INTRODUCTORY NUCLEAR PHYSICS

Kenneth S. Krane

Oregon State University

JOHN WILEY & SONS

New York • Chichester • Brisbane • Toronto • Singapore



Copyright © 1988, by John Wiley & Sons, Inc.

All rights reserved. Published simultaneously in Canada.

Reproduction or translation of any part of
this work beyond that permitted by Sections
107 and 108 of the 1976 United States Copyright
Act without the permission of the copyright
owner is unlawful. Requests for permission
or further information should be addressed to
the Permissions Department, John Wiley & Sons.

Library of Congress Cataloging in Publication Data:

Krane, Kenneth S.
Introductory nuclear physics.

Rev. ed. of Introductory nuclear physics/David Halliday. 2nd. ed. 1955.
1. Nuclear physics. I. Halliday, David, 1916 –
Introductory nuclear physics. II. Title.
QC777.K73 1987 539.7 87-10623
ISBN 0-471-80553-X

Printed in the United States of America

10 9 8 7 6 5 4 3 2

PREFACE

This work began as a collaborative attempt with David Halliday to revise and update the second edition of his classic text *Introductory Nuclear Physics* (New York: Wiley, 1955). As the project evolved, it became clear that, owing to other commitments, Professor Halliday would be able to devote only limited time to the project and he therefore volunteered to remove himself from active participation, a proposal to which I reluctantly and regretfully agreed. He was kind enough to sign over to me the rights to use the material from the previous edition.

I first encountered Halliday's text as an undergraduate physics major, and it was perhaps my first real introduction to nuclear physics. I recall being impressed by its clarity and its readability, and in preparing this new version, I have tried to preserve these elements, which are among the strengths of the previous work.

Audience This text is written primarily for an undergraduate audience, but could be used in introductory graduate surveys of nuclear physics as well. It can be used specifically for physics majors as part of a survey of modern physics, but could (with an appropriate selection of material) serve as an introductory course for other areas of nuclear science and technology, including nuclear chemistry, nuclear engineering, radiation biology, and nuclear medicine.

Background It is expected that students have a previous background in quantum physics, either at the introductory level [such as the author's text *Modern Physics* (New York: Wiley, 1983)] or at a more advanced, but still undergraduate level. (A brief summary of the needed quantum background is given in Chapter 2.) The text is therefore designed in a "two-track" mode, so that the material that requires the advanced work in quantum mechanics, for instance, transition probabilities or matrix elements, can be separated from the rest of the text by skipping those sections that require such a background. This can be done without interrupting the logical flow of the discussion.

Mathematical background at the level of differential equations should be sufficient for most applications.

Emphasis There are two features that distinguish the present book. The first is the emphasis on breadth. The presentation of a broad selection of material permits the instructor to tailor a curriculum to meet the needs of any particular

student audience. The complete text is somewhat short for a full-year course, but too long for a course of quarter or semester length. The instructor is therefore able to select material that will provide students with the broadest possible introduction to the field of nuclear physics, consistent with the time available for the course.

The second feature is the unabashedly experimental and phenomenological emphasis and orientation of the presentation. The discussions of decay and reaction phenomena are accompanied with examples of experimental studies from the literature. These examples have been carefully selected following searches for papers that present data in the clearest possible manner and that relate most directly to the matter under discussion. These original experiments are discussed, often with accompanying diagrams of apparatus, and results *with uncertainties* are given, all in the attempt to convince students that progress in nuclear physics sprang not exclusively from the forehead of Fermi, but instead has been painstakingly won in the laboratory. At the same time, the rationale and motivation for the experiments are discussed, and their contributions to the theory are emphasized.

Organization The book is divided into four units: Basic Nuclear Structure, Nuclear Decay and Radioactivity, Nuclear Reactions, and Extensions and Applications. The first unit presents background material on nuclear sizes and shapes, discusses the two-nucleon problem, and presents an introduction to nuclear models. These latter two topics can be skipped without loss of continuity in an abbreviated course. The second unit on decay and radioactivity presents the traditional topics, with new material included to bring nuclear decay nearly into the current era (the recently discovered "heavy" decay modes, such as ^{14}C, double β decay, β-delayed nucleon emission, Mössbauer effect, and so on). The third unit surveys nuclear reactions, including fission and fusion and their applications. The final unit deals with topics that fall only loosely under the nuclear physics classification, including hyperfine interactions, particle physics, nuclear astrophysics, and general applications including nuclear medicine. The emphasis here is on the overlap with other physics and nonphysics specialties, including atomic physics, high-energy physics, cosmology, chemistry, and medicine. Much of this material, particularly in Chapters 18 and 19, represents accomplishments of the last couple of years and therefore, as in all such volatile areas, may be outdated before the book is published. Even if this should occur, however, the instructor is presented with a golden opportunity to make important points about progress in science. Chapter 20 features applications involving similarly recent developments, such as PET scans. The material in this last unit builds to a considerable degree on the previous material; it would be very unwise, for example, to attempt the material on meson physics or particle physics without a firm grounding in nuclear reactions.

Sequence Chapters or sections that can be omitted without loss of continuity in an abbreviated reading are indicated with asterisks (*) in the table of contents. An introductory short course in nuclear physics could be based on Chapters 1, 2, 3, 6, 8, 9, 10, and 11, which cover the fundamental aspects of nuclear decay and reactions, but little of nuclear structure. Fission and fusion can be added from

Chapters 13 and 14. Detectors and accelerators can be included with material selected from Chapters 7 and 15.

The last unit (Chapters 16 to 20) deals with applications and does not necessarily follow Chapter 15 in sequence. In fact, most of this material could be incorporated at any time after Chapter 11 (Nuclear Reactions). Chapter 16, covering spins and moments, could even be moved into the first unit after Chapter 3. Chapter 19 (Nuclear Astrophysics) requires background material on fission and fusion from Chapters 13 and 14.

Most of the text can be understood with only a minimal background in quantum mechanics. Chapters or sections that require a greater background (but still at the undergraduate level) are indicated in the table of contents with a dagger (†).

Many undergraduates, in my experience, struggle with even the most basic aspects of the quantum theory of angular momentum, and more abstract concepts, such as isospin, can present them with serious difficulties. For this reason, the introduction of isospin is delayed until it is absolutely necessary in Chapter 11 (Nuclear Reactions) where references to its application to beta and gamma decays are given to show its importance to those cases as well. No attempt is made to use isospin coupling theory to calculate amplitudes or cross sections. In an abbreviated coverage, it is therefore possible to omit completely any discussion of isospin, but it absolutely must be included before attempting Chapters 17 and 18 on meson and particle physics.

Notation Standard notation has been adopted, which unfortunately overworks the symbol T to represent kinetic energy, temperature, and isospin. The particle physicist's choice of I for isospin and J for nuclear spin leaves no obvious alternative for the total electronic angular momentum. Therefore, I has been reserved for the total nuclear angular momentum, J for the total electronic angular momentum, and T for the isospin. To be consistent, the same scheme is extended into the particle physics regime in Chapters 17 and 18, even though it may be contrary to the generally accepted notation in particle physics. The lowercase j refers to the total angular momentum of a single nucleon or atomic electron.

References No attempt has been made to produce an historically accurate set of references to original work. This omission is done partly out of my insecurity about assuming the role of historian of science and partly out of the conviction that references tend to clutter, rather than illuminate, textbooks that are aimed largely at undergraduates. Historical discussions have been kept to a minimum, although major insights are identified with their sources. The history of nuclear physics, which so closely accompanies the revolutions wrought in twentieth-century physics by relativity and quantum theory, is a fascinating study in itself, and I encourage serious students to pursue it. In stark contrast to modern works, the classic papers are surprisingly readable. Many references to these early papers can be found in Halliday's book or in the collection by Robert T. Beyer, *Foundations of Nuclear Physics* (New York: Dover, 1949), which contains reprints of 13 pivotal papers and a classified bibliography of essentially every nuclear physics publication up to 1947.

Each chapter in this textbook is followed with a list of references for further reading, where more detailed or extensive treatments can be found. Included in the lists are review papers as well as popular-level books and articles.

Several of the end-of-chapter problems require use of systematic tabulations of nuclear properties, for which the student should have ready access to the current edition of the *Table of Isotopes* or to a complete collection of the *Nuclear Data Sheets*.

Acknowledgments Many individuals read chapters or sections of the manuscript. I am grateful for the assistance of the following professional colleagues and friends: David Arnett, Carroll Bingham, Merle Bunker, H. K. Carter, Charles W. Drake, W. A. Fowler, Roger J. Hanson, Andrew Klein, Elliot J. Krane, Rubin H. Landau, Victor A. Madsen, Harvey Marshak, David K. McDaniels, Frank A. Rickey, Kandula S. R. Sastry, Larry Schecter, E. Brooks Shera, Richard R. Silbar, Paul Simms, Rolf M. Steffen, Gary Steigman, Morton M. Sternheim, Albert W. Stetz, and Ken Toth. They made many wise and valuable suggestions, and I thank them for their efforts. Many of the problems were checked by Milton Sagen and Paula Sonawala. Hundreds of original illustrations were requested of and generously supplied by nuclear scientists from throughout the world. Kathy Haag typed the original manuscript with truly astounding speed and accuracy and in the process helped to keep its preparation on schedule. The staff at John Wiley & Sons were exceedingly helpful and supportive, including physics editor Robert McConnin, copy editors Virginia Dunn and Deborah Herbert, and production supervisor Charlene Cassimire. Finally, without the kind support and encouragement of David Halliday, this work would not have been possible.

Corvallis, Oregon
February 1987

Kenneth S. Krane

CONTENTS

UNIT I BASIC NUCLEAR STRUCTURE

Chapter 1 BASIC CONCEPTS 2

1.1 History and Overview 3
1.2 Some Introductory Terminology 4
1.3 Nuclear Properties 5
1.4 Units and Dimensions 7

Chapter 2 ELEMENTS OF QUANTUM MECHANICS 9

2.1 Quantum Behavior 9
2.2 Principles of Quantum Mechanics 12
2.3 Problems in One Dimension 15
2.4 Problems in Three Dimensions 25
2.5 Quantum Theory of Angular Momentum 34
2.6 Parity 37
2.7 Quantum Statistics 39
2.8 Transitions Between States 40

Chapter 3 NUCLEAR PROPERTIES 44

3.1 The Nuclear Radius 44
3.2 Mass and Abundance of Nuclides 59
3.3 Nuclear Binding Energy 65
3.4 Nuclear Angular Momentum and Parity 70
3.5 Nuclear Electromagnetic Moments 71
3.6 Nuclear Excited States 75

***Chapter 4** THE FORCE BETWEEN NUCLEONS 80

4.1 The Deuteron 80
†4.2 Nucleon-Nucleon Scattering 86
4.3 Proton-Proton and Neutron-Neutron Interactions 96
4.4 Properties of the Nuclear Force 100
4.5 The Exchange Force Model 108

*Denotes material that can be omitted without loss of continuity in an abbreviated reading.
†Denotes material that requires somewhat greater familiarity with quantum mechanics.

*Chapter 5 NUCLEAR MODELS 116

5.1 The Shell Model 117
5.2 Even-*Z*, Even-*N* Nuclei and Collective Structure 134
5.3 More Realistic Nuclear Models 149

UNIT II NUCLEAR DECAY AND RADIOACTIVITY

Chapter 6 RADIOACTIVE DECAY 160

6.1 The Radioactive Decay Law 161
†6.2 Quantum Theory of Radiative Decays 165
6.3 Production and Decay of Radioactivity 169
6.4 Growth of Daughter Activities 170
6.5 Types of Decays 173
6.6 Natural Radioactivity 178
*6.7 Radioactive Dating 181
*6.8 Units for Measuring Radiation 184

*Chapter 7 DETECTING NUCLEAR RADIATIONS 192

7.1 Interactions of Radiation with Matter 193
7.2 Gas-Filled Counters 204
7.3 Scintillation Detectors 207
7.4 Semiconductor Detectors 213
7.5 Counting Statistics 217
7.6 Energy Measurements 220
7.7 Coincidence Measurements and Time Resolution 227
7.8 Measurement of Nuclear Lifetimes 230
7.9 Other Detector Types 236

Chapter 8 ALPHA DECAY 246

8.1 Why Alpha Decay Occurs 246
8.2 Basic Alpha Decay Processes 247
8.3 Alpha Decay Systematics 249
†8.4 Theory of Alpha Emission 251
8.5 Angular Momentum and Parity in Alpha Decay 257
*8.6 Alpha Decay Spectroscopy 261

Chapter 9 BETA DECAY 272

9.1 Energy Release in Beta Decay 273
†9.2 Fermi Theory of Beta Decay 277
9.3 The "Classical" Experimental Tests of the Fermi Theory 282
9.4 Angular Momentum and Parity Selection Rules 289
9.5 Comparative Half-Lives and Forbidden Decays 292

*9.6 Neutrino Physics 295
*9.7 Double Beta Decay 298
*9.8 Beta-Delayed Nucleon Emission 302
*9.9 Nonconservation of Parity 309
*9.10 Beta Spectroscopy 315

Chapter 10 GAMMA DECAY 327

10.1 Energetics of Gamma Decay 327
10.2 Classical Electromagnetic Radiation 328
†10.3 Transition to Quantum Mechanics 331
10.4 Angular Momentum and Parity Selection Rules 333
10.5 Angular Distribution and Polarization Measurements 335
10.6 Internal Conversion 341
10.7 Lifetimes for Gamma Emission 348
*10.8 Gamma-Ray Spectroscopy 351
*10.9 Nuclear Resonance Fluorescence and the Mössbauer Effect 361

UNIT III NUCLEAR REACTIONS

Chapter 11 NUCLEAR REACTIONS 378

11.1 Types of Reactions and Conservation Laws 378
11.2 Energetics of Nuclear Reactions 380
11.3 Isospin 388
11.4 Reaction Cross Sections 392
11.5 Experimental Techniques 395
11.6 Coulomb Scattering 396
11.7 Nuclear Scattering 405
†11.8 Scattering and Reaction Cross Sections 408
*11.9 The Optical Model 413
11.10 Compound-Nucleus Reactions 416
11.11 Direct Reactions 419
*11.12 Resonance Reactions 424
*11.13 Heavy-Ion Reactions 431

***Chapter 12** NEUTRON PHYSICS 444

12.1 Neutron Sources 445
12.2 Absorption and Moderation of Neutrons 447
12.3 Neutron Detectors 451
12.4 Neutron Reactions and Cross Sections 456
12.5 Neutron Capture 462
12.6 Interference and Diffraction with Neutrons 465

Chapter 13 NUCLEAR FISSION 478

13.1 Why Nuclei Fission 479
13.2 Characteristics of Fission 484

13.3 Energy in Fission 488
*13.4 Fission and Nuclear Structure 493
13.5 Controlled Fission Reactions 501
13.6 Fission Reactors 506
*13.7 Radioactive Fission Products 512
*13.8 A Natural Fission Reactor 516
13.9 Fission Explosives 520

Chapter 14 NUCLEAR FUSION 528

14.1 Basic Fusion Processes 529
14.2 Characteristics of Fusion 530
*14.3 Solar Fusion 534
14.4 Controlled Fusion Reactors 538
14.5 Thermonuclear Weapons 553

***Chapter 15** ACCELERATORS 559

15.1 Electrostatic Accelerators 563
15.2 Cyclotron Accelerators 571
15.3 Synchrotrons 581
15.4 Linear Accelerators 588
15.5 Colliding-Beam Accelerators 593

UNIT IV EXTENSIONS AND APPLICATIONS

***Chapter 16** NUCLEAR SPIN AND MOMENTS 602

16.1 Nuclear Spin 602
16.2 Nuclear Moments 605
16.3 Hyperfine Structure 610
16.4 Measuring Nuclear Moments 619

***Chapter 17** MESON PHYSICS 653

17.1 Yukawa's Hypothesis 653
17.2 Properties of Pi Mesons 656
17.3 Pion-Nucleon Reactions 671
17.4 Meson Resonances 679
17.5 Strange Mesons and Baryons 686
17.6 CP Violation in K Decay 692

***Chapter 18** PARTICLE PHYSICS 701

18.1 Particle Interactions and Families 701
18.2 Symmetries and Conservation Laws 710
18.3 The Quark Model 718
18.4 Colored Quarks and Gluons 721
18.5 Reactions and Decays in the Quark Model 725
18.6 Charm, Beauty, and Truth 733
18.7 Quark Dynamics 742
18.8 Grand Unified Theories 746

***Chapter 19** NUCLEAR ASTROPHYSICS 755

19.1 The Hot Big Bang Cosmology 756
19.2 Particle and Nuclear Interactions in the Early Universe 760
19.3 Primordial Nucleosynthesis 764
19.4 Stellar Nucleosynthesis ($A \lesssim 60$) 769
19.5 Stellar Nucleosynthesis ($A > 60$) 776
19.6 Nuclear Cosmochronology 780

***Chapter 20** APPLICATIONS OF NUCLEAR PHYSICS 788

20.1 Trace Element Analysis 788
20.2 Mass Spectrometry with Accelerators 794
20.3 Alpha-Decay Applications 796
20.4 Diagnostic Nuclear Medicine 800
20.5 Therapeutic Nuclear Medicine 808

Appendix A SPECIAL RELATIVITY 815

Appendix B CENTER-OF-MASS REFERENCE FRAME 818

Appendix C TABLE OF NUCLEAR PROPERTIES 822

Credits 834

Index 835

UNIT I
BASIC NUCLEAR STRUCTURE

1

BASIC CONCEPTS

Whether we date the origin of nuclear physics from Becquerel's discovery of radioactivity in 1896 or Rutherford's hypothesis of the existence of the nucleus in 1911, it is clear that experimental and theoretical studies in nuclear physics have played a prominent role in the development of twentieth century physics. As a result of these studies, a chronology of which is given on the inside of the front cover of this book, we have today a reasonably good understanding of the properties of nuclei and of the structure that is responsible for those properties. Furthermore, techniques of nuclear physics have important applications in other areas, including atomic and solid-state physics. Laboratory experiments in nuclear physics have been applied to the understanding of an incredible variety of problems, from the interactions of quarks (the most fundamental particles of which matter is composed), to the processes that occurred during the early evolution of the universe just after the Big Bang. Today physicians use techniques learned from nuclear physics experiments to perform diagnosis and therapy in areas deep inside the body without recourse to surgery; but other techniques learned from nuclear physics experiments are used to build fearsome weapons of mass destruction, whose proliferation is a constant threat to our future. No other field of science comes readily to mind in which theory encompasses so broad a spectrum, from the most microscopic to the cosmic, nor is there another field in which direct applications of basic research contain the potential for the ultimate limits of good and evil.

Nuclear physics lacks a coherent theoretical formulation that would permit us to analyze and interpret all phenomena in a fundamental way; atomic physics has such a formulation in quantum electrodynamics, which permits calculations of some observable quantities to more than six significant figures. As a result, we must discuss nuclear physics in a phenomenological way, using a different formulation to describe each different type of phenomenon, such as α decay, β decay, direct reactions, or fission. Within each type, our ability to interpret experimental results and predict new results is relatively complete, yet the methods and formulation that apply to one phenomenon often are not applicable to another. In place of a single unifying theory there are islands of coherent knowledge in a sea of seemingly uncorrelated observations. Some of the most fundamental problems of nuclear physics, such as the exact nature of the forces

that hold the nucleus together, are yet unsolved. In recent years, much progress has been made toward understanding the basic force between the quarks that are the ultimate constituents of matter, and indeed attempts have been made at applying this knowledge to nuclei, but these efforts have thus far not contributed to the clarification of nuclear properties.

We therefore adopt in this text the phenomenological approach, discussing each type of measurement, the theoretical formulation used in its analysis, and the insight into nuclear structure gained from its interpretation. We begin with a summary of the basic aspects of nuclear theory, and then turn to the experiments that contribute to our knowledge of structure, first radioactive decay and then nuclear reactions. Finally, we discuss special topics that contribute to microscopic nuclear structure, the relationship of nuclear physics to other disciplines, and applications to other areas of research and technology.

1.1 HISTORY AND OVERVIEW

The search for the fundamental nature of matter had its beginnings in the speculations of the early Greek philosophers; in particular, Democritus in the fourth century B.C. believed that each kind of material could be subdivided into smaller and smaller bits until one reached the very limit beyond which no further division was possible. This *atom* of material, invisible to the naked eye, was to Democritus the basic constituent particle of matter. For the next 2400 years, this idea remained only a speculation, until investigators in the early nineteenth century applied the methods of *experimental science* to this problem and from their studies obtained the evidence needed to raise the idea of atomism to the level of a full-fledged scientific theory. Today, with our tendency toward the specialization and compartmentalization of science, we would probably classify these early scientists (Dalton, Avogadro, Faraday) as chemists. Once the chemists had elucidated the kinds of atoms, the rules governing their combinations in matter, and their systematic classification (Mendeleev's periodic table), it was only natural that the next step would be a study of the fundamental properties of individual atoms of the various elements, an activity that we would today classify as atomic physics. These studies led to the discovery in 1896 by Becquerel of the radioactivity of certain species of atoms and to the further identification of radioactive substances by the Curies in 1898. Rutherford next took up the study of these radiations and their properties; once he had achieved an understanding of the nature of the radiations, he turned them around and used them as probes of the atoms themselves. In the process he proposed in 1911 the existence of the atomic nucleus, the confirmation of which (through the painstaking experiments of Geiger and Marsden) provided a new branch of science, nuclear physics, dedicated to studying matter at its most fundamental level. Investigations into the properties of the nucleus have continued from Rutherford's time to the present. In the 1940s and 1950s, it was discovered that there was yet another level of structure even more elementary and fundamental than the nucleus. Studies of the particles that contribute to the structure at this level are today carried out in the realm of elementary particle (or high energy) physics.

Thus nuclear physics can be regarded as the descendent of chemistry and atomic physics and in turn the progenitor of particle physics. Although nuclear

physics no longer occupies center stage in the search for the ultimate components of matter, experiments with nuclei continue to contribute to the understanding of basic interactions. Investigation of nuclear properties and the laws governing the structure of nuclei is an active and productive area of physical research in its own right, and practical applications, such as smoke detectors, cardiac pacemakers, and medical imaging devices, have become common. Thus nuclear physics has in reality three aspects: probing the fundamental particles and their interactions, classifying and interpreting the properties of nuclei, and providing technological advances that benefit society.

1.2 SOME INTRODUCTORY TERMINOLOGY

A nuclear species is characterized by the total amount of positive charge in the nucleus and by its total number of mass units. The net nuclear charge is equal to $+Ze$, where Z is the *atomic number* and e is the magnitude of the electronic charge. The fundamental positively charged particle in the nucleus is the *proton*, which is the nucleus of the simplest atom, hydrogen. A nucleus of atomic number Z therefore contains Z protons, and an electrically neutral atom therefore must contain Z negatively charged electrons. Since the mass of the electrons is negligible compared with the proton mass ($m_p \simeq 2000 m_e$), the electron can often be ignored in discussions of the mass of an atom. The *mass number* of a nuclear species, indicated by the symbol A, is the integer nearest to the ratio between the nuclear mass and the fundamental mass unit, defined so that the proton has a mass of nearly one unit. (We will discuss mass units in more detail in Chapter 3.) For nearly all nuclei, A is greater than Z, in most cases by a factor of two or more. Thus there must be other massive components in the nucleus. Before 1932, it was believed that the nucleus contained A protons, in order to provide the proper mass, along with $A - Z$ *nuclear* electrons to give a net positive charge of Ze. However, the presence of electrons within the nucleus is unsatisfactory for several reasons:

1. The nuclear electrons would need to be bound to the protons by a very strong force, stronger even than the Coulomb force. Yet no evidence for this strong force exists between protons and *atomic* electrons.
2. If we were to confine electrons in a region of space as small as a nucleus ($\Delta x \sim 10^{-14}$ m), the uncertainty principle would require that these electrons have a momentum distribution with a range $\Delta p \sim \hbar/\Delta x = 20$ MeV/c. Electrons that are emitted from the nucleus in radioactive β decay have energies generally less than 1 MeV; never do we see decay electrons with 20 MeV energies. Thus the existence of 20 MeV electrons in the nucleus is not confirmed by observation.
3. The total intrinsic angular momentum (spin) of nuclei for which $A - Z$ is odd would disagree with observed values if A protons and $A - Z$ electrons were present in the nucleus. Consider the nucleus of deuterium ($A = 2$, $Z = 1$), which according to the proton-electron hypothesis would contain 2 protons and 1 electron. The proton and electron each have intrinsic angular momentum (spin) of $\frac{1}{2}$, and the quantum mechanical rules for adding spins of particles would require that these three spins of $\frac{1}{2}$ combine to a total of either $\frac{3}{2}$ or $\frac{1}{2}$. Yet the observed spin of the deuterium nucleus is 1.

4. Nuclei containing unpaired electrons would be expected to have magnetic dipole moments far greater than those observed. If a single electron were present in a deuterium nucleus, for example, we would expect the nucleus to have a magnetic dipole moment about the same size as that of an electron, but the observed magnetic moment of the deuterium nucleus is about $\frac{1}{2000}$ of the electron's magnetic moment.

Of course it is possible to invent all sorts of ad hoc reasons for the above arguments to be wrong, but the necessity for doing so was eliminated in 1932 when the *neutron* was discovered by Chadwick. The neutron is electrically neutral and has a mass about equal to the proton mass (actually about 0.1% larger). Thus a nucleus with Z protons and $A - Z$ neutrons has the proper total mass *and* charge, without the need to introduce nuclear electrons. When we wish to indicate a specific nuclear species, or *nuclide*, we generally use the form ${}^{A}_{Z}\mathrm{X}_{N}$, where X is the chemical symbol and N is the *neutron number*, $A - Z$. The symbols for some nuclides are ${}^{1}_{1}\mathrm{H}_{0}$, ${}^{238}_{92}\mathrm{U}_{146}$, ${}^{56}_{26}\mathrm{Fe}_{30}$. The chemical symbol and the atomic number Z are redundant—every H nucleus has $Z = 1$, every U nucleus has $Z = 92$, and so on. It is therefore not necessary to write Z. It is also not necessary to write N, since we can always find it from $A - Z$. Thus $^{238}\mathrm{U}$ is a perfectly valid way to indicate that particular nuclide; a glance at the periodic table tells us that U has $Z = 92$, and therefore $^{238}\mathrm{U}$ has $238 - 92 = 146$ neutrons. You may find the symbols for nuclides written sometimes with Z and N, and sometimes without them. When we are trying to balance Z and N in a decay or reaction process, it is convenient to have them written down; at other times it is cumbersome and unnecessary to write them.

Neutrons and protons are the two members of the family of *nucleons*. When we wish simply to discuss nuclear particles without reference to whether they are protons or neutrons, we use the term nucleons. Thus a nucleus of mass number A contains A nucleons.

When we analyze samples of many naturally occurring elements, we find that nuclides with a given atomic number can have several different mass numbers; that is, a nuclide with Z protons can have a variety of different neutron numbers. Nuclides with the same proton number but different neutron numbers are called *isotopes*; for example, the element chlorine has two isotopes that are stable against radioactive decay, $^{35}\mathrm{Cl}$ and $^{37}\mathrm{Cl}$. It also has many other unstable isotopes that are artificially produced in nuclear reactions; these are the radioactive isotopes (or *radioisotopes*) of Cl.

It is often convenient to refer to a sequence of nuclides with the same N but different Z; these are called *isotones*. The stable isotones with $N = 1$ are $^{2}\mathrm{H}$ and $^{3}\mathrm{He}$. Nuclides with the same mass number A are known as *isobars*; thus stable $^{3}\mathrm{He}$ and radioactive $^{3}\mathrm{H}$ are isobars.

1.3 NUCLEAR PROPERTIES

Once we have identified a nuclide, we can then set about to measure its properties, among which (to be discussed later in this text) are mass, radius, relative abundance (for stable nuclides), decay modes and half-lives (for radioactive nuclides), reaction modes and cross sections, spin, magnetic dipole and electric quadrupole moments, and excited states. Thus far we have identified

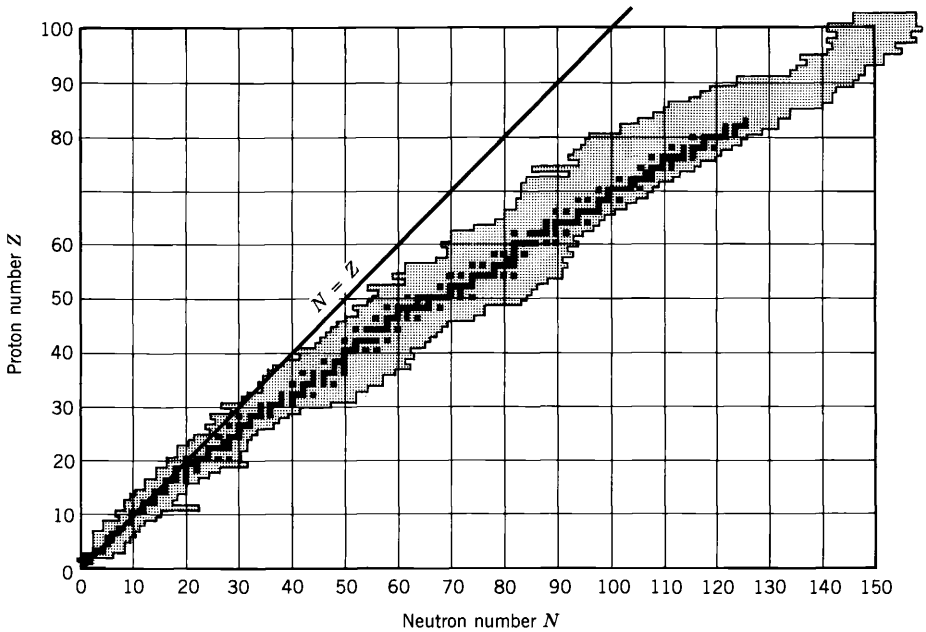


Figure 1.1 Stable nuclei are shown in dark shading and known radioactive nuclei are in light shading.

nuclides with 108 different atomic numbers (0 to 107); counting all the different isotopes, the total number of nuclides is well over 1000, and the number of carefully studied new nuclides is growing rapidly owing to new accelerators dedicated to studying the isotopes far from their stable isobars. Figure 1.1 shows a representation of the stable and known radioactive nuclides.

As one might expect, cataloging all of the measured properties of these many nuclides is a formidable task. An equally formidable task is the retrieval of that information: if we require the best current experimental value of the decay modes of an isotope or the spin and magnetic moment of another, where do we look?

Nuclear physicists generally publish the results of their investigations in journals that are read by other nuclear physicists; in this way, researchers from distant laboratories are aware of one another's activities and can exchange ideas. Some of the more common journals in which to find such communications are *Physical Review*, Section C (abbreviated *Phys. Rev. C*), *Physical Review Letters* (*Phys. Rev. Lett.*), *Physics Letters*, Section B (*Phys. Lett. B*), *Nuclear Physics*, Section A (*Nucl. Phys. A*), *Zeitschrift für Physik*, Section A (*Z. Phys. A*), and *Journal of Physics*, Section G (*J. Phys. G*). These journals are generally published monthly, and by reading them (or by scanning the table of contents), we can find out about the results of different researchers. Many college and university libraries subscribe to these journals, and the study of nuclear physics is often aided by browsing through a selection of current research papers.

Unfortunately, browsing through current journals usually does not help us to locate the specific nuclear physics information we are seeking, unless we happen to stumble across an article on that topic. For this reason, there are many sources of compiled nuclear physics information that summarize nuclear properties and

give references to the literature where the original publication may be consulted. A one-volume summary of the properties of all known nuclides is the *Table of Isotopes*, edited by M. Lederer and V. Shirley (New York: Wiley, 1978). A copy of this indispensible work is owned by every nuclear physicist. A more current updating of nuclear data can be found in the *Nuclear Data Sheets*, which not only publish regular updated collections of information for each set of isobars, but also give an annual summary of all published papers in nuclear physics, classified by nuclide. This information is published in journal form and is also carried by many libraries. It is therefore a relatively easy process to check the recently published work concerning a certain nuclide.

Two other review works are the *Atomic Data and Nuclear Data Tables*, which regularly produces compilations of nuclear properties (for example, β or γ transition rates or fission energies), and the *Annual Review of Nuclear and Particle Science* (formerly called the *Annual Review of Nuclear Science*), which each year publishes a collection of review papers on current topics in nuclear and particle physics.

1.4 UNITS AND DIMENSIONS

In nuclear physics we encounter lengths of the order of 10^{-15} m, which is one femtometer (fm). This unit is colloquially known as one fermi, in honor of the pioneer Italian-American nuclear physicist, Enrico Fermi. Nuclear sizes range from about 1 fm for a single nucleon to about 7 fm for the heaviest nuclei.

The time scale of nuclear phenomena has an enormous range. Some nuclei, such as ^{5}He or ^{8}Be, break apart in times of the order of 10^{-20} s. Many nuclear reactions take place on this time scale, which is roughly the length of time that the reacting nuclei are within range of each other's nuclear force. Electromagnetic (γ) decays of nuclei occur generally within lifetimes of the order of 10^{-9} s (nanosecond, ns) to 10^{-12} s (picosecond, ps), but many decays occur with much shorter or longer lifetimes. α and β decays occur with even longer lifetimes, often minutes or hours, but sometimes thousands or even millions of years.

Nuclear energies are conveniently measured in millions of electron-volts (MeV), where 1 eV = 1.602×10^{-19} J is the energy gained by a single unit of electronic charge when accelerated through a potential difference of one volt. Typical β and γ decay energies are in the range of 1 MeV, and low-energy nuclear reactions take place with kinetic energies of order 10 MeV. Such energies are far smaller than the nuclear rest energies, and so we are justified in using nonrelativistic formulas for energy and momentum of the nucleons, but β-decay electrons must be treated relativistically.

Nuclear masses are measured in terms of the *unified atomic mass unit*, u, defined such that the mass of an *atom* of ^{12}C is exactly 12 u. Thus the nucleons have masses of approximately 1 u. In analyzing nuclear decays and reactions, we generally work with mass energies rather than with the masses themselves. The conversion factor is 1 u = 931.502 MeV, so the nucleons have mass energies of approximately 1000 MeV. The conversion of mass to energy is of course done using the fundamental result from special relativity, $E = mc^2$; thus we are free to work either with masses or energies at our convenience, and in these units $c^2 = 931.502$ MeV/u.

REFERENCES FOR ADDITIONAL READING

The following comprehensive nuclear physics texts provide explanations or formulations alternative to those of this book. Those at the introductory level are at about the same level as the present text; higher-level texts often form the basis for more advanced graduate courses in nuclear physics. No attempt has been made to produce a complete list of reference works; rather, these are the ones the author has found most useful in preparing this book.

These "classic" texts now mostly outdated but still containing much useful material are interesting for gaining historical perspective: R. D. Evans, *The Atomic Nucleus* (New York: McGraw-Hill, 1955) (For 20 years, since his graduate-student days, the most frequently used book on the author's shelves. Its binding has all but deteriorated, but its completeness and clarity remain.); David Halliday, *Introductory Nuclear Physics* (New York: Wiley, 1955); I. Kaplan, *Nuclear Physics* (Reading, MA: Addison-Wesley, 1955).

Introductory texts complementary to this text are: W. E. Burcham, *Nuclear Physics: An Introduction* (London: Longman, 1973); B. L. Cohen, *Concepts of Nuclear Physics* (New York: McGraw-Hill, 1971); Harald A. Enge, *Introduction to Nuclear Physics* (Reading, MA: Addison-Wesley, 1966); Robert A. Howard, *Nuclear Physics* (Belmont, CA: Wadsworth, 1963); Walter E. Meyerhof, *Elements of Nuclear Physics* (New York: McGraw-Hill, 1967); Haro Von Buttlar, *Nuclear Physics: An Introduction* (New York: Academic Press, 1968).

Intermediate texts, covering much the same material as the present one but distinguished primarily by a more rigorous use of quantum mechanics, are: M. G. Bowler, *Nuclear Physics* (Oxford: Pergamon, 1973); Emilio Segré, *Nuclei and Particles* (Reading, MA: W. A. Benjamin, 1977).

Advanced texts, primarily for graduate courses, but still containing much material of a more basic nature, are: Hans Frauenfelder and Ernest M. Henley, *Subatomic Physics* (Englewood Cliffs, NJ: Prentice-Hall, 1974); M. A. Preston, *Physics of the Nucleus* (Reading, MA: Addison-Wesley, 1962).

Advanced works, more monographs than texts in nature, are: John M. Blatt and Victor F. Weisskopf, *Theoretical Nuclear Physics* (New York: Wiley, 1952); A. Bohr and B. R. Mottelson, *Nuclear Structure* (New York: W. A. Benjamin, 1969); A. deShalit and H. Feshbach, *Theoretical Nuclear Physics* (New York: Wiley, 1974).

2

ELEMENTS OF QUANTUM MECHANICS

Nucleons in a nucleus do not behave like classical particles, colliding like billiard balls. Instead, the *wave behavior* of the nucleons determines the properties of the nucleus, and to analyze this behavior requires that we use the mathematical techniques of quantum mechanics.

From a variety of scattering experiments, we know that the nucleons in a nucleus are in motion with kinetic energies of the order of 10 MeV. This energy is small compared with the nucleon rest energy (about 1000 MeV), and so we can with confidence use *nonrelativistic* quantum mechanics.

To give a complete introduction to quantum mechanics would require a text larger than the present one. In this chapter, we summarize some of the important concepts that we will need later in this book. We assume a previous introduction to the concepts of modern physics and a familiarity with some of the early experiments that could not be understood using classical physics; these experiments include thermal (blackbody) radiation, Compton scattering, and the photoelectric effect. At the end of this chapter is a list of several introductory modern physics texts for review. Included in the list are more advanced quantum physics texts, which contain more complete and rigorous discussions of the topics summarized in this chapter.

2.1 QUANTUM BEHAVIOR

Quantum mechanics is a mathematical formulation that enables us to calculate the wave behavior of material particles. It is not at all *a priori* evident that such behavior should occur, but the suggestion follows by analogy with the quantum behavior of light. Before 1900, light was generally believed to be a wave phenomenon, but the work of Planck in 1900 (analyzing blackbody radiation) and Einstein in 1905 (analyzing the photoelectric effect) showed that it was also necessary to consider light as if its energy were delivered not smoothly and continuously as a wave but instead in concentrated bundles or "quanta," in effect "particles of light."

The analogy between matter and light was made in 1924 by de Broglie, drawing on the previous work of Einstein and Compton. If light, which we

generally regard as a wave phenomenon, also has particle aspects, then (so de Broglie argued) might not matter, which we generally regard as composed of particles, also have a wave aspect? Again proceeding by analogy with light, de Broglie postulated that associated with a "particle" moving with momentum p is a "wave" of wavelength $\lambda = h/p$ where h is Planck's constant. The wavelength defined in this way is generally called the de Broglie wavelength. Experimental confirmation of de Broglie's hypothesis soon followed in 1927 through the experiments of Thomson and of Davisson and Germer. They showed that electrons (particles) were diffracted like waves with the de Broglie wavelength.

The de Broglie theory was successful in these instances, but it is incomplete and unsatisfying for several reasons. For one, we seldom see particles with a unique momentum p; if the momentum of a particle changes, such as when it is acted upon by an external force, its wavelength must change, but the de Broglie relationship lacks the capability to enable computation of the dynamical behavior of the waves. For this we need a more complete mathematical theory, which was supplied by Schrödinger in 1925 and which we review in Section 2 of this chapter. A second objection to the de Broglie theory is its reliance on classical concepts and terminology. "Particle" and "wave" are mutually exclusive sorts of behaviors, but the de Broglie relationship involves classical particles with uniquely defined momenta and classical waves with uniquely defined wavelengths. A classical particle has a definite position in space. Now, according to de Broglie, that localized particle is to be represented by a pure wave that extends throughout all space and has no beginning, end, or easily identifiable "position."

The solution to this dilemma requires us to discard the classical idea of "particle" when we enter the domain of quantum physics. The size of a classical particle is the same in every experiment we may do; the "size" of a quantum particle varies with the experiment we perform. Quantum physics forces us to sacrifice the objective reality of a concept such as "size" and instead to substitute an operational definition that depends on the experiment that is being done. Thus an electron may have a certain size in one experiment and a very different size in another. Only through this coupling of the observing system and the observed object can we define observations in quantum physics. A particle, then, is *localized* within some region of space of dimension Δx. It is likely to be found in that region and unlikely to be found elsewhere. The dimension Δx of an electron is determined by the kind of experiment we do—it may be the dimension of a block of material if we are studying electrical conduction in solids, or the dimension of a single atom if we are studying atomic physics, or of a nucleus if we are studying β decay. The wave that characterizes the particle has large amplitude in the region Δx and small amplitude elsewhere. The single de Broglie wave corresponding to the unique momentum component p_x had a large amplitude everywhere; thus a definite momentum (wavelength) corresponds to a completely unlocalized particle. To localize the particle, we must add (superpose) other wavelengths corresponding to other momenta p_x, so that we make the resultant wave small outside the region Δx. *We improve our knowledge of* Δx *at the expense of our knowledge of* p_x. *The very act of confining the particle to* Δx *destroys the precision of our knowledge of* p_x *and introduces a range of values* Δp_x. If we try to make a *simultaneous* determination of x and p_x, our result will show

that each is uncertain by the respective amounts Δx and Δp_x, which are related by the Heisenberg uncertainty relationship

$$\Delta x \, \Delta p_x \geq \frac{\hbar}{2} \tag{2.1}$$

with similar expressions for the y and z components. (The symbol $\hbar$, read as "h-bar," is $h/2\pi$ where h is Planck's constant.) The key word here is "simultaneous"—we can indeed measure x with arbitrarily small uncertainty ($\Delta x = 0$) if we are willing to sacrifice all simultaneous knowledge of the momentum of the particle. Having made that determination, we could then make an arbitrarily precise measurement of the *new* momentum ($\Delta p_x = 0$), which would simultaneously destroy our previous precise knowledge of its position.

We describe the particle by a "wave packet," a collection of waves, representing a range of momenta Δp_x around p_x, with an amplitude that is reasonably large only within the region Δx about x. A particle is localized in a region of space defined by its wave packet; the wave packet contains all of the available information about the particle. Whenever we use the term "particle" we really mean "wave packet"; although we often speak of electrons or nucleons as if they had an independent existence, our knowledge of them is limited by the uncertainty relationship to the information contained in the wave packet that describes their particular situation.

These arguments about uncertainty hold for other kinds of measurements as well. The energy E of a system is related to the frequency ν of its de Broglie wave according to $E = h\nu$. To determine E precisely, we must observe for a sufficiently long time interval Δt so that we can determine ν precisely. The uncertainty relationship in this case is

$$\Delta E \, \Delta t \geq \frac{\hbar}{2} \tag{2.2}$$

If a system lives for a time Δt, we cannot determine its energy except to within an uncertainty ΔE. The energy of a system that is absolutely stable against decay can be measured with arbitrarily small uncertainty; for all decaying systems there is an uncertainty in energy, commonly called the energy "width."

A third uncertainty relationship involves the angular momentum. Classically, we can determine all three components ℓ_x, ℓ_y, ℓ_z of the angular momentum vector $\boldsymbol{\ell}$. In quantum mechanics, when we try to improve our knowledge of one component, it is at the expense of our knowledge of the other two components. Let us choose to measure the z component, and let the location of the projection of $\boldsymbol{\ell}$ in the xy plane be characterized by the azimuthal angle ϕ. Then

$$\Delta \ell_z \, \Delta \phi \geq \frac{\hbar}{2} \tag{2.3}$$

If we know ℓ_z exactly, then we know nothing at all about ϕ. We can think of $\boldsymbol{\ell}$ as rotating or precessing about the z axis, keeping ℓ_z fixed but allowing all possible ℓ_x and ℓ_y, so that ϕ is completely uncertain.

2.2 PRINCIPLES OF QUANTUM MECHANICS

The mathematical aspects of nonrelativistic quantum mechanics are determined by solutions to the *Schrödinger equation*. In one dimension, the time-independent Schrödinger equation for a particle of mass m with potential energy $V(x)$ is

$$-\frac{\hbar^2}{2m}\frac{d^2\psi}{dx^2} + V(x)\,\psi(x) = E\,\psi(x) \tag{2.4}$$

where $\psi(x)$ is the Schrödinger *wave function*. The wave function is the mathematical description of the wave packet. In general, this equation will have solutions only for certain values of the energy E; these values, which usually result from applying boundary conditions to $\psi(x)$, are known as the energy *eigenvalues*. The complete solution, including the time dependence, is

$$\Psi(x, t) = \psi(x)\, e^{-i\omega t} \tag{2.5}$$

where $\omega = E/\hbar$.

An important condition on the wave function is that ψ and its first derivative $d\psi/dx$ must be continuous across any boundary; in fact, the same situation applies to classical waves. Whenever there is a boundary between two media, let us say at $x = a$, we must have

$$\lim_{\varepsilon \to 0} [\psi(a + \varepsilon) - \psi(a - \varepsilon)] = 0 \tag{2.6a}$$

and

$$\lim_{\varepsilon \to 0} \left[\left(\frac{d\psi}{dx} \right)_{x=a+\varepsilon} - \left(\frac{d\psi}{dx} \right)_{x=a-\varepsilon} \right] = 0 \tag{2.6b}$$

It is permitted to violate condition 2.6*b* if there is an *infinite* discontinuity in $V(x)$; however, condition 2.6*a* must always be true.

Another condition on ψ, which originates from the interpretation of probability density to be discussed below, is that ψ must remain finite. Any solution for the Schrödinger equation that allows ψ to become infinite must be discarded.

Knowledge of the wave function $\Psi(x, t)$ for a system enables us to calculate many properties of the system. For example, the probability to find the particle (the wave packet) between x and $x + dx$ is

$$P(x)\, dx = \Psi^*(x, t)\, \Psi(x, t)\, dx \tag{2.7}$$

where Ψ^* is the complex conjugate of Ψ. The quantity $\Psi^* \Psi$ is known as the *probability density*. The probability to find the particle between the limits x_1 and x_2 is the integral of all the infinitesimal probabilities:

$$P = \int_{x_1}^{x_2} \Psi^* \Psi\, dx \tag{2.8}$$

The total probability to find the particle must be 1:

$$\int_{-\infty}^{\infty} \Psi^* \Psi\, dx = 1 \tag{2.9}$$

This condition is known as the *normalization condition* and in effect it determines any multiplicative constants included in Ψ. All physically meaningful wave functions must be properly normalized.

Any function of x, $f(x)$, can be evaluated for this quantum mechanical system. The values that we measure for $f(x)$ are determined by the probability density, and the average value of $f(x)$ is determined by finding the contribution to the average for each value of x:

$$\langle f \rangle = \int \Psi^* f \Psi \, dx \tag{2.10}$$

Average values computed in this way are called quantum mechanical *expectation values*.

We must be a bit careful how we interpret these expectation values. Quantum mechanics deals with statistical outcomes, and many of our calculations are really statistical averages. If we prepare a large number of identical systems and measure $f(x)$ for each of them, the average of these measurements will be $\langle f \rangle$. One of the unsatisfying aspects of quantum theory is its inability to predict with certainty the outcome of an experiment; all we can do is predict the statistical average of a large number of measurements.

Often we must compute the average values of quantities that are not simple functions of x. For example, how can we compute $\langle p_x \rangle$? Since p_x is not a function of x, we cannot use Equation 2.10 for this calculation. The solution to this difficulty comes from the mathematics of quantum theory. Corresponding to each classical variable, there is a quantum mechanical *operator*. An operator is a symbol that directs us to perform a mathematical operation, such as exp or sin or d/dx. We adopt the convention that the operator acts only on the variable or function immediately to its right, unless we indicate otherwise by grouping functions in parentheses. This convention means that it is very important to remember the form of Equation 2.10; the operator is "sandwiched" between Ψ^* and Ψ, and operates only on Ψ. Two of the most common operators encountered in quantum mechanics are the momentum operator, $p_x = -i\hbar \partial/\partial x$ and the energy, $E = i\hbar \partial/\partial t$. Notice that the first term on the left of the Schrödinger equation 2.4 is just $p_x^2/2m$, which we can regard as the kinetic energy operator. Notice also that the *operator* E applied to $\Psi(x, t)$ in Equation 2.5 gives the *number* E multiplying $\Psi(x, t)$.

We can now evaluate the expectation value of the x component of the momentum:

$$\begin{aligned} \langle p_x \rangle &= \int \Psi^* \left(-i\hbar \frac{\partial}{\partial x} \right) \Psi \, dx \\ &= -i\hbar \int \Psi^* \frac{\partial \Psi}{\partial x} \, dx \end{aligned} \tag{2.11}$$

One very important feature emerges from these calculations: when we take the complex conjugate of Ψ as given by Equation 2.5, the time-dependent factor becomes $e^{+i\omega t}$, and therefore the time dependence cancels from Equations 2.7–2.11. None of the observable properties of the system depend on the time. Such conditions are known for obvious reasons as *stationary states*; a system in a stationary state stays in that state for all times and all of the dynamical variables are constants of the motion. This is of course an idealization—no system lives forever, but many systems can be regarded as being in states that are approxi-

mately stationary. Thus an atom can make a transition from one "stationary" excited state to another "stationary" state.

Associated with the wave function Ψ is the *particle current density* j:

$$j = \frac{\hbar}{2mi}\left(\Psi^* \frac{\partial \Psi}{\partial x} - \Psi \frac{\partial \Psi^*}{\partial x}\right) \tag{2.12}$$

This quantity is analogous to an electric current, in that it gives the number of particles per second passing any point x.

In three dimensions, the form of the Schrödinger equation depends on the coordinate system in which we choose to work. In Cartesian coordinates, the potential energy is a function of (x, y, z) and the Schrödinger equation is

$$-\frac{\hbar^2}{2m}\left(\frac{\partial^2 \psi}{\partial x^2} + \frac{\partial^2 \psi}{\partial y^2} + \frac{\partial^2 \psi}{\partial z^2}\right) + V(x, y, z)\psi(x, y, z) = E\psi(x, y, z) \tag{2.13}$$

The complete time-dependent solution is again

$$\Psi(x, y, z, t) = \psi(x, y, z)\, e^{-i\omega t} \tag{2.14}$$

The probability density $\Psi^* \Psi$ now gives the probability per unit volume; the probability to find the particle in the volume element $dv = dx\, dy\, dz$ at x, y, z is

$$P\, dv = \Psi^* \Psi\, dv \tag{2.15}$$

To find the total probability in some volume V, we must do a triple integral over x, y, and z. All of the other properties discussed above for the one-dimensional system can easily be extended to the three-dimensional system.

Since nuclei are approximately spherical, the Cartesian coordinate system is not the most appropriate one. Instead, we must work in spherical polar coordinates (r, θ, ϕ), which are shown in Figure 2.1. In this case the Schrödinger equation is

$$-\frac{\hbar^2}{2m}\left[\frac{\partial^2 \psi}{\partial r^2} + \frac{2}{r}\frac{\partial \psi}{\partial r} + \frac{1}{r^2 \sin\theta}\frac{\partial}{\partial \theta}\left(\sin\theta \frac{\partial \psi}{\partial \theta}\right) + \frac{1}{r^2 \sin^2\theta}\frac{\partial^2 \psi}{\partial \phi^2}\right]$$
$$+ V(r, \theta, \phi)\psi(r, \theta, \phi) = E\psi(r, \theta, \phi) \tag{2.16}$$

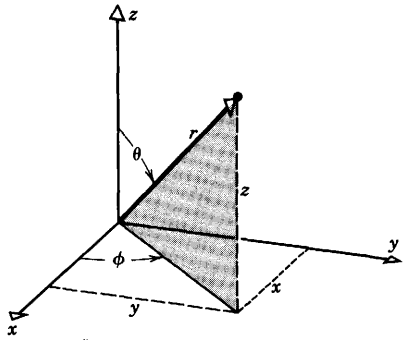


Figure 2.1 Spherical polar coordinate system, showing the relationship to Cartesian coordinates.

All of the previous considerations apply in this case as well, with the volume element

$$dv = r^2 \sin\theta \, dr \, d\theta \, d\phi \tag{2.17}$$

The following two sections illustrate the application of these principles, first with the mathematically simpler one-dimensional problems and then with the more physical three-dimensional problems.

2.3 PROBLEMS IN ONE DIMENSION

The Free Particle

For this case, no forces act and we take $V(x) = 0$ everywhere. We can then rewrite Equation 2.4 as

$$\frac{d^2\psi}{dx^2} = -\frac{2mE}{\hbar^2}\psi \tag{2.18}$$

The solution to this differential equation can be written

$$\psi(x) = A' \sin kx + B' \cos kx \tag{2.19}$$

or, equivalently

$$\psi(x) = A e^{ikx} + B e^{-ikx} \tag{2.20}$$

where $k^2 = 2mE/\hbar^2$ and where A and B (or A' and B') are constants.

The time-dependent wave function is

$$\Psi(x, t) = A e^{i(kx-\omega t)} + B e^{-i(kx+\omega t)} \tag{2.21}$$

The first term represents a wave traveling in the positive x direction, while the second term represents a wave traveling in the negative x direction. The intensities of these waves are given by the squares of the respective amplitudes, $|A|^2$ and $|B|^2$. Since there are no boundary conditions, there are no restrictions on the energy E; all values of E give solutions to the equation. The normalization condition 2.9 cannot be applied in this case, because integrals of $\sin^2$ or $\cos^2$ do not converge in $x = -\infty$ to $+\infty$. Instead, we use a different normalization system for such constant potentials. Suppose we have a source such as an accelerator located at $x = -\infty$, emitting particles at a rate I particles per second, with momentum $p = \hbar k$ in the positive x direction. Since the particles are traveling in the positive x direction, we can set B to zero—the intensity of the wave representing particles traveling in the negative x direction must vanish if there are no particles traveling in that direction. The particle current is, according to Equation 2.12,

$$j = \frac{\hbar k}{m}|A|^2 \tag{2.22}$$

which must be equal to the current of I particles per second emitted by the source. Thus we can take $A = \sqrt{mI/\hbar k}$.

Step Potential, $E > V_0$

The potential is

$$\begin{aligned} V(x) &= 0 \qquad x < 0 \\ &= V_0 \qquad x > 0 \end{aligned} \tag{2.23}$$

where $V_0 > 0$. Let us call $x < 0$ region 1 and $x > 0$ region 2. Then in region 1, the Schrödinger equation is identical with Equation 2.18 and the solutions ψ_1 are given by Equation 2.20 with $k = k_1 = \sqrt{2mE/\hbar^2}$. In region 2, the Schrödinger equation is

$$\frac{d^2\psi_2}{dx^2} = -\frac{2m(E - V_0)}{\hbar^2}\psi_2 \tag{2.24}$$

Since $E > V_0$, we can write the solution as

$$\psi_2 = Ce^{ik_2x} + De^{-ik_2x} \tag{2.25}$$

where $k_2 = \sqrt{2m(E - V_0)/\hbar^2}$.

Applying the boundary conditions at $x = 0$ gives

$$A + B = C + D \tag{2.26a}$$

from Equation 2.6*a*, and

$$k_1(A - B) = k_2(C - D) \tag{2.26b}$$

from Equation 2.6*b*.

Let's assume that particles are incident on the step from a source at $x = -\infty$. Then the A term in ψ_1 represents the *incident wave* (the wave in $x < 0$ traveling toward the step at $x = 0$), the B term in ψ_1 represents the *reflected wave* (the wave in $x < 0$ traveling back toward $x = -\infty$), and the C term in ψ_2 represents the *transmitted wave* (the wave in $x > 0$ traveling away from $x = 0$). The D term cannot represent any part of this problem because there is no way for a wave to be moving toward the origin in region 2, and so we eliminate this term by setting D to zero. Solving Equations 2.26*a* and 2.26*b*, we have

$$B = A\frac{1 - k_2/k_1}{1 + k_2/k_1} \tag{2.27}$$

$$C = A\frac{2}{1 + k_2/k_1} \tag{2.28}$$

The *reflection coefficient* R is defined as the current in the reflected wave divided by the incident current:

$$R = \frac{j_{\text{reflected}}}{j_{\text{incident}}} \tag{2.29}$$

and using Equation 2.22 we find

$$R = \frac{|B|^2}{|A|^2} = \left(\frac{1 - k_2/k_1}{1 + k_2/k_1}\right)^2 \tag{2.30}$$

The *transmission coefficient* T is similarly defined as the fraction of the incident

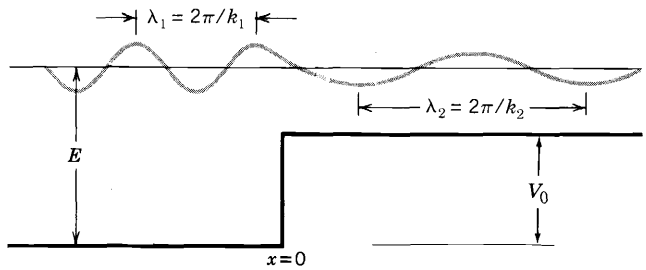


Figure 2.2 The wave function of a particle of energy E encountering a step of height V_0 for the case $E > V_0$. The de Broglie wavelength changes from λ_1 to λ_2 when the particle crosses the step, but ψ and $d\psi/dx$ are continuous at $x = 0$.

current that is transmitted past the boundary:

$$T = \frac{j_{\text{transmitted}}}{j_{\text{incident}}} \tag{2.31}$$

and thus

$$T = \frac{k_2}{k_1}\frac{|C|^2}{|A|^2} = \frac{4k_2/k_1}{(1 + k_2/k_1)^2} \tag{2.32}$$

Notice that $R + T = 1$, as expected. The resulting solution is illustrated in Figure 2.2.

This is a simple example of a *scattering* problem. In Chapter 4 we show how these concepts can be extended to three dimensions and applied to nucleon–nucleon scattering problems.

Step Potential, $E < V_0$

In this case, the potential is still given by Equation 2.23, and the solution for region 1 ($x < 0$) is identical with the previous calculation. In region 2, the Schrödinger equation gives

$$\frac{d^2\psi_2}{dx^2} = \frac{2m}{\hbar^2}(V_0 - E)\psi_2 \tag{2.33}$$

which has the solution

$$\psi_2 = Ce^{k_2 x} + De^{-k_2 x} \tag{2.34}$$

where $k_2 = \sqrt{2m(V_0 - E)/\hbar^2}$. Note that for *constant* potentials, the solutions are either oscillatory like Equation 2.19 or 2.20 when $E > V_0$, or exponential like Equation 2.34 when $E < V_0$. Although the mathematical forms may be different for nonconstant potentials $V(x)$, the general behavior is preserved: oscillatory (though not necessarily sinusoidal) when $E > V(x)$ and exponential when $E < V(x)$.

This solution, Equation 2.34, must be valid for the entire range $x > 0$. Since the first term would become infinite for $x \to \infty$, we must set $C = 0$ to keep the wave function finite. The D term in ψ_2 illustrates an important difference between classical and quantum physics, *the penetration of the wave function into*

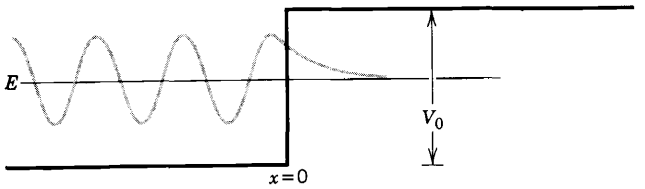


Figure 2.3 The wave function of a particle of energy E encountering a step of height V_0, for the case $E < V_0$. The wave function decreases exponentially in the classically forbidden region, where the classical kinetic energy would be negative. At $x = 0$, ψ and $d\psi/dx$ are continuous.

the classically forbidden region. All (classical) *particles* are reflected at the boundary; the quantum mechanical *wave packet*, on the other hand, can penetrate a short distance into the forbidden region. The (classical) particle is never directly *observed* in that region; since $E < V_0$, the kinetic energy would be negative in region 2. The solution is illustrated in Figure 2.3

Barrier Potential, $E > V_0$

The potential is

$$\begin{aligned} V(x) &= 0 \qquad x < 0 \\ &= V_0 \qquad 0 \le x \le a \\ &= 0 \qquad x > a \end{aligned} \tag{2.35}$$

In the three regions 1, 2, and 3, the solutions are

$$\begin{aligned} \psi_1 &= A e^{ik_1 x} + B e^{-ik_1 x} \\ \psi_2 &= C e^{ik_2 x} + D e^{-ik_2 x} \\ \psi_3 &= F e^{ik_3 x} + G e^{-ik_3 x} \end{aligned} \tag{2.36}$$

where $k_1 = k_3 = \sqrt{2mE/\hbar^2}$ and $k_2 = \sqrt{2m(E - V_0)/\hbar^2}$.

Using the continuity conditions at $x = 0$ and at $x = a$, and assuming again that particles are incident from $x = -\infty$ (so that G can be set to zero), after considerable algebraic manipulation we can find the transmission coefficient $T = |F|^2/|A|^2$:

$$T = \frac{1}{1 + \frac{1}{4}\dfrac{V_0^2}{E(E - V_0)}\sin^2 k_2 a} \tag{2.37}$$

The solution is illustrated in Figure 2.4.

Barrier Potential, $E < V_0$

For this case, the ψ_1 and ψ_3 solutions are as above, but ψ_2 becomes

$$\psi_2 = C e^{k_2 x} + D e^{-k_2 x} \tag{2.38}$$

where now $k_2 = \sqrt{2m(V_0 - E)/\hbar^2}$. Because region 2 extends only from $x = 0$

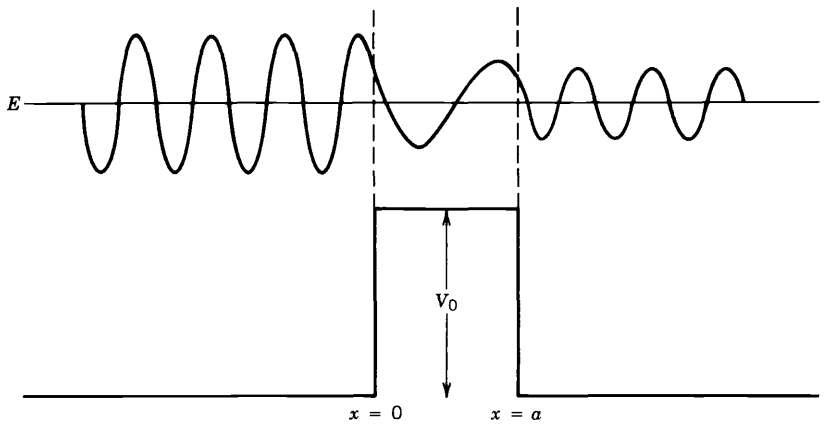


Figure 2.4 The wave function of a particle of energy $E > V_0$ encountering a barrier potential. The particle is incident from the left. The wave undergoes reflections at both boundaries, and the transmitted wave emerges with smaller amplitude.

to $x = a$, the question of an exponential solution going to infinity does not arise, so we cannot set C or D to zero.

Again, applying the boundary conditions at $x = 0$ and $x = a$ permits the solution for the transmission coefficient:

$$T = \frac{1}{1 + \frac{1}{4}\frac{V_0^2}{E(V_0 - E)}\sinh^2 k_2 a} \tag{2.39}$$

Classically, we would expect $T = 0$—the particle is not permitted to enter the forbidden region where it would have negative kinetic energy. The quantum wave can penetrate the barrier and give a nonzero probability to find the particle beyond the barrier. The solution is illustrated in Figure 2.5.

This phenomenon of *barrier penetration* or quantum mechanical *tunneling* has important applications in nuclear physics, especially in the theory of α decay, which we discuss in Chapter 8.

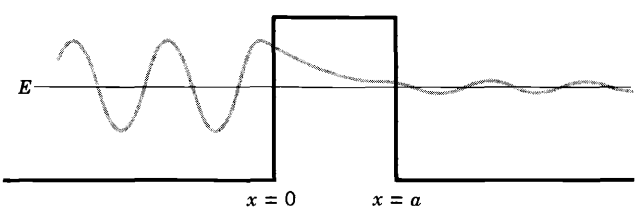


Figure 2.5 The wave function of a particle of energy $E < V_0$ encountering a barrier potential (the particle would be incident from the left in the figure). The wavelength is the same on both sides of the barrier, but the amplitude beyond the barrier is much less than the original amplitude. The particle can never be observed, inside the barrier (where it would have negative kinetic energy) but it can be observed *beyond* the barrier.

The Infinite Well

The potential is (see Figure 2.6)

$$\begin{aligned} V(x) &= \infty \qquad x < 0, \quad x > a \\ &= 0 \qquad 0 \leq x \leq a \end{aligned} \tag{2.40}$$

That is, the particle is trapped between $x = 0$ and $x = a$. The walls at $x = 0$ and $x = a$ are absolutely impenetrable; thus the particle is never outside the well and $\psi = 0$ for $x < 0$ and for $x > a$. Inside the well, the Schrödinger equation has the form of Equation 2.18, and we will choose a solution in the form of Equation 2.19:

$$\psi = A \sin kx + B \cos kx \tag{2.41}$$

The continuity condition on ψ at $x = 0$ gives $\psi(0) = 0$, which is true only for $B = 0$. At $x = a$, the continuity condition on ψ gives

$$A \sin ka = 0 \tag{2.42}$$

The solution $A = 0$ is not acceptable, for that would give $\psi = 0$ everywhere. Thus $\sin ka = 0$, or

$$ka = n\pi \qquad n = 1, 2, 3, \ldots \tag{2.43}$$

and

$$E_n = \frac{\hbar^2 k^2}{2m} = \frac{\hbar^2 \pi^2}{2ma^2} n^2 \tag{2.44}$$

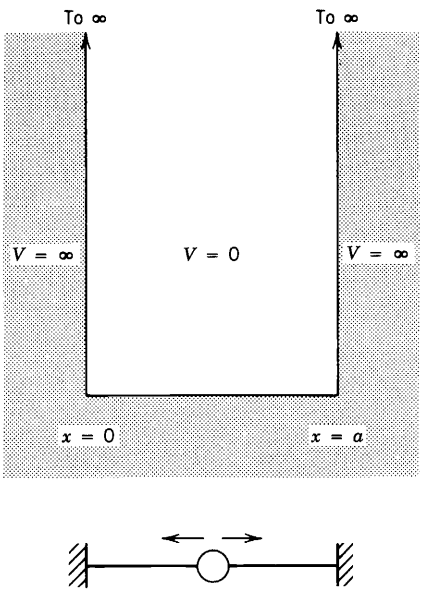


Figure 2.6 A particle moves freely in the one-dimensional region $0 \leq x \leq a$ but is excluded completely from $x < 0$ and $x > a$. A bead sliding without friction on a wire and bouncing elastically from the walls is a simple physical example.

Here the energy is *quantized*—only certain values of the energy are permitted. The energy spectrum is illustrated in Figure 2.7. These states are *bound states*, in which the potential confines the particle to a certain region of space.

The corresponding wave functions are

$$\psi_n = \sqrt{\frac{2}{a}} \sin \frac{n\pi x}{a} \tag{2.45}$$

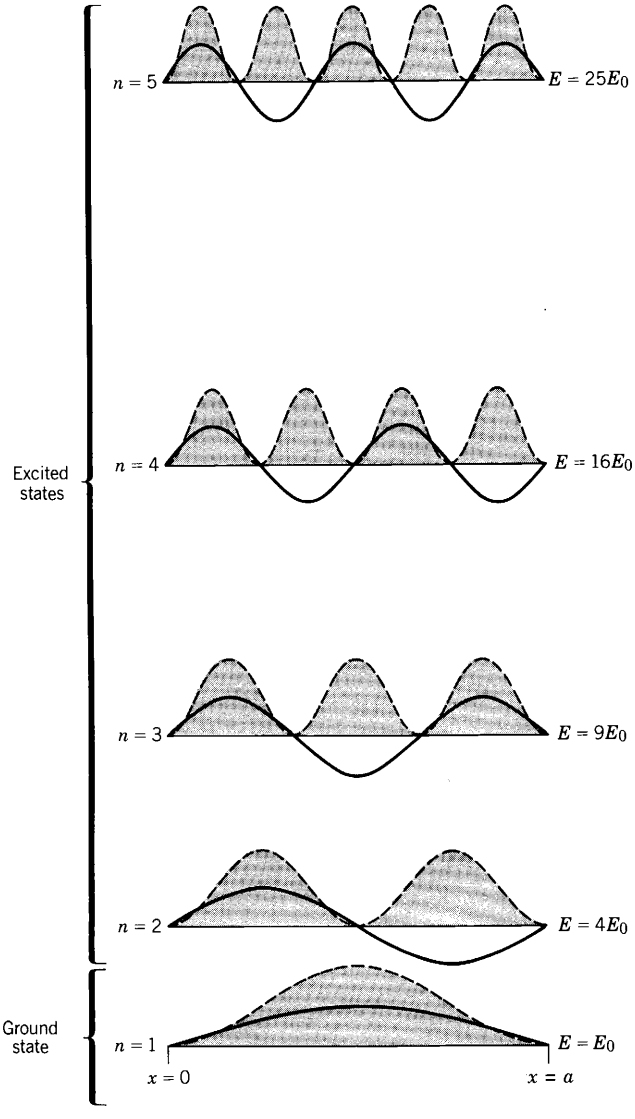


Figure 2.7 The permitted energy levels of the one-dimensional infinite square well. The wave function for each level is shown by the solid curve, and the shaded region gives the probability density for each level. The energy E_0 is $\hbar^2\pi^2 / 2ma^2$.

where the constant A has been evaluated using Equation 2.9. The probability densities $|\psi|^2$ of some of the lower states are illustrated in Figure 2.7.

The Finite Potential Well

For this case we assume the well has depth V_0 between $+a/2$ and $-a/2$:

$$\begin{aligned} V(x) &= V_0 \qquad |x| > a/2 \\ &= 0 \qquad |x| < a/2 \end{aligned} \tag{2.46}$$

We look for *bound-state* solutions, with $E < V_0$. The solutions are

$$\begin{aligned} \psi_1 &= A e^{k_1 x} + B e^{-k_1 x} \qquad x < -a/2 \\ \psi_2 &= C e^{ik_2 x} + D e^{-ik_2 x} \qquad -a/2 \le x \le a/2 \\ \psi_3 &= F e^{k_1 x} + G e^{-k_1 x} \qquad x > a/2 \end{aligned} \tag{2.47}$$

where $k_1 = \sqrt{2m(V_0 - E)/\hbar^2}$ and $k_2 = \sqrt{2mE/\hbar^2}$. To keep the wave function finite in region 1 when $x \to -\infty$, we must have $B = 0$, and to keep it finite in region 3 for $x \to +\infty$, we require $F = 0$.

Applying the continuity conditions at $x = -a/2$ and at $x = +a/2$, we find the following two relationships:

$$k_2 \tan \frac{k_2 a}{2} = k_1 \tag{2.48a}$$

or

$$-k_2 \cot \frac{k_2 a}{2} = k_1 \tag{2.48b}$$

These transcendental equations cannot be solved directly. They can be solved numerically on a computer, or graphically. The graphical solutions are easiest if we rewrite Equations 2.48 in the following form:

$$\alpha \tan \alpha = (P^2 - \alpha^2)^{1/2} \tag{2.49a}$$

$$-\alpha \cot \alpha = (P^2 - \alpha^2)^{1/2} \tag{2.49b}$$

where $\alpha = k_2 a/2$ and $P = (mV_0 a^2/2\hbar^2)^{1/2}$. The right side of these equations defines a circle of radius P, while the left side gives a tangentlike function with several discrete branches. The solutions are determined by the points where the circle intersects the tangent function, as shown in Figure 2.8. *Therefore, the number of solutions is determined by the radius P, and thus by the depth V_0 of the well.* (Contrast this with the infinite well, which had an infinite number of bound states.) For example, when $P < \pi/2$, there is only one bound state. For $\pi/2 < P < \pi$ there are two bound states. Conversely, if we studied a system of this sort and found only one bound state, we could deduce some limits on the depth of the well. As we will discuss in Chapter 4, a similar technique allows us to estimate the depth of the nuclear potential, because the deuteron, the simplest two-nucleon bound system, has only one bound state.

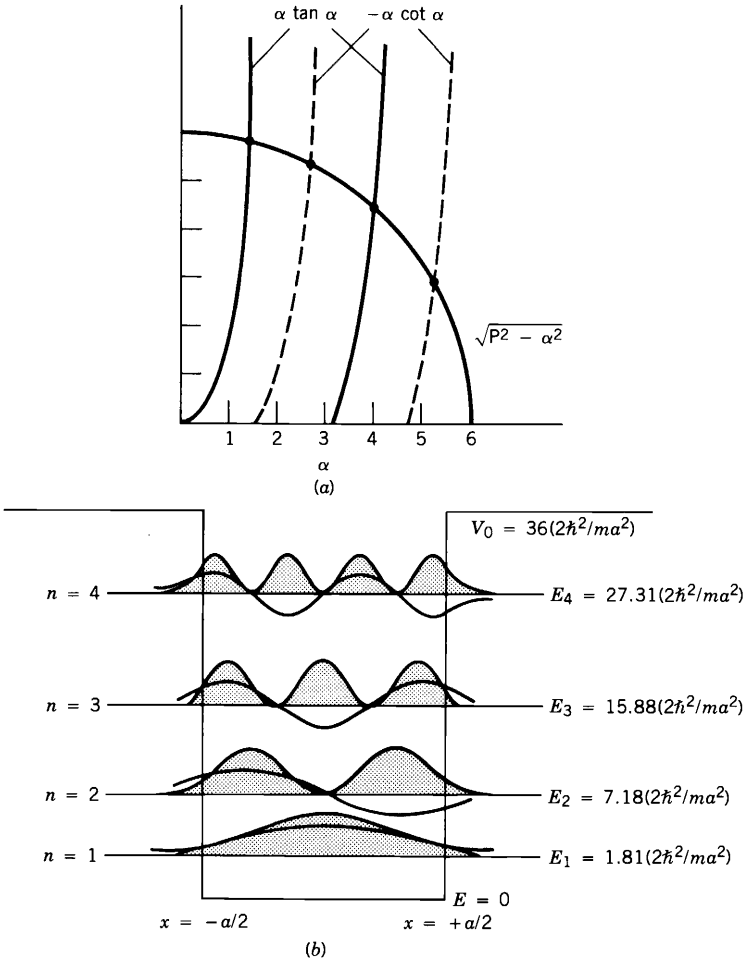


Figure 2.8 (*a*) The graphical solution of Equations 2.49*a* and 2.49*b*. For the case of $P = 6$ (chosen arbitrarily) there are four solutions at $\alpha = 1.345, 2.679, 3.985$, and 5.226. (*b*) The wave functions and probability densities (shaded) for the four states. (Compare with the infinite well shown in Figure 2.7.)

The Simple Harmonic Oscillator

Any reasonably well-behaved potential can be expanded in a Taylor series about the point x_0:

$$V(x) = V(x_0) + \left(\frac{dV}{dx}\right)_{x=x_0}(x - x_0) + \frac{1}{2}\left(\frac{d^2V}{dx^2}\right)_{x=x_0}(x - x_0)^2 + \cdots \tag{2.50}$$

If x_0 is a potential minimum, the second term in the series vanishes, and since the first term contributes only a constant to the energy, the interesting term is the third term. Thus to a first approximation, near its minimum the system behaves

Table 2.1 Sample Wave Functions of the One-Dimensional Simple Harmonic Oscillator

n	E_n	$\psi_n(x)$
0	$\frac{1}{2}\hbar\omega_0$	$\pi^{-1/4}\, e^{-\alpha^2 x^2/2}$
1	$\frac{3}{2}\hbar\omega_0$	$2^{-1/2}\pi^{-1/4}(2\alpha x)\, e^{-\alpha^2 x^2/2}$
2	$\frac{5}{2}\hbar\omega_0$	$2^{-3/2}\pi^{-1/4}(4\alpha^2 x^2 - 2)\, e^{-\alpha^2 x^2/2}$
3	$\frac{7}{2}\hbar\omega_0$	$(1/4\sqrt{3}\,\pi^{1/4})(8\alpha^3 x^3 - 12\alpha x)\, e^{-\alpha^2 x^2/2}$
4	$\frac{9}{2}\hbar\omega_0$	$(1/8\sqrt{6}\,\pi^{1/4})(16\alpha^4 x^4 - 48\alpha^2 x^2 + 12)\, e^{-\alpha^2 x^2/2}$

$E_n = \hbar\omega_0(n + \frac{1}{2})$

$\psi_n(x) = (2^n n!\sqrt{\pi})^{-1/2} H_n(\alpha x)\, e^{-\alpha^2 x^2/2}$

where $H_n(\alpha x)$ is a Hermite polynomial

like a simple harmonic oscillator, which has the similar potential $\frac{1}{2}k(x - x_0)^2$. The study of the simple harmonic oscillator therefore is important for understanding a variety of systems.

For our system, we choose the potential energy

$$V(x) = \tfrac{1}{2}kx^2 \tag{2.51}$$

for all x. The Schrödinger equation for this case is solved through the substitution $\psi(x) = h(x)\, e^{-\alpha^2 x^2/2}$, where $\alpha^2 = \sqrt{km}/\hbar$. The function $h(x)$ turns out to be a simple polynomial in x. The degree of the polynomial (the highest power of x that appears) is determined by the quantum number n that labels the energy states, which are also found from the solution to the Schrödinger equation:

$$E_n = \hbar\omega_0\left(n + \tfrac{1}{2}\right) \qquad n = 0, 1, 2, 3, \ldots \tag{2.52}$$

where $\omega_0 = \sqrt{k/m}$, the classical angular frequency of the oscillator. Some of the resulting wave functions are listed in Table 2.1, and the corresponding energy levels and probability densities are illustrated in Figure 2.9. Notice that the probabilities resemble those of Figure 2.8; where $E > V$, the solution oscillates somewhat sinusoidally, while for $E < V$ (beyond the classical turning points where the oscillator comes to rest and reverses its motion) the solution decays exponentially. This solution also shows penetration of the probability density into the classically forbidden region.

A noteworthy feature of this solution is that the energy levels are equally spaced. Also, because the potential is infinitely deep, there are infinitely many bound states.

Summary

By studying these one-dimensional problems, we learn several important details about the wave properties of particles.

1. Quantum waves can undergo reflection and transmission when they encounter a potential barrier; this behavior is very similar to that of classical waves.
2. A wave packet can penetrate into the classically forbidden region and appear beyond a potential barrier that it does not have enough energy to overcome.

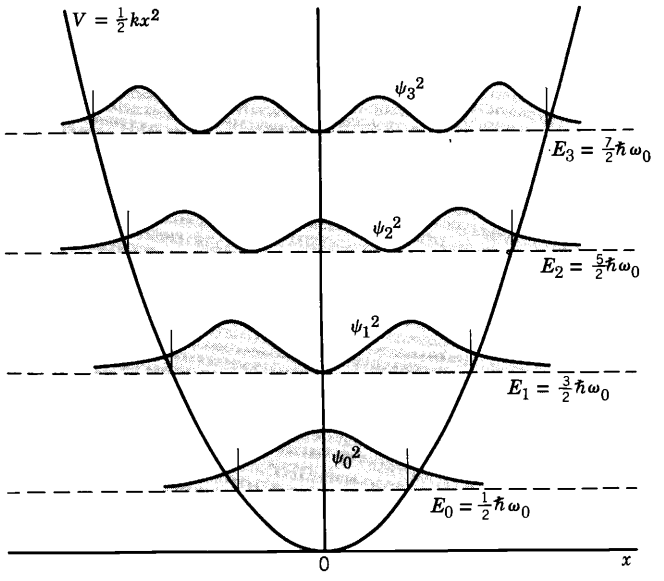


Figure 2.9 The lowest few energy levels and corresponding probability densities of the harmonic oscillator.

3. Wave functions oscillate whenever $E > V(x)$ and decay exponentially whenever $E < V(x)$.
4. When a potential confines a particle to a region of space, bound-state wave functions can result. The particle is permitted only a set of discrete energy values; the number of allowed energy values is determined by the depth of the potential well.

2.4 PROBLEMS IN THREE DIMENSIONS

The Infinite Cartesian Well

We begin with a problem in Cartesian coordinates that illustrates an important feature present in three-dimensional problems but not in one-dimensional problems. The potential in this case is

$$\begin{aligned} V(x, y, z) &= 0 \qquad 0 \le x \le a, \quad 0 \le y \le a, \quad 0 \le z \le a \\ &= \infty \qquad x < 0, \quad x > a, \quad y < 0, \quad y > a, \quad z < 0, \quad z > a \end{aligned} \tag{2.53}$$

The particle is thus confined to a cubical box of dimension a. Beyond the impenetrable walls of the well, $\psi = 0$ as before. Inside the well, the Schrödinger equation is

$$-\frac{\hbar^2}{2m}\left(\frac{\partial^2\psi}{\partial x^2} + \frac{\partial^2\psi}{\partial y^2} + \frac{\partial^2\psi}{\partial z^2}\right) = E\psi(x, y, z) \tag{2.54}$$

The usual procedure for solving partial differential equations is to try to find a

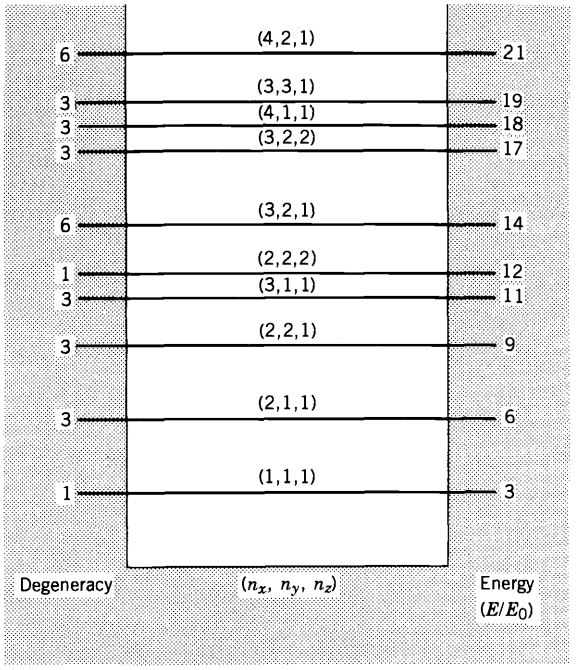


Figure 2.10 Energy levels of a particle confined to a three-dimensional cubical box. The energy is given in units of $E_0 = \hbar^2\pi^2 / 2ma^2$.

separable solution, with $\psi(x, y, z) = X(x)\,Y(y)\,Z(z)$, where X, Y, and Z are each functions of a single variable. We will skip the mathematical details and give only the result of the calculation:

$$\psi_{n_x n_y n_z}(x, y, z) = \sqrt{\left(\frac{2}{a}\right)^3} \sin\frac{n_x\pi x}{a} \sin\frac{n_y\pi y}{a} \sin\frac{n_z\pi z}{a} \tag{2.55}$$

$$E_{n_x n_y n_z} = \frac{\hbar^2\pi^2}{2ma^2}\left(n_x^2 + n_y^2 + n_z^2\right) \tag{2.56}$$

where n_x, n_y, and n_z are independent integers greater than zero. The lowest state, the ground state, has quantum numbers $(n_x, n_y, n_z) = (1, 1, 1)$. Its probability distribution would show a maximum at the center of the box ($x = y = z = a/2$), falling gradually to zero at the walls like $\sin^2$.

The first excited state has three possible sets of quantum numbers: (2, 1, 1), (1, 2, 1), and (1, 1, 2). Each of these distinct and independent states has a different wave function, and therefore a different probability density and different expectation values of the physical observables, *but they all have the same energy*. This situation is known as *degeneracy*; the first excited state is threefold degenerate. Degeneracy is extremely important for atomic structure since it tells us how many electrons can be put in each atomic subshell. We will soon discuss its similar role in the nuclear shell model.

Figure 2.10 shows the lower portion of the energy spectrum of excited states. Notice that the spacing and ordering do not have the regularity of the one-dimensional problem.

The Infinite Spherical Well

If we work in spherical coordinates with a potential that depends only on r (not on θ or ϕ), another new feature arises that will be important in our subsequent investigations of nuclear structure. When we search for separable solutions, of the form $\psi(r, \theta, \phi) = R(r)\,\Theta(\theta)\,\Phi(\phi)$, the central potential $V(r)$ appears only in the radial part of the separation equation, and the angular parts can be solved directly. The differential equation for $\Phi(\phi)$ is

$$\frac{d^2\Phi}{d\phi^2} + m_\ell^2\,\Phi = 0 \tag{2.57}$$

where m_ℓ^2 is the separation constant.

The solution is

$$\Phi_{m_\ell}(\phi) = \frac{1}{\sqrt{2\pi}}\,e^{im_\ell\phi} \tag{2.58}$$

where $m_\ell = 0, \pm 1, \pm 2, \ldots$. The equation for $\Theta(\theta)$ is

$$\frac{1}{\sin\theta}\frac{d}{d\theta}\left(\sin\theta\frac{d\Theta}{d\theta}\right) + \left[\ell(\ell+1) - \frac{m_\ell^2}{\sin^2\theta}\right]\Theta = 0 \tag{2.59}$$

where $\ell = 0, 1, 2, 3, \ldots$ and $m_\ell = 0, \pm 1, \pm 2, \ldots, \pm\ell$. The solution $\Theta_{\ell m_\ell}(\theta)$ can be expressed as a polynomial of degree ℓ in $\sin\theta$ or $\cos\theta$. Together, and normalized, $\Phi_{m_\ell}(\phi)$ and $\Theta_{\ell m_\ell}(\theta)$ give the *spherical harmonics* $Y_{\ell m_\ell}(\theta, \phi)$, some examples of which are listed in Table 2.2. These functions give the angular part of the solution to the Schrödinger equation for *any central potential* $V(r)$. For example, it is these angular functions that give the spatial properties of atomic orbitals that are responsible for molecular bonds.

For each potential $V(r)$, all we need to do is to find a solution of the radial equation

$$-\frac{\hbar^2}{2m}\left(\frac{d^2R}{dr^2} + \frac{2}{r}\frac{dR}{dr}\right) + \left[V(r) + \frac{\ell(\ell+1)\hbar^2}{2mr^2}\right]R = ER \tag{2.60}$$

Table 2.2 Spherical Harmonics for Some Low ℓ Values

ℓ	m_ℓ	$Y_{\ell m_\ell}(\theta, \phi) = \Theta_{\ell m_\ell}(\theta)\,\Phi_{m_\ell}(\phi)$
0	0	$(1/4\pi)^{1/2}$
1	0	$(3/4\pi)^{1/2}\cos\theta$
1	± 1	$\mp(3/8\pi)^{1/2}\sin\theta\,e^{\pm i\phi}$
2	0	$(5/16\pi)^{1/2}(3\cos^2\theta - 1)$
2	± 1	$\mp(15/8\pi)^{1/2}\sin\theta\cos\theta\,e^{\pm i\phi}$
2	± 2	$(15/32\pi)^{1/2}\sin^2\theta\,e^{\pm 2i\phi}$

$$\Phi_{m_\ell}(\phi) = \frac{1}{\sqrt{2\pi}}\,e^{im_\ell\phi}$$

$$\Theta_{\ell m_\ell}(\theta) = \left[\frac{2\ell+1}{2}\frac{(\ell - m_\ell)!}{(\ell + m_\ell)!}\right]^{1/2} P_\ell^{m_\ell}(\theta)$$

where $P_\ell^{m_\ell}(\theta)$ is the associated Legendre polynomial

Table 2.3 Spherical Bessel Functions — Sample Expressions and Limits

$$j_0(kr) = \frac{\sin kr}{kr}$$

$$j_1(kr) = \frac{\sin kr}{(kr)^2} - \frac{\cos kr}{kr}$$

$$j_2(kr) = \frac{3\sin kr}{(kr)^3} - \frac{3\cos kr}{(kr)^2} - \frac{\sin kr}{kr}$$

$$j_\ell(kr) \cong \frac{(kr)^\ell}{1 \cdot 3 \cdot 5 \cdots (2\ell+1)} \qquad kr \to 0$$

$$j_\ell(kr) \cong \frac{\sin(kr - \ell\pi/2)}{kr} \qquad kr \to \infty$$

$$j_\ell(kr) = \left(-\frac{r}{k}\right)^\ell \left(\frac{1}{r}\frac{d}{dr}\right)^\ell j_0(kr)$$

The $\ell(\ell+1)$ term is generally written as an addition to the potential; it is called the "centrifugal potential" and it acts like a potential that keeps the particle away from the origin when $\ell > 0$.

As an example, we consider the case of the infinite spherical well,

$$\begin{aligned} V(r) &= 0 \qquad r < a \\ &= \infty \qquad r > a \end{aligned} \tag{2.61}$$

We require again that $R(r) = 0$ for $r > a$, since the walls of the infinite well are impenetrable. Inside the well, the solution to Equation 2.60 for $V = 0$ can be expressed in terms of the oscillatory functions known as *spherical Bessel functions* $j_\ell(kr)$, some of which are listed in Table 2.3. To find the energy eigenvalues, we proceed exactly as in the one-dimensional problem and apply the continuity condition on ψ at $r = a$. This gives

$$j_\ell(ka) = 0 \tag{2.62}$$

This is in effect a transcendental equation, which must be solved numerically. Tables of the spherical Bessel functions are available that can be consulted to find the zeros for any given value of ℓ.* For example, we consider the case $\ell = 0$. From the tables we find $j_0(x) = 0$ at $x = 3.14, 6.28, 9.42, 12.57$, and so on. For $\ell = 1$, the first few zeros of $j_1(x)$ are at $x = 4.49, 7.73, 10.90, 14.07$. Since $E = \hbar^2k^2/2m$, we can then solve for the allowed values of the energies. Repeating this process for $\ell = 2$, $\ell = 3$, and so on, we would be able to construct a spectrum of the energy states, as is shown in Figure 2.11. As in the case of the Cartesian well, the regularity of the one-dimensional problem is not present. Also, note that the levels are again degenerate—since the energy depends only on ℓ, the wave functions with different m_ℓ values all have the same energy. Thus, in the case of the level with $\ell = 2$, the possible wave functions are $j_2(kr)Y_{22}(\theta, \phi)$,

*M. Abramowitz and I. A. Stegun, *Handbook of Mathematical Functions* (New York: Dover, 1965).

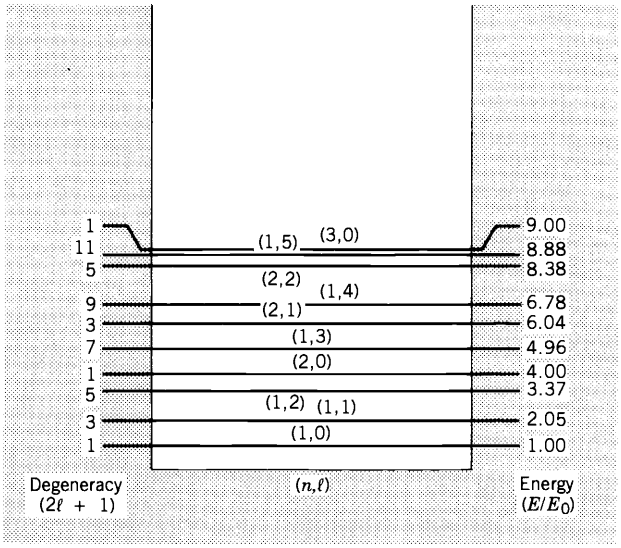


Figure 2.11 Energy levels of a particle confined to a three-dimensional spherical container. The energy is given in units of $E_0 = \hbar^2\pi^2 / 2ma^2$. Compare with the spacings and degeneracies of Figure 2.10. The quantum number n does not arise directly in the solution in this case; it serves to number the states of a given ℓ.

$j_2(kr)Y_{21}(\theta, \phi)$, $j_2(kr)Y_{20}(\theta, \phi)$, $j_2(kr)Y_{2-1}(\theta, \phi)$, and $j_2(kr)Y_{2-2}(\theta, \phi)$, for a fivefold degeneracy. In fact, since m_ℓ is restricted to the values 0, ± 1, $\pm 2, \ldots, \pm \ell$, there are exactly $2\ell + 1$ possible $Y_{\ell m_\ell}$ for a given ℓ, and thus each level has a degeneracy of $2\ell + 1$. (This situation is very similar to the case of electronic orbits in atoms, in which there is also a central potential. The capacity of each atomic subshell contains the factor of $2\ell + 1$, which likewise arises from the m_ℓ degeneracy.)

The probability to locate the particle in a volume dv is given by $|\psi|^2\, dv$, where the volume element was given in Equation 2.17. Such three-dimensional distributions are difficult to represent graphically, so we often consider the radial and angular parts separately. To find the radial probability density, which gives the probability to find the particle between r and $r + dr$ averaged over all angles, we integrate the probability density over θ and ϕ:

$$P(r)\, dr = \int |\psi|^2\, dv$$

$$= r^2 |R(r)|^2\, dr \int \sin\theta\, d\theta \int d\phi\, |Y_{\ell m_\ell}|^2 \tag{2.63}$$

The spherical harmonics $Y_{\ell m_\ell}$ are themselves normalized, so that the integral gives 1, and thus

$$P(r) = r^2 |R(r)|^2 \tag{2.64}$$

Some sample radial probability distributions for the infinite well are shown in Figure 2.12.

The angular dependence of the probability density for any central potential is given by $|Y_{\ell m_\ell}(\theta, \phi)|^2$, some samples of which are illustrated in Figure 2.13.

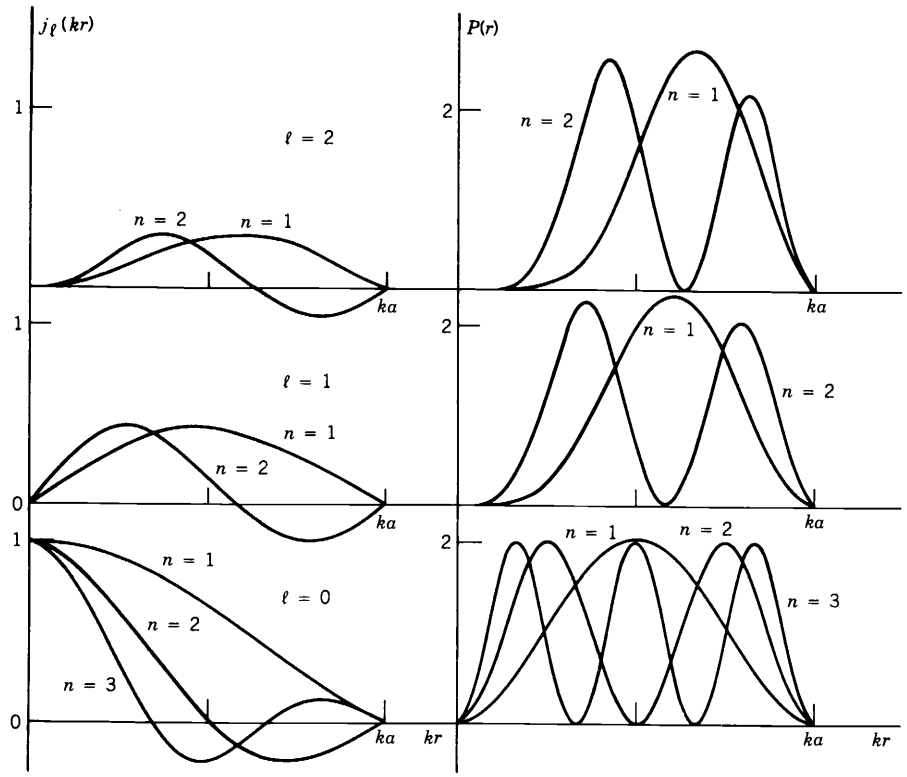


Figure 2.12 The left side shows, for some of the lower energy levels, the unnormalized $j_\ell(kr)$, adjusted so that $j_\ell(ka) = 0$. The right side shows the corresponding normalized radial probability density, r^2R^2. Note that all j_ℓ vanish at the origin except j_0, and that all probability densities vanish at $r = 0$. Also, note how the "centrifugal repulsion" pushes corresponding maxima in $P(r)$ away from the origin as ℓ increases.

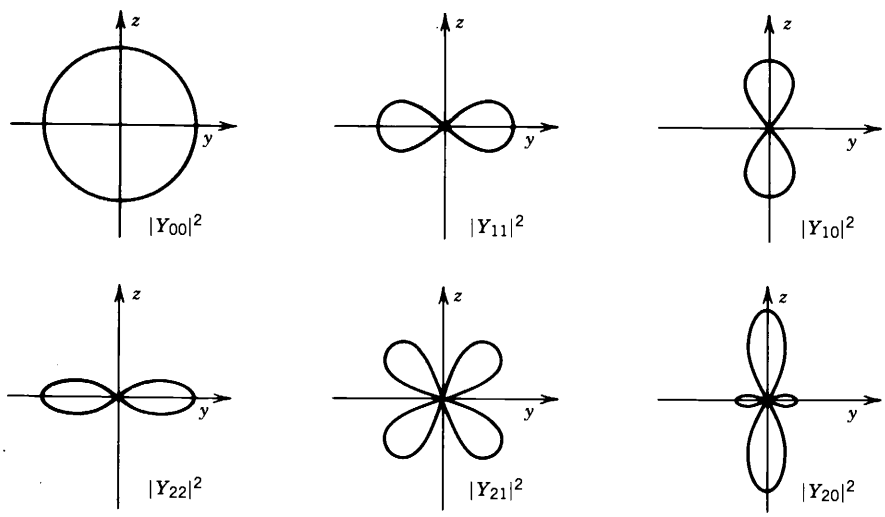


Figure 2.13 Spatial probability distributions resulting from the $Y_{\ell m_\ell}$. The three-dimensional representations can be obtained by rotating each figure about the z axis.

Table 2.4 Sample Radial Wave Functions for Three-Dimensional Simple Harmonic Oscillator

n	ℓ	E_n	$R(r)$
0	0	$\frac{3}{2}\hbar\omega_0$	$(2\alpha^{3/2}/\pi^{1/4})\, e^{-\alpha^2 r^2/2}$
1	1	$\frac{5}{2}\hbar\omega_0$	$(2\alpha^{3/2}\sqrt{2}/\sqrt{3}\,\pi^{1/4})(\alpha r)\, e^{-\alpha^2 r^2/2}$
2	0	$\frac{7}{2}\hbar\omega_0$	$(2\alpha^{3/2}\sqrt{2}/\sqrt{3}\,\pi^{1/4})(\frac{3}{2} - \alpha^2 r^2)\, e^{-\alpha^2 r^2/2}$
2	2	$\frac{7}{2}\hbar\omega_0$	$(4\alpha^{3/2}/\sqrt{15}\,\pi^{1/4})(\alpha^2 r^2)\, e^{-\alpha^2 r^2/2}$
3	1	$\frac{9}{2}\hbar\omega_0$	$(4\alpha^{3/2}/\sqrt{15}\,\pi^{1/4})(\frac{5}{2}\alpha r - \alpha^3 r^3)\, e^{-\alpha^2 r^2/2}$
3	3	$\frac{9}{2}\hbar\omega_0$	$(4\alpha^{3/2}\sqrt{2}/\sqrt{105}\,\pi^{1/4})(\alpha^3 r^3)\, e^{-\alpha^2 r^2/2}$
4	0	$\frac{11}{2}\hbar\omega_0$	$(4\alpha^{3/2}\sqrt{2}/\sqrt{15}\,\pi^{1/4})(\frac{15}{8} - \frac{5}{2}\alpha^2 r^2 + \frac{1}{2}\alpha^4 r^4)\, e^{-\alpha^2 r^2/2}$
4	2	$\frac{11}{2}\hbar\omega_0$	$(4\alpha^{3/2}\sqrt{2}/\sqrt{105}\,\pi^{1/4})(\frac{7}{2}\alpha^2 r^2 - \alpha^4 r^4)\, e^{-\alpha^2 r^2/2}$
4	4	$\frac{11}{2}\hbar\omega_0$	$(8\alpha^{3/2}/3\sqrt{105}\,\pi^{1/4})\, \alpha^4 r^4\, e^{-\alpha^2 r^2/2}$

Note the similarity in form (polynomial × exponential) between these solutions and those of the one-dimensional problem shown in Table 2.1. In this case the polynomials are called Laguerre polynomials. The solutions are discussed in J. L. Powell and B. Crasemann, *Quantum Mechanics* (Reading, MA: Addison-Wesley, 1961), Chapter 7.

The Simple Harmonic Oscillator

We consider a central oscillator potential, $V(r) = \frac{1}{2}kr^2$. The angular part of the solution to the Schrödinger equation is $Y_{\ell m_\ell}(\theta, \phi)$ for all central potentials, so all we need to consider here is the solution to the radial equation. As in the one-dimensional case, the solution can be expressed as the product of an exponential and a finite polynomial. Some representative solutions are listed in Table 2.4, and the corresponding radial probability densities are illustrated in Figure 2.14. The general properties of the one-dimensional solutions are also present in this case: oscillation in the classically allowed region, and exponential decay in the classically forbidden region.

The energy levels are given by

$$E_n = \hbar\omega_0\left(n + \tfrac{3}{2}\right) \tag{2.65}$$

where $n = 0, 1, 2, 3, \ldots$. The energy does not depend on ℓ, but not all ℓ values are permitted. From the mathematical solution of the radial equation, the restrictions on ℓ are as follows: ℓ can be at most equal to n and takes only even or only odd values as n is even or odd. For $n = 5$, the permitted values of ℓ are 1, 3, and 5; for $n = 4$, the values of ℓ are 0, 2, and 4. Since the energies do not depend on m_ℓ either, there is an additional degeneracy of $2\ell + 1$ for each ℓ value. Thus the $n = 5$ level has a degeneracy of $[(2 \times 1 + 1) + (2 \times 3 + 1) + (2 \times 5 + 1)] = 21$, while the $n = 4$ level has a degeneracy of $[(2 \times 0 + 1) + (2 \times 2 + 1) + (2 \times 4 + 1)] = 15$. Figure 2.15 shows some of the energy levels and their degeneracies, which are equal to $\frac{1}{2}(n + 1)(n + 2)$.

The Coulomb Potential

The attractive Coulomb potential energy also has a simple central form, $V(r) = -Ze^2/4\pi\epsilon_0 r$, for the interaction between electrical charges $+Ze$ and $-e$, such as in the case of a single electron in an atom of atomic number Z. The angular

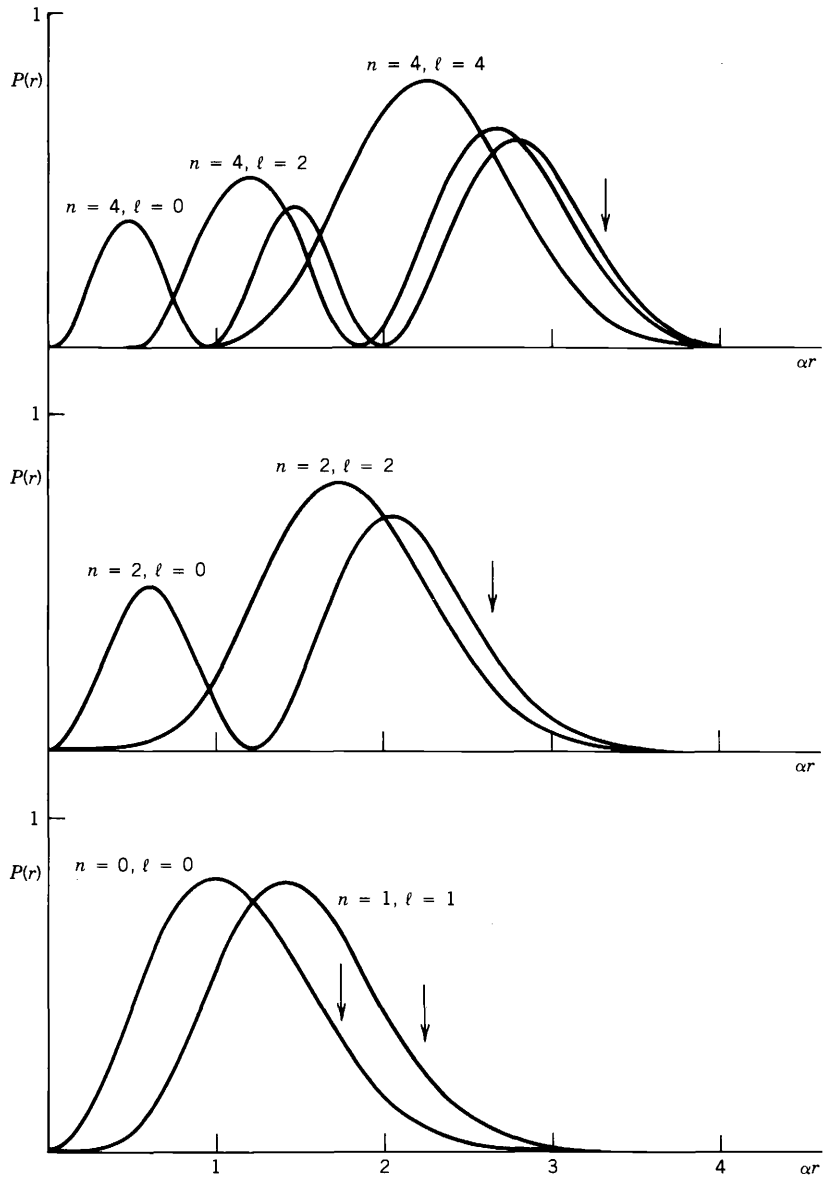


Figure 2.14 Radial probabililty densities for some states of the three-dimensional harmonic oscillator. The vertical arrows mark the classical turning points. As in Figure 2.12, note that $P(r)$ vanishes for $r = 0$ (but note from Table 2.4 that $R(r)$ is nonvanishing at $r = 0$ only for $\ell = 0$). Also note the "centrifugal repulsion" for the larger ℓ values.

part of the wave function is again given by $Y_{\ell m_\ell}(\theta, \phi)$, and some of the radial wave functions $R(r)$ are listed in Table 2.5. The energy levels are $E_n = (-mZ^2e^4/32\pi^2\epsilon_0{}^2\hbar^2n^2)$ and are shown in Figure 2.16; the radial probability density is plotted for several states in Figure 2.17. The relationship between n and ℓ is different from what it was for the oscillator potential: for each level n, the permitted values of ℓ are $0, 1, 2, \ldots, (n-1)$. The total degeneracy of each

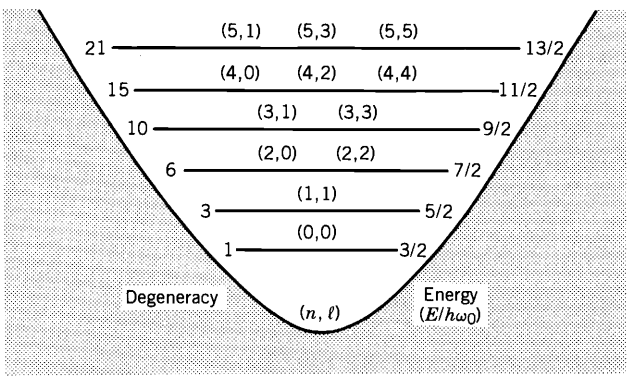


Figure 2.15 Some of the lower energy levels of a particle in a central three-dimensional oscillator potential.

Table 2.5 Coulomb (Hydrogenic) Radial Wave Functions

n	ℓ	$R(r)$
1	0	$2(Z/a_0)^{3/2}\, e^{-Zr/a_0}$
2	0	$(Z/2a_0)^{3/2}(2 - Zr/a_0)\, e^{-Zr/2a_0}$
2	1	$3^{-1/2}(Z/2a_0)^{3/2}(Zr/a_0)\, e^{-Zr/2a_0}$
3	0	$\frac{2}{3}(Z/3a_0)^{3/2}[3 - 2Zr/a_0 + 2(Zr/3a_0)^2]\, e^{-Zr/3a_0}$
3	1	$(4\sqrt{2}/9)(Z/3a_0)^{3/2}(Zr/a_0)(1 - Zr/6a_0)\, e^{-Zr/3a_0}$
3	2	$(2\sqrt{2}/27\sqrt{5})(Z/3a_0)^{3/2}(Zr/a_0)^2\, e^{-Zr/3a_0}$

The radial wave functions have the mathematical form of associated Laguerre polynomials multiplied by exponentials. The Bohr radius a_0 is $4\pi\epsilon_0\hbar^2/me^2$. For a discussion of these solutions, see L. Pauling and E. B. Wilson, *Introduction to Quantum Mechanics* (New York: McGraw-Hill, 1935), Chapter 5.

energy level, including the various ℓ values and the $2\ell + 1$ degeneracy of each, is n^2.

Summary

The mathematical techniques of finding and using solutions to the Schrödinger equation in three dimensions are similar to the techniques we illustrated previously for one-dimensional problems. There are two important new features in the three-dimensional calculations that do not arise in the one-dimensional calculations: (1) The energy levels are *degenerate*—several different wave functions can have the same energy. The degeneracies will have the same effect in the nuclear shell model that the ℓ and m_ℓ degeneracies of the energy levels of the Coulomb potential have in the atomic shell model—they tell us how many particles can occupy each energy level. (2) When the potential depends only on r (not on θ or ϕ), the wave functions can be assigned a definite angular momentum quantum number ℓ. These new features will have important consequences when we discuss

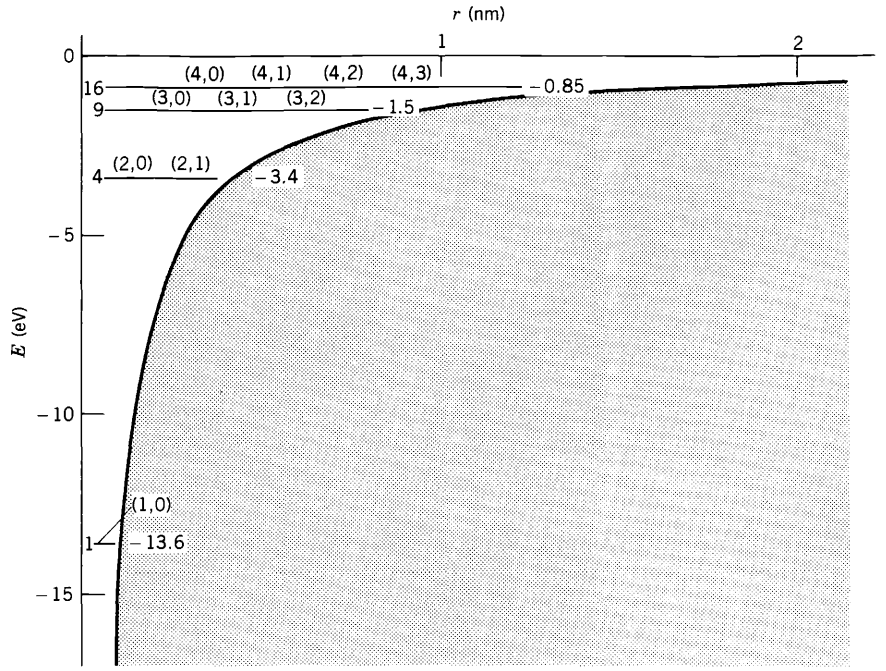


Figure 2.16 The lower energy levels in a Coulomb potential, shown for $Z = 1$ (hydrogen atom). The states are labeled with (n, ℓ); the degeneracies are indicated on the left and the energy values on the right.

nuclear models in Chapter 5. The behavior of angular momentum in quantum theory is discussed in the next section.

2.5 QUANTUM THEORY OF ANGULAR MOMENTUM

In solutions of the Schrödinger equation for three-dimensional problems, the quantum number ℓ plays a prominent role. In atomic physics, for example, it serves to label different electron wave functions and to tell us something about the spatial behavior of the wave functions. This *angular momentum quantum number* has the same function in all three-dimensional problems involving central potentials, where $V = V(r)$.

In classical physics, the angular momentum $\boldsymbol{\ell}$ of a particle moving with linear momentum $\boldsymbol{p}$ at a location $\boldsymbol{r}$ from a reference point is defined as

$$\boldsymbol{\ell} = \boldsymbol{r} \times \boldsymbol{p} \tag{2.66}$$

In quantum mechanics, we can evaluate the expectation value of the angular momentum by analogy with Equation 2.10. We first consider the magnitude of the angular momentum, and for this purpose it is simplest to calculate ℓ^2. We must first find a quantum mechanical *operator* for ℓ^2, as we discussed in Section 2.2. This can be done simply by replacing the components of $\boldsymbol{p}$ with their operator equivalents: $p_x = -i\hbar\,\partial/\partial x$, $p_y = -i\hbar\,\partial/\partial y$, $p_z = -i\hbar\,\partial/\partial z$. Evaluating the cross product then gives terms of the form $\ell_x = yp_z - zp_y$, and finally computing $\langle \ell^2 \rangle = \langle \ell_x^2 + \ell_y^2 + \ell_z^2 \rangle$ gives the remarkably simple result, which is

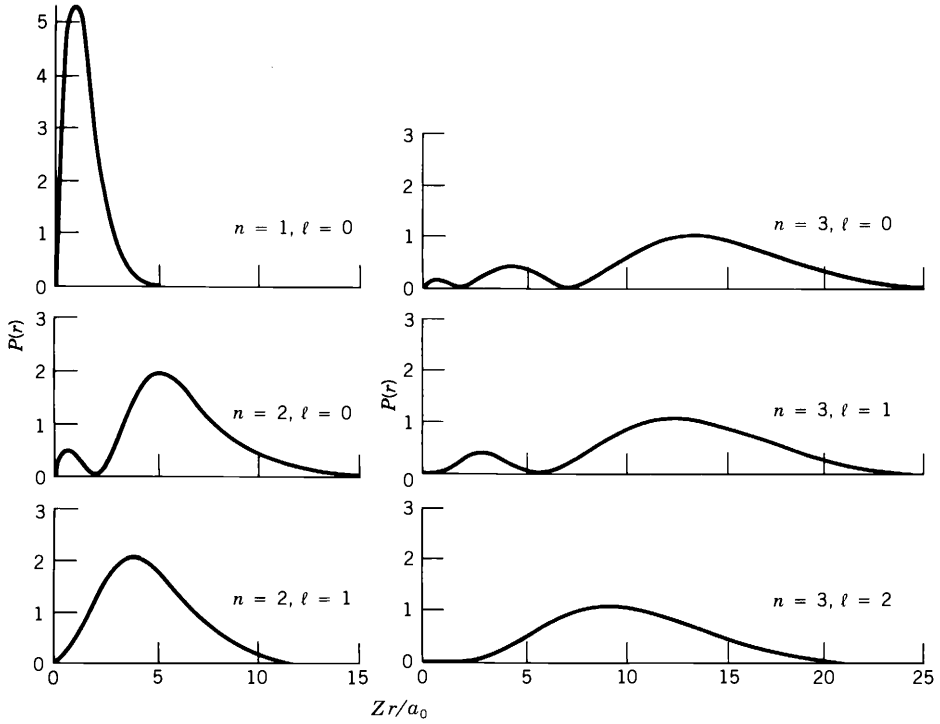


Figure 2.17 Radial probability distributions for a particle in a Coulomb potential (hydrogenic atom). The probability vanishes at $r = 0$, but as before the $\ell = 0$ wave functions do not. This property becomes especially important for phenomena that depend on the overlap of atomic wave functions with the nucleus — only $\ell = 0$ states contribute substantially to such phenomena (electron capture, hyperfine structure, etc.). Why doesn't the "centrifugal repulsion" appear to occur in this case?

independent of the form of $R(r)$,

$$\langle \ell^2 \rangle = \hbar^2 \ell(\ell + 1) \tag{2.67}$$

That is, whenever we have a central potential, which gives a wave function $R(r)Y_{\ell m_\ell}(\theta, \phi)$, the magnitude of the angular momentum is fixed at the value given by Equation 2.67; *the angular momentum is a constant of the motion* (as it is in classical physics for central potentials). The atomic substates with a given ℓ value are labeled using *spectroscopic notation*; we use the same spectroscopic notation in nuclear physics: s for $\ell = 0$, p for $\ell = 1$, and so on. These are summarized in Table 2.6.

When we now try to find the direction of ℓ, we run into a barrier imposed by the uncertainty principle: quantum mechanics permits us to know exactly only

Table 2.6 Spectroscopic Notation

ℓ value	0	1	2	3	4	5	6
Symbol	s	p	d	f	g	h	i

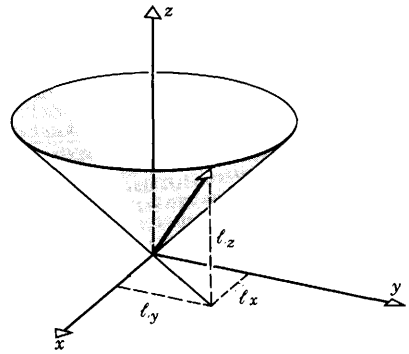


Figure 2.18 The vector ℓ precesses rapidly about the z axis, so that ℓ_z stays constant, but ℓ_x and ℓ_y are variable.

one component of ℓ at a time. Once we determine the value of one component, the other two components are completely indeterminate. (This is a fundamental limitation, and no amount of trickery can get us around it. It is the very act of measuring one component that *makes* the other two indeterminate. When we measure ℓ_x, we force ℓ_y and ℓ_z into indeterminacy; when we then measure ℓ_y for the same system, our previous knowledge of ℓ_x is destroyed as ℓ_x is now forced into indeterminacy.) By convention, we usually choose the z component of ℓ to be determined, and computing $\langle \ell_z \rangle$ as described above,

$$\langle \ell_z \rangle = \hbar m_\ell \tag{2.68}$$

where $m_\ell = 0, \pm 1, \pm 2, \ldots, \pm \ell$. Notice that $|\langle \ell_z \rangle| < |\ell| = \hbar\sqrt{\ell(\ell+1)}$—the z component of the vector is always less than its length. If $|\langle \ell_z \rangle| = |\ell|$ were permitted, then we would have exact knowledge of all three components of ℓ (ℓ_x and ℓ_y would be zero if ℓ were permitted to align with the z axis). The conventional vector representation of this indeterminacy is shown in Figure 2.18—ℓ rotates or precesses about the z axis keeping ℓ_z fixed but varying ℓ_x and ℓ_y.

The complete description of an electronic state in an atom requires the introduction of a new quantum number, the *intrinsic angular momentum* or *spin*. For the electron, the spin quantum number is $s = \frac{1}{2}$. The spin can be treated as an angular momentum (although it cannot be represented in terms of classical variables, because it has no classical analog). Thus

$$\langle \boldsymbol{s}^2 \rangle = \hbar^2 s(s+1) \tag{2.69}$$

$$\langle s_z \rangle = \hbar m_s \qquad \left(m_s = \pm \tfrac{1}{2}\right) \tag{2.70}$$

It is often useful to imagine the spin as a vector $\boldsymbol{s}$ with possible z components $\pm \frac{1}{2}\hbar$.

Nucleons, like electrons, have spin quantum numbers of $\frac{1}{2}$. A nucleon moving in a central potential with orbital angular momentum ℓ and spin $\boldsymbol{s}$ has a *total angular momentum*

$$\boldsymbol{j} = \boldsymbol{\ell} + \boldsymbol{s} \tag{2.71}$$

The total angular momentum $\boldsymbol{j}$ behaves in a manner similar to ℓ and $\boldsymbol{s}$:

$$\langle \boldsymbol{j}^2 \rangle = \hbar^2 j(j+1) \tag{2.72}$$

$$\langle j_z \rangle = \langle \ell_z + s_z \rangle = \hbar m_j \tag{2.73}$$

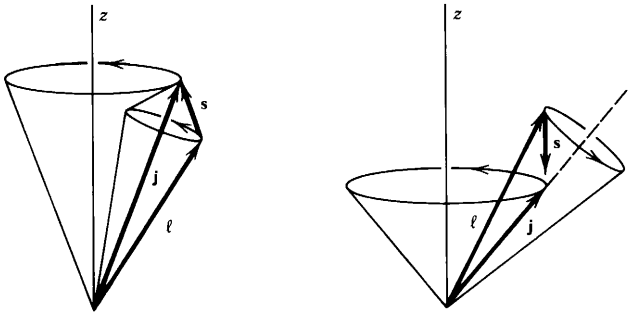


Figure 2.19 The coupling of orbital angular momentum ℓ to spin angular momentum s giving total angular momentum j. (*a*) Coupling giving $j = \ell + \frac{1}{2}$. The vectors ℓ and s have definite lengths, as does j. The combined ℓ and s vectors rotate or precess about the direction of j; in this coupling the z components ℓ_z and s_z thus do not have definite values. The vector j precesses about the z direction so that j_z has a definite value. (*b*) The similar case of $j = \ell - \frac{1}{2}$. In interpreting both figures, keep in mind that all such representations of vectors governed by the rules of quantum mechanics are at best symbolic and at worst misleading.

where $m_j = -j, -j+1, \ldots, j-1, j$ and where j is the total angular momentum quantum number. From Equations 2.68, 2.70, and 2.73 it is apparent that

$$m_j = m_\ell + m_s = m_\ell \pm \tfrac{1}{2} \tag{2.74}$$

Since m_ℓ is always an integer, m_j must be half-integral ($\pm \frac{1}{2}, \pm \frac{3}{2}, \pm \frac{5}{2}, \ldots$) and thus j must be half-integral. The vector coupling of Equation 2.71 suggests only two possible values for j: $\ell + \frac{1}{2}$ or $\ell - \frac{1}{2}$, which are illustrated in Figure 2.19.

Usually, we indicate the j value as a subscript in spectroscopic notation. Thus, for $\ell = 1$ (p states), there are two possible j values: $\ell + \frac{1}{2} = \frac{3}{2}$ and $\ell - \frac{1}{2} = \frac{1}{2}$. We would indicate these states as $p_{3/2}$ and $p_{1/2}$. When there is an additional quantum number, such as a principal quantum number n (or perhaps just an index which counts the states in order of increasing energy), we indicate it as $2p_{3/2}$, $3p_{3/2}$, and so on.

In atoms, it is often useful for us to picture the electrons as moving in well defined orbits with definite ℓ and j. It is not at all obvious that a similar picture is useful for nucleons inside the nucleus, and thus it is not clear that ℓ and j will be useful labels. We discuss this topic in detail when we consider the nuclear shell model in Chapter 5.

2.6 PARITY

The parity operation causes a reflection of all of the coordinates through the origin: $\boldsymbol{r} \to -\boldsymbol{r}$. In Cartesian coordinates, this means $x \to -x$, $y \to -y$, $z \to -z$; in spherical coordinates, $r \to r$, $\theta \to \pi - \theta$, $\phi \to \phi + \pi$. If a system is left unchanged by the parity operation, then we expect that none of the observable properties should change as a result of the reflection. Since the values we measure for the observable quantities depend on $|\psi|^2$, then we have the following reasonable assertion:

$$\text{If } V(\boldsymbol{r}) = V(-\boldsymbol{r}), \quad \text{then } |\psi(\boldsymbol{r})|^2 = |\psi(-\boldsymbol{r})|^2.$$

This assertion, whose reverse is also true, has two important consequences for our work in nuclear physics:

1. If $|\psi(\boldsymbol{r})|^2 = |\psi(-\boldsymbol{r})|^2$ then $\psi(-\boldsymbol{r}) = \pm\psi(\boldsymbol{r})$. That is, the parity operation has either of two effects on a wave function. The case $\psi(-\boldsymbol{r}) = +\psi(\boldsymbol{r})$ is known as *positive* or *even* parity, while the case $\psi(-\boldsymbol{r}) = -\psi(\boldsymbol{r})$ is *negative* or *odd* parity. If the potential $V(\boldsymbol{r})$ is left unchanged by the parity operation, then the resulting stationary-state wave functions must be of either even or odd parity. Mixed-parity wave functions are not permitted. Recall our solutions for the one-dimensional harmonic oscillator. The potential $\frac{1}{2}kx^2$ is certainly invariant with respect to the parity operation $x \to -x$. The wave functions listed in Table 2.1 have either only odd powers of x, and therefore odd parity, or only even powers of x, and therefore even parity. Polynomials mixing odd and even powers do not occur. Also, review the solutions for the finite potential well. Since the well lies between $x = +a/2$ and $x = -a/2$, the potential is symmetric with respect to the parity operation: $V(x) = V(-x)$. Notice the solutions illustrated in Figure 2.8. For some of the solutions, $\psi(-x) = \psi(x)$ and their parity is even; the other solutions have $\psi(-x) = -\psi(x)$ and odd parity.

 In three dimensions, the parity operation applied to the $Y_{\ell m_\ell}$ gives a phase $(-1)^\ell$:

$$Y_{\ell m_\ell}(\pi - \theta, \phi + \pi) = (-1)^\ell Y_{\ell m_\ell}(\theta, \phi) \tag{2.75}$$

 Central potentials, which depend only on the magnitude of $\boldsymbol{r}$, are thus invariant with respect to parity, and their wave functions have definite parity, odd if ℓ is odd and even if ℓ is even.

 The wave function for a system of many particles is formed from the product of the wave functions for the individual particles. The parity of the combined wave function will be even if the combined wave function represents any number of even-parity particles or an even number of odd-parity particles; it will be odd if there is an odd number of odd-parity particles. Thus nuclear states can be assigned a definite parity, odd or even. This is usually indicated along with the total angular momentum for that state, as for example, $\frac{5}{2}^+$ or $\frac{3}{2}^-$. In Chapter 10 we will discuss how the parity of a state can be determined experimentally.

2. The second consequence of the parity rule is based on its converse. If we find a system for which $|\psi(\boldsymbol{r})|^2 \neq |\psi(-\boldsymbol{r})|^2$, then we must conclude that $V(\boldsymbol{r}) \neq V(-\boldsymbol{r})$; that is, the system is *not* invariant with respect to parity. In 1957 it was discovered that certain nuclear processes (β decays) gave observable quantities whose measured values did not respect the parity symmety. On the other hand, no evidence has yet been obtained that either the strong nuclear interaction or the electromagnetic interaction violate parity. The establishment of parity violation in β decay was one of the most dramatic discoveries in nuclear physics and has had profound influences on the development of theories of fundamental interactions between particles. A description of these experiments is given in Section 9.9.

2.7 QUANTUM STATISTICS

When we group several particles together to make a larger quantum system (several nucleons in a nucleus, several electrons in an atom, several atoms in a molecule) a new quantum effect arises if the particles are indistinguishable from one another. Let us consider the case of two particles, for example, the two electrons in a helium atom. Suppose one electron is described by coordinates $\boldsymbol{r}_1$ and is in the state ψ_A, while the other electron is described by coordinates $\boldsymbol{r}_2$ and is in the state ψ_B. The combined wave function is the product of the two component wave functions; thus $\psi = \psi_A(\boldsymbol{r}_1)\psi_B(\boldsymbol{r}_2)$. Now suppose the two electrons are interchanged so that the new wave function is $\psi' = \psi_B(\boldsymbol{r}_1)\psi_A(\boldsymbol{r}_2)$. Is there any measurement we could do to detect whether this interchange had taken place?

If the electrons are truly *indistinguishable*, the answer to this question must be no. There is no *observational scheme* for distinguishing the "first electron" from the "second electron." Thus we have a result that is somewhat similar to our result for the parity operation: *Probability densities must be invariant with respect to exchange of identical particles.* That is, the exchanged wave function ψ_{21} can at most differ only in sign from the original wave function ψ_{12}. We therefore have two cases. If the sign does not change upon exchange of the particles, we have a *symmetric* wave function; for symmetric wave functions, $\psi_{12} = \psi_{21}$. If the exchange changes the sign, we have an *antisymmetric* wave function, for which $\psi_{21} = -\psi_{12}$. *All combined wave functions representing identical particles must be either completely symmetric or completely antisymmetric.* No "mixed symmetry" wave functions are allowed.

When we turn to our laboratory experiments to verify these assertions, we find a further classification to which there are no known exceptions: all particles with integral spins $(0, 1, 2, \ldots)$ have symmetric combined wave functions, while all particles with half-integral spins $(\frac{1}{2}, \frac{3}{2}, \frac{5}{2}, \ldots)$ have antisymmetric combined wave functions.

The above two-particle functions ψ and ψ' will not do for combined wave functions because they are neither symmetric nor antisymmetric. That is, ψ' does not at all look like either ψ or $-\psi$. Instead, consider the following combined wave function:

$$\psi_{12} = \frac{1}{\sqrt{2}}[\psi_A(\boldsymbol{r}_1)\psi_B(\boldsymbol{r}_2) \pm \psi_B(\boldsymbol{r}_1)\psi_A(\boldsymbol{r}_2)] \tag{2.76}$$

If we choose the plus sign, then the combined wave function is symmetric with respect to interchange of the particles. If we choose the minus sign then the result is an antisymmetric wave function. The factor of $1/\sqrt{2}$ ensures that the resulting combination is normalized (assuming that each of the component wave functions is itself normalized).

A special case arises when we have identical quantum states A and B. (We can regard A and B as representing a set of quantum numbers.) When A is the same as B, the antisymmetric combination wave function vanishes identically, and so its probability density is always zero. *The probability to find two identical particles of half-integral spin in the same quantum state must always vanish.* This is of course

just the *Pauli exclusion principle*, which determines why atomic subshells fill in a certain way. This vanishing of the antisymmetric wave function is the mathematical basis of the Pauli principle. No such vanishing occurs for the symmetric combination, so there is nothing to prevent identical particles of integral spin from occupying the same quantum state.

Later in this text, we apply the Pauli principle to nucleons and show its importance in understanding the nuclear shell model. We also construct some simple antisymmetric wave functions for the quarks that make up nucleons and other similar particles.

2.8 TRANSITIONS BETWEEN STATES

A true stationary state lives forever. The expectation values of physical observables, computed from the wave function of a stationary state, do not change with time. In particular, the expectation value of the energy is constant in time. The energy of the state is precisely determined, and the uncertainty in the energy,

$$\Delta E = \sqrt{\langle E^2 \rangle - \langle E \rangle^2} \tag{2.77}$$

vanishes, because $\langle E^2 \rangle = \langle E \rangle^2$ for this case. The Heisenberg relationship, $\Delta E \, \Delta t \geq \hbar/2$, then implies that $\Delta t = \infty$. Thus a state with an exact energy lives forever; its lifetime against decay (to lower excited states, for example) is infinite.

Now suppose our system is subject to a weak perturbing potential V', in addition to the original potential V. In the absence of V', we can solve the Schrödinger equation for the potential V and find a set of eigenstates ψ_n and corresponding eigenvalues E_n. If we now include the weak additional potential V', we find that the states are approximately, but not exactly, the previous eigenstates ψ_n of V. This weak additional potential permits the system to make transitions between the "approximate" eigenstates ψ_n. Thus, under the interaction with a weak electromagnetic field, a hydrogen atom can make transitions, such as 2p $\rightarrow$ 1s or 3d $\rightarrow$ 2p. We still describe the various levels as if they were eigenstates of the system.

Even though a system may make a transition from an initial energy state E_i to a final state E_f, energy must be conserved. Thus the total decay energy must be constant. If the final state E_f is of lower energy than E_i, the energy difference $E_i - E_f$ must appear as radiation emitted in the decay. In transitions between atomic or nuclear excited states, a photon is emitted to carry the energy $E_i - E_f$.

A nonstationary state has a nonzero energy uncertainty ΔE. This quantity is often called the "width" of the state and is usually represented by Γ. The *lifetime* τ of this state (the mean or average time it lives before making a transition to a lower state) can be estimated from the uncertainty principle by associating τ with the time Δt during which we are permitted to carry out a measurement of the energy of the state. Thus $\tau \simeq \hbar/\Gamma$. The *decay probability* or *transition probability* λ (the number of decays per unit time) is inversely related to the mean lifetime τ:

$$\lambda = \frac{1}{\tau} \tag{2.78}$$

It would be very useful to have a way to calculate λ or τ directly from the nuclear wave functions. We can do this if we have knowledge of (1) the initial

and final wave functions ψ_i and ψ_f, which we regard as approximate stationary states of the potential V; and (2) the interaction V' that causes the transition between the states. The calculation of λ is too detailed for this text, but can be found in any advanced text on quantum mechanics. We will merely state the result, which is known as *Fermi's Golden Rule*:

$$\lambda = \frac{2\pi}{\hbar} |V'_{fi}|^2 \rho(E_f) \tag{2.79}$$

The quantity V'_{fi} has the form of an expectation value:

$$V'_{fi} = \int \psi_f^* V' \psi_i \, dv \tag{2.80}$$

Notice again the ordering of the states f and i in the integral. The integral V'_{fi} is sometimes called the *matrix element* of the transition operator V'. This terminology comes from an alternative formulation of quantum mechanics based on matrices instead of differential equations. Be sure to take special notice that *the decay probability depends on the square of the transition matrix element.*

The quantity $\rho(E_f)$ is known as the *density of final states*. It is the number of states per unit energy interval at E_f, and it must be included for the following reason: if the final state E_f is a single isolated state, then the decay probability will be much smaller than it would be in the case that there are many, many states in a narrow band near E_f. If there is a large density of states near E_f, there are more possible final states that can be reached by the transition and thus a larger transition probability. The density of final states must be computed based on the type of decay that occurs, and we shall consider examples when we discuss β decay, γ decay, and scattering cross sections.

REFERENCES FOR ADDITIONAL READING

The following introductory (sophomore-junior) modern physics texts provide background material necessary for the study of quantum mechanics: A. Beiser, *Concepts of Modern Physics*, 3rd ed. (New York: McGraw-Hill, 1981); K. S. Krane, *Modern Physics* (New York: Wiley, 1983); P. A. Tipler, *Modern Physics* (New York: Worth, 1978); R. T. Weidner and R. L. Sells, *Elementary Modern Physics*, 3rd ed. (Boston: Allyn and Bacon, 1980).

Quantum mechanics references at about the same level as the present text are listed below: R. Eisberg and R. Resnick, *Quantum Physics of Atoms, Molecules, Solids, Nuclei, and Particles*, 2nd ed. (New York: Wiley, 1985); A. P. French and E. F. Taylor, *An Introduction to Quantum Physics* (New York: Norton, 1978); R. B. Leighton, *Principles of Modern Physics* (New York: McGraw-Hill, 1969); D. S. Saxon, *Elementary Quantum Mechanics* (San Francisco: Holden-Day, 1968).

Advanced quantum texts, which can be consulted to find more detailed discussions of topics discussed only briefly in this text, are the following: C. Cohen-Tannoudji, B. Diu, and F. Laloë, *Quantum Mechanics* (New York: Wiley-Interscience, 1977); D. Park, *Introduction to the Quantum Theory*, 2nd ed. (New York: McGraw-Hill, 1974); E. Merzbacher, *Quantum Mechanics*, 2nd ed. (New York: Wiley, 1970).

PROBLEMS

1. Derive Equation 2.37 and plot the transmission coefficient as a function of the energy E of the incident particle. Comment on the behavior of T.
2. Derive Equation 2.39 and plot the transmission coefficient as a function of E.
3. Solve the Schrödinger equation for the following potential:

$$\begin{aligned} V(x) &= \infty & x &< 0 \\ &= -V_0 & 0 &< x < a \\ &= 0 & x &> a \end{aligned}$$

 Here V_0 is positive and solutions are needed for energies $E > 0$. Evaluate all undetermined coefficients in terms of a single common coefficient, but do not attempt to normalize the wave function. Assume particles are incident from $x = -\infty$.
4. Find the number of bound states and their energies in the finite one-dimensional square well when $P = 10$.
5. Find the solution to the "half" harmonic oscillator:

$$\begin{aligned} V(x) &= \infty & x &< 0 \\ &= \tfrac{1}{2}kx^2 & x &> 0 \end{aligned}$$

 Compare the energy values and wave functions with those of the full harmonic oscillator. Why are some of the full solutions present and some missing in the "half" problem?
6. For the ground state and first two excited states of the one-dimensional simple harmonic oscillator, find the probability for the particle to be beyond the classical turning points.
7. (a) For the ground state of the one-dimensional simple harmonic oscillator, evaluate $\langle x \rangle$ and $\langle x^2 \rangle$.
 (b) Find $\Delta x = [\langle x^2 \rangle - \langle x \rangle^2]^{1/2}$.
 (c) Without carrying out any additional calculations, evaluate $\langle p_x \rangle$ and $\langle p_x^2 \rangle$. (*Hint:* Find $\langle p_x^2/2m \rangle$.)
 (d) Evaluate Δp_x and the product $\Delta x \cdot \Delta p_x$. A wave packet with this shape (called a Gaussian shape) is known as a "minimum-uncertainty" wave packet. Why?
8. (a) Find the wave functions and energy levels for a particle confined to a two-dimensional rectangular box, with

$$\begin{aligned} V(x, y) &= 0 & -a \le x \le +a, -b \le y \le +b \\ &= \infty & |x| > a, |y| > b \end{aligned}$$

 (b) Make a diagram similar to Figure 2.10 showing the levels and degeneracies for $b = a$ and for $b = 2a$.
9. Continue Figure 2.10 upward to $50E_0$.
10. Continue Figure 2.11 upward to $20E_0$.

11. Carry out the separation procedure necessary to obtain the solution to Equation 2.54.

12. Show that the first four radial wave functions listed in Table 2.4 are solutions to the Schrödinger equation corresponding to the proper value of the energy, and also show that they are normalized.

13. Find the solutions to the one-dimensional infinite square well when the potential extends from $-a/2$ to $+a/2$ instead of from 0 to $+a$. Is the potential invariant with respect to parity? Are the wave functions? Discuss the assignment of odd and even parity to the solutions.

14. Find the angle between the angular momentum vector $\boldsymbol{\ell}$ and the z axis for all possible orientations when $\ell = 3$.

15. (a) What are the possible values of j for f states?
(b) What are the corresponding m_j?
(c) How many total m_j states are there?
(d) How many states would there be if we instead used the labels m_ℓ and m_s?

16. A combined wave function representing the total spin S of three electrons can be represented as $\psi = \psi_1(m_s)\psi_2(m_s)\psi_3(m_s)$ where $m_s = \pm \frac{1}{2}$ for a spin-$\frac{1}{2}$ electron. (a) List all such possible wave functions and their total projection M_S. (b) Identify the number of M_S values with the number of different values of the total spin S. (Some values of S may occur more than once.) (c) Draw simple vector diagrams showing how the different couplings of $\boldsymbol{s}_1$, $\boldsymbol{s}_2$, and $\boldsymbol{s}_3$ can lead to the deduced number and values of S. (*Hint:* First couple two of the spins, and then couple the third to the possible resultants of the first two.) (d) In the coupling of four electrons, give the possible values of S and their multiplicity, and show that the number of M_S states agrees with what would be expected from tabulating the possible wave functions.

3

NUCLEAR PROPERTIES

Like many systems governed by the laws of quantum mechanics, the nucleus is a somewhat enigmatic and mysterious object whose properties are much more difficult to characterize than are those of macroscopic objects. The list of instructions needed to build an exact replica of a French colonial house or a '57 Chevy is relatively short; the list of instructions necessary to characterize all of the mutual interactions of the 50 nucleons in a medium weight nucleus could contain as many as 50! or about 10^{64} terms! We must therefore select a different approach and try to specify the overall characteristics of the entire nucleus. Are there a few physical properties that can be listed to give an adequate description of any nucleus?

To a considerable extent, we can describe a nucleus by a relatively small number of parameters: electric charge, radius, mass, binding energy, angular momentum, parity, magnetic dipole and electric quadrupole moments, and energies of excited states. These are the *static properties* of nuclei that we consider in this chapter. In later chapters we discuss the *dynamic properties* of nuclei, including decay and reaction probabilities. To understand these static and dynamic properties in terms of the interaction between individual nucleons is the formidable challenge that confronts the nuclear physicist.

3.1 THE NUCLEAR RADIUS

Like the radius of an atom, the radius of a nucleus is not a precisely defined quantity; neither atoms nor nuclei are solid spheres with abrupt boundaries. Both the Coulomb potential that binds the atom and the resulting electronic charge distribution extend to infinity, although both become negligibly small at distances far beyond the atomic radius (10^{-10} m). What is required is an "operational definition" of what we are to take as the value of the atomic radius. For instance, we might define the atomic radius to be the largest mean radius of the various electronic states populated in an atom. Such a property would be exceedingly difficult to measure, and so more practical definitions are used, such as the spacing between atoms in ionic compounds containing the atom of interest. This also leads to some difficulties since we obtain different radii for an atom when it is in different compounds or in different valence states.

For nuclei, the situation is better in some aspects and worse in others. As we will soon discuss, the density of nucleons and the nuclear potential have a similar spatial dependence—relatively constant over short distances beyond which they drop rapidly to zero. It is therefore relatively natural to characterize the nuclear shape with two parameters: the mean radius, where the density is half its central value, and the "skin thickness," over which the density drops from near its maximum to near its minimum. (In Section 5 of this chapter, we discuss a third parameter, which is necessary to characterize nuclei whose shape is not spherical.)

The problems we face result from the difficulty in determining just what it is that the distribution is describing; the radius that we measure depends on the kind of experiment we are doing to measure the nuclear shape. In some experiments, such as high-energy electron scattering, muonic X rays, optical and X-ray isotope shifts, and energy differences of mirror nuclei, we measure the Coulomb interaction of a charged particle with the nucleus. These experiments would then determine the *distribution of nuclear charge* (primarily the distribution of protons but also involving somewhat the distribution of neutrons, because of their internal structure). In other experiments, such as Rutherford scattering, α decay, and pionic X rays, we measure the strong nuclear interaction of nuclear particles, and we would determine the distribution of nucleons, called the *distribution of nuclear matter*.

The Distribution of Nuclear Charge

Our usual means for determining the size and shape of an object is to examine the radiation scattered from it (which is, after all, what we do when we look at an object or take its photograph). To see the object and its details, the wavelength of the radiation must be smaller than the dimensions of the object; otherwise the effects of diffraction will partially or completely obscure the image. For nuclei, with a diameter of about 10 fm, we require $\lambda \lesssim 10$ fm, corresponding to $p \gtrsim 100$ MeV/c. Beams of electrons with energies 100 MeV to 1 GeV can be produced with high-energy accelerators, such as the Stanford linear accelerator, and can be analyzed with a precise spectrometer to select only those electrons that are elastically scattered from the selected nuclear target. Figure 3.1 shows an example of the results of such an experiment. The first minimum in the diffractionlike pattern can clearly be seen; for diffraction by a circular disk of diameter D, the first minimum should appear at $\theta = \sin^{-1}(1.22\lambda/D)$, and the resulting estimates for the nuclear radii are 2.6 fm for ^{16}O and 2.3 fm for ^{12}C. These are, however, only rough estimates because potential scattering is a three-dimensional problem only approximately related to diffraction by a two-dimensional disk.

Figure 3.2 shows the results of elastic scattering from a heavy nucleus, ^{208}Pb. Several minima in the diffractionlike pattern can be seen. These minima do not fall to zero like diffraction minima seen with light incident on an opaque disk, because the nucleus does not have a sharp boundary.

Let us try to make this problem more quantitative. The initial electron wave function is of the form $e^{i\boldsymbol{k}_i \cdot \boldsymbol{r}}$, appropriate for a free particle of momentum $\boldsymbol{p}_i = \hbar \boldsymbol{k}_i$. The scattered electron can also be regarded as a free particle of momentum $\boldsymbol{p}_f = \hbar \boldsymbol{k}_f$ and wave function $e^{i\boldsymbol{k}_f \cdot \boldsymbol{r}}$. The interaction $V(r)$ converts the initial wave into the scattered wave, and according to Equation 2.80 the probabil-

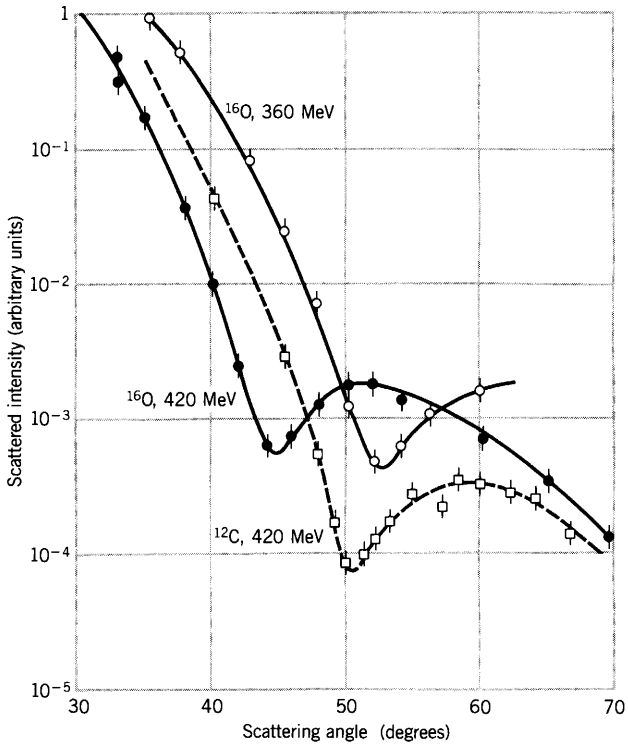


Figure 3.1 Electron scattering from ^{16}O and ^{12}C. The shape of the cross section is somewhat similar to that of diffraction patterns obtained with light waves. The data come from early experiments at the Stanford Linear Accelerator Center (H. F. Ehrenberg et al., *Phys. Rev.* **113**, 666 (1959)).

ity for the transition will be proportional to the square of the quantity

$$F(\boldsymbol{k}_i, \boldsymbol{k}_f) = \int \psi_f^* V(r) \psi_i \, dv \tag{3.1}$$

$$F(\boldsymbol{q}) = \int e^{i\boldsymbol{q}\cdot\boldsymbol{r}} V(r) \, dv \tag{3.2}$$

apart from a normalization constant, which is chosen so that $F(0) = 1$. Here $\boldsymbol{q} = \boldsymbol{k}_i - \boldsymbol{k}_f$, which is essentially the momentum change of the scattered electron. The interaction $V(r)$ depends on the nuclear charge density $Ze\rho_e(\boldsymbol{r}')$, where $\boldsymbol{r}'$ is a coordinate describing a point in the nuclear volume and ρ_e gives the distribution of nuclear charge. That is, as indicated in Figure 3.3, an electron located at $\boldsymbol{r}$ feels a potential energy due to the element of charge dQ located at $\boldsymbol{r}'$:

$$\begin{aligned} dV &= -\frac{e\,dQ}{4\pi\epsilon_0|\boldsymbol{r} - \boldsymbol{r}'|} \\ &= -\frac{Ze^2\rho_e(\boldsymbol{r}')\,dv'}{4\pi\epsilon_0|\boldsymbol{r} - \boldsymbol{r}'|} \end{aligned} \tag{3.3}$$

To find the complete interaction energy $V(r)$, we sum over all of the contribu-

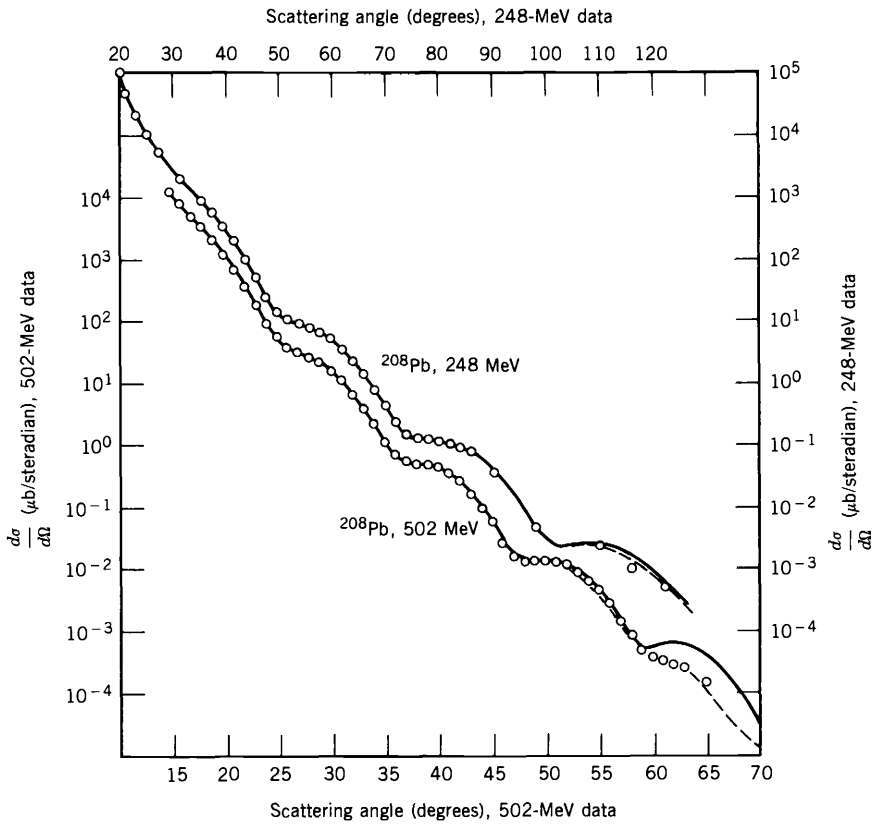


Figure 3.2 Elastic scattering of electrons from ^{208}Pb. Note the different vertical and horizontal scales for the two energies. This also shows diffractionlike behavior, but lacks sharp minima. (J. Heisenberg et al., *Phys. Rev. Lett.* **23**, 1402 (1969).)

tions dQ within the nucleus:

$$V(r) = -\frac{Ze^2}{4\pi\epsilon_0}\int \frac{\rho_e(\boldsymbol{r}')\,dv'}{|\boldsymbol{r}-\boldsymbol{r}'|} \tag{3.4}$$

Writing $\boldsymbol{q}\cdot\boldsymbol{r} = qr\sin\theta$ in Equation 3.2 and integrating over $\boldsymbol{r}$, the properly normalized result is

$$F(\boldsymbol{q}) = \int e^{i\boldsymbol{q}\cdot\boldsymbol{r}'}\rho_e(\boldsymbol{r}')\,dv' \tag{3.5}$$

and if $\rho_e(\boldsymbol{r}')$ depends only on the magnitude r' (not on θ' or ϕ') we obtain

$$F(q) = \frac{4\pi}{q}\int \sin qr'\rho_e(r')r'\,dr' \tag{3.6}$$

This quantity is a function of q, the magnitude of $\boldsymbol{q}$. Since we originally assumed that the scattering was elastic, then $|\boldsymbol{p}_i| = |\boldsymbol{p}_f|$ and q is merely a function of the scattering angle α between $\boldsymbol{p}_i$ and $\boldsymbol{p}_f$; a bit of vector manipulation shows $q = (2p/\hbar)\sin\alpha/2$ where p is the momentum of the electron. Measuring the scattering probability as a function of the angle α then gives us the dependence

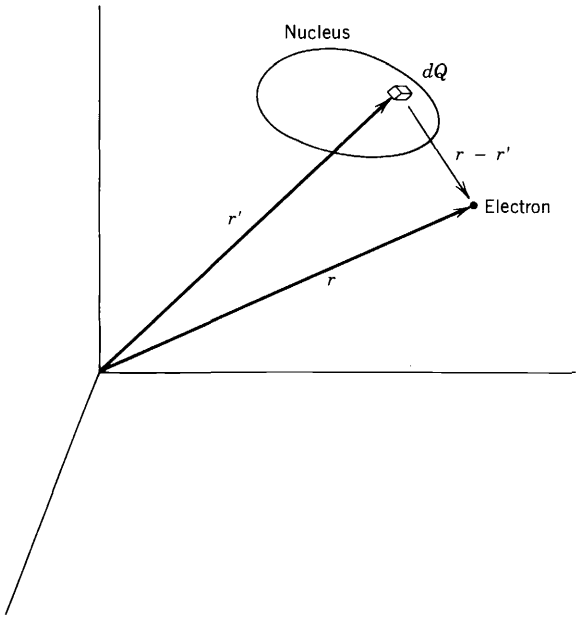


Figure 3.3 The geometry of scattering experiments. The origin of coordinates is located arbitrarily. The vector $\boldsymbol{r}'$ locates an element of charge dQ within the nucleus, and the vector $\boldsymbol{r}$ defines the position of the electron.

of Equation 3.6 on q. The quantity $F(q)$ is known as a form factor, and the numerical inversion of Equation 3.6, actually an inverse Fourier transformation, then gives us $\rho_e(r')$.

The results of this procedure for several different nuclei are shown in Figure 3.4. One remarkable conclusion is obvious—the central nuclear charge density is nearly the same for all nuclei. Nucleons do not seem to congregate near the center of the nucleus, but instead have a fairly constant distribution out to the surface. (The conclusion from measurements of the nuclear matter distribution is the same.) Thus *the number of nucleons per unit volume is roughly constant*:

$$\frac{A}{\frac{4}{3}\pi R^3} \sim \text{constant} \tag{3.7}$$

where R is the mean nuclear radius. Thus $R \propto A^{1/3}$, and defining the proportionality constant R_0 gives

$$R = R_0 A^{1/3} \tag{3.8}$$

From electron scattering measurements, such as those in Figure 3.4, it is concluded that $R_0 \simeq 1.2$ fm. These measurements give the most detailed descriptions of the complete nuclear charge distribution.

Figure 3.4 also shows how diffuse the nuclear surface appears to be. The charge density is roughly constant out to a certain point and then drops relatively slowly to zero. The distance over which this drop occurs is nearly independent of the size of the nucleus, and is usually taken to be constant. We define the *skin*

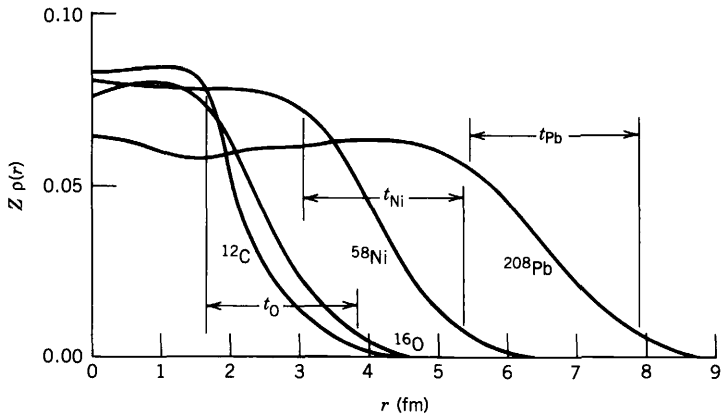


Figure 3.4 The radial charge distribution of several nuclei determined from electron scattering. The skin thickness t is shown for O, Ni, and Pb; its value is roughly constant at 2.3 fm. The central density changes very little from the lightest nuclei to the heaviest. These distributions were adapted from R. C. Barrett and D. F. Jackson, *Nuclear Sizes and Structure* (Oxford: Clarendon, 1977), which gives more detail on methods of determining $\rho(r)$.

thickness parameter t as the distance over which the charge density falls from 90% of its central value to 10%. The value of t is approximately 2.3 fm.

Figure 3.5 shows a more quantitative determination of the relationship between the nuclear radius and mass number, based on electron scattering results. The root mean square (rms) radius, $\langle r^2 \rangle^{1/2}$, is deduced directly from the distribution of scattered electrons; for a uniformly charged sphere $\langle r^2 \rangle = \frac{3}{5}R^2$, where R is the radius of the sphere. Figure 3.5 shows that the dependence of R on $A^{1/3}$ is approximately valid over the range from the lightest to the heaviest nuclei. From the slope of the line, we deduce $R_0 = 1.23$ fm.

The nuclear charge density can also be examined by a careful study of atomic transitions. In solving the Schrödinger equation for the case of the atom with a single electron, it is always assumed that the electron feels the Coulomb attraction of a *point* nucleus, $V(r) = -Ze^2/4\pi\epsilon_0 r$. Since real nuclei are not points, the electron wave function can penetrate to $r < R$, and thus the electron spends part of its time *inside* the nuclear charge distribution, where it feels a very different interaction. In particular, as $r \to 0$, $V(r)$ will not tend toward infinity for a nucleus with a nonzero radius. As a rough approximation, we can assume the nucleus to be a uniformly charged sphere of radius R, for which the potential energy of the electron for $r \leq R$ is

$$V'(r) = -\frac{Ze^2}{4\pi\epsilon_0 R}\left\{\frac{3}{2} - \frac{1}{2}\left(\frac{r}{R}\right)^2\right\} \tag{3.9}$$

while for $r \geq R$, the potential energy has the point-nucleus form.

The total energy E of the electron in a state ψ_n of a point nucleus depends in part on the expectation value of the potential energy

$$\langle V \rangle = \int \psi_n^* V \psi_n \, dv \tag{3.10}$$

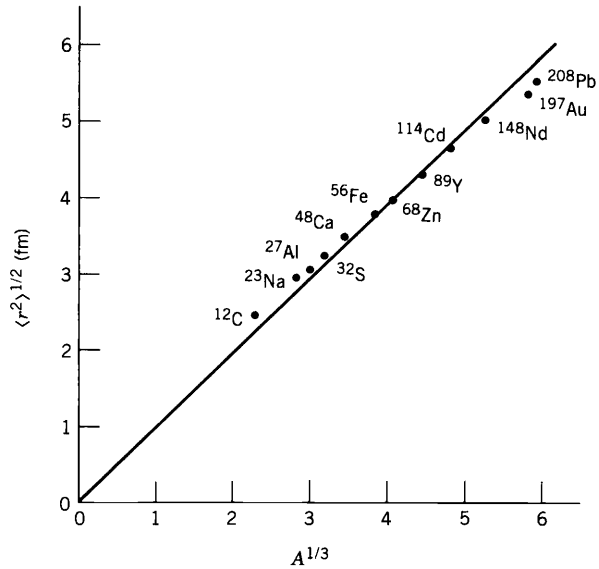


Figure 3.5 The rms nuclear radius determined from electron scattering experiments. The slope of the straight line gives $R_0 = 1.23$ fm. (The line is not a true fit to the data points, but is forced to go through the origin to satisfy the equation $R = R_0 A^{1/3}$.) The error bars are typically smaller than the size of the points (± 0.01 fm). More complete listings of data and references can be found in the review of C. W. de Jager et al., *Atomic Data and Nuclear Data Tables* **14**, 479 (1974).

where V is the point-nucleus Coulomb potential energy. If we assume (as a first approximation) that changing from a point nucleus to a uniformly charged spherical nucleus does not significantly change the electronic wave function ψ_n, then the energy E' of the electron in a state of a uniformly charged spherical nucleus depends on the expectation value of the potential V':

$$\langle V' \rangle = \int_{r<R} \psi_n^* V' \psi_n \, dv + \int_{r>R} \psi_n^* V \psi_n \, dv \tag{3.11}$$

where the second integral involves only the $1/r$ potential energy. The effect of the spherical nucleus is thus to change the energy of the electronic states, relative to the point-nucleus value, by $\Delta E = E' - E = \langle V' \rangle - \langle V \rangle$; the latter step follows directly from our assumption that the wave functions are the same, in which case the kinetic energy terms in E and E' are identical. Using the 1s hydrogenic wave function from Table 2.5, we find

$$\Delta E = \frac{e^2}{4\pi\epsilon_0} \frac{4Z^4}{a_0^3} \int_0^R e^{-2Zr/a_0} \left(\frac{1}{r} - \frac{3}{2R} + \frac{1}{2} \frac{r^2}{R^3} \right) r^2 \, dr \tag{3.12}$$

The exponential factor in the integrand is nearly unity, because $R/a_0 \simeq 10^{-5}$, and evaluating the remaining terms gives

$$\Delta E = \frac{2}{5} \frac{Z^4 e^2}{4\pi\epsilon_0} \frac{R^2}{a_0^3} \tag{3.13}$$

This ΔE is the difference between the energy of the 1s state in an atom with a "point" nucleus and the 1s energy in an atom with a uniformly charged nucleus of radius R. The latter is a fair approximation to real nuclei (as suggested by Figure 3.4); if we could only find a supply of atoms with "point" nuclei we could measure ΔE and deduce R! Since no such nuclei exist, the next best strategy would be to determine E' from measurement (from K X rays, for example) and to calculate the point-nucleus value E from the 1s atomic wave function. Unfortunately, the atomic wave functions are not known with sufficient precision to do this—ΔE is a very small difference, perhaps 10^{-4} of E, and the simple hydrogenlike 1s wave functions are not good enough to calculate E to a precision of 1 part in 10^4 (relativistic effects and the presence of other electrons are two factors that also influence the 1s energy). Thus a single measurement of the energy of a K X ray cannot be used to deduce the nuclear radius.

Let's instead measure and compare the K X-ray energies (resulting from $2p \rightarrow 1s$ electronic transitions) in two neighboring isotopes of mass numbers A and A'. Letting $E_K(A)$ and $E_K(A')$ represent the observed K X-ray energies, we have

$$E_K(A) - E_K(A') = E_{2p}(A) - E_{1s}(A) - E_{2p}(A') + E_{1s}(A') \quad (3.14)$$

If we assume that the 2p energy difference is negligible (recall from Chapter 2 that p-electron wave functions vanish at $r = 0$), the remaining 1s energy difference reduces to the difference between the ΔE values of Equation 3.13, because $E_{1s} \equiv E' = E + \Delta E$ and the "point" nucleus values E would be the same for the isotopes A and A'. Thus

$$\begin{aligned} E_K(A) - E_K(A') &= \Delta E(A') - \Delta E(A) \\ &= -\frac{2}{5}\frac{Z^4e^2}{4\pi\epsilon_0}\frac{1}{a_0^3}R_0^2(A^{2/3} - A'^{2/3}) \end{aligned} \quad (3.15)$$

The quantity $E_K(A) - E_K(A')$ is called the K X-ray *isotope shift*, and a plot against $A^{2/3}$ of a sequence of isotope shifts of different isotopes A all compared with the same reference A' should give a straight line from whose slope we could deduce R_0. Figure 3.6 is an example of such a plot for some isotopes of Hg. The agreement with the $A^{2/3}$ dependence is excellent. The slope, however, does not give a reasonable value of R_0, because the 1s wave function used in Equation 3.12 is not a very good representation of the true 1s wave function. The calculated K X-ray energies, for example, are about 10% lower than the observed values. Detailed calculations that treat the 1s electron relativistically and take into account the effect of other electrons give a more realistic relationship between the slope of Figure 3.6 and the value of R_0. The resulting values are in the range of 1.2 fm, in agreement with the results of electron scattering experiments.

It is also possible to measure isotope shifts for the *optical* radiations in atoms (those transitions among the outer electronic shells that produce visible light). Because these electronic orbits lie much further from the nucleus than the 1s orbit, their wave functions integrated over the nuclear volume, as in Equation 3.12, give much smaller shifts than we obtain for the inner 1s electrons. In Chapter 2 we showed that s states ($\ell = 0$ wave functions) give nonzero limits on

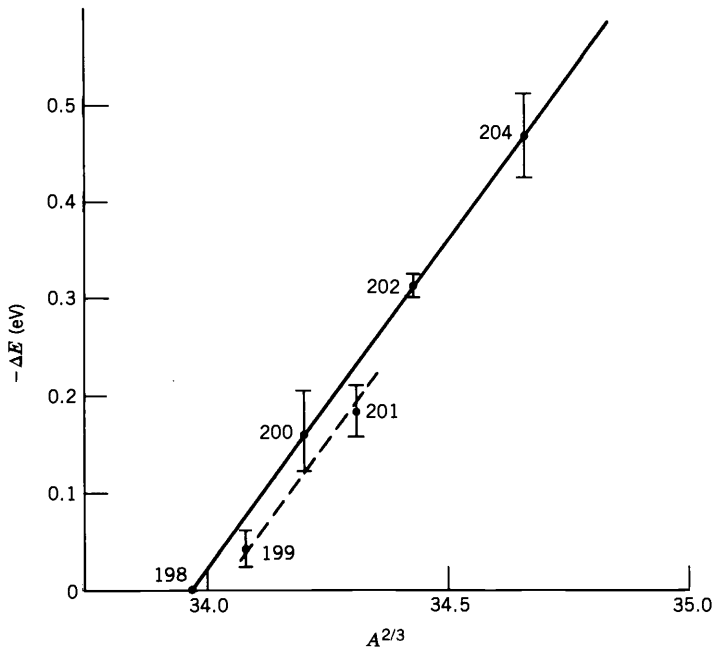


Figure 3.6 K X-ray isotope shifts in Hg. The energy of the K X ray in Hg is about 100 keV, so the relative isotope shift is of the order of 10^{-6}. The data show the predicted dependence on $A^{2/3}$. There is an "odd-even" shift in radius of odd-mass nuclei relative to their even-A neighbors, brought about by the orbit of the odd particle. For this reason, odd-A isotopes must be plotted separately from even-A isotopes. Both groups, however, show the $A^{2/3}$ dependence. The data are taken from P. L. Lee et al., *Phys. Rev. C* **17**, 1859 (1978).

ψ at small r. If the optical transitions involve s states, their isotope shifts can be large enough to be measured precisely, especially using modern techniques of laser interferometry. Figure 3.7 shows an example of optical shifts in Hg isotopes; again the expected $A^{2/3}$ dependence is consistent with the data. Measurements across a large range of nuclei are consistent with $R_0 = 1.2$ fm.

These effects of the nuclear size on X-ray and optical transitions are very small, about 10^{-4} to 10^{-6} of the transition energy. The reason these effects are so small has to do with the difference in scale of 10^4 between the Bohr radius a_0 and the nuclear radius R. For integrals of the form of Equation 3.12 to give large effects, the atomic wave function should be large at values of r near R, but instead the atomic wave functions are large near $r = a_0/Z$, which is far greater than R. We can improve on this situation by using a *muonic atom*. The muon is a particle identical to the electron in all characteristics except its mass, which is 207 times the electronic mass. Since the Bohr radius depends inversely on the mass, the muonic orbits have $1/207$ the radius of the corresponding electronic orbits. In fact, in a heavy nucleus like Pb, the muonic 1s orbit has its mean radius *inside* the nuclear radius R; the effect of the nuclear size is a factor of 2 in the transition energies, a considerable improvement over the factor of 10^{-4} to 10^{-6} in electronic transitions.

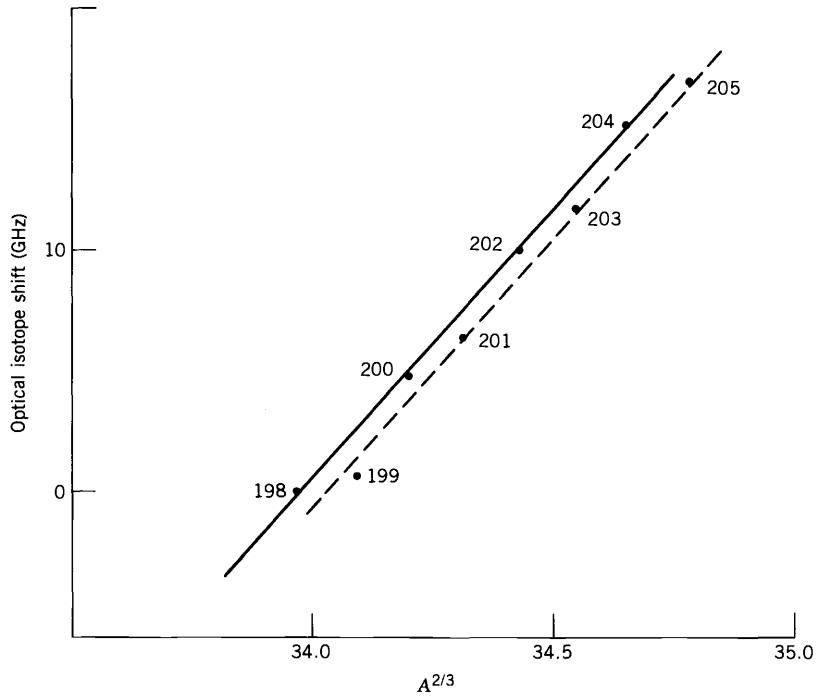


Figure 3.7 Optical isotope shifts in Hg isotopes from 198 to 205, measured relative to 198. These data were obtained through laser spectroscopy; the experimental uncertainties are about $\pm 1\%$. The optical transition used for these measurements has a wavelength of 253.7 nm, and the isotope shift is therefore about one part in 10^7. Compare these results with Figure 3.6. Data taken from J. Bonn et al., *Z. Phys. A* **276**, 203 (1976).

Muons are not present in ordinary matter, but must be made artificially using large accelerators that produce intense beams of π mesons. The π mesons then decay rapidly (10^{-8} s) to muons. (The properties of muons and π mesons are discussed in Chapters 17 and 18.) Beams of the resulting muons are then focused onto a suitably chosen target; atoms of the target capture the muons into orbits similar to electronic orbits. Initially the muon is in a state of very high principal quantum number n, and as the muon cascades down toward its 1s ground state, photons are emitted, in analogy with the photons emitted in electronic transitions between energy levels. The energy levels of atomic hydrogen depend directly on the electronic mass; we therefore expect the muonic energy levels and transition energies to be 207 times their electronic counterparts. Since ordinary K X rays are in the energy range of tens of keV, muonic K X rays will have energies of a few MeV. Figure 3.8 shows some typical muonic K X rays; the isotope shift is large compared with the isotope shift of electronic K X rays, which is typically 10^{-2} eV per unit change in A.

In contrast to the case with electronic K X rays, where uncertainties in atomic wave functions made it difficult to interpret the isotope shifts, we can use the observed muonic X-ray energies directly to compute the parameters of the nuclear charge distribution. Figure 3.9 shows the deduced rms radii, based once

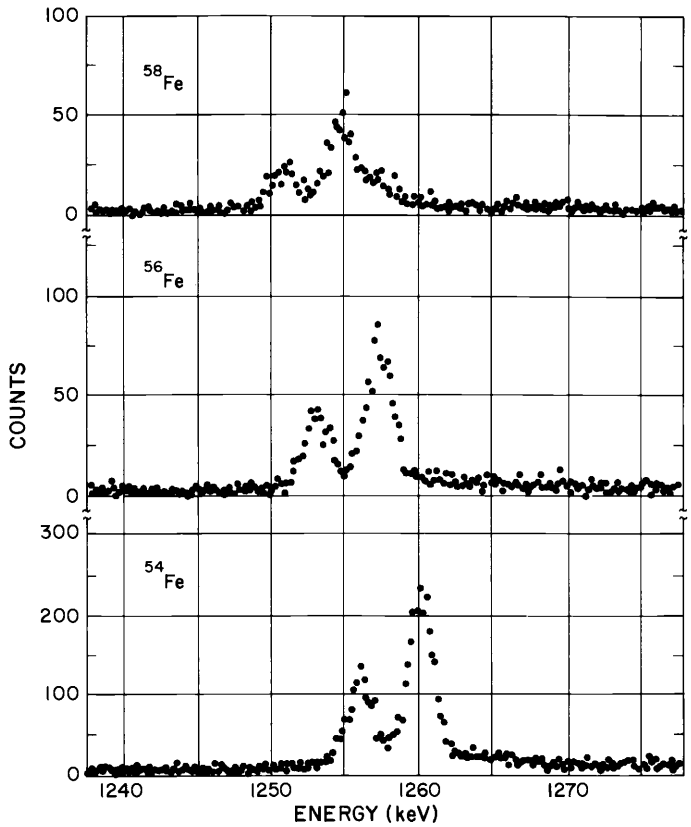


Figure 3.8 The muonic K X rays in some Fe isotopes. The two peaks show the $2p_{3/2}$ to $1s_{1/2}$ and $2p_{1/2}$ to $1s_{1/2}$ transitions, which have relative intensities in the ratio 2 : 1 determined by the statistical weight $(2j + 1)$ of the initial state. The isotope shift can clearly be seen as the change in energy of the transitions. The effect is about 0.4%, which should be compared with the 10^{-6} effect obtained with electronic K X rays (Figure 3.6). From E. B. Shera et al., *Phys. Rev. C* **14**, 731 (1976).

again on the model of the uniformly charged sphere. The data are roughly consistent with $R_0 A^{1/3}$, with $R_0 = 1.25$ fm.

Yet another way to determine the nuclear charge radius is from direct measurement of the Coulomb energy differences of nuclei. Consider, for example, ${}^3_1\mathrm{H}_2$ and ${}^3_2\mathrm{He}_1$. To get from ^{3}He to ^{3}H, we must change a proton into a neutron. As we discuss in Chapter 4, there is strong evidence which suggests that the *nuclear* force does not distinguish between protons and neutrons. Changing a proton into a neutron should therefore not affect the *nuclear* energy of the three-nucleon system; only the Coulomb energy should change, because the two protons in ^{3}He experience a repulsion that is not present in ^{3}H. The energy difference between ^{3}He and ^{3}H is thus a measure of the Coulomb energy of the second proton, and the usual formula for the Coulomb repulsion energy can be used to calculate the distance between the protons and thus the size of the nucleus.

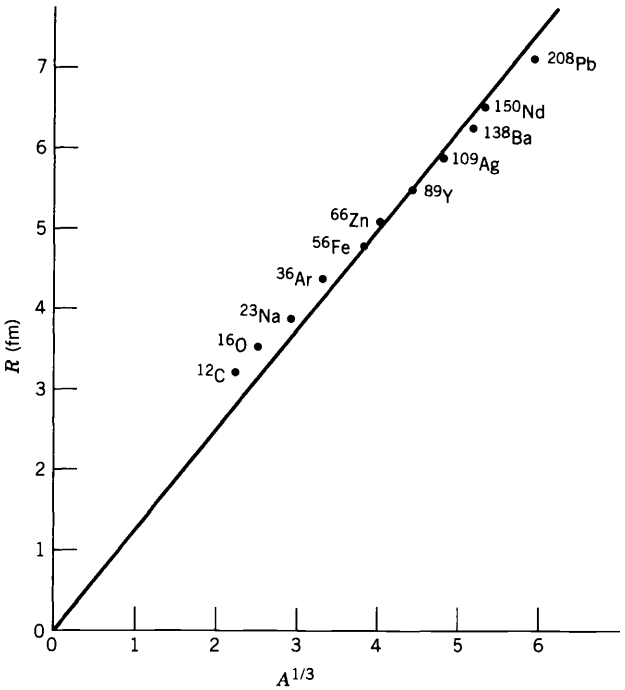


Figure 3.9 The mean nuclear radius determined from muonic X-ray measurements. As in Figure 3.5, the data depend roughly linearly on $A^{1/3}$ (again forcing the line to go through the origin). The slope of the line gives $R_0 = 1.25$ fm. The data are taken from a review of muonic X-ray determinations of nuclear charge distributions by R. Engfer et al., *Atomic Data and Nuclear Data Tables* **14**, 509 (1974).

Consider now a more complex nucleus, such as $^{238}_{92}U_{146}$. If we try to change a proton to a neutron we now have a very different circumstance, because the 92nd proton would become the 147th neutron. Because neutrons and protons each must obey the Pauli principle, the orbital of the 92nd proton will differ from the orbital of the 147th neutron, and in general it is not possible to calculate this effect to sufficient accuracy to be able to extract the Coulomb energy. The situation is resolved if we choose a case (as with ^{3}He–^{3}H) in which no change of orbital is involved, that is, in which the number of the last proton that makes the change is identical to the number of the last neutron after the change. The Z of the first nucleus must equal the N of the second (and thus the N of the first equals the Z of the second). Such pairs of nuclei are called *mirror nuclei* because one is changed into the other by "reflecting" in a mirror that exchanges protons and neutrons. Examples of such pairs of mirror nuclei are $^{13}_{7}N_6$ and $^{13}_{6}C_7$, or $^{39}_{20}Ca_{19}$ and $^{39}_{19}K_{20}$.

The Coulomb energy of a uniformly charged sphere of radius R is

$$E_c = \frac{3}{5}\frac{1}{4\pi\epsilon_0}\frac{Q^2}{R} \tag{3.16}$$

where Q is the total charge of the sphere. The difference in Coulomb energy

between the mirror pairs is thus

$$\Delta E_c = \frac{3}{5}\frac{e^2}{4\pi\epsilon_0 R}\left[Z^2 - (Z-1)^2\right]$$

$$= \frac{3}{5}\frac{e^2}{4\pi\epsilon_0 R}(2Z-1) \tag{3.17}$$

Since Z represents the nucleus of higher atomic number, the N of that nucleus must be $Z - 1$, and so $A = 2Z - 1$. With $R = R_0 A^{1/3}$,

$$\Delta E_c = \frac{3}{5}\frac{e^2}{4\pi\epsilon_0 R_0}A^{2/3} \tag{3.18}$$

These Coulomb energy differences can be directly measured in two ways. One of the nuclei in the pair can decay to the other through *nuclear β decay*, in which a proton changes into a neutron with the emission of a positive electron (positron). The maximum energy of the positron is a measure of the energy difference between the nuclei. A second method of measuring the energy difference is through nuclear reactions; for example, when a nucleus such as ^{11}B is bombarded with protons, occasionally a neutron will be emitted leaving the residual nucleus ^{11}C. The minimum proton energy necessary to cause this reaction is a measure of the energy difference between ^{11}B and ^{11}C. (We discuss β decay in Chapter 9 and reaction kinematics in Chapter 11.) The measured energy differences are plotted against $A^{2/3}$ in Figure 3.10. As expected from Equation 3.18, the dependence is very nearly linear. The slope of the line gives $R_0 = 1.22$ fm.

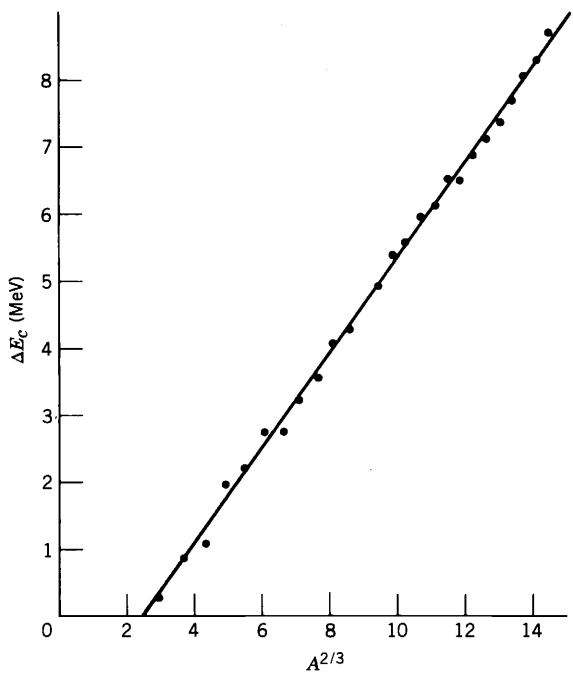


Figure 3.10 Coulomb energy differences of mirror nuclei. The data show the expected $A^{2/3}$ dependence, and the slope of the line gives $R_0 = 1.22$ fm.

Even though these measurements of the nuclear charge radius use very different techniques, they all give essentially the same results: the nuclear radius varies with mass number as $R_0 A^{1/3}$, with $R_0 = 1.2 - 1.25$ fm.

The Distribution of Nuclear Matter

An experiment that involves the nuclear force between two nuclei will often provide a measure of the nuclear radius. The determination of the spatial variation of the force between nuclei enables the calculation of the nuclear radii. In this case the radius is characteristic of the *nuclear*, rather than the *Coulomb*, force; these radii therefore reflect the distribution of all nucleons in a nucleus, not only the protons.

As an example of a measurement that determines the size of the nuclear matter distribution, we consider an experiment in which a ^{4}He nucleus (α particle) is scattered from a much heavier target of ^{197}Au. If the separation between the two nuclei is always greater than the sum of their radii, each is always beyond the range of the other's nuclear force, so only the Coulomb force acts. (This situation is known as Rutherford scattering and is discussed in Chapter 11.) The probability for scattering at a certain angle depends on the energy of the incident particle exactly as predicted by the Rutherford formula, when the energy of the incident particle is below a certain value. As the energy of the incident α particle is increased, the Coulomb repulsion of the nuclei is overcome and they may approach close enough to allow the nuclear force to act. In this case the Rutherford formula no longer holds. Figure 3.11 shows an example of this effect.

For another example, we consider the form of radioactive decay in which an α particle is emitted from the nucleus (see Chapter 8 for a complete discussion of α decay). The α particle must escape the nuclear potential and penetrate a Coulomb potential barrier, as indicated in Figure 3.12. The α decay probabilities can be calculated from a standard barrier-penetration approach using the Schrödinger equation. These calculated values depend on the nuclear matter radius R, and comparisons with measured decay probabilities permit values of R to be deduced.

A third method for determining the nuclear matter radius is the measurement of the energy of π-mesic X rays. This method is very similar to the muonic X-ray technique discussed above for measuring the charge radius. The difference between the two techniques results from differences between muons and π mesons: the muons interact with the nucleus through the Coulomb force, while the π mesons interact with the nucleus through the nuclear and the Coulomb forces. Like the muons, the negatively charged π mesons cascade through electronlike orbits and emit photons known as π-mesic X rays. When the π-meson wave functions begin to overlap with the nucleus, the energy levels are shifted somewhat from values calculated using only the Coulomb interaction. In addition, the π mesons can be directly absorbed into the nucleus, especially from the inner orbits; thus there are fewer X-ray transitions among these inner levels. The "disappearance rate" of π mesons gives another way to determine the nuclear radius.

All of these effects could in principle be used as a basis for deducing the nuclear radius. However, the calculations are very sensitive to the exact onset of

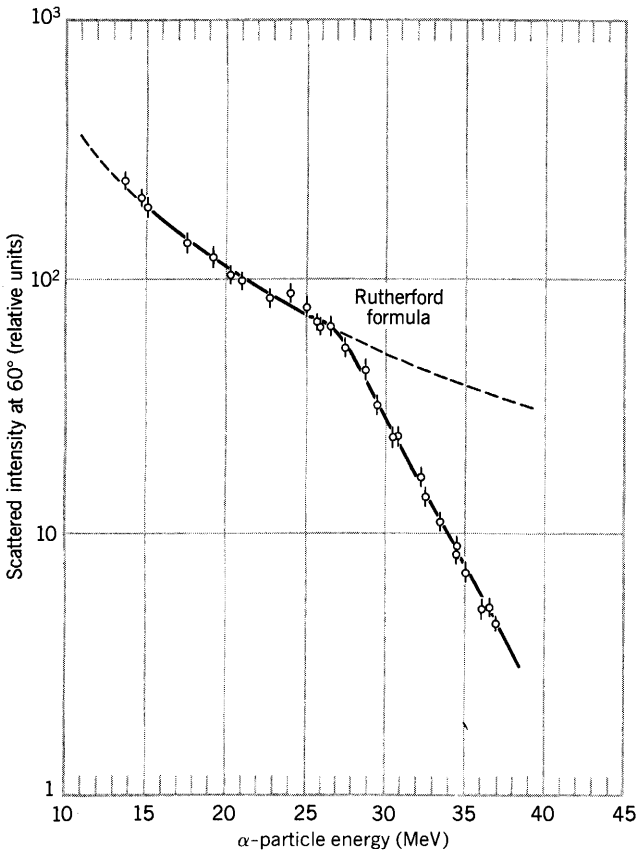


Figure 3.11 The breakdown of the Rutherford scattering formula. When the incident α particle gets close enough to the target Pb nucleus so that they can interact through the nuclear force (in addition to the Coulomb force that acts when they are far apart) the Rutherford formula no longer holds. The point at which this breakdown occurs gives a measure of the size of the nucleus. Adapted from a review of α particle scattering by R. M. Eisberg and C. E. Porter, *Rev. Mod. Phys.* **33**, 190 (1961).

overlap between the probe particle and the nuclear matter distribution. For these calculations it is therefore very wrong to use the "uniform sphere" model of assuming a constant density out to R and zero beyond R. We should instead use a distribution, such as those of Figure 3.4, with a proper tail beyond the mean radius.

We will not go into the details of the calculations, which are far more complicated than our previous calculations of the charge radius. We merely give the result, which may seem a bit surprising: *the charge and matter radii of nuclei are nearly equal, to within about 0.1 fm.* Both show the $A^{1/3}$ dependence with $R_0 \simeq 1.2$ fm. Because heavy nuclei have about 50% more neutrons than protons, we might have expected the neutron radius to be somewhat larger than the proton radius; however, the proton repulsion tends to push the protons outward and the neutron–proton force tends to pull the neutrons inward, until the

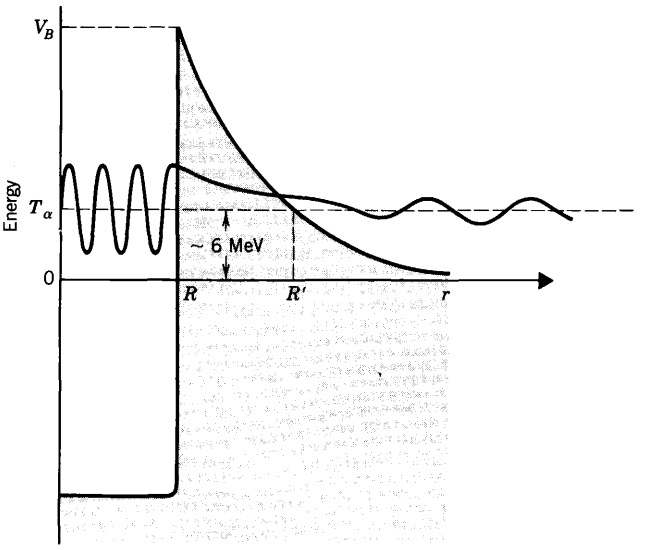


Figure 3.12 Barrier penetration in α decay. The half-life for α emission depends on the probability to penetrate the barrier, which in turn depends on its thickness. The measured half-lives can thus be used to determine the radius R where the nuclear force ends and the Coulomb repulsion begins.

neutrons and protons are so completely intermixed that the charge and matter radii are nearly equal.

3.2 MASS AND ABUNDANCE OF NUCLIDES

In Appendix C is a table of measured values of the masses and abundances of neutral *atoms* of various stable and radioactive nuclei. Even though we must analyze the energy balance in nuclear reactions and decays using nuclear masses, it is conventional to tabulate the masses of neutral atoms. It may therefore be necessary to correct for the mass and binding energy of the electrons.

As we probe ever deeper into the constituents of matter, the binding energy becomes ever greater in comparison with the rest energy of the bound system. In a hydrogen atom, the binding energy of 13.6 eV constitutes only 1.4×10^{-8} of the total rest energy of the atom. In a simple nucleus, such as deuterium, the binding energy of 2.2 MeV is 1.2×10^{-3} of the total mass energy. The deuteron is relatively weakly bound and thus this number is rather low compared with typical nuclei, for which the fraction would be more like 8×10^{-3}. At a yet deeper level, three massive quarks make up a nucleon. The masses of the quarks are not known (no free quarks have yet been confirmed experimentally and quarks may not be permitted to exist in a free state), but it is possible that they may be greater than 100 GeV/c^2. If so, the binding energy of the quarks in a nucleon would be a fraction greater than 0.99 of the total mass of the quarks—3 quarks of total rest energy of perhaps 300 GeV combine to produce a nucleon of rest energy 1 GeV!

It is therefore not possible to separate a discussion of nuclear mass from a discussion of nuclear binding energy; if it were, then nuclei would have masses

given by $Zm_p + Nm_n$, and the subject would hardly be of interest. In this section, we confine our discussion to the experimental determination of nuclear masses, treating the nucleus as a simple object with no internal structure. In the next section we analyze the measured masses to determine the binding energy.

The measurement of nuclear masses occupies an extremely important place in the development of nuclear physics. Mass spectrometry was the first technique of high precision available to the experimenter, and since the mass of a nucleus increases in a regular way with the addition of one proton or neutron, measuring masses permitted the entire scheme of stable isotopes to be mapped. Not so with atomic physics—nineteenth-century measurements of average atomic weights led to discrepancies in the atomic periodic table, such as misordering of elements cobalt and nickel, cobalt being heavier but preceding nickel in the proper ordering based on atomic *number* not atomic *weight*. Equally as important, no understanding of nuclear structure can be successful unless we can explain the variation in nuclear properties from one isotope to another; before we can measure such properties, we must determine which isotopes are present and simultaneously attempt to separate them from one another for experimental investigations.

To determine the nuclear masses and relative abundances in a sample of ordinary matter, which even for a pure element may be a mixture of different isotopes, we must have a way to separate the isotopes from one another by their masses. The mere separation of isotopes does not require an instrument of great sensitivity—neighboring isotopes of medium-weight nuclei differ in mass by about 1%. To measure masses to precisions of order 10^{-6} requires instruments of much greater sophistication, known as *mass spectroscopes*. The separated masses may be focused to make an image on a photographic plate, in which case the instrument is called a *spectrograph*; or the masses may pass through a detecting slit and be recorded electronically (as a current, for instance), in which case we would have a *spectrometer*. A schematic diagram of a typical mass spectrograph is shown in Figure 3.13.

All mass spectroscopes begin with an *ion source*, which produces a beam of ionized atoms or molecules. Often a vapor of the material under study is bombarded with electrons to produce the ions; in other cases the ions can be formed as a result of a spark discharge between electrodes coated with the material. Ions emerging from the source have a broad range of velocities, as might be expected for a thermal distribution, and of course many different masses might be included.

The next element is a *velocity selector*, consisting of perpendicular electric and magnetic fields. The $\boldsymbol{E}$ field would exert a force qE that would tend to divert the ions upward in Figure 3.13; the $\boldsymbol{B}$ field would exert a downward force qvB. Ions pass through undeflected if the forces cancel, for which

$$qE = qvB$$

$$v = \frac{E}{B} \tag{3.19}$$

The final element is a momentum selector, which is essentially a uniform magnetic field that bends the beam into a circular path with radius r determined

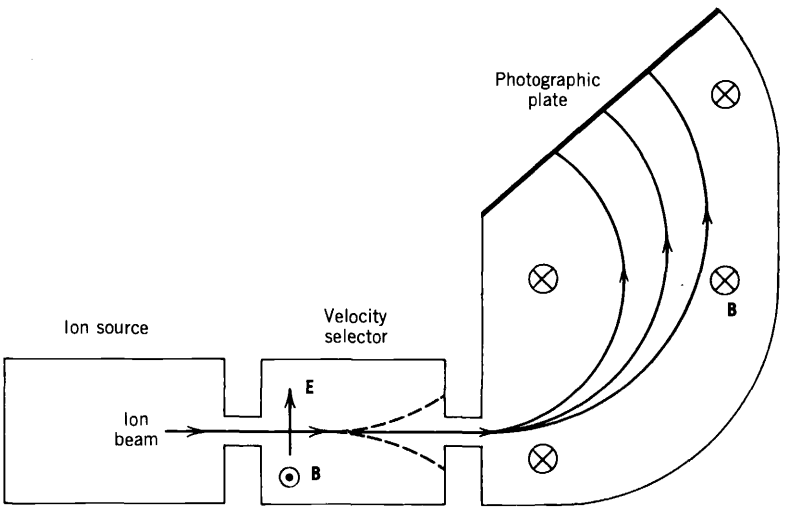


Figure 3.13 Schematic diagram of mass spectrograph. An ion source produces a beam with a thermal distribution of velocities. A velocity selector passes only those ions with a particular velocity (others being deflected as shown), and momentum selection by a uniform magnetic field permits identification of individual masses.

by the momentum:

$$mv = qBr$$

$$r = \frac{mv}{qB} \tag{3.20}$$

Since q, B, and v are uniquely determined, each different mass m appears at a particular r. Often the magnetic fields of the velocity and momentum selectors are common, in which case

$$m = \frac{qrB^2}{E} \tag{3.21}$$

To determine masses to one part in 10^6, we must know all quantities in Equation 3.21 to that precision, which hardly seems possible. In practice we could calibrate for one particular mass, and then determine all masses by relative measurements. The fixed point on the atomic mass scale is ^{12}C, which is taken to be exactly 12.000000 u. To determine the mass of another atom, such as ^1H, we would need to make considerable changes in E and B, and it is perhaps questionable whether the calibration would be valid to one part in 10^6 over such a range. It would be preferable to measure the smaller difference between two nearly equal masses. For example, let us set the apparatus for mass 128 and measure the difference between the molecular masses of C_9H_{20} (nonane) and $C_{10}H_8$ (naphthalene). This difference is measured to be $\Delta = 0.09390032 \pm 0.00000012$ u. Neglecting corrections for the difference in the molecular binding energies of the two molecules (which is of the order of 10^{-9} u), we can write

$$\Delta = m(C_9H_{20}) - m(C_{10}H_8) = 12m(^1H) - m(^{12}C)$$

Thus

$$\begin{aligned} m(^1\mathrm{H}) &= \tfrac{1}{12}\left[m(^{12}\mathrm{C}) + \Delta\right] \\ &= 1.00000000 + \tfrac{1}{12}\Delta \\ &= 1.00782503 \pm 0.00000001 \text{ u} \end{aligned}$$

Given this accurate value we could then set the apparatus for mass 28 and determine the difference between C_2H_4 and N_2:

$$\begin{aligned} \Delta &= m(C_2H_4) - m(N_2) = 2m(^{12}\mathrm{C}) + 4m(^1\mathrm{H}) - 2m(^{14}\mathrm{N}) \\ &= 0.025152196 \pm 0.000000030 \text{ u} \end{aligned}$$

from which we find:

$$m(^{14}\mathrm{N}) = m(^{12}\mathrm{C}) + 2m(^1\mathrm{H}) - \tfrac{1}{2}\Delta = 14.00307396 \pm 0.00000002 \text{ u}$$

This system of measuring small differences between close-lying masses is known as the *mass doublet* method, and you can see how it gives extremely precise mass values. Notice in particular how the 1 part in 10^6 uncertainties in the measured Δ values give uncertainties in the deduced atomic masses of the order of 1 part in 10^8 or 10^9.

It is also possible to determine mass differences by measuring the energies of particles in nuclear reactions. Consider the nuclear reaction $x + X \rightarrow y + Y$, in which a projectile x is incident on a stationary target X. By measuring the kinetic energies of the reacting particles, we can determine the difference in masses, which is known as the Q value of the reaction:

$$Q = \left[m(x) + m(X) - m(y) - m(Y)\right]c^2 \tag{3.22}$$

(We consider reaction Q values in detail in Section 11.2.) For example, consider the reaction $^1\mathrm{H} + {}^{14}\mathrm{N} \rightarrow {}^{12}\mathrm{N} + {}^3\mathrm{H}$. From mass doublet measurements we know that $m(^1\mathrm{H}) = 1.007825$ u, $m(^{14}\mathrm{N}) = 14.003074$ u, and $m(^3\mathrm{H}) = 3.016049$ u. The measured Q value is -22.1355 ± 0.0010 MeV. We thus deduce

$$\begin{aligned} m(^{12}\mathrm{N}) &= m(^1\mathrm{H}) + m(^{14}\mathrm{N}) - m(^3\mathrm{H}) - Q/c^2 \\ &= 12.018613 \pm 0.000001 \text{ u} \end{aligned}$$

The main contribution to the uncertainty of the deduced mass comes from the Q value; the $^1\mathrm{H}$, $^3\mathrm{H}$, and $^{14}\mathrm{N}$ masses are known to much greater precision. The nuclide $^{12}\mathrm{N}$ is unstable and decays with a half-life of only 0.01 s, which is far too short to allow its mass to be measured with a mass spectrometer. The nuclear reaction method allows us to determine the masses of unstable nuclides whose masses cannot be measured directly.

Nuclide Abundances The mass spectrometer also permits us to measure the relative abundances of the various isotopes of an element. Measuring the current passing through an exit slit (which replaces the photographic plate of Figure 3.13) as we scan the mass range by varying E or B, we can produce results such as those shown in Figure 3.14. From the relative areas of the peaks, we can

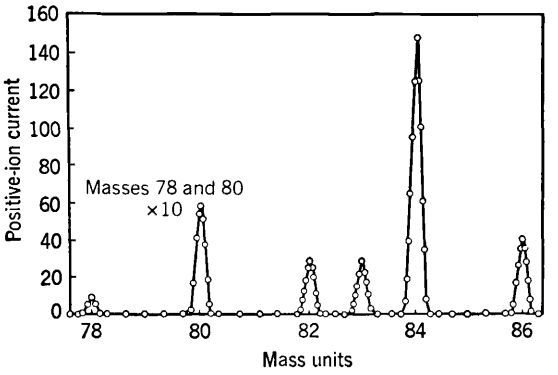


Figure 3.14 A mass-spectrum analysis of krypton. The ordinates for the peaks at mass positions 78 and 80 should be divided by 10 to show these peaks in their true relation to the others.

determine the abundances of the stable isotopes of krypton:

^{78}Kr	0.356%	^{83}Kr	11.5%
^{80}Kr	2.27%	^{84}Kr	57.0%
^{82}Kr	11.6%	^{86}Kr	17.3%

The masses that do not appear in the scan (^{79}Kr, ^{81}Kr, ^{85}Kr, plus those below ^{78}Kr and above ^{86}Kr) are radioactive and are not present in natural krypton. A typical sample of natural krypton would consist of a mixture of the six stable isotopes with the above relative composition. If we add the measured masses of the six stable isotopes with the abundances as relative weighting factors, we can compute the "average" atomic mass of krypton

$$\begin{aligned} m &= 0.00356m(^{78}\text{Kr}) + 0.0227m(^{80}\text{Kr}) + \cdots \\ &= 83.8 \text{ u} \end{aligned}$$

which is identical with the accepted atomic mass of Kr, such as is normally given in the periodic table of the elements.

Separated Isotopes If we set the mass spectrometer on a single mass and collect for a very long time, we can accumulate a large quantity of a particular isotope, enough to use for laboratory experiments. Some mass spectrometers are designed to process large quantities of material (often at the expense of another characteristic of the equipment, such as its ability to resolve nearby masses as in Figure 3.14); the isotope separation facility at Oak Ridge National Laboratory is an example. Separated isotopes, which can be purchased from these facilities, are used for an enormous variety of experiments, not only in nuclear physics, where work with separated isotopes enables us to measure specific properties such as cross sections associated with a particular isotope, but also in other fields including chemistry or biology. For example, we can observe the ingestion of nutrients by plants using stable isotopes as an alternative to using radioactive tracers. Ordinary carbon is about 99% ^{12}C and 1% ^{13}C; nitrogen is 99.6% ^{14}N and 0.4% ^{15}N. If we surround a plant with an atmosphere of CO_2 made from

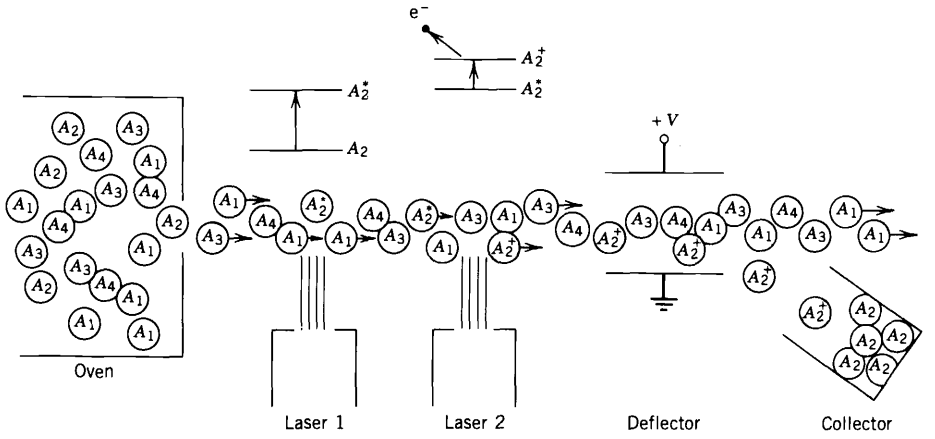


Figure 3.15 Laser isotope separation. The beam of neutral atoms from the oven is a mixture of four isotopes A_1, A_2, A_3, and A_4. The first laser is tuned to the transition corresponding to the resonant excitation of isotope A_2 to a certain excited state; because of the sharpness of the laser energy and the isotope shift that gives that particular transition a different energy in the other isotopes, only A_2 is excited. The second laser has a broad energy profile, so that many free-electron states can be reached in the ionization of the atoms; but because only the A_2 isotopes are in the excited state, only the A_2 atoms are ionized. The A_2 ions are then deflected and collected.

^{13}C, and if we use fertilizers made with ^{15}N instead of ^{14}N, we can then study how these isotopes are incorporated into the plant. The longest-lived radioactive isotope of nitrogen has a half-life of 10 min; thus, long-term studies with radioactive tracers would not be possible, and in addition radioactive decays could adversely affect the plant and the personnel who must care for them.

Laser Isotope Separation A completely different technique for separating isotopes takes advantage of the extremely sharp (that is, monochromatic) beams available from lasers. As discussed in the last section, the optical radiations of different isotopes of the same element do not have exactly the same energy; the differences in nuclear size cause small variations in the transition energies, called the *isotope shift*. Laser beams are sufficiently sharp so that they can be tuned to excite electrons in one isotope of a mixture of isotopes but not in the others. A schematic representation of the process is shown in Figure 3.15. A beam of neutral atoms passes through a laser beam, which is tuned so that electrons in the desired isotope (but not in the others) will absorb the radiation and make a transition to a particular excited state. A second laser beam is set to a wavelength that corresponds to ionization of the excited atoms. The final energy states of the free electron are continuous rather than quantized, and hence the second laser should have a broad energy profile; this will not result in the ionization of the unwanted isotopes because only those that have been excited by the first laser have electrons in the excited state. After passing through the second laser, the beam consists of ionized atoms of one isotope and neutral atoms of all the others; the ionized atoms can be removed from the beam by an electric field and collected.

3.3 NUCLEAR BINDING ENERGY

The mass energy $m_N c^2$ of a certain nuclide is its atomic mass energy $m_A c^2$ less the total mass energy of Z electrons and the total *electronic* binding energy:

$$m_N c^2 = m_A c^2 - Z m_e c^2 + \sum_{i=1}^{Z} B_i \tag{3.23}$$

where B_i is the binding energy of the ith electron. Electronic binding energies are of order 10–100 keV in heavy atoms, while atomic mass energies are of order $A \times 1000$ MeV; thus to a precision of about 1 part in 10^6 we can neglect the last term of Equation 3.23. (Even this 10^{-6} precision does not affect measurements in nuclear physics because we usually work with *differences* in mass energies, such as in determining decay or reaction energies; the effects of electron binding energies tend to cancel in these differences.)

The *binding energy* B of a nucleus is the difference in mass energy between a nucleus ${}^{A}_{Z}\mathrm{X}_N$ and its constituent Z protons and N neutrons:

$$B = \left\{ Z m_p + N m_n - \left[m({}^{A}\mathrm{X}) - Z m_e \right] \right\} c^2 \tag{3.24}$$

where we have dropped the subscript from m_A—from now on, unless we indicate otherwise, we shall always be dealing with *atomic* masses.

Grouping the Z proton and electron masses into Z neutral hydrogen atoms, we can rewrite Equation 3.24 as

$$B = \left[Z m({}^{1}\mathrm{H}) + N m_n - m({}^{A}\mathrm{X}) \right] c^2 \tag{3.25}$$

With the masses generally given in atomic mass units, it is convenient to include the unit conversion factor in c^2, thus: $c^2 = 931.50$ MeV/u.

We occasionally find atomic mass tables in which, rather than $m({}^{A}\mathrm{X})$, what is given is the *mass defect* $\Delta = (m - A)c^2$. Given the mass defect, it is possible to use Equation 3.25 to deduce the atomic mass.

Other useful and interesting properties that are often tabulated are the neutron and proton separation energies. The *neutron separation energy* S_n is the amount of energy that is needed to remove a neutron from a nucleus ${}^{A}_{Z}\mathrm{X}_N$, equal to the difference in binding energies between ${}^{A}_{Z}\mathrm{X}_N$ and ${}^{A-1}_{Z}\mathrm{X}_{N-1}$:

$$\begin{aligned} S_n &= B\left({}^{A}_{Z}\mathrm{X}_N\right) - B\left({}^{A-1}_{Z}\mathrm{X}_{N-1}\right) \\ &= \left[m\left({}^{A-1}_{Z}\mathrm{X}_{N-1}\right) - m\left({}^{A}_{Z}\mathrm{X}_N\right) + m_n \right] c^2 \end{aligned} \tag{3.26}$$

In a similar way we can define the *proton separation energy* S_p as the energy needed to remove a proton:

$$\begin{aligned} S_p &= B\left({}^{A}_{Z}\mathrm{X}_N\right) - B\left({}^{A-1}_{Z-1}\mathrm{X}_N\right) \\ &= \left[m\left({}^{A-1}_{Z-1}\mathrm{X}_N\right) - m\left({}^{A}_{Z}\mathrm{X}_N\right) + m({}^{1}\mathrm{H}) \right] c^2 \end{aligned} \tag{3.27}$$

The hydrogen mass appears in this equation instead of the proton mass, since we are always working with *atomic* masses; you can see immediately how the Z electron masses cancel from Equations 3.26 and 3.27.

The neutron and proton separation energies are analogous to the ionization energies in atomic physics—they tell us about the binding of the outermost or

Table 3.1 Some Mass Defects and Separation Energies

Nuclide	Δ (MeV)	S_n (MeV)	S_p (MeV)
^{16}O	−4.737	15.66	12.13
^{17}O	−0.810	4.14	13.78
^{17}F	+1.952	16.81	0.60
^{40}Ca	−34.847	15.64	8.33
^{41}Ca	−35.138	8.36	8.89
^{41}Sc	−28.644	16.19	1.09
^{208}Pb	−21.759	7.37	8.01
^{209}Pb	−17.624	3.94	8.15
^{209}Bi	−18.268	7.46	3.80

valence nucleons. Just like the atomic ionization energies, the separation energies show evidence for nuclear shell structure that is similar to atomic shell structure. We therefore delay discussion of the systematics of separation energies until we discuss nuclear models in Chapter 5. Table 3.1 gives some representative values of mass defects and separation energies.

As with many other nuclear properties that we will discuss, we gain valuable clues to nuclear structure from a *systematic* study of nuclear binding energy. Since the binding energy increases more or less linearly with A, it is general practice to show the average binding energy per nucleon, B/A, as a function of A. Figure 3.16 shows the variation of B/A with nucleon number. Several remarkable features are immediately apparent. First of all, the curve is relatively constant except for the very light nuclei. The average binding energy of most nuclei is, to within 10%, about 8 MeV per nucleon. Second, we note that the curve reaches a peak near $A = 60$, where the nuclei are most tightly bound. This suggests we can "gain" (that is, release) energy in two ways—below $A = 60$, by assembling lighter nuclei into heavier nuclei, or above $A = 60$, by breaking heavier nuclei into lighter nuclei. In either case we "climb the curve of binding energy" and liberate nuclear energy; the first method is known as *nuclear fusion* and the second as *nuclear fission*. These important subjects are discussed in Chapters 13 and 14.

Attempting to understand this curve of binding energy leads us to the *semiempirical mass formula*, in which we try to use a few general parameters to characterize the variation of B with A.

The most obvious term to include in estimating B/A is the constant term, since to lowest order $B \propto A$. The contribution to the binding energy from this "volume" term is thus $B = a_v A$ where a_v is a constant to be determined, which should be of order 8 MeV. This linear dependence of B on A is in fact somewhat surprising, and gives us our first insight into the properties of the nuclear force. If every nucleon attracted all of the others, then the binding energy would be proportional to $A(A-1)$, or roughly to A^2. Since B varies linearly with A, this suggests that each nucleon attracts only its closest neighbors, and *not* all of the other nucleons. From electron scattering we learned that the nuclear density is roughly constant, and thus each nucleon has about the same number of neigh-

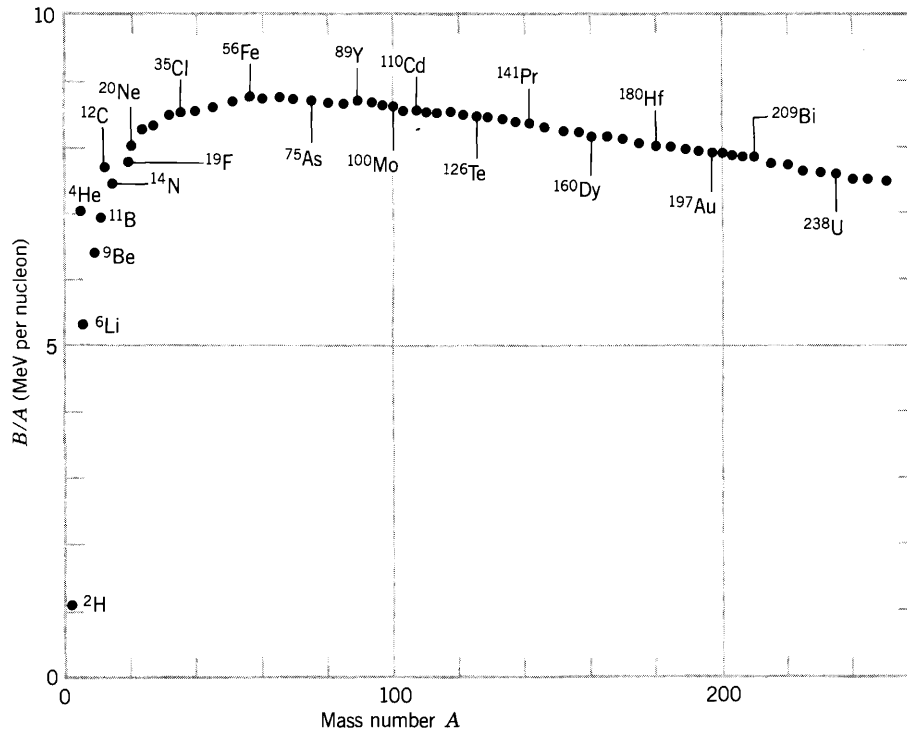


Figure 3.16 The binding energy per nucleon.

bors; each nucleon thus contributes roughly the same amount to the binding energy.

An exception to the above argument is a nucleon on the nuclear surface, which is surrounded by fewer neighbors and thus less tightly bound than those in the central region. These nucleons do not contribute to B quite as much as those in the center, and thus $B = a_v A$ overestimates B by giving full weight to the surface nucleons. We must therefore subtract from B a term proportional to the nuclear surface area. The surface area of the nucleus is proportional to R^2 or to $A^{2/3}$, since $R \propto A^{1/3}$. Thus the surface nucleons contribute to the binding energy a term of the form $-a_s A^{2/3}$.

Our binding energy formula must also include the Coulomb repulsion of the protons, which likewise tends to make the nucleus less tightly bound. Since each proton repels all of the others, this term is proportional to $Z(Z-1)$, and we may do an exact calculation, assuming a uniformly charged sphere, to obtain $-\frac{3}{5}(e^2/4\pi\epsilon_0 R_0)Z(Z-1)/A^{1/3}$ where the negative sign implies a reduction in binding energy. The constants evaluate to 0.72 MeV with $R_0 = 1.2$ fm; we can allow this constant to be adjustable by replacing it with a general Coulomb constant a_c.

We also note, from our study of the distribution of stable and radioactive isotopes (Figure 1.1), that stable nuclei have $Z \simeq A/2$. (The explanation for this effect will come from our discussion of the shell model in Chapter 5.) If our binding energy formula is to be realistic in describing the stable nuclei that are

actually observed, it must take this effect into account. (Otherwise it would allow stable isotopes of hydrogen with hundreds of neutrons!) This term is very important for light nuclei, for which $Z \simeq A/2$ is more strictly observed. For heavy nuclei, this term becomes less important, because the rapid increase in the Coulomb repulsion term requires additional neutrons for nuclear stability. A possible form for this term, called the symmetry term because it tends to make the nucleus symmetric in protons and neutrons, is $-a_{\text{sym}}(A - 2Z)^2/A$ which has the correct form of favoring nuclei with $Z = A/2$ and reducing in importance for large A.

Finally, we must include another term that accounts for the tendency of like nucleons to couple pairwise to especially stable configurations. When we have an odd number of nucleons (odd Z and even N, or even Z and odd N), this term does not contribute. However, when both Z and N are odd, we gain binding energy by converting one of the odd protons into a neutron (or vice versa) so that it can now form a pair with its formerly odd partner. We find evidence for this *pairing force* simply by looking at the stable nuclei found in nature—there are only four nuclei with odd N and Z (^{2}H, ^{6}Li, ^{10}B, ^{14}N), but 167 with even N and Z. This pairing energy δ is usually expressed as $+a_p A^{-3/4}$ for Z and N even, $-a_p A^{-3/4}$ for Z and N odd, and zero for A odd.

Combining these five terms we get the complete binding energy:

$$B = a_v A - a_s A^{2/3} - a_c Z(Z-1)A^{-1/3} - a_{\text{sym}}\frac{(A-2Z)^2}{A} + \delta \tag{3.28}$$

and using this expression for B we have the *semiempirical mass formula*:

$$M(Z, A) = Zm(^1\text{H}) + Nm_n - B(Z, A)/c^2 \tag{3.29}$$

The constants must be adjusted to give the best agreement with the experimental curve of Figure 3.16. A particular choice of $a_v = 15.5$ MeV, $a_s = 16.8$ MeV, $a_c = 0.72$ MeV, $a_{\text{sym}} = 23$ MeV, $a_p = 34$ MeV, gives the result shown in Figure 3.17, which reproduces the observed behavior of B rather well.

The importance of the semiempirical mass formula is not that it allows us to predict any new or exotic phenomena of nuclear physics. Rather, it should be regarded as a first attempt to apply nuclear models to understand the systematic behavior of a nuclear property, in this case the binding energy. It includes several different varieties of nuclear models: the *liquid-drop model*, which treats some of the gross collective features of nuclei in a way similar to the calculation of the properties of a droplet of liquid (indeed, the first three terms of Equation 3.28 would also appear in a calculation of the energy of a charged liquid droplet), and the *shell model*, which deals more with individual nucleons and is responsible for the last two terms of Equation 3.28.

For constant A, Equation 3.29 represents a parabola of M vs. Z. The parabola will be centered about the point where Equation 3.29 reaches a minimum. To compare this result with the behavior of actual nuclei, we must find the minimum, where $\partial M/\partial Z = 0$:

$$Z_{\text{min}} = \frac{[m_n - m(^1\text{H})] + a_c A^{-1/3} + 4a_{\text{sym}}}{2a_c A^{-1/3} + 8a_{\text{sym}}A^{-1}} \tag{3.30}$$

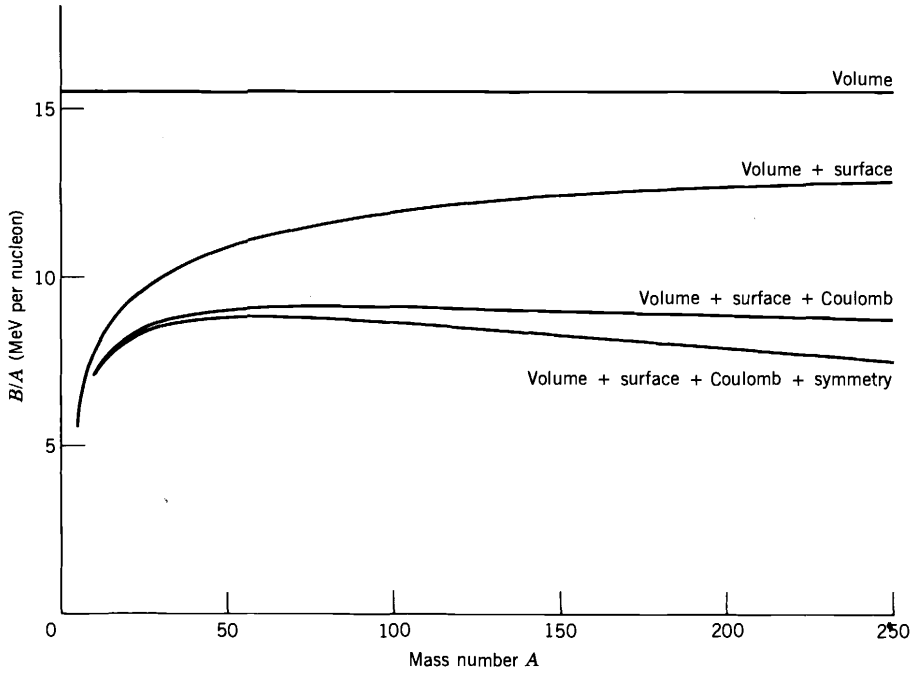


Figure 3.17 The contributions of the various terms in the semiempirical mass formula to the binding energy per nucleon.

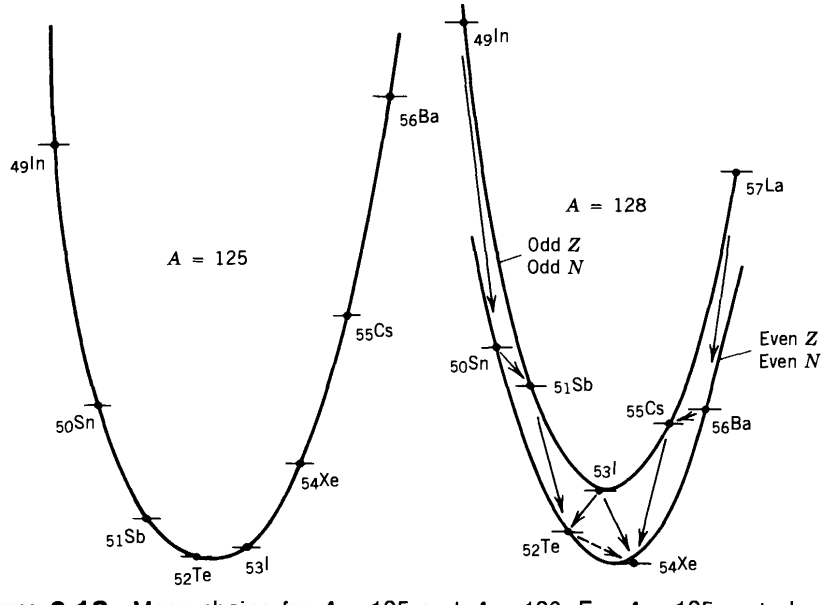


Figure 3.18 Mass chains for $A = 125$ and $A = 128$. For $A = 125$, note how the energy differences between neighboring isotopes increase as we go further from the stable member at the energy minimum. For $A = 128$, note the effect of the pairing term; in particular, ^{128}I can decay in either direction, and it is energetically possible for ^{128}Te to decay directly to ^{128}Xe by the process known as double β decay.

With $a_c = 0.72$ MeV and $a_{sym} = 23$ MeV, it follows that the first two terms in the numerator are negligible, and so

$$Z_{min} \simeq \frac{A}{2} \frac{1}{1 + \frac{1}{4}A^{2/3}a_c/a_{sym}} \tag{3.31}$$

For small A, $Z_{min} \simeq A/2$ as expected, but for large A, $Z_{min} < A/2$. For heavy nuclei, Equation 3.31 gives $Z/A \simeq 0.41$, consistent with observed values for heavy stable nuclei.

Figure 3.18 shows a typical odd-A decay chain for $A = 125$, leading to the stable nucleus at $Z = 52$. The unstable nuclei approach stability by converting a neutron into a proton or a proton into a neutron by radioactive β decay. Notice how the decay energy (that is, the mass difference between neighboring isobars) increases as we go further from stability. For even A, the pairing term gives two parabolas, displaced by 2δ. This permits two unusual effects, not seen in odd-A decays: (1) some odd-Z, odd-N nuclei can decay in either direction, converting a neutron to a proton or a proton to a neutron; (2) certain *double β decays* can become energetically possible, in which the decay may change 2 protons to 2 neutrons. Both of these effects are discussed in Chapter 9.

3.4 NUCLEAR ANGULAR MOMENTUM AND PARITY

In Section 2.5 we discussed the coupling of orbital angular momentum $\boldsymbol{\ell}$ and spin $\boldsymbol{s}$ to give total angular momentum $\boldsymbol{j}$. To the extent that the nuclear potential is central, $\boldsymbol{\ell}$ and $\boldsymbol{s}$ (and therefore $\boldsymbol{j}$) will be constants of the motion. In the quantum mechanical sense, we can therefore label every nucleon with the corresponding quantum numbers ℓ, s, and j. The total angular momentum of a nucleus containing A nucleons would then be the vector sum of the angular momenta of all the nucleons. This total angular momentum is usually called the *nuclear spin* and is represented by the symbol I. The angular momentum I has all of the usual properties of quantum mechanical angular momentum vectors: $I^2 = \hbar^2 I(I + 1)$ and $I_z = m\hbar$ $(m = -I, \ldots, +I)$. For many applications involving angular momentum, the nucleus behaves as if it were a single entity with an intrinsic angular momentum of I. In ordinary magnetic fields, for example, we can observe the nuclear Zeeman effect, as the state I splits up into its $2I + 1$ individual substates $m = -I, -I + 1, \ldots, I - 1, I$. These substates are equally spaced, as in the atomic normal Zeeman effect. If we could apply an incredibly strong magnetic field, so strong that the coupling between the nucleons were broken, we would see each individual j splitting into its $2j + 1$ substates. Atomic physics also has an analogy here: when we apply large magnetic fields we can break the coupling between the electronic $\boldsymbol{\ell}$ and $\boldsymbol{s}$ and separate the $2\ell + 1$ components of $\boldsymbol{\ell}$ and the $2s + 1$ components of $\boldsymbol{s}$. No fields of sufficient strength to break the coupling of the nucleons can be produced. We therefore observe the behavior of I as if the nucleus were only a single "spinning" particle. For this reason, the spin (total angular momentum) $\boldsymbol{I}$ and the corresponding spin quantum number I are used to describe nuclear states.

To avoid confusion, we will always use I to denote the nuclear spin; we will use j to represent the total angular momentum of a single nucleon. It will often

be the case that a single valence particle determines all of the nuclear properties; in that case, $I = j$. In other cases, it may be necessary to consider two valence particles, in which case $\boldsymbol{I} = \boldsymbol{j}_1 + \boldsymbol{j}_2$, and several different resultant values of I may be possible. Sometimes the odd particle and the remaining core of nucleons each contribute to the angular momentum, with $\boldsymbol{I} = \boldsymbol{j}_{\text{particle}} + \boldsymbol{j}_{\text{core}}$.

One important restriction on the allowed values of I comes from considering the possible z components of the total angular momentum of the individual nucleons. Each j must be half-integral ($\frac{1}{2}, \frac{3}{2}, \frac{5}{2}, \ldots$) and thus its only possible z components are likewise half-integral ($\pm\frac{1}{2}\hbar, \pm\frac{3}{2}\hbar, \pm\frac{5}{2}\hbar, \ldots$). If we have an even number of nucleons, there will be an even number of half-integral components, with the result that the z component of the total I can take only integral values. This requires that I itself be an integer. If the number of nucleons is odd, the total z component must be half-integral and so must the total I. We therefore require the following rules:

odd-A nuclei: I = half-integral

even-A nuclei: I = integral

The measured values of the nuclear spin can tell us a great deal about the nuclear structure. For example, of the hundreds of known (stable and radioactive) even-Z, even-N nuclei, all have spin-0 ground states. This is evidence for the nuclear pairing force we discussed in the previous section; the nucleons couple together in spin-0 pairs, giving a total I of zero. As a corollary, the ground state spin of an odd-A nucleus must be equal to the j of the odd proton or neutron. We discuss this point further when we consider the nuclear shell model in Chapter 5.

Along with the nuclear spin, the *parity* is also used to label nuclear states. The parity can take either + (even) or − (odd) values. If we knew the wave function of every nucleon, we could determine the nuclear parity by multiplying together the parities of each of the A nucleons, ending with a result π either + or −: $\pi = \pi_1\pi_2 \cdots \pi_A$. However, in practice no such procedure is possible, for we generally cannot assign a definite wave function of known parity to every nucleon. Like the spin I, we regard the parity π as an "overall" property of the whole nucleus. It can be directly measured using a variety of techniques of nuclear decays and reactions. The parity is denoted by a + or − superscript to the nuclear spin, as I^{π}. Examples are 0^+, 2^-, $\frac{1}{2}^-$, $\frac{5}{2}^+$. There is no direct theoretical relationship between I and π; for any value of I, it is possible to have either $\pi = +$ or $\pi = -$.

3.5 NUCLEAR ELECTROMAGNETIC MOMENTS

Much of what we know about nuclear structure comes from studying not the strong nuclear interaction of nuclei with their surroundings, but instead the much weaker electromagnetic interaction. That is, the strong nuclear interaction establishes the distribution and motion of nucleons in the nucleus, and we probe that distribution with the electromagnetic interaction. In doing so, we can use electromagnetic fields that have less effect on the motion of nucleons than the

strong force of the nuclear environment; thus our measurements do not seriously distort the object we are trying to measure.

Any distribution of electric charges and currents produces electric and magnetic fields that vary with distance in a characteristic fashion. It is customary to assign to the charge and current distribution an electromagnetic *multipole moment* associated with each characteristic spatial dependence—the $1/r^2$ electric field arises from the net charge, which we can assign as the zeroth or *monopole* moment; the $1/r^3$ electric field arises from the first or *dipole* moment; the $1/r^4$ electric field arises from the second or *quadrupole* moment, and so on. The magnetic multipole moments behave similarly, with the exception of the monopole moment; as far as we know, magnetic monopoles either do not exist or are exceedingly rare, and thus the magnetic monopole field ($\propto 1/r^2$) does not contribute. Electromagnetic theory gives us a recipe for calculating the various electric and magnetic multipole moments, and the same recipe can be carried over into the nuclear regime using quantum mechanics, by treating the multipole moments in operator form and calculating their expectation values for various nuclear states. These expectation values can then be directly compared with the experimental values we measure in the laboratory. Techniques for measuring the nuclear moments are discussed in Chapter 16.

The simplest distributions of charges and currents give only the lowest order multipole fields. A spherical charge distribution gives only a monopole (Coulomb) field; the higher order fields all vanish. A circular current loop gives only a magnetic dipole field. Nature has not been arbitrary in the construction of nuclei; if a simple, symmetric structure (consistent with the nuclear interaction) is possible, then nuclei tend to acquire that structure. It is therefore usually necessary to measure or calculate only the lowest order multipole moments to characterize the electromagnetic properties of the nucleus.

Another restriction on the multipole moments comes about from the symmetry of the nucleus, and is directly related to the parity of the nuclear states. Each electromagnetic multipole moment has a parity, determined by the behavior of the multipole operator when $\boldsymbol{r} \rightarrow -\boldsymbol{r}$. The parity of electric moments is $(-1)^L$, where L is the order of the moment ($L = 0$ for monopole, $L = 1$ for dipole, $L = 2$ for quadrupole, etc.); for magnetic moments the parity is $(-1)^{L+1}$. When we compute the expectation value of a moment, we must evaluate an integral of the form $\int \psi^* \mathcal{O} \psi \, dv$, where $\mathcal{O}$ is the appropriate electromagnetic operator. The parity of ψ itself is not important; because ψ appears twice in the integral, whether $\psi \rightarrow +\psi$ or $\psi \rightarrow -\psi$ does not change the integrand. If, however, $\mathcal{O}$ has odd parity, then the integrand is an odd function of the coordinates and must vanish identically. *Thus all odd-parity static multipole moments must vanish*—electric dipole, magnetic quadrupole, electric octupole ($L = 3$), and so on.

The monopole electric moment is just the net nuclear charge Ze. The next nonvanishing moment is the *magnetic dipole moment* μ. A circular loop carrying current i and enclosing area A has a magnetic moment of magnitude $|\mu| = iA$; if the current is caused by a charge e, moving with speed v in a circle of radius r (with period $2\pi r/v$), then

$$|\mu| = \frac{e}{(2\pi r/v)} \pi r^2 = \frac{evr}{2} = \frac{e}{2m} |\ell| \tag{3.32}$$

where $|\boldsymbol{\ell}|$ is the classical angular momentum mvr. In quantum mechanics, we operationally *define* the observable magnetic moment to correspond to the direction of greatest component of $\boldsymbol{\ell}$; thus we can take Equation 3.32 directly into the quantum regime by replacing $\boldsymbol{\ell}$ with the expectation value relative to the axis where it has maximum projection, which is $m_\ell \hbar$ with $m_\ell = +\ell$. Thus

$$\mu = \frac{e\hbar}{2m}\ell \tag{3.33}$$

where now ℓ is the angular momentum quantum number of the orbit.

The quantity $e\hbar/2m$ is called a *magneton*. For atomic motion we use the electron mass and obtain the *Bohr magneton* $\mu_B = 5.7884 \times 10^{-5}$ eV/T. Putting in the proton mass we have the *nuclear magneton* $\mu_N = 3.1525 \times 10^{-8}$ eV/T. Note that $\mu_N \ll \mu_B$ owing to the difference in the masses; thus under most circumstances atomic magnetism has much larger effects than nuclear magnetism. Ordinary magnetic interactions of matter (ferromagnetism, for instance) are determined by atomic magnetism; only in very special circumstances can we observe the effects of nuclear magnetism (see Chapter 16).

We can rewrite Equation 3.33 in a more useful form:

$$\mu = g_\ell \ell \mu_N \tag{3.34}$$

where g_ℓ is the *g factor* associated with the orbital angular momentum ℓ. For protons $g_\ell = 1$; because neutrons have no electric charge, we can use Equation 3.34 to describe the orbital motion of neutrons if we put $g_\ell = 0$.

We have thus far been considering only the orbital motion of nucleons. Protons and neutrons, like electrons, also have intrinsic or spin magnetic moments, which have no classical analog but which we write in the same form as Equation 3.34:

$$\mu = g_s s \mu_N \tag{3.35}$$

where $s = \frac{1}{2}$ for protons, neutrons, and electrons. The quantity g_s is known as the *spin g factor* and is calculated by solving a relativistic quantum mechanical equation. For a spin-$\frac{1}{2}$ point particle such as the electron, the Dirac equation gives $g_s = 2$, and measurement is quite consistent with that value for the electron: $g_s = 2.0023$. The difference between g_s and 2 is quite small and can be very accurately computed using the higher order corrections of quantum electrodynamics. On the other hand, for free nucleons, the experimental values are far from the expected value for point particles:

$$\text{proton:} \quad g_s = 5.5856912 \pm 0.0000022$$

$$\text{neutron:} \quad g_s = -3.8260837 \pm 0.0000018$$

(The measured magnetic moments, in nuclear magnetons, are just half the g_s factors.) Not only is the proton value far from the expected value of 2 for a point particle, but the uncharged neutron has a nonzero magnetic moment! Here is perhaps our first evidence that the nucleons are not elementary point particles like the electron, but have an internal structure; the internal structure of the nucleons must be due to charged particles in motion, whose resulting currents give the observed spin magnetic moments. It is interesting to note that g_s for the proton is greater than its expected value by about 3.6, while g_s for the neutron is

Table 3.2 Sample Values of Nuclear Magnetic Dipole Moments

Nuclide	$\mu(\mu_N)$
n	−1.9130418
p	+2.7928456
^{2}H (D)	+0.8574376
^{17}O	−1.89379
^{57}Fe	+0.09062293
^{57}Co	+4.733
^{93}Nb	+6.1705

All values refer to the nuclear ground states; uncertainties are typically a few parts in the last digit. For a complete tabulation, see V. S. Shirley, in *Table of Isotopes* (Wiley: New York, 1978), Appendix VII.

less than its expected value (zero) by roughly the same amount. Formerly these differences between the expected and measured g_s values were ascribed to the clouds of π mesons that surround nucleons, with positive and neutral π mesons in the proton's cloud, and negative and neutral π mesons in the neutron's cloud. The equal and opposite contributions of the meson cloud are therefore not surprising. In present theories we consider the nucleons as composed of three quarks; adding the magnetic moments of the quarks gives the nucleon magnetic moments directly (see Chapter 18).

In nuclei, the pairing force favors the coupling of nucleons so that their orbital angular momentum and spin angular momentum each add to zero. Thus the paired nucleons do not contribute to the magnetic moment, and we need only consider a few valence nucleons. If this were not so, we might expect on statistical grounds alone to see a few heavy nuclei with very large magnetic moments, perhaps tens of nuclear magnetons. However, no nucleus has been observed with a magnetic dipole moment larger than about $6\mu_N$.

Table 3.2 gives some representative values of nuclear magnetic dipole moments. Because of the pairing force, we can analyze these magnetic moments to learn about the nuclear structure. In Chapter 4, we discuss the magnetic moment of the deuteron, and in Chapter 5 we consider how nuclear models predict the magnetic moments of heavier nuclei.

The next nonvanishing moment is the *electric quadrupole moment*. The quadrupole moment eQ of a classical point charge e is of the form $e(3z^2 - r^2)$. If the particle moves with spherical symmetry, then (on the average) $z^2 = x^2 = y^2 = r^2/3$ and the quadrupole moment vanishes. If the particle moves in a classical flat orbit, say in the xy plane, then $z = 0$ and $Q = -r^2$. The quadrupole moment in quantum mechanics is

$$eQ = e\int \psi^*(3z^2 - r^2)\psi \, dv \tag{3.36}$$

for a single proton; for an orbiting neutron, $Q = 0$. If $|\psi|^2$ is spherically symmetric, then $Q = 0$. If $|\psi|^2$ is concentrated in the xy plane ($z \cong 0$), then

Table 3.3 Some Values of Nuclear Electric Quadrupole Moments

Nuclide	Q (b)
^{2}H (D)	+0.00288
^{17}O	−0.02578
^{59}Co	+0.40
^{63}Cu	−0.209
^{133}Cs	−0.003
^{161}Dy	+2.4
^{176}Lu	+8.0
^{209}Bi	−0.37

All values refer to nuclear ground states; uncertainties are typically a few parts in the last digit. For a complete tabulation, see V. S. Shirley, in *Table of Isotopes* (Wiley: New York, 1978), Appendix VII.

$Q \sim -\langle r^2 \rangle$, while if $|\psi|^2$ is concentrated along the z axis ($z \cong r$), we might have $Q \sim +2\langle r^2 \rangle$. Here $\langle r^2 \rangle$ is the mean-square radius of the orbit. Once again the pairing force is helpful, for if the paired nucleons move in spherically symmetric orbits, they do not contribute to Q. We might therefore expect that for many nuclei, the quadrupole moment can be estimated from the valence nucleon, which we can assume to orbit near the surface, so $r = R_0 A^{1/3}$. We therefore estimate $|eQ| \leq eR_0^2 A^{2/3}$, which ranges from about 6×10^{-30} em^2 for light nuclei to 50×10^{-30} em^2 for heavy nuclei. The unit of 10^{-28} m^2 is used frequently in nuclear reaction studies for cross sections, and is known as a *barn* (b). This unit is also convenient for measuring quadrupole moments; thus the expected maximum is from 0.06 to 0.5 eb. As you can see from Table 3.3, many nuclei do fall within that range, but several, especially in the rare-earth region, are far outside. Here the quadrupole moment is giving important information—the model of the single particle cannot explain the large observed quadrupole moments. Most or all of the protons must somehow collectively contribute to have such a large Q. The assumption of a spherically symmetric core of paired nucleons is not valid for these nuclei. The core in certain nuclei can take on a static nonspherical shape that can give a large quadrupole moment. The properties of such strongly deformed nuclei are discussed in Chapter 5.

3.6 NUCLEAR EXCITED STATES

Just as we learn about atoms by studying their excited states, we study nuclear structure in part through the properties of nuclear excited states. (And like atomic excited states, the nuclear excited states are unstable and decay rapidly to the ground state.) In atoms, we make excited states by moving individual electrons to higher energy orbits, and we can do the same for individual nucleons; thus the excited states can reveal something about the orbits of individual nucleons. We have already several times in this chapter referred to the complementary single-particle and collective structure of nuclei—we can also

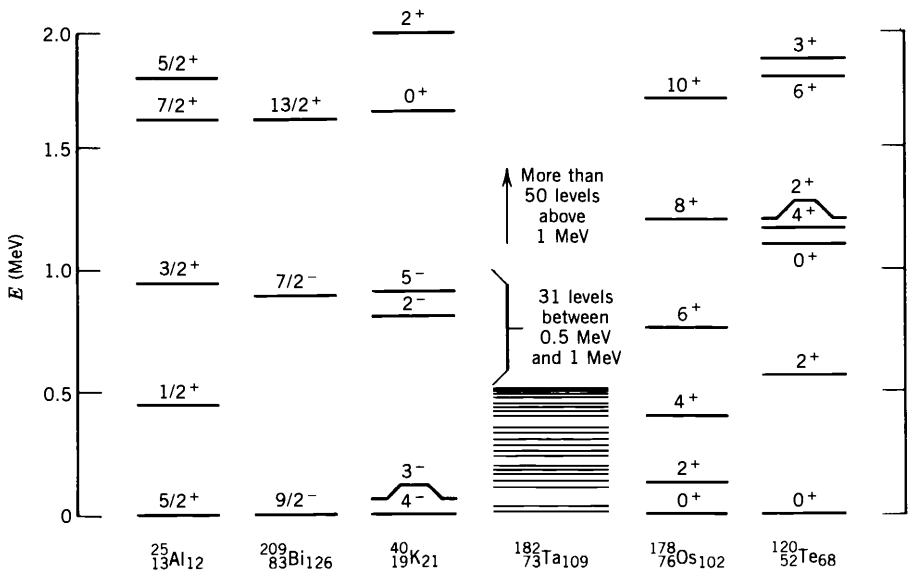


Figure 3.19 Some sample level schemes showing the excited states below 2 MeV. Some nuclei, such as ^{209}Bi, show great simplicity, while others, such as ^{182}Ta, show great complexity. There is a regularity associated with the levels of ^{178}Os that is duplicated in all even-Z, even-N nuclei in the range $150 \leq A \leq 190$. Structures similar to ^{120}Te are found in many nuclei in the range $50 \leq A \leq 150$.

produce excited states by adding energy to the core of paired nucleons. This energy can take the form of collective rotation or vibrations of the entire core, or it might even break one of the pairs, thereby adding two additional valence nucleons.

Part of the goal of nuclear spectroscopy is to observe the possible excited states and to measure their properties. The experimental techniques available include all manner of radioactive decay and nuclear reaction studies that we will consider in detail in subsequent sections. Among the properties we should like to measure for each excited state are: energy of excitation, lifetime and mode(s) of decay, spin and parity, magnetic dipole moment, and electric quadrupole moment. With more than 1000 individual nuclides, each of which may have hundreds of excited states, the tasks of measuring, tabulating, and interpreting these data are almost overwhelming.

Figure 3.19 shows some sample nuclear level schemes. A few of the excited states are identified as originating from excitations of the valence nucleons or the core; such identifications come about only after the properties listed above have been measured and have been compared with the predictions of calculations based on either single particle or collective core excitations, to see which agrees best with experiment. In subsequent chapters, we will explore the experimental techniques used to extract this information and nuclear models used to interpret it. Only through difficult and precise experiments, and through calculations involving the most powerful computers now available, can we obtain such detailed interpretations of nuclear structure.

REFERENCES FOR ADDITIONAL READING

Two essential references on nuclear charge and mass distributions are Roger C. Barrett and Daphne F. Jackson, *Nuclear Sizes and Structure* (Oxford: Clarendon, 1977), and the collection of articles on nuclear charge and moment distributions in *Atomic Data and Nuclear Data Tables* **14**, 479–653 (1974).

A collection of reprints of articles relating to electron scattering is R. Hofstadter, *Nuclear and Nucleon Structure* (New York: Benjamin, 1963). The use of muonic atoms to determine nuclear charge distributions is reviewed by C. S. Wu and L. Wilets, *Ann. Rev. Nucl. Sci*, **19**, 527 (1969). General techniques of using lasers to do high-resolution optical spectroscopy to study nuclear properties are discussed in D. E. Murnick and M. S. Feld, *Ann. Rev. Nucl. Sci.* **29**, 411 (1979). For more detail on the semiempirical mass formula, see R. D. Evans, *The Atomic Nucleus* (New York: McGraw-Hill, 1955), Chapter 11.

PROBLEMS

1. Show that the mean-square charge radius of a uniformly charged sphere is $\langle r^2 \rangle = 3R^2/5$.
2. (a) Derive Equation 3.9. (b) Fill in the missing steps in the derivation of Equation 3.13 beginning with Equation 3.9.
3. Compute the form factors $F(q)$ for the following charge distributions:
 (a) $\rho(r) = \rho_0, \quad r < R$ (b) $\rho(r) = \rho_0 e^{-(\ln 2) r^2/R^2}$
 $= 0, \quad r > R$
4. A nuclear charge distribution more realistic than the uniformly charged distribution is the Fermi distribution, $\rho(r) = \rho_0\{1 + \exp[(r - R)/a]\}^{-1}$. (a) Sketch this distribution and compare with Figure 3.4. (b) Find the value of a if $t = 2.3$ fm. (c) What is the significance of the parameter R? (d) Evaluate $\langle r^2 \rangle$ according to this distribution.
5. Why is the electron screening correction, which is a great difficulty for analyzing electronic X rays, not a problem for muonic X rays?
6. (a) Using a one-electron model, evaluate the energies of the muonic K X rays in Fe assuming a point nucleus, and compare with the energies shown in Figure 3.8. (b) Evaluate the correction ΔE due to the finite nuclear size. Compare the corrected value with the measured energies.
7. (a) From the known masses of ^{15}O and ^{15}N, compute the difference in binding energy. (b) Assuming this difference to arise from the difference in Coulomb energy, compute the nuclear radius of ^{15}O and ^{15}N.
8. Given the following mass doublet values (in units of 10^{-6} u), compute the corresponding values for the atomic mass of ^{37}Cl:

$$m(C_3H) - m(^{37}Cl) = 41922.2 \pm 0.3$$
$$m(C_2D_8) - m(^{37}ClH_3) = 123436.5 \pm 0.1$$
$$m(C_3H_6O_2) - m(^{37}Cl_2) = 104974.24 \pm 0.08$$

 Here D $\equiv {}^2H$, C $\equiv {}^{12}C$, and O $\equiv {}^{16}O$. Include in your calculation the effect of uncertainties in the H, D, O, and C masses.

9. Compute the total binding energy and the binding energy per nucleon for (a) ^{7}Li; (b) ^{20}Ne; (c) ^{56}Fe; (d) ^{235}U.
10. For each of the following nuclei, use the semiempirical mass formula to compute the total binding energy and the Coulomb energy: (a) ^{21}Ne; (b) ^{57}Fe; (c) ^{209}Bi; (d) ^{256}Fm.
11. Compute the mass defects of (a) ^{32}S; (b) ^{20}F; (c) ^{238}U.
12. Given the following mass defects, find the corresponding atomic mass: (a) ^{24}Na: -8.418 MeV; (b) ^{144}Sm: -81.964 MeV; (c) ^{240}Pu: $+50.123$ MeV.
13. Evaluate (a) the neutron separation energies of ^{7}Li, ^{91}Zr, and ^{236}U; (b) the proton separation energies of ^{20}Ne, ^{55}Mn, and ^{197}Au.
14. Examine carefully the S_n and S_p values given in Table 3.1 and draw conclusions about the strength of the binding of the last proton or neutron in the mirror pairs (^{17}O, ^{17}F) and (^{41}Ca, ^{41}Sc). Try to account for general or systematic behavior. Compare the nucleon separation energies in nuclei with identical numbers of protons or neutrons (for example, S_n in ^{16}O and ^{17}F or S_p in ^{16}O and ^{17}O). Extend these systematics by evaluating and tabulating the S_n and S_p for ^{4}He, ^{5}He, ^{5}Li and for ^{56}Ni, ^{57}Ni, and ^{57}Cu. (*Note*: Nuclei with Z or N equal to 2, 8, 20, or 28 have unusual stability. We explore the reasons for this behavior in Chapter 5.)
15. Use the semiempirical mass formula to obtain an expression for the two-neutron separation energy when $A \gg 1$. (*Hint:* A differential method is far easier than an algebraic one for this problem.) Estimate the size of the various terms and discuss the A dependence. Compare with the following data for Al and Te:

^{25}Al	31.82 MeV	^{117}Te	18.89 MeV	^{124}Te	16.36 MeV
^{26}Al	28.30 MeV	^{118}Te	18.45 MeV	^{125}Te	16.00 MeV
^{27}Al	24.42 MeV	^{119}Te	18.17 MeV	^{126}Te	15.69 MeV
^{28}Al	20.78 MeV	^{120}Te	17.88 MeV	^{127}Te	15.41 MeV
^{29}Al	17.16 MeV	^{121}Te	17.46 MeV	^{128}Te	15.07 MeV
^{30}Al	15.19 MeV	^{122}Te	17.04 MeV	^{129}Te	14.86 MeV
^{31}Al	13.03 MeV	^{123}Te	16.80 MeV	^{130}Te	14.50 MeV

Why do we choose two-neutron, rather than one-neutron, separation energies for this comparison?

16. In analogy with the previous problem, use the semiempirical mass formula to find approximate expressions for the variation of S_p with A holding Z constant. Obtain data for several sets of isotopes, plot the data, and compare with the predictions of the semiempirical mass formula.
17. The spin-parity of ^{9}Be and ^{9}B are both $\frac{3}{2}^{-}$. Assuming in both cases that the spin and parity are characteristic only of the odd nucleon, show how it is possible to obtain the observed spin-parity of ^{10}B (3^{+}). What other spin-parity combinations could also appear? (These are observed as excited states of ^{10}B.)
18. Let's suppose we can form ^{3}He or ^{3}H by adding a proton or a neutron to ^{2}H, which has spin equal to 1 and even parity. Let ℓ be the orbital angular

momentum of the added nucleon relative to the ^{2}H center of mass: What are the possible values of the total angular momentum of ^{3}H or ^{3}He? Given that the ground-state parity of ^{3}H and ^{3}He is even, which of these can be eliminated? What is the most likely value of the ground-state angular momentum of ^{3}H or ^{3}He? Can you make a similar argument based on removing a proton or a neutron from ^{4}He? (What is the ground-state spin-parity of ^{4}He?) How would you account for the spin-parity of ^{5}Li and ^{5}He ($\frac{3}{2}^-$)?

19. (a) Consider a neutron as consisting of a proton plus a negative π meson in an $\ell = 1$ orbital state. What would be the orbital magnetic dipole moment of such a configuration? Express your result as a multiple of the proton's magnetic moment. (b) Is it possible to account for the observed neutron magnetic moment from such a model? Suppose the neutron wave function consisted of two pieces, one corresponding to a $g = 0$ "Dirac" neutron and the other to proton-plus-π meson. What would be the relative sizes of the two pieces of the wave function? (Assume the proton also to behave like an ideal Dirac particle.) (c) Repeat the previous analysis for the proton magnetic moment; that is, consider the proton as part pure Dirac proton, plus part Dirac neutron with orbiting positive π meson in $\ell = 1$ state.

20. Suppose the proton magnetic moment were to be interpreted as due to the rotational motion of a positive spherical uniform charge distribution of radius R spinning about its axis with angular speed ω. (a) Show that $\mu = e\omega R^2/5$ by integrating over the charge distribution. (b) Using the classical relationship between angular momentum and rotational speed, show that $\omega R^2 = s/0.4m$. (c) Finally, obtain $\mu = (e/2m)s$, which is analogous to Equation 3.32.

21. Calculate the electric quadrupole moment of a uniformly charged ellipsoid of revolution of semimajor axis b and semiminor axis a.

4

THE FORCE BETWEEN NUCLEONS

Even before describing any further experiments to study the force between two nucleons, we can already guess at a few of the properties of the nucleon–nucleon force:

1. At short distances it is stronger than the Coulomb force; the nuclear force can overcome the Coulomb repulsion of protons in the nucleus.
2. At long distances, of the order of atomic sizes, the nuclear force is negligibly feeble; the interactions among nuclei in a molecule can be understood based only on the Coulomb force.
3. Some particles are immune from the nuclear force; there is no evidence from atomic structure, for example, that electrons feel the nuclear force at all.

As we begin to do experiments specifically to explore the properties of the nuclear force, we find several other remarkable properties:

4. The nucleon–nucleon force seems to be nearly independent of whether the nucleons are neutrons or protons. This property is called *charge independence*.
5. The nucleon–nucleon force depends on whether the spins of the nucleons are parallel or antiparallel.
6. The nucleon–nucleon force includes a repulsive term, which keeps the nucleons at a certain average separation.
7. The nucleon–nucleon force has a noncentral or *tensor* component. This part of the force does not conserve orbital angular momentum, which is a constant of the motion under central forces.

In this chapter we explore these properties in detail, discuss how they are measured, and propose some possible forms for the basic nucleon–nucleon interaction.

4.1 THE DEUTERON

A *deuteron* (^{2}H nucleus) consists of a neutron and a proton. (A neutral atom of ^{2}H is called *deuterium*.) It is the simplest bound state of nucleons and therefore gives us an ideal system for studying the nucleon–nucleon interaction. For

nuclear physicists, the deuteron should be what the hydrogen atom is for atomic physicists. Just as the measured Balmer series of electromagnetic transitions between the excited states of hydrogen led to an understanding of the structure of hydrogen, so should the electromagnetic transitions between the excited states of the deuteron lead to an understanding of its structure. Unfortunately, there are *no excited states* of the deuteron—it is such a weakly bound system that the only "excited states" are unbound systems consisting of a free proton and neutron.

Binding Energy

The binding energy of the deuteron is a very precisely measured quantity, which can be determined in three different ways. By spectroscopy, we can directly determine the mass of the deuteron, and we can use Equation 3.25 to find the binding energy. Using the mass doublet method described in Section 3.2, the following determinations have been made (we use the symbol D for ^{2}H):

$$m(C_6H_{12}) - m(C_6D_6) = (9.289710 \pm 0.000024) \times 10^{-3} \text{ u}$$

and

$$m(C_5D_{12}) - m(C_6D_6) = (84.610626 \pm 0.000090) \times 10^{-3} \text{ u}.$$

From the first difference we find, using 1.007825037 u for the ^{1}H mass,

$$m(^2\text{H}) = 2.014101789 \pm 0.000000021 \text{ u}$$

and from the second,

$$m(^2\text{H}) = 2.014101771 \pm 0.000000015 \text{ u}$$

These precise values are in very good agreement, and using the measured ^{1}H and neutron masses we can find the binding energy

$$B = [m(^1\text{H}) + m(\text{n}) - m(^2\text{H})]c^2 = 2.22463 \pm 0.00004 \text{ MeV}$$

We can also determine this binding energy directly by bringing a proton and a neutron together to form ^{2}H and measuring the energy of the γ-ray photon that is emitted:

$$^1\text{H} + \text{n} \rightarrow {}^2\text{H} + \gamma$$

The deduced binding energy, which is equal to the observed energy of the photon less a small recoil correction, is 2.224589 $\pm$ 0.000002 MeV, in excellent agreement with the mass spectroscopic value. A third method uses the reverse reaction, called *photodissociation*,

$$\gamma + {}^2\text{H} \rightarrow {}^1\text{H} + \text{n}$$

in which a γ-ray photon breaks apart a deuteron. The minimum γ-ray energy that accomplishes this process is equal to the binding energy (again, corrected for the recoil of the final products). The observed value is 2.224 $\pm$ 0.002 MeV, in good agreement with the mass spectroscopic value.

As we discussed in Section 3.3, the average binding energy per nucleon is about 8 MeV. The deuteron is therefore very weakly bound compared with typical nuclei. Let's see how we can analyze this result to study the properties of the deuteron.

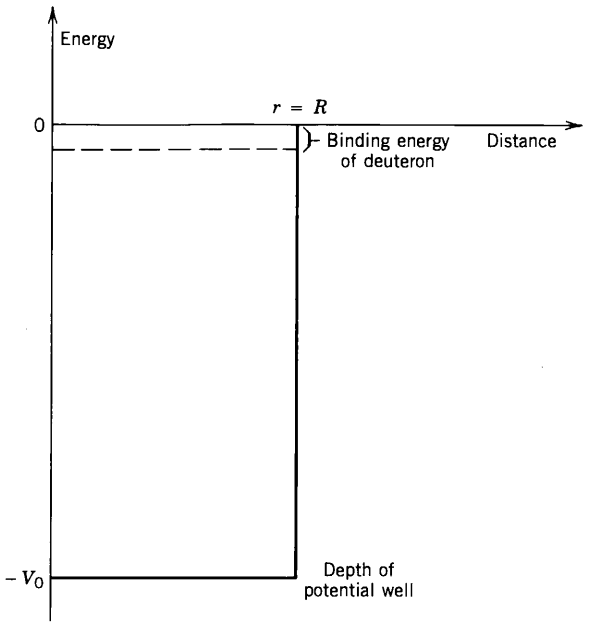


Figure 4.1 The spherical square-well potential is an approximation to the nuclear potential. The depth is $-V_0$, where V_0 is deduced to be about 35 MeV. The bound state of the deuteron, at an energy of about -2 MeV, is very close to the top of the well.

To simplify the analysis of the deuteron, we will assume that we can represent the nucleon–nucleon potential as a three-dimensional square well, as shown in Figure 4.1:

$$\begin{aligned} V(r) &= -V_0 \qquad \text{for } r < R \\ &= 0 \qquad\quad \text{for } r > R \end{aligned} \tag{4.1}$$

This is of course an oversimplification, but it is sufficient for at least some qualitative conclusions. Here r represents the separation between the proton and the neutron, so R is in effect a measure of the *diameter* of the deuteron. Let's assume that the lowest energy state of the deuteron, just like the lowest energy state of the hydrogen atom, has $\ell = 0$. (We justify this assumption later in this section when we discuss the spin of the deuteron.) If we define the radial part of $\psi(\boldsymbol{r})$ as $u(r)/r$, then we can rewrite Equation 2.60 as

$$-\frac{\hbar^2}{2m}\frac{d^2u}{dr^2} + V(r)u(r) = Eu(r) \tag{4.2}$$

This expression looks exactly like the one-dimensional Equation 2.4, and the solutions can be written in analogy with Equations 2.47. For $r < R$,

$$u(r) = A \sin k_1 r + B \cos k_1 r \tag{4.3}$$

with $k_1 = \sqrt{2m(E + V_0)/\hbar^2}$, and for $r > R$,

$$u(r) = Ce^{-k_2 r} + De^{+k_2 r} \tag{4.4}$$

with $k_2 = \sqrt{-2mE/\hbar^2}$. (Remember, $E < 0$ for bound states.) To keep the wave

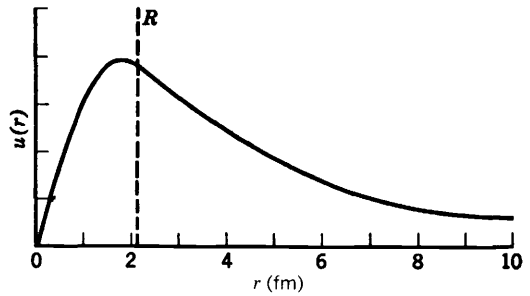


Figure 4.2 The deuteron wave function for $R = 2.1$ fm. Note how the exponential joins smoothly to the sine at $r = R$, so that both $u(r)$ and du/dr are continuous. If the wave function did not "turn over" inside $r = R$, it would not be possible to connect smoothly to a decaying exponential (negative slope) and there would be no bound state.

function finite for $r \to \infty$ we must have $D = 0$, and to keep it finite for $r \to 0$ we must have $B = 0$. (ψ depends on $u(r)/r$; as $r \to 0$, $u(r)$ also must go to zero.) Applying the continuity conditions on u and du/dr at $r = R$, we obtain

$$k_1 \cot k_1 R = -k_2 \tag{4.5}$$

This transcendental equation gives a relationship between V_0 and R. From electron scattering experiments, the rms charge radius of the deuteron is known to be about 2.1 fm, which provides a reasonable first estimate for R. Solving Equation 4.5 numerically (see Problem 6 at the end of this chapter) the result is $V_0 = 35$ MeV. This is actually quite a reasonable estimate of the strength of the nucleon–nucleon potential, even in more complex nuclei. (Note, however, that the proton and neutron are very likely to be found at separations greater than R; see Problem 4.)

We can see from Figure 4.1 how close the deuteron is to the top of the well. If the nucleon–nucleon force were just a bit weaker, the deuteron bound state would not exist (see Problem 3). We are fortunate that it does, however, because the formation of deuterium from hydrogen is the first step not only in the proton-proton cycle of fusion by which our sun makes its energy, but also in the formation of stable matter from the primordial hydrogen that filled the early universe. If no stable two-nucleon bound state existed, we would not be here to discuss it! (For more on the cosmological consequences of the formation of deuterium in the early universe, see Chapter 19.)

The deuteron wave function is shown in Figure 4.2. The weak binding means that $\psi(r)$ is just barely able to "turn over" in the well so as to connect at $r = R$ with the negative slope of the decaying exponential.

Spin and Parity

The total angular momentum $\boldsymbol{I}$ of the deuteron should have three components: the individual spins $\boldsymbol{s}_n$ and $\boldsymbol{s}_p$ of the neutron and proton (each equal to $\frac{1}{2}$), and the orbital angular momentum $\boldsymbol{\ell}$ of the nucleons as they move about their common center of mass:

$$\boldsymbol{I} = \boldsymbol{s}_n + \boldsymbol{s}_p + \boldsymbol{\ell} \tag{4.6}$$

When we solved the Schrödinger equation for the deuteron, we assumed $\ell = 0$ in analogy with the lowest bound state (the 1s state) in atomic hydrogen. The measured spin of the deuteron is $I = 1$ (how this is measured is discussed in Chapter 16). Since the neutron and proton spins can be either parallel (for a total of 1) or antiparallel (for a total of zero), there are four ways to couple $\boldsymbol{s}_n$, $\boldsymbol{s}_p$, and ℓ to get a total I of 1:

(a) $\boldsymbol{s}_n$ and $\boldsymbol{s}_p$ parallel with $\ell = 0$,
(b) $\boldsymbol{s}_n$ and $\boldsymbol{s}_p$ antiparallel with $\ell = 1$,
(c) $\boldsymbol{s}_n$ and $\boldsymbol{s}_p$ parallel with $\ell = 1$,
(d) $\boldsymbol{s}_n$ and $\boldsymbol{s}_p$ parallel with $\ell = 2$.

Another property of the deuteron that we can determine is its *parity* (even or odd), the behavior of its wave function when $\boldsymbol{r} \rightarrow -\boldsymbol{r}$ (see Section 2.6). By studying the reactions involving deuterons and the property of the photon emitted during the formation of deuterons, we know that its parity is even. In Section 2.6 we discussed that the parity associated with orbital motion is $(-1)^{\ell}$, even parity for $\ell = 0$ (s states) and $\ell = 2$ (d states) and odd parity for $\ell = 1$ (p states). The observed even parity allows us to eliminate the combinations of spins that include $\ell = 1$, leaving $\ell = 0$ and $\ell = 2$ as possibilities. The spin and parity of the deuteron are therefore consistent with $\ell = 0$ as we assumed, but of course we cannot yet exclude the possibility of $\ell = 2$.

Magnetic Dipole Moment

In Section 3.5 we discussed the spin and orbital contributions to the magnetic dipole moment. If the $\ell = 0$ assumption is correct, there should be no orbital contribution to the magnetic moment, and we can assume the total magnetic moment to be simply the combination of the neutron and proton magnetic moments:

$$\begin{aligned} \boldsymbol{\mu} &= \boldsymbol{\mu}_n + \boldsymbol{\mu}_p \\ &= \frac{g_{sn}\mu_N}{\hbar}\boldsymbol{s}_n + \frac{g_{sp}\mu_N}{\hbar}\boldsymbol{s}_p \end{aligned} \tag{4.7}$$

where $g_{sn} = -3.826084$ and $g_{sp} = 5.585691$. As we did in Section 3.5, we take the observed magnetic moment to be the z component of $\boldsymbol{\mu}$ when the spins have their maximum value ($+\frac{1}{2}\hbar$):

$$\begin{aligned} \mu &= \tfrac{1}{2}\mu_N(g_{sn} + g_{sp}) \\ &= 0.879804\,\mu_N \end{aligned} \tag{4.8}$$

The observed value is $0.8574376 \pm 0.0000004\ \mu_N$, in good but not quite exact agreement with the calculated value. The small discrepancy can be ascribed to any of a number of factors, such as contributions from the mesons exchanged between the neutron and proton; in the context of the present discussion, we can assume the discrepancy to arise from a small mixture of d state ($\ell = 2$) in the deuteron wave function:

$$\psi = a_s\,\psi(\ell = 0) + a_d\,\psi(\ell = 2) \tag{4.9}$$

Calculating the magnetic moment from this wave function gives

$$\mu = a_s^2 \mu(\ell = 0) + a_d^2 \mu(\ell = 2) \tag{4.10}$$

where $\mu(\ell = 0)$ is the value calculated in Equation 4.8 and $\mu(\ell = 2) = \frac{1}{4}(3 - g_{sp} - g_{sn})\mu_N$ is the value calculated for a d state. The observed value is consistent with $a_s^2 = 0.96$, $a_d^2 = 0.04$; that is, the deuteron is 96% $\ell = 0$ and only 4% $\ell = 2$. The assumption of the pure $\ell = 0$ state, which we made in calculating the well depth, is thus pretty good but not quite exact.

Electric Quadrupole Moment

The bare neutron and proton have no electric quadrupole moment, and so any measured nonzero value for the quadrupole moment must be due to the orbital motion. Thus the pure $\ell = 0$ wave function would have a vanishing quadrupole moment. The observed quadrupole moment is

$$Q = 0.00288 \pm 0.00002 \text{ b}$$

which, while small by comparison with many other nuclei, is certainly not zero.

The mixed wave function of Equation 4.9, when used as in Equation 3.36 to evaluate Q, gives two contributions, one proportional to a_d^2 and another proportional to the cross-term $a_s a_d$. Performing the calculation we obtain

$$Q = \frac{\sqrt{2}}{10} a_s a_d \langle r^2 \rangle_{sd} - \frac{1}{20} a_d^2 \langle r^2 \rangle_{dd} \tag{4.11}$$

where $\langle r^2 \rangle_{sd} = \int r^2 R_s(r) R_d(r) r^2 \, dr$ is the integral of r^2 over the radial wave functions; $\langle r^2 \rangle_{dd}$ is similarly defined. To calculate Q we must know the deuteron d-state wave function, which is not directly measurable. Using the realistic phenomenological potentials discussed later in this chapter gives reasonable values for Q with d-state admixtures of several percent, consistent with the value of 4% deduced from the magnetic moment.

This good agreement between the d-state admixtures deduced from μ and Q should be regarded as a happy accident and not taken too seriously. In the case of the magnetic dipole moment, there is no reason to expect that it is correct to use the free-nucleon magnetic moments in nuclei. (In fact, in the next chapter we see that there is strong evidence to the contrary.) Unfortunately, a nucleon in a deuteron lies somewhere between a free nucleon and a strongly bound nucleon in a nucleus, and we have no firm clues about what values to take for the magnetic moments. Spin-orbit interactions, relativistic effects, and meson exchanges may have greater effects on μ than the d-state admixture (but may cancel one another's effects). For the quadrupole moment, the poor knowledge of the d-state wave function makes the deduced d-state admixture uncertain. (It would probably be more valid to regard the calculation of Q, using a known d-state mixture, as a test of the d-state wave function.) Other experiments, particularly scattering experiments using deuterons as targets, also give d-state admixtures in the range of 4%. Thus our conclusions from the magnetic dipole and electric quadrupole moments may be valid after all!

It is important that we have an accurate knowledge of the d-state wave function because the mixing of ℓ values in the deuteron is the best evidence we have for the noncentral (tensor) character of the nuclear force.

4.2 NUCLEON–NUCLEON SCATTERING

Although the study of the deuteron gives us a number of clues about the nucleon–nucleon interaction, the total amount of information available is limited. Because there are no excited states, we can only study the dynamics of the nucleon–nucleon interaction in the configuration of the deuteron: $\ell = 0$, parallel spins, 2-fm separation. (Excited states, if they were present, might have different ℓ values or spin orientations.) To study the nucleon–nucleon interaction in different configurations, we can perform nucleon–nucleon scattering experiments, in which an incident beam of nucleons is scattered from a target of nucleons. If the target is a nucleus with many nucleons, then there will be several target nucleons within the range of the nuclear potential of the incident nucleon; in this case the observed scattering of a single nucleon will include the complicated effects of multiple encounters, making it very difficult to extract the properties of the interaction between individual nucleons. We therefore select a target of hydrogen so that incident particles can scatter from the individual protons. (It is still possible to have multiple scattering, but in this case it must occur through scattering first from one proton, then from another that is quite far from the first on the scale of nuclear dimensions. If the probability for a single encounter is small, the probability for multiple encounters will be negligible. This is very different from the case of scattering from a heavier nucleus, in which each single encounter with a target nucleus consists of many nucleon–nucleon interactions.)

Before we discuss the nuclear scattering problem, let's look at an analogous problem in optics, the diffraction of waves at a small slit or obstacle, as shown in Figure 4.3. The diffraction pattern produced by an obstacle is very similar to that produced by a slit of the same size. Nuclear scattering more resembles diffraction by the obstacle, so we will concentrate our discussion on it. There are three features of the optical diffraction that are analogous to the scattering of nucleons:

1. The incident wave is represented by a plane wave, while far from the obstacle the scattered wave fronts are spherical. The total energy content of any expanding spherical wave front cannot vary; thus its intensity (per unit area) must decrease like r^{-2} and its amplitude must decrease like r^{-1}.
2. Along the surface of any spherical scattered wave front, the diffraction is responsible for a variation in intensity of the radiation. The intensity thus depends on angular coordinates θ and ϕ.
3. A radiation detector placed at any point far from the obstacle would record both incident and scattered waves.

To solve the nucleon–nucleon scattering problem using quantum mechanics, we will again assume that we can represent the interaction by a square-well potential, as we did in the previous section for the deuteron. In fact, the only difference between this calculation and that of the deuteron is that we are concerned with free incident particles with $E > 0$. We will again simplify the Schrödinger equation by assuming $\ell = 0$. The justification for this assumption has nothing to do with that of the identical assumption made in the calculation for the deuteron. Consider an incident nucleon striking a target nucleon just at its surface; that is, the *impact parameter* (the perpendicular distance from the center of the target nucleon to the line of flight of the incident nucleon) is of the order of $R \simeq 1$ fm. If the incident particle has velocity v, its angular momentum

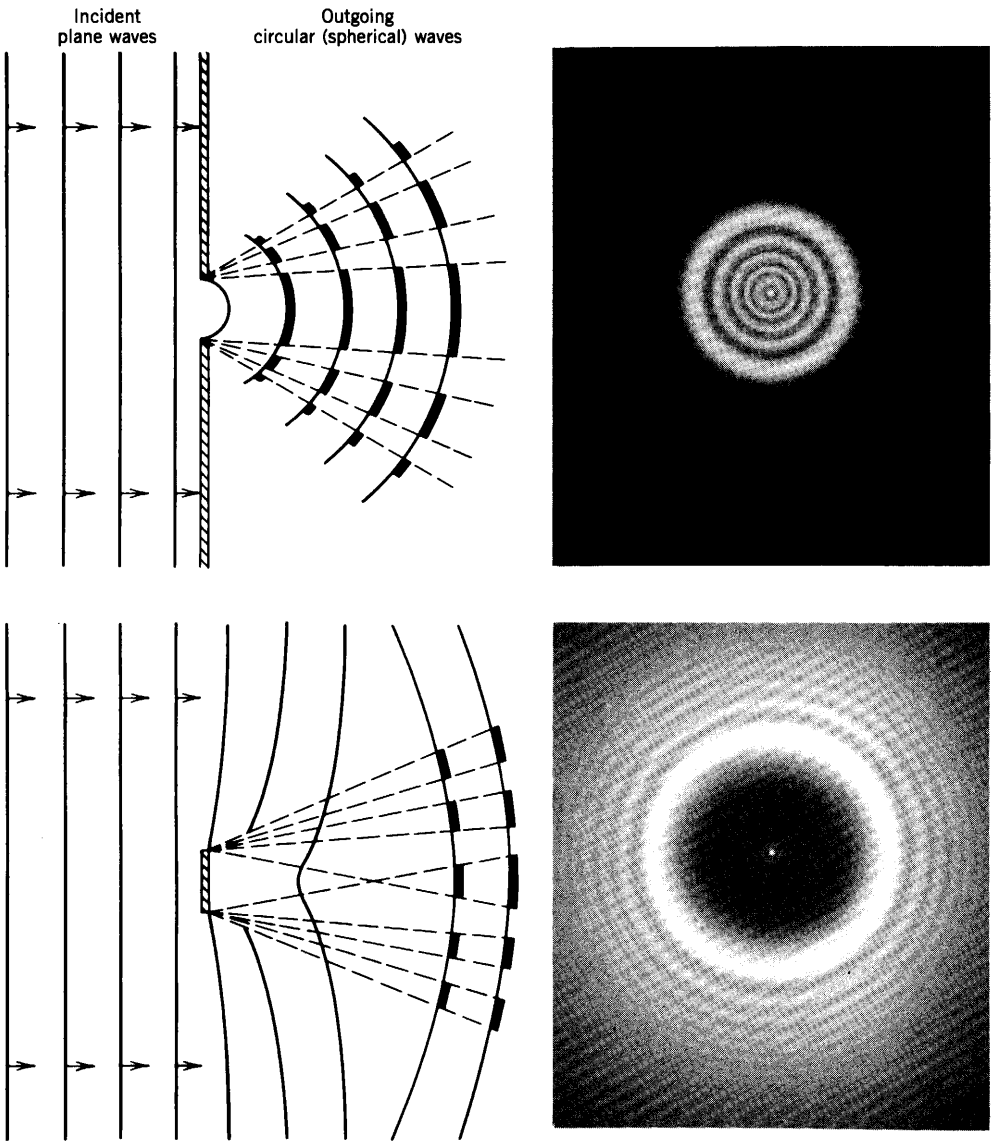


Figure 4.3 Representation of scattering by (top) a small opening and (bottom) a small obstacle. The shading of the wavefronts shows regions of large and small intensity. On the right are shown photographs of diffraction by a circular opening and an opaque circular disk. Source of photographs: M. Cagnet, M. Francon, and J. C. Thrierr, *Atlas of Optical Phenomena* (Berlin: Springer-Verlag, 1962).

relative to the target is mvR. The relative angular momentum between the nucleons must be quantized in units of $\hbar$; that is, $mvR = \ell\hbar$ in semiclassical notation. If $mvR \ll \hbar$, then only $\ell = 0$ interactions are likely to occur. Thus $v \ll \hbar/mR$ and the corresponding kinetic energy is estimated as

$$T = \tfrac{1}{2}mv^2 \ll \frac{\hbar^2}{2mR^2} = \frac{\hbar^2c^2}{2mc^2R^2} = \frac{(200\ \text{MeV} \cdot \text{fm})^2}{2(1000\ \text{MeV})(1\ \text{fm})^2} = 20\ \text{MeV}$$

If the incident energy is far below 20 MeV, the $\ell = 0$ assumption is justified. We will consider only low-energy scattering, for which the $\ell = 0$ assumption is valid.

The nucleon–nucleon scattering problem will be solved in the center-of-mass coordinate system (see Appendix B). The mass appearing in the Schrödinger equation is the reduced mass, which in this case is about half the nucleon mass.

The solution to the square-well problem for $r < R$ is given by Equation 4.3; as before, $B = 0$ in order that $u(r)/r$ remain finite for $r \to 0$. For $r > R$, the wave function is

$$u(r) = C' \sin k_2 r + D' \cos k_2 r \tag{4.12}$$

with $k_2 = \sqrt{2mE/\hbar^2}$. It is convenient to rewrite Equation 4.12 as

$$u(r) = C \sin(k_2 r + \delta) \tag{4.13}$$

where

$$C' = C \cos\delta \quad \text{and} \quad D' = C \sin\delta \tag{4.14}$$

The boundary conditions on u and du/dr at $r = R$ give

$$C \sin(k_2 R + \delta) = A \sin k_1 R \tag{4.15}$$

and

$$k_2 C \cos(k_2 R + \delta) = k_1 A \cos k_1 R \tag{4.16}$$

Dividing,

$$k_2 \cot(k_2 R + \delta) = k_1 \cot k_1 R \tag{4.17}$$

Again, we have a transcendental equation to solve; given E (which we control through the energy of the incident particle), V_0, and R, we can in principle solve for δ.

Before we discuss the methods for extracting the parameter δ from Equation 4.17, we examine how δ enters the solution to the Schrödinger equation. As $V_0 \to 0$ (in which case no scattering occurs), $k_1 \to k_2$ and $\delta \to 0$. This is just the free particle solution. The effect of V_0 on the wave function is indicated in Figure 4.4. The wave function at $r > R$ has the same form as the free particle, but it has experienced a *phase shift* δ. The nodes (zeros) of the wave function are "pulled" toward the origin by the attractive potential. (A repulsive potential would "push" the nodes away from the origin and would give a negative phase shift.) We can analyze the incident waves into components according to their angular momentum relative to the target: $\ell = 0$ (which we have been considering so far), $\ell = 1$, and so on. Associated with each ℓ there will be a different solution to the Schrödinger equation and a different phase shift δ_ℓ.

Let us see how our square-well problem relates to more general scattering theory. The incident wave is (as in the optical analogy) a plane wave traveling in the z direction:

$$\psi_{\text{incident}} = Ae^{ikz} \tag{4.18}$$

Let the target be located at the origin. Multiplying by the time-dependent factor gives

$$\psi(z, t) = Ae^{i(kz - \omega t)} \tag{4.19}$$

which always moves in the $+z$ direction (toward the target for $z < 0$ and away

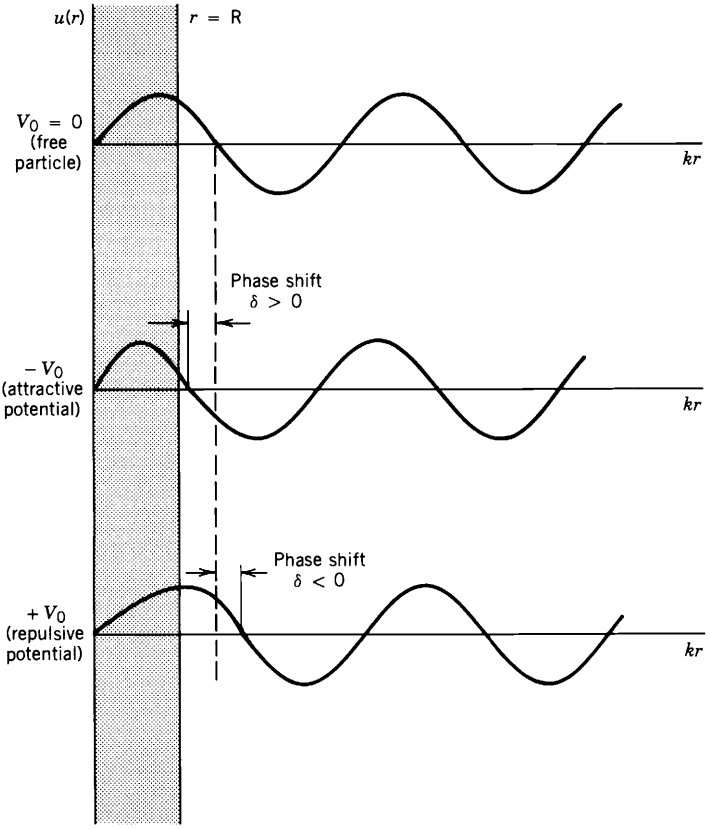


Figure 4.4 The effect of a scattering potential is to shift the phase of the scattered wave at points beyond the scattering regions, where the wave function is that of a free particle.

from it for $z > 0$). It is mathematically easier to work with spherical waves e^{ikr}/r and e^{-ikr}/r, and multiplying with $e^{-i\omega t}$ shows that e^{ikr} gives an outgoing wave and e^{-ikr} gives an incoming wave. (A more rigorous treatment of scattering theory, including terms with $\ell > 0$, is given in Chapter 11.) For $\ell = 0$ we can take

$$\psi_{\text{incident}} = \frac{A}{2ik}\left[\frac{e^{ikr}}{r} - \frac{e^{-ikr}}{r}\right] \tag{4.20}$$

The minus sign between the two terms keeps ψ finite for $r \to 0$, and using the coefficient A for both terms sets the amplitudes of the incoming and outgoing waves to be equal. We assume that the scattering does not create or destroy particles, and thus the scattering cannot change the amplitudes of the e^{ikr} or e^{-ikr} terms (since the squared amplitudes give the probabilities to detect incoming or outgoing particles). *All that can result from the scattering is a change in phase of the outgoing wave*:

$$\psi(r) = \frac{A}{2ik}\left[\frac{e^{i(kr+\beta)}}{r} - \frac{e^{-ikr}}{r}\right] \tag{4.21}$$

where β is the change in phase.

Manipulation of Equation 4.13 gives the relationship between β and δ_0:

$$\begin{aligned}\psi(r) &= \frac{C}{r}\sin(kr + \delta_0) \\ &= \frac{C}{r}\frac{e^{i(kr+\delta_0)} - e^{-i(kr+\delta_0)}}{2i} \\ &= \frac{C}{2i}e^{-i\delta_0}\left[\frac{e^{i(kr+2\delta_0)}}{r} - \frac{e^{-ikr}}{r}\right]\end{aligned} \tag{4.22}$$

Thus $\beta = 2\delta_0$ and $A = kCe^{-i\delta_0}$.

To evaluate the probability for scattering, we need the amplitude of the scattered wave. The wave function ψ represents all waves in the region $r > R$, and to find the amplitude of only the scattered wave we must subtract away the incident amplitude:

$$\begin{aligned}\psi_{\text{scattered}} &= \psi - \psi_{\text{incident}} \\ &= \frac{A}{2ik}(e^{2i\delta_0} - 1)\frac{e^{ikr}}{r}\end{aligned} \tag{4.23}$$

The current of scattered particles per unit area can be found using Equation 2.12 extended to three dimensions:

$$j_{\text{scattered}} = \frac{\hbar}{2mi}\left(\psi^*\frac{\partial\psi}{\partial r} - \frac{\partial\psi^*}{\partial r}\psi\right) \tag{4.24}$$

$$= \frac{\hbar|A|^2}{mkr^2}\sin^2\delta_0 \tag{4.25}$$

and the incident current is, in analogy with Equation 2.22

$$j_{\text{incident}} = \frac{\hbar k|A|^2}{m} \tag{4.26}$$

The scattered current is uniformly distributed over a sphere of radius r. An element of area $r^2\,d\Omega$ on that sphere subtends a solid angle $d\Omega = \sin\theta\,d\theta\,d\phi$ at the scattering center; see Figure 4.5. The *differential cross section* $d\sigma/d\Omega$ is the probability per unit solid angle that an incident particle is scattered into the solid angle $d\Omega$; the probability $d\sigma$ that an incident particle is scattered into $d\Omega$ is the ratio of the scattered current through $d\Omega$ to the incident current:

$$d\sigma = \frac{(j_{\text{scattered}})(r^2\,d\Omega)}{j_{\text{incident}}} \tag{4.27}$$

Using Equations 4.25 and 4.26 for the scattered and incident currents, we obtain

$$\frac{d\sigma}{d\Omega} = \frac{\sin^2\delta_0}{k^2} \tag{4.28}$$

The *total cross section* σ is the total probability to be scattered in any direction:

$$\sigma = \int \frac{d\sigma}{d\Omega}\,d\Omega \tag{4.29}$$

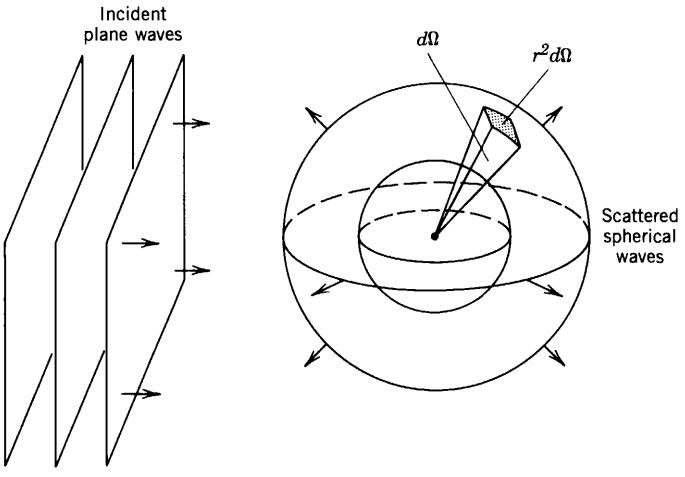


Figure 4.5 The basic geometry of scattering.

In general, $d\sigma/d\Omega$ varies with direction over the surface of the sphere; in the special case of $\ell = 0$ scattering, $d\sigma/d\Omega$ is constant and comes out of the integral:

$$\sigma = 4\pi \frac{d\sigma}{d\Omega}$$

$$= \frac{4\pi \sin^2 \delta_0}{k^2} \tag{4.30}$$

Thus the $\ell = 0$ phase shift is directly related to the probability for scattering to occur. That is, we can evaluate δ_0 from our simple square-well model, Equation 4.17, find the total cross section from Equation 4.30, and compare with the experimental cross section.

We now return to the analysis of Equation 4.17. Let us assume the incident energy is small, say $E \lesssim 10$ keV. Then $k_1 = \sqrt{2m(V_0 + E)/\hbar^2} \simeq 0.92\ \text{fm}^{-1}$, with $V_0 = 35$ MeV from our analysis of the deuteron bound state, and $k_2 = \sqrt{2mE/\hbar^2} \lesssim 0.016\ \text{fm}^{-1}$. If we let the right side of Equation 4.17 equal $-\alpha$,

$$\alpha = -k_1 \cot k_1 R \tag{4.31}$$

then a bit of trigonometric manipulation gives

$$\sin^2 \delta_0 = \frac{\cos k_2 R + (\alpha/k_2) \sin k_2 R}{1 + \alpha^2/k_2^2} \tag{4.32}$$

and so

$$\sigma = \frac{4\pi}{k_2^2 + \alpha^2}\left(\cos k_2 R + \frac{\alpha}{k_2} \sin k_2 R\right) \tag{4.33}$$

Using $R \approx 2$ fm from the study of the ^{2}H bound state gives $\alpha \approx 0.2\ \text{fm}^{-1}$. Thus $k_2^2 \ll \alpha^2$ and $k_2 R \ll 1$, giving

$$\sigma \simeq \frac{4\pi}{\alpha^2}(1 + \alpha R) = 4.6\ \text{b} \tag{4.34}$$

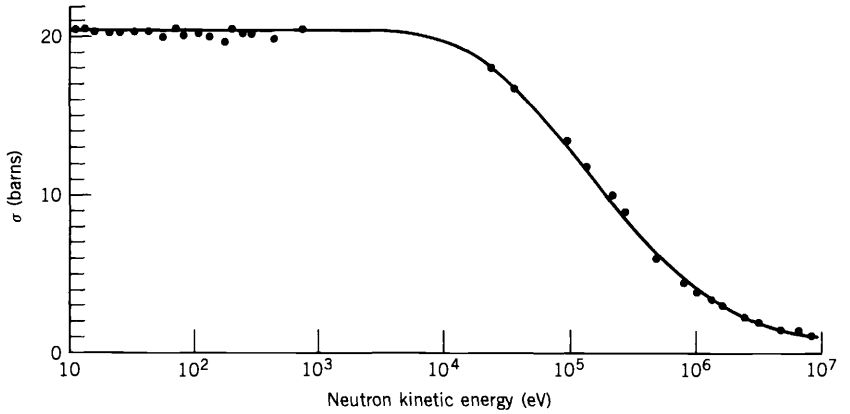


Figure 4.6 The neutron–proton scattering cross section at low energy. Data taken from a review by R. K. Adair, *Rev. Mod. Phys.* **22**, 249 (1950), with additional recent results from T. L. Houk, *Phys. Rev. C* **3**, 1886 (1970).

where 1 barn (b) = 10^{-28} m^2. This result suggests that the cross section should be constant at low energy and should have a value close to 4–5 b.

Figure 4.6 shows the experimental cross sections for scattering of neutrons by protons. The cross section is indeed constant at low energy, and it decreases with E at large energy as Equation 4.33 predicts, but the low-energy cross section, 20.4 b, is not in agreement with our calculated value of 4–5 b.

For the solution to this discrepancy, we must study the relative spins of the incident and scattered nucleons. The proton and neutron spins (each $\frac{1}{2}$) can combine to give a total spin $\boldsymbol{S} = \boldsymbol{s}_p + \boldsymbol{s}_n$ that can have magnitude either 0 or 1. The $S = 1$ combination has three orientations (corresponding to z components $+1, 0, -1$) and the $S = 0$ combination has only a single orientation. For that reason, the $S = 1$ combination is called a *triplet* state and the $S = 0$ combination is called a *singlet* state. Of the four possible relative spin orientations, three are associated with the triplet state and one with the singlet state. As the incident nucleon approaches the target, the probability of being in a triplet state is 3/4 and the probability of being in a singlet state is 1/4. If the scattering cross section is different for the singlet and triplet states, then

$$\sigma = \tfrac{3}{4}\sigma_t + \tfrac{1}{4}\sigma_s \tag{4.35}$$

where σ_t and σ_s are the cross sections for scattering in the triplet and singlet states, respectively. In estimating the cross section in Equation 4.34, we used parameters obtained from the deuteron, which is in a $S = 1$ state. We therefore take $\sigma_t = 4.6$ b and using the measured value of $\sigma = 20.4$ b for the low-energy cross section, we deduce

$$\sigma_s = 67.8 \text{ b}$$

This calculation indicates that there is an enormous difference between the cross sections in the singlet and triplet states—that is, *the nuclear force must be spin dependent.*

Even from our investigation of the deuteron, we should have concluded that the force is spin dependent. If the neutron–proton force did *not* depend on the

relative direction of the spins, then we would expect to find deuteron bound states with $S = 0$ and $S = 1$ at essentially the same energy. Because we find no $S = 0$ bound state, we conclude that the force must be spin dependent.

We can verify our conclusions about the singlet and triplet cross sections in a variety of ways. One method is to scatter very low energy neutrons from hydrogen *molecules*. Molecular hydrogen has two forms, known as orthohydrogen and parahydrogen. In orthohydrogen the two proton spins are parallel, while in parahydrogen they are antiparallel. The difference between the neutron scattering cross sections of ortho- and parahydrogen is evidence of the spin-dependent part of the nucleon–nucleon force.

Our discussion of the cross section for neutron–proton scattering is inadequate for analysis of scattering of neutrons from H_2 molecules. Very low energy neutrons ($E < 0.01$ eV) have a de Broglie wavelength larger than 0.05 nm, thus greater than the separation of the two protons in H_2. The uncertainty principle requires that the size of the wave packet that describes a particle be no smaller than its de Broglie wavelength. Thus the wave packet of the incident neutron overlaps simultaneously with both protons in H_2, even though the range of the nuclear force of the individual neutron–proton interactions remains of the order of 1 fm. The scattered neutron waves ψ_1 and ψ_2 from the two protons will therefore combine *coherently*; that is, they will interfere, and the cross section depends on $|\psi_1 + \psi_2|^2$, not $|\psi_1|^2 + |\psi_2|^2$. We cannot therefore simply add the cross sections from the two individual scatterings. (At higher energy, where the de Broglie wavelength would be small compared with the separation of the protons, the scattered waves would not interfere and we could indeed add the cross sections directly. The reason for choosing to work at very low energy is partly to observe the interference effect and partly to prevent the neutron from transferring enough energy to the H_2 molecule to start it rotating, which would complicate the analysis. The minimum rotational energy is about 0.015 eV, and so neutrons with energies in the range of 0.01 eV do not excite rotational states of the molecule.)

To analyze the interference effect in problems of this sort, we introduce the *scattering length* a, defined such that the low-energy cross section is equal to $4\pi a^2$:

$$\lim_{k \to 0} \sigma = 4\pi a^2 \tag{4.36}$$

Comparison with Equation 4.30 shows that

$$a = \pm \lim_{k \to 0} \frac{\sin \delta_0}{k} \tag{4.37}$$

The choice of sign is arbitrary, but it is conventional to choose the minus sign.

Even though the scattering length has the dimension of length, it is a parameter that represents the strength of the scattering, *not* its range. To see this, we note from Equation 4.37 that δ_0 must approach 0 at low energy in order that a remain finite. Equation 4.23 for the scattered wave function can be written for small δ_0 as

$$\psi_{\text{scattered}} \simeq A \frac{\delta_0}{k} \frac{e^{ikr}}{r} = -Aa \frac{e^{ikr}}{r} \tag{4.38}$$

Thus a gives in effect the amplitude of the scattered wave.

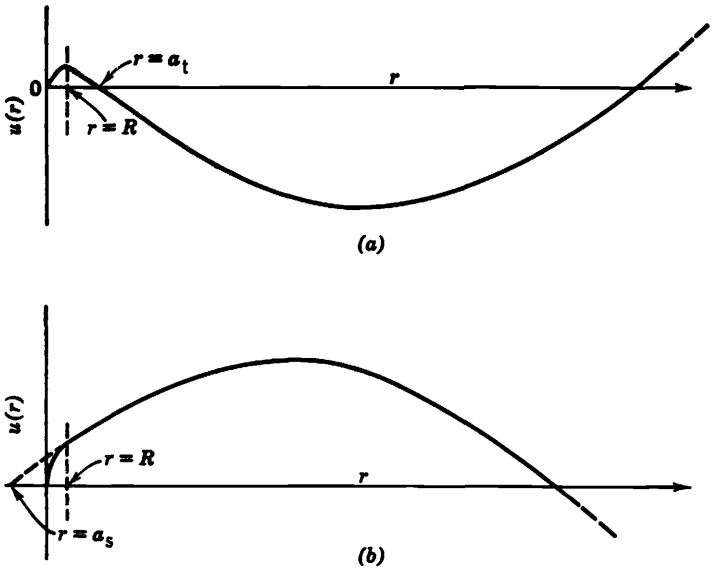


Figure 4.7 (*a*) Wave function for triplet np scattering for a laboratory neutron energy of ~ 200 keV and a well radius of 2.1 fm. Note the positive scattering length. (*b*) Wave function exhibiting a negative scattering length. This happens to be the case for singlet np scattering.

The sign of the scattering length also carries physical information. Figure 4.7 shows representations of the triplet and singlet scattered wave functions $u(r)$. At low energy we can write $a \simeq -\delta_0/k$ and the scattered wave function, Equation 4.13, becomes

$$u(r) = C \sin k_2(r - a) \tag{4.39}$$

The value of a is given by the point at which $u(r)$ passes through zero. The triplet wave function for $r < R$ looks just like the bound state wave function for the deuteron: $u(r)$ "turns over" for $r < R$ to form the bound state. The value of a_t is therefore positive. Because there is no singlet bound state, $u(r)$ does not "turn over" for $r < R$, so it reaches the boundary at $r = R$ with positive slope. When we make the smooth connection at $r = R$ to the wave function beyond the potential and extrapolate to $u(r) = 0$, we find that a_s, the singlet scattering length, is negative.

Our estimate $\sigma_t = 4.6$ b from the properties of the deuteron leads to $a_t = +6.1$ fm, and the estimate of $\sigma_s = 67.8$ b needed to reproduce the observed total cross section gives $a_s = -23.2$ fm.

The theory of neutron scattering from ortho- and parahydrogen gives

$$\sigma_{\text{para}} = 5.7(3a_t + a_s)^2 \tag{4.40}$$

$$\sigma_{\text{ortho}} = \sigma_{\text{para}} + 12.9(a_t - a_s)^2 \tag{4.41}$$

where the numerical coefficients depend on the speed of the incident neutron. Equations 4.40 and 4.41 are written for neutrons of about 770 m/s, slower even than "thermal" neutrons (2200 m/s). The measured cross sections, corrected for

absorption, for neutrons of this speed are $\sigma_{para} = 3.2 \pm 0.2$ b and $\sigma_{ortho} = 108 \pm 1$ b. If the nuclear force were independent of spin, we would have $\sigma_t = \sigma_s$ and $a_t = a_s$; thus σ_{para} and σ_{ortho} would be the same. The great difference between the measured values shows that $a_t \neq a_s$, and it also suggests that a_t and a_s must have different signs, so that $-3a_t \simeq a_s$ in order to make σ_{para} small. Solving Equations 4.40 and 4.41 for a_s and a_t gives

$$a_s = -23.55 \pm 0.12 \text{ fm}$$

$$a_t = +5.35 \pm 0.06 \text{ fm}$$

consistent with the values deduced previously from σ_t and σ_s. A description of these experiments can be found in G. L. Squires and A. T. Stewart, *Proc. Roy. Soc.* (*London*) **A230**, 19 (1955).

There are several other experiments that are sensitive to the singlet and triplet scattering lengths; these include neutron diffraction by crystals that contain hydrogen (such as hydrides) as well as the total reflection of neutron beams at small angles from hydrogen-rich materials (such as hydrocarbons). These techniques give results in good agreement with the above values for a_s and a_t.

The theory we have outlined is valid only for $\ell = 0$ scattering of low-energy incident particles. The $\ell = 0$ restriction required particles of incident energies below 20 MeV, while our other low-energy approximations required eV or keV energies. As we increase the energy of the incident particle, we will violate Equation 4.36 long before we reach energies of 20 MeV. We therefore still have $\ell = 0$ scattering, but at these energies (of order 1 MeV) equations such as 4.38 are not valid. This case is generally treated in the *effective range approximation*, in which we take

$$k \cot \delta_0 = \frac{1}{a} + \frac{1}{2} r_0 k^2 + \cdots \tag{4.42}$$

and where terms in higher powers of k are neglected. The quantity a is the zero-energy scattering length we already defined (and, in fact, this reduces to Equation 4.37 in the $k \to 0$ limit), and the quantity r_0 is a new parameter, the *effective range*. One of the advantages of this representation is that a and r_0 characterize the nuclear potential independent of its shape; that is, we could repeat all of the calculations done in this section with a potential other than the square well, and we would deduce identical values of a and r_0 from analyzing the experimental cross sections. Of course there is an accompanying disadvantage in that we can learn little about the shape of the nuclear potential from an analysis in which calculations with different potentials give identical results!

Like the scattering lengths, the effective range is different for singlet and triplet states. From a variety of scattering experiments we can deduce the best set of $\ell = 0$ parameters for the neutron–proton interaction:

$$a_s = -23.715 \pm 0.015 \text{ fm} \qquad a_t = 5.423 \pm 0.005 \text{ fm}$$

$$r_{0s} = 2.73 \pm 0.03 \text{ fm} \qquad r_{0t} = 1.748 \pm 0.006 \text{ fm}$$

As a final comment regarding the singlet and triplet neutron–proton interactions, we can try to estimate the energy of the singlet n-p state relative to the

bound triplet state at −2.22 MeV. Using Equations 4.34, 4.31, and 4.5 we would deduce that the energy of the singlet state is about +77 keV. Thus the singlet state is only slightly unbound.

4.3 PROTON–PROTON AND NEUTRON–NEUTRON INTERACTIONS

There is one very important difference between the scattering of identical nucleons (proton–proton and neutron–neutron scattering) and the scattering of different nucleons (neutron–proton scattering). This difference comes about because the identical projectile and target nucleons must be described by a common wave function, as discussed in Section 2.7. Because nucleons have spin $\frac{1}{2}$, their wave functions must be antisymmetric with respect to interchange of the nucleons. If we again consider only low-energy scattering, so that $\ell = 0$, interchanging the spatial coordinates of the two particles gives no change in sign. (This situation is somewhat analogous to the parity operation described in Section 2.6.) Thus the wave function is symmetric with respect to interchange of spatial coordinates and must therefore be antisymmetric with respect to interchange of spin coordinates in order that the total (spatial times spin) wave function be antisymmetric. The antisymmetric spin wave function is of the form of Equation 2.76 and must correspond to a total combined spin of 0; that is, the spin orientations must be different. *Only singlet spin states can thus contribute to the scattering.* (At higher energies, the antisymmetric $\ell = 1$ spatial states can occur, accompanied by only the symmetric triplet spin states.)

The derivation of the differential cross section relies on another feature of quantum physics. Consider Figure 4.8, which represents the scattering of two identical particles in the center of mass reference frame. Since the particles are

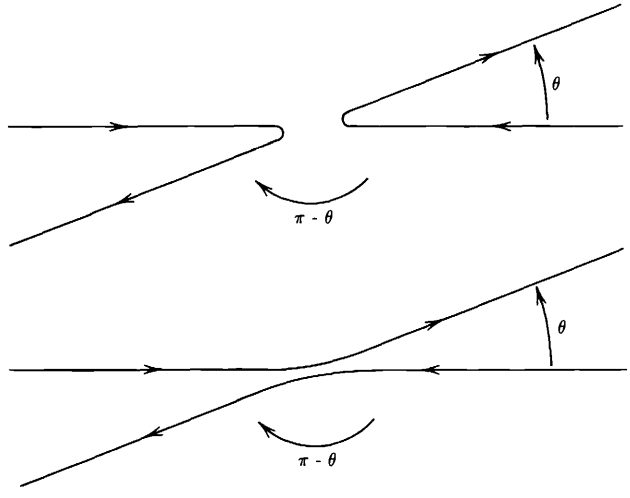


Figure 4.8 Scattering of identical particles in the center-of-mass system. One particle emerges at the angle θ and the other at $\pi - \theta$; because the particles are identical, there is no way to tell which particle emerges at which angle, and therefore we cannot distinguish the two cases shown.

identical, there is no experimental way to distinguish the two situations in the figure. The scattered wave function must therefore include contributions for scattering at θ and at $\pi - \theta$. When we square the scattered wave function to calculate the cross section, there will be a term proportional to the interference between the parts of the wave function that give scattering at θ and at $\pi - \theta$. This interference is a purely quantum effect that has no classical analog.

Let's first consider scattering between two protons; the wave function must describe both Coulomb and nuclear scattering, and there will be an additional Coulomb-nuclear interference term in the cross section. (The scattered wave function must include one term resulting from Coulomb scattering and another resulting from nuclear scattering; the Coulomb term must vanish in the limit $e \to 0$, and the nuclear term must vanish as the nuclear potential vanishes, in which case $\delta_0 \to 0$. When we square the wave function to find the cross section, we get a term that includes both the Coulomb and nuclear scattering.) The derivation of the cross section is beyond the level of this text; for discussions of its derivation and of early work on proton–proton scattering, see J. D. Jackson and J. M. Blatt, *Rev. Mod. Phys.* **22**, 77 (1950). The differential cross section is

$$\frac{d\sigma}{d\Omega} = \left(\frac{e^2}{4\pi\epsilon_0}\right)^2 \frac{1}{4T^2}\left\{\frac{1}{\sin^4(\theta/2)} + \frac{1}{\cos^4(\theta/2)} - \frac{\cos\left[\eta \ln \tan^2(\theta/2)\right]}{\sin^2(\theta/2)\cos^2(\theta/2)}\right.$$
$$- \frac{2}{\eta}(\sin\delta_0)\left(\frac{\cos\left[\delta_0 + \eta \ln \sin^2(\theta/2)\right]}{\sin^2(\theta/2)} + \frac{\cos\left[\delta_0 + \eta \ln \cos^2(\theta/2)\right]}{\cos^2(\theta/2)}\right)$$
$$\left. + \frac{4}{\eta^2}\sin^2\delta_0\right\} \tag{4.43}$$

Here T is the *laboratory* kinetic energy of the incident proton (assuming the target proton to be at rest), θ is the scattering angle in the center-of-mass system, δ_0 the $\ell = 0$ phase shift for pure nuclear scattering, and $\eta = (e^2/4\pi\epsilon_0\hbar c)\beta^{-1} = \alpha/\beta$, where α is the fine-structure constant (with a value of nearly $\frac{1}{137}$) and $\beta = v/c$ is the (dimensionless) relative velocity of the protons. The six terms in brackets in Equation 4.43 can be readily identified: (1) The $\sin^{-4}(\theta/2)$ is characteristic of Coulomb scattering, also known as Rutherford scattering. We discuss this further in Chapter 11. (2) Since the two protons are identical, we cannot tell the case in which the incident proton comes out at θ and the target proton at $\pi - \theta$ (in the center-of-mass system) from the case in which the incident proton comes out at $\pi - \theta$ and the target proton at θ. Thus the scattering cross section must include a characteristic Coulomb (Rutherford) term $\sin^{-4}(\pi - \theta)/2 = \cos^{-4}(\theta/2)$. (3) This term describes the interference between Coulomb scattering at θ and at $\pi - \theta$. (4 and 5) These two terms result from the interference between Coulomb and nuclear scattering. (6) The last term is the pure nuclear scattering term. In the limit $e \to 0$ (pure nuclear scattering), only this term survives and Equation 4.43 reduces to Equation 4.28, as it should.

Although it may be complicated in practice, the procedure for studying the proton–proton interaction is simple in concept: since δ_0 is the only unknown in Equation 4.43, we can measure the differential scattering cross section as a function of angle (for a specific incident kinetic energy) and extract δ_0 from the

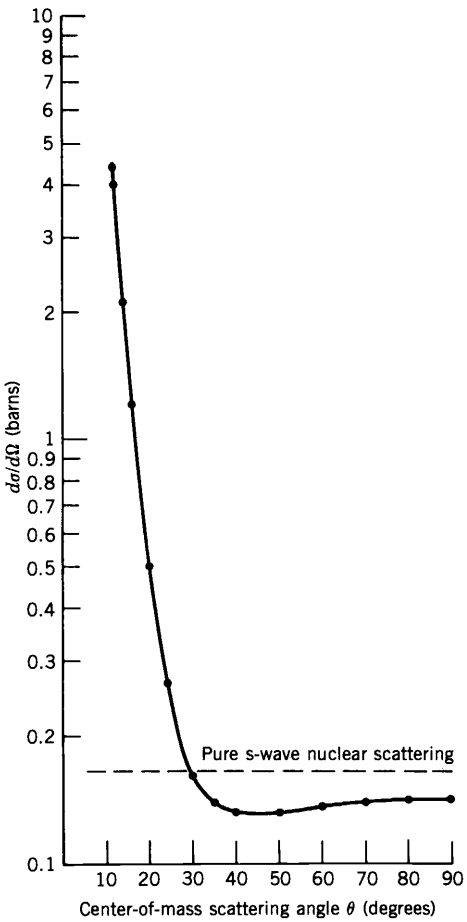


Figure 4.9 The cross section for low-energy proton–proton scattering at an incident proton energy of 3.037 MeV. Fitting the data points to Equation 4.43 gives the s-wave phase shift $\delta_0 = 50.966°$. The cross section for pure nuclear scattering would be 0.165 b; the observation of values of the cross section *smaller* than the pure nuclear value is evidence of the interference between the Coulomb and nuclear parts of the wave function. Data from D. J. Knecht et al., *Phys. Rev.* **148**, 1031 (1966).

best fit of the results to Equation 4.43. Figure 4.9 shows an example of such data, from which it is deduced that $\delta_0 = 50.966°$ at $T = 3.037$ MeV. From many such experiments we can observe the dependence of δ_0 on energy, as shown in Figure 4.10.

The next step in the interpretation of these data is to represent the scattering in terms of energy-independent quantities such as the scattering length and effective range, as we did in Equation 4.42. Unfortunately, this cannot easily be done because the Coulomb interaction has infinite range and even in the $k \to 0$ limit we cannot neglect the higher-order terms of Equation 4.42. With certain modifications, however, it is possible to obtain an expression incorporating the effects of Coulomb and nuclear scattering in a form similar to Equation 4.42 and thus to

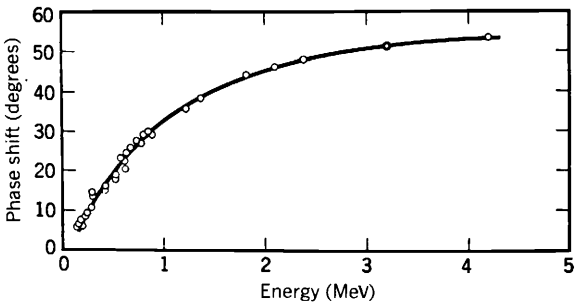


Figure 4.10 The s-wave phase shift for pp scattering as deduced from the experimental results of several workers.

obtain values for the proton–proton scattering length and effective range:

$$a = -7.82 \pm 0.01 \text{ fm}$$
$$r_0 = 2.79 \pm 0.02 \text{ fm}$$

The effective range is entirely consistent with the *singlet* np values deduced in the previous section. The scattering length, which measures the strength of the interaction, includes Coulomb as well as nuclear effects and thus cannot be compared directly with the corresponding np value. (It is, however, important to note that a is negative, suggesting that there is no pp bound state; that is, the nucleus ^{2}He does not exist.) The comparison of the pp and np scattering lengths will be discussed further in the next section.

The study of neutron–neutron scattering should be free of the effects of the Coulomb interaction that made the analysis of proton–proton scattering so complicated. Here the difficulty is an experimental one—although beams of neutrons are readily available, targets of free neutrons are not. Measurement of neutron–neutron scattering parameters therefore requires that we use a nuclear reaction to create two neutrons in relative motion within the range of each other's nuclear force. As the two neutrons separate, we have in effect a scattering experiment. Unfortunately, such reactions must also create a third particle, which will have interactions with both of the neutrons (individually and collectively), but the necessary corrections can be calculated with sufficient precision to enable values to be extracted for the neutron–neutron scattering length and effective range. The experiments that have been reported include the breakup of a deuteron following capture of a negative π meson ($\pi^- + {}^2\text{H} \rightarrow 2\text{n} + \gamma$) and following neutron scattering ($\text{n} + {}^2\text{H} \rightarrow 2\text{n} + \text{p}$). It is also possible to deduce the nn parameters from comparison of mirror reactions such as ${}^3\text{He} + {}^2\text{H} \rightarrow {}^3\text{H} + 2\text{p}$ and ${}^3\text{H} + {}^2\text{H} \rightarrow {}^3\text{He} + 2\text{n}$, using known pp parameters as an aid in calculating the final-state effects of the three particles. The analysis of these (and other) experiments gives the neutron–neutron parameters

$$a = -16.6 \pm 0.5 \text{ fm}$$
$$r_0 = 2.66 \pm 0.15 \text{ fm}$$

As with the proton–proton interaction, the negative scattering length shows that the two neutrons do not form a stable bound state. (It is tempting, but

incorrect, to explain the nonexistence of the di-proton as arising from Coulomb repulsion. No such temptation exists for the di-neutron, the nonexistence of which must arise from the spin dependence of the nuclear interaction. Reviewing the evidence, we first learned that the deuteron ground state is a spin triplet and that no bound spin singlet state exists. We then argued that, because identical fermions must have total antisymmetric wave functions and because the lowest state is expected to be a spatially symmetric $\ell = 0$ state, the di-proton and di-neutron systems must have antisymmetric, or singlet, spin states which are unbound.)

4.4 PROPERTIES OF THE NUCLEAR FORCE

Based on the low-energy properties described in the previous sections, we can learn many details about the nuclear force. When we include results from higher energy experiments, still more details emerge. In this section we summarize the main features of the internucleon force and in the next section we discuss a particular representation for the force that reproduces many of these details.

The Interaction between Two Nucleons Consists to Lowest Order of an Attractive Central Potential

In this chapter we have used for this potential a square-well form, which simplifies the calculations and reproduces the observed data fairly well. Other more realistic forms could just as well have been chosen, but the essential conclusions would not change (in fact, the effective range approximation is virtually independent of the shape assumed for the potential). The common characteristic of these potentials is that they depend only on the internucleon distance r. We therefore represent this central term as $V_c(r)$. The experimental program to study $V_c(r)$ would be to measure the energy dependence of nucleon–nucleon parameters such as scattering phase shifts, and then to try to choose the form for $V_c(r)$ that best reproduces those parameters.

The Nucleon–Nucleon Interaction is Strongly Spin Dependent

This observation follows from the failure to observe a singlet bound state of the deuteron and also from the measured differences between the singlet and triplet cross sections. What is the form of an additional term that must be added to the potential to account for this effect? Obviously the term must depend on the spins of the two nucleons, $\boldsymbol{s}_1$ and $\boldsymbol{s}_2$, but not all possible combinations of $\boldsymbol{s}_1$ and $\boldsymbol{s}_2$ are permitted. The nuclear force must satisfy certain symmetries, which restrict the possible forms that the potential could have. Examples of these symmetries are *parity* ($\boldsymbol{r} \rightarrow -\boldsymbol{r}$) and *time reversal* ($t \rightarrow -t$). Experiments indicate that, to a high degree of precision (one part in 10^7 for parity and one part in 10^3 for time reversal), the internucleon potential is invariant with respect to these operations. Under the parity operator, which involves spatial reflection, angular momentum vectors are unchanged. This statement may seem somewhat surprising, because upon inverting a coordinate system we would naturally expect all vectors defined

in that coordinate system to invert. However, angular momentum is not a true or polar vector; it is a pseudo- or axial vector that does not invert when $\boldsymbol{r} \rightarrow -\boldsymbol{r}$. This follows directly from the definition $\boldsymbol{r} \times \boldsymbol{p}$ or can be inferred from a diagram of a spinning object. Under the time-reversal operation, all motions (including linear and angular momentum) are reversed. Thus terms such as $\boldsymbol{s}_1$ or $\boldsymbol{s}_2$ or a linear combination $A\boldsymbol{s}_1 + B\boldsymbol{s}_2$ in the potential would violate time-reversal invariance and cannot be part of the nuclear potential; terms such as s_1^2, s_2^2, or $\boldsymbol{s}_1 \cdot \boldsymbol{s}_2$ are invariant with respect to time reversal and are therefore allowed. (All of these terms are also invariant with respect to parity.) The simplest term involving both nucleon spins is $\boldsymbol{s}_1 \cdot \boldsymbol{s}_2$. Let's consider the value of $\boldsymbol{s}_1 \cdot \boldsymbol{s}_2$ for singlet and triplet states. To do this we evaluate the total spin $\boldsymbol{S} = \boldsymbol{s}_1 + \boldsymbol{s}_2$

$$\begin{aligned} \boldsymbol{S}^2 = \boldsymbol{S} \cdot \boldsymbol{S} &= (\boldsymbol{s}_1 + \boldsymbol{s}_2) \cdot (\boldsymbol{s}_1 + \boldsymbol{s}_2) \\ &= s_1^2 + s_2^2 + 2\boldsymbol{s}_1 \cdot \boldsymbol{s}_2 \end{aligned}$$

Thus

$$\boldsymbol{s}_1 \cdot \boldsymbol{s}_2 = \tfrac{1}{2}\left(\boldsymbol{S}^2 - s_1^2 - s_2^2\right) \tag{4.44}$$

To evaluate this expression, we must remember that in quantum mechanics all squared angular momenta evaluate as $s^2 = \hbar^2 s(s+1)$; see Section 2.5 and Equation 2.69.

$$\langle \boldsymbol{s}_1 \cdot \boldsymbol{s}_2 \rangle = \tfrac{1}{2}\left[S(S+1) - s_1(s_1+1) - s_2(s_2+1)\right]\hbar^2 \tag{4.45}$$

With nucleon spins s_1 and s_2 of $\frac{1}{2}$, the value of $\boldsymbol{s}_1 \cdot \boldsymbol{s}_2$ is, for triplet ($S = 1$) states:

$$\langle \boldsymbol{s}_1 \cdot \boldsymbol{s}_2 \rangle = \tfrac{1}{2}\left[1(1+1) - \tfrac{1}{2}\left(\tfrac{1}{2}+1\right) - \tfrac{1}{2}\left(\tfrac{1}{2}+1\right)\right]\hbar^2 = \tfrac{1}{4}\hbar^2 \tag{4.46}$$

and for singlet ($S = 0$) states:

$$\langle \boldsymbol{s}_1 \cdot \boldsymbol{s}_2 \rangle = \tfrac{1}{2}\left[0(0+1) - \tfrac{1}{2}\left(\tfrac{1}{2}+1\right) - \tfrac{1}{2}\left(\tfrac{1}{2}+1\right)\right]\hbar^2 = -\tfrac{3}{4}\hbar^2 \tag{4.47}$$

Thus a spin-dependent expression of the form $\boldsymbol{s}_1 \cdot \boldsymbol{s}_2 V_s(r)$ can be included in the potential and will have the effect of giving different calculated cross sections for singlet and triplet states. The magnitude of V_s can be adjusted to give the correct differences between the singlet and triplet cross sections and the radial dependence can be adjusted to give the proper dependence on energy.

We could also write the potential including V_c and V_s as

$$V(r) = -\left(\frac{\boldsymbol{s}_1 \cdot \boldsymbol{s}_2}{\hbar^2} - \tfrac{1}{4}\right)V_1(r) + \left(\frac{\boldsymbol{s}_1 \cdot \boldsymbol{s}_2}{\hbar^2} + \tfrac{3}{4}\right)V_3(r) \tag{4.48}$$

where $V_1(r)$ and $V_3(r)$ are potentials that separately give the proper singlet and triplet behaviors.

The Internucleon Potential Includes a Noncentral Term, Known as a Tensor Potential

Evidence for the tensor force comes primarily from the observed quadrupole moment of the ground state of the deuteron. An s-state ($\ell = 0$) wave function is spherically symmetric; the electric quadrupole moment vanishes. Wave functions with mixed ℓ states must result from noncentral potentials. This tensor force

must be of the form $V(\boldsymbol{r})$, instead of $V(r)$. For a single nucleon, the choice of a certain direction in space is obviously arbitrary; nucleons do not distinguish north from south or east from west. The only reference direction for a nucleon is its spin, and thus only terms of the form $\boldsymbol{s} \cdot \boldsymbol{r}$ or $\boldsymbol{s} \times \boldsymbol{r}$, which relate $\boldsymbol{r}$ to the direction of $\boldsymbol{s}$, can contribute. To satisfy the requirements of parity invariance, there must be an even number of factors of $\boldsymbol{r}$, and so for two nucleons the potential must depend on terms such as $(\boldsymbol{s}_1 \cdot \boldsymbol{r})(\boldsymbol{s}_2 \cdot \boldsymbol{r})$ or $(\boldsymbol{s}_1 \times \boldsymbol{r}) \cdot (\boldsymbol{s}_2 \times \boldsymbol{r})$. Using vector identities we can show that the second form can be written in terms of the first and the additional term $\boldsymbol{s}_1 \cdot \boldsymbol{s}_2$, which we already included in $V(r)$. Thus without loss of generality we can choose the tensor contribution to the internucleon potential to be of the form $V_T(r)S_{12}$, where $V_T(r)$ gives the force the proper radial dependence and magnitude, and

$$S_{12} = 3(\boldsymbol{s}_1 \cdot \boldsymbol{r})(\boldsymbol{s}_2 \cdot \boldsymbol{r})/r^2 - \boldsymbol{s}_1 \cdot \boldsymbol{s}_2 \tag{4.49}$$

which gives the force its proper tensor character and also averages to zero over all angles.

The Nucleon–Nucleon Force Is Charge Symmetric

This means that the proton–proton interaction is identical to the neutron–neutron interaction, after we correct for the Coulomb force in the proton–proton system. Here "charge" refers to the character of the nucleon (proton or neutron) and not to electric charge. Evidence in support of this assertion comes from the equality of the pp and nn scattering lengths and effective ranges. Of course, the pp parameters must first be corrected for the Coulomb interaction. When this is done, the resulting singlet pp parameters are

$$a = -17.1 \pm 0.2 \text{ fm}$$

$$r_0 = 2.84 \pm 0.03 \text{ fm}$$

These are in very good agreement with the measured nn parameters ($a = -16.6 \pm 0.5$ fm, $r_0 = 2.66 \pm 0.15$ fm), which strongly supports the notion of charge symmetry.

The Nucleon–Nucleon Force Is Nearly Charge Independent

This means that (in analogous spin states) the three *nuclear* forces nn, pp, *and* pn are identical, again correcting for the pp Coulomb force. Charge independence is thus a stronger requirement than charge symmetry. Here the evidence is not so conclusive; in fact, the singlet np scattering length (-23.7 fm) seems to differ substantially from the pp and nn scattering lengths (-17 fm). However, we see from Figure 4.11 that large negative scattering lengths are extraordinarily sensitive to the nuclear wave function near $r = R$, and a very small change in ψ can give a large change in the scattering length. Thus the large difference between the scattering lengths may correspond to a very small difference (of order 1%) between the potentials, which (as we see in the next section) is easily explained by the exchange force model.

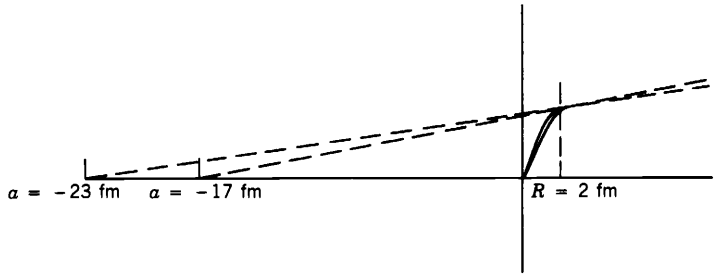


Figure 4.11 Very small changes in the nucleon–nucleon wave function near $r = R$ can lead to substantial differences in the scattering length when the extrapolation is made (compare Figure 4.7*b*).

The Nucleon–Nucleon Interaction Becomes Repulsive at Short Distances

This conclusion follows from qualitative considerations of the nuclear density: as we add more nucleons, the nucleus grows in such a way that its central density remains roughly constant, and thus something is keeping the nucleons from crowding too closely together. More quantitatively, we can study nucleon–nucleon scattering at higher energies. Figure 4.12 shows the deduced singlet s-wave phase shifts for nucleon–nucleon scattering up to 500 MeV. (At these energies, phase shifts from higher partial waves, p and d for example, also contribute to the cross

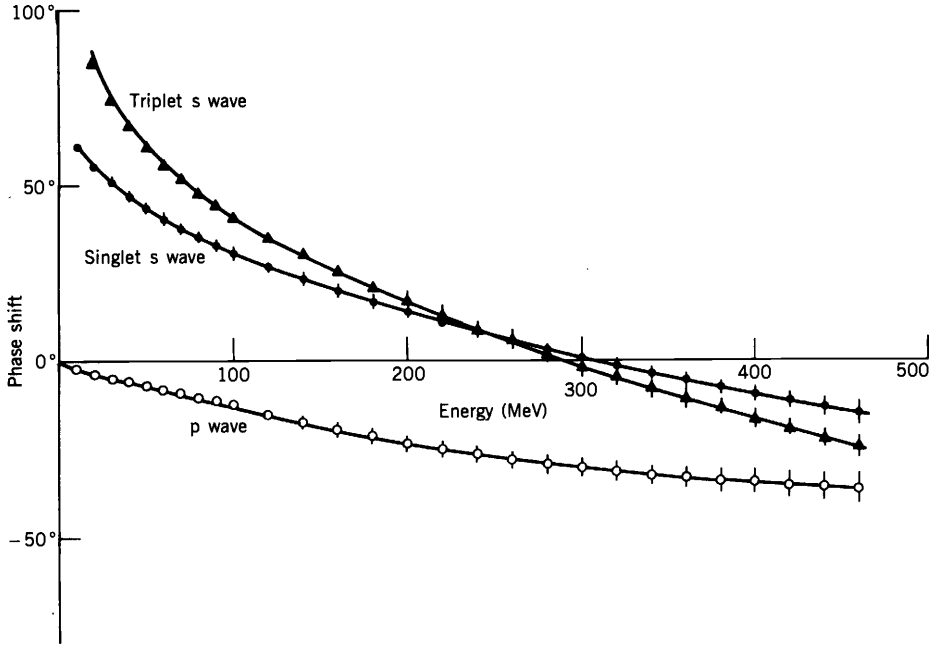


Figure 4.12 The phase shifts from neutron–proton scattering at medium energies. The change in the s-wave phase shift from positive to negative at about 300 MeV shows that at these energies the incident nucleon is probing a repulsive core in the nucleon–nucleon interaction. ▲, $^3S_1$; ●, $^1S_0$; O, $^1P_1$. Data from M. MacGregor et al., *Phys. Rev.* **182**, 1714 (1969).

sections. The s-wave phase shifts can be easily extracted from the differential scattering measurements of $d\sigma/d\Omega$ vs θ because they do not depend on θ.) At about 300 MeV, the s-wave phase shift becomes *negative*, corresponding to a change from an attractive to a repulsive force. To account for the repulsive core, we must modify the potentials we use in our calculations. For example, again choosing a square-well form to simplify the calculation, we might try

$$\begin{aligned} V(r) &= +\infty && r < R_{\text{core}} \\ &= -V_0 && R_{\text{core}} \leq r \leq R \\ &= 0 && r > R \end{aligned} \tag{4.50}$$

and we can adjust R_{core} until we get satisfactory agreement with the observed s-wave phase shifts. The value $R_{\text{core}} \simeq 0.5$ fm gives agreement with the observed phase shifts.

The Nucleon–Nucleon Interaction May Also Depend on the Relative Velocity or Momentum of the Nucleons

Forces depending on velocity or momentum cannot be represented by a scalar potential, but we can include these forces in a reasonable manner by introducing terms linear in $\boldsymbol{p}$, quadratic in $\boldsymbol{p}$, and so on, with each term including a characteristic $V(r)$. Under the parity operation, $\boldsymbol{p} \rightarrow -\boldsymbol{p}$, and also under time reversal $\boldsymbol{p} \rightarrow -\boldsymbol{p}$. Thus any term simply linear in $\boldsymbol{p}$ is unacceptable because it violates both parity and time-reversal invariance. Terms of the form $\boldsymbol{r} \cdot \boldsymbol{p}$ or $\boldsymbol{r} \times \boldsymbol{p}$ are invariant with respect to parity, but still violate time reversal. A possible structure for this term that is first order in $\boldsymbol{p}$ and invariant with respect to both parity and time reversal is $V(r)(\boldsymbol{r} \times \boldsymbol{p}) \cdot \boldsymbol{S}$, where $\boldsymbol{S} = \boldsymbol{s}_1 + \boldsymbol{s}_2$ is the total spin of the two nucleons. The relative angular momentum of the nucleons is $\boldsymbol{\ell} = \boldsymbol{r} \times \boldsymbol{p}$, and therefore this term, known as the *spin-orbit term* in analogy with atomic physics, is written $V_{\text{so}}(r)\boldsymbol{\ell} \cdot \boldsymbol{S}$. Although higher-order terms may be present, this is the only first-order term in $\boldsymbol{p}$ that satisfies the symmetries of both parity and time reversal.

The experimental evidence in support of the spin-orbit interaction comes from the observation that scattered nucleons can have their spins aligned, or *polarized*, in certain directions. The polarization of the nucleons in a beam (or in a target) is defined as

$$P = \frac{N(\uparrow) - N(\downarrow)}{N(\uparrow) + N(\downarrow)} \tag{4.51}$$

where $N(\uparrow)$ and $N(\downarrow)$ refer to the number of nucleons with their spins pointed up and down, respectively. Values of P range from $+1$, for a 100% spin-up polarized beam, to -1, for a 100% spin-down polarized beam. An unpolarized beam, with $P = 0$, has equal numbers of nucleons with spins pointing up and down.

Consider the scattering experiment shown in Figure 4.13*a*, in which an unpolarized beam (shown as a mixture of spin-up and spin-down nucleons) is incident on a spin-up target nucleon. Let's suppose the nucleon–nucleon interaction causes the incident spin-up nucleons to be scattered to the left at angle θ

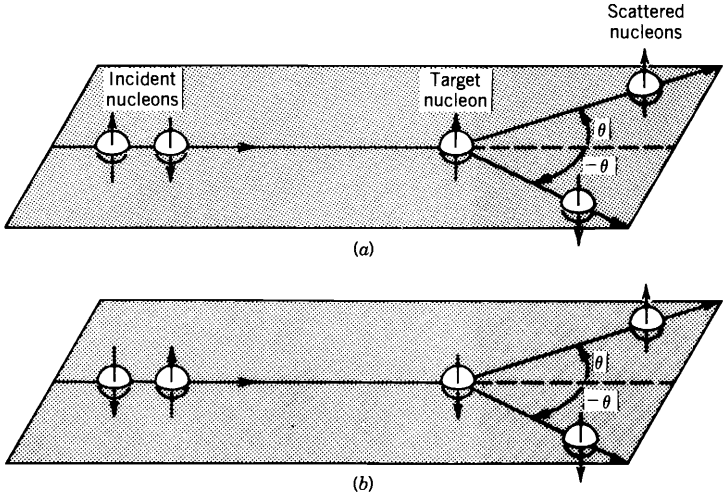


Figure 4.13 An unpolarized beam (shown as a mixture of spin-up and spin-down nucleons) is scattered from a target that can have either spin up or spin down. In part *a*, the incident nucleons with spin up are scattered to the left at angle θ, while those with spin down are scattered to the right at $-\theta$. Part *b* can be obtained from part *a* by viewing from below or by rotating 180° about the beam direction; it shows that the same conclusions follow in scattering from a spin-down polarized target.

and the incident spin-down nucleons to be scattered to the right at angle $-\theta$. Part *b* of the figure shows the *same experiment* viewed from below or else rotated 180° about the direction of the incident beam. We can also interpret Figure 4.13*b* as the scattering of an unpolarized beam from a spin-down target nucleon, and once again the spin-up incident nucleons scatter to the left and the spin-down nucleons scatter to the right. The results would be the same, even in an unpolarized target, which would contain a mixture of spin-up and spin-down nucleons: when an unpolarized beam is scattered from an unpolarized target, the spin-up scattered nucleons appear preferentially at θ and the spin-down scattered nucleons at $-\theta$.

Although this situation may appear superficially to violate reflection symmetry (parity), you can convince yourself that this is not so by sketching the experiment and its mirror image. Parity is conserved if at angle θ we observe a net polarization P, while at angle $-\theta$ we observe a net polarization of $-P$.

Let's now see how the spin-orbit interaction can give rise to this type of scattering with polarization. Figure 4.14 shows two nucleons with spin up incident on a spin up target, so that $S = 1$. (Scattering that includes only s waves must be spherically symmetric, and therefore there can be no polarizations. The p-wave ($\ell = 1$) scattering of identical nucleons has an antisymmetric spatial wave function and therefore a symmetric spin wave function.) Let's assume that $V_{so}(r)$ is negative. For incident nucleon 1, $\boldsymbol{\ell} = \boldsymbol{r} \times \boldsymbol{p}$ is down (into the page), and therefore $\boldsymbol{\ell} \cdot \boldsymbol{S}$ is negative because $\boldsymbol{\ell}$ and $\boldsymbol{S}$ point in opposite directions. The combination $V_{so}(r)\boldsymbol{\ell} \cdot \boldsymbol{S}$ is positive and so there is a repulsive force between the

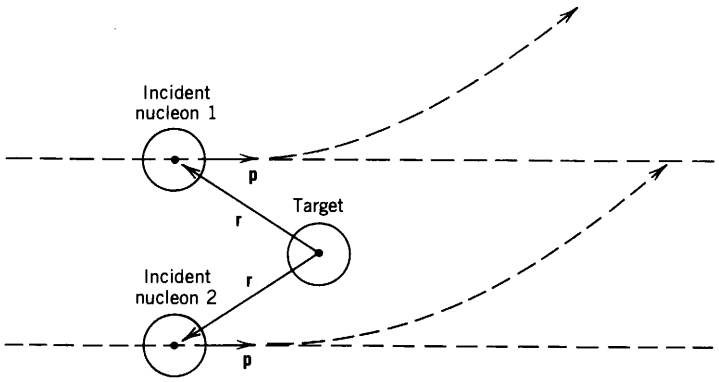


Figure 4.14 Top view of nucleon–nucleon scattering experiment. All spins point up (out of the paper). Incident nucleon 1 has $\boldsymbol{r} \times \boldsymbol{p}$ into the paper, and thus $\boldsymbol{\ell} \cdot \boldsymbol{S}$ is negative, giving a repulsive force and scattering to the left. Incident nucleon 2 has $\boldsymbol{r} \times \boldsymbol{p}$ out of the paper, resulting in an attractive force and again scattering to the left.

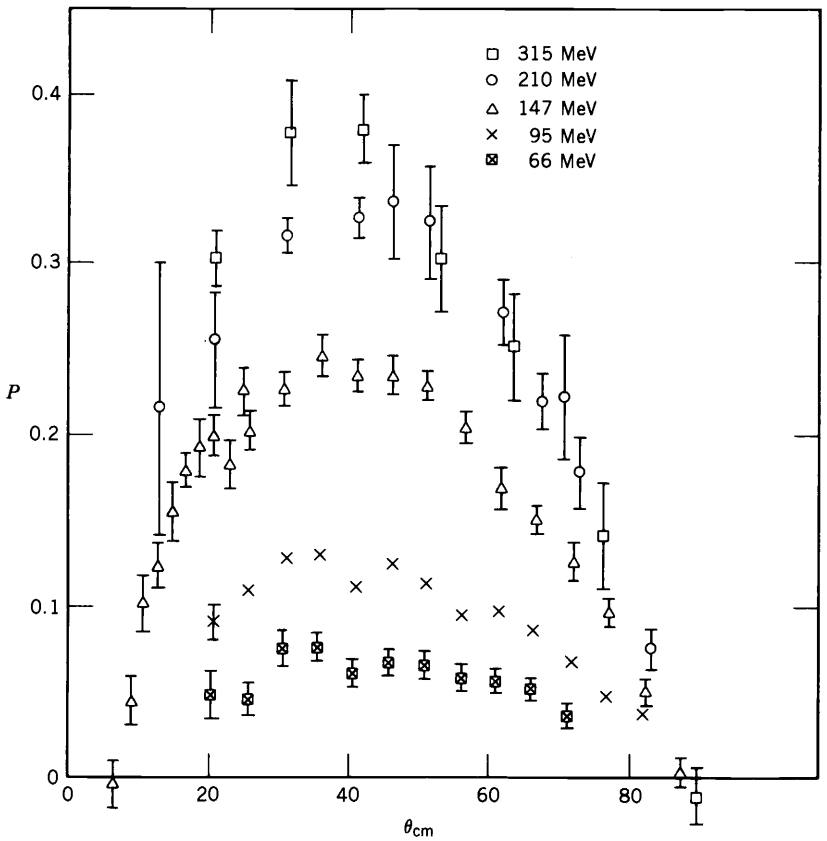


Figure 4.15 As the incident energy in proton–proton scattering increases, the maximum polarization increases. From R. Wilson, *The Nucleon–Nucleon Interaction* (New York: Wiley-Interscience, 1963).

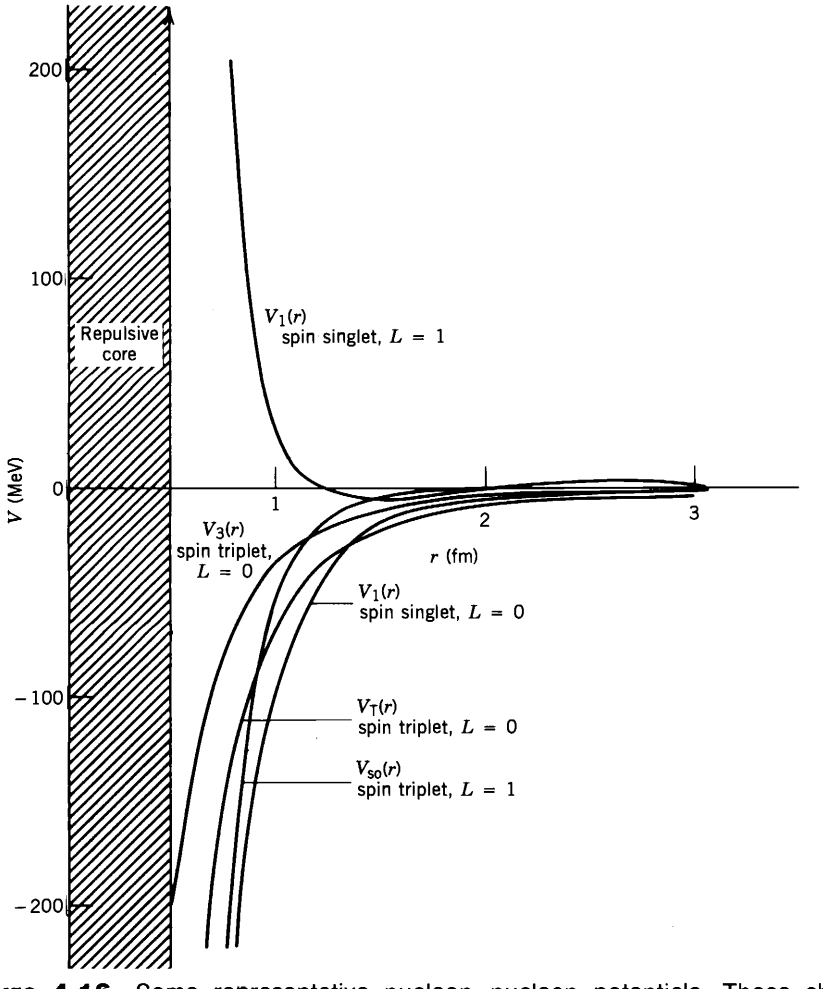


Figure 4.16 Some representative nucleon–nucleon potentials. Those shown include the attractive singlet and triplet terms that contribute to s-wave scattering, the repulsive term that gives one type of p-wave ($L = 1$) scattering, and the attractive tensor and spin-orbit terms. All potentials have a repulsive core at $r = 0.49$ fm. These curves are based on an early set of functional forms proposed by T. Hamada and I. D. Johnston, *Nucl. Phys.* **34**, 382 (1962); other relatively similar forms are in current use.

target and incident nucleon 1, which is pushed to the left. For nucleon 2, ℓ points up, $\ell \cdot S$ is positive, and the interaction is attractive; incident nucleon 2 is pulled toward the target and also appears on the left side. Spin-up incident nucleons are therefore preferentially scattered to the left and (by a similar argument) spin-down nucleons to the right. Thus the spin-orbit force can produce polarized scattered beams when unpolarized particles are incident on a target.

At low energy, where s-wave scattering dominates, we expect no polarization. As the incident energy increases, the contribution of p-wave scattering increases and there should be a corresponding increase in the polarization. Figure 4.15

shows that this expectation is correct. From the variation of P with θ and with energy, we can make deductions about the form of $V_{so}(r)$.

The general topic of polarization in nuclear reactions is far more complicated than we have indicated in this brief discussion. We should also consider the effect on the measured cross sections of using polarized beams and polarized targets, which we do in Chapter 11.

From this enormous set of experimental information (total and differential cross sections, spin dependence, polarizations), it is possible to propose a set of phenomenological potentials $V(r)$ that give reasonable agreement with the observed nucleon–nucleon data. These potentials can then be used in calculations for more complicated nuclei. As an example, Figure 4.16 illustrates one such set of potentials. As is usually the case, negative potentials give an attractive force and positive potentials give a repulsive force. Notice how the potentials incorporate such features as the range of the interactions, the repulsive core, the strong attractive s-wave phase shifts, the repulsive p-wave phase shifts, and charge independence (since no distinctions are made for the characters of the nucleons).

4.5 THE EXCHANGE FORCE MODEL

The phenomenological potentials discussed in the previous section have been fairly successful in accounting for a variety of measured properties of the nucleon–nucleon interaction. Of course, the ability of these potentials to give accurate predictions would be improved if we added more terms to the interaction. For example, we could have included a term that is second-order in the momentum dependence (proportional to ℓ^2), we could write potentials that are different for each ℓ value, and so on. Each new term in the potential may improve the calculation, but it may be at the expense of simplicity. It also serves to make us lose sight of our main objective: to understand the nucleon–nucleon interaction. Simply because we have included enough potentials to do accurate calculations does not mean we have improved our understanding of the fundamental character of the nucleon–nucleon interaction. We therefore try to postulate a physical mechanism for the nucleon–nucleon force that will yield potentials similar to those that have already proven to be successful in calculations.

A successful mechanism is that of the *exchange force*. There are two principal arguments in support of the presence of exchange forces in nuclei. The first comes from the saturation of nuclear forces. The experimental support for saturation comes from the relatively constant nuclear density and binding energy per nucleon as we go to heavier nuclei. A given nucleon seems to attract only a small number of near neighbors, but it also repels at small distances to keep those neighbors from getting too close. (We explained this behavior in the previous section by choosing a central potential that was of finite range and had a repulsive core.) We encounter exactly the same sort of behavior in molecules. When we bring two atoms together to form a diatomic molecule, such as one with covalent bonding, electrons are shared or exchanged between the two atoms, and a stable molecule forms with the atoms in equilibrium separated by a certain

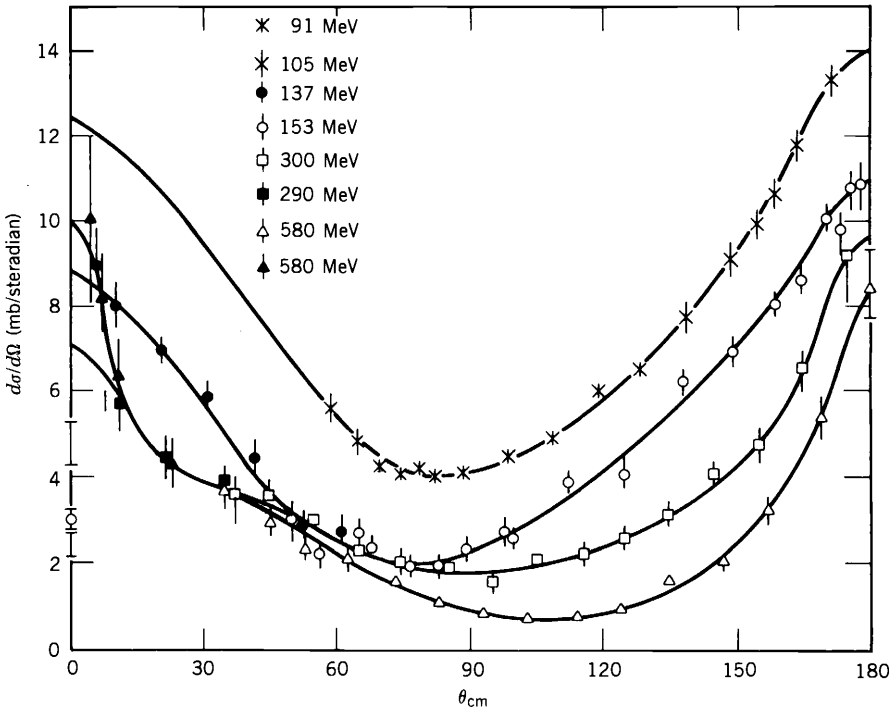


Figure 4.17 The neutron–proton differential cross section at medium energies. The strong forward-scattering peak (near 0°) is expected; the equally strong backward peak (near 180°) is evidence for the exchange force. From R. Wilson, *The Nucleon–Nucleon Interaction* (New York: Wiley-Interscience, 1963).

distance. If we try to force the atoms closer together, the overlap of the filled electronic shells causes a strong repulsive force. Furthermore, approaching the molecule with a third atom may result only in very weak forces between the first two atoms and the third; if all of the valence electrons are occupied in the first set of bonds, none are available to form new bonds. Nuclear forces show a similar saturation character.

Another argument in favor of the exchange force model comes from the study of np scattering at high energies. Figure 4.17 shows the np differential cross section. There is a strong peak in the cross section at forward angles near 0°, corresponding to a small momentum transfer between the projectile and the target. We can estimate the extent of this forward peak by studying the maximum momentum transfer in the following way: For small deflection angles, $\sin\theta \simeq \theta = \Delta p/p$ where p is the momentum of the incident particle and Δp is the transverse momentum added during the collision. If F is the average force that acts during the collision time Δt, then $\Delta p = F\Delta t$. The force F is $-dV/dr$, and thus the average force should be of the order of V_0/R, where V_0 is the depth of the nucleon–nucleon square-well potential and R is its range. (Even if the actual potential is not at all constant, such as the central term of Figure 4.16, the average value of dV/dr should be of the order of V_0/R.) The collision time Δt

should be of the order of R/v, where v is the projectile velocity. Thus

$$\theta \simeq \frac{\Delta p}{p} = \frac{F\Delta t}{p} = \frac{1}{p}\frac{V_0}{R}\frac{R}{v} = \frac{V_0}{pv} = \frac{V_0}{2T} \tag{4.52}$$

where T is the projectile kinetic energy. For the energies shown in Figure 4.17, this gives values of θ in the range of 10° or smaller. We certainly do not expect to see a peak at 180°! Although it is tempting to regard this "backward" peak in the center of mass frame as the result of a head-on collision in which the incident particle has its motion reversed, our estimate above indicates such an explanation is not likely to be correct.

A more successful explanation can be found in the exchange model if, during the collision, the neutron and proton exchange places. That is, the forward-moving neutron becomes a proton and the backward-moving (in the center-of-mass system) proton becomes a neutron. The incident nucleon then reappears in the laboratory as a forward-moving nucleon (now a proton), consistent with our estimate of the small deflection angle in nucleon–nucleon scattering.

In summary, both the saturation of nuclear forces and the strong backward peak in np scattering are explained by exchange forces. In the former case, "something" is exchanged between nucleons to produce a sort of saturated bond. In the second case, "something" is exchanged between nucleons and actually changes their character.

In the early development of classical physics, objects were said to interact by means of "action at a distance." Somehow one object mysteriously transmitted through space its force on the other object. The great development in nineteenth-century theoretical physics was the introduction of the concept of *fields*, according to which one object establishes throughout space a force field (electromagnetic and gravitational fields are examples) and the second object interacts only with the field, not directly with the first object. Maxwell showed in the case of electromagnetism how the fields were transmitted through space. The major development of twentieth-century physics is quantum mechanics, according to which all exchanges of energy must occur in bundles of a discrete size. The classical field is smooth and continuous, and to bring classical field theory into agreement with quantum theory, the field itself must be quantized. That is, according to quantum field theory, the first object does not set up a classical field throughout space but instead emits field quanta. The second object can then absorb those field quanta (and reemit them back to the first object). The two objects interact directly with the exchanged field quanta and therefore indirectly with each other.

In view of the preceding discussion, it is natural to associate the "something" that is exchanged in the nucleon–nucleon interaction with quanta of the nuclear field. For a spin-$\frac{1}{2}$ neutron to turn into a spin-$\frac{1}{2}$ proton, it is clear that the exchanged particle must have integral spin (0 or 1) and must carry electric charge. In addition, if we wish to apply the same exchange-force concepts to nn and pp interactions, there must also be an uncharged variety of exchanged particle. Based on the observed range of the nuclear force, we can estimate the mass of the exchanged particle. Let us assume that a nucleon (which we denote by N, to include both neutrons and protons) emits a particle x. A second nucleon

absorbs the particle x:

$$N_1 \rightarrow N_1 + x$$
$$x + N_2 \rightarrow N_2$$

How is it possible for a nucleon to emit a particle of mass energy $m_x c^2$ and still remain a nucleon, without violating conservation of energy? It is not possible, unless the emission and reabsorption take place within a short enough time Δt that we are unaware energy conservation has been violated. Since the limits of our ability to measure an energy (and therefore to determine whether energy is conserved) are restricted by the uncertainty principle, if $\Delta t < \hbar/(m_x c^2)$, we will be unaware that energy conservation has been violated by an amount $\Delta E = m_x c^2$. The maximum range of the force is determined by the maximum distance that the particle x can travel in the time Δt. If it moves at speeds of the order of c, then the range R can be at most

$$R = c\,\Delta t = \frac{\hbar c}{m_x c^2} = \frac{200 \text{ MeV} \cdot \text{fm}}{m_x c^2} \tag{4.53}$$

where we have used a convenient approximation for $\hbar c$. Equation 4.53 gives a useful relationship between the mass energy of the exchanged particles and the range of the force. For nuclear forces with a range of about 1 fm, it is clear that we must have an exchanged particle with a mass energy of the order of 200 MeV.

Such particles that exist only for fleeting instants and allow us to violate conservation of energy (and momentum—the emitting and absorbing nucleons do not recoil) are known as *virtual* particles. We can observe the force that results from the exchange of virtual particles, but we cannot observe the particles themselves during the exchange. (Exchanged virtual particles can be identical with ordinary particles, however. According to field theory, the Coulomb interaction between electric charges can be regarded as the exchange of virtual photons, which have properties in common with ordinary real photons.)

The exchanged particles that carry the nuclear force are called *mesons* (from the Greek "meso" meaning middle, because the predicted mass was between the masses of the electron and the nucleon). The lightest of the mesons, the π-meson or simply *pion*, is responsible for the major portion of the longer range (1.0 to 1.5 fm) part of the nucleon–nucleon potential. To satisfy all the varieties of the exchanges needed in the two-nucleon system, there must be three pions, with electric charges of $+1$, 0, and -1. The pions have spin 0 and rest energies of 139.6 MeV (for $\pi^{\pm}$) and 135.0 MeV (for π^0). At shorter ranges (0.5–1.0 fm), two-pion exchange is probably responsible for the nuclear binding; at much shorter ranges (0.25 fm) the exchange of ω mesons ($mc^2 = 783$ MeV) may contribute to the repulsive core whereas the exchange of ρ mesons ($mc^2 = 769$ MeV) may provide the spin-orbit part of the interaction. Further properties of these mesons are discussed in Chapter 17.

The differing masses for the charged and neutral pions may explain the possible small violation of charge independence we discussed previously. The single pion that is exchanged between two identical nucleons must be a π^0:

$$n_1 \rightarrow n_1 + \pi^0 \qquad \pi^0 + n_2 \rightarrow n_2$$

or

$$p_1 \rightarrow p_1 + \pi^0 \qquad \pi^0 + p_2 \rightarrow p_2$$

Charged pion exchange will not work:

$$n_1 \rightarrow p_1 + \pi^- \qquad \text{but } \pi^- + n_2 \rightarrow ?$$

$$p_1 \rightarrow n_1 + \pi^+ \qquad \text{but } \pi^+ + p_2 \rightarrow ?$$

because there are no nucleons with charges -1 or $+2$. (There are *excited states* of the nucleon with these charges, as we discuss in Chapters 17 and 18, but these high-energy states are unlikely to contribute substantially to the low-energy experiments we have discussed in this chapter.) However, the neutron–proton interaction can be carried by charged as well as neutral pions:

$$n_1 \rightarrow n_1 + \pi^0 \qquad \pi^0 + p_2 \rightarrow p_2$$

$$n_1 \rightarrow p_1 + \pi^- \qquad \pi^- + p_2 \rightarrow n_2$$

This additional term in the np interaction (and the difference in mass between the charged and neutral pions) may be responsible for the small difference in the potential that produces the observed difference in the scattering lengths.

The meson-exchange theory of nuclear forces was first worked out by Yukawa in 1935; some details of his work are summarized in Chapter 17. Meson exchange can be represented by a potential in the basic form of $r^{-1}e^{-r/R}$, where R is the range of the force ($R = \hbar/m_\pi c = 1.5$ fm for pions). A more detailed form for the one-pion exchange potential (called OPEP in the literature) is

$$V(r) = \frac{g_\pi^2 (m_\pi c^2)^3}{3(Mc^2)^2 \hbar^2} \left[\boldsymbol{s}_1 \cdot \boldsymbol{s}_2 + S_{12} \left(1 + \frac{3R}{r} + \frac{3R^2}{r^2} \right) \right] \frac{e^{-r/R}}{r/R} \qquad (4.54)$$

Here g_π^2 is a dimensionless coupling constant that gives the strength of the interaction (just as e^2 gives the strength of the electromagnetic interaction) and M is the nucleon mass. This particular potential describes only the long-range part of the nucleon–nucleon interaction; other aspects of the interaction are described by other potentials.

The exchange-force model enjoyed a remarkable success in accounting for the properties of the nucleon–nucleon system. The forces are based on the exchange of virtual mesons, all of which can be produced in the laboratory and studied directly. The pion is the lightest of the mesons and therefore has the longest range. Exploring the nucleus with higher energy probes (with shorter de Broglie wavelengths) allows us to study phenomena that are responsible for the finer details of the nuclear structure, such as those that occur only over very short distances. These phenomena are interpreted as arising from the exchange of heavier mesons. Studying the spatial and spin dependence of these detailed interactions allows us to deduce the properties of the hypothetical exchanged meson. On the other hand, particle physicists are able to observe a large variety of mesons from high-energy collisions done with large accelerators. Among the debris from those collisions they can observe many varieties of new particles and catalog their properties. Nuclear physicists are then able to choose from this list candidates for the mesons exchanged in various details of the nucleon–nucleon interaction. This slightly oversimplified view nevertheless emphasizes the close historical relationship between nuclear physics and elementary particle physics.

REFERENCES FOR ADDITIONAL READING

For similar treatments of the nucleon–nucleon interaction, see H. Enge, *Introduction to Nuclear Physics* (Reading: Addison-Wesley, 1966), Chapters 2 and 3; R. D. Evans, *The Atomic Nucleus* (New York: McGraw-Hill, 1955), Chapter 10; E. Segrè, *Nuclei and Particles* (Reading, MA: Benjamin, 1977), Chapter 10.

Monographs devoted to the nucleon–nucleon interaction are H. A. Bethe and P. Morrison, *Elementary Nuclear Theory* (New York: Wiley, 1956); M. J. Moravcsik, *The Two Nucleon Interaction* (Oxford: Clarendon, 1963); R. Wilson, *The Nucleon–Nucleon Interaction* (New York: Wiley, 1963).

A review of early work on nucleon–nucleon scattering can be found in R. K. Adair, *Rev. Mod. Phys.* **22**, 249 (1950). Analyses of scattering data to extract phase shifts and other parameters are reviewed by M. H. MacGregor, M. J. Moravcsik, and H. P. Stapp, *Ann. Rev. Nucl. Sci.* **10**, 291 (1960), and H. P. Noyes, *Ann. Rev. Nucl. Sci.* **22**, 465 (1972). See also M. H. MacGregor, *Phys. Today* **22**, 21 (December 1969).

PROBLEMS

1. What is the minimum photon energy necessary to dissociate ^{2}H? Take the binding energy to be 2.224589 MeV.
2. (a) Use the continuity and normalization conditions to evaluate the coefficients A and C in the deuteron wave functions, Equations 4.3 and 4.4.
 (b) From the resulting wave function, evaluate the root-mean-square radius of the deuteron.
3. The condition for the existence of a bound state in the square-well potential can be determined through the following steps:
 (a) Using the complete normalized wave function, Equations 4.3 and 4.4, show that the expectation value of the potential energy is

$$\langle V \rangle = \int \psi^* V \psi \, dv = -V_0 A^2 \left[\tfrac{1}{2} R - \frac{1}{4k_1} \sin 2k_1 R \right]$$

 (b) Show that the expectation value of the kinetic energy is

$$\langle T \rangle = \frac{\hbar^2}{2m} \int_0^\infty \left| \frac{\partial \psi}{\partial r} \right|^2 dv$$

$$= \frac{\hbar^2}{2m} A^2 \left[\tfrac{1}{2} k_1^2 R + \tfrac{1}{4} k_1 \sin 2k_1 R + \frac{k_2}{2} \sin^2 k_1 R \right]$$

 (c) Show that, for a bound state to exist, it must be true that $\langle T \rangle < -\langle V \rangle$.
 (d) Finally, show that a bound state will exist only for $V_0 \geq \pi^2 \hbar^2 / 8mR^2$ and evaluate the minimum depth of the potential that gives a bound state of the deuteron.

(*Note:* This calculation is valid only in three-dimensional problems. In the one-dimensional square well (indeed, in all reasonably well-behaved

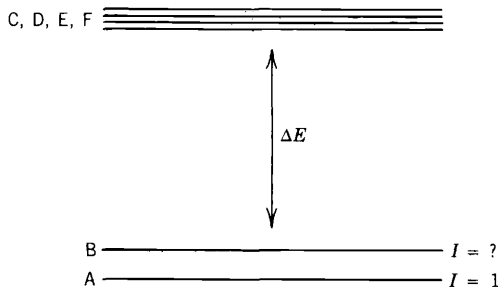
attractive one-dimensional potentials) there is always at least one bound state. Only in three-dimensional problems is there a critical depth for the existence of a bound state. See C. A. Kocher, *Am. J. Phys.* **45**, 71 (1977).)

4. What fraction of the time do the neutron and proton in the deuteron spend beyond the range of their nuclear force?
5. From Equation 4.5, plot V_0 against R for R in the range of 1.0 to 3.0 fm. Discuss the sensitivity of V_0 to R.
6. (a) Show that Equation 4.5 can be written in the transcendental form $x = -\tan bx$, where $x = \sqrt{-(V_0 + E)/E}$. Evaluate the parameter b for $R = 2$ fm. Note that in Equation 4.2, m is the reduced mass $m_p m_n/(m_p + m_n)$, which is approximately $m_p/2$. (b) Solve the transcendental equation in two ways: graphically and iteratively using a programmable calculator or computer. For a review of using iterative techniques on similar equations, see K. S. Krane, *Am. J. Phys.* **50**, 521 (1982).
7. Assuming a deuteron wave function of the form of Equation 4.9, deduce why there is a cross-term (that is, a term proportional to $a_s a_d$) in the expression for the electric quadrupole moment, Equation 4.11, but not in the expression for the magnetic dipole moment, Equation 4.10.
8. Evaluate the energy of the magnetic dipole–dipole interaction in the deuteron, and compare with the nuclear binding energy. Consider separately the cases in which the nucleon spins are perpendicular to and parallel to the line joining the nucleons.
9. Find the scattering cross section of the "hard sphere":

$$V(r) = \infty \qquad \text{for } r < R$$
$$= 0 \qquad \text{for } r > R$$

10. Suppose the binding energy of the deuteron were much weaker, say 10 keV. Evaluate the resulting neutron–proton s-wave cross section.
11. Show that the singlet neutron–proton state is unbound and evaluate its energy.
12. Antiprotons ($\bar{p}$) and antineutrons ($\bar{n}$) can be produced at several accelerator facilities throughout the world. Discuss the properties of the following systems in comparison with those discussed in this chapter: (a) $\bar{n}\bar{p}$ bound state; (b) $n\bar{p}$ bound state; (c) $\bar{n}p$ s-wave scattering; (d) $\bar{p}p$ scattering.
13. Solve the Schrödinger equation for the potential given in Equation 4.50 for s-wave neutron–proton scattering. Find an expression that relates the s-wave phase shift to the core radius, and find the value of R_{core} that causes the phase shift to go negative, as in Figure 4.12.
14. In a measurement of the pp differential cross section, the result $d\sigma/d\Omega = 0.111$ b/steradian was obtained at a laboratory energy of 4.2 MeV and a laboratory scattering angle of 30°. What is the corresponding s-wave phase shift?
15. Suppose the nucleon–nucleon force were stronger, so that the deuteron had the following bound states:

 State A is the "well-known" ground state with the properties discussed in this chapter. State B is very close to state A. At a large energy gap ΔE



above states A and B are four states, C, D, E, and F. There are no other states near C, D, E, and F.

(a) What is the most likely value of the relative orbital angular momentum of the nucleons in state B? What is the relative orientation of the nucleon intrinsic spins in state B, and what is the resulting value of the total angular momentum I in state B?

(b) In states C, D, E, and F the nucleons have the same relative orbital angular momentum (but different from state A). Make a reasonable guess at the value of the orbital angular momentum and justify your choice.

(c) By considering the possible couplings of the orbital angular momentum and the intrinsic spins of the two nucleons, show that there must be only four states in the excited multiplet, and give the four possible values of the total angular momentum I and the parity.

(d) Assuming the energy gap ΔE to result primarily from the "centripetal" contribution to the potential, estimate ΔE. Be sure to justify any choice of parameters you use in your estimate.

16. Low-energy (s-wave) neutrons are scattered from protons, and the distribution of "recoil" protons is to be observed and analyzed. Let the neutron scattering angle be θ in the laboratory coordinate system, and let the incident neutron kinetic energy be T_n. (a) Show that the protons emerge at an angle $\phi = 90° - \theta$ with respect to the direction of the incident neutrons. (b) Show that $T'_n = T_n \cos^2\theta$ and $T'_p = T_n \sin^2\theta$, where T' signifies the energy after the scattering. (c) Show that the laboratory and center-of-mass cross sections are related by $(d\sigma/d\Omega)_{lab} = (4\cos\theta)(d\sigma/d\Omega)_{cm}$. (d) Given that the scattering is independent of direction in the center-of-mass system, show that (in the laboratory system) $d\sigma/dT'_p = \sigma/T_n$, where σ is the total cross section. This latter result shows that the number of recoil protons observed at any particular energy T'_p ($0 \leq T'_p \leq T_n$) is independent of T'_p. (e) What is the angular distribution of the recoil protons in the laboratory?

5

NUCLEAR MODELS

At this point it is tempting to try to extend the ideas of the previous chapter to heavier nuclei. Unfortunately, we run into several fundamental difficulties when we do. One difficulty arises from the mathematics of solving the many-body problem. If we again assume an oversimplified form for the nuclear potential, such as a square well or an harmonic oscillator, we could in principle write down a set of coupled equations describing the mutual interactions of the A nucleons. These equations cannot be solved analytically, but instead must be attacked using numerical methods. A second difficulty has to do with the nature of the nuclear force itself. There is evidence to suggest that the nucleons interact not only through mutual two-body forces, but through three-body forces as well. That is, the force on nucleon 1 not only depends on the individual positions of nucleons 2 and 3, it contains an *additional* contribution that arises from the correlation of the positions of nucleons 2 and 3. Such forces have no classical analog.

In principle it is possible to do additional scattering experiments in the three-body system to try (in analogy with the two-body studies described in Chapter 4) to extract some parameters that describe the three-body forces. However, we quickly reach a point at which such a microscopic approach obscures, rather than illuminates, the essential physics of the nucleus. It is somewhat like trying to obtain a microscopic description of the properties of a gas by studying the interactions of its atoms and then trying to solve the dynamical equations that describe the interatomic forces. Most of the physical insight into the properties of a gas comes from a few general parameters such as pressure and temperature, rather than from a detailed microscopic theory.

We therefore adopt the following approach for nuclei. We choose a deliberately oversimplified theory, but one that is mathematically tractable and rich in physical insight. If that theory is fairly successful in accounting for at least a few nuclear properties, we can then improve it by adding additional terms. Through such operations we construct a *nuclear model*, a simplified view of nuclear structure that still contains the essentials of nuclear physics. A successful model must satisfy two criteria: (1) it must reasonably well account for previously measured nuclear properties, and (2) it must predict additional properties that can be measured in new experiments. This system of modeling complex processes is a common one in many areas of science; biochemists model the complex processes such as occur in the replication of genes, and atmospheric

scientists model the complex dynamics of air and water currents that affect climate.

5.1 THE SHELL MODEL

Atomic theory based on the shell model has provided remarkable clarification of the complicated details of atomic structure. Nuclear physicists therefore attempted to use a similar theory to attack the problem of nuclear structure, in the hope of similar success in clarifying the properties of nuclei. In the atomic shell model, we fill the shells with electrons in order of increasing energy, consistent with the requirement of the Pauli principle. When we do so, we obtain an inert core of filled shells and some number of valence electrons; the model then assumes that atomic properties are determined primarily by the valence electrons. When we compare some measured properties of atomic systems with the predictions of the model, we find remarkable agreement. In particular, we see regular and smooth variations of atomic properties *within* a subshell, but rather sudden and dramatic changes in the properties when we fill one subshell and enter the next. Figure 5.1 shows the effects of a change in subshell on the ionic radius and ionization energy of the elements.

When we try to carry this model over to the nuclear realm, we immediately encounter several objections. In the atomic case, the potential is supplied by the Coulomb field of the nucleus; the subshells ("orbits") are established by an external agent. We can solve the Schrödinger equation for this potential and calculate the energies of the subshells into which electrons can then be placed. In the nucleus, there is no such external agent; the nucleons move in a potential that they themselves create.

Another appealing aspect of atomic shell theory is the existence of spatial orbits. It is often very useful to describe atomic properties in terms of spatial orbits of the electrons. The electrons can move in those orbits relatively free of collisions with other electrons. Nucleons have a relatively large diameter compared with the size of the nucleus. How can we regard the nucleons as moving in well defined orbits when a single nucleon can make many collisions during each orbit?

First let's examine the experimental evidence that supports the existence of nuclear shells. Figure 5.2 shows measured proton and neutron separation energies, plotted as deviations from the predictions of the semiempirical mass formula, Equation 3.28. (The gross changes in nuclear binding are removed by plotting the data in this form, allowing the shell effects to become more apparent.) The similarity with Figure 5.1 is striking—the separation energy, like the atomic ionization energy, increases gradually with N or Z except for a few sharp drops that occur at the same neutron and proton numbers. We are led to guess that the sharp discontinuities in the separation energy correspond (as in the atomic case) to the filling of major shells. Figure 5.3 shows some additional evidence from a variety of experiments; the sudden and discontinuous behavior occurs at the same proton or neutron numbers as in the case of the separation energies. These so-called "magic numbers" (Z or N = 2, 8, 20, 28, 50, 82, and 126) represent the effects of filled major shells, and any successful theory must be able to account for the existence of shell closures at those occupation numbers.

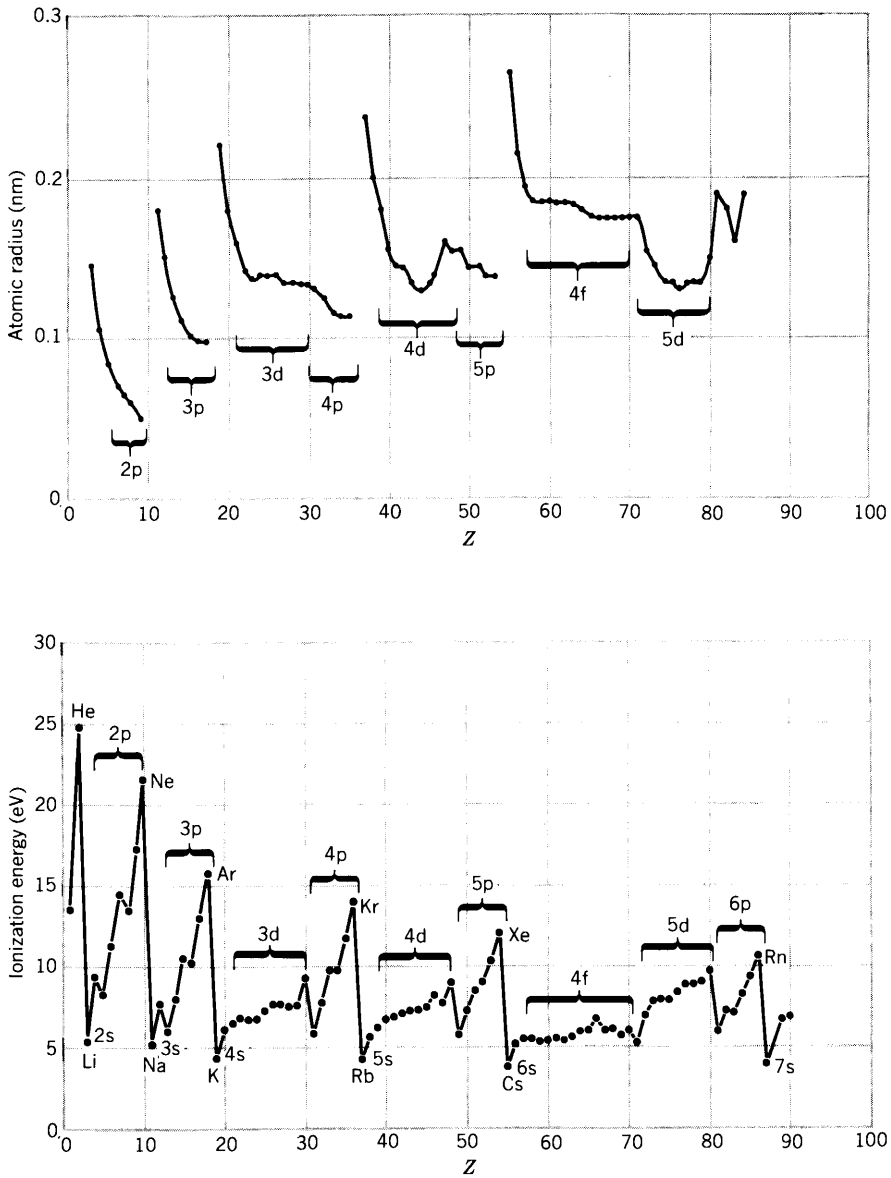


Figure 5.1 Atomic radius (top) and ionization energy (bottom) of the elements. The smooth variations in these properties correspond to the gradual filling of an atomic shell, and the sudden jumps show transitions to the next shell.

The question of the existence of a nuclear potential is dealt with by the fundamental assumption of the shell model: the motion of a single nucleon is governed by a potential caused by all of the other nucleons. If we treat each individual nucleon in this way, then we can allow the nucleons in turn to occupy the energy levels of a series of subshells.

The existence of definite spatial orbits depends on the Pauli principle. Consider in a heavy nucleus a collision between two nucleons in a state near the very

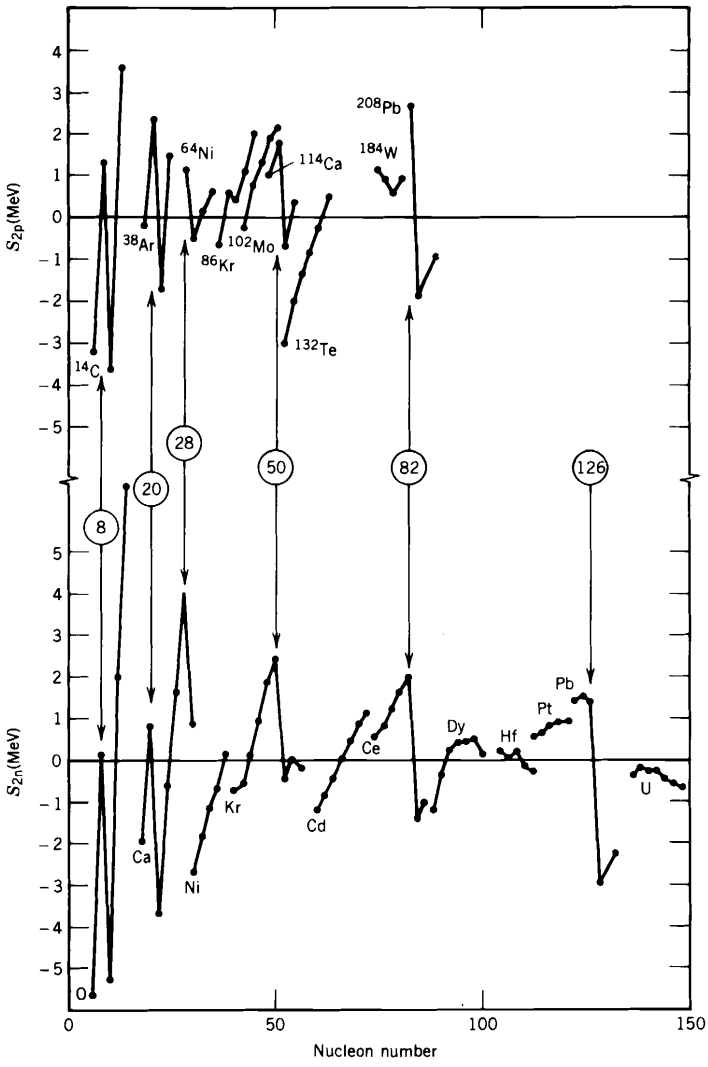


Figure 5.2 (Top) Two-proton separation energies of sequences of isotones (constant N). The lowest Z member of each sequence is noted. (Bottom) Two-neutron separation energies of sequences of isotopes. The sudden changes at the indicated "magic numbers" are apparent. The data plotted are differences between the measured values and the predictions of the semiempirical mass formula. Measured values are from the 1977 atomic mass tables (A. H. Wapstra and K. Bos, *Atomic Data and Nuclear Data Tables* **19**, 215 (1977)).

bottom of the potential well. When the nucleons collide they will transfer energy to one another, but if all of the energy levels are filled up to the level of the valence nucleons, there is no way for one of the nucleons to gain energy except to move up to the valence level. The other levels near the original level are filled and cannot accept an additional nucleon. Such a transfer, from a low-lying level to the valence band, requires more energy than the nucleons are likely to transfer in

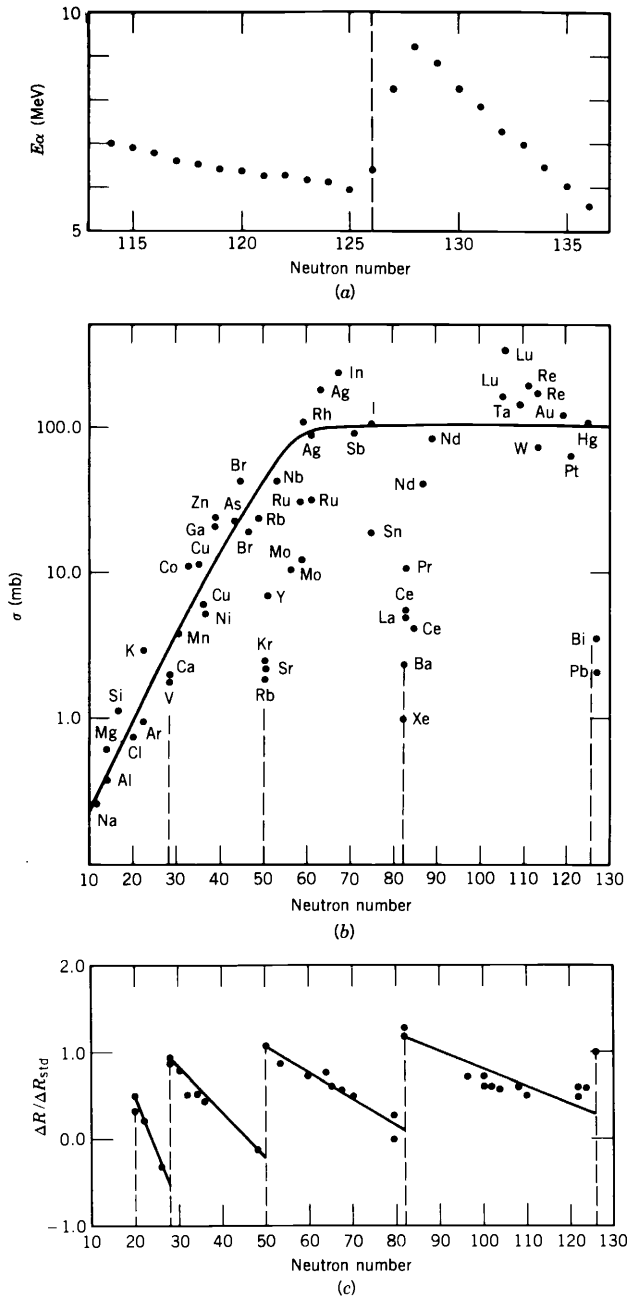


Figure 5.3 Additional evidence for nuclear shell structure. (*a*) Energies of α particles emitted by isotopes of Rn. Note the sudden increase when the *daughter* has $N = 126$ (i.e., when the parent has $N = 128$). If the daughter nucleus is more tightly bound, the α decay is able to carry away more energy. (*b*) Neutron-capture cross sections of various nuclei. Note the decreases by roughly two orders of magnitude near $N = 50$, 82, and 126. (*c*) Change in the nuclear charge radius when $\Delta N = 2$. Note the sudden jumps at 20, 28, 50, 82, and 126 and compare with Figure 5.1. To emphasize the shell effects, the radius difference ΔR has been divided by the standard ΔR expected from the $A^{1/3}$ dependence. From E. B. Shera et al., *Phys. Rev. C* **14**, 731 (1976).

a collision. Thus the collisions cannot occur, and the nucleons can indeed orbit as if they were transparent to one another!

Shell Model Potential

The first step in developing the shell model is the choice of the potential, and we begin by considering two potentials for which we solved the three-dimensional Schrödinger equation in Chapter 2: the infinite well and the harmonic oscillator. The energy levels we obtained are shown in Figure 5.4. As in the case of atomic physics, the degeneracy of each level is the the number of nucleons that can be put in each level, namely $2(2\ell + 1)$. The factor of $(2\ell + 1)$ arises from the m_ℓ degeneracy, and the additional factor of 2 comes from the m_s degeneracy. As in atomic physics, we use spectroscopic notation to label the levels, with one important exception: the index n is *not* the principal quantum number, but simply counts the number of levels with that ℓ value. Thus 1d means the first (lowest) d state, 2d means the second, and so on. (In atomic spectroscopic notation, there are no 1d or 2d states.) Figure 5.4 also shows the occupation

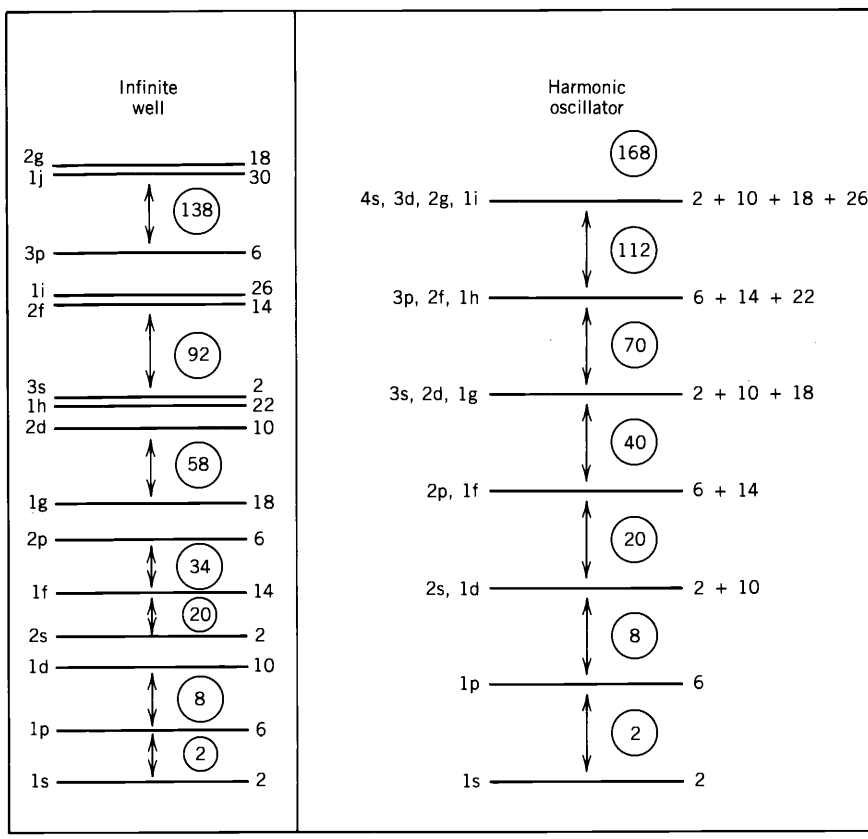


Figure 5.4 Shell structure obtained with infinite well and harmonic oscillator potentials. The capacity of each level is indicated to its right. Large gaps occur between the levels, which we associate with closed shells. The circled numbers indicate the total number of nucleons at each shell closure.

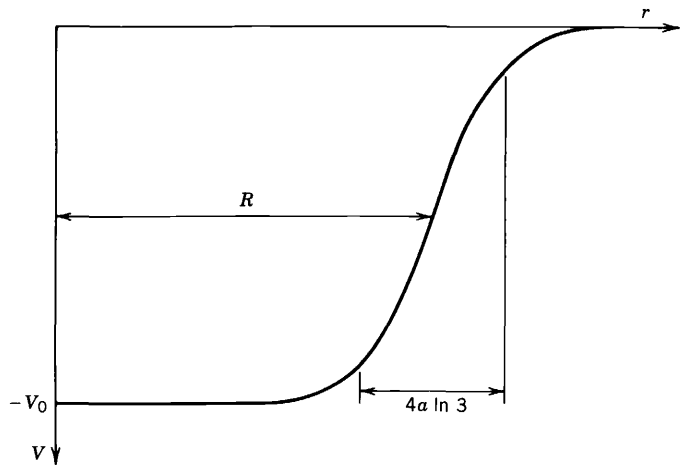


Figure 5.5 A realistic form for the shell-model potential. The "skin thickness" $4a \ln 3$ is the distance over which the potential changes from $0.9V_0$ to $0.1V_0$.

number of each level and the cumulative number of nucleons that would correspond to the filling of major shells. (Neutrons and protons, being nonidentical particles, are counted separately. Thus the 1s level can hold 2 protons as well as 2 neutrons.) It is encouraging to see the magic numbers of 2, 8, and 20 emerging in both of these schemes, but the higher levels do not correspond at all to the observed magic numbers.

As a first step in improving the model, we try to choose a more realistic potential. The infinite well is not a good approximation to the nuclear potential for several reasons: To separate a neutron or proton, we must supply enough energy to take it out of the well—an infinite amount! In addition, the nuclear potential does not have a sharp edge, but rather closely approximates the nuclear charge and matter distribution, falling smoothly to zero beyond the mean radius R. The harmonic oscillator, on the other hand, does not have a sharp enough edge, and it also requires infinite separation energies. Instead, we choose an intermediate form:

$$V(r) = \frac{-V_0}{1 + \exp[(r - R)/a]} \tag{5.1}$$

which is sketched in Figure 5.5. The parameters R and a give, respectively, the mean radius and skin thickness, and their values are chosen in accordance with the measurements discussed in Chapter 3: $R = 1.25A^{1/3}$ fm and $a = 0.524$ fm. The well depth V_0 is adjusted to give the proper separation energies and is of order 50 MeV. The resulting energy levels are shown in Figure 5.6; the effect of the potential, as compared with the harmonic oscillator (Figure 5.4) is to remove the ℓ degeneracies of the major shells. As we go higher in energy, the splitting becomes more and more severe, eventually becoming as large as the spacing between the oscillator levels themselves. Filling the shells in order with $2(2\ell + 1)$ nucleons, we again get the magic numbers 2, 8, and 20, but the higher magic numbers do not emerge from the calculations.

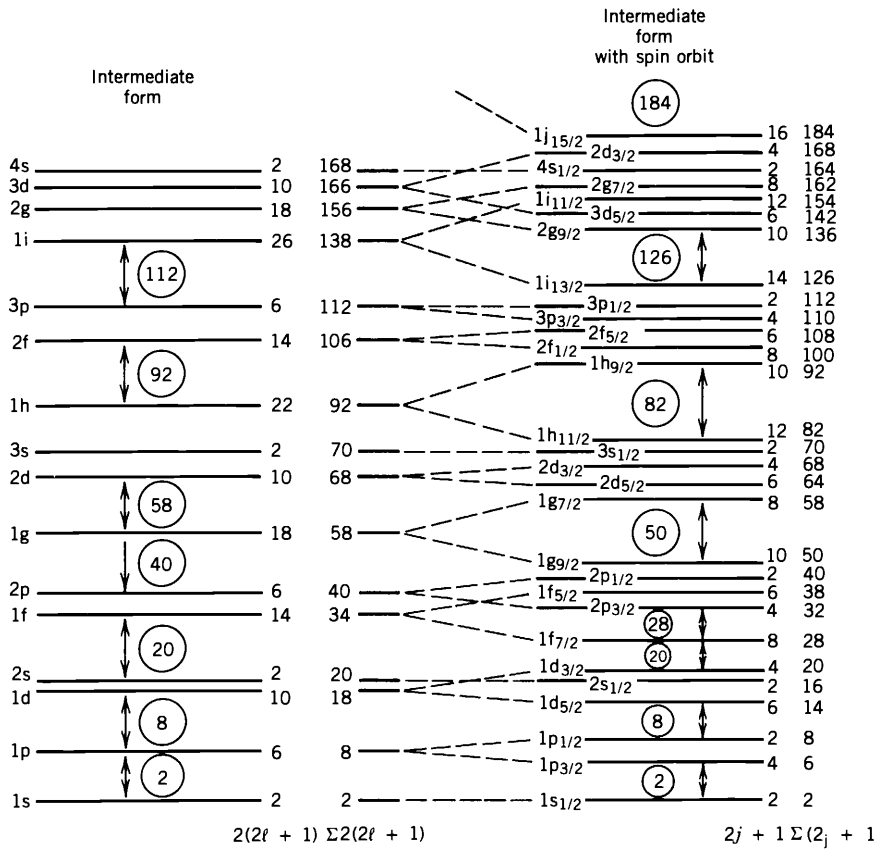


Figure 5.6 At the left are the energy levels calculated with the potential of Figure 5.5. To the right of each level are shown its capacity and the cumulative number of nucleons up to that level. The right side of the figure shows the effect of the spin-orbit interaction, which splits the levels with $\ell > 0$ into two new levels. The shell effect is quite apparent, and the magic numbers are exactly reproduced.

Spin-Orbit Potential

How can we modify the potential to give the proper magic numbers? We certainly cannot make a radical change in the potential, because we do not want to destroy the physical content of the model—Equation 5.1 is already a very good guess at how the nuclear potential *should* look. It is therefore necessary to add various terms to Equation 5.1 to try to improve the situation. In the 1940s, many unsuccessful attempts were made at finding the needed correction; success was finally achieved by Mayer, Haxel, Suess, and Jensen who showed in 1949 that the inclusion of a *spin-orbit* potential could give the proper separation of the subshells.

Once again, we are borrowing an idea from our colleagues, the atomic physicists. In atomic physics the spin-orbit interaction, which causes the observed fine structure of spectral lines, comes about because of the electromagnetic interaction of the electron's magnetic moment with the magnetic field generated by its motion about the nucleus. The effects are typically very small, perhaps one

part in 10^5 in the spacing of atomic levels. No such electromagnetic interaction would be strong enough to give the substantial changes in the *nuclear* level spacing needed to generate the observed magic numbers. Nevertheless we adopt the concept of a *nuclear* spin-orbit force of the same form as the atomic spin-orbit force but certainly *not* electromagnetic in origin. In fact, we know from the scattering experiments discussed in Chapter 4 that there is strong evidence for a nucleon–nucleon spin-orbit force.

The spin-orbit interaction is written as $V_{so}(r)\boldsymbol{\ell}\cdot\boldsymbol{s}$, but the form of $V_{so}(r)$ is not particularly important. It is the $\boldsymbol{\ell}\cdot\boldsymbol{s}$ factor that causes the reordering of the levels. As in atomic physics, in the presence of a spin-orbit interaction it is appropriate to label the states with the *total angular momentum* $\boldsymbol{j} = \boldsymbol{\ell} + \boldsymbol{s}$. A single nucleon has $s = \frac{1}{2}$, so the possible values of the total angular momentum quantum number are $j = \ell + \frac{1}{2}$ or $j = \ell - \frac{1}{2}$ (except for $\ell = 0$, in which case only $j = \frac{1}{2}$ is allowed). The expectation value of $\boldsymbol{\ell}\cdot\boldsymbol{s}$ can be calculated using a common trick. We first evaluate $\boldsymbol{j}^2 = (\boldsymbol{\ell} + \boldsymbol{s})^2$:

$$\begin{aligned} \boldsymbol{j}^2 &= \boldsymbol{\ell}^2 + 2\boldsymbol{\ell}\cdot\boldsymbol{s} + \boldsymbol{s}^2 \\ \boldsymbol{\ell}\cdot\boldsymbol{s} &= \tfrac{1}{2}\left(\boldsymbol{j}^2 - \boldsymbol{\ell}^2 - \boldsymbol{s}^2\right) \end{aligned} \tag{5.2}$$

Putting in the expectation values gives

$$\langle \boldsymbol{\ell}\cdot\boldsymbol{s} \rangle = \tfrac{1}{2}\left[j(j+1) - \ell(\ell+1) - s(s+1) \right]\hbar^2 \tag{5.3}$$

Consider a level such as the 1f level ($\ell = 3$), which has a degeneracy of $2(2\ell + 1) = 14$. The possible j values are $\ell \pm \frac{1}{2} = \frac{5}{2}$ or $\frac{7}{2}$. Thus we have the levels $1f_{5/2}$ and $1f_{7/2}$. The degeneracy of each level is $(2j + 1)$, which comes from the m_j values. (With spin-orbit interactions, m_s and m_ℓ are no longer "good" quantum numbers and can no longer be used to label states or to count degeneracies.) The capacity of the $1f_{5/2}$ level is therefore 6 and that of $1f_{7/2}$ is 8, giving again 14 states (the number of possible states must be preserved; we are only grouping them differently). For the $1f_{5/2}$ and $1f_{7/2}$ states, which are known as a spin-orbit pair or doublet, there is an energy separation that is proportional to the value of $\langle \boldsymbol{\ell}\cdot\boldsymbol{s} \rangle$ for each state. Indeed, for any pair of states with $\ell > 0$, we can compute the energy difference using Equation 5.3:

$$\langle \boldsymbol{\ell}\cdot\boldsymbol{s} \rangle_{j=\ell+1/2} - \langle \boldsymbol{\ell}\cdot\boldsymbol{s} \rangle_{j=\ell-1/2} = \tfrac{1}{2}(2\ell + 1)\hbar^2 \tag{5.4}$$

The energy splitting increases with increasing ℓ. Consider the effect of choosing $V_{so}(r)$ to be negative, so that the member of the pair with the larger j is pushed downward. Figure 5.6 shows the effect of this splitting. The $1f_{7/2}$ level now appears in the gap between the second and third shells; its capacity of 8 nucleons gives the magic number 28. (The p and d splittings do not result in any major regrouping of the levels.) The next major effect of the spin-orbit term is on the 1g level. The $1g_{9/2}$ state is pushed down all the way to the next lower major shell; its capacity of 10 nucleons adds to the previous total of 40 for that shell to give the magic number of 50. A similar effect occurs at the top of each major shell. In each case the lower energy member of the spin-orbit pair from the next shell is pushed down into the lower shell, and the remaining magic numbers follow exactly as expected. (We even predict a new one, at 184, which has not yet been seen.)

As an example of the application of the shell model, consider the filling of levels needed to produce ${}^{15}_{8}\mathrm{O}$ and ${}^{17}_{8}\mathrm{O}$. The 8 protons fill a major shell and do not

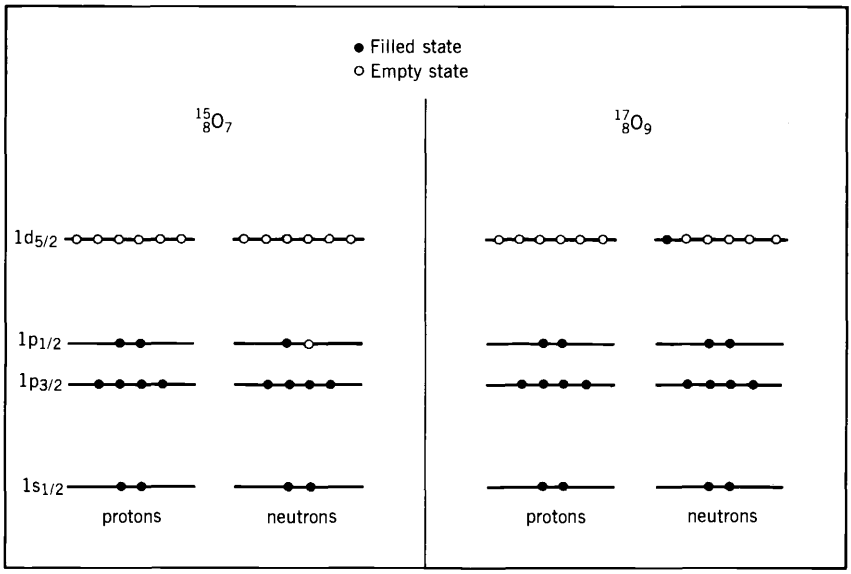


Figure 5.7 The filling of shells in ^{15}O and ^{17}O. The filled proton shells do not contribute to the structure; the properties of the ground state are determined primarily by the odd neutron.

contribute to the structure. Figure 5.7 shows the filling of levels. The extreme limit of the shell model asserts that only the single unpaired nucleon determines the properties of the nucleus. In the case of ^{15}O, the unpaired neutron is in the $p_{1/2}$ shell; we would therefore predict that the ground state of ^{15}O has spin $\frac{1}{2}$ and odd parity, since the parity is determined by $(-1)^{\ell}$. The ground state of ^{17}O should be characteristic of a $d_{5/2}$ neutron with spin $\frac{5}{2}$ and even parity. These two predictions are in exact agreement with the observed spin-parity assignments, and in fact similar agreements are found throughout the range of odd-A nuclei where the shell model is valid (generally $A < 150$ and $190 < A < 220$, for reasons to be discussed later in this chapter). This success in accounting for the observed ground-state spin-parity assignments was a great triumph for the shell model.

Magnetic Dipole Moments

Another case in which the shell model gives a reasonable (but not so exact) agreement with observed nuclear properties is in the case of magnetic dipole moments. You will recall from Chapter 3 that the magnetic moment is computed from the expectation value of the magnetic moment operator in the state with maximum z projection of angular momentum. Thus, including both ℓ and s terms, we must evaluate

$$\mu = \mu_N(g_\ell \ell_z + g_s s_z)/\hbar \tag{5.5}$$

when $j_z = j\hbar$. This cannot be evaluated directly, since ℓ_z and s_z do not have precisely defined values when we work in a system in which j is precisely defined. We can rewrite this expression, using $\boldsymbol{j} = \boldsymbol{\ell} + \boldsymbol{s}$, as

$$\mu = [g_\ell j_z + (g_s - g_\ell)s_z]\mu_N/\hbar \tag{5.6}$$

and, taking the expectation value when $j_z = j\hbar$, the result is

$$\langle\mu\rangle = [g_\ell j + (g_s - g_\ell)\langle s_z\rangle/\hbar]\mu_N \tag{5.7}$$

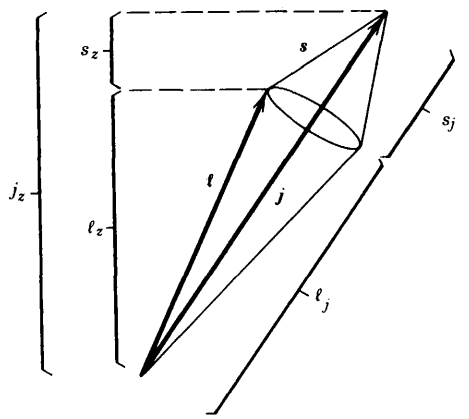


Figure 5.8 As the total angular momentum $\boldsymbol{j}$ precesses about the z axis keeping j_z constant, the vectors $\boldsymbol{\ell}$ and $\boldsymbol{s}$ precess about $\boldsymbol{j}$. The components of $\boldsymbol{\ell}$ and $\boldsymbol{s}$ along $\boldsymbol{j}$ remain constant, but ℓ_z and s_z vary.

The expection value of $\langle s_z \rangle$ can be quickly computed by recalling that $\boldsymbol{j}$ is the only vector of interest in this problem—the $\boldsymbol{\ell}$ and $\boldsymbol{s}$ vectors are meaningful only in their relationship to $\boldsymbol{j}$. Specifically, when we compute $\langle s_z \rangle$ the only surviving part will be from the component of $\boldsymbol{s}$ along $\boldsymbol{j}$, as suggested by the vector diagram of Figure 5.8. The instantaneous value of s_z varies, but its component along $\boldsymbol{j}$ remains constant. We therefore need an expression for the vector $\boldsymbol{s}_j$, the component of $\boldsymbol{s}$ along $\boldsymbol{j}$. The unit vector along j is $\boldsymbol{j}/|\boldsymbol{j}|$, and the component of $\boldsymbol{s}$ along $\boldsymbol{j}$ is $|\boldsymbol{s} \cdot \boldsymbol{j}|/|\boldsymbol{j}|$. The vector $\boldsymbol{s}_j$ is therefore $\boldsymbol{j}|\boldsymbol{s} \cdot \boldsymbol{j}|/|\boldsymbol{j}|^2$, and replacing all quantities by their expectation values gives

$$\langle s_z \rangle = \frac{j}{2j(j+1)}\left[j(j+1) - \ell(\ell+1) + s(s+1)\right]\hbar \tag{5.8}$$

where $\boldsymbol{s} \cdot \boldsymbol{j} = \boldsymbol{s} \cdot (\boldsymbol{\ell} + \boldsymbol{s})$ is computed using Equation 5.3. Thus for $j = \ell + \frac{1}{2}$, $\langle s_z \rangle = \hbar/2$, while for $j = \ell - \frac{1}{2}$ we have $\langle s_z \rangle = -\hbar j/2(j+1)$. The corresponding magnetic moments are

$$\begin{aligned} j &= \ell + \tfrac{1}{2} \qquad \langle \mu \rangle = \left[g_\ell\left(j - \tfrac{1}{2}\right) + \tfrac{1}{2}g_s\right]\mu_N \\ j &= \ell - \tfrac{1}{2} \qquad \langle \mu \rangle = \left[g_\ell \frac{j\left(j+\frac{3}{2}\right)}{(j+1)} - \frac{1}{2}\frac{1}{j+1}g_s\right]\mu_N \end{aligned} \tag{5.9}$$

Figure 5.9 shows a comparison of these calculated values with measured values for shell-model odd-A nuclei. The computed values are shown as solid lines and are known as the Schmidt lines; this calculation was first done by Schmidt in 1937. The experimental values fall within the limits of the Schmidt lines, but are generally smaller in magnitude and have considerable scatter. One defect of this theory is the assumption that g_s for a nucleon in a nucleus is the same as g_s for a free nucleon. We discussed in Chapter 3 how the spin g factors of nucleons differ considerably from the value of 2 expected for "elementary" spin-$\frac{1}{2}$ particles. If we regard the substantial differences as arising from the "meson cloud" that surrounds the nucleon, then it is not at all surprising that the meson cloud in nuclei, where there are other surrounding nucleons and mesons, differs from what it is for free nucleons. It is customary to account for this effect by (somewhat

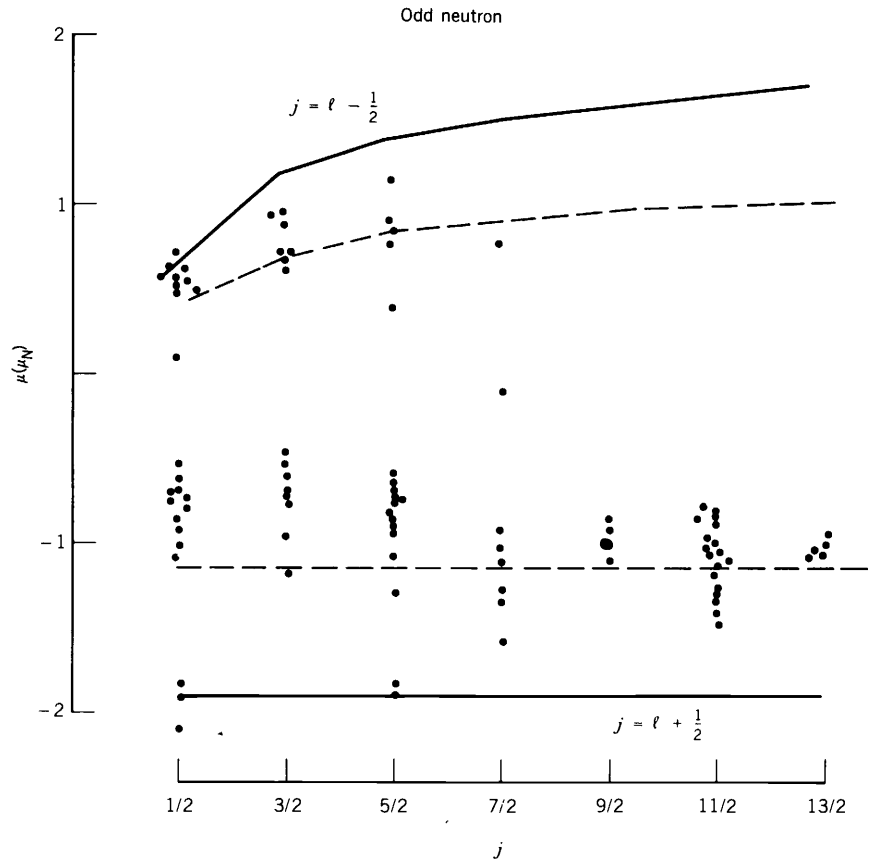


Figure 5.9 Experimental values for the magnetic moments of odd-neutron and odd-proton shell-model nuclei. The Schmidt lines are shown as solid for $g_s = g_s(\text{free})$ and dashed for $g_s = 0.6g_s(\text{free})$.

arbitrarily) reducing the g_s factor; for example, the lines for $g_s = 0.6g_s(\text{free})$ are shown in Figure 5.9. The overall agreement with experiment is better, but the scatter of the points suggests that the model is oversimplifying the calculation of magnetic moments. Nevertheless, the success in indicating the general trend of the observed magnetic moments suggests that the shell model gives us at least an approximate understanding of the structure of these nuclei.

Electric Quadrupole Moments

The calculation of electric quadrupole moments in the shell model is done by evaluating the electric quadrupole operator, $3z^2 - r^2$, in a state in which the total angular momentum of the odd particle has its maximum projection along the z axis (that is, $m_j = +j$). Let's assume for now that the odd particle is a proton. If its angular momentum is aligned (as closely as quantum mechanics allows) with the z axis, then it must be orbiting mostly in the xy plane. As we indicated in the discussion following Equation 3.36, this would give a negative quadrupole

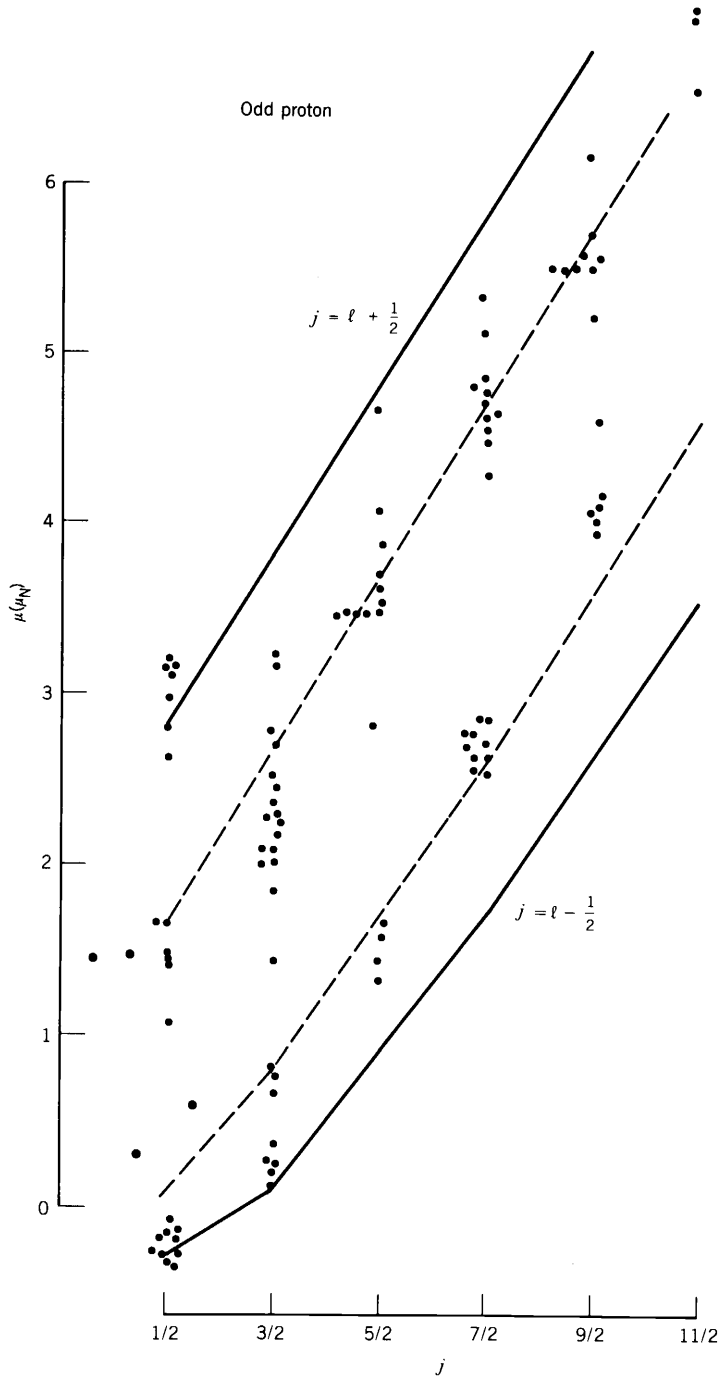


Figure 5.9 Continued.

Table 5.1 Shell-Model Quadrupole Moments

Shell-Model State	Calculated Q (single proton)	Measured Q			
		Single Particle		Single Hole	
		p	n	p	n
$1p_{3/2}$	−0.013	−0.0366(^{7}Li)		+0.0407(^{11}B)	+0.053(^{9}Be)
$1d_{5/2}$	−0.036	−0.12(^{19}F)	−0.026(^{17}O)	+0.140(^{27}Al)	+0.201(^{25}Mg)
$1d_{3/2}$	−0.037	−0.08249(^{35}Cl)	−0.064(^{33}S)	+0.056(^{39}K)	+0.45(^{35}S)
$1f_{7/2}$	−0.071	−0.26(^{43}Sc)	−0.080(^{41}Ca)	+0.40(^{59}Co)	+0.24(^{49}Ti)
$2p_{3/2}$	−0.055	−0.209(^{63}Cu)	−0.0285(^{53}Cr)	+0.195(^{67}Ga)	+0.20(^{57}Fe)
$1f_{5/2}$	−0.086		−0.20(^{61}Ni)	+0.274(^{85}Rb)	+0.15(^{67}Zn)
$1g_{9/2}$	−0.13	−0.32(^{93}Nb)	−0.17(^{73}Ge)	+0.86(^{115}In)	+0.45(^{85}Kr)
$1g_{7/2}$	−0.14	−0.49(^{123}Sb)		+0.20(^{139}La)	
$2d_{5/2}$	−0.12	−0.36(^{121}Sb)	−0.236(^{91}Zr)		+0.44(^{111}Cd)

Data for this table are derived primarily from the compilation of V. S. Shirley in the *Table of Isotopes*, 7th ed. (New York: Wiley, 1978). The uncertainties in the values are typically a few parts in the last quoted significant digit.

moment of the order of $Q \approx -\langle r^2 \rangle$. Some experimental values of quadrupole moments of nuclei that have one proton beyond a filled subshell are listed in Table 5.1. Values of $\langle r^2 \rangle$ range from 0.03 b for $A = 7$ to 0.3 b for $A = 209$, and thus the measured values are in good agreement with our expectations.

A more refined quantum mechanical calculation gives the single-particle quadrupole moment of an odd proton in a shell-model state j:

$$\langle Q_{sp} \rangle = -\frac{2j-1}{2(j+1)} \langle r^2 \rangle \tag{5.10}$$

For a uniformly charged sphere, $\langle r^2 \rangle = \frac{3}{5}R^2 = \frac{3}{5}R_0^2 A^{2/3}$. Using these results, we can compute the quadrupole moments for the nuclei shown in Table 5.1. The calculated values have the correct sign but are about a factor of 2–3 too small.

A more disturbing difficulty concerns nuclei with an odd neutron. An uncharged neutron outside a filled subshell should have no quadrupole moment at all. From Table 5.1 we see that the odd-neutron values are generally smaller than the odd-proton values, but they are most definitely not zero.

When a subshell contains more than a single particle, all of the particles in the subshell can contribute to the quadrupole moment. Since the capacity of any subshell is $2j + 1$, the number of nucleons in an unfilled subshell will range from 1 to $2j$. The corresponding quadrupole moment is

$$\langle Q \rangle = \langle Q_{sp} \rangle \left[1 - 2\frac{n-1}{2j-1} \right] \tag{5.11}$$

where n is the number of nucleons in the subshell ($1 \leq n \leq 2j$) and Q_{sp} is the

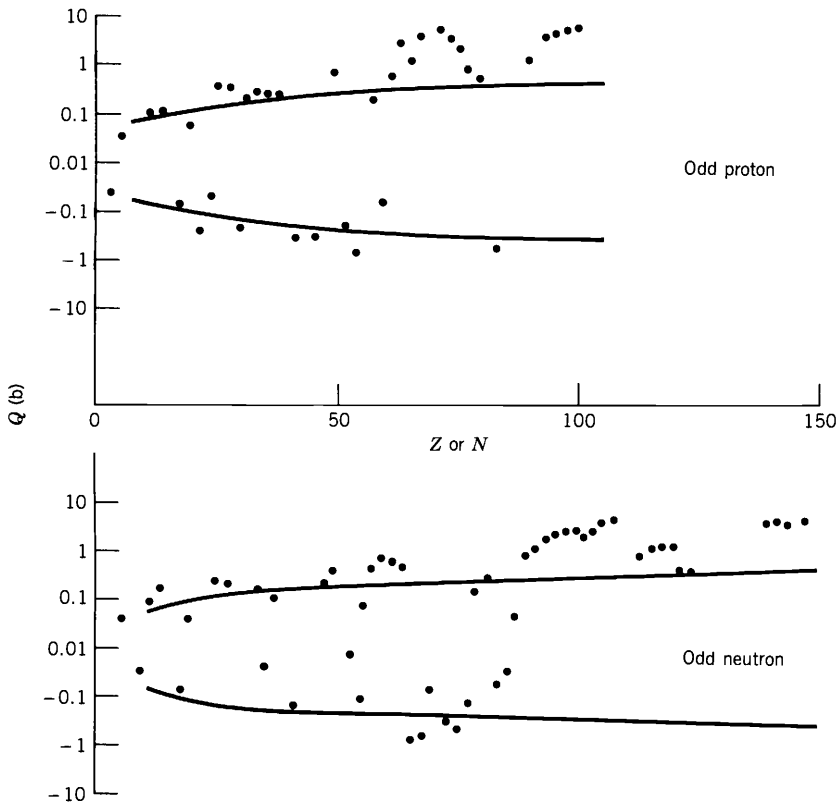


Figure 5.10 Experimental values of electric quadrupole moments of odd-neutron and odd-proton nuclei. The solid lines show the limits $Q \sim \langle r^2 \rangle$ expected for shell-model nuclei. The data are within the limits, except for the regions $60 < Z < 80$, $Z > 90$, $90 < N < 120$, and $N > 140$, where the experimental values are more than an order of magnitude larger than predicted by the shell model.

single-particle quadrupole moment given in Equation 5.10. When $n = 1$, $Q = Q_{sp}$, but when $n = 2j$ (corresponding to a subshell that lacks only one nucleon from being filled), $Q = -Q_{sp}$. Table 5.1 shows the quadrupole moments of these so-called "hole" states, and you can see that to a very good approximation, $Q(\text{particle}) = -Q(\text{hole})$. In particular, the quadrupole moments of the hole states are positive and opposite in sign to the quadrupole moments of the particle states.

Before we are overcome with enthusiasm with the success of this simple model, let us look at the entire systematic behavior of the quadrupole moments. Figure 5.10 summarizes the measured quadrupole moments of the ground states of odd-mass nuclei. There is some evidence for the change in sign of Q predicted by Equation 5.11, but the situation is not entirely symmetric—there are far more positive than negative quadrupole moments. Even worse, the model fails to predict the extremely large quadrupole moments of several barns observed for certain heavy nuclei. The explanations for these failures give us insight into other aspects of nuclear structure that cannot be explained within the shell model. We discuss these new features in the last two sections of this chapter.

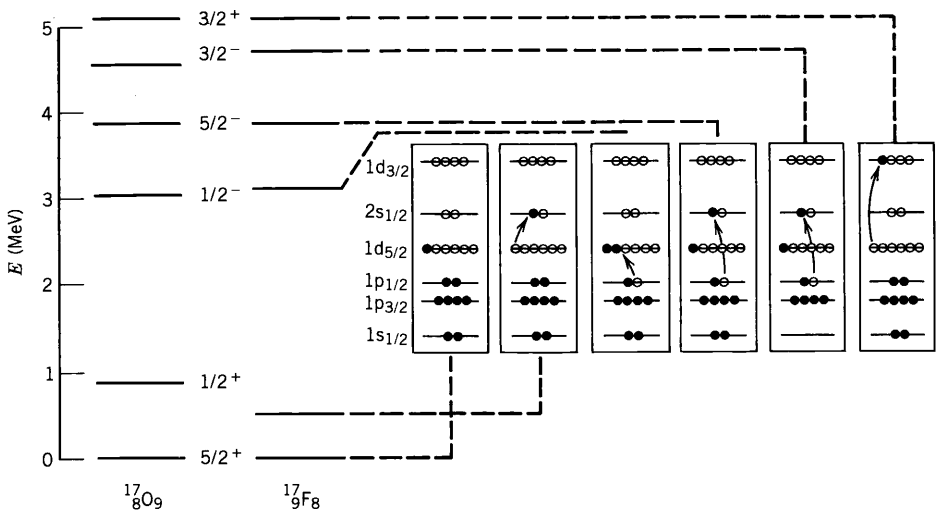


Figure 5.11 Shell-model interpretation of the levels of ^{17}O and ^{17}F. All levels below about 5 MeV are shown, and the similarity between the levels of the two nuclei suggests they have common structures, determined by the valence nucleons. The even-parity states are easily explained by the excitation of the single odd nucleon from the $d_{5/2}$ ground state to $2s_{1/2}$ or $1d_{3/2}$. The odd-parity states have more complicated structures; one possible configuration is shown, but others are also important.

Valence Nucleons

The shell model, despite its simplicity, is successful in accounting for the spins and parities of nearly all odd-A ground states, and is somewhat less successful (but still satisfactory) in accounting for magnetic dipole and electric quadrupole moments. The particular application of the shell model that we have considered is known as the *extreme independent particle model.* The basic assumption of the extreme independent particle model is that all nucleons but one are paired, and the nuclear properties arise from the motion of the single unpaired nucleon. This is obviously an oversimplification, and as a next better approximation we can treat all of the particles in the unfilled subshell. Thus in a nucleus such as $^{43}_{20}Ca_{23}$, with three neutrons beyond the closed shell at $N = 20$, the extreme version of the shell model considers only the 23rd neutron, but a more complete shell model calculation should consider all three valence neutrons. For $^{45}_{22}Ti_{23}$, we should take into account all five particles (2 protons, 3 neutrons) beyond the closed shells at $Z = 20$ and $N = 20$.

If the extreme independent particle model were valid, we should be able to reproduce diagrams like Figure 5.6 by studying the excited states of nuclei. Let's examine some examples of this procedure. Figure 5.11 shows some of the excited states of $^{17}_{8}O_9$ and $^{17}_{9}F_8$, each of which has only one nucleon beyond a doubly magic ($Z = 8$, $N = 8$) core. The ground state is $\frac{5}{2}^+$, as expected for the $d_{5/2}$ shell-model state of the 9th nucleon. From Figure 5.6 we would expect to find excited states with spin-parity assignments of $\frac{1}{2}^+$ and $\frac{3}{2}^+$, corresponding to the $1s_{1/2}$ and $1d_{3/2}$ shell-model levels. According to this assumption, when we add

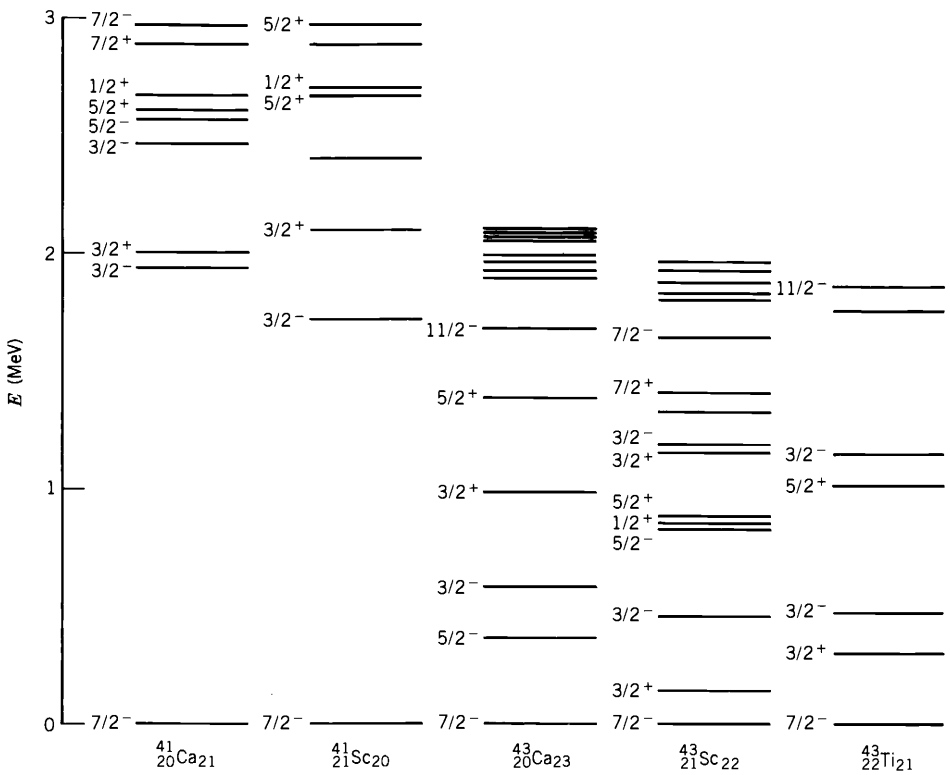


Figure 5.12 Energy levels of nuclei with odd particles in the $1f_{7/2}$ shell.

energy to the nucleus, the core remains inert and the odd particle absorbs the energy and moves to higher shell-model levels. The expected $\frac{1}{2}^+$ shell-model state appears as the first excited state, and the $\frac{3}{2}^+$ state is much higher, but how can we account for $\frac{1}{2}^-$, $\frac{3}{2}^-$, and $\frac{5}{2}^-$? (The negative parity $2p_{1/2}$, $2p_{3/2}$, and $1f_{5/2}$ shell-model states are well above the $1d_{3/2}$ state, which should therefore appear lower.) Figure 5.11 shows one possible explanation for the $\frac{1}{2}^-$ state: instead of exciting the odd nucleon to a higher state, we break the pair in the $1p_{1/2}$ level and excite one of the nucleons to pair with the nucleon in the $d_{5/2}$ level. The odd nucleon is now in the $1p_{1/2}$ state, giving us a $\frac{1}{2}^-$ excited state. (Because the pairing energy increases with ℓ, it is actually energetically favorable to break an $\ell = 1$ pair and form an $\ell = 2$ pair.) Verification of this hypothesis requires that we determine by experiment whether the properties of the $\frac{1}{2}^-$ state agree with those expected for a $p_{1/2}$ shell-model state. A similar assumption might do as well for the $\frac{3}{2}^-$ state (breaking a $p_{3/2}$ pair), but that still does not explain the $\frac{5}{2}^-$ state or the many other excited states.

In Figure 5.12, we show a similar situation for nuclei in the $1f_{7/2}$ shell. The $\frac{7}{2}^-$ ground state ($1f_{7/2}$) and the $\frac{3}{2}^-$ excited state ($2p_{3/2}$) appear as expected in the nuclei ^{41}Ca and ^{41}Sc, each of which has only a single nucleon beyond a doubly magic ($Z = 20$, $N = 20$) core. In ^{43}Ca, the structure is clearly quite different from that of ^{41}Ca. Many more low-lying states are present. These states come

from the coupling of three particles in the $1f_{7/2}$ shell and illustrate the difference between the complete shell model and its extreme independent particle limit. If only the odd particle were important, ^{43}Ca should be similar to ^{41}Ca. In ^{43}Sc, you can see how the 21st and 22nd neutrons, which would be ignored in the extreme independent particle limit, have a great effect on the structure. Similarly, the level scheme of ^{43}Ti shows that the 21st and 22nd protons have a great effect on the shell-model levels of the 21st neutron.

In addition to spin-parity assignments, magnetic dipole moments, electric quadrupole moments, and excited states, the shell model can also be used to calculate the probability of making a transition from one state to another as a result of a radioactive decay or a nuclear reaction. We examine the shell model predictions for these processes in later chapters.

Let's conclude this discussion of the shell model with a brief discussion of the question we raised at the beginning—how can we be sure that the very concept of a nucleon with definite orbital properties remains valid deep in the nuclear interior? After all, many of the tests of the shell model involve such nuclear properties as the spin and electromagnetic moments of the valence particles, all of which are concentrated near the nuclear surface. Likewise, many experimental probes of the nucleus, including other particles that feel the nuclear force, tell us mostly about the surface properties. To answer the question we have proposed,

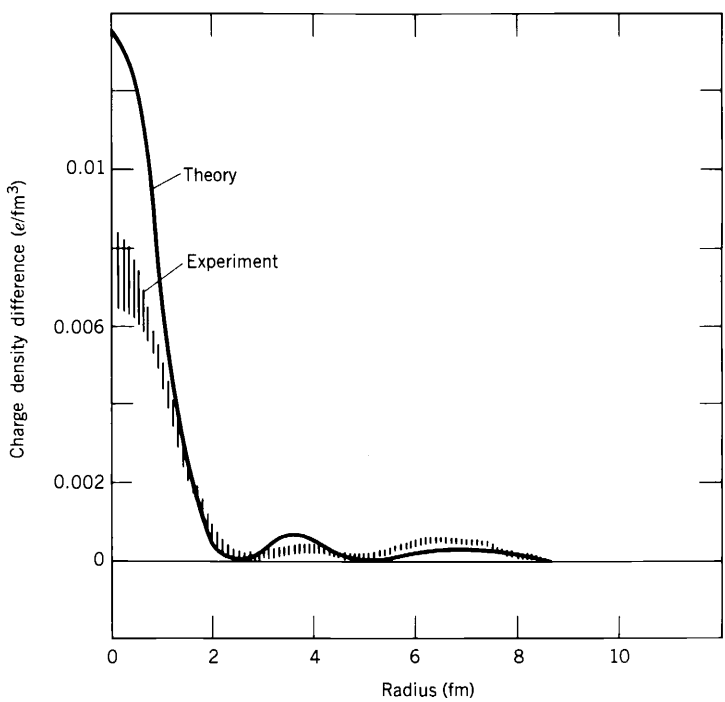


Figure 5.13 The difference in charge density between ^{205}Tl and ^{206}Pb, as determined by electron scattering. The curve marked "theory" is just the square of a harmonic oscillator 3s wave function. The theory reproduces the variations in the charge density extremely well. Experimental data are from J. M. Cavedon et al., *Phys. Rev. Lett.* **49**, 978 (1982).

what is needed is a probe that reaches deep into the nucleus, and we must use that probe to measure a nuclear property that characterizes the interior of the nucleus and not its surface. For a probe we choose high-energy electrons, as we did in studying the nuclear charge distribution in Chapter 3. The property that is to be measured is the charge density of a single nucleon in its orbit, which is equivalent to the square of its wave function, $|\psi|^2$. Reviewing Figure 2.12 we recall that only s-state wave functions penetrate deep into the nuclear interior; for other states $\psi \to 0$ as $r \to 0$. For our experiment we therefore choose a nucleus such as $^{205}_{81}\mathrm{Tl}_{124}$, which lacks a single proton in the $3s_{1/2}$ orbit from filling all subshells below the $Z = 82$ gap. How can we measure the contribution of just the $3s_{1/2}$ proton to the charge distribution and ignore the other protons? We can do so by measuring the *difference* in charge distribution between ^{205}Tl and $^{206}_{82}\mathrm{Pb}_{124}$, which has the filled proton shell. Any difference between the charge distributions of these two nuclei must be due to the extra $3s_{1/2}$ proton in ^{206}Pb. Figure 5.13 shows the experimentally observed difference in the charge distributions as measured in a recent experiment. The comparison with $|\psi|^2$ for a 3s wave function is very successful (using the same harmonic oscillator wave function plotted in Figure 2.12, except that here we plot $|\psi|^2$, *not* r^2R^2), thus confirming the validity of the assumption about nucleon orbits retaining their character deep in the nuclear interior. From such experiments we gain confidence that the independent-particle description, so vital to the shell model, is not just a convenience for analyzing measurements near the nuclear surface, but instead is a valid representation of the behavior of nucleons throughout the nucleus.

5.2 EVEN-*Z*, EVEN-*N* NUCLEI AND COLLECTIVE STRUCTURE

Now let's try to understand the structure of nuclei with even numbers of protons and neutrons (known as *even-even* nuclei). As an example, consider the case of ^{130}Sn, shown in Figure 5.14. The shell model predicts that all even-even nuclei will have 0^+ (spin 0, even parity) ground states, because all of the nucleons are paired. According to the shell model, the 50 protons of ^{130}Sn fill the $g_{9/2}$ shell and the 80 neutrons lack 2 from filling the $h_{11/2}$ shell to complete the magic number of $N = 82$. To form an excited state, we can break one of the pairs and excite a nucleon to a higher level; the coupling between the two odd nucleons then determines the spin and parity of the levels. Promoting one of the $g_{9/2}$ protons or $h_{11/2}$ neutrons to a higher level requires a great deal of energy, because the gap between the major shells must be crossed (see Figure 5.6). We therefore expect that the major components of the wave functions of the lower excited states will consist of neutron excitation within the last occupied major shell. For example, if we assume that the ground-state configuration of ^{130}Sn consists of filled $s_{1/2}$ and $d_{3/2}$ subshells and 10 neutrons (out of a possible 12) occupying the $h_{11/2}$ subshell, then we could form an excited state by breaking the $s_{1/2}$ pair and promoting one of the $s_{1/2}$ neutrons to the $h_{11/2}$ subshell. Thus we would have one neutron in the $s_{1/2}$ subshell and 11 neutrons in the $h_{11/2}$ subshell. The properties of such a system would be determined mainly by the coupling of the $s_{1/2}$ neutron with the unpaired $h_{11/2}$ neutron. Coupling angular momenta j_1 and j_2 in quantum mechanics gives values from the sum $j_1 + j_2$ to

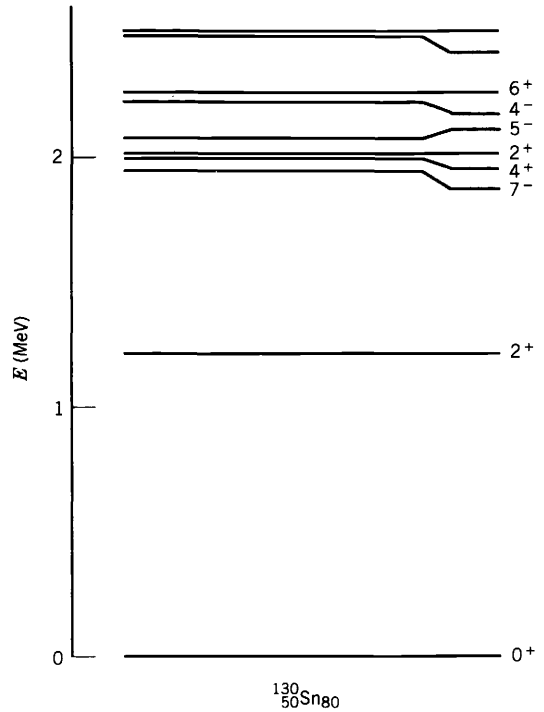


Figure 5.14 The low-lying energy levels of ^{130}Sn.

the difference $|j_1 - j_2|$ in integer steps. In this case the possible resultants are $\frac{11}{2} + \frac{1}{2} = 6$ and $\frac{11}{2} - \frac{1}{2} = 5$. Another possibility would be to break one of the $d_{3/2}$ pairs and again place an odd neutron in the $h_{11/2}$ subshell. This would give resulting angular momenta ranging from $\frac{11}{2} + \frac{3}{2} = 7$ to $\frac{11}{2} - \frac{3}{2} = 4$. Because the $s_{1/2}$ and $d_{3/2}$ neutrons have even parity and the $h_{11/2}$ neutron has odd parity, all of these couplings will give states with odd parity. If we examine the ^{130}Sn level scheme, we do indeed see several odd parity states with spins in the range of 4–7 with energies about 2 MeV. This energy is characteristic of what is needed to break a pair and excite a particle within a shell, and so we have a strong indication that we understand those states. Another possibility to form excited states would be to break one of the $h_{11/2}$ pairs and, keeping both members of the pair in the $h_{11/2}$ subshell, merely recouple them to a spin different from 0; according to the angular momentum coupling rules, the possibilities would be anything from $\frac{11}{2} + \frac{11}{2} = 11$ to $\frac{11}{2} - \frac{11}{2} = 0$. The two $h_{11/2}$ neutrons must be treated as identical particles and must therefore be described by a properly symmetrized wave function. This requirement restricts the resultant coupled spin to even values, and thus the possibilities are $0^+, 2^+, 4^+, 6^+, 8^+, 10^+$. There are several candidates for these states in the 2-MeV region, and here again the shell model seems to give us a reasonable description of the level structure.

A major exception to this successful interpretation is the 2^+ state at about 1.2 MeV. Restricting our discussion to the neutron states, what are the possible ways to couple two neutrons to get 2^+? As discussed above, the two $h_{11/2}$ neutrons can couple to 2^+. We can also excite a pair of $d_{3/2}$ neutrons to the $h_{11/2}$ subshell

(thus filling that shell and making an especially stable configuration), then break the coupling of the two remaining $d_{3/2}$ neutrons and recouple them to 2^+. Yet another possibility would be to place the pair of $s_{1/2}$ neutrons into the $h_{11/2}$ subshell, and excite one of the $d_{3/2}$ neutrons to the $s_{1/2}$ subshell. We would then have an odd neutron in each of the $d_{3/2}$ and $s_{1/2}$ subshells, which could couple to 2^+. However, in all these cases we must first break a pair, and thus the resulting states would be expected at about 2 MeV.

Of course, the shell-model description is only an approximation, and it is unlikely that "pure" shell-model states will appear in a complex level scheme. A better approach is to recognize that if we wish to use the shell model as a means to interpret the structure, then the physical states must be described as combinations of shell-model states, thus:

$$\psi(2^+) = a\psi(\nu h_{11/2} \oplus \nu h_{11/2}) + b\psi(\nu d_{3/2} \oplus \nu d_{3/2}) + c\psi(\nu d_{3/2} \oplus \nu s_{1/2}) + \cdots \tag{5.12}$$

where ν stands for neutron and the $\oplus$ indicates that we are doing the proper angular momentum coupling to get the 2^+ resultant. The puzzle of the low-lying 2^+ state can now be rephrased as follows: Each of the constituent states has an energy of about 2 MeV. What is it about the nuclear interaction that gives the right mixture of expansion coefficients $a, b, c, \ldots$ to force the state down to an energy of 1.2 MeV?

Our first thought is that this structure may be a result of the particular shell-model levels occupied by the valence particles of ^{130}Sn. We therefore examine other even-even nuclei and find this remarkable fact: of the hundreds of known even-even nuclei in the shell-model region, *each one* has an "anomalous" 2^+ state at an energy at or below one-half of the energy needed to break a pair. In all but a very few cases, this 2^+ state is the lowest excited state. The occurrence of this state is thus not an accident resulting from the shell-model structure of ^{130}Sn. Instead it is a *general property* of even-Z, even-N nuclei, valid throughout the entire mass range, independent of which particular shell-model states happen to be occupied. We will see that there are other general properties that are common to all nuclei, and it is reasonable to identify those properties not with the motion of a few valence nucleons, but instead with the entire nucleus. Such properties are known as *collective properties* and their origin lies in the nuclear collective motion, in which many nucleons contribute cooperatively to the nuclear properties. The collective properties vary smoothly and gradually with mass number and are mostly independent of the number and kind of valence nucleons outside of filled subshells (although the valence nucleons may contribute shell structure that couples with the collective structure).

In Figures 5.15 and 5.16 are shown four different properties of even-even nuclei that reveal collective behavior. The energy of the first 2^+ excited state (Figure 5.15*a*) seems to decrease rather smoothly as a function of A (excepting the regions near closed shells). The region from about $A = 150$ to $A = 190$ shows values of $E(2^+)$ that are both exceptionally small and remarkably constant. Again excepting nuclei near closed shells, the ratio $E(4^+)/E(2^+)$ (Figure 5.15*b*)

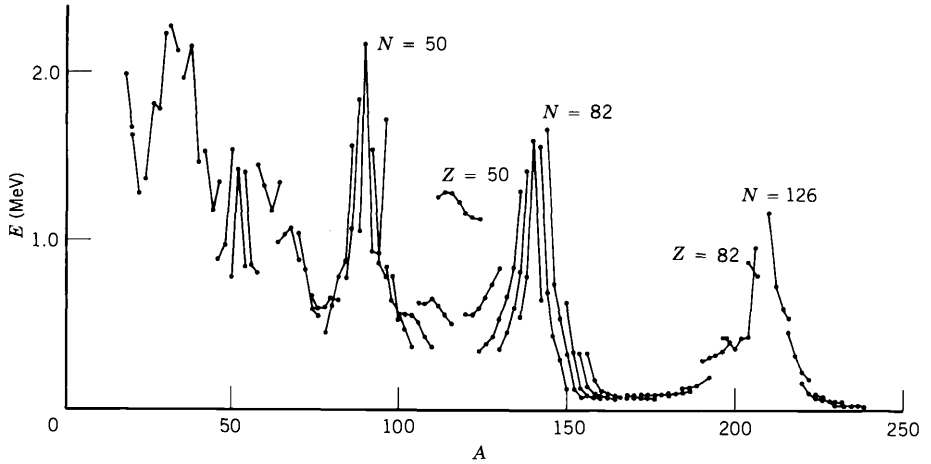


Figure 5.15*a* Energies of lowest 2^+ states of even-Z, even-N nuclei. The lines connect sequences of isotopes.

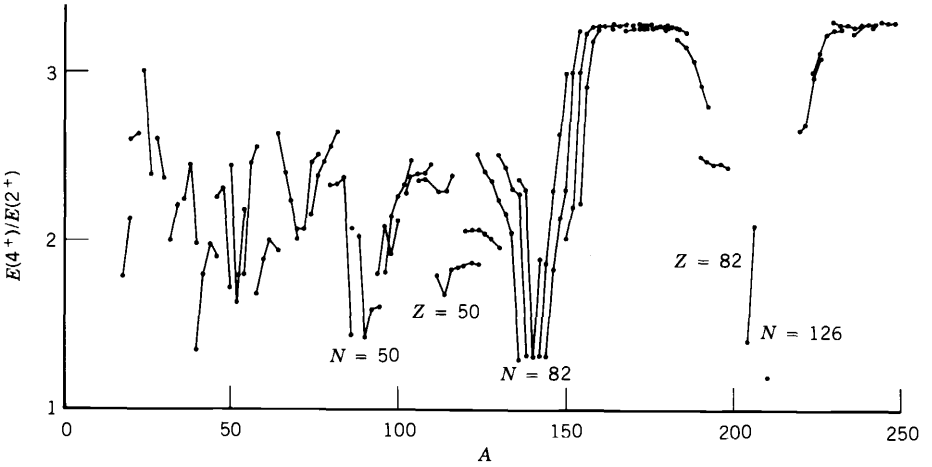


Figure 5.15*b* The ratio $E(4^+) / E(2^+)$ for the lowest 2^+ and 4^+ states of even-Z, even-N nuclei. The lines connect sequences of isotopes.

is roughly 2.0 for nuclei below $A = 150$ and very constant at 3.3 for $150 < A < 190$ and $A > 230$. The magnetic moments of the 2^+ states (Figure 5.16*a*) are fairly constant in the range 0.7–1.0, and the electric quadrupole moments (Figure 5.16*b*) are small for $A < 150$ and much larger for $A > 150$. These illustrations suggest that we must consider two types of collective structure, for the nuclei with $A < 150$ seem to show one set of properties and the nuclei with $150 < A < 190$ show quite a different set.

The nuclei with $A < 150$ are generally treated in terms of a model based on vibrations about a spherical equilibrium shape, while nuclei with A between 150 and 190 show structures most characteristic of rotations of a nonspherical system. Vibrations and rotations are the two major types of collective nuclear

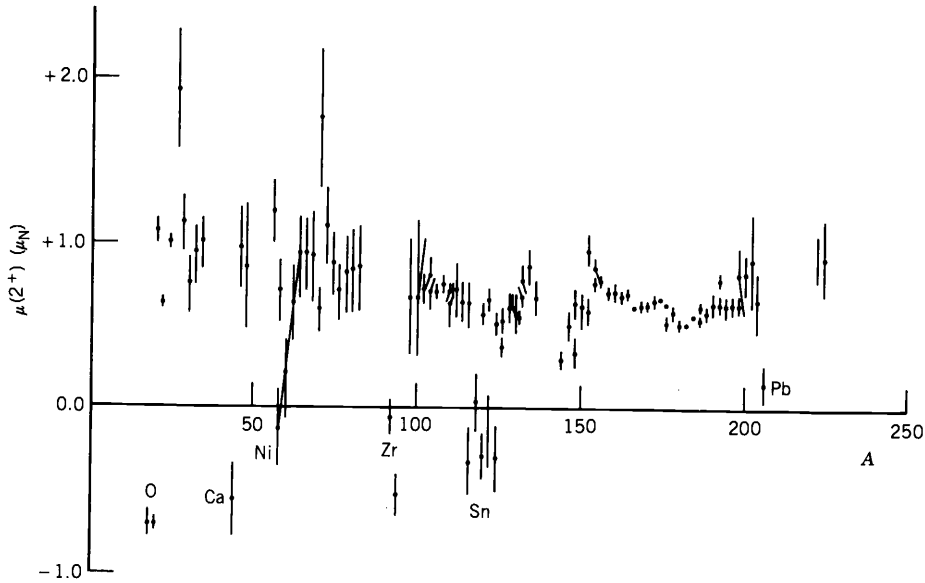


Figure 5.16*a* Magnetic moments of lowest 2^+ states of even-Z, even-N nuclei. Shell-model nuclei showing noncollective behavior are indicated.

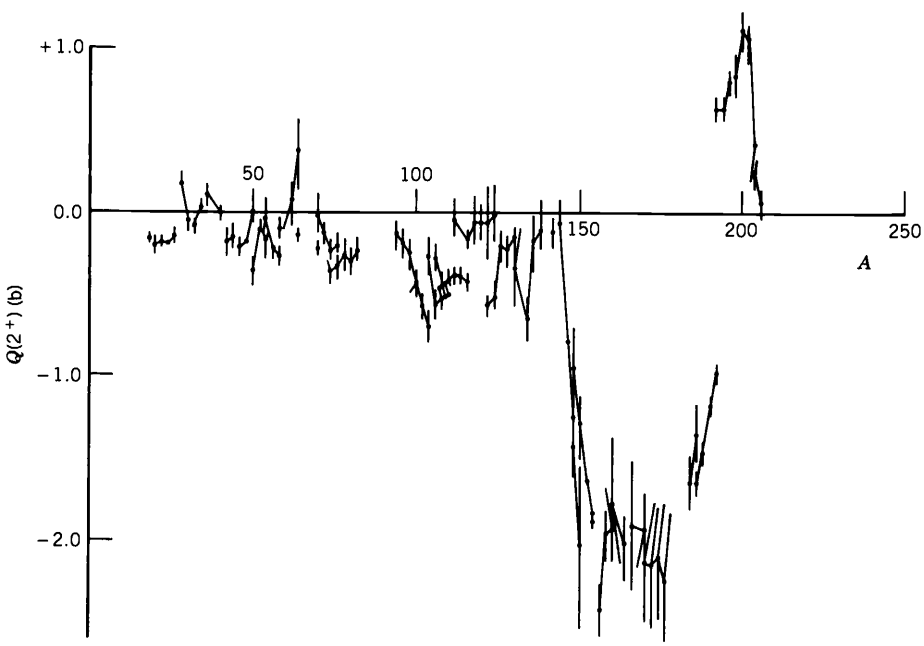


Figure 5.16*b* Electric quadrupole moments of lowest 2^+ states of even-Z, even-N nuclei. The lines connect sequences of isotopes.

motion, and we will consider each in turn. The collective nuclear model is often called the "liquid drop" model, for the vibrations and rotations of a nucleus resemble those of a suspended drop of liquid and can be treated with a similar mathematical analysis.

Nuclear Vibrations

Imagining a liquid drop vibrating at high frequency, we can get a good idea of the physics of nuclear vibrations. Although the average shape is spherical, the instantaneous shape is not. It is convenient to give the instantaneous coordinate $R(t)$ of a point on the nuclear surface at (θ, ϕ), as shown in Figure 5.17, in terms of the spherical harmonics $Y_{\lambda\mu}(\theta, \phi)$. Each spherical harmonic component will have an amplitude $\alpha_{\lambda\mu}(t)$:

$$R(t) = R_{\text{av}} + \sum_{\lambda \geq 1} \sum_{\mu=-\lambda}^{+\lambda} \alpha_{\lambda\mu}(t) Y_{\lambda\mu}(\theta, \phi) \tag{5.13}$$

The $\alpha_{\lambda\mu}$ are not completely arbitrary; reflection symmetry requires that $\alpha_{\lambda\mu} = \alpha_{\lambda-\mu}$, and if we assume the nuclear fluid to be incompressible, further restrictions apply. The constant ($\lambda = 0$) term is incorporated into the average radius R_{av}, which is just $R_0 A^{1/3}$. A typical $\lambda = 1$ vibration, known as a *dipole* vibration, is shown in Figure 5.18. Notice that this gives a net displacement of the center of mass and therefore cannot result from the action of internal nuclear forces. We therefore consider the next lowest mode, the $\lambda = 2$ (quadrupole) vibration. In analogy with the quantum theory of electromagnetism, in which a unit of electromagnetic energy is called a photon, a quantum of vibrational energy is

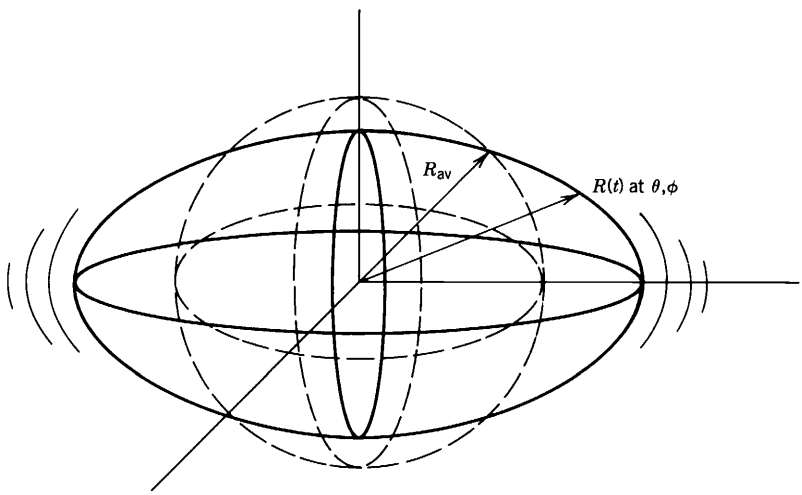


Figure 5.17 A vibrating nucleus with a spherical equilibrium shape. The time-dependent coordinate $R(t)$ locates a point on the surface in the direction θ, ϕ.

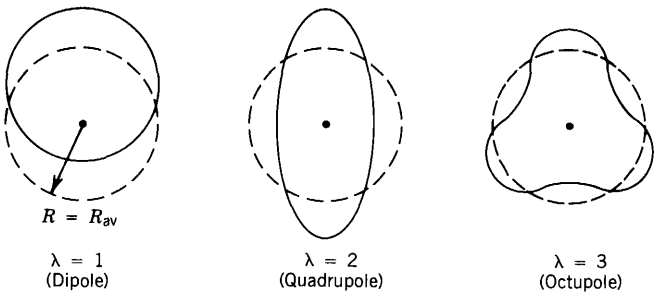


Figure 5.18 The lowest three vibrational modes of a nucleus. The drawings represent a slice through the midplane. The dashed lines show the spherical equilibrium shape and the solid lines show an instantaneous view of the vibrating surface.

called a *phonon*. Whenever we produce mechanical vibrations, we can equivalently say that we are producing vibrational phonons. A single unit of $\lambda = 2$ nuclear vibration is thus a *quadrupole phonon*.

Let's consider the effect of adding one unit of vibrational energy (a quadrupole phonon) to the 0^+ ground state of an even-even nucleus. The $\lambda = 2$ phonon carries 2 units of angular momentum (it adds a $Y_{2\mu}$ dependence to the nuclear wave function, just like a $Y_{\ell m}$ with $\ell = 2$) and even parity, since the parity of a $Y_{\ell m}$ is $(-1)^{\ell}$. Adding two units of angular momentum to a 0^+ state gives only a 2^+ state, in exact agreement with the observed spin-parity of first excited states of spherical even-Z, even-N nuclei. (The energy of the quadrupole phonon is not predicted by this theory and must be regarded as an adjustable parameter.) Suppose now we add a second quadrupole phonon. There are 5 possible components μ for each phonon and therefore 25 possible combinations of the $\lambda\mu$ for the two phonons, as enumerated in Table 5.2. Let's try to examine the resulting sums. There is one possible combination with total $\mu = +4$. It is natural to associate this with a transfer of 4 units of angular momentum (a $Y_{\ell m}$ with $m = +4$ and therefore $\ell = 4$). There are two combinations with total $\mu = +3$: $(\mu_1 = +1,\ \mu_2 = +2)$ and $(\mu_1 = +2,\ \mu_2 = +1)$. However, when we make the proper symmetric combination of the phonon wave functions (phonons, with integer spins, must have symmetric total wave functions; see Section 2.7), only

Table 5.2 Combinations of z Projections of Two Quadrupole Phonons into a Resultant Total z Component[a]

	μ_1				
μ_2	−2	−1	0	+1	+2
−2	−4	−3	−2	−1	0
−1	−3	−2	−1	0	+1
0	−2	−1	0	+1	+2
+1	−1	0	+1	+2	+3
+2	0	+1	+2	+3	+4

[a] The entries show $\mu = \mu_1 + \mu_2$.

one combination appears. There are three combinations that give $\mu = +2$: $(\mu_1, \mu_2) = (+2, 0)$, $(+1, +1)$, and $(0, +2)$. The first and third must be combined into a symmetric wave function; the $(+1, +1)$ combination is already symmetric. Continuing in this way, we would find not 25 but 15 possible allowed combinations: one with $\mu = +4$, one with $\mu = +3$, two with $\mu = +2$, two with $\mu = +1$, three with $\mu = 0$, two with $\mu = -1$, two with $\mu = -2$, one with $\mu = -3$ and one with $\mu = -4$. We can group these in the following way:

$$\ell = 4 \qquad \mu = +4, +3, +2, +1, 0, -1, -2, -3, -4$$
$$\ell = 2 \qquad \mu = +2, +1, 0, -1, -2$$
$$\ell = 0 \qquad \mu = 0$$

Thus we expect a triplet of states with spins $0^+, 2^+, 4^+$ at twice the energy of the first 2^+ state (since two identical phonons carry twice as much energy as one). This $0^+, 2^+, 4^+$ triplet is a common feature of vibrational nuclei and gives strong support to this model. The three states are never exactly at the same energy, owing to additional effects not considered in this simple model. A similar calculation for three quadrupole phonons gives states $0^+, 2^+, 3^+, 4^+, 6^+$ (see Problem 10).

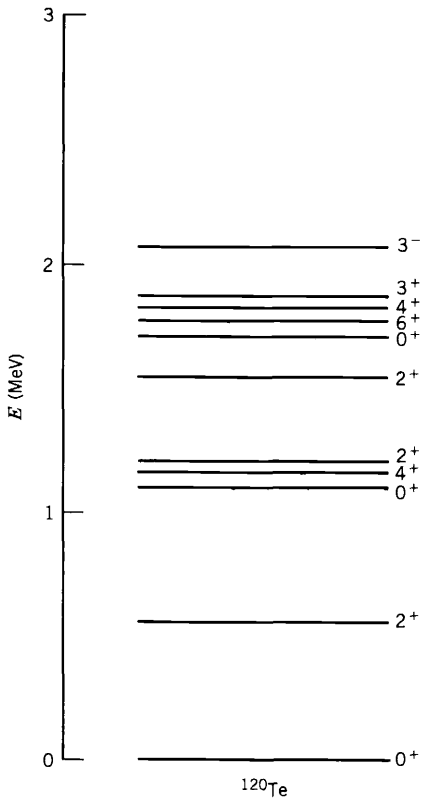


Figure 5.19 The low-lying levels of ^{120}Te. The single quadrupole phonon state (first 2^+), the two-phonon triplet, and the three-phonon quintuplet are obviously seen. The 3^- state presumably is due to the octupole vibration. Above 2 MeV the structure becomes quite complicated, and no vibrational patterns can be seen.

The next highest mode of vibration is the $\lambda = 3$ *octupole* mode, which carries three units of angular momentum and negative parity. Adding a single octupole phonon to the 0^+ ground state gives a 3^- state. Such states are also commonly found in vibrational nuclei, usually at energies somewhat above the two-phonon triplet. As we go higher in energy, the vibrational structure begins to give way to particle excitation corresponding to the breaking of a pair in the ground state. These excitations are very complicated to handle and are not a part of the collective structure of nuclei.

The vibrational model makes several predictions that can be tested in the laboratory. If the equilibrium shape is spherical, the quadrupole moments of the first 2^+ state should vanish; Figure 5.16*b* showed they are small and often vanishing in the region $A < 150$. The magnetic moments of the first 2^+ states are predicted to be $2(Z/A)$, which is in the range 0.8–1.0 for the nuclei considered; this is also in reasonable agreement with experiment. The predicted ratio $E(4^+)/E(2^+)$ is 2.0, if the 4^+ state is a member of the two-phonon triplet and the 2^+ state is the first excited state; Figure 5.15*b* shows reasonable agreement with this prediction in the range $A < 150$. In Chapter 10 we show the good agreement with γ-ray transition probabilities as well. Figure 5.19 shows an example of the low-lying level structure of a typical "vibrational" nucleus, and many of the predicted features are readily apparent. Thus the spherical vibrational model gives us quite an accurate picture of the structure of these nuclei.

Nuclear Rotations

Rotational motion can be observed only in nuclei with nonspherical equilibrium shapes. These nuclei can have substantial distortions from spherical shape and are often called *deformed nuclei*. They are found in the mass ranges $150 < A < 190$ and $A > 220$ (rare earths and actinides). Figure 5.10 showed that the odd-mass nuclei in these regions also have quadrupole moments that are unexpectedly large. A common representation of the shape of these nuclei is that of an ellipsoid of revolution (Figure 5.20), the surface of which is described by

$$R(\theta, \phi) = R_{\text{av}}[1 + \beta Y_{20}(\theta, \phi)] \tag{5.14}$$

which is independent of ϕ and therefore gives the nucleus cylindrical symmetry. The *deformation parameter* β is related to the eccentricity of the ellipse as

$$\beta = \frac{4}{3}\sqrt{\frac{\pi}{5}}\frac{\Delta R}{R_{\text{av}}} \tag{5.15}$$

where ΔR is the difference between the semimajor and semiminor axes of the ellipse. It is customary (although not quite exact) to take $R_{\text{av}} = R_0 A^{1/3}$. The approximation is not exact because the volume of the nucleus described by Equation 5.14 is not quite $\frac{4}{3}\pi R_{\text{av}}^3$; see Problem 11. The axis of symmetry of Equation 5.14 is the reference axis relative to which θ is defined. When $\beta > 0$, the nucleus has the elongated form of a *prolate* ellipsoid; when $\beta < 0$, the nucleus has the flattened form of an *oblate* ellipsoid.

One indicator of the stable deformation of a nucleus is a large electric quadrupole moment, such as those shown in Figure 5.10. The relationship

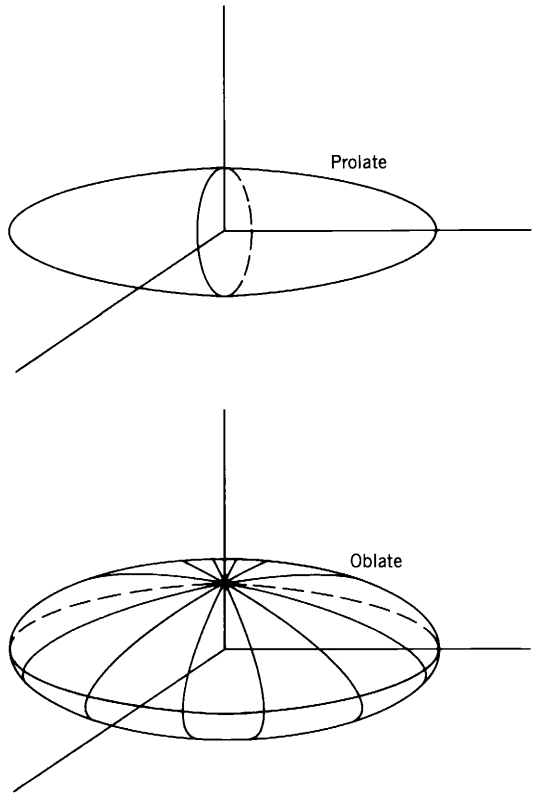


Figure 5.20 Equilibrium shapes of nuclei with permanent deformations. These sketches differ from Figures 5.17 and 5.18 in that these do not represent snapshots of a moving surface at a particular instant of time, but instead show the static shape of the nucleus.

between the deformation parameter and the quadrupole moment is

$$Q_0 = \frac{3}{\sqrt{5\pi}} R_{\text{av}}^2 Z\beta(1 + 0.16\beta) \tag{5.16}$$

The quadrupole moment Q_0 is known as the *intrinsic* quadrupole moment and would only be observed in a frame of reference in which the nucleus were at rest. In the laboratory frame of reference, the nucleus is rotating and quite a different quadrupole moment Q is measured. In fact, as indicated in Figure 5.21, rotating a prolate intrinsic distribution about an axis perpendicular to the symmetry axis (no rotations can be observed parallel to the symmetry axis) gives a time-averaged oblate distribution. Thus for $Q_0 > 0$, we would observe $Q < 0$. The relationship between Q and Q_0 depends on the nuclear angular momentum; for 2^+ states, $Q = -\frac{2}{7}Q_0$. Figure 5.16*b* shows $Q \simeq -2$ b for nuclei in the region of stable permanent deformations ($150 \leq A \leq 190$), and so $Q_0 \simeq +7$ b. From Equation 5.16, we would deduce $\beta \simeq 0.29$. This corresponds to a substantial deviation from a spherical nucleus; the difference in the lengths of the semimajor and semiminor axes is, according to Equation 5.15, about 0.3 of the nuclear radius.

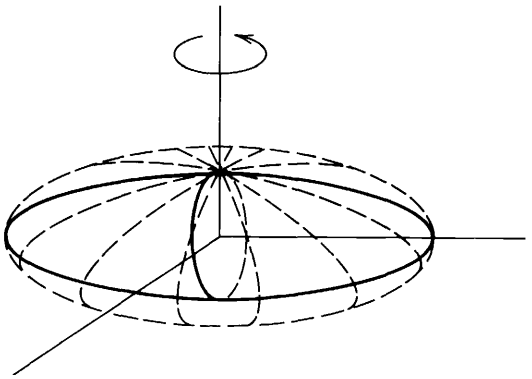


Figure 5.21 Rotating a static prolate distribution about an axis perpendicular to its symmetry axis gives in effect a smeared-out oblate (flattened) distribution.

The kinetic energy of a rotating object is $\frac{1}{2}\mathscr{I}\omega^2$, where $\mathscr{I}$ is the moment of inertia. In terms of the angular momentum $\ell = \mathscr{I}\omega$, the energy is $\ell^2/2\mathscr{I}$. Taking the quantum mechanical value of ℓ^2, and letting I represent the angular momentum quantum number, gives

$$E = \frac{\hbar^2}{2\mathscr{I}} I(I+1) \tag{5.17}$$

for the energies of a rotating object in quantum mechanics. Increasing the quantum number I corresponds to adding rotational energy to the nucleus, and the nuclear excited states form a sequence known as a *rotational band*. (Excited states in molecules also form rotational bands, corresponding to rotations of the molecule about its center of mass.) The ground state of an even-Z, even-N nucleus is always a 0^+ state, and the mirror symmetry of the nucleus restricts the sequence of rotational states in this special case to *even* values of I. We therefore expect to see the following sequence of states:

$$\begin{aligned} E(0^+) &= 0 \\ E(2^+) &= 6(\hbar^2/2\mathscr{I}) \\ E(4^+) &= 20(\hbar^2/2\mathscr{I}) \\ E(6^+) &= 42(\hbar^2/2\mathscr{I}) \\ E(8^+) &= 72(\hbar^2/2\mathscr{I}) \end{aligned}$$

and so on.

Figure 5.22 shows the excited states of a typical rotational nucleus. The first excited state is at $E(2^+) = 91.4$ keV, and thus we have $\hbar^2/2\mathscr{I} = 15.2$ keV. The energies of the next few states in the ground-state rotational band are computed to be

$$\begin{aligned} E(4^+) &= 20(\hbar^2/2\mathscr{I}) = 305 \text{ keV} \qquad \text{(measured 300 keV)} \\ E(6^+) &= 42(\hbar^2/2\mathscr{I}) = 640 \text{ keV} \qquad \text{(measured 614 keV)} \\ E(8^+) &= 72(\hbar^2/2\mathscr{I}) = 1097 \text{ keV} \qquad \text{(measured 1025 keV)} \end{aligned}$$

The calculated energy levels are not quite exact (perhaps because the nucleus behaves somewhat like a fluid of nucleons and not quite like a rigid object with a fixed moment of inertia), but are good enough to give us confidence that we have at least a rough idea of the origin of the excited levels. In particular, the predicted

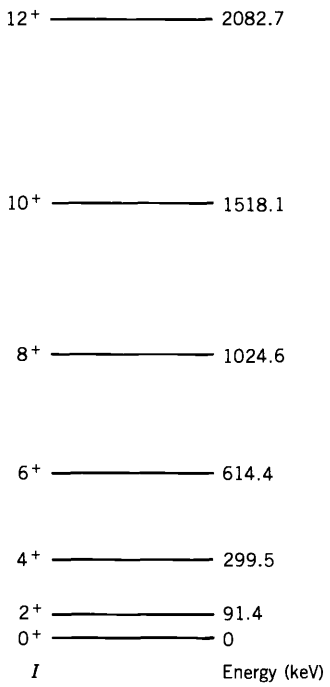


Figure 5.22 The excited states resulting from rotation of the ground state in ^{164}Er.

ratio $E(4^+)/E(2^+)$ is 3.33, in remarkable agreement with the systematics of nuclear levels for $150 < A < 190$ and $A > 230$ shown in Figure 5.15*b*.

We can gain some insight into the structure of deformed nuclei by considering the moment of inertia in two extreme cases. A solid ellipsoid of revolution of mass M whose surface is described by Equation 5.14 has a rigid moment of inertia

$$\mathscr{I}_{\text{rigid}} = \tfrac{2}{5}MR_{\text{av}}^2(1 + 0.31\beta) \tag{5.18}$$

which of course reduces to the familiar value for a sphere when $\beta = 0$. For a typical nucleus in the deformed region ($A \approx 170$), this gives a rotational energy constant

$$\frac{\hbar^2}{2\mathscr{I}_{\text{rigid}}} \cong 6 \text{ keV}$$

which is of the right order of magnitude but is too small compared with the observed values (about 15 keV for $E(2^+) = 90$ keV). That is, the rigid moment of inertia is too large by about a factor of 2–3. We can take the other extreme and regard the nucleus as a fluid inside a rotating ellipsoidal vessel, which would give a moment of inertia

$$\mathscr{I}_{\text{fluid}} = \frac{9}{8\pi}MR_{\text{av}}^2\beta \tag{5.19}$$

from which we would estimate

$$\frac{\hbar^2}{2\mathscr{I}_{\text{fluid}}} \cong 90 \text{ keV}$$

The fluid moment inertia is thus too small, and we conclude $\mathscr{I}_{\text{rigid}} > \mathscr{I} > \mathscr{I}_{\text{fluid}}$. The rotational behavior is thus intermediate between a rigid object, in which the particles are tightly bonded together, and a fluid, in which the particles are only weakly bonded. (We probably should have guessed this result, based on our studies of the nuclear force. Strong forces exist between a nucleon and its immediate neighbors only, and thus a nucleus does not show the long-range structure that would characterize a rigid solid.)

Another indication of the lack of rigidity of the nucleus is the increase in the moment of inertia that occurs at high angular momentum or rotational frequency. This effect, called "centrifugal stretching," is seen most often in heavy-ion reactions, to be discussed in Section 11.13.

Of course, the nucleus has no "vessel" to define the shape of the rotating fluid; it is the potential supplied by the nucleons themselves which gives the nucleus its shape. The next issue to be faced is whether the concept of a shape has any meaning for a rotating nucleus. If the rotation is very fast compared with the speed of nucleons in their "orbits" defined by the nuclear potential (as seen in a frame of reference in which the nucleus is at rest), then the concept of a static nuclear shape is not very meaningful because the motion of the nucleons will be dominated by the rotation. The average kinetic energy of a nucleon in a nucleus is of the order of 20 MeV, corresponding to a speed of approximately $0.2c$. This is a reasonable estimate for the speed of internal motion of the nucleons. The angular velocity of a rotating state is $\omega = \sqrt{2E/\mathscr{I}}$, where E is the energy of the state. For the first rotational state, $\omega \simeq 1.1 \times 10^{20}$ rad/s and a nucleon near the surface would rotate with a tangential speed of $v \simeq 0.002c$. The rotational motion is therefore far slower than the internal motion. The correct picture of a rotating deformed nucleus is therefore a stable equilibrium shape determined by nucleons in rapid internal motion in the nuclear potential, with the entire resulting distribution rotating sufficiently slowly that the rotation has little effect on the nuclear structure or on the nucleon orbits. (The rotational model is sometimes described as "adiabatic" for this reason.)

It is also possible to form other kinds of excited states upon which new rotational bands can be built. Examples of such states, known as *intrinsic states* because they change the intrinsic structure of the nucleus, are vibrational states (in which the nucleus vibrates about a deformed equilibrium shape) and pair-breaking particle excitations. If the intrinsic state has spin different from zero, the rotational band built on that state will have the sequence of spins I, $I + 1$, $I + 2, \ldots$. The vibrational states in deformed nuclei are of two types: β vibrations, in which the deformation parameter β oscillates and the nucleus preserves its cylindrical symmetry, and γ vibrations, in which the cylindrical symmetry is violated. (Picture a nucleus shaped like a football. β vibrations correspond to pushing and pulling on the ends of the football, while γ vibrations correspond to pushing and pulling on its sides.) Both the vibrational states and the particle excitations occur at energies of about 1 MeV, while the rotational spacing is much smaller (typically $\hbar^2/2\mathscr{I} \simeq 10$–$20$ keV).

Figure 5.23 shows the complete low-energy structure of ^{164}Er. Although the entire set of excited states shows no obvious patterns, knowing the spin-parity assignments helps us to group the states into rotational bands, which show the characteristic $I(I + 1)$ spacing. Other properties of the excited states (for example, γ-ray emission probabilities) also help us to identify the structure.

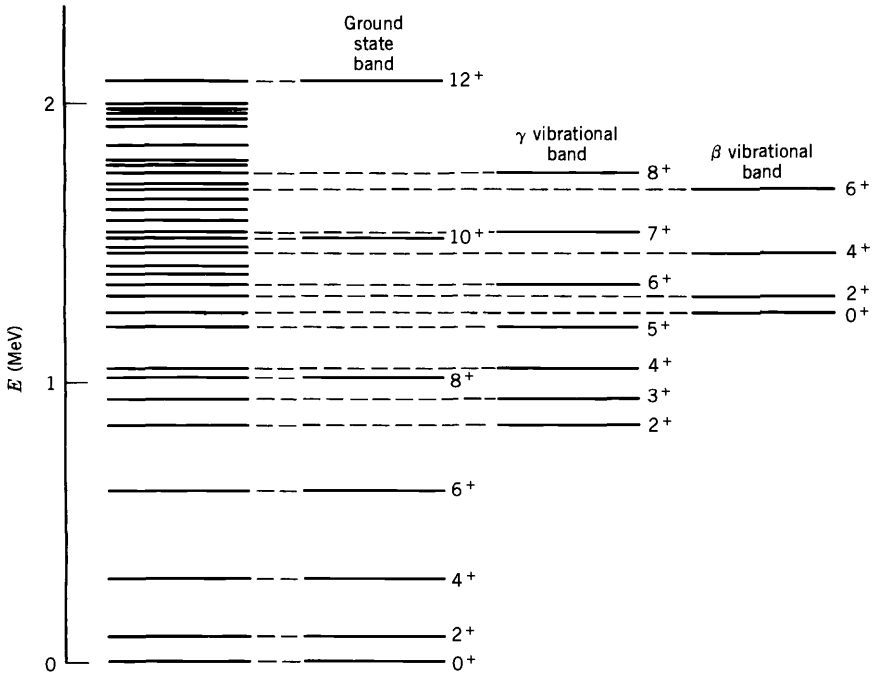


Figure 5.23 The states of ^{164}Er below 2 MeV. Most of the states are identified with three rotational bands: one built on the deformed ground state, a second built on a γ-type vibration (in which the surface vibrates transverse to the symmetry axis), and a third built on a β-type vibration (in which the surface vibrates along the symmetry axis). Many of the other excited states originate from pair-breaking particle excitations and their associated rotational bands.

Both the vibrational and rotational collective motions give the nucleus a magnetic moment. We can regard the movement of the protons as an electric current, and a single proton moving with angular momentum quantum number ℓ would give a magnetic moment $\mu = \ell\mu_N$. However, the entire angular momentum of a nuclear state does not arise from the protons alone; the neutrons also contribute, and if we assume that the protons and neutrons move with identical collective motions (a reasonable but not quite exact assumption), we would predict that the protons contribute to the total nuclear angular momentum a fraction of nearly Z/A. (We assume that the collective motion of the neutrons does not contribute to the magnetic moment, and we also assume that the protons and neutrons are all coupled pairwise so that the spin magnetic moments do not contribute.) The collective model thus predicts for the magnetic moment of a vibrational or rotational state of angular momentum I

$$\mu(I) = I\frac{Z}{A}\mu_N \tag{5.20}$$

For light nuclei, $Z/A \simeq 0.5$ and $\mu(2) \simeq +1\mu_N$, while for heavier nuclei, $Z/A \simeq 0.4$ and $\mu(2) \simeq +0.8\mu_N$. Figure 5.16*a* shows that, with the exception of closed-shell nuclei (for which the collective model is not valid), the magnetic moments of the 2^+ states are in very good agreement with this prediction.

As a final point in this brief introduction to nuclear collective motion, we must try to justify the origin of collective behavior based on a more microscopic approach to nuclear structure. This is especially true for rotational nuclei with permanent deformations. We have already seen how well the shell model with a spherically symmetric potential works for many nuclei. We can easily allow the shell-model potential to vibrate about equilibrium when energy is added to the nucleus, and so the vibrational motion can be handled in a natural way in the shell model. As we learned in our discussion of the ^{130}Sn structure at the beginning of this section, we can analyze the collective vibrational structure from an even more microscopic approach; for example, we consider all valence nucleons (those outside closed shells), find all possible couplings (including those that break pairs) giving 2^+ resultant spins, and try to find the correct mixture of wave functions that gives the observed 2^+ first excited state. If there are many possible couplings, this procedure may turn out to be mathematically complex, but the essentials of the shell model on which it is based are not significantly different from the extreme independent particle model we considered in the previous section. This approach works for spherical nuclei, but it does not lead naturally to a rotational nucleus with a permanent deformation.

Here is the critical question: How do shell-model orbits, calculated using a spherical potential, result in a nonspherical nucleus? We get a clue to the answer to this question by superimposing a diagram showing the "magic numbers" on a

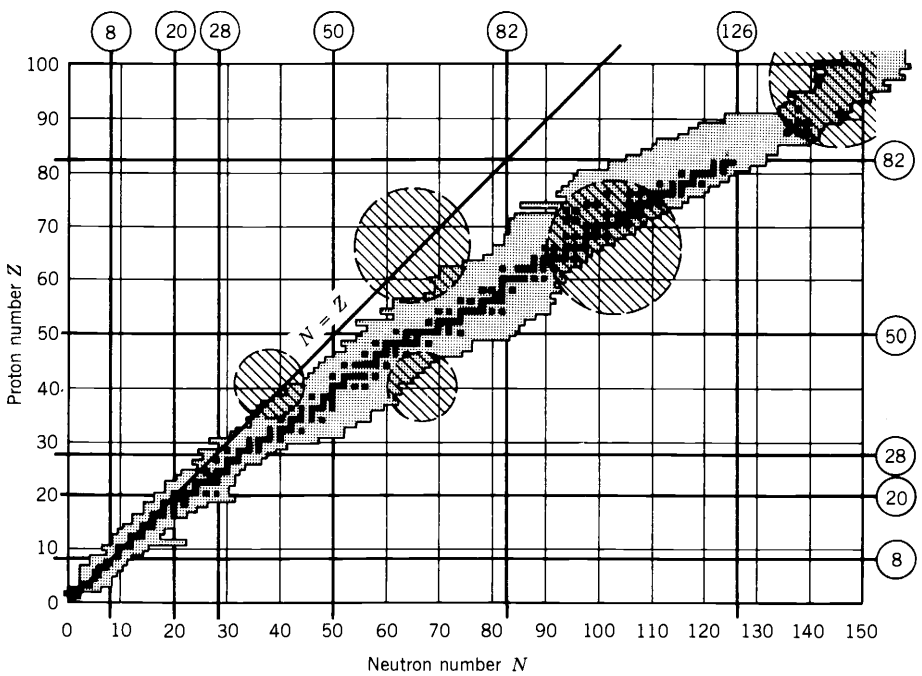


Figure 5.24 The crosshatched areas show the regions far from closed shells where we expect that the cooperative effects of many single-particle shell-model states may combine to produce a permanent nuclear deformation. Such deformed nuclei have been identified in all of the regions where the crosshatched areas overlap the known nuclei.

chart of the known nuclear species, as shown in Figure 5.24. The deformed nuclei exist only in regions far from filled neutron *and* proton shells. Just as the cooperative effect of a few nucleon pairs outside of a filled shell was responsible for the microscopic structure of the vibrations of spherical nuclei, the cooperative effect of many valence nucleon pairs can distort the "core" of nucleons until the equilibrium shape becomes strongly deformed.

5.3 MORE REALISTIC NUCLEAR MODELS

Both the shell model for odd-A nuclei and the collective model for even-even nuclei are idealizations that are only approximately valid for real nuclei, which are far more complex in their structure than our simple models suggest. Moreover, in real nuclei we cannot "turn off" one type of structure and consider only the other. Thus even very collective nuclei show single-particle effects, while the core of nucleons in shell-model nuclei may contribute collective effects that we have ignored up to this point. The structure of most nuclei cannot be quite so neatly divided between single-particle and collective motion, and usually we must consider a combination of both. Such a *unified nuclear model* is mathematically too complicated to be discussed here, and hence we will merely illustrate a few of the resulting properties of nuclei and try to relate them to the more elementary aspects of the shell and collective models.

Many-Particle Shell Model

In our study of the shell model, we considered only the effects due to the last unpaired single particle. A more realistic approach for odd-A nuclei would be to include all particles outside of closed shells. Let us consider for example the nuclei with odd Z or N between 20 and 28, so that the odd nucleons are in the $f_{7/2}$ shell. For simplicity, we shall confine our discussion to one kind of nucleon only, and thus we require not only that there be an even number of the other kind of nucleon, but also that it be a magic number. Figure 5.25 shows the lower excited states of several such nuclei. The nuclei whose structure is determined by a *single* particle (^{41}Ca and ^{55}Co) show the expected levels—a $\frac{7}{2}^-$ ground state, corresponding to the single odd $f_{7/2}$ particle (or vacancy, in the case of ^{55}Co, since a single vacancy or hole in a shell behaves like a single particle in the shell), and a $\frac{3}{2}^-$ excited state at about 2 MeV, corresponding to exciting the single odd particle to the $p_{3/2}$ state. The nuclei with 3 or 5 particles in the $f_{7/2}$ level show a much richer spectrum of states, and in particular the very low negative-parity states cannot be explained by the extreme single-particle shell model. If the $\frac{5}{2}^-$ state, for instance, originated from the excitation of a single particle to the $f_{5/2}$ shell, we would expect it to appear above 2 MeV because the $f_{5/2}$ level occurs above the $p_{3/2}$ level (see Figure 5.6); the lowest $\frac{5}{2}^-$ level in the single-particle nuclei occurs at 2.6 MeV (in ^{41}Ca) and 3.3 MeV (in ^{55}Co).

We use the shorthand notation $(f_{7/2})^n$ to indicate the configuration with n particles in the $f_{7/2}$ shell, and we consider the possible resultant values of I for the configuration $(f_{7/2})^3$. (From the symmetry between particles and holes, the levels of three holes, or five particles, in the $f_{7/2}$ shell will be the same.) Because

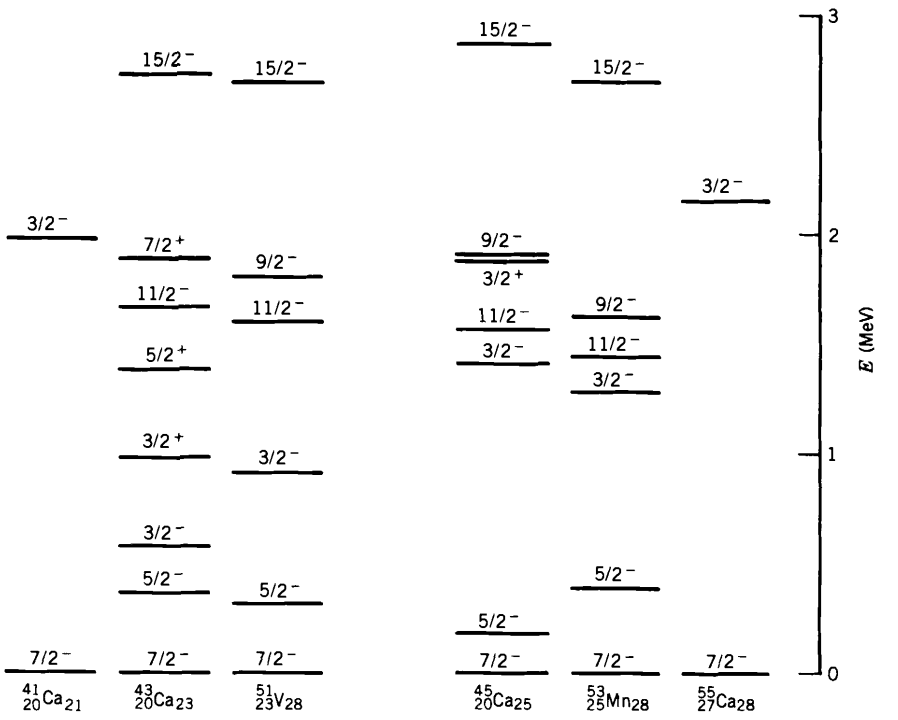


Figure 5.25 Excited states of some nuclei with valence particles in the $f_{7/2}$ shell. All known levels below about 2 MeV are shown, and in addition the $\frac{15}{2}^-$ state is included.

the nucleons have half-integral spins, they must obey the Pauli principle, and thus no two particles can have the same set of quantum numbers. Each particle in the shell model is described by the angular momentum $j = \frac{7}{2}$, which can have the projections or z components corresponding to $m = \pm\frac{1}{2}, \pm\frac{3}{2}, \pm\frac{5}{2}, \pm\frac{7}{2}$. The Pauli principle requires that each of the 3 particles have a different value of m. Immediately we conclude that the maximum value of the total projection, $M = m_1 + m_2 + m_3$, for the three particles is $+\frac{7}{2} + \frac{5}{2} + \frac{3}{2} = +\frac{15}{2}$. (Without the Pauli principle, the maximum would be $\frac{21}{2}$.) We therefore expect to find no state in the configuration $(f_{7/2})^3$ with I greater than $\frac{15}{2}$; the maximum resultant angular momentum is $I = \frac{15}{2}$, which can have all possible M from $+\frac{15}{2}$ to $-\frac{15}{2}$. The next highest possible M is $\frac{13}{2}$, which can only be obtained from $+\frac{7}{2} + \frac{5}{2} + \frac{1}{2}$ ($+\frac{7}{2} + \frac{3}{2} + \frac{3}{2}$ is not permitted, nor is $+\frac{7}{2} + \frac{7}{2} - \frac{1}{2}$). This single $M = \frac{13}{2}$ state must belong to the M states we have already assigned to the $I = \frac{15}{2}$ configuration; thus we have no possibility to have a $I = \frac{13}{2}$ resultant. Continuing in this way, we find two possibilities to obtain $M = +\frac{11}{2}$ ($+\frac{7}{2} + \frac{3}{2} + \frac{1}{2}$ and $+\frac{7}{2} + \frac{5}{2} - \frac{1}{2}$); there are thus two possible $M = +\frac{11}{2}$ states, one for the $I = \frac{15}{2}$ configuration and another that we can assign to $I = \frac{11}{2}$. Extending this reasoning, we expect to find the following states for $(f_{7/2})^3$ or $(f_{7/2})^5$: $I = \frac{15}{2}, \frac{11}{2}, \frac{9}{2}, \frac{7}{2}, \frac{5}{2}$, and $\frac{3}{2}$. Because each of the three or five particles has negative parity, the resultant parity is $(-1)^3$. The nuclei shown in Figure 5.25 show low-lying negative-parity states with the expected spins (and also with the expected absences—no low-lying $\frac{1}{2}^-$ or $\frac{13}{2}^-$ states appear).

Although this analysis is reasonably successful, it is incomplete—if we do indeed treat all valence particles as independent and equivalent, then the energy of a level should be independent of the orientation of the different m's—that is, all of the resultant I's should have the same energy. This is obviously not even approximately true; in the case of the $(f_{7/2})^3$ multiplet, the energy splitting between the highest and lowest energy levels is 2.7 MeV, about the same energy as pair-breaking and particle-exciting interactions. We can analyze these energy splittings in terms of a *residual interaction* between the valence particles, and thus the level structure of these nuclei gives us in effect a way to probe the nucleon–nucleon interaction in an environment different from the free-nucleon studies we discussed in Chapter 4.

As a final comment, we state without proof that the configurations with n particles in the same shell have another common feature that lends itself to experimental test—their magnetic moments should all be proportional to I. That is, given two different states 1 and 2 belonging to the same configuration, we expect

$$\frac{\mu_1}{\mu_2} = \frac{I_1}{I_2} \tag{5.21}$$

Unfortunately, few of the excited-state magnetic moments are well enough known to test this prediction. In the case of ^{51}V, the ground-state moment is $\mu = +5.1514 \pm 0.0001\ \mu_N$ and the moment of the first excited state is $\mu = +3.86 \pm 0.33\ \mu_N$. The ratio of the moments is thus 1.33 ± 0.11, in agreement with the expected ratio $\frac{7}{2}/\frac{5}{2} = 1.4$. In the case of ^{53}Mn, the ratio of moments of the same states is $5.024 \pm 0.007\ \mu_N/3.25 \pm 0.30\ \mu_N = 1.55 \pm 0.14$. The evidence from the magnetic moments thus supports our assumption about the nature of these states.

Single-Particle States in Deformed Nuclei

The calculated levels of the nuclear shell model are based on the assumption that the nuclear potential is spherical. We know, however, that this is not true for nuclei in the range $150 \leq A \leq 190$ and $A > 230$. For these nuclei we should use a shell-model potential that approximates the actual nuclear shape, specifically a rotational ellipsoid. In calculations using the Schrödinger equation with a non-spherical potential, the angular momentum ℓ is no longer a "good" quantum number; that is, we cannot identify states by their spectroscopic notation (s, p, d, f, etc.) as we did for the spherical shell model. To put it another way, the states that result from the calculation have mixtures of different ℓ values (but based on consideration of parity, we expect mixtures of only even or only odd ℓ values).

In the spherical case, the energy levels of each single particle state have a degeneracy of $(2j + 1)$. (That is, relative to any arbitrary axis of our choice, all $2j + 1$ possible orientations of j are equivalent.) If the potential has a deformed shape, this will no longer be true—*the energy levels in the deformed potential depend on the spatial orientation of the orbit*. More precisely, the energy depends on the component of j along the symmetry axis of the core. For example, an $f_{7/2}$

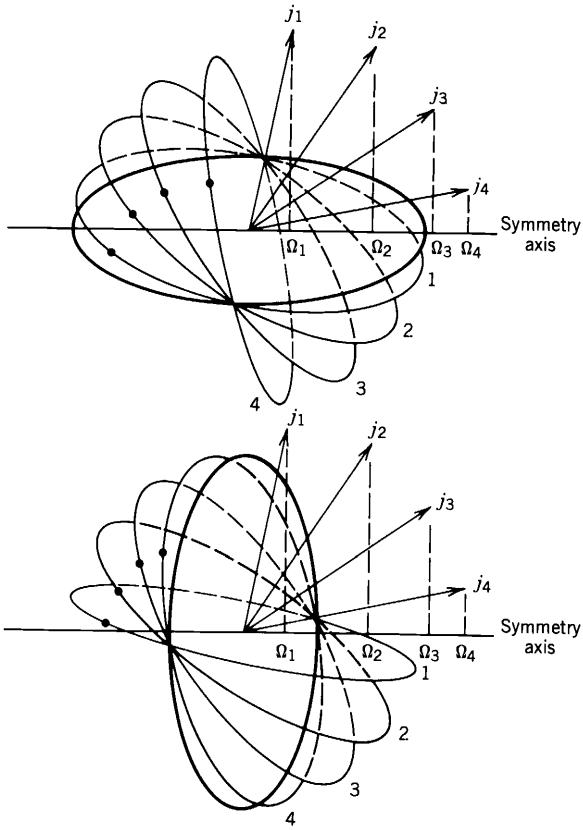


Figure 5.26 Single-particle orbits with $j = \frac{7}{2}$ and their possible projections along the symmetry axis, for prolate (top) and oblate (bottom) deformations. The possible projections are $\Omega_1 = \frac{1}{2}$, $\Omega_2 = \frac{3}{2}$, $\Omega_3 = \frac{5}{2}$, and $\Omega_4 = \frac{7}{2}$. (For clarity, only the positive projections are shown.) Note that in the prolate case, orbit 1 lies closest (on the average) to the core and will interact most strongly with the core; in the oblate case, it is orbit 4 that has the strongest interaction with the core.

nucleon can have eight possible components of j, ranging from $-\frac{7}{2}$ to $+\frac{7}{2}$. This component of j along the symmetry axis is generally denoted by Ω. Because the nuclei have reflection symmetry for either of the two possible directions of the symmetry axis, the components $+\Omega$ and $-\Omega$ will have the same energy, giving the levels a degeneracy of 2. That is, what we previously called the $f_{7/2}$ state splits up into four states if we deform the central potential; these states are labeled $\Omega = \frac{1}{2}, \frac{3}{2}, \frac{5}{2}, \frac{7}{2}$ and all have negative parity. Figure 5.26 indicates the different possible "orbits" of the odd particle for prolate and oblate deformations. For prolate deformations, the orbit with the smallest possible Ω (equal to $\frac{1}{2}$) interacts most strongly with the core and is thus more tightly bound and lowest in energy. The situation is different for oblate deformations, in which the orbit with maximum Ω (equal to j) has the strongest interaction with the core and the lowest energy. Figure 5.27 shows how the $f_{7/2}$ states would split as the deformation is increased.

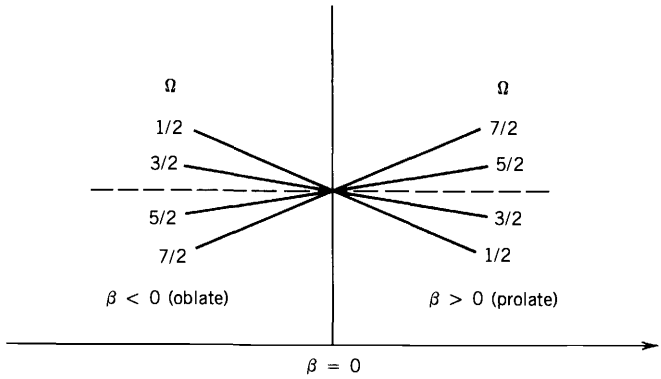


Figure 5.27 This shows directly the effect of the various orientations of the $f_{7/2}$ orbit. As shown in Figure 5.26, the orbit with component $\Omega = \frac{1}{2}$ along the symmetry axis has the strongest interaction with the *prolate* core and therefore lies lowest in energy. For an *oblate* core, it is the $\Omega = \frac{7}{2}$ component that lies lowest.

Of course, we must keep in mind that Figures 5.26 and 5.27 are not strictly correct because the spherical single-particle quantum numbers ℓ and j are not valid when the potential is deformed. The negative parity state with $\Omega = \frac{5}{2}$, for example, cannot be identified with the $f_{7/2}$ state, even though it approaches that state as $\beta \to 0$. The wave function of the $\Omega = \frac{5}{2}$ state can be expressed as a mixture (or linear combination) of many different ℓ and j (but only with $j \geq \frac{5}{2}$, in order to get a component of $\frac{5}{2}$). It is customary to make the approximation that states from different major oscillator shells (see Figures 5.4 and 5.6) do not mix. Thus, for example, the $\Omega = \frac{5}{2}$ state that approaches the $2f_{7/2}$ level as $\beta \to 0$ will include contributions from only those states of the 5th oscillator shell ($2f_{5/2}$, $2f_{7/2}$, $1h_{9/2}$, $1h_{11/2}$). The 4th and 6th oscillator shells have the opposite parity and so will not mix, and the next odd-parity shells are far away and do not mix strongly. Writing the spherical wave functions as $\psi_{N\ell j}$, we must have

$$\psi'(\Omega) = \sum_{\ell j} a(N\ell j)\psi_{N\ell j} \tag{5.22}$$

where $\psi'(\Omega)$ represents the wave function of the deformed state Ω and where $a(N\ell j)$ are the expansion coefficients. For the $\Omega = \frac{5}{2}$ state

$$\psi'(\Omega) = a\left(53\tfrac{5}{2}\right)\psi_{53\frac{5}{2}} + a\left(53\tfrac{7}{2}\right)\psi_{53\frac{7}{2}} + a\left(55\tfrac{9}{2}\right)\psi_{55\frac{9}{2}} + a\left(55\tfrac{11}{2}\right)\psi_{55\frac{11}{2}} \tag{5.23}$$

The coefficients $a(N\ell j)$ can be obtained by solving the Schrödinger equation for the deformed potential, which was first done by S. G. Nilsson in 1955. The coefficients will vary with β, and of course for $\beta \to 0$ we expect $a(53\frac{7}{2})$ to approach 1 while the others all approach 0. For $\beta = 0.3$ (a typical prolate deformation), Nilsson calculated the values

$$a\left(53\tfrac{5}{2}\right) = 0.267 \qquad a\left(53\tfrac{7}{2}\right) = 0.832$$
$$a\left(55\tfrac{9}{2}\right) = 0.415 \qquad a\left(55\tfrac{11}{2}\right) = -0.255$$

for the $\Omega = \frac{5}{2}$ level we have been considering.

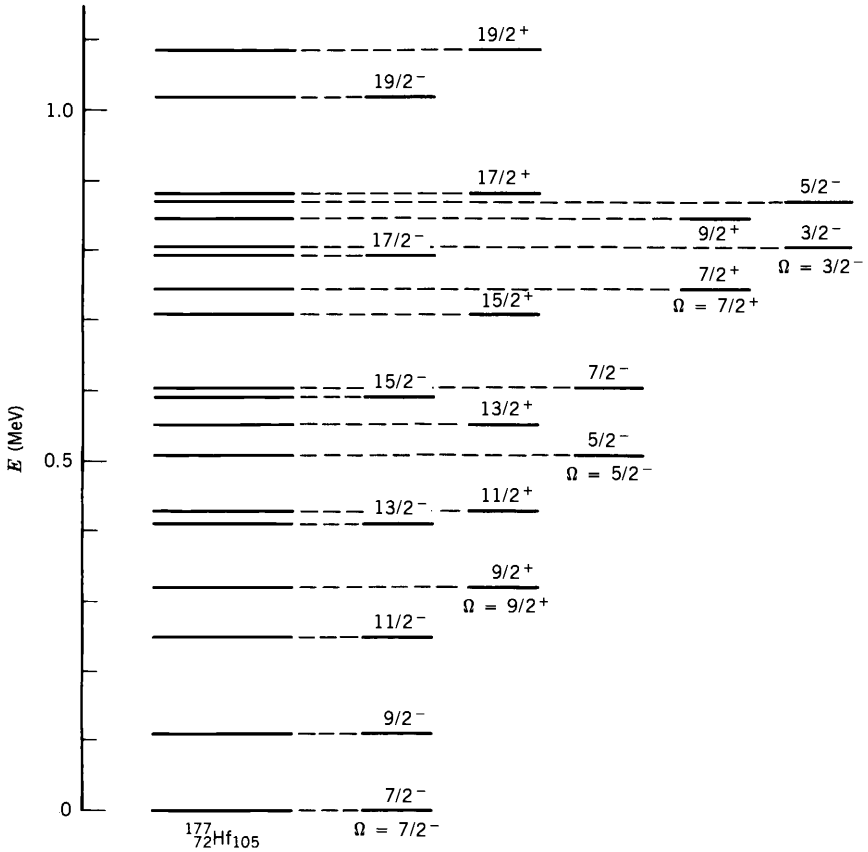


Figure 5.28 The energy levels of ^{177}Hf. As in the case of ^{164}Er (Figure 5.23), knowledge of the spin-parity assignments helps us to group the states into rotational bands. The lowest state in each band has $I = \Omega$, and the higher states follow the $I(I + 1)$ energy spacing.

Given such wave functions for single-particle states in deformed nuclei, we can then allow the nuclei to rotate, and we expect to find a sequence of rotational states, following the $I(I + 1)$ energy spacing, built on each single-particle state. The lowest state of the rotational band has $I = \Omega$, and as rotational energy is added the angular momentum increases in the sequence $I = \Omega, \Omega + 1, \Omega + 2, \ldots$. Figure 5.28 shows the energy levels of the nucleus ^{177}Hf, in which two well-developed rotational bands have been found and several other single-particle states have been identified.

To interpret the observed single-particle levels, we require a diagram similar to Figure 5.27 but which shows all possible single-particle states and how their energies vary with deformation. Such a diagram is shown in Figure 5.29 for the neutron states that are appropriate to the $150 \leq A \leq 190$ region. Recalling that the degeneracy of each deformed single-particle level is 2, we proceed exactly as we did in the spherical shell model, placing two neutrons in each state up to $N = 105$ and two protons in each state up to $Z = 72$. We can invoke the pairing argument to neglect the single-particle states of the protons and examine the possible levels of the 105th neutron for the typical deformation of $\beta \approx 0.3$. You

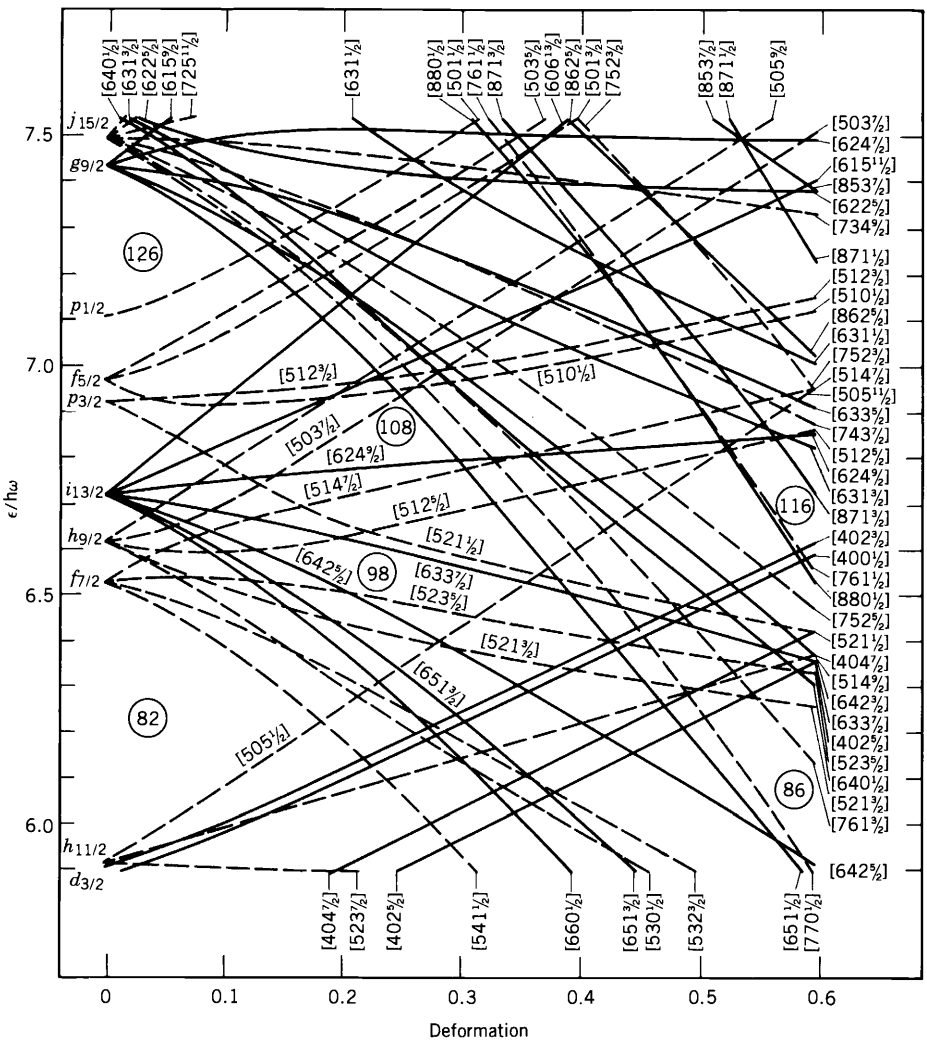


Figure 5.29 Energy levels for neutrons in a prolate deformed potential. The deformation is measured essentially by the parameter β. The numbers in the brackets label the states; for our purposes, we are interested only in the first number, which is the principal quantum number N of the oscillator shell and therefore tells us the parity of the state $(-1)^N$, and the last number, which is the component Ω. Solid lines show states with even parity, and dashed lines show odd parity. For a deformation between 0.2 and 0.3 (typical for nuclei in this region) the 105th neutron of ^{177}Hf would go into the state $[514\frac{7}{2}]$, that is, an odd-parity state with $\Omega = \frac{7}{2}$. A small excitation takes it into the state $[624\frac{9}{2}]$, an even parity state with $\Omega = \frac{9}{2}$. Both intrinsic states (and their associated rotational bands) can be seen in Figure 5.28. Other observed states in ^{177}Hf result from breaking a pair of neutrons in a lower state and exciting one to pair with the $\frac{7}{2}^-$ neutron. In this way, for instance, we could produce a single neutron in the state $[512\frac{5}{2}]$, which gives the odd-parity $\Omega = \frac{5}{2}$ state in ^{177}Hf. From C. Gustafson et al., *Ark. Fys.* **36**, 613 (1967).

can see from the diagram that the expected single-particle levels correspond exactly with the observed levels of ^{177}Hf.

The general structure of the odd-A deformed nuclei is thus characterized by rotational bands built on single-particle states calculated from the deformed shell-model potential. The proton and neutron states are filled (two nucleons per state), and the nuclear properties are determined in the extreme single-particle limit by the properties of the odd particle. This model, with the wave functions calculated by Nilsson, has had extraordinary success in accounting for the nuclear properties in this region. In general, the calculations based on the properties of the odd particle have been far more successful in the deformed region than have the analogous calculations in the spherical region.

In this chapter we have discussed evidence for types of nuclear structure based on the *static* properties of nuclei—energy levels, spin-parity assignments, magnetic dipole and electric quadrupole moments. The wave functions that result from solving the Schrödinger equation for these various models permit many other features of nuclear structure to be calculated, particularly the transitions between different nuclear states. Often the evidence for collective structure, for instance, may be inconclusive based on the energy levels alone, while the transition probabilities between the excited states may give definitive proof of collective effects. It may also be the case that a specific excited state may have alternative interpretations—for example, a vibrational state or a 2-particle coupling. Studying the transition probabilities will usually help us to discriminate between these competing interpretations. The complete study of nuclear structure therefore requires that we study *radioactive decays*, which give spontaneous transitions between states, and *nuclear reactions*, in which the experimenter can select the initial and final states. In both cases, we can compare calculated decay and reaction probabilities with their experimental values in order to draw conclusions about the structure of nuclear states. The methods of each of these areas of *nuclear spectroscopy* will occupy us for most of the remainder of this text.

REFERENCES FOR ADDITIONAL READING

Nuclear physics texts providing more detailed and advanced information on nuclear models are the following: B. L. Cohen, *Concepts of Nuclear Physics* (New York: McGraw-Hill, 1971), Chapters 4–6; H. Frauenfelder and E. M. Henley, *Subatomic Physics* (Englewood Cliffs, NJ: Prentice-Hall, 1974), Chapters 14–16; M. A. Preston, *Physics of the Nucleus* (Reading, MA: Addison-Wesley, 1962), Chapters 7–10.

Two essential monographs, covering respectively the shell model and the collective model, have been written by recipients of the Nobel Prize for their work on nuclear models: M. G. Mayer and J. H. D. Jensen, *Elementary Theory of Nuclear Shell Structure* (New York: Wiley, 1955) and A. Bohr and B. R. Mottelson, *Nuclear Structure* (Reading, MA: Benjamin, 1975), Vol. 2 (Vol. 1 treats the shell model). Another comprehensive but advanced work is J. M. Eisenberg and W. Greiner, *Nuclear Models* (Amsterdam: North-Holland, 1970).

PROBLEMS

1. Give the expected shell-model spin and parity assignments for the ground states of (a) ^{7}Li; (b) ^{11}B; (c) ^{15}C; (d) ^{17}F; (e) ^{31}P; (f) ^{141}Pr.
2. The low-lying levels of ^{13}C are ground state, $\frac{1}{2}^-$; 3.09 MeV, $\frac{1}{2}^+$; 3.68 MeV, $\frac{3}{2}^-$; 3.85 MeV, $\frac{5}{2}^+$. The next states are about 7 MeV and above. Interpret these four states according to the shell model.
3. The level scheme of Figure 5.6 would lead us to expect $I^\pi = \frac{11}{2}^-$ for the ground state of ^{203}Tl ($Z = 81$), while the observed value is $\frac{1}{2}^+$. A similar case occurs in ^{207}Pb ($N = 125$) and ^{199}Hg ($N = 119$), where $\frac{13}{2}^+$ is expected but $\frac{1}{2}^-$ is observed. Given that the pairing force increases strongly with ℓ, give the shell-model configurations for these nuclei that are consistent with the observed spin-parity assignments.
4. Figure 5.6 is only a schematic, average representation of the shell-model single-particle states. The energies of the states will vary with the proton number and neutron number. To illustrate this effect, consider the available states of the 51st proton in Sb isotopes. Make a chart in the style of Figure 5.25 showing the $\frac{5}{2}^+$ and $\frac{7}{2}^+$ states in ^{113}Sb to ^{133}Sb. (Consult the *Table of Isotopes* and the Nuclear Data Sheets for information on the energy levels.) Discuss the relative positions of the $g_{7/2}$ and $d_{5/2}$ *proton* states as a function of *neutron* number.
5. In the single-particle shell model, the ground state of a nucleus with an odd proton and an odd neutron is determined from the coupling of the proton and neutron shell-model states: $\boldsymbol{I} = \boldsymbol{j}_p + \boldsymbol{j}_n$. Consider the following nuclei: ^{16}N – 2^-; ^{12}B – 1^+; ^{34}P – 1^+; ^{28}Al – 3^+. Draw simple vector diagrams illustrating these couplings, then replace $\boldsymbol{j}_p$ and $\boldsymbol{j}_n$, respectively, by $\boldsymbol{\ell}_p + \boldsymbol{s}_p$ and $\boldsymbol{\ell}_n + \boldsymbol{s}_n$. Examine your four diagrams and deduce an empirical rule for the relative orientation of $\boldsymbol{s}_p$ and $\boldsymbol{s}_n$ in the ground state. Finally, use your empirical rule to predict the I^π assignments of ^{26}Na and ^{28}Na.
6. (a) If the energy of a single-particle state in the absence of spin-orbit splitting is E_0, find the energies of the two members of the spin-orbit doublet whose difference is given by Equation 5.4. (b) Show that the "center of gravity" of the doublet is E_0.
7. Compute the expected shell-model quadrupole moment of ^{209}Bi ($\frac{9}{2}^-$) and compare with the experimental value, -0.37 b.
8. Compute the values of the magnetic dipole moments expected from the shell model, and compare with the experimental values:

Nuclide	I^π	μ(exp) (μ_N)
^{75}Ge	$\frac{1}{2}^-$	+0.510
^{87}Sr	$\frac{9}{2}^+$	−1.093
^{91}Zr	$\frac{5}{2}^+$	−1.304
^{47}Sc	$\frac{7}{2}^-$	+5.34
^{147}Eu	$\frac{11}{2}^-$	+6.06

9. Compute the vibrational frequency associated with typical quadrupole vibrations. Taking typical values for decay lifetimes of 2^+ states in vibrational nuclei (you can find these in the *Table of Isotopes*, for example), comment on whether the decays generally occur on a shorter or longer time scale than the nuclear vibrations. If α represents the vibrational amplitude, as in Equation 5.13, could we observe quantities dependent on $\langle\alpha\rangle$? On $\langle\alpha^2\rangle$?
10. By tabulating the possible m states of three quadrupole ($\ell = 2$) phonons, and their symmetrized combinations, show that the permitted resultant states are 0^+, 2^+, 3^+, 4^+, and 6^+.
11. Find the volume of the nucleus whose surface is described by Equation 5.14.
12. Consider a uniformly charged ellipsoidal nucleus whose surface is described by Equation 5.14. Show that the electric quadrupole moment, defined by Equation 3.36, is given by Equation 5.16.
13. The levels of ^{174}Hf show two similar rotational bands, with energies given as follows (in MeV):

	$E(0^+)$	$E(2^+)$	$E(4^+)$	$E(6^+)$	$E(8^+)$	$E(10^+)$	$E(12^+)$
Band 1	0	0.091	0.297	0.608	1.010	1.486	2.021
Band 2	0.827	0.900	1.063	1.307	1.630	2.026	2.489

Compare the moments of inertia of these two bands, and comment on any difference.

14. The low-lying levels of ^{17}O and ^{19}O differ primarily in the presence of states of $I^\pi = \frac{3}{2}^+$ and $\frac{9}{2}^+$ in ^{19}O; these two states have no counterparts in ^{17}O. Show that these two states could result from the configuration $(d_{5/2})^3$ and thus are not expected in ^{17}O.
15. The nucleus ^{24}Mg has a 2^+ first excited state at 1.369 MeV and a 4^+ second excited state at 4.123 MeV. The 2^+ state has a magnetic dipole moment of 1.02 μ_N and an electric quadrupole moment of -0.27 b. Which model would be most likely to provide an accurate description of these states? Justify your choice by calculating parameters appropriate to your choice of model.

UNIT II
NUCLEAR DECAY AND RADIOACTIVITY

8

ALPHA DECAY

Alpha particles were first identified as the least penetrating of the radiations emitted by naturally occurring materials. In 1903, Rutherford measured their charge-to-mass ratio by deflecting α particles from the decay of radium in electric and magnetic fields. Despite the difficulty of these early experiments, Rutherford's result was only about 25% higher than the presently accepted value. In 1909 Rutherford showed that, as suspected, the α particles were in fact helium nuclei; in his experiments the particles entered an evacuated thin-walled chamber by penetrating its walls, and after several days of collecting, atomic spectroscopy revealed the presence of helium gas inside the chamber.

Many heavy nuclei, especially those of the naturally occurring radioactive series, decay though α emission. Only exceedingly rarely does any other spontaneous radioactive process result in the emission of nucleons; we do not, for example, observe deuteron emission as a natural decay process. There must therefore be a special reason that nuclei choose α emission over other possible decay modes. In this chapter we examine this question and study the α decay process in detail. We also show how α spectroscopy can help us to understand nuclear structure.

8.1 WHY α DECAY OCCURS

Alpha emission is a Coulomb repulsion effect. It becomes increasingly important for heavy nuclei because the disruptive Coulomb force increases with size at a faster rate (namely, as Z^2) than does the specific nuclear binding force, which increases approximately as A.

Why is the α particle chosen as the agent for the spontaneous carrying away of positive charge? When we call a process *spontaneous* we mean that some kinetic energy has suddenly appeared in the system for no apparent cause; this energy must come from a decrease in the mass of the system. The α particle, because it is a very stable and tightly bound structure, has a relatively small mass compared with the mass of its separate constituents. It is particularly favored as an emitted particle if we hope to have the disintegration products as light as possible and thus get the largest possible release of kinetic energy.

Table 8.1 Energy Release (Q value) for Various Modes of Decay of ^{232}U[a]

Emitted Particle	Energy Release (MeV)	Emitted Particle	Energy Release (MeV)
n	−7.26	^{4}He	+5.41
^{1}H	−6.12	^{5}He	−2.59
^{2}H	−10.70	^{6}He	−6.19
^{3}H	−10.24	^{6}Li	−3.79
^{3}He	−9.92	^{7}Li	−1.94

[a] Computed from known masses.

For a typical α emitter ^{232}U (72 y) we can compute, from the known masses, the energy release for various emitted particles. Table 8.1 summarizes the results. Of the particles considered, spontaneous decay is energetically possible *only* for the α particle. A positive disintegration energy results for some slightly heavier particles than those listed, ^{8}Be or ^{12}C, for example. We will show, however (Section 8.4), that the partial disintegration constant for emission of such heavy particles is normally vanishingly small compared with that for α emission. Such decays would be so rare that in practice they would almost never be noticed. This suggests that if a nucleus is to be recognized as an alpha emitter it is not enough for α decay to be energetically possible. The disintegration constant must also not be too small or else α emission will occur so rarely that it may not be detected. With present techniques this means that the half-life must be less than about 10^{16} y. Also, β decay, if it has a much higher partial disintegration constant, can mask the α decay. Most nuclei with $A > 190$ (and many with $150 < A < 190$) are energetically unstable against α emission but only about one-half of them can meet these other requirements.

8.2 BASIC α DECAY PROCESSES

The spontaneous emission of an α particle can be represented by the following process:

$$ {}^{A}_{Z}X_{N} \rightarrow {}^{A-4}_{Z-2}X'_{N-2} + \alpha $$

The α particle, as was shown by Rutherford, is a nucleus of ^{4}He, consisting of two neutrons and two protons. To understand the decay process, we must study the conservation of energy, linear momentum, and angular momentum.

Let's first consider the conservation of energy in the α decay process. We assume the initial decaying nucleus X to be at rest. Then the energy of the initial system is just the rest energy of X, $m_X c^2$. The final state consists of X′ and α, each of which will be in motion (to conserve linear momentum). Thus the final total energy is $m_{X'}c^2 + T_{X'} + m_\alpha c^2 + T_\alpha$, where T represents the kinetic energy of the final particles. Thus conservation of energy gives

$$ m_X c^2 = m_{X'}c^2 + T_{X'} + m_\alpha c^2 + T_\alpha \tag{8.1} $$

or

$$ (m_X - m_{X'} - m_\alpha)c^2 = T_{X'} + T_\alpha \tag{8.2} $$

The quantity on the left side of Equation 8.2 is the net energy released in the decay, called the Q value:

$$Q = (m_X - m_{X'} - m_\alpha)c^2 \tag{8.3}$$

and the decay will occur spontaneously only if $Q > 0$. (The decay Q values for ^{232}U were listed in Table 8.1.) Q values can be calculated from *atomic* mass tables because even though Equation 8.3 represents a *nuclear* process, the electron masses will cancel in the subtraction. When the masses are in atomic mass units (u), expressing c^2 as 931.502 MeV/u gives Q values directly in MeV.

The Q value is also equal to the total kinetic energy given to the decay fragments:

$$Q = T_{X'} + T_\alpha \tag{8.4}$$

If the original nucleus X is at rest, then its linear momentum is zero, and conservation of linear momentum then requires that X′ and α move with equal and opposite momenta in order that the final momentum also be zero:

$$p_\alpha = p_{X'} \tag{8.5}$$

α decays typically release about 5 MeV of energy. Thus for both X′ and α, $T \ll mc^2$ and we may safely use nonrelativistic kinematics. Writing $T = p^2/2m$ and using Equations 8.4 and 8.5 gives the kinetic energy of the α particle in terms of the Q value:

$$T_\alpha = \frac{Q}{(1 + m_\alpha/m_{X'})} \tag{8.6}$$

Because the mass ratio is small compared with 1 (recall that X′ represents a heavy nucleus), it is usually sufficiently accurate to express this ratio simply as $4/(A - 4)$, which gives, with $A \gg 4$,

$$T_\alpha = Q(1 - 4/A) \tag{8.7}$$

Typically, the α particle carries about 98% of the Q value, with the much heavier nuclear fragment X′ carrying only about 2%. (This *recoil* energy of the heavy fragment is not entirely negligible. For a typical Q value of 5 MeV, the recoiling nucleus has an energy of the order of 100 keV. This energy is far in excess of that which binds atoms in solids, and thus the recoiling nucleus, if it is near the surface of the radioactive source, escapes from the source and can spread to the surroundings. If the α decay is part of a decay chain, then the recoiling daughter nucleus may itself be radioactive, and these recoils can result in the spread of radioactive material. Fortunately, the heavy recoil nuclei have an extremely short range in matter and their spread can be prevented by a thin coating, such as Mylar or lacquer, placed over the radioactive sample.)

The kinetic energy of an α particle can be measured directly with a magnetic spectrometer, and so the Q value of a decay can be determined. This gives us a way to determine atomic masses, such as in a case in which we might know the mass of long-lived X as a result of direct measurement but X′ is so short-lived that its mass cannot be determined by direct measurement.

8.3 α DECAY SYSTEMATICS

One feature of α decay is so striking that it was noticed as long ago as 1911, the year that Rutherford "discovered" the nucleus. Geiger and Nuttall noticed that α emitters with large disintegration energies had short half-lives and conversely. The variation is astonishingly rapid as we may see from the limiting cases of ^{232}Th (1.4×10^{10} y; $Q = 4.08$ MeV) and ^{218}Th (1.0×10^{-7} s; $Q = 9.85$ MeV). A factor of 2 in energy means a factor of 10^{24} in half-life! The theoretical explanation of this Geiger-Nuttall rule in 1928 was one of the first triumphs of quantum mechanics.

A plot of log $t_{1/2}$ against Q in which all α emitters are included shows a considerable scatter about the general Geiger-Nuttall trend. Very smooth curves result, however, if we plot only α emitters with the same Z and if further we select from this group only those with Z and N both even (Figure 8.1). Even-odd, odd-even, and odd-odd nuclei obey the general trend but do not plot into quite such smooth curves; their periods are 2–1000 times longer than those for even-even types with the same Z and Q.

It is interesting that ^{235}U (even Z, odd N) is one of these "extra-long-life" types. If its half-life were 1000 times shorter, this important nucleus would not occur in nature, and we probably would not have nuclear reactors today! We see in Chapter 13 that the same feature that apparently accounts for the long life against α decay, namely the odd neutron, also makes ^{235}U very susceptible to fission by thermal neutrons.

Figure 8.2 shows another important systematic relationship for α emitters. Looking for the moment only at the data for $A > 212$, we see that adding neutrons to a nucleus reduces the disintegration energy, which, because of the

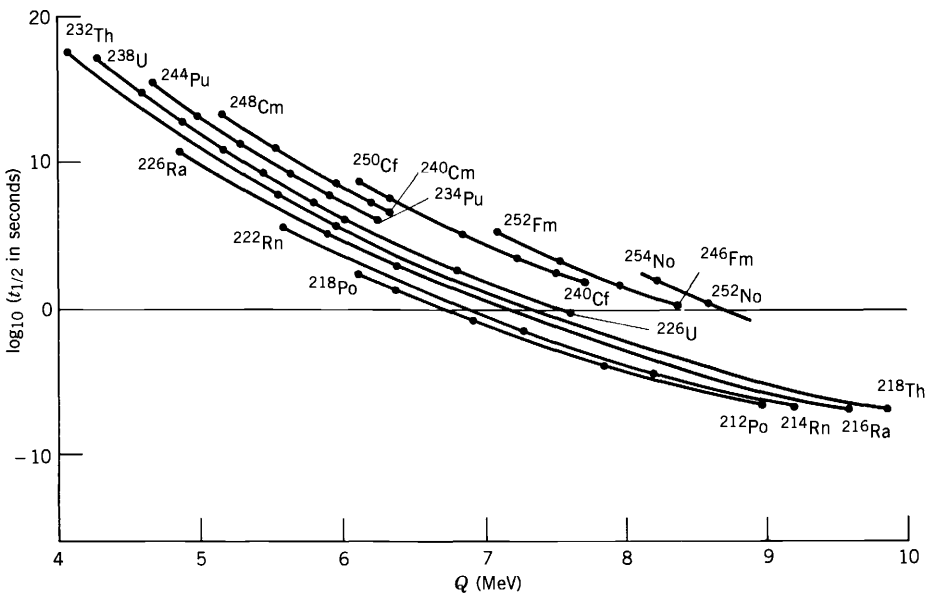


Figure 8.1 The inverse relationship between α-decay half-life and decay energy, called the Geiger-Nuttall rule. Only even-Z, even-N nuclei are shown. The solid lines connect the data points.

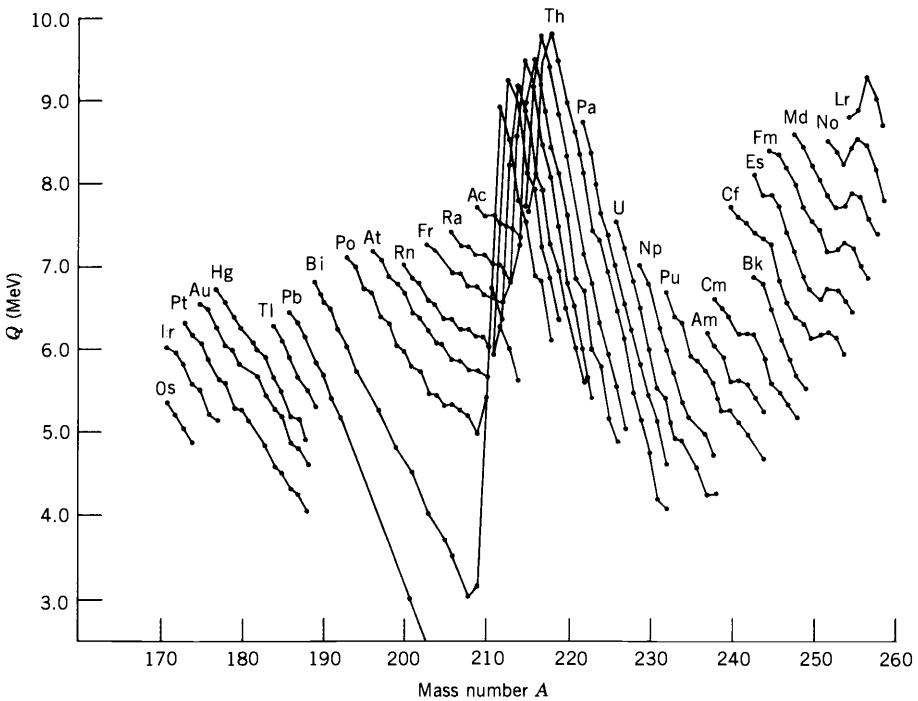


Figure 8.2 Energy released in α decay for various isotopic sequences of heavy nuclei. In contrast to Figure 8.1, both odd-A and even-A isotopes are shown, and a small amount of odd-even staggering can be seen. The effects of the shell closures at $N = 126$ (large dip in data) and $Z = 82$ (larger than average spacing between Po, Bi, and Pb sequences) are apparent.

Geiger-Nuttall rule, increases the half-life. The nucleus becomes more stable. A striking discontinuity near $A = 212$ occurs where $N = 126$ and is another example of nuclear shell structure.

We can compare the systematic dependence of Q on A with the prediction of the semiempirical mass formula, Equation 3.28.

$$Q = B(^4\text{He}) + B(Z-2, A-4) - B(Z, A) \tag{8.8}$$

$$\cong 28.3 - 4a_v + \tfrac{8}{3}a_s A^{-1/3} + 4a_c Z A^{-1/3}(1 - Z/3A)$$

$$-4a_{sym}(1 - 2Z/A)^2 + 3a_p A^{-7/4} \tag{8.9}$$

where the approximation in Equation 8.9 is $Z, A \gg 1$. For ^{226}Th, this formula gives $Q = 6.75$ MeV, not too far from the measured value of 6.45 MeV. What is perhaps more significant is that the general trend of Figure 8.2 is reproduced: for ^{232}Th, Equation 8.9 gives $Q = 5.71$ MeV (to be compared with $Q = 4.08$ MeV), while for ^{220}Th the formula gives $Q = 7.77$ MeV (compared with $Q = 8.95$ MeV). Keep in mind that the parameters of the semiempirical mass formula are chosen to give rough agreement with observed binding energies across the entire range of nuclei. It is important that the formula gives us rough agreement with the decay Q values and that it correctly gives $Q > 0$ for the heavy nuclei. It also

correctly predicts the decrease of Q with increasing A for a sequence of isotopes such as those of thorium, although it gives too small a change of Q with A (the formula gives $\Delta Q = -0.17$ MeV per unit change in A, while for Th the observed average change is $\Delta Q = -0.40$ MeV per unit change in A).

8.4 THEORY OF α EMISSION

The general features of Figure 8.1 can be accounted for by a quantum mechanical theory developed in 1928 almost simultaneously by Gamow and by Gurney and Condon. In this theory an α particle is assumed to move in a spherical region determined by the *daughter* nucleus. The central feature of this *one-body model* is that the α particle is preformed inside the parent nucleus. Actually there is not much reason to believe that α particles do exist separately within heavy nuclei; nevertheless, the theory works quite well, especially for even-even nuclei. This success of the theory does not prove that α particles are preformed, but merely that they behave as if they were.

Figure 8.3 shows a plot, suitable for purposes of the theory, of the potential energy between the α particle and the residual nucleus for various distances between their centers. The horizontal line Q is the disintegration energy. Note that the Coulomb potential is extended inward to a radius a and then arbitrarily cut off. The radius a can be taken as the sum of the radius of the residual nucleus and of the α particle. There are three regions of interest. In the spherical region $r < a$ we are inside the nucleus and speak of a potential well of depth $-V_0$, where V_0 is taken as a positive number. Classically the α particle can move in this region, with a kinetic energy $Q + V_0$ but it cannot escape from it. The annular-shell region $a < r < b$ forms a potential barrier because here the potential energy

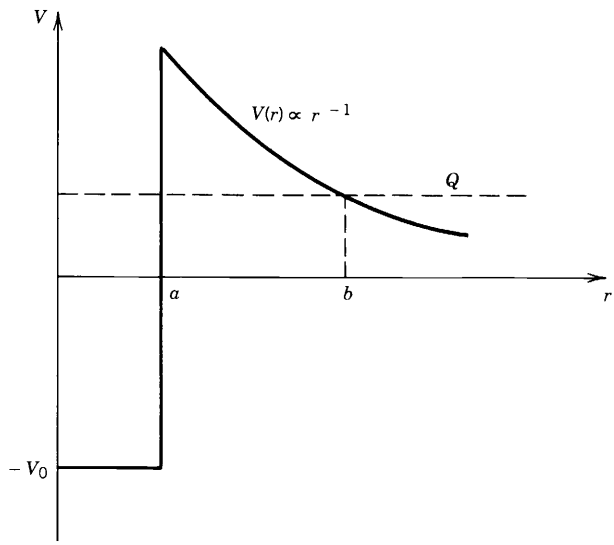


Figure 8.3 Relative potential energy of α-particle, daughter-nucleus system as a function of their separation. Inside the nuclear surface at $r = a$, the potential is represented as a square well; beyond the surface, only the Coulomb repulsion operates. The α particle tunnels through the Coulomb barrier from a to b.

is more than the total available energy Q. Classically the α particle cannot enter this region from either direction, just as a tennis ball dropped from a certain height cannot rebound higher; in each case the kinetic energy would have to be negative. The region $r > b$ is a classically permitted region outside the barrier.

From the classical point of view, an α particle in the spherical potential well would sharply reverse its motion every time it tried to pass beyond $r = a$. Quantum mechanically, however, there is a chance of "leakage" or "tunnelling" through such a barrier. This barrier accounts for the fact that α-unstable nuclei do not decay immediately. The α particle within the nucleus must present itself again and again at the barrier surface until it finally penetrates. In ^{238}U, for example, the leakage probability is so small that the α particle, on the average, must make $\sim 10^{38}$ tries before it escapes ($\sim 10^{21}$ per second for $\sim 10^{9}$ years)!

The barrier also operates in reverse, in the case of α-particle scattering by nuclei (see Sections 3.1 and 11.6). Alpha particles incident on the barrier from outside the nucleus usually scatter in the Coulomb field if the incident energy is well below the barrier height. Tunnelling through the barrier, so that the nuclear force between the particle and target can cause nuclear reactions, is a relatively improbable process at low energy. The theoretical analysis of nuclear reactions induced by charged particles uses a formalism similar to that of α decay to calculate the barrier penetration probability. Fusion reactions, such as those responsible for the energy released in stars, also are analyzed using the barrier penetration approach (see Section 14.2).

The disintegration constant of an α emitter is given in the one-body theory by

$$\lambda = fP \tag{8.10}$$

where f is the frequency with which the α particle presents itself at the barrier and P is the probability of transmission through the barrier.

Equation 8.10 suggests that our treatment is going to be semiclassical in that our discussion of the situation for $r < a$ is very "billiard-ballish." A rigorous wave-mechanical treatment, however, gives about the same results for this problem. The quantity f is roughly of the order of v/a where v is the relative velocity of the α particle as it rattles about inside the nucleus. We can find v from the kinetic energy of the α particle for $r < a$. Estimating $V_0 \approx 35$ MeV for a typical well depth gives $f \approx 6 \times 10^{21}$/s for $Q \approx 5$ MeV. We will see later that we do not need to know f very precisely to check the theory.

The barrier penetration probability P must be obtained from a quantum mechanical calculation similar to the one-dimensional problem discussed in Section 2.3. Let's first use the result of that calculation, Equation 2.39, to estimate the probability P. Of course, the calculation that led to Equation 2.39 was based on a one-dimensional rectangular barrier, which is not directly applicable to the $1/r$ Coulomb potential, but we can at least find a rough order-of-magnitude estimate. The result, Equation 2.39, depends on the width of the barrier and on its height (called V_0 for the rectangular barrier) above the energy E of the particle. The Coulomb barrier of Figure 8.3 has height B at $r = a$, where

$$B = \frac{1}{4\pi\epsilon_0}\frac{zZ'e^2}{a} \tag{8.11}$$

In this expression the α particle has charge ze and the daughter nucleus, which

provides the Coulomb repulsion, has charge $Z'e = (Z - z)e$. The height of the barrier thus varies from $(B - Q)$ above the particle's energy at $r = a$ to zero at $r = b$, and we can take a representative average height to be $\frac{1}{2}(B - Q)$. We can similarly choose a representative average width to be $\frac{1}{2}(b - a)$. The factor k_2 of Equation 2.39 then becomes $\sqrt{(2m/\hbar^2) \cdot \frac{1}{2}(B - Q)}$. For a typical heavy nucleus ($Z = 90$, $a = 7.5$ fm), the barrier height B is about 34 MeV, so the factor k_2 is about 1.6 fm^{-1}. The radius b at which the α particle "leaves" the barrier is found from the equality of the particle's energy and the potential energy:

$$b = \frac{1}{4\pi\epsilon_0}\frac{zZ'e^2}{Q} \tag{8.12}$$

and for a typical case of a heavy nucleus with $Q \approx 6$ MeV, $b \approx 42$ fm. Thus $k_2 \cdot \frac{1}{2}(b - a) \gg 1$ and we can approximate Equation 2.39 as

$$P \cong e^{-2k_2 \cdot (1/2)(b-a)} \tag{8.13}$$

since the factors in front of the exponential are of unit order of magnitude. For the case we are estimating here, $P \sim 2 \times 10^{-25}$ and thus $\lambda \sim 10^{-3}$/s and $t_{1/2} \sim 700$ s. A slight change of Q to 5 MeV changes P to 1×10^{-30} and $t_{1/2} \sim 10^8$ s. Even this very crude calculation is able to explain the many orders of magnitude change of $t_{1/2}$ between $Q = 5$ MeV and $Q = 6$ MeV, as illustrated in Figure 8.1.

The exact quantum mechanical calculation is very similar in spirit to the crude estimate above. We can think of the Coulomb barrier as made up of a sequence of infinitesimal rectangular barriers of height $V(r) = zZ'e^2/4\pi\epsilon_0 r$ and width dr. The probability to penetrate each infinitesimal barrier, which extends from r to $r + dr$, is

$$dP = \exp\left\{-2\,dr\sqrt{(2m/\hbar^2)[V(r) - Q]}\right\} \tag{8.14}$$

The probability to penetrate the complete barrier is

$$P = e^{-2G} \tag{8.15}$$

where the *Gamow factor* G is

$$G = \sqrt{\frac{2m}{\hbar^2}}\int_a^b [V(r) - Q]^{1/2}\,dr \tag{8.16}$$

which can be evaluated as

$$G = \sqrt{\frac{2m}{\hbar^2 Q}}\frac{zZ'e^2}{4\pi\epsilon_0}\left[\arccos\sqrt{x} - \sqrt{x(1-x)}\right] \tag{8.17}$$

where $x = a/b = Q/B$. The quantity in brackets in Equation 8.17 is approximately $\pi/2 - 2x^{1/2}$ when $x \ll 1$, as is the case for most decays of interest. Thus the result of the quantum mechanical calculation for the half-life of α decay is

$$t_{1/2} = 0.693\frac{a}{c}\sqrt{\frac{mc^2}{2(V_0 + Q)}}\exp\left\{2\sqrt{\frac{2mc^2}{(\hbar c)^2 Q}}\frac{zZ'e^2}{4\pi\epsilon_0}\left(\frac{\pi}{2} - 2\sqrt{\frac{Q}{B}}\right)\right\} \tag{8.18}$$

Table 8.2 Calculated α-Decay Half-lives for Th Isotopes

		$t_{1/2}$ (s)	
A	Q (MeV)	Measured	Calculated
220	8.95	10^{-5}	3.3×10^{-7}
222	8.13	2.8×10^{-3}	6.3×10^{-5}
224	7.31	1.04	3.3×10^{-2}
226	6.45	1854	6.0×10^{1}
228	5.52	6.0×10^{7}	2.4×10^{6}
230	4.77	2.5×10^{12}	1.0×10^{11}
232	4.08	4.4×10^{17}	2.6×10^{16}

The results of this calculation for the even isotopes of Th are shown in Table 8.2. The agreement is not exact, but the calculation is able to reproduce the trend of the half-lives within 1–2 orders of magnitude over a range of more than 20 orders of magnitude. We have neglected several important details in the calculation: we did not consider the initial and final nuclear wave functions (Fermi's Golden Rule, Equation 2.79, must be used to evaluate the decay probability), we did not consider the angular momentum carried by the α particle, and we assumed the nucleus to be spherical with a mean radius of $1.25A^{1/3}$ fm. The latter approximation has a very substantial influence on the calculated half-lives. The nuclei with $A \gtrsim 230$ have strongly deformed shapes, and the calculated half-lives are extremely sensitive to small changes in the assumed mean radius. For instance, changing the mean radius to $1.20A^{1/3}$ (a 4% change in a) changes the half-lives by a factor of 5! In fact, because of this extreme sensitivity, the procedure is often reversed—the measured half-lives are used to deduce the nuclear radius; what actually comes out of the calculation is more like the sum of the radii of the nucleus X′ and the α particle, if we assume their charge distributions to have a sharp edge. This result can then be used to obtain an estimate of the nuclear radius; see, for example, L. Marquez, *J. Phys. Lett.* **42**, 181 (1981).

Even though this oversimplified theory is not strictly correct, it gives us a good estimate of the decay half-lives. It also enables us to understand why other decays into light particles are not commonly seen, even though they may be allowed by the Q value. For example, the decay $^{220}\text{Th} \rightarrow {}^{12}\text{C} + {}^{208}\text{Po}$ would have a Q value of 32.1 MeV, and carrying through the calculation using Equation 8.18 gives $t_{1/2} = 2.3 \times 10^{6}$ s for the ^{220}Th decay into ^{12}C. This is a factor of 10^{13} longer than the α-decay half-life and thus the decay will not easily be observable.

Recently, just such a decay mode has in fact been observed, the first example of a spontaneous decay process involving emission of a particle heavier than an α. The decay of ^{223}Ra normally proceeds by α emission with a half-life of 11.2 d, but there has now been discovered the decay process $^{223}\text{Ra} \rightarrow {}^{14}\text{C} + {}^{209}\text{Pb}$. The probability for this process is very small, about 10^{-9} relative to the α decay. Figure 8.4 indicates the heroic efforts that are necessary to observe the process. To confirm that the emitted particle is ^{14}C requires the $\Delta E \cdot T$ technique discussed in Chapter 7. Figure 8.4 shows a portion of the high-energy end of the tail of the hyperbola expected for observation of carbon. From the mass tables,

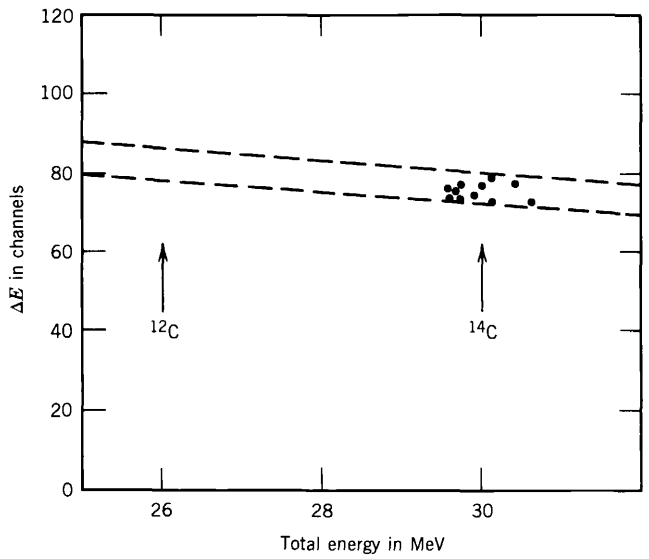


Figure 8.4 A portion of the tail of the $\Delta E \cdot T$ hyperbola showing the observed ^{14}C events from the decay of ^{223}Ra. The dashed lines show the limits expected for carbon. The 11 ^{14}C events result from 6 months of counting. From H. J. Rose and G. A. Jones, *Nature* **307**, 245 (1984). Reprinted by permission, copyright © Macmillan Journals Limited.

the decay Q value is calculated to be 31.8 MeV, which (when corrected for the recoil) gives a ^{14}C kinetic energy of 29.8 MeV. By contrast, the calculated energy for ^{12}C emission would be about 26 MeV. The total of 11 events observed represents about *six months* of counting with a source of 3.3 μCi of ^{223}Ra in secular equilibrium with 21-y ^{227}Ac, a member of the naturally occurring actinium series beginning with ^{235}U.

Calculating the Gamow factor for ^{14}C emission gives a decay probability of about 10^{-3} relative to α emission; the discrepancy between the calculated and observed (10^{-9}) values results from the assumptions about the preformation of the particle inside the nucleus. You will recall that our theory of α decay is based on the assumption that the α is preformed inside the nucleus. What the experiment tells us is that the probability for forming ^{14}C clusters inside the nucleus is about 10^{-6} relative to the probability to preform α's.

For a description of the experiment, see H. J. Rose and G. A. Jones, *Nature* **307**, 245 (1984). Emission of ^{14}C from several other nuclei in this region has also been observed, and emission of heavier decay fragments, including ^{24}Ne, has been reported.

Going in the opposite direction, we can use Equation 8.18 with $z = 1$ to evaluate the half-life for proton decay—that is, the spontaneous emission of a proton by an unstable nucleus. In this case the Coulomb barrier will be only half as high as it is for α decay, but these decays are inhibited for a stronger reason: the Q values for proton decay are generally negative and so the decays are absolutely forbidden by energy conservation. Such decays have recently been observed for a few proton-rich unstable nuclei, which are formed in nuclear reactions by bombarding a target with $N \approx Z$ using a projectile having $N \approx Z$.

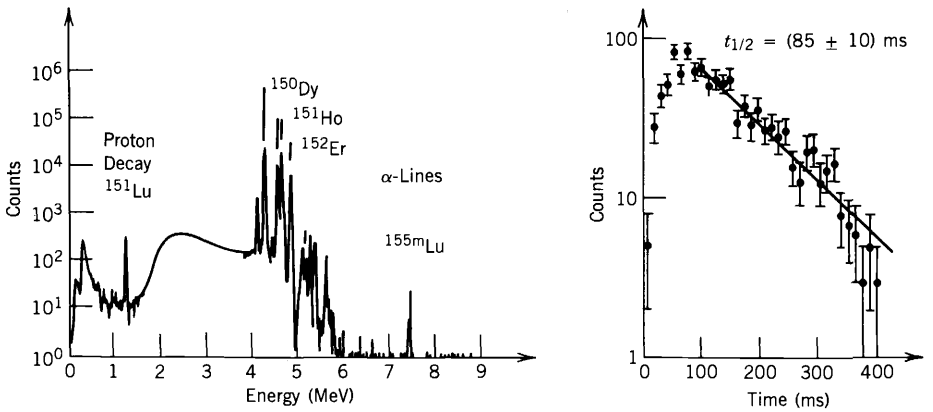


Figure 8.5 (Left) Charged-particle spectrum emitted in the radioactive decays of products of the reaction ^{96}Ru + ^{58}Ni. The peaks above 4 MeV represent α decays; the 1.2-MeV peak is from proton emission. (Right) The decay with time of the proton peak gives a half-life of 85 ms. From S. Hofmann et al., *Z. Phys. A* **305**, 111 (1982).

This creates a heavy nucleus with $N \approx Z$, a very unstable configuration, and proton emission may be energetically possible, as the nucleus tries to relieve itself of its proton excess. The Q value for proton decay can be found by a slight modification of Equation 8.3, which gives exactly the negative of the proton separation energy, Equation 3.27. Proton decay will be energetically possible when the Q value is positive and therefore when the separation energy is negative. A glance at the mass tabulations (see A. H. Wapstra and G. Audi, *Nucl. Phys. A* **432**, 1 (1985)) shows only a few very rare cases in which the proton separation energy is negative, and even these are not directly measured but instead obtained by extrapolations from more stable nuclei.

In an experiment reported by Hofmann *et al.*, *Z. Phys. A* **305**, 111 (1982), a target of ^{96}Ru was bombarded with ^{58}Ni projectiles. Figure 8.5 shows the spectrum of light particles emitted following the reaction. The more energetic peaks are identified as α decays from unstable nuclei in the neighborhood of $A = 150$ produced in the reaction. The peak at 1.239 MeV was identified as a proton using $\Delta E \cdot T$ techniques as described in Chapter 7. Its half-life was measured as 85 ms, as shown in Figure 8.5. The decay was assigned to the isotope ^{151}Lu based on a series of indirect arguments; unfortunately, reactions such as this produce many different products, and it is often a difficult task to identify the source of the observed radiations. This experiment thus provides evidence for the decay $^{151}\text{Lu} \rightarrow {}^{150}\text{Yb} + \text{p}$.

Study of decays such as this enables us to extend our knowledge of nuclear mass systematics far beyond the previous limits; for instance, at the time of this work ^{151}Lu was three protons further from stability than the previous last known isobar (^{151}Er). Figure 8.6 shows the Q_p values deduced from known masses and from extrapolations based on systematics. The value for ^{151}Lu lies right on the theoretical calculation, giving confidence to both the identification of the isotope and to the theoretical calculation.

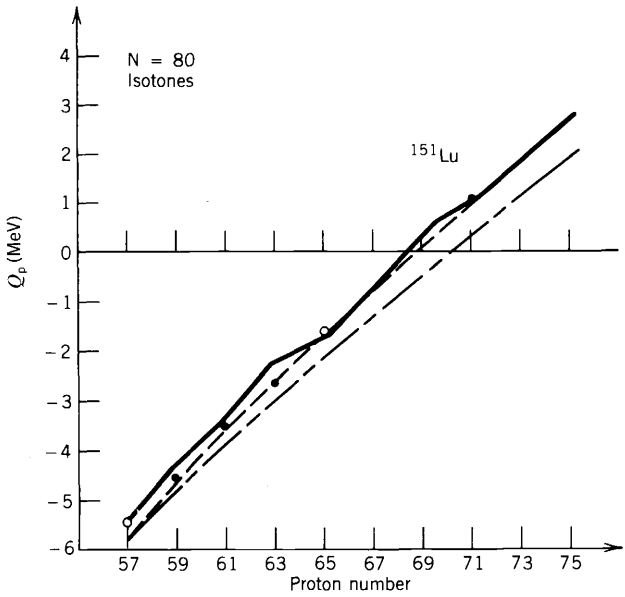


Figure 8.6 Proton-decay energies of $N = 80$ isotones. The solid lines are theoretical calculations based on nuclear mass formulas (somewhat like the semiempirical mass formula). Only for ^{151}Lu is the decay energy positive. From S. Hofmann et al., *Z. Phys. A* **305**, 111 (1982).

Using Equation 8.18 for the half-life gives a value of about 1.7 μs, too small by nearly 5 orders of magnitude. For this reason, it has been proposed that the decay is inhibited by differences in the nuclear structure of the initial and final states (or possibly by a large angular momentum change in the decay, examples of which are discussed in the next section).

8.5 ANGULAR MOMENTUM AND PARITY IN α DECAY

We have up to this point neglected to discuss the angular momentum carried by the α particle. In a transition from an initial nuclear state of angular momentum I_i to a final state I_f, the angular momentum of the α particle can range between $I_i + I_f$ and $|I_i - I_f|$. The nucleus ^{4}He consists of two protons and two neutrons, all in 1s states and all with their spins coupled pairwise to 0. The spin of the α particle is therefore zero, and the total angular momentum carried by an α particle in a decay process is purely orbital in character. We will designate this by ℓ_α. The α particle wave function is then represented by a $Y_{\ell m}$ with $\ell = \ell_\alpha$; thus the parity change associated with α emission is $(-1)^{\ell_\alpha}$, and we have a parity *selection rule*, indicating which transitions are permitted and which are absolutely forbidden by conservation of parity: if the initial and final parities are the same, then ℓ_α must be even; if the parities are different, then ℓ_α must be odd.

To study the applications of these rules, we must recognize that we have also neglected one very significant feature of α decay—a given initial state can populate many different final states in the daughter nucleus. This property is

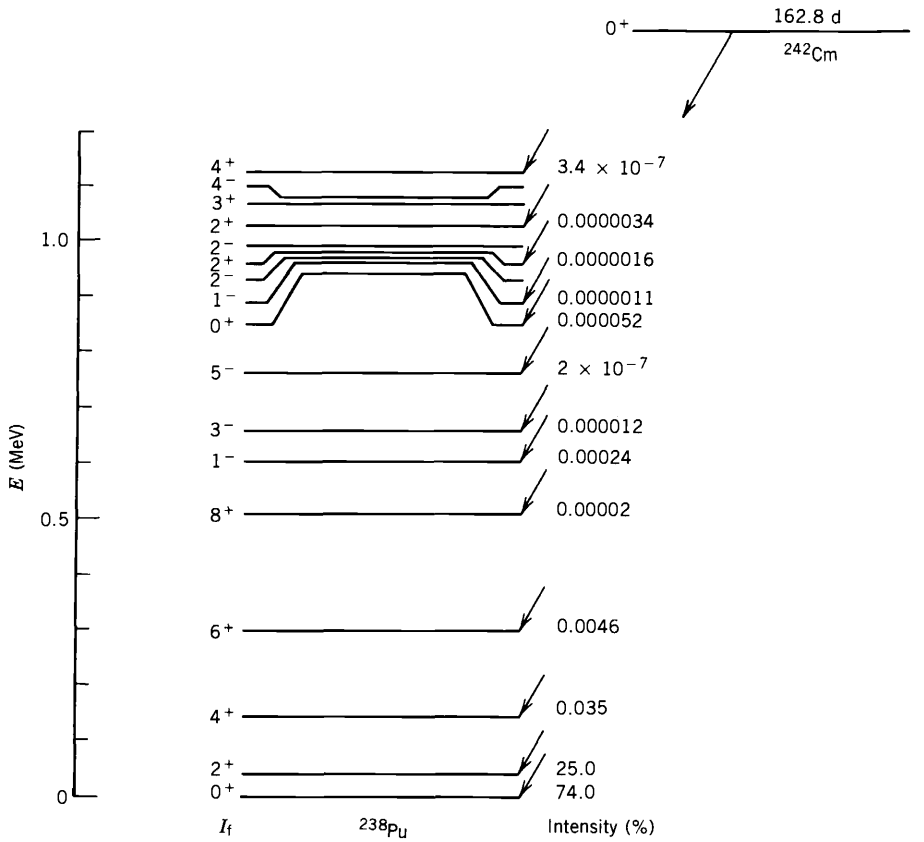


Figure 8.7 α decay of ^{242}Cm to different excited states of ^{238}Pu. The intensity of each α-decay branch is given to the right of the level.

sometimes known as the "fine structure" of α decay, but of course has nothing whatever to do with atomic fine structure. Figure 8.7 shows the α decay of ^{242}Cm. The initial state is spin zero, and thus the angular momentum of the α particle ℓ_α is equal to the angular momentum of the final nuclear state I_f. You can see that many different states of ^{238}Pu are populated. The α decays have different Q values (given by the Q value for decay to the ground state, 6.216 MeV, less the excitation energy of the excited state) and different intensities. The intensity depends on the wave functions of the initial and final states, and also depends on the angular momentum ℓ_α. In Equation 2.60, it was shown how the "centrifugal potential" $\ell(\ell+1)\hbar^2/2mr^2$ must be included in spherical coordinates. This term, which is always positive, has the effect of raising the potential energy for $a < r < b$ and thus increasing the thickness of the barrier which must be penetrated. Consider for example the 0^+, 2^+, 4^+, 6^+, and 8^+ states of the ground-state rotational band. The decay to the 2^+ state has less intensity than the decay to the ground state for two reasons—the "centrifugal potential" raises the barrier by about 0.5 MeV, and the excitation energy lowers Q by 0.044 MeV. The decay intensity continues to decrease for these same reasons as we go up the band to the 8^+ state. If we use our previous theory for the decay rates, taking

into account the increasing effective B and decreasing Q, we obtain the following estimates for the relative decay branches: 0^+, 76%; 2^+, 23%; 4^+, 1.5%; 6^+, 0.077%; 8^+, 8.4×10^{-5}%. These results are not in exact agreement with the observed decay intensities, but they do give us a rough idea of the origin of the decrease in intensity.

Once we go above the ground-state band, the α decay intensities become very small, of the order of 10^{-6}% of the total decay intensity. This situation results from the poor match of initial and final wave functions—many of these excited states originate with vibrations or pair-breaking particle excitations, which are not at all similar to the paired, vibrationless 0^+ ground state of ^{242}Cm. You should note that there are some states for which there is no observed decay intensity at all. These include the 2^- states at 0.968 and 0.986 MeV, the 3^+ state at 1.070 MeV, and the 4^- state at 1.083 MeV. Alpha decay to these states is absolutely forbidden by the parity selection rule. For example, a $0 \rightarrow 3$ decay must have $\ell_\alpha = 3$, which must give a change in parity between initial and final states. Thus $0^+ \rightarrow 3^-$ is possible, but not $0^+ \rightarrow 3^+$. Similarly, $0 \rightarrow 2$ and $0 \rightarrow 4$

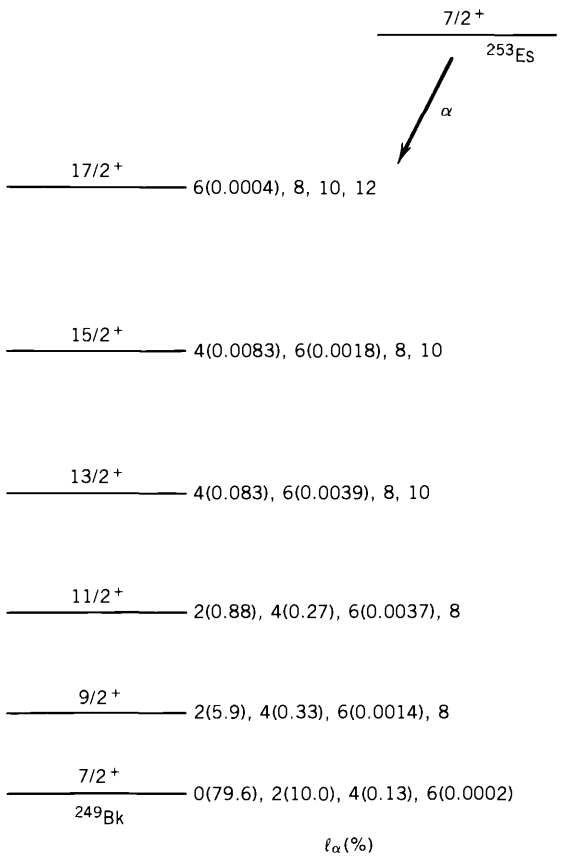


Figure 8.8 Intensities of various α-decay angular momentum components in the decay of ^{253}Es. For $\ell_\alpha = 8$ and higher, the intensities are not known but are presumably negligibly small. From the results of a study of spin-aligned α decays by A. J. Soinski et al., *Phys. Rev. C* **2**, 2379 (1970).

decays cannot change the parity, and so $0^+ \rightarrow 2^-$ and $0^+ \rightarrow 4^-$ are not permitted.

When neither the initial nor the final states have spin 0, the situation is not so simple and there are no absolutely forbidden decays. For example, the decay $2^- \rightarrow 2^+$ must have odd ℓ_α (because of the change in parity), and the angular momentum coupling rules require $0 \leq \ell_\alpha \leq 4$. Thus it is possible to have this decay with $\ell_\alpha = 1$ or 3. The next question that occurs is whether $\ell_\alpha = 1$ or $\ell_\alpha = 3$ is favored and by how much. Our previous discussion would lead us to guess that the $\ell_\alpha = 1$ intensity is roughly an order of magnitude greater than the $\ell_\alpha = 3$ intensity. However, measuring only the energy or the intensity of the decay gives us no information about how the total decay intensity is divided among the possible values of ℓ_α. To make the determination of the relative contributions of the different ℓ values, it is necessary to measure the angular distribution of the α particles. The emission of an $\ell = 1$ α particle is governed by a $Y_1(\theta, \phi)$, while an $\ell = 3$ α decay is emitted with a distribution according to $Y_3(\theta, \phi)$. If we determine the spatial distribution of these decays, we could in principle determine the relative amounts of the different ℓ values.

To do this experiment we must first align the spins of our α-radioactive nuclei, such as by aligning their magnetic dipole or electric quadrupole moments in a magnetic field or in a crystalline electric field gradient. Keeping the spins aligned requires that the nuclei must be cooled to a temperature at which the thermal motion is not sufficient to destroy the alignment; generally temperatures below 0.01 K are required (that is, less than 0.01 degree above the absolute zero of temperature!).

As an example of such an experiment, we consider the decay of ^{253}Es to states of the ground-state rotational band of ^{249}Bk. The possible ℓ values are indicated in Figure 8.8, and the results of measuring the α-particle angular distributions help us to determine the relative contribution of the different values of ℓ_α.

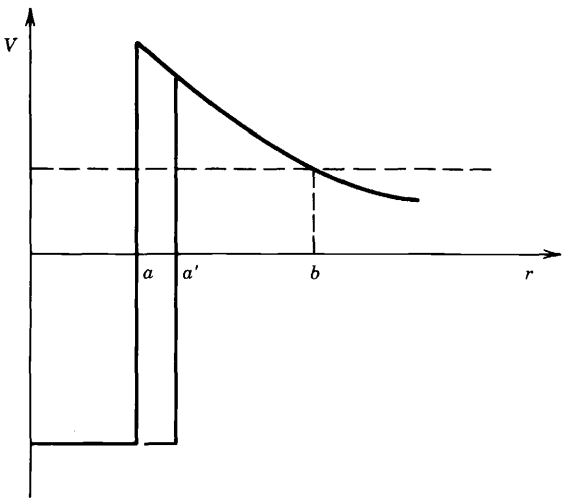


Figure 8.9 In a deformed nucleus, α particles escaping from the poles enter the Coulomb barrier at the larger separation a', and must therefore penetrate a lower, thinner barrier. It is therefore more probable to observe emission from the poles than from the equator.

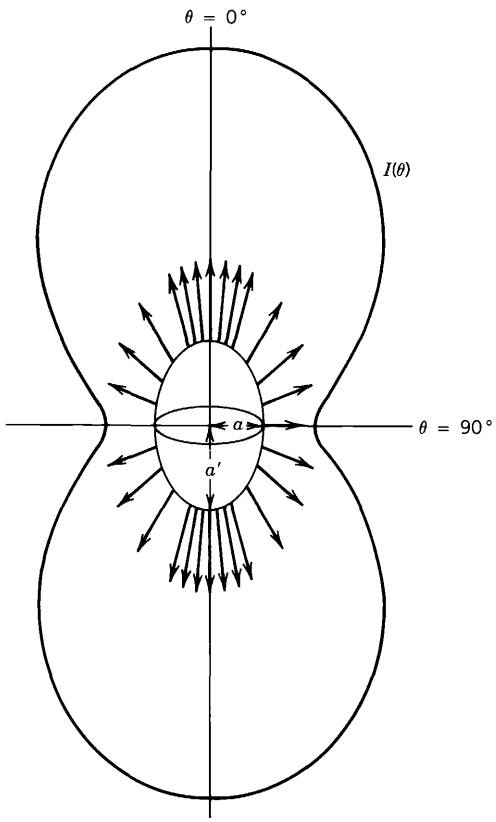


Figure 8.10 Intensity distribution of α particles emitted from the deformed nucleus at the center of the figure. The polar plot of intensity shows a pronounced angular distribution effect.

Since many α-emitting nuclei are deformed, these angular distribution measurements can also help us to answer another question: if we assume a stable prolate (elongated) nucleus, will more α's be emitted from the poles or from the equator? Figure 8.9 suggests a possible answer to this question: at the larger radius of the poles, the α particle feels a weaker Coulomb potential and must therefore penetrate a thinner and lower barrier. We therefore expect that polar emission ought to be more likely than equatorial emission. Figure 8.10 shows the angular distribution of α emission relative to the symmetry axis. You can see that emission from the poles is 3–4 times more probable than emission from the equator, exactly as we expect on the basis of the potential.

8.6 α DECAY SPECTROSCOPY

The final topic in our discussion of α decay is this: What can we learn about the energy levels of nuclei by studying α decay?

Let's consider, for example, the 5.3-h decay of ^{251}Fm to levels of ^{247}Cf. (The levels of ^{247}Cf are also populated in the beta decay of ^{247}Es, but the half-life of that decay is so short, 4.7 min, that it is more difficult to use as a detailed probe of the level structure of ^{247}Cf.)

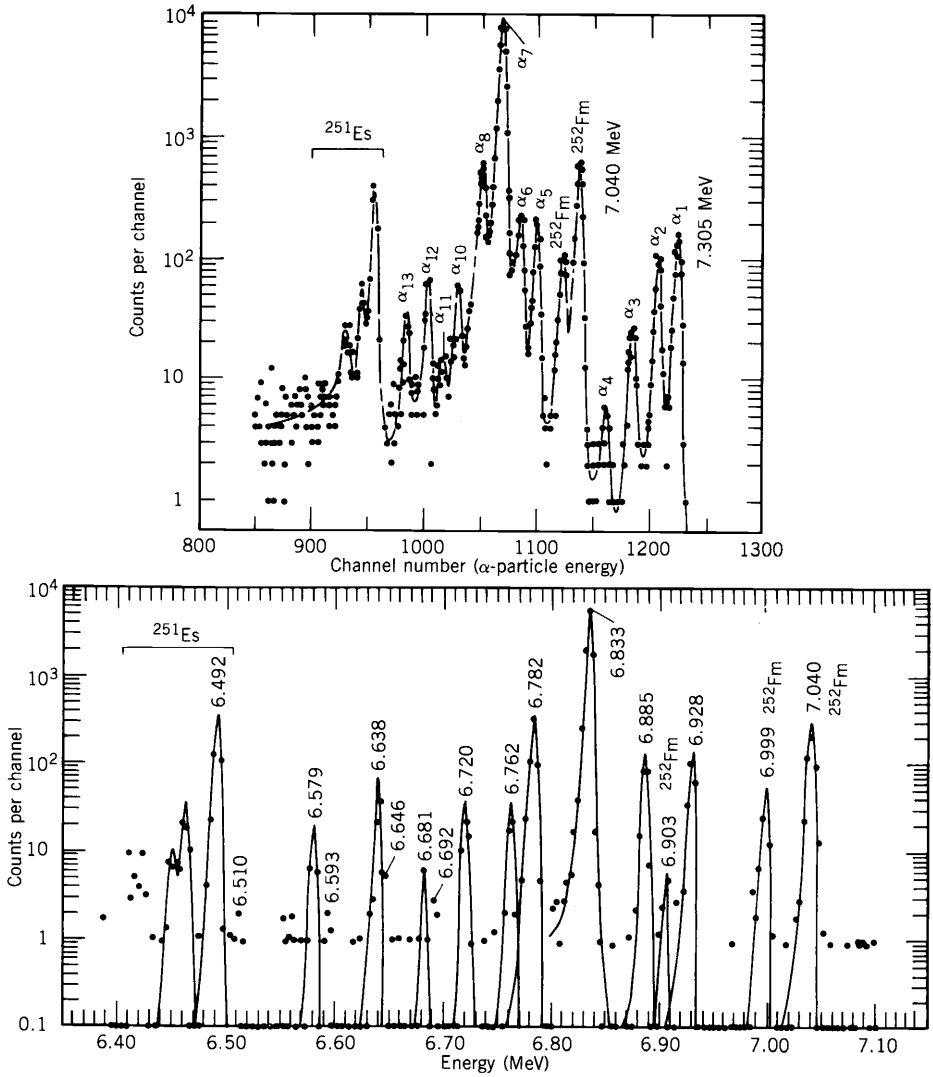


Figure 8.11 α spectrum from the decay of ^{251}Fm. The top portion shows the spectrum as observed with a Si detector. The bottom shows a portion of the same spectrum observed with a magnetic spectrometer, whose superior energy resolution enables observation of the 6.762-MeV decay, which would be missed in the upper spectrum. From Ahmad et al., *Phys. Rev. C* **8**, 737 (1973).

Figure 8.11 shows the energy spectrum of α decays from the decay of ^{251}Fm. As you can see, there are 13 distinct groups of α particles; each group presumably represents the decay to a different excited state of ^{247}Cf. How can we use this information to construct the level scheme of ^{247}Cf? Based on the α spectrum, we first must find the energy and intensity of each α group. The energy is found by comparing with decays of known energy (the impurity decays from the ^{252}Fm contaminant are helpful for this) and the intensity is found from the area of each peak. The result of this analysis is shown in Table 8.3, along with the uncertainties that come mostly from the counting statistics for each peak. (Notice that the

Table 8.3 α Decays from ^{251}Fm

α Group	α Energy (keV)	Decay Energy (keV)	Excited-State Energy (keV)	α Intensity (%)
α_1	7305 ± 3	7423	0	1.5 ± 0.1
α_2	7251 ± 3	7368	55	0.93 ± 0.08
α_3	7184 ± 3	7300	123	0.29 ± 0.03
α_4	7106 ± 5	7221	202	~ 0.05
α_5	6928 ± 2	7040	383	1.8 ± 0.1
α_6	6885 ± 2	6996	427	1.7 ± 0.1
α_7	6833 ± 2	6944	479	87.0 ± 0.9
α_8	6782 ± 2	6892	531	4.8 ± 0.2
α_9	6762 ± 3	6872	552	0.38 ± 0.06
α_{10}	6720 ± 3	6829	594	0.44 ± 0.04
α_{11}	6681 ± 4	6789	634	0.07 ± 0.03
α_{12}	6638 ± 3	6745	678	0.56 ± 0.06
α_{13}	6579 ± 3	6686	738	0.26 ± 0.04

strongest peaks have the smallest *relative* uncertainties.) To find the decay energies (that is, the relative energies of the nuclear states), we must use Equation 8.7, since the measured α energies are only the kinetic energies. These are also shown in Table 8.3.

The different ^{247}Cf excited states will quickly decay to the ground state by emitting γ-ray photons, so in constructing the decay scheme it is helpful to have the energies and intensities of the γ rays as well. Figure 8.12 shows the observed γ rays and Table 8.4 shows the deduced energies and intensities.

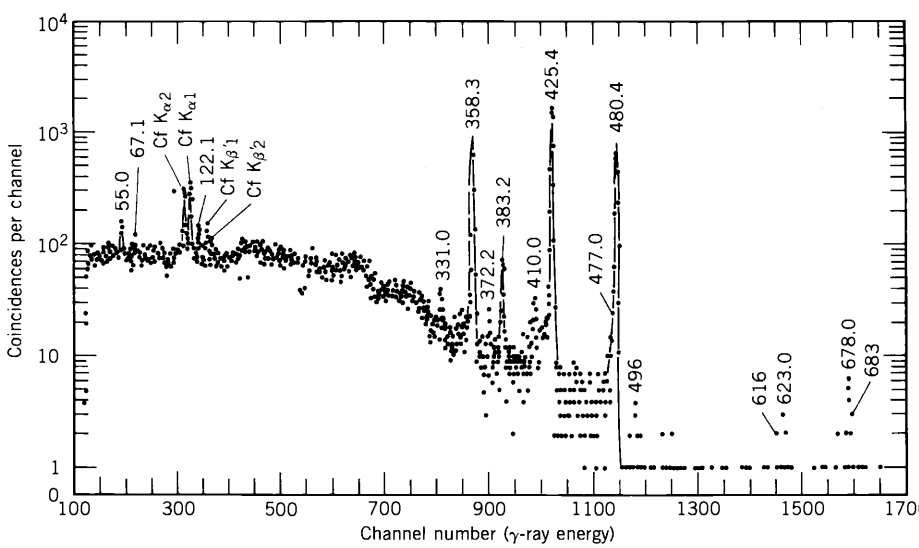


Figure 8.12 γ-ray spectrum of ^{251}Fm in coincidence with all α decays in the range 6.0 to 7.7 MeV. The spectrum was obtained with a Ge(Li) detector.

Table 8.4 γ Rays in ^{247}Cf following α Decay of ^{251}Fm

Energy (keV)	Intensity (% of decays)	Energy (keV)	Intensity (% of decays)
55.0 ± 0.2	0.58 ± 0.08	425.4 ± 0.1	51 ± 4
67.1 ± 0.2	0.28 ± 0.05	477.0 ± 0.3	0.54 ± 0.08
122.1 ± 0.2	0.28 ± 0.05	480.4 ± 0.1	21 ± 2
331.0 ± 0.3	0.35 ± 0.07	496 ± 1	~ 0.08
358.3 ± 0.1	17 ± 1.5	616 ± 1	~ 0.05
372.2 ± 0.4	0.25 ± 0.05	623.0 ± 0.8	0.07 ± 0.02
382.2 ± 0.3	1.2 ± 0.13	678.0 ± 0.8	0.26 ± 0.06
410.0 ± 0.3	0.50 ± 0.07	683 ± 1	~ 0.04

Now the detective work comes. Let's assume (and here we must be very careful, as we see in the next example) that the highest energy α decay populates the ground state of ^{247}Cf. (In an even-even nucleus, this would be a very good assumption, because $0^+ \rightarrow 0^+$ α decays are very strong and not inhibited by any differences between the wave functions of the initial and final nuclear states. In an odd-A nucleus, the initial and final ground states may have very different characters so that the decay to the ground state may be very weak or even vanishing.) The decay just lower in energy differs from the ground-state decay by about 55 keV. Assuming this to populate the first excited state, we are pleased to find among the γ transitions one of energy 55 keV, which presumably represents the transition between the first excited state and the ground state. The next α decay populates a state at 123 ± 3 keV above the ground state, and we find among the γ rays one of energy 122.1 keV, which corresponds to a transition from the second excited state to the ground state. We also find a transition of energy 67.1 (= 122.1 − 55.0) keV, which results from transitions between the second and first excited states.

Let's guess that these three states (with assumed energies 0, 55.0 keV, 122.1 keV) form a rotational band whose states, we recall from the discussion of odd-A deformed nuclei in Section 5.3, have angular momenta $I = \Omega, \Omega + 1, \Omega + 2, \ldots$, where Ω is the component of the angular momentum of the odd particle along the symmetry axis. The energy difference between the first excited state and ground state should then be

$$\Delta E_{21} \equiv E_2 - E_1 = \frac{\hbar^2}{2\mathscr{I}}[(\Omega + 1)(\Omega + 2) - \Omega(\Omega + 1)]$$
$$= \frac{\hbar^2}{2\mathscr{I}} 2(\Omega + 1) \tag{8.19}$$

where we have used $E = (\hbar^2/2\mathscr{I})I(I + 1)$ for the energy of rotational states. Similarly, the difference between the ground state and second excited state is

$$\Delta E_{31} \equiv E_3 - E_1 = \frac{\hbar^2}{2\mathscr{I}}[(\Omega + 2)(\Omega + 3) - \Omega(\Omega + 1)]$$
$$= \frac{\hbar^2}{2\mathscr{I}} 2(2\Omega + 3) \tag{8.20}$$

Combining these results with the experimental values, $\Delta E_{21} = 55.0$ keV and $\Delta E_{31} = 122.1$ keV, we conclude $\Omega = 3.5 \pm 0.2$ (that is, $\Omega = \frac{7}{2}$) and $\hbar^2/2\mathscr{I} = 6.11 \pm 0.02$ keV. These three states thus seem to form a rotational band with $I = \frac{7}{2}, \frac{9}{2}, \frac{11}{2}$. With our deduced values we can predict the energy of the $\frac{13}{2}$ state:

$$\Delta E_{41} = \frac{\hbar^2}{2\mathscr{I}}\left[\frac{13}{2}\cdot\frac{15}{2} - \frac{7}{2}\cdot\frac{9}{2}\right] = 201.6 \text{ keV}$$

and the $\frac{15}{2}$ state

$$\Delta E_{51} = \frac{\hbar^2}{2\mathscr{I}}\left[\frac{15}{2}\cdot\frac{17}{2} - \frac{7}{2}\cdot\frac{9}{2}\right] = 293.3 \text{ keV}$$

Apparently, the $\frac{13}{2}$ state is populated by the very weak α_4 decay, but its γ decays may be too weak to be seen in the spectrum of Figure 8.12. The decay to the $\frac{15}{2}$ state is not observed.

The interpretation of the remaining states is aided by α-γ coincidence studies, in which we electronically select only those γ transitions that follow a given α decay within a certain short time interval (in this case 110 ns). Since this time is long compared with typical lifetimes of nuclear states, all γ rays that follow the α decay will be recorded, even those that follow indirectly (such as the case in which two γ's are emitted in cascade, one following the other). The following coincidence relationships were observed:

Coincidence Gate	γ Rays (keV)
α_5	383.2
α_6	372.2, 383.2
α_7	55.0, 67.1, 122.1, 358.3, 425.4, 480.4
α_8	331.0, 358.3, 410.0, 425.4, 477.0, 480.4
α_{12}	623.0, 678.0

The decay α_5 goes to a state at 383.2 keV, which then goes directly to the ground state by emitting a single γ ray. The decay α_6 populates a state at about 427 keV. There is no coincident γ ray of that energy, which indicates no direct transition to the ground state, but there is a transition of energy 372.2 keV which, when added to 55.0 keV, gives 427.2 keV, very close to the energy of the state. We therefore conclude that this state, at 427.2 keV, decays to the first excited state at 55.0 keV. There is also a coincident transition at 383.2 keV, and thus this state at 427.2 keV must decay to the previously established state at 383.2 keV, by emitting a γ ray of energy $427.2 - 383.2 = 44.0$ keV; this γ ray is not observed. The decay α_7 to the state at 480.4 keV shows decays to the ground state and to the 55.0 and 122.1 keV states ($425.4 + 55.0 = 480.4$; $358.3 + 122.1 = 480.4$). Similarly, the decay α_8 to a state of 532.0 keV shows direct transitions to the lower states ($331.0 + 201.0 = 532.0$; $410.0 + 122.1 = 532.1$; $477.0 + 55.0 = 532.0$) but not directly to the ground state. It also shows coincident transitions that originate from the 480.4-keV level, so there must be a transition of energy 51.6 keV ($= 532.0 - 480.4$). In a similar fashion we analyze the other α and γ decays, and Figure 8.13 shows the resulting decay scheme.

For the states above the ground-state band, the assignment of spins and intrinsic angular momentum Ω is not as easy as it was for the states of the

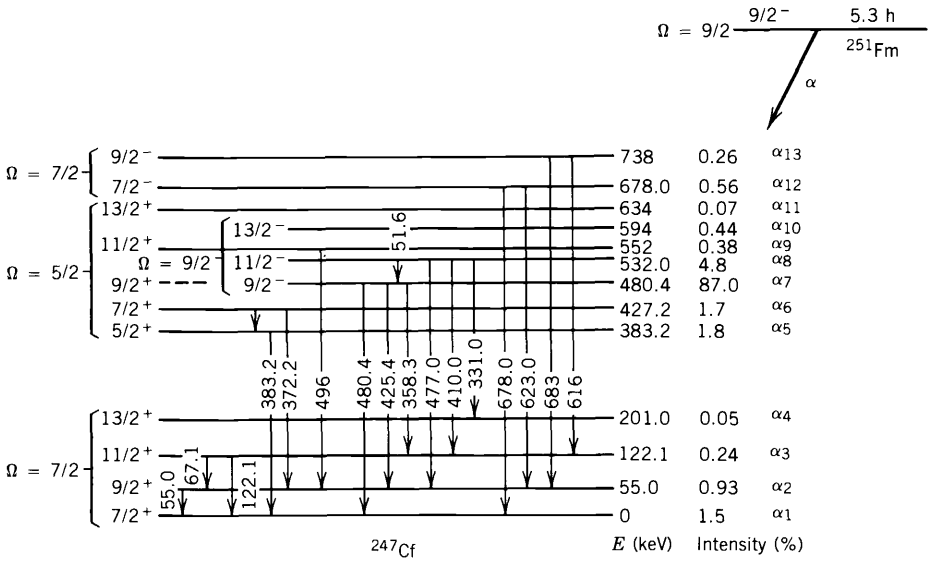


Figure 8.13 The decay scheme of ^{251}Fm to levels of ^{247}Cf deduced from α and γ spectroscopy. The spin assignments for the higher levels are deduced using γ-ray and internal conversion techniques described in Chapter 10.

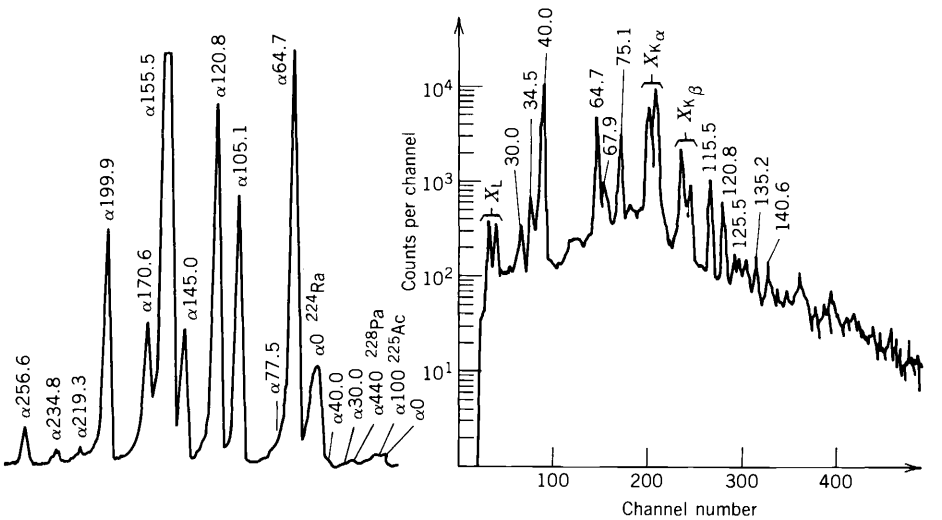


Figure 8.14 α (left) and γ (right) spectra from the decay of ^{229}Pa to ^{225}Ac. The α peaks are labeled according to the excited state populated in ^{225}Ac; thus α105.1 indicates the decay leading to the excited state at 105.1 keV. Prominent peaks from impurities are also indicated. The γ spectrum is taken in coincidence with all α's. From P. Aguer et al., *Nucl. Phys. A* **202**, 37 (1973).

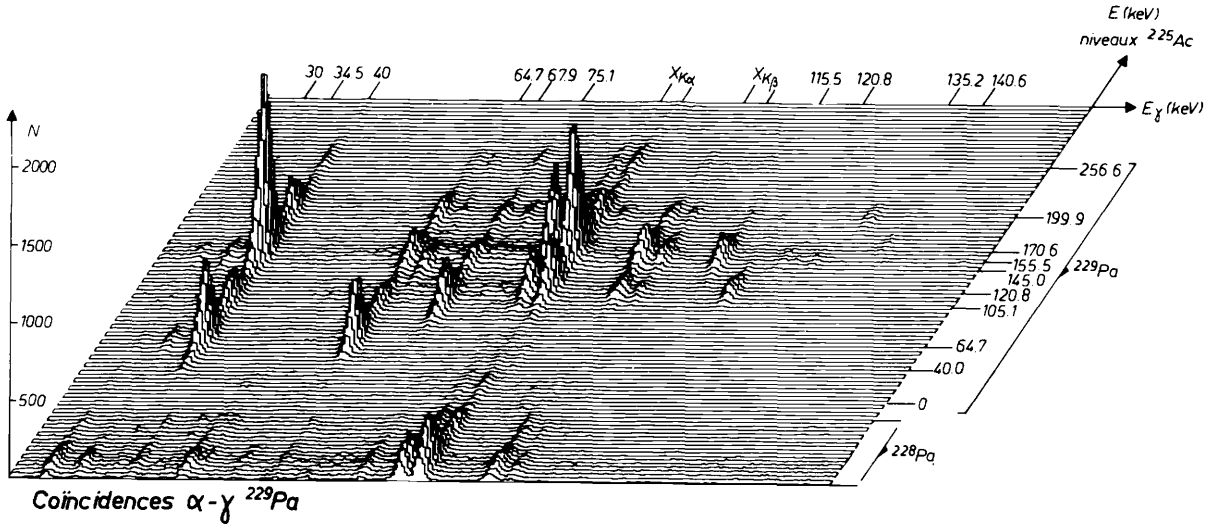
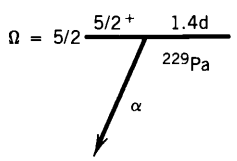


Figure 8.15 Three-dimensional (sometimes called two-parameter) representation of α-γ coincidences in the decay of ^{229}Pa. The horizontal axis shows γ-ray energies, labeled along the top. The oblique axis gives α-decay energies, labeled to indicate the ^{225}Ac state populated in the decay. The vertical axis gives the intensity of the coincidence relationship.

ground-state rotational band. To make these assignments, we need additional information from the γ decays; these measurements are discussed in Chapter 10.

Notice the strong α branch to the state at 480.4 keV. This occurs because the wave functions of the initial and final states are identical—both come from the same $\Omega = \frac{9}{2}$ deformed single-particle state—and the result is that more than 93% of the decay intensity goes to states of that so-called "favored" band. The observed decay rates can be compared with values calculated for various deformed single-particle states using the Nilsson wave functions, and in general there is good agreement between the measured and calculated results, both for the favored and unfavored decays. It is such comparisons between theory and experiment that allow us to assign the single-particle states because the intrinsic Ω and Nilsson assignments are not directly measurable.

The data for this discussion were taken from I. Ahmad, J. Milsted, R. K. Sjoblom, J. Lerner, and P. R. Fields, *Phys. Rev. C* **8**, 737 (1973). Theoretical calculations of α transition amplitudes for states in even-A and odd-A deformed nuclei of the actinide region can be found in J. K. Poggenburg, H. J. Mang, and J. O. Rasmussen, *Phys. Rev.* **181**, 1697 (1969).



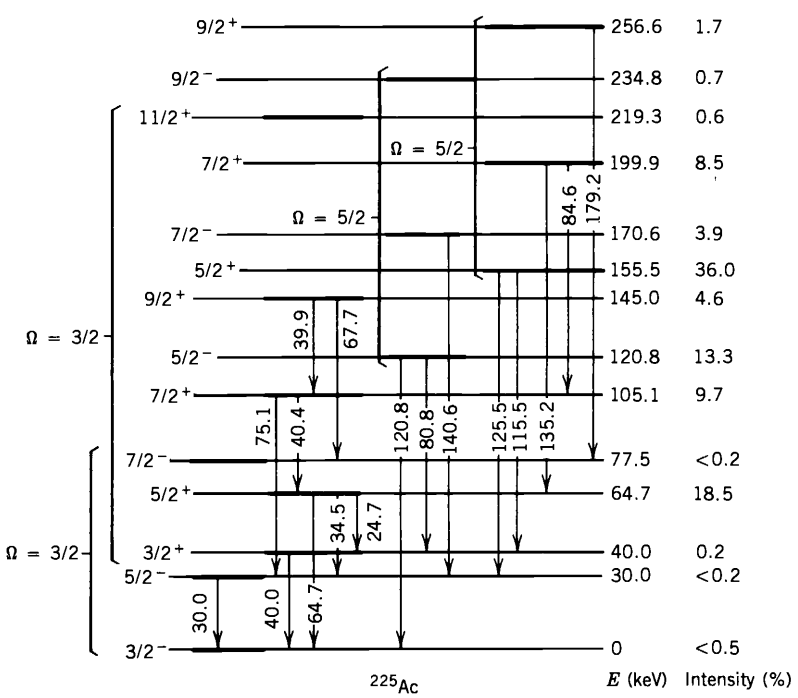


Figure 8.16 Decay scheme of ^{229}Pa deduced from α and γ spectroscopy.

Another example of the study of nuclear spectroscopy through α decay is illustrated in Figures 8.14–8.16. Figure 8.14 shows the α and γ spectra from the decay $^{229}Pa \rightarrow {}^{225}Ac$, and you can see that the decay to the ground state (labeled α_0) cannot be verified. Again, the α-γ coincidences help to elucidate the decay scheme, and a particularly instructive way to illustrate the coincidences is shown in Figure 8.15. Each peak in this three-dimensional spectrum represents a definite coincidence relationship between the α and the γ that label the axes. The information derived from the coincidence studies is used to make the decay scheme shown in Figure 8.16. Four rotational bands are identified in ^{225}Ac, positive and negative parity bands with $\Omega = \frac{3}{2}$ and $\frac{5}{2}$. The decaying ^{229}Pa is assigned $\frac{5}{2}^+$, so in this case the favored decay to the $\frac{5}{2}^+$ band in the daughter has about 46% of the decay intensity. The decay to the $\frac{3}{2}^-$ ground-state rotational band is strongly inhibited by the nuclear wave functions, resulting in the very weak (and possibly nonexistent) decay to the ground state. In this case it would lead to errors if we had assumed that the highest energy observed α group ($\alpha_{64.7}$, or $\alpha_{40.0}$ if we looked carefully) corresponded to transitions to the ground state.

The data for the ^{229}Pa decay come from P. Aguer, A. Peghaire, and C. F. Liang, *Nucl. Phys. A* **202**, 37 (1973).

REFERENCES FOR ADDITIONAL READING

Somewhat more extensive discussions of α decay can be found in Chapter 16 of R. D. Evans, *The Atomic Nucleus* (New York: McGraw-Hill, 1955), and in Chapter 13 of I. Kaplan, *Nuclear Physics* (Reading, MA: Addison-Wesley, 1955). For surveys of α-decay theory, see H. J. Mang, *Ann. Rev. Nucl. Sci.* **14**, 1 (1964), and J. O. Rasmussen, "Alpha Decay," in *Alpha-, Beta- and Gamma-Ray Spectroscopy*, edited by K. Siegbahn (Amsterdam: North-Holland, 1965), Chapter XI. A discussion of the use of α decay for nuclear spectroscopy is that of F. S. Stephens, in *Nuclear Spectroscopy*, part A, edited by F. Ajzenberg-Selove (New York: Academic, 1959), Section I.E.2.

PROBLEMS

1. Find the Q values of the following decays:
 (a) $^{247}Bk \rightarrow {}^{243}Am + \alpha$; (b) $^{251}Cf \rightarrow {}^{247}Cm + \alpha$; (c) $^{230}Th \rightarrow {}^{226}Ra + \alpha$.
2. For each decay given in Problem 1, calculate the kinetic energy and velocity of the daughter nucleus after the decay.
3. From the known atomic masses, compute the Q values of the decays:
 (a) $^{242}Pu \rightarrow {}^{238}U + \alpha$
 (b) $^{208}Po \rightarrow {}^{204}Pb + \alpha$
 (c) $^{208}Po \rightarrow {}^{196}Pt + {}^{12}C$
 (d) $^{210}Bi \rightarrow {}^{208}Pb + {}^{2}H$
4. In the decay of ^{242}Cm to ^{238}Pu, the maximum α energy is 6112.9 ± 0.1 keV. Given the mass of ^{238}Pu, find the mass of ^{242}Cm.
5. The highest energy α particle emitted in the decay of ^{238}U to ^{234}Th is 4196 ± 4 keV. From this information and the known mass of ^{238}U, compute the mass of ^{234}Th.

6. Use the uncertainty principle to estimate the minimum speed and kinetic energy of an α particle confined to the interior of a heavy nucleus.
7. (a) Compute the Q values for the decays $^{224}\text{Ra} \rightarrow {}^{212}\text{Pb} + {}^{12}\text{C}$ and $^{224}\text{Ra} \rightarrow {}^{210}\text{Pb} + {}^{14}\text{C}$. (b) Estimate the half-lives for these two possible decay processes. ^{224}Ra is an α emitter with a half-life of 3.66 days.
8. The Q value for the α decay of ^{203}Tl is calculated to be 0.91 MeV from the masses of the initial and final nuclei. Estimate the half-life of ^{203}Tl and explain why we call ^{203}Tl a "stable" nucleus.
9. Use the semiempirical mass formula to estimate the α-decay energy of ^{242}Cf and compare with the measured value (see Figure 8.1).
10. For the α decay of ^{226}Ra to ^{222}Rn ($Q = 4.869$ MeV), compute the expected half-lives for values of the ^{222}Rn radius of 7.0, 8.0, 9.0, and 10.0 fm. Estimate the nuclear radius required to give the measured half-life (1602 years); deduce the corresponding value of R_0 and interpret.
11. Using a scale similar to that of Figure 8.2, plot Equation 8.9 and show that it reproduces the general trend of the Q values. Choose appropriate values of Z corresponding to each A.
12. Make a drawing to scale of the Coulomb potential barrier encountered in the α decay of ^{242}Cm ($Z = 96$) to ^{238}Pu ($Z = 94$), for which $Q = 6.217$ MeV. Assume $R_0 = 1.5$ fm, to account for the diffuseness of the nuclear surface. Show also the Coulomb-plus-centrifugal barrier for the $\ell = 2$ decay to the first excited state (44 keV). Now use a method analogous to that of Equation 8.13 to estimate the reduction in the decay probability caused by the additional barrier, and correspondingly estimate the ratio of the α branching intensities to the ground and first excited states of ^{238}Pu. (Don't forget to reduce the Q value for decays to the excited state.) Compare your estimate with the actual intensities given in Figure 8.7.
13. Equations 8.1 to 8.5 are strictly correct even using relativistic mechanics; however, Equations 8.6 and 8.7 were obtained by assuming a nonrelativistic form for the kinetic energy. Using relativistic expressions for p and T, derive relativistic versions of Equations 8.6 and 8.7 and calculate the error made by neglecting these corrections for a 6-MeV α particle.
14. Consider the strongly distorted nucleus ^{252}Fm with $\varepsilon = 0.3$. That is, the nucleus is shaped like an ellipsoid of revolution with semimajor axis $a' = R(1 + \varepsilon)$ and semiminor axis $a = R(1 + \varepsilon)^{-1/2}$, where R is the mean radius. Using a potential of the form of Figure 8.9, estimate the relative probabilities of polar and equatorial emission of α particles.
15. In a semiclassical picture, an $\ell = 0$ α particle is emitted along a line that passes through the center of the nucleus. (a) How far from the center of the nucleus must $\ell = 1$ and $\ell = 2$ α particles be emitted? Assume $Q = 6$ MeV for a heavy nucleus ($A = 230$). (b) What would be the recoil rotational kinetic energy if all of the recoil went into rotational motion of the daughter nucleus?
16. Use data from available reference material (*Table of Isotopes*, *Atomic Mass Tables*) to plot a series of curves showing α-decay Q values against Z for constant A. Use Equation 8.9 to analyze the graph.

17. In the decay $^{228}\text{Th} \rightarrow {}^{224}\text{Ra} + \alpha$, the highest energy α particle has an energy 5.423 MeV and the next highest energy is 5.341 MeV. (a) The highest energy decay populates the ^{224}Ra ground state. Why is it natural to expect this to be so? (b) Compute the Q value for the decay from the measured α energy. (c) Compute the energy of the first excited state of ^{224}Ra.

18. The Q value of the decay $^{233}\text{U} \rightarrow {}^{229}\text{Th} + \alpha$ is 4.909 MeV. Excited states of ^{229}Th at 29, 42, 72, and 97 keV are populated in the decay. Compute the energies of the five most energetic α groups emitted in the ^{233}U decay.

19. The five highest energy α's emitted by ^{242}Cm (Figure 8.7) have energies (in MeV) of 6.113, 6.070, 5.972, 5.817, 5.609. Each state is connected with the state directly below it by a γ transition. Calculate the energies of the γ rays.

20. The α decay of a nucleus near mass 200 has two components of energies 4.687 and 4.650 MeV. Neither populates the ground state of the daughter, but each is followed by a γ ray, of respective energy 266 and 305 keV. No other γ rays are seen. (a) From this information, construct a decay scheme. (b) The decaying parent state has spin 1 and negative parity, and the ground state of the daughter has spin zero and also negative parity. Explain why there is no direct α decay to the ground state.

21. The α decay of ^{244}Cm populates a 0^+ excited state in ^{240}Pu at 0.861 MeV with an intensity of $1.6 \times 10^{-4}\%$, while the 0^+ ground state is populated with an intensity of 76.7%. Estimate the ratio between these decay intensities from the theory of α decay and compare with the experimental value.

22. In a certain decay process, a nucleus in the vicinity of mass 240 emits α particles with the following energies (in MeV): 5.545 (α_0), 5.513 (α_1), 5.486 (α_2), 5.469 (α_3), 5.443 (α_4), 5.417 (α_5), and 5.389 (α_6). The following γ rays in the daughter nucleus are seen (energies in keV): 26 (γ_1), 33 (γ_2), 43 (γ_3), 56 (γ_4), 60 (γ_5), 99 (γ_6), 103 (γ_7), and 125 (γ_8). Construct a decay scheme from this information, assuming α_0 populates the ground state of the daughter.

23. For the decay of ^{253}Es to ^{249}Bk illustrated in Figure 8.8: (a) Estimate the intensities of the $\ell_\alpha = 0$, 2, 4, and 6 contributions to the decay to the ground state and compare with the measured values. (b) Assuming the $\ell_\alpha = 2$ component to be dominant, estimate the relative intensities of the decays to the $\frac{9}{2}^+$ and $\frac{11}{2}^+$ states. The ground-state Q value is 6.747 MeV, and the excited states are at 42 keV ($\frac{9}{2}^+$) and 94 keV ($\frac{11}{2}^+$).

24. The decay of ^{253}Es ($I = \frac{7}{2}$, $\pi = +$) leads to a sequence of negative-parity states in ^{249}Bk with $I = \frac{3}{2}, \frac{5}{2}, \frac{7}{2}, \frac{9}{2}, \frac{11}{2}, \frac{13}{2}$. For each state, find the permitted values of ℓ_α.

9

BETA DECAY

The emission of ordinary negative electrons from the nucleus was among the earliest observed radioactive decay phenomena. The inverse process, capture by a nucleus of an electron from its atomic orbital, was not observed until 1938 when Alvarez detected the characteristic X rays emitted in the filling of the vacancy left by the captured electron. The Joliot-Curies in 1934 first observed the related process of positive electron (positron) emission in radioactive decay, only two years after the positron had been discovered in cosmic rays. These three nuclear processes are closely related and are grouped under the common name *beta* (β) *decay*.

The most basic β decay process is the conversion of a proton to a neutron or of a neutron into a proton. In a nucleus, β decay changes both Z and N by one unit: $Z \rightarrow Z \pm 1$, $N \rightarrow N \mp 1$ so that $A = Z + N$ remains constant. Thus β decay provides a convenient way for an unstable nucleus to "slide down" the mass parabola (Figure 3.18, for example) of constant A and to approach the stable isobar.

In contrast with α decay, progress in understanding β decay has been achieved at an extremely slow pace, and often the experimental results have created new puzzles that challenged existing theories. Just as Rutherford's early experiments showed α particles to be identical with ^{4}He nuclei, other early experiments showed the negative β particles to have the same electric charge and charge-to-mass ratio as ordinary electrons. In Section 1.2, we discussed the evidence against the presence of electrons as nuclear constituents, and so we must regard the β decay process as "creating" an electron from the available decay energy at the instant of decay; this electron is then immediately ejected from the nucleus. This situation contrasts with α decay, in which the α particle may be regarded as having a previous existence in the nucleus.

The basic decay processes are thus:

$$\mathrm{n} \rightarrow \mathrm{p} + \mathrm{e}^- \quad \text{negative beta decay } (\beta^-)$$

$$\mathrm{p} \rightarrow \mathrm{n} + \mathrm{e}^+ \quad \text{positive beta decay } (\beta^+)$$

$$\mathrm{p} + \mathrm{e}^- \rightarrow \mathrm{n} \quad \text{orbital electron capture } (\varepsilon)$$

These processes are not complete, for there is yet another particle (a neutrino or antineutrino) involved in each. The latter two processes occur only for protons

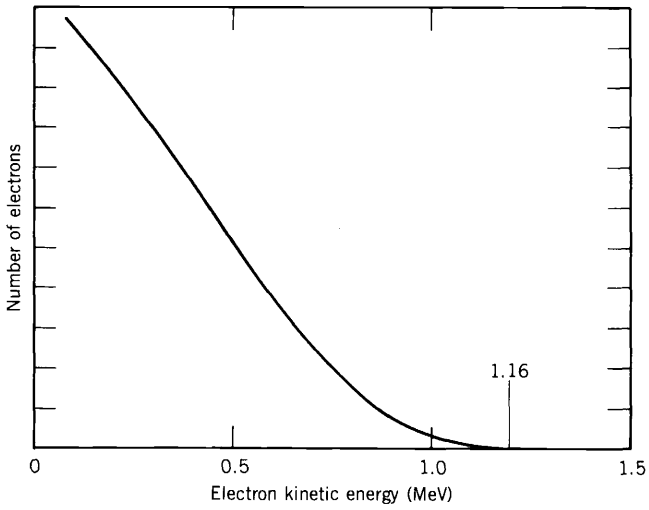


Figure 9.1 The continuous electron distribution from the β decay of ^{210}Bi (also called RaE in the literature).

bound in nuclei; they are energetically forbidden for free protons or for protons in hydrogen atoms.

9.1 ENERGY RELEASE IN β DECAY

The continuous energy distribution of the β-decay electrons was a confusing experimental result in the 1920s. Alpha particles are emitted with sharp, well-defined energies, equal to the difference in mass energy between the initial and final states (less the small recoil corrections); all α decays connecting the same initial and final states have exactly the same kinetic energies. Beta particles have a continuous distribution of energies, from zero up to an upper limit (the endpoint energy) which is equal to the energy difference between the initial and final states. If β decay were, like α decay, a two-body process, we would expect all of the β particles to have a unique energy, but virtually all of the emitted particles have a smaller energy. For instance, we might expect on the basis of nuclear mass differences that the β particles from ^{210}Bi would be emitted with a kinetic energy of 1.16 MeV, yet we find a continuous distribution from 0 up to 1.16 MeV (Figure 9.1).

An early attempt to account for this "missing" energy hypothesized that the β's are actually emitted with 1.16 MeV of kinetic energy, but lose energy, such as by collisions with atomic electrons, before they reach the detection system. Such a possibility was eliminated by very precise calorimetric experiments that confined a β source and measured its decay energy by the heating effect. If a portion of the energy were transferred to the atomic electrons, a corresponding rise in temperature should be observed. These experiments showed that the shape of the spectrum shown in Figure 9.1 is a characteristic of the decay electrons themselves and not a result of any subsequent interactions.

To account for this energy release, Pauli in 1931 proposed that there was emitted in the decay process a second particle, later named by Fermi the

neutrino. The neutrino carries the "missing" energy and, because it is highly penetrating radiation, it is not stopped within the calorimeter, thus accounting for the failure of those experiments to record its energy. Conservation of electric charge requires the neutrino to be electrically neutral, and angular momentum conservation and statistical considerations in the decay process require the neutrino to have (like the electron) a spin of $\frac{1}{2}$. Experiment shows that there are in fact two different kinds of neutrinos emitted in β decay (and yet other varieties emitted in other decay processes; see Chapter 18). These are called the *neutrino* and the *antineutrino* and indicated by ν and $\bar{\nu}$. It is the antineutrino which is emitted in β^- decay and the neutrino which is emitted in β^+ decay and electron capture. In discussing β decay, the term "neutrino" is often used to refer to both neutrinos and antineutrinos, although it is of course necessary to distinguish between them in writing decay processes; the same is true for "electron."

To demonstrate β-decay energetics we first consider the decay of the free neutron (which occurs with a half-life of about 10 min),

$$\mathrm{n} \rightarrow \mathrm{p} + \mathrm{e}^- + \bar{\nu}.$$

As we did in the case of α decay, we define the Q value to be the difference between the initial and final *nuclear* mass energies.

$$Q = (m_\mathrm{n} - m_\mathrm{p} - m_\mathrm{e} - m_{\bar{\nu}})c^2 \tag{9.1}$$

and for decays of neutrons at rest,

$$Q = T_\mathrm{p} + T_\mathrm{e} + T_{\bar{\nu}} \tag{9.2}$$

For the moment we will ignore the proton recoil kinetic energy T_p, which amounts to only 0.3 keV. The antineutrino and electron will then share the decay energy, which accounts for the continuous electron spectrum. The maximum-energy electrons correspond to minimum-energy antineutrinos, and when the antineutrinos have vanishingly small energies, $Q \simeq (T_\mathrm{e})_\mathrm{max}$. The measured maximum energy of the electrons is 0.782 ± 0.013 MeV. Using the measured neutron, electron, and proton masses, we can compute the Q value:

$$\begin{aligned} Q &= m_\mathrm{n}c^2 - m_\mathrm{p}c^2 - m_\mathrm{e}c^2 - m_{\bar{\nu}}c^2 \\ &= 939.573 \text{ MeV} - 938.280 \text{ MeV} - 0.511 \text{ MeV} - m_{\bar{\nu}}c^2 \\ &= 0.782 \text{ MeV} - m_{\bar{\nu}}c^2 \end{aligned}$$

Thus to within the precision of the measured maximum energy (about 13 keV) we may regard the antineutrino as massless. Other experiments provide more stringent upper limits, as we discuss in Section 9.6, and for the present discussion we take the masses of the neutrino and antineutrino to be identically zero.

Conservation of linear momentum can be used to identify β decay as a three-body process, but this requires measuring the momentum of the recoiling nucleus in coincidence with the momentum of the electron. These experiments are difficult, for the low-energy nucleus ($T \lesssim$ keV) is easily scattered, but they have been done in a few cases, from which it can be deduced that the vector sum of the linear momenta of the electron and the recoiling nucleus is consistent with an unobserved third particle carrying the "missing" energy and having a rest mass of zero or nearly zero. Whatever its mass might be, the existence of the

additional particle is absolutely required by these experiments, for the momenta of the electron and nucleus certainly do not sum to zero, as they would in a two-body decay.

Because the neutrino is massless, it moves with the speed of light and its total relativistic energy E_ν is the same as its kinetic energy; we will use E_ν to represent neutrino energies. (A review of the concepts and formulas of relativistic kinematics may be found in Appendix A.) For the electron, we will use both its kinetic energy T_e and its total relativistic energy E_e, which are of course related by $E_e = T_e + m_e c^2$. (Decay energies are typically of order MeV; thus the nonrelativistic approximation $T \ll mc^2$ is certainly not valid for the decay electrons, and we *must* use relativistic kinematics.) The nuclear recoil is of very low energy and can be treated nonrelativistically.

Let's consider a typical negative β-decay process in a nucleus:

$$\begin{aligned} {}^{A}_{Z}X_N &\rightarrow {}_{Z+1}{}^{A}X'_{N-1} + e^- + \bar{\nu} \\ Q_{\beta^-} &= \left[m_N({}^{A}_{Z}X) - m_N({}_{Z+1}{}^{A}X') - m_e\right]c^2 \end{aligned} \tag{9.3}$$

where m_N indicates *nuclear* masses. To convert nuclear masses into the tabulated neutral atomic masses, which we denote as $m({}^{A}X)$, we use

$$m({}^{A}X)c^2 = m_N({}^{A}X)c^2 + Zm_e c^2 - \sum_{i=1}^{Z} B_i \tag{9.4}$$

where B_i represents the binding energy of the ith electron. In terms of atomic masses,

$$\begin{aligned} Q_{\beta^-} = &\left\{\left[m({}^{A}X) - Zm_e\right] - \left[m({}^{A}X') - (Z+1)m_e\right] - m_e\right\}c^2 \\ &+ \left\{\sum_{i=1}^{Z} B_i - \sum_{i=1}^{Z+1} B_i\right\} \end{aligned} \tag{9.5}$$

Notice that the electron masses cancel in this case. Neglecting the differences in electron binding energy, we therefore find

$$Q_{\beta^-} = \left[m({}^{A}X) - m({}^{A}X')\right]c^2 \tag{9.6}$$

where the masses are neutral atomic masses. The Q value represents the energy shared by the electron and neutrino:

$$Q_{\beta^-} = T_e + E_{\bar{\nu}} \tag{9.7}$$

and it follows that each has its maximum when the other approaches zero:

$$(T_e)_{\max} = (E_{\bar{\nu}})_{\max} = Q_{\beta^-} \tag{9.8}$$

In the case of the $^{210}\text{Bi} \rightarrow {}^{210}\text{Po}$ decay, the mass tables give

$$\begin{aligned} Q_{\beta^-} &= \left[m({}^{210}\text{Bi}) - m({}^{210}\text{Po})\right]c^2 \\ &= (209.984095\ \text{u} - 209.982848\ \text{u})(931.502\ \text{MeV/u}) \\ &= 1.161\ \text{MeV} \end{aligned}$$

Figure 9.1 showed $(T_e)_{\max} = 1.16$ MeV, in agreement with the value expected from Q_{β^-}. Actually, this is really not an agreement between two independent values. The value of Q_{β^-} is used in this case to *determine* the mass of ^{210}Po, with

the mass of ^{210}Bi determined from that of ^{209}Bi using neutron capture. Equation 9.6 is used with the measured Q_{β^-} to obtain $m(^A\mathrm{X}')$.

In the case of positron decay, a typical decay process is

$$ {}^A_Z\mathrm{X}_N \rightarrow {}_{Z-1}{}^A\mathrm{X}'_{N+1} + \mathrm{e}^+ + \nu $$

and a calculation similar to the previous one shows

$$ Q_{\beta^+} = \left[m(^A\mathrm{X}) - m(^A\mathrm{X}') - 2m_\mathrm{e}\right]c^2 \tag{9.9} $$

again using *atomic* masses. Notice that the electron masses *do not* cancel in this case.

For electron-capture processes, such as

$$ {}^A_Z\mathrm{X}_N + \mathrm{e}^- \rightarrow {}_{Z-1}{}^A\mathrm{X}'_{N+1} + \nu $$

the calculation of the Q value must take into account that the atom X′ is in an *atomic* excited state immediately after the capture. That is, if the capture takes place from an inner shell, the K shell for instance, an electronic vacancy in that shell results. The vacancy is quickly filled as electrons from higher shells make downward transitions and emit characteristic X rays. Whether one X ray is emitted or several, the total X-ray energy is equal to the binding energy of the captured electron. Thus the atomic mass of X′ immediately after the decay is greater than the mass of X′ in its atomic ground state by B_n, the binding energy of the captured n-shell electron (n = K, L, ...). The Q value is then

$$ Q_\varepsilon = \left[m(^A\mathrm{X}) - m(^A\mathrm{X}')\right]c^2 - B_n \tag{9.10} $$

Positive beta decay and electron capture both lead from the initial nucleus ${}^A_Z\mathrm{X}_N$ to the final nucleus ${}_{Z-1}{}^A\mathrm{X}'_{N+1}$, but note that both may not always be energetically possible (Q must be positive for any decay process). Nuclei for which β^+ decay is energetically possible may also undergo electron capture, but the reverse is not true—it is possible to have $Q > 0$ for electron capture while $Q < 0$ for β^+ decay. The atomic mass energy difference must be at least $2m_ec^2 = 1.022$ MeV to permit β^+ decay.

In positron decay, expressions of the form of Equations 9.7 and 9.8 show that there is a continuous distribution of neutrino energies up to Q_{β^+} (less the usually negligible nuclear recoil). In electron capture, however, the two-body final state results in unique values for the recoil energy and E_ν. Neglecting the recoil, a monoenergetic neutrino with energy Q_ε is emitted.

All of the above expressions refer to decays between nuclear ground states. If the final nuclear state X′ is an excited state, the Q value must be accordingly

Table 9.1 Typical β-Decay Processes

Decay	Type	Q (MeV)	$t_{1/2}$
$^{23}\mathrm{Ne} \rightarrow {}^{23}\mathrm{Na} + \mathrm{e}^- + \bar{\nu}$	β^-	4.38	38 s
$^{99}\mathrm{Tc} \rightarrow {}^{99}\mathrm{Ru} + \mathrm{e}^- + \bar{\nu}$	β^-	0.29	2.1×10^5 y
$^{25}\mathrm{Al} \rightarrow {}^{25}\mathrm{Mg} + \mathrm{e}^+ + \nu$	β^+	3.26	7.2 s
$^{124}\mathrm{I} \rightarrow {}^{124}\mathrm{Te} + \mathrm{e}^+ + \nu$	β^+	2.14	4.2 d
$^{15}\mathrm{O} + \mathrm{e}^- \rightarrow {}^{15}\mathrm{N} + \nu$	ε	2.75	1.22 s
$^{41}\mathrm{Ca} + \mathrm{e}^- \rightarrow {}^{41}\mathrm{K} + \nu$	ε	0.43	1.0×10^5 y

decreased by the excitation energy of the state:

$$Q_{ex} = Q_{ground} - E_{ex} \tag{9.11}$$

Table 9.1 shows some typical β decay processes, their energy releases, and their half-lives.

9.2 FERMI THEORY OF β DECAY

In our calculation of α-decay half-lives in Chapter 8, we found that the barrier penetration probability was the critical factor in determining the half-life. In negative β decay there is no such barrier to penetrate and even in β^+ decay, it is possible to show from even a rough calculation that the exponential factor in the barrier penetration probability is of order unity. There are other important differences between α and β decay which suggest to us that we must use a completely different approach for the calculation of transition probabilities in β decay: (1) The electron and neutrino do not exist before the decay process, and therefore we must account for the formation of those particles. (2) The electron and neutrino must be treated relativistically. (3) The continuous distribution of electron energies must result from the calculation.

In 1934, Fermi developed a successful theory of β decay based on Pauli's neutrino hypothesis. The essential features of the decay can be derived from the basic expression for the transition probability caused by an interaction that is weak compared with the interaction that forms the quasi-stationary states. This is certainly true for β decay, in which the characteristic times (the half-lives, typically of order seconds or longer) are far longer than the characteristic nuclear time (10^{-20} s). The result of this calculation, treating the decay-causing interaction as a weak perturbation, is Fermi's Golden Rule, a general result for any transition rate previously given in Equation 2.79:

$$\lambda = \frac{2\pi}{\hbar} |V_{fi}|^2 \rho(E_f) \tag{9.12}$$

The matrix element V_{fi} is the integral of the interaction V between the initial and final quasi-stationary states of the system:

$$V_{fi} = \int \psi_f^* V \psi_i \, dv \tag{9.13}$$

The factor $\rho(E_f)$ is the density of final states, which can also be written as dn/dE_f, the number dn of final states in the energy interval dE_f. A given transition is more likely to occur if there is a large number of accessible final states.

Fermi did not know the mathematical form of V for β decay that would have permitted calculations using Equations 9.12 and 9.13. Instead, he considered all possible forms consistent with special relativity, and he showed that V could be replaced with one of five mathematical operators O_X, where the subscript X gives the form of the operator O (that is, its transformation properties): X = V (vector), A (axial vector), S (scalar), P (pseudoscalar), or T (tensor). Which of these is correct for β decay can be revealed only through experiments that study

the symmetries and the spatial properties of the decay products, and it took 20 years (and several mistaken conclusions) for the correct V–A form to be deduced.

The final state wave function must include not only the nucleus but also the electron and neutrino. For electron capture or neutrino capture, the forms would be similar, but the appropriate wave function would appear in the initial state. For β decay, the interaction matrix element then has the form

$$V_{\mathrm{fi}} = g\int[\psi_{\mathrm{f}}^{*}\varphi_{\mathrm{e}}^{*}\varphi_{\nu}^{*}]O_X\psi_i\,dv \tag{9.14}$$

where now ψ_{f} refers only to the final nuclear wave function and φ_{e} and φ_{ν} give the wave functions of the electron and neutrino. The quantity in square brackets represents the entire final system after the decay. The value of the constant g determines the strength of the interaction; the electronic charge e plays a similar role in the interaction between an atom and the electromagnetic field.

The density of states factor determines (to lowest order) the shape of the beta energy spectrum. To find the density of states, we need to know the number of final states accessible to the decay products. Let us suppose in the decay that we have an electron (or positron) emitted with momentum $\boldsymbol{p}$ and a neutrino (or antineutrino) with momentum $\boldsymbol{q}$. We are interested at this point only in the *shape* of the energy spectrum, and thus the directions of $\boldsymbol{p}$ and $\boldsymbol{q}$ are of no interest. If we imagine a coordinate system whose axes are labeled p_x, p_y, p_z, then the locus of the points representing a specific value of $|\boldsymbol{p}| = (p_x^2 + p_y^2 + p_z^2)^{1/2}$ is a sphere of radius $p = |\boldsymbol{p}|$. More specifically, the locus of points representing momenta in the range dp at p is a spherical shell of radius p and thickness dp, thus having volume $4\pi p^2\,dp$. If the electron is confined to a box of volume V (this step is taken only for completeness and to permit the wave function to be normalized; the actual volume will cancel from the final result), then the number of final electron states dn_{e}, corresponding to momenta in the range p to $p + dp$, is

$$dn_{\mathrm{e}} = \frac{4\pi p^2\,dp\,V}{h^3} \tag{9.15}$$

where the factor h^3 is included to make the result a dimensionless pure number.* Similarly, the number of neutrino states is

$$dn_{\nu} = \frac{4\pi q^2\,dq\,V}{h^3} \tag{9.16}$$

and the number of final states which have simultaneously an electron and a neutrino with the proper momenta is

$$d^2n = dn_{\mathrm{e}}\,dn_{\nu} = \frac{(4\pi)^2V^2p^2\,dp\,q^2\,dq}{h^6} \tag{9.17}$$

*The available spatial and momentum states are counted in six-dimensional (x, y, z, p_x, p_y, p_z) *phase space*; the unit volume in phase space is h^3.

The electron and neutrino wave functions have the usual free-particle form, normalized within the volume V:

$$\varphi_e(\boldsymbol{r}) = \frac{1}{\sqrt{V}} e^{i\boldsymbol{p}\cdot\boldsymbol{r}/\hbar}$$
$$\varphi_\nu(\boldsymbol{r}) = \frac{1}{\sqrt{V}} e^{i\boldsymbol{q}\cdot\boldsymbol{r}/\hbar} \tag{9.18}$$

For an electron with 1 MeV kinetic energy, $p = 1.4$ MeV/c and $p/\hbar = 0.007$ fm^{-1}. Thus over the nuclear volume, $pr \ll 1$ and we can expand the exponentials, keeping only the first term:

$$e^{i\boldsymbol{p}\cdot\boldsymbol{r}/\hbar} = 1 + \frac{i\boldsymbol{p}\cdot\boldsymbol{r}}{\hbar} + \cdots \cong 1$$
$$e^{i\boldsymbol{q}\cdot\boldsymbol{r}/\hbar} = 1 + \frac{i\boldsymbol{q}\cdot\boldsymbol{r}}{\hbar} + \cdots \cong 1 \tag{9.19}$$

This approximation is known as the *allowed* approximation.

In this approximation, the only factors that depend on the electron or neutrino energy come from the density of states. Let's assume we are trying to calculate the momentum and energy distributions of the emitted electrons. The partial decay rate for electrons and neutrinos with the proper momenta is

$$d\lambda = \frac{2\pi}{\hbar} g^2 |M_{fi}|^2 (4\pi)^2 \frac{p^2\, dp\, q^2}{h^6} \frac{dq}{dE_f} \tag{9.20}$$

where $M_{fi} = \int \psi_f^* O_X \psi_i \, dv$ is the *nuclear matrix element*. The final energy E_f is just $E_e + E_\nu = E_e + qc$, and so $dq/dE_f = 1/c$ at fixed E_e. As far as the shape of the electron spectrum is concerned, all of the factors in Equation 9.20 that do not involve the momentum (including M_{fi}, which for the present we assume to be independent of p) can be combined into a constant C, and the resulting distribution gives the number of electrons with momentum between p and $p + dp$:

$$N(p)\, dp = Cp^2 q^2\, dp \tag{9.21}$$

If Q is the decay energy, then ignoring the negligible nuclear recoil energy,

$$q = \frac{Q - T_e}{c} = \frac{Q - \sqrt{p^2c^2 + m_e^2c^4} + m_e c^2}{c} \tag{9.22}$$

and the spectrum shape is given by

$$N(p) = \frac{C}{c^2} p^2 (Q - T_e)^2 \tag{9.23}$$

$$= \frac{C}{c^2} p^2 \left[Q - \sqrt{p^2c^2 + m_e^2c^4} + m_e c^2\right]^2 \tag{9.24}$$

This function vanishes at $p = 0$ and also at the endpoint where $T_e = Q$; its shape is shown in Figure 9.2.

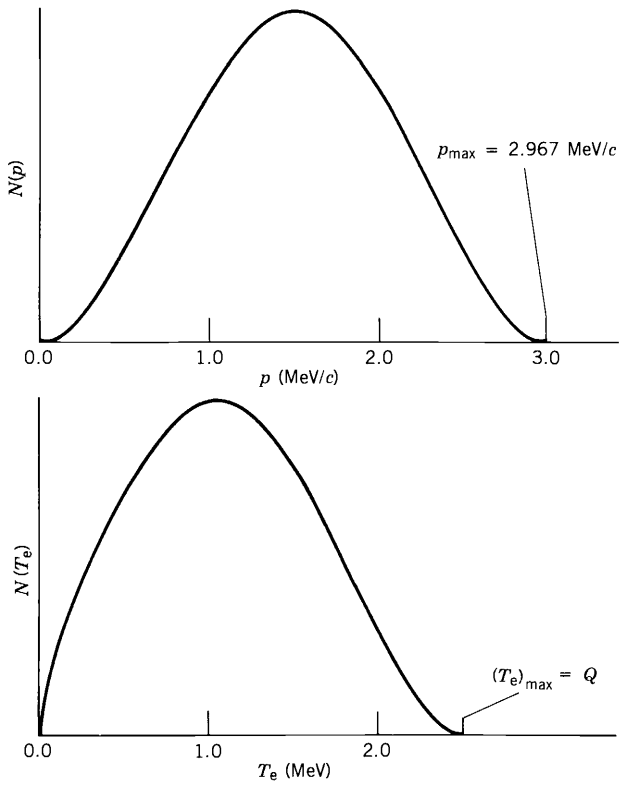


Figure 9.2 Expected electron energy and momentum distributions, from Equations 9.24 and 9.25. These distributions are drawn for $Q = 2.5$ MeV.

More frequently we are interested in the energy spectrum, for electrons with kinetic energy between T_e and $T_e + dT_e$. With $c^2 p\, dp = (T_e + m_e c^2)\, dT_e$, we have

$$N(T_e) = \frac{C}{c^5}\left(T_e^2 + 2T_e m_e c^2\right)^{1/2}(Q - T_e)^2\left(T_e + m_e c^2\right) \qquad (9.25)$$

This distribution, which also vanishes at $T_e = 0$ and at $T_e = Q$, is shown in Figure 9.2.

In Figure 9.3, the β^+ and β^- decays of ^{64}Cu are compared with the predictions of the theory. As you can see, the general shape of Figure 9.2 is evident, but there are systematic differences between theory and experiment. These differences originate with the Coulomb interaction between the β particle and the daughter nucleus. Semiclassically, we can interpret the shapes of the momentum distributions of Figure 9.3 as a Coulomb repulsion of β^+ by the nucleus, giving fewer low-energy positrons, and a Coulomb attraction of β^-, giving more low-energy electrons. From the more correct standpoint of quantum mechanics, we should instead refer to the change in the electron plane wave, Equation 9.19, brought about by the Coulomb potential inside the nucleus. The quantum mechanical calculation of the effect of the nuclear Coulomb field on the electron wave function is beyond the level of this text. It modifies the spectrum by introducing an additional factor, the *Fermi function* $F(Z', p)$ or $F(Z', T_e)$, where Z' is the atomic number of the daughter nucleus. Finally, we must

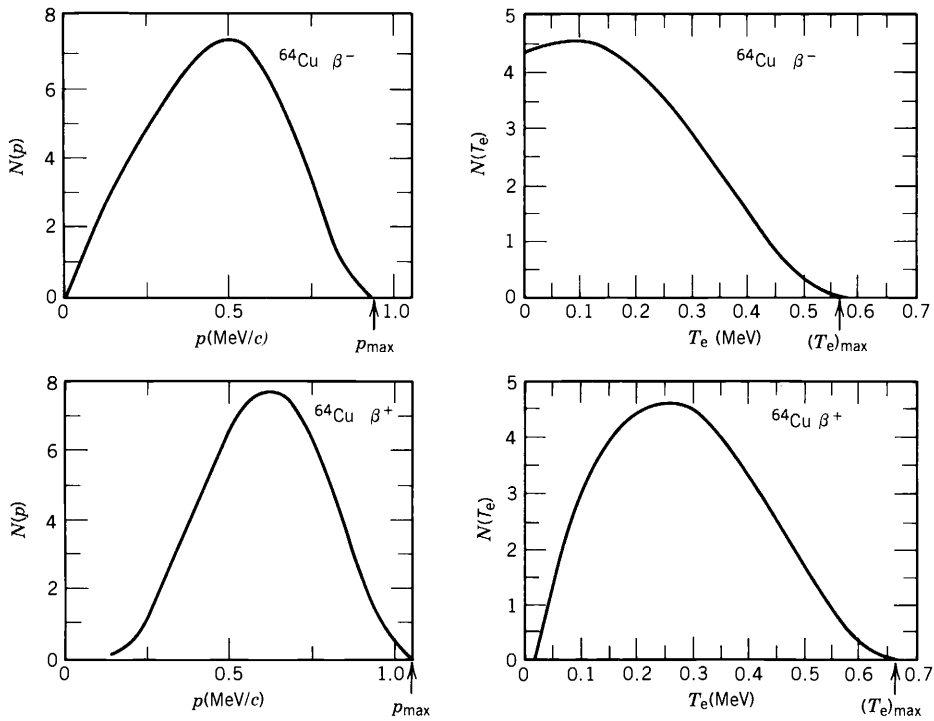


Figure 9.3 Momentum and kinetic energy spectra of electrons and positrons emitted in the decay of ^{64}Cu. Compare with Figure 9.2; the differences arise from the Coulomb interactions with the daughter nucleus. From R. D. Evans, *The Atomic Nucleus* (New York: McGraw-Hill, 1955).

consider the effect of the nuclear matrix element, M_{fi}, which we have up to now assumed not to influence the shape of the spectrum. This approximation (also called the allowed approximation) is often found to be a very good one, but there are some cases in which it is very bad—in fact, there are cases in which M_{fi} vanishes in the allowed approximation, giving no spectrum at all! In such cases, we must take the next terms of the plane wave expansion, Equations 9.19, which introduce yet another momentum dependence. Such cases are called, somewhat incorrectly, *forbidden* decays; these decays are not absolutely forbidden, but as we will learn subsequently, they are less likely to occur than allowed decays and therefore tend to have longer half-lives. The degree to which a transition is forbidden depends on how far we must take the expansion of the plane wave to find a nonvanishing nuclear matrix element. Thus the first term beyond the 1 gives first-forbidden decays, the next term gives second-forbidden, and so on. We will see in Section 9.4 how the angular momentum and parity selection rules restrict the kinds of decay that can occur.

The complete β spectrum then includes three factors:

1. The *statistical factor* $p^2(Q - T_e)^2$, derived from the number of final states accessible to the emitted particles.
2. The Fermi function $F(Z', p)$, which accounts for the influence of the nuclear Coulomb field.

3. The nuclear matrix element $|M_{fi}|^2$, which accounts for the effects of particular initial and final nuclear states and which may include an additional electron and neutrino momentum dependence $S(p, q)$ from forbidden terms:

$$N(p) \propto p^2(Q - T_e)^2 F(Z', p)|M_{fi}|^2 S(p, q) \tag{9.26}$$

9.3 THE "CLASSICAL" EXPERIMENTAL TESTS OF THE FERMI THEORY

The Shape of the β Spectrum

In the allowed approximation, we can rewrite Equation 9.26 as

$$(Q - T_e) \propto \sqrt{\frac{N(p)}{p^2 F(Z', p)}} \tag{9.27}$$

and plotting $\sqrt{N(p)/p^2F(Z', p)}$ against T_e should give a straight line which intercepts the x axis at the decay energy Q. Such a plot is called a *Kurie plot* (sometimes a Fermi plot or a Fermi-Kurie plot). An example of a Kurie plot is shown in Figure 9.4. The linear nature of this plot gives us confidence in the theory as it has been developed, and also gives us a convenient way to determine the decay endpoint energy (and therefore the Q value).

In the case of forbidden decays, the standard Kurie plot does not give a straight line, but we can restore the linearity of the plot if we instead graph $\sqrt{N(p)/p^2F(Z', p)S(p, q)}$ against T_e, where S is the momentum dependence that results from the higher-order term in the expansion of the plane wave. The function S is known as the *shape factor*; for certain first-forbidden decays, for example, it is simply $p^2 + q^2$.

Including the shape factor gives a linear plot, as Figure 9.5 shows.

The Total Decay Rate

To find the total decay rate, we must integrate Equation 9.20 over all values of the electron momentum p, keeping the neutrino momentum at the value determined by Equation 9.22, which of course also depends on p. Thus, for allowed decays,

$$\lambda = \frac{g^2|M_{fi}|^2}{2\pi^3\hbar^7c^3}\int_0^{p_{max}} F(Z', p)p^2(Q - T_e)^2\,dp \tag{9.28}$$

The integral will ultimately depend only on Z' and on the maximum electron total energy E_0 (since $cp_{max} = \sqrt{E_0^2 - m_e^2c^4}$), and we therefore represent it as

$$f(Z', E_0) = \frac{1}{(m_ec)^3(m_ec^2)^2}\int_0^{p_{max}} F(Z', p)p^2(E_0 - E_e)^2\,dp \tag{9.29}$$

where the constants have been included to make f dimensionless. The function $f(Z', E_0)$ is known as the *Fermi integral* and has been tabulated for values of Z' and E_0.

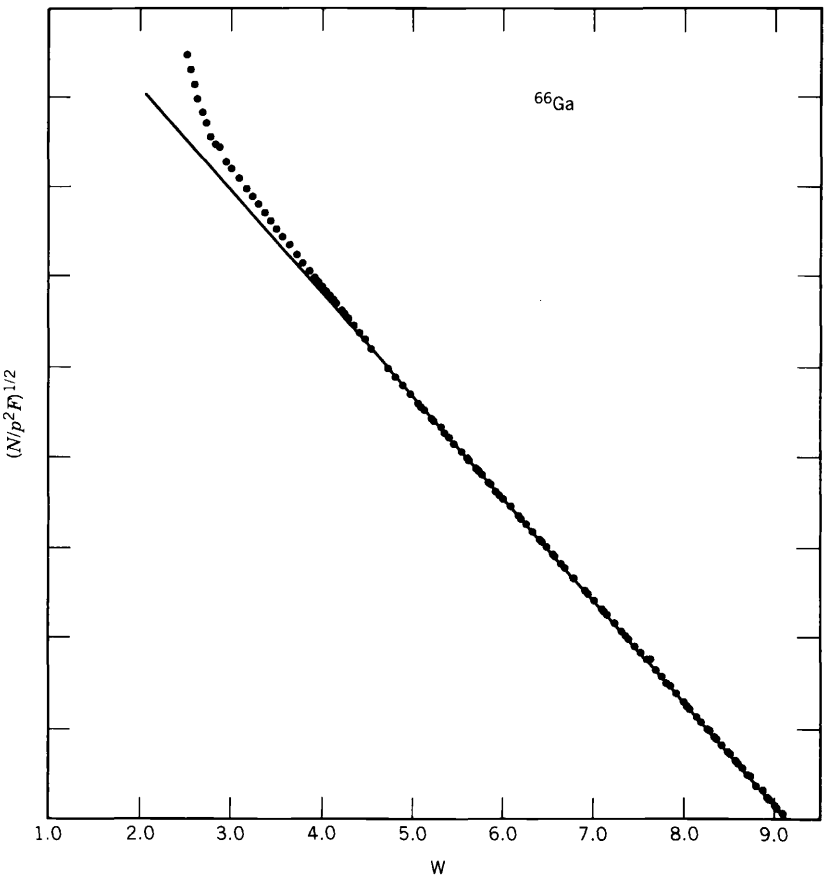


Figure 9.4 Fermi–Kurie plot of allowed $0^+ \rightarrow 0^+$ decay of ^{66}Ga. The horizontal scale is the relativistic *total* energy ($T_e + m_e c^2$) in units of $m_e c^2$. The deviation from the straight line at low energy arises from the scattering of low-energy electrons within the radioactive source. From D. C. Camp and L. M. Langer, *Phys. Rev.* **129**, 1782 (1963).

With $\lambda = 0.693/t_{1/2}$, we have

$$ft_{1/2} = 0.693 \frac{2\pi^3 \hbar^7}{g^2 m_e^5 c^4 |M_{fi}|^2} \tag{9.30}$$

The quantity on the left side of Equation 9.30 is called the *comparative half-life* or *ft value*. It gives us a way to compare the β-decay probabilities in different nuclei—Equation 9.28 shows that the decay rate depends on Z' and on E_0, and this dependence is incorporated into f, so that *differences in ft values must be due to differences in the nuclear matrix element* and thus to differences in the nuclear wave function.

As in the case of α decay, there is an enormous range of half-lives in β decay —ft values range from about 10^3 to 10^{20} s. For this reason, what is often quoted is the value of $\log_{10} ft$ (with t given in seconds). The decays with the shortest comparative half-lives ($\log ft \simeq 3$–4) are known as *superallowed* decays. Some of

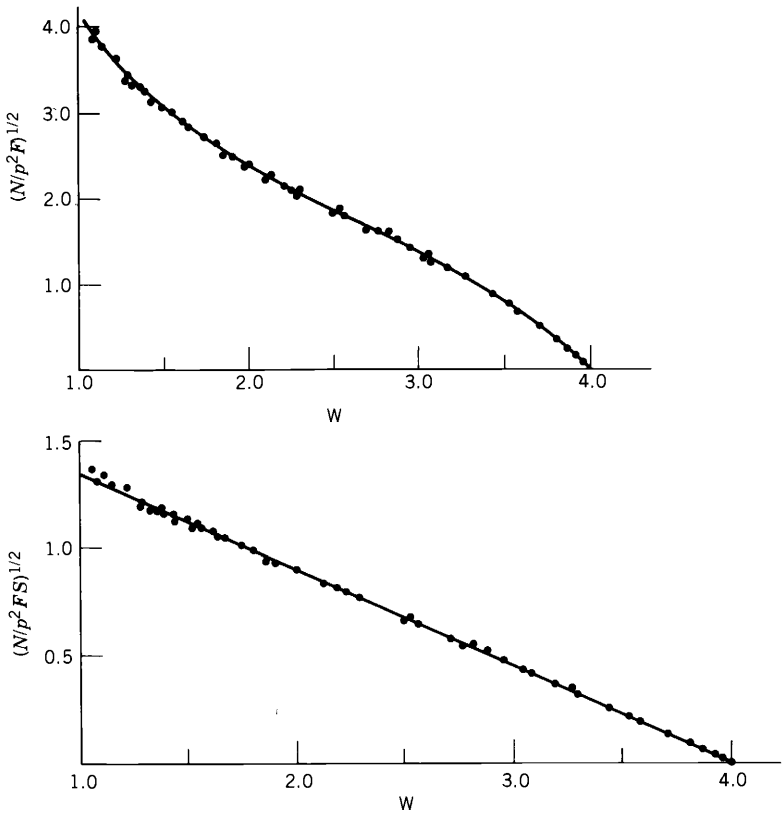


Figure 9.5 Uncorrected Fermi–Kurie plot in the β decay of ^{91}Y (top). The linearity is restored if the shape factor $S(p, q)$ is included; for this type of first-forbidden decay, the shape factor $p^2 + q^2$ gives a linear plot (bottom). Data from L. M. Langer and H. C. Price, *Phys. Rev.* **75**, 1109 (1949).

the superallowed decays have 0^+ initial and final states, in which case the nuclear matrix element can be calculated quite easily: $M_{\text{fi}} = \sqrt{2}$. The log ft values for $0^+ \rightarrow 0^+$ decays should all be identical. Table 9.2 shows the log ft values of all known $0^+ \rightarrow 0^+$ superallowed transitions, and within experimental error the values appear to be quite constant. Moreover, with $M_{\text{fi}} = \sqrt{2}$, we can use Equation 9.30 to find a value of the β-decay strength constant

$$g = 0.88 \times 10^{-4} \text{ MeV} \cdot \text{fm}^3$$

To make this constant more comparable to other fundamental constants, we should express it in a dimensionless form. We can then compare it with dimensionless constants of other interactions (the fine structure constant which characterizes the electromagnetic interaction, for instance). Letting M, L, and T represent, respectively, the dimensions of mass, length, and time, the dimensions of g are $M^1L^5T^{-2}$, and no combinations of the fundamental constants $\hbar$ (dimension $M^1L^2T^{-1}$) and c (dimension L^1T^{-1}) can be used to convert g into a dimensionless constant. (For instance, $\hbar c^3$ has dimension $M^1L^5T^{-5}$, and so $g/\hbar c^3$ has dimension T^3.) Let us therefore introduce an arbitrary mass m and

Table 9.2 *ft* Values for $0^+ \rightarrow 0^+$ Superallowed Decays

Decay	*ft* (s)
$^{10}C \rightarrow {}^{10}B$	3100 ± 31
$^{14}O \rightarrow {}^{14}N$	3092 ± 4
$^{18}Ne \rightarrow {}^{18}F$	3084 ± 76
$^{22}Mg \rightarrow {}^{22}Na$	3014 ± 78
$^{26}Al \rightarrow {}^{26}Mg$	3081 ± 4
$^{26}Si \rightarrow {}^{26}Al$	3052 ± 51
$^{30}S \rightarrow {}^{30}P$	3120 ± 82
$^{34}Cl \rightarrow {}^{34}S$	3087 ± 9
$^{34}Ar \rightarrow {}^{34}Cl$	3101 ± 20
$^{38}K \rightarrow {}^{38}Ar$	3102 ± 8
$^{38}Ca \rightarrow {}^{38}K$	3145 ± 138
$^{42}Sc \rightarrow {}^{42}Ca$	3091 ± 7
$^{42}Ti \rightarrow {}^{42}Sc$	3275 ± 1039
$^{46}V \rightarrow {}^{46}Ti$	3082 ± 13
$^{46}Cr \rightarrow {}^{46}V$	2834 ± 657
$^{50}Mn \rightarrow {}^{50}Cr$	3086 ± 8
$^{54}Co \rightarrow {}^{54}Fe$	3091 ± 5
$^{62}Ga \rightarrow {}^{62}Zn$	2549 ± 1280

try to choose the exponents i, j, and k so that $g/m^i\hbar^j c^k$ is dimensionless. A solution immediately follows with $i = -2$, $j = 3$, $k = -1$. Thus the desired ratio, indicated by G, is

$$G = \frac{g}{m^{-2}\hbar^3 c^{-1}} = g\frac{m^2 c}{\hbar^3} \tag{9.31}$$

There is no clear indication of what value to use for the mass in Equation 9.31. If we are concerned with the nucleon–nucleon interaction, it is appropriate to use the nucleon mass, in which case the resulting dimensionless strength constant is $G = 1.0 \times 10^{-5}$. The comparable constant describing the pion—nucleon interaction, denoted by g_π^2 in Chapter 4, is of order unity. We can therefore rank the four basic nucleon–nucleon interactions in order of strength:

pion-nucleon ("strong")	1
electromagnetic	10^{-2}
β decay ("weak")	10^{-5}
gravitational	10^{-39}

(The last entry follows from a similar conversion of the universal gravitational constant into dimensionless form also using the nucleon mass.) The β-decay interaction is one of a general class of phenomena known collectively as *weak interactions*, all of which are characterized by the strength parameter g. The Fermi theory is remarkably successful in describing these phenomena, to the extent that they are frequently discussed as examples of the *universal Fermi*

interaction. Nevertheless, the Fermi theory fails in several respects to account for some details of the weak interaction (details which are unimportant for the present discussion of β decay). A theory that describes the weak interaction in terms of exchanged particles (just as the strong nuclear force was described in Chapter 4) is more successful in explaining these properties. The recently discovered exchanged particles (with the unfortunate name *intermediate vector bosons*) are discussed in more detail in Chapter 18.

The Mass of the Neutrino

The Fermi theory is based on the *assumption* that the rest mass of the neutrino is zero. Superficially, it might seem that the neutrino rest mass would be a reasonably easy quantity to measure in order to verify this assumption. Looking back at Equations 9.1 and 9.2, or their equivalents for nuclei with $A > 1$, we immediately see a method to test the assumption. We can calculate the decay Q value (including a possible nonzero value of the neutrino mass) from Equation 9.6 or 9.9, and we can measure the Q value, as in Equation 9.8, from the maximum energy of the β particles. Comparison of these two values then permits a value for the neutrino mass to be deduced.

From this procedure we can conclude that the neutrino rest mass is smaller than about 1 keV/c^2, but we cannot extend far below that limit because the measured atomic masses used to compute Q have precisions of the order of keV, and the deduced endpoint energies also have experimental uncertainties of the order of keV. A superior method uses the shape of the β spectrum near the upper limit. If $m_\nu \neq 0$ then Equation 9.22 is no longer strictly valid. However, if $m_\nu c^2 \ll Q$, then over most of the observed β spectrum $E_\nu \gg m_\nu c^2$ and the neutrino can be treated in the extreme relativistic approximation $E_\nu \approx qc$. In this case, Equation 9.22 will be a very good approximation and the neutrino mass will have a negligible effect. Near the endpoint of the β spectrum, however, the neutrino energy approaches zero and at some point we would expect $E_\nu \sim m_\nu c^2$, in which case our previous calculation of the statistical factor for the spectrum shape is incorrect. Still closer to the endpoint, the neutrino kinetic energy becomes still smaller and we may begin to treat it nonrelativistically, so that $q^2 = 2m_\nu T_\nu$ and

$$N(p) \propto p^2\left[Q - \sqrt{p^2c^2 + m_e^2c^4} + m_e c^2\right]^{1/2} \tag{9.32}$$

which follows from a procedure similar to that used to obtain Equation 9.24, except that for $m_\nu > 0$ we must use $dq/dE_f = m_\nu/q$ in the nonrelativistic limit. Also,

$$N(T_e) \propto \left(T_e^2 + 2T_e m_e c^2\right)^{1/2}(Q - T_e)^{1/2}\left(T_e + m_e c^2\right) \tag{9.33}$$

The quantity in square brackets in Equations 9.32 and 9.24, which is just $(Q - T_e)$, vanishes at the endpoint. Thus at the endpoint $dN/dp \to 0$ if $m_\nu = 0$, while $dN/dp \to \infty$ if $m_\nu > 0$. That is, the momentum spectrum approaches the

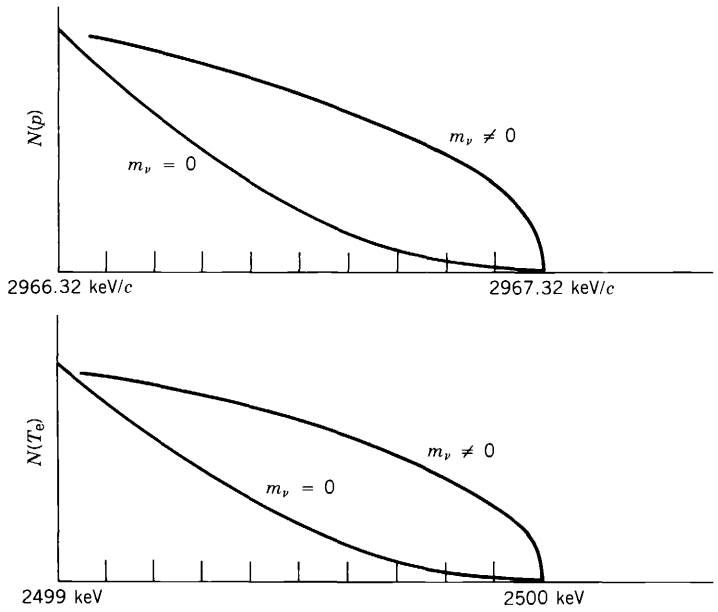


Figure 9.6 Expanded view of the upper 1-keV region of the momentum and energy spectra of Figure 9.2. The normalizations are arbitrary; what is significant is the difference in the shape of the spectra for $m_\nu = 0$ and $m_\nu \neq 0$. For $m_\nu = 0$, the slope goes to zero at the endpoint; for $m_\nu \neq 0$, the slope at the endpoint is infinite.

endpoint with zero slope for $m_\nu = 0$ and with infinite slope for $m_\nu > 0$. The slope of the energy spectrum, dN/dT_e, behaves identically. We can therefore study the limit on the neutrino mass by looking at the slope at the endpoint of the spectrum, as suggested by Figure 9.6. Unfortunately $N(p)$ and $N(T_e)$ also approach zero here, and we must study the slope of a continuously diminishing (and therefore statistically worsening) quantity of data.

The most attractive choice for an experimental measurement of this sort would be a decay with a small Q (so that the relative magnitude of the effect is larger) and one in which the atomic states before and after the decay are well understood, so that the important corrections for the influence of different atomic states can be calculated. (The effects of the atomic states are negligible in most β-decay experiments, but in this case in which we are searching for a very small effect, they become important.) The decay of ^{3}H (tritium) is an appropriate candidate under both criteria. Its Q value is relatively small (18.6 keV), and the one-electron atomic wave functions are well known. (In fact, the calculation of the state of the resulting ^{3}He ion is a standard problem in first-year quantum mechanics.) Figure 9.7 illustrates some of the more precise experimental results. Langer and Moffat originally reported an upper limit of $m_\nu c^2 < 200$ eV, while two decades later, Bergkvist reduced the limit to 60 eV. One recent result may indicate a nonzero mass with a probable value between 14 and 46 eV, while others suggest an upper limit of about 20 eV. Several experiments are currently being performed to resolve this question and possibly to reduce the upper limit.

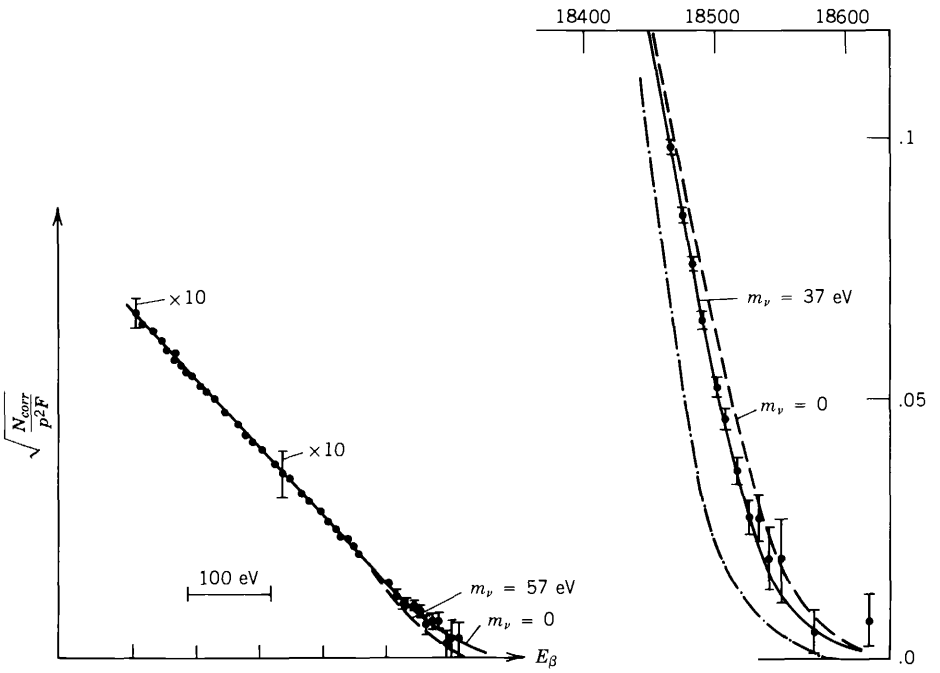


Figure 9.7 Experimental determination of the neutrino mass from the β decay of tritium (^{3}H). The data at left, from K.-E. Bergkvist, *Nucl. Phys. B* **39**, 317 (1972), are consistent with a mass of zero and indicate an upper limit of around 60 eV. The more recent data of V. A. Lubimov et al., *Phys. Lett. B* **94**, 266 (1980), seem to indicate a nonzero value of about 30 eV; however, these data are subject to corrections for instrumental resolution and atomic-state effects and may be consistent with a vanishing mass.

Why is so much effort expended to pursue these measurements? The neutrino mass has very important implications for two areas of physics that on the surface may seem to be unrelated. If the neutrinos have mass, then the "electroweak" theoretical formulism, which treats the weak and electromagnetic interactions as different aspects of the same basic force, permits electron-type neutrinos, those emitted in β decay, to convert into other types of neutrinos, called muon and τ neutrinos (see Chapter 18). This conversion may perhaps explain why the number of neutrinos we observe coming from the sun is only about one-third of what it is expected to be, based on current theories of solar fusion. At the other end of the scale, there seems to be more matter holding the universe together than we can observe with even the most powerful telescopes. This matter is nonluminous, meaning it is not observed to emit any sort of radiation. The Big Bang cosmology, which seems to explain nearly all of the observed astronomical phenomena, predicts that the present universe should be full of neutrinos from the early universe, with a present concentration of the order of $10^8/m^3$. If these neutrinos were massless, they could not supply the necessary gravitational attraction to "close" the universe (that is, to halt and reverse the expansion), but with rest masses as low as 5 eV, they would provide sufficient mass-energy density. The study of the neutrino mass thus has direct and immediate bearing not only on nuclear and particle physics, but on solar physics and cosmology as well.

9.4 ANGULAR MOMENTUM AND PARITY SELECTION RULES

Allowed Decays

In the allowed approximation, we replaced the electron and neutrino wave functions with their values at the origin; that is, we regard the electron and neutrino to have been created at $r = 0$. In this case they cannot carry any *orbital* angular momentum, and the only change in the angular momentum of the nucleus must result from the spins of the electron and neutrino, each of which has the value $s = \frac{1}{2}$. These two spins can be parallel (total $S = 1$) or antiparallel (total $S = 0$). If the spins are antiparallel (which is known as a *Fermi* decay) then in the allowed approximation ($\ell = 0$) there can be no change in the nuclear spin: $\Delta I = |I_i - I_f| = 0$. If the electron and neutrino spins are parallel (which is called a *Gamow-Teller* decay) in the allowed approximation, they carry a total angular momentum of 1 unit and thus I_i and I_f must be coupled through a vector of length 1: $\boldsymbol{I}_i = \boldsymbol{I}_f + \mathbf{1}$. This is possible only if $\Delta I = 0$ or 1 (except for $I_i = 0$ and $I_f = 0$, in which case only the Fermi transition can contribute).

If the electron and neutrino carry no orbital angular momentum, then the parities of the initial and final states must be identical since the parity associated with orbital angular momentum ℓ is $(-1)^\ell$.

We therefore have the following *selection rules* for *allowed β decay*:

$$\Delta I = 0, 1 \qquad \Delta\pi \text{ (parity change)} = \text{no}$$

Some examples of allowed β decay are

$^{14}O \rightarrow {}^{14}N^*$ This $0^+ \rightarrow 0^+$ decay to an excited state of ^{14}N must be pure Fermi type (because $0^+ \rightarrow 0^+$ decays cannot be accomplished through a Gamow-Teller decay, which must carry one unit of angular momentum). Other examples include $^{34}\text{Cl} \rightarrow {}^{34}\text{S}$ and $^{10}\text{C} \rightarrow {}^{10}\text{B}^*$, both of which are $0^+ \rightarrow 0^+$.

$^6He \rightarrow {}^6Li$ This decay is $0^+ \rightarrow 1^+$, which must be a pure Gamow-Teller transition. Other allowed pure Gamow-Teller decays include $^{13}\text{B} \rightarrow {}^{13}\text{C}$ ($\frac{3}{2}^- \rightarrow \frac{1}{2}^-$), $^{230}\text{Pa} \rightarrow {}^{230}\text{Th}^*$ ($2^- \rightarrow 3^-$), and $^{111}\text{Sn} \rightarrow {}^{111}\text{In}$ ($\frac{7}{2}^+ \rightarrow \frac{9}{2}^+$).

$n \rightarrow p$ In this case $\Delta I = 0$ ($\frac{1}{2}^+ \rightarrow \frac{1}{2}^+$), and so both the Fermi (F) and Gamow-Teller (GT) selection rules are satisfied. This is an example of a "mixed" F + GT transition, in which the exact proportions of F and GT are determined by the initial and final nuclear wave functions. It is convenient to define the ratio y of the Fermi and Gamow-Teller *amplitudes* (that is, matrix elements):

$$y = \frac{g_F M_F}{g_{GT} M_{GT}} \tag{9.34}$$

where M_F and M_{GT} are the actual Fermi and Gamow-Teller nuclear matrix elements. We allow for the possibility that the Fermi and Gamow-Teller strength constants may differ by defining g_F and g_{GT} as the constants analogous to the single constant g that appears in Equation 9.28. (In the decay rate, we should replace $g^2|M_{fi}|^2$ with $g_F^2|M_F|^2 + g_{GT}^2|M_{GT}|^2$.) We assume g_F to be identical to the value g deduced from the superallowed ($0^+ \rightarrow 0^+$) Fermi

decays. For neutron decay, the Fermi matrix element can be simply calculated: $|M_F| = 1$. Since the decay rate is proportional to $g_F^2 M_F^2(1 + y^{-2})$, the neutron decay rate permits a calculation of the ratio y, which yields the value 0.467 ± 0.003. That is, the decay is 82% Gamow-Teller and 18% Fermi.

In general, the initial and final nuclear wave functions make calculating M_F and M_{GT} a complicated and difficult process, but in one special group of decays the calculation is simplified. That group is the *mirror decays*, which we previously considered in Section 3.1. In decays such as ${}^{41}_{21}Sc_{20} \rightarrow {}^{41}_{20}Ca_{21}$, where the 21st proton becomes the 21st neutron, no change of wave function is involved. Except for minor differences due to the Coulomb interaction, the initial and final wave functions are identical, and the calculation of M_F and M_{GT} is easily done. For these nuclei, g_F and M_F have the same values as they do for the decay of the free neutron.

This result may seem somewhat surprising because in a nucleus, a nucleon does not behave at all like a free nucleon, primarily because of the cloud of mesons that surrounds a nucleon as it participates in exchange interactions with its neighbors. The hypothesis that Fermi interactions of nucleons in nuclei are unchanged by the surrounding mesons is called the *conserved vector current* (CVC) hypothesis. (The term "vector" refers to the transformation properties of the operator that causes the Fermi part of the decay; the Gamow-Teller part arises from an "axial vector" type of interaction.) The CVC hypothesis can be understood by analogy with the electromagnetic interaction. The electric charge is not changed by the transformation $p \leftrightarrow n + \pi^+$ which is part of the exchange interaction in which a proton may participate. Electric charge is conserved in this process and the Coulomb interaction is unchanged. (The electrons bound to the nucleus by Coulomb forces are unaware of the transformation.) On the other hand, magnetic interactions are substantially changed by $p \leftrightarrow n + \pi^+$, as we discussed when we considered shell-model magnetic moments in Section 5.1. In β decay, g_F (like electric charge) is unaffected by the surrounding mesons, while g_{GT} (like magnetic moments) may be affected by the meson cloud. In some nuclei, the change amounts to 20–30%. The matrix element M_{GT} also varies with the particular shell model state of the nucleon that makes the transition.

Table 9.3 Ratio of Fermi to Gamow-Teller Matrix Elements

	Decay	$y = g_F M_F / g_{GT} M_{GT}$	%F	%GT
Mirror	$n \rightarrow p$	0.467 ± 0.003	18	82
decays	${}^3H \rightarrow {}^3He$	0.479 ± 0.001	19	81
	${}^{13}N \rightarrow {}^{13}C$	1.779 ± 0.006	76	24
	${}^{21}Na \rightarrow {}^{21}Ne$	1.416 ± 0.012	67	33
	${}^{41}Sc \rightarrow {}^{41}Ca$	0.949 ± 0.003	47	53
Nonmirror	${}^{24}Na \rightarrow {}^{24}Mg$	-0.021 ± 0.007	0.044	99.956
decays	${}^{41}Ar \rightarrow {}^{41}K$	$+0.027 \pm 0.011$	0.073	99.927
	${}^{46}Sc \rightarrow {}^{46}Ti$	-0.023 ± 0.005	0.053	99.947
	${}^{52}Mn \rightarrow {}^{52}Cr$	-0.144 ± 0.006	2	98
	${}^{65}Ni \rightarrow {}^{65}Cu$	-0.002 ± 0.019	< 0.04	> 99.96

Table 9.3 shows a summary of values of the ratio y of the Fermi and Gamow-Teller amplitudes for some mirror nuclei, assuming the CVC hypothesis (g_F is unchanged from its value for neutron decay) and taking $|M_F| = 1$. These values are derived from decay rates.

For decays in which the initial and final wave functions are very different, the Fermi matrix element vanishes, and so measuring the ratio y for these decays is a way to test the purity of the wave functions. Table 9.3 includes some representative values of y for transitions in other than mirror nuclei. These values come from measuring the angular distribution of the β particles relative to a particular direction (similar to studies with α decays discussed in Chapter 8). You can see that the values are in general quite small, showing that the Fermi transitions are inhibited and thus that the wave functions are relatively pure.

Forbidden Decays

The designation of decays as "forbidden" is really somewhat of a misnomer. These decays are usually less probable than allowed decays (and have generally longer half-lives, as we discuss in the next section), but if the allowed matrix elements happen to vanish, then the forbidden decays are the only ones that can occur.

The most frequent occurrence of a forbidden decay is when the initial and final states have opposite parities, and thus the selection rule for allowed decay is violated. To accomplish the change in parity, the electron and neutrino must be emitted with an odd value of the orbital angular momentum relative to the nucleus. Let us consider, for example, a 1-MeV decay process. If the electron is given all the decay energy, its momentum is 1.4 MeV/c and the maximum angular momentum it can carry relative to the nucleus is $pR = 8.4$ MeV·fm/c taking $R = 6$ fm as a typical nuclear radius. In units of $\hbar$, this is equivalent to $pR/\hbar = 0.04$. Thus, while it is less likely to have $\ell = 1$ decays relative to $\ell = 0$, decays with $\ell = 3, 5, 7, \ldots$ are extremely unlikely, and we can for the moment consider only those forbidden decays with $\ell = 1$. These are called *first-forbidden* decays, and like the allowed decays they have Fermi types, with the electron and neutrino spins opposite ($S = 0$), and Gamow-Teller types, with the spins parallel ($S = 1$). The coupling of $S = 0$ with $\ell = 1$ for the Fermi decays gives total angular momentum of one unit carried by the beta decay, so that $\Delta I = 0$ or 1 (but not $0 \rightarrow 0$). Coupling $S = 1$ with $\ell = 1$ for the Gamow-Teller decays gives 0, 1, or 2 units of total angular momentum, so that $\Delta I = 0$, 1, or 2. Thus the *selection rules* for first-forbidden decays are

$$\Delta I = 0, 1, 2 \qquad \Delta\pi = \text{yes}$$

In contrast to the relative simplicity of allowed decays, there are six different matrix elements for first-forbidden decays, and the analysis of decay rates or angular distributions becomes very complicated. We will merely cite some of the many examples of first-forbidden decays:

$$^{17}\text{N} \rightarrow {}^{17}\text{O} \qquad (\tfrac{1}{2}^- \rightarrow \tfrac{5}{2}^+)$$

$$^{76}\text{Br} \rightarrow {}^{76}\text{Se} \qquad (1^- \rightarrow 0^+)$$

$$^{122}\text{Sb} \rightarrow {}^{122}\text{Sn}^* \qquad (2^- \rightarrow 2^+)$$

Transitions with $\Delta I \geq 2$, but with no change in parity, are permitted by neither the allowed nor the first-forbidden selection rules. For these transitions we must look to the $\ell = 2$ β emission, and consequently these are known as *second-forbidden* decays. When we couple $S = 0$ or 1 to $\ell = 2$, we can in principle change the nuclear spin by any amount from $\Delta I = 0$ to $\Delta I = 3$ (with certain exceptions, such as $0 \rightarrow 0$ and $\frac{1}{2} \rightarrow \frac{1}{2}$). The $\Delta I = 0$ and 1 cases fall within the selection rules for allowed decays, and we expect that the contribution of the second-forbidden terms to those decays will be negligible (perhaps 10^{-3} to 10^{-4} in angular distributions, and 10^{-6} to 10^{-8} in the spectrum shape). Excepting these cases, the selection rules for the second-forbidden decays are

$$\Delta I = 2,3 \qquad \Delta\pi = \text{no}$$

Examples of second-forbidden decays are

$$^{22}\text{Na} \rightarrow {}^{22}\text{Ne} \quad (3^+ \rightarrow 0^+)$$

$$^{137}\text{Cs} \rightarrow {}^{137}\text{Ba} \quad \left(\tfrac{7}{2}^+ \rightarrow \tfrac{3}{2}^+\right)$$

Continuing this process, we would find third-forbidden decays ($\ell = 3$), in which the selection rules not also satisfied by first-forbidden processes are $\Delta I = 3$ or 4 and $\Delta\pi = \text{yes}$:

$$^{87}\text{Rb} \rightarrow {}^{87}\text{Sr} \quad \left(\tfrac{3}{2}^- \rightarrow \tfrac{9}{2}^+\right)$$

$$^{40}\text{K} \rightarrow {}^{40}\text{Ca} \quad (4^- \rightarrow 0^+)$$

In very unusual circumstances, even fourth-forbidden decays ($\ell = 4$) may occur, with $\Delta I = 4$ or 5 and $\Delta\pi = \text{no}$:

$$^{115}\text{In} \rightarrow {}^{115}\text{Sn} \left(\tfrac{9}{2}^+ \rightarrow \tfrac{1}{2}^+\right)$$

We will learn in the next section that the higher the order of forbiddenness, the more unlikely is the decay. Given the chance, a nucleus prefers to decay by allowed or first-forbidden decays, and higher orders are generally too weak to observe. Only when no other decay mode is possible can we observe these extremely rare third- and fourth-forbidden decays.

9.5 COMPARATIVE HALF-LIVES AND FORBIDDEN DECAYS

Beta-decay half-lives encompass an enormous range, from the order of milliseconds to about 10^{16} years. Part of this variation must be due to the poor match-up of the initial and final nuclear wave functions, but it is hard to imagine that nuclear wave functions are so purely one configuration or another that this effect can account for any but a relatively small part of this variation over 26 orders of magnitude.

The true source of the variation in half-lives is the relative difficulty of creating a β particle and a neutrino in an angular momentum state with $\ell > 0$. As we found in the previous section, a typical (classical) angular momentum for a 1-MeV β particle has a maximum value of the order of $\ell \sim 0.04\hbar$. That is, the probability is very small for the electron and neutrino to be emitted in a state with quantum number $\ell > 0$.

We can make this qualitative estimate more quantitative by considering the wave functions of the electron and neutrino, which are taken to be of the form of plane waves, $e^{i\boldsymbol{p}\cdot\boldsymbol{r}/\hbar}$. Expanding the exponential gives $1 + (i\boldsymbol{p} \cdot \boldsymbol{r})/\hbar + \frac{1}{2}[(i\boldsymbol{p} \cdot \boldsymbol{r})/\hbar]^2 + \cdots$. The first term (after sandwiching between the initial and final nuclear wave functions and including the appropriate spin terms) is responsible for *allowed* decays. In the event that the nuclear wave functions cause this term to vanish (they may be of opposite parity, for instance) then we must go to the next term, in which the nuclear part (excepting the spin) is $\int \psi_f^* \boldsymbol{r} \psi_i \, dv$. Such terms are responsible for the *first-forbidden* decays. The average value of $\boldsymbol{p} \cdot \boldsymbol{r}/\hbar$, integrated over the nuclear volume, is of order 0.01, as we found above. The transition probability is proportional to the square of the integral, and so the probability for first-forbidden decays is only about 10^{-4} that for allowed decays.

The integral also vanishes unless the initial and final states have opposite parities, which can be shown, for example, by writing $\boldsymbol{r}$ in terms of $Y_1(\theta, \phi)$. This gives again the selection rule $\Delta\pi$ = yes for first-forbidden decays, as discussed in the previous section.

Each succeeding term in the expansion of the exponential form of the plane wave gives a higher order of forbiddenness, and each gives a transition probability smaller than that of the previous term by a factor of the order of $(\boldsymbol{p} \cdot \boldsymbol{r}/\hbar)^2$, or about 10^{-4}.

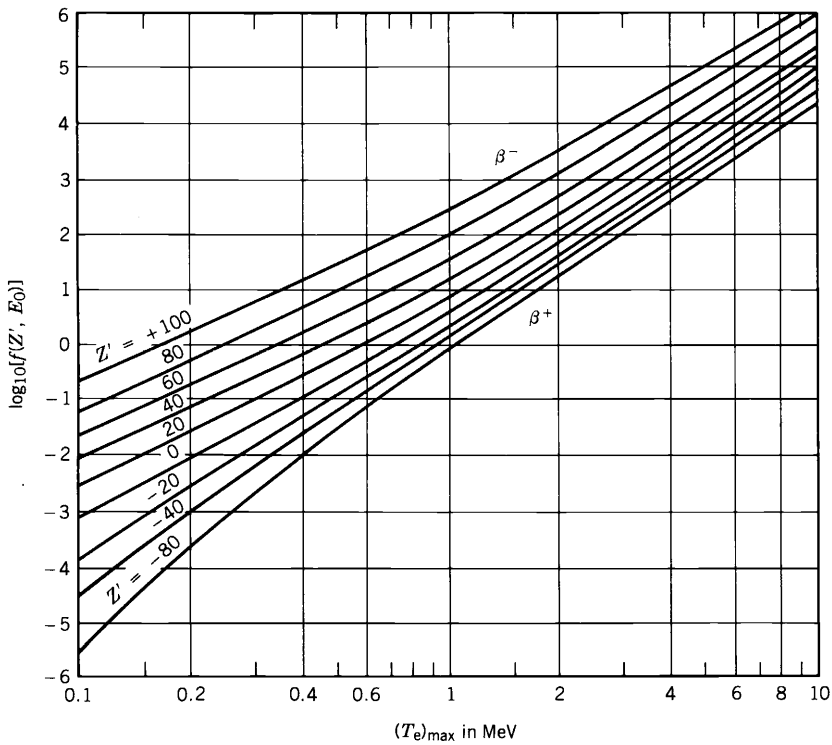


Figure 9.8 The Fermi integral, defined by Equation 9.29. The atomic number Z' refers to the daughter nucleus; the curves for positive Z' are for β^- decay, while negative Z' is for β^+ decay. From R. D. Evans, *The Atomic Nucleus* (New York: McGraw-Hill, 1955).

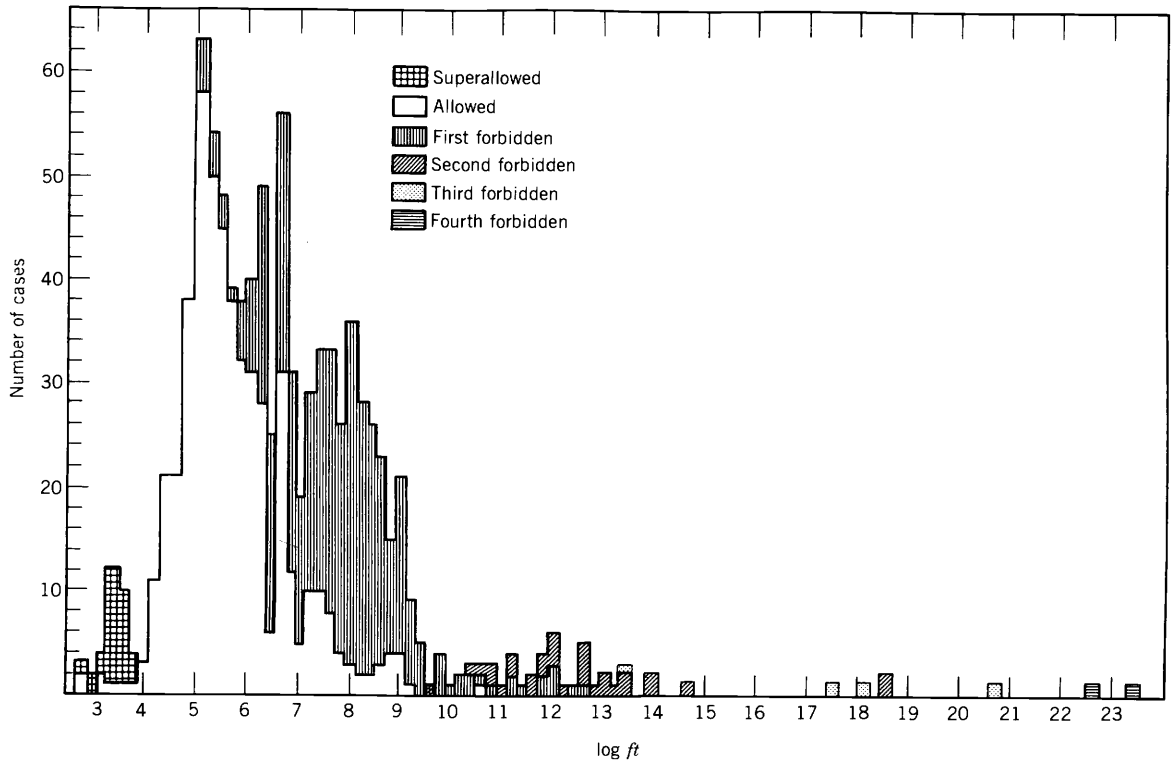


Figure 9.9 Systematics of experimental log *ft* values. From W. Meyerhof, *Elements of Nuclear Physics* (New York: McGraw-Hill, 1967).

To compare the half-lives of different β transitions, we must first correct for the variation in the β decay probability that results from differences in the daughter atomic number Z' or in the endpoint energy E_0. This is done through the *Fermi integral function* $f(Z', E_0)$, which was defined in Section 9.3. If we know the *partial* half-life for a certain decay process, we can find $f(Z', E_0)$ from curves such as those of Figure 9.8. The product $ft_{1/2}$ is the *comparative half-life* or ft value, which is usually given as $\log_{10} ft$, where $t_{1/2}$ is always in seconds.

As an example, we consider the β^- decay of ^{203}Hg. The half-life is 46.8 days, so $\log_{10} t_{1/2} = 6.6$. The Q value for the decay to ^{203}Tl is 0.491 MeV. However, essentially 100% of the decay goes to the 279-keV excited state of ^{203}Tl, and so the β endpoint energy will be $0.491 - 0.279 = 0.212$ MeV. From Figure 9.8 we estimate $\log_{10} f = -0.1$, and thus

$$\log_{10} ft = \log_{10} f + \log_{10} t_{1/2} = -0.1 + 6.6 = 6.5$$

For a second example, we take the β^+ decay of ^{22}Na to the ground state of ^{22}Ne ($Z' = 10$). The half-life is 2.60 years but the branching ratio to the ground state is only 0.06%. Thus the partial half-life is 2.60 years$/6 \times 10^{-4}$, so that $\log_{10} t_{1/2} = 11.1$. The Q value for β^+ decay is 1.8 MeV, so from Figure 9.8 we estimate $\log_{10} f = 1.6$, and $\log_{10} ft = 11.1 + 1.6 = 12.7$.

In compilations of nuclear decay information, the $\log ft$ values are given directly. We can determine the type of decay (allowed, nth-forbidden) based on the angular momentum and parity selection rules, and we can then try to relate the experimental $\log ft$ values with the order of forbiddenness. Figure 9.9 summarizes the experimental values of $\log ft$ for different types of decays, and you can see that there is indeed an effect of the order we estimated—each additional degree of forbiddenness increases the $\log ft$ value by about 3.5, representing a reduction in the transition probability by 3×10^{-4}. (There is also a great deal of scatter within each type of decay, a large part of which is probably due to the effects of the particular initial and final nuclear wave functions.)

Most allowed decays have $\log ft$ values in the range 3.5 to 7.5, and first-forbidden decays generally fall in the range 6.0 to 9.0. There are relatively fewer known second-forbidden decays, which have $\log ft$ values from about 10 to 13, and the third-forbidden decays (four cases) range from about 14 to 20. There are two known fourth-forbidden decays, with $\log ft$ about 23.

The value of summaries of this kind of information is in their *predictive ability*; for example, if we are studying a previously unknown decay scheme for which we measure $\log ft = 5.0$, the decay is most probably of the allowed type, which permits us to assign the initial and final states the same parity and to conclude that their spins differ by at most one unit. We shall see the value of such deductions when we discuss β spectroscopy in Section 9.10.

9.6 NEUTRINO PHYSICS

A process closely related to β decay is capture of a neutrino (or an antineutrino) by a nucleon:

$$\bar{\nu} + \mathrm{p} \rightarrow \mathrm{n} + \mathrm{e}^+$$
$$\nu + \mathrm{n} \rightarrow \mathrm{p} + \mathrm{e}^-$$

which sometimes is called *inverse β decay*.

Let's first discuss why only these processes occur and not others such as capture of a neutrino by a proton or of an antineutrino by a neutron. Electrons and neutrinos belong to a class of particles called *leptons*; the antiparticles e^+ and $\bar{\nu}$ are *antileptons*. Based on observations of many processes and failure to observe certain others, the *law of lepton conservation* is deduced: the total number of leptons minus antileptons on each side of a decay or reaction process must be the same. Many sensitive searches have been made to find violations of this law, but none have yet been found. The reaction $\nu + p \rightarrow n + e^+$, which conserves electric charge and nucleon number, does not conserve lepton number and is therefore, according to our present understanding of fundamental processes, absolutely forbidden.

The failure to observe such reactions is in fact one of our best indicators that ν and $\bar{\nu}$ are really different particles. The electron and positron differ in the sign of their electric charge (and in properties that depend on electric charge, such as magnetic moment). But ν and $\bar{\nu}$ are uncharged (and as uncharged point particles, have vanishing magnetic moments). They are thus immune from the electromagnetic interaction, which is often used to distinguish particles from antiparticles.

As we discussed in Section 9.1, the existence of the neutrino was inferred from the failure of β decay to conform to the well-established conservation laws of energy and momentum conservation. Direct observation of the neutrinos did not occur until 25 years following Pauli's original proposal. To understand the difficulty of catching the elusive neutrino, we can try to estimate the probability for the basic neutrino capture reaction. Let us, in analogy with Equation 4.27, define the cross section for the reaction $\bar{\nu} + p \rightarrow n + e^+$ as

$$\sigma = \frac{\text{probability per target atom for the reaction to occur}}{\text{incident flux of } \bar{\nu}} \tag{9.35}$$

The reaction probability can be calculated using Fermi's Golden Rule, as in Equation 9.12. For the matrix element V_{fi} we can take $(1/V)gM_{fi}$, as we did in the calculation based on the allowed approximation leading to Equation 9.20. Neglecting the recoil of the neutron, the density of final states comes only from the electron and is given by Equation 9.15. Finally, we can adapt the form of Equation 4.26 for the incident flux of $\bar{\nu}$, using the plane wave form of Equation 9.18 and recalling that the quantity $\hbar k/m$ came from the velocity of the incident particle, which is c for neutrinos. The resulting cross section is thus

$$\sigma = \frac{\dfrac{2\pi}{\hbar}\dfrac{g^2}{V^2}|M_{fi}|^2\dfrac{4\pi p^2\,dp\,V}{h^3\,dE}}{c/V} \tag{9.36}$$

Using $dp/dE = E/c^2p$ gives

$$\sigma = \frac{2\pi}{\hbar c}g^2|M_{fi}|^2\frac{4\pi pE}{c^2h^3} \tag{9.37}$$

To make a numerical estimate, let us use the nuclear matrix element we found for the case of neutron β decay in Section 9.4, $g^2|M_{fi}|^2 = g_F^2(1 + y^{-2}) \simeq 5.6g_F^2$; for g_F we take the value deduced from the superallowed β decays. We choose an incident antineutrino energy of 2.5 MeV, somewhat above the minimum energy of 1.8 MeV needed to initiate the reaction (because $m_pc^2 < m_nc^2$, we must

supply the additional needed mass energy through the incident antineutrino), and thus the electron energy is 1.21 MeV. Putting in all of the numerical factors, the resulting cross section is 1.2×10^{-19} b $= 1.2 \times 10^{-43}$ cm^2. We can appreciate this incredibly small cross section (compare with the low-energy nucleon–nucleon scattering cross section of 20 b!) by evaluating the probability for a neutrino to be captured in passing through a typical solid, which contains of the order of 10^{24} protons per cm^3. The neutrino has a reaction cross section of about 10^{-43} cm^2 for each proton it encounters, and in passing through 1 cm^3 of material a neutrino will encounter about 10^{24} protons. The net reaction probability is $(10^{-43}\ \text{cm}^2)(10^{24}\ \text{cm}^{-3}) = 10^{-19}\ \text{cm}^{-1}$; that is, the reaction probability is about 10^{-19} for each cm of material through which the neutrino passes. To have a reasonable probability to be captured, the neutrino must pass through about 10^{19} cm of material, or about 10 light-years. No wonder it took 25 years to find one!

The actual experimental detection was done through an ingenious and painstaking series of experiments carried out in the 1950s by Reines and Cowan. As a source of $\bar{\nu}$ they used a nuclear reactor, since the neutron-rich fission products undergo negative β decay and consequently emit $\bar{\nu}$. The average emission rate is about 6 $\bar{\nu}$ per fission, and the net flux of $\bar{\nu}$ was about 10^{13} per cm^2 per second. For their neutrino detector, Reines and Cowan used a liquid scintillator (rich in free protons) into which a Cd compound had been introduced. The capture of $\bar{\nu}$ by a proton gives a neutron and a positron; the positron quickly annihilates ($e^- + e^+ \rightarrow 2\gamma$) in the scintillator and gives a flash of light. The neutron travels through the solution and is gradually slowed, until finally it is captured by a Cd nucleus, which has a large neutron-capture cross section. Following the neutron capture, ^{114}Cd is left in a highly excited state, which quickly emits a 9.1-MeV γ ray. The characteristic signal of a $\bar{\nu}$ is thus a light signal from the positron annihilation radiation (0.511-MeV photons) followed about 10 μs later (the time necessary for the neutron to be slowed and captured) by the 9.1-MeV neutron capture γ ray. Using a tank containing of the order of 10^6 cm^3 of scintillator, Reines and Cowan observed a few events per hour that were candidates for $\bar{\nu}$ captures. To determine conclusively that these were indeed $\bar{\nu}$ captures, many additional experiments were necessary, following which the conclusion was inescapable—the $\bar{\nu}$ is a real particle, and not just a figment of Pauli's and Fermi's fertile imaginations.

To demonstrate that $\bar{\nu}$ capture by *neutrons* is not possible, a related experiment was done by Davis and co-workers. They used a large tank of CCl_4 in an attempt to observe $\bar{\nu} + {}^{37}\text{Cl} \rightarrow e^- + {}^{37}\text{Ar}$, again with reactor antineutrons. By purging the tank periodically and searching for the presence of radioactive ^{37}Ar in the removed gas, Davis was able to conclude that the reaction was not observed, indicating that ν and $\bar{\nu}$ are in fact different particles.

We are thus resolved to the fact that ν and $\bar{\nu}$ are different particles, but we have not yet specified just what is the fundamental property that distinguishes ν from $\bar{\nu}$. Experimentally, there is one property: all $\bar{\nu}$ have their spin vectors parallel to their momentum vectors, while all ν have spin opposite to momentum. This property is called the *helicity* and is defined to be

$$h = \frac{\boldsymbol{s} \cdot \boldsymbol{p}}{|\boldsymbol{s} \cdot \boldsymbol{p}|} \tag{9.38}$$

which has the value of $+1$ for $\bar{\nu}$ and -1 for ν. (It is often said that $\bar{\nu}$ is "right-handed" and ν is "left-handed" because the precession of s about p traces out a pattern analogous to the threads of a right-handed screw for $\bar{\nu}$ and of a left-handed screw for ν.) Electrons from β decay have a similar property, with $h = -v/c$ for e^- and $h = +v/c$ for e^+, but this is not an intrinsic property of all e^+ and e^-, only those emitted in β decay. Electrons in atoms have no definite helicities, nor do positrons that originate from pair production ($\gamma \rightarrow e^+ + e^-$). *All* ν and $\bar{\nu}$, however, have definite helicities, right-handed for $\bar{\nu}$ and left-handed for ν.

Davis has used a similar technique to observe ν emitted by the sun as a result of fusion processes. (Fusion of light nuclei tends to produce neutron-deficient products, which undergo β^+ decay and thus emit ν rather than $\bar{\nu}$.) To shield against events produced by cosmic rays (a problem in his earlier experiments), Davis has placed his CCl_4 tank at the bottom of a 1500-m deep mine, and has spent more than 10 years counting these solar neutrinos. These are especially important because they come to us directly from the core of the sun, where the nuclear reactions occur; the light we see, on the other hand, comes from the sun's surface and contains relatively little direct information about processes that are now going on in the core.) The expected rate of conversion of ^{37}Cl to ^{37}Ar by solar neutrinos in Davis' tank is about *one atom per day*; yet despite years of heroic efforts, the observed rate is only about one-third of the expected value, which represents either an error in the assumptions made regarding the rate of neutrino emission by the sun (and thus a shortcoming of our present theory of solar processes) or an error in our present theories of properties of the neutrino.

9.7 DOUBLE-β DECAY

Consider the decay of ^{48}Ca (Figure 9.10). The Q value for β^- decay to ^{48}Sc is 0.281 MeV, but the only ^{48}Sc states accessible to the decay would be the 4^+, 5^+, and 6^+ states, which would require either fourth- or sixth-forbidden decays. If we take our previous empirical estimate of $\log ft \sim 23$ for fourth-forbidden decays, then (with $\log f \simeq -2$ from Figure 9.8) we estimate $\log t \sim 25$ or $t_{1/2} \sim 10^{25}$ s (10^{18} y). It is thus not surprising that we should regard ^{48}Ca as a "stable" nucleus.

An alternative possible decay is the *double-β* ($\beta\beta$) *decay* $^{48}Ca \rightarrow {}^{48}Ti + 2e^- + 2\bar{\nu}$. This is a direct process, which does not require the ^{48}Sc intermediate state. (In fact, as we shall discuss, in most of the possible $\beta\beta$ decays, the intermediate state is of greater energy then the initial state and is energetically impossible to reach.) The advantage of this process over the single β decay (in this case) is the $0^+ \rightarrow 0^+$ nature of the transition, which would place it in the superallowed, rather than the fourth-forbidden, category.

We can make a rough estimate of the probability for such decay by rewriting Equation 9.30 for single-β decay as

$$\lambda_\beta = \left(\frac{m_e c^2}{\hbar}\right)\left\{fg^2\frac{m_e^4 c^2 |M_{fi}|^2}{2\pi^3\hbar^6}\right\} \tag{9.39}$$

The first term has a value of approximately 0.8×10^{21} s^{-1} and can be considered

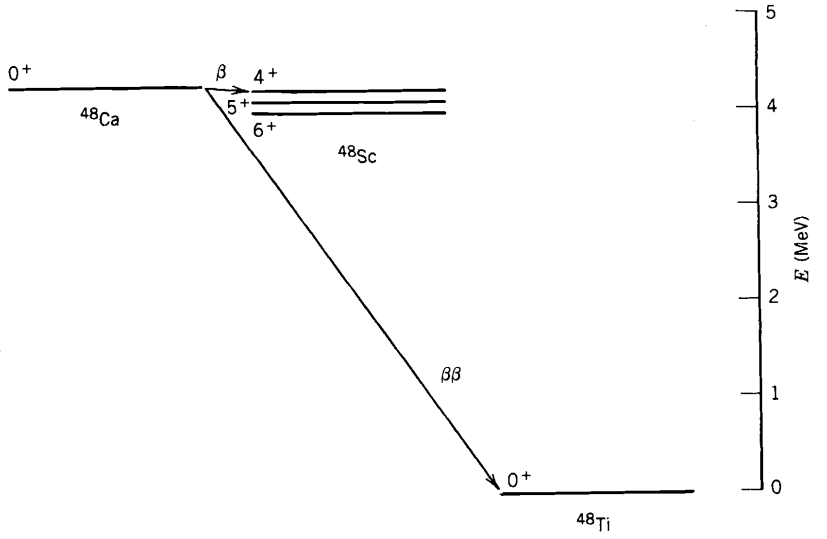


Figure 9.10 The decay of ^{48}Ca. The superallowed $\beta\beta$ decay to ^{48}Ti is an alternative to the fourth-forbidden single-β decay to ^{48}Sc.

the dimensional scaling factor. The remaining term is dimensionless and contains all of the information on the β decay and nuclear transition probabilities. It has a value of $1.5 \times 10^{-25}\, f$ (using $|M_{fi}| = \sqrt{2}$).

The decay rate for $\beta\beta$ decay then ought to be approximately given by

$$\lambda_{\beta\beta} = \left(\frac{m_e c^2}{\hbar}\right)\left\{ fg^2 \frac{m_e^4 c^2 |M_{fi}|^2}{2\pi^3 \hbar^6} \right\}^2 \tag{9.40}$$

which gives a half-life of the order of 10^{17} years, comparable with the value for single-β decay (although this simple calculation should not be taken too seriously).

Double-beta decay can also occur in cases in which the intermediate state cannot be reached by the single decay mode. Consider the case of ^{128}Te, shown in Figure 9.11. The decay ^{128}Te $\rightarrow$ ^{128}I has a *negative* Q value of -1.26 MeV, and is therefore not possible. Yet the $\beta\beta$ decay ^{128}Te $\rightarrow$ ^{128}Xe is energetically possible, with $Q = 0.87$ MeV. In fact, such situations provide the most likely candidates

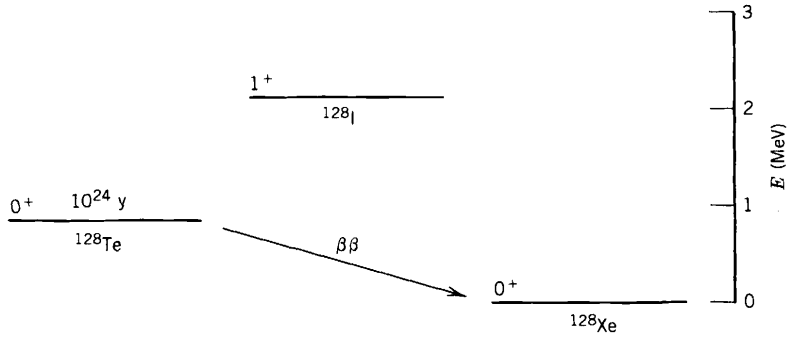


Figure 9.11 Single-β decay of ^{128}Te is energetically forbidden, but $\beta\beta$ decay to ^{128}Xe is possible. See Figure 3.18 to understand the relative masses of these nuclei.

for observing $\beta\beta$ decays because we do *not* want to study the case of two successive decays through an energetically accessible intermediate state.

There are two basic approaches to the observation of $\beta\beta$ decay. The first is the mass spectroscopic method, in which we search for the stable daughter nuclei in minerals of known geological age. If, for example, we were to find an excess abundance of ^{128}Xe (relative to its abundance in atmospheric Xe, for example) in a tellurium-bearing rock, we could deduce an estimate for the $\beta\beta$-decay half-life of ^{128}Te to ^{128}Xe. Making the reasonable assumption that the $\beta\beta$-decay half-life is long compared with the age T of the rock, the number of Xe resulting from the $\beta\beta$ decay is

$$N_{\text{Xe}} = N_{\text{Te}}(1 - e^{-\lambda T}) \cong N_{\text{Te}}\frac{0.693T}{t_{1/2}} \tag{9.41}$$

and so

$$t_{1/2} \cong 0.693T\frac{N_{\text{Te}}}{N_{\text{Xe}}} \tag{9.42}$$

The number of Te and Xe nuclei can be determined using mass spectroscopic techniques, and thus the $\beta\beta$-decay half-life may be found. Some typical values obtained using this method are

$$^{128}\text{Te} \rightarrow {}^{128}\text{Xe} \qquad (3.5 \pm 1.0) \times 10^{24}\ \text{y}$$

$$^{130}\text{Te} \rightarrow {}^{130}\text{Xe} \qquad (2.2 \pm 0.6) \times 10^{21}\ \text{y}$$

$$^{82}\text{Se} \rightarrow {}^{82}\text{Kr} \qquad (1.7 \pm 0.3) \times 10^{20}\ \text{y}$$

The direct detection of $\beta\beta$ decay is obviously frustrated by the long half-lives —from one mole of sample, we would expect of the order of one decay per year in the worst case above and one per day in the best case. Experiments with such low count rates always suffer from spurious background counts, such as those from natural radioactivity or cosmic rays, and shielding against these unwanted counts severely taxes the skill of the experimenter. For example, one experiment was done under 4000 m of rock in a tunnel under Mont Blanc on the border between France and Italy!

A recent experiment reported by Moe and Lowenthal used strips of ^{82}Se in a cloud chamber to search for evidence of $\beta\beta$ decays. Figure 9.12 shows examples of a typical event in which two electrons were emitted. Also shown for comparison is another event in which an α particle track originates from the same location as the two electrons; this event probably results from the natural radioactive background, most likely from the decay of ^{214}Bi in the uranium series. A more sensitive search for $\beta\beta$ events by Elliott, Hahn, and Moe, reported in *Phys. Rev. Lett.* **56**, 2582 (1986), showed approximately 30 events possibly associated with $\beta\beta$ decays in more than 3000 h of measuring time. The deduced lower limit on the $\beta\beta$ half-life is 1.0×10^{20} y, in agreement with the geochemical result listed above.

Although the direct method is exceedingly difficult and subject to many possible systematic uncertainties, it is extremely important to pursue these studies because they are sensitive to the critical question of *lepton conservation* (which we

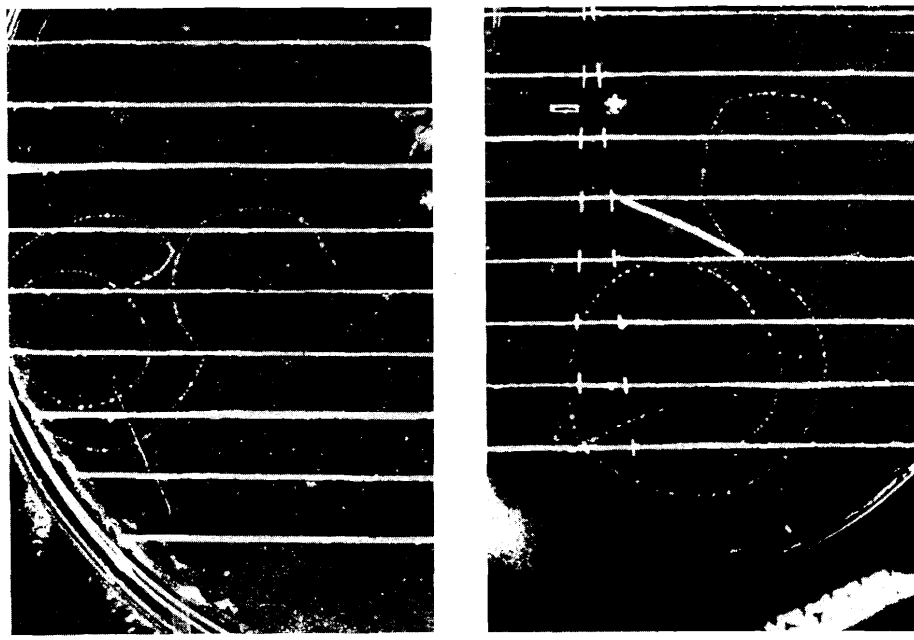


Figure 9.12 Cloud chamber photograph of a suspected $\beta\beta$-decay event from ^{82}Se. The horizontal lines are strips of ^{82}Se source material. The $\beta\beta$-decay event is the pair of curved tracks originating from one of the strips in the exact center of the photograph at left. There are also background events due to natural radioactivity; these produce two β-decay electrons in succession (as in the natural radioactive chain of decays, Figure 6.10) and an α particle. Note the two electron tracks and the heavy α track originating from a common point near the center of the photograph on the right. A magnetic field perpendicular to the plane of the photos curves the tracks, so that the electron momentum can be deduced. From M. K. Moe and D. D. Lowenthal, *Phys. Rev. C* **22**, 2186 (1980).

discuss in greater detail in Chapter 18). If ν and $\bar{\nu}$ are not really distinct particles (that is, if they are coupled together or are linear combinations of yet other fundamental particles), then "neutrinoless" $\beta\beta$ decay would be possible:

$$ {}^{A}_{Z}\mathrm{X}_{N} \rightarrow {}^{A}_{Z+2}\mathrm{X}''_{N-2} + 2\mathrm{e}^{-} $$

(In essence, we can think of this process as follows: the first β decay proceeds through the virtual and energetically inaccessible intermediate state ${}^{A}_{Z+1}\mathrm{X}'_{N-1}$. The emitted $\bar{\nu}$ turns into a ν and is reabsorbed by the virtual intermediate state giving $\nu + {}^{A}_{Z+1}\mathrm{X}'_{N-1} \rightarrow \mathrm{e}^{-} + {}^{A}_{Z+2}\mathrm{X}''_{N-2}$. The net process therefore results in the emission of two β's and no ν's.)

An experiment designed to search for neutrinoless $\beta\beta$ decay has been done in the case of ^{76}Ge. Here a Ge detector is used both as the source of the decaying nuclei and as the detector of the decays. The total available decay energy is 2.04 MeV, and if the two electrons stop within the detector, it should record a single event with an energy of 2.04 MeV. The difficulty here is to reduce the background (from natural radioactivity, man-made radioactive contaminants, and cosmic rays) to a low enough level so that the 2.04-MeV region can be searched for a

peak. The Mont Blanc experiment mentioned above was of this type and obtained a lower limit on the half-life of 5×10^{21} y. In another underground experiment, reported recently by Avignone et al., *Phys. Rev. C* **34**, 666 (1986), extraordinary measures were taken to surround the detector only with material that would not contribute substantially to the background (stainless steel screws, which showed contamination from ^{60}Co, were replaced with brass, and rubber O-rings were replaced with indium). After 9 months of counting, there was no visible peak at 2.04 MeV, and the half-life was deduced to be greater than 10^{23} y. These experiments are continuing, in the hope that continued improvements in sensitivity will enable both the two-neutrino and the neutrinoless $\beta\beta$ decays to be observed directly.

Although the theoretical interpretations are difficult, it may be that the search for evidence of neutrinoless $\beta\beta$ decay will be an important source of information on the fundamental character of the neutrinos. The emission-reabsorption process described above, for instance, is impossible for massless neutrinos with definite helicities (± 1), and so the observation of the neutrinoless $\beta\beta$ decay would immediately suggest that the "classical" properties of the neutrino are not correct.

9.8 BETA-DELAYED NUCLEON EMISSION

Gamma rays are not the only form of radiation that can be emitted from nuclear *excited* states that are populated following β decay. Occasionally the states are unstable against the emission of one or more nucleons. The nucleon emission itself occurs rapidly (so that it competes with γ emission), and thus overall the nucleon emission occurs with a half-life characteristic of the β decay.

For decays of nuclei only one or two places from the most stable isobar of each mass number A, the decay energies are small (1–2 MeV), and nucleon emission is forbidden by energetics. Far from the stable nuclei, the decay energies may become large enough to populate highly excited states, which may then decay through nucleon emission. A schematic diagram of this process for proton emission is shown in Figure 9.13. The original β-decaying parent is called the *precursor*; the nucleons themselves come from the *emitter* and eventually lead to states in the *daughter*.

Interest in delayed nucleon emission has increased in recent years in concert with experimental studies of nuclei far from stability. Additional interest comes from the importance of delayed neutrons in the control of nuclear reactors (see Chapter 13). However, the discovery of the phenomenon dates from the early history of nuclear physics—Rutherford in 1916 reported "long-range alpha particles" following the β decay of ^{212}Bi. The main branch in this β decay goes to the ground state of ^{212}Po, which in turn emits α particles with an energy of 8.784 MeV. (Since the α-decaying state is a 0^+ ground state of an even-even nucleus, the decay proceeds virtually 100% to the ground state of ^{208}Pb.) A small number of α's, however, were observed with *higher* energies (9.495 MeV, 0.0035%; 10.422 MeV, 0.0020%; 10.543 MeV, 0.017%). Lower energies would have indicated decays *to* excited states of ^{208}Pb, but higher energies must indicate decays *from* excited states of ^{212}Po. Similar behavior was observed in the decay of ^{214}Bi.

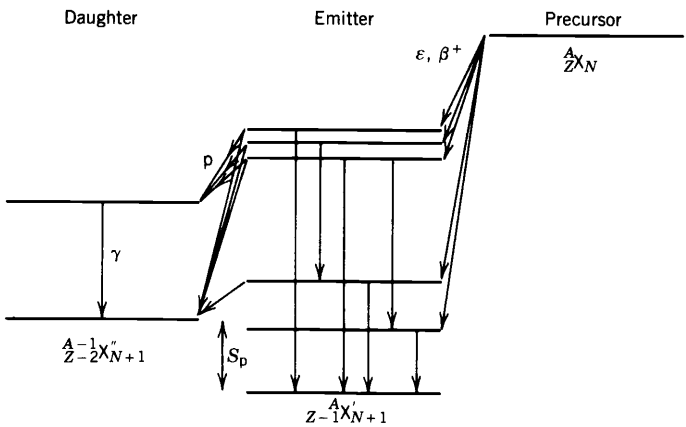


Figure 9.13 Schematic of β-delayed nucleon emission. The β decay of the precursor populates highly excited states in the emitter that are unstable with respect to nucleon emission. Note that the energy of the excited state in the emitter equals the sum of the energy of the emitted nucleon plus the nucleon separation energy between X′ and X″ (plus the small correction for the recoil of the emitting nucleus).

The calculation of the energy spectra of the emitted nucleons is a complicated process, requiring knowledge of the spectrum of excited states in the emitter, the probabilities for β decay from the precursor to each state of the emitter, and the probabilities of nucleon decay for each state of the emitter to the accessible states of the daughter. The difficulty is compounded in heavy nuclei by the large density of excited states—the average spacing between excited states at high energy may be of order eV, far smaller than our ability to resolve individual proton or neutron groups; thus all we observe in such cases is a broad distribution, similar in structure to the continuous distribution in β decay but originating from a very different effect. Because of these difficulties, we shall not discuss the theory of delayed nucleon emission; rather, we shall give some examples of experimental studies and their significance.

The energetics of β-delayed nucleon emission are relatively simple. Reference to Figure 9.13 shows immediately that the process can occur as long as the β-decay energy is greater than the nucleon separation energy: $Q_\beta > S_N$ (where N = n or p). Whenever this process is energetically permitted, there will always be competing processes; for example, γ decay of the emitting state or β decays to lower levels in the emitter that cannot decay by particle emission.

The information that we derive from β-delayed nucleon emission is mainly of two types: (1) Since the decay is a two-body process (emitted nucleon plus daughter nucleus), the nucleons emerge with a distinct energy, which gives directly the energy difference between the initial and final states. The energy levels in the daughter are usually well known, and so the energy of the emitted nucleon is in effect a measure of the energy of the excited state of the emitter. (2) From the relative probability of nucleon emission from different states in the emitter, we can deduce the relative population of these states in the β decay of the precursor. This provides information on the β-decay matrix elements. Because the highly excited states in the emitter are so close together, they nearly

form a continuum, and it is more appropriate to consider a β-decay strength function $S_\beta(E_x)$, which gives the average β-decay intensity leading to excited states in the vicinity of excitation energy E_x. Usually there are few selection rules inhibiting β decay to states at this high excitation, and so the β-decay strength function is rather featureless and is roughly proportional to the density of states $\rho(E_x)$. However, there is always one particular state that is so similar in character to the precursor that the majority of the β decays populate that state (it has a particularly large Fermi-type matrix element). The state is known as the *isobaric analog state* (or simply, analog state) because its structure is analogous to the original decaying state in the neighboring isobar. The β-decay strength leading to the analog state (and its energy) can often be determined only through the technique of β-delayed nucleon emission.

As an example of a typical experiment, we consider the β-delayed neutron emission from ^{17}N, which decays by negative β emission to ^{17}O. Figure 9.14 shows three readily identifiable neutron groups, with energies 383, 1171, and 1700 keV; we assume that three excited states of ^{17}O are populated in the β decay and that each emits a neutron to form ^{16}O. Let us assume that these decays go directly to the ground state of ^{16}O. (This is certainly not going to be true in general, but ^{16}O has its first excited state at more than 6 MeV; we will see that it is not possible that the ^{17}N β decay could have enough energy to populate such a highly excited state.)

To analyze the energy transfer in the decay, we first need the neutron separation energy of ^{17}O; using Equation 3.26:

$$\begin{aligned} S_n &= \left[m(^{16}\mathrm{O}) - m(^{17}\mathrm{O}) + m_n\right]c^2 \\ &= (15.99491464\,\mathrm{u} - 16.9991306\,\mathrm{u} + 1.008664967\,\mathrm{u})931.502\,\mathrm{MeV/u} \\ &= 4.144\,\mathrm{MeV} \end{aligned}$$

This is the energy that must be supplied to remove a neutron from ^{17}O. Let's regard the initial state of the system as ^{17}O in an excited state with energy E_x. The initial energy is therefore $m(^{17}\mathrm{O})c^2 + E_x$. The final energy is $m(^{16}\mathrm{O})c^2 + E_x' + m_nc^2 + T_n + T_R$, where T_n is the neutron kinetic energy and T_R is the energy of the ^{16}O recoil, which must occur to conserve momentum. We have included a possible excitation energy of ^{16}O in the term E_x'; later we will show it must be zero in this case. Energy conservation gives

$$m(^{17}\mathrm{O})c^2 + E_x = m(^{16}\mathrm{O})c^2 + E_x' + m_nc^2 + T_n + T_R$$

or

$$E_x = E_x' + T_n + T_R + S_n \tag{9.43}$$

which is a general result. The recoil correction is obtained by application of conservation of momentum, yielding

$$T_R = T_n\left(\frac{m_n}{m_R}\right) \approx T_n\frac{1}{A-1} \tag{9.44}$$

where m_R is the mass of the recoiling nucleus. Since this is a small correction, we can approximate m_n/m_R by $1/(A-1)$. The final result is

$$E_x = E_x' + \frac{A}{A-1}T_n + S_n \tag{9.45}$$

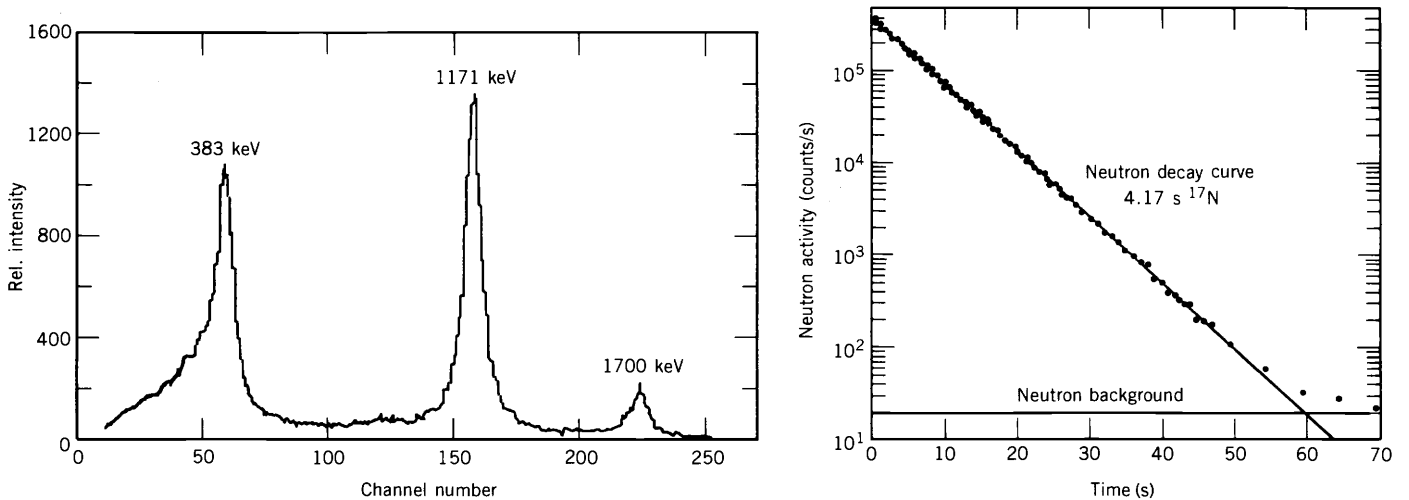


Figure 9.14 Beta-delayed neutrons following the decay of ^{17}N. The neutron energy spectrum is shown at the left; the decay of the neutron activity with time is at the right. From H. Ohm et al., *Nucl. Phys. A* **274**, 45 (1976).

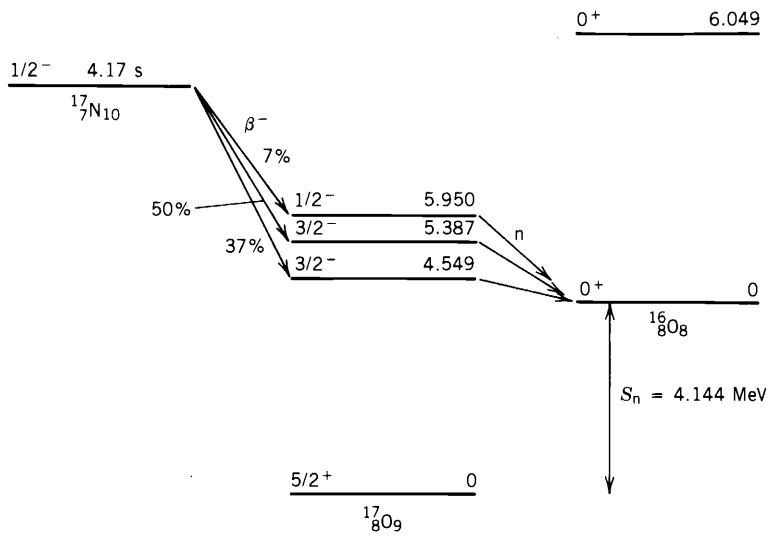


Figure 9.15 The β-delayed neutron decay of ^{17}N.

Assuming $E_x' = 0$ for ^{16}O, the three measured ^{17}N β-delayed neutron energies give excitation energies of 4.551, 5.388, and 5.950 MeV. Nuclear reactions can also be used to measure the energies of the ^{17}O excited states, and three states are found in reaction studies with the energies we have just calculated. If we were to consider the possibility to reach excited states in ^{16}O (that is, $E_x' \geq 6.049$ MeV, the first excited state in ^{16}O), then the lowest possible excitation in ^{17}O would be 10.6 MeV, which is greater than the Q value of the ^{17}N β decay (8.68 MeV). Excited states in ^{16}O are therefore not populated in this decay.

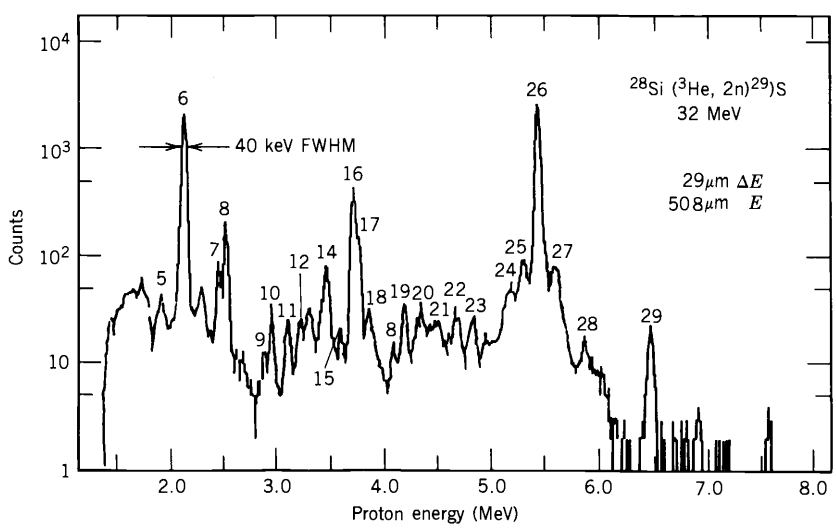


Figure 9.16 Protons emitted following the β decay of ^{29}S. The protons were observed using a $\Delta E \cdot E$ telescope of Si detectors. The numbers refer to specific proton decays of excited state of ^{29}P. Data from D. J. Vieira et al., *Phys. Rev. C* **19**, 177 (1979).

Figure 9.14 also shows the rate of neutron emission as a function of time, which gives the half-life of ^{17}N to be 4.17 s. This half-life is far too long for the decay to be a direct neutron emission process and it must therefore be a β-delayed emission process. The resulting decay is shown in Figure 9.15.

Proton emission will occur most easily from nuclei with an excess of protons, which is certainly the case for ^{29}S ($Z = 16$, $N = 13$). The activity is formed through the reaction $^{28}Si + {}^{3}He \rightarrow {}^{29}S + 2n$, which essentially adds two protons and removes a neutron from the stable initial nucleus ($Z = 14$, $N = 14$). The

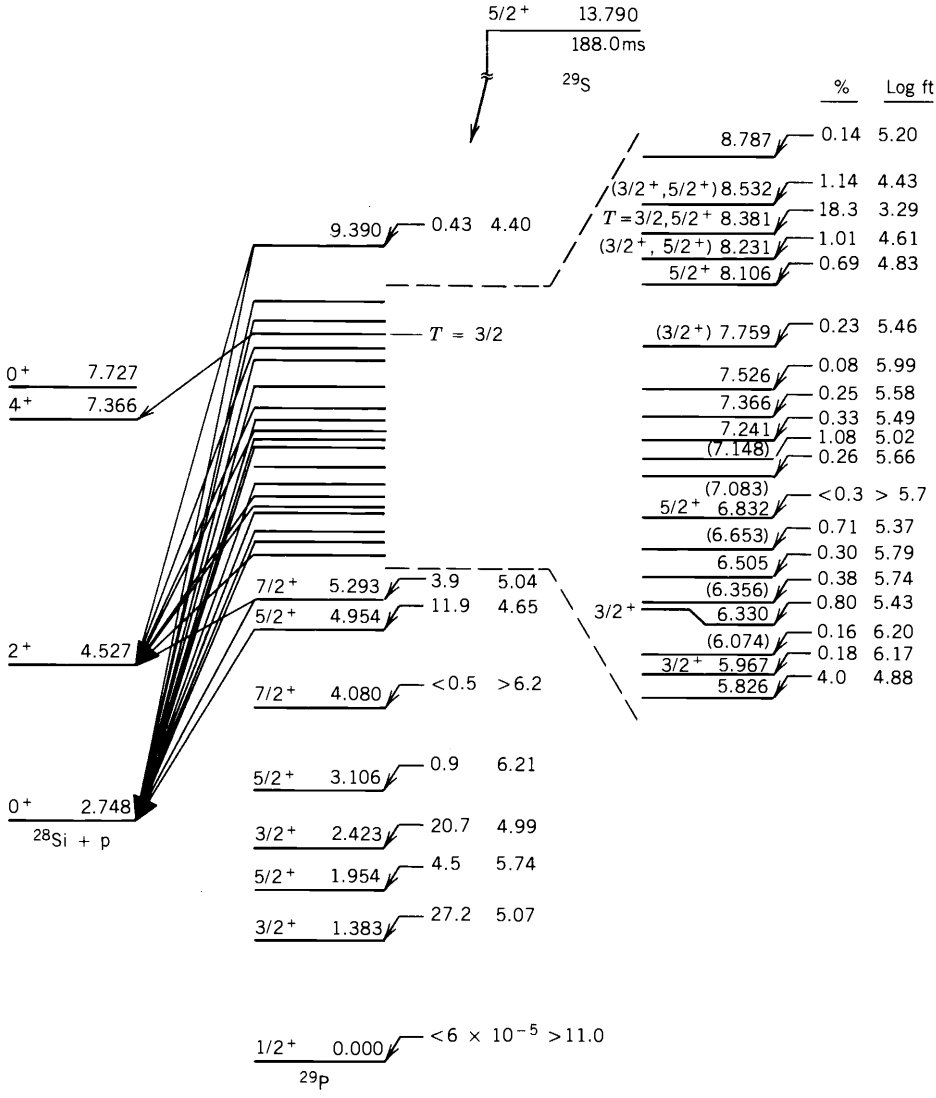


Figure 9.17 Excited states of ^{29}P deduced from the β-delayed proton decay of ^{29}S. The *ft* values are deduced from the intensity of the observed protons. Note the strong decay branch (small *ft* value) in the decay to the state at 8.381 MeV, which is the analog state of the ^{29}S ground state.

precursor ^{29}S decays by β^+ emission to states in the emitter ^{29}P, which then emits protons leading to final states in ^{28}Si. Figure 9.16 shows the observed proton spectrum, and Figure 9.17 illustrates the assignment of these proton groups to known initial and final states in ^{29}P and ^{28}Si. Many of the arguments for placing these decays proceed indirectly; for example, the energy difference between the 0^+ ground state and 2^+ first excited state in ^{28}Si is known to be 1.778 MeV, and thus two proton groups differing in energy by 1.778 MeV can be assumed to lead from the same state in the emitter to these two different final states in the daughter (groups 16 and 26, 18 and 27, 22 and 29). The analog state is associated with the strong groups 16 and 26; its log ft value of 3.29 is characteristic of superallowed decays, as expected for this strongly favored transition.

As we go to heavier nuclei, the density of excited states in the emitter becomes so large that the spacing between levels is smaller than the energy resolution of the detector. When this occurs, it is no longer possible to make the above identification of decays from specific states in the emitter, and only broad, average features of the decay can be discussed (Figure 9.18).

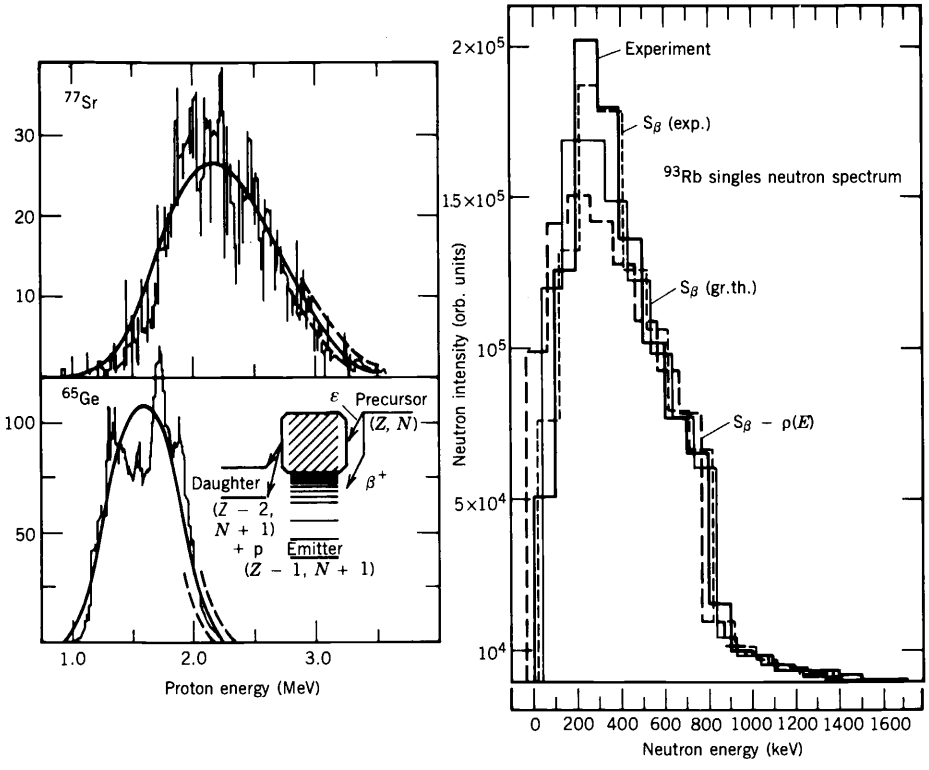


Figure 9.18 Proton (left) and neutron (right) emission following β decay in heavy nuclei. The spacing between excited states in the emitter is so small that we observe only a broad distribution, rather than the individual peaks of Figures 9.14 and 9.16. Attempts to fit the experimental data are based on statistical models, rather than on detailed calculations of individual nuclear states. Proton data from J. C. Hardy et al., *Phys. Lett. B* **63**, 27 (1976); neutron data from K.-L. Kratz et al., *Z. Phys. A* **306**, 239 (1982).

9.9 NONCONSERVATION OF PARITY

The parity operation (as distinguished from the parity quantum number) consists of reflecting all of the coordinates of a system: $\boldsymbol{r} \rightarrow -\boldsymbol{r}$. If the parity operation gives us a physical system or set of equations that obeys the same laws as the original system, we conclude that the system is invariant with respect to parity. The original and reflected systems would both represent possible states of nature, and in fact we could not distinguish in any fundamental way the original system from its reflection.

Of course, the macroscopic world *does* show a definite preference for one direction over another—for example, we humans tend to have our hearts on the left side of our bodies. There is no law of nature that demands that this be so, and we could construct a perfectly acceptable human with the heart on the right side. It is the reflection symmetry of the laws of nature themselves with which we are concerned, not the accidental arrangement of the objects governed by the laws.

In fact, there are three different "reflections" with which we frequently work. The first is the spatial reflection $\boldsymbol{r} \rightarrow -\boldsymbol{r}$, which is the parity (P) operation. The second "reflection" consists of replacing all particles with their antiparticles; this operation is called *charge conjugation* (C), although there are properties in addition to electric charge that are reversed in this operation. The third operation is *time reversal* (T), in which we replace t by $-t$ and in effect reverse the direction in time of all of the processes in the system. Figure 9.19 shows how three basic processes would appear under the P, C, and T operations. Notice especially that there are some vectors that change sign under P (coordinates, velocity, force, electric field) and some that do not (angular momentum, magnetic field, torque). The former are called true or polar vectors and the latter are pseudo- or axial vectors. Figure 9.20 shows a complete view of a rotating object reflected through the origin. You can see quite clearly that the angular momentum vector does not change direction upon reflection.

In each case shown in Figure 9.19, the reflected image represents a real physical situation that we could achieve in the laboratory, and we believe that gravity and electromagnetism are invariant with respect to P, C, and T.

One way of testing the invariance of the nuclear interaction to P, C, and T would be to perform the series of experiments described in Figure 9.21. In the original experiment, a reaction between particles A and B produces C and D. We could test P by interchanging the particles (for example, have projectile B incident on target A, instead of projectile A incident on target B). We could test C by doing the reaction with antiparticles and T by reacting particles C and D to produce A and B. In each case we could compare the probability of the reversed reaction with that of the original, and if the probabilities proved to be identical, we could conclude that P, C, and T were invariant operations for the nuclear interaction.

In the case of decays $A \rightarrow B + C$, we could perform the same type of tests, as shown in the figure, and could again study the invariance of P, C, and T in decay processes.

We must take care how we test the P operation because, as shown in the figure, the reflected experiment is identical to what we would observe if we turned the page around or stood on our heads to observe the decay or reaction process.

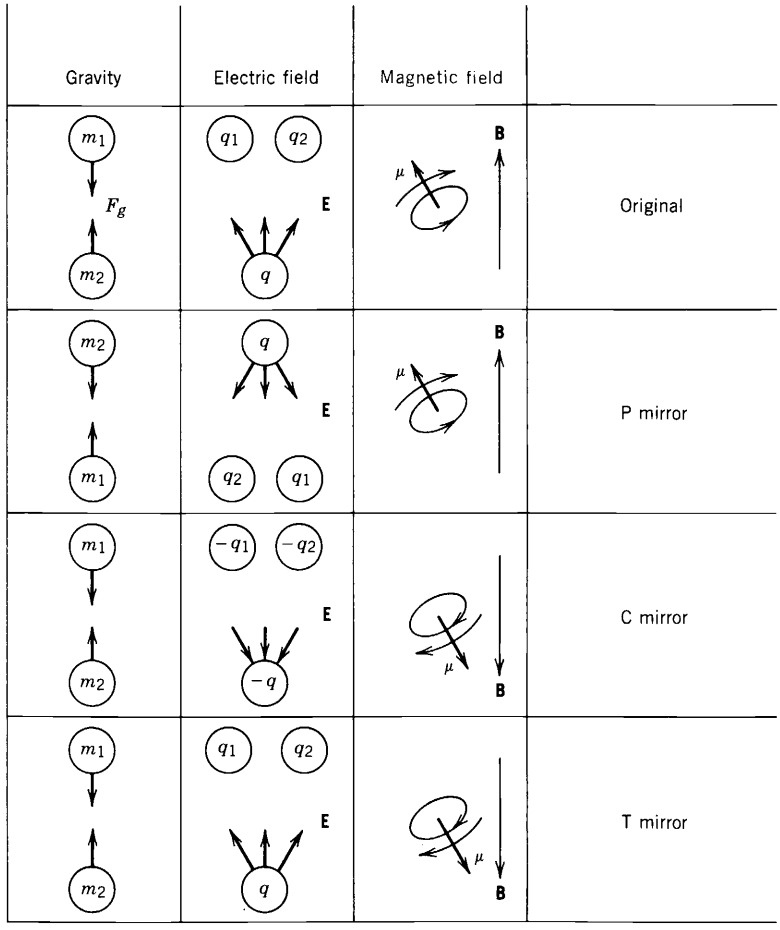


Figure 9.19 The effect of P, C, and T reversal on gravitational and electromagnetic interactions. In all cases the reversed diagrams represent possible physical situations, and thus these interactions are invariant under P, C, and T.

Since our goal is not to test the invariance of the laws of nature to physicists standing on their heads, we must have some way more clearly to identify the reflected process.

One way is to assume the decaying particle A to have a spin vector that is pointing in a specific direction. The spin does not change direction under P, but it certainly does if we view it upside down. Thus the original experiment shows particle B emitted in the same direction as the spin of A, while the reflected experiment shows B emitted opposite to the spin of A. Quite clearly the experiment differs from its reflection. If, however, we have a large number of A nuclei, all with spins aligned in the same direction, and if they tend to emit B's in equal numbers along the spin and opposite to the spin, then once again the experiment looks like its image. Here then is a way to test P directly—we simply

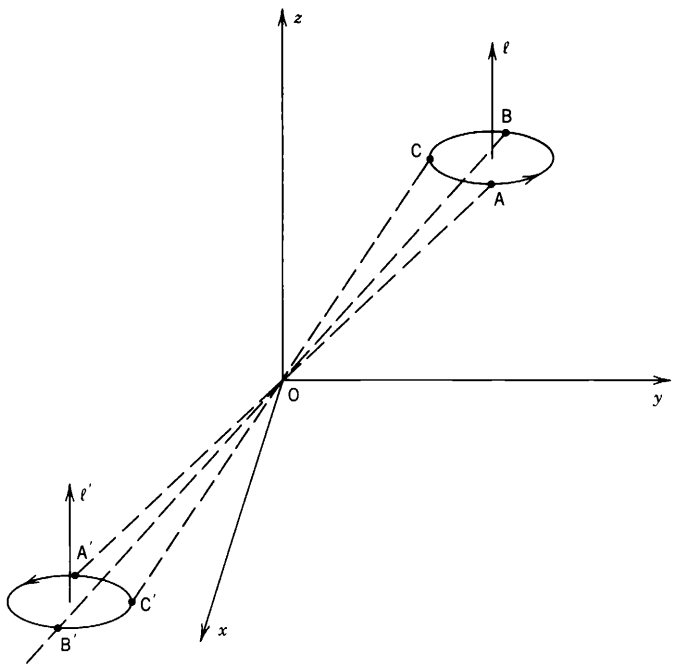


Figure 9.20 The effect of the P operation on a rotating object. If coordinates A, B, and C in the orbit are reflected through the origin ($\boldsymbol{r} \rightarrow -\boldsymbol{r}$), coordinates A′, B′, and C′ result. As the original particle travels from A to B to C, the reflected particle travels from A′ to B′ to C′, and using the right-hand rule to define the direction of the angular momentum indicates that both $\boldsymbol{\ell}$ and $\boldsymbol{\ell}'$ point upward. Thus $\boldsymbol{\ell}$ is a vector that does not change sign under P; such vectors are called *axial vectors*. (Vectors such $\boldsymbol{r}$ that do change sign under P are called *polar vectors*.)

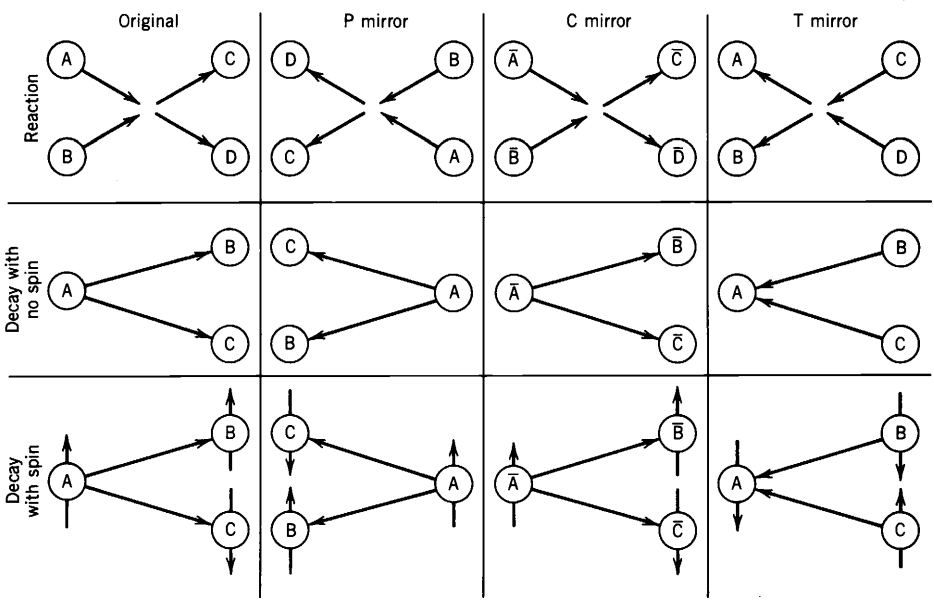


Figure 9.21 Nuclear physics tests of P, C, and T.

align the spins of some decaying nuclei and look to see if the decay products are emitted equally in both directions or preferentially in one direction.

In 1956, T. D. Lee and C. N. Yang pointed out that P had not yet been tested in β decay, even though it had been well tested in other nuclear decay and reaction processes. They were led to this assertion by an unusual situation called the θ-τ puzzle. At that time there were two particles, called θ and τ, which appeared to have identical spins, masses, and lifetimes; this suggested that θ and τ were in fact the same particle. Yet the decays of these particles lead to final states of different parities. Since the decays were governed by a process similar to nuclear β decay, Lee and Yang suggested that θ and τ were the same particle (today called a K meson) which could decay into final states of differing parities *if the P operation were not an invariant process for β decay.*

Several experimental groups set out to test the suggestion of Lee and Yang, and a successful experiment was soon done by C. S. Wu and her co-workers using the β decay of ^{60}Co. They aligned the ^{60}Co spins by aligning their magnetic dipole moments in a magnetic field at very low temperature ($T \sim 0.01$ K, low enough so that thermal motion would not destroy the alignment). Reversing the magnetic field direction reversed the spins and in effect accomplished the reflection. If β particles would have been observed in equal numbers along and opposite to the magnetic field, then β decay would have been invariant with respect to the P operation. What was observed in fact was that at least 70% of the β particles were emitted opposite to the nuclear spin. Figure 9.22 shows the original data of Wu and colleagues, and you can see quite clearly that the β counting rate reverses as the magnetic field direction is reversed.

Twenty-five years after the original experiment, Wu's research group repeated the ^{60}Co experiment with new apparatus that represented considerably advanced technology for cooling the nuclei, polarizing their spins, and detecting the β particles. Figure 9.23 shows the result of this new experiment, which demonstrates quite clearly the parity-violating effect.

Figure 9.24 shows schematically the ^{60}Co experiment and its reflection in the P mirror. In the P-reflected experiment, the electrons are emitted preferentially along, rather than opposite to, the direction of the magnetic field. Since this represents a state of affairs that is not observed in nature, it must be concluded that, at least as far as β decay is concerned, the P operation is not a valid symmetry. There is yet another surprising result that follows from this experiment. Consider the reflection of the original experiment in the C mirror, also shown in Figure 9.24. The electrons flowing in the wires that produce the magnetic field become positrons, so that the magnetic field reverses. In the C-reflected experiment, the β particles are now emitted preferentially *along* the magnetic field. Thus matter and antimatter behave differently in beta decay, which is a violation of the C symmetry. (In his book *The Ambidextrous Universe*, Martin Gardner discusses how this experiment can be used to try to decide whether an extraterrestrial civilization, with whom we may someday be in communication, is composed of matter or antimatter.)

If, however, we reflect the experiment in a mirror that simultaneously performs both the P and C operations, as shown in Figure 9.24, the original experiment is restored. Even though the separate C and P operations are not valid symmetries, the CP combination is. (We discuss in Chapter 17 that certain decays of the K

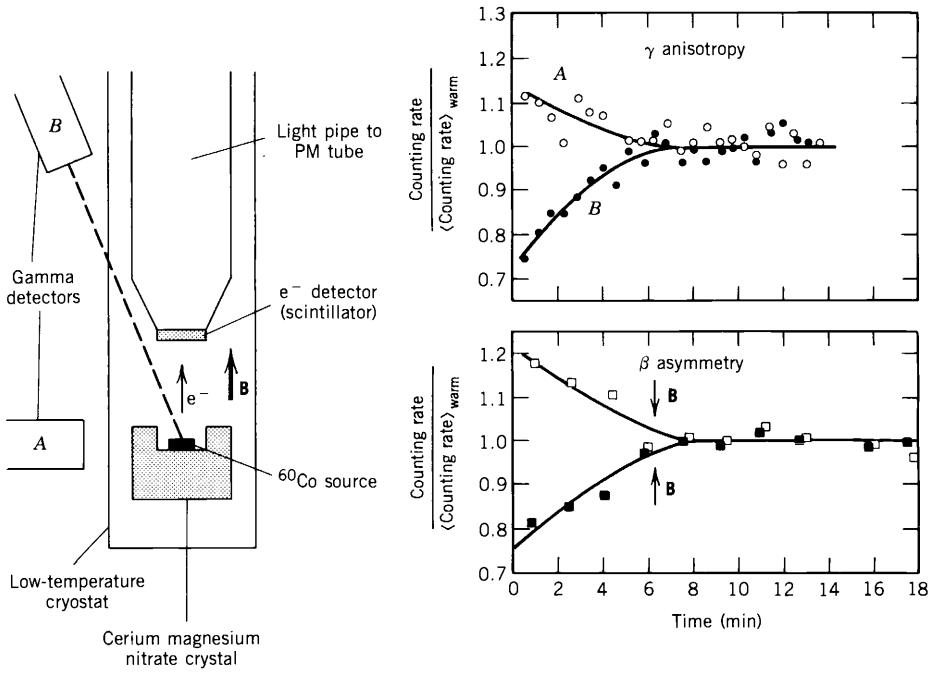


Figure 9.22 Schematic arrangement of experimental test of parity violation in the decay of ^{60}Co. At left is shown the apparatus; the cerium magnesium nitrate crystal is used to cool the radioactive source to about 0.01 K. At bottom right is shown the observed β counting rates; reversing the magnetic field direction is equivalent to subjecting the nuclei to the P operation (see Figures 9.21 and 9.24). If P were *not* violated, there would be no asymmetry and the field-up and field-down curves would coincide. The vanishing of the asymmetry at about 8 min is due to the gradual warming of the source and the corresponding loss in polarization of the ^{60}Co nuclei, as is demonstrated by the observed γ-ray counting rates. Data from C. S. Wu et al., *Phys. Rev.* **105**, 1413 (1957).

meson, which are analogous to β decays, even violate to a small extent the CP invariance. There is as yet no evidence that the CP symmetry is violated in ordinary nuclear β decay.)

Before we leave this topic, we should discuss the effect of the P nonconservation on nuclear spectroscopy. The interaction between nucleons in a nucleus consists of two parts: the "strong" part, which arises primarily from π meson exchange and which respects the P symmetry, and the "weak" part, which comes from the same interaction responsible for β decay:

$$V_{\text{nuclear}} = V_{\text{strong}} + V_{\text{weak}} \tag{9.46}$$

Typically, the effects of V_{weak} on nuclear spectroscopy are very small compared with those of V_{strong}, but V_{weak} has a property that V_{strong} lacks—it violates the P symmetry. As far as nuclear states are concerned, the effect of V_{weak} is to add to the nuclear wave function a small contribution of the "wrong" parity:

$$\psi = \psi^{(\pi)} + F\psi^{(-\pi)} \tag{9.47}$$

where F is of order 10^{-7}. Under most circumstances, this small addition to the

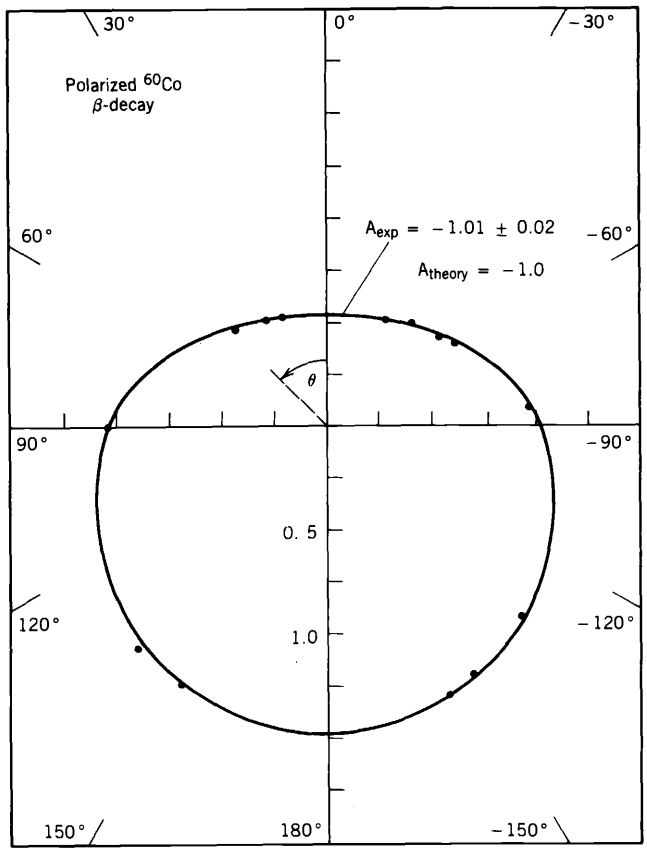


Figure 9.23 Improved results of C. S. Wu and co-workers on the parity violation in the ^{60}Co β decay. The data points (plotted on a polar diagram) give the observed β intensity at an angle θ with respect to the direction of polarization (spin direction) of the decaying ^{60}Co nuclei. The solid curve represents the prediction of the Fermi theory, according to which the intensity should vary as $1 + AP\cos\theta$, where P is a parameter that depends primarily on the nuclear polarization. If parity were *not* violated in β decay, the intensities at 0 and 180° would be equal. From L. M. Chirovsky et al., *Phys. Lett. B* **94**, 127 (1980).

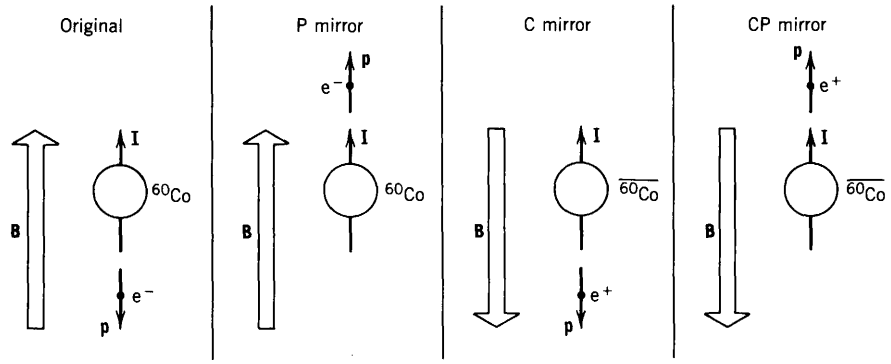


Figure 9.24 The polarized ^{60}Co experiment in the P, C, and combined CP mirrors.

wave function has no observable consequences for nuclear spectroscopy, but there are two cases in particular in which the effects can be observable. In the first, nuclear γ radiation emitted by a polarized nucleus acquires a small difference in intensity between the directions along and opposite to the polarizing magnetic field. This is exactly analogous to the ^{60}Co experiment, but is generally a very small effect (of the order of one part in 10^7) because it arises only from the small part of the wave function and the regular part $\psi^{(\pi)}$ gives no difference in the two intensities. In one very favorable case in the decay of the ^{180}Hf isomeric state, described in K. S. Krane et al., *Phys. Rev. C* **4**, 1906 (1971), the difference is about 2%, but in general it is much smaller and probably beyond our ability to measure. A second type of observation involves the search for a process that would ordinarily be absolutely forbidden if F were zero. For example, consider the α decay of the 2^- level of ^{16}O to the 0^+ ground state of ^{12}C. The selection rules for α decay absolutely forbid $2^- \rightarrow 0^+$ decays (see Section 8.5), but if the 2^- state includes a small piece of 2^+ state, the decay is permitted to occur with a very small intensity proportional to F^2. Based on a careful study of the α decay of the excited states of ^{16}O, Neubeck et al. discovered a weak branch which they assigned to the parity-violating $2^- \rightarrow 0^+$ transition. The partial half-life for this transition was deduced to be 7×10^{-7} s. By way of comparison, Equation 8.18 gives for the half-life of an ordinary α transition (with $Q = 1.7$ MeV, $B = 3.8$ MeV) the value 2×10^{-21} s. The α decay intensity is thus indeed of order F^2 (10^{-14}), as expected for this P-violating process. A description of this difficult experiment can be found in *Phys. Rev. C* **10**, 320 (1974).

9.10 BETA SPECTROSCOPY

In this section we explore some techniques for deducing the properties of nuclear states (especially excitation energies and spin-parity assignments) through measurements of β decays. This process is complicated by two features of the β-decay process (as compared with α decay, for instance): (1) The β spectrum is continuous. The study of decay processes such as those discussed in Section 8.6 is

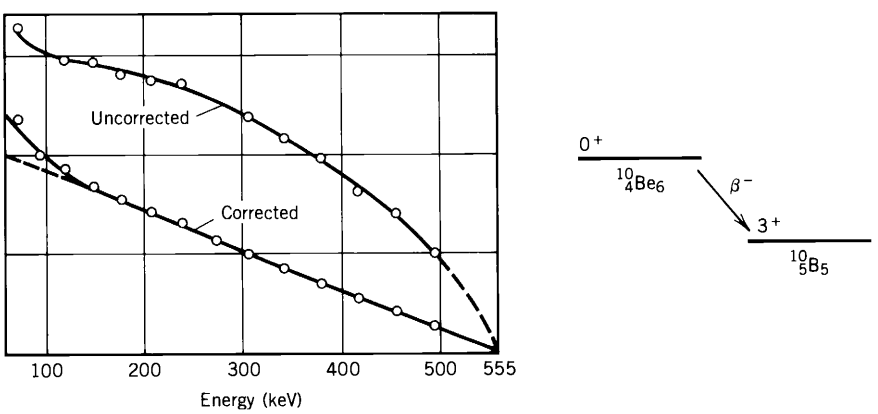


Figure 9.25 Uncorrected Fermi–Kurie plot for ^{10}Be decay and correction for shape factor for second-forbidden transition. Data from L. Feldman and C. S. Wu, *Phys. Rev.* **87**, 1091 (1952).

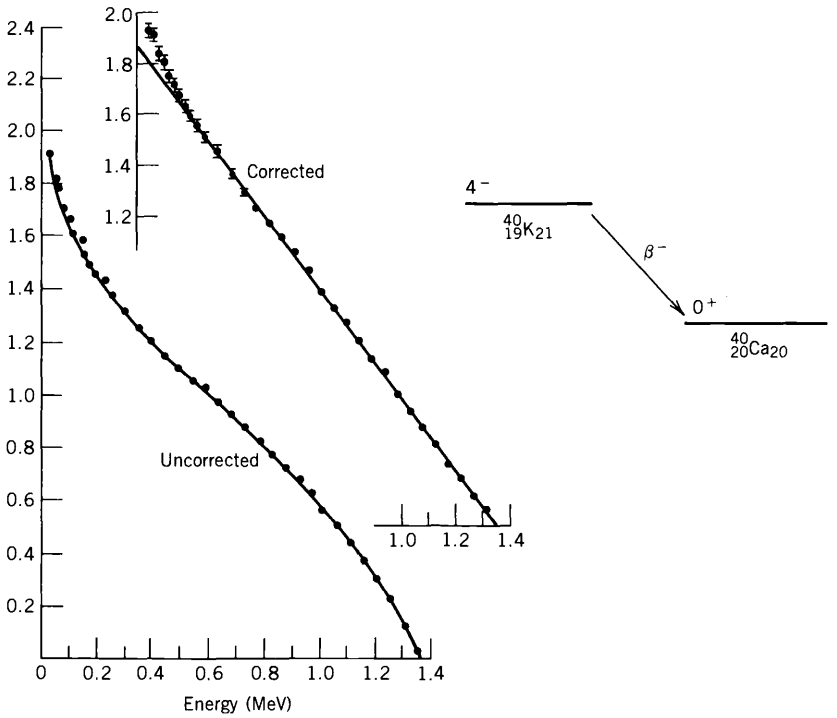


Figure 9.26 Uncorrected Fermi–Kurie plot for the decay of ^{40}K and correction for shape factor of third-forbidden transition. Data from W. H. Kelly et al., *Nucl. Phys.* **11**, 492 (1959).

not possible for β decays with many branches, for we cannot reliably "unfold" the various components. (2) The β selection rules are not absolute—the ranges of ft values often overlap and cannot be used to make absolute deductions of decay types, and the measurement of the angular momentum carried by the β particle is not sufficient to fix the relative parities of the initial and final states. There are, however, many cases in which it is possible to derive spectroscopic information from the decays.

Although the shape of the β spectrum and the half-life (actually, the ft value) of the decay are not absolute indicators of the decay type, they do give us strong clues about the type of decay (and therefore the relative spin-parity assignments of the initial and final nuclear states). As discussed in Section 9.3, a linear Fermi–Kurie plot with no shape factor strongly suggests a decay of the allowed type, and we would therefore expect $\Delta I = 0$ or 1 and $\Delta\pi$ = no. A nonlinear Fermi–Kurie plot that is linearized by the shape factor $S = p^2 + q^2$ is, as shown in Figure 9.5, most likely of a first-forbidden type.

Figures 9.25 and 9.26 show additional examples of the use of the shape of the decay to deduce the properties of the initial state. The Fermi–Kurie plot for the decay of ^{10}Be is linearized by a shape factor characteristic of $\Delta I = 3$, $\Delta\pi$ = no second-forbidden decays. Like all even-Z, even-N nuclei, ^{10}Be has a 0^+ ground state, and so we immediately deduce the assignment of 3^+ for the ^{10}B final state.

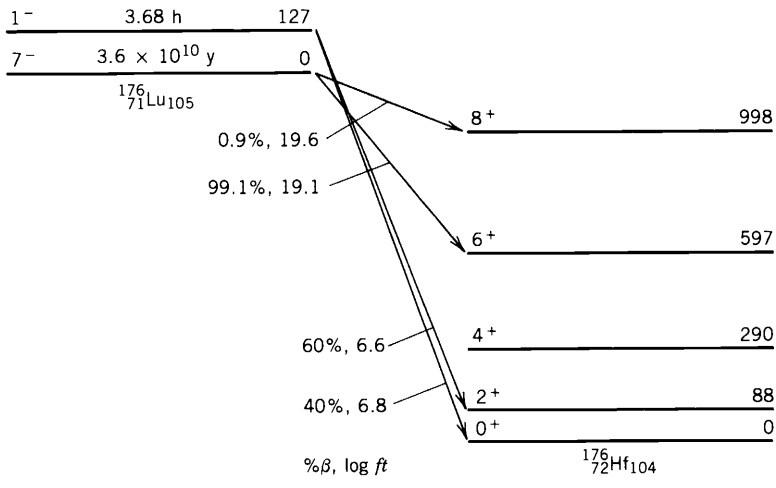


Figure 9.27 The β decay of ^{176}Lu. Level energies are given in keV.

Moreover, the log ft value of 13.4 is consistent with that expected for second-forbidden decays. The ^{40}K decay proceeds primarily by β^- decay to ^{40}Ca. The Fermi–Kurie plot is linearized by a shape factor characteristic of a $\Delta I = 4$, $\Delta\pi$ = yes third-forbidden decay. The final state is the ^{40}Ca ground state, which is certainly 0^+. The initial state is therefore 4^-. The log ft of 18.1 also suggests a third-forbidden process.

On the other hand, we must be careful not to rely too much on the empirical rules for log ft values, which are merely based on systematics and not on any theory. In the decay of ^{176}Lu (Figure 9.27) the log ft is 19.1, while from the known spin-parity assignments we expect a first-forbidden decay (the log ft values for which usually fall in the range 8–12). It is useful to remind ourselves that a log ft of 19 means that the β decay is slowed or inhibited by a factor of 10^7 relative to a decay with log ft of 12. The extreme effect in the ^{176}Lu decay comes about from the unusually poor match of the initial and final nuclear wave functions.

A case in which two different β groups contribute to the decay is illustrated by the decay of ^{72}Zn (Figure 9.28). The weaker group can be reliably seen only through β-γ coincidence measurements. The linear Fermi–Kurie plots and the small log ft values suggest allowed decays, consistent with the 1^+ assignments to both final states.

A more extreme example comes from the decay of ^{177}Lu (Figure 9.29) in which through careful measurement it is possible to deduce four separate groups. The unfolding procedure begins with the highest group, which is assumed to have a nearly linear Fermi–Kurie plot. Extrapolating the linear high-energy portion backward and subtracting, the remaining spectrum shows an endpoint of 385 keV, and repeating the process reveals two additional components.

We cannot tell directly whether the highest-energy component represents a decay to the ground state of ^{177}Hf, but we can show that it does by computing the Q value for the decay to the ground state. Because ^{177}Lu is radioactive, its mass cannot be measured directly, but we can deduce it through measuring the

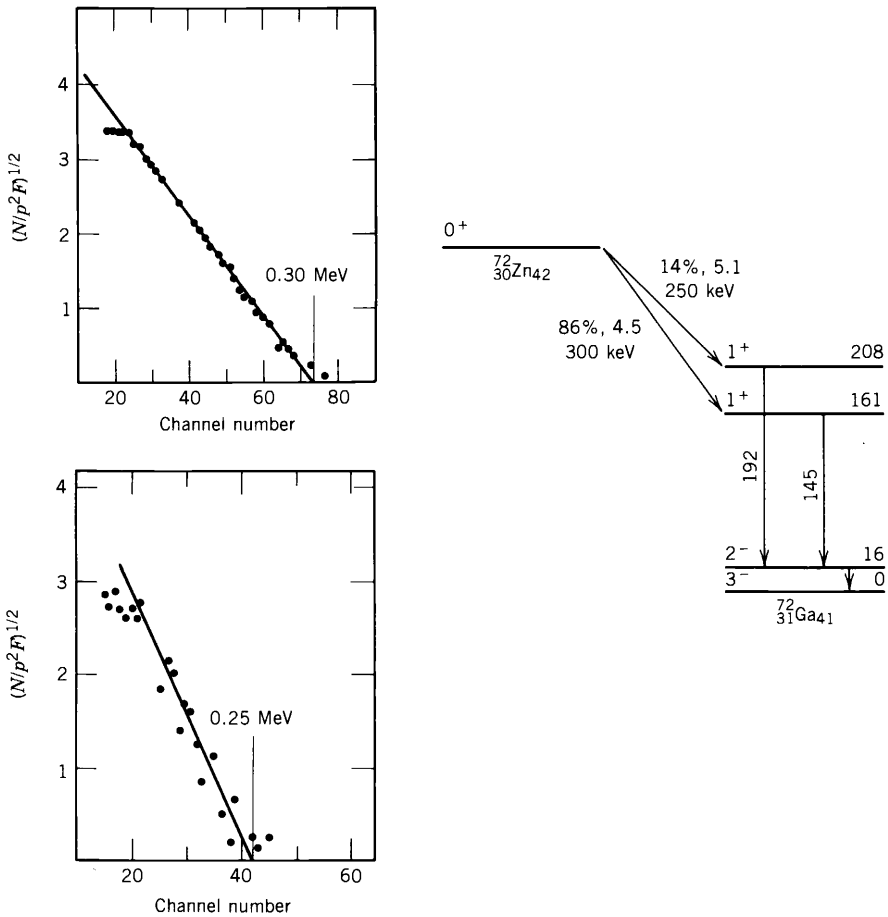


Figure 9.28 β decay of ^{72}Zn. In this case, there are two decays, but the stripping method cannot reliably be used to find the much weaker, lower energy component. At left are shown Fermi–Kurie plots of β's in coincidence with the 192-keV (bottom) and 145-keV (top) γ rays. The coincidences enable the unambiguous separation of the two decays, the determination of their endpoints, and the demonstration of the linearity of their Fermi–Kurie plots. Data from M. Ishihara, *J. Phys. Soc. Jpn.* **18**, 1111 (1963).

energy released when a low-energy neutron is added to stable ^{176}Lu to form ^{177}Lu. This energy is determined to be 7.0726 $\pm$ 0.0006 MeV, and thus

$$m(^{177}\text{Lu}) = m(^{176}\text{Lu}) + m(\text{n}) - 7.0726\ \text{MeV}/c^2$$
$$= 176.943766 \pm 0.000006\ \text{u}$$

where the latter step is made using the known ^{176}Lu mass. We can now find

$$Q_\beta = m(^{177}\text{Lu}) - m(^{177}\text{Hf})$$
$$= 496 \pm 8\ \text{keV}$$

in excellent agreement with the energy of the highest β group. We therefore conclude that this group populates the ^{177}Hf ground state, with the lower groups

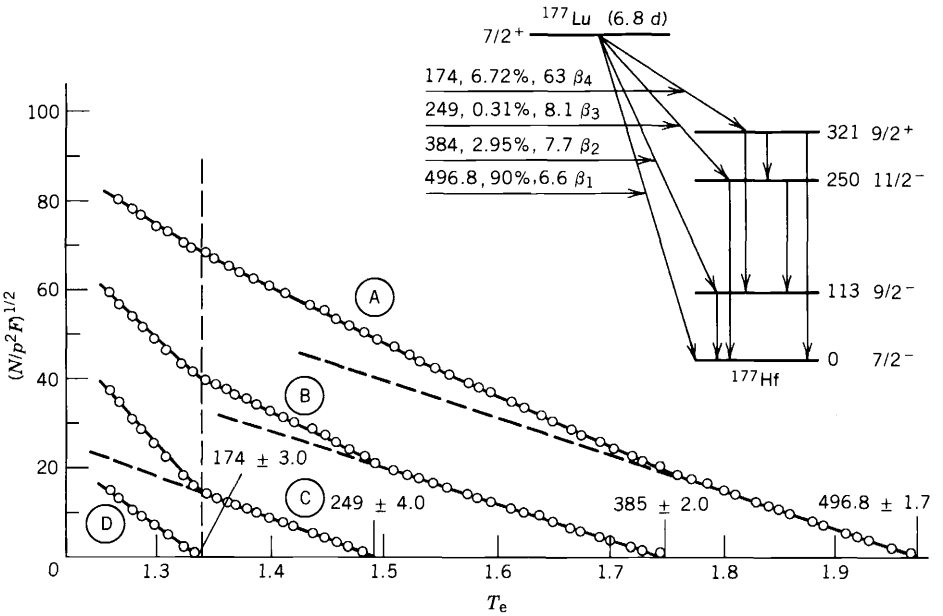


Figure 9.29 Fermi–Kurie plot of the β decay of ^{177}Lu. Curve A represents the complete β spectrum. Extrapolating the high-energy portion (which presumably includes only a single component) gives the dashed line, and the difference between the extrapolated line and curve A gives curve B. The linear portion of curve B gives the endpoint of the next component, and repeating the procedure gives curves C and D. The resulting decay scheme is shown in the inset. Data from M. S. El-Nesr and E. Bashandy, *Nucl. Phys.* **31**, 128 (1962).

populating successively higher states at energies of 112 keV (= 497 − 385), 248 keV (= 497 − 249), and 323 keV (= 497 − 174). The γ spectrum shows results consistent with these deductions, as we discuss in Section 10.8. The 113-keV γ ray, for example, represents the transition from the first excited state to the ground state, and the β spectrum in coincidence with the 113-keV γ ray shows only the 385-keV component.

As a final example of a spectroscopic study, we consider the decay of ^{126}I, which can occur either through negative or positive β emission. The Fermi–Kurie plot (Figure 9.30) is definitely nonlinear at the high end, but when the upper end is corrected by the shape factor for a $\Delta I = 2$, $\Delta\pi$ = yes first-forbidden decay, it becomes linear and the stripping reveals three groups. Only the two lower groups are in coincidence with γ radiation, suggesting that the highest group populates the ^{126}Xe ground state (0^+) and thus that the decaying state must be 2^- (because the highest group is $\Delta I = 2$, $\Delta\pi$ = yes). The other groups must populate excited states at 385 keV (= 1250 − 865) and 865 keV (= 1250 − 385). (It is coincidental that the numbers happen to be interchangeable.) The positron spectrum (Figure 9.31) similarly shows two groups which by the same argument populate the ground and first excited (670-keV) state of ^{126}Te. The γ spectrum shows strong transitions of energies 389, 492, 666, 754, 880, and 1420 keV, which can be placed as shown in Figure 9.32, based on the observed β endpoints. The spins of the first excited states are 2^+, and the second excited states must be 2^+ as well,

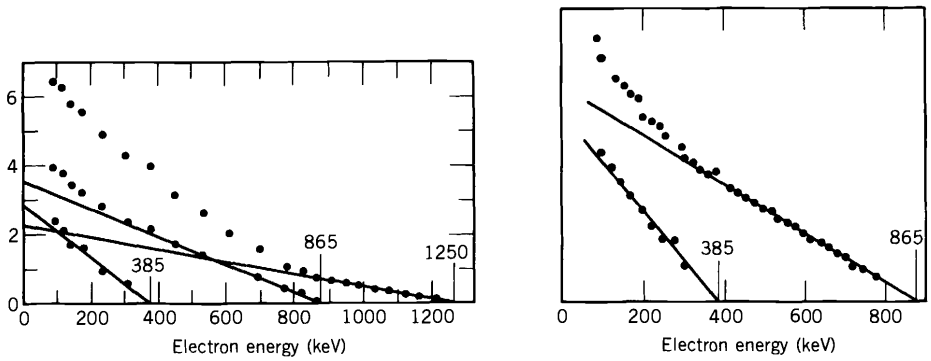


Figure 9.30 Electron spectrum from the β decay of ^{126}I. The singles spectrum (left) shows three components, using a stripping procedure as in Figure 9.29. The coincidence spectrum with gamma radiation (right) does not show the highest energy component; if it is coincident with no γ radiations, it must be a transition to the ground state. Data from L. Koerts et al., *Phys. Rev.* **98**, 1230 (1955).

based on the similarity of the log ft values and the observed "crossover" transition to the ground state.

The calculation of β matrix elements from nuclear wave functions is a difficult process, and so we usually are content to compare experimental results from different but similar decays. For example, consider the mirror decays of ^{12}B and ^{12}N to ^{12}C (Figure 9.33). The ft values to the different excited states are virtually identical for the β^- and β^+ decays. The transition of the 7th proton into the 6th

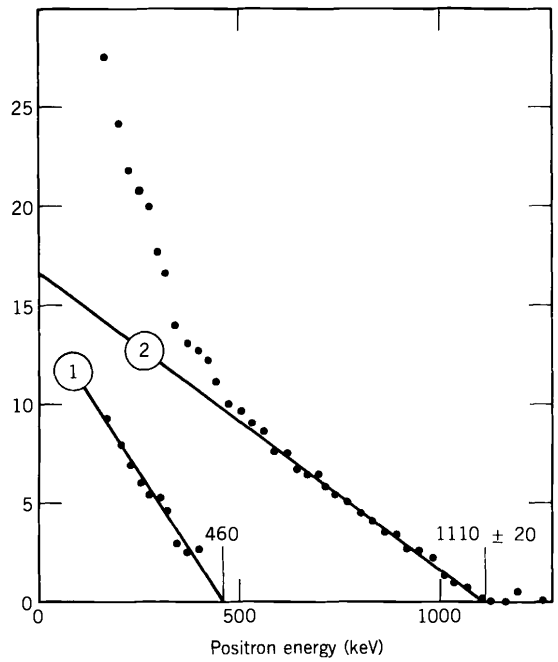


Figure 9.31 Positron spectrum from the β decay of ^{126}I. Stripping reveals two components. Data from L. Koerts et al., *Phys. Rev.* **98**, 1230 (1955).

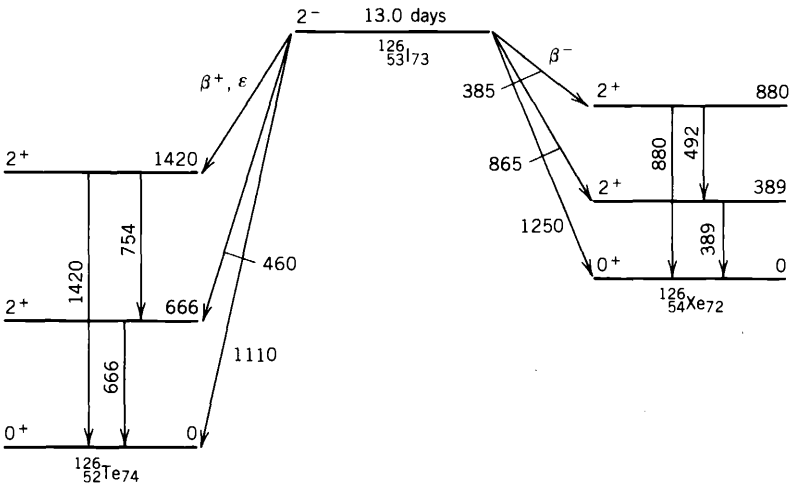


Figure 9.32 Decay scheme of ^{126}I, showing β and γ information. Energies of β's, γ's, and levels are given in keV.

neutron would be expected to involve initial and final nuclear wave functions (based on the shell model) identical with those in the transition of the 7th neutron into the 6th proton. The *ft* values are consistent with this expectation. The transition of the proton into a neutron that leaves the neutron in the same shell-model state as the initial proton results in the population of the 15.11-MeV excited state of ^{12}C. This state therefore has the same nuclear wave functions as the ^{12}B and ^{12}N ground states (except for the difference between protons and neutrons) and is the *analog state* of ^{12}B and ^{12}N. The particularly small *ft* value in the decay of ^{12}N to this state emphasizes its interpretation as the analog state.

Finally, let's look at the information on nuclear wave functions that can be obtained from β decay. In particular, we examine the transitions between odd neutrons and protons within the $f_{7/2}$ shell. (That is, one $f_{7/2}$ nucleon is transformed into another.) Let us look specifically at cases in odd-A nuclei involving $\Delta I = 0$, allowed decays between states of spin-parity $\frac{7}{2}^-$. The simplest example is

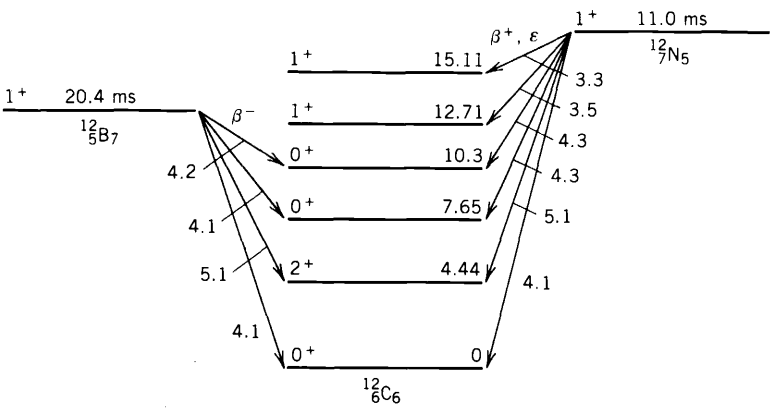


Figure 9.33 Beta decays of ^{12}B and ^{12}N to ^{12}C. Note the similarities in the log *ft* values for the β^+ and β^- decays leading to the same final state in ^{12}C.

Table 9.4 β Decays in the $f_{7/2}$ Shell ($\frac{7}{2}^- \rightarrow \frac{7}{2}^-$)

${}^{A}_{Z}X_{N} \rightarrow {}^{A}_{Z'}X'_{N'}$	$\lvert Z - N' \rvert = \lvert N - Z' \rvert$	$\log ft$
${}^{41}_{21}Sc_{20} \rightarrow {}^{41}_{20}Ca_{21}$	0	3.5
${}^{43}_{22}Ti_{21} \rightarrow {}^{43}_{21}Sc_{22}$	0	3.5
${}^{45}_{23}V_{22} \rightarrow {}^{45}_{22}Ti_{23}$	0	3.6
${}^{53}_{27}Co_{26} \rightarrow {}^{53}_{26}Fe_{27}$	0	3.6
${}^{43}_{21}Sc_{22} \rightarrow {}^{43}_{20}Ca_{23}$	2	5.0
${}^{45}_{22}Ti_{23} \rightarrow {}^{45}_{21}Sc_{24}$	2	4.6
${}^{53}_{26}Fe_{27} \rightarrow {}^{53}_{25}Mn_{28}$	2	5.2
${}^{45}_{20}Ca_{25} \rightarrow {}^{45}_{21}Sc_{24}$	4	6.0
${}^{47}_{21}Sc_{26} \rightarrow {}^{47}_{22}Ti_{25}$	4	5.3
${}^{49}_{23}V_{26} \rightarrow {}^{49}_{22}Ti_{27}$	4	6.2
${}^{51}_{24}Cr_{27} \rightarrow {}^{51}_{23}V_{28}$	4	5.4
${}^{47}_{20}Ca_{27} \rightarrow {}^{47}_{21}Sc_{26}$	6	8.5
${}^{49}_{21}Sc_{28} \rightarrow {}^{49}_{22}Ti_{27}$	6	5.7

the decay of ^{41}Sc to ^{41}Ca, in which a single proton outside the doubly magic ^{40}Ca core changes into a single neutron. No change of nuclear wave function is involved, and the observed log *ft* for this decay is 3.5, placing it in the superallowed category. (This is an example of a *mirror* decay.) In the extreme independent particle shell model, all odd particles are treated equivalently, and we might therefore expect the decay ^{47}Ca to ^{47}Sc (also $\frac{7}{2}^-$ to $\frac{7}{2}^-$) to show a similar log *ft*. However, the observed value is 8.5—the decay is slower by a factor of 10^5! The transition of the 27th neutron to the 21st proton is thus a more complicated process, and the other six neutrons in the $f_{7/2}$ shell must have a significant influence on the decay. (Some general features of these many-particle states were discussed in Section 5.3.) Table 9.4 summarizes the observed $\frac{7}{2}^-$ to $\frac{7}{2}^-$ β decays of the $f_{7/2}$ shell nuclei ($20 \leq N, Z \leq 28$). You can see that decays in which the odd particle is not required to change its state ($Z - N' = N - Z' = 0$) have log *ft* values in the superallowed category (about 3.5); as the value of $Z - N'$ increases, the change of state is correspondingly greater and the log *ft* increases, on the average by about one unit (a factor of 10 in the half-life) for each step in $Z - N'$.

REFERENCES FOR ADDITIONAL READING

Other references on "classical" β decay include Chapter 13 of J. M. Blatt and V. F. Weisskopf, *Theoretical Nuclear Physics* (New York: Wiley, 1952); Chapter 17 of R. D. Evans, *The Atomic Nucleus* (New York: McGraw-Hill, 1955); and I. Kaplan, *Nuclear Physics* (Reading, MA: Addison-Wesley, 1955).

More comprehensive reference works, ranging from elementary to advanced material, include H. F. Schopper, *Weak Interactions and Nuclear Beta Decay* (Amsterdam: North-Holland, 1966); C. S. Wu and S. A. Moszkowski, *Beta*

Decay (New York: Wiley-Interscience, 1966); E. J. Konopinski, *The Theory of Beta Decay* (Oxford: Oxford University Press, 1966); M. Morita, *Beta Decay and Muon Capture* (Reading, MA: Benjamin, 1973). An introductory work which includes reprints of some of the classic papers on β decay is C. Strachan, *The Theory of Beta Decay* (Oxford: Pergamon, 1969).

Beta spectroscopy is the subject of C. S. Wu, in *Nuclear Spectroscopy*, part A, edited by F. Ajzenberg-Selove (New York: Academic, 1959), Section I.E.1. A survey of measurements of the shapes of β spectra can be found in H. Daniel, *Rev. Mod. Phys.* **40**, 659 (1968). Many details of β decay are discussed in Chapters 22–24 of *Alpha-, Beta- and Gamma-Ray Spectroscopy*, edited by K. Siegbahn (Amsterdam: North-Holland, 1965).

A general elementary work on neutrino physics is G. M. Lewis, *Neutrinos* (London: Wykeham, 1970). A useful review of the early experimental work can be found in J. S. Allen, *The Neutrino* (Princeton, NJ: Princeton University Press, 1958). A survey of the literature about neutrinos is given in the resource letter of L. M. Lederman, *Am. J. Phys.* **38**, 129 (1970). For a discussion of the solar neutrino experiment, see the article by John Bahcall in the July 1969 issue of *Scientific American*.

Reviews of β-delayed nucleon emission can be found in J. Cerny and J. C. Hardy, *Ann. Rev. Nucl. Sci.* **27**, 333 (1977), and in J. C. Hardy, *Nuclear Spectroscopy and Reactions*, edited by J. Cerny (New York: Academic, 1974), Chapter 8B.

A popular-level treatment of parity is Martin Gardner, *The Ambidextrous Universe* (New York: Scribner, 1979).

Double-beta decay is reviewed in D. Bryman and C. Picciotto, *Rev. Mod. Phys.* **50**, 11 (1978).

PROBLEMS

1. Compute the Q values for the following β^- decays: (a) $^{65}\text{Ni} \rightarrow {}^{65}\text{Cu}$; (b) $^{11}\text{Be} \rightarrow {}^{11}\text{B}$; (c) $^{193}\text{Os} \rightarrow {}^{193}\text{Ir}$.
2. Compute the Q values for the following β^+ and ε decays: (a) $^{10}\text{C} \rightarrow {}^{10}\text{B}$; (b) $^{152}\text{Eu} \rightarrow {}^{152}\text{Sm}$; (c) $^{89}\text{Zr} \rightarrow {}^{89}\text{Y}$.
3. ^{196}Au can decay by β^-, β^+, and ε. Find the Q values for the three decay modes.
4. The maximum kinetic energy of the positron spectrum emitted in the decay $^{11}\text{C} \rightarrow {}^{11}\text{B}$ is 1.983 ± 0.003 MeV. Use this information and the known mass of ^{11}B to calculate the mass of ^{11}C.
5. In the decay of ^{6}He to ^{6}Li, the maximum β kinetic energy is 3.510 ± 0.004 MeV. Find the mass of ^{6}He, given the mass of ^{6}Li.
6. In the decay of ^{47}Ca to ^{47}Sc, what energy is given to the neutrino when the electron has a kinetic energy of 1.100 MeV?
7. The β decay of ^{191}Os leads only to an excited state of ^{191}Ir at 171 keV. Compute the maximum kinetic energy of the β spectrum.
8. (a) If the β-decay energy is large compared with $m_e c^2$, find a simplified form of Equation 9.25 and show that the average value of T_e (not the value

of T_e where $N(T_e)$ has its maximum) is equal to $Q/2$. (b) In the case of β-decay energies that are small compared with $m_e c^2$, show that the average value of T_e is $Q/3$.

9. Supply the missing component(s) in the following processes:
(a) $\bar{\nu} + {}^3\mathrm{He} \rightarrow$
(b) ${}^6\mathrm{He} \rightarrow {}^6\mathrm{Li} + \mathrm{e}^- +$
(c) $\mathrm{e}^- + {}^8\mathrm{B} \rightarrow$
(d) $\nu + {}^{12}\mathrm{C} \rightarrow$
(e) ${}^{40}\mathrm{K} \rightarrow \nu +$
(f) ${}^{40}\mathrm{K} \rightarrow \bar{\nu} +$

10. What is the kinetic energy given to the proton in the decay of the neutron when (a) the electron has negligibly small kinetic energy; (b) the neutrino has negligibly small energy?

11. One of the processes that is most likely responsible for the production of neutrinos in the sun is the electron-capture decay of ${}^7\mathrm{Be}$. Compute the energy of the emitted neutrino and the kinetic energy of the ${}^7\mathrm{Li}$ nucleus.

12. Defining the Q value as $(m_i - m_f)c^2$, compute the range of neutrino energies in the solar fusion reaction $\mathrm{p} + \mathrm{p} \rightarrow \mathrm{d} + \mathrm{e}^+ + \nu$. Assume the initial protons to have negligible kinetic energies.

13. (a) For neutrino capture reactions $\nu + {}^A\mathrm{X} \rightarrow \mathrm{e}^- + {}^A\mathrm{X}'$, show that the Q value, defined as in the case of decays as $Q = (m_i - m_f)c^2$, is just $[m({}^A\mathrm{X}) - m({}^A\mathrm{X}')]c^2$ using atomic masses. (b) Neglecting the small kinetic energy given to the final nucleus (to conserve momentum), this Q value is equal to the minimum energy the neutrino must have to cause the reaction. Compute the minimum neutrino energy necessary for capture by ${}^{37}\mathrm{Cl}$, by ${}^{71}\mathrm{Ga}$, and by ${}^{115}\mathrm{In}$. (c) In the Davis experiment (Section 9.6), ${}^{37}\mathrm{Cl}$ is used to detect ν from solar fusion; ${}^{71}\mathrm{Ga}$ and ${}^{115}\mathrm{In}$ have also been proposed as solar neutrino detectors. Comment on the use of these detectors to observe neutrinos from the basic fusion reaction $\mathrm{p} + \mathrm{p} \rightarrow \mathrm{d} + \mathrm{e}^+ + \nu$ (see Problem 12) and from the decay of ${}^7\mathrm{Be}$ (see Problem 11).

14. Classify the following decays according to degree of forbiddenness:
(a) ${}^{89}\mathrm{Sr}\ (\frac{5}{2}^+) \rightarrow {}^{89}\mathrm{Y}\ (\frac{1}{2}^-)$
(b) ${}^{36}\mathrm{Cl}\ (2^+) \rightarrow {}^{36}\mathrm{Ar}\ (0^+)$
(c) ${}^{26}\mathrm{Al}\ (5^+) \rightarrow {}^{26}\mathrm{Mg}^*\ (2^+)$
(d) ${}^{26}\mathrm{Si}\ (0^+) \rightarrow {}^{26}\mathrm{Al}^*\ (0^+) \rightarrow {}^{26}\mathrm{Mg}\ (0^+)$
(e) ${}^{97}\mathrm{Zr}\ (\frac{1}{2}^+) \rightarrow {}^{97}\mathrm{Nb}^*(\frac{1}{2}^-)$

15. Show that the slope of the electron energy spectrum for allowed decays is zero near $T_e = Q$ if $m_\nu = 0$ but becomes infinite if $m_\nu \neq 0$.

16. Electron-capture decays can originate with any atomic shell K, L, ... For a wide range of nuclei, the L-capture probability is about 11% of the K-capture probability. Justify this ratio with an estimate based on the probability to locate an orbital electron near the nucleus. For this rough estimate, ignore any effects of electron screening.

17. (a) Consider a $0^+ \rightarrow 0^+$ β^- decay. Using the helicity, Equation 9.38, of the emitted e^- and ν, deduce whether the e^- and ν tend to be emitted parallel

or antiparallel to one another. (b) Repeat for a $1^+ \rightarrow 0^+$ β^- decay. (c) What are the implications of these results for the recoil of the nucleus? (d) Would any of your conclusions differ in the case of β^+ decay?

18. ^{20}Na decays to an excited state of ^{20}Ne through the emission of positrons of maximum kinetic energy 5.55 MeV. The excited state decays by α emission to the ground state of ^{16}O. Compute the energy of the emitted α.

19. Following the decay of ^{17}Ne, a highly excited state in ^{17}F emits a 10.597 MeV proton in decaying to the ground state of ^{16}O. What is the maximum energy of the positrons emitted in the decay to the ^{17}F excited state?

20. A certain β-decay process has three components, with maximum energies 0.672, 0.536, and 0.256 MeV. The first component has two coincident γ rays: 0.468 and 0.316 MeV, which are also coincident with each other. The second component has coincident γ's of 0.604, 0.308, 0.136, 0.468, 0.612, 0.296, and 0.316 MeV. The third β component is in coincidence with all of the above, plus 0.885, 0.589, 0.416, and 0.280 MeV. Use this information to construct a decay scheme and find the mass difference between the nuclear ground states.

21. The decay of ^{198}Au to ^{198}Pt by electron capture has not been observed, even though the very similar decay of ^{196}Au to ^{196}Pt by electron capture proceeds strongly. Examine the spectroscopic features of these decays and explain why the ^{198}Au electron-capture decay is not observed. (Use the *Table of Isotopes* or a similar spectroscopic reference.)

22. From collections of nuclear spectroscopic data, find and tabulate *ft* values for $\frac{3}{2}^+ \rightarrow \frac{1}{2}^+$ allowed decays in the region of N or $Z = 14$ to 20 ($d_{3/2}$ and $s_{1/2}$ shells). Also tabulate the allowed $\frac{3}{2}^- \rightarrow \frac{1}{2}^-$ decays for N or $Z = 2$ to 8 ($p_{3/2}$ and $p_{1/2}$ shells). Discuss any systematic differences between the two sets of values.

23. Using systematic collections of nuclear data (such as the *Table of Isotopes* or the *Nuclear Data Sheets*), tabulate the available information on $0^+ \rightarrow 0^+$ β transitions between $f_{7/2}$ nuclei ($20 \leq Z, N \leq 28$). Discuss the coupling of the odd proton and odd neutron, and explain the observed *ft* values.

24. Tabulate the available information on $g_{9/2} \rightarrow g_{7/2}$ positron decays of odd-mass nuclei; $g_{9/2}$ protons are generally found in the range $40 \leq Z \leq 50$, and $g_{7/2}$ neutrons are usually between $N = 50$ and $N = 66$. Try to account for the *ft* values. (*Note*: The GT decay is sometimes called a "spin-flip" process.)

25. There are many β-decaying odd-Z, odd-N nuclei with 2^- spin-parity assignments. These can decay to the 0^+ ground state or the 2^+ first excited state of the neighboring even-Z, even-N nucleus. (a) Use a general nuclear spectroscopy reference (*Table of Isotopes* or the *Nuclear Data Sheets*) to tabulate the *ft* values for the 2^+ and 0^+ final states from as many of these decay processes as you can find. (b) The $2^- \rightarrow 0^+$ decay is a first-forbidden process, in which the β decay must carry 2 units of total angular momentum, while in the $2^- \rightarrow 2^+$ decay it can carry 0, 1, or 2 units of angular momentum. Use your compilations of *ft* values to make some general conclusions on the relative probability of the β decay carrying 2 units of

angular momentum. (c) To examine whether there might be an explanation for this effect in terms of the 0^+ and 2^+ nuclear wave functions, make a similar tabulation of decays from 1^- states, that is, of $1^- \rightarrow 0^+$ and $1^- \rightarrow 2^+$ decays. Both these first-forbidden decays carry one unit of total angular momentum. (Why?) Do you observe a systematic difference in *ft* values between 0^+ and 2^+ final states? What do you conclude about the probable effect of the final nuclear state on the β decays from 2^- initial states?

26. There are several examples of allowed β decays that have larger than average *ft* values, which can be explained with reference to the nuclear structure. Consider, for example, the following cases: (a) $^{65}\text{Ni} \rightarrow {}^{65}\text{Cu}$ and $^{65}\text{Zn} \rightarrow {}^{65}\text{Cu}$, in which the ground state-ground state decays are both $\frac{5}{2}^-$ to $\frac{3}{2}^-$ Gamow-Teller decays, but the *ft* values are 1–2 orders of magnitude larger than for allowed decays to other low-lying states; (b) $^{115}\text{Te} \rightarrow {}^{115}\text{Sb}$ and $^{115}\text{Sb} \rightarrow {}^{115}\text{Sn}^*$; in the ^{115}Te decay, the $\frac{7}{2}^+ \rightarrow \frac{5}{2}^+$ transition to the ^{115}Sb ground state is not seen, and in the ^{115}Sb decay, a $\frac{7}{2}^+$ low-lying excited state is populated only weakly, with an *ft* value again 1–2 orders of magnitude larger than values for neighboring excited states. Find the shell model identification of these states and thus explain why the allowed decay mode is inhibited. Use the *Table of Isotopes* to find other examples of inhibited decays with the same shell-model assignments.

10

GAMMA DECAY

Most α and β decays, and in fact most nuclear reactions as well, leave the final nucleus in an excited state. These excited states decay rapidly to the ground state through the emission of one or more γ rays, which are photons of electromagnetic radiation like X rays or visible light. Gamma rays have energies typically in the range of 0.1 to 10 MeV, characteristic of the energy difference between nuclear states, and thus corresponding wavelengths between 10^4 and 100 fm. These wavelengths are far shorter than those of the other types of electromagnetic radiations that we normally encounter; visible light, for example, has wavelengths 10^6 times longer than γ rays.

The detail and richness of our knowledge of nuclear spectroscopy depends on what we know of the excited states, and so studies of γ-ray emission have become the standard technique of nuclear spectroscopy. Other factors that contribute to the popularity and utility of this method include the relative ease of observing γ rays (negligible absorption and scattering in air, for instance, contrary to the behavior of α and β radiations) and the accuracy with which their energies (and thus by deduction the energies of the excited states) can be measured. Furthermore, studying γ emission and its competing process, internal conversion, allows us to deduce the spins and parities of the excited states.

10.1 ENERGETICS OF γ DECAY

Let's consider the decay of a nucleus of mass M at rest, from an initial excited state E_i to a final state E_f. To conserve linear momentum, the final nucleus will not be at rest but must have a recoil momentum p_R and corresponding recoil kinetic energy T_R, which we assume to be nonrelativistic ($T_R = p_R^2/2M$). Conservation of total energy and momentum give

$$\begin{aligned} E_i &= E_f + E_\gamma + T_R \\ 0 &= \boldsymbol{p}_R + \boldsymbol{p}_\gamma \end{aligned} \tag{10.1}$$

It follows that $p_R = p_\gamma$; the nucleus recoils with a momentum equal and opposite to that of the γ ray. Defining $\Delta E = E_i - E_f$ and using the relativistic relationship $E_\gamma = cp_\gamma$,

$$\Delta E = E_\gamma + \frac{E_\gamma^2}{2Mc^2} \tag{10.2}$$

which has the solution

$$E_\gamma = Mc^2\left[-1 \pm \left(1 + 2\frac{\Delta E}{Mc^2}\right)^{1/2}\right] \tag{10.3}$$

The energy differences ΔE are typically of the order of MeV, while the rest energies Mc^2 are of order $A \times 10^3$ MeV, where A is the mass number. Thus $\Delta E \ll Mc^2$ and to a precision of the order of 10^{-4} to 10^{-5} we keep only the first three terms in the expansion of the square root:

$$E_\gamma \cong \Delta E - \frac{(\Delta E)^2}{2Mc^2} \tag{10.4}$$

which also follows directly from Equation 10.2 with the approximation $\Delta E \cong E_\gamma$.

The actual γ-ray energy is thus diminished somewhat from the maximum available decay energy ΔE. This recoil correction to the energy is generally negligible, amounting to a 10^{-5} correction that is usually far smaller than the experimental uncertainty with which we can measure energies. There is one circumstance in which the recoil plays an important role; this case, known as the Mössbauer effect, is discussed in Section 10.9. Except for this case, we will in the remainder of this chapter assume $E_\gamma = \Delta E$.

For low-energy γ rays, the recoil energy is less than 1 eV and has a negligible effect. High-energy γ rays (such as the 5–10-MeV radiations emitted following neutron capture) give recoils in the range of 100 eV, which may be sufficient to drive the recoiling atom from its position in a solid lattice. Effects of this sort are known as *radiation damage* and have an important place in the study of solids.

10.2 CLASSICAL ELECTROMAGNETIC RADIATION

As you will recall from your study of modern physics, electromagnetic radiation can be treated either as a classical wave phenomenon or else as a quantum phenomenon. The type of treatment we use is determined by the kind of physical effect we are trying to describe. For analyzing radiations from individual atoms and nuclei the quantum description is most appropriate, but we can more easily understand the quantum calculations of electromagnetic radiation if we first review the classical description.

Static (i.e., constant in time) distributions of charges and currents give static electric and magnetic fields. In Section 3.5, we discussed how these fields can be analyzed in terms of the *multipole moments* of the charge distribution—dipole moment, quadrupole moment, and so on. These multipole moments give characteristic fields, and we can conveniently study the dipole field, quadrupole field, and so on.

If the charge and current distributions vary with time, particularly if they vary sinusoidally with circular frequency ω, a *radiation field* is produced. The radiation field (which is studied at a distance from the source that is large compared with the size of the source) can be analyzed, like the static field, in terms of its multipole character. As an example, we consider the lowest multipole order, the dipole field.

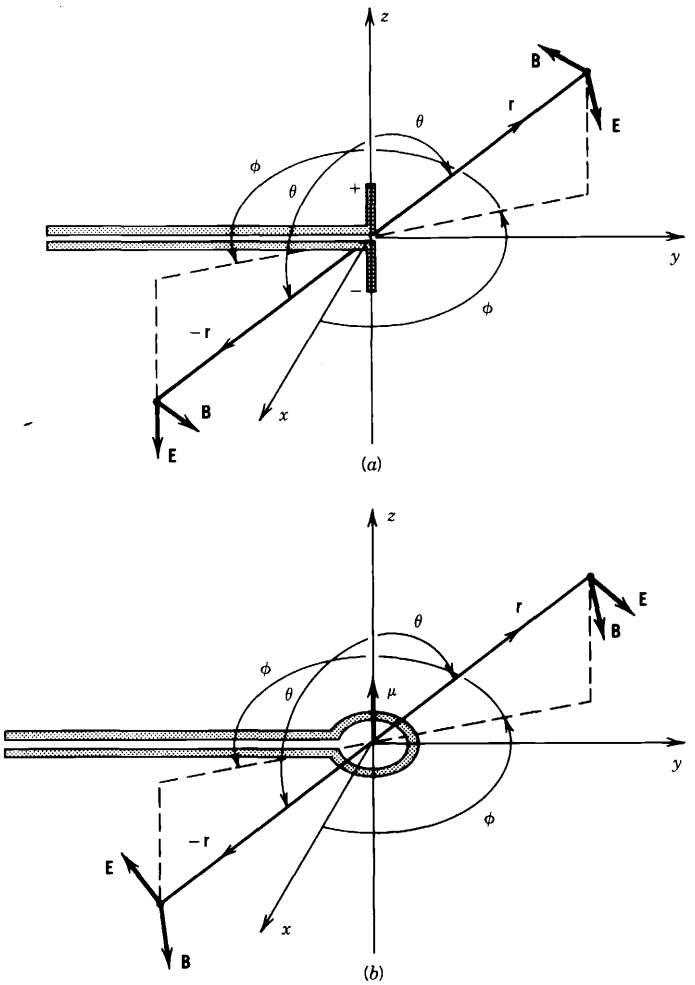


Figure 10.1 Electric and magnetic fields from (*a*) an electric dipole and (*b*) a magnetic dipole. In each case the dipole moment is along the z axis. The vectors show the radiation fields $\boldsymbol{E}$ and $\boldsymbol{B}$ at a particular instant of time. The wires along the negative y axes should be imagined as connected to a current source of frequency ω, and to be twisted so as to make no contribution themselves to the radiation. Also shown are the behaviors of $\boldsymbol{E}$ and $\boldsymbol{B}$ under the spatial reflection $\boldsymbol{r} \rightarrow -\boldsymbol{r}$; note the differences between the two cases.

A static *electric* dipole consists of equal and opposite charges $+q$ and $-q$ separated by a fixed distance z; the electric dipole moment is then $d = qz$. A static *magnetic* dipole can be represented as a circular current loop of current i enclosing area A; the magnetic dipole moment is $\mu = iA$. We can produce electromagnetic radiation fields by varying the dipole moments; for example, we can allow the charges to oscillate along the z axis, so that $d(t) = qz \cos \omega t$, thereby producing an electric dipole radiation field. Similarly, we could vary the current so that $\mu(t) = iA \cos \omega t$. Figure 10.1 shows the radiation fields produced in these two cases. The alternating electric dipole, Figure 10.1*a*, can be regarded

as a linear current element, for which the magnetic field lines form circles concentric with the z axis. The magnetic field vector $\boldsymbol{B}$ is tangent to the circles, and the electric field direction must be chosen so that $\boldsymbol{E} \times \boldsymbol{B}$ is in the direction of propagation of the radiation. The magnetic dipole, Figure 10.1*b*, has the magnetic field lines that we often associate with a bar magnet.

There are three characteristics of the dipole radiation field that are important for us to consider:

1. The power radiated into a small element of area, in a direction at an angle θ with respect to the z axis, varies as $\sin^2\theta$. The average radiated power can be calculated based on wave theory or on quantum theory, and by the correspondence principle the two calculations must agree when we extend the quantum result to the classical limit. This characteristic $\sin^2\theta$ dependence of dipole radiation must therefore be a characteristic result of the quantum calculation as well. Higher order multipoles, such as quadrupole radiation, have a different angular distribution. In fact, as we shall see, measuring the angular distribution of the radiation is a convenient way to determine which multipoles are present in the radiation.
2. Electric and magnetic dipole fields have opposite parity. Consider the effect of the transformation $\boldsymbol{r} \rightarrow -\boldsymbol{r}$. The magnetic field of the electric dipole clearly changes sign; thus $\boldsymbol{B}(\boldsymbol{r}) = -\boldsymbol{B}(-\boldsymbol{r})$. For the magnetic dipole, on the other hand, there is no change of sign, so $\boldsymbol{B}(\boldsymbol{r}) = \boldsymbol{B}(-\boldsymbol{r})$. Thus the electric and magnetic dipoles, which give identical angular distributions, differ in the parity of the radiation fields. Electric dipole radiation has odd parity, while magnetic dipole radiation has even parity.
3. The average radiated power (energy emitted per unit time) is

$$P = \frac{1}{12\pi\epsilon_0}\frac{\omega^4}{c^3}d^2 \tag{10.5}$$

for electric dipoles, and

$$P = \frac{1}{12\pi\epsilon_0}\frac{\omega^4}{c^5}\mu^2 \tag{10.6}$$

for magnetic dipoles. Here d and μ represent the *amplitudes* of the time-varying dipole moments.

Without entering into a detailed discussion of electromagnetic theory, we can extend these properties of dipole radiation to multipole radiation in general. We first define the index L of the radiation so that 2^L is the multipole order ($L = 1$ for dipole, $L = 2$ for quadrupole, and so on). With E for electric and M for magnetic, we can generalize the above three properties of dipole radiation.

1. The angular distribution of 2^L-pole radiation, relative to a properly chosen direction, is governed by the *Legendre polynomial* $P_{2L}(\cos\theta)$. The most common cases are dipole, for which $P_2 = \frac{1}{2}(3\cos^2\theta - 1)$, and quadrupole, with $P_4 = \frac{1}{8}(35\cos^4\theta - 30\cos^2\theta + 3)$.

2. The parity of the radiation field is

$$\pi(ML) = (-1)^{L+1}$$
$$\pi(EL) = (-1)^{L} \tag{10.7}$$

Notice that electric and magnetic multipoles of the same order always have opposite parity.

3. The radiated power is, using $\sigma = E$ or M to represent electric or magnetic radiation,

$$P(\sigma L) = \frac{2(L+1)c}{\epsilon_0 L[(2L+1)!!]^2}\left(\frac{\omega}{c}\right)^{2L+2}[m(\sigma L)]^2 \tag{10.8}$$

where $m(\sigma L)$ is the amplitude of the (time-varying) electric or magnetic multipole moment, and where the double factorial $(2L+1)!!$ indicates $(2L+1)\cdot(2L-1)\cdots 3\cdot 1$. The generalized multipole moment $m(\sigma L)$ differs, for $L = 1$, from the electric dipole moment d and magnetic dipole moment μ through some relatively unimportant numerical factors of order unity. From now on, we shall deal only with the generalized moments in our discussion of γ radiation.

10.3 TRANSITION TO QUANTUM MECHANICS

To carry the classical theory into the quantum domain, all we must do is quantize the sources of the radiation field, the classical multipole moments. In Equation 10.8, it is necessary to replace the *multipole moments* by appropriate *multipole operators* that change the nucleus from its initial state ψ_i to the final state ψ_f. As we have discussed for α and β radiation, the decay probability is governed by the *matrix element* of the *multipole operator*

$$m_{fi}(\sigma L) = \int \psi_f^* m(\sigma L)\psi_i \, dv \tag{10.9}$$

The integral is carried out over the volume of the nucleus. We shall not discuss the form of the operator $m(\sigma L)$, except to say that its function is to change the nuclear state from ψ_i to ψ_f while simultaneously creating a photon of the proper energy, parity, and multipole order.

If we regard Equation 10.8 as the energy radiated per unit time in the form of photons, each of which has energy $\hbar\omega$, then the probability per unit time for photon emission (that is, the decay constant) is

$$\lambda(\sigma L) = \frac{P(\sigma L)}{\hbar\omega} = \frac{2(L+1)}{\epsilon_0 \hbar L[(2L+1)!!]^2}\left(\frac{\omega}{c}\right)^{2L+1}[m_{fi}(\sigma L)]^2 \tag{10.10}$$

This expression for the decay constant can be carried no further until we evaluate the matrix element $m_{fi}(\sigma L)$, which requires knowledge of the initial and final wave functions. We can simplify the calculation and make some corresponding estimates of the γ-ray emission probabilities if we assume the transition is due to a single proton that changes from one shell-model state to another. In the case of electric transitions, the multipole operator includes a term of the form $er^L Y_{LM}(\theta, \phi)$, which reduces to ez for $L = 1$ (dipole) radiation as expected, and to $e(3z^2 - r^2)$ for $L = 2$ (quadrupole) radiation, analogous to the calculation of

the static quadrupole moment in Equation 3.36. If we take the radial parts of the nuclear wave functions ψ_i and ψ_f to be constant up to the nuclear radius R and zero for $r > R$, then the radial part of the transition probability is of the form

$$\int_0^R r^2 r^L \, dr \Big/ \int_0^R r^2 \, dr = \frac{3}{L+3} R^L \tag{10.11}$$

where the integral in the denominator is included for normalization and the r^2 factor comes from the volume element. Including this factor in the matrix element, and replacing the angular integrals by unity, which is also a reasonable estimate, the EL transition probability is estimated to be

$$\lambda(EL) \cong \frac{8\pi(L+1)}{L[(2L+1)!!]^2} \frac{e^2}{4\pi\epsilon_0 \hbar c} \left(\frac{E}{\hbar c}\right)^{2L+1} \left(\frac{3}{L+3}\right)^2 c R^{2L} \tag{10.12}$$

With $R = R_0 A^{1/3}$, we can make the following estimates for some of the lower multipole orders

$$\begin{aligned} \lambda(E1) &= 1.0 \times 10^{14} A^{2/3} E^3 \\ \lambda(E2) &= 7.3 \times 10^{7} A^{4/3} E^5 \\ \lambda(E3) &= 34 A^2 E^7 \\ \lambda(E4) &= 1.1 \times 10^{-5} A^{8/3} E^9 \end{aligned} \tag{10.13}$$

where λ is in s^{-1} and E is in MeV.

For magnetic transitions, the radial integral includes the term r^{L-1}, and the same assumption as above about the constancy of the nuclear wave function gives the factor $3R^{L-1}/(L+2)$. The magnetic operator also includes a factor that depends on the nuclear magnetic moment of the proton. The result for the ML transition probability is

$$\begin{aligned} \lambda(ML) \cong \frac{8\pi(L+1)}{L[(2L+1)!!]^2} &\left(\mu_p - \frac{1}{L+1}\right)^2 \left(\frac{\hbar}{m_p c}\right)^2 \left(\frac{e^2}{4\pi\epsilon_0 \hbar c}\right) \\ &\times \left(\frac{E}{\hbar c}\right)^{2L+1} \left(\frac{3}{L+2}\right)^2 c R^{2L-2} \end{aligned} \tag{10.14}$$

where again several angular momentum factors of order unity have been neglected. It is customary to replace the factor $[\mu_p - 1/(L+1)]^2$ by 10, which gives the following estimates for the lower multiple orders*:

$$\begin{aligned} \lambda(M1) &= 5.6 \times 10^{13} E^3 \\ \lambda(M2) &= 3.5 \times 10^{7} A^{2/3} E^5 \\ \lambda(M3) &= 16 A^{4/3} E^7 \\ \lambda(M4) &= 4.5 \times 10^{-6} A^2 E^9 \end{aligned} \tag{10.15}$$

*The numerical coefficients in Equation 10.15 differ slightly from those sometimes found in the literature. The difference arises because the factor $3/(L+2)$ in Equation 10.14 is often replaced by $3/(L+3)$, to make Equation 10.14 look more like Equation 10.12. We choose to maintain the form of Equation 10.14, so that to agree with some ML Weisskopf estimates in the literature, Equations 10.15 must be multiplied by $(L+2)^2/(L+3)^2$.

These estimates for the transition rates are known as *Weisskopf estimates* and are not meant to be true theoretical calculations to be compared with measured transition rates. Instead, they provide us with reasonable relative comparisons of the transition rates. For example, if the observed decay rate of a certain γ transition is many orders of magnitude smaller than the Weisskopf estimate, we might suspect that a poor match-up of initial and final wave functions is slowing the transition. Similarly, if the transition rate were much greater than the Weisskopf estimate, we might guess that more than one single nucleon is responsible for the transition.

Based on the Weisskopf estimates, we can immediately draw two conclusions about transition probabilities: (1) The lower multipolarities are dominant—increasing the multipole order by one unit reduces the transition probability by a factor of about 10^{-5}. A similar effect occurs in atoms, in which the most common transitions are dipole. (2) For a given multipole order, electric radiation is more likely than magnetic radiation by about two orders of magnitude in medium and heavy nuclei. We shall see in Section 10.7 how these expectations agree with observations.

10.4 ANGULAR MOMENTUM AND PARITY SELECTION RULES

A classical electromagnetic field produced by oscillating charges and currents transmits not only energy but angular momentum as well. If, for example, we surround the charges and currents with a large spherical absorbing shell, the shell can be made to rotate by the absorbed radiation. The rate at which angular momentum is radiated is proportional to the rate at which energy is radiated.

When we go over to the quantum limit, we can preserve the proportionality if each photon carries a definite angular momentum. The multipole operator of order L includes the factor $Y_{LM}(\theta, \phi)$, which is associated with an angular momentum L. We therefore conclude that a multipole of order L transfers an angular momentum of $L\hbar$ per photon.

Let's consider a γ transition from an initial excited state of angular momentum I_i and parity π_i to a final state I_f and π_f. For the moment we will assume $I_i \neq I_f$. Conservation of angular momentum requires that the total initial angular momentum be equal to the total final angular momentum. In vector terms,

$$\boldsymbol{I}_i = \boldsymbol{L} + \boldsymbol{I}_f$$

Since $\boldsymbol{I}_i$, $\boldsymbol{L}$, and $\boldsymbol{I}_f$ must form a closed vector triangle, the possible values of L are restricted. The largest possible value of L is $I_i + I_f$ and the smallest possible value is $|I_i - I_f|$. For example, if $I_i = \frac{3}{2}$ and $I_f = \frac{5}{2}$, the possible values of L are 1, 2, 3, and 4; the radiation field in this case would consist of a mixture of dipole, quadrupole, octupole ($L = 3$) and hexadecapole ($L = 4$) radiation.

Whether the emitted radiation is of the electric or magnetic type is determined by the relative parity of the initial and final levels. If there is no change in parity ($\Delta\pi$ = no), then the radiation field must have even parity; if the parity changes in the transition ($\Delta\pi$ = yes), then the radiation field must have odd parity. As shown by Equation 10.7, electric and magnetic multipoles differ in their parities. Electric transitions have even parity if L = even, while magnetic transitions have

even parity if L = odd. Therefore a $\Delta\pi$ = no transition would consist of even electric multipoles and odd magnetic multipoles. A $\Delta\pi$ = yes transition, on the other hand, would consist of odd electric and even magnetic multipoles. In our previous example ($I_i = \frac{3}{2}$ to $I_f = \frac{5}{2}$), let us assume that $\pi_i = \pi_f$, so that $\Delta\pi$ = no. We have already concluded that $L = 1, 2, 3$, or 4. The $L = 1$ radiation must be of magnetic character (odd magnetic and even electric multipoles for $\Delta\pi$ = no), the $L = 2$ radiation of electric character, and so on. The radiation field must thus be $M1$, $E2$, $M3$, and $E4$ radiation. If our two states had $\pi_i = -\pi_f$ ($\Delta\pi$ = yes) then the radiation field would be $E1$, $M2$, $E3$, and $M4$ radiation.

We therefore have the following angular momentum and parity *selection rules*:

$$\begin{aligned} &|I_i - I_f| \leq L \leq I_i + I_f \qquad (\text{no } L = 0) \\ &\Delta\pi = \text{no:} \qquad \text{even electric, odd magnetic} \\ &\Delta\pi = \text{yes:} \qquad \text{odd electric, even magnetic} \end{aligned} \tag{10.16}$$

The exception to the angular momentum selection rule occurs when $I_i = I_f$ because *there are no monopole* ($L = 0$) *transitions* in which a single photon is emitted. Classically, the monopole moment is just the electric charge, which does not vary with time. (A spherical charge distribution of radius R gives only a pure $1/r^2$ Coulomb field for $r > R$. Even if we allow the sphere to undergo radial oscillations, the Coulomb field for $r > R$ is unaffected and no radiation is produced.) For transitions in which $I_i = I_f$, the lowest possible γ-ray multipole order is dipole ($L = 1$).

The case in which either I_i or I_f is zero is particularly simple, for then only a pure multipole transition is emitted. For example, the first excited 2^+ ($I_i = 2$, π_i = even) state in even-Z, even-N nuclei decays to the 0^+ ground state through the emission of a pure electric quadrupole ($E2$) transition. The above selection rules give immediately $L = 2$ and electric radiation for $\Delta\pi$ = no.

For $I_i = I_f = 0$, the selection rules would give only $L = 0$, which as we have already discussed is not permitted for radiative transitions. A few even-even nuclei have 0^+ first excited states, which are forbidden to decay to the 0^+ ground state by γ emission. These states decay instead through *internal conversion*, which we discuss in Section 10.6. In this process the excitation energy is emitted by ejecting an *orbital* electron, the wave function of which penetrates the nuclear volume and samples the monopole distribution at $r < R$, where the potential *does* fluctuate.

Usually the spins I_i and I_f have values for which the selection rules permit several multipoles to be emitted. The single-particle (Weisskopf) estimates permit us to make some general predictions about which multipole is most likely to be emitted. Let us consider the previous example of an $I_i = \frac{3}{2}^+$ to $I_f = \frac{5}{2}^+$ transition ($M1$, $E2$, $M3$, $E4$). We assume a medium-weight nucleus ($A = 125$, so $A^{2/3} = 25$) and a transition energy $E = 1$ MeV. The estimates (Equations 10.13 and 10.15) give emission probabilities in the ratio

$$\lambda(M1) : \lambda(E2) : \lambda(M3) : \lambda(E4) = 1 : 1.4 \times 10^{-3} : 2.1 \times 10^{-10} : 1.3 \times 10^{-13}$$

You can see that the lower multipoles ($M1$ and $E2$) are far more likely than the higher ones. In practice we could regard this transition as being composed of $M1$ radiation with possibly a small mixture of $E2$. If the transition were $\Delta\pi$ = yes,

the multipoles would be $E1$, $M2$, $E3$, $M4$ with the ratios

$$\lambda(E1):\lambda(M2):\lambda(E3):\lambda(M4) = 1:2.3\times10^{-7}:2.1\times10^{-10}:2.1\times10^{-17}$$

Here only the $E1$ is expected to contribute to the transition.

There are rather general expectations, based on the single-particle estimates:

1. The lowest permitted multipole usually dominates.
2. Electric multipole emission is more probable than the same magnetic multipole emission by a factor of order 10^2 for medium and heavy nuclei. (Of course, the selection rules prohibit EL and ML from competing in the same radiation field.)
3. Emission of multipole $L+1$ is less probable than emission of multipole L by a factor of the order of about 10^{-5}.
4. Combining 2 and 3, we have the following (here $L' = L+1$)

$$\frac{\lambda(EL')}{\lambda(ML)} = \frac{\lambda(EL')}{\lambda(EL)}\cdot\frac{\lambda(EL)}{\lambda(ML)} \approx 10^{-5}\times10^{2} \approx 10^{-3}$$

$$\frac{\lambda(ML')}{\lambda(EL)} = \frac{\lambda(ML')}{\lambda(ML)}\cdot\frac{\lambda(ML)}{\lambda(EL)} \approx 10^{-5}\times10^{-2} \approx 10^{-7}$$

You can thus see why $M2$ competes with $E1$ far less effectively than $E2$ competes with $M1$. Keep in mind, however, that these are only estimates based on some very crude approximations. The properties of specific nuclear states can modify these estimates by many orders of magnitude; for example, we often find cases in which $\lambda(E2) > \lambda(M1)$, especially in transitions between vibrational or rotational collective states.

10.5 ANGULAR DISTRIBUTION AND POLARIZATION MEASUREMENTS

In this section we consider the experimental techniques that help us to distinguish one multipole from another. Measuring the energy of a γ ray emitted in a certain transition gives us no information on the multipole character, and even if we know I_i and I_f, all we can do is restrict the range of possible L values, not determine how much of each is present. (In fact, more frequently the reverse process is used—we might know I_f and restrict the range of I_i by measuring L.) Even measuring the lifetime is of limited usefulness because of the many assumptions made in obtaining the Weisskopf estimates. To determine the multipole order of the γ radiation, we must measure the angular distribution of the radiation, and to distinguish electric from magnetic radiations, it is necessary to do additional measurements, such as to measure the polarization of the radiation.

By way of illustration, let us consider a dipole transition from $I_i = 1$ to $I_f = 0$. The initial state includes three sublevels with $m_i = +1, 0, -1$; the final state has only one sublevel, with $m_f = 0$. The angular distribution generally depends on the values of m_i and m_f. For example, in the case $m_i = 0$ to $m_f = 0$, the γ

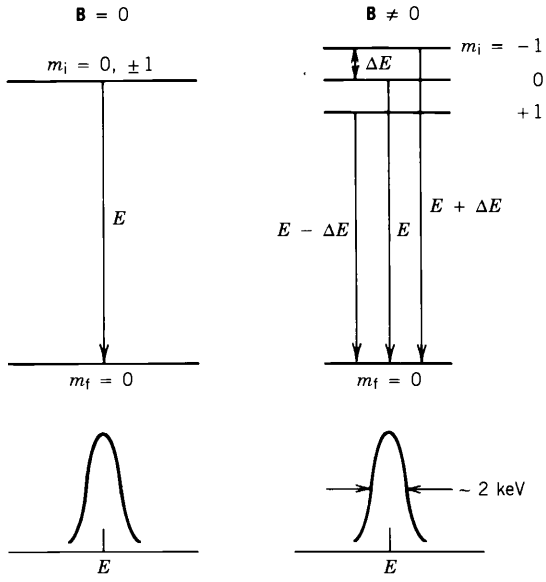


Figure 10.2 The nuclear Zeeman effect. In a magnetic field B, the $2I_i + 1$ sublevels of the state I_i are split into equally spaced states differing in energy by $\Delta E = \mu B / I_i$; for the case illustrated, $I_i = 1$, $2I_i + 1 = 3$, $I_f = 0$, and $\Delta E = \mu B$. Three transitions satisfy the dipole selection rule $\Delta m = 0, \pm 1$. The observed γ emission lines are shown below each diagram; because the energy resolution is much greater than the splitting ΔE, we cannot resolve the individual components.

emission probability varies as $\sin^2\theta$ (where the angle is defined with respect to the z axis that we use to measure the components of $\boldsymbol{I}_i$). This is in fact the quantum analog of the case of radiation from the classical dipole we considered in Section 10.2. The transitions from $m_i = \pm 1$ to $m_f = 0$ have angular distributions that vary as $\frac{1}{2}(1 + \cos^2\theta)$.

If we could pick out one of the three initial m states and measure the angular distribution of only that component of the transition, we would observe the characteristic angular distribution. The simplest scheme to do this would be to place the nuclei in a very strong magnetic field, so that the interaction of the magnetic moment μ of level I_i would give a splitting of that level depending on the relative orientations of $\boldsymbol{I}_i$ and the field $\boldsymbol{B}$. (This is exactly analogous to the Zeeman effect in atoms.) Figure 10.2 shows a representation of this situation. Before the field is turned on, there is one transition of energy E. When the field is present, the splitting of the levels gives three transitions of energy E, $E + \Delta E$, and $E - \Delta E$, where $\Delta E = \mu B$. If we could pick out only the component with energy $E + \Delta E$, for example, we would see the $\frac{1}{2}(1 + \cos^2\theta)$ distribution, relative to the direction of the field. We can estimate the magnitude of ΔE—for a typical magnetic moment of 1 nuclear magneton in a large field of 10 T, $\Delta E \simeq 10^{-6}$ eV. This small value of ΔE is far below the energy differences we can resolve with γ-ray detectors, which typically cannot separate or resolve transitions within 2 keV of each other. Thus what we actually observe is a mixture of all possible $m_i \rightarrow m_f$ ($+1 \rightarrow 0$, $0 \rightarrow 0$, $-1 \rightarrow 0$). If we let $W(\theta)$ represent the

observed angular distribution, then

$$W(\theta) = \sum_{m_i} p(m_i) W_{m_i \to m_f}(\theta)$$

where $p(m_i)$ is the *population* of the initial state, the fraction of the nuclei that occupies each sublevel.

Under normal circumstances all the populations are equal, $p(+1) = p(0) = p(-1) = \frac{1}{3}$, so that

$$W(\theta) \propto \tfrac{1}{3}\left[\tfrac{1}{2}(1 + \cos^2\theta)\right] + \tfrac{1}{3}(\sin^2\theta) + \tfrac{1}{3}\left[\tfrac{1}{2}(1 + \cos^2\theta)\right] = \text{constant}$$

that is, the angular distribution disappears and the radiation intensity is independent of direction.

There are two methods that can be used to create unequal populations $p(m_i)$ resulting in nonconstant $W(\theta)$. In the first method, we place the nuclei in a strong magnetic field, as we described previously, but at the same time we cool them to very low temperature, so low that the populations are made unequal by the Boltzmann distribution, $p(m_i) \propto e^{-m_i(\Delta E/kT)}$. To have unequal populations,

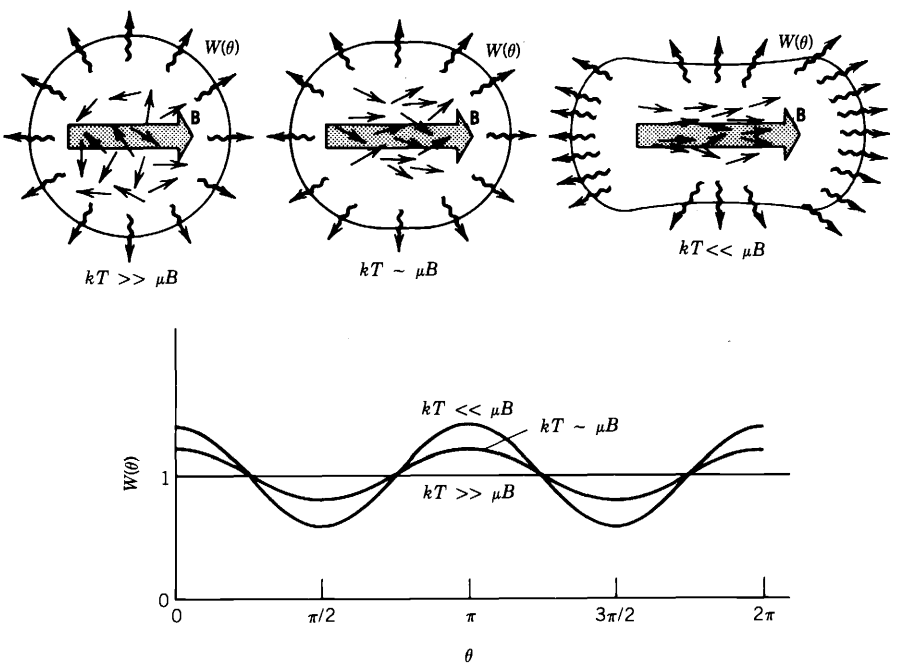


Figure 10.3 Angular distributions of nuclei with spins oriented at low temperatures. At top left is shown the distribution of radiation expected at high temperature; the magnetic field has essentially no effect in orienting the nuclear spins because of the thermal motion. At intermediate temperature (top center), the spins begin to align with the field, and the radiation distribution becomes nonuniform. At very low temperature, the spins are essentially completely aligned with the field. Measuring the angular distribution for dipole radiation would give the results shown at the bottom.

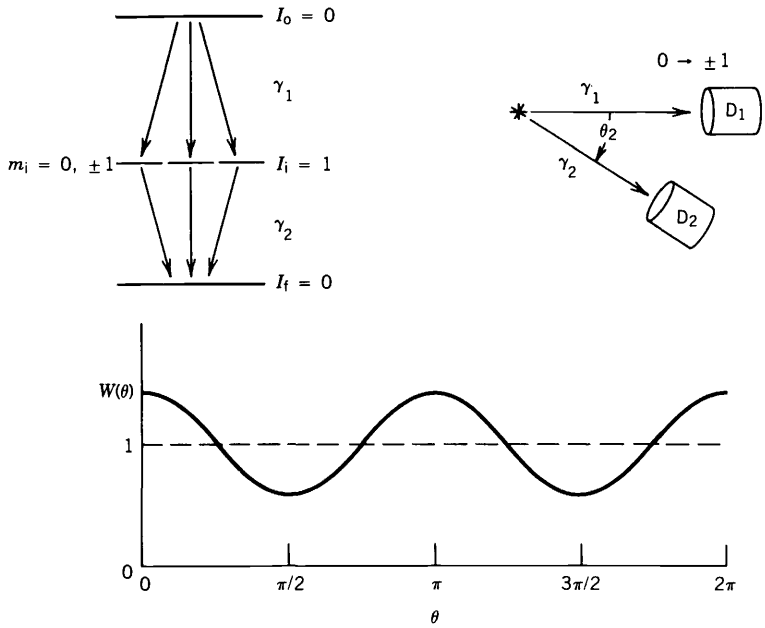


Figure 10.4 Angular correlation measurements. In a cascade of two radiations, here assumed to be $0 \rightarrow 1 \rightarrow 0$, the angular distribution of γ_2 is measured relative to the direction of γ_1. A typical result for two dipole transitions is shown at the bottom.

the exponential must be different from one, which means ΔE must be of the order of kT. (At high temperature, say room temperature, $kT \simeq 1/40$ eV, and $\Delta E \ll kT$, with the previous estimate of 10^{-6} eV for ΔE.) To have $\Delta E \sim kT$, we must cool the nuclei to $T \sim 0.01$ K. This is accomplished using continuously operating refrigerators, called helium dilution refrigerators, and this method, called low-temperature *nuclear orientation*, has become a powerful technique for determining γ-ray multipole characters and for inferring nuclear spin assignments. Figure 10.3 shows representative angular distributions for dipole radiation. Note that in this method we still cannot distinguish one component of the transition from another; we merely create a situation in which the various components contribute to the mixture with unequal weights.

The second method consists of creating an unequal mixture of populations $p(m_i)$ by observing a previous radiation. Let us assume for simplicity that the level I_i is populated by a transition from a state of spin $I_0 = 0$, so that there is a *cascade* $0 \rightarrow 1 \rightarrow 0$ of two radiations γ_1 and γ_2, as shown in Figure 10.4. Let's observe the first radiation in a certain direction, which we use to define the z axis; the second radiation is observed in a direction that makes an angle θ_2 with respect to the axis. With respect to the z axis, the first radiation has the same angular distribution we discussed above; for $m_0 = 0$ to $m_i = 0$, the distribution is proportional to $\sin^2 \theta_1$ and for $m_0 = 0$ to $m_i = \pm 1$, to $\frac{1}{2}(1 + \cos^2 \theta_1)$. Since we *define* the z axis by the direction of γ_1, it follows that $\theta_1 = 0$, and so the $0 \rightarrow 0$ transition cannot be emitted in that direction. That is, the nuclei for which γ_2 is observed following γ_1 must have a population of $p(m_i) = 0$ for $m_i = 0$. Thus the

angular distribution of γ_2 relative to γ_1 is

$$W(\theta) \propto \tfrac{1}{2}\left[\tfrac{1}{2}(1 + \cos^2\theta)\right] + 0(\sin^2\theta) + \tfrac{1}{2}\left[\tfrac{1}{2}(1 + \cos^2\theta)\right] \propto 1 + \cos^2\theta$$

This type of experiment is called an *angular correlation*; again, we do not observe the individual components of γ_2, but we create an unequal m-state population distribution of the state I_i.

We have considered these examples of angular distribution measurements for the simplest case of pure dipole radiation. In general, the angular distribution or correlation of multipole radiation is of the form of a polynomial in even powers of $\cos\theta$:

$$W(\theta) = 1 + \sum_{k=1}^{L} a_{2k} \cos^{2k}\theta \tag{10.17}$$

where the coefficients a_{2k} depend on I_i, I_f, and L, and also on whether we are doing a low-temperature angular distribution or an angular correlation experiment. For example, for the angular correlation $4^+ \xrightarrow{\gamma_1} 2^+ \xrightarrow{\gamma_2} 0^+$, where γ_1 and γ_2 are $E2$ radiation (γ_2 is pure $E2$ by the selection rules (Equation 10.16); γ_1 has a negligible mixture of $M3$ and higher multipoles), $a_2 = \frac{1}{8}$ and $a_4 = \frac{1}{24}$, while for

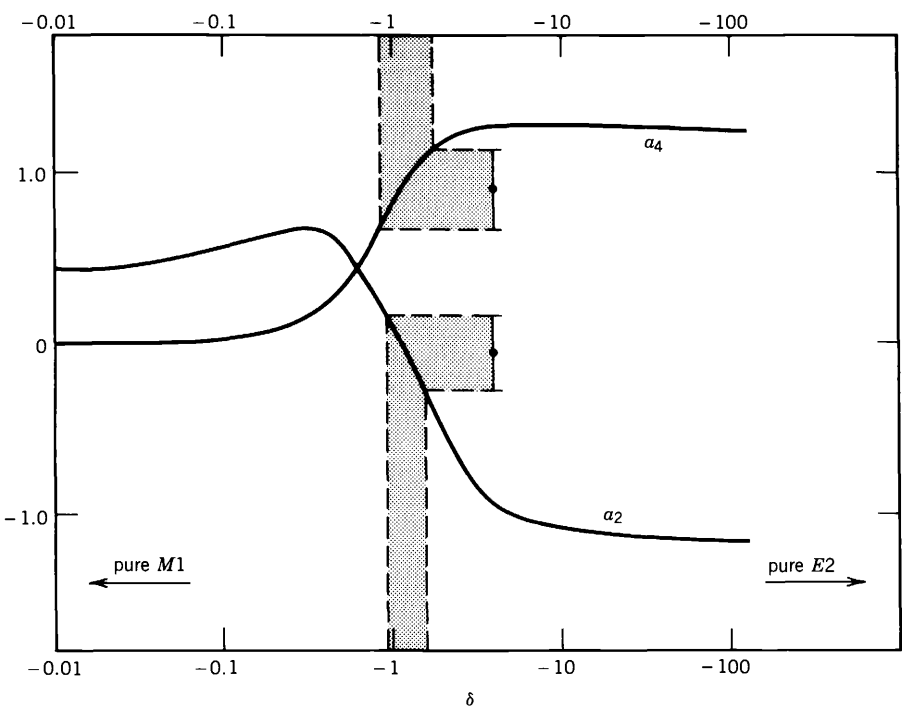


Figure 10.5 Analysis of angular correlation data for the ratio of $E2$ to $M1$ matrix elements in a transition. The vertical error bars show the ranges of the experimentally determined a_2 and a_4, each of which gives a corresponding value for δ. The a_2 and a_4 curves are derived from theory for this $2 \rightarrow 2 \rightarrow 0$ cascade in ^{110}Cd. Data from K. S. Krane and R. M. Steffen, *Phys. Rev. C* **2**, 724 (1970).

$0^+ \rightarrow 2^+ \rightarrow 0^+$ the angular correlation is $a_2 = -3$, $a_4 = 4$. Returning to the original goal of this discussion, let us consider the angular correlation for $2^+ \xrightarrow{\gamma_1} 2^+ \xrightarrow{\gamma_2} 0^+$, where γ_1 is a mixture of $M1$ and $E2$ (neglecting the higher multipoles). The coefficients a_2 and a_4 depend on the relative amounts of $M1$ and $E2$ radiation; Figure 10.5 shows a_2 and a_4 as they vary with the parameter δ, which essentially is $m_{fi}(E2)/m_{fi}(M1)$, where $m_{fi}(\sigma L)$ is the transition matrix element defined by Equation 10.9. The fraction of $E2$ radiation is $\delta^2/(1 + \delta^2)$ and the fraction of $M1$ radiation is $1/(1 + \delta^2)$. As an example, the case of the 818–658-keV $2^+ \rightarrow 2^+ \rightarrow 0^+$ cascade in ^{110}Cd has the measured values $a_2 = -0.06 \pm 0.22$, $a_4 = 0.89 \pm 0.24$. As shown in Figure 10.5, the deduced ratio of the multipole matrix elements is $\delta = -1.2 \pm 0.2$, corresponding to the 818-keV radiation being 59% $E2$ and 41% $M1$. This accurate knowledge of multipole character is extremely important in evaluating nuclear models and deducing partial lifetimes, as we discuss in Section 10.7. Thus angular distribution and correlation measurements have an extremely important role in nuclear spectroscopy.

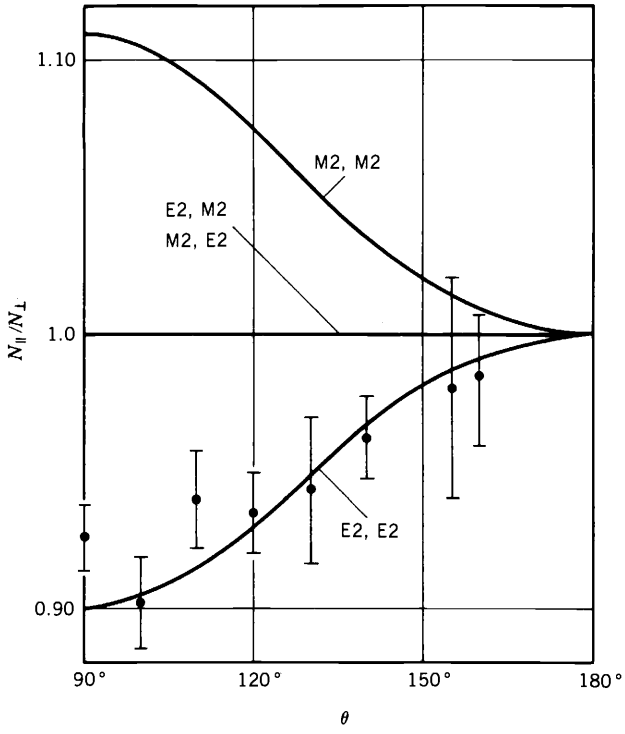


Figure 10.6 An angular correlation measurement in which the linear polarization of the radiation is measured. The angle θ refers, as in Figures 10.4 and 7.43, to the angle between the two radiations. Data shown are for two transitions in the decay of ^{46}Sc, obtained by F. Metzger and M. Deutsch, *Phys. Rev.* **78**, 551 (1950). Theoretical curves are drawn for various combinations of $E2$ and $M2$ radiations. The results indicate convincingly that both transitions must be of $E2$ character, consistent with the presently known $4^+ \rightarrow 2^+ \rightarrow 0^+$ level scheme.

To determine whether the radiation is electric or magnetic in character, additional measurements are necessary for in the angular distribution a_2 and a_4 are identical for E and M radiation. In Figure 10.1, you can see that the $\boldsymbol{E}$ vector of the radiation field is parallel to the dipole axis for electric radiation but normal to it for magnetic radiation. The same characteristic carries into the complete quantum description, and we can distinguish E from M radiation by determining the directional relationship between the axis of the emitting nucleus, the direction of the emitted radiation, and its $\boldsymbol{E}$ field. The plane formed by the radiation propagation direction $\boldsymbol{r}$ and the field $\boldsymbol{E}$ is called the *plane of polarization*. (Given $\boldsymbol{r}$ and $\boldsymbol{E}$, we can deduce $\boldsymbol{B}$ because the radiation propagates in the direction $\boldsymbol{E} \times \boldsymbol{B}$. Choosing $\boldsymbol{r}$ and $\boldsymbol{E}$ to define the polarization is merely a convention and has no intrinsic significance.) As in the previous measurement, we must begin with an unequal distribution of m states. (In the classical case, this would be equivalent to knowing the direction of the axis of the dipole since it is possible that a given direction for $\boldsymbol{E}$ can correspond to an electric dipole in the z direction or a magnetic dipole in the y direction.)

This type of measurement is called a *linear polarization distribution* and is usually accomplished by taking advantage of the polarization dependence of Compton scattering (see Section 7.9 and Figure 7.43). Figure 10.6 shows an example of an angular correlation in which the linear polarization of γ_2 is observed. As before, the observation of the previous radiation γ_1 in effect provides the unequal m-state distribution, and we measure the linear polarization of γ_2 by the intensity of the Compton-scattered photons as a function of ϕ.

10.6 INTERNAL CONVERSION

Internal conversion is an electromagnetic process that competes with γ emission. In this case the electromagnetic multipole fields of the nucleus do not result in the emission of a photon; instead, the fields interact with the atomic electrons and cause one of the electrons to be emitted from the atom. In contrast to β decay, the electron is not created in the decay process but rather is a previously existing electron in an atomic orbit. For this reason internal conversion decay rates can be altered slightly by changing the chemical environment of the atom, thus changing somewhat the atomic orbits. Keep in mind, however, that this is *not* a two-step process in which a photon is first emitted by the nucleus and then knocks loose an orbiting electron by a process analogous to the photoelectric effect; such a process would have a negligibly small probability to occur.

The transition energy ΔE appears in this case as the kinetic energy T_e of the emitted electron, less the binding energy B that must be supplied to knock the electron loose from its atomic shell:

$$T_e = \Delta E - B \tag{10.18}$$

As we did in our discussion of nuclear binding energy, we take B to be a positive number. The energy of a bound state is of course negative, and we regard the binding energy as that which we must supply to go from that state up to zero energy. Because the electron binding energy varies with the atomic orbital, for a

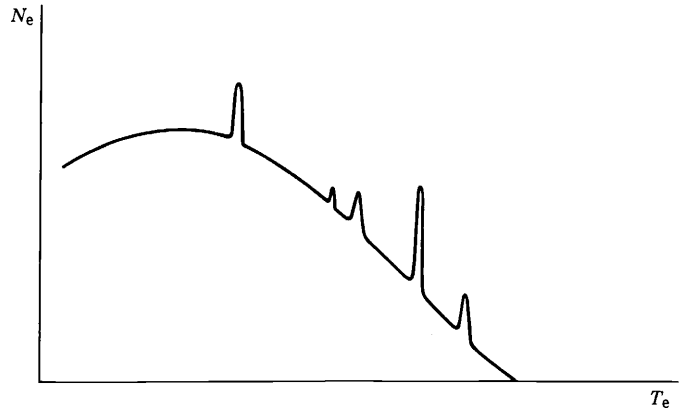


Figure 10.7 A typical electron spectrum such as might be emitted from a radioactive nucleus. A few discrete conversion electron peaks ride on the continuous background from β decay.

given transition ΔE there will be internal conversion electrons emitted with differing energies. The observed electron spectrum from a source with a single γ emission thus consists of a number of individual components; these are discrete components, however, and not at all continuous like the electrons emitted in β decay. Most radioactive sources will emit both β-decay and internal conversion electrons, and it is relatively easy to pick out the discrete conversion electron peaks riding on the continuous β spectrum (Figure 10.7).

Equation 10.18 suggests that the internal conversion process has a threshold energy equal to the electron binding energy in a particular shell; as a result, the conversion electrons are labeled according to the electronic shell from which they come: K, L, M, and so on, corresponding to principal atomic quantum numbers $n = 1, 2, 3, \ldots$. Furthermore, if we observe at very high resolution, we can even see the substructure corresponding to the individual electrons in the shell. For example, the L ($n = 2$) shell has the atomic orbitals $2s_{1/2}$, $2p_{1/2}$, and $2p_{3/2}$; electrons originating from these shells are called, respectively, L_I, L_{II}, and L_{III} conversion electrons.

Following the conversion process, the atom is left with a vacancy in one of the electronic shells. This vacancy is filled very rapidly by electrons from higher shells, and thus we observe characteristic X-ray emission accompanying the conversion electrons. For this reason, when we study the γ emission from a radioactive source we usually find X rays near the low-energy end of the spectrum.

As an illustration of the calculation of electron energies, consider the β decay of ^{203}Hg to ^{203}Tl, following which a single γ ray of energy 279.190 keV is emitted. To calculate the energies of the conversion electrons, we must look up the electron binding energies in the *daughter* Tl because it is from that atom that the electron emission takes place. (We will assume that the atomic shells have enough time to settle down between the β emission and the subsequent γ or conversion electron emission; this may not necessarily be true and will depend on the chemical environment and on the lifetime of the excited state.) Electron binding energies are conveniently tabulated in Appendix III of the *Table of*

Isotopes. For Tl, we find the following:

$$B(\mathrm{K}) = 85.529 \text{ keV}$$
$$B(\mathrm{L_I}) = 15.347 \text{ keV}$$
$$B(\mathrm{L_{II}}) = 14.698 \text{ keV}$$
$$B(\mathrm{L_{III}}) = 12.657 \text{ keV}$$
$$B(\mathrm{M_I}) = 3.704 \text{ keV}$$

and so on through the M, N, and O shells. We therefore expect to find conversion electrons emitted with the following energies:

$$T_e(\mathrm{K}) = 279.190 - 85.529 = 193.661 \text{ keV}$$
$$T_e(\mathrm{L_I}) = 279.190 - 15.347 = 263.843 \text{ keV}$$
$$T_e(\mathrm{L_{II}}) = 279.190 - 14.698 = 264.492 \text{ keV}$$
$$T_e(\mathrm{L_{III}}) = 279.190 - 12.657 = 266.533 \text{ keV}$$
$$T_e(\mathrm{M_I}) = 279.190 - 3.704 = 275.486 \text{ keV}$$

Figure 10.8 shows the electron spectrum for ^{203}Hg. You can see the continuous β spectrum as well as the electron lines at the energies we have calculated.

One feature that is immediately apparent is the varying intensities of the conversion electrons from the decay. This variation, as we shall see, depends on the multipole character of the radiation field; in fact, measuring the relative probabilities of conversion electron emission is one of the primary ways to determine multipole characters.

In some cases, internal conversion is heavily favored over γ emission; in others it may be completely negligible compared with γ emission. As a general rule, it is necessary to correct for internal conversion when calculating the probability for γ emission. That is, if we know the half-life of a particular nuclear level, then the total decay probability λ_t (equal to $0.693/t_{1/2}$) has two components, one (λ_γ) arising from γ emission and another (λ_e) arising from internal conversion:

$$\lambda_t = \lambda_\gamma + \lambda_e \tag{10.19}$$

The level decays more rapidly through the combined process than it would if we considered γ emission alone. It is (as we shall see) convenient to define the *internal conversion coefficient* α as

$$\alpha = \frac{\lambda_e}{\lambda_\gamma} \tag{10.20}$$

That is, α gives the probability of electron emission relative to γ emission and ranges from very small (≈ 0) to very large. The total decay probability then becomes

$$\lambda_t = \lambda_\gamma(1 + \alpha) \tag{10.21}$$

We let α represent the *total* internal conversion coefficient and define *partial* coefficients representing the individual atomic shells:

$$\begin{aligned}\lambda_t &= \lambda_\gamma + \lambda_{e,\mathrm{K}} + \lambda_{e,\mathrm{L}} + \lambda_{e,\mathrm{M}} + \cdots \\ &= \lambda_\gamma(1 + \alpha_\mathrm{K} + \alpha_\mathrm{L} + \alpha_\mathrm{M} + \cdots)\end{aligned} \tag{10.22}$$

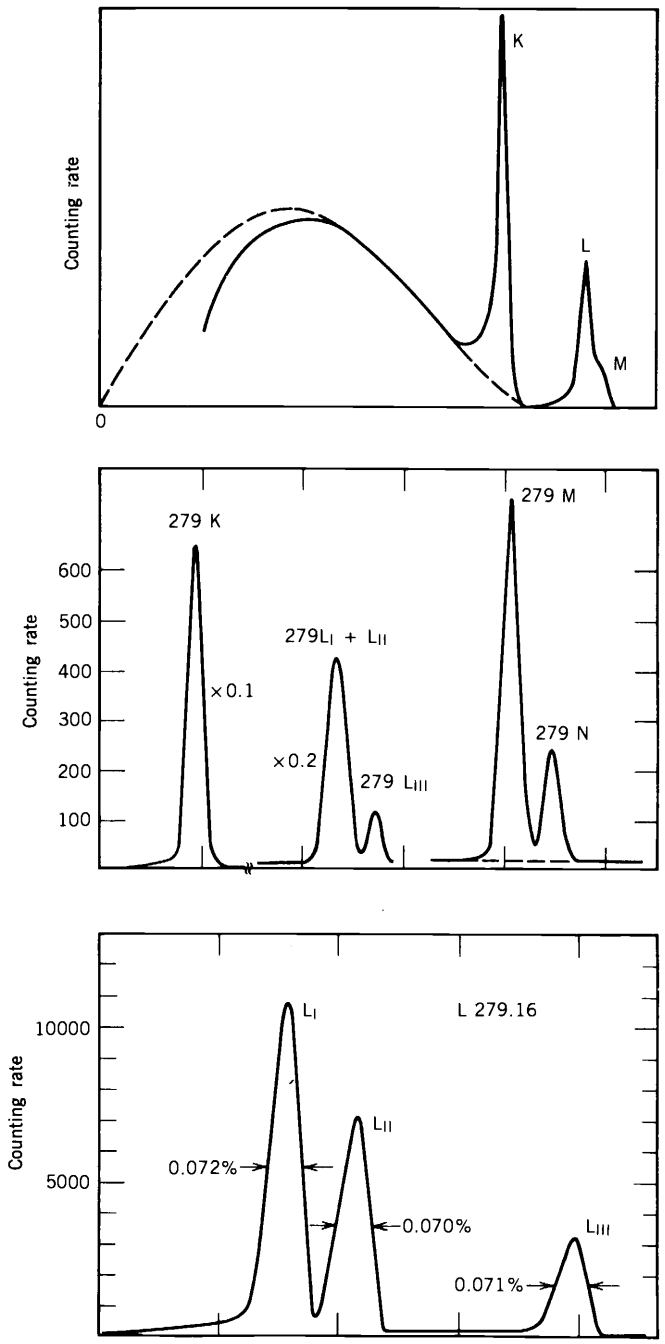


Figure 10.8 Electron spectrum from the decay of ^{203}Hg. At top, the continuous β spectrum can be seen, along with the K and unresolved L and M conversion lines. In the middle is shown the conversion spectrum at higher resolution; the L and M lines are now well separated, and even L_{III} is resolved. At yet higher resolution (bottom) L_I and L_{II} are clearly separated. *Sources*: (top) A. H. Wapstra et al., *Physica* **20**, 169 (1954); (middle) Z. Sujkowski, *Ark. Fys.* **20**, 243 (1961); (bottom) C. J. Herrlander and R. L. Graham, *Nucl. Phys.* **58**, 544 (1964).

and thus

$$\alpha = \alpha_K + \alpha_L + \alpha_M + \cdots \tag{10.23}$$

Of course, considering the subshells, we could break these down further, such as

$$\alpha_L = \alpha_{L_I} + \alpha_{L_{II}} + \alpha_{L_{III}} \tag{10.24}$$

and similarly for other shells.

The calculation of internal conversion coefficients is a difficult process, beyond the level of the present text. Let's instead try to justify some of the general results and indicate the way in which the calculation differs from the similar calculation for γ emission. Because the process is electromagnetic in origin, the matrix element that governs the process is quite similar to that of Equation 10.9 with two exceptions: the initial state includes a bound electron, so that $\psi_i = \psi_{i,N}\psi_{i,e}$ where N indicates the nuclear wave function and e indicates the electron wave function. Similarly, $\psi_f = \psi_{f,N}\psi_{f,e}$ where in this case $\psi_{f,e}$ is the free-particle wave function $e^{-i\boldsymbol{k}\cdot\boldsymbol{r}_e}$. To a very good approximation, the atomic wave function varies relatively little over the nucleus, and we can replace $\psi_{i,e}(\boldsymbol{r}_e)$ with its value at $\boldsymbol{r}_e = 0$. The important detail, however, is that all of the specifically nuclear information is contained in $\psi_{i,N}$ and $\psi_{f,N}$, and that the same electromagnetic multipole operator $m(\sigma L)$ governs both γ emission and internal conversion. The *nuclear* part of the matrix element of Equation 10.9 is therefore identical for both processes:

$$\begin{aligned} \lambda_\gamma(\sigma L) &\propto |m_{fi}(\sigma L)|^2 \\ \lambda_e(\sigma L) &\propto |m_{fi}(\sigma L)|^2 \end{aligned} \tag{10.25}$$

and thus the internal conversion coefficient α, the ratio of λ_e and λ_γ, is *independent* of the details of nuclear structure. The coefficient α will depend on the atomic number of the atom in which the process occurs, and on the energy of the transition and its multipolarity (hence, indirectly on the nuclear structure). We can therefore calculate and display general tables or graphs of α for different Z, T_e, and L.

We are oversimplifying here just a bit because the electron wave function $\psi_{i,e}$ does penetrate the nucleus and does sample the specific nuclear wave function, but it has a very slight, usually negligible, effect on the conversion coefficient.

A nonrelativistic calculation gives the following instructive results for electric (E) and magnetic (M) multipoles:

$$\alpha(EL) \cong \frac{Z^3}{n^3}\left(\frac{L}{L+1}\right)\left(\frac{e^2}{4\pi\epsilon_0\hbar c}\right)^4\left(\frac{2m_ec^2}{E}\right)^{L+5/2} \tag{10.26}$$

$$\alpha(ML) \cong \frac{Z^3}{n^3}\left(\frac{e^2}{4\pi\epsilon_0\hbar c}\right)^4\left(\frac{2m_ec^2}{E}\right)^{L+3/2} \tag{10.27}$$

In these expressions, Z is the atomic number of the atom in which the conversion takes place (the daughter, in the case of transitions following β decay) and n is the principal quantum number of the bound electron wave function; the factor $(Z/n)^3$ comes from the term $|\psi_{i,e}(0)|^2$ that appears in the conversion rate (the hydrogenic wave functions of Table 2.5 show the factor $(Z/n)^{3/2}$ in the nor-

malization constant). The dimensionless factor ($e^2/4\pi\epsilon_0\hbar c$) is the fine structure constant with a value close to $\frac{1}{137}$.

These expressions for the conversion coefficients are only approximate, for the electron must be treated relativistically (transition energies are typically 0.5–1 MeV, so it is *not* true that $T_e \ll m_e c^2$) and the "point" nucleus Coulomb wave functions such as those of Table 2.5 do not properly take into account the important effects that occur when the electron penetrates the nucleus. Tabulations of conversion coefficients based on more rigorous calculations are listed at the end of the chapter. The approximate expressions do, however, illustrate a number of features of the conversion coefficients:

1. They increase as Z^3, and so the conversion process is more important for heavy nuclei than for light nuclei. For example, the 1.27-MeV $E2$ transition in $^{22}_{10}$Ne has $\alpha_K = 6.8 \times 10^{-6}$ and the 1.22-MeV $E2$ transition in $^{182}_{74}$W has $\alpha_K = 2.5 \times 10^{-3}$; their ratio is very nearly equal to $(10/74)^3$, as expected.
2. The conversion coefficient decreases rapidly with increasing transition energy. (In contrast, the probability for γ emission increases rapidly with energy.) For example, in ^{56}Co there are three $M1$ transitions, with energies 158 keV ($\alpha_K = 0.011$), 270 keV ($\alpha_K = 0.0034$), and 812 keV ($\alpha_K = 0.00025$). These decrease approximately as $E^{-2.5}$, as expected based on Equation 10.27.
3. The conversion coefficients increase rapidly as the multipole order increases; in fact, for the higher L values, conversion electron emission may be far more probable than γ emission. For example, in ^{99}Tc there is an $M1$ transition of 141 keV with $\alpha_K = 0.10$, while an $M4$ transition of 143 keV has $\alpha_K = 30$. Based on Equation 10.27 we would expect the ratio $\alpha_K(143)/\alpha_K(141)$ to be about $(2m_e c^2/E)^3$, or about 370, which is quite consistent with the observed ratio (about 300).
4. The conversion coefficients for higher atomic shells ($n > 1$) decrease like $1/n^3$. Thus for a given transition, we might roughly expect $\alpha_K/\alpha_L \simeq 8$. Using the correct electronic wave functions will cause this estimate to vary considerably, but many experimental values of α_K/α_L do fall in the range of 3–6, so even in this case our estimate serves us well.

We therefore expect relatively large K-shell conversion coefficients for low-energy, high-multipolarity transitions in heavy nuclei, with smaller values in other cases (higher atomic shells, higher transition energy, lighter nuclei, lower multipoles).

While these estimates give us reasonable qualitative values, for quantitative comparisons with experimental results, we must do detailed computations of the conversion coefficients, using the proper atomic wave functions. Figure 10.9 shows some results of such calculations. Notice that the coefficients differ considerably for EL and ML transitions; thus measurement of α allows us to determine the relative parities of nuclear states.

There is one other application for which internal conversion is an essential tool —the observation of $E0$ transitions, which are forbidden to go by electromagnetic radiation because the nuclear monopole moment (that is, its charge) cannot radiate to points external to the nucleus. The $E0$ transition is particularly important in decays from 0^+ initial states to 0^+ final states, which cannot occur

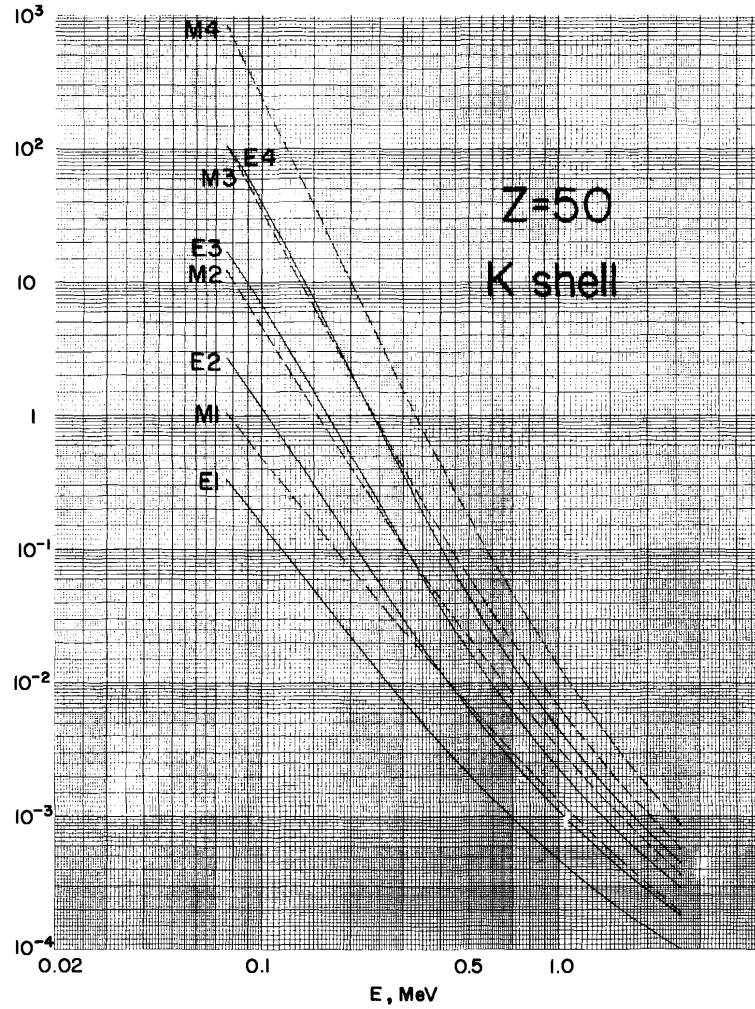


Figure 10.9 K-shell internal conversion coefficients for $Z = 50$. From *Table of Isotopes*, edited by C. M. Lederer and V. S. Shirley (New York: Wiley, 1978).

by any other direct process. We can regard the nucleus in this case as a spherically symmetric ball of charge; the only possible motion is a pulsation, which does not alter the electric field at points external to the sphere and thus produces no radiation. Electronic orbits that do not vanish near $r = 0$ (that is, s states) can sample the varying potential *within* the pulsating nucleus, and so a transfer of energy to the electron is possible.

Because no γ rays are emitted, it is not possible to define a conversion coefficient (α is infinite for $\lambda_\gamma = 0$). We can illustrate a particular case in which the decay occurs by the ^{72}Ge level scheme shown in Figure 10.10. The excited 0^+ state decays to the ground state by $E0$ conversion with a half-life of 0.42 μs. The nearby 2^+ state can decay by γ emission much more rapidly; the internal conversion coefficient for that decay is only 4.9×10^{-4}. Comparison of these rates will involve evaluating the nuclear matrix elements (because we cannot take

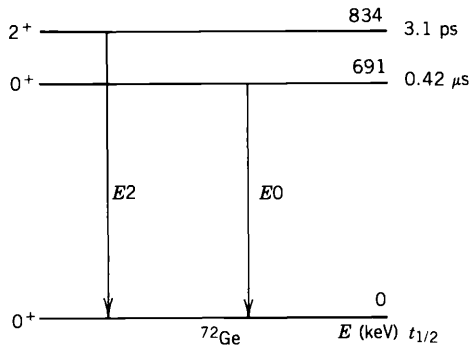


Figure 10.10 Energy levels in ^{72}Ge.

the ratio λ_e/λ_γ for the $E0$ transition, its matrix elements do not cancel), but may reveal to us something about the internal structure of the excited 0^+ state.

10.7 LIFETIMES FOR γ EMISSION

In Chapter 7, we discussed techniques for measuring the half-lives of excited states. One primary usefulness of these experimental values is for comparing with theoretical values calculated on the basis of different models of the nucleus. If we compare various calculated values with the experimental one, we can often draw some conclusions about the structure of the nucleus.

Before we do this, we must first evaluate the *partial* decay rate for γ emission, as we did at the end of Section 6.5. Let's consider the example of the decay shown in Figure 10.11. The half-life of the 1317-keV level has been measured to be 8.7 ps. Its total decay constant is therefore

$$\lambda_t = \frac{0.693}{t_{1/2}} = \frac{0.693}{8.7 \times 10^{-12}\ \text{s}} = 8.0 \times 10^{10}\ \text{s}^{-1}$$

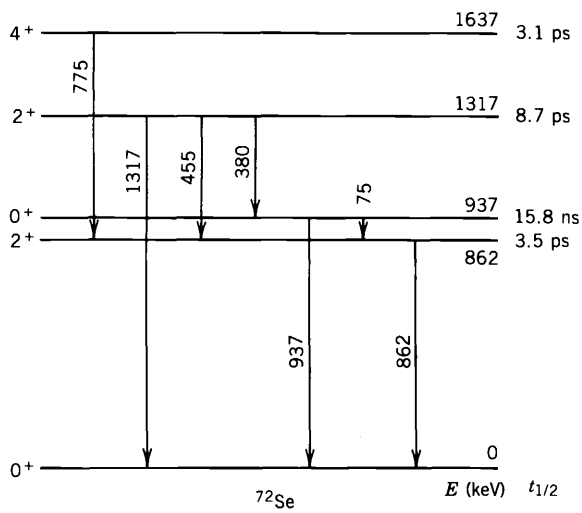


Figure 10.11 Energy levels in ^{72}Se.

This decay rate is just the sum of the decay rates of the three transitions that depopulate the state:

$$\begin{aligned}\lambda_t &= \lambda_{t,1317} + \lambda_{t,455} + \lambda_{t,380} \\ &= \lambda_{\gamma,1317}(1 + \alpha_{1317}) + \lambda_{\gamma,455}(1 + \alpha_{455}) + \lambda_{\gamma,380}(1 + \alpha_{380})\end{aligned}$$

The conversion coefficients can be found in standard reference works (they have not been measured in this case) and are sufficiently small (< 0.01) that they can be neglected (compared with 1) to the precision of this calculation. Thus

$$\lambda_t = \lambda_{\gamma,1317} + \lambda_{\gamma,455} + \lambda_{\gamma,380}$$

The relative intensities of the three γ rays have been measured to be

$$\lambda_{\gamma,1317} : \lambda_{\gamma,455} : \lambda_{\gamma,380} = 51 : 39 : 10$$

and so the partial decay rates for the three γ rays are

$$\lambda_{\gamma,1317} = 0.51(8.0 \times 10^{10}\ \text{s}^{-1}) = 4.1 \times 10^{10}\ \text{s}^{-1}$$

$$\lambda_{\gamma,455} = 0.39(8.0 \times 10^{10}\ \text{s}^{-1}) = 3.1 \times 10^{10}\ \text{s}^{-1}$$

$$\lambda_{\gamma,380} = 0.10(8.0 \times 10^{10}\ \text{s}^{-1}) = 0.80 \times 10^{10}\ \text{s}^{-1}$$

It is these *partial rates for* γ *emission* that can be compared with calculated values, such as the Weisskopf estimates of Equation 10.13. Let us calculate the expected values of $\lambda(E2)$:

$$\lambda_{E2,1317} = 8.7 \times 10^{10}\ \text{s}^{-1}$$

$$\lambda_{E2,455} = 4.3 \times 10^{8}\ \text{s}^{-1}$$

$$\lambda_{E2,380} = 1.7 \times 10^{8}\ \text{s}^{-1}$$

The case of the 937-keV level ($t_{1/2} = 15.8$ ns) can be handled similarly:

$$\lambda_t = \frac{0.693}{15.8\ \text{ns}} = 4.39 \times 10^{7}\ \text{s}^{-1}$$

$$\begin{aligned}\lambda_t &= \lambda_{t,937} + \lambda_{t,75} \\ &= \lambda_{e,937} + \lambda_{\gamma,75}(1 + \alpha_{75})\end{aligned}$$

because the 937-keV transition is of the $0 \rightarrow 0$, $E0$ type we discussed in the previous section. The total conversion coefficient of the 75-keV transition is about 2.4 (from tables or graphs). Experimentally, it is known that $\lambda_{\gamma,75} : \lambda_{e,937} = 73 : 27$, and thus

$$\lambda_{e,937} = 4.3 \times 10^{6}\ \text{s}^{-1}$$

$$\lambda_{\gamma,75} = 1.16 \times 10^{7}\ \text{s}^{-1}$$

Finally, for the 862-keV transition, we find

$$\lambda_{\gamma,862} = 2.0 \times 10^{11}\ \text{s}^{-1}$$

From the Weisskopf estimates, we would compute

$$\lambda_{E2,75} = 5.2 \times 10^{4}\ \text{s}^{-1}$$

$$\lambda_{E2,862} = 1.0 \times 10^{10}\ \text{s}^{-1}$$

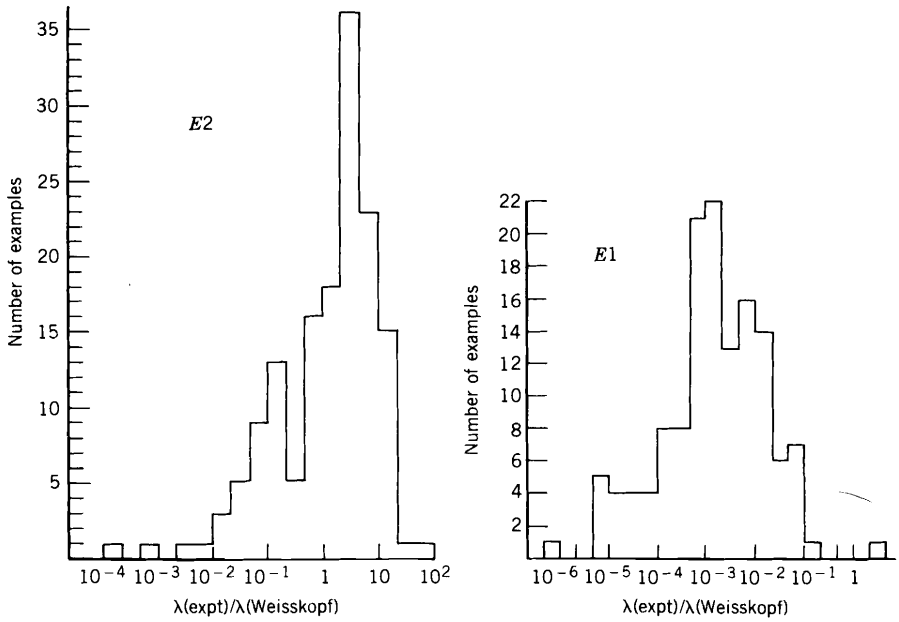


Figure 10.12 Systematics of $E2$ and $E1$ transitions. The figures show the number of cases versus the ratio between the observed decay rate and the value calculated from the Weisskopf formulas. From S. J. Skorka et al., *Nucl. Data* **2**, 347 (1966).

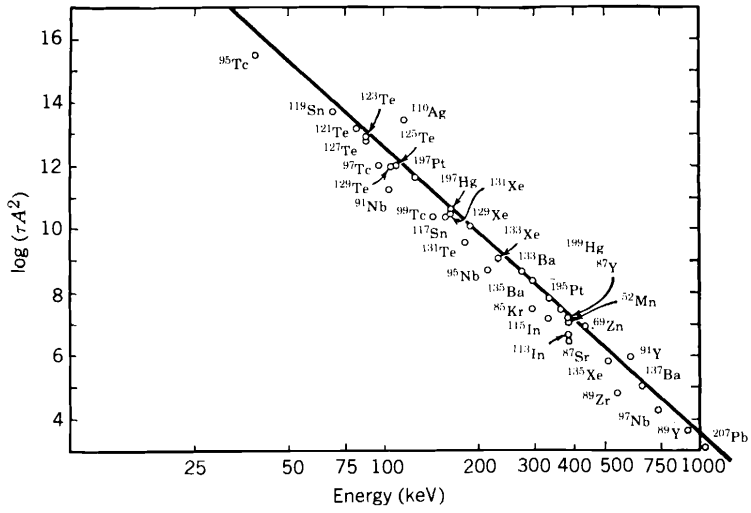


Figure 10.13 Systematics of $M4$ transitions. The data are plotted in terms of the mean life (the reciprocal of the decay constant λ). The straight line is determined from Equation 10.15. Note especially the good agreement between the data points and the expected E^{-9} dependence. From M. Goldhaber and A. W. Sunyar, *Phys. Rev.* **83**, 906 (1951).

One feature that generally emerges from these calculations is that the measured transition rates are frequently at least an order of magnitude larger than the Weisskopf estimates for $E2$ transitions. This is strong evidence for the *collective* aspects of nuclear structure discussed in Chapter 5—the Weisskopf estimates are based on the assumption that the transition arises from the motion of a *single nucleon*, and the fact that these are too small indicates that *many* nucleons must be taking part in the transition. Figure 10.12 summarizes similar results for many $E2$ transitions, and you can see that this enhancement or acceleration of the single-particle $E2$ rate is quite a common feature. No such effect occurs for $E1$ transitions, which are generally slower than the single-particle rates. On the other hand, consider Figure 10.13 which shows the systematic behavior of $M4$ transitions. Here the agreement between theory and experiment is excellent.

10.8 GAMMA-RAY SPECTROSCOPY

The study of the γ radiations emitted by radioactive sources is one of the primary means to learn about the structure of excited nuclear states. Gamma-ray detection is relatively easy to accomplish, and can be done at high resolution (transitions a mere 2 keV apart can be cleanly separated by good γ detectors) and with high precision (uncertainties of a few eV in typical cases and more than an order of magnitude better in the best cases). Knowledge of the locations and properties of the excited states is essential for the evaluation of calculations based on any nuclear model, and γ-ray spectroscopy is the most direct, precise, and often the easiest way to obtain that information.

Let's consider how the "ideal" γ-ray experiments might proceed to provide us with the information we need about nuclear excited states:

1. A spectrum of the γ rays shows us the energies and intensities of the transitions.
2. Coincidence measurements give us clues about how these transitions might be arranged among the excited states.
3. Measuring internal conversion coefficients can give clues about the character of the radiation and the relative spins and parities of the initial and final states. Additional clues may come from angular distribution and correlation measurements.
4. Absolute transition probabilities can be found by determining the half-lives of the levels.

As a first example, we consider the decay of ^{108m}Ag ($t_{1/2}$ = 127 y). Figure 10.14 shows the conversion electron and γ-ray spectra, and Table 10.1 shows the deduced relative γ and electron intensities.

The first excited state of ^{108}Pd is known from many nuclear reaction studies to be at an energy of 434 keV and to be a 2^+ state, as in nearly all even-Z, even-N nuclei. We therefore recognize the 434-keV transition shown in Table 10.1 as representing the decay of this state, and we assume the transition to be a pure $E2$, $2^+ \rightarrow 0^+$ transition. From conversion coefficient tables, we can determine that the theoretical conversion coefficients are $\alpha_K(434) = 7.89 \times 10^{-3}$, $\alpha_{L+M+\cdots} = 1.0 \times 10^{-3}$. Given the intensities from Table 10.1, the remaining conversion

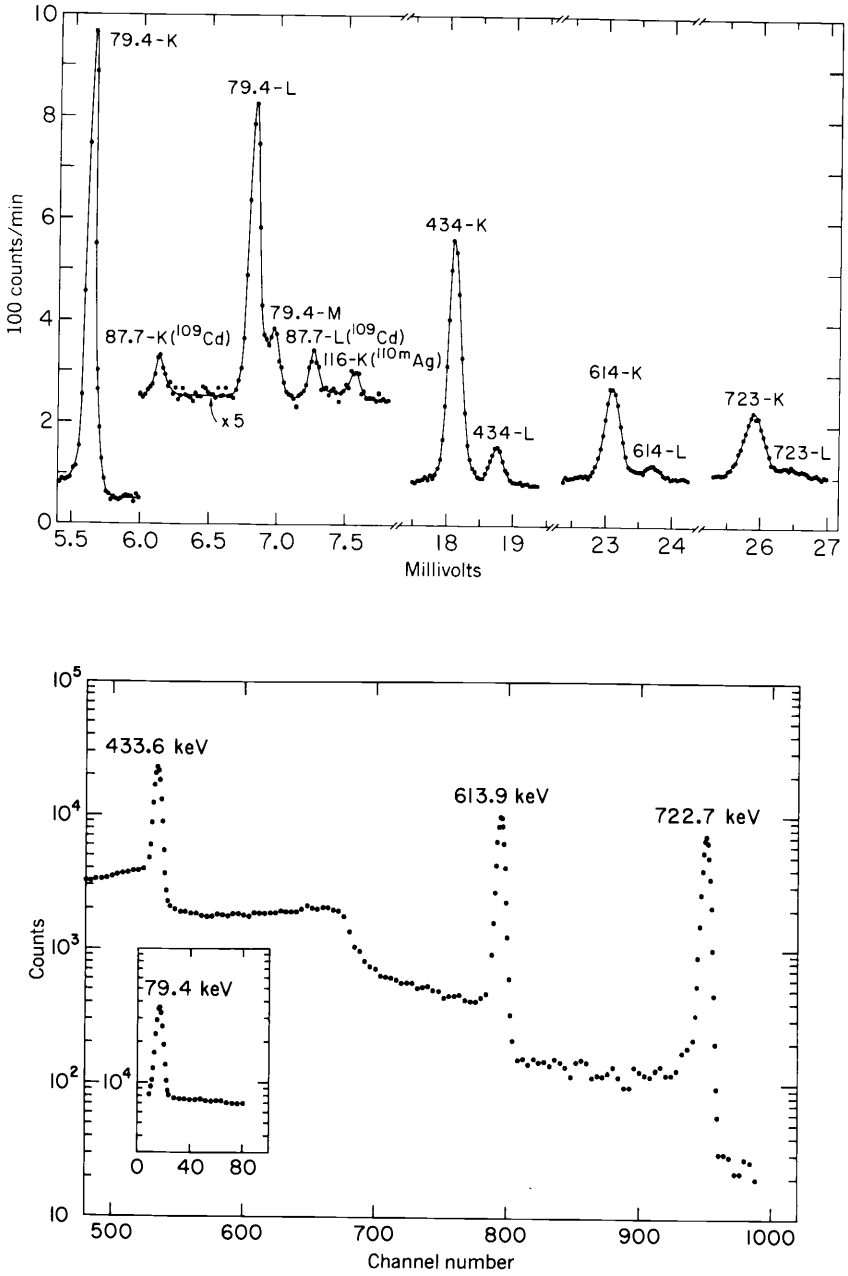


Figure 10.14 Gamma-ray (bottom) and conversion electron (top) spectra following the ^{108m}Ag decay. The γ spectrum was obtained with a Ge(Li) detector. The electron spectrum, obtained with a magnetic spectrometer, shows the high resolution necessary to separate the K and L lines. From O. C. Kistner and A. W. Sunyar, *Phys. Rev.* **143**, 918 (1966).

Table 10.1 Conversion Electron and γ-Ray Intensities of Transitions Following the Decay of ^{108m}Ag

Transition Energy (keV)	Relative γ Intensity	Relative Electron Intensity	Conversion Coefficient (units of 10^{-3})	
			Experimental	Theoretical
79.2	7.3 ± 0.8	204 ± 10 (K)	220 ± 26	270 (*E*1), 710 (*M*1), 2400 (*E*2)
		25 ± 2 (L)	27 ± 4	33 (*E*1), 88 (*M*1), 777 (*E*2)
434.0	≡ 100	≡ 100 (K)	≡ 7.89	7.89 (*E*2)
		14.8 ± 2.3 (L + ···)	1.17 ± 0.18	1.02 (*E*2)
614.4	103 ± 3	37 ± 3 (K)	2.83 ± 0.24	1.03 (*E*1), 3.01 (*M*1), 2.92 (*E*2)
		5.1 ± 1.6 (L + ···)	0.39 ± 0.12	0.12 (*E*1), 0.35 (*M*1), 0.36 (*E*2)
632.9	0.16 ± 0.02			
723.0	102 ± 3	25.0 ± 1.2 (K)	1.93 ± 0.11	0.72 (*E*1), 2.06 (*M*1), 1.91 (*E*2)
		4.6 ± 0.8 (L + ···)	0.35 ± 0.06	0.08 (*E*1), 0.24 (*M*1), 0.23 (*E*2)

Source: Experimental data from O. C. Kistner and A. W. Sunyar, *Phys. Rev.* **143**, 918 (1966).

coefficients can be computed in the following way:

$$\alpha_K(434) = \frac{I_K(434)}{I_\gamma(434)}$$

$$\alpha_K(614) = \frac{I_K(614)}{I_\gamma(614)}$$

where I represents the tabulated intensities.

Since we have *relative*, rather than *absolute*, intensities, we form the ratio

$$\frac{\alpha_K(614)}{\alpha_K(434)} = \frac{I_K(614)}{I_K(434)} \cdot \frac{I_\gamma(434)}{I_\gamma(614)}$$

$$\alpha_K(614) = \alpha_K(434) \cdot \frac{I_K(614)}{I_K(434)} \cdot \frac{I_\gamma(434)}{I_\gamma(614)}$$

$$= 7.89 \times 10^{-3} \cdot \frac{37 \pm 3}{100} \cdot \frac{100}{103 \pm 3}$$

$$= (2.83 \pm 0.24) \times 10^{-3}$$

From a similar procedure, the remaining conversion coefficients can be calculated, as listed in Table 10.1, and from tabulated values, we can find the theoretical values also listed in the table.

The 614- and 723-keV transitions are either $M1$ or $E2$ character, but from the conversion coefficients we cannot decide which is correct because it happens (for this atomic number and γ-ray energy range) the $M1$ and $E2$ values are nearly equal.

Further information can be obtained from coincidence experiments, illustrated in Figure 10.15. The low-energy end of the electron spectrum shows another

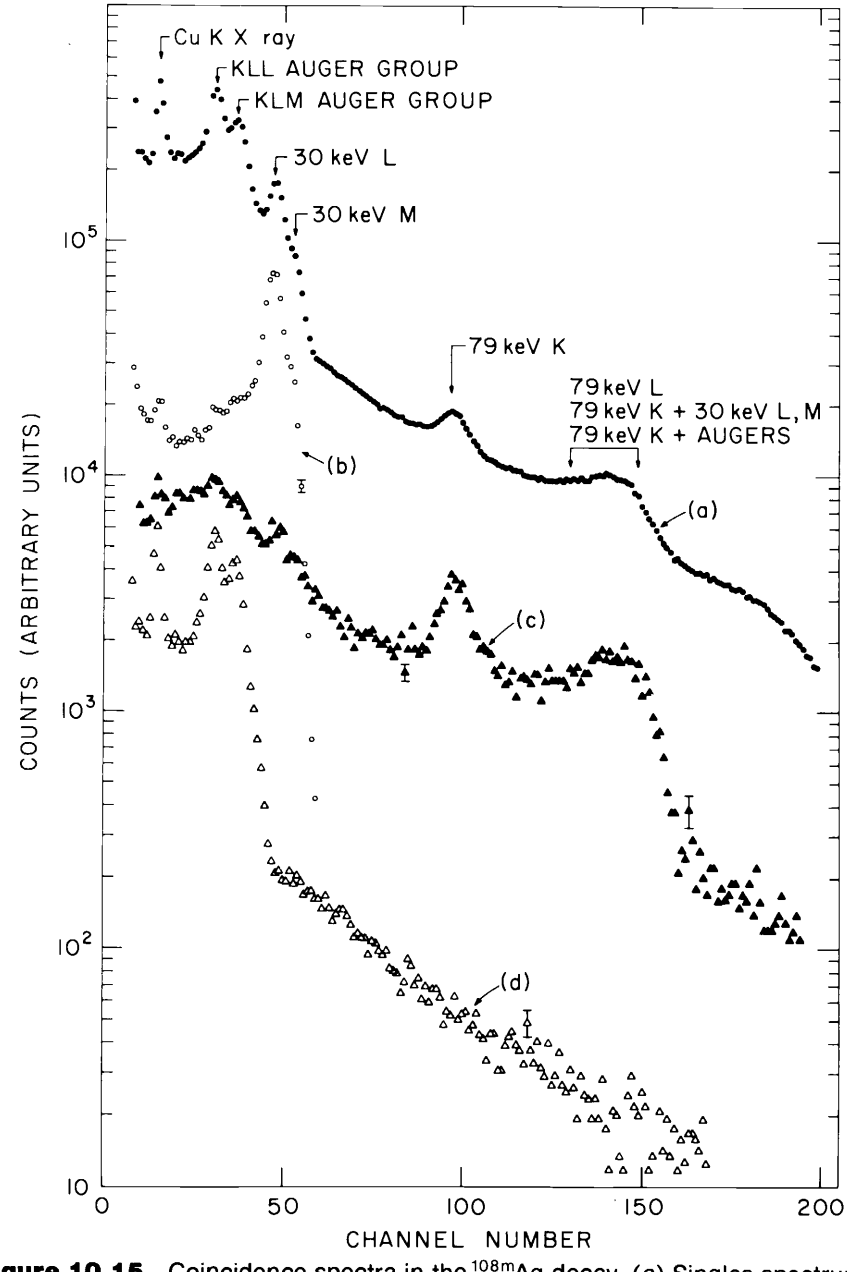


Figure 10.15 Coincidence spectra in the ^{108m}Ag decay. (*a*) Singles spectrum for comparison. (*b*) Spectrum in coincidence with 79-keV γ ray. (*c*) Spectrum in coincidence with K X rays. (*d*) Spectrum in coincidence with 434-, 614-, and 723-keV γ's. From O. C. Kistner and A. W. Sunyar, *Phys. Rev.* **143**, 918 (1966).

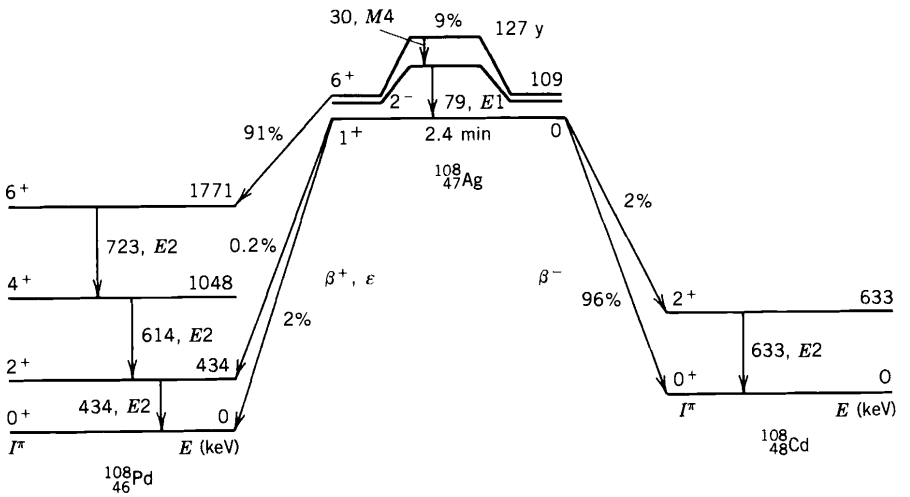


Figure 10.16 Decay scheme of ^{108}Ag. The 127-y isomer decays 91% by β decay and 9% through γ rays. The branching ratios of the β decay of the 2.4-min ground state are also shown.

transition, of energy 30.4 keV; its γ intensity is too low to be observed, but from the relative subshell intensities $L_I/(L_{II} + L_{III})$ it is deduced to be of $M4$ character. Neither this transition nor the 79.2-keV transition are in coincidence with the 434-, 614-, or 723-keV transitions. This strongly suggests that the 30.4- and 79.2-keV transitions take place in ^{108}Ag following the decay of the isomer. Furthermore, the coincidence relationship among the 434-, 614-, and 723-keV transitions suggests that they follow one another in cascade.

The resulting decay scheme deduced on the basis of these (and other) data is shown in Figure 10.16. The spins of the 1048- and 1771-keV levels are deduced from angular correlation and linear polarization measurements, and the transitions are then of $E2$ multipolarity. The 633-keV transition is deduced to take place in ^{108}Cd, and must follow the decay of the ^{108}Ag ground state. (Otherwise, the β decay would be $6^+ \rightarrow 2^+$, a fourth-forbidden process not likely to be observed.)

The 127-y isomeric state decays 91% by an allowed β decay to the 6^+ state in ^{108}Pd, which then decays through the cascade of three transitions. Because there is negligible β feeding of the 4^+ or 2^+ levels (the 2^+ level is fed by only 0.2% of 9% of the decays), the three transitions should all have the same total (γ plus electron) intensity, as can be confirmed from the data of Table 10.1. The ^{108}Ag ground state decays through four different allowed β branches, with a half-life of 2.4 min.

As a second example, we consider the decay of isomeric ^{180m}Hf. A γ-ray spectrum is shown in Figure 10.17, and the deduced γ intensities and conversion coefficients are shown in Table 10.2. The conversion coefficients of the 93-, 215-, 332-, and 443-keV transitions strongly suggest $E2$ multipolarity, while for 57- and 501-keV, they suggest $E1$ and $E3$, respectively.

Since ^{180}Hf is an even-Z, even-N nucleus, we expect the first excited state to be a 2^+ state, and such a state has been identified at 93 keV from a variety of experiments. In this region, we expect the sequence of $0^+, 2^+, 4^+, 6^+, \ldots$ rota-

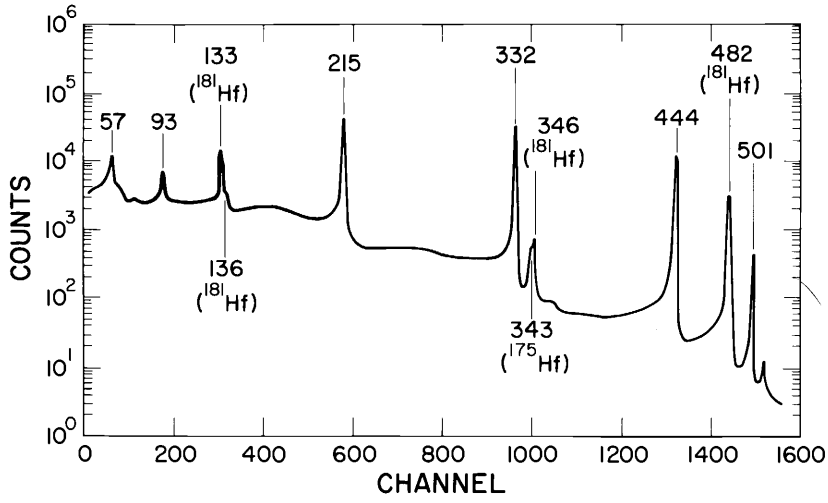


Figure 10.17 Gamma ray spectrum from the decay of ^{180m}Hf. The radioactive sample was made by neutron activation, which also produced other isotopes of Hf; γ rays from these other isotopes are labeled.

tional states with characteristic $I(I + 1)$ spacing, and so we expect to find a 4^+ state at an energy of $\frac{10}{3}$ of the 2^+ energy, or 310 keV, with a 4^+–2^+ transition of energy 310 − 93 = 217 keV. This is presumably the 215-keV $E2$ transition seen in the γ spectrum. The 6^+ state is expected at 651 keV, and the 6^+–4^+ transition should be of energy 651 − 310 = 341 keV, which we identify with the observed 332-keV transition. The 8^+ energy is expected to be 1116 keV, and the 8^+–6^+ transition (1116 − 651 = 465 keV) we guess to be the observed 443 keV. To place the 57- and 501-keV transitions, we notice the energy sum 57.5 + 443.2 = 500.7, which strongly suggests that a level 57.5 keV above the 8^+ level emits both the 57.5- and 500.7-keV transitions, with the 500.7-keV transition proceeding directly to the 6^+ state in parallel with the cascade 57.5 + 443.2 keV. To check this assumption, we examine the total intensities of the transitions, which we find, according to Equation 10.21, by $I_T = I_\gamma(1 + \alpha)$, where α is the *total* conversion coefficient (the sum of the individual coefficients). From the data of Table 10.2, the following relative intensities can be computed:

$$I_T(57.5) = 87.1 \pm 2.9 \qquad I_T(332.3) = 105.3 \pm 1.1$$
$$I_T(93.3) = 108.1 \pm 4.8 \qquad I_T(443.2) = 89.7 \pm 1.6$$
$$I_T(215.3) = 103.4 \pm 1.0 \qquad I_T(500.7) = 16.2 \pm 0.4$$

Note that, within the uncertainties, $I_T(93.3) = I_T(215.3) = I_T(332.3)$, as expected for transitions emitted in a cascade, one following the other. The 443.2 intensity is smaller, suggesting an alternative branch to the 6^+ state other than through the 443.2-keV, 8^+–6^+ transition, consistent with the assumption that the 500.7-keV transition goes to the 6^+ state. Finally, note that $I_T(57.5) = I_T(443.2)$, suggesting they are in cascade, and that $I_T(57.5) + I_T(500.7) = I_T(332.3)$, suggesting the two branches that feed the 6^+ level, one by the 57.5-keV transition and another by the 500.7-keV transition.

Table 10.2 Gamma Decays of ^{180m}Hf

Transition Energy (keV)	Relative γ Intensity	Conversion Coefficient: Experiment (atomic shell)	Conversion Coefficient: Theory (multipole)
57.5	51.3 ± 1.2	0.430 ± 0.029 (L)	0.452 (*E*1)
		0.083 ± 0.007 (M)	0.105 (*E*1)
		0.023 ± 0.004 (N + ···)	0.031 (*E*1)
93.3	17.6 ± 0.4	≡ 1.10 (K)	1.10 (*E*2)
		3.13 ± 0.19 (L)	2.72 (*E*2)
		0.91 ± 0.11 (M + ···)	0.85 (*E*2)
215.3	86.2 ± 0.8	0.123 ± 0.009 (K)	0.14 (*E*2)
		0.077 ± 0.011 (L)	0.071 (*E*2)
332.3	≡ 100.0 ± 1.0	0.038 ± 0.003 (K)	0.042 (*E*2)
		0.015 ± 0.002 (L)	0.013 (*E*2)
443.2	87.7 ± 1.6	0.0189 ± 0.0017 (K)	0.020 (*E*2)
		0.0044 ± 0.0007 (L)	0.005 (*E*2)
500.7	15.4 ± 0.4	0.037 ± 0.012 (K)	0.124 (*M*2), 0.038 (*E*3)
		0.016 ± 0.005 (L)	0.062 (*M*2), 0.016 (*E*3)

Source: Data for this table came from various sources compiled in the *Nuclear Data Sheets* **15**, 559 (1975).

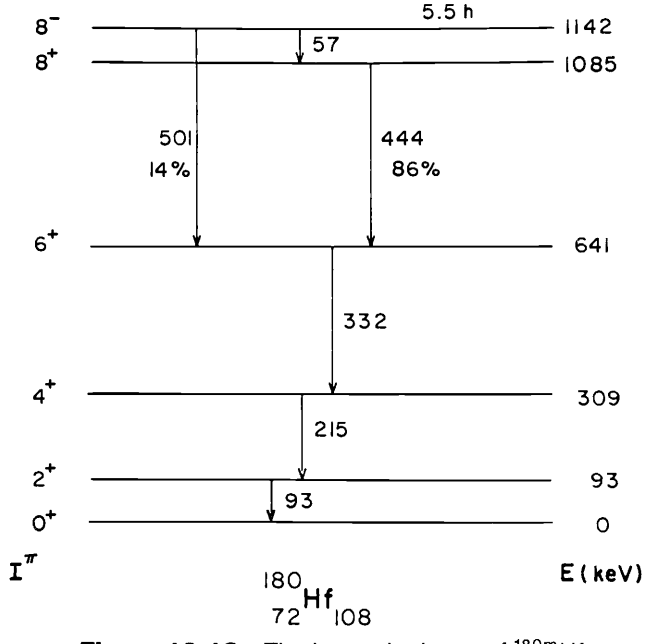


Figure 10.18 The isomeric decay of ^{180m}Hf.

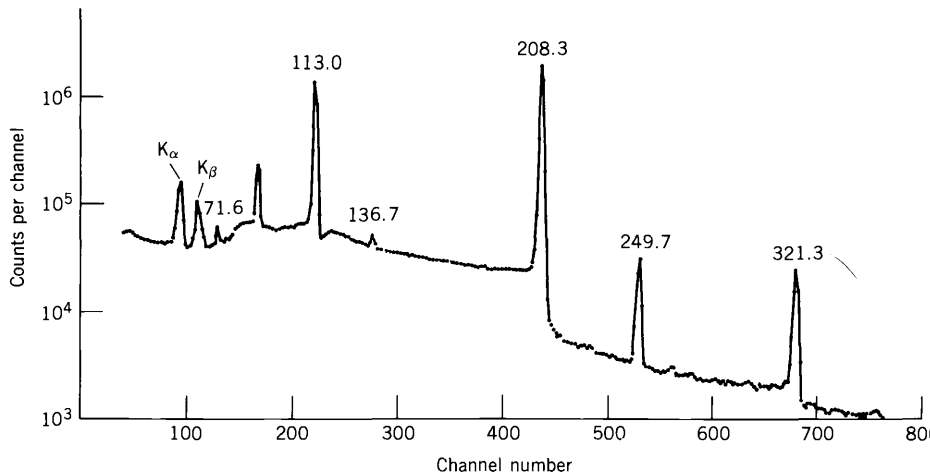


Figure 10.19 Gamma-ray spectrum from the decay of ^{177}Lu. The peak at about 90 keV is from an impurity activity produced in this neutron-activated sample. (Data from the author's laboratory.)

The parity of the level that emits the 57.5- and 500.7-keV transitions must be negative (because of their $E1$ and $E3$ characters, respectively), and its spin must be 7, 8, or 9 to permit decay to 8^+ via the $E1$ transition. We can eliminate the 7^- possibility because it would allow the 500.7-keV transition to 6^+ to be of $E1$ character, and 9^- can be eliminated by angular correlation experiments, which show the 500.7-keV transition to have a small ($\approx 3\%$) $M2$ component, which the conversion coefficients are not sensitive enough to reveal.

The resulting decay scheme is shown in Figure 10.18. Of course, many additional measurements are required to confirm that our guesses based on the γ

Table 10.3 γ Transitions in the Decay of ^{177}Lu

Transition Energy (keV)	Relative γ Intensity	Conversion Coefficient	
		Experiment (atomic shell)	Theory (multipole)
71.6	2.4 ± 0.1	0.90 ± 0.11 (K)	0.72 ($E1$), 92.0 ($M2$)
		0.087 ± 0.010 (L_I)	0.071 ($E1$), 24.3 ($M2$)
113.0	≡ 100	0.78 ± 0.05 (K)	2.4 ($M1$), 0.74 ($E2$)
		0.091 ± 0.011 (L_I)	0.345 ($M1$), 0.076 ($E2$)
136.7	0.92 ± 0.06	0.49 ± 0.08 (K)	1.45 ($M1$), 0.48 ($E2$)
		0.08 ± 0.02 (L_I)	0.20 ($M1$), 0.05 ($E2$)
208.3	164 ± 10	0.046 ± 0.004 (K)	0.046 ($E1$), 2.05 ($M2$)
		0.0063 ± 0.0006 (L_I)	0.0053 ($E1$), 0.38 ($M2$)
249.7	3.0 ± 0.2	0.101 ± 0.009 (K)	0.26 ($M1$), 0.094 ($E2$)
321.3	3.6 ± 0.2	0.102 ± 0.013 (K)	0.0155 ($E1$), 0.49 ($M2$)
		0.017 ± 0.002 (L_I)	0.0018 ($E1$), 0.081 ($M2$)

Sources: Gamma-ray data from A. J. Haverfield et al., *Nucl. Phys. A* **94**, 337 (1967). Electron conversion data from A. P. Agnihotry et al., *Phys. Rev. C* **9**, 336 (1974).

decays are in fact correct. The 5.5-h half-life is one of the longest known for γ-emitting isomers.

For our final example, we consider the 6.7-day decay of ^{177}Lu. The γ-ray spectrum is shown in Figure 10.19 and the γ and conversion data are listed in Table 10.3. The β decays of ^{177}Lu to ^{177}Hf were discussed in Section 9.10; there are four decays, leading to the ground state and to excited states at 113, 250, and 321 keV. Transitions from each of these states to the ground state can be seen among those listed in Table 10.3, and we therefore assume the excited states to be at energies of 113.0, 249.7, and 321.3 keV. (These γ energies are determined to about ± 0.1 keV, while the β energies are determined only to ± 2–3 keV.) We also find in the transitions of Table 10.3 all possible transitions connecting the excited states:

$$321.3 - 249.7 \text{ keV} = 71.6 \text{ keV}$$
$$321.3 - 113.0 \text{ keV} = 208.3 \text{ keV}$$
$$249.7 - 113.0 \text{ keV} = 136.7 \text{ keV}$$

The ground state and first two excited states of ^{177}Hf are known to be the lowest states of a rotational band with spins $\frac{7}{2}^-, \frac{9}{2}^-, \frac{11}{2}^-, \ldots$. We would expect the 113.0-keV transition to be $\frac{9}{2}^- \rightarrow \frac{7}{2}^-$ and thus of $M1 + E2$ character, the 136.7-keV transition to be $\frac{11}{2}^- \rightarrow \frac{9}{2}^-$ and likewise $M1 + E2$, and the 249.7-keV transition to be $\frac{11}{2}^- \rightarrow \frac{7}{2}^-$ $E2$. These expectations are consistent with the conversion coefficients. The 321.3 level decays to all three lower levels through $E1 + M2$ transitions, and thus only a $\frac{9}{2}^+$ assignment is possible.

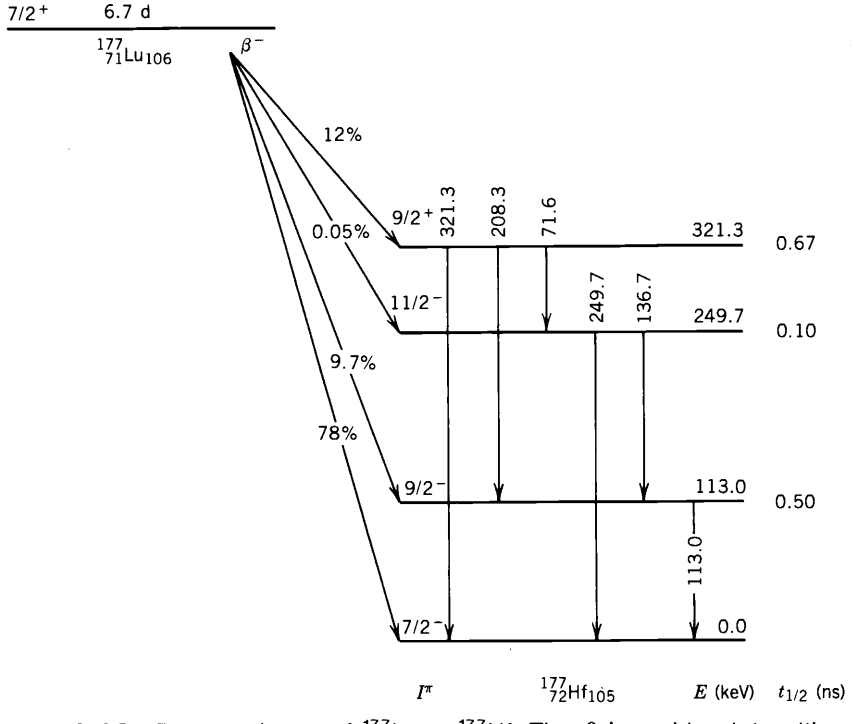


Figure 10.20 Decay scheme of ^{177}Lu to ^{177}Hf. The β branching intensities are deduced indirectly from the γ-ray intensities and differ from those of Figure 9.29.

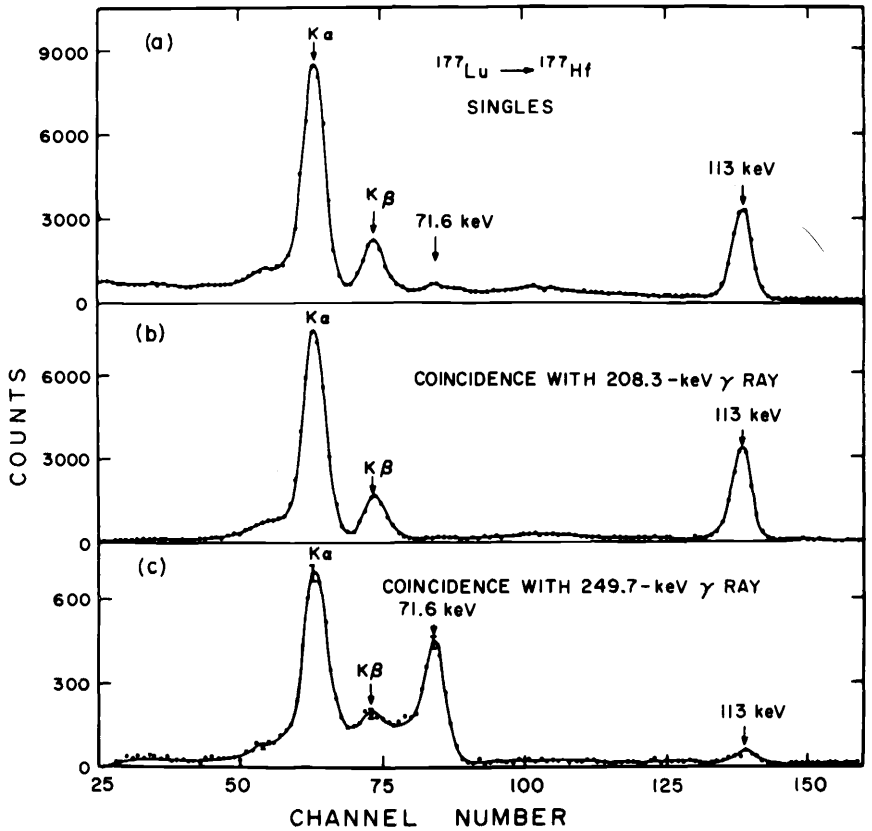


Figure 10.21 Coincidence spectra from the ^{177}Lu decay. Note the strong coincidence between 208 and 113; also note how the 71.6-keV peak, which is barely observable in the singles spectrum at the top, appears prominently in coincidence with 249.7 keV. (The small apparent 113.0-keV peak in the 249.7 keV coincidence spectrum is an artifact.) Data from A. P. Agnihotry et al., *Phys. Rev. C* **9**, 336 (1974).

The postulated decay scheme is shown in Figure 10.20. To verify our assumptions about the placement of the transitions, we can do γ-ray coincidence measurements, an example of which is shown in Figure 10.21. The coincidence spectrum shows quite plainly the 113.0–208.3 and 71.6–249.7 coincidence relationships.

As a final note on this decay, we point out that the L-subshell ratios can determine the relative $M1$ and $E2$ components of the 113.0-keV transition. Figure 10.22 shows the dependence of the L_I/L_{III} and L_I/L_{II} ratios on the $E2$ component. These very precise data show that the transition is 94–95% $E2$ and thus only 5–6% $M1$. In this case, the nuclear wave functions enhance the $E2$ transition probability to such an extent that $E2$ dominates over $M1$.

In this section we have given some examples of decay schemes that can be elucidated through γ-ray and conversion electron spectroscopy. It is of course impossible to isolate any one technique from all others in determining the properties of nuclear states, but from the examples discussed here you should

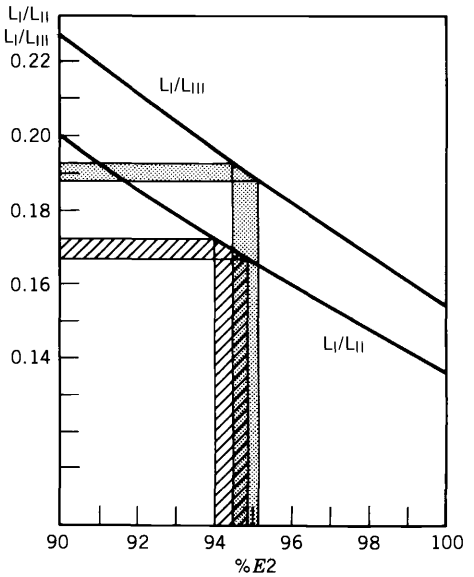


Figure 10.22 Determination of the $E2$ fraction of the 113.0-keV transition in ^{177}Hf from L-subshell data. The horizontal bars give the ranges of the experimental L-subshell ratios, and the vertical bars give the corresponding $E2$ fractions. The transition is deduced to be 94–95% $E2$ (and thus 5–6% $M1$). Data from S. Högberg et al., *Z. Phys.* **254**, 89 (1972).

appreciate the detailed and precise information that can be obtained from these methods.

10.9 NUCLEAR RESONANCE FLUORESCENCE AND THE MÖSSBAUER EFFECT

The inverse process of γ-ray emission is γ-ray absorption—a nucleus in its ground state absorbs a photon of energy E_γ and jumps to an excited state at an energy ΔE above the ground state. The relationship between E_γ and ΔE follows from a procedure similar to that used to obtain Equation 10.4:

$$\Delta E = E_\gamma - \frac{E_\gamma^2}{2Mc^2} \tag{10.28}$$

if we assume the absorbing nucleus to be initially at rest. The difference between ΔE and E_γ comes about because of the recoil of the nucleus after absorbing the photon.

Let us assume we have a source of γ radiation of continuously variable energy. The cross section for resonant absorption of a photon is

$$\sigma_0 = 2\pi\left(\frac{\hbar c}{E_\gamma}\right)^2 \frac{2I_e + 1}{2I_g + 1} \frac{1}{1 + \alpha} \tag{10.29}$$

where α is the total conversion coefficient and I_g and I_e are the spin quantum

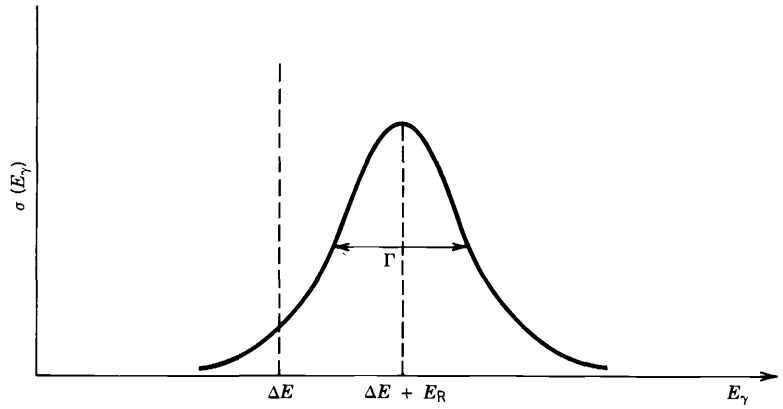


Figure 10.23 The resonant absorption cross section of Equation 10.30. The recoil energy E_R shifts the resonance slightly from the value $E_\gamma = \Delta E$ expected in the absence of recoil.

numbers of the ground and excited states. Because the energy of the excited state is not "sharp," the absorption will take place even when the γ energy differs somewhat from the resonant value. As we discussed in Chapter 6, any state that has a mean life τ has a width $\Gamma = \hbar/\tau$, and measurement of the energy of the state gives a distribution of the form of Equation 6.20 and Figure 6.3. If we were to pass a beam of photons through a collection of bare nuclei (so as to eliminate scattering and absorption processes due to atomic electrons), then the resonant absorption cross section is

$$\sigma(E_\gamma) = \sigma_0 \frac{(\Gamma/2)^2}{\left[E_\gamma - (\Delta E + E_R)\right]^2 + (\Gamma/2)^2} \tag{10.30}$$

where E_R is the recoil correction $E_\gamma^2/2Mc^2$. This distribution is plotted in Figure 10.23. For typical nuclear states of mean lives ns to ps, the widths will be in the range of 10^{-6} to 10^{-3} eV.

Figure 10.24 shows a schematic view of the resonant absorption experiment. As E_γ is varied, the resonance curve of Figure 10.23 is traced. At energies E_γ far

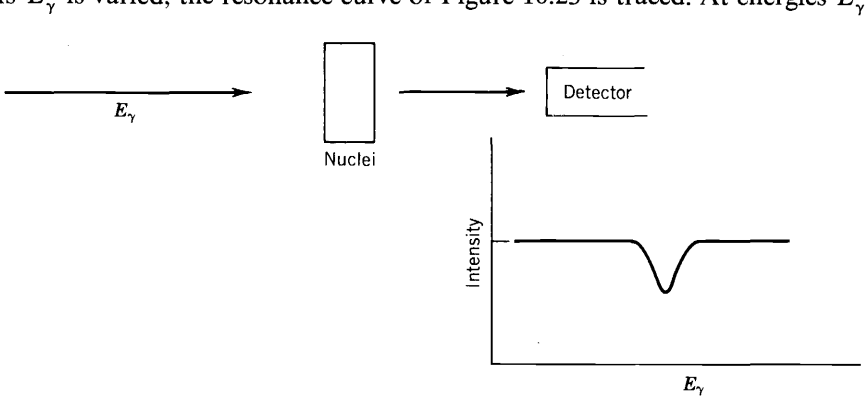


Figure 10.24 Schematic of an experiment to observe resonant absorption by nuclei.

from the resonance, the nuclei are transparent to the radiation, and no absorption occurs. At the resonance, the transmitted intensity reaches a minimum value.

In practice, we would be unlikely to observe the *natural linewidth* Γ. A primary additional contributor to the observed linewidth is the *Doppler broadening* Δ, which arises because the nuclei are not at rest (as we assumed) but in fact are in thermal motion at any temperature T. The photons as emitted or absorbed in the lab frame appear Doppler shifted with energies $E'_\gamma = E_\gamma(1 \pm v_x/c)$, where v_x is the velocity component along the photon direction. If the motion of the nuclei is represented by the usual Maxwell velocity distribution $e^{-[(1/2)mv_x^2]/kT}$ there will be a distribution of energies of the form $e^{-(mc^2/2kT)(1-E'_\gamma/E_\gamma)^2}$. This gives a Gaussian distribution of width

$$\Delta = 2\sqrt{\ln 2}\, E_\gamma \sqrt{\frac{2kT}{Mc^2}} \tag{10.31}$$

At room temperature, $kT \simeq 0.025$ eV, and for a 100-keV transition in a medium-weight nucleus $\Delta \simeq 0.1$ eV, which dominates the natural linewidth for most nuclear transitions. Even cooling to low temperature (for instance, to 4 K in thermal contact with a reservoir of liquid helium) reduces the width by only an order of magnitude to 0.01 eV. The width observed in experiments such as that of Figure 10.24 will be a combination of the natural linewidth plus additional contributions including Doppler broadening.

Tunable sources of photons of the sort needed for the resonance experiment do not exist. (The best one can do is the continuous electromagnetic spectrum from bremsstrahlung or synchrotron radiation produced by charged-particle accelerators capable of reaching relativistic energies.) In our laboratories, we must therefore make do with ordinary sources of γ radiation that emit only at discrete energies. However, to do the resonant absorption, we must find a radioactive source that emits a γ ray of an energy within at most 0.1 eV of the desired resonant energy $\Delta E + E_R$. It is of course extremely unlikely to find such radiation, and with the proper multipole character besides. It therefore makes sense for us to try to use a source in which the γ radiation is emitted in the same *downward* transition that we are trying to excite *upward* by resonant absorption. Consider, for example, the decay of ^{198}Au; following the β decay to ^{198}Hg, a single strong γ-ray of energy 412 keV is emitted. If we now allow that γ ray to fall upon a target of stable ^{198}Hg nuclei, there is a possibility of absorption and excitation from the ground state to the 412-keV excited state. The mean life of the 412-keV state is 32 ps, corresponding to a width of 2×10^{-5} eV. The recoil energy E_R is $E_\gamma^2/2Mc^2 = 0.46$ eV, and it is important to note that the recoil affects both the *emitted* and *absorbed* transitions. That is, the emitted radiation has energy $\Delta E - E_R$, while for absorption we must supply an energy of $\Delta E + E_R$. The situation is indicated in Figure 10.25, in which we have assumed the lines to have the room-temperature Doppler width of 0.36 eV. As you can see, there is minimal overlap between the emission and absorption lines, and thus little probability of resonant excitation.

(Contrast this with the case of atomic radiation. Optical transitions have energies of a few eV; the recoil correction in Hg would be 2.7×10^{-12} eV and there would be almost complete overlap between the profile of the source and

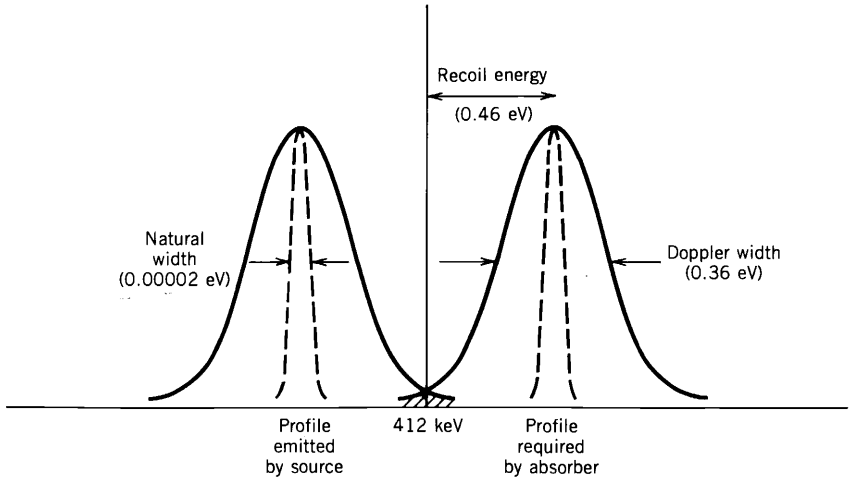


Figure 10.25 The emitted radiation is shifted downward in energy by E_R, while the absorption requires an energy shifted upward by E_R. Because of the Doppler (thermal) broadening, there is a small overlap (shaded region) between the emission and absorption lines. The natural width has been greatly exaggerated on the energy scale of the diagram.

absorber transitions. Atomic resonant absorption experiments are thus relatively easy to perform.)

There are several techniques for overcoming the energy difference $2E_R$ between the source and absorber transitions. The first consists of raising the temperature, thereby increasing the Doppler broadening and the overlap of the profiles. A second method is to move the source toward the absorber at high speed to Doppler shift the emitted energy by an amount $2E_R$. Since the Doppler-shifted energy is $E'_\gamma = E_\gamma(1 + v/c)$, the speed required is

$$v = c\frac{2E_R}{E_\gamma} \tag{10.32}$$

which gives $2.2 \times 10^{-6}c$, or 670 m/s. Experiments of this type are usually done by attaching the source to the tip of a rotor in a centrifuge spinning at 10^4–10^5 revolutions per minute. Figure 10.26 shows examples of results from the thermal-broadening and centrifuge techniques.

The most successful and useful technique for defeating the recoil problem is called the Mössbauer effect. In 1958, Rudolf Mössbauer performed a resonant absorption experiment using a source of ^{191}Ir ($E_\gamma = 129$ keV; $E_R = 0.047$ eV). The emitting and absorbing nuclei were bound in a crystal lattice. Typical binding energies of an atom in a lattice are 1–10 eV, and thus there is not enough recoil energy available for the atom to leave its lattice site. The effect is somewhat like the difference between hitting a single brick with a baseball bat and hitting one brick in a solid brick wall—the entire solid lattice absorbs the recoil momentum. The mass that appears in the expression for the recoil energy becomes the mass of the entire solid, rather than the mass of one atom. In addition, a certain fraction of the atoms in a lattice (determined from statistical considerations) is in the vibrational ground state of thermal motion and thus

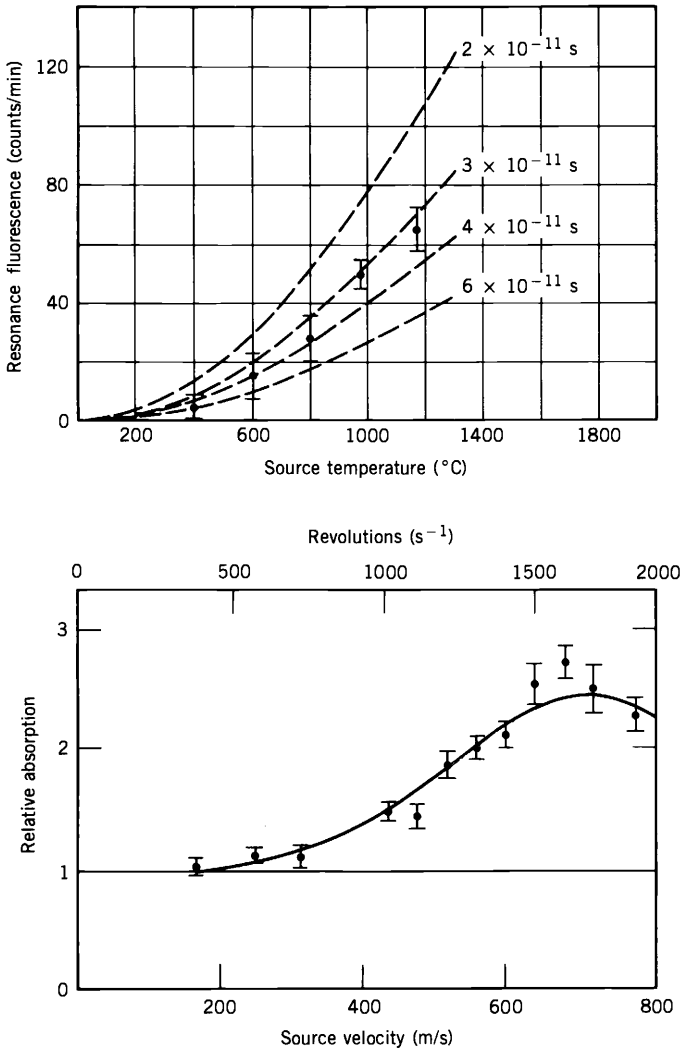


Figure 10.26 Thermal broadening (top) and centrifuge (bottom) techniques for observing nuclear resonance in ^{198}Hg. The data points at top show increasing resonant absorption as the temperature is increased (broadening the lines in Figure 10.25 and increasing the overlap). The dashed lines show the expected behavior for different excited-state lifetimes (that is, for different natural widths). From these data the lifetime is determined to be about 30 ps. The graph at bottom shows the result of Doppler shifting the radiation emitted by the source, by attaching it to the tip of a rotor. In this case, the emission line in Figure 10.25 is being moved to higher energy until it overlaps the absorption line. As estimated, this occurs at about 670 m/s. Thermal data from F. R. Metzger and W. B. Todd, *Phys. Rev.* **95**, 853 (1954); rotor data from W. G. Davey and P. B. Moon, *Proc. Phys. Soc. London A* **66**, 956 (1953).

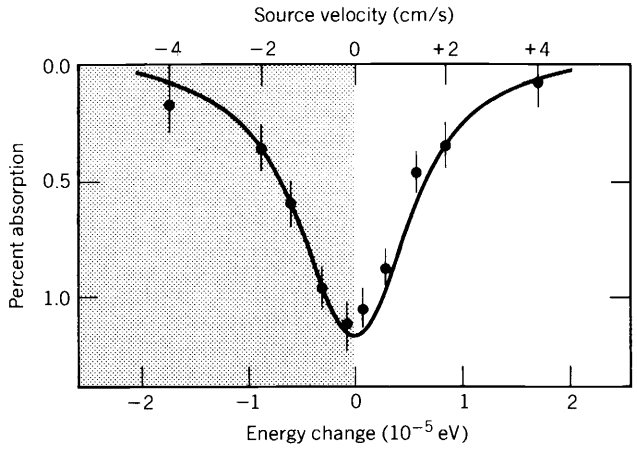


Figure 10.27 Mössbauer effect using 129-keV γ ray from ^{191}Ir. Because (1) the natural linewidth is obtained, and (2) the recoil is eliminated, there is essentially complete overlap between source and absorber. Doppler-shifting the source energy by an amount slightly greater that the natural linewidth (10^{-5} eV) is sufficient to destroy the resonance. From original data by R. Mössbauer, *Z. Naturforsch. A* **14**, 211 (1959).

shows very little thermal Doppler broadening. The result is very narrow and overlapping emission and absorption lines, each characterized by the natural linewidth (3×10^{-6} eV in ^{191}Ir). To demonstrate this phenomenon, we have only to move the source and absorber relative to one another at low speed; if the speed is such that the Doppler shift is greater than the natural linewidth, the resonance will be destroyed. For a total linewidth of 6×10^{-6} eV (because both source and absorber have the natural width), the necessary speed is about $5 \times 10^{-11}c$, or about 15 mm/s, a considerable improvement over the 700 m/s needed for the centrifuge experiment! Figure 10.27 shows the resulting resonance, first obtained by Mössbauer in 1958.

What is remarkable about the Mössbauer effect is its extreme precision for the measurement of relative energies. For instance, suppose we modified the environment of the source or absorber nuclei in such a way that the energy difference between the initial and final nuclear states shifted by a very small amount δE. Using the Mössbauer effect, we should be able to measure this shift, as long is it is of the same order as the width of the resonance. (If the shift is too small compared with the width of the resonance, it is very difficult to measure.) In the case of ^{191}Ir, where the observed width is about 10^{-5} eV, this would amount to measuring a change in energy of 10^{-5} eV out of a gamma-ray energy of 10^{5} eV, or an effect of one part in 10^{10}. In ^{57}Fe, which is more frequently used for the Mössbauer effect, the observed (natural) linewidth is of order 10^{-8} eV, and in this case experimental effects of the order of one part in 10^{12} can be measured!

Although we will not go into the details of the theory of the Mössbauer effect, it is worthwhile to consider briefly one other aspect of the resonance, its depth, which is determined by the fraction of the nuclei in the lattice that emits (or absorbs) with no recoil. The calculation of the recoil-free fraction f depends on properties of the solid more detailed than the simple question of whether or not

the recoil energy exceeds the lattice binding energy. Solids can absorb energy in many ways other than by removing atoms from their lattice sites. At low energies and temperatures, the primary way is through lattice vibrations, called *phonons*. (Propagation of these phonons through a lattice is responsible for familiar properties such as mechanical and acoustical waves.) These vibrations occur at a spectrum of frequencies, from zero up to a maximum, ω_{max}. The energy corresponding to the highest vibrational frequency is usually expressed in terms of the corresponding temperature, called the *Debye temperature*, θ_D, defined so that $\hbar\omega_{max} = k\theta_D$, where k is the Boltzmann constant. For typical materials, $\hbar\omega_{max} \sim 0.01$ eV and $\theta_D \sim 1000$ K. The recoilless fraction is

$$f = \exp\left[-\frac{\langle x^2\rangle}{(\lambda/2\pi)^2}\right] \tag{10.33}$$

where $\langle x^2\rangle$ is the mean-square vibrational amplitude of the emitting nucleus and λ is the wavelength of the γ ray. Using the Bose-Einstein distribution function for the vibrational phonon spectrum permits the calculation of the mean-square amplitude, and gives for the recoilless fraction

$$f = \exp\left\{-\frac{6E_R}{k\theta_D}\left[\frac{1}{4} + \left(\frac{T}{\theta_D}\right)^2 \int_0^{\theta_D/T} \frac{x\,dx}{e^x - 1}\right]\right\} \tag{10.34}$$

At low temperatures $T \ll \theta_D$, the last term in the exponent is negligible. Values of θ_D do not vary greatly among metals ($\theta_D \sim 400$ K for Fe and 300 K for Ir), so the recoil energy E_R is essential in determining the recoilless fraction. For the 14.4 keV transition of ^{57}Fe, $E_R = 0.002$ eV and $f = 0.92$, while for Ir, $f \approx 0.1$. (The second term in the exponent of Equation 10.34 is always negative, and thus this term will work to make f smaller than these low-temperature estimates.) Because recoilless processes are needed in both the source and absorber, the overall recoilless fraction is determined by the product of the factors in the source and absorber. It is therefore not surprising that Mössbauer's original experiment with Ir showed an effect of only 1%, while Fe shows a much larger effect.

The Mössbauer effect has found applications in an enormous variety of areas. Its primary usefulness is in those applications in which we must determine the properties of the physical or chemical environment of a nucleus, but an important exploitation of the extreme precision of the method was the determination of the change in energy of photons falling in the gravitational field of the Earth, called the *gravitational red shift*. One of the cornerstones of Einstein's General Theory of Relativity is the Principle of Equivalence, according to which the effects of a local uniform gravitational field cannot be distinguished from those of a uniformly accelerated reference frame. If we were to observe the emission and absorption of radiation in an accelerated reference frame, in which H is the distance between the source and absorber, then in the time H/c necessary for radiation to travel from the source to the absorber, the absorber would acquire a velocity gH/c, where g is the acceleration, chosen to be numerically equal (and in the opposite direction) to the gravitational acceleration of the uniform field. The radiation photons are therefore Doppler shifted,

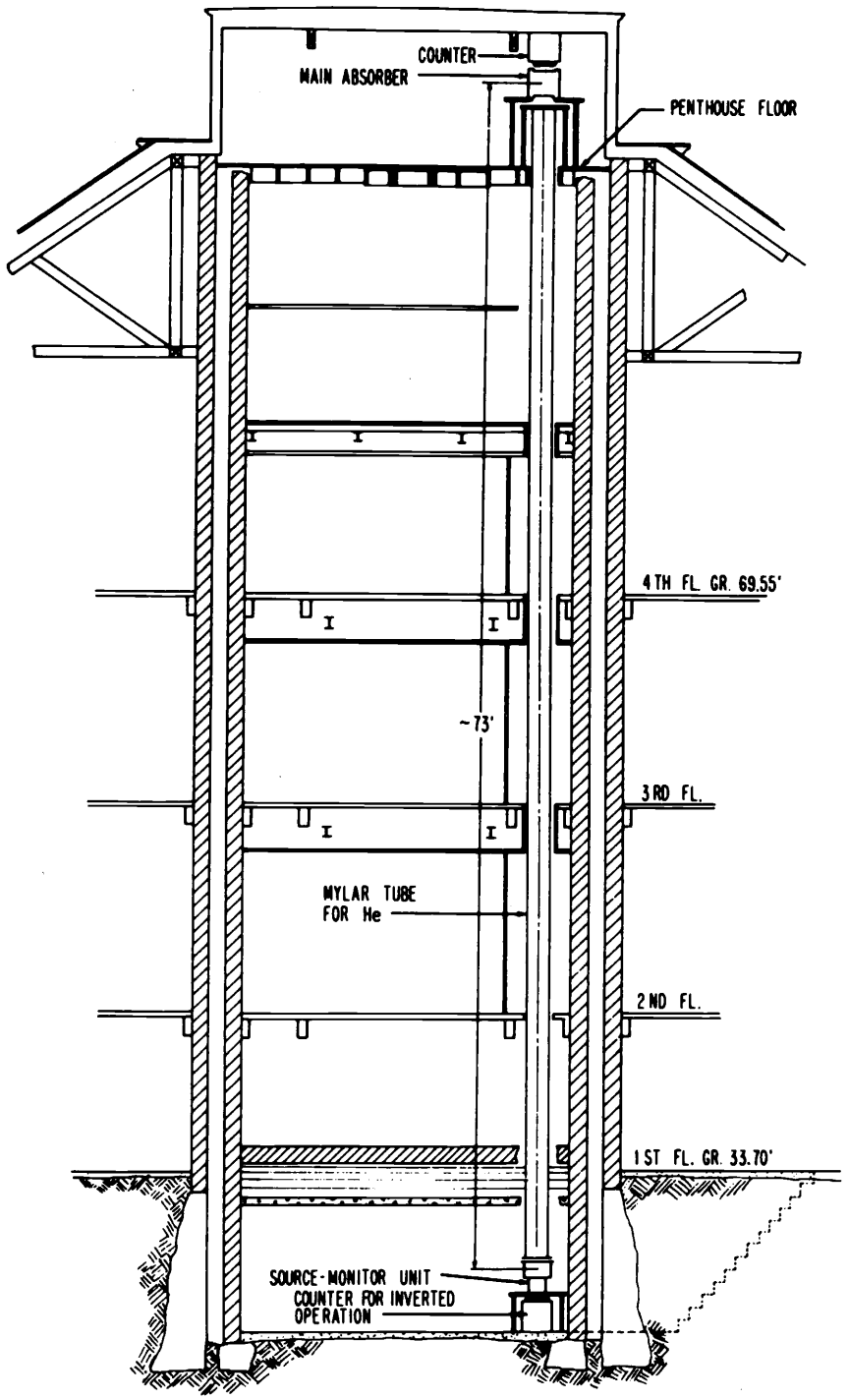


Figure 10.28 Schematic view of the gravitational red shift experiment in the Harvard tower. To reduce absorption in air, the 14.4-keV photons traveled in He gas in a Mylar tube. In the configuration shown, the source is at the bottom and the absorber and counter are at the top. From R. V. Pound, in *Mössbauer Spectroscopy II*, edited by U. Gonser (Berlin: Springer-Verlag, 1981), p. 31.

according to

$$\frac{\Delta E}{E} = \frac{\Delta v}{c} = \frac{gH}{c^2} \tag{10.35}$$

This amounts to about 1×10^{-16} per meter in the Earth's gravitational field.

In the original experiment of Pound and Rebka, *Phys. Rev. Lett.* **4**, 337 (1960), ^{57}Fe was used (from a 1-Ci source of ^{57}Co), and the 14.4-keV photons were allowed to travel 22.5 m up the tower of the Jefferson Physical Laboratory at Harvard (Figure 10.28). The expected effect was of order 2×10^{-15}, which required heroic efforts even for ^{57}Fe with a sensitivity (Γ/E_γ) of roughly 3×10^{-13}. To observe the small shift (about 10^{-2} of the width of the resonance), Pound and Rebka concentrated on the portions of the sides of the resonance curve with the largest slope. To reduce systematic effects, it was necessary to monitor with great precision the temperature of the source and absorber (temperature differences between source and absorber would cause unequal Doppler broadenings, which would simulate a shift in the peak) and periodically to interchange source and absorber to allow the photons to travel in the opposite direction. After four months of experiments, the result was $\Delta E/E = (4.902 \pm 0.041) \times 10^{-15}$, compared with the expected value 4.905×10^{-15} for the 45-m round trip. This careful experiment represents one of the most precise tests of the General Theory of Relativity, and it would not have been possible without the great sensitivity provided by the Mössbauer effect. [For a review of this experiment, see R. V. Pound, in *Mössbauer Spectroscopy II*, edited by U. Gonser (Berlin: Springer-Verlag, 1981), p. 31.]

As mentioned above, perhaps the primary application of the Mössbauer effect has been in studying the interaction of nuclei with their physical and chemical environments. The interaction of nuclear electromagnetic moments with the fields

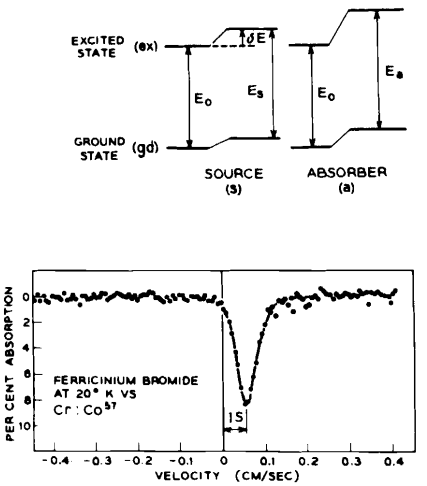


Figure 10.29 The isomer shift. In different materials, the ground and excited states show different shifts from the overlap of electronic wave functions with the nucleus. The effect on the resonance is to shift it away from zero relative velocity. From G. K. Wertheim, *Mössbauer Effect: Principles and Applications* (New York: Academic, 1964).

of the environment is usually called *hyperfine interactions*, and will be discussed in more detail in Chapter 16. For the present, we give a few examples of the application of Mössbauer spectroscopy to their study.

In the first case, we measure simply the effect of the penetration of atomic wave functions into the nuclear volume. This quantity, called ΔE in Equation 3.12, represents the difference in energy between electronic levels calculated for a "point" nucleus and for a uniformly charged spherical nucleus of radius R. Although our goal in Chapter 3 was to calculate the effect on the atomic levels, a bit of thought should convince you that nuclear levels should be shifted by an equal but opposite energy because the observed total (atomic + nuclear) energy cannot change under the influence of internal forces. If we let E_0 represent the photon energy in the absence of this effect ($E_0 = E_e - E_g$, where e is the excited state and g is the ground state), then the observed energy is

$$\begin{aligned} E &= (E_e + \Delta E_e) - (E_g + \Delta E_g) \\ &= E_0 + \Delta E_e - \Delta E_g \end{aligned} \tag{10.36}$$

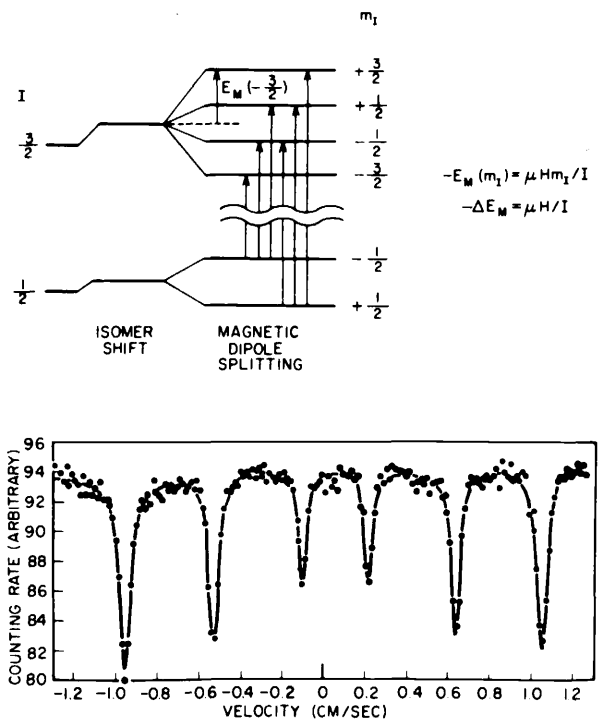
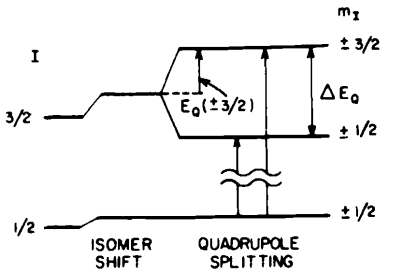


Figure 10.30 Magnetic dipole splitting of nuclear levels observed with the Mössbauer effect. At top right are shown the nuclear m states split by a magnetic field. If the ground state and excited state have different nuclear magnetic dipole moments, the energy splittings ΔE_M will be different, as shown; in the case illustrated, the moments also have opposite signs. For dipole transitions, only $\Delta m_I = 0$ or ± 1 can occur, so 6 individual components are seen. From G. K. Wertheim, *Mössbauer Effect: Principles and Applications* (New York: Academic, 1964).

because the ground and excited states will have different nuclear wave functions and thus different radii. If the source and absorber in a Mössbauer experiment had the same chemical environment, the resonance would not be affected, but if the source and absorber are different, then the transition energies are slightly different. In this case, one of the peaks in Figure 10.25 would be shifted somewhat, relative to where it appears when the source and absorber are similar. The effect on the Mössbauer spectrum is to shift the center of the resonance away from zero velocity. This effect is called the *isomer shift* (or sometimes *chemical shift*) and is illustrated in Figure 10.29. You can see that this is a small effect, of the order of one part in 10^{12}.

In another kind of hyperfine coupling, we study the splitting of the nuclear levels in a magnetic field. In atomic physics, the effect of a magnetic field on spectral lines is called the *Zeeman effect* and corresponds to the removal of the m degeneracy of a level of angular momentum I in a magnetic field—the field splits the level into $2I + 1$ equally spaced sublevels. Atomic wavelengths are typically shifted by one part in 10^4 by the Zeeman effect; nuclear magnetic moments are only 10^{-3} of atomic magnetic moments, and nuclear transition energies are 10^5 of atomic energies, and so the resulting nuclear effect is one part in 10^{12}. Figure



$$E_Q(m_I) = eqQ\left[\frac{3m_I^2 - I(I+1)}{4I(2I-1)}\right]$$

$$\Delta E_Q = E_Q(3/2) - E_Q(1/2) = \frac{eqQ}{2}$$

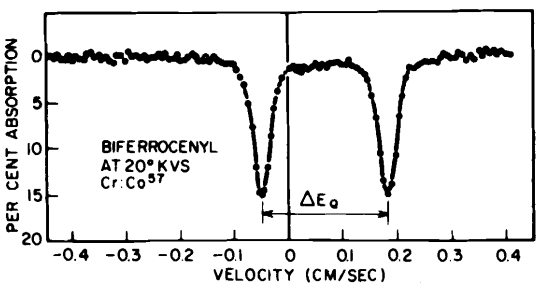


Figure 10.31 Electric quadrupole hyperfine splitting. In the expression for the splitting energy, Q represents the nuclear electric quadrupole moment and q is the electric field gradient (sometimes called V_{zz} or $\partial^2 V / \partial z^2$). In this case only two lines appear; in addition there is an isomer shift that moves the center of the Mössbauer spectrum away from zero velocity. From G. K. Wertheim, *Mössbauer Effect: Principles and Applications* (New York: Academic, 1964).

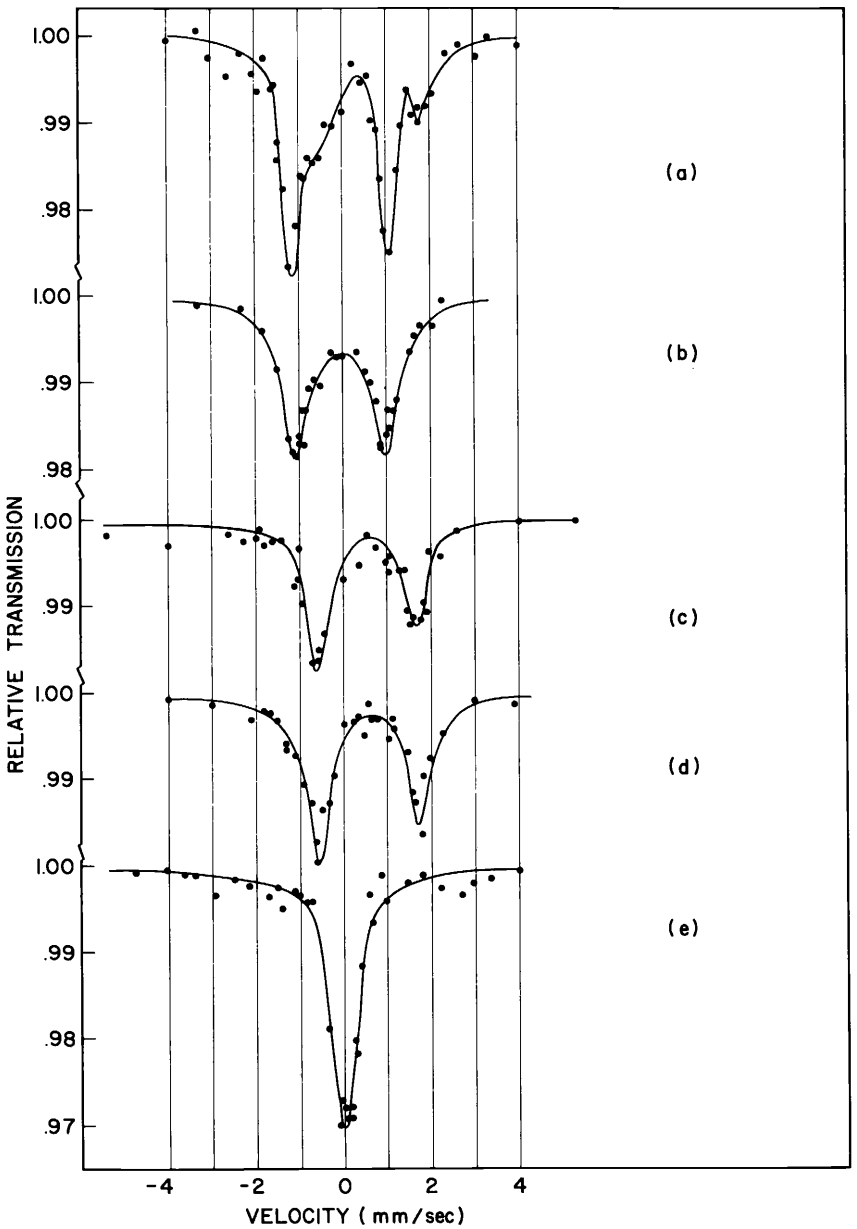


Figure 10.32 Mössbauer effect experiments showing the differing chemical environments of Fe in hemoglobin. The source for these experiments was ^{57}Co (which decays to ^{57}Fe) in Pt; absorbers were (*a*) rat red cells at 4 K, (*b*) oxygenated rat hemoglobin at 77 K, (*c*) human hemoglobin in CO_2 at 77 K, (*d*) human hemoglobin in N_2 at 77 K, and (*e*) human hemoglobin in CO at 77 K. Note the different isomer shifts and electric quadrupole splittings. From U. Gonser et al., *Science* **143**, 680 (1964). Copyright © 1964, AAAS.

10.30 shows an example of this for ^{57}Fe. An isomer shift is present, in addition to the magnetic hyperfine structure. The magnetic moments of the ground and excited states are unequal, and in fact the Mössbauer spectrum can give the magnetic moment of the excited state to great precision, when (as in ^{57}Fe) the ground state is stable and its moment is precisely known. It is also possible, if the moment is known, to deduce the size of the magnetic field, the determination of which can give important clues about atomic structure.

Finally, the nuclear quadrupole moment can interact with an electric field gradient to give an electric quadrupole splitting. This splitting is proportional to m^2 and thus does not distinguish between $+m$ and $-m$. Furthermore, it vanishes when $I = \frac{1}{2}$. Figure 10.31 shows an example in the case of ^{57}Fe. Note that 2 lines appear in the case of electric quadrupole interactions in ^{57}Fe (whereas 6 appear in the magnetic dipole case). For other isotopes having different ground-state and excited-state spins, the number of lines will be different.

These same studies can be extended to materials with a variety of applications. For example, the protein hemoglobin gives blood its red color and is responsible for binding to the oxygen in the bloodstream. Hemoglobin is rich in Fe and can therefore be used in Mössbauer experiments. Figure 10.32 shows some typical results. Oxygenated blood shows a quadrupole-split Mössbauer spectrum, but with an isomer shift slightly different from that of deoxygenated blood. Venous blood shows a mixture of the two types. Blood exposed to CO shows neither quadrupole splitting nor isomer shift. Oxygenated hemoglobin shows magnetic dipole splittings when placed in a strong magnetic field; deoxygenated hemoglobin does not. All of the above refer to the ferrous ion (Fe^{2+}); ferric ions (Fe^{3+}), the presence of which may indicate certain blood diseases, give very different Mössbauer spectra.

REFERENCES FOR ADDITIONAL READING

A comprehensive work on electromagnetic multipole radiation is M. E. Rose, *Multipole Fields* (New York: Wiley, 1955); Chapter 12 of J. M. Blatt and V. F. Weisskopf, *Theoretical Nuclear Physics* (New York: Wiley, 1952) also discusses classical multipole radiation. The quantum mechanics of the electromagnetic radiation field is considered in detail in Sections 3.1–3.9 of M. G. Bowler, *Nuclear Physics* (Oxford: Pergamon, 1973). Also of interest are Chapters 15 (multipole radiation) and 16 (internal conversion) of *Alpha-, Beta- and Gamma-Ray Spectroscopy*, edited by K. Siegbahn (Amsterdam: North-Holland, 1965).

Many theoretical and experimental aspects of γ emission are reviewed in *The Electromagnetic Interaction in Nuclear Spectroscopy*, edited by W. D. Hamilton (Amsterdam: North-Holland, 1975).

Tabulations of theoretical conversion coefficients can be found in R. S. Hager and E. C. Seltzer, *Nuclear Data Tables A* **4**, 1 (1968); F. Rösel, H. M. Fries, K. Alder, and H. C. Pauli, *Atomic Data and Nuclear Data Tables* **21**, 91 (1978); L. A. Sliv and I. M. Band, in *Alpha-, Beta- and Gamma-Ray Spectroscopy*, edited by K. Siegbahn (Amsterdam: North-Holland, 1965), Appendix 5.

The Mössbauer effect is reviewed in G. K. Weitheim, *Mössbauer Effect: Principles and Applications* (New York: Academic, 1964), and T. C. Gibb,

Principles of Mössbauer Spectroscopy (New York: Halsted, 1976). Collections of recent papers on the application of the Mössbauer effect are *Applications of Mössbauer Spectroscopy*, Vols. I and II, edited by Richard L. Cohen (New York: Academic, 1976 and 1980), and *Mössbauer Spectroscopy*, edited by U. Gonser (Berlin: Springer-Verlag, 1981).

PROBLEMS

1. Each of the following nuclei emits a photon in a γ transition between an excited state and the ground state. Given the energy of the photon, find the energy of the excited state and comment on the relationship between the nuclear recoil energy and the experimental uncertainty in the photon energy: (a) 320.08419 $\pm$ 0.00042 keV in ^{51}V; (b) 1475.786 $\pm$ 0.005 keV in ^{110}Cd; (c) 1274.545 $\pm$ 0.017 keV in ^{22}Ne; (d) 3451.152 $\pm$ 0.047 keV in ^{56}Fe; (e) 884.54174 $\pm$ 0.00074 keV in ^{192}Ir.
2. Following the decay of ^{198}Au, three γ's are observed to be emitted from states in ^{198}Hg; their energies (in keV) are γ_1, 411.80441 $\pm$ 0.00015; γ_2, 675.88743 $\pm$ 0.00069; and γ_3, 1087.69033 $\pm$ 0.00074. It is suggested that there are two excited states E_1 and E_2 in ^{198}Hg that are populated in the decay, and that the γ's correspond respectively to the transitions $E_1 \rightarrow E_0$, $E_2 \rightarrow E_1$, and $E_2 \rightarrow E_0$ (where E_0 represents the ground state). If this hypothesis were correct, we would expect $E_{\gamma_1} + E_{\gamma_2} = E_{\gamma_3}$, which is almost but not quite true according to the experimental uncertainties. Show how the proper inclusion of the nuclear recoil resolves the discrepancy.
3. The calculation of the emission probability for electric quadrupole radiation involves a term of the form of Equation 3.36, with the proper labeling of initial and final wave functions. From such an integral, verify the parity selection rule for electric quadrupole transitions.
4. (a) For a light nucleus ($A \approx 10$), compute the ratio of the emission probabilities for quadrupole and dipole radiation according to the Weisskopf estimates. Consider all possible choices for the parities of the initial and final states. (b) Repeat for a heavy nucleus ($A \approx 200$).
5. In a nucleus described by the rotational model (see Figure 5.22), the second excited state is always 4^+. This state decays by $E2$ radiation to the 2^+ state. Justify this observation by calculating, using the Weisskopf estimates, the ratio between the $E2$ decay probability and (a) the octupole ($L = 3$) and hexadecapole ($L = 4$) decays to the 2^+ state and (b) the hexadecapole decay to the ground state. (*Note*: These are collective rotational states, for which the Weisskopf estimates should not be taken too seriously.)
6. For the following γ transitions, give all permitted multipoles and indicate which multipole might be the most intense in the emitted radiation.
 (a) $\frac{9}{2}^- \rightarrow \frac{7}{2}^+$ (d) $4^+ \rightarrow 2^+$
 (b) $\frac{1}{2}^- \rightarrow \frac{7}{2}^-$ (e) $\frac{11}{2}^- \rightarrow \frac{3}{2}^+$
 (c) $1^- \rightarrow 2^+$ (f) $3^+ \rightarrow 3^+$
7. A certain decay process leads to final states in an even-Z, even-N nucleus and gives only three γ rays of energies 100, 200, and 300 keV, which are

found to be (respectively) of $E1$, $E2$, and $E3$ multipolarity. Construct two different possible level schemes for this nucleus (consistent with known systematics of nuclear structure) and label the states with their most likely spin-parity assignments. Suggest experiments that might distinguish between your proposed level schemes.

8. A nucleus has the following sequence of states beginning with the ground state: $\frac{3}{2}^+$, $\frac{7}{2}^+$, $\frac{5}{2}^+$, $\frac{1}{2}^-$, and $\frac{3}{2}^-$. Draw a level scheme showing the intense γ transitions likely to be emitted and indicate their multipole assignment.

9. The isomeric 2^+ state of ^{60}Co at 58.6 keV decays to the 5^+ ground state. Internal conversion competes with γ emission; the observed internal conversion coefficients are $\alpha_K = 41$, $\alpha_L = 7$, $\alpha_M = 1$. (a) Compute the expected half-life of the 2^+ state if the transition multipolarity is assumed to be $M3$, and compare with the observed half-life of 10.5 min. (b) If the transition also contained a small component of $E4$ radiation, how would your estimate for the half-life be affected? (c) The 2^+ state also decays by direct β emission to ^{60}Ni. The maximum β energy is 1.55 MeV and the log ft is 7.2. The 2^+ state decays 0.25% by β emission and 99.75% by γ emission and internal conversion. What is the effect on the calculated half-life of including the β emission?

10. An even-Z, even-N nucleus has the following sequence of levels above its 0^+ ground state: 2^+ (89 keV), 4^+ (288 keV), 6^+ (585 keV), 0^+ (1050 keV), 2^+ (1129 keV). (a) Draw an energy level diagram and show all reasonably probable γ transitions and their dominant multipole assignments. (b) By considering also internal conversion, what additional transitions and multipoles would appear?

11. (a) Pick half a dozen or so typical examples of $2^+ \rightarrow 0^+$ transitions from the first excited states of "rotational" nuclei, $150 < A < 190$. (Use standard reference works for nuclear spectroscopic data.) Compute the ratio between the observed γ decay rate and the corresponding Weisskopf estimate. Be sure to correct the measured lifetimes for internal conversion if necessary. (b) Repeat for "vibrational" nuclei, $60 < A < 150$, excluding cases at closed shells. (c) Draw any apparent conclusion about the difference between "rotational" and "vibrational" γ transitions.

12. The *Table of Isotopes* shows multipole assignments of γ transitions and lifetimes of excited states. By searching through the data given there, prepare a graph similar to Figure 10.13 showing the lifetimes for $M2$ transitions. Verify the dependence on the transition energy. (Be sure to use the *partial* lifetime in the cases in which a level can decay through several transitions.) Among the cases you should consider are ^{39}Ar, ^{73}As, ^{147}Eu, ^{165}Ho, ^{181}Ta, and ^{182}W, but you should find many other instances as well.

13. Among the nuclei in which there are known $E4$ transitions are ^{44}Sc, ^{52}Mn, ^{86}Rb, ^{93}Mo, ^{114}In, and ^{202}Pb. Look up the partial lifetimes for these transitions from collections of spectroscopic data, and compare with values calculated from the Weisskopf estimates.

14. The isotope ^{113}Cd captures a very low-energy neutron, leading to an excited state of ^{114}Cd, which emits a γ ray leading directly to the ^{114}Cd ground

state. (a) Find the energy of the γ ray, neglecting the nuclear recoil. (b) Calculate the kinetic energy of the recoiling ^{114}Cd.

15. In Section 5.2, the states of the vibrational model for even-Z, even-N nuclei up to the 0^+, 2^+, 3^+, 4^+, 6^+ three-phonon multiplet were discussed. The model also gives selection rules for γ emission: the phonon number must change by exactly one unit, and only $E2$ transitions are permitted. Draw a vibrational level scheme showing all permitted γ transitions starting with the three-phonon multiplet (use Figure 5.19 as a basis).

16. A certain decay scheme shows the following γ energies (in keV): 32.7, 42.1, 74.8, 84.0, 126.1, and 158.8. Coincidence studies reveal two features of the decay: only one of the γ's has none of the others in coincidence with it, and none of the γ's is in coincidence with more than three of the others. The γ's are preceded by a β decay that populates only one level. From this information suggest a possible level scheme. (*Note*: There are two different arrangements of the γ's that are consistent with the information given.)

17. In a study of the conversion electrons emitted in a decay process, the following electron energies were measured (in keV): 207.40, 204.64, 193.36, 157.57, 154.81, 143.53, 125.10, 75.27, 49.03, 46.27, 34.99. The electron binding energies are known to be 83.10 keV (K shell), 14.84 keV (L shell), 3.56 keV (M shell), and 0.80 keV (N shell). What is the minimum number of γ's that can produce the observed electron groups, and what are the γ energies?

18. Based on the information given in Figure 10.18 and Table 10.2, find all partial lifetimes for γ and electron emission for the 8^- level of ^{180}Hf.

19. For each of the following Mössbauer-effect transitions compute the natural width, the Doppler width at room temperature, the Doppler width at liquid helium temperature (4 K), and the nuclear recoil energy: (a) 73 keV, 6.3 ns in ^{193}Ir; (b) 14.4 keV, 98 ns in ^{57}Fe; (c) 6.2 keV, 6.8 μs in ^{181}Ta; (d) 23.9 keV, 17.8 ns in ^{119}Sn; (e) 95 keV, 22 ps in ^{165}Ho. Half-lives are given.

20. The absorption of the 27.8 keV magnetic dipole Mössbauer transition in ^{129}I takes the nucleus from its $\frac{7}{2}^+$ ground state to a $\frac{5}{2}^+$ excited state. The values of the magnetic dipole and electric quadrupole moments are: $\mu(\frac{7}{2}) = +2.6\ \mu_N$, $\mu(\frac{5}{2}) = +2.8\ \mu_N$, $Q(\frac{7}{2}) = -0.55$ b, $Q(\frac{5}{2}) = -0.68$ b. Make a sketch of the m-state splittings (similar to Figures 10.30 and 10.31) for the magnetic dipole and electric quadrupole cases and show the number of components in the Mössbauer spectrum. *Hint*: The magnetic field (B or H) and the electric field gradient (q or V_{zz}) can be regarded as positive.

21. In most of our work in nuclear physics, we regard the decay constant λ as a true constant for a given nuclear species. However, in this chapter and in the previous chapter you have studied two processes in which the nuclear decay rate could be sensitive to the chemical state of the atom. Discuss these two processes and explain how the atomic state might influence the nuclear decay rate. [For a discussion and some examples of cases in which this can occur, see the review by G. T. Emery, *Ann. Rev. Nucl. Sci.* **22**, 165 (1972).]

UNIT III
NUCLEAR REACTIONS

11

NUCLEAR REACTIONS

If energetic particles from a reactor or accelerator (or even from a radioactive source) are allowed to fall upon bulk matter, there is the possibility of a nuclear reaction taking place. The first such nuclear reactions were done in Rutherford's laboratory, using α particles from a radioactive source. In some of these early experiments, the α particles merely rebounded elastically from the target nuclei; this phenomenon, known ever since as Rutherford scattering, gave us the first evidence for the existence of atomic nuclei. In other experiments, Rutherford was able to observe a change or transmutation of nuclear species, as in this reaction done in 1919:

$$\alpha + {}^{14}\mathrm{N} \rightarrow {}^{17}\mathrm{O} + \mathrm{p}$$

The first particle accelerator capable of inducing nuclear reactions was built by Cockcroft and Walton, who in 1930 observed the reaction

$$\mathrm{p} + {}^{7}\mathrm{Li} \rightarrow {}^{4}\mathrm{He} + \alpha$$

In this chapter we discuss various types of nuclear reactions and their properties. In most cases, we deal with light projectiles, usually $A \leq 4$, incident on heavy targets; there is, however, much current interest in reactions induced by accelerating heavy ions (usually $A \leq 40$, but even beams as heavy as uranium are considered). We also deal only with reactions that are classified as "low energy," that is, of the order of 10 MeV per nucleon or less. In the range of 100 MeV–1 GeV, called "medium energy," meson production can take place, and protons and neutrons can transform into each other. At "high energy," all sorts of exotic particles can be produced, and we can even rearrange the quarks that are the constituents of nucleons. We discuss these latter types of reactions in Chapters 17 and 18.

11.1 TYPES OF REACTIONS AND CONSERVATION LAWS

A typical nuclear reaction is written

$$\mathrm{a} + \mathrm{X} \rightarrow \mathrm{Y} + \mathrm{b}$$

where a is the accelerated projectile, X is the target (usually stationary in the

laboratory), and Y and b are the reaction products. Usually, Y will be a heavy product that stops in the target and is not directly observed, while b is a light particle that can be detected and measured. Generally, a and b will be nucleons or light nuclei, but occasionally b will be a γ ray, in which case the reaction is called *radiative capture*. (If a is a γ ray, the reaction is called the *nuclear photoeffect*.)

An alternative and compact way of indicating the same reaction is

$$X(a, b)Y$$

which is convenient because it gives us a natural way to refer to a general class of reactions with common properties, for example (α, n) or (n, γ) reactions.

We classify reactions in many ways. If the incident and outgoing particles are the same (and correspondingly X and Y are the same nucleus), it is a *scattering* process, *elastic* if Y and b are in their ground states and *inelastic* if Y or b is in an excited state (from which it will generally decay quickly by γ emission). Sometimes a and b are the same particle, but the reaction causes yet another nucleon to be ejected separately (so that there are three particles in the final state); this is called a *knockout* reaction. In a *transfer reaction*, one or two nucleons are transferred between projectile and target, such as an incoming deuteron turning into an outgoing proton or neutron, thereby adding one nucleon to the target X to form Y. Reactions can also be classified by the mechanism that governs the process. In *direct reactions* (of which transfer reactions are an important subgroup), only very few nucleons take part in the reaction, with the remaining nucleons of the target serving as passive spectators. Such reactions might insert or remove a single nucleon from a shell-model state and might therefore serve as ways to explore the shell structure of nuclei. Many excited states of Y can be reached in these reactions. The other extreme is the *compound nucleus* mechanism, in which the incoming and target nuclei merge briefly for a complete sharing of energy before the outgoing nucleon is ejected, somewhat like evaporation of a molecule from a hot liquid. Between these two extremes are the *resonance reactions*, in which the incoming particle forms a "quasibound" state before the outgoing particle is ejected.

Observables

We have at our disposal techniques for measuring the energies of the outgoing particles to high precision (perhaps 10 keV resolution with a magnetic spectrometer). We can determine the direction of emission of the outgoing particle, and observe its angular distribution (usually relative to the axis of the original beam) by counting the number emitted at various angles. The *differential cross section* is obtained from the probability to observe particle b with a certain energy and at a certain angle (θ, ϕ) with respect to the beam axis. Integrating the differential cross section over all angles, we get the total cross section for particle b to be emitted at a certain energy (which is also sometimes called a differential cross section). We can also integrate over all energies of b to get the absolute total cross section, which is in effect the probability to form nucleus Y in the reaction.

This quantity is of interest in, for instance, neutron activation or radioisotope production.

By doing *polarization* experiments, we can deduce the spin orientation of the product nucleus Y or perhaps the spin dependence of the reaction cross section. For these experiments we may need an incident beam of polarized particles, a target of polarized nuclei, and a spectrometer for analyzing the polarization of the outgoing particle b.

We can simultaneously observe the γ radiations or conversion electrons from the decay of excited states of Y. This is usually done in coincidence with the particle b to help us decide which excited states the radiations come from. We can also observe the angular distribution of the γ radiations, as an aid in interpreting the properties of the excited states, especially in deducing their spin-parity assignments.

Conservation Laws

In analyzing nuclear reactions, we apply the same conservation laws we applied in studying radioactive decays. *Conservation of total energy and linear momentum* can be used to relate the unknown but perhaps measurable energies of the products to the known and controllable energy of the projectile. We can thus use the measured energy of b to deduce the excitation energy of states of Y or the mass difference between X and Y. *Conservation of proton and neutron number* is a result of the low energy of the process, in which no meson formation or quark rearrangement take place. (The weak interaction is also negligible on the time scale of nuclear reactions, about 10^{-16} to 10^{-22} s.) At higher energies we still conserve total nucleon (or, as we discuss in Chapter 18, baryon) number, but at low energy we conserve *separately* proton number *and* neutron number. *Conservation of angular momentum* enables us to relate the spin assignments of the reacting particles and the orbital angular momentum carried by the outgoing particle, which can be deduced by measuring its angular distribution. We can thus deduce the spin assignments of nuclear states. *Conservation of parity* also applies; the net parity *before* the reaction must equal the net parity *after* the reaction. If we know the orbital angular momentum of the outgoing particle, we can use the $(-1)^{\ell}$ rule and the other known parities in the reaction to deduce unknown parities of excited states. In Section 11.3 we discuss yet another quantity that is conserved in nuclear reactions.

11.2 ENERGETICS OF NUCLEAR REACTIONS

Conservation of total relativistic energy in our basic reaction gives

$$m_X c^2 + T_X + m_a c^2 + T_a = m_Y c^2 + T_Y + m_b c^2 + T_b \qquad (11.1)$$

where the T's are kinetic energies (for which we can use the nonrelativistic approximation $\frac{1}{2}mv^2$ at low energy) and the m's are rest masses. We define the *reaction Q value*, in analogy with radioactive decay Q values, as the initial mass

energy minus the final mass energy:

$$\begin{aligned} Q &= (m_{\text{initial}} - m_{\text{final}})c^2 \\ &= (m_X + m_a - m_Y - m_b)c^2 \end{aligned} \tag{11.2}$$

which is the same as the excess kinetic energy of the *final* products:

$$\begin{aligned} Q &= T_{\text{final}} - T_{\text{initial}} \\ &= T_Y + T_b - T_X - T_a \end{aligned} \tag{11.3}$$

The Q value may be positive, negative, or zero. If $Q > 0$ ($m_{\text{initial}} > m_{\text{final}}$ or $T_{\text{final}} > T_{\text{initial}}$) the reaction is said to be *exoergic* or *exothermic*; in this case nuclear mass or binding energy is released as kinetic energy of the final products. When $Q < 0$ ($m_{\text{initial}} < m_{\text{final}}$ or $T_{\text{final}} < T_{\text{initial}}$) the reaction is *endoergic* or *endothermic*, and initial kinetic energy is converted into nuclear mass or binding energy. The changes in mass and energy must of course be related by the familiar expression from special relativity, $\Delta E = \Delta mc^2$—any change in the kinetic energy of the system of reacting particles must be balanced by an equal change in its rest energy.

Equations 11.1–11.3 are valid in any frame of reference in which we choose to work. Let's apply them first to the laboratory reference frame, in which the target nuclei are considered to be at rest (room-temperature thermal energies are negligible on the MeV scale of nuclear reactions). If we define a reaction plane by the direction of the incident beam and one of the outgoing particles, then conserving the component of momentum perpendicular to that plane shows immediately that the motion of the second outgoing particle must lie in the plane as well. Figure 11.1 shows the basic geometry in the reaction plane. Conserving linear momentum along and perpendicular to the beam direction gives

$$p_a = p_b \cos\theta + p_Y \cos\xi \tag{11.4a}$$

$$0 = p_b \sin\theta - p_Y \sin\xi \tag{11.4b}$$

Regarding Q as a known quantity and T_a (and therefore p_a) as a parameter that we control, Equations 11.3 and 11.4a, b represent three equations in four unknowns (θ, ξ, T_b, and T_Y) which have no unique solution. If, as is usually the case, we do not observe particle Y, we can eliminate ξ and T_Y from the equations

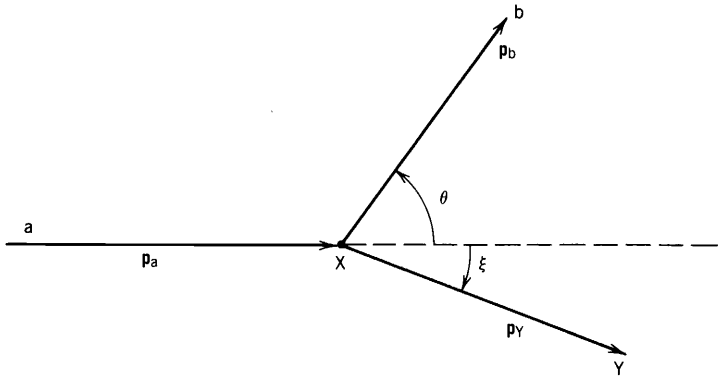


Figure 11.1 Basic reaction geometry for a + X → b + Y.

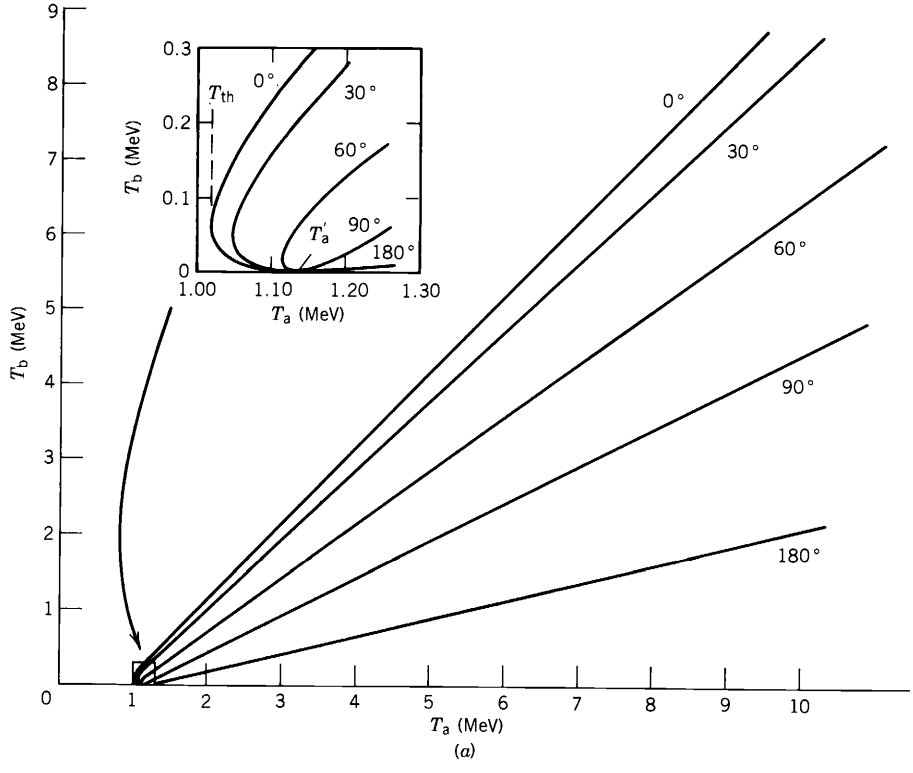


Figure 11.2 (*a*) T_a vs T_b for the reaction $^3H(p, n)^3He$. The inset shows the region of double-valued behavior near 1.0 MeV.

to find a relationship between T_b and θ:

$$T_b^{1/2} = \frac{(m_a m_b T_a)^{1/2} \cos\theta \pm \left\{ m_a m_b T_a \cos^2\theta + (m_Y + m_b)[m_Y Q + (m_Y - m_a)T_a] \right\}^{1/2}}{m_Y + m_b} \tag{11.5}$$

This expression is plotted in Figure 11.2*a* for the reaction $^3H(p, n)^3He$, for which $Q = -763.75$ keV. Except for a very small energy region between 1.019 and 1.147 MeV, there is a one-to-one correspondence (for a given T_a) between T_b and θ. That is, keeping the incident energy fixed, choosing a value of θ to observe the outgoing particles automatically then selects their energy.

Several other features of Figure 11.2 are apparent, which you should be able to show explicitly from Equation 11.5:

1. There is an absolute minimum value of T_a below which the reaction is not possible. This occurs only for $Q < 0$ and is called the *threshold energy* T_{th}:

$$T_{th} = (-Q)\frac{m_Y + m_b}{m_Y + m_b - m_a} \tag{11.6}$$

The threshold condition always occurs for $\theta = 0°$ (and therefore $\xi = 0°$)—the products Y and b move in a common direction (but still as separate nuclei).

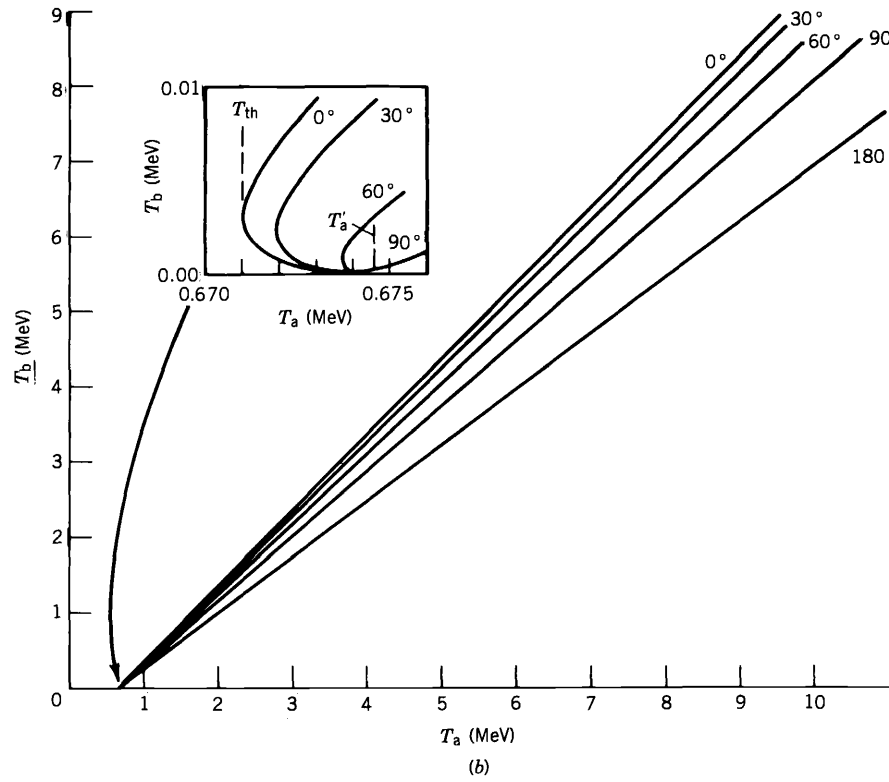


Figure 11.2 (*b*) T_a vs T_b for the reaction $^{14}C(p,n)^{14}N$. The inset shows the double-valued region.

No energy is "wasted" in giving them momentum transverse to the beam direction. If $Q > 0$, there is no threshold condition and the reaction will "go" even for very small energies, although we may have to contend with Coulomb barriers not considered here and which will tend to keep a and X outside the range of each other's nuclear force.

2. The double-valued situation occurs for incident energies between T_{th} and the upper limit

$$T_a' = (-Q)\frac{m_Y}{m_Y - m_a} \tag{11.7}$$

This also occurs only for $Q < 0$, and is important only for reactions involving nuclei of comparable masses. Using Equations 11.6 and 11.7 we can approximate this range as

$$T_a' - T_{th} \cong T_{th}\frac{m_a m_b}{m_Y(m_Y - m_a)}\left(1 - \frac{m_b}{m_Y} + \cdots\right) \tag{11.8}$$

and you can see that if a and b have mass numbers of 4 or less and if Y is a medium or heavy nucleus, then the range $(T_a' - T_{th})$ becomes much smaller

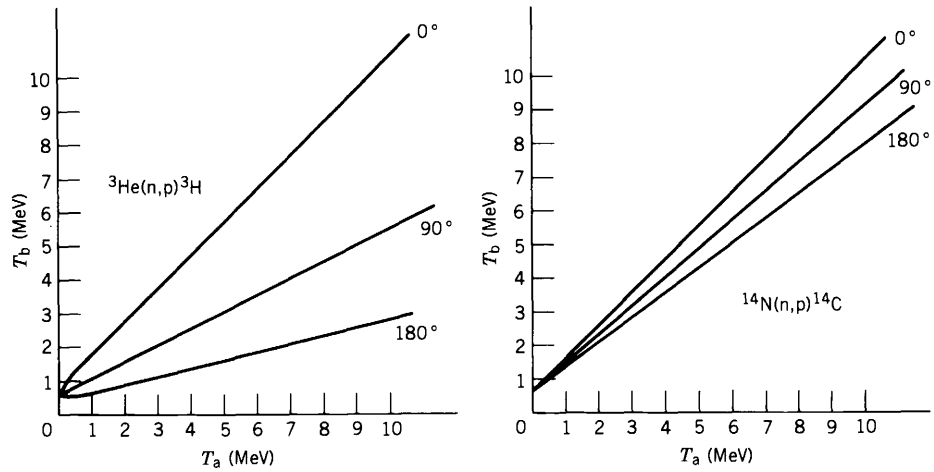


Figure 11.3 T_a vs T_b for the reactions ^{3}He(n, p)^3H and ^{14}N(n, p)^{14}C. No double-valued behavior occurs.

than 1% of the threshold energy. Figure 11.2*b* shows the double-valued region for the reaction ^{14}C(p, n)^{14}N.

3. There is also a maximum angle θ_m at which this double-valued behavior occurs, the value for which is determined for T_a in the permitted range by the vanishing of the argument in the square root of Equation 11.5:

$$\cos^2 \theta_m = -\frac{(m_Y + m_b)[m_Y Q + (m_Y - m_a)T_a]}{m_a m_b T_a} \tag{11.9}$$

When $T_a = T_a'$, the double-valued behavior occurs between $\theta = 0°$ and $\theta_m = 90°$; near $T_a = T_{th}$ it occurs only near $\theta_m = 0°$.

4. Reactions with $Q > 0$ have neither a threshold nor a double-valued behavior, as you can see by reversing the reactions shown in Figures 11.2*a* and 11.2*b*, ^{3}He(n, p)^3H and ^{14}N(n, p)^{14}C, for which we can in each case make the single transformation $-Q \rightarrow +Q$. Figure 11.3 shows the T_b vs T_a graphs for these cases. The reactions occur down to $T_a \rightarrow 0$ (no threshold), and the curves are single-valued for all θ and T_a.

If, for a given θ and T_a, we measure T_b, then we can determine the Q value of the reaction and deduce the mass relationships among the constituents. If we know m_a, m_b, and m_X, we then have a way of determining the mass of Y. Solving Equation 11.5 for Q, we obtain

$$Q = T_b\left(1 + \frac{m_b}{m_Y}\right) - T_a\left(1 - \frac{m_a}{m_Y}\right) - 2\left(\frac{m_a}{m_Y}\frac{m_b}{m_Y}T_a T_b\right)^{1/2}\cos\theta \tag{11.10}$$

This procedure is not strictly valid, for m_Y also appears on the right side of the equation, but it is usually of sufficient accuracy to replace the masses with the integer mass numbers, especially if we measure at 90° where the last term vanishes.

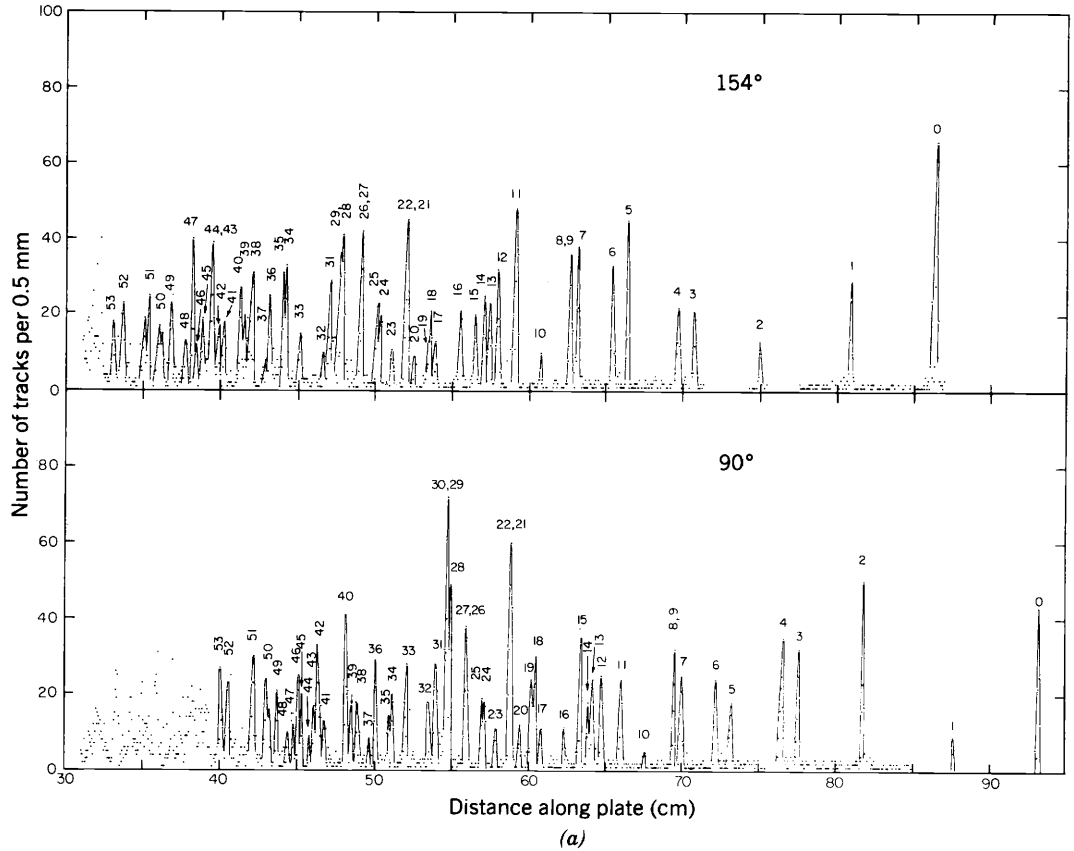
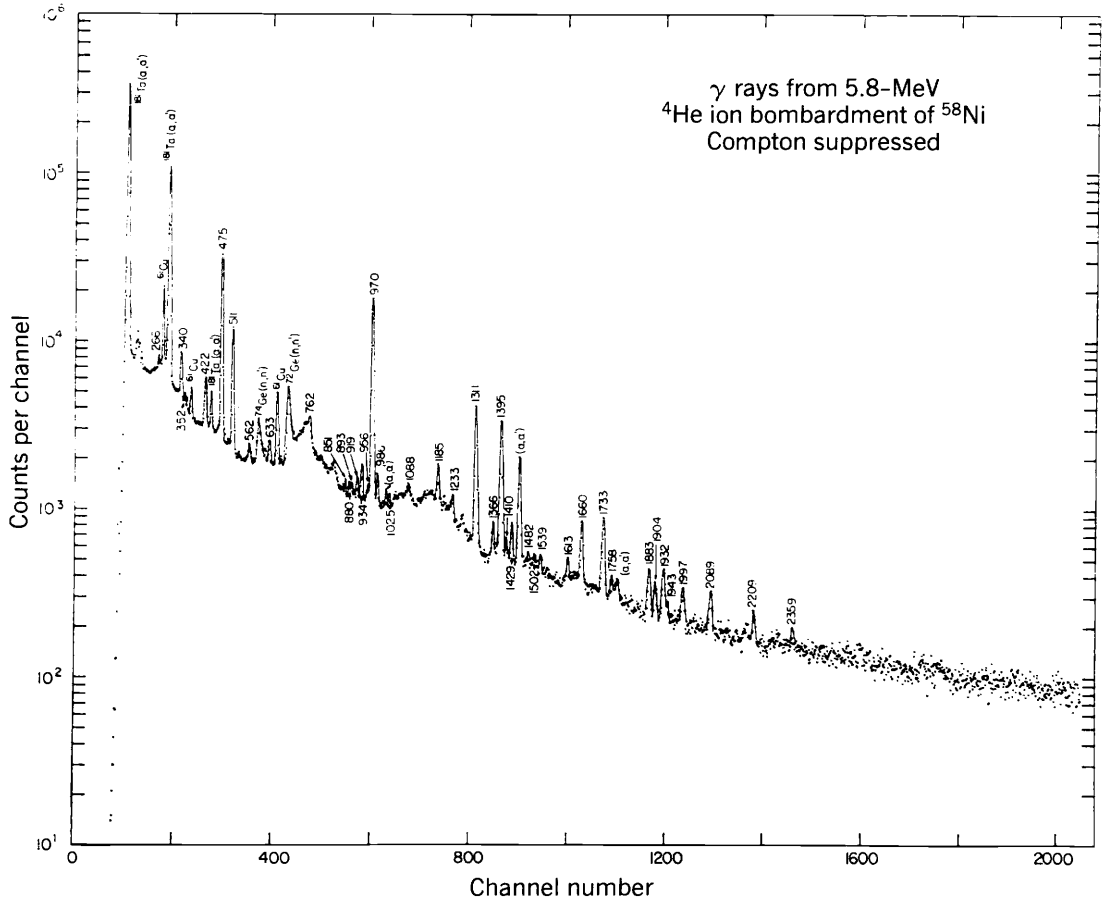
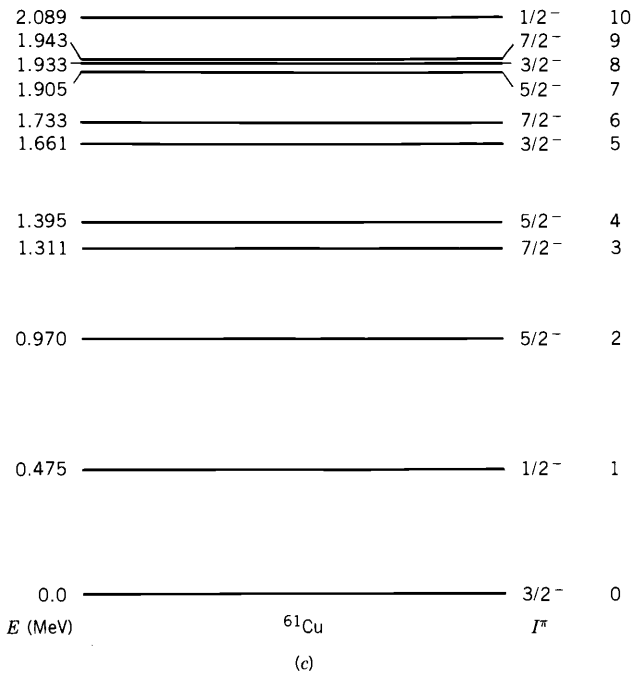


Figure 11.4 (*a*) Spectrum of protons from the reaction $^{58}Ni(^{4}He, p)^{61}Cu$. The highest energy proton group populates the ground state of ^{61}Cu, while the remaining groups lead to excited states (numbered 1, 2, 3, ...). The spectra taken at angles of 90 and 154° show a very dramatic angular dependence; note especially the change in the cross section for groups 1 and 2 at the two angles. (*b*) γ rays following the reaction. (*c*) Deduced partial level scheme of ^{61}Cu. Data from E. J. Hoffman, D. G. Sarantites, and N.-H. Lu, *Nucl. Phys. A* **173**, 146 (1971).



(b)

Figure 11.4 Continued.



(c)

Figure 11.4 Continued.

As an example of the application of this technique, we consider the reaction ^{26}Mg(^{7}Li, ^{8}B)^{25}Ne. The nucleus ^{26}Mg already has a neutron excess, and the removal of two additional protons in the reaction results in the final nucleus ^{25}Ne with a large excess of neutrons. Data reported by Wilcox et al., *Phys. Rev. Lett.* **30**, 866 (1973), show a ^{8}B peak about 55.8 MeV observed at a lab angle of 10° when the incident ^{7}Li beam energy is 78.9 MeV. Using Equation 11.10 with mass numbers instead of masses gives $Q = -22.27$ MeV, which gives 24.99790 u for the mass of ^{25}Ne. Iterating the calculation a second time with the actual masses instead of the mass numbers does not change the result even at this level of precision.

If the reaction reaches excited states of Y, the Q-value equation should include the mass energy of the excited state.

$$\begin{aligned} Q_{ex} &= (m_X + m_a - m_Y^* - m_b)c^2 \\ &= Q_0 - E_{ex} \end{aligned} \tag{11.11}$$

where Q_0 is the Q value corresponding to the ground state of Y, and where we have used $m_Y^* c^2 = m_Y c^2 + E_{ex}$ as the mass energy of the excited state (E_{ex} is the excitation energy above the ground state). The largest observed value of T_b is normally for reactions leading to the ground state, and we can thus use Equation 11.10 to find Q_0. Successively smaller values of T_b correspond to higher excited states, and by measuring T_b we can deduce Q_{ex} and the excitation energy E_{ex}.

Figure 11.4 shows an example of this kind of measurement. The peaks in the figure serve to determine T_b, from which the following Q values and excited-state

energies are obtained (energy uncertainties are about ± 0.005 MeV):

Peak	Q (MeV)	E_{ex} (MeV)
0	3.152	0.0
1	3.631	0.479
2	4.122	0.970
3	4.464	1.312
4	4.547	1.395
5	4.810	1.658
6	4.884	1.732
7	5.061	1.919
8, 9	5.090	1.938
10	5.240	2.088

leading to the excited states shown in the figure. The spectrum of the γ rays emitted following the reaction is also shown in the figure, and transitions can be seen corresponding to each of the deduced values of E_{ex} and therefore interpreted as direct transitions from the excited state to the ground state. Finally, angular distribution studies following the reaction can be used to deduce the spin-parity assignments of the excited states, leading to the level scheme shown in the figure. Notice how the various bits of data complement and supplement one another in building up the level scheme; from the γ rays alone, for example, we cannot tell which transitions connect the ground state with an excited state and therefore what the energies are of the excited states. The proton spectrum, however, gives us the excited-state energies directly, and turning to the γ-ray energies, which can be measured with greater precision, we can obtain more precise values for the energies of the states.

11.3 ISOSPIN

The interactions of a nucleon with its surroundings (other nucleons, for instance) in most cases do not depend on whether the nucleon has spin components $m_s = +\frac{1}{2}$ or $m_s = -\frac{1}{2}$ relative to an arbitrarily chosen z axis. That is, there is no need to distinguish in the formalism of nuclear physics between a "spin-up" nucleon and a "spin-down" nucleon. The multiplicity of spin orientations (two, for a single nucleon) may enter into the equations, for example in the statistics of the interaction, but the actual value of the projection does not appear. The exception to this situation comes about when a magnetic field is applied; the magnetic interaction of a nucleon depends on its spin component relative to the direction of the external field.

The charge independence of nuclear forces means that in most instances we do not need to distinguish in the formalism between neutrons and protons, and this leads us to group them together as members of a common family, the nucleons. The formalism for nuclear interactions may depend on the multiplicity of nucleon states (two) but it is independent of whether the nucleons are protons or

neutrons. The exception, of course, is the electromagnetic interaction, which can distinguish between protons and neutrons; with respect to the strong nuclear force alone, the symmetry between neutrons and protons remains valid.

This two-state degeneracy leads naturally to a formalism analogous to that of the magnetic interaction of a spin-$\frac{1}{2}$ particle. The neutron and proton are treated as two different states of a single particle, the nucleon. The nucleon is assigned a fictitious spin vector, called the *isospin*.* The two degenerate nuclear states of the nucleon in the absence of electromagnetic fields, like the two degenerate spin states of a nucleon in the absence of a magnetic field, are then "isospin-up," which we arbitrarily assign to the proton, and "isospin-down," the neutron.† That is, for a nucleon with isospin quantum number $t = \frac{1}{2}$, a proton has $m_t = +\frac{1}{2}$ and a neutron has $m_t = -\frac{1}{2}$. These projections are measured with respect to an arbitrary axis called the "3-axis" in a coordinate system whose axes are labeled 1, 2, and 3, in order to distinguish it from the laboratory z axis of the x, y, z coordinate system. The isospin obeys the usual rules for angular momentum vectors; thus we use an isospin vector $\boldsymbol{t}$ of length $\sqrt{t(t+1)}\,\hbar$ and with 3-axis projections $t_3 = m_t\hbar$.

For a system of several nucleons, the isospin follows coupling rules identical with the rules of ordinary angular momentum vectors. A two-nucleon system, for example, can have total isospin T of 0 or 1, corresponding (semiclassically) to the antiparallel or parallel orientations of the two isospin-$\frac{1}{2}$ vectors. The 3-axis component of the total isospin vector, T_3, is the sum of the 3-axis components of the individual nucleons, and thus for any nucleus,

$$T_3 = \tfrac{1}{2}(Z - N) \tag{11.12}$$

expressed in units of $\hbar$ which will not be shown explicitly.

For a given nucleus, T_3 is determined by the number of neutrons and protons. For any value of T_3, the total isospin quantum number T can take any value at least as great as $|T_3|$. Two related questions that immediately follow are: Can we assign the quantum number T to individual nuclear states? Is such an assignment useful, for example, in predicting decay or reaction probabilities?

We consider as an example the two-nucleon system, which can have T of 0 or 1. There are thus four possible 3-axis components: $T_3 = +1$ (two protons), $T_3 = -1$ (two neutrons), and two combinations with $T_3 = 0$ (one proton and one neutron). The first two states must have $T = 1$, while the latter two can have $T = 0$ and $T = 1$. If the nuclear interaction is perfectly charge independent (and if we "turn off" the electromagnetic interaction), then the three 3-axis projections of $T = 1$ $(+1, 0, -1)$ must have the same energy, while the single $T = 0$ state may have a different energy. In fact, we know that the isospin triplet (which is the $I = 0$ singlet of ordinary spin) is unbound, as discussed in Chapter 4.

*Isospin is often called *isotopic spin* or *isobaric spin*, the former because the value of its projection, equal to $\frac{1}{2}(Z - N)$, distinguishes between isotopes and the latter because the isospin quantum number is valid to label isobaric multiplets. The name "isospin" avoids the controversy and is now the generally accepted term.

†Originally, nuclear physicists defined the neutron as the isospin-up member of the nucleon family. Particle physicists also use isospin to label the different charge states of strongly interacting particles, but they stress the connection with electric charge by choosing isospin-up for the proton. This choice has now been accepted by nuclear physicists as well.

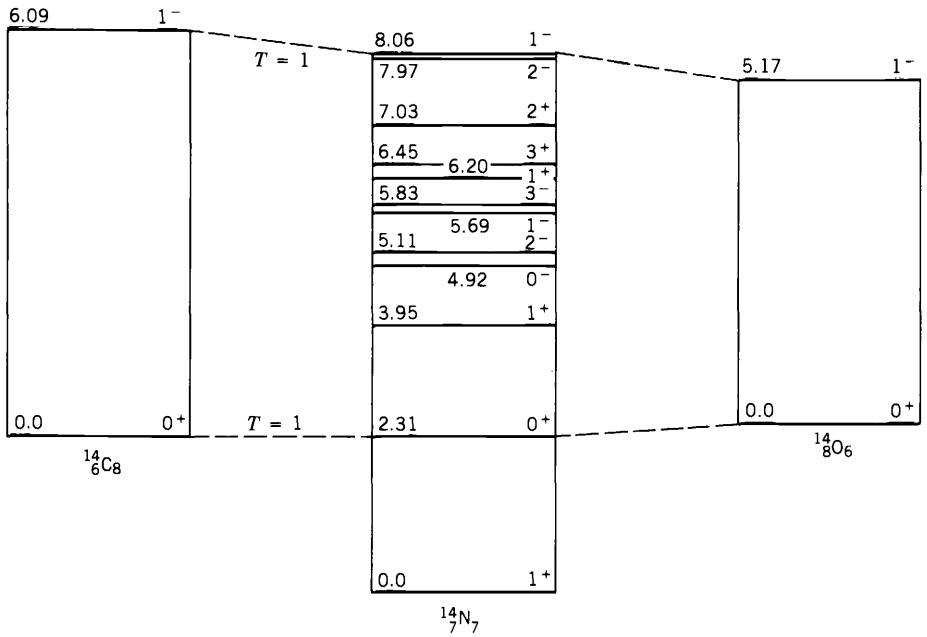


Figure 11.5 Lower energy levels of $A = 14$ isobars. The ground states of ^{14}C and ^{14}O have been shifted relative to ^{14}N by the neutron-proton mass difference and the Coulomb energy; the respective shifts are 2.36 and 2.44 MeV. Energy levels in ^{14}C and ^{14}O have $T = 1$; levels in ^{14}N have $T = 0$ except the $T = 1$ levels at 2.31 and 8.06 MeV. Based on data compiled by F. Ajzenberg-Selove, *Nucl. Phys. A* **449**, 53 (1986).

A clearer example of the isospin assignments can be found in the nuclei of the $A = 14$ system. Figure 11.5 shows the states of ^{14}C ($T_3 = -1$), ^{14}N ($T_3 = 0$), and ^{14}O ($T_3 = +1$). For ^{14}N, we know that any integer T can give a 3-axis component of 0, and the possible values of T therefore range from 0 up to a maximum of $A/2$ or 7. The tendency toward nuclear symmetry (reflected in the symmetry term of the semiempirical mass formula) implies that the lowest states will most likely have $T = |T_3|$, that is, the smallest possible value of T. This will certainly apply to the ground state, but the excited states must be assigned on the basis of reaction or decay studies or symmetry arguments. In Figure 11.5, the energies have been adjusted so that the neutron-proton mass difference (an electromagnetic effect) and the Coulomb energy of the nucleus have been removed. The energies of the states should then be due only to the nuclear force. Note that the energies of the 0^+ states in the three nuclei are nearly identical; these are the states of the $T = 1$ triplet. Similar agreement is obtained for the 1^- triplet.

Such speculations regarding the T assignments can be verified through decay and reaction studies. For example, angular momentum coupling theory leads to selection rules for $E1$ transitions: ΔT must be 0 or ± 1, except that transitions from $T = 0$ to $T = 0$ are forbidden and $\Delta T = 0$ transitions are forbidden in nuclei with $T_3 = 0$. To test these rules, we examine the half-lives for the 1^- to 0^+ $E1$ transitions in ^{14}O, ^{14}C, and ^{14}N. The measured half-lives of the analogous states are, respectively, 1.2×10^{-4}, < 7, and 27 fs. The ^{14}N transition, which is a

$\Delta T = 0$ $E1$ transition in a $T_3 = 0$ nucleus, is forbidden by the isospin selection rule and is indeed strongly inhibited, as its longer half-life indicates. (The Weisskopf estimate for the half-life is about 7×10^{-3} fs.)

Consider also the decay of the 1^-, $T = 0$ level at 5.69 MeV in ^{14}N. The $E1$ decay to the 1^+, $T = 0$ ground state should be inhibited by the selection rule, while the $E1$ decay to the 0^+, $T = 1$ level at 2.31 MeV is permitted. The higher energy transition ought to be greater in intensity by about a factor of 5, owing to the E^3 dependence of the $E1$ transition probability, yet the lower energy transition is observed to have about twice the intensity. The effect of the isospin selection rule is a reduction in the expected relative intensity of the 5.69-MeV $E1$ transition by about an order of magnitude.

Similar selection rules operate in β decay. The Fermi matrix element is forbidden unless $\Delta T = 0$, which is the case in the mirror decays listed in the top half of Table 9.3. The nonmirror decays are those with $\Delta T = 1$, and the Fermi contribution to the transition is reduced by several orders of magnitude by the violation of the isospin selection rule. The 0^+ to 0^+ decays, which on the basis of ordinary angular momentum alone should be pure Fermi decays of the superallowed category as in Table 9.2, are inhibited by three orders of magnitude if $\Delta T \neq 0$; the log ft values rise from about 3.5 for the $\Delta T = 0$ decays permitted by the isospin selection rule to 7 or larger for the $\Delta T \neq 0$ isospin-forbidden decays.

Nuclear reactions also show effects of isospin. Because the nuclear force does not distinguish between protons and neutrons, the isospin must be absolutely conserved in all nuclear reactions. The 3-axis component is automatically conserved when the numbers of protons and neutrons remain constant, but it is also true that the total isospin quantum number T remains invariant in reactions. Consider the reaction $^{16}\text{O} + {}^2\text{H} \rightarrow {}^{14}\text{N} + {}^4\text{He}$, leading to states in ^{14}N. All four reacting particles have $T = 0$ ground states; thus T is conserved if the product particles remain in their ground states. Excitation of ^{4}He is unlikely in low-energy reactions, for its first excited state is above 20 MeV, and thus it is expected that only $T = 0$ excited states in ^{14}N can be reached in the reaction; the 2.31-MeV, $T = 1$ state should not be populated. Any small population observed for that state must arise from isospin impurities in the reacting particles. The cross section to reach the 2.31-MeV state is observed to be about 2 orders of magnitude smaller than the cross sections to reach the neighboring $T = 0$ states, showing the effectiveness of the isospin selection rule. In the similar reaction $^{12}\text{C}(\alpha, \text{d})^{14}\text{N}$ the cross section for the 2.31-MeV state is 3 orders of magnitude smaller than the isospin-allowed cross sections, and in $^{10}\text{B}(^6\text{Li}, \text{d})^{14}\text{N}$ and $^{12}\text{C}(^6\text{Li}, \alpha)^{14}\text{N}$ it is at least two orders of magnitude smaller. By way of contrast, in $^{10}\text{B}(^7\text{Li}, ^3\text{H})^{14}\text{N}$, the $T = 1$ level is populated with a strength comparable to that of the neighboring $T = 0$ level; the isospin selection rule does not inhibit the probability to reach the $T = 1$ level. (The initial nuclei have a total T of $\frac{1}{2}$; the $\frac{1}{2}$ isospin of ^{3}H can couple to either $T = 0$ or $T = 1$ in ^{14}N to give a resultant of $\frac{1}{2}$.)

The members of an isospin multiplet, as for example pairs of mirror nuclei or a set of the three states connected by the dashed lines in Figure 11.5, are called *isobaric analog states*, a term which was previously introduced in the discussion of β decay in Section 9.8. The analog states in neighboring nuclei have identical nucleon wave functions, except for the change in the number of protons and neutrons. In the ^{14}C and ^{14}O ground states, the nucleons are strongly coupled

pairwise (with two coupled proton holes in ^{14}C and two coupled neutron holes in ^{14}O), and the 2.31-MeV analog state in ^{14}N must have a similar wave function, with the odd proton hole and neutron hole strongly paired.

Because analog states are obtained by exchanging a proton for a neutron, they tend to be strongly populated in β decay (see Figure 9.17) and in (p, n) or (n, p) reactions. In medium and heavy nuclei, placing a proton into a state formerly occupied by a neutron involves a large energy transfer, because with $N > Z$ the newly placed neutron occupies a considerably higher shell-model state than the former proton. Analog states may appear in medium and heavy nuclei at energies of 10 MeV and above, and thus they generally do not contribute to low-energy reaction and decay studies.

11.4 REACTION CROSS SECTIONS

In Chapter 4 we considered the nature of cross sections and the application to nucleon-nucleon scattering. In this section we give some more general definitions of various measurable quantities that are loosely grouped under the heading "cross section."

Roughly speaking, the cross section is a measure of the relative probability for the reaction to occur. If we have a detector placed to record particle b emitted in a direction (θ, ϕ) with respect to the beam direction, the detector defines a small solid angle $d\Omega$ at the target nucleus (Figure 11.6). Let the current of incident particles be I_a particles per unit time, and let the target show to the beam N target nuclei per unit area. If the outgoing particles appear at a rate R_b, then the reaction cross section is

$$\sigma = \frac{R_b}{I_a N} \tag{11.13}$$

Defined in this way, σ has the dimension of area per nucleus, but it may be very much larger or smaller than the geometrical area of the disc of the target nucleus

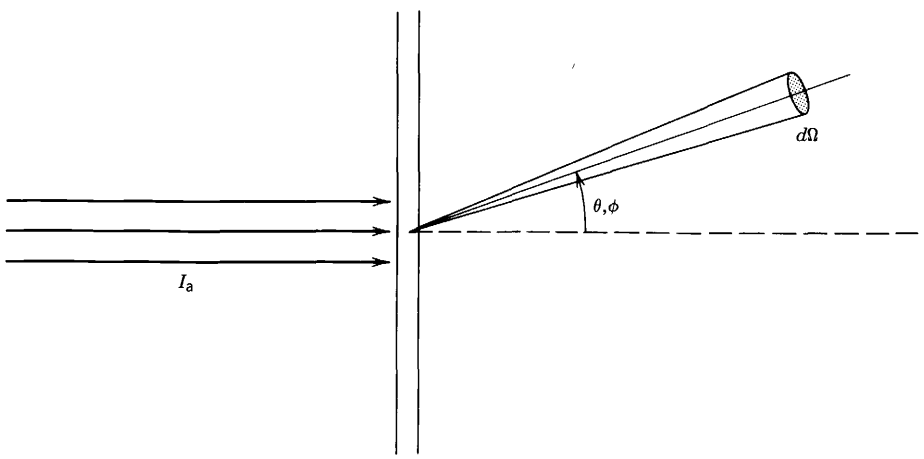


Figure 11.6 Reaction geometry showing incident beam, target, and outgoing beam going into solid angle $d\Omega$ at θ, ϕ.

seen by the incoming beam. For a typical nucleus of radius $R = 6$ fm, the geometrical area πR^2 is about 100 fm^2 = 1 b; for neutron capture by ^{135}Xe, the cross section is about 10^6 b, while for other much more improbable reactions the cross section may be measured in millibarns or microbarns. You should think of σ as a quantity which has the dimension of an area, but which is proportional to the reaction probability.

Our detector occupies only a small solid angle $d\Omega$ and therefore does not observe *all* of the outgoing particles; only a small fraction dR_b are actually counted, and therefore only a fraction of the cross section $d\sigma$ will be deduced. Moreover, the outgoing particles will not in general be emitted uniformly in all directions, but will have an angular distribution that will depend on θ and possibly also on ϕ. It we let this angular distribution function be arbitrarily represented by $r(\theta, \phi)$, then $dR_b = r(\theta, \phi)\, d\Omega/4\pi$. (The 4π is introduced to make $d\Omega/4\pi$ a pure fraction.) Then

$$\frac{d\sigma}{d\Omega} = \frac{r(\theta, \phi)}{4\pi I_a N} \tag{11.14}$$

The quantity $d\sigma/d\Omega$ is called the *differential cross section*, and its measurement gives us important information on the angular distribution of the reaction products. In the literature, it is often called $\sigma(\theta, \phi)$ or $\sigma(\theta)$ or sometimes (unfortunately) just "cross section." (If you see a graph of "cross section" vs θ, you should know that what is intended is differential cross section.) Because solid angle is measured in steradians (the surface of a sphere subtends a solid angle of 4π steradians at its center), units of differential cross section are barns/steradian. The reaction cross section σ can be found by integrating $d\sigma/d\Omega$ over all angles; with $d\Omega = \sin\theta\, d\theta\, d\phi$ we have*

$$\sigma = \int \frac{d\sigma}{d\Omega}\, d\Omega = \int_0^{\pi} \sin\theta\, d\theta \int_0^{2\pi} d\phi\, \frac{d\sigma}{d\Omega} \tag{11.15}$$

Notice that if $d\sigma/d\Omega$ is constant (independent of angle), the integral gives $\sigma = 4\pi(d\sigma/d\Omega)$. This justifies the insertion of the constant 4π into Equation 11.14, for now $r(\theta, \phi)$ reduces to the constant R_b and Equation 11.14 agrees with Equation 11.13.

In many nuclear physics applications, we are not concerned simply with the probability to find particle b emitted at a certain angle; we also want to find it with a certain energy, corresponding to a particular energy of the residual nucleus Y. We therefore must modify the definition of cross section to give the probability to observe b in the angular range of $d\Omega$ and in the energy range dE_b. This gives the so-called *doubly differential cross section* $d^2\sigma/dE_b\, d\Omega$. In the literature, this additional energy dependence is often not explicitly stated; usually the cross sections are plotted as $d\sigma/d\Omega$ vs θ *leading to a specific final energy state*. This is in reality $d^2\sigma/dE_b\, d\Omega$, although it may not be labeled as such. For discrete states, there may be only a single level within the energy range dE_b, and the

*An element of area on the surface of a sphere is $r^2\, d\Omega$ or $r^2 \sin\theta\, d\theta\, d\phi$ in spherical coordinates. Hence $d\Omega = \sin\theta\, d\theta\, d\phi$.

Table 11.1 Reaction Cross Sections

Cross Sections	Symbol	Technique	Possible Application
Total	σ_t	Attenuation of beam	Shielding
Reaction	σ	Integrate over all angles and all energies of b (all excited states of Y)	Production of radioisotope Y in a nuclear reaction
Differential (Angular)	$d\sigma/d\Omega$	Observe b at (θ, ϕ) but integrate over all energies	Formation of beam of b particles in a certain direction (or recoil of Y in a certain direction)
Differential (Energy)	$d\sigma/dE$	Don't observe b, but observe excitation of Y by subsequent γ emission	Study of decay of excited states of Y
Doubly differential	$d^2\sigma/dE_b\, d\Omega$	Observe b at (θ, ϕ) at a specific energy	Information on excited states of Y by angular distribution of b

distinction becomes unimportant. If, on the other hand, we do not observe the direction of particle b (by surrounding the target area with 4π solid angle of detectors, or by not observing b at all), then we measure yet another differential cross section $d\sigma/dE$, where now E may represent an excitation energy of Y.

There is still another cross section that may be of interest, the *total cross section* σ_t. Here, for a specific incident particle a, we add the reaction cross sections σ for all possible different outgoing particles b, no matter what their direction or energy. Such a determination would tell us the probability for an incident particle to have *any reaction at all* with the target and thus be removed from the beam of incident particles. This can be deduced directly by measuring the loss in intensity of a collimated beam in passing through a certain thickness of the target material.

When we discuss a specific reaction then, the exact meaning of the term cross section will depend on exactly what we measure. Table 11.1 summarizes these different measurements, how they might be accomplished, and the application to which the result might be put. For example, if we wish to produce a radioactive isotope as the residual nucleus Y, we have absolutely no interest in the direction of emission of particle b, nor in the excited states of Y that may be populated, for they will quickly decay by γ emission to the ground state of Y. The literature often does not discriminate carefully among these definitions, and often they are called merely "cross section." It is almost always obvious in context which cross section is meant, and therefore not strictly necessary to distinguish carefully among them.

11.5 EXPERIMENTAL TECHNIQUES

A typical nuclear reaction study requires a beam of particles, a target, and a detection system. Beams of charged particles are produced by a variety of different types of accelerators (see Chapter 15), and neutron beams are available from nuclear reactors and as secondary beams from charged-particle accelerators. To do precision spectroscopy of the outgoing particle b and the residual nucleus Y, the beam must satisfy several criteria:

1. It must be *highly collimated and focused*, so that we have a precise reference direction to determine θ and ϕ for angular distribution measurements.
2. It must have a *sharply defined energy*; otherwise, in trying to observe a specific excited state by finding Q_{ex} and E_{ex} from Equation 11.5, we might find that variations in T_a would give two or more different E_{ex} for the same T_b.
3. It must be of *high intensity*, so that we can gather the necessary statistics for precise experiments.
4. If we wish to do timing measurements (such as to measure the lifetimes of excited states of Y), the beam must be *sharply pulsed* to provide a reference signal for the formation of the state, and the pulses must be separated in time by at least the time resolution of the measuring apparatus and preferably by a time of the order of the one we are trying to measure.
5. Under ideal circumstances, the accelerator beam should be *easily selectable*—we should be able to change the incident energy T_a or even the type of incident particle in a reasonable time. The stringent tuning requirements of modern large accelerators and the demands that high currents put on ion sources make this requirement hard to meet in practice. Accelerator beam time is often scheduled far in advance (6 months to a year is common), so that experiments with common beam requirements can be grouped together, thus minimizing the beam tuning time.
6. The intensity of the incident beam should be nearly *constant and easily measurable*, for we must know it to determine the cross section. If we move a detector from one position to another, we must know if the change in the observed rate of detection of particle b comes from the angular dependence of the differential cross section or merely from a change in the incident beam intensity.
7. The beam may be *polarized* (that is, the spins of the incident particles all aligned in a certain direction) or *unpolarized*, according to the desire of the experimenters.
8. The beam must be transported to the target through a *high-vacuum system* so as to prevent beam degradation and production of unwanted products by collisions with air molecules.

Types of targets vary widely, according to the goals of the experiment. If we want to measure the yield of a reaction (that is, σ or σ_t), perhaps through observation of the attenuation of the beam or the decay of radioisotope Y, then we may choose a thick, solid target. Such a target might degrade, scatter, or even

stop the outgoing particles b, which does not bother us in this kind of measurement. On the other hand, if we wish to observe b unaffected by interactions in the target, a very thin target is required. Thin metal foils are often used as targets, but for nonmetals, including compounds such as oxides, the target material is often placed on a thin backing, which does not contribute to the reaction or affect the passage of particle b. For many applications, extremely rare (and often expensive) targets of separated isotopes are used. A high-intensity, highly focused beam (typically a few mm in diameter) delivers considerable thermal power to the target (absorption of 1 μA of 10 MeV protons delivers 10 W), which is enough to burn up thin targets; therefore a way must be found to cool the target and extract the heat generated by the beam. As with the beam, it should be relatively easy to change targets so that valuable beam time is not wasted. For some applications, it may be desirable to polarize the spins of the target nuclei.

The detectors may consist of some (or all) of the following: particle detectors or detector telescopes to determine the energy and type of the outgoing particles, magnetic spectrometers for good energy resolution (sometimes necessary to identify close-lying excited states of Y), position-sensitive particle detectors (such as multiwire proportional counters) to do accurate angular distribution work, γ-ray detectors to observe the de-excitation of the excited states of Y (possibly in coincidence with particle b), polarimeters to measure the polarization of the particles b, and so on. Because beam time is a precious commodity at a modern accelerator facility, the emphasis is always on getting the largest amount of data in the shortest possible time. Therefore multidetector configurations are very common; many signals arrive simultaneously at the detectors and are stored by an on-line computer system for later "re-play" and analysis. (Keeping the beam and the detectors going during the experiment usually demands all the attention of the experimenters and leaves little time for data analysis!)

11.6 COULOMB SCATTERING

Because the nucleus has a distribution of electric charge, it can be studied by the electric (Coulomb) scattering of a beam of charged particles. This scattering may be either elastic or inelastic.

Elastic Coulomb scattering is called *Rutherford scattering* because early (1911–1913) experiments on the scattering of α particles in Rutherford's laboratory by Geiger and Marsden led originally to the discovery of the existence of the nucleus. The basic geometry for the scattering is shown in Figure 11.7. As is always the case for unbound orbits in a $1/r^2$ force, the scattered particle follows a hyperbolic path. (We will assume the target nucleus to be infinitely massive, so that the scattering center remains fixed.) The particle approaches the target nucleus along a straight line that would pass a distance b from the nucleus in the absence of the repulsive force; this distance is called the *impact parameter*. The scattering angle is θ. Very far from the nucleus, the incident particle has negligible Coulomb potential energy; its total energy is thus only the incident kinetic energy $T_a = \frac{1}{2}mv_0^2$. Its angular momentum relative to the target nucleus is $|\boldsymbol{r} \times m\boldsymbol{v}| = mv_0 b$ at large distances. In passing close to the target nucleus, the particle reaches a minimum separation distance r_{min} (which depends on b), the

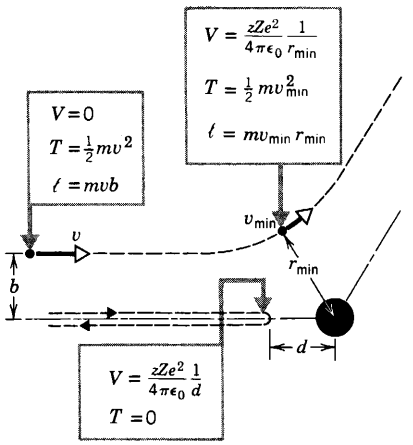


Figure 11.7 The trajectory of a particle undergoing Rutherford scattering, showing the closest approach to the target nucleus.

absolute minimum value of which occurs in a head-on collision ($b = 0$), in which the particle comes instantaneously to rest before reversing its motion. At this point it has exchanged its initial kinetic energy for Coulomb potential energy:

$$\tfrac{1}{2}mv_0^2 = \frac{1}{4\pi\epsilon_0}\frac{zZe^2}{d} \tag{11.16}$$

where ze is the charge of the projectile and Ze the target. The distance d is called the *distance of closest approach*. At intermediate points in the trajectory, the energy is partly kinetic and partly potential; conservation of energy gives (for any value of the impact parameter)

$$\tfrac{1}{2}mv_0^2 = \tfrac{1}{2}mv^2 + \frac{1}{4\pi\epsilon_0}\frac{zZe^2}{r} \tag{11.17}$$

The scattering has cylindrical symmetry about the beam axis (because the Coulomb force is symmetric), and therefore the cross section is independent of the azimuthal angle ϕ. We therefore work in a ring or annular geometry (Figure 11.8). Particles with impact parameters between b and $b + db$ are scattered into the ring at angles between θ and $\theta + d\theta$. Let the target have n nuclei per unit volume, and assume the target to be thin enough so that it is unlikely to have any "shadowing" of one nucleus by another. The target is considered to be a foil of thickness x. Then the number of nuclei per unit area is nx, and the fraction df of the incident particles that pass through the annular ring of area $2\pi b\,db$ is

$$df = nx(2\pi b\,db) \tag{11.18}$$

The fraction f with impact parameters less than b is

$$f = nx\pi b^2 \tag{11.19}$$

If particles scattered with impact parameter b emerge at angle θ, then Equation 11.19 also gives the fraction that are scattered at angles greater than θ, but to carry the discussion further we need a relationship between b and θ. (We are

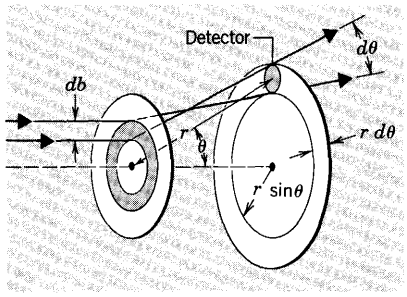


Figure 11.8 Particles entering the ring between b and $b + db$ are distributed uniformly along a ring of angular width $d\theta$. A detector is at a distance r from the scattering foil.

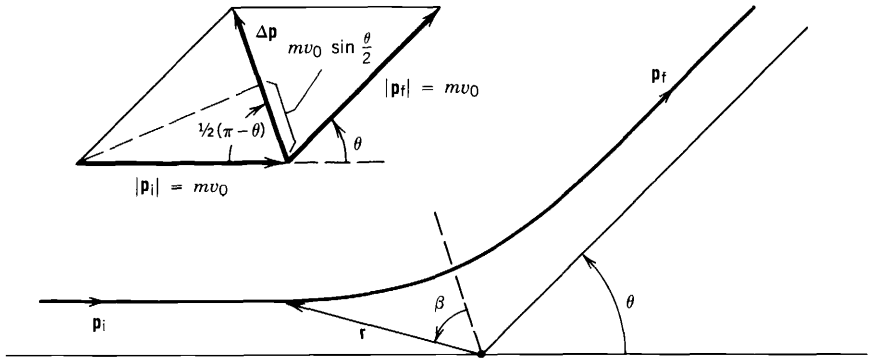


Figure 11.9 The hyperbolic trajectory of a scattered particle. The instantaneous coordinates are r, β. The change in momentum is $\Delta \boldsymbol{p}$, in the direction of the dashed line that bisects $(\pi - \theta)$.

assuming that each incident particle is scattered only once—more about this assumption later.)

The net linear momentum of the scattered particles changes in direction only; far from the scattering, the incident and the final linear momentum are both mv_0. (This follows from the assumption that the target is so massive that it does not move.) The change in the momentum vector, as shown in Figure 11.9, is a vector of magnitude

$$\Delta p = 2mv_0 \sin \frac{\theta}{2} \tag{11.20}$$

in the direction of the bisector of $\pi - \theta$. According to Newton's second law in the form $F = dp/dt$, this is equal to the net impulse of the Coulomb force in that direction:

$$\Delta p = \int dp = \int F\,dt = \frac{zZe^2}{4\pi\epsilon_0} \int \frac{dt}{r^2} \cos\beta \tag{11.21}$$

where β is the angle between the bisector and instantaneous vector $\boldsymbol{r}$ locating the particle. In the initial position far from the scattering, which we take to be time $t = 0$, the angle β has the value $-(\pi/2 - \theta/2)$; in the final position ($t = \infty$), the angle β is $+(\pi/2 - \theta/2)$.

The instantaneous velocity $\boldsymbol{v}$ can be written in terms of radial (along $\boldsymbol{r}$) and tangential components:

$$\boldsymbol{v} = \frac{dr}{dt}\hat{r} + r\frac{d\beta}{dt}\hat{\beta} \tag{11.22}$$

where $\hat{r}$ and $\hat{\beta}$ indicate unit vectors in the radial and tangential directions, respectively. Only the tangential component contributes to the angular momentum about the nucleus:

$$\ell = |m\boldsymbol{r} \times \boldsymbol{v}| = mr^2\frac{d\beta}{dt} \tag{11.23}$$

Far from the nucleus, the angular momentum has the value mv_0b; conservation of angular momentum gives

$$\begin{aligned} mv_0b &= mr^2\frac{d\beta}{dt} \\ \frac{dt}{r^2} &= \frac{d\beta}{v_0b} \end{aligned} \tag{11.24}$$

and substituting into Equation 11.21 gives

$$\begin{aligned} \Delta p &= \frac{zZe^2}{4\pi\epsilon_0 v_0 b}\int_{-(\pi/2-\theta/2)}^{+(\pi/2-\theta/2)} \cos\beta\, d\beta \\ &= \frac{zZe^2}{2\pi\epsilon_0 v_0 b}\cos\frac{\theta}{2} \end{aligned} \tag{11.25}$$

Combining this result with Equation 11.20 gives the needed relationship between b and θ:

$$b = \frac{d}{2}\cot\frac{\theta}{2} \tag{11.26}$$

where d is the distance of closest approach from Equation 11.16. Combining Equations 11.18 and 11.26,

$$|df| = \pi n x\frac{d^2}{4}\cot\frac{\theta}{2}\csc^2\frac{\theta}{2}\,d\theta \tag{11.27}$$

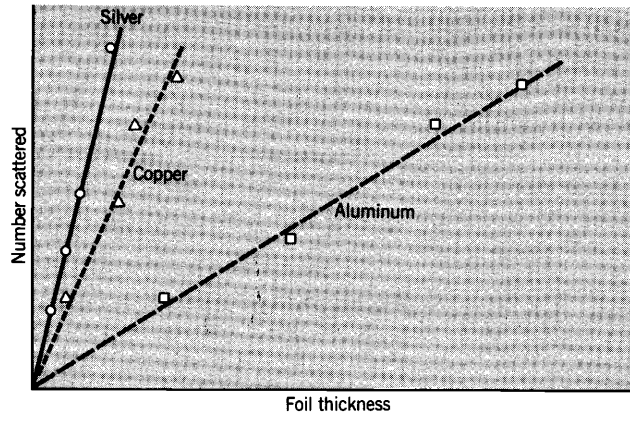
and the rate at which particles reach the ring, per unit solid angle, is

$$r(\theta,\phi) = \frac{I_a|df|}{d\Omega/4\pi} \tag{11.28}$$

where I_a is the rate at which incident particles fall on the target (and hence $I_a|df|$ is the number that fall between b and $b + db$). With $d\Omega = 2\pi\sin\theta\, d\theta$ for the ring geometry (that is, $\sin\theta\, d\theta\, d\phi$ integrated over ϕ), the net result is

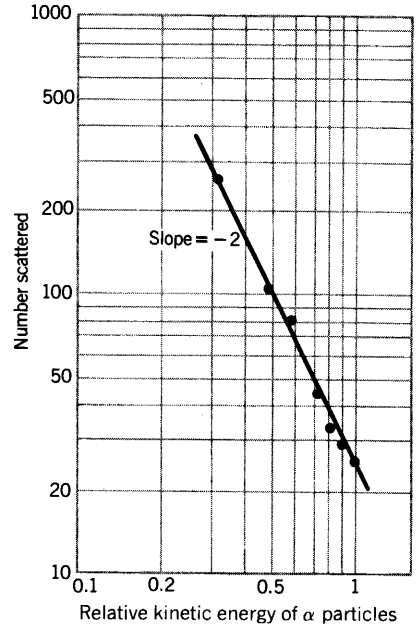
$$\frac{d\sigma}{d\Omega} = \left(\frac{zZe^2}{4\pi\epsilon_0}\right)^2\left(\frac{1}{4T_a}\right)^2\frac{1}{\sin^4\dfrac{\theta}{2}} \tag{11.29}$$

This is the differential cross section for Rutherford scattering, usually called the



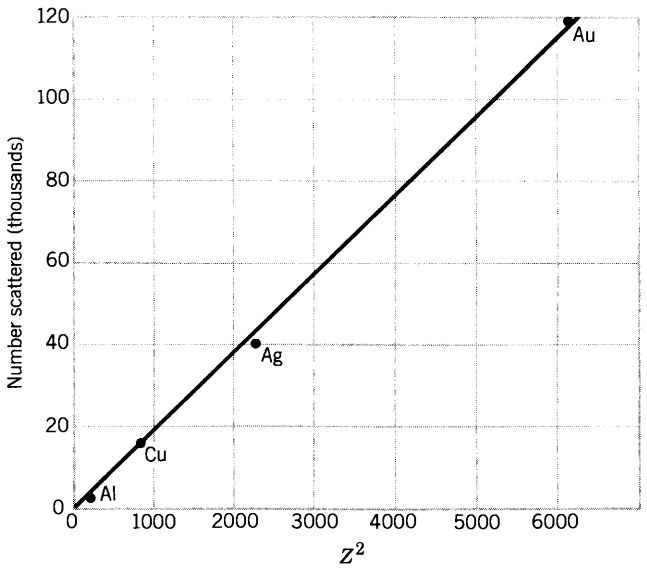
(a)

Figure 11.10 (*a*) The dependence of scattering rate on foil thickness for three different scattering foils.



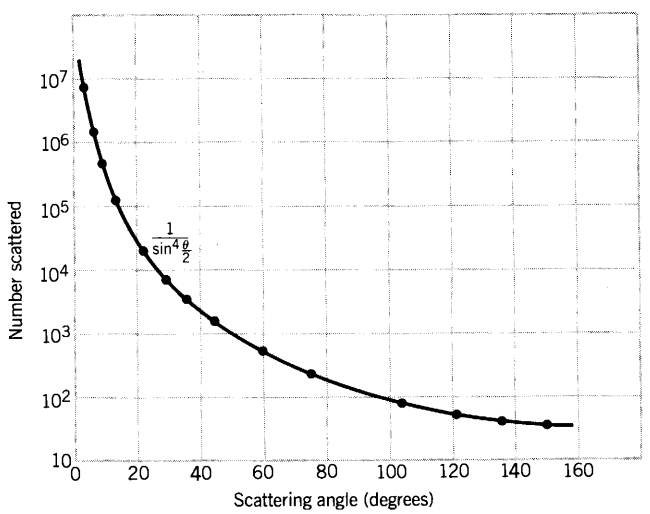
(c)

Figure 11.10 (*c*) The dependence of scattering rate on the kinetic energy of the incident α particles for scattering by a single foil. Note the log-log scale; the slope of -2 shows that $\log N \propto -2 \log T$, or $N \propto T^{-2}$, as expected from the Rutherford formula.



(b)

Figure 11.10 (*b*) The dependence of scattering rate on the nuclear charge Z for foils of different materials. The data are plotted against Z^2



(d)

Figure 11.10 (*d*) The dependence of scattering rate on the scattering angle θ, using a gold foil. The $\sin^{-4}(\theta/2)$ dependence is exactly as predicted by the Rutherford formula.

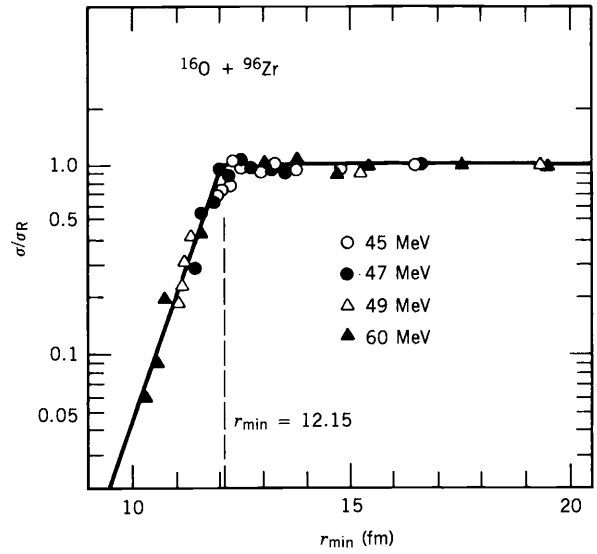


Figure 11.11 Elastic scattering of ^{16}O from ^{96}Zr at several incident energies. The horizontal axis shows the minimum separation distance r_{min} between projectile and target, which varies with b and therefore with θ. The vertical axis shows the cross section in terms of the calculated Rutherford cross section. Nuclear scattering effects appear at separations of less than 12.15 fm; this corresponds to $R_0 = 1.7$ fm, considerably greater than the mean radius of 1.25 fm, but consistent with a "skin thickness" of about 0.5 fm which allows the two nuclear distributions to overlap at these larger distances. From P. R. Christensen et al., *Nucl. Phys. A* **207**, 33 (1973).

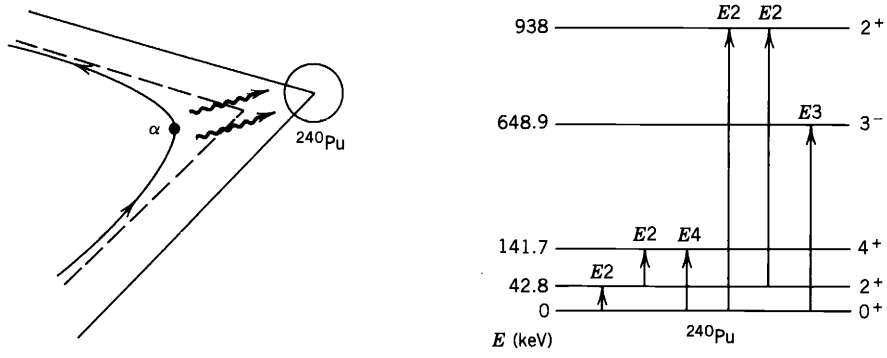


Figure 11.12 Inelastic Coulomb scattering (Coulomb excitation). The projectile exchanges energy with the target through the Coulomb interaction (exchanged photons are shown as wavy lines) and the target ^{240}Pu, originally in its ground state, can be driven to excited states. Several different modes of excitation are shown, including two-step processes. The spectrum of inelastically scattered α's shows which excited states of ^{240}Pu have been excited. Data from C. E. Bemis, Jr., et al., *Phys. Rev. C* **8**, 1466 (1973).

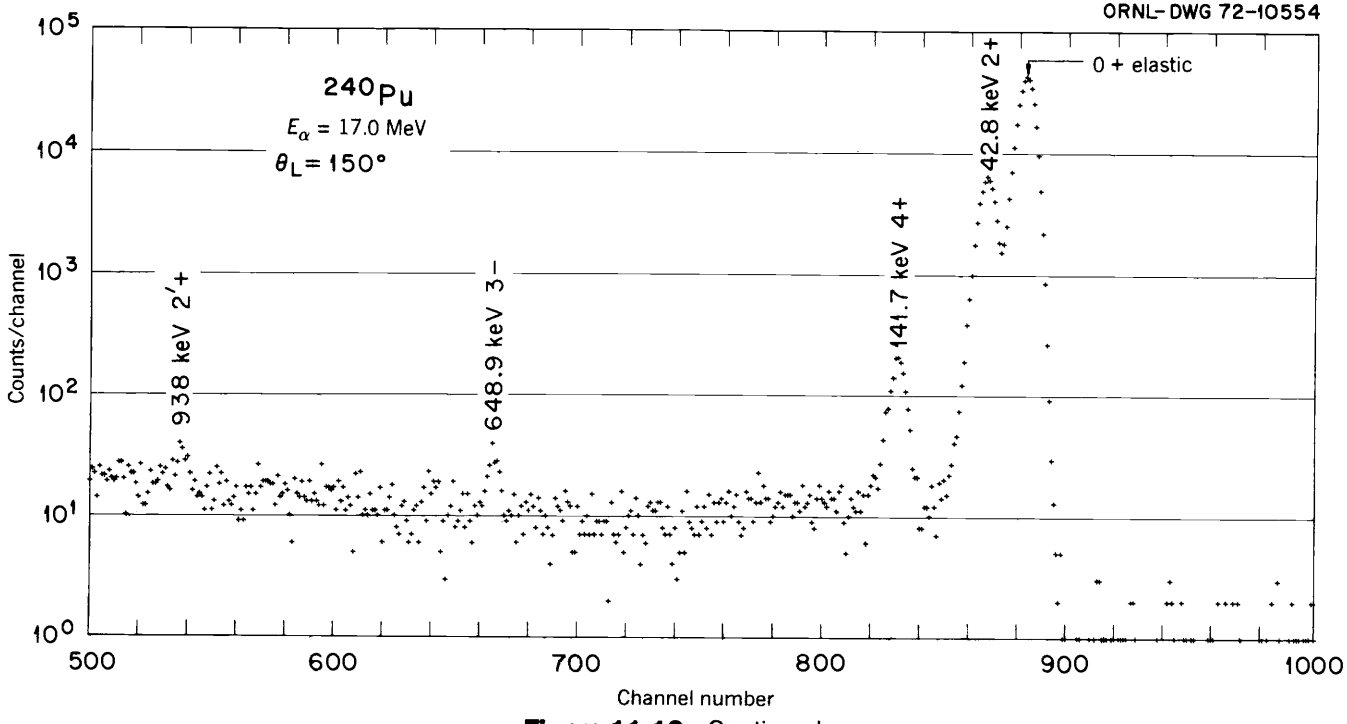


Figure 11.12 Continued.

Rutherford cross section. Note especially the $\sin^{-4}(\theta/2)$ dependence, which is characteristic.

In a difficult and painstaking series of experiments, Geiger and Marsden verified three aspects of the Rutherford formula: the dependence on Z^2, T_a^{-2}, and $\sin^{-4}(\theta/2)$. Figure 11.10 shows the excellent agreement with the predictions of the formula.

The most noteworthy aspect of the scattering experiment, and the detail that led Rutherford to his concept of the nuclear atom, is the fraction scattered at large angles, say beyond 90°. For example, we consider a gold foil of thickness 2.0×10^{-4} cm, on which 8.0 MeV α's are incident. From Equation 11.26, we find $b = 14$ fm, from which Equation 11.19 gives $f = 7.5 \times 10^{-5}$. This is a large fraction to be scattered at such angles and requires a dense, compact nucleus as the scatterer.

Let's look at the situation for small angles. For the above gold foil, there are about 12×10^{18} nuclei/cm^2, or of the order of 0.003 nm lateral spacing between nuclei, as seen by an incoming α particle. This means about $\frac{2}{3}$ of the α particles have an impact parameter of 0.001 nm or greater. For this impact parameter, the scattering angle is 1.6°. Thus the mean scattering angle is of order 1° or less. To appear at large angles, we must have either many scatterings, each at a small angle, or a single scattering at large angle. Of course, if there are many individual scatterings of a random nature, some will tend to increase the net scattering angle and others will tend to decrease it. To observe scattering at a total angle of about $N\theta_{\text{mean}}$, there must be about N^2 individual scatterings. If we observe scattering at a fixed angle θ much larger than 1° and if we vary the thickness x of the scattering foil, then we expect the probability to observe scattered particles to vary as $\sqrt{x}$ for multiple scattering, while it should vary with x in the case of single scattering (simply because there are linearly more chances to have single large-angle scattering as the number of nuclei increases). Figure 11.10*a* shows the variation of the number of scattered particles with x, and the linear behavior is quite apparent.

Our treatment of Rutherford scattering has been based entirely on classical concepts; no quantum effects are included. In particular, the uncertainty principle renders doubtful any treatment based on fixed trajectories and particle orbits. Any attempt to locate a particle with an impact parameter of arbitrarily small uncertainty would introduce a large uncertainty in the transverse momentum and thus in the scattering angle. We are not discussing the experimental difficulty of "aiming" a beam with a specific impact parameter; the range of impact parameters is automatically included in the variation with θ of $d\sigma/d\Omega$. What we discuss here is whether the assumption of a definite trajectory has introduced pathological errors into the derivation of the Rutherford cross section.

Corresponding to an uncertainty Δb in the impact parameter will be an uncertainty Δp in the transverse momentum of order $\hbar/\Delta b$. Our classical derivation makes sense only if $\Delta b \ll b$ and $\Delta p \ll p_{\text{transverse}}$:

$$b\,\Delta p_{\text{transverse}} \gg \Delta b\,\Delta p \gtrsim \hbar$$

$$\frac{b\,\Delta p_{\text{transverse}}}{\hbar} \gg 1 \tag{11.30}$$

We consider two extreme cases: (1) 90° scattering, for which $b = d/2 = 14$ fm and $\Delta p_{\text{transverse}} = mv_0 = 250$ MeV/c, where we have assumed 8-MeV α's incident on gold. For this case the ratio in Equation 11.30 is about 18, reasonably far from the quantum limit. (2) Small-angle scattering ($\theta \simeq 1°$), with $b = 1600$ fm and $\Delta p_{\text{transverse}} \simeq mv_0 \tan\theta \simeq 4$ MeV/c. The ratio is now about 32, again far from the quantum limit.

Ultimately what justifies the classical calculation is a happy accident of quantum physics: the quantum calculation of the Coulomb scattering cross section gives the same result as the classical calculation, Equation 11.29. This is a peculiarity of the $1/r^2$ force, in which the exact quantum result contains no factors of $\hbar$, and thus the "classical limit" of $\hbar \to 0$ leaves the quantum result unchanged.

As we increase the energy of the incident particle, we will eventually reach a point where the distance of closest approach decreases to the nuclear radius, and thus the projectile and target feel each other's nuclear force. The Rutherford formula, which was derived on the basis of Coulomb interactions only, fails at that point to account for the cross section, as we illustrated in Figure 3.11. (The cross section then includes Coulomb and nuclear parts, as in the case of proton-proton scattering, Equation 4.43.) The internuclear separation at which the Rutherford formula fails is then a measure of the nuclear radius, as illustrated in Figure 11.11.

Up to now we have considered only elastic Coulomb scattering. Inelastic Coulomb scattering is called *Coulomb excitation*; after the encounter the nucleus (and possibly, although not usually, the projectile) is left in an excited state, from which it decays rapidly with the emission of γ rays. We can think of this process as the emission and absorption of virtual photons, with the most likely mode being $E2$. This process has therefore been extensively used to study the first excited 2^+ states of even-Z, even-N nuclei. Because the $0^+ \to 2^+$ photon absorption probability is closely related to the $2^+ \to 0^+$ photon emission probability, the Coulomb excitation probability can give a measure of the half-life of the 2^+ state. Moreover, since the 2^+ state lives much longer than the time it takes for the encounter between target and projectile, there is a second-order interaction between the projectile and the excited-state nuclei of the target. This can have several effects, including photon absorption causing a $2^+ \to 4^+$ upward transition and a change in the m-state population of the 2^+ state from the interaction of its quadrupole moment with the electric field gradient of the moving projectile.

Figure 11.12 shows some sample results from inelastic Coulomb scattering. The reduced energy of the detected particles exactly matches the energy simultaneously observed in γ-ray emission from the excited states.

11.7 NUCLEAR SCATTERING

The elastic nuclear scattering of particles bears a strong resemblance to a familiar problem from optics: the diffraction of light by an opaque disk (Figures 4.3 and 11.13). In the optical case, diffraction at the sharp edge results in a series of maxima and minima; the first minimum occurs at $\theta \sim \lambda/R$, the succeeding minima are roughly (but not exactly) equally spaced, and the intervening maxima are of steadily and substantially decreasing intensity.

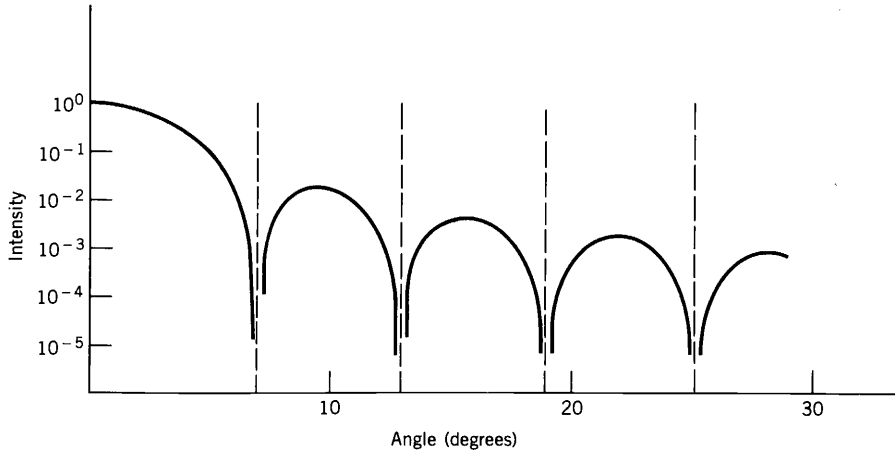


Figure 11.13 Diffraction pattern of light incident on a circular aperture; a circular disk gives a similar pattern. The minima have intensity of zero. The curve is drawn for a wavelength equal to ten times the diameter of the aperture or disk.

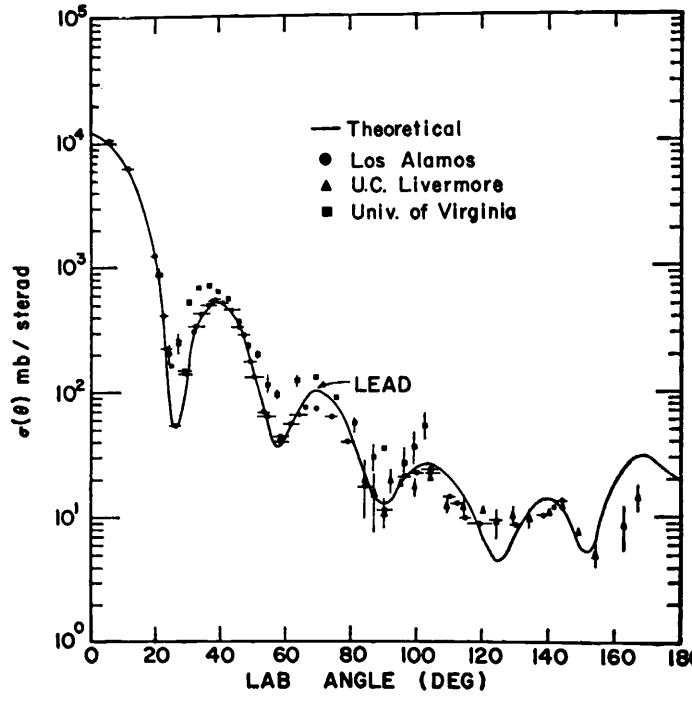


Figure 11.14 Elastic scattering of 14-MeV neutrons from Pb. From S. Fernbach, *Rev. Mod. Phys.* **30**, 414 (1958).

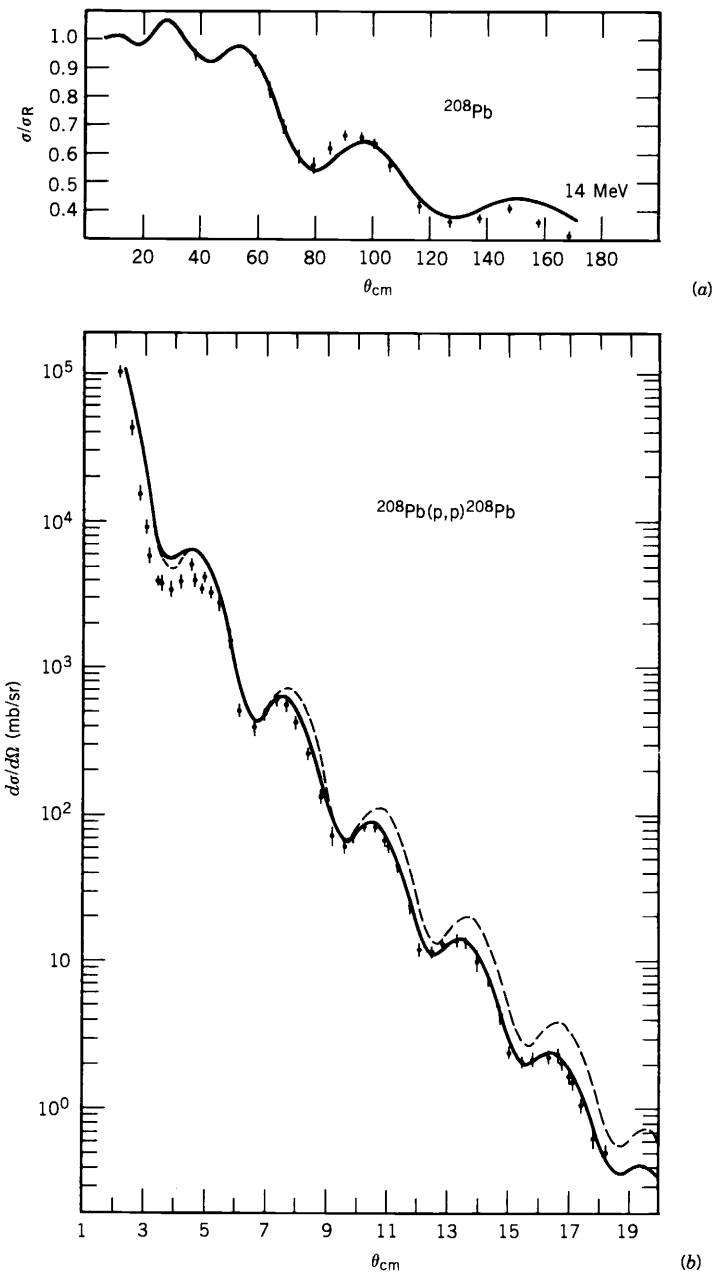


Figure 11.15 Elastic scattering of protons from ^{208}Pb. In (*a*), at low energy (14 MeV), the diffraction-like behavior occurs only at large angles (beyond 60°), where nuclear scattering occurs, because the closest distance between projectile and target (12.6 fm at 60° from the Rutherford formulas) agrees with the internuclear distance appropriate for nuclear interactions (11.8 fm), calculated using $R_0 = 1.7$ fm, as in Figure 11.11. Compare this figure with that for neutron scattering at the same energy, Figure 11.14. In (*b*), the incident energy is 1050 MeV and the Coulomb barrier is easily penetrated, so diffraction effects occur at small angles. (*a*) From J. S. Eck and W. J. Thompson, *Nucl. Phys. A* **237**, 83 (1975). (*b*) From G. Igo, in *High Energy Physics and Nuclear Structure— 1975,* edited by D. Nagle et al. (New York: American Institute of Physics, 1975).

A nucleus is a strongly absorbing object for nucleons, and thus the analogy with the opaque disk is quite valid. For charged particles, we must deal with the interference between nuclear and Coulomb scattering, as in Figure 4.9 and Equation 4.43. It is this effect that is responsible for the deviation of scattering cross sections from the Rutherford formula, as shown in Figure 11.11. If we wish to observe the elastic scattering of nucleons, in the form of the "diffraction-like" pattern, we must eliminate the effects of Rutherford scattering, which we can do in either of two ways. The first is to use uncharged neutrons as the scattered particle. Figure 11.14 shows an example of neutron elastic scattering. One particular difference between the nuclear scattering and optical diffraction is that the minima do not fall to zero. This is a direct result of the diffuseness of the nuclear surface—nuclei do not have sharp edges.

For charged particles, we must take two steps to reduce the effect of interference with Coulomb scattering: we work at higher energy, so that the Rutherford cross section is small and the projectile can more easily penetrate to feel the nuclear interaction, and we observe at larger angles, where again the Rutherford cross section is small and where the small impact parameter also helps to guarantee nuclear penetration. An example of nucleon elastic scattering is shown in Figure 11.15. Again, the diffraction-like effects are apparent.

One result of nucleon elastic scattering studies is the determination of the nuclear radius. Although the value may depend somewhat on the potential model used to analyze the scattering (such as the square well discussed in Chapter 4), the results are generally quite consistent with $R = R_0 A^{1/3}$ with $R_0 = 1.25$ fm as in other studies. In Section 11.9 we discuss in more detail the implication of these experiments on our knowledge of the potential.

Inelastic nuclear scattering, like inelastic Coulomb scattering, results when the target nucleus takes energy from the projectile and reaches excited states. (It is also possible for projectiles to be placed in excited states; we ignore this effect for now.) If we measure the energy distribution of scattered projectiles at a fixed angle, we observe a single elastic peak, which is the highest energy scattered projectile. Each inelastic peak corresponds to a specific excited state of the target nucleus. Figure 11.4 showed an example of inelastic nuclear scattering, and another example is discussed in Section 11.11. From the locations of the inelastic peaks, we can learn the energies of the excited states; from their relative heights we learn the relative cross sections for excitation of each state, which tells us something of the wave function of the excited state. We can also measure an angular distribution of scattered projectiles for any excited state, from which we can learn the spin and parity of the excited states.

11.8 SCATTERING AND REACTION CROSS SECTIONS

In this section we cover some details of reaction cross sections more thoroughly than in our previous discussion in Section 4.2. You may wish to review that discussion before proceeding.

We take the z axis to be the direction of the incident beam and assume it can be represented by a plane wave e^{ikz} corresponding to momentum $p = \hbar k$. The outgoing particles will be represented by spherical waves, and so the manipula-

tions become easier if we express the incident plane wave as a superposition of spherical waves:

$$\psi_{\text{inc}} = Ae^{ikz} = A\sum_{\ell=0}^{\infty} i^{\ell}(2\ell+1)\,j_{\ell}(kr)\,P_{\ell}(\cos\theta) \tag{11.31}$$

where A is an appropriately chosen normalization constant. The radial functions $j_{\ell}(kr)$ are *spherical Bessel functions* which were previously given in Table 2.3; they are solutions to the radial part of the Schrödinger equation, Equation 2.60, in a region far from the target where the nuclear potential vanishes. The angular functions $P_{\ell}(\cos\theta)$ are Legendre polynomials:

$$\begin{aligned} P_0(\cos\theta) &= 1 \\ P_1(\cos\theta) &= \cos\theta \\ P_2(\cos\theta) &= \tfrac{1}{2}(3\cos^2\theta - 1) \end{aligned} \tag{11.32}$$

This expansion of the incident (and eventually, the scattered) wave is called the *partial wave expansion*, with each partial wave corresponding to a specific angular momentum ℓ. Such a procedure is valid if the nuclear potential is assumed to be central. What makes the method useful is that it is often sufficient to consider the effect of the nuclear potential on at most only a few of the lowest partial waves (such as $\ell = 0$ or s-wave nucleon-nucleon scattering discussed in Chapter 4). If the particles of momentum p interact with impact parameter b, then the (semiclassical) relative angular momentum will be

$$\ell\hbar = pb$$

or

$$b = \ell\frac{\hbar}{p} = \ell\frac{\lambda}{2\pi} = \ell\lambda\!\!\!^{-} \tag{11.33}$$

where $\lambda\!\!\!^{-} = \lambda/2\pi$ is called the *reduced* de Broglie wavelength. Incidently, $\lambda\!\!\!^{-} = k^{-1}$.

According to quantum mechanics, ℓ can only be defined in integer units, and thus the semiclassical estimate should be revised somewhat. That is, particles with (semiclassical) angular momenta between $0\hbar$ and $1\hbar$ will interact through impact parameters between 0 and $\lambda\!\!\!^{-}$, and thus effectively over an area (cross section) of at most $\pi\lambda\!\!\!^{-2}$. With $\hbar \le \ell \le 2\hbar$, the cross section is a ring of inner radius $\lambda\!\!\!^{-}$ and outer radius $2\lambda\!\!\!^{-}$, and thus of area $3\pi\lambda\!\!\!^{-2}$. We can thus divide the interaction area into a number of zones, each corresponding to a specific angular momentum ℓ and each having area $\pi[(\ell+1)\lambda\!\!\!^{-}]^2 - \pi(\ell\lambda\!\!\!^{-})^2 = (2\ell+1)\pi\lambda\!\!\!^{-2}$. We can estimate the maximum impact parameter for nuclear scattering to be about $R = R_1 + R_2$ (the sum of the radii of the incident and target nuclei), and thus the maximum ℓ value likely to occur is $R/\lambda\!\!\!^{-}$, and the total cross section is correspondingly

$$\sigma = \sum_{\ell=0}^{R/\lambda\!\!\!^{-}} (2\ell+1)\pi\lambda\!\!\!^{-2} = \pi(R+\lambda\!\!\!^{-})^2 \tag{11.34}$$

This is a reasonable estimate, for it includes not only an interaction distance R, but it allows the incident particle's wave nature to spread over a distance of the order of $\lambda\!\!\!^{-}$, making the effective interaction radius $(R + \lambda\!\!\!^{-})$. We will see later how the exact calculation modifies this estimate.

When the wave is far from the nucleus, the $j_\ell(kr)$ have the following convenient expansion:

$$j_\ell(kr) \cong \frac{\sin\left(kr - \frac{1}{2}\ell\pi\right)}{kr} \qquad (kr \gg \ell)$$

$$= i\frac{e^{-i(kr-\ell\pi/2)} - e^{+i(kr-\ell\pi/2)}}{2kr} \tag{11.35}$$

so that

$$\psi_{\text{inc}} = \frac{A}{2kr}\sum_{\ell=0}^{\infty} i^{\ell+1}(2\ell+1)[e^{-i(kr-\ell\pi/2)} - e^{+i(kr-\ell\pi/2)}]P_\ell(\cos\theta) \tag{11.36}$$

The first term in brackets, involving e^{-ikr}, represents an incoming spherical wave converging on the target, while the second term, in e^{+ikr}, represents an outgoing spherical wave emerging from the target nucleus. The superposition of these two spherical waves, of course, gives the plane wave.

The scattering can affect only the outgoing wave, and can affect it in either of two ways: through a change in phase (as in the phase shift discussed in Chapter 4), and through a change in amplitude. The change in amplitude suggests that there may be fewer particles coming out than there were going in, which may appear to be a loss in the net number of particles. However, keep in mind that the wave function represents only those particles of momentum $\hbar k$. If there is inelastic scattering (or some other nuclear reaction), the energy (or even the identity) of the outgoing particle may change. It is therefore not surprising that there may be fewer particles in the e^{ikr} term following inelastic scattering. It has become customary to refer to a specific set of conditions (exclusive of direction of travel) of the outgoing particle and residual nucleus as a reaction *channel*. The reaction may thus proceed through the elastic channel or through any one of many inelastic channels. Some channels may be *closed* to the reacting particles, if there is not enough energy or angular momentum to permit a specific final configuration to be reached.

We account for the changes in the ℓth outgoing partial wave by introducing the complex coefficient η_ℓ into the outgoing (e^{ikr}) term of Equation 11.36:

$$\psi = \frac{A}{2kr}\sum_{\ell=0}^{\infty} i^{\ell+1}(2\ell+1)\left[e^{-i(kr-\ell\pi/2)} - \eta_\ell e^{+i(kr-\ell\pi/2)}\right]P_\ell(\cos\theta) \tag{11.37}$$

This wave represents a superposition of the incident and scattered waves: $\psi = \psi_{\text{inc}} + \psi_{\text{sc}}$, exactly as in Equation 4.23. To find the scattered wave itself, we subtract Equation 11.37 from Equation 11.36:

$$\psi_{\text{sc}} = \frac{A}{2kr}\sum_{\ell=0}^{\infty} i^{\ell+1}(2\ell+1)(1-\eta_\ell)e^{i(kr-\ell\pi/2)}P_\ell(\cos\theta)$$

$$= \frac{A}{2k}\frac{e^{ikr}}{r}\sum_{\ell=0}^{\infty}(2\ell+1)i(1-\eta_\ell)P_\ell(\cos\theta) \tag{11.38}$$

Because we have accounted for only those parts of ψ_{sc} with wave number k identical with the incident wave, this represents only *elastic scattering*. As we did in Equation 4.24 we now find the scattered current density:

$$j_{sc} = \frac{\hbar}{2mi}\left(\psi_{sc}^{*}\frac{\partial\psi_{sc}}{\partial r} - \frac{\partial\psi_{sc}^{*}}{\partial r}\psi_{sc}\right) \tag{11.39}$$

$$= |A|^2\frac{\hbar}{4mkr^2}\left|\sum_{\ell=0}^{\infty}(2\ell+1)i(1-\eta_\ell)P_\ell(\cos\theta)\right|^2 \tag{11.40}$$

The incident current is identical with Equation 4.26:

$$j_{inc} = \frac{\hbar k}{m}|A|^2 \tag{11.41}$$

and by analogy with Equation 4.27, the differential cross section is

$$\frac{d\sigma}{d\Omega} = \frac{1}{4k^2}\left|\sum_{\ell=0}^{\infty}(2\ell+1)i(1-\eta_\ell)P_\ell(\cos\theta)\right|^2 \tag{11.42}$$

To find the total cross section, we require the integral of the Legendre polynomials:

$$\int P_\ell(\cos\theta)P_{\ell'}(\cos\theta)\sin\theta\,d\theta\,d\phi = \frac{4\pi}{2\ell+1} \qquad \text{if } \ell = \ell'$$

$$= 0 \qquad \text{if } \ell \neq \ell' \tag{11.43}$$

Thus

$$\sigma_{sc} = \sum_{\ell=0}^{\infty}\pi\lambda\!\!\!^{-2}(2\ell+1)|1-\eta_\ell|^2 \tag{11.44}$$

If elastic scattering were the only process that could occur, then $|\eta_\ell| = 1$ and it is conventional to write $\eta_\ell = e^{2i\delta_\ell}$ where δ_ℓ is the *phase shift* of the ℓth partial wave. For this case, $|1-\eta_\ell|^2 = 4\sin^2\delta_\ell$ and

$$\sigma_{sc} = \sum_{\ell=0}^{\infty}4\pi\lambda\!\!\!^{-2}(2\ell+1)\sin^2\delta_\ell \tag{11.45}$$

which reduces directly to Equation 4.30 for $\ell = 0$.

If there are other processes in addition to elastic scattering (inelastic scattering or other reactions) then Equation 11.45 is not valid, because $|\eta_\ell| < 1$. We group all of these processes together under the term *reaction cross section* σ_r, where we take "reaction" to mean all nuclear processes *except* elastic scattering. To find this cross section, we must examine Equation 11.37 to find the rate at which particles are "disappearing" from the channel with wave number k. That is, we find the difference between the incoming current and the outgoing current using,

respectively, the first and second terms of Equation 11.37:

$$|j_{\text{in}}| - |j_{\text{out}}| = \frac{|A|^2\hbar}{4mkr^2}\left\{\left|\sum_{\ell=0}^{\infty}(2\ell+1)i^{\ell+1}e^{i\ell\pi/2}P_\ell(\cos\theta)\right|^2 - \left|\sum_{\ell=0}^{\infty}(2\ell+1)i^{\ell+1}\eta_\ell e^{-i\ell\pi/2}P_\ell(\cos\theta)\right|^2\right\} \quad (11.46)$$

and the reaction cross section becomes

$$\sigma_r = \sum_{\ell=0}^{\infty}\pi\lambda\!\!\!^{-2}(2\ell+1)(1-|\eta_\ell|^2) \quad (11.47)$$

The *total* cross section, including all processes, is

$$\begin{aligned}\sigma_t &= \sigma_{sc} + \sigma_r \\ &= \sum_{\ell=0}^{\infty}2\pi\lambda\!\!\!^{-2}(2\ell+1)(1-\text{Re}\,\eta_\ell)\end{aligned} \quad (11.48)$$

You should note the following details about these results:

1. It is possible to have elastic scattering in the absence of other processes; that is, if $|\eta_\ell| = 1$, then Equation 11.47 vanishes. It is *not* possible, however, to have reactions without also having elastic scattering; that is, any choice of η_ℓ for which $\sigma_r \neq 0$ for a given partial wave automatically gives $\sigma_{sc} \neq 0$ for that partial wave. We can understand this with reference to the diffraction model of scattering we considered in Section 11.7. If particles are removed from the incident beam, creating a "shadow" behind the target nucleus, incident particles will be diffracted into the shadow.
2. For a "black disk" absorber, as in Equation 11.34, in which all partial waves are completely absorbed up to $\ell = R/\lambda\!\!\!^{-}$ ($\eta_\ell = 0$ for complete absorption) and unaffected for $\ell > R/\lambda\!\!\!^{-}$ ($\eta_\ell = 1$), then

$$\sigma_{sc} = \pi(R + \lambda\!\!\!^{-})^2 \quad (11.49)$$

and

$$\sigma_r = \pi(R + \lambda\!\!\!^{-})^2 \quad (11.50)$$

so that

$$\sigma_t = 2\pi(R + \lambda\!\!\!^{-})^2 \quad (11.51)$$

The total cross section is *twice* the geometrical area! The explanation for this nonclassical effect can also be found in the "shadow" region—the target nucleus cannot simply absorb and throw a sharp shadow. It must also diffract into the shadow region.

The program for using these results to study nuclear structure is similar to that of Chapter 4 for nucleon–nucleon scattering. We can guess at a form for the nuclear potential, solve the Schrödinger equation inside the interaction region

$0 \leq r \leq R$, and match boundary conditions at the surface. In this way we should be able to calculate η_ℓ and, by comparison with experimental values of σ_{sc} and σ_r, evaluate whether our chosen form for the potential is reasonable. In practice this is very difficult for all but the elastic channel because all of the inelastic and reaction channels are coupled together leading to a complicated system of coupled equations. We discuss one particular technique, the optical model for elastic scattering, in Section 11.9.

11.9 THE OPTICAL MODEL

A simple model used to account in a general way for elastic scattering in the presence of absorptive effects is the *optical model*, so called because the calculation resembles that of light incident on a somewhat opaque glass sphere. (The model is also called the "cloudy crystal ball model.")

In this model, we represent the scattering in terms of a complex potential $U(r)$:

$$U(r) = V(r) + iW(r) \tag{11.52}$$

where the real functions V and W are selected to give the potential its proper radial dependence. The real part, $V(r)$, is responsible for the elastic scattering; it describes the ordinary nuclear interaction between target and projectile and may therefore be very similar to a shell-model potential. The imaginary part, $W(r)$, is responsible for the absorption. We can demonstrate this by considering a square-well form for $U(r)$:

$$\begin{aligned} U(r) &= -V_0 - iW_0 \qquad r < R \\ &= 0 \qquad\qquad\quad r > R \end{aligned} \tag{11.53}$$

The outgoing scattered wave we take to be in the form of e^{ikr}/r, with $k = \sqrt{2m(E + V_0 + iW_0)/\hbar^2}$, which follows from solving the Schrödinger equation in the usual way for this potential. The wave number k is thus complex: $k = k_r + ik_i$, where k_r and k_i are the real and imaginary parts, respectively. The wave function behaves like $e^{ik_r r} \cdot e^{-k_i r}/r$, and the radial probability density is proportional to $e^{-2k_i r}$. The wave is therefore exponentially attenuated as it passes through the nucleus. (Choosing $W_0 > 0$ in Equation 11.53 gives a loss in intensity, rather than a gain.) If we assume that the absorption is relatively weak (that is, W_0 is small compared with $E + V_0$), then we can use the binomial theorem to expand the expression for k:

$$k \cong \sqrt{\frac{2m(E + V_0)}{\hbar^2}} + \frac{iW_0}{2}\sqrt{\frac{2m}{\hbar^2}\left(\frac{1}{E + V_0}\right)} \tag{11.54}$$

The usual shell-model potential has a depth V_0 of the order of 40 MeV, and we can take $E = 10$ MeV for a typical low-energy projectile. The distance over which the intensity is attenuated by e^{-1} (a sort of mean free path) is

$$d = \frac{1}{2k_i} = \frac{1}{W_0}\sqrt{\frac{\hbar^2(E + V_0)}{2m}} \tag{11.55}$$

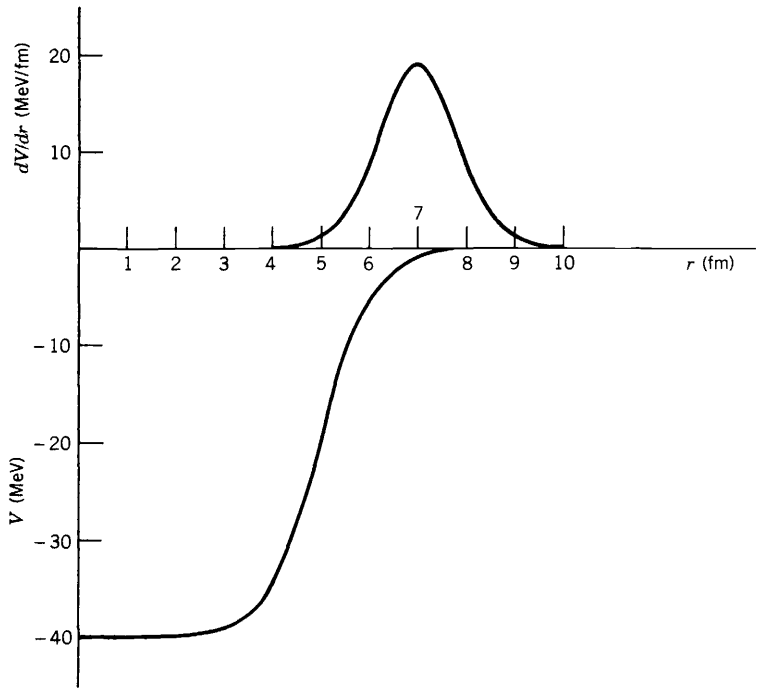


Figure 11.16 The optical model functions $V(r)$ and $W(r) = dV/dr$. Typical parameters chosen are $V_0 = 40$ MeV, $R = 1.25A^{1/3}$, $a = 0.523$ fm, and $A = 64$.

If this distance is to be at most of the order of the nuclear radius (say, 3 fm) then $W_0 \simeq 11$ MeV. Thus for the usual case, in which absorption is relatively weaker than elastic scattering, we estimate $|V| \sim 40$ MeV, $|W| \sim 10$ MeV.

The procedure for applying the optical model might be as follows: First, we must choose a form for the potential. The square-well form is often adequate (with $R \simeq 1.4A^{1/3}$, a bit larger than usual to account for the diffuse nuclear surface), but a more detailed form is often chosen:

$$V(r) = \frac{-V_0}{1 + e^{(r-R)/a}} \tag{11.56}$$

exactly as in the case of the shell model, Equation 5.1. The constants V_0, R, and a are adjusted to give the best fits with the scattering data. The absorptive part $W(r)$ at low energies must have a very different form. Because of the exclusion principle, the tightly bound nucleons in the nuclear interior cannot participate in absorbing incident nucleons. Only the "valence" nucleons near the surface can absorb the relatively low energy carried by the incident particle. The function $W(r)$ is thus often chosen as proportional to dV/dr, which has the proper shape of being large only near the surface, as shown in Figure 11.16. (At higher energy, where the inner nucleons can also participate in absorption, $W(r)$ may look more like $V(r)$.) A *spin-orbit* term is also included in modern optical potentials. It is also peaked near the surface, because the spin density of the inner nucleons vanishes. Finally, a Coulomb term must be included if the incident particle is

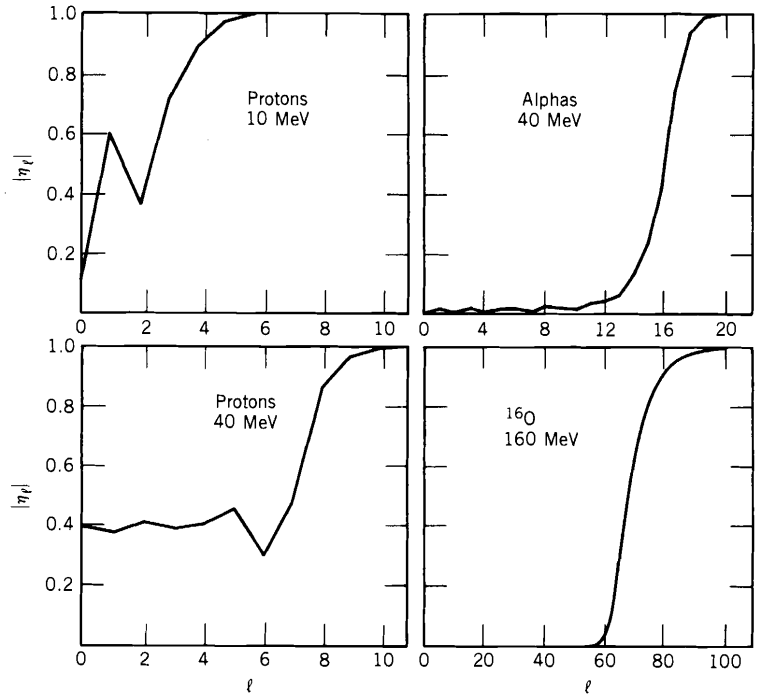


Figure 11.17 Magnitudes of complex scattering amplitudes η_ℓ for scattering of various projectiles on a target of ^{58}Ni. The approach of $|\eta_\ell|$ to 1 at higher energy corresponds to $\sigma_r \to 0$, so that few particles are absorbed and only elastic scattering takes place. From G. R. Satchler, *Introduction to Nuclear Reactions* (Wiley: New York, 1980).

charged. For the chosen potential, the Schrödinger equation can be solved, and equating boundary conditions at $r = R$, as we did in Chapter 4 for the nucleon-nucleon problem, gives the complex scattering amplitudes η_ℓ, which can be used to compare calculated cross sections with experiment. Figure 11.17 shows examples of some η_ℓ values.

The complete optical model fits to scattering data often are very impressive. Figure 11.18 shows an example of several fits to elastic scattering cross sections and polarizations.

The optical model is useful only in discussing average behavior in reactions such as scattering. Many of the interesting features of the microscopic structure of nuclei are accounted for indirectly only in this average way. The calculation using the optical model, as described in this section, does not deal with where the absorbed particles actually go; they simply disappear from the elastic channel. In fact, the many interactions between the nucleons of the target and projectile are so complicated that representing them by a single potential is itself a significant approximation. Nevertheless, the optical model is successful in accounting for elastic and inelastic scattering and leads us to an understanding of the interactions of nuclei.

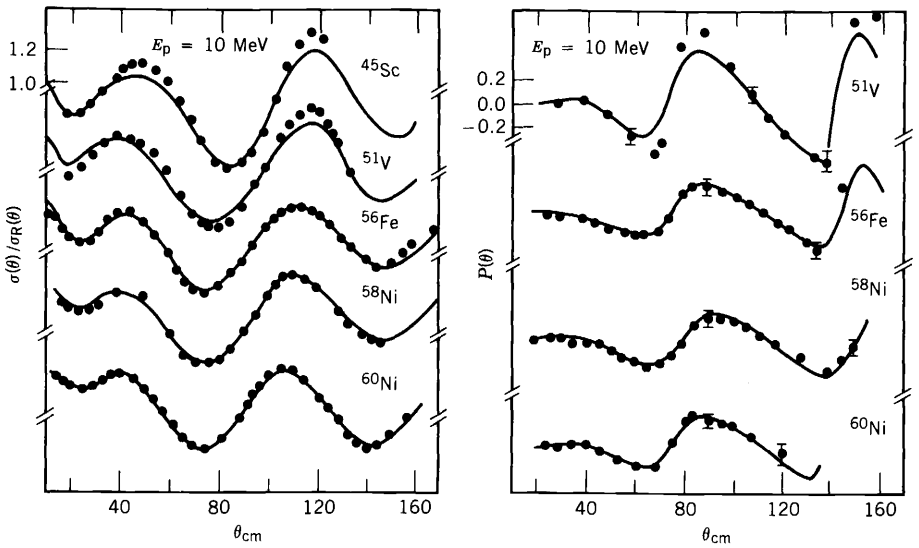


Figure 11.18 Optical-model fits to differential cross sections (at left, shown as a ratio to the Rutherford cross section) and polarizations, for 10-MeV protons scattered elastically from various targets. The solid lines are the fits to the data using the best set of optical-model parameters. From F. D. Becchetti, Jr., and G. W. Greenlees, *Phys. Rev.* **182**, 1190 (1969).

11.10 COMPOUND-NUCLEUS REACTIONS

Suppose an incident particle enters a target nucleus with an impact parameter small compared with the nuclear radius. It then will have a high probability of interacting with one of the nucleons of the target, possibly through a simple scattering. The recoiling struck nucleon and the incident particle (now with less energy) can each make successive collisions with other nucleons, and after several such interactions, the incident energy is shared among many of the nucleons of the combined system of projectile + target. The average increase in energy of any single nucleon is not enough to free it from the nucleus, but as many more-or-less random collisions occur, there is a statistical distribution in energies and a small probability for a single nucleon to gain a large enough share of the energy to escape, much as molecules evaporate from a hot liquid.

Such reactions have a definite intermediate state, after the absorption of the incident particle but before the emission of the outgoing particle (or particles). This intermediate state is called the *compound nucleus*. Symbolically then the reaction a + X → Y + b becomes

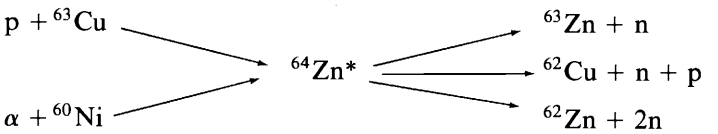
$$a + X \rightarrow C^* \rightarrow Y + b$$

where C* indicates the compound nucleus.

As might be assumed from seeing the reaction written in this form, we can consider a reaction that proceeds through the compound nucleus to be a two-step process: the formation and then the subsequent decay of the compound nucleus. A given compound nucleus may decay in a variety of different ways, and essential to the compound-nucleus model of nuclear reactions is the assumption that *the*

relative probability for decay into any specific set of final products is independent of the means of formation of the compound nucleus. The decay probability depends only on the total energy given to the system; in effect, the compound nucleus "forgets" the process of formation and decays governed primarily by statistical rules.

Let's consider a specific example. The compound nucleus $^{64}Zn^*$ can be formed through several reaction processes, including $p + {}^{63}Cu$ and $\alpha + {}^{60}Ni$. It can also decay in a variety of ways, including $^{63}Zn + n$, $^{62}Zn + 2n$, and $^{62}Cu + p + n$. That is



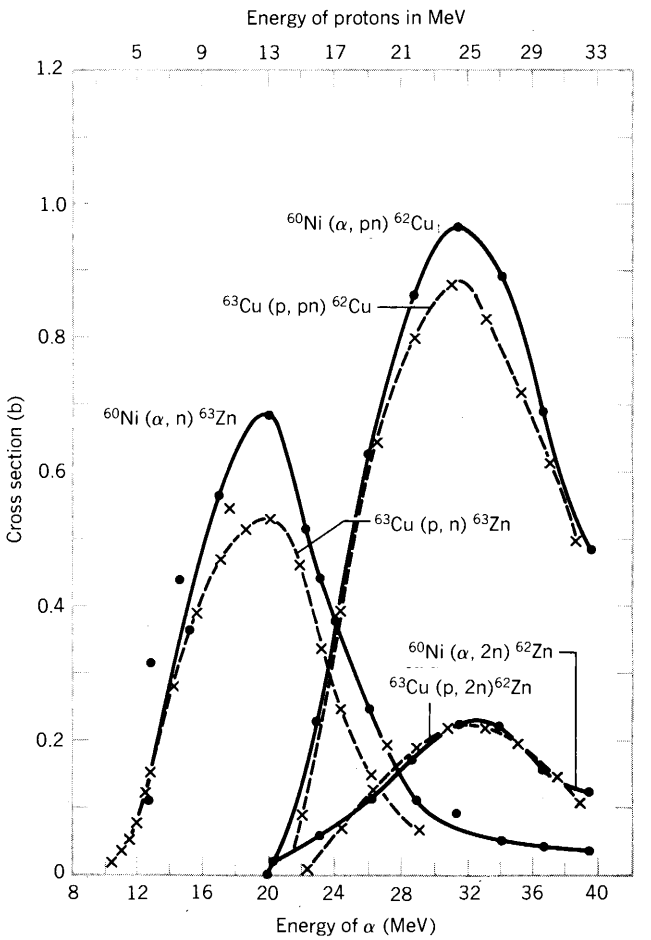


Figure 11.19 Cross sections for different reactions leading to the compound nucleus ^{64}Zn show very similar characteristics, consistent with the basic assumptions of the compound nucleus model. From S. N. Goshal, *Phys. Rev.* **80**, 939 (1950).

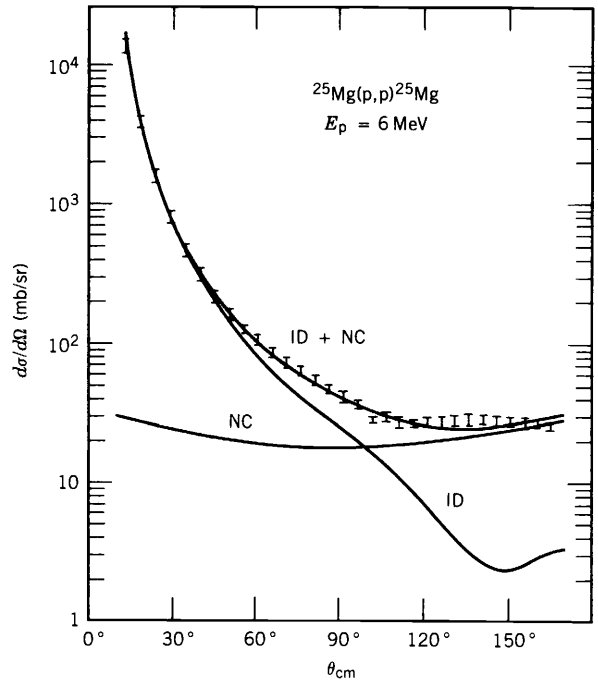


Figure 11.20 The curve marked NC shows the contribution from compound-nucleus formation to the cross section of the reaction ^{25}Mg(p, p)^{25}Mg. The curve marked ID shows the contribution from direct reactions. Note that the direct part has a strong angular dependence, while the compound-nucleus part shows little angular dependence. From A. Gallmann et al., *Nucl. Phys.* **88**, 654 (1966).

If this model were correct, we would expect for example that the relative cross sections for ^{63}Cu(p, n)^{63}Zn and ^{60}Ni(α, n)^{63}Zn would be the same at incident energies that give the same excitation energy to ^{64}Zn*. Figure 11.19 shows the cross sections for the three final states, with the energy scales for the incident protons and α's shifted so that they correspond to a common excitation of the compound nucleus. The agreement between the three pairs of cross sections is remarkably good, showing that indeed, the decay of ^{64}Zn* into any specific final state is nearly independent of how it was originally formed.

The compound-nucleus model works best for low incident energies (10–20 MeV), where the incident projectile has a small chance of escaping from the nucleus with its identity and most of its energy intact. It also works best for medium-weight and heavy nuclei, where the nuclear interior is large enough to absorb the incident energy.

Another characteristic of compound-nucleus reactions is the angular distribution of the products. Because of the random interactions among the nucleons, we expect the outgoing particle to be emitted with a nearly isotropic angular distribution (that is, the same in all directions). This expectation is quite consistent with experiment, as shown in Figure 11.20. In cases in which a heavy ion is the incident particle, large amounts of angular momentum can be transferred to the compound nucleus, and to extract that angular momentum the

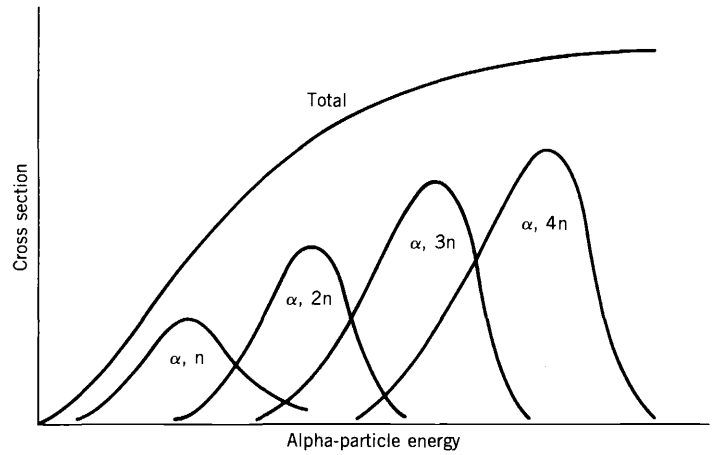


Figure 11.21 At higher incident energies, it is more likely that additional neutrons will "evaporate" from the compound nucleus.

emitted particles tend to be emitted at right angles to the angular momentum, and thus preferentially at 0 and 180°. With light projectiles, this effect is negligible.

The "evaporation" analogy mentioned previously is really quite appropriate. In fact, the more energy we give to the compound nucleus, the more particles are likely to evaporate. For each final state, the cross section has the Gaussian-like shape shown in Figure 11.19. Figure 11.21 shows the cross sections for $(\alpha, x\text{n})$ reactions, where $x = 1, 2, 3, \ldots$. For each reaction, the cross section increases to a maximum and then decreases as the higher energy makes it more likely for an additional neutron to be emitted.

11.11 DIRECT REACTIONS

At the opposite extreme from compound-nucleus reactions are *direct* reactions, in which the incident particle interacts primarily at the surface of the target nucleus; such reactions are also called *peripheral* processes. As the energy of the incident particle is increased, its de Broglie wavelength decreases, until it becomes more likely to interact with a nucleon-sized object than with a nucleus-sized object. A 1-MeV incident nucleon has a de Broglie wavelength of about 4 fm, and thus does not "see" individual nucleons; it is more likely to interact through a compound-nucleus reaction. A 20-MeV nucleon has a de Broglie wavelength of about 1 fm and therefore may be able to participate in direct processes. Direct processes are most likely to involve one nucleon or very few valence nucleons near the surface of the target nucleus.

Of course, it may be possible to have direct and compound-nucleus processes both contribute to a given reaction. How can we distinguish their contributions or decide which may be more important? There are two principal differences that can be observed experimentally: (1) Direct processes occur very rapidly, in a time of the order of 10^{-22} s, while compound-nuclear processes typically take much longer, perhaps 10^{-16} to 10^{-18} s. This additional time is necessary for the

distribution and reconcentration of the incident energy. There are ingenious experimental techniques for distinguishing between these two incredibly short intervals of time. (2) The angular distributions of the outgoing particles in direct reactions tend to be more sharply peaked than in the case of compound-nuclear reactions.

Inelastic scattering could proceed either through a direct process or a compound nucleus, largely depending on the energy of the incident particle. The *deuteron stripping reaction* (d, n), which is an example of a *transfer reaction* in which a single proton is transferred from projectile to target, may also go by either mechanism. Another deuteron stripping reaction (d, p) may be more likely to go by a direct process, for the "evaporation" of protons from the compound nucleus is inhibited by the Coulomb barrier. The (α, n) reaction is less likely to be a direct process, for it would involve a single transfer of three nucleons into valence states of the target, a highly improbable process.

One particularly important application of single-particle transfer reactions, especially (d, p) and (d, n), is the study of low-lying shell-model excited states. Several such states may be populated in a given reaction; we can choose a particular excited state from the energy of the outgoing nucleon. Once we have done so, we would like to determine just which shell-model state it is. For this we need the angular distribution of the emitted particles, which often give the spin and parity of the state that is populated in a particular reaction. Angular distributions therefore are of critical importance in studies of transfer reactions. (*Pickup reactions*, for example (p, d), in which the projectile takes a nucleon from the target, also give information on single-particle states.)

Let's consider in somewhat more detail the angular momentum transfer in a deuteron stripping reaction. In the geometry of Figure 11.22, an incident particle with momentum $\boldsymbol{p}_a$ gives an outgoing particle with momentum $\boldsymbol{p}_b$, while the residual nucleus (target nucleus plus transferred nucleon) must recoil with momentum $\boldsymbol{p} = \boldsymbol{p}_a - \boldsymbol{p}_b$. In a direct process, we may assume that the transferred nucleon instantaneously has the recoil momentum and that it must be placed in an orbit with orbital angular momentum $\ell = Rp$, assuming that the interaction

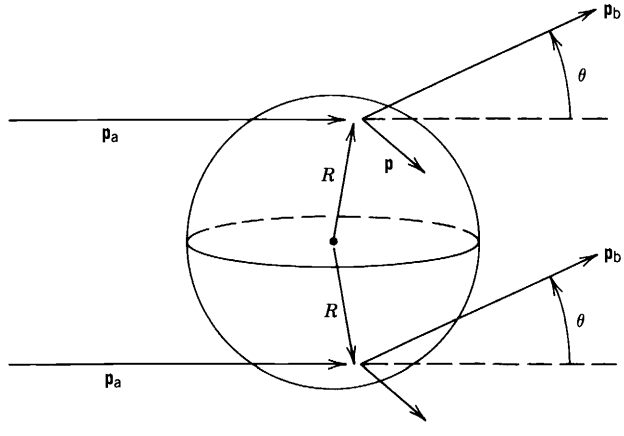


Figure 11.22 Geometry for direct reactions occurring primarily on the nuclear surface.

takes place at the surface of the nucleus. The momentum vectors are related by the law of cosines:

$$p^2 = p_a^2 + p_b^2 - 2p_a p_b \cos\theta$$
$$= (p_a - p_b)^2 + 2p_a p_b(1 - \cos\theta) \tag{11.57}$$

Given the energies of the incident and outgoing particles, we then have a direct relationship between ℓ and θ—particles emerging at a given angle should correspond to a specific angular momentum of the orbiting particle.

Consider a specific example, the (d, p) reaction on ^{90}Zr leading to single neutron shell-model states in ^{91}Zr. The Q value is about 5 MeV, so an incident deuteron at 5 MeV gives a proton at about 10 MeV, less any excitation in ^{91}Zr. Since at these energies $p_a \simeq p_b \simeq 140$ MeV/c, Equation 11.57 gives

$$\ell = \left[\frac{2c^2 p_a p_b(2\sin^2\theta/2)}{\hbar^2 c^2/R^2}\right]^{1/2} \cong 8\sin\frac{\theta}{2}$$

For each angular momentum transfer, we expect to find outgoing protons at the following angles: $\ell = 0$, 0°; $\ell = 1$, 14°; $\ell = 2$, 29°; $\ell = 3$, 44°.

This simple semiclassical estimate will be changed by the intrinsic spins of the particles, which we neglected. There will also be interference between scatterings that occur on opposite sides of the nucleus, as shown in Figure 11.22. These interferences result in maxima and minima in the angular distributions.

Figure 11.23 shows the result of studies of (d, p) reactions on ^{90}Zr. You can see several low-lying states in the proton spectrum, and from their angular distributions we can assign them to specific spins and parities in ^{91}Zr. Notice the appearance of maxima and minima in the angular distribution. The angular momentum transfer, as usual, also gives us the change in parity of the reactions, ℓ = even for no change in parity and ℓ = odd for a change in parity. If we are studying shell-model states in odd-A nuclei by single-particle transfer reactions such as (d, p), we will use an even-Z, even-N nucleus as target, and so the initial spin and parity are 0^+. If the orbital angular momentum transferred is ℓ, then the final nuclear state reached will be $\ell \pm \frac{1}{2}$, allowing for the contribution of the spin of the transferred nucleon. For $\ell = 2$, for instance, we can reach states of $j = \frac{3}{2}$ or $\frac{5}{2}$, both with even parity.

The complete theory of direct reactions is far too detailed for this text, but we can sketch the outline of the calculation as an exercise in applications of the principles of quantum mechanics. The transition amplitude for the system to go from the initial state (X + a) to the final state (Y + b) is governed by the usual quantum mechanical matrix element:

$$M = \int \psi_Y^* \psi_b^* V \psi_X \psi_a \, dv \tag{11.58}$$

The interaction V must be a very complicated function of many nuclear coordinates. A simplifying assumption is the plane-wave *Born approximation*, in which ψ_a and ψ_b are treated as plane waves. Expanding the resulting exponential $e^{i\mathbf{p}\cdot\mathbf{r}/\hbar}$ using a spherical wave expansion of the form of Equation 11.31 and making the simplifying assumption that the interaction takes place on the nuclear

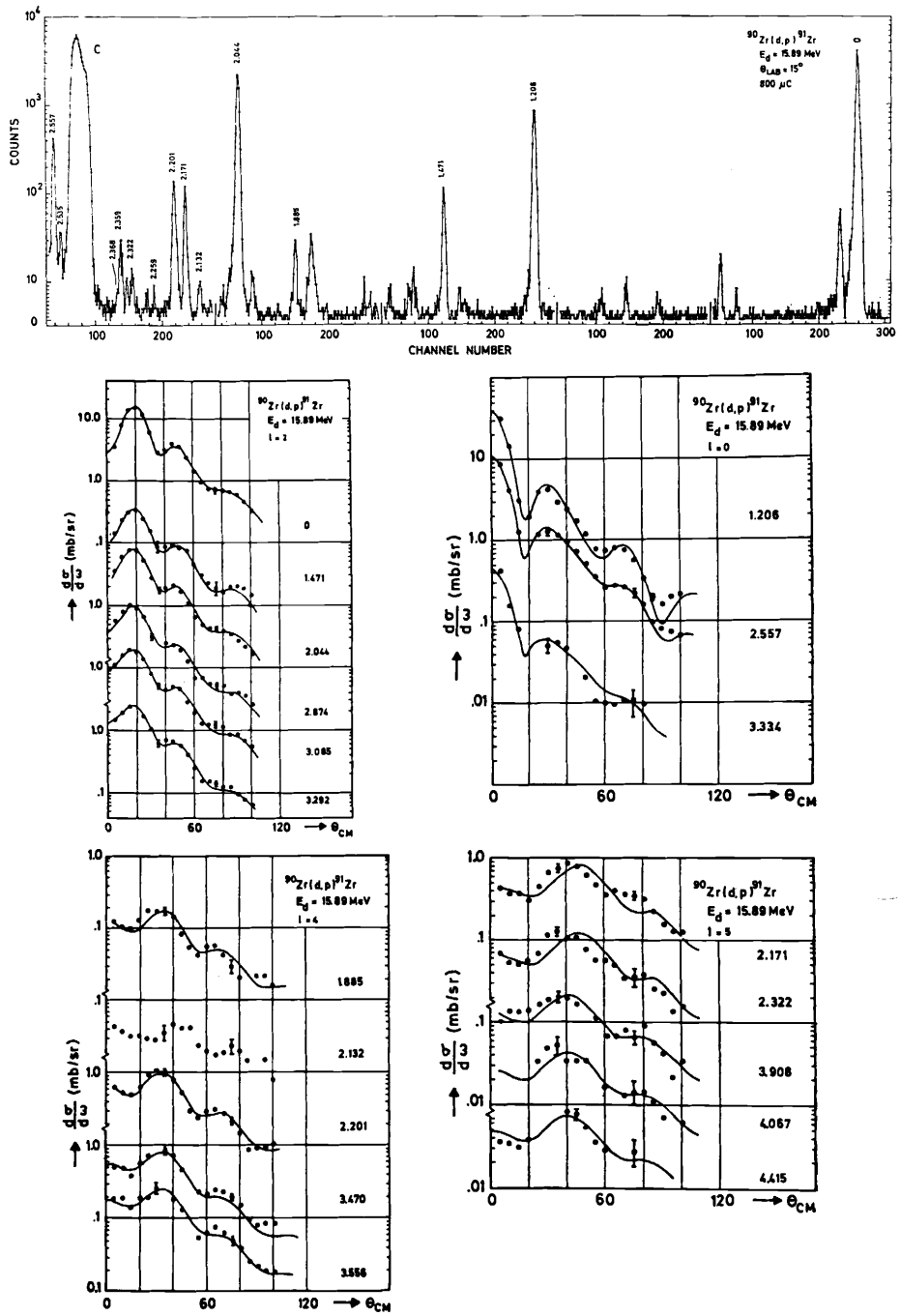


Figure 11.23 (top) Proton spectrum from ^{90}Zr(d, p)^{91}Zr. Peaks are identified with the final states in ^{91}Zr populated. The large peak at the left is from a carbon impurity. (bottom) Angular distributions fitted to determine the ℓ value. Note that the location of the first maximum shifts to larger angles with increasing ℓ, as predicted by Equation 11.57. See Figure 11.24 for the deduced excited states. Data from H. P. Blok et al., *Nucl. Phys. A* **273**, 142 (1976).

surface, so the integral is evaluated only at $r = R$, the matrix element is proportional to $j_\ell(kR)$ where $k = p/\hbar$ contains the explicit angular dependence through Equation 11.57. The cross section then depends on $[j_\ell(kR)]^2$, which gives results of the form of Figure 11.23.

Taking this calculation one step further, we use the optical model to account for the fact that the incoming and outgoing plane waves are changed (or distorted) by the nucleus. This gives the *distorted-wave Born approximation*, or DWBA. We can even put in explicit shell-model wave functions for the final state, and ultimately we find a differential cross section for the reaction. Because there are no "pure" shell-model states, the calculated cross section may describe many different final states. Each will have a differential cross section whose shape can be accurately calculated based on this model, but the amplitude of the cross section for any particular state depends on the fraction of the pure shell-model state included in the wave function for that state. The measured cross section is thus reduced from the calculated shell-model single-particle value by a number

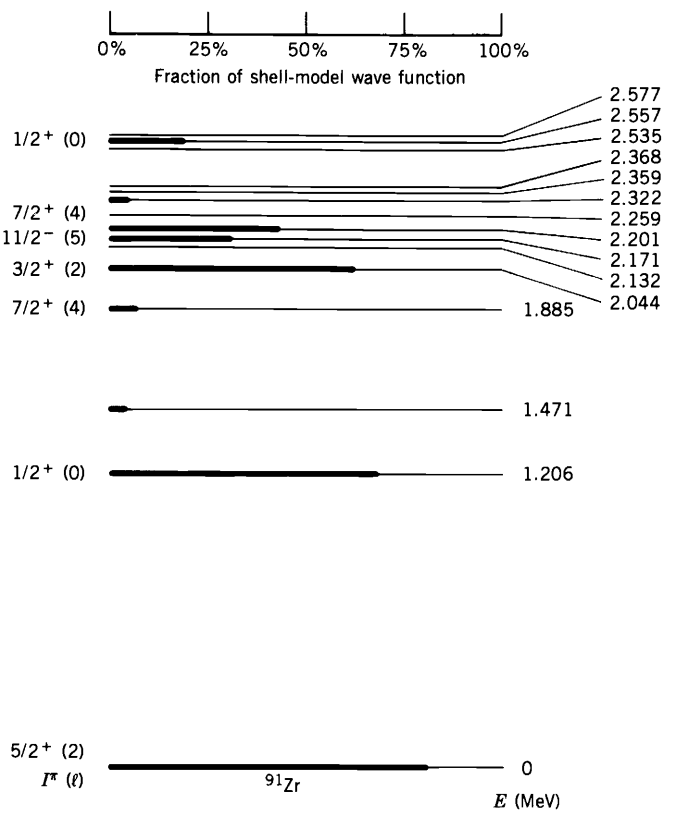


Figure 11.24 Deduced level scheme for ^{91}Zr. Each ℓ value (except zero) deduced from the angular distributions of Figure 11.23 leads to a definite parity assignment but to two possible I values, $\ell \pm \frac{1}{2}$. Which one is correct must be determined from other experiments. The fraction of the single-particle strengths represented by each level is indicated by the length of the shading; thus the ground state is nearly pure $d_{5/2}$ shell-model state.

between 0 and 1 called the *spectroscopic factor* S:

$$\left(\frac{d\sigma}{d\Omega}\right)_{\text{meas}} = S\left(\frac{d\sigma}{d\Omega}\right)_{\text{calc}} \tag{11.59}$$

A pure shell-model state would have $S = 1$. In practice we often find the shell-model wave function to be distributed over many states. Figure 11.24 shows examples of the spectroscopic factors measured for ^{91}Zr.

11.12 RESONANCE REACTIONS

The compound-nucleus model of nuclear reactions treats the unbound nuclear states as if they formed a structureless continuum. That is, there may be discrete nuclear states, but there are so many of them and they are so close together that they form a continuous spectrum. Each of these supposed discrete states is unstable against decay and therefore has a certain *width*; when the states are so numerous that their spacing is much less than the widths of the individual states, the compound-nucleus continuum results.

The bound states studied by direct reactions are at the opposite end of the scale. Because they are stable against particle emission, their mean lives are much longer (for example, characteristic of γ decay) and their corresponding widths are much smaller. A state with a lifetime of 1 ps, for instance, has a width of about 10^{-3} eV, far smaller than the typical spacing of bound states. We are therefore justified in treating these as discrete states with definite wavefunctions.

Between these two extremes is the *resonance* region—discrete levels in the compound-nucleus region. These levels have a high probability of formation (large cross sections), and their widths are very small because at low incident energy, where these resonances are most likely to occur, the quasibound state that is formed usually has only two modes of decay available to it—re-ejecting the incident particle, as in elastic or inelastic scattering, or γ emission.

To obtain a qualitative understanding of the formation of resonances, we represent the nuclear potential seen by the captured particle as a square well. The oscillatory wave functions inside and outside the well must be matched smoothly, as we did in Figure 4.7*a* for nucleon-nucleon scattering. Figure 11.25 shows several examples of how this might occur. Depending on the phase of the wave function inside the nucleus, the smooth matching can result in substantial variations between the relative amplitudes of the wave functions inside and outside the nucleus. In case (*a*), the incident particle has relatively little probability to penetrate the nucleus and form a quasibound state; in case (*c*), there is a very high probability to penetrate. As we vary the energy of the incident particle, we vary the relative phase of the inner and outer wave functions; the location of the matching point *and* the relative amplitudes vary accordingly. Only for certain incident energies do we achieve the conditions shown in part (*c*) of Figure 11.25. These are the energies of the *resonances* in the cross section.

In a single, isolated resonance of energy E_R and width Γ, the energy profile of the cross section in the vicinity of the resonance will have the character of the energy distribution of any decaying state of lifetime $\tau = \hbar/\Gamma$; see, for example, Equation 6.20 or Figure 6.3. The resonance will occur where the total cross

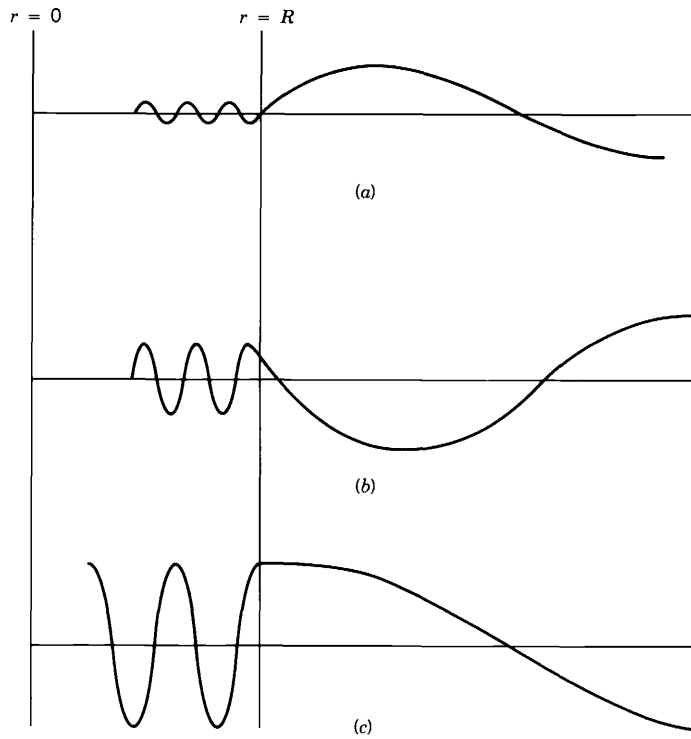


Figure 11.25 (*a*) Far from resonance, the exterior and interior wave functions match badly, and little penetration of the nucleus occurs. (*b*) As the match improves, there is a higher probability to penetrate. (*c*) At resonance the amplitudes match exactly, the incident particle penetrates easily, and the cross section rises to a maximum.

section has a maximum; from Equation 11.48, assuming only one partial wave ℓ is important for the resonant state, there will be a scattering resonance where $\eta_\ell = -1$, corresponding to a phase shift $\delta_\ell = \pi/2$.

The shape of the resonance can be obtained by expanding the phase shift about the value $\delta_\ell = \pi/2$. Better convergence of the Taylor series expansion is obtained if we expand the cotangent of δ_ℓ:

$$\cot \delta_\ell(E) = \cot \delta_\ell(E_R) + (E - E_R)\left(\frac{\partial \cot \delta_\ell}{\partial E}\right)_{E=E_R} + \tfrac{1}{2}(E - E_R)^2\left(\frac{\partial^2 \cot \delta_\ell}{\partial E^2}\right)_{E=E_R} + \cdots \tag{11.60}$$

in which

$$\left(\frac{\partial \cot \delta_\ell}{\partial E}\right)_{E=E_R} = -\left(\frac{\partial \delta_\ell}{\partial E}\right)_{E=E_R} \tag{11.61}$$

Defining the width Γ as

$$\Gamma = 2\left(\frac{\partial \delta_\ell}{\partial E}\right)^{-1}_{E=E_R} \tag{11.62}$$

then it can be shown that the second-order term vanishes, and thus (neglecting higher-order terms)

$$\cot \delta_\ell = -\frac{(E - E_R)}{\Gamma/2} \tag{11.63}$$

Because Γ is the full width of the resonance, the cross section should fall to half of the central value at $E - E_R = \pm\Gamma/2$. From Equation 11.63, this occurs when $\cot \delta_\ell = \pm 1$, or $\delta_\ell = \pi/4$, $3\pi/4$ (compared with $\delta_\ell = \pi/2$ at the center of the resonance). The cross section depends on $\sin^2 \delta_\ell$, which does indeed fall to half the central value at $\delta_\ell = \pi/4$ and $3\pi/4$. The width defined by Equation 11.62 is thus entirely consistent with the width shown in Figure 6.3.

From Equation 11.63, we find

$$\sin \delta_\ell = \frac{\Gamma/2}{\left[(E - E_R)^2 + \Gamma^2/4\right]^{1/2}} \tag{11.64}$$

and the scattering cross section becomes, using Equation 11.45

$$\sigma_{sc} = \frac{\pi}{k^2}(2\ell + 1)\frac{\Gamma^2}{(E - E_R)^2 + \Gamma^2/4} \tag{11.65}$$

This result can be generalized in two ways. In the first place, we can account for the effect of reacting particles with spin. If s_a and s_X are the spins of the incident and target particles, and if I is the total angular momentum of the resonance,

$$\boldsymbol{I} = \boldsymbol{s}_a + \boldsymbol{s}_X + \boldsymbol{\ell} \tag{11.66}$$

then the factor $(2\ell + 1)$ in Equation 11.65 should be replaced by the more general statistical factor

$$g = \frac{2I + 1}{(2s_a + 1)(2s_X + 1)} \tag{11.67}$$

Note that g reduces to $(2\ell + 1)$ for spinless particles.

The second change we must make is to allow for partial entrance and exit widths. If the resonance has many ways to decay, then the total width Γ is the sum of all the partial widths Γ_i

$$\Gamma = \sum_i \Gamma_i \tag{11.68}$$

The Γ^2 factor in the denominator of Equation 11.65 is related to the decay width of the resonant state and therefore to its lifetime: $\Gamma = \hbar/\tau$. The observation of only a single entrance or exit channel does not affect this factor, for the resonance always decays with the same lifetime τ. In the analogous situation in

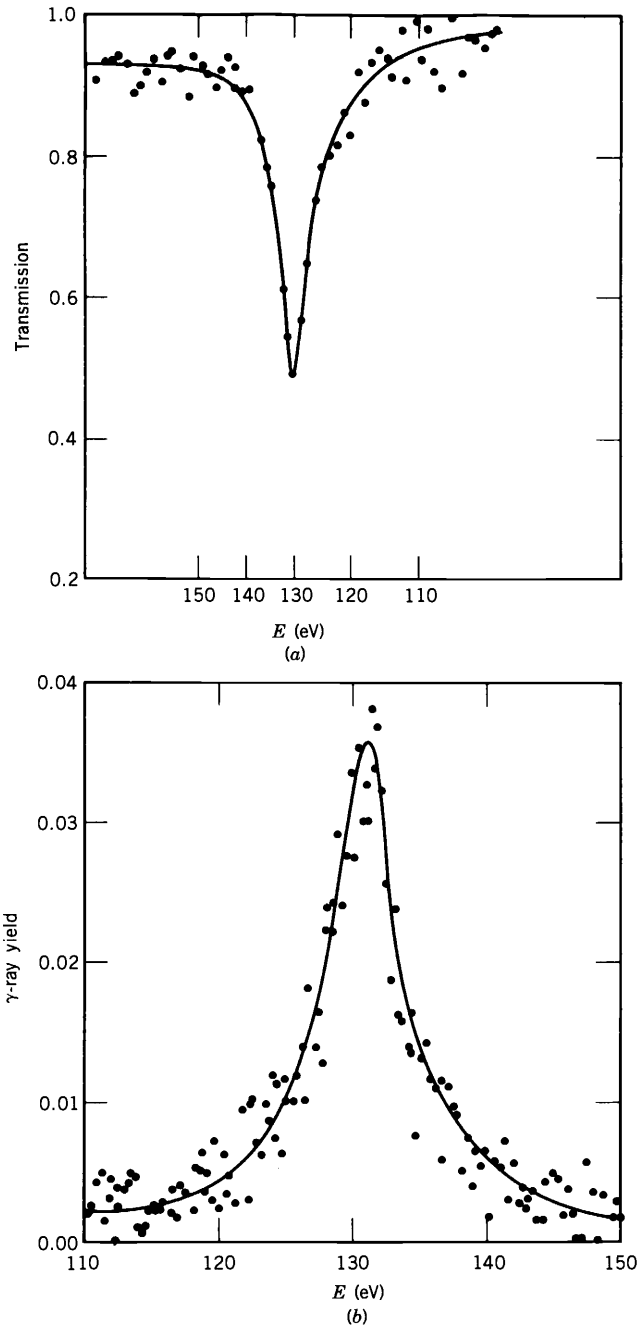


Figure 11.26 130-eV neutron resonance in scattering from ^{59}Co. Part (*a*) shows the intensity of neutrons transmitted through a target of ^{59}Co; at the resonance there is the highest probability for a reaction and the intensity of the transmitted beam drops to a minimum. In (*b*), the γ-ray yield is shown for neutron radiative capture by ^{59}Co. Here the yield of γ rays is maximum where the reaction has the largest probability. From J. E. Lynn, *The Theory of Neutron Resonance Reactions* (Oxford: Clarendon, 1968).

radioactive decay, the activity decays with time according to the total decay constant, even though we might observe only a single branch with a very different partial decay constant. The Γ^2 factor in the numerator, on the other hand, is directly related to the formation of the resonance and to its probability to decay into a particular exit channel. In the case of elastic scattering, for which Equation 11.65 was derived, the entrance and exit channels are identical. That is, for the reaction a + X → a + X, we should use the partial widths Γ_{aX} of the entrance and exit channels:

$$\sigma = \frac{\pi}{k^2} g \frac{(\Gamma_{aX})^2}{(E - E_R)^2 + \Gamma^2/4} \tag{11.69}$$

Similarly, for the reaction a + X → b + Y, a different exit width must be used:

$$\sigma = \frac{\pi}{k^2} g \frac{\Gamma_{aX}\Gamma_{bY}}{(E - E_R)^2 + \Gamma^2/4} \tag{11.70}$$

Equations 11.69 and 11.70 are examples of the *Breit-Wigner formula* for the shape of a single, isolated resonance. Figure 11.26 shows such a resonance with the Breit-Wigner shape. The cross section for resonant absorption of γ radiation has a similar shape, as given by Equations 10.29 and 10.30.

Many elastic scattering resonances have shapes slightly different from that suggested by the Breit-Wigner formula. This originates with another contribution to the reaction amplitude from direct scattering of the incident particle by the nuclear potential, without forming the resonant state. This alternative process is called *potential scattering* or *shape-elastic scattering*. Potential scattering and

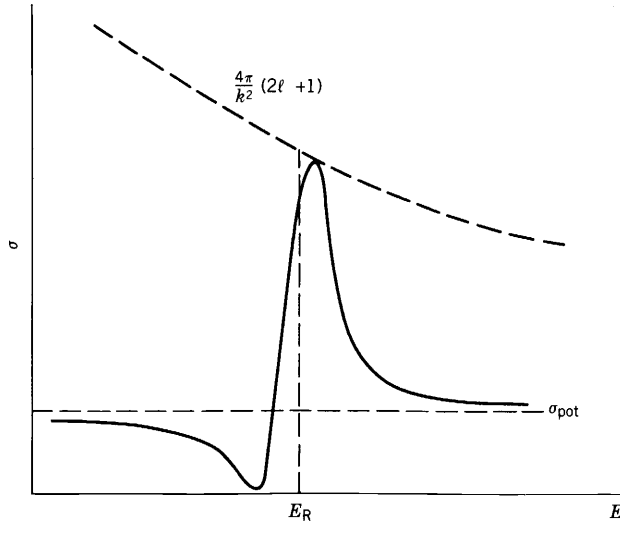


Figure 11.27 Interference between resonance and potential scattering produces resonances with this characteristic shape.

resonant scattering both contribute to the elastic scattering amplitude, and interference between the two processes causes variation in the cross section. Interference can cause the combined cross section to be smaller than it would be for either process alone. It is therefore not correct simply to add the cross sections for the two processes. We can account for the two processes by writing

$$\eta_\ell = e^{2i(\delta_{\ell R}+\delta_{\ell P})} \tag{11.71}$$

where $\delta_{\ell R}$ is the resonant phase shift, as in Equations 11.63 or 11.64, and $\delta_{\ell P}$ is an additional contribution to the phase shift from potential scattering. From

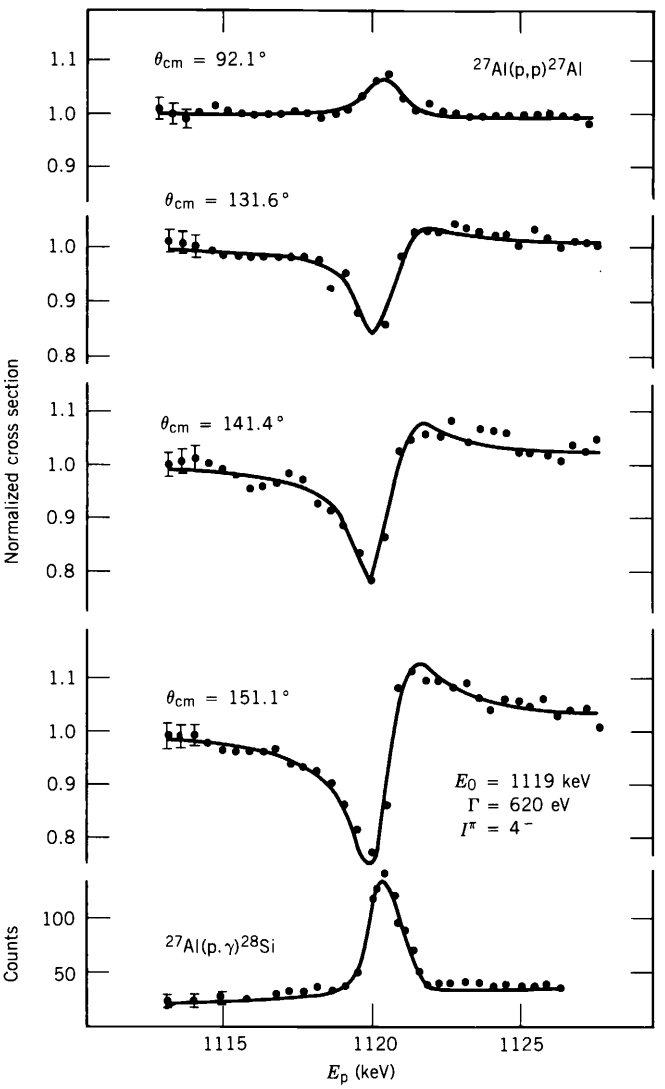


Figure 11.28 Resonances in the reaction ^{27}Al(p, p)^{27}Al. The resonances occur in the nucleus ^{28}Si. Note that the (p, γ) yield shows a resonance at the same energy. From A. Tveter, *Nucl. Phys. A* **185**, 433 (1972).

Equation 11.44 we find the cross section

$$\sigma_{sc} = \frac{\pi}{k^2}(2\ell + 1)\left|e^{-2i\delta_{\ell P}} - 1 + \frac{i\Gamma}{(E - E_R) + i\Gamma/2}\right|^2 \tag{11.72}$$

Far from the resonance, $(E - E_R) \gg \Gamma/2$ and the potential scattering term dominates:

$$\sigma \cong \sigma_{pot} = \frac{4\pi}{k^2}(2\ell + 1)\sin^2\delta_{\ell P} \tag{11.73}$$

At $E = E_R$, the resonant term dominates and

$$\sigma \cong \sigma_{res} = \frac{4\pi}{k^2}(2\ell + 1) \tag{11.74}$$

Near the resonance there is interference between the two terms, which produces the characteristic shape shown in Figure 11.27. According to this model, we

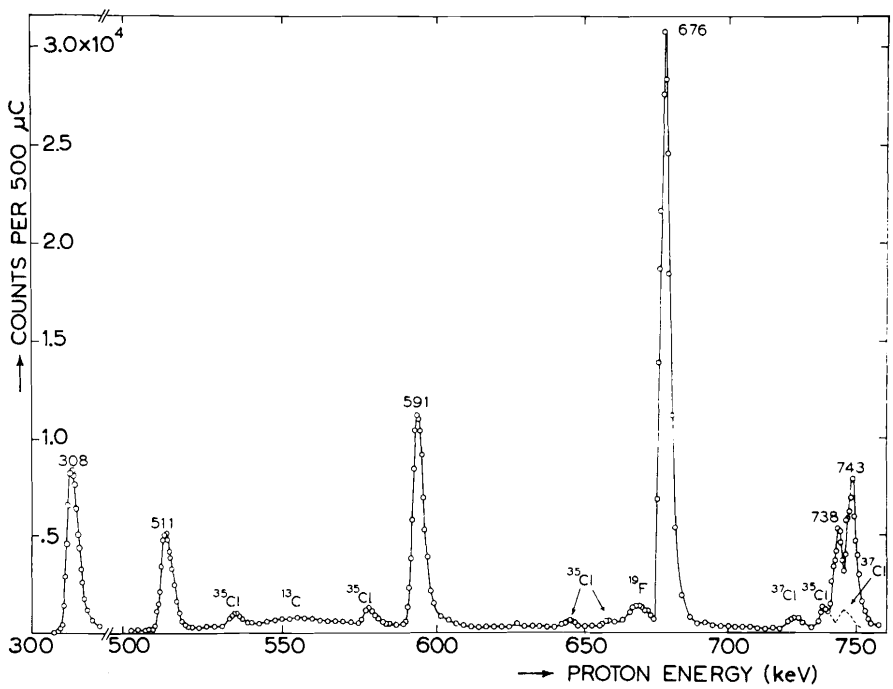


Figure 11.29 Resonances observed in the radiative proton capture by ^{23}Na. In this case, the total yield of γ rays in the energy range 3 – 13 MeV was measured as a function of the incident proton energy. The Cl peaks appear because the target used was NaCl. From P. W. M. Glaudemans and P. M. Endt, *Nucl. Phys.* **30**, 30 (1962).

expect an interference "dip" on the low-E side of the resonance. The resonance height should decrease roughly as k^{-2} (that is, as E^{-1}) with increasing incident energy, and the nonresonant "background" from potential scattering should remain roughly constant. Figure 11.28 shows scattering cross sections with the resonant structure clearly visible. The expectations of the resonance model are clearly fulfilled.

Radiative capture reactions also show a resonant structure. Figure 11.29 shows examples of (p, γ) reactions. Note that this is not a γ spectrum in the conventional sense—the horizontal axis shows the incident proton energy, not the emitted γ energy.

Resonances observed in neutron scattering are discussed in more detail in Chapter 12.

11.13 HEAVY-ION REACTIONS

From the point of view of nuclear reactions, a heavy ion is defined to be any projectile with $A > 4$. Accelerators devoted to the study of heavy-ion reactions can produce beams of ions up to ^{238}U, at typical energies of the order of 1–10 MeV per nucleon, although much higher energies are also possible.

The variety of processes than can occur in heavy-ion reactions is indicated schematically in Figure 11.30. At large impact parameters, Coulomb effects dominate, and Rutherford scattering or Coulomb excitation may occur. When the nuclear densities of the target and projectile just begin to overlap, nuclear reactions can occur, and at small overlap ordinary elastic or inelastic scattering and few-nucleon transfer through direct reactions may occur, as discussed previously in this chapter.

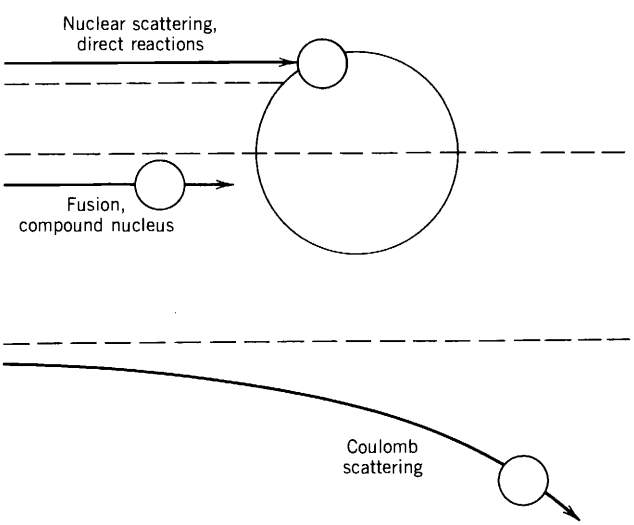


Figure 11.30 Processes in heavy-ion scattering depend on the impact parameter, when energies are large enough to penetrate the Coulomb barrier.

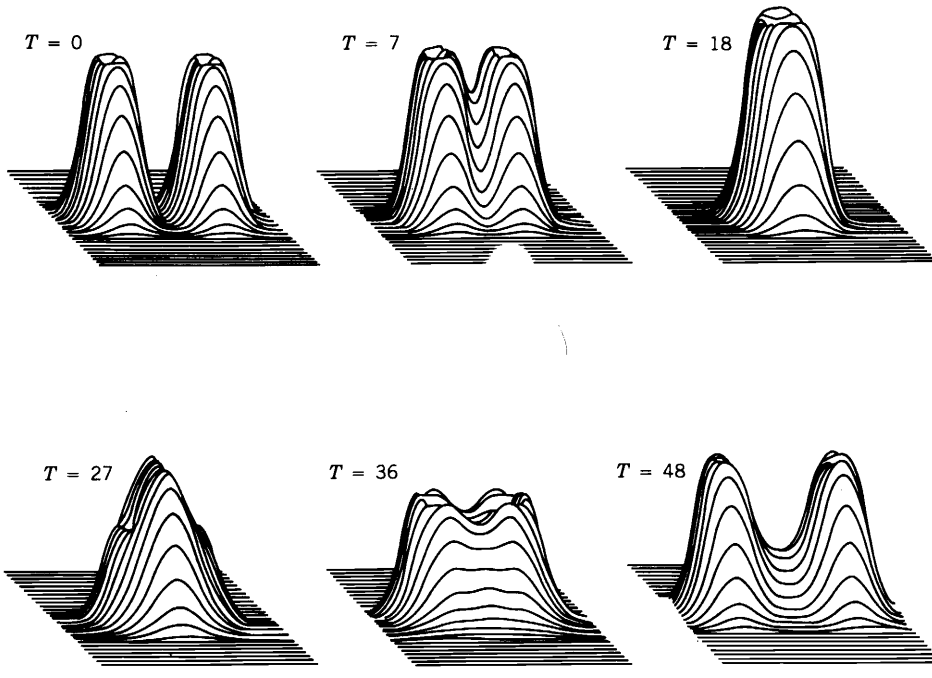


Figure 11.31 Two ^{12}C nuclei colliding, shown at various times (each unit of time is 3.3×10^{-24} s, and the area shown represents 1 fm^2). The vertical scale shows the nuclear density, which reaches a peak at $T = 11$. Note the internal oscillations that occur before the compound system breaks apart. The energy of the incident projectile was about 700 MeV. (Courtesy Ronald Y. Cusson and Joachim Maruhn, Oak Ridge National Laboratory; from *Scientific American*, p. 59, December 1978.)

At small impact parameters, new and unusual features emerge in these reactions. If the impact parameter is small enough that the nuclei can overlap completely, a compound nucleus, representing complete fusion of the two nuclei, can form as an intermediate state. However, to overcome the repulsive Coulomb barrier, the incident ion must be quite energetic, and thus the compound nucleus is formed with a considerable excitation energy. This compound nucleus may be an unusual state of nuclear matter that cannot be achieved in reactions with light nuclei. Because of the large incident energy, the compound nucleus may achieve a density or a "temperature" (that is, a mean internal kinetic energy per nucleon) beyond what can be achieved in reactions with light ions. The analysis of these compound states and their decay modes thus represent a challenge for nuclear theory—can we extrapolate from an equation of state for "ordinary" nuclear matter to one for "extraordinary" nuclear matter? Figure 11.31 shows an attempt to calculate the intermediate states through which the highly excited compound nucleus ^{24}Mg progresses in the course of the reaction $^{12}C + {}^{12}C$.

Once the excited compound state is formed, there are many channels available for its decay. It can split more-or-less in half, either through the original entrance channel ($^{24}Mg \rightarrow {}^{12}C + {}^{12}C$) or through a closely related channel ($^{24}Mg \rightarrow {}^{15}O$

$+{}^{9}$Be). For heavier nuclei, the study of the fission mode provides a check on theories derived from the study of the more familiar cases of transuranic fission, described in Chapter 13.

A more probable means of decay of the compound nucleus is through particle emission, for fission is inhibited by a substantial Coulomb barrier. Emission of charged particles (protons or α's) is also inhibited by a Coulomb barrier. In reactions with heavy nuclei the compound nucleus is extremely proton rich, but the preferred decay mode is still neutron emission; this remains so, even for heavy nuclei with a proton excess of 10–20 or more. It is thus possible to study nuclei far from stability on the proton-rich side through (HI, xn) reactions, where HI indicates any heavy ion and x may be in the range 5–10.

A particular application of these reactions is in the search for stable or nearly stable nuclei of *superheavy elements*. The transuranic atoms that have been studied through the neutron capture–β-decay technique move up the atomic number scale in single steps, but the technique loses its applicability for the nuclei around $Z = 104$ or 105, where the half-lives become very short ($\sim$ seconds) for decay by spontaneous fission. As Z increases, the spontaneous fission half-life should continue to decrease (because the Coulomb energy, which makes the nucleus more unstable to fission, increases like Z^2), until we approach the region of the next closed shell or "magic number" for protons, which has been calculated to be $Z = 114$ (rather than 126, as is already known for neutrons).

It is possible to search for superheavy nuclei directly, by bombarding the heaviest possible quasistable targets ($^{249}_{98}$Cf, with $t_{1/2} = 351$ y) with beams such as ^{32}S or ^{40}Ca, in the hope of producing stable products around $Z = 114$, $N = 164$ following few-nucleon emission from the compound state. Another possibility would be to produce a highly unstable, extremely heavy compound state in a reaction such as $^{238}\text{U} + {}^{238}\text{U}$, in the hope that one of the fission decay channels would have a high probability of producing a stable superheavy nucleus. To date no success has been reported from either of these approaches, but the effort continues.

Another unique feature of heavy-ion reactions is the transfer of large amounts of angular momentum to the compound nucleus. For example, in the reaction

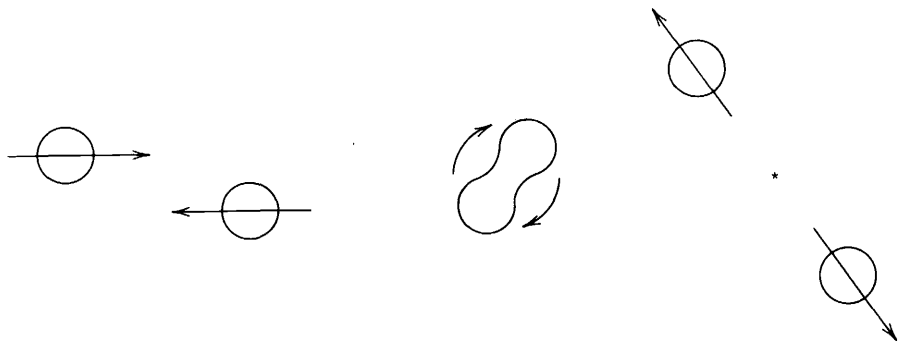
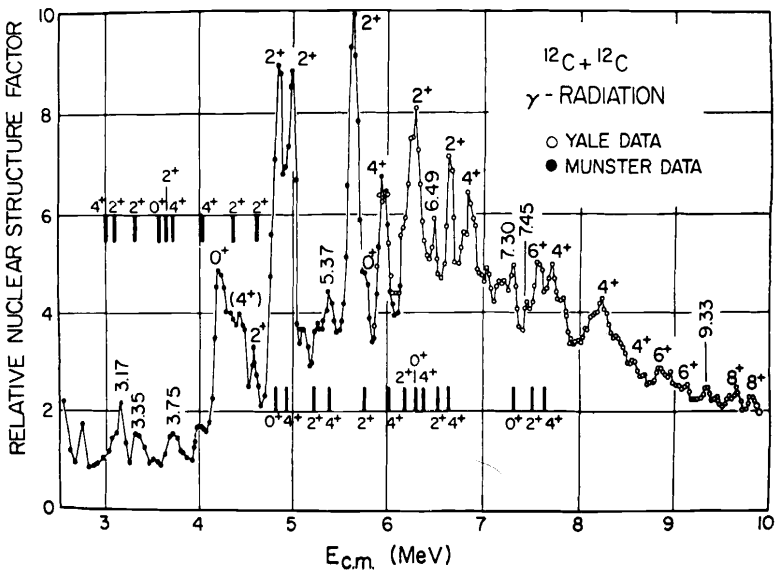
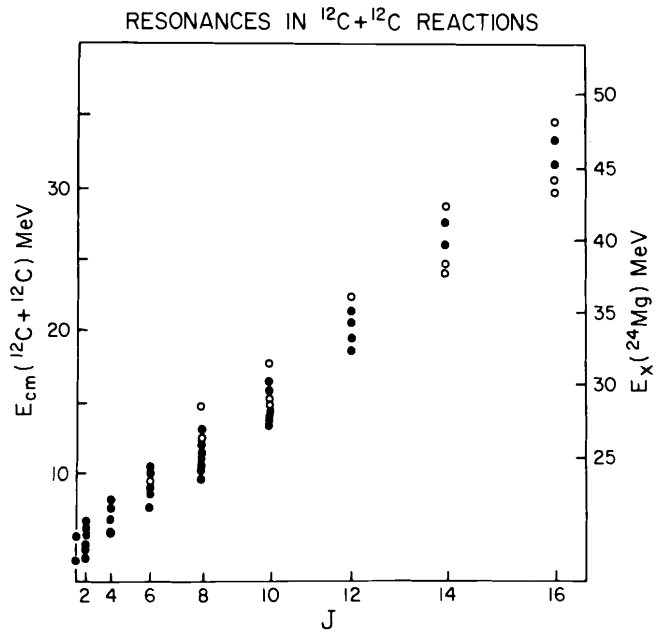


Figure 11.32 In nuclear molecule formation, there is not quite complete fusion of the two particles; they retain a "memory" of their previous character and break apart accordingly. The internal energy of the system can show rotational and vibrational structures, just like an ordinary molecule.



(a)



(b)

Figure 11.33 (*a*) The $^{12}C + ^{12}C$ molecular states. The vertical scale shows the cross section with the "uninteresting" Coulomb penetrability factor removed, leaving the nuclear structure factor. The resonances are labeled with the spin-parity assignments which can be grouped into rotational sequences $0^+, 2^+, 4^+, 6^+, \ldots$. (*b*) Plotting the internal excitation energies of the resonances against $I(I+1)$ reveals that the states do indeed form rotational sequences. From T. M. Cormier, *Ann. Rev. Nucl. Particle Sci.* **32**, 271 (1982).

$^{40}Ca + {}^{197}Au$, the Coulomb barrier is about 200 MeV. If we use 200 MeV incident ^{40}Ca, a grazing collision will provide about $140\hbar$ of angular momentum to the system. Even at collisions with smaller impact parameters, it would not be unusual to transfer an angular momentum of $\ell \gtrsim 40\hbar$ to the compound system. At such rotational velocities, the nuclear force may not be able to provide the necessary centripetal acceleration, and the compound system may be completely unstable and therefore unable to form. In such a case, a new type of system is possible, called a *nuclear molecule*. Figure 11.32 illustrates the process schematically. The two nuclei do not form a compound system, corresponding to complete sharing of the incident energy. Instead a system analogous to a diatomic molecule is formed, exists for a short time, and then breaks apart in the same configuration as the incident particles. Because the decay occurs into the original particles, the combined system retains a considerable "memory" of its formation, contrary to the basic assumption of the compound-nucleus model. Evidence for such molecular states comes from observing the rotational and vibrational excitations that correspond closely with those observed in ordinary molecules. Figure 11.33 shows an example of the states observed in the $^{12}C + {}^{12}C$ nuclear molecule. Resonances in the cross section correspond to the rotational and vibrational states permitted in the molecular system.

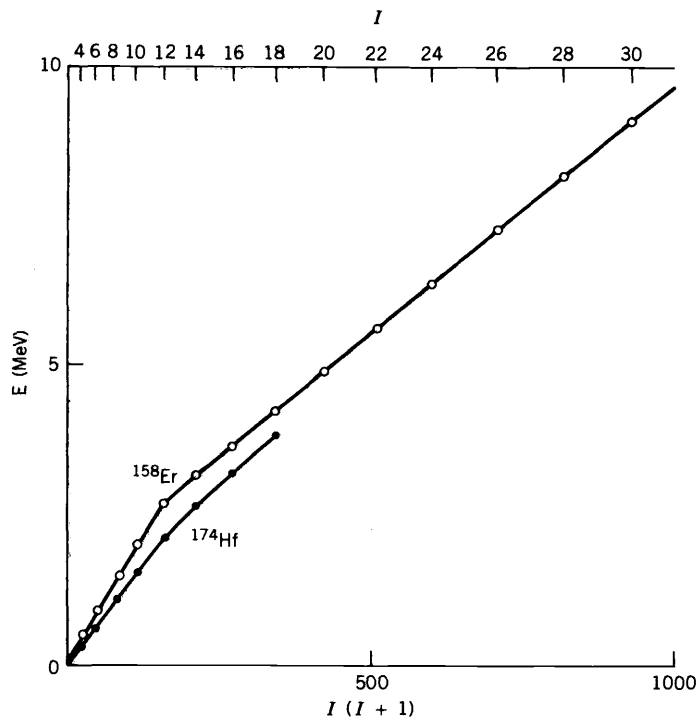


Figure 11.34 Rotational energies of ^{158}Er and ^{174}Hf. Neither case shows the expected linear dependence of E on $I(I + 1)$, but in ^{174}Hf the deviation is relatively gradual, while in ^{158}Er there appears to be a sudden change in slope (and therefore in moment of inertia) in the neighborhood of $I = 12-14$.

In heavier nuclei, highly excited states with $\ell \gtrsim 40$–$50\hbar$ can be populated in the compound system. The emission of a few neutrons from the excited system can change the angular momentum only little (a 5-MeV neutron carries at most only $\ell \sim 3\hbar$), and following the neutron emission, excited bound states in the final nucleus can be formed with angular momentum quantum numbers of 40 or so. Assuming the product nucleus to be of the deformed even-Z, even-N variety, the excited states will show a rotational spectrum of the type illustrated in Figure 5.22. The rotational energies are given by Equation 5.17:

$$E = \frac{\hbar^2}{2\mathscr{I}} I(I+1) \tag{11.75}$$

and the states should cascade down toward the ground state through a sequence of $E2$ γ transitions as in Figure 10.18. The observation of these cascade $E2$ transitions provides a way to study these excited states. In particular, we can study whether the assumption of a fixed, constant moment of inertia $\mathscr{I}$ remains valid at such high excitations. One way to test this assumption is to plot the energies of the states against $I(I+1)$ and to see if the slope remains constant, as predicted by Equation 11.75. Figure 11.34 is an example of such a plot, and there appears to be some deviation from the expected linear behavior.

There is a more instructive way to plot the data on the rotational structure. From Equation 11.75, the energy of a transition from state I to the next lower state $I-2$ is

$$E(I) - E(I-2) = \frac{\hbar^2}{2\mathscr{I}}(4I-2) \tag{11.76}$$

The transition energies should increase linearly with I; Figure 11.35 shows that this is true for the lower transitions, but becomes less valid as we go to larger I, and in fact the behavior changes completely at about $I = 16$, but then seems to restore itself as we go to higher states.

Let's assume that the moment of inertia is not constant, but increases gradually as we go to more rapidly rotating states; this effect, known classically as "centrifugal stretching," would not occur for a rigid rotor but would occur for a fluid. Because rotating nuclei have moments of inertia somewhere between that of a rigid rotor and of a fluid, as described in Equations 5.18 and 5.19, it is not surprising that centrifugal stretching occurs. Representing the rotational energy in terms of the rotational frequency

$$E = \tfrac{1}{2}\mathscr{I}\omega^2 \tag{11.77}$$

we can then assume $\mathscr{I}$ varies either with increasing angular momentum,

$$\mathscr{I} = \mathscr{I}_0 + kI(I+1) \tag{11.78}$$

or with increasing rotational frequency,

$$\mathscr{I} = \mathscr{I}_0 + k'\omega^2 \tag{11.79}$$

where k and k' are appropriate proportionality constants. From Equation 11.76,

$$\frac{2\mathscr{I}}{\hbar^2} = \frac{4I-2}{E(I) - E(I-2)} \tag{11.80}$$

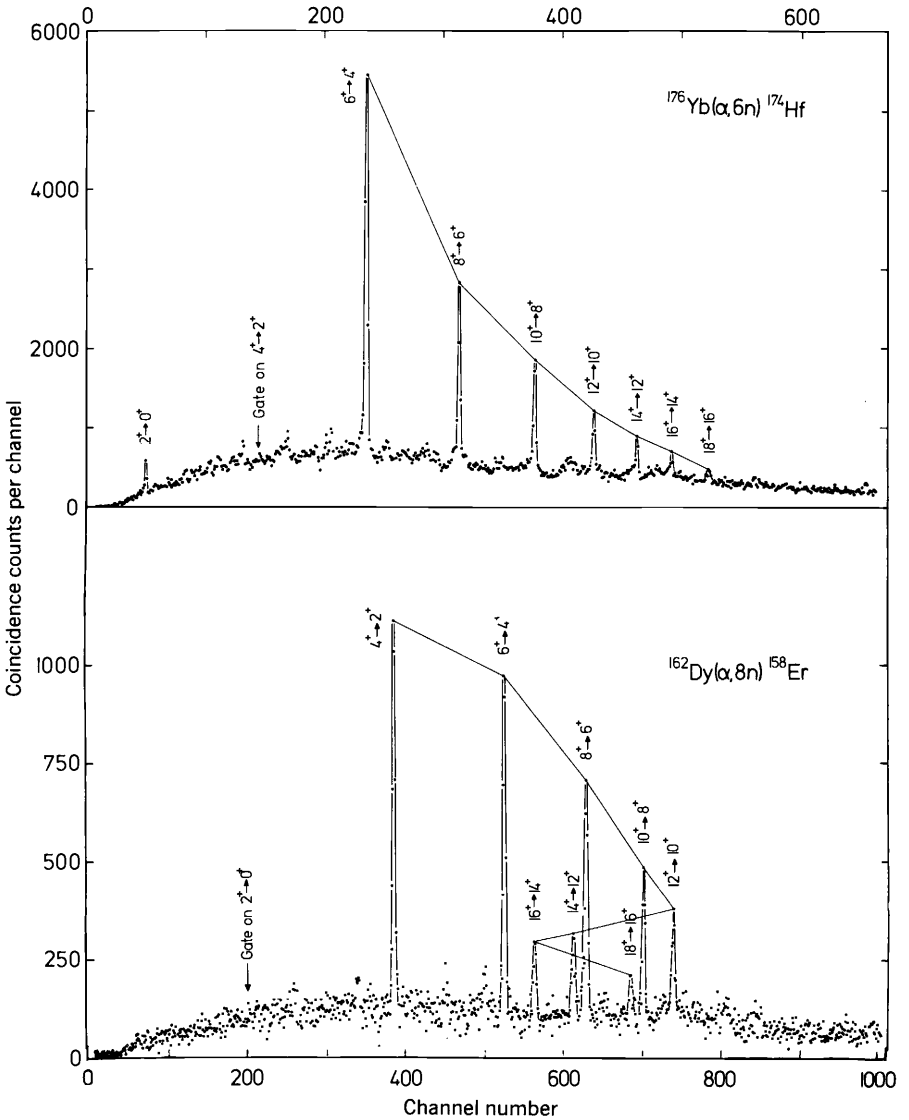


Figure 11.35 γ-ray spectra of transitions between rotational states in ^{158}Er and ^{174}Hf. For a perfect rotor, the γ-ray energies should increase monotonically with I. This is so for ^{174}Hf, but for ^{158}Er the energy begins to *decrease* with I in the range $I = 12-16$, and after $I = 16$ the energy again begins to increase. From R. M. Lieder and H. Ryde, in *Advances in Nuclear Physics*, Vol. 10, edited by M. Baranger and E. Vogt (New York: Plenum, 1978).

and plotting $\mathscr{I}$, measured in these units, against ω^2, we ought to see either a constant $\mathscr{I}_0$ if no stretching occurs, or a linear behavior. Figure 11.36 shows an example of such a relationship. There appears to be a gradual increase in $\mathscr{I}$ among the lower angular momentum states, then a radical change in behavior around $I = 16$, and then a return to the gradual stretching. This effect is known as *backbending*, and occurs because the rotational energy exceeds the energy

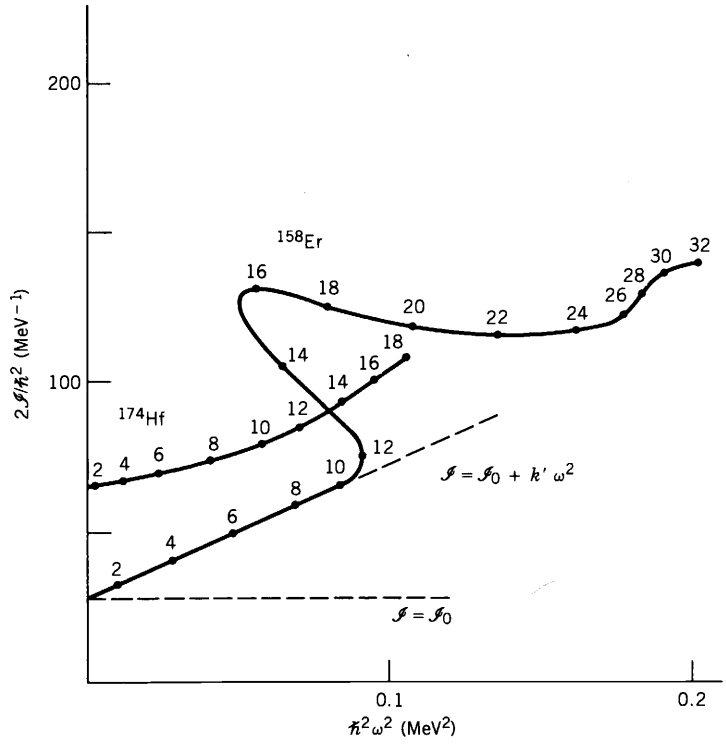


Figure 11.36 Moment of inertia, from Equation 11.80, as a function of $\hbar^2\omega^2$, from the semiclassical formula $\frac{1}{4}[E(I) - E(I-2)]^2$. Note the gradual increase in the moment of inertia for the lower states in both ^{158}Er and ^{174}Hf, and note also the backbending in ^{158}Er.

needed to break a pair of coupled nucleons. When that occurs (at an energy corresponding to $I = 16$), the unpaired nucleons go into different orbits and change the nuclear moment of inertia. The situation then remains stable until about $I = 30$, where another pair is broken and another change in moment of inertia occurs.

The study of the properties of nuclei at high angular momentum is another example of an unusual state of nuclear matter accessible only through heavy-ion reactions.

A final example of the nuclear structure studies that can be done through heavy-ion reactions is the α-particle transfer reaction, such as (^{16}O, ^{12}C). In our discussion of α decay in Chapter 8, we alluded to the "preformation" of the α particle inside the nucleus. Because the α particle is such a stable structure, we can consider the nucleons in a nucleus to have a high probability of occasionally forming an α particle, even in nuclei that do not α decay. This leads to the *α-cluster* model of nuclei, in which we look for nuclear structure characteristic of such clusters. States populated in (^{16}O, ^{12}C) reactions, in which four nucleons are simultaneously transferred to the target nucleus, might be analyzed in terms of the transfer of an α cluster from ^{16}O to the target. Figure 11.37 illustrates the cross sections for the formation of states in ^{20}Ne through α-transfer reactions.

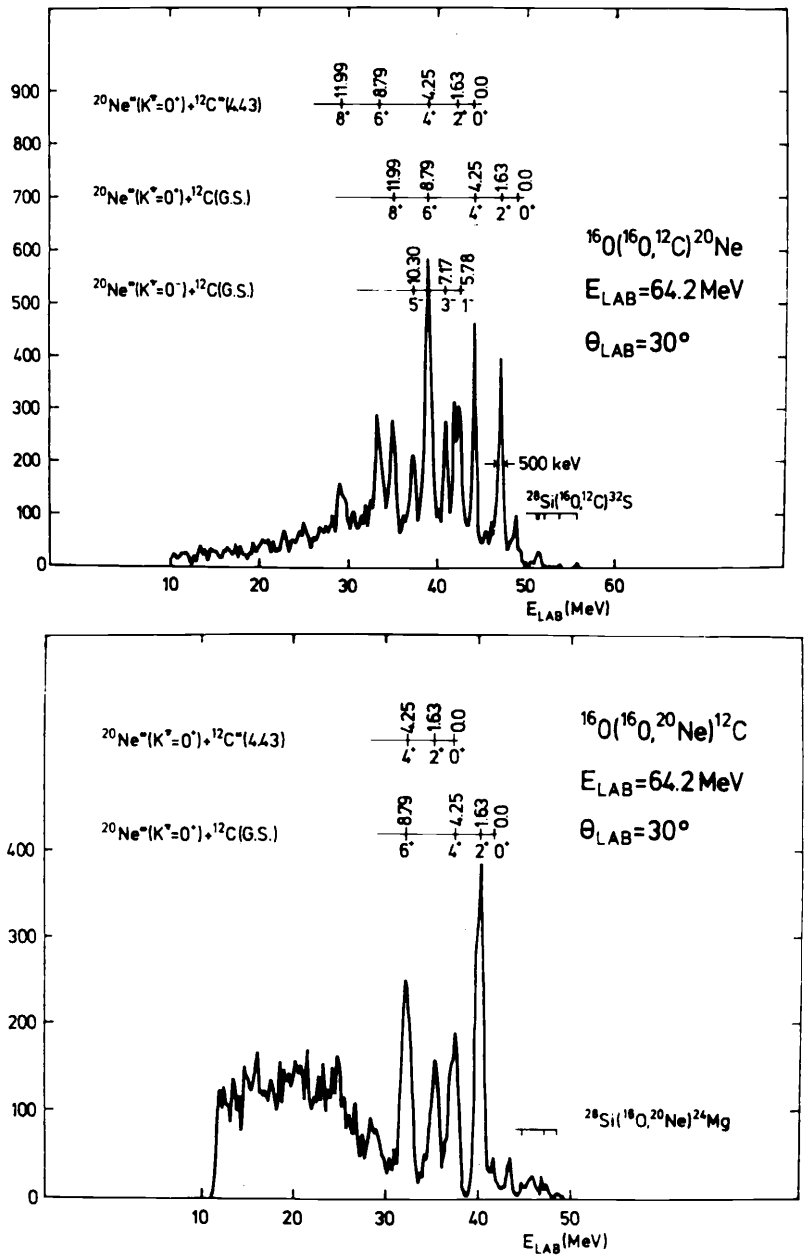


Figure 11.37 α-particle transfer reactions leading to ^{20}Ne. At top is the observed ^{12}C spectrum and at bottom is the ^{20}Ne spectrum. Individual excited states in ^{20}Ne are labeled, with some peaks in the spectrum assigned to reactions in which ^{12}C is left in its first excited state at 4.43 MeV. On the following page are shown the excited states of ^{20}Ne. Notice the selectivity of the reaction in populating certain states and not others; the dashed lines show states that are not populated in the reaction. Because the ^{16}O projectile and target are doubly closed-shell nuclei ($Z = 8, N = 8$), the observed states in ^{20}Ne correspond to the addition of an α particle to a doubly magic core; that is, the four valence nucleons are coupled to a resultant spin of zero, but can carry a net orbital angular momentum. Only a small subset of the ^{20}Ne states will have this character. Data from H. H. Rossner et al., *Nucl. Phys. A* **218**, 606 (1974).

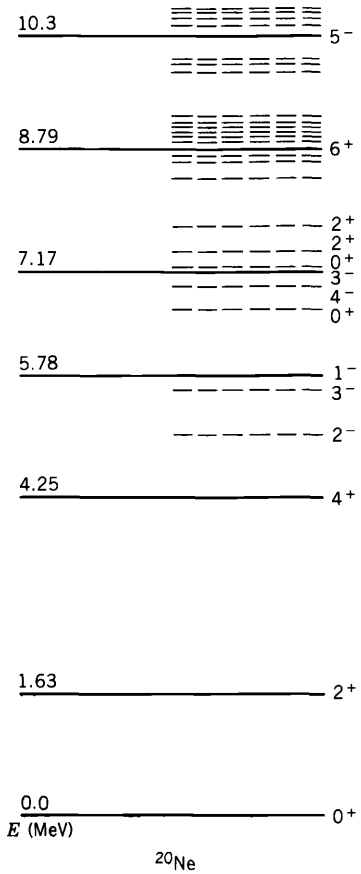


Figure 11.37 Continued.

REFERENCES FOR ADDITIONAL READING

A more complete description of nuclear reactions, at about the same level as this chapter, is by G. R. Satchler, *Introduction to Nuclear Reactions* (New York: Wiley, 1980). A reference at a similar level is I. E. McCarthy, *Nuclear Reactions* (Oxford: Pergamon, 1966). A more advanced text is P. E. Hodgson, *Nuclear Reactions and Nuclear Structure* (Oxford: Clarendon, 1971).

The most comprehensive recent review of all aspects of nuclear reactions is the four-part collection, *Nuclear Spectroscopy and Reactions*, edited by Joseph Cerny (New York: Academic, 1974). It includes chapters on direct reactions, resonance reactions, scattering, Coulomb excitation, and heavy-ion reactions, as well as material on experimental techniques.

Comprehensive summaries of the role of isospin in nuclear decays and reactions can be found in *Isospin in Nuclear Physics*, edited by D. H. Wilkinson (Amsterdam: North-Holland, 1969). Wilkinson's introduction is highly recommended as a review of the historical development of isospin and of nuclear theory.

Effects at high rotational velocities are discussed by R. M. Lieder and H. Ryde, in *Advances in Nuclear Physics*, Vol. 10, edited by M. Baranger and E. Vogt (New

York: Plenum, 1978); see also the brief review by R. M. Diamond and F. S. Stephens, *Nature* **310**, 457 (1984).

PROBLEMS

1. Complete the following reactions:

$$^{27}\text{Al} + \text{p} \rightarrow \quad + \text{n}$$

$$^{32}\text{S} + \alpha \rightarrow \quad + \gamma$$

$$^{197}\text{Au} + ^{12}\text{C} \rightarrow ^{206}\text{At} +$$

$$^{116}\text{Sn} + \quad \rightarrow ^{117}\text{Sn} + \text{p}$$

2. (a) Solve Equations 11.3 and 11.4 for $\cos\theta$. (b) Determine the relationship between $\cos\theta$ and p_b for elastic scattering. (c) Show that there is a maximum value of θ only when $m_a > m_Y$. (d) Find the maximum angle at which α particles appear after elastic scattering from hydrogen and from deuterium.
3. It is desired to study the first excited state of ^{16}O, which is at an energy of 6.049 MeV. (a) Using the (α, n) reaction on a target of ^{13}C, what is the minimum energy of incident alphas which will populate the excited state? (b) In what direction will the resulting neutrons travel? (c) If it is desired to detect the neutrons at 90° to the incident beam, what is the minimum α energy that can result in the excited state being populated?
4. (a) In Coulomb scattering of 7.50-MeV protons by a target of ^7Li, what is the energy of the elastically scattered protons at 90°? (b) What is the energy of the inelastically scattered protons at 90° when the ^7Li is left in its first excited state (0.477 MeV)?
5. The (n, p) reaction can be regarded as equivalent to β^+ decay in that the same initial and final nuclei are involved. Derive a general expression relating the Q value of the (n, p) reaction to the maximum energy release in β^+ decay. Find several examples to verify your derived relationship.
6. The Q value for the reaction $^9\text{Be}(\text{p}, \text{d})^8\text{Be}$ is 559.5 ± 0.4 keV. Use this value along with the accurately known masses of ^9Be, ^2H, and ^1H to find the mass of ^8Be.
7. (a) Calculate the Q value of the reaction $\text{p} + ^4\text{He} \rightarrow ^2\text{H} + ^3\text{He}$. (b) What is the threshold energy for protons incident on He? For α's incident on hydrogen?
8. For the reaction $^2\text{H} + ^2\text{H} \rightarrow ^3\text{He} + \text{n}$, plot the energy of the outgoing neutron as a function of angle for ^2H incident on ^2H at rest. Use incident energies of 0.00, 2.50, and 5.00 MeV.
9. Compute the Q values for the reactions (a) $^6\text{Li} + \text{p} \rightarrow ^3\text{He} + ^4\text{He}$; (b) $^{59}\text{Co} + \text{p} \rightarrow \text{n} + ^{59}\text{Ni}$; (c) $^{40}\text{Ca} + \alpha \rightarrow \text{n} + ^{43}\text{Ti}$.
10. For the following endoergic reactions, find the Q value and the threshold kinetic energy, assuming in each case that the lighter particle is incident on the heavier particle at rest: (a) $^7\text{Li} + \text{p} \rightarrow ^7\text{Be} + \text{n}$; (b) $^{12}\text{C} + \text{p} \rightarrow \text{n} + ^{12}\text{N}$; (c) $^{35}\text{Cl} + \alpha \rightarrow \text{n} + ^{38}\text{K}$.

11. At threshold, the product particles Y + b move at the same velocity. Use momentum conservation to derive a relationship between T_a and T_b at threshold, and then substitute your expression into Equation 11.5 to obtain the threshold condition (11.6).

12. It is desired to study the low-lying excited states of ^{35}Cl (1.219, 1.763, 2.646, 2.694, 3.003, 3.163 MeV) through the $^{32}S(\alpha, p)$ reaction. (a) With incident α particles of 5.000 MeV, which of these excited states can be reached? (b) Again with 5.000-MeV incident α's, find the proton energies observed at 0, 45, and 90°.

13. In the reaction $^{7}Li + p \rightarrow {}^{4}He + {}^{4}He$ (18.6 MeV protons incident on a lithium target) the differential cross section (in the center-of-mass system) reaches a maximum of about 1.67 barns/steradian at a center-of-mass angle of 75°. (a) Sketch the reaction kinematics in the laboratory system, labeling all momenta, directions, and energies. (b) Assuming a target thickness of 1.0 mg/cm^2 and a beam of protons of current 1.0 μA spread over an area of 1 cm^2, find the number of α particles per second in the above geometry that would strike a detector of area 0.5 cm^2 located 12.0 cm from the target.

14. The radioactive isotope ^{15}O, which has important medical applications (see Chapter 20), can be produced in the reaction $^{12}C(\alpha, n)$. (a) The cross section reaches a peak when the laboratory energy of the incident α particles is 14.6 MeV. What is the excitation energy of the compound nuclear state? (b) The reaction cross section at the above incident energy is 25 mb. Assuming a carbon target of 0.10 mg/cm^2 and a current of 20 nA of α's, compute the ^{15}O activity that results after 4.0 min of irradiation.

15. In a Coulomb excitation experiment, α particles are inelastically scattered from ^{160}Dy nuclei. (a) If the incident energy is 5.600 MeV, what is the energy of the elastically scattered α's observed at $\theta = 150°$? (b) States in ^{160}Dy are known at 2^+(0.087 MeV), 4^+(0.284 MeV), and 2^+(0.966 MeV). Considering only the $E2$ excitation mode, find the energies of the inelastically scattered α's observed at 150°.

16. What should be the incident energy of a beam of protons to be Coulomb scattered by gold nuclei, if it is desired that the minimum distance between projectile and target should correspond to the two nuclei just touching at their surfaces?

17. Alpha particles of energy 8.0 MeV are incident at a rate of 3.0×10^7 per second on a gold foil of thickness 4.0×10^{-6} m. A detector in the form of an annular ring is placed 3.0 cm from the scattering foil and concentric with the beam direction; the annulus has an inner radius of 0.50 cm and an outer radius of 0.70 cm. What is the rate at which scattered particles strike the detector?

18. Alpha particles of energy 6.50 MeV are Coulomb scattered by a gold foil. (a) What is the impact parameter when the scattered particles are observed at 90°? (b) Again for scattering at 90°, find the smallest distance between the α particles and the nucleus, and also find the kinetic and potential energies of the α particle at that distance.

19. Protons of energy 4.00 MeV are Coulomb scattered by a silver foil of thickness 4.0×10^{-6} m. What fraction of the incident protons is scattered at angles (a) beyond 90°? (b) Less than 10°? (c) Between 5 and 10°?

20. Derive Equations 11.49–11.51 for "black disk" scattering.

21. Give the compound nucleus resulting from protons bombarding an aluminum target, and give at least five different ways for the compound nucleus to decay.

22. For the states of ^{61}Cu populated in the (α, p) reaction, Figure 11.4, find the ℓ transfer for each of the states.

23. In the (d, p) reaction leading to states in ^{91}Zr, as shown in Figures 11.23 and 11.24, discuss the possible final angular momentum states if the reaction could proceed by a compound-nucleus mechanism. As an example, consider whether it still is possible to associate a final $I^{\pi} = \frac{7}{2}^{+}$ state uniquely with $\ell = 4$. Discuss other final states as well.

24. The low-lying levels of ^{43}Sc were illustrated in Figure 5.12. It is desired to populate the states up to the $\frac{7}{2}^{-}$ excited state with the (d, n) reaction. Estimate the most likely angle for the outgoing neutrons for each excited state. (Try to estimate the excited-state energies from the figure.)

25. The (d, p) reaction on ^{49}Ti ($\frac{7}{2}^{-}$ ground state) populates the "collective" 0^{+}, 2^{+}, and 4^{+} states at 0.000, 1.555, and 2.675 MeV (respectively) in ^{50}Ti. What are the angular momentum values transferred in the direct reaction?

26. The (^{3}He, p) reaction on an even-Z, even-N target leads to certain final states identified with the transfer of either $\ell = 0$, 2, or 4. (a) For each choice, list the possible spin-parity assignments in the final nucleus. (b) In some cases, the analysis suggests that certain states are populated by a mixture of $\ell = 0$ and $\ell = 2$, while others are populated by a mixture of $\ell = 2$ and $\ell = 4$. Is it possible to make a unique determination of the final spin in either of these cases?

27. The (d, p) reaction on ^{52}Cr leads to the $\frac{3}{2}^{-}$ ground state of ^{53}Cr. How would the analysis of the angular momentum transfer in this reaction differ between an analysis in terms of direct reactions and one in terms of compound-nucleus reactions?

12

NEUTRON PHYSICS

As the uncharged member of the nucleon pair, the neutron plays a fundamental role in the study of nuclear forces. Unaffected by the Coulomb barrier, neutrons of even very low energy (eV or less) can penetrate the nucleus and initiate nuclear reactions. In contrast, part of our lack of understanding of processes in the interior of stars results from the difficulty of studying proton-induced reactions at energies as low as keV. On the other hand, the lack of Coulomb interaction presents some experimental problems when using neutrons as a nuclear probe: energy selection and focusing of an incident neutron beam are difficult, and neutrons do not produce primary ionization events in detectors (neutrons passing through matter have negligible interactions with the atomic electrons).

The first experimental observation of the neutron occurred in 1930, when Bothe and Becker bombarded beryllium with α particles (from radioactive decay) and obtained a very penetrating but nonionizing radiation, which they assumed to be a high-energy γ ray. Soon thereafter, Curie and Joliot noticed that when this radiation fell on paraffin, an energetic proton was emitted. From the range of these protons, they determined their energy to be 5.3 MeV. If the radiation under study were indeed γ's, protons could be knocked loose from paraffin by a Compton-like collision; from the Compton-scattering formula, they computed that the energy of this "γ radiation" would be at least 52 MeV to release such protons. An emitted γ of such an energy seemed extremely unlikely. In 1932, Chadwick provided the correct explanation, identifying the unknown radiation as a neutral (therefore penetrating and nonionizing) particle with a mass nearly the same as that of the proton. Thus in a head-on collision, a 5.3-MeV neutron could transfer its energy entirely to the struck proton. Chadwick did additional recoil experiments with neutrons and confirmed his hypothesis, and he is generally credited with being the discoverer of the neutron.

The free neutron is unstable against β decay, with a half-life of 10.6 min. In nuclei, the bound neutron may be much longer-lived (even stable) or much shorter-lived. Despite the instability of free neutrons, their properties are measured to high precision, particularly the magnetic dipole moment, $\mu = -1.91304184 \pm 0.00000088\ \mu_N$, and the neutron-proton mass difference, $m_n - m_p = 1.29340 \pm 0.00003$ MeV.

Basic research with neutrons goes back almost to the earliest days of nuclear physics, and it continues to be a vital and exciting research field today. For example, interference effects with neutron beams have permitted some basic

aspects of quantum mechanics to be demonstrated for the first time. The *electric* dipole moment of the neutron should vanish if the neutron were an elementary particle or even a composite particle in which the binding forces were symmetric with respect to the parity and time-reversal operations. Many careful and detailed experiments have been done, and all indicate a vanishing electric dipole moment, but the limit has been pushed so low (10^{-25} e · cm) that it is almost possible to distinguish among certain competing theories for the interactions among the elementary particles. The so-called Grand Unified Theories that attempt to unify the strong (nuclear), electromagnetic, and weak (β-decay) interactions predict that the conservation of nucleon number (actually baryon number) can break down, and that a neutron could convert into its antiparticle, the antineutron, and then back again to a neutron. No evidence has yet been seen for this effect either, but current research is trying to improve the limits on our knowledge of the neutron-antineutron conversion frequency.

12.1 NEUTRON SOURCES

Beams of neutrons can be produced from a variety of nuclear reactions. We cannot accelerate neutrons as we can charged particles, but we can start with high-energy neutrons and reduce their energy through collisions with atoms of various materials. This process of slowing is called "moderating" the neutrons. The resulting neutrons can have very low energies, which by convention are given the following designations:

Thermal	$E \simeq 0.025$ eV
Epithermal	$E \sim 1$ eV
Slow	$E \sim 1$ keV
Fast	$E = 100$ keV–10 MeV

α-Beryllium Sources The reaction responsible for the discovery of the neutron can be used to produce a source of neutrons suitable for use in the laboratory. The stable isotope of beryllium, ^{9}Be, has a relatively loosely bound neutron (1.7 MeV binding energy). If a typical α particle from a radioactive decay (5–6 MeV) strikes a ^{9}Be nucleus, a neutron can be released:

$$^{4}\text{He} + {}^{9}\text{Be} \rightarrow {}^{12}\text{C} + \text{n}$$

The Q value for this reaction is 5.7 MeV. If we mix together a long-lived α-emitting material, such as ^{226}Ra, and ^{9}Be, there will be a constant rate of neutron production. From ^{226}Ra and its daughters there are α's emitted with energies from about 5 to nearly 8 MeV, and thus we find neutrons with an energy spectrum up to 13 MeV. The neutrons are not monoenergetic because of (1) the many α groups, (2) the slowing of α's that will occur by collision in any solid material, (3) the various directions of emission that can occur for the neutrons relative to the α's (whose direction we do not know), and (4) the possibility that ^{12}C is left in an excited state. The most probable neutron energy is about 5 MeV, and the neutron production rate is about 10^{7} neutrons per second for each Ci of ^{226}Ra. A typical neutron spectrum is shown in Figure 12.1.

Because of the high γ emission of ^{226}Ra and its daughters, the radium-beryllium neutron source has largely been replaced with sources using ^{210}Po (138 d),

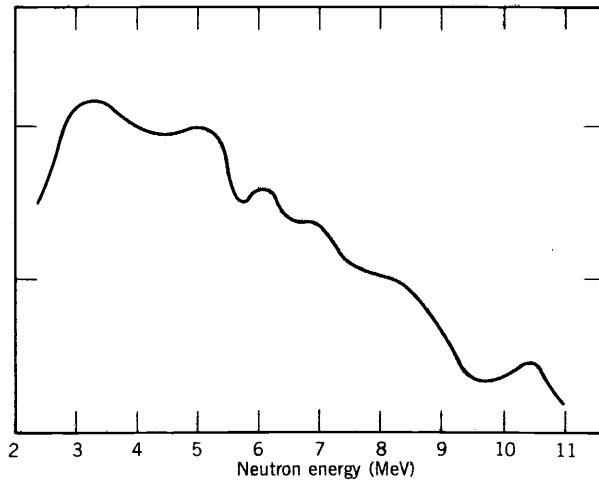


Figure 12.1 Neutron energy spectrum from a Ra-Be source, measured with a proton recoil counter. Several neutron groups are present; they result from reactions induced by α's with differing energies and in which the ^{12}C is left either in the ground state or the 4.43- or 7.6-MeV excited states.

^{238}Pu (86 y), and ^{241}Am (458 y). These sources produce about $2–3 \times 10^6$ neutrons per second per Ci of α activity.

Photoneutron Sources In a process similar to the (α, n) sources discussed above, we can use the (γ, n) reaction to produce neutrons. The advantage of photoneutron production is that we can make the neutrons more nearly monoenergetic, particularly if the photon source is nearly monoenergetic. For example, ^{24}Na emits a γ of 2.76 MeV, absorption of which would be sufficient to overcome the neutron binding energy of ^9Be:

$$\gamma + {}^9Be \rightarrow {}^8Be + n$$

The yield is acceptable (2×10^6 neutrons/s per Ci of ^{24}Na), but the half-life is short (15 h). The neutron energy is about 0.8 MeV. A longer-lived isotope ^{124}Sb (60 d) emits a strong γ whose energy just exceeds the ^9Be neutron binding energy; the emitted neutron has a much lower energy, about 24 keV.

Spontaneous Fission A common source of neutrons is the spontaneous fission of isotopes such as ^{252}Cf (2.65 y). Neutrons are produced directly in the fission process, at a rate of about 4 per fission. The fission occurs in only about 3% of the decays (α decay accounts for the rest), and the neutron production rate is 2.3×10^{12} neutrons/s per gram of ^{252}Cf or 4.3×10^9 n/s per Ci of ^{252}Cf. The neutron energies are characteristic of fission—a continuous distribution with an average energy of 1–3 MeV.

Nuclear Reactions There are of course many nuclear reactions that produce neutrons. These require an accelerator to produce a beam of particles to initiate the reaction, and thus they are not as convenient as the radioactive-decay type of sources discussed previously. However, by carefully selecting the incident energy and the angle at which we observe the emitted neutron, we can obtain a

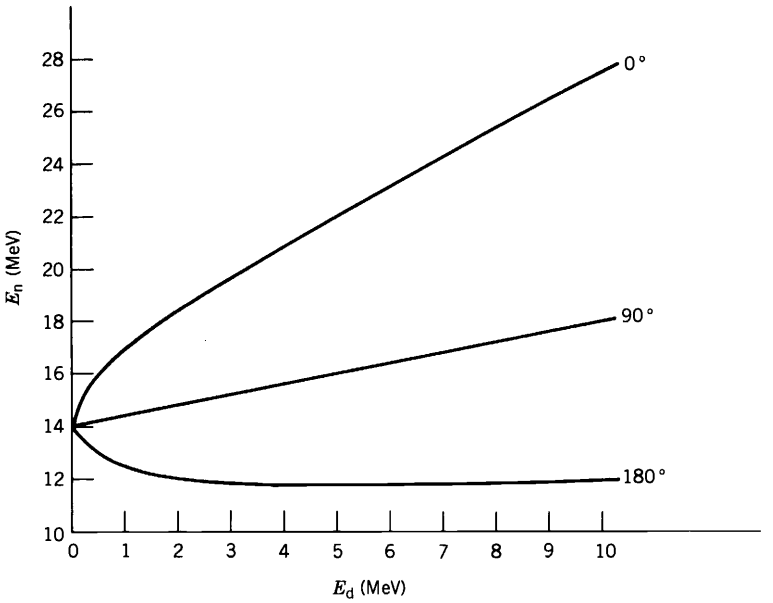


Figure 12.2 Neutrons emitted in the $^3H(d, n)^4He$ reaction.

reasonably monoenergetic beam of almost any desired energy. Some reactions that might be used are

$$^3H + d \rightarrow {}^4He + n \qquad Q = +17.6 \text{ MeV}$$
$$^9Be + {}^4He \rightarrow {}^{12}C + n \qquad Q = +5.7 \text{ MeV}$$
$$^7Li + p \rightarrow {}^7Be + n \qquad Q = -1.6 \text{ MeV}$$
$$^2H + d \rightarrow {}^3He + n \qquad Q = +3.3 \text{ MeV}$$

Figure 12.2 illustrates the dependence of the neutron energy in the first of these reactions on the incident energy and on the direction of the outgoing neutron.

Reactor Sources The neutron flux near the core of a nuclear fission reactor can be quite high—typically 10^{14} neutrons/cm^2/s. The energy spectrum extends to 5–7 MeV but peaks at 1–2 MeV. These neutrons are generally reduced to thermal energies within the reactor, but there are also fast neutrons present in the core. Cutting a small hole in the shielding of the reactor vessel permits a beam of neutrons to be extracted into the laboratory for experiments. The high neutron fluxes from a reactor are particularly useful for production of radioisotopes by neutron capture, as in neutron activation analysis.

12.2 ABSORPTION AND MODERATION OF NEUTRONS

As a beam of neutrons travels through bulk matter, the intensity will decrease as neutrons are removed from the beam by nuclear reactions. For fast neutrons, many reactions such as (n, p), (n, α), or (n, 2n) are possible, but for slow or thermal neutrons the primary cause of their disappearance is capture, in the form

of the (n, γ) reaction. Often the cross sections for these capture reactions are dominated by one or more resonances, where the cross section becomes very large. Off resonance, the cross section decreases with increasing velocity like v^{-1}; thus as the neutrons slow down (become moderated) due to elastic and inelastic scattering processes, absorption becomes more probable. Neutrons with initial energy in the 1-MeV range would undergo many scattering processes until their energies were reduced to the eV range, where they would have a high probability of resonant or nonresonant absorption.

In crossing a thickness dx of material, the neutrons will encounter $n\,dx$ atoms per unit surface area of the beam or the material, where n is the number of atoms per unit volume of the material. If σ_t is the total cross section (including scattering processes, which will tend to divert neutrons from the beam), then the loss in intensity I is

$$dI = -I\sigma_t n\,dx \tag{12.1}$$

and the intensity decreases with absorber thickness according to an exponential relationship:

$$I = I_0 e^{-\sigma_t n x} \tag{12.2}$$

Keep in mind that this expression refers only to monoenergetic neutrons—the original intensity of neutrons of a certain energy decreases according to Equation 12.2. Of course, we may at the same time be creating neutrons of lower energy (by scattering, for example), which may have a very different cross section, but this effect is not included in Equation 12.2. We therefore cannot use it reliably to calculate the decrease in the *total number* of neutrons, only the change in intensity of those with a given initial energy.

Let's consider an elastic collision between a neutron of initial energy E and velocity v with a target atom of mass A initially at rest. Elementary application of the laws of conservation of energy and linear momentum gives the ratio between the final neutron energy E' and the initial energy:

$$\frac{E'}{E} = \frac{A^2 + 1 + 2A\cos\theta}{(A+1)^2} \tag{12.3}$$

where θ is the scattering angle in the center-of-mass system (but E and E' are measured in the laboratory system). For no scattering ($\theta = 0$), Equation 12.3 gives $E'/E = 1$, as it should. The maximum energy loss occurs for a head-on collision ($\theta = 180°$):

$$\left(\frac{E'}{E}\right)_{\min} = \left(\frac{A-1}{A+1}\right)^2 \tag{12.4}$$

Notice that for $A = 1$ (scattering from hydrogen), the neutron gives all its energy to the struck proton.

For neutron energies of about 10 MeV and below, the scattering is mostly s wave and thus (in the center-of-mass system) largely independent of θ. The values of E'/E are uniformly distributed between $E'/E = 1$ and the minimum value given by Equation 12.4, as shown in Figure 12.3*a*.

Because each neutron will scatter many times, we must repeatedly calculate the energy loss. In the case of the second scattering, the incident neutrons are no

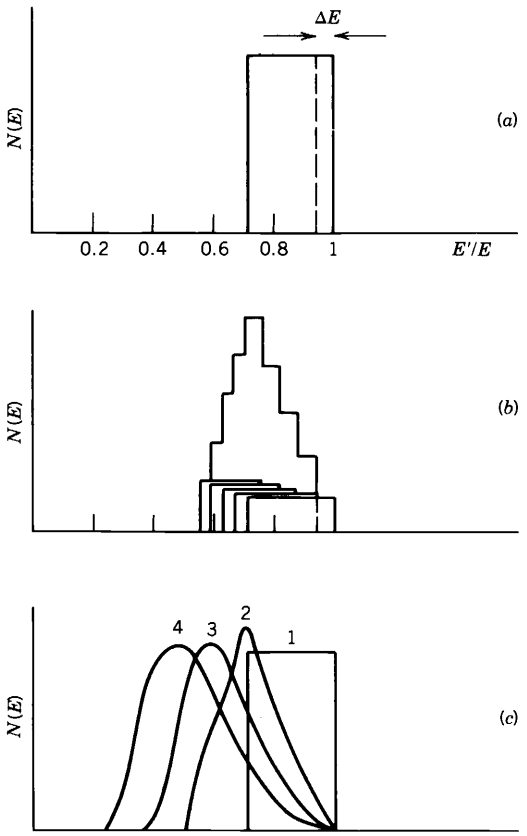


Figure 12.3 (*a*) A monoenergetic neutron of energy E gives, after a single s-wave scattering from ^{12}C, a flat distribution of laboratory energies E' from $0.72E$ to E. (*b*) Dividing the scattered distribution into five narrow, nearly monoenergetic distributions of width ΔE, we get after a second scattering the five flat distributions shown, whose sum is the peaked distribution. (*c*) An exact calculation of the energy distribution after 1, 2, 3, and 4 scatterings.

longer monoenergetic but rather are distributed as in Figure 12.3*a*. We can approximate this effect by considering each interval of width ΔE to be a new generation of approximately monoenergetic neutrons giving the result shown in Figure 12.3*b*. Continuing this process, we obtain the succeeding "generations" of energy distributions shown in Figure 12.3*c*.

To make the calculations more quantitative, we define the parameter ξ to represent the average value of $\log(E/E')$ after a single collision:

$$\xi = \left[\log \frac{E}{E'}\right]_{\text{av}} \tag{12.5}$$

$$= \frac{\int \log\left[\dfrac{(A+1)^2}{A^2+1+2A\cos\theta}\right] d\Omega}{\int d\Omega} \tag{12.6}$$

Table 12.1 Moderating Properties of Various Nuclei

Nucleus	ξ	n (for thermalization)
^{1}H	1.00	18
^{2}H	0.725	25
^{4}He	0.425	43
^{12}C	0.158	110
^{238}U	0.0084	2200

where $d\Omega$ is the element of solid angle in the center-of-mass system. Here again we assume the scattering to be isotropic. Carrying out the integration gives

$$\xi = 1 + \frac{(A-1)^2}{2A} \log \frac{A-1}{A+1} \tag{12.7}$$

The average value of log E' is decreased after each collision by an amount ξ, and after n collisions, the average value of log E' is log E'_n:

$$\log E'_n = \log E - n\xi \tag{12.8}$$

which follows directly from Equation 12.5.

Table 12.1 shows values of ξ for some commonly used moderators. If our goal is to reduce the average neutron energy from that which is typical for neutrons emitted in fission ($E \sim 2$ MeV) to that which is characteristic of thermal motion ($E'_n \sim 0.025$ eV), the number of generations of collisions is shown in Table 12.1.

The previous calculation has assumed the atoms from which the neutrons scatter to be at rest. This is certainly a good approximation for MeV neutrons, but as thermal energies are approached, we find the thermal motion of the atoms of the moderator to be comparable to the speeds of the neutrons. The scattering in this case is better analyzed using statistical mechanics, and we can simply assume that after a sufficient time the neutrons will reach thermal equilibrium with the moderator at a temperature T. In this case, the neutrons are described by a Maxwellian speed distribution:

$$f(v)\,dv = 4\pi n \left(\frac{m}{2\pi kT}\right)^{3/2} v^2 e^{-mv^2/2kT}\,dv \tag{12.9}$$

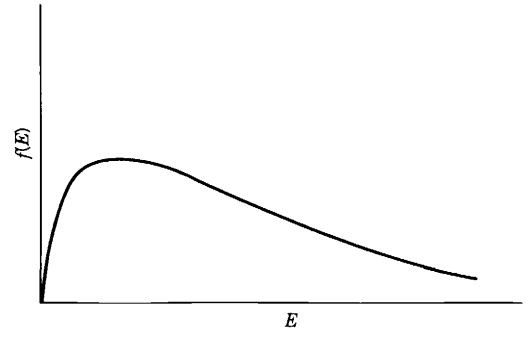


Figure 12.4 Maxwellian energy distribution, a representation of the neutron energy spectrum after many scatterings.

where $f(v)\,dv$ gives the fraction of neutrons with speeds between v and $v + dv$. Here m is the neutron mass and n is the total number of neutrons per unit volume. Rewriting this in terms of energy gives

$$f(E)\,dE = \frac{2\pi n}{(\pi kT)^{3/2}} E^{1/2} e^{-E/kT}\,dE \tag{12.10}$$

which is illustrated in Figure 12.4 and looks similar to Figure 12.3*c*, showing the thermalizing effect of even a few generations of collisions.

12.3 NEUTRON DETECTORS

Because neutrons produce no direct ionization events, neutron detectors must be based on detecting the secondary events produced by nuclear reactions, such as (n, p), (n, α), (n, γ), or (n, fission), or by nuclear scattering from light charged particles, which are then detected.

For slow and thermal neutrons, detectors based on the (n, p) and (n, α) reactions provide a direct means for observing neutrons from the signal left by the energetic p or α resulting from the reaction. The isotope ^{10}B is commonly used, by producing an ionization chamber or a proportional counter filled with BF_3 gas or lined with boron metal or a boron compound. The reaction is

$$^{10}\mathrm{B} + \mathrm{n} \rightarrow {}^{7}\mathrm{Li}^{*} + \alpha$$

where the ^{7}Li is preferentially left in an excited state with energy 0.48 MeV. (Natural boron consists of about 20% of the isotope ^{10}B, so materials enriched in ^{10}B increase the efficiency of the detector.) For thermal neutrons, the cross section is about 3840 b, a very large value, and the cross section follows the $1/v$ law up to about 100 keV, so the dependence of cross section on incident energy is featureless (no resonances are present) and predictable (Figure 12.5).

There is also another advantage of the $1/v$ dependence of the cross section. Suppose we are observing a collimated beam of neutrons or an isotropic flux (perhaps near the core of a reactor) that has a velocity distribution of $n(v)\,dv$ neutrons per unit volume with speeds between v and $v + dv$. The flux passing through the detector will be $n(v)v\,dv$, and if the counter contains N boron nuclei each with cross section σ, the probability per second of an interaction (or counting rate, if we are able to detect and count every interaction) is

$$dR = N\sigma n(v)v\,dv \tag{12.11}$$

for neutrons of speeds between v and $v + dv$. For neutrons of all speeds, the total counting rate is

$$R = \int N\sigma n(v)v\,dv \tag{12.12}$$

$$= NC\int n(v)\,dv \tag{12.13}$$

where the last step assumes that $\sigma \propto v^{-1}$, so that the product σv is the constant C. The integral then gives the total number of neutrons per unit volume n, and

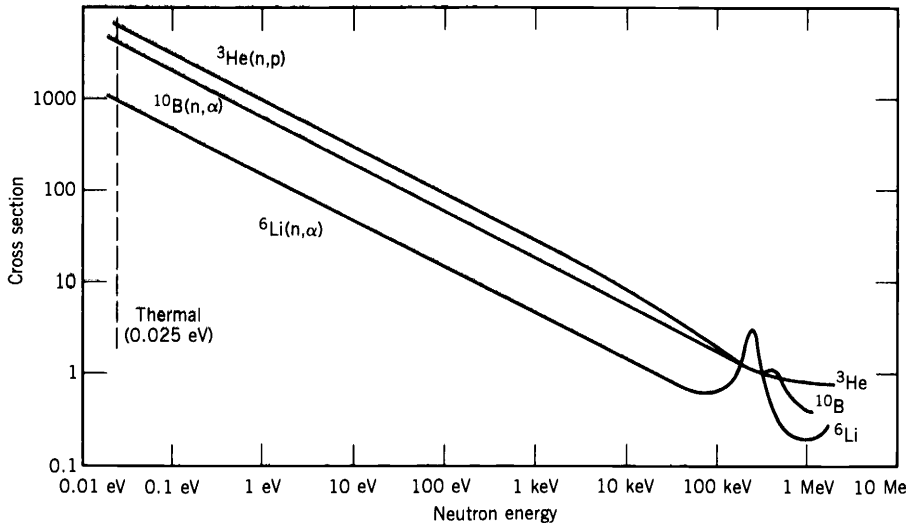


Figure 12.5 Neutron cross sections for ^{3}He(n, p), ^{10}B(n, α), and ^{6}Li(n,α). The cross section shows the $1/v$ behavior for $E < 1$ keV, but begins to show resonances above 100 keV.

the counting rate is

$$R = NCn \tag{12.14}$$

That is, R is directly proportional to the neutron density for *any distribution of velocities* as long as we can neglect any contributions to the neutron flux outside the $1/v$ region of cross section.

The Q value for the reaction leading to the ^{7}Li excited state is 2.31 MeV, and for incident neutrons of kinetic energy small compared with this value, momentum conservation requires the sharing of energy between ^{7}Li and α so that the α is given a kinetic energy of 1.47 MeV. The kinetic energy of the incident neutron, if it is in the eV or even keV range, will not substantially modify this value. Unless either particle strikes the wall, we will detect simultaneously the ^{7}Li ($T = 0.84$ MeV) as well, and the neutron then leaves as its signature a 2.31-MeV energy loss in the counter. Because we cannot measure MeV energies to eV or keV precision in a proportional counter, we cannot use such a device to measure such low neutron energies.

Other similar devices are based on ^{6}Li (n, α), with $Q = 4.78$ MeV and $\sigma = 940$ b for thermal neutrons, and ^{3}He (n, p), with $Q = 0.765$ MeV and $\sigma = 5330$ b. A comparison of the neutron cross sections for these reactions is shown in Figure 12.5.

Another way of measuring neutron intensities is by exposing to the neutrons a material which becomes radioactive after neutron capture and which has a known capture cross section for neutrons of a particular energy. If we remove the material from the neutron flux and measure the induced radioactivity (using a γ-ray detector, for example), we can determine the neutron flux.

Among the earliest devices used for determining neutron energies were mechanical devices, for example the velocity selector, a rotating shutter made of a highly absorbing material, such as Cd for thermal neutrons (Figure 12.6). This

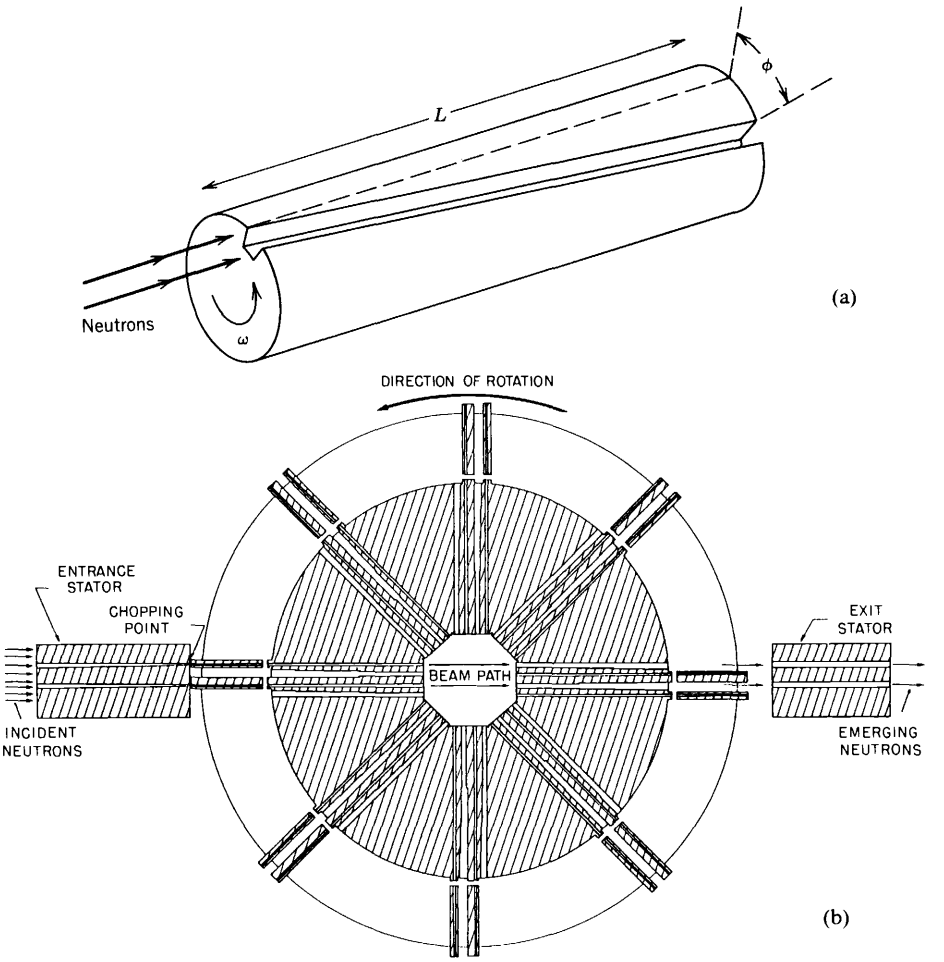


Figure 12.6 (*a*) Neutron velocity selector, consisting of a rotating cylinder with one or more helical slots cut into its surface. The cylinder is made of a material, such as cadmium, with a high absorption for neutrons. The selector will pass neutrons of velocity v that travel the length L of the cylinder in the time that it takes it to rotate through the angle ϕ; that is, $t = L/v = \phi/\omega$, so that $v = L\omega/\phi$. Changing the angular speed ω permits selection of the neutron velocity. (*b*) Rotating shutter or "chopper" for producing pulses of neutrons. A continuous stream of neutrons enters from the left and a pulse of neutrons emerges at right if the rotor slits line up with the entrance slits. The rotor is made of stainless steel with phenolic slits. From R. E. Chrien, in *Neutron Sources for Basic Physics and Applications*, edited by S. Cierjacks (Oxford: Pergamon, 1983).

device is practical only for velocities in the thermal region, but it can be used to select neutrons from the continuous velocity distribution such as is produced by a reactor.

Another way of measuring velocities is through a variant of the time-of-flight technique (see Section 7.9 and Figure 7.39). If we have neutrons in a short pulse, we can time their travel over a distance of several meters (thermal neutrons have

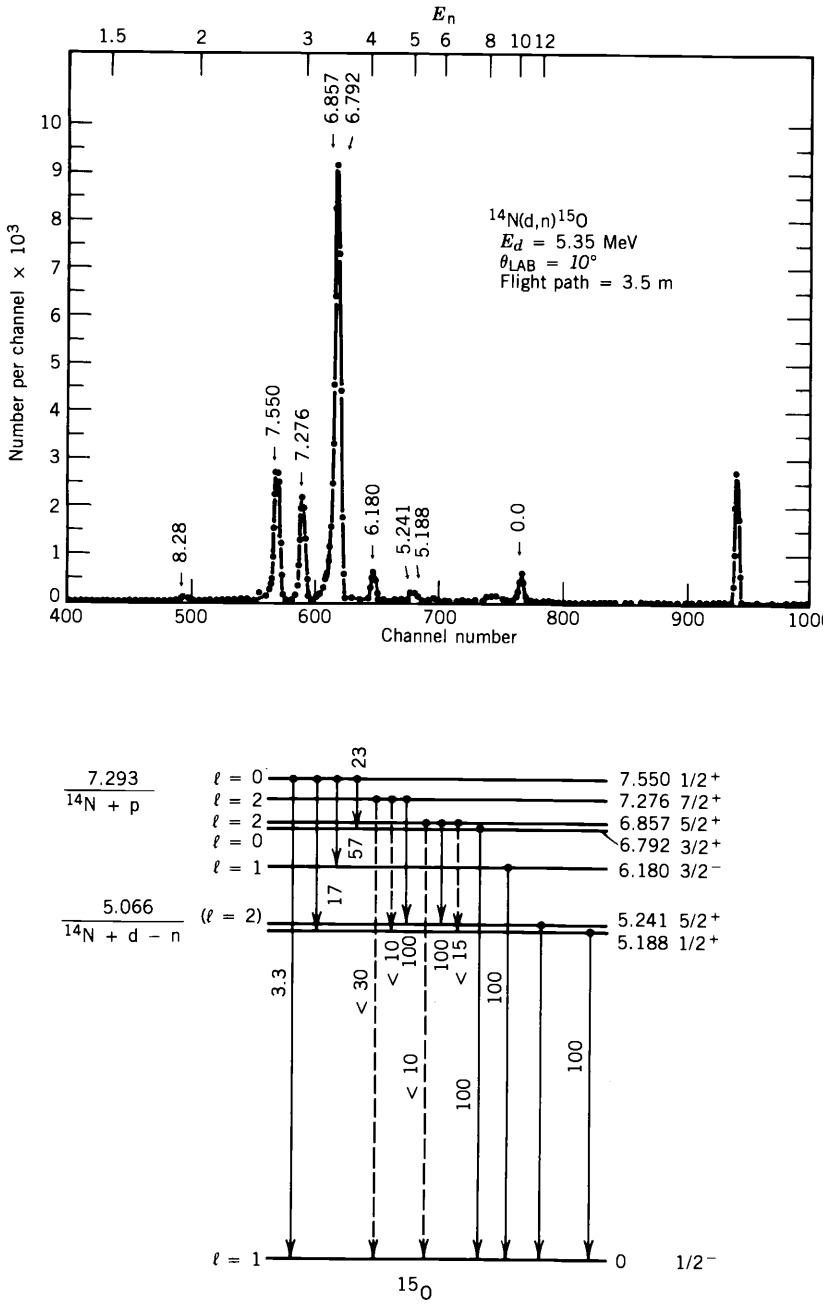


Figure 12.7 Time-of-flight spectrum of neutrons emitted in the reaction ^{14}N(d, n)^{15}O. Timing was done with reference to a pulsed beam of deuterons. The peak at far right comes from γ rays, which of course travel at the highest possible speed. The neutron peaks correspond to the ground and excited states of ^{15}O, as shown. The ℓ values come from measurement of the angular distribution of the cross section, or $d\sigma/d\Omega$. From R. C. Ritter, E. Sheldon, and M. Strang, *Nucl. Phys.* *A* **140**, 609 (1970).

$v = 2200$ m/s, and the time of travel is thus an easily measurable 10^{-3} s). For higher energies, longer flight paths of order 100 m and increased sensitivity of short-timing techniques can give accurate velocity measurements for neutrons up to MeV energies.

The initial pulse of neutrons for a timing measurement can be provided by a "chopper" of the kind shown in Figure 12.6, or else by a pulsed charged-particle accelerator, in which the neutrons are produced through reactions such as those listed in Section 12.1. If the initial pulse includes a wide range of velocities, the start-stop technique using a time-to-amplitude converter can display the energy spectrum of the neutrons, as in Figure 12.7.

Very precise energy determinations can be done in the thermal region using crystal diffraction. Thermal neutrons have a de Broglie wavelength of about 0.1 nm, about the same as the spacing between atoms in a crystal lattice. If a beam of thermal neutrons is incident on a crystal, the wave nature of the beam will be revealed through a set of interference maxima that occur at angles determined by the Bragg condition:

$$n\lambda = 2d \sin \theta \tag{12.15}$$

where d is the lattice spacing, n the order of the interference maximum, and θ the angle the incident and reflected beams make with the surface of the crystal. This technique, which is used frequently to study the crystalline properties or atomic spacing of materials, is discussed in Section 12.6.

For measurement of the energies of fast neutrons, the most common method is to use the recoil following elastic scattering between the neutron and a light target (H, ^{2}H, ^{3}He, ^{4}He, etc.). This elastic scattering was previously discussed in Section 12.2 in connection with neutron moderation, and we can use the results derived in that section. In the discussion following Equation 12.4, we showed that the scattered neutron has a continuous range of energies from $E' = E$ down to the minimum value given by Equation 12.4. The struck nucleus has a corresponding recoil energy

$$E_R = E - E' \tag{12.16}$$

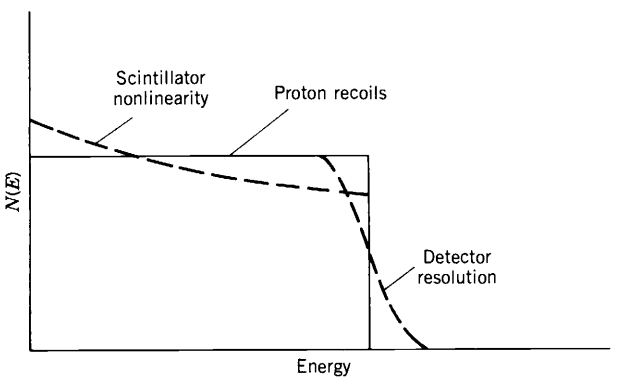


Figure 12.8 An ideal spectrum of proton recoils (from monoenergetic incident neutrons) can be distorted by detector resolution and scintillator nonlinearity.

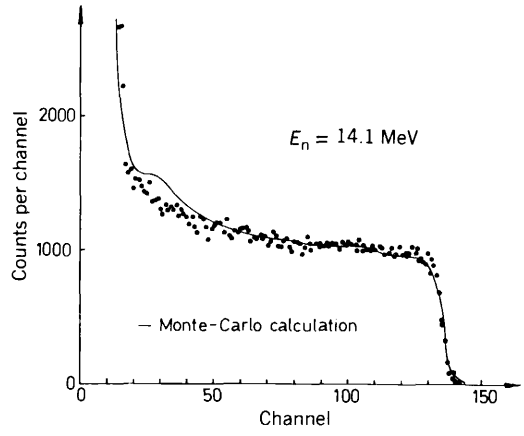


Figure 12.9 Spectrum of monoenergetic 14-MeV neutrons observed in an organic scintillator. From M. Bormann et al., *Nucl. Instrum. Methods* **88**, 245 (1970).

ranging from zero up to a maximum

$$(E_R)_{max} = E - (E')_{min}$$

$$= E\frac{4A}{(A+1)^2} \tag{12.17}$$

For hydrogen, $(E_R)_{max} = E$, while for ^{3}He, $(E_R)_{max} = 0.75E$. The response of an ideal proton recoil detector to monoenergetic neutrons is shown in Figure 12.8.

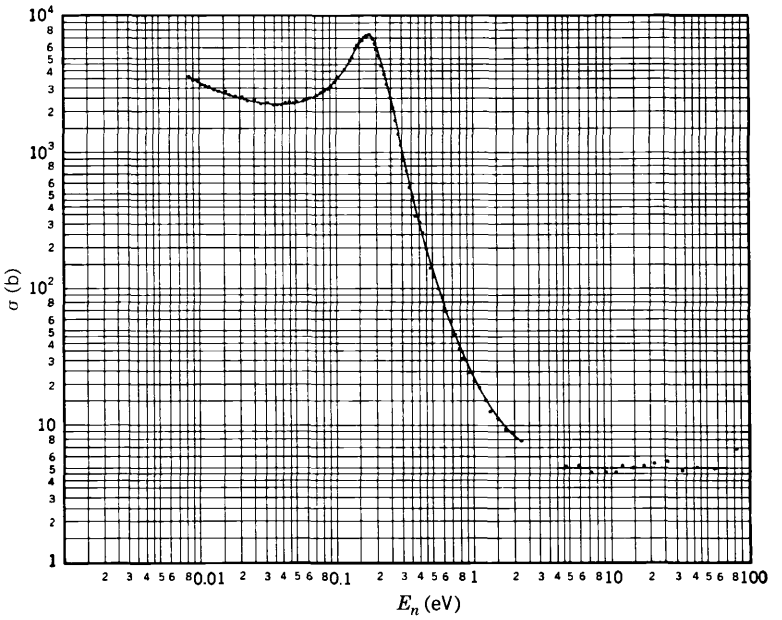
The proton recoil signal is normally observed by using a scintillating material that is rich in hydrogen, such as plastic or an organic liquid. The scintillator therefore serves as both the proton target for the neutron and the detector for the recoiling proton. Taking into account the energy resolution of the scintillator and geometrical effects, the observed energy spectrum for monoenergetic neutrons looks like the continuous distribution shown in Figure 12.9. If the incident neutrons have several distinct energy components, the unfolding of the superimposed spectra of recoils may be difficult.

The efficiency of proton-recoil scintillation detectors for MeV neutrons can be of the order of 50%.

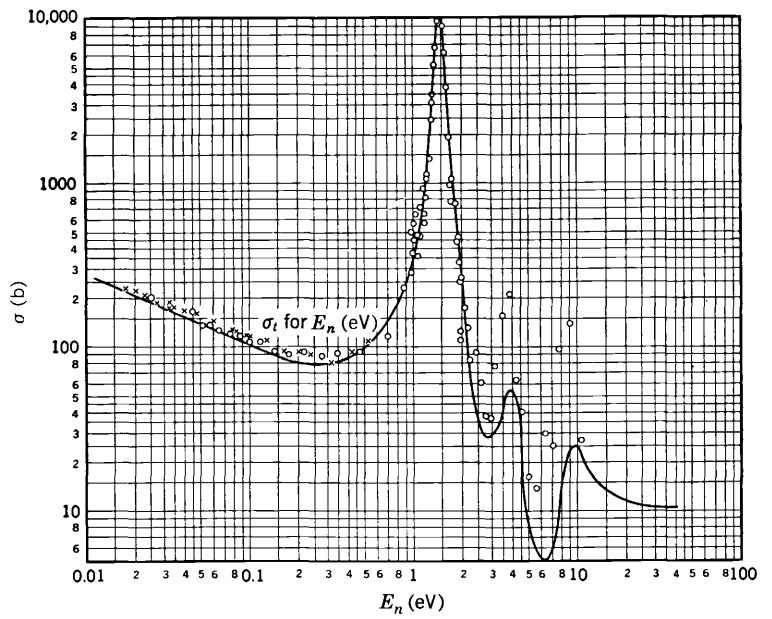
12.4 NEUTRON REACTIONS AND CROSS SECTIONS

The formalism for analyzing nuclear reactions has already been discussed in Chapter 11. In this section we give some examples of applications to neutron-induced reactions and show the specific aspects of nuclear structure that can be probed.

Let's first consider the $1/v$ dependence of the low-energy neutron cross section. We can obtain this result using two very different approaches. In Section 11.8, we obtained an estimate for the reaction cross section, Equation 11.50, of



(a)



(b)

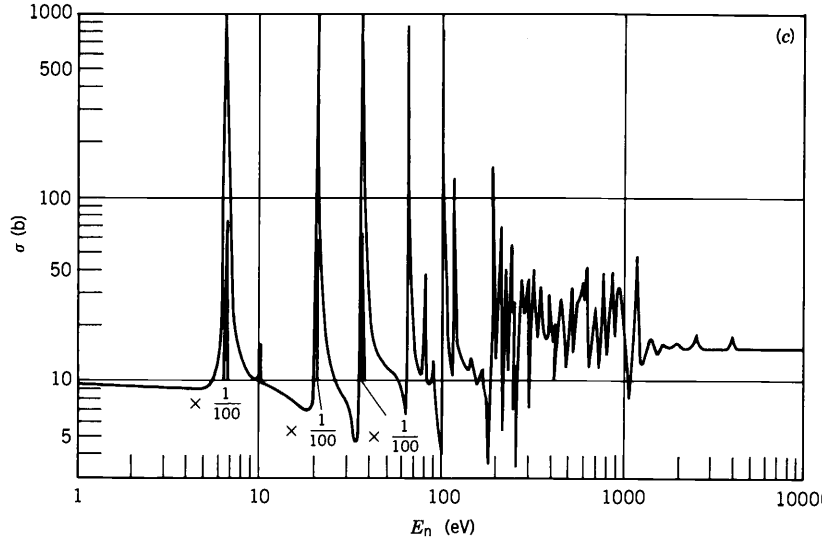
Figure 12.10 Resonances in neutron total cross sections. (*a*) A single isolated resonance superimposed on a $1/v$ background in Cd. (*b*) Several close-lying resonances in In. (*c*) Many sharp peaks in the resonance region in ^{238}U. (*d*) In ^{32}S, the relative heights of the resonance peaks are indications of the spin of the resonances. *Sources*: (*a*), (*b*) H. H. Goldsmith et al., *Rev. Mod. Phys.* **19**, 259 (1947); (*c*) D. J. Hughes and R. B. Schwartz, Brookhaven National Laboratory Report BNL 325 (1958); (*d*) J. M. Blatt and V. F. Weisskopf, *Theoretical Nuclear Physics* (New York: Wiley, 1952).

$\sigma_r = \pi(R + \lambda\!\!\!^{-})^2$ based on a total absorption model. A primary modification to this estimate would include the reflection of the incident neutron wave function at the nuclear surface—how likely is it that the incident particle will penetrate to the region of nuclear potential, where it can be absorbed?

The transmission probability for a rectangular potential barrier was calculated in Section 2.3, and including this factor the cross section is estimated as

$$\sigma = \pi(R + \lambda\!\!\!^{-})^2 \frac{4kK}{(k + K)^2} \tag{12.18}$$

where $K = \sqrt{2m(E + V_0)/\hbar^2}$ for a barrier of depth $-V_0$, and $k = \sqrt{2mE/\hbar^2}$.



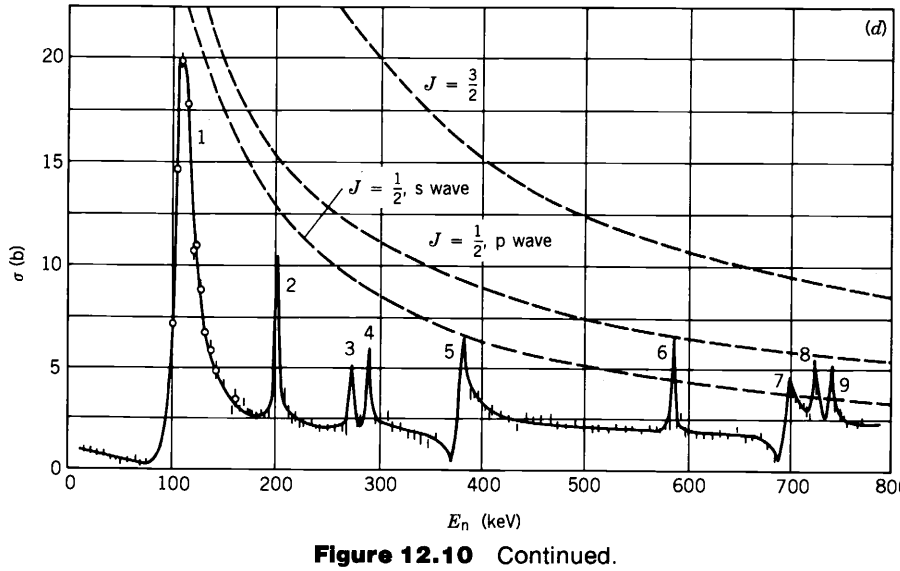


Figure 12.10 Continued.

For low-energy neutrons, $E \ll V_0$ and $k \ll K$; also $\lambda\!\!\!^{-} = k^{-1} \gg R$, so

$$\sigma \cong \frac{4\pi}{kK} \tag{12.19}$$

and since $k = p/\hbar = mv/\hbar$, we have the $1/v$ dependence of the cross section.

A similar result can be obtained from quite another approach, using the single-level resonance formula, Equation 11.70. Following neutron capture, the primary decay mechanism is γ emission, the probability for which is virtually independent of any small variation in the resonance or incident energy. We can therefore take Γ as independent of the neutron energy. The neutron width Γ_n, which refers to the entrance channel, is dependent on the density of final states dn/dE available to the captured neutron, which according to Equation 9.15 is proportional to the velocity of the neutron. (This is somewhat similar to α decay, in which the decay probability includes a factor proportional to v that originates from considering the frequency with which the α particle presents itself to the nuclear barrier in preparation for decay.) Far from the resonance, $E \ll E_R$ and

$$\sigma \cong \frac{\pi}{k^2} \frac{\Gamma_n \Gamma}{E_R^2 + \Gamma^2/4} \propto \frac{1}{v} \tag{12.20}$$

when $\Gamma_n \propto v$.

As indicated by the cross sections plotted in Figure 12.5, the $1/v$ law is followed quite accurately for reactions far from the resonance region.

In the resonance region there is no exact theory for predicting the location of the resonances; the structure may be dominated by a single, isolated resonance (as in Cd, Figure 12.10*a*), or a complex structure (as in In and U, Figures 12.10*b*

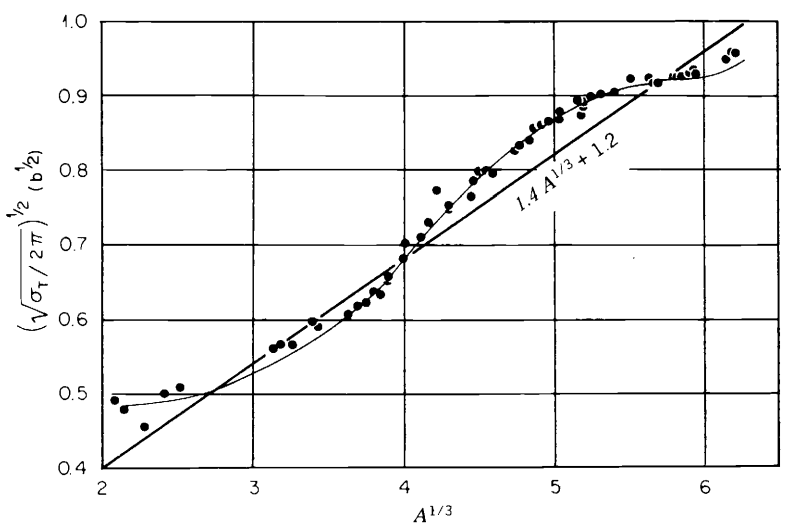


Figure 12.11 Total cross section for 14-MeV neutrons, plotted against $A^{1/3}$. The straight line represents $R + \lambda\!\!\!^{-} = 1.4A^{1/3} + 1.2$ fm, and it fits the data reasonably well. The curve through the data points is an improved calculation using the optical model. From G. R. Satchler, *Introduction to Nuclear Reactions* (Halstead: New York, 1980).

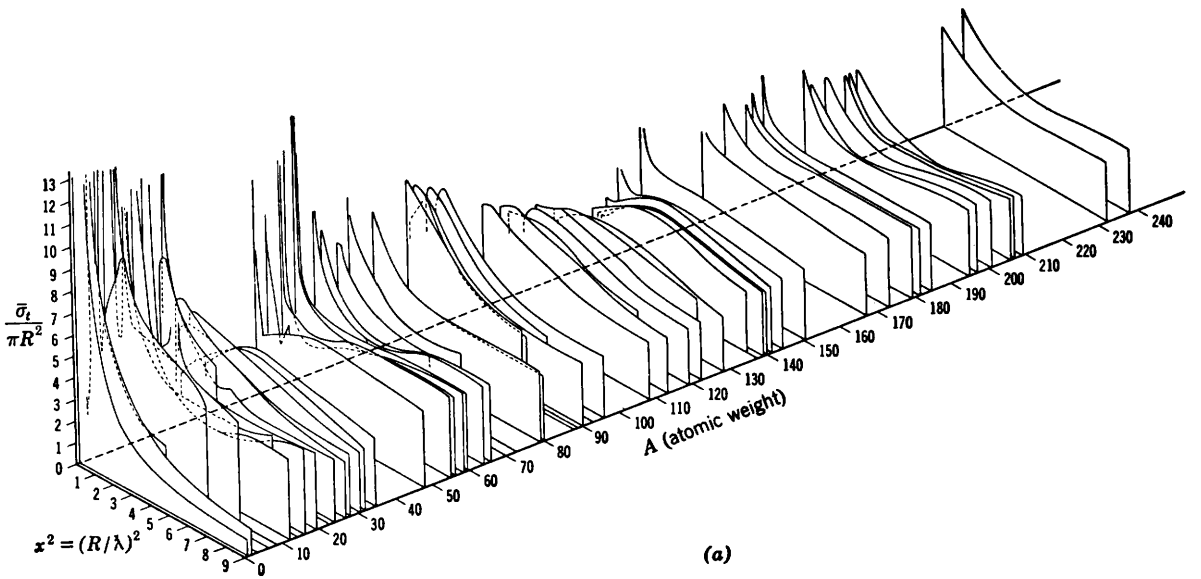


Figure 12.12 The total cross section, in units of πR^2, for neutrons of various energies (x^2 is an energy parameter in dimensionless form). The top curves (*a*) represent experimental results, and the bottom curves (*b*) are the results of calculations using the optical model.

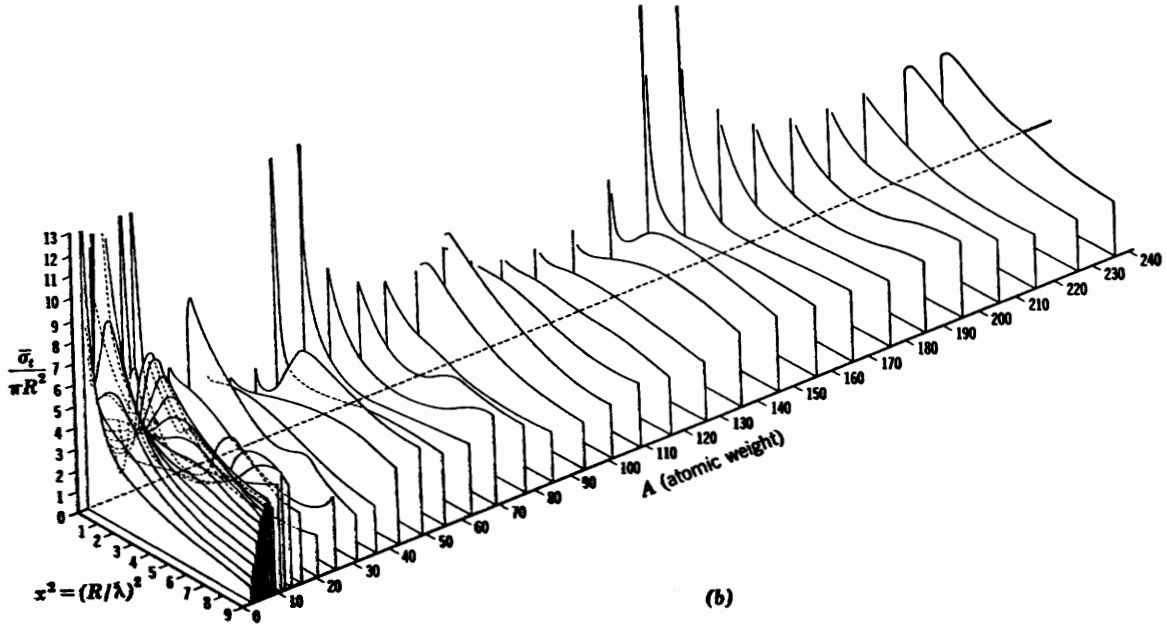


Figure 12.12 Continued.

and c). In some cases, the intensity of a resonance can be used to determine its spin. For instance, in the resonance structure of ^{32}S (which is an even-even, spin zero nucleus), s-wave capture leads to a resonance with total spin $I = \frac{1}{2}$ (from the intrinsic spin of the neutron). P-wave capture can give $I = \frac{1}{2}$ or $\frac{3}{2}$, depending on whether the ℓ and the s of the neutron are antiparallel or parallel. The relationship between the cross section at resonance and ℓ is slightly more complicated than the $(2\ell + 1)$ dependence predicted in Equation 11.47, but the general effect of the increase in cross sections is apparent.

As we move to higher incident energies, the microscopic properties become less important because the observed structure often represents an average over many overlapping resonances. An indication of the applicability of an average property is obtained from the geometrical estimate for the *total* cross section, Equation 11.51. Figure 12.11 shows the quantity $(\sigma_t/2\pi)^{1/2}$ plotted to show $R + \lambda\!\!\!^{-}$, where $R = R_0 A^{1/3}$ and $\lambda\!\!\!^{-} = 1.2$ fm for 14-MeV neutrons. The radius R_0 is taken as 1.4 fm, somewhat larger than the usual estimate of 1.25 fm because it takes into account the skin thickness of the nuclear interaction.

The variations of the total cross section with energy and with A are indicated by Figure 12.12. We can use the optical model (Section 11.9) to calculate the neutron total cross section for these nuclei, with the results also shown in Figure 12.12. The agreement with the observed gross structure is reasonably good.

12.5 NEUTRON CAPTURE

Figure 12.13 shows some of the processes that can occur following neutron capture. Although it is of course possible to re-emit the neutron, for heavy nuclei and very low energy incident neutrons this mode of decay of the compound or resonant state is suppressed, and γ emission is the most probable decay process.

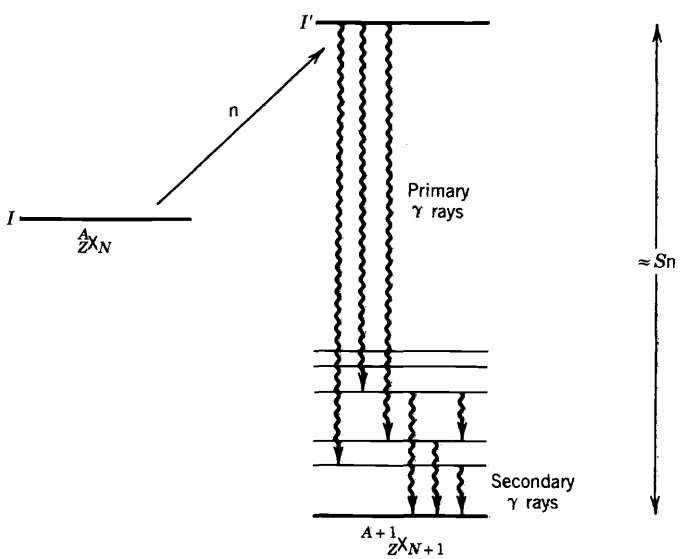


Figure 12.13 Low-energy neutron capture leads to a state I', which emits primary γ rays followed by secondary γ rays.

(Charged-particle emission is inhibited by the Coulomb barrier and unlikely to occur in any but the very lightest nuclei.) The excitation energy E_x of A' is just $S_n + E_n$, the neutron separation energy plus the energy of the incident neutron. For low-energy neutrons, E_x is typically 5–10 MeV.

Neutron capture reactions can be used to determine the energy and spin-parity assignments of the capturing states. Let's assume the original nucleus had spin I and parity π (+ or −). The spin I' of the capturing state is determined by the neutron orbital angular momentum ℓ and spin angular momentum s added to that of the target nucleus:

$$I' = I + \ell + s \tag{12.21}$$

and the parities are related by

$$\pi' = \pi(-1)^{\ell} \tag{12.22}$$

For incident neutrons in the thermal range of energies, only s-wave capture will occur, for which $I' = I \pm \frac{1}{2}$ (excepting $I = 0$, in which case $I' = \frac{1}{2}$ only) and $\pi' = \pi$.

The capture state can usually be treated as a compound-nuclear state, that is, as many unresolved individual levels having $I' = I + \frac{1}{2}$ and $I' = I - \frac{1}{2}$. Occasionally, the capture may be dominated by one or a few resonances, and in certain selected cases it is possible to populate only only the $I' = I + \frac{1}{2}$ or $I' = I - \frac{1}{2}$ resonances by aligning the spins of the target nuclei either parallel or antiparallel to the neutron spins.

In the γ decay of the capture state, all excited states of A' can be populated to some extent, limited only by the selection rules for γ radiation. For dipole radiation, the maximum change in spin is one unit, and thus the primary radiation (that which comes directly from the capture state) reaches states with spins from $I' + 1$ to $I' - 1$. Taking into account the relationship between I' and I, the excited states populated by the primary radiation will have spins ranging from $I - \frac{3}{2}$ to $I + \frac{3}{2}$ (except for $I \leq 1$). For dipole radiation, the emission probability is proportional to E_γ^3, as in Equation 10.12. It is therefore most likely to observe the highest energy transitions, that is, those that populate the lowest excited states. The γ spectrum therefore shows two principal components: the *primary* component, consisting of direct 5–10-MeV radiations from the capture state to lower excited states, usually below 2 MeV, and the *secondary* component, consisting of low-energy radiations between the low-lying excited states.

Electric dipole primary radiation is roughly 100 times more likely than magnetic dipole, and so it is most likely to populate lower excited states whose parity is opposite to that of the capture state. However, magnetic dipole radiation is often present, as is radiation of multipole order higher than dipole; these radiations are usually far less intense than the electric dipole radiation.

One of the useful features in studying neutron capture γ rays is that the primary radiation is almost completely unselective in populating the lower excited states—no strong selection rules based on nuclear structure will forbid primary decays to any particular excited state. Thus if, for instance, the capture state has $I' = 4$, we expect dipole radiation to populate directly *all* spin 3, 4, and 5 states. This is in contrast to α or β decay, in which the emission process is governed by selection rules which may forbid decays to states that, considering

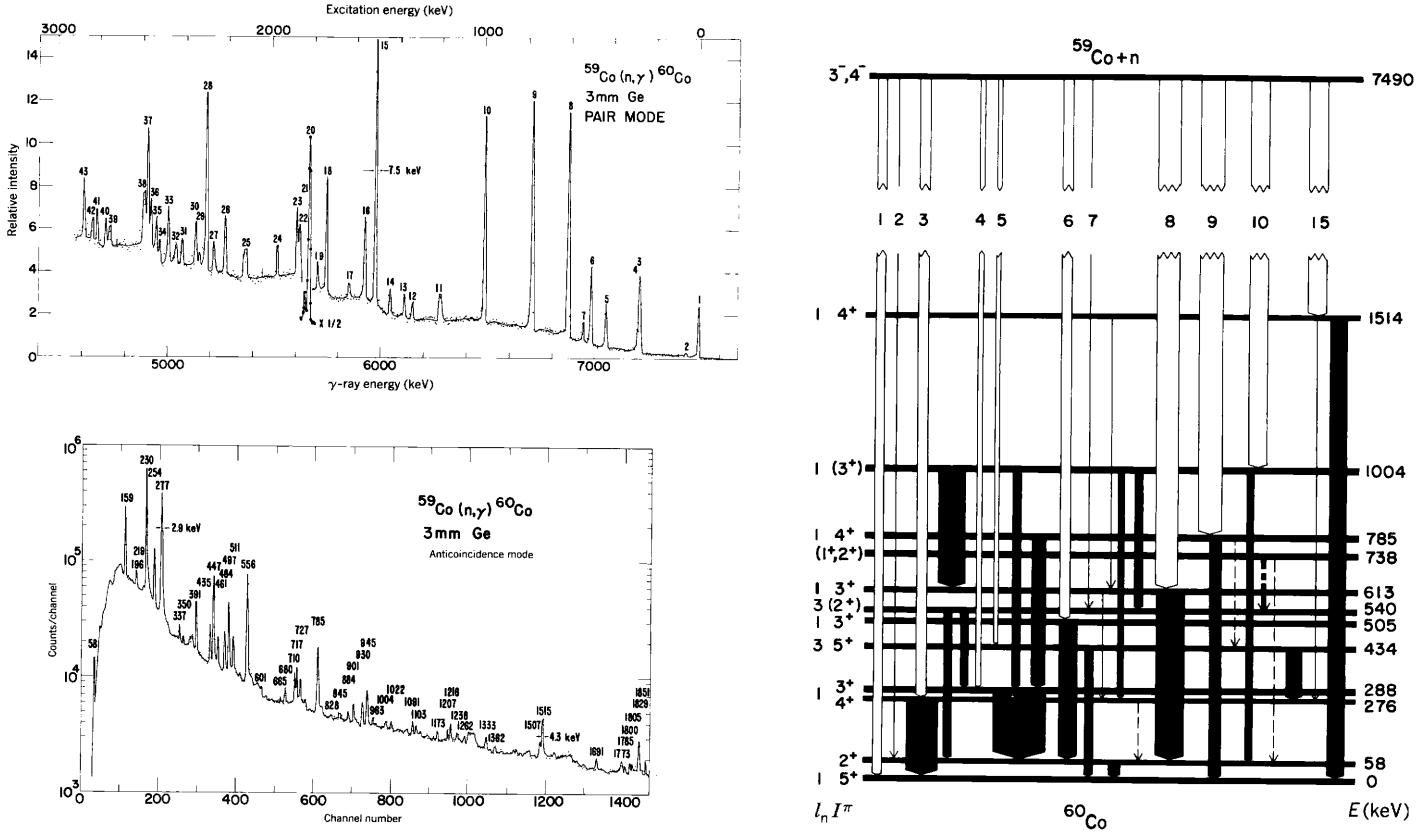


Figure 12.14 Gamma rays following thermal neutron capture by ^{59}Co. (Top left) Primary transitions from the capture state, shown in white on the level scheme at right. (Bottom left) Secondary transitions between the low-lying excited states, shown in black at right. Because ^{59}Co has spin $\frac{7}{2}$ and negative parity, the capture state must be a combination of spin-parity 3^- and 4^-. Electric dipole primary transitions will populate only low-lying 2^+, 3^+, 4^+, and 5^+ states, as shown. No primary transition leading to the 1^+ state at 738 keV is expected, and none is observed. Because the capture state is mostly 4^-, the 2^+ states are only weakly populated (the thickness of the lines at right is proportional to the transition intensity); note transitions number 2 and 7. Data from E. B. Shera and D. W. Hafemeister, *Phys. Rev.* **150**, 894 (1966).

angular momentum couplings only, we might expect to be populated. Neutron capture can therefore serve as a rather *complete* means of spectroscopy of excited states—if we can only unravel what must be a very complicated spectrum of radiations, we should be able to learn a great deal about the number and location of excited states.

Figure 12.14 shows an example of the primary and secondary γ radiations emitted following neutron capture, including the detailed structure of the excited states that can be deduced.

Another application of the (n, γ) reaction occurs when the ground state (or a long-lived isomeric state) of A' is itself radioactive. We therefore accumulate activity of A' (usually without bothering to observe the decay γ's from the capture state). The activity builds up according to Equation 6.24, which can be expressed in the following useful form:

$$\mathscr{A} = 0.602 \frac{m}{A} \sigma \frac{\phi}{3.7 \times 10^{10}} (1 - e^{-\lambda t}) \tag{12.23}$$

where $\mathscr{A}$ is the activity in Curies, m/A is the dimensionless ratio between the mass of the target and its atomic mass, σ is the capture cross section (usually for thermal neutrons) in units of barns, ϕ is the neutron flux in neutrons/cm^2/s, and t is the duration of the neutron bombardment.

This technique has a variety of applications: with a known cross section, measuring $\mathscr{A}$ gives the neutron flux, and thus we have a measure of neutron intensity. If ϕ is known, on the other hand, we can determine unknown cross sections. The most common application, however, is to use cases with known ϕ and σ to do qualitative analysis to determine m. After exposing an unknown sample to neutrons, we can observe many different radiations from the radioactive decays of those isotopes that can be produced by neutron capture. Careful measurement of the γ-ray spectrum permits the determination of which isotopes are present and in what quantities, and we can thus deduce the original quantities present in the irradiated sample. This technique is called *neutron activation analysis* and it has important applications in a variety of areas, including environmental pollution research, archeology, and forensic science. We discuss this application of nuclear techniques in Chapter 20.

12.6 INTERFERENCE AND DIFFRACTION WITH NEUTRONS

Beams of neutrons provide an excellent way to observe effects depending on the wave behavior of material particles. In Chapter 11 we saw examples of the diffraction of nucleons in scattering from nuclei, in cases in which the wavelength of the incident particle was comparable to the nuclear size. By moving to other ranges of wavelengths, however, we can observe effects such as single and double slit or thin film interference, which are more frequently demonstrated only with optical radiations.

In Figure 12.15 are shown results from single-slit and double-slit interference experiments. The interference effects are very apparent and remind us of the analogous results using light waves.

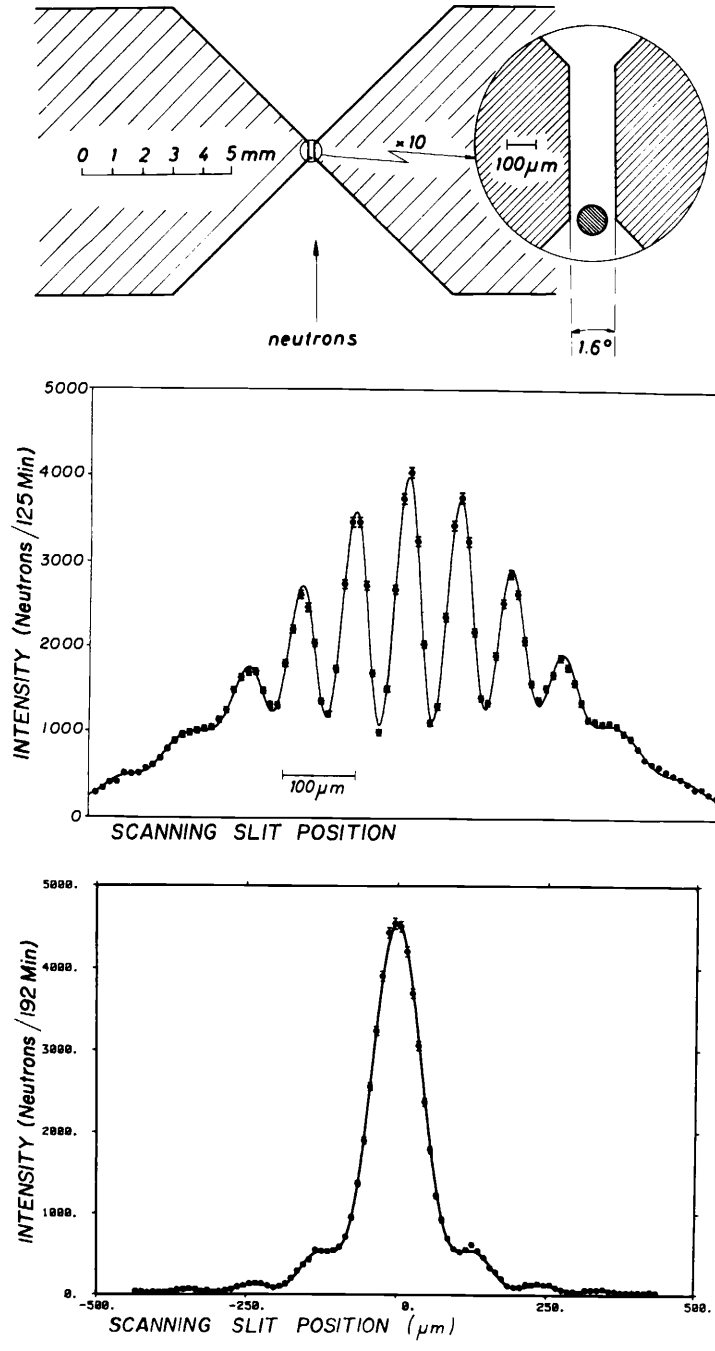


Figure 12.15 (Top) Double-slit apparatus for neutrons. A highly absorbing boron wire is mounted in the gap between two pieces of neutron-absorbing glass to form a double slit. (Middle) Double-slit interference pattern. The dots are the experimental points and the curve is calculated from the Schrödinger equation for a neutron wavelength of 1.845 nm. (Bottom) A single-slit interference pattern. All figures from A. Zeilinger, R. Gaehler, C. G. Shull, and W. Treimer, in *Neutron Scattering—1981*, edited by J. Faber (New York: American Institute of Physics, 1982), p. 93.

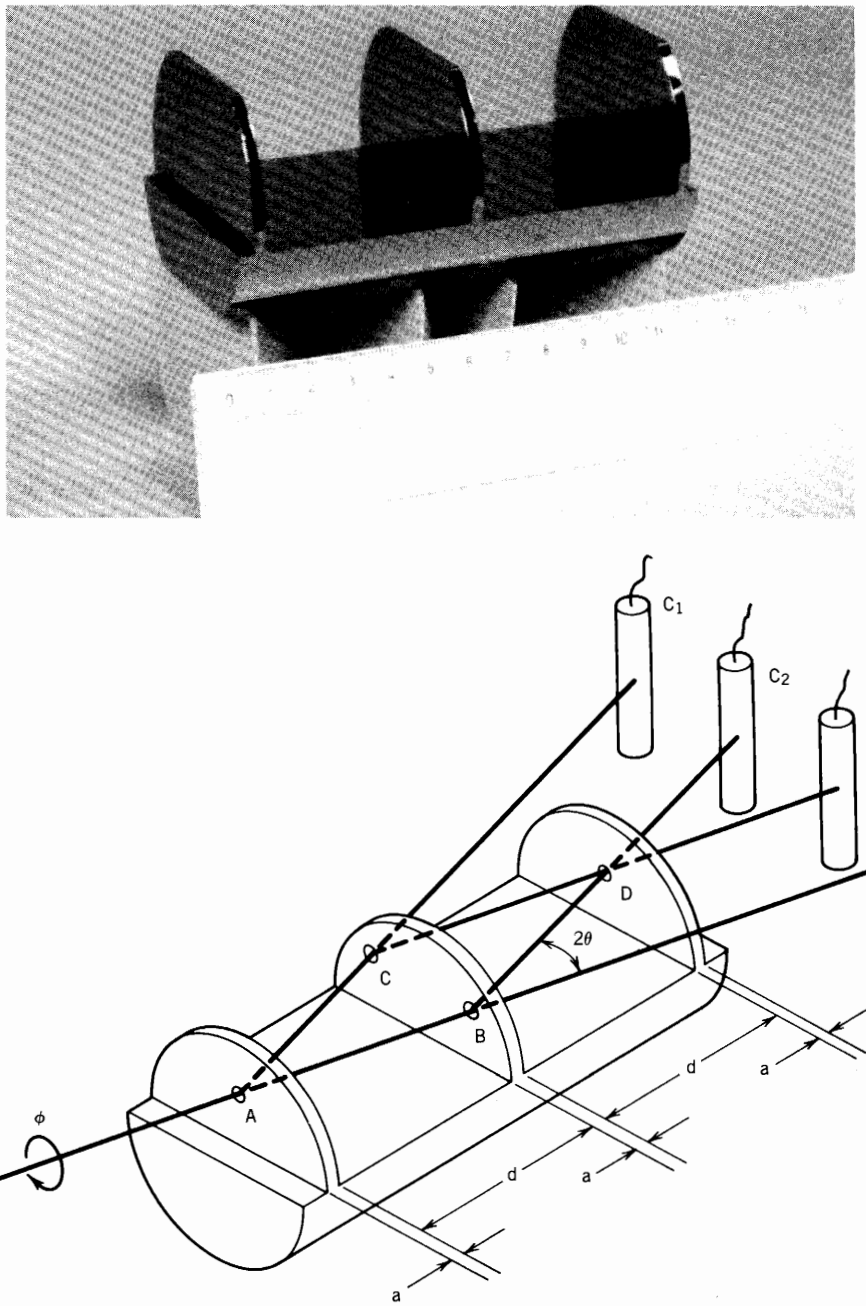


Figure 12.16 (Top) Photograph of neutron interferometer, carved from a single block of silicon 5 cm in diameter and 9 cm long. The three slabs are attached to the base as they were in the original crystal, and therefore the atoms in the slabs are spatially coherent. Photograph courtesy of Professor Samuel A. Werner. (Bottom) Schematic diagram of interferometer. Counter C_1 counts the non-interfering beam, while C_2 and C_3 count the two interfering beams which re-combine at D. From S. A. Werner, J.-L. Staudenmann, R. Colella, and A. W. Overhauser, in *Neutron Interferometry*, edited by U. Bonse and H. Rauch (Oxford: Clarendon Press, 1979), p. 209.

The most ingenious demonstrations of neutron interference have been done with the interferometer shown in Figure 12.16. The device consists of three identical "beam splitters," each of which passes an undeviated transmitted beam and a diffracted beam deflected by an angle 2θ. (We discuss neutron diffraction later in this section.) To obtain identical diffractions at the three beam splitters and to guarantee precise alignment of the three planes, the entire apparatus was carved from a large single crystal of silicon, of length 9 cm and diameter 5 cm. The function of the third slab is to recombine the two interfering beams BD and CD into outgoing beams that contain the interference information as a net intensity variation. (The variations in the two beams are complementary to one another and contain the same information.) Without the recombination done by the third crystal, the interference would occur only at the single point D where the interfering beams cross. Figure 12.17 shows the interference effects observed with this device.

The neutron interferometer has been used in two remarkable experiments which demonstrate aspects of quantum behavior that have not been accessible to testing by any other means. In the first of these, the interferometer was rotated about the horizontal axis AB in Figure 12.16. At a certain value of the rotation angle, one of the beams, ABD for instance, will lie at a greater height than the other (ACD) and will therefore experience a different gravitational potential, mgy. The differing gravitational potential between the two beams causes a relative phase shift that changes the way they interfere when they are recombined. As the angle ϕ (which measures the rotation about the axis) is varied, the intensity in the recombined beam will vary accordingly. Figure 12.18 shows the resulting variation in intenity as ϕ is varied. This experiment, done 50 years after de Broglie's work and after the introduction of the Schrödinger equation, is the first to demonstrate that the Schrödinger equation and the laws of quantum mechanics apply to gravitational fields. The experimental result shows great sensitivity to physical parameters—it was possible to deduce the sag in the crystal caused by bending under its own weight (about 2 nm) and also to observe the Coriolis effect on the two neutron paths due to the rotation of the Earth.

Another unusual and fundamental interferometry experiment with neutrons is done by causing one of the neutron paths (AB, for example) to pass through a magnetic field. In the region of the magnetic field, the magnetic moment of the neutron will precess about the field direction, and this precession causes a change in the phase of the neutron wave function, which is again observed as a variation in the intensity of the recombined beam.

Quantum mechanics predicts an unusual (and previously untested) result for spin-$\frac{1}{2}$ particles—the phase of the wave function upon rotation by an angle α is $e^{is\alpha}$, where s is the spin in units of $\hbar$. When α is 2π (360°), the phase is $e^{i\pi}$ or -1. Thus a complete 360° rotation of the system causes a change in phase of the wave function! This is certainly a nonclassical effect, for in classical physics a 360° rotation leaves all equations unchanged. However, the change in phase of the interfering beams will cause the interference to go from, for instance, a maximum (corresponding to $|\psi|^2 = |\psi_{ACD} + \psi_{ABD}|^2$) to a minimum ($|\psi|^2 = |\psi_{ACD} - \psi_{ABD}|^2$). The neutron interference experiments not only observed the effects of the spin precession of the neutrons, they demonstrated for the first time that a 720° rotation, not a 360° rotation, is required to bring the system back to

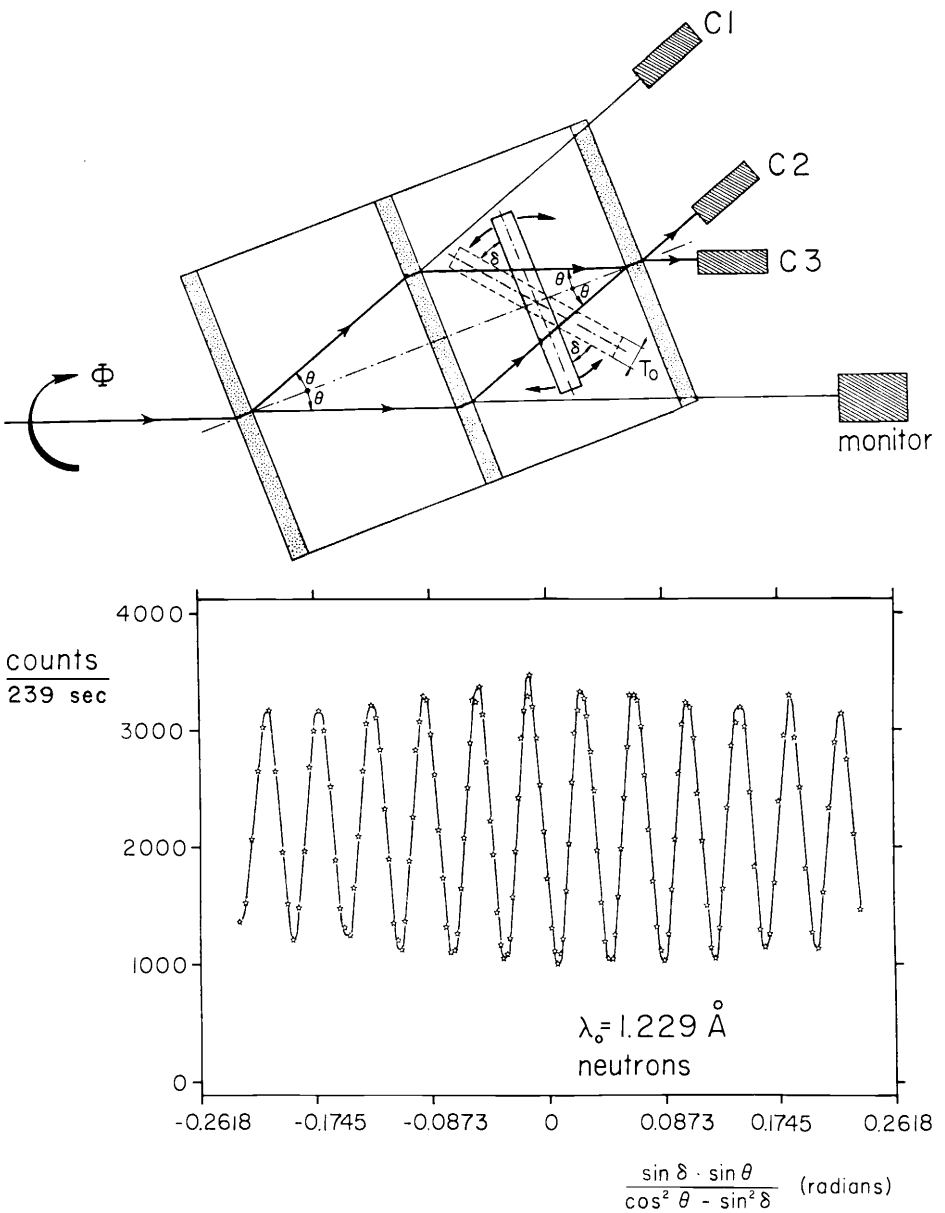


Figure 12.17 A silicon slab placed between the second and third diffracting planes is free to rotate (angle δ in the figure at top). As it does, the two neutron beams must pass through different thicknesses of silicon, which causes a phase shift and a change in intensity when they are recombined. The lower part of the figure shows the observed intensity variation, measured in counter C_3, as δ is varied. From S. Werner, J.-L. Staudenmann, R. Colella, and A. W. Overhauser, in *Neutron Interferometry*, edited by U. Bonse and H. Rauch (Oxford: Clarendon, 1979), p. 209.

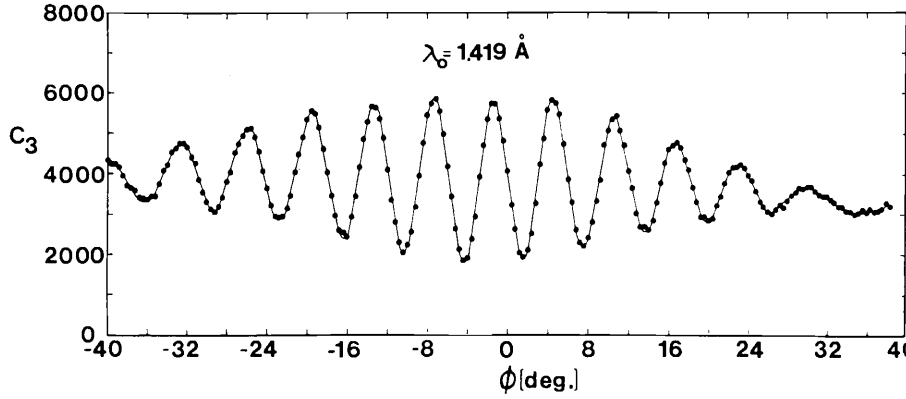


Figure 12.18 Neutron interference in a gravitational field. As the interferometer rotates by the angle ϕ about a horizontal axis, as in Figure 12.17, the two interfering beams change gravitational potentials, which causes a phase difference and a corresponding intensity variation in the recombined beams, as shown. Notice that a rotation of 3–4° changes the counting rate in detector C_3 by a factor of 3. From S. Werner, J.-L. Staudenmann, R. Colella, and A. W. Overhauser, in *Neutron Interferometry*, edited by U. Bonse and H. Rauch (Oxford: Clarendon, 1979), p. 209.

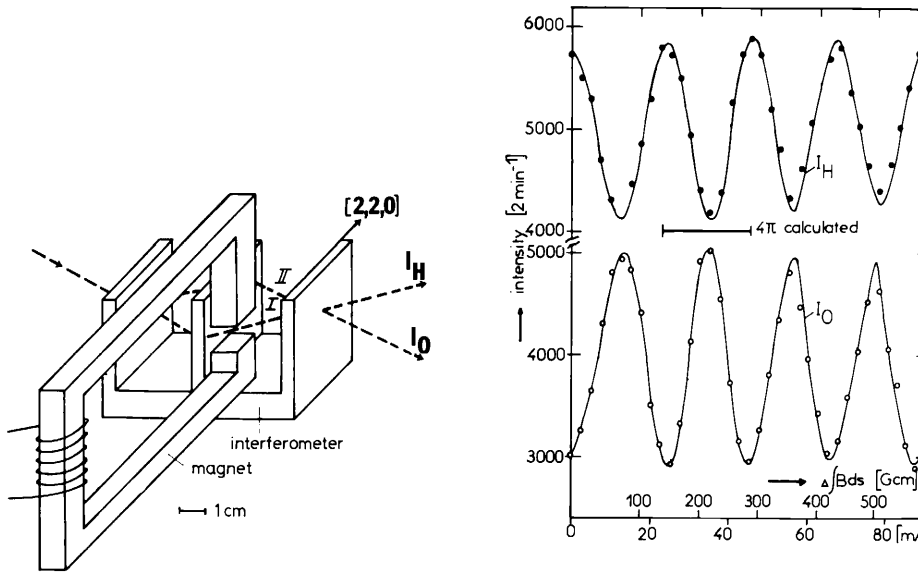


Figure 12.19 Neutron interferometer used to demonstrate rotation of neutron spins in a magnetic field. Unpolarized neutrons of $\lambda = 1.8$ nm are incident on the interferometer; one of the interfering beams passes through the magnetic field, the strength of which may be varied. The neutron spins in branch I precess relative to those in branch II. The data show that a phase change of 4π is necessary to obtain constructive interference. From H. Rauch et al., *Phys. Lett. A* **54**, 425 (1975).

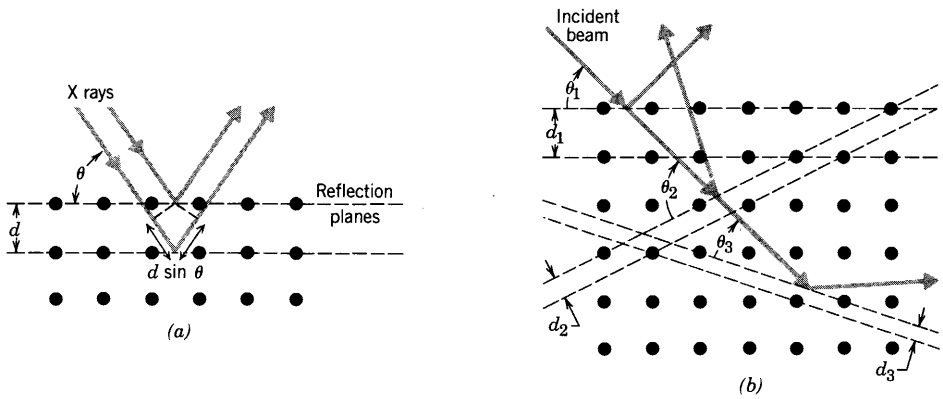


Figure 12.20 (*a*) An incident beam can be reflected from two adjacent parallel rows of atoms in a lattice. If the path difference, $2d\sin\theta$, is an integral number of wavelengths, there will be constructive interference. (*b*) There are many possible ways to choose the set of parallel reflecting lattice planes. Corresponding to each will be a particular value of θ and of d.

its original configuration. Figure 12.19 shows the variation in the interfering intensity as the magnetic field is varied.

Probably the most frequent application of neutron interference is in the diffraction of neutrons by crystals. The diffraction can be used to provide a source or a detector of monoenergetic neutrons, or it can be used to study crystal structures of materials. Figure 12.20 illustrates the basic application of the Bragg law, Equation 12.15, to the diffraction by a single crystal. For neutrons whose wavelengths are about the same order as the crystalline atomic spacing d, interference results in an apparent "reflection" from planes drawn through atoms of the lattice. Typical atomic spacings in solids are of order 0.1 nm, and a de Broglie wavelength of 0.1 nm corresponds to thermal neutron energies.

The choice of a particular set of reflection planes is arbitrary; Figure 12.20 also shows several other choices, corresponding to different angles θ and different spacings d. In three dimensions, we can specify the choice of planes with a set of indices that give essentially the number of fundamental lattice spacings along the three coordinate axes. Figure 12.21 shows some examples of different lattice planes in three dimensions.

The intensity at any particular reflection may be a complicated function of crystal properties and neutron scattering amplitudes (which may involve coherent sums over different isotopes that may be present in the crystal). Figure 12.22 is an example of a scattering spectrum taken for neutrons of a particular wavelength. The scattering sample in this case was a powder consisting of many micro-crystals, so that all possible orientations are simultaneously observed.

An alternative approach would be to begin with a beam of neutrons containing a mixture of energies, such as might be obtained from a reactor. If the beam falls on a scattering crystal, at a certain angle (as in Figure 12.23) we will observe monoenergetic neutrons that satisfy the Bragg condition (assuming that the same angle does not happen to satisfy the Bragg condition for a different wavelength and set of crystal planes). If we change the angle θ slightly, the same Bragg condition will be satisfied for a slightly different wavelength or energy. We thus

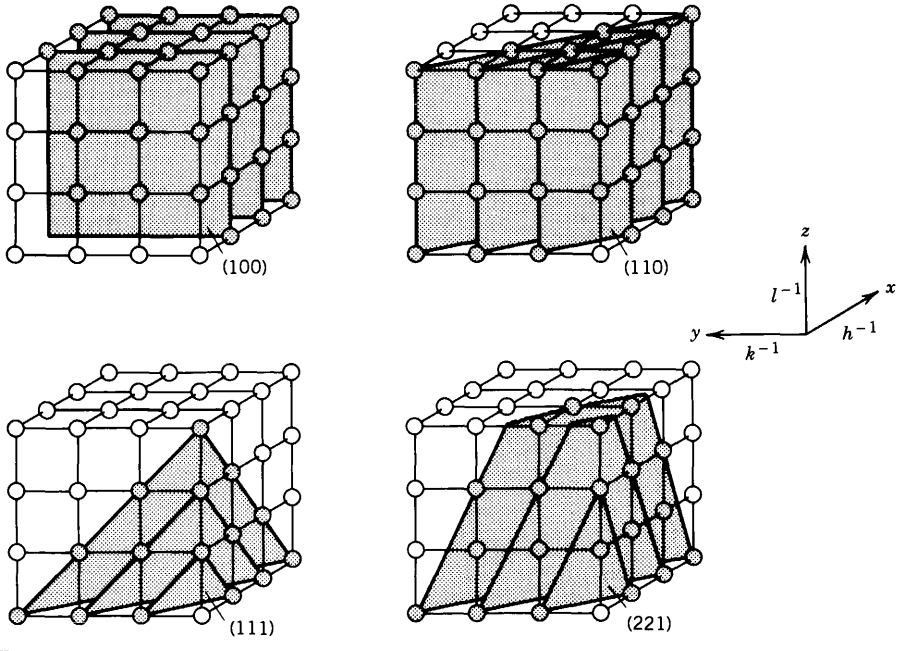


Figure 12.21 Planes of atoms in three-dimensional cubic lattice (this is a three-dimensional analog of Figure 12.20*b*). The indices (*hkl*) give integers in the ratio of the *inverse* of the coordinates of the plane with respect to the three directional axes x, y, z. Thus $x = 1$, $y = \infty$, $z = \infty$ (upper left) reduces to (100); $x = 1$, $y = 1$, $z = 2$ (lower right) becomes $(11\frac{1}{2})$ and then (221) by changing to integers in the same ratio.

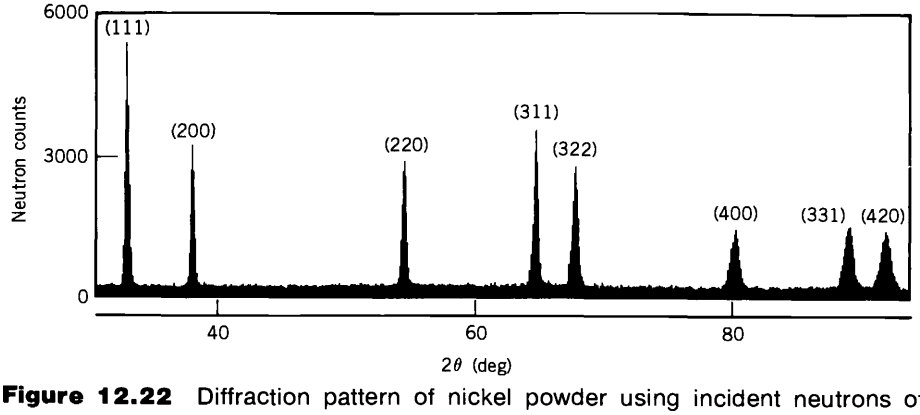


Figure 12.22 Diffraction pattern of nickel powder using incident neutrons of wavelength 0.114 nm. The scattering angle 2θ is plotted, and the peaks are labeled with the indices of the lattice planes, as in Figure 12.21. From G. E. Bacon, *Neutron Diffraction* (Oxford: Clarendon, 1975).

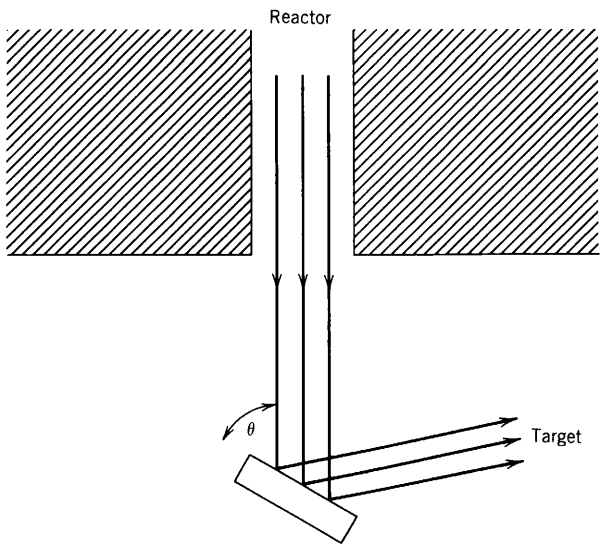


Figure 12.23 Monochromator for producing a beam of monoenergetic neutrons. A collimated beam of reactor neutrons with a broad spectrum of wavelengths is Bragg reflected from a single crystal. For a particular value of θ, there will be an interference maximum for a certain wavelength, and thus by varying θ we can choose the wavelength. As in Figure 12.20*b*, there may be other Bragg reflected peaks at other angles, which are not shown.

have a *neutron monochromator*, a source of neutrons of any particular energy, with a spread in energy determined by the angular spread of the beam.

Powder diffraction patterns such as shown in Figure 12.22 can be used to deduce the type of crystal structure, as in the cubic lattice characteristic of nickel. Similar studies are possible for more complex systems, including the relatively disordered structures of liquids and glasses, and the exceedingly complicated structures of biological molecules.

The primary mechanism for neutron scattering is the nuclear scattering that we have discussed previously in this chapter and in Chapter 11. An alternative mechanism is *magnetic* scattering, in which the neutron magnetic moment scatters from the electronic magnetic moment. If it is possible to separate nuclear from magnetic scattering (as, for instance, by using polarized neutrons), it is possible to deduce magnetic structures, which can be more complicated and more interesting than the physical arrangement of atoms in the lattice. Figure 12.24 shows the neutron diffraction pattern of MnO above and below the Néel temperature, which is for antiferromagnets what the Curie temperature is for ferromagnets. Below the Néel temperature, MnO is antiferromagnetic, in which there are alternating layers with opposite spin orientations. (In a ferromagnetic structure, all spins would be parallel.) Figure 12.25 shows a representation of the structure. The basic distance needed for the structure to repeat itself (called the *unit cell* dimension) is twice what it would be if we were above the Néel temperature where the magnetic structure repeats in nonalternating fashion. There is a factor of 2 difference in the basic distance d that appears in the Bragg

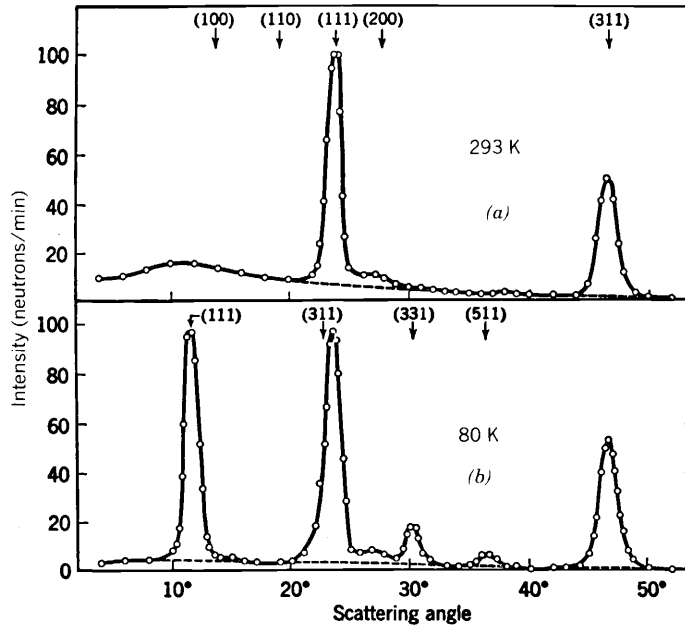


Figure 12.24 The neutron diffraction pattern of MnO (*a*) above and (*b*) below the antiferromagnetic transition temperature. Notice the factor of 2 difference in the location of the 111 peak. From C. G. Shull and J. S. Smart, *Phys. Rev.* **76**, 1256 (1949).

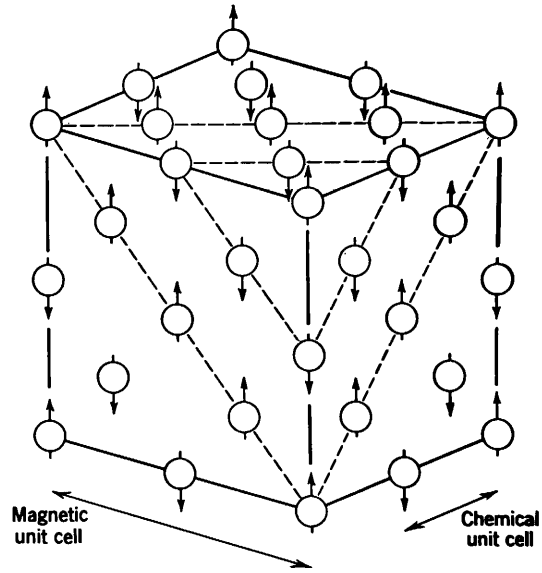


Figure 12.25 The crystal structure of MnO. In the antiferromagnetic structure, the lattice repeats over a distance of $2a$ (where a is the spacing of the Mn atoms) while at high temperature the spins are all aligned and the lattice repeats over a distance of a.

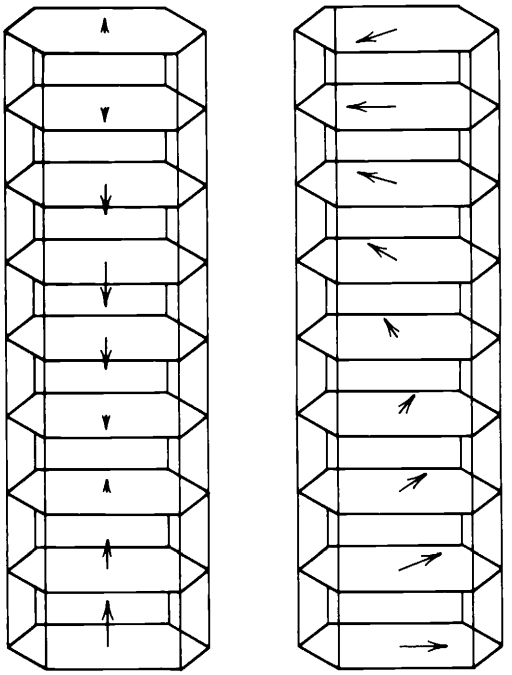


Figure 12.26 Two examples of rare-earth magnetic structures studied by neutron diffraction. The basic crystal structure is that of stacked planes of hexagonal arrays of atoms. The arrows show the effective magnetic dipole moments. The structure at left is characteristic of erbium metal in the temperature range 52–85 K, and that at right describes terbium in the range of 220–230 K. Below 220 K, the terbium moment does not rotate from one plane to the next, but points in a fixed direction. Below 20 K, erbium shows a moment that has a rotating component in the hexagonal plane and a perpendicular component of fixed magnitude.

equation, and the result is that the peaks for magnetic scattering appear at values of θ such that $\sin\theta$ is half what it would be for nuclear scattering.

The rare-earth metals have rather similar crystal structures of the hexagonal type, but very different magnetic properties that also change with temperature as in the case of MnO. In some cases the electronic magnetic moment is perpendicular to the hexagonal plane, but may be modulated in unusual ways from one layer to the next, as for example several layers pointing up and then several down, or else sinusoidally. In other structures, the electronic moment lies in the hexagonal plane, but it rotates through a certain angle from one layer to the next. These magnetic structures, illustrated in Figure 12.26, can be studied only through neutron diffraction.

REFERENCES FOR ADDITIONAL READING

A nontechnical introduction to neutron physics is D. J. Hughes, *The Neutron Story* (New York: Doubleday, 1959). Modern research with extremely low-energy neutrons is described in "Ultracold Neutrons" by R. Golub, W. Mampe, J. M. Pendlebury, and P. Ageron in the June 1979 issue of *Scientific American*.

For general surveys of neutron physics, see L. F. Curtiss, *Introduction to Neutron Physics* (Princeton, NJ: Van Nostrand, 1959); D. J. Hughes, *Pile Neutron Research* (Cambridge: Addison-Wesley, 1953); D. J. Hughes, *Neutron Optics* (New York: Interscience, 1954).

For more advanced and detailed references, see I. I. Gurevich and L. V. Tarasov, *Low-Energy Neutron Physics* (Amsterdam: North-Holland, 1968); J. E. Lynn, *The Theory of Neutron Resonance Reactions* (Oxford: Clarendon, 1968); *Fast Neutron Physics*, edited by J. B. Marion and J. L. Fowler (New York: Interscience, 1960); C. G. Windsor, *Pulsed Neutron Scattering* (New York: Halsted, 1981).

A comprehensive survey of neutron diffraction is G. E. Bacon, *Neutron Diffraction*, 3rd ed. (Oxford: Clarendon, 1975).

Reports on recent work with neutrons can be found in *Neutron Sources for Basic Physics and Applications*, edited by S. Cierjacks (Oxford: Pergamon, 1983); *Neutron Interferometry*, edited by U. Bonse and H. Rauch (Oxford: Clarendon, 1979); *Neutron Scattering—1981*, edited by John Faber, Jr. (New York: American Institute of Physics, 1982).

PROBLEMS

1. In the reaction $\alpha + {}^{9}\mathrm{Be} \rightarrow {}^{12}\mathrm{C} + \mathrm{n}$, find the maximum and minimum neutron energies when the incident α energy is (a) 7.0 MeV; (b) 1.0 MeV.
2. If the neutrons in Problem 1 are emitted uniformly in space, sketch their energy spectrum, that is, the relative number emitted at each energy from the minimum to the maximum.
3. A 5.00-MeV proton beam is available to produce neutrons from the reaction ${}^{7}\mathrm{Li}(\mathrm{p}, \mathrm{n}){}^{7}\mathrm{Be}$. A neutron beam of 1.75 MeV is needed for a particular experiment. (a) In what direction relative to the incident beam should we look to find 1.75-MeV neutrons? (b) If we extract the neutrons through a 1-cm aperture located 10 cm from the reaction target, what will be the energy spread of the neutron beam?
4. Neutrons were first observed through the "knock-on" protons produced in direct head-on scattering. If protons are observed at an energy of 5.3 MeV, compute the incident energy if the incident particle is (a) a photon, or (b) a neutron.
5. A neutron of kinetic energy E scatters elastically from a target atom at rest. Find the maximum energy lost by the neutron if the target is (a) ${}^{2}\mathrm{H}$; (b) ${}^{12}\mathrm{C}$; (c) ${}^{238}\mathrm{U}$.
6. For neutron moderation by protons, make a sketch showing the average energy of a beam of initial 2.0-MeV neutrons as a function of time, assuming the mean time between collisions is t. How long does it take for the neutrons to lose 50% of their energy? How long for 90%?
7. A point source of fast neutrons (a radium-beryllium source, for example) is placed at the center of a tank of water. Make a sketch showing the density of thermal neutrons as a function of the distance from the source. Your sketch should indicate general features only; don't try to be too specific. The

mean free path of neutrons in water is a few centimeters for fast neutrons to a few tenths of a centimeter for slow neutrons.

8. Derive Equation 12.7.

9. Find the number of collisions necessary to reduce the energy of a 1 MeV neutron to 1 eV in scattering by (a) hydrogen; (b) carbon; (c) beryllium; (d) iron.

10. In scattering between incident neutrons and target protons at rest, show that the angle between the two scattered particles is always 90°.

11. The intensity of a source of thermal neutrons is to be measured by counting the induced radioactivity in a thin foil of indium metal exposed to the neutrons. The foil is 3.0×3.0 mm in area and 1.0 μm in thickness. The activation of ^{115}In to ^{116}In ($t_{1/2} = 54$ min) takes place with a cross section of 160 b for thermal neutrons. The foil is irradiated for 1 min, but after the conclusion of the irradiation, the counting of the decays from the foil cannot be started for 30 min. The efficiency of the detecting system is only 2.4×10^{-4}, and in 1 h of counting 4.85×10^4 counts are accumulated. What is the thermal neutron flux?

12. In low-energy neutron capture by ^{55}Mn, the following primary γ transitions are seen (energies in MeV): 7.2703, 7.2438, 7.1597, 7.0578, 6.9287. (a) Deduce the corresponding energies of the ^{56}Mn excited states. (b) ^{55}Mn has $I^\pi = \frac{5}{2}^-$. What are the possible I^π assignments of the ^{56}Mn excited states populated through primary transitions?

13. (a) ^{143}Nd has a $\frac{7}{2}^-$ ground state. Following thermal neutron capture, would you expect to see a strong primary transition from the capture state to the ^{144}Nd ground state? (b) Would you expect the same in the case of capture by ^{119}Sn ($\frac{1}{2}^+$)?

14. A beam of neutrons of energy 50 keV is incident on a slab of graphite of thickness 2.5 cm. The transmitted beam has intensity of 26% of the original beam. What value does this indicate for the scattering phase shift? (It is a good approximation to neglect all but the s-wave phase shift. Why?)

15. A beam of neutrons of wavelength λ is incident in the x direction on a crystal represented by the cubic lattice of Figure 12.21. The spacing between neighboring atoms along the coordinate axes is a. (a) Find the spacing d between the lattice planes for the 4 cases in terms of a. (b) Find the direction in space of the scattered neutrons in each case for the first-order interference.

13

NUCLEAR FISSION

The development of nuclear physics occurred very rapidly in the 1930s. Following the discovery of the neutron by Chadwick in 1932, it was a natural next step to study the effects of exposing various nuclei to neutrons (in effect, carrying on the work begun a few years earlier with charged-particle beams from the first accelerators). Enrico Fermi and his co-workers in Italy exposed many elements to neutrons and studied the induced radioactivity following neutron capture. They discovered that many nuclei decay by β^- emission following neutron capture, as the nuclei try to compensate for the excess neutron by converting a neutron to a proton. The result is a residual nucleus of atomic number one unit higher. (Fermi received the Nobel Prize in 1938 for this work.) The next natural step was to use this technique to increase the atomic number to produce *transuranic* elements, those beyond the heaviest naturally occurring element (uranium) found in nature. Indeed, the technique of irradiating uranium with neutrons did reveal β^- activities that were at first identified with new transuranic elements, but efforts to separate these elements chemically to study their properties produced confusing results. In particular, the induced activity appeared to show a chemical behavior similar to barium; consequently it was at first assumed to be radium, which appears just below barium in the periodic table and thus has atomic structure and chemical properties very similar to those of barium. However, radium is produced from uranium through the (n, 2α) reaction, which must be very improbable. In 1939, using careful radiochemical techniques, Hahn and Strassmann showed that in fact the induced activity was barium itself and not merely something chemically similar to it. Further work revealed many other intermediate-mass nuclei formed in the bombardment of uranium by neutrons, and experiments using ionization chambers showed that the energy released following neutron capture was very large, of the order of 100 MeV and certainly far greater than any previously observed α-decay energy. With this evidence, Meitner and Frisch in 1939 proposed that the uranium nuclei following neutron capture are highly unstable and split nearly in half or *fission* (a term borrowed from the biologists' description of cell division).

Fission results primarily from the competition between the nuclear and Coulomb forces in heavy nuclei. The total nuclear binding energy increases roughly in proportion to A, while the Coulomb repulsion energy of the protons

increases faster, like Z^2. If we regard the emission of a heavy fragment as a decay process similar to α decay, then we can regard heavy nuclei as residing very close to the top of the potential well in Figure 8.3, where the Coulomb barrier is very thin and easily penetrable. Fission can thus occur spontaneously as a natural decay process, or it can be induced through the absorption of a relatively low-energy particle, such as a neutron or a photon (producing excited states or compound-nuclear states that are high enough in energy to surmount or more easily penetrate the barrier).

Although any nucleus will fission if we provide enough excitation energy, as a practical matter the process is important only for heavy nuclei (thorium and beyond). The applicability of fission for obtaining large total energy releases was realized soon after its discovery, for another characteristic of the process is that every neutron-induced fission event produces, in addition to the two heavy fragments, several neutrons which can themselves induce new fission events. This *chain reaction* of fissions can occur very rapidly and without control, as in a fission explosive, or slowly and under careful control, as in a fission reactor. Because of these spectacular and awesome applications, nuclear fission plays a prominent role in many technical processes and in political decisions as well.

13.1 WHY NUCLEI FISSION

The energetic preference for nuclei to fission can be understood immediately from the binding energy per nucleon, Figure 3.16. A heavy nucleus in the uranium region has a binding energy of about 7.6 MeV/nucleon. If ^{238}U were to divide into two equal fragments with $A \simeq 119$, their binding energy per nucleon would be about 8.5 MeV. Going to a more tightly bound system means that energy must be released; that is, the energy changes from bound $^{238}_{92}$U at $-238 \times 7.6 = -1809$ MeV to two bound $^{119}_{46}$Pd nuclei at $-2 \times 119 \times 8.5 = -2033$ MeV. To conserve energy, the final state must include an extra 214 MeV, which can appear in a variety of forms (neutrons, β and γ emissions from the fragments) but which appears primarily ($\sim 80\%$) as kinetic energy of the fragments as Coulomb repulsion drives them apart. In calculating decay probabilities, there is a term that depends on the energy release—the more energy is released, the more ways there are for the decay products to share the energy, the greater the number of final states to decay into, and the higher the decay probability. With such a large energy release, fission ought to be a decay means that is readily available for these nuclei as they "climb the curve of binding energy."

While the fission decay mode does indeed exist, it is not nearly so probable as our discussion might indicate—it does not compete successfully with the spontaneous α decay of ^{238}U ($t_{1/2} = 4.5 \times 10^9$ y, while the partial half-life for fission is about 10^{16} y), and it does not become an important decay process until we get to nuclei of mass 250 and above. What inhibits the fission process is the Coulomb barrier, which also inhibits the analogous α-decay process. If we divide ^{238}U into two identical fragments that are just touching at their surfaces (separation = R_1

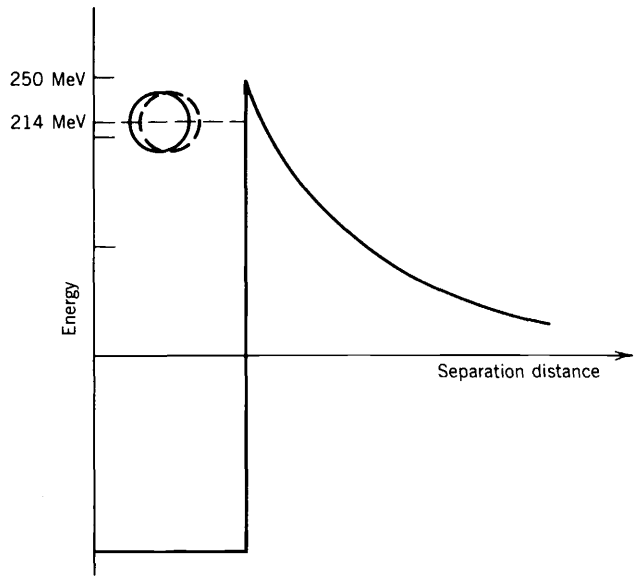


Figure 13.1 Inside its nuclear potential well, ^{238}U may perhaps exist instantaneously as two fragments of ^{119}Pd, but the Coulomb barrier prevents them from separating.

$+ R_2$ where $R_1 = R_2 = 1.25(119)^{1/3} = 6.1$ fm), the Coulomb barrier is

$$V = \frac{1}{4\pi\epsilon_0}\frac{Z_1 Z_2 e^2}{R}$$

$$= (1.44 \text{ MeV} \cdot \text{fm})\frac{(46)^2}{12.2 \text{ fm}} = 250 \text{ MeV}$$

If we regard the zero of our energy scale to be the two fragments at rest separated by an infinite distance, then we can represent this system by Figure 13.1. Inside the region of nuclear potential, ^{238}U can exist as two ^{119}Pd nuclei because of the enormous number of final states accessible with a 214-MeV energy release. However, the Coulomb barrier prevents the fragments from separating, and the decay probability is small because the barrier cannot be penetrated.

This very crude calculation may indicate why fission is inhibited from readily occurring, but it should not be taken too seriously because the numbers we have used (250 MeV for the barrier height and 214 MeV for the energy release) are only estimates and can easily be modified by 10 to 20%. For example, the assumption that ^{238}U splits into two identical fragments may not be very realistic. If the two fragments have masses and atomic numbers in roughly a 2 : 1 ratio, such as $^{79}_{30}Zn$ and $^{159}_{62}Sm$, the Coulomb barrier height is reduced from 250 to 221 MeV. The release of a few neutrons will change the mass numbers of the final fragments and can produce more nearly stable and tightly bound fragments (nuclei such as ^{119}Pd, ^{79}Zn, and ^{159}Sm have a large neutron excess and are unlikely to be formed in fission). Also, the Coulomb barrier calculation based on a sharp edge at $R = R_1 + R_2$ is quite unlikely to be strictly correct.

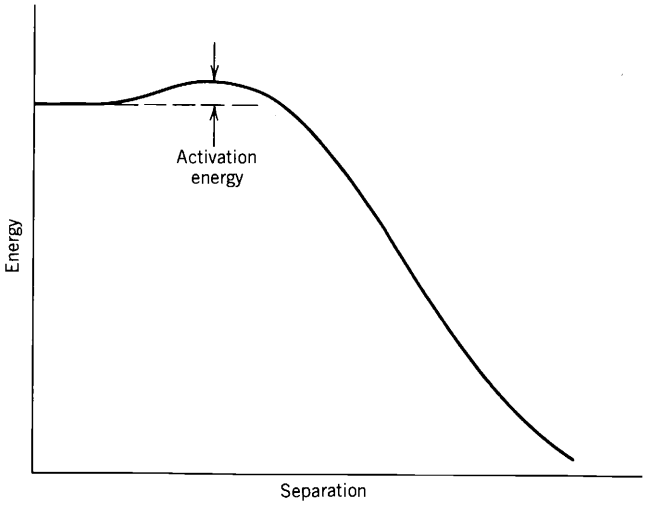


Figure 13.2 A smooth potential barrier opposing the spontaneous fission of ^{238}U. To surmount the fission barrier, we must supply an amount of energy equal to the activation energy.

What is certainly true, though, is that the height of the Coulomb barrier is *roughly* equal to the energy released in fission of heavy nuclei, and there are certain to be *some* nuclei for which the energy release puts the two fragments just below the Coulomb barrier, giving them a reasonably good chance to penetrate. These are the *spontaneously fissioning* nuclei, for which fission competes successfully with other radioactive decay processes. There may be others whose separated state would put them *above* the barrier and that would (if formed) instantly spontaneously fission. Such nuclei of course do not exist in nature; calculations suggest that the barrier against fission is zero at about $A = 300$. Still other nuclei may be far enough below the barrier that spontaneous fission is not observed, but absorption of a relatively small amount of energy, such as from a low-energy neutron or photon, forms an intermediate state (perhaps a compound nuclear state) that is at or above the barrier so that *induced fission* occurs readily, that is, it competes successfully with other modes of decay of the compound nucleus. If the intermediate state is below the barrier, fission is inhibited and other decay modes, including re-emission of the absorbed particle, may dominate. Subthreshold fission may have important implications for nuclear structure for there are often resonances that can enhance the fission probability, as we discuss in Section 13.4. The ability of a nucleus to undergo induced fission will depend critically on the energy of the intermediate system; for some nuclei, absorption of thermal neutrons may be sufficient to push them over the barrier, while for others, fast (MeV) neutrons may be required. Figure 13.2 shows a more realistic representation of the fission barrier for heavy nuclei.

A more detailed calculation of the energy needed to induce fission is shown in Figure 13.3, which gives essentially the height of the fission barrier above the ground state (usually called the *activation energy*). This calculation is based on the liquid-drop model, which treats only average nuclear properties; the inclusion of more sophisticated effects based on the shell model modifies the calculation

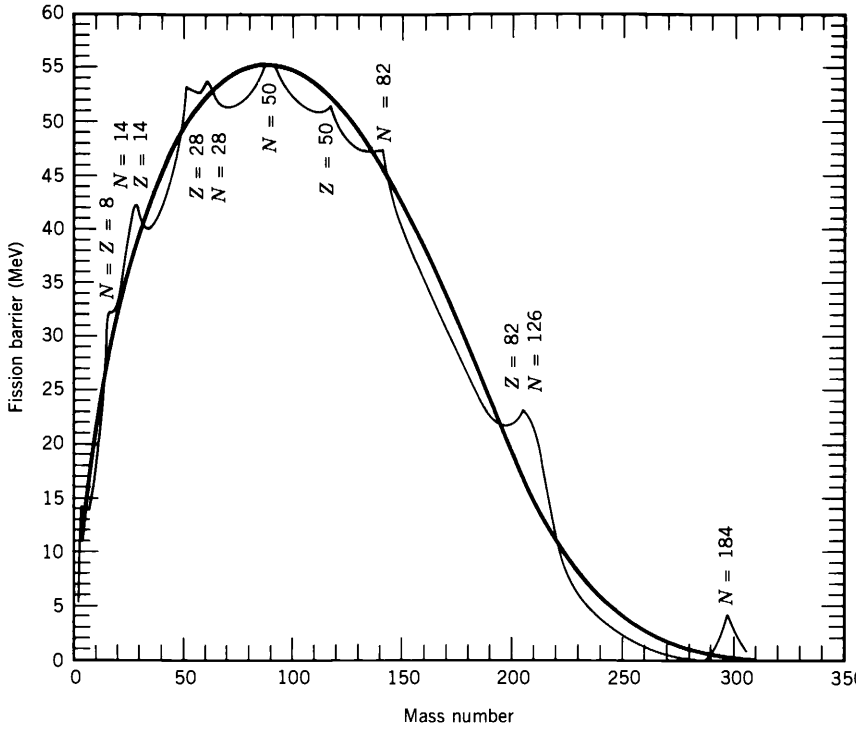


Figure 13.3 Variation of fission activation energy with mass number. The dark curve is based on the liquid-drop model, calculated only for the most stable isotope at each mass number, and the light curve shows the effect of including shell structure. Note the typical 5-MeV energies around uranium, the vanishing energy around mass 280 (making these nuclei extremely unstable to spontaneous fission), and the stability around mass 300 from the expected neutron shell closure. From W. D. Myers and W. J. Swiatecki, *Nucl. Phys.* **81**, 1 (1966).

somewhat and suggests that certain super-heavy nuclei around $A = 300$ may be more stable against fission. Other consequences of shell structure are discussed in Section 13.4.

An instructive approach to understanding fission can be obtained from the semiempirical mass formula, Equation 3.28. Let us consider the effect on the binding energy of an initially spherical nucleus that we gradually stretch. The stretching can be done to keep the volume constant, but the surface and Coulomb terms, which were calculated originally for spherical nuclei, will certainly be affected by the stretching. We represent the stretched nucleus as an ellipsoid of revolution, which has a volume of $\frac{4}{3}\pi ab^2$, where a is the semimajor axis and b is the semiminor axis. The deviation of the ellipsoid from a sphere of radius R is given in terms of a distortion parameter ε as

$$\begin{aligned} a &= R(1 + \varepsilon) \\ b &= R(1 + \varepsilon)^{-1/2} \end{aligned} \tag{13.1}$$

where ε is the eccentricity of the ellipse and is related to the deformation parameter β defined in Equation 5.15 as $\varepsilon = \beta\sqrt{5/4\pi}$. Note that $R^3 =$

ab^2, which keeps the volume constant as we increase the distortion. As a sphere is stretched to distort it into an ellipsoid, its surface area increases as $S = 4\pi R^2(1 + \frac{2}{5}\varepsilon^2 + \cdots)$; the surface energy term in the semiempirical mass formula increases accordingly. The Coulomb energy term can be shown to be modified by the factor $(1 - \frac{1}{5}\varepsilon^2 + \cdots)$, and thus the *difference* in energy (actually the decrease in binding energy) between a spherical nucleus and an ellipsoid of the same volume is

$$\begin{aligned}\Delta E &= B(\varepsilon) - B(\varepsilon = 0) \\ &= -a_s A^{2/3}\left(1 + \tfrac{2}{5}\varepsilon^2 + \cdots\right) - a_c Z^2 A^{-1/3}\left(1 - \tfrac{1}{5}\varepsilon^2 + \cdots\right) \\ &\quad + a_s A^{2/3} + a_c Z^2 A^{-1/3} \\ &\cong \left(-\tfrac{2}{5}a_s A^{2/3} + \tfrac{1}{5}a_c Z^2 A^{-1/3}\right)\varepsilon^2 \qquad (13.2)\end{aligned}$$

If the second term is larger than the first, the energy difference is positive—we *gain* energy through the stretching, and the more the nucleus is stretched, the more energy is gained. Such a nucleus is unstable against this stretching and will readily undergo fission. Therefore, for spontaneous fission, the condition is

$$\tfrac{1}{5}a_c Z^2 A^{-1/3} > \tfrac{2}{5}a_s A^{2/3}$$

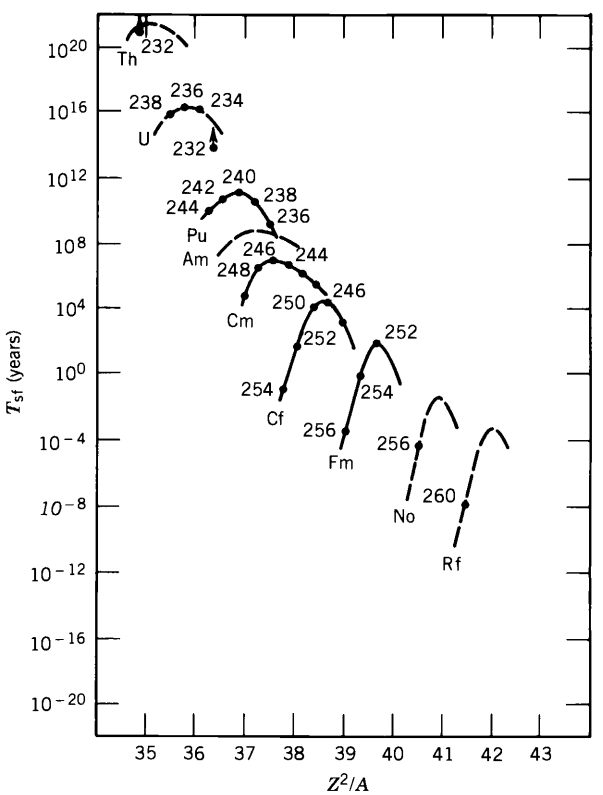


Figure 13.4 Lifetimes for spontaneous fission. There is a general trend of decreasing lifetime with increasing Z^2/A. From V. M. Strutinsky and H. C. Pauli, in *Physics and Chemistry of Fission* (Vienna: IAEA, 1969), p. 155.



Figure 13.5 Representation of nuclear shapes in fission.

and using the values of a_s and a_c gives

$$\frac{Z^2}{A} > 47 \tag{13.3}$$

This estimate must be modified somewhat to account for quantum mechanical barrier penetration, which permits spontaneous fission even when the deformation energy is negative. Furthermore, the nuclei in the region around uranium have permanent equilibrium deformation—the equilibrium shape is ellipsoidal rather than spherical. Nevertheless, the parameter Z^2/A does serve as a rough indicator of the ability of a nucleus to fission spontaneously, as shown in Figure 13.4. The larger the value of Z^2/A, the shorter is the half-life for spontaneous fission. Extrapolating the spontaneous fission half-lives gives about 10^{-20} s for $Z^2/A \simeq 47$; thus the fission would occur "instantly" on the nuclear time scale for nuclei beyond the critical value of Z^2/A. No such nuclei are known, however, but a nucleus with $A = 300$ and $Z/A = 0.4$ has $Z^2/A = 48$, so this estimate is consistent with the zero activation energy for $A = 300$ as shown in Figure 13.3.

From a physical standpoint, what occurs during stretching can be described by the sequence of drawings shown in Figure 13.5. As the distortion becomes more extreme, the center becomes "pinched off" and the nucleus fissions.

13.2 CHARACTERISTICS OF FISSION

Mass Distribution of Fragments

A typical neutron-induced fission reaction is

$$^{235}\text{U} + \text{n} \rightarrow {}^{93}\text{Rb} + {}^{141}\text{Cs} + 2\text{n}$$

which is possible for incident neutrons of thermal energies. The fission products are not determined uniquely—there is a distribution of masses of the two fission products of the form shown in Figure 13.6. The distribution must be symmetric about the center—for every heavy fragment, there must be a corresponding light fragment, but notice that fission into equal or nearly equal fragments ($A_1 \approx A_2$) is less probable by a factor of about 600 relative to the maximum yield of fragments with $A_1 \simeq 95$ and $A_2 \simeq 140$. Surprisingly, a convincing explanation for this mass distribution, which is characteristic of low-energy fission processes, has not been found. In contrast, fissions induced by very energetic particles show mass distributions that favor equal-mass fragments.

Number of Emitted Neutrons

The fission fragments in the vicinity of $A = 95$ and $A = 140$ must share 92 protons. If they do so in rough proportion to their masses, the nuclei formed will be ${}^{95}_{37}\text{Rb}_{58}$ and ${}^{140}_{55}\text{Cs}_{85}$. These nuclei are extremely rich in neutrons—the most

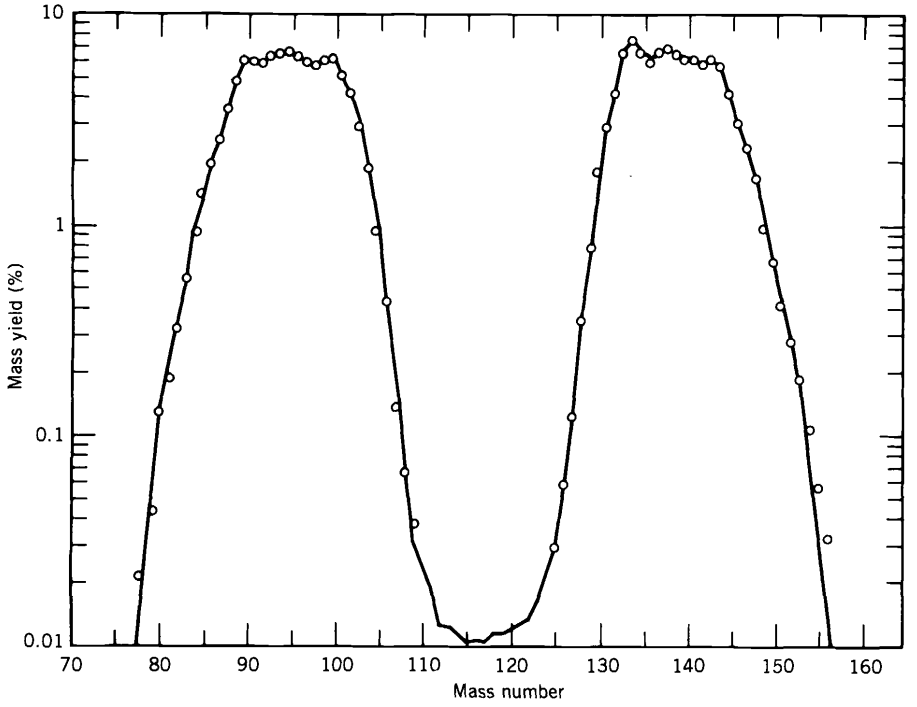


Figure 13.6 Mass distribution of fission fragments from thermal fission of ^{235}U. Note the symmetry of the heavy and light distributions, even in the small variations near the maxima. From G. J. Dilorio, *Direct Physical Measurement of Mass Yields in Thermal Fission of Uranium 235* (New York: Garland, 1979).

stable nuclei in this mass region have $Z/A \simeq 0.41$, while for these fission products, $Z/A = 0.39$. The stable $A = 95$ isobar has $Z = 42$, and the stable $A = 140$ isobar has $Z = 58$. The fission fragments shed this neutron excess through emission of one or more neutrons *at the instant of fission* (within 10^{-16} s). These neutrons are known as *prompt neutrons*, and the number of prompt neutrons emitted in a given fission event will vary with the nature of the two fragments (and with the energy of the incident particle in the case of induced fission). The average number of prompt neutrons, called ν, is characteristic of the particular fission process; for thermal neutron-induced fission, the experimentally observed values of ν are 2.48 for ^{233}U, 2.42 for ^{235}U, and 2.86 for ^{239}Pu. The distribution about the mean shows the statistical behavior expected for an evaporation process, as illustrated by Figure 13.7. The Gaussian distribution that governs the neutron emission is remarkably independent of the fissioning nucleus, as all nuclei seem to follow the same behavior.

In addition to the prompt neutrons, *delayed neutrons* are often emitted in fission. These neutrons are emitted following the β decay of the fission fragments and are examples of the β-delayed nucleon emission discussed in Section 9.8. The delay times are typically quite short, usually of the order of seconds. Figure 13.8 shows a typical case. Following the 6-s β decay of ^{93}Rb, ^{93}Sr is left in a highly excited state, the energy of which happens to exceed the neutron separation

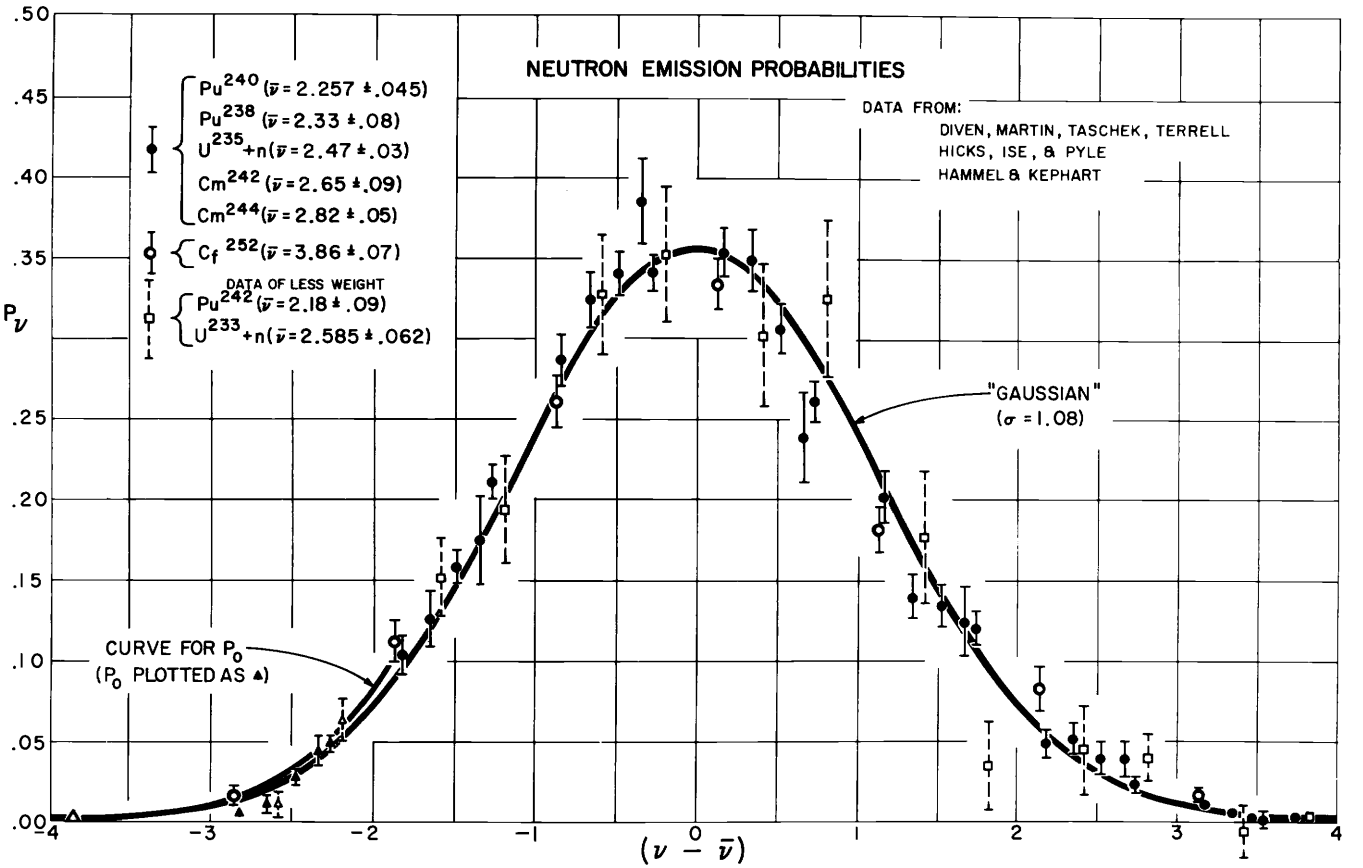


Figure 13.7 Distribution of fission neutrons. Even though the average number of neutrons $\bar{\nu}$ changes with the fissioning nucleus, the distribution about the average is independent of the original nucleus. From J. Terrell, in *Physics and Chemistry of Fission*, Vol. 2 (Vienna: IAEA, 1965), p. 3.

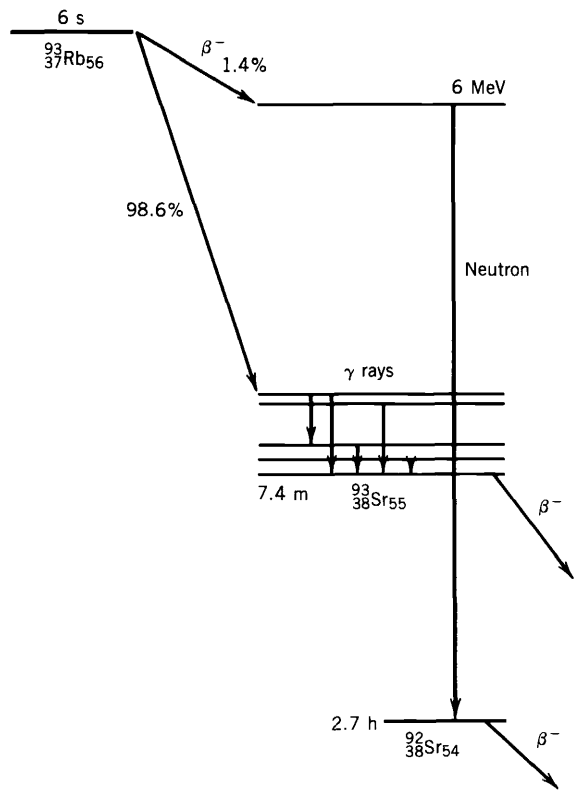


Figure 13.8 Delayed neutron emission from ^{93}Rb. After the original β decay, the excited state of ^{93}Sr has enough energy to decay by neutron emission to ^{92}Sr. The neutrons are delayed relative to the prompt fission neutrons by a time characteristic of the mean lifetime of ^{93}Rb.

energy. The state therefore can decay by neutron emission in competition with γ emission; in this case, the neutron branch occurs with an intensity of 1.4%.

The total intensity of delayed neutrons amounts to about 1 per 100 fissions, but these neutrons are essential for the control of nuclear reactors. No mechanical system could respond rapidly enough to prevent statistical variations in the prompt neutrons from causing the reactor to run out of control, but it is indeed possible to achieve control using the delayed neutrons.

Radioactive Decay Processes

The initial fission products are highly radioactive and decay toward stable isobars by emitting many β and γ radiations (which contribute ultimately to the total energy release in fission). Some sample decay chains are

$$^{93}\text{Rb} \xrightarrow{6\text{ s}} {}^{93}\text{Sr} \xrightarrow{7\text{ min}} {}^{93}\text{Y} \xrightarrow{10\text{ h}} {}^{93}\text{Zr} \xrightarrow{10^6\text{ y}} {}^{93}\text{Nb}$$

$$^{141}\text{Cs} \xrightarrow{25\text{ s}} {}^{141}\text{Ba} \xrightarrow{18\text{ min}} {}^{141}\text{La} \xrightarrow{4\text{ h}} {}^{141}\text{Ce} \xrightarrow{33\text{ d}} {}^{141}\text{Pr}$$

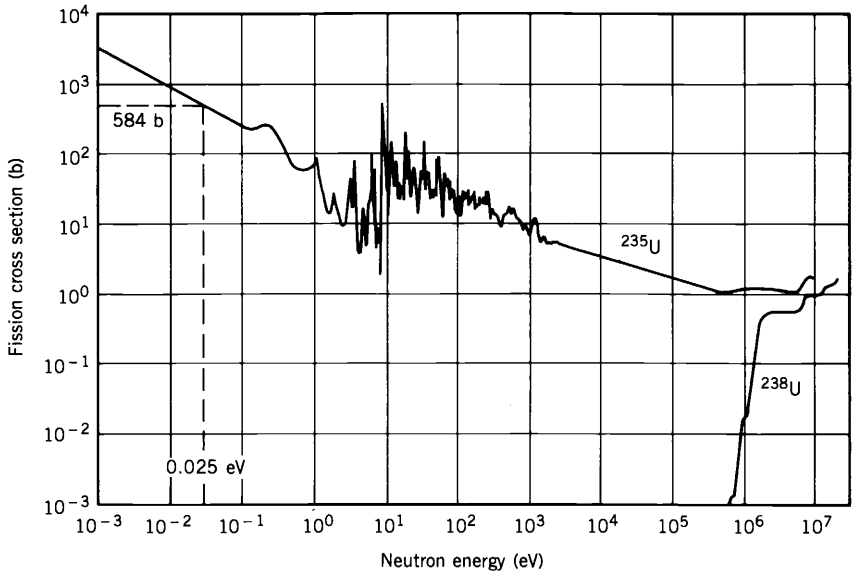


Figure 13.9 Cross sections for neutron-induced fission of ^{235}U and ^{238}U.

These radioactive products are the waste products of nuclear reactors. Many decay very quickly, but others have long half-lives, especially near the stable members of the series.

Fission Cross Sections

Figure 13.9 shows the cross sections for neutron-induced fission of ^{235}U and ^{238}U. The ^{235}U cross section shows many features in common with the neutron cross sections we considered in Chapter 11. The thermal region shows the usual $1/v$ dependence of the cross section, and numerous resonances dominate the structure in the region 1–100 eV. For ^{235}U, the thermal cross section for fission (584 b) dominates over scattering (9 b) and radiative capture (97 b). Note also that the thermal cross section is 3 orders of magnitude larger than the cross section for fast neutrons. If we wish to use the MeV neutrons emitted in fission to induce new fission events, the neutrons must first be moderated to thermal energies to increase the cross section. For ^{238}U, there is no fission at all in the thermal region; only for fast neutron energies will fission occur. This extreme difference in behavior, as we see in the next section, results from the relationship between the excitation energy of the compound system and the activation energy needed to overcome the barrier.

13.3 ENERGY IN FISSION

In this section we consider in more detail the energy involved in fission. When ^{235}U captures a neutron to form the compound state ^{236}U*, the *excitation energy* is

$$E_{ex} = \left[m(^{236}\text{U}^*) - m(^{236}\text{U})\right]c^2$$

The energy of the compound state can be found directly from the mass energies of ^{235}U and n, if we assume the neutron's kinetic energy is so small (i.e., in the thermal region) that it is negligible.

$$\begin{aligned} m(^{236}\text{U}^*) &= m(^{235}\text{U}) + m_n \\ &= (235.043924\ \text{u} + 1.008665\ \text{u}) \\ &= 236.052589\ \text{u} \\ E_{ex} &= (236.052589\ \text{u} - 236.045563\ \text{u})\ 931.502\ \text{MeV/u} \\ &= 6.5\ \text{MeV} \end{aligned}$$

The activation energy (energy needed to overcome the fission barrier, as in Figure 13.2) for ^{236}U is calculated also to be 6.2 MeV. Thus, the energy needed to excite ^{236}U into a fissionable state (the activation energy) is exceeded by the energy we get by adding a neutron to ^{235}U. This means that ^{235}U can be fissioned with zero-energy neutrons, consistent with its large observed fission cross section in the thermal region.

A similar calculation for $^{238}\text{U} + \text{n} \rightarrow {}^{239}\text{U}^*$ gives $E_{ex} = 4.8$ MeV, which is far smaller than the calculated activation energy of ^{239}U, 6.6 MeV. (Table 13.1 and Figure 13.10 give calculated activation energies for nuclei in this region.) Neutrons of at least MeV energy are therefore required for fission of ^{238}U, which is consistent with the observed threshold for neutron-induced fission of ^{238}U, as indicated in Figure 13.9.

The primary explanation for the extreme differences in the fissionability of ^{235}U and ^{238}U thus lies in the difference between their excitation energies, respectively 6.5 and 4.8 MeV. This difference in turn can be understood in terms

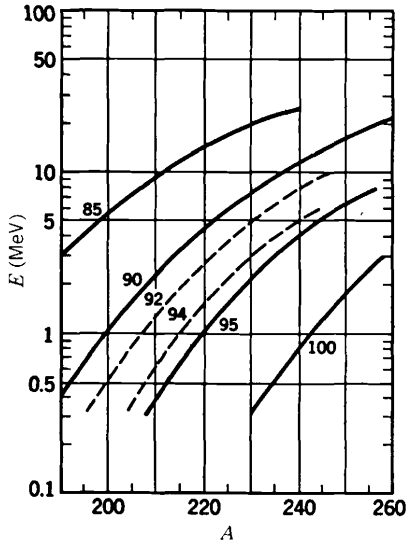


Figure 13.10 Activation energies of heavy nuclei. This graph shows the explicit *A* and *Z* dependence (which is not shown in Figure 13.3), calculated using the liquid-drop model. From S. Frankel and N. Metropolis, *Phys. Rev.* **72**, 914 (1947).

Table 13.1 Fission Cross Sections for Thermal Neutrons

Nuclide	Cross Section (b)	$A + 1$ Activation Energy (MeV)
$^{227}_{90}Th_{137}$	200 ± 20	
$^{228}_{90}Th_{138}$	< 0.3	
$^{229}_{90}Th_{139}$	30 ± 3	8.3
$^{230}_{90}Th_{140}$	< 0.001	8.3
$^{230}_{91}Pa_{139}$	1500 ± 300	7.6
$^{231}_{91}Pa_{140}$	0.019 ± 0.003	7.6
$^{232}_{91}Pa_{141}$	700 ± 100	7.2
$^{233}_{91}Pa_{142}$	< 0.1	7.1
$^{231}_{92}U_{139}$	300 ± 300	6.8
$^{232}_{92}U_{140}$	76 ± 4	6.9
$^{233}_{92}U_{141}$	530 ± 5	6.5
$^{234}_{92}U_{142}$	< 0.005	6.5
$^{235}_{92}U_{143}$	584 ± 1	6.2
$^{238}_{92}U_{146}$	$(2.7 \pm 0.3) \times 10^{-6}$	6.6
$^{234}_{93}Np_{141}$	1000 ± 400	5.9
$^{236}_{93}Np_{143}$	3000 ± 600	5.9
$^{237}_{93}Np_{144}$	0.020 ± 0.005	6.2
$^{238}_{93}Np_{145}$	17 ± 1	6.0
$^{239}_{93}Np_{146}$	< 0.001	6.3
$^{238}_{94}Pu_{144}$	17 ± 1	6.2
$^{239}_{94}Pu_{145}$	742 ± 3	6.0
$^{240}_{94}Pu_{146}$	< 0.08	6.3
$^{241}_{94}Pu_{147}$	1010 ± 10	6.0
$^{242}_{94}Pu_{148}$	< 0.2	6.2
$^{241}_{95}Am_{146}$	3.24 ± 0.15	6.5
$^{242}_{95}Am_{147}$	2100 ± 200	6.2
$^{243}_{95}Am_{148}$	< 0.08	6.3
$^{244}_{95}Am_{149}$	2200 ± 300	6.0
$^{243}_{96}Cm_{147}$	$610 + 30$	6.1
$^{244}_{96}Cm_{148}$	1.0 ± 0.5	6.3
$^{245}_{96}Cm_{149}$	2000 ± 200	5.9
$^{246}_{96}Cm_{150}$	0.2 ± 0.1	6.0

of the pairing energy term δ of the semiempirical mass formula, Equation 3.28. Figure 13.11 illustrates the effect of the pairing term. The binding energy of ^{236}U is increased (that is, its ground-state energy is lowered) by an amount δ, which is roughly 0.56 MeV; the excitation energy is correspondingly increased by δ over what it would be in the absence of pairing. In the case of ^{238}U, the energy of the ground state *before capture* is lowered by δ, and as a result the energy of the

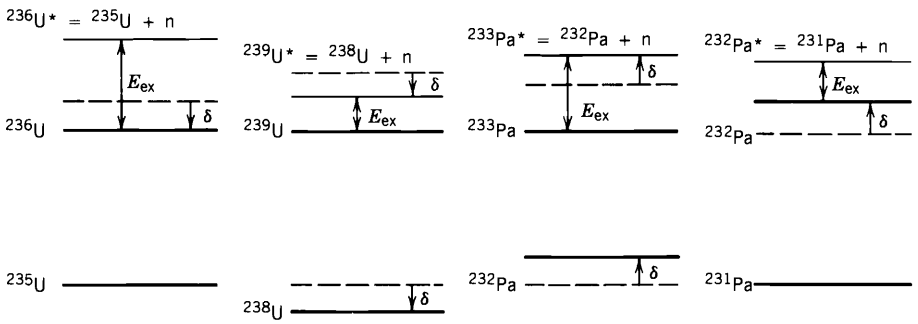


Figure 13.11 Effect of pairing on excitation energies. The dashed levels show the nuclear energies in the absence of pairing, which are then raised or lowered by the amount δ when the effect of pairing is included.

capture state is correspondingly lower. The excitation energy is therefore *reduced* by δ relative to its value without the pairing force term. The difference in excitation energy between $^{235}U + n$ and $^{238}U + n$ is therefore about 2δ or 1.1 MeV, which nicely accounts for most of the observed difference.

Similar considerations based on the pairing force lead us to expect the following additional results, as indicated in Figure 13.11—an increase in the excitation energy for neutron-induced fission in ^{232}Pa and a decrease in ^{231}Pa. We therefore expect that ^{232}Pa will fission more easily with thermal neutrons than will ^{231}Pa. Table 13.1 shows the thermal neutron cross sections for a variety of nuclei in this region. You can see quite clearly that neutron capture by *any* odd-N nucleus will lead to a more stable (paired) even-N configuration, with a corresponding increase in E_{ex} by δ. Capture by even-N nuclei will lead to reductions in E_{ex} by the same amount. We therefore expect that odd-N nuclei will in general have much larger thermal neutron cross sections than even-N nuclei, and the data listed in Table 13.1 are consistent with this expectation. The large fission cross sections of ^{235}U and ^{239}Pu owe much to the pairing force!

We now turn to a consideration of the energy released in fission and where it goes. Let us begin by considering a specific set of final products:

$$^{235}U + n \rightarrow ^{236}U^* \rightarrow ^{93}Rb + ^{141}Cs + 2n$$

Using the masses of ^{93}Rb (92.92172 u) and ^{141}Cs (140.91949 u), the Q value is computed to be 181 MeV. Other final products (possibly with a different number of neutrons emitted) will give energy releases of roughly the same magnitude, and it is quite reasonable to take 200 MeV as an average figure for the energy released in the fission of ^{235}U. (This value is consistent with the estimate of 0.9 MeV per nucleon introduced earlier, and also with the Coulomb repulsion energy of the two fragments separated roughly by $R = R_1 + R_2$.) The Coulomb repulsion will drive the two fragments apart, converting the potential energy to kinetic, and giving them of order 200 MeV of kinetic energy in the process. Figure 13.12 shows the observed energy distribution of the two fission fragments. There are two highly probable energies, at about 66 and 98 MeV. These correspond to the heavy and the light fragment, respectively. Because the neutrons carry very little momentum, conservation of momentum requires that the two fragments have nearly equal (and opposite) momenta: $m_1v_1 = m_2v_2$, from which it is easy to see that the ratio between the kinetic energies should be the inverse of the ratio of the

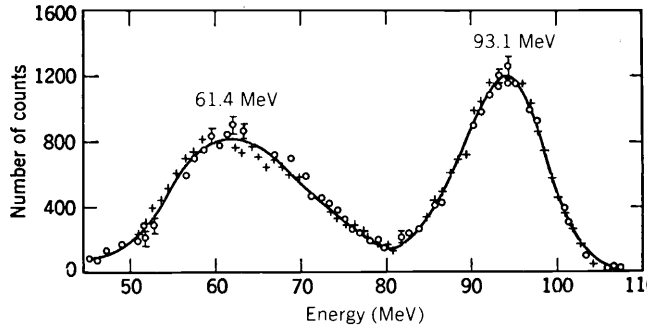


Figure 13.12 Energy distribution of fission fragments from thermal fission of ^{235}U. These data were taken with an ion chamber, which subsequent work showed to be slightly miscalibrated for fission fragments; the deduced energies are about 5 MeV too low. From J. L. Fowler and L. Rosen, *Phys. Rev.* **72**, 926 (1947).

masses:

$$\frac{\frac{1}{2}m_1v_1^2}{\frac{1}{2}m_2v_2^2} = \frac{m_2}{m_1} \tag{13.4}$$

The ratio 66 MeV/98 MeV = 0.67 is entirely consistent with the ratio of the most probable masses obtained from Figure 13.6, $(140/95)^{-1} = 0.68$. This distribution of energies thus appears to be characteristic of the distribution of masses, and suggests that on the average 165 MeV or roughly 80% of the fission energy appears as kinetic energy of the fragments.

Figure 13.13 shows the distribution of prompt neutron energies following fission of ^{235}U. The mean energy is about 2 MeV, and with an average of about 2.5 neutrons per fission, the average energy carried by the neutrons in fission is about 5 MeV. This also suggests that the average neutron carries a momentum only 2% that of either of the fragments, thus justifying neglecting the neutron momentum in the estimate of Equation 13.4.

Other energy releases in fission appear as follows:

prompt γ rays, 8 MeV

β decays from radioactive fragments, 19 MeV

γ decays from radioactive fragments, 7 MeV

These are only estimates and will obviously depend on the exact nature of the fragments and their decays; within 1–2 MeV, they are characteristic of most decays. The prompt γ's are emitted essentially at the instant of fission (later than the prompt neutrons, perhaps, but still within 10^{-14} s.) The β and γ radiations are emitted according to the decay schemes of the chain of heavy and light fission fragments. The β energy is, on the average, about 30–40% given to β particles with the remainder ($\sim$ 12 MeV) going to neutrinos. The neutrino energy is lost and contributes neither to the energy recovery or heating of reactor fuel nor to the dangers posed by radioactive waste products.

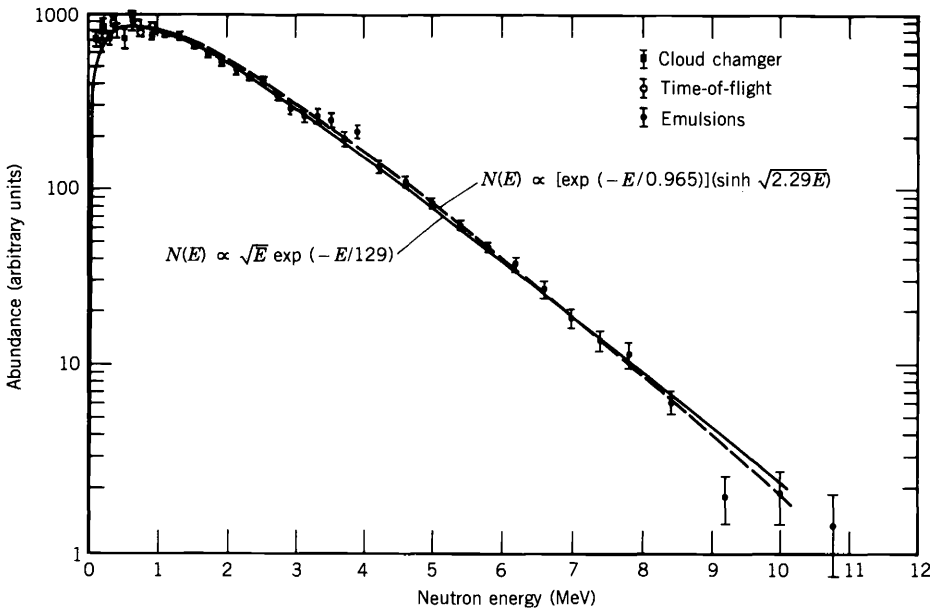


Figure 13.13 Energy spectrum of neutrons emitted in the thermal-neutron fission of ^{235}U. From R. B. Leachman, in *Proceedings of the International Conference on the Peaceful Uses of Atomic Energy*, Vol. 2 (New York: United Nations, 1956), p. 193.

13.4 FISSION AND NUCLEAR STRUCTURE

Fission is generally treated as a collective phenomenon according to the liquid-drop model, and the analogy with a charged drop of liquid is not only helpful analytically, but also provides a useful mental image of the process. It is therefore perhaps surprising to learn that shell effects play an important and in many cases a decisive role in determining the outcome of fission. As a clue to the importance of shell structure we consider in somewhat more detail the asymmetric mass distribution of the fragments (Figure 13.6). Figure 13.14 shows the mass distributions for ^{236}U and for several other fissioning nuclei of heavier mass. These distributions reveal an unexpected feature—the mass distributions for the heavy fragments overlap quite well, while the lighter fragment shows a large variation. Comparing ^{236}U with ^{256}Fm, we note that Z, N, and A all increase by about 8.5%, and if the liquid-drop model of fission were a complete description of the process, we should expect both the heavy and light fragment distributions to shift by about 8.5% between ^{236}U and ^{256}Fm; that is, the average masses should go from about 95 and 140 in ^{236}U to about 103 and 152 in ^{256}Fm. Instead, the observed average masses in ^{256}Fm are about 114 and 141. The 20 additional mass units in ^{256}Fm nearly all find themselves given to the lighter fragment.

A more dramatic indication of this effect is illustrated in Figure 13.15, which shows the average masses of the light and heavy fragments over a mass range from 228 to 256. The average mass of the heavy fragment stays nearly constant at about 140, while the average mass of the lighter fragment increases linearly as A increases. Throughout this entire range, the added nucleons all go to the lighter

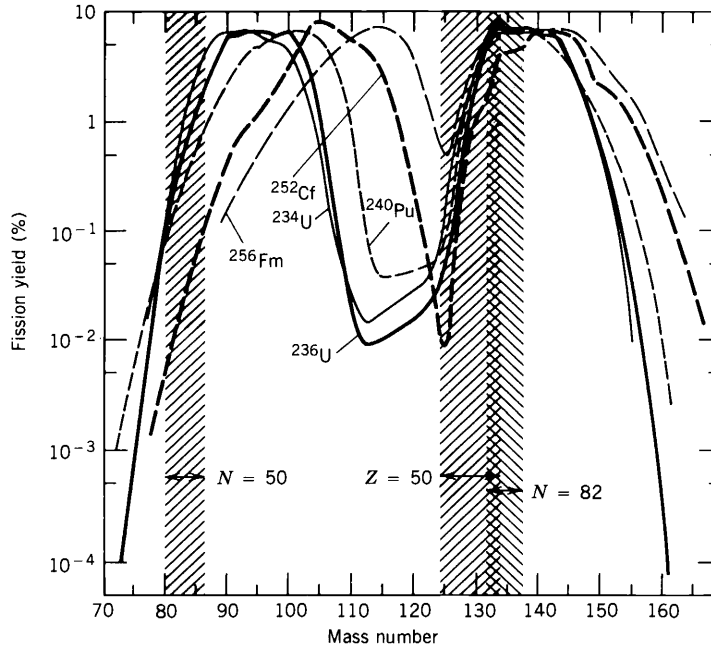


Figure 13.14 Mass distribution of fission fragments from thermal-neutron fission of ^{233}U, ^{235}U, and ^{239}Pu, along with spontaneous fission of ^{252}Cf and ^{256}Fm. Shaded areas show approximate locations of closed-shell nuclei. From A. C. Wahl, in *Physics and Chemistry of Fission*, Vol. I (Vienna: IAEA, 1965), p. 317. Data for ^{256}Fm from K. F. Flynn et al., *Phys. Rev. C* **5**, 1725 (1972).

fragment, while in a liquid-drop fission we would expect the average masses to scale roughly with the mass of the drop.

The explanation for this unusual observed behavior lies with the shell model. Figure 13.14 shows the regions in which we would expect to find fission fragments with shell-model "magic numbers" of protons or neutrons. That is, for $Z = 50$ we have a stable nucleus with $Z/A = 0.4$ (and thus with $A = 125$) and neutron-rich fission products ranging down to a minimum of about $Z/A \simeq 0.38$ (corresponding to $A = 132$ and thus about 7 neutrons from stability). Just at the lower edge of the heavy fragment mass distribution there is the doubly magic nucleus $^{132}_{50}\mathrm{Sn}_{82}$. This exceptionally stable configuration determines the low edge of the mass distribution of the heavier fragment. No such effect occurs for the lighter fragment, and indeed the light fragment mass distribution has practically no overlap even with singly magic nuclei and is thus unaffected by shell closures.

The most drastic effect of shell structure occurs in the fission barrier itself. As we begin to stretch the nucleus (characterized by an eccentricity parameter ε), the energy increases like ε^2 as in Equation 13.2, giving an approximate parabolic dependence. The single-particle states in the now deformed nucleus vary with deformation as in Figure 5.29. Notice that for some states in Figure 5.29, the energy increases with deformation, while for some others it decreases. If the valence nucleons are in a state that happens to have a positive slope, the net increase in energy with deformation will be a bit faster than the parabola, for the single-particle energy also increases with ε. At some point, however, as ε

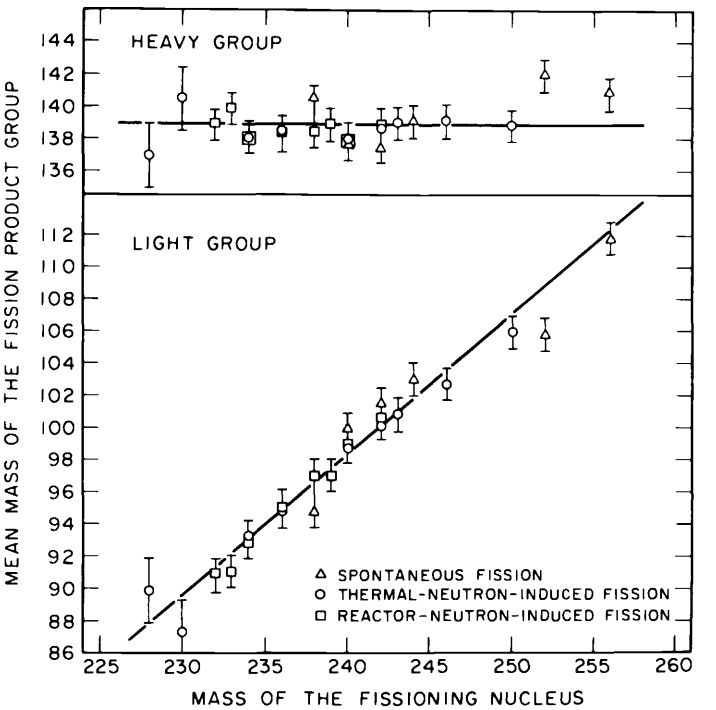


Figure 13.15 Dependence of average masses of heavy and light groups of fission fragments on mass of fissioning nucleus. From K. F. Flynn et al., *Phys. Rev. C* **5**, 1725 (1972).

increases in Figure 5.29 we encounter a crossing with a state of negative slope. The valence particle, choosing the state of lowest energy, now follows the new state, and the net change of energy with ε is a bit *below* the parabola. It remains so until a new crossing with a state whose energy increases with ε, so that the total energy is once again above the parabola. This oscillation due to the changing behavior of the valence particles with ε is shown in Figure 13.16. At the point where fission begins to occur, the form of the single barrier that was shown in Figure 13.2 becomes modified and the energy dependence introduced by the single-particle shell structure results in a fission barrier with two humps. The net effect is that to have a high probability to fission, we no longer need to excite the nucleus so it is close to the top of the barrier. If we excite it above the bottom of the well between the two humps, penetration of the two thinner barriers becomes more probable and fission can occur.

The introduction of the double-humped barrier was necessary following the 1962 discovery of *fission (or shape) isomers*—isomeric excited states with unusually short half-lives for spontaneous fission. Several dozens of the fission isomers are known today. They are typically at excitations of 2–3 MeV (and thus far below the barrier height of 6–7 MeV), but their half-lives for spontaneous fission are in the range of 10^{-6}–10^{-9} s. It was postulated that these isomers were actually states in the intermediate potential well and could decay either by fission through a relatively thin barrier, or by γ emission back to the ground state. Figure 13.17 illustrates the situation. The ordinary ground state is usually one of

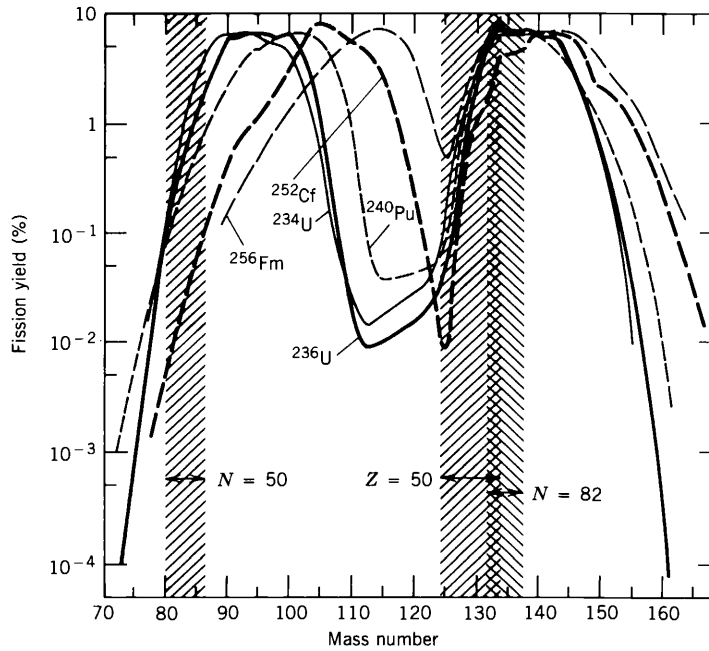


Figure 13.14 Mass distribution of fission fragments from thermal-neutron fission of ^{233}U, ^{235}U, and ^{239}Pu, along with spontaneous fission of ^{252}Cf and ^{256}Fm. Shaded areas show approximate locations of closed-shell nuclei. From A. C. Wahl, in *Physics and Chemistry of Fission*, Vol. I (Vienna: IAEA, 1965), p. 317. Data for ^{256}Fm from K. F. Flynn et al., *Phys. Rev. C* **5**, 1725 (1972).

fragment, while in a liquid-drop fission we would expect the average masses to scale roughly with the mass of the drop.

The explanation for this unusual observed behavior lies with the shell model. Figure 13.14 shows the regions in which we would expect to find fission fragments with shell-model "magic numbers" of protons or neutrons. That is, for $Z = 50$ we have a stable nucleus with $Z/A = 0.4$ (and thus with $A = 125$) and neutron-rich fission products ranging down to a minimum of about $Z/A \simeq 0.38$ (corresponding to $A = 132$ and thus about 7 neutrons from stability). Just at the lower edge of the heavy fragment mass distribution there is the doubly magic nucleus $^{132}_{50}\mathrm{Sn}_{82}$. This exceptionally stable configuration determines the low edge of the mass distribution of the heavier fragment. No such effect occurs for the lighter fragment, and indeed the light fragment mass distribution has practically no overlap even with singly magic nuclei and is thus unaffected by shell closures.

The most drastic effect of shell structure occurs in the fission barrier itself. As we begin to stretch the nucleus (characterized by an eccentricity parameter ε), the energy increases like ε^2 as in Equation 13.2, giving an approximate parabolic dependence. The single-particle states in the now deformed nucleus vary with deformation as in Figure 5.29. Notice that for some states in Figure 5.29, the energy increases with deformation, while for some others it decreases. If the valence nucleons are in a state that happens to have a positive slope, the net increase in energy with deformation will be a bit faster than the parabola, for the single-particle energy also increases with ε. At some point, however, as ε

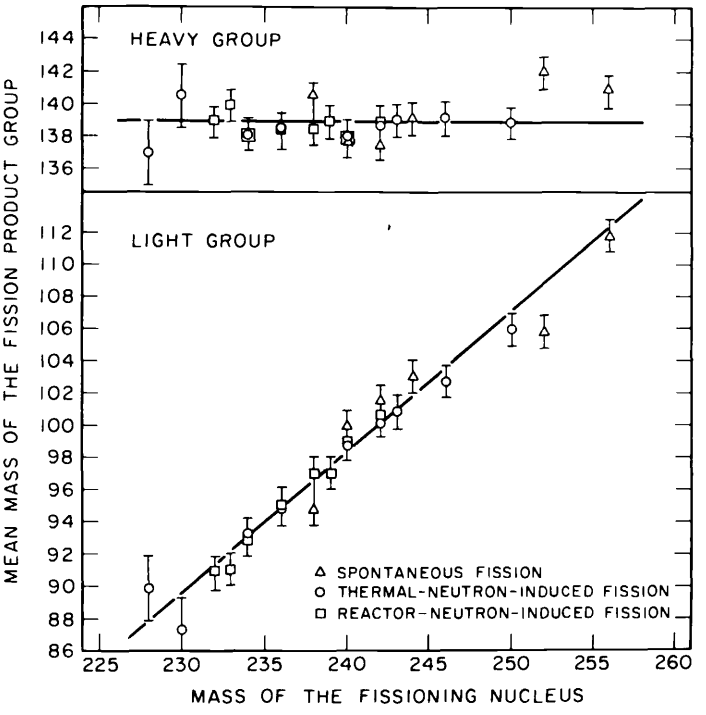


Figure 13.15 Dependence of average masses of heavy and light groups of fission fragments on mass of fissioning nucleus. From K. F. Flynn et al., *Phys. Rev. C* **5**, 1725 (1972).

increases in Figure 5.29 we encounter a crossing with a state of negative slope. The valence particle, choosing the state of lowest energy, now follows the new state, and the net change of energy with ε is a bit *below* the parabola. It remains so until a new crossing with a state whose energy increases with ε, so that the total energy is once again above the parabola. This oscillation due to the changing behavior of the valence particles with ε is shown in Figure 13.16. At the point where fission begins to occur, the form of the single barrier that was shown in Figure 13.2 becomes modified and the energy dependence introduced by the single-particle shell structure results in a fission barrier with two humps. The net effect is that to have a high probability to fission, we no longer need to excite the nucleus so it is close to the top of the barrier. If we excite it above the bottom of the well between the two humps, penetration of the two thinner barriers becomes more probable and fission can occur.

The introduction of the double-humped barrier was necessary following the 1962 discovery of *fission (or shape) isomers*—isomeric excited states with unusually short half-lives for spontaneous fission. Several dozens of the fission isomers are known today. They are typically at excitations of 2–3 MeV (and thus far below the barrier height of 6–7 MeV), but their half-lives for spontaneous fission are in the range of 10^{-6}–10^{-9} s. It was postulated that these isomers were actually states in the intermediate potential well and could decay either by fission through a relatively thin barrier, or by γ emission back to the ground state. Figure 13.17 illustrates the situation. The ordinary ground state is usually one of

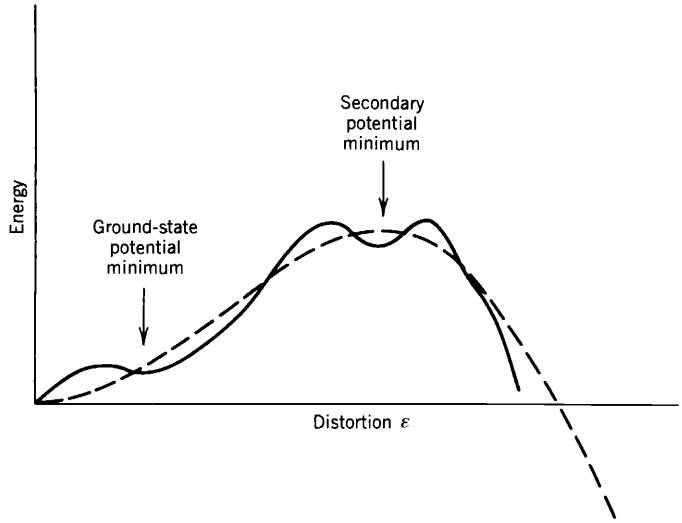


Figure 13.16 The dashed line shows the nuclear energy in the absence of shell effects; it is a much magnified section of Figure 13.2 and is approximately parabolic for small distortions. The solid line oscillates above and below the dashed line owing to the shell structure; the result is a distorted ground-state potential minumum and a more distorted secondary potential minimum.

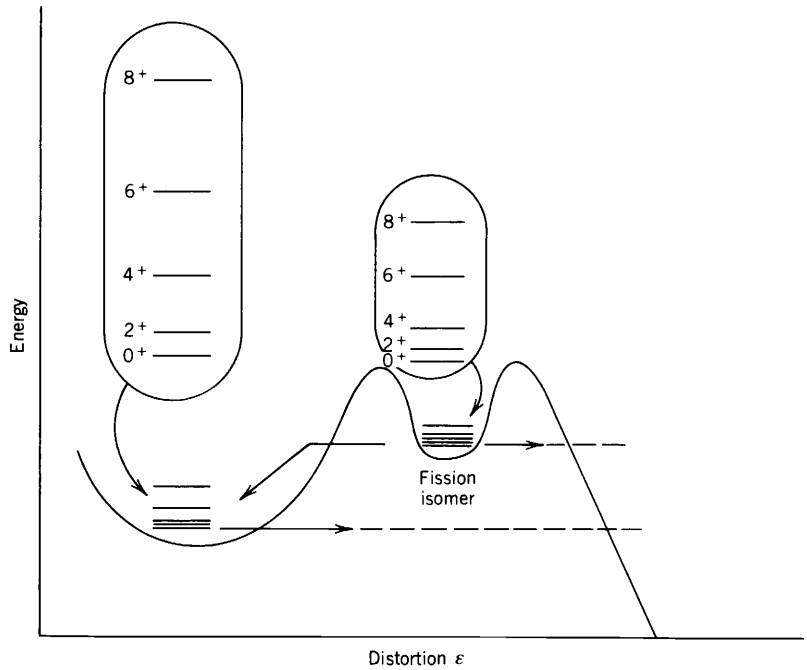


Figure 13.17 Fission isomers are states in the secondary potential well. They have a higher probability to fission compared with the ordinary ground state because they must penetrate a much thinner potential barrier. The rotational excited states show that the second well corresponds to a larger deformation and therefore to a larger moment of inertia.

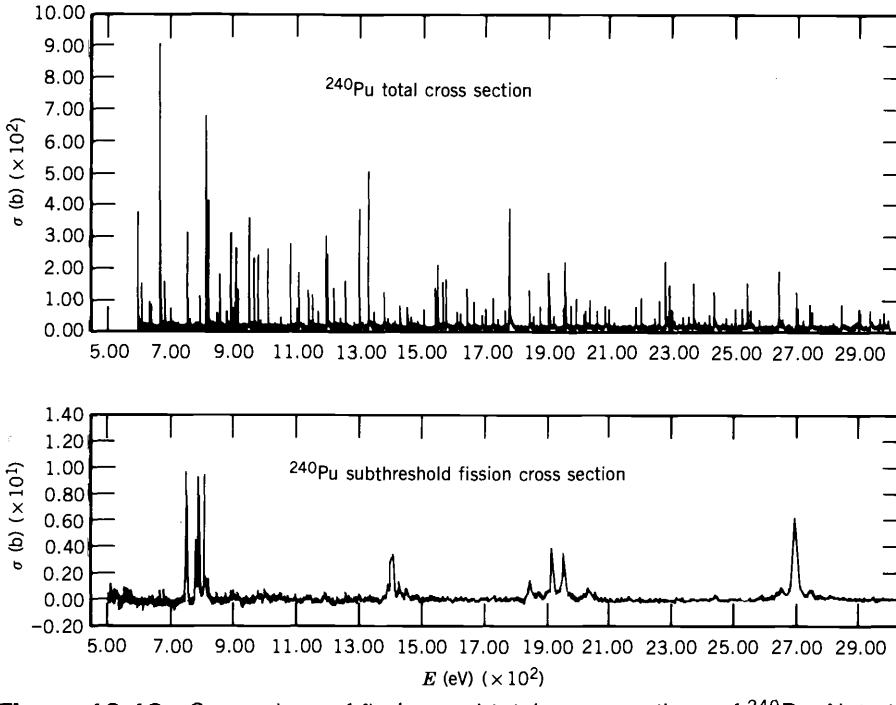


Figure 13.18 Comparison of fission and total cross sections of ^{240}Pu. Note the grouping of the fission resonances. From V. M. Strutinsky and H. C. Pauli, in *Physics and Chemistry of Fission* (Vienna: IAEA, 1969), p. 155.

modest stable deformation, and the well corresponds to states of a much larger deformation. It is easy to see why these states have spontaneous fission lifetimes short compared with the ground states.

This explanation of the fission isomers was confirmed by measurements of the rotational spectra of the excited states in the second potential well. The rotational spectrum was presented in Equation 5.17. As the deformation increases, the moment of inertia becomes larger and the rotational states become closer together in energy. Figure 13.17 shows two sequences of rotational states, one corresponding to about twice the moment of inertia of the other. These states have been identified from the observation of the $E2$ γ transitions between them.

Another influence of the second potential well is on the structure of the resonances in the fission cross section. As in Figure 13.9, there are many individual fission resonances in the eV–keV region. We can regard these resonances as originating from excited states in the first potential well. In *any* nucleus, at an excitation of 6 MeV following neutron capture, the level density is very high, and there are many states separated in energy by an average spacing of the order of eV. Not all of these excited compound states following neutron capture are likely to fission. Figure 13.18 compares the fission cross sections with the total neutron cross section for ^{240}Pu. You can see that the fission picks out a few of the resonances that are likely to fission. The other resonances decay through other processes, perhaps by γ or neutron emission.

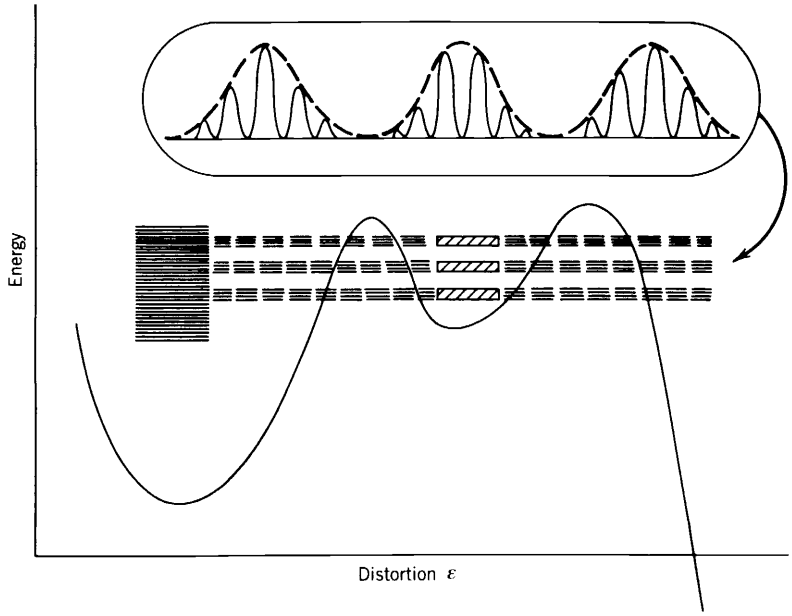


Figure 13.19 There are many closely spaced states in the first well and a few broad, widely separated states in the second well. Fission resonances occur where states in the first well match in energy (and in spin-parity) with states in the second well. If we reach these selected states in the first well, we will observe them to fission with high probability. The resultant fission resonant structure is shown.

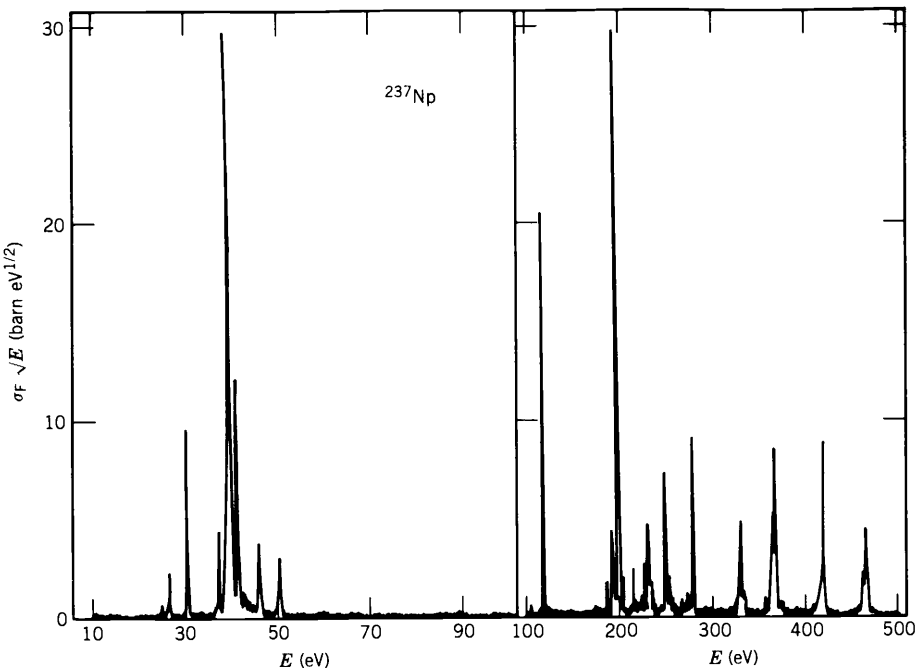


Figure 13.20 Fission resonances in ^{237}Np. The broad peaks in the low-resolution spectrum at right are the many unresolved states corresponding to the broad states of the second well. A high-resolution view of a resonance around 40 eV is shown at left, which reveals the narrow states characteristic of the first well. From D. Paya et al., *Physics and Chemistry of Fission* (Vienna: IAEA, 1969), p. 307.

A closer inspection of Figure 13.18 shows a more interesting effect—the fission resonances appear to cluster in well-separated groups. This effect occurs because the second well is not quite as deep as the first. The density of states of any nucleus depends on the excitation energy above the ground state—the higher we go above the ground state, the closer together are the states. States in the second well at the same energy as those in the first well are on the average further apart —perhaps the average spacing is 100–1000 eV in the second well and 1–10 eV in the first well. Another difference is that states in the second well have a higher probability to fission (because they must penetrate only one barrier) and thus a greater width than states in the first well. Figure 13.19 gives a schematic view of the relationship between the states in the two wells, showing how the fissioning states are selected through their overlap in energy between narrow, closely spaced states in the first well, and broader, more widely spaced states in the second well. The effect on the cross section is also shown and gives rise to the resonance structure shown in Figure 13.18.

The actual neutron fission resonances involve relatively complicated couplings of wave functions representing states in the first and second wells. Because angular momentum and parity are always good quantum numbers, we can combine the states only if they have the same angular momentum. Each of the broad states in the second well has a definite spin-parity assignment, and it will

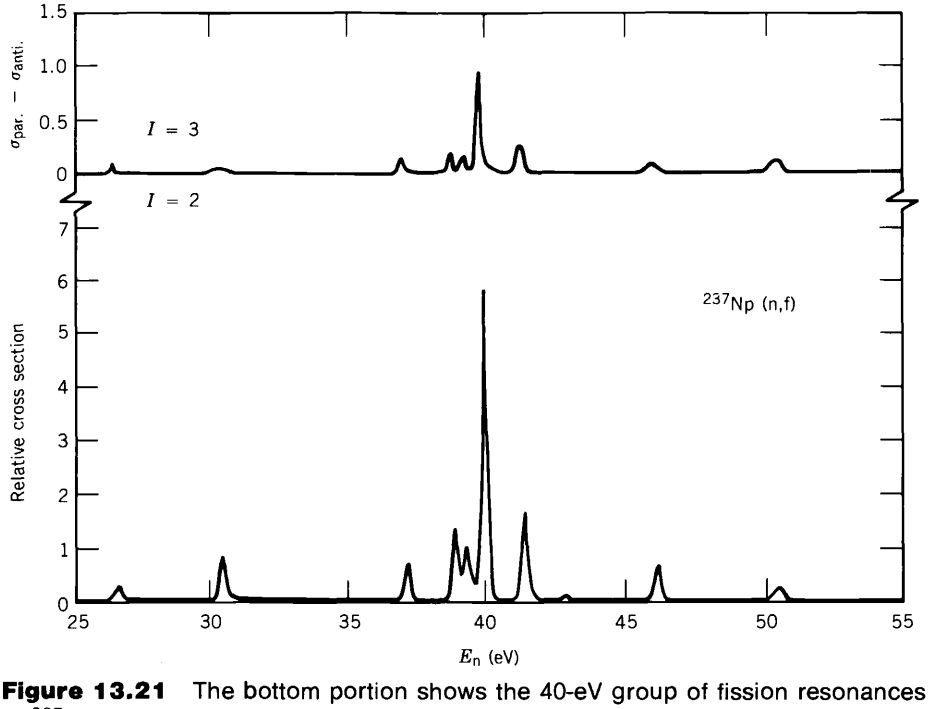


Figure 13.21 The bottom portion shows the 40-eV group of fission resonances of ^{237}Np, as in Figure 13.20. The top portion shows the difference in cross section between neutron and ^{237}Np spins parallel and antiparallel, which should be positive for $I = 3$ and negative for $I = 2$. Clearly the entire group has $I = 3$, consistent with the common origin of the states with the broad resonance of the second well. From G. A. Keyworth et al., *Phys. Rev. C* **8**, 2352 (1973).

couple only with overlapping states from the first well of the same spin-parity assignment. Thus not all of the states of the first well within the energy width of a state of the second well will show these enhanced resonant fission cross sections; only those with the proper spin-parity assignment. If we excite the states in the first well by capture of s-wave neutrons, the only possible spin assignments of the levels in the first well are $I + \frac{1}{2}$ and $I - \frac{1}{2}$, where I is the spin of the original target nucleus. We therefore expect that the groupings consist of many resonances with identical spin-parity assignments within each group (but possibly differing from one group to another). Verification of this hypothesis comes from experiments done using fission induced by polarized neutrons incident on polarized targets. For example, consider the case of ^{237}Np ($I = \frac{5}{2}$). The capture states can be $I = 2$ or 3. If we do the experiment with the spins of the incident neutrons parallel to those of the target, only $I = 3$ states can be populated, and we ought to be able to pick out the $I = 3$ resonances. Figure 13.20 shows the fission cross section for ^{237}Np. The broad unresolved peaks are the states of the second well, each containing many individual states. A high-resolution view of the resonance near 40 eV is shown in Figure 13.21, and the cross section

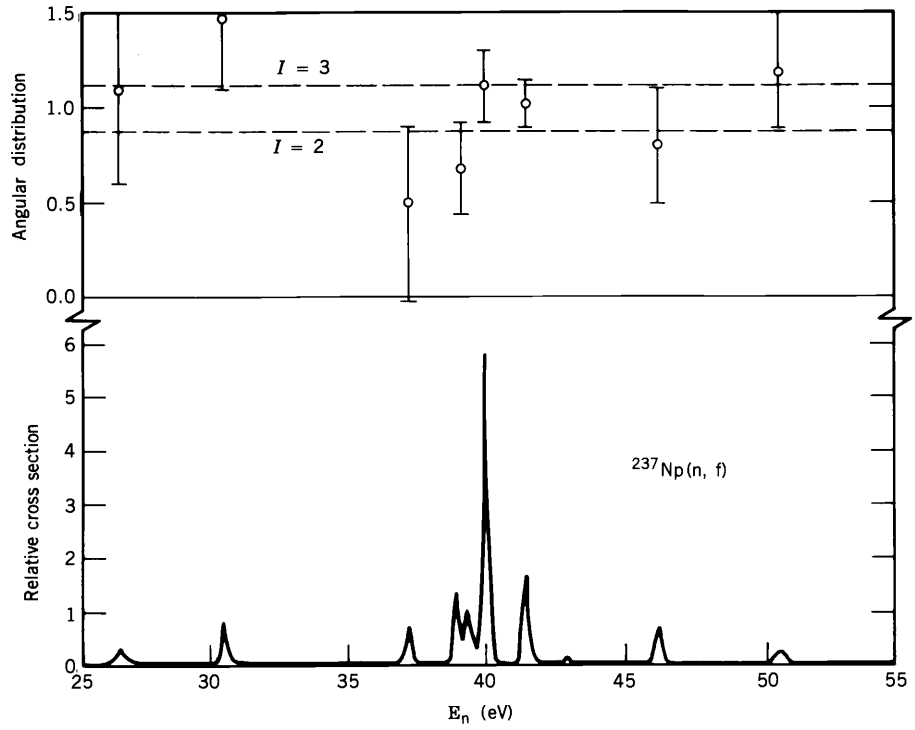


Figure 13.22 As in Figure 13.21, the bottom portion shows the region of the 40-eV group of fission resonances of ^{237}Np. The top shows the angular distribution coefficient of the fission fragments from aligned ^{237}Np. The results are generally consistent with $I = 3$, but do not discriminate between $I = 2$ and $I = 3$ as well as the data of Figure 13.21. From R. Kuiken, N. J. Pattenden, and H. Postma, *Nucl. Phys.* *A* **196**, 389 (1972).

measured with neutron and target spins parallel shows every peak of the multiplet, indicating they all have $I = 3$. The 120-eV broad resonance is also observed to be $I = 3$, while the groups at about 230 and 375 eV are $I = 2$.

An alternative approach to this same end is to study the angular distribution of the fragments produced following unpolarized neutron capture on nuclei whose spins are aligned. Figure 13.22 shows a sample set of results for the 40-eV group of resonances in ^{237}Np. Although the discrimination between $I = 2$ and $I = 3$ is not as absolute as in the case of the studies with polarized neutrons, the data do indicate similar conclusions regarding $I = 3$ for this group of resonances.

13.5 CONTROLLED FISSION REACTIONS

Let's consider an infinitely large mass of uranium, which we will for the present assume to be of natural isotopic composition (0.72% ^{235}U, 99.28% ^{238}U). A single fission event will produce, on the average, about 2.5 neutrons. Each of these "second-generation" neutrons is capable of producing yet another fission event producing still more neutrons, and so on. This process is the *chain reaction*. Each fission event releases about 200 MeV in the form of kinetic energy of heavy fragments (that is, heat) and radiation.

It is convenient to define the *neutron reproduction factor* k_∞ (for an infinite medium, that is, ignoring loss of neutrons through leakage at the surface). The reproduction factor gives the net change in the number of thermal neutrons from one generation to the next; on the average, each thermal neutron produces k_∞ new thermal neutrons. For a chain reaction to continue, we must have $k_\infty \geq 1$. Although we have an average of 2.5 neutrons emitted per fission, these are *fast neutrons*, for which the fission cross section is small. It is advantageous to *moderate* these neutrons to thermal velocities because of the large thermal cross section (about 580 b) resulting from the $1/v$ law. In the process, many neutrons can become absorbed or otherwise lost to the chain reaction, and the 2.5 fast neutrons per fission can easily become < 1 thermal neutron, effectively halting the reaction.

As we discussed in Section 12.2, neutrons lose energy in elastic collisions with nuclei, and a popular choice for a moderator is carbon in the form of graphite blocks. (The best choice for a moderator is the lightest nucleus, to which the neutron transfers the largest possible energy in an elastic collision. Carbon is a reasonable choice because it is available as a solid, thus with a high density of scattering atoms, and is inexpensive and easy to handle.) A lattice of blocks of uranium alternating with graphite is called a chain-reacting *pile*, and the first such pile was constructed by Fermi and his collaborators in a squash court at the University of Chicago in 1942. If the reproduction factor k (for a finite pile) is exactly 1.0, the pile is said to be *critical*; for $k < 1$, the pile is *subcritical* and for $k > 1$ it is *supercritical*. To maintain a steady release of energy, we would like for the pile to be exactly critical.

To calculate the reproduction factor k_∞, we must follow the fate of a collection of thermal neutrons from one generation to the next. Let's assume we have N thermal neutrons in the present generation. Even though each fission produces on

the average ν neutrons, we will *not* have νN fast fission neutrons immediately available, for not every one of the original collection will cause a fission event. Some will be absorbed through other processes, most notably (n, γ) reactions in both ^{235}U and ^{238}U. We define η as the mean number of fission neutrons produced per original thermal neutron. It is clear that $\eta < \nu$, for some of the original thermal neutrons do not cause fissions. If we let σ_f represent the fission cross section and σ_a the cross section for other absorptive processes (both of these cross sections are evaluated for thermal neutrons), then the relative probability for a neutron to cause fission is $\sigma_f/(\sigma_f + \sigma_a)$ and

$$\eta = \nu \frac{\sigma_f}{\sigma_f + \sigma_a} \tag{13.5}$$

For ^{235}U, $\sigma_f = 584$ b and $\sigma_a = 97$ b, so that $\eta = 2.08$ fast neutrons are produced per thermal neutron. ^{238}U is not fissionable with thermal neutrons, and so $\sigma_f = 0$, but $\sigma_a = 2.75$ b. For a natural mixture of ^{235}U and ^{238}U, the effective fission and absorption cross sections are

$$\sigma_f = \frac{0.72}{100}\sigma_f(235) + \frac{99.28}{100}\sigma_f(238)$$
$$= 4.20 \text{ b}$$
$$\sigma_a = \frac{0.72}{100}\sigma_a(235) + \frac{99.28}{100}\sigma_a(238)$$
$$= 3.43 \text{ b}$$

and the effective value of η becomes 1.33. This is already very close to 1.0, so we must minimize other ways that neutrons can be lost, in order to obtain a critical reactor. If we use enriched uranium, in which the fraction of ^{235}U is raised to 3%, the effective value of η becomes 1.84, considerably further from the critical value and allowing more neutrons to be lost by other means and still maintain the criticality condition.

At this point the N thermal neutrons have been partly absorbed and the remainder have caused fissions, and we now have ηN fast neutrons which must be reduced to thermal energies. As these fast neutrons journey through the chain-reacting pile, some of them may encounter ^{238}U nuclei which have a small cross section (about 1 b) for fission by fast neutrons. This causes a small increase in the number of neutrons, so we introduce a new factor ε, the *fast fission factor*; the number of fast neutrons is now $\eta\varepsilon N$. The value of ε is about 1.03 for natural uranium.

Moderation of the neutrons is accomplished by intermixing the reactor fuel with a light moderator, such as carbon, usually in the form of graphite. As indicated in Table 12.1, it takes about 100 collisions with carbon for MeV neutrons to be thermalized. In the process, they must pass through the region from 10–100 eV, in which ^{238}U has many capture resonances (Figure 13.23) with cross sections in the range of 1000 b (greater than the ^{235}U fission cross section). If we are to have any thermal neutrons at all, we must find a way for the neutrons to avoid resonance capture. If the uranium and the graphite are intimately mixed, such as in the form of fine powders, it will be almost impossible for neutrons to avoid resonant capture in ^{238}U. In this kind of mixture, a neutron may scatter

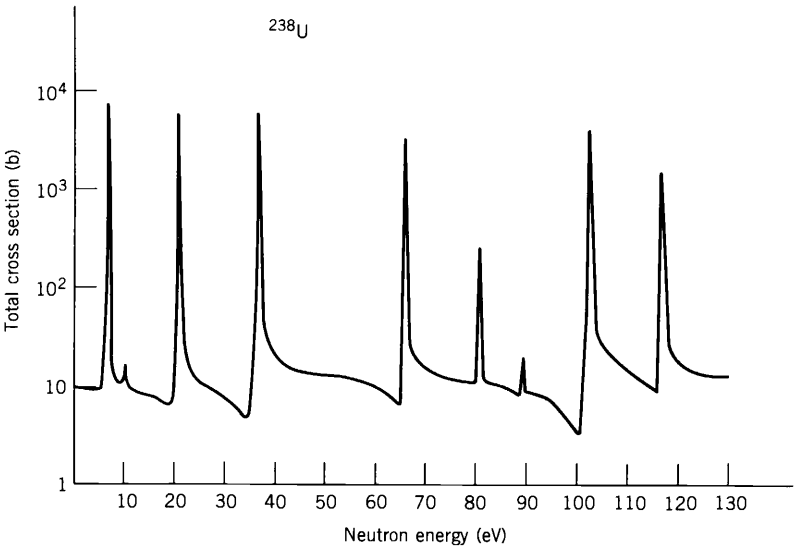


Figure 13.23 Neutron-capture resonance region of ^{238}U.

very few times from carbon before encountering a ^{238}U nucleus, and therefore will very likely pass near ^{238}U when its energy is in the critical region. If we make the lumps of graphite larger, we will eventually reach a configuration in which the neutrons can be completely thermalized through many scatterings without leaving the graphite and encountering any ^{238}U. In this way it is possible to avoid the dangerous resonance region. The average distance needed by a fission neutron to slow to thermal energies in graphite is about 19 cm. If we therefore construct the pile as a matrix of uranium fuel elements separated by about 19 cm of graphite, we minimize the neutron losses due to resonant capture. Of course, it will still be possible for some neutrons to wander too close to the surface of the graphite and enter the uranium before they are fully thermalized, and thus resonant capture cannot be completely eliminated. We account for this effect by including a reduction factor p, the *resonance escape probability*, in the number of neutrons remaining after thermalization, now $\eta\varepsilon pN$. A typical value of p might be 0.9.

Once the neutrons are successfully thermalized, we must immediately get them into the uranium, so the graphite lumps mustn't be made too large. In any case, there is a probability of capture of thermal neutrons by graphite and by any structural components of the reactor (such as the material used to encapsulate the fuel elements). One reason for choosing carbon as a moderator is that it has a very small thermal cross section (0.0034 b), but there is a lot of it present. The *thermal utilization factor* f gives the fraction of the thermal neutrons that are actually available to ^{235}U and ^{238}U. This factor may also typically be about 0.9.

The number of neutrons which finally survive capture by the moderator and other materials is $\eta\varepsilon pfN$, and whether this is greater or smaller than the original number N determines the criticality of the reactor. The reproduction factor is

$$k_\infty = \eta\varepsilon pf \tag{13.6}$$

which is known for obvious reasons as the *four-factor formula*. Figure 13.24 shows the processes that can occur to neutrons during a reactor cycle.

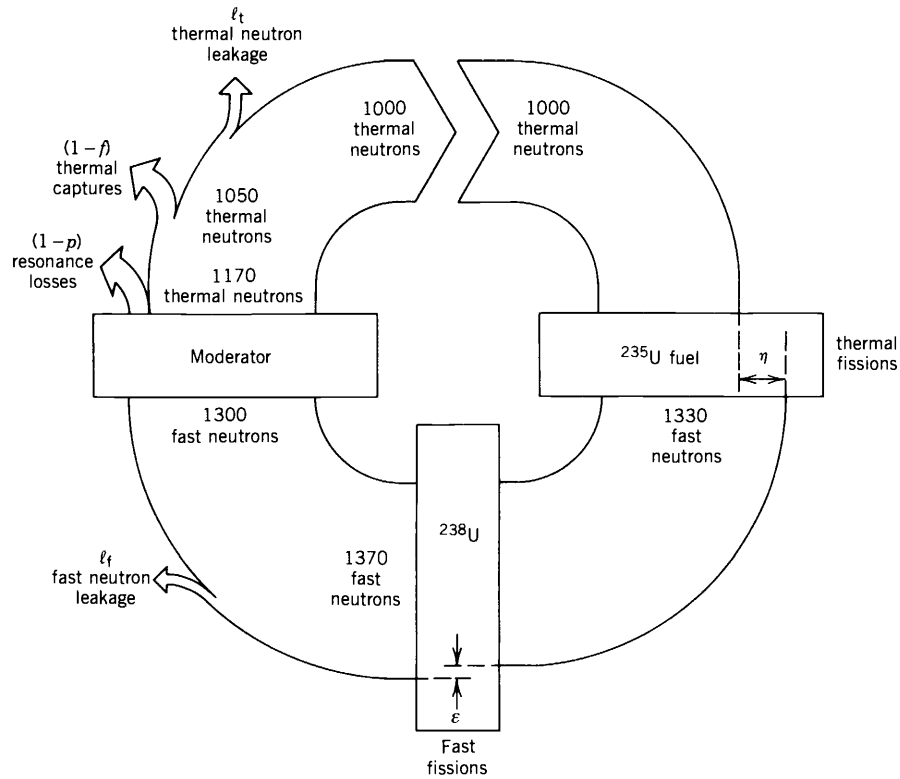


Figure 13.24 Schematic representation of processes occurring during a single generation of neutrons. The cycle has been drawn for a reproduction factor k of exactly 1.000.

The actual design of the pile will be a compromise of attempts to optimize the three factors that depend on the geometry (ε, p, f). For instance, large lumps of U tend to reduce p because resonant absorption occurs primarily on the surface; that is, a neutron of energy 10–100 eV that enters a uranium lump is unlikely to get very far before absorption. The uranium in the center of the lump never sees such neutrons, and that central mass of uranium can be treated from the perspective of resonant absorption as if it were not present. The larger the lumps of uranium, the more effective is the surface in shielding the central uranium from neutron absorption. On the other hand, if the lumps become too large, the same effect occurs for the thermal neutrons that cause fission—more fission occurs near the surface and the density of thermal neutrons decreases toward the center of the lump of uranium.

Using the four factors estimated for the natural uranium and graphite pile, the reproduction factor is estimated to be $k_\infty = 1.11$. This estimate is still not appropriate for an actual pile, for we have ignored leakage of neutrons at the surface. This leakage must be considered both for fast neutrons and for thermalized neutrons. If ℓ_f and ℓ_t are the fractions of each that are lost, the complete formula for the reproduction factor is

$$k = \eta\varepsilon pf(1 - \ell_f)(1 - \ell_t) \tag{13.7}$$

The larger the pile, the smaller is the surface area to volume ratio and the smaller is the fraction of neutrons that leak. If ℓ_f and ℓ_t are small, then $k_\infty - k \approx k(\ell_f + \ell_t)$. We expect that the total leakage $(\ell_f + \ell_t)$ decreases as the surface area increases. Furthermore, the leakage must increase with the distance a neutron is able to travel before absorption. This distance is called the *migration length* M and it includes two contributions: the diffusion length L_d for thermal neutrons, the distance a thermal neutron can travel on the average before absorption, and the slowing distance L_s over which a fast neutron slows to thermal energies:

$$M = \left(L_d^2 + L_s^2\right)^{1/2} \tag{13.8}$$

For graphite, $L_s = 18.7$ cm and $L_d = 50.8$ cm.

If the pile has dimension R (radius, if it is spherical, or length of a side if a cube), it is reasonable to suppose that $(k_\infty - k) \propto R^{-2}$ and also that $k_\infty - k$ depends on M; if these are the only physical parameters involved, then from a dimensional analysis we expect

$$k_\infty - k \propto \frac{M^2}{R^2} \tag{13.9}$$

and there will be a critical size R_c corresponding to $k = 1$

$$R_c \propto \frac{M}{\sqrt{k_\infty - 1}} \tag{13.10}$$

The proportionality constant needed to make Equation 13.10 an equality depends on the geometry but is of order unity. For a spherical arrangement,

$$R_c = \frac{\pi M}{\sqrt{k_\infty - 1}} \tag{13.11}$$

and our estimates for the natural uranium-graphite reactor give $R_c = 5$ m. A spherical lattice of radius 5 m consisting of uranium and graphite blocks should "go critical." The size can be decreased somewhat by surrounding the pile with a material that reflects escaping neutrons back into the pile.

Before leaving this brief introduction to reactor theory, let's consider the time constants involved in neutron multiplication. The neutrons are characterized by a time constant τ, which includes the time necessary to moderate (about 10^{-6} s) and a diffusion time at thermal energies before absorption (about 10^{-3} s). If the reproduction factor is k, and if there are N neutrons at time t, then there are, on the average, kN neutrons at time $t + \tau$, k^2N at time $t + 2\tau$, and so on. In a short time interval dt, the increase is

$$dN = (kN - N)\frac{dt}{\tau} \tag{13.12}$$

from which

$$N(t) = N_0 e^{(k-1)t/\tau} \tag{13.13}$$

If $k = 1$, then $N =$ constant; this would be the desired operating mode of a reactor. If $k < 1$, the number of neutrons decays exponentially. If $k > 1$, the number of neutrons grows exponentially with time, with a time constant char-

acterized by $\tau/(k-1)$. Even if the reactor is just slightly supercritical ($k = 1.01$), the time constant is of order 0.1 s. It would be dangerous to operate a reactor in which the number of neutrons could increase by a factor of e^{10} ($= 22{,}000$) in 1 s. In practice, control of the number of neutrons is achieved by inserting into the pile a material such as cadmium, which is highly absorptive of thermal neutrons; the cadmium *control rods* are under mechanical control and can be gradually removed from the pile or rapidly inserted. If the pile is designed so that it is just slightly subcritical for prompt neutrons, the small number of delayed neutrons can be used to achieve critical operation, and since the delayed-neutron decay time constants are fairly long (seconds to minutes) the control rods can be manipulated to achieve a constant reaction rate.

13.6 FISSION REACTORS

Nuclear reactor engineering is a complex discipline and we cannot do it justice with a short summary. Nevertheless, there are enough general properties and categories of reactors that it is instructive to try to list them and describe some of them.

All reactors consist of the same essential elements: the *fuel*, or fissile material; a *moderator* to thermalize the neutrons (which may not be present in a reactor using fast neutrons); a *reflector* surrounding the *core* (fuel elements plus moderators) to reduce neutron leakage and thereby reduce the critical size of a reactor; a *containment vessel* to prevent the escape of radioactive fission products, some of which are gases; *shielding* to prevent neutrons and γ rays from causing biological harm to operating personnel; a *coolant* to remove heat from the core; a *control system* allowing the operator to control the power level and to keep it constant during normal operation; and various *emergency systems* designed to prevent runaway operation in the event of a failure of the control or coolant systems.

Types of reactors The first and perhaps most basic classification is the use for which the reactor is intended, and we can loosely define three categories: power generation, research, and conversion. *Power reactors* are nothing more than devices for extracting the kinetic energy of the fission fragments as heat and converting the heat energy to electrical energy, perhaps by boiling water and driving a turbine with the resulting steam. Design considerations for power reactors therefore involve as much attention to thermodynamic details of the efficiency of heat engines as to nuclear engineering. The fuel assembly represents a relatively small fraction of the cost of a power reactor; most of the expenses are associated with the shielding and containment vessel and with the electrical generating equipment. It is therefore economically advantageous to build large power reactors; 10 reactors each producing 100 MW are far more costly than a single 1000-MW reactor. The corresponding thermal wastes are, however, considerable; it must be emphasized that these thermal wastes have nothing to do with the specific nuclear nature of the power source—*any* 1000 MW heat engine is, according to the Second Law of Thermodynamics, going to discharge a great deal of heat in a relatively confined area. (In addition, the nuclear power plant operates at somewhat lower thermodynamic efficiency than a fossil-fuel plant,

and therefore discharges more heat.)

Research reactors are generally designed to produce neutrons for research in areas such as nuclear or solid-state physics. These generally operate at low power levels, in the range of 1–10 MW. Principal design features of research reactors may be large neutron flux (10^{13} n/cm^2/s is typical, but specialized reactors may exceed that by 1–2 orders of magnitude in steady operation and by considerably more in pulsed operation), ease of access to the neutrons (many research reactors have a beam pipe leading from the region of the core to a research facility outside the shielding, for example, a neutron diffraction apparatus to study crystal structures), and quality of neutron spectrum (a *thermal column* is a block of graphite near the core of sufficient thickness to eliminate fast neutrons and allow small samples placed within it to be exposed to neutrons with a relatively pure thermal spectrum).

Converters are reactors designed to have high efficiency for converting material that is not fissionable with thermal neutrons to material that is. The specific conversions that are generally used are ^{238}U to ^{239}Pu and ^{232}Th to ^{233}U. In both cases, the conversion involves the capture of a neutron followed by two β decays:

$$^{238}\mathrm{U} + \mathrm{n} \rightarrow {}^{239}\mathrm{U} \xrightarrow{23\ \mathrm{min}} {}^{239}\mathrm{Np} + \beta^- + \bar{\nu}$$

$$\downarrow 2.3\ \mathrm{d}$$

$$\rightarrow {}^{239}\mathrm{Pu} + \beta^- + \bar{\nu}$$

$$^{232}\mathrm{Th} + \mathrm{n} \rightarrow {}^{233}\mathrm{Th} \xrightarrow{22\ \mathrm{min}} {}^{233}\mathrm{Pa} + \beta^- + \bar{\nu}$$

$$\downarrow 27\ \mathrm{d}$$

$$\rightarrow {}^{233}\mathrm{U} + \beta^- + \bar{\nu}$$

Isotopes such as ^{238}U and ^{232}Th, which can be converted to thermally fissile material, are called *fertile*. In principle it is possible to design a reactor in which the value of η were at least 2.0. With two neutrons emitted per neutron absorbed in the fuel, one neutron could go to sustaining the chain reactions and the other to the fertile material. Assuming other losses could be minimized, if $\eta > 2$ then a reactor could produce more fissile material than it consumed. Such a reactor is called a *breeder*. For thermal neutrons, ^{239}Pu has $\eta = 2.1$ and it is unlikely that losses of neutrons (resonance capture, leakage, etc.) could be kept low enough to permit breeding. For fast (MeV) neutrons, $\eta = 3$ for ^{239}Pu and breeding becomes a strong possibility. Much research has therefore gone into the design and construction of fast breeder reactors. One advantage of this method of production of fissile material is that, following a sufficient time of breeding, the newly made fissile material can be separated from the fertile material by chemical means, which are considerably easier than the methods that must be used to separate fissile and nonfissile isotopes such as ^{235}U and ^{238}U from one another.

Neutron Energy It is possible to design reactors to operate with thermal, intermediate, or fast neutrons. In the last section, the neutron budget for thermal reactors was discussed. One advantage of the intermediate-energy (eV to keV) reactor is that it requires considerably less volume than a thermal reactor, and

these reactors were originally developed for use in propulsion, as for example in submarines. Fast reactors require no moderator at all (and consequently cannot use a moderating material such as water as coolant circulating through the fuel). Because of the lower cross sections for fast neutrons, fast reactors require of the order of 10–100 times the fuel of thermal reactors providing the same power; however, because of the lack of a moderator, the core of a fast reactor occupies a much smaller volume than the core of a thermal reactor.

Type of Fuel The most commonly used fuels are natural uranium (0.72% ^{235}U), enriched uranium (> 0.72% ^{235}U), ^{239}Pu, and ^{233}U. The latter two are obtained from chemical processing of fertile material from converter or breeder reactors. Enriched uranium, which is the most commonly used fuel in power reactors, is produced in quantity at great expense from processes sensitive to the small mass difference between ^{235}U and ^{238}U. One such process is *gaseous diffusion*, in which uranium hexafluoride gas (UF_6) is forced through a porous barrier. The diffusion coefficient of a gas is inversely proportional to the square root of its mass, and the lighter isotope diffuses slightly more rapidly owing to its higher average speed in a mixture of ^{235}U and ^{238}U at thermal equilibrium. (The mean kinetic energies will be equal, so the molecule with the lighter mass has the higher speed.) The enrichment after a single passage through the barrier is very small, of the order of 0.4% *relative* (that is, the original 0.72% of ^{235}U becomes $1.004 \times 0.72\%$), a very small increase, and the process must be repeated *thousands* of times before highly enriched (nearly pure) ^{235}U can be obtained. Highly enriched ^{235}U and ^{239}Pu are bomb-grade fissile materials, while uranium at 2–3% enrichment, used in certain types of reactors, is not.

Moderator The ideal moderator would (1) be cheap and abundant, (2) be chemically stable, (3) have a mass of nearly one (to absorb the maximum amount of energy in a collision with a neutron), (4) be a liquid or a solid so its density will be high, and (5) have a minimal neutron capture cross section. Carbon, in the form of graphite, satisfies (1), (2), (4), and (5), and we must compensate for a relatively small loss in neutron energy per collision by increasing the amount of moderator. Ordinary water satisfies (1), (2), (3), and (4), but the protons in water have a very high cross section to capture a neutron ($n + p \rightarrow d + \gamma$). Heavy water ($D_2O$) has a very small neutron capture cross section, but captures that do occur lead to radioactive tritium, a particularly nasty product for biological systems. It is also quite rare and relatively expensive to separate, although it is not nearly so difficult to separate deuterium from ordinary hydrogen as it is one isotope of uranium from another; the mass ratio of 2 : 1 leads to quite dramatic effects. Because of the small capture cross section, heavy-water moderated reactors can use natural uranium as fuel; the extra neutron absorption in light-water moderated reactors requires enriched uranium. Beryllium ($Z = 4$) and BeO are also used as moderators, but are difficult to work with and dangerous poisons.

Assembly Reactors are usually classified as *heterogeneous* when the moderator and fuel are lumped, or *homogeneous* when they are mixed together. Homogeneous reactors are more tractable to mathematical analysis then heterogeneous

reactors, for which the calculation of the thermal utilization factor f and the resonance escape probability p can be difficult. A homogeneous natural uranium-graphite mixture cannot go critical, but a heterogeneous arrangement can.

Coolant The coolant is an essential element of the reactor for without it the heat generated would melt the core (called "meltdown"). In the design of power

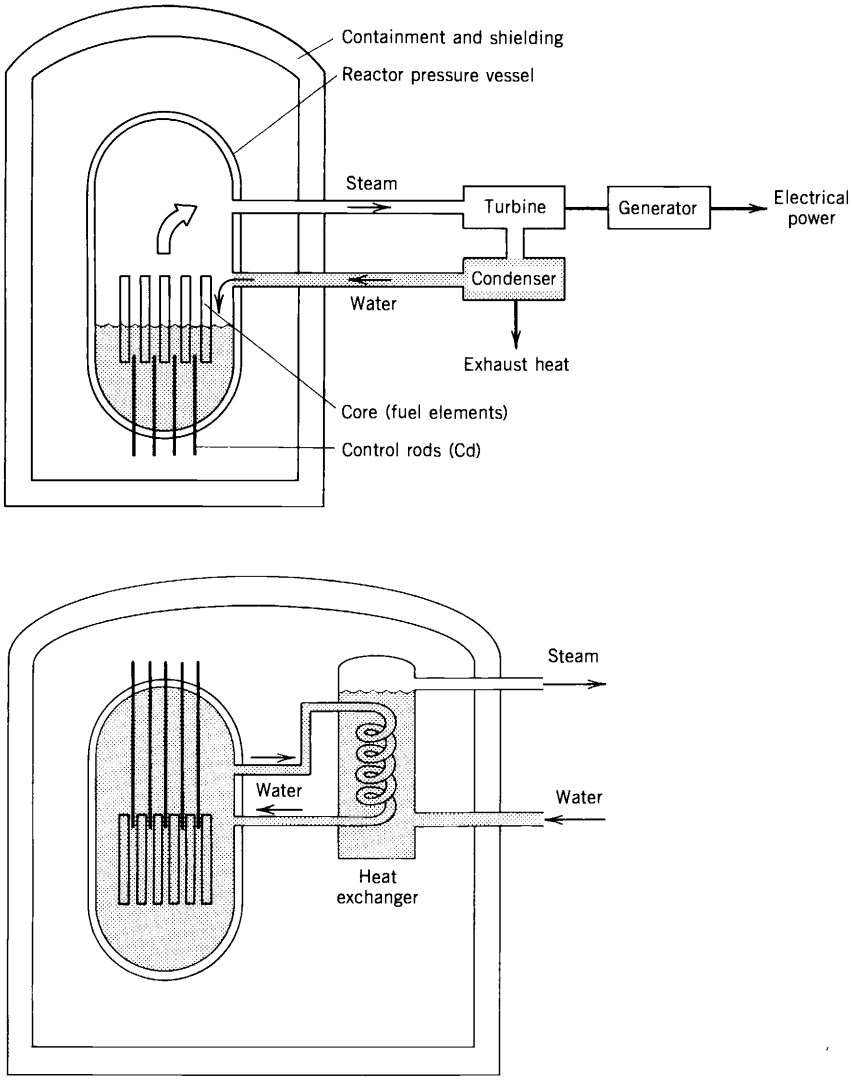


Figure 13.25 Schematic diagram of boiling-water (top) and pressurized-water (bottom) reactors. The core consists of a number of rods containing pellets of uranium oxide in a metal (zirconium alloy or stainless steel) housing. Control rods of cadmium can be inserted into the core to absorb neutrons and keep the power level stable. The boiling-water reactor is shown driving electrical generating equipment. Many details, including the important emergency core cooling system, are omitted.

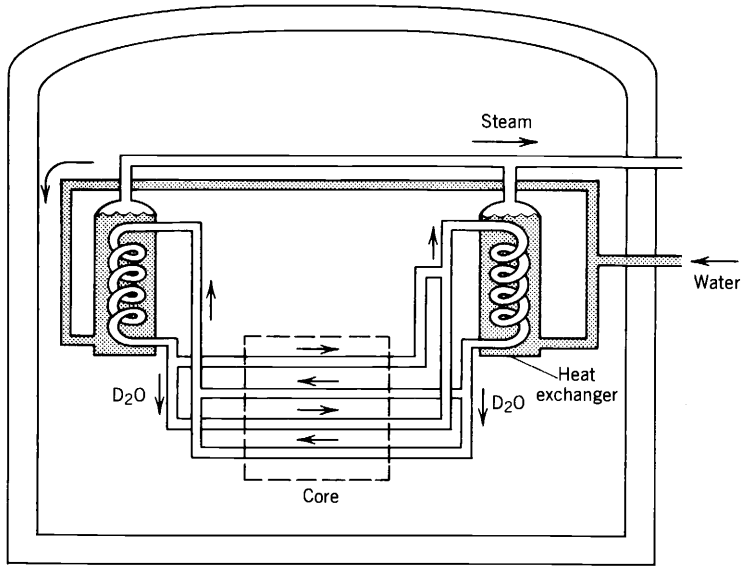


Figure 13.26 Schematic diagram of Canadian deuterium-uranium (CANDU) reactor. A closed system of D_2O circulates through the core and then exchanges heat with ordinary water, the steam from which can drive a turbine. The D_2O is under pressure to keep it in the liquid state.

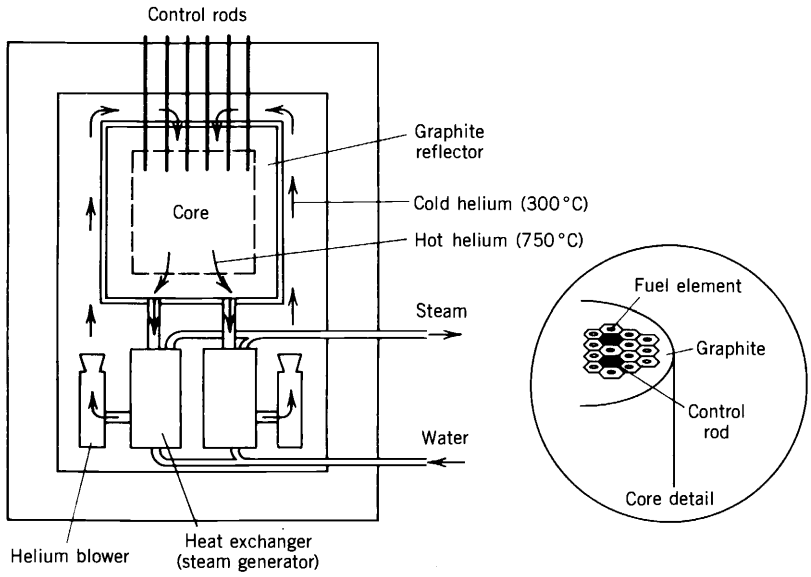


Figure 13.27 Schematic diagram of gas-cooled reactor. Helium gas flows through the core to extract the heat; the helium is then used to produce steam. A detail of the core is shown at right. The fuel elements are in the form of hexagonal rods containing the fissionable material, graphite moderator, and a channel for gas flow. The core is surrounded with a graphite reflector.

reactors, an essential feature is the ability of the coolant to transfer heat efficiently. Coolant materials can be gases (air, CO_2, helium), water or other liquids, or even liquid metals, which have a large heat capacity. Because steam has a small heat capacity, reactors that use water as a coolant may keep it under high pressure (of order 100 atmospheres) allowing it to remain as a liquid well above its normal boiling point. These are called *pressurized-water reactors*. Liquid sodium has been studied as a coolant in fast breeder reactors, which have a high density of fuel, thus requiring efficient heat transfers from a relatively small volume, and which cannot permit the moderating effect of water as coolant. Although liquid sodium is extremely corrosive and becomes radioactive through its large capture cross section, its high boiling temperature allows it to remain a liquid under ordinary pressure and eliminates the need for a high-pressure system.

Based on these design considerations, we can now examine some of the common reactor systems. Figure 13.25 illustrates the boiling-water and pressurized-water reactors, which might be used for power generation. These designs use ordinary (light) water as both moderator and coolant. The boiling-water reactor circulates water through the core (as moderator) and then into the generating apparatus as steam. A strong pressure vessel is needed to contain the steam. Even though pure water does not become radioactive (except for a tiny fraction of ^{18}O which has a very small neutron capture cross section), impurities even at the level of parts per million will become highly radioactive in the large neutron flux at the reactor core, and the design calls for the circulation of this radioactive steam beyond the containment vessel. The pressurized-water reactor

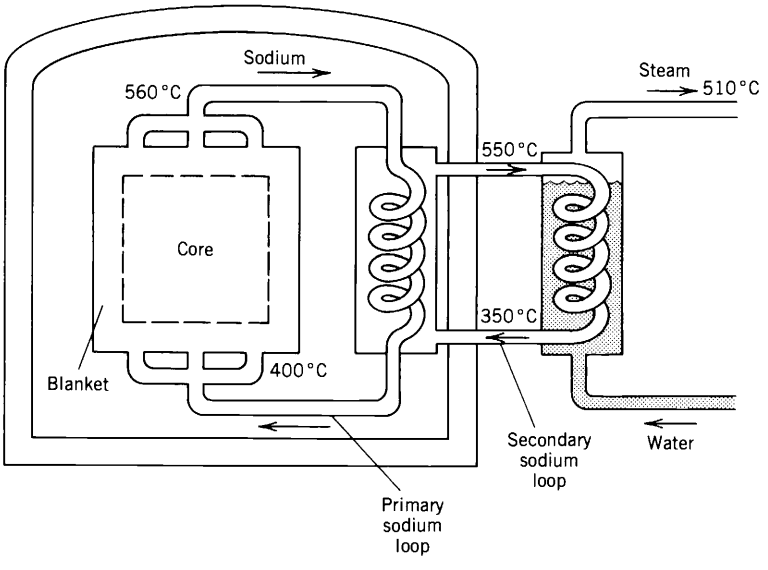


Figure 13.28 Schematic diagram of a liquid-sodium-cooled fast breeder reactor. The core may consist of ^{235}U and ^{239}Pu, while the blanket contains the fertile ^{238}U that will breed into fissionable material. An intermediate heat exchanger is necessary to keep sodium and water (which react explosively) from simultaneously being present in the reactor core, and also to keep water away from the highly radioactive sodium in the primary loop.

eliminates this potential danger by exchanging heat between the high-pressure water that circulates through the core and a separate steam line to drive the electrical generators. As mentioned previously, reactors moderated with light water must use enriched uranium; enrichments of 2–3% are typical for these reactors. Because of the relative availability of enriched uranium in the United States, many reactors have been built with these basic designs using light water.

Canada, on the other hand, has a supply of natural uranium and the ability to produce heavy water, and so the Canadian power reactors are moderated with D_2O (and use either D_2O or H_2O as coolant). Figure 13.26 shows the basic design of a heavy-water moderated reactor.

Graphite-moderated reactors are of the lumped (heterogeneous) arrangement and can use natural or enriched uranium as fuel. Most designs are gas cooled, as shown in Figure 13.27. Fuel assemblies are constructed to permit easy gas flow for good heat transfer. Most of the power reactors in Great Britain are graphite-moderated, gas-cooled reactors.

An example of a fast reactor is the liquid-sodium fast breeder reactor, illustrated in Figure 13.28.

13.7 RADIOACTIVE FISSION PRODUCTS

The two nuclear fragments produced in fission have an excess of neutrons and therefore undergo negative β decay to reach the stable isobar in the mass chain of each. These radioactive fission products and their decays are important for several reasons: (1) A small portion (10–15%) of the fission energy is released through these β and γ emissions. After the reactor is shut down (that is, after the control rods are inserted and fission is halted), the heat generated by these decay processes continues and decreases on a time scale characteristic of the radioactive decay half-lives of the products. (2) As each chain approaches stability, two effects occur—the decay energy decreases (see Figure 3.18) and the half-life increases. The residue of very long-lived ($t_{1/2} \sim$ years) decaying products constitutes the major share of the hazardous waste product of nuclear reactors. (3) Certain of the fission products that accumulate in the fuel elements during reactor operation can interfere with the fission process because of their large neutron-capture cross sections. (4) Many of the radioactive products have important research applications, and extraction from spent fuel elements is the only economic means of producing some of these isotopes. We will discuss each of these four topics in turn.

As was estimated in Section 13.3, the total β-decay energy from the fragment decays is about 19 MeV. This of course represents several sequential decays, perhaps ranging in energy from 6–7 MeV down to 1 MeV as stability is approached. In each decaying nucleus, there will be many excited states that can be populated; however, the β-emission probability, Equation 9.28, favors higher energy decays, and therefore the most probable decays are those carrying the largest energies and populating the lowest excited states of the daughter nucleus. It is for this reason that the average γ-decay energy from the fission products is only about 7 MeV, much smaller than the β energy.

The β-decay energy is shared by the electron and the antineutrino. The antineutrino escapes from the fuel element and contributes neither to the decay

heating nor to the radiation. The mean energy given to the electron is about 0.3–0.4 of the decay energy, and thus on the average only 6–8 MeV of the 19 MeV appears as heat.

To calculate the actual energy that appears as β and γ decays, we must know exactly which isotopes are produced, and we must also know all of the β and γ branching intensities and decay probabilities. Much of this information is not available, especially for the shorter-lived fission products at the beginning of the decay chains. Instead, we take an average figure, based on estimates of the mass differences and half-lives:

$$\beta(t) = 1.26t^{-1.2} \text{ MeV/s} \tag{13.14}$$

$$\gamma(t) = 1.40t^{-1.2} \text{ MeV/s} \tag{13.15}$$

where β and γ give the power per fission deposited as β and γ decays, respectively, as functions of the time for t between 1 and 10^6 s.

As a reactor is operated, fission products are continuously produced while others decay. When the reactor is shut down, the energy of the still-decaying products will depend on how long the reactor has operated and at what power level. If the reactor operates from time 0 to time T, the power emitted as β and γ decays at time t after the shutdown is

$$P(t) = 4.10 \times 10^{11}\left[t^{-0.2} - (t + T)^{-0.2}\right] \text{ MeV/s} \tag{13.16}$$

per watt of original operating level. (That is, if the reactor operated before shutdown at 10^3 MW, multiply this expression by 10^9.) Figure 13.29 shows the

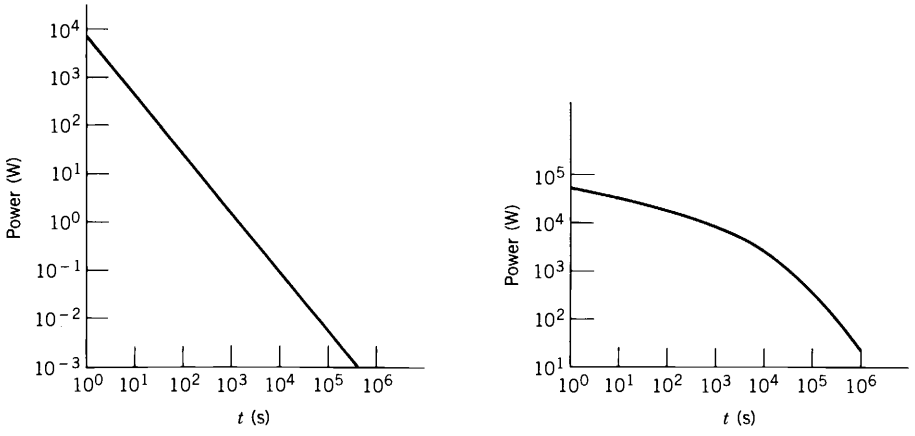


Figure 13.29 (Left) Power deposited from β or γ decays of radioactive fission products per second of reactor operation for a 1-MW reactor (3.1×10^{16} fissions/s). (Right) Total radioactive decay heat from a 1-MW reactor at time t following shutdown, after the reactor has been operating for $T = 8$ h. Note that the decay power remains at or above 1% of the reactor power for a time of order 1 h after the shutdown. For power reactors, scale both figures upward by a factor of 1000.

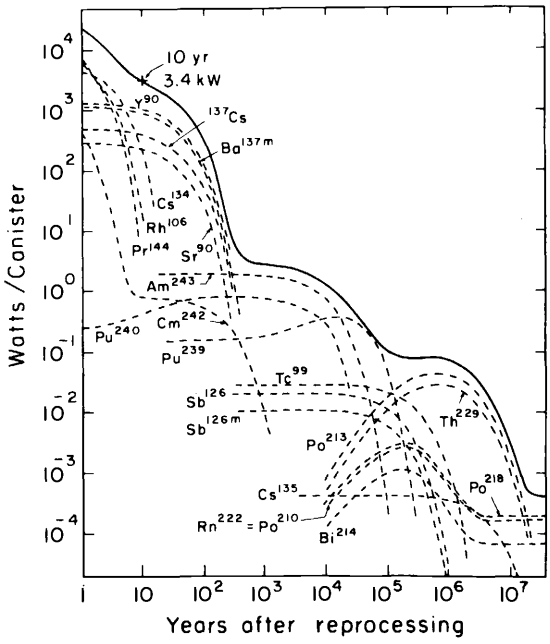


Figure 13.30 Radioactive power produced from decays of fission products and actinides. This amount of power would result from the waste products of a 1000-MW power reactor operating for about one month. The solid curve is the sum of the contributions of the individual isotopes. From B. L. Cohen, *Rev. Mod. Phys.* **49**, 1 (1977).

decay of the β and γ activities and the decay power level after shutdown, called *after-heat*, of a research reactor operating at 1 MW.

When we consider the longer-lived activities that might characterize spent fuel elements, we are interested in a time scale of the order of years. Figure 13.30 shows the activities of the long-lived fission products and actinides. After reprocessing, these activities must be isolated from biological systems for times of the order of 10^5–10^6 y. Several schemes have been suggested for achieving this isolation, but no system has yet been adopted that can guarantee isolation over this time scale. Any leakage into groundwater or the food chain would be expected to result in an increase in deaths from cancer. It is, however, interesting to note that over the long time periods involved, the burn-up of uranium through fission actually *reduces* the natural background and the consequent risk of cancer. This natural background radiation is released into the environment in the burning of coal, and it is released in particulate form, which poses a special hazard to the lungs. It is estimated that a coal-burning power plant operating at 1000 MW annually releases into the atmosphere 23 kg of uranium and 46 kg of thorium, along with their radioactive decay products, most notably radon. The radiation exposure to the general population from coal-burning power plants is several times that of nuclear power reactors. We know far more about the risks of exposure to radioactive fission products than we know about the effects of this radioactive release from coal-burning power plants.

Prominent among the fission products that can actually modify reactor operation is ^{135}Xe, which can be formed directly in ^{235}U fission (with a yield of 0.2%)

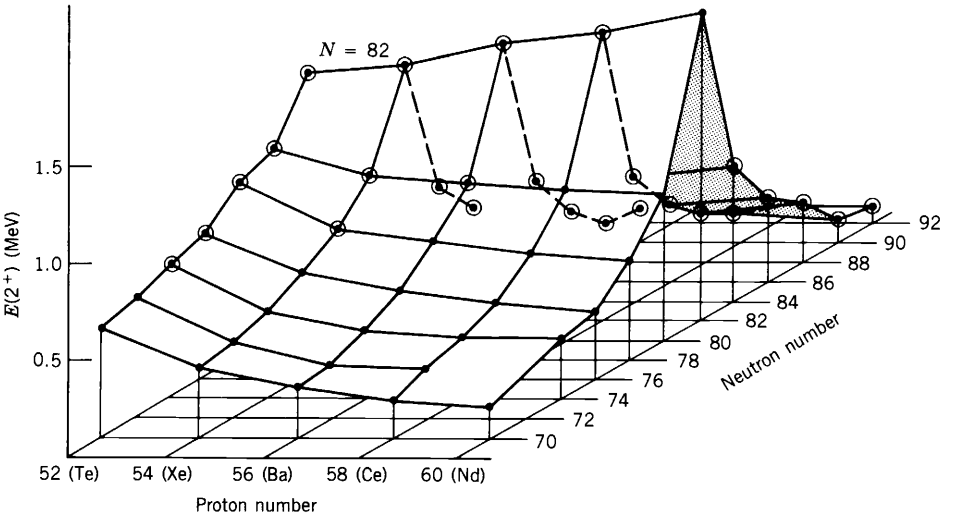


Figure 13.31 Energies of first excited 2^+ states of even-Z, even-N nuclei in the mass-140 region. The closed shell at $N = 82$ is apparent from the systematic peak in the 2^+ energy, and the rapid decrease to low energies beyond the peak is characteristic of nuclei with nonspherical equilibrium shapes (deformed nuclei). The circled points are those on the neutron-rich side studied from the decay of fission fragments.

or as a result of the decay of ^{135}I (which has a higher yield, about 6.4%). The mass-135 decay chain is

$$^{135}\text{Sb} \xrightarrow{1.7\text{ s}} {}^{135}\text{Te} \xrightarrow{19\text{ s}} {}^{135}\text{I} \xrightarrow{6.6\text{ h}} {}^{135}\text{Xe} \xrightarrow{9.1\text{ h}} {}^{135}\text{Cs} \xrightarrow{3\text{ My}} {}^{135}\text{Ba}$$

The Sb and Te activities decay in a time short compared with the effects we are considering here, so we will consider the ^{135}I as the primary activity in the sequence. In a time scale of the order of hours, there is a build-up of ^{135}Xe, which has a thermal neutron capture cross section of 2.7×10^6 b. This large cross section tends to reduce the number of thermal neutrons available for fission, and there must be a corresponding correction in the control system if the reactor power level is to remain constant. This effect of ^{135}Xe (and other isotopes) is called *fission product poisoning*. (See Problems 14 and 15.)

Fission products have many applications in research. The most apparent is the study of the nuclear spectroscopy in the decays of the fission products. For example, the interesting region around mass 140–150 has been carefully studied from the γ decays of separated fragments. To do careful and precise spectroscopy, it is important to deal with only a single decay, and so methods have been developed for rapid chemical and mass separation of fission products, so that the short-lived fragments can also be studied. Figure 13.31 shows an example of what can be learned from these studies. As neutrons are added beyond the neutron shell closure at $N = 82$, nuclei begin to acquire a stable deformation, as indicated by the decrease of the energy of the first excited 2^+ state. To study the effect of adding additional neutrons, it is necessary to go to more neutron-rich nuclei, for which the short-lived fission products are essential.

Fission products with medical applications include iodine isotopes ^{131}I and ^{132}I, which are used in studies of the human thyroid gland. The thyroid takes in iodine from the blood plasma and uses the iodine to manufacture thyroxine, the hormone that regulates metabolism. The isotope ^{131}I ($t_{1/2}$ = 8.0 d) is obtained from fission products and is administered to the patient in an oral dose of several μCi. A γ-ray detector placed at the patient's neck can follow the build-up of radioactive iodine in the thyroid. In this way, it is possible to diagnose overactive and underactive thyroid function. The isotope ^{132}I ($t_{1/2}$ = 2.3 h) is also used, and because of its shorter half-life, the radiation dose absorbed by the patient is much smaller. The short half-life would ordinarily result in difficulties in extracting and purifying the isotope before too much of it had decayed; however, ^{132}I is the daughter of 78-h ^{132}Te, and it is possible to "milk" ^{132}I from a source of ^{132}Te, for instance, by treating it with a solvent that dissolves I but not Te.

Much larger doses ($\sim$ mCi) of radioactive iodine are used to reduce the functioning of an overactive thyroid, and still larger doses ($\sim$ Ci) can be used to treat cancers of the thyroid.

Iodine is convenient to obtain from fission products because of its volatility—heating the spent fuel converts the iodine to gas and makes it possible to extract it without resorting to dangerous chemical procedures. Other gaseous fission products include Xe, which can be administered to patients by inhalation and used to measure lung function.

13.8 A NATURAL FISSION REACTOR

Fission of course occurs as a natural process, through the spontaneous decay of certain heavy nuclei. Many of these heavy nuclei have decay half-lives that are short compared with the time since their formation (most likely in supernova explosions), and so they do not now exist in nature, but we can infer their former presence by the fission products they leave behind. A particular example is ^{244}Pu, with $t_{1/2} = 81 \times 10^6$ y. Assuming that the solar system formed primarily from the debris of a supernova explosion that occurred at least 4.5×10^9 y ago, nearly all of the ^{244}Pu that might have been formed would long since have decayed away, leaving behind the products of its fission. One popular place to search for such records of the early universe is in meteorites, which are unaffected by the geological evolution and possible redistribution of minerals that have taken place on Earth. Indeed, such meteorites show an excess isotopic abundance of ^{136}Xe, which is assumed to be due to the spontaneous fission of ^{244}Pu.

Extrapolating back over geological time is possible because there are few naturally occurring phenomena that can alter relative isotopic abundances over time scales of the order of 10^9 years. The isotopic abundances we observe today are fixed by those that resulted from the supernova explosion (see Chapter 19 for a discussion of the formation of the elements), with modifications from the radioactive decay of unstable isotopes. Furthermore, we expect that these processes are common throughout the solar system, including in solid extraterrestrial minerals that we observe as meteorites. In the case of Xe, which forms no chemical compounds under normal conditions, the primordial isotopes were released during the era when the Earth was molten and they have been thor-

oughly mixed in the atmosphere. In meteorites, this has not occurred, and often the Xe produced by primordial fissions can be released from microscopic inclusions within the mineral and analyzed by mass spectroscopy to reveal isotopic abundances different from terrestrial Xe.

Owing to the need for exact control of ^{235}U enrichments, its natural abundance has been carefully and precisely measured in minerals from a variety of sources. The accepted value is 0.00720 ± 0.00001 for the fraction of ^{235}U in natural uranium. The small limit of uncertainty not only represents the precision of the measured values, but is also indicative of the variation in samples from very different locations where uranium is mined—the western United States, Canada, Australia, and Africa; even the rocks returned from the moon by the Apollo missions show the same value.

Of course, we expect this ratio to vary over geological time because both ^{235}U and ^{238}U are radioactive, with ^{235}U having a shorter half-life (7.0×10^8 y) than ^{238}U (4.5×10^9 y). Because of the shorter half-life, ^{235}U decays more rapidly than ^{238}U, and in times past ^{235}U must have had a greater relative abundance. If $t = 0$ represents the present, and if N_5 and N_8 represent, respectively, the number of 235 and 238 nuclei and λ_5 and λ_8 their decay constants, then the present abundance is

$$r(0) = \frac{N_5(0)}{N_5(0) + N_8(0)} = 0.00720 \tag{13.17}$$

and previous abundances were

$$r(t) = \frac{N_5(0)\, e^{-\lambda_5 t}}{N_5(0)\, e^{-\lambda_5 t} + N_8(0)\, e^{-\lambda_8 t}} \tag{13.18}$$

where t is negative. Figure 13.32 is a plot of this ratio. Notice that about 2×10^9 years ago, the ^{235}U fraction was of order 3%; as we know from our previous discussion of water-moderated reactors, with ^{235}U enrichments of 3% the neutron absorption in natural water as moderator does not prevent the construction of a critical assembly. Going further back, we might postulate that the extreme conditions in a supernova (where the heavy elements may have been produced) would not be expected to discriminate significantly between ^{235}U and ^{238}U (recall the similarity of the fast neutron cross sections, Figure 13.9). Thus the extrapolation back to about $r = 0.5$ should give an estimate of the time of formation of these elements; Figure 13.32 shows this to be about 6×10^9 y, consistent with values obtained from other sources for the age of the solar system. See Section 19.6 for a more rigorous discussion of the $^{235}U/^{238}U$ ratio and its use in dating the galaxy.

Because of the extreme precision and uniformity of the measured abundance of ^{235}U, even small anomalies are particularly apparent. In 1972, a sample of uranium, mined at Oklo in what is now the Republic of Gabon on the west coast of Africa, was analyzed by the French Atomic Energy Commission and showed a ^{235}U abundance of only 0.00717, about 3 standard deviations below the accepted value. This small deviation was enough to excite their curiosity, and analysis of additional samples showed even smaller ^{235}U abundances, as low as 0.00440. Since the only known process that could lead to a reduction in ^{235}U concentra-

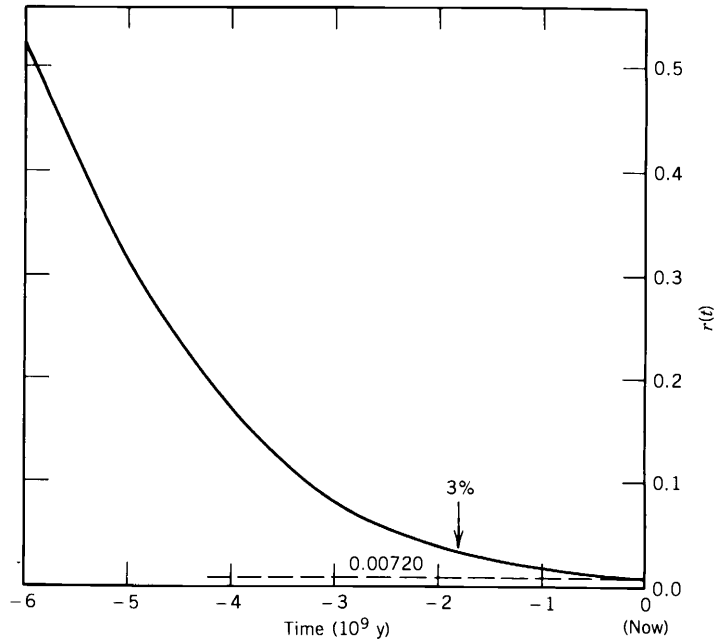


Figure 13.32 Fraction of ^{235}U in natural uranium. The present fraction is 0.0072, and 2×10^9 y ago it was about 3%.

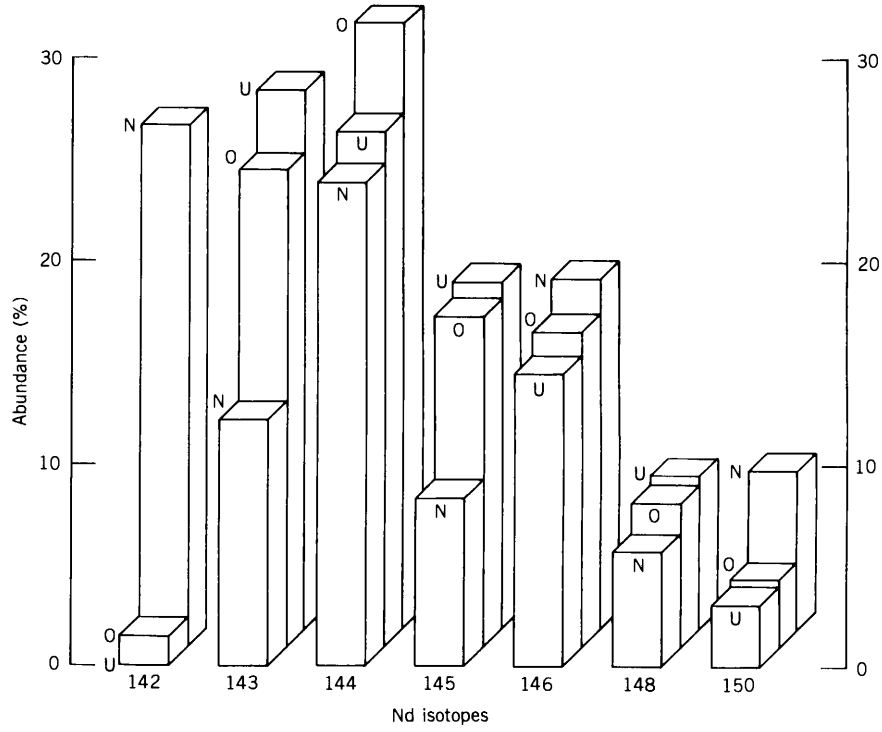


Figure 13.33 Abundances of neodymium isotopes. N indicates the abundance of natural Nd, U indicates abundances in ^{235}U fission, and O indicates the observed abundances in the Oklo ore samples. The Oklo abundances are in much better agreement with those of ^{235}U fission than with those of natural Nd.

tion is fission by low-energy neutrons, the French workers theorized that a natural nuclear reactor operated in the Oklo site about 2×10^9 y ago, when the ^{235}U abundance was high enough ($\sim$ 3%) to permit the operation of a reactor moderated by groundwater. Of course, the reactor could have operated even before 2×10^9 y ago; however, the formation of deposits of uranium such as in the Oklo region requires the transport of uranyl ions (UO_2^{2+}) in groundwater, and it is now believed that before the evolution of oxygen-producing bacteria about 2×10^9 y ago there was insufficient oxygen in the water to have formed the uranium deposit. Thus the need for highly oxygenated water and for ^{235}U enrichments of 3% place fairly rigid limits on the age of the reactor.

Estimating the total size of the uranium deposit and its deficiency of ^{235}U, it has been calculated that about *5 tons* of ^{235}U were fissioned; with 200 MeV released per fission, this amounts to a total energy release of 2×10^{30} MeV, or about 10^8 MW·h. A contemporary power reactor, by comparison, may operate at about 10^3 MW. However, it is unlikely that the Oklo reactor operated at this power level for the boiling of the water would have removed the moderator and terminated the reactor until groundwater could collect again. The average power level was probably more like 0.01 MW, suggesting that the reactor may have operated for 10^{10} h, or 10^6 y!

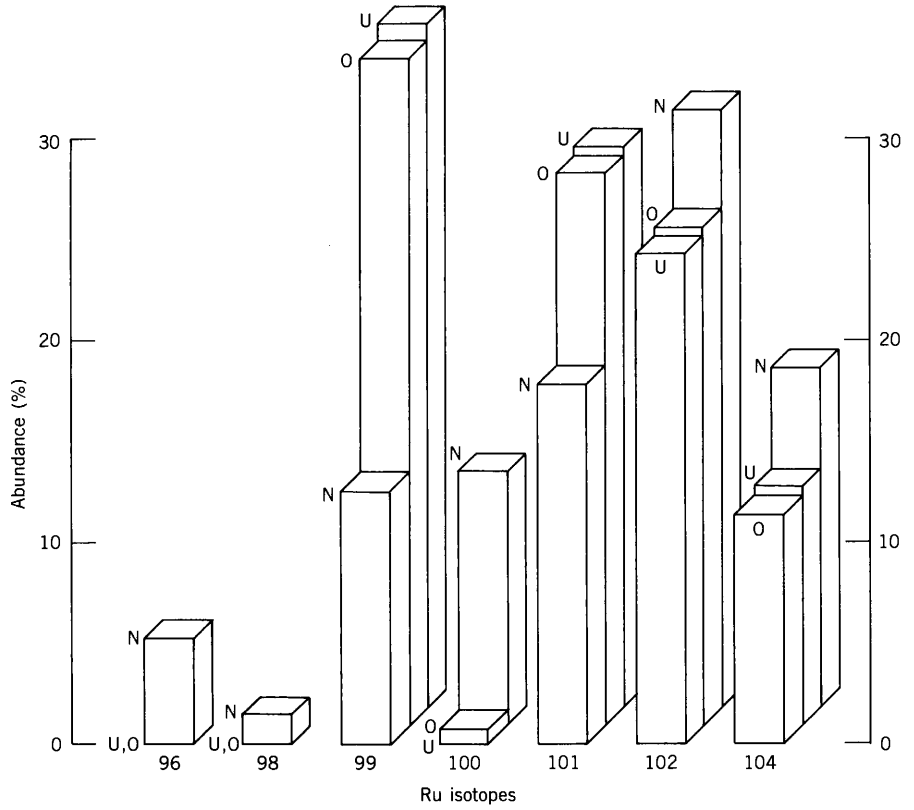
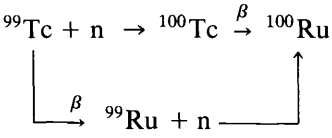


Figure 13.34 Abundances of ruthenium isotopes from natural Ru (N), uranium fission (U), and Oklo deposits (O). As in the case of the Nd isotopes, the Oklo abundances agree with those of fission and disagree with those of natural Ru.

Confirmation of the remarkable hypothesis of the natural reactor was found in the observation of the abundances of fission products in the Oklo minerals. Figure 13.33 shows the relative abundances of Nd isotopes in natural Nd, in the Oklo deposits, and in residues of ^{235}U fission products. The disagreement of the Oklo Nd abundances with natural Nd and the agreement with the fission distribution supports the identification of the natural reactor. Figure 13.34 shows similar relationships for the abundances of the Ru isotopes. The ^{100}Ru abundance differs slightly from that of the ordinary fission of ^{235}U. This small excess is believed due to neutron capture by (radioactive) fission product ^{99}Tc, from the chain



Of the two possible paths leading to ^{100}Ru, the upper one has the larger cross section, and the long half-life of ^{99}Tc (2.1×10^5 y) ensures that it will be present long enough to capture a neutron. The observed excess of ^{100}Ru can be used to estimate the duration of the Oklo reactor, and the values obtained are about 10^6 y, in agreement with the estimate based on the ^{235}U depletion.

One final interesting feature of the Oklo reactor should be mentioned—the fission products are still in place in the reactor zone and have migrated very little. Despite climatic changes, no substantial movement of these fission products has taken place over the past 2×10^9 y. This suggests that there may be merit in the present schemes for burying waste products of power reactors in geologically stable formations.

13.9 FISSION EXPLOSIVES

If the exponential increase in energy release of a supercritical assembly of ^{235}U or ^{239}Pu is permitted to continue without control, a highly unstable situation will rapidly occur. The energy released in the fissionable material must be dissipated, and in doing so will often blow apart the fissionable fuel, thereby rendering it subcritical. In a reactor core, the ^{235}U is neither sufficiently enriched nor sufficiently concentrated to result in an explosion, even if it were allowed to go supercritical. To make a nuclear explosive, it is necessary to collect subcritical pieces into a supercritical assembly, and to do it so quickly that the exponential fission energy release produces the desired blast effects before the inertia of the supercritical mass is overcome and the fuel itself is blown apart into a subcritical state.

Two basic designs were employed to construct fission-based explosives. The first is the gun type, illustrated in Figure 13.35. In this case the mass of pure ^{235}U is cut into a sphere with a plug removed from its center. The plug is then fired rapidly into the center of the sphere, and the assembly goes supercritical. The bomb that was dropped on Hiroshima, Japan, in 1945 was of this type. The energy release was about 10^{14} J, or equivalent to a conventional bomb containing

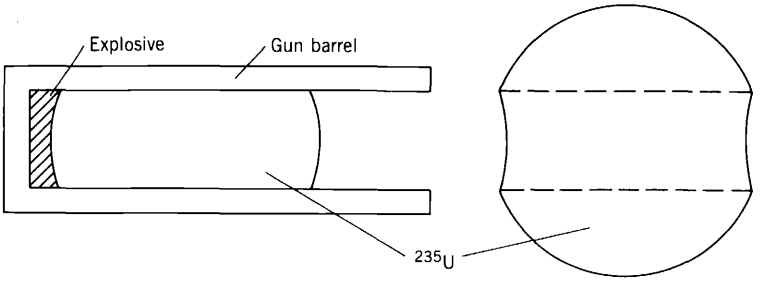


Figure 13.35 The gun-type design of the ^{235}U explosive. Not shown are the tamper, which surrounds the critical mass and reflects escaping neutrons back into the explosive, and the initiator, a source of neutrons that guarantees that a neutron will be present to begin the chain reaction at the instant the critical mass is achieved.

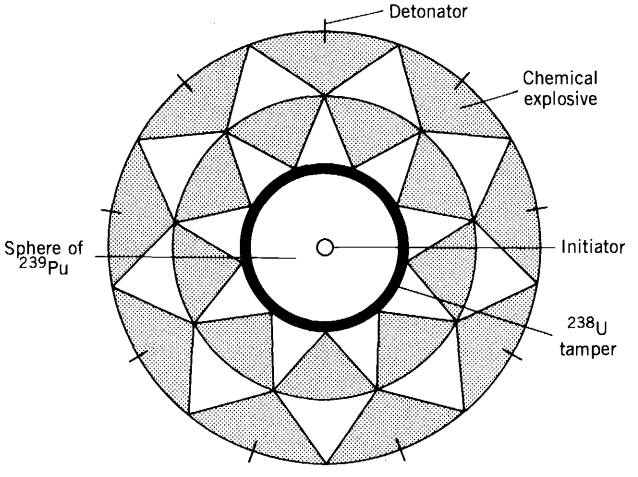


Figure 13.36 The ^{239}Pu implosion bomb. Detonation of the conventional explosive compresses the ^{239}Pu core into a supercritical state. An initiator at the center provides neutrons to begin the chain reaction. The ^{238}U tamper reflects neutrons back into the core (and can also provide additional neutrons through fissions induced by escaping fast neutrons).

about 20 kilotons of TNT. (The energy release from one ton of TNT is about 4×10^9 J.)

A second design is the implosion type, illustrated in Figure 13.36. Here a solid spherical subcritical mass of fissionable material is surrounded by a spherical shell of conventional explosives. When the conventional explosives are detonated in exact synchronization, a spherical shock wave compresses the fissionable material into a supercritical state. The first nuclear explosive, tested near Alamogordo, New Mexico, in 1945 and the one later dropped on Nagasaki, Japan, were of this type. The yields of these weapons were, like the ^{235}U bomb, in the range of 20 kilotons of TNT equivalent.

Although many of the details of the construction of fission explosives are classified, based on the known physical dimensions (see Figure 13.37), we can estimate that the fissile material occupies a sphere of perhaps 10 cm diameter,

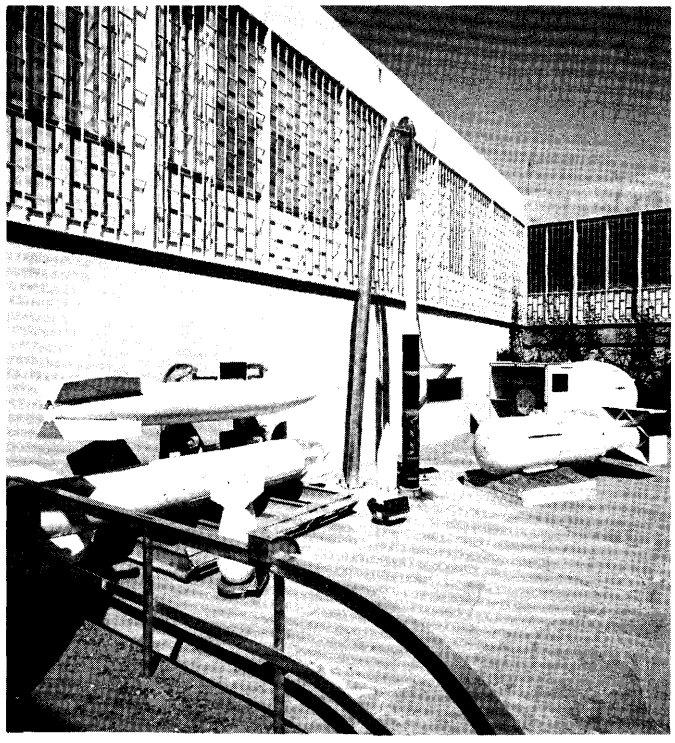


Figure 13.37 The large casing on the right side is from "Fat Man," the plutonium implosion-type weapon. The smaller one in front of it is "Little Boy," a ^{235}U gun-barrel type. The smaller casings on the left are from kiloton-range tactical weapons, and the upper casing at left is from a thermonuclear explosive. Photo courtesy Los Alamos National Laboratory.

and thus has a mass of roughly 10 kg. (The fast-neutron fission cross sections for ^{235}U and ^{239}Pu are in the range 1–2 b, where the mean free path of a neutron would be of order 10 cm. The size is thus determined by the distance over which a neutron has a high probability of interacting.) An energy release of 10^{14} J (20 kilotons of TNT equivalent) would require about 3×10^{24} fission events (at 200 MeV released per fission), which corresponds to the complete fissioning of the atoms in about 1 kg of fissile material. Thus only 10% of the fuel in the explosive actually fissions before the energy released reduces the density of the fissile materials to the subcritical region.

The effects of nuclear explosives fall into several categories: the blast itself (a rapidly spreading shock wave), heat radiation (sometimes called a "fireball"), direct nuclear radiation (mostly neutrons and γ rays from fission), and indirect nuclear radiation (from the radioactive decays of fission products).

The direct blast damage from a nuclear explosion can be considered as a rapidly expanding spherical wavefront carrying a sudden increase and a following decrease in air pressure. The energy density in this spherical wavefront decreases like $1/r^2$ from a purely geometrical effect, but even at a distance of 1 km from a 20-kiloton explosion, the increase in pressure is of order one atmosphere, sufficient to destroy brick buildings. At 2 km, the pressure increase would be only

about 0.25 atmosphere, or perhaps 3 psi, which is sufficient to destroy wood-frame buildings and to send debris flying at speeds of the order 100 miles/h.

The heat radiation also decreases like $1/r^2$ as the heat wave spreads, but it also decreases by an additional exponential factor from absorption and scattering by the atmosphere. At a distance of 2 km from a 20-kiloton explosion, the heat wave (which arrives within about 2 s following the explosion) is still sufficient to produce third-degree burns on exposed skin and to ignite flammable materials such as wood and cloth. An indirect effect of the many fires produced by this radiation is the "firestorm," in which the heat rising from the fires produces ground-level winds of 50–100 miles/h which increase the intensity of the fires and help to spread them. (This is not a specifically nuclear effect; incendiary bombing raids with conventional bombs produce the same effect, but a nuclear explosion is capable of producing a firestorm from a single bomb.)

Direct nuclear radiations (neutrons and γ's) also decrease both like $1/r^2$ and exponentially, and the distance over which lethal doses of radiation would be received is roughly the same as the distance for severe blast damage or fatal burns (of the order of 1 km for a 20-kiloton explosion) in unprotected population. Even the smaller doses received at greater distances can have severe long-term effects, including increased incidences of leukemia, cancer, and genetic defects.

The long-lived radioactive products of fission are generally vaporized in the explosion and fall to the ground as radioactive fallout. Some of this material can be carried, as a vaporized cloud, high into the atmosphere where it is spread by prevailing high-altitude winds. This "cloud" of radioactivity may circulate in the upper atmosphere for a year or more as it gradually falls back to the ground. Many short-lived products decay during this time, and the major isotopes remaining after this period are ^{90}Sr and ^{137}Cs. The isotope ^{90}Sr is particularly worrisome, for it is chemically similar to calcium and can concentrate in the bones, where its decays can produce bone cancer.

If the bomb is exploded low enough above the ground that material from the surface of the Earth is vaporized by the fireball, then this additional vaporized material can mix with the cloud of vaporized fission products and condense into particles as the fireball spreads and cools. These particles fall back to the ground relatively rapidly (over several hours) and over a range determined by the low-altitude local winds. Population downwind from the blast, even tens or hundreds of miles, can be exposed to serious, perhaps even lethal, doses of radiation from the decay of shorter-lived fission products. (Hence, we can distinguish two basic ways to detonate a nuclear explosive—a high-altitude "air burst," the goal of which is blast damage over a relatively large area and which might be used as a means of destruction of cities, and a low-altitude "ground burst" which concentrates the blast damage over a smaller area, such as might be desired in an attack against blast-hardened underground missile silos, but which produces extreme levels of local fallout in the process.)

As awesome and frightening as these effects of nuclear explosions may be, it is even more frightening that within a decade after the development of fission weapons came the testing of fusion-based thermonuclear weapons, with yields 1000 times as great. Even though many of these effects we have discussed scale as the square root or cube root of the yield, the resulting complete destruction of a

population center of 10-mile radius (e.g., most of metropolitan New York City or Los Angeles) from a single explosion is truly staggering. The principles, yields, and effects of thermonuclear weapons are considered in Section 14.5.

REFERENCES FOR ADDITIONAL READING

A comprehensive and advanced work on the theory of nuclear fission is R. Vandenbosch and J. R. Huizenga, *Nuclear Fission* (New York: Academic, 1973); a similar work is L. Wilets, *Theories of Nuclear Fission* (Oxford: Clarendon, 1964). The early paper on the application of the liquid-drop model to fission by N. Bohr and J. Wheeler, *Phys. Rev.* **56**, 426 (1939) is essential reading. Also of historical interest is H. G. Graetzer and D. L. Anderson, *The Discovery of Nuclear Fission: A Documentary History* (New York: Van Nostrand, 1971).

For general reviews of fission, see also I. Halpern, *Ann. Rev. Nucl. Sci.* **9**, 245 (1959) and J. S. Fraser and J. C. D. Milton, *Ann. Rev. Nucl. Sci.* **16**, 379 (1966).

Experimental data on fission studies, especially cross sections, have been collected in a series of conference reports under the title *Physics and Chemistry of Fission* and published serially by the International Atomic Energy Agency (Vienna). A similar series of Proceedings of International Conferences on the Peaceful Uses of Atomic Energy has been published by the United Nations.

A popular-level review of nuclear energy and its effects is D. R. Inglis, *Nuclear Energy—Its Physics and Its Social Challenge* (Reading, MA: Addison-Wesley, 1973).

There are many texts and monographs on reactor physics and design, including: I. R. Cameron, *Nuclear Fission Reactors* (New York: Plenum, 1982); J. R. Lamarsh, *Introduction to Nuclear Reactor Theory* (Reading, MA: Addison-Wesley, 1966); J. J. Duderstadt and L. J. Hamilton, *Nuclear Reactor Analysis* (New York: Wiley, 1976); L. Massimo, *Physics of High-Temperature Reactors* (Oxford: Pergamon, 1976).

Breeder reactors are reviewed by W. Häfele, D. Faude, E. A. Fischer, and H. J. Lane, *Ann. Rev. Nucl. Sci.* **20**, 393 (1970), and A. M. Perry and A. M. Weinberg, *Ann. Rev. Nucl. Sci.* **22**, 317 (1972).

For a survey of the problems of management of radioactive wastes, see Bernard L. Cohen, *Rev. Mod. Phys.* **49**, 1 (1977) and *Am. J. Phys.* **54**, 38 (1986); a review of this topic by a study group of the American Physical Society was published in *Rev. Mod. Phys.* **50**, S1 (1978). The radiation released from coal-burning power plants is discussed by J. P. McBride et al., *Science* **202**, 1045 (1978).

Many technical details of reactor safety and radiation protection are reviewed in *Nuclear Power and Its Environmental Effects*, by S. Glasstone and W. H. Jordan, published by the American Nuclear Society in 1980. The American Association of Physics Teachers has published six papers given at a 1982 symposium on nuclear power; see *The Status of the Nuclear Enterprise*, edited by Morris W. Firebaugh.

The Oklo reactor is reviewed in the conference proceedings, *The Oklo Phenomenon*, published by the International Atomic Energy Agency (Vienna) in 1975. Other references to Oklo are P. K. Kuroda, *The Origin of the Chemical Elements*

and the Oklo Phenomenon (Berlin: Springer-Verlag, 1982) and M. Maurette, *Ann. Rev. Nucl. Sci.* **26**, 319 (1976). For a popular-level account, see G. A. Cowan, "A Natural Fission Reactor," in the July 1976 issue of *Scientific American*.

Fission-based nuclear explosives are now mainly of historical interest (references for fusion explosives, including the effects of nuclear weapons, will be given in the next chapter). The now-declassified summary of the wartime work on the Manhattan Project can be found in H. D. Smyth, *Atomic Energy for Military Purposes* (Washington, DC: U.S. Government Printing Office, 1946). More details of the work at Los Alamos are described in L. Lamont, *Day of Trinity* (New York: Atheneum, 1965). A similar work, describing a more personal view of bomb design, is John McPhee, *The Curve of Binding Energy* (New York: Farrar, Strauss and Giroux, 1974). A recent historical work from the British perspective is A. McKay, *The Making of the Atomic Age* (Oxford: Oxford University Press, 1984).

PROBLEMS

1. Compute the energy release (Q value) of: (a) $^{235}\mathrm{U} + \mathrm{n} \rightarrow {}^{90}\mathrm{Kr} + {}^{144}\mathrm{Ba} + ?$; (b) $^{239}\mathrm{Pu} + \gamma \rightarrow {}^{92}\mathrm{Sr} + ? + 3\mathrm{n}$; (c) $^{252}\mathrm{Cf} \rightarrow {}^{106}\mathrm{Nb} + ? + 4\mathrm{n}$.
2. In the fission of $^{236}\mathrm{U}$ into two fragments A_1 and $A_2 = 236 - A_1$, plot the Coulomb repulsion energy of the two fragments if they are formed just touching at their surfaces. Consider all values of A_1 from 1 to 235, and assume each fragment has the same Z/A ratio as $^{236}\mathrm{U}$.
3. $^{252}\mathrm{Cf}$ has a half-life of 2.64 y and a spontaneous fission branch of 3.09%. How many fission neutrons per second are emitted per milligram of $^{252}\mathrm{Cf}$? (See Figure 13.7.)
4. The isotope $^{254}\mathrm{Cf}$ decays almost exclusively by spontaneous fission, with a half-life of 60.5 days. The energy released is about 225 MeV per fission. (a) Calculate the total fission power produced by 1.0 μg of $^{254}\mathrm{Cf}$. (b) Assuming Cf to behave like an ordinary metal, what would be the rise in temperature of the Cf sample per minute from the fission heating?
5. Estimate the neutron energy needed to produce fission of $^{208}\mathrm{Pb}$. Is it likely that such neutrons would be released in the fission, making possible a self-sustaining reaction?
6. Given that the activation energy of $^{236}\mathrm{U}$ is 6.2 MeV, what is the minimum-energy α particle that can produce fission following bombardment of a $^{232}\mathrm{Th}$ target?
7. Compare the excitation and activation energies for thermal neutron-induced fission of (a) $^{239}\mathrm{Pu}$; (b) $^{231}\mathrm{Pa}$; (c) $^{237}\mathrm{Np}$; (d) $^{238}\mathrm{Np}$.
8. Which of the following heavy nuclei would you expect to have large thermal cross sections? (Use arguments based on the pairing-energy discussion given in Section 13.3.) (a) $^{251}\mathrm{Cf}$; (b) $^{253}\mathrm{Es}$; (c) $^{255}\mathrm{Fm}$; (d) $^{250}\mathrm{Bk}$.
9. Use Figure 13.7 to estimate the fraction of neutron-induced fissions of $^{235}\mathrm{U}$ that produce no prompt neutrons.
10. Discuss the formation of $^{244}\mathrm{Pu}$ in the core of a reactor operating with enriched uranium as a fuel. (Information on cross sections and decays can

be found in the *Table of Isotopes*.) This isotope is one of the longest-lived remnants of supernova explosions, in which it is also formed through neutron captures.

11. In ^{239}Pu, the thermal fission cross section is 742 b, while the cross section for other (nonfission) absorptive processes is 267 b. Each fission produces, on the average, 2.86 fast neutrons. What is the mean number of fission neutrons produced by ^{239}Pu per thermal neutron?

12. In calculating the heat deposited in a reactor core by the radioactive decays of the fission products, is it necessary to know the details of β and γ spectroscopy of each decay process? That is, given the Q value of each decay, we know the sum of the total β and γ energies emitted in each decay process. Is this knowledge sufficient for calculating the decay heat? Give some examples to justify your arguments.

13. In a water-moderated uranium reactor, what will be the effect on the fission rate of an increase in the temperature of the core? Consider especially the possible qualitative effects of temperature on p and f.

14. Consider the fission product poisoning by ^{135}I and ^{135}Xe. Let I be produced directly in fission with yield $\gamma_I = 6.4\%$ per fission, and let it be depleted by its decay (to ^{135}Xe) and by neutron capture (to ^{136}I). Let Xe be produced directly in fission ($\gamma_{Xe} = 0.23\%$) and indirectly in ^{135}I decay, and let Xe be depleted by its decay and by neutron capture. (a) Write differential equations for the change dn in the number density of I and of Xe resulting from these processes. Your results should be in terms of the fission cross section σ_f, the neutron flux ϕ, the number density n_U of fissionable U, the decay constants λ_I and λ_{Xe}, the capture cross sections σ_I (7 b) and σ_{Xe} (2.7×10^6 b), and the yields γ_I and γ_{Xe}. (b) Show that the neutron capture contribution can be neglected for I but not for Xe. (c) Subject to the initial conditions $n_I(0) = 0$ and $n_{Xe}(0) = 0$ and assuming n_U and ϕ to be constant, solve the differential equations to obtain $n_I(t)$ and $n_{Xe}(t)$. Show that the equilibrium values at large t are $n_I = \gamma_I \sigma_f n_U \phi / \lambda_I$ and $n_{Xe} = (\gamma_I + \gamma_{Xe})\sigma_f n_U \phi / (\lambda_{Xe} + \sigma_{Xe}\phi)$. (d) After reaching equilibrium, the reactor is shut down at $t = t_0$. In terms of $t' = t - t_0$, find $n_I(t')$ and $n_{Xe}(t')$; sketch their behavior from $t = 0$ to $t \gg t_0$. What problems might arise in starting the reactor again?

15. Another example of fission product poisoning (see previous problem) occurs in the mass-149 decay chain, $^{149}\text{Nd} \rightarrow {}^{149}\text{Pm} \rightarrow {}^{149}\text{Sm}$. The thermal cross sections are 1400 b for ^{149}Pm and 42,000 b for ^{149}Sm. Calculate and plot the number density of Sm nuclei as a function of time in a reactor that operates at a constant power level (keeping ϕ constant) for several weeks, following which it is turned off. (*Hint*: Nd decays sufficiently rapidly on this time scale that you may assume the Pm to be formed only directly in fission with yield $\gamma_{Pm} = 1.13\%$.)

16. (a) Given a collection of n thermal neutrons in a natural uranium reactor, how many ^{235}U atoms (of N total fuel atoms) disappear following the absorption of these neutrons? (b) How many ^{239}Pu atoms appear? Consider the production of ^{239}U from absorption of the original thermal neutrons and also of the secondary fast fission neutrons, taking $p = 0.9$ and $\varepsilon = 1.0$.

(c) The ratio between the numbers found in (b) and (a) is called the *conversion ratio* and represents a measure of whether a converter reactor will function as a breeder, that is, produce more fuel than it consumes. Evaluate the conversion ratio and comment. (d) Repeat the calculation for a reactor fueled with a mixture of 1% fissile ^{233}U ($\sigma_f = 530$ b, $\sigma_a = 47.7$ b, $\nu = 2.49$) and 99% fertile ^{232}Th ($\sigma_f = 0$, $\sigma_a = 7.4$ b).

17. Suppose you were given the assignment of calculating the time dependence of radioactive decay heat produced by fission products after a reactor is shut down. List the information you would need, and discuss whether the needed input data could be measured or estimated. Carefully specify any assumptions that would need to be made. Be as realistic as possible in your approach to this problem—your resources of time and money needed to do experiments are not infinite.

18. The thermal utilization factor f depends on the ratio of the total number of captures in the fuel to the number in the fuel plus everything else (moderator, structural components, etc.). Suppose we have a homogeneous, graphite-moderated reactor containing 20 times as much graphite (by weight) as uranium; the uranium is enriched to 2% in ^{235}U. Compute the thermal utilization factor. How would the calculation be different in a heterogeneous (lumped) arrangement?

14

NUCLEAR FUSION

Figure 3.16 suggests an alternative to fission for extracting energy from the nucleus—we can climb the binding energy curve toward the more stable nuclei by beginning with the very light nuclei, rather than the very heavy nuclei as in fission. That is, if we combine two light nuclei into a nucleus below $A = 56$, energy is released. This process is called *nuclear fusion* because two light nuclei are fused into a heavier one.

As an energy source, fusion has several obvious advantages over fission: the light nuclei are plentiful and easy to obtain, and the end products of fusion are usually light, stable nuclei rather than heavy radioactive ones. There is one considerable disadvantage, however: before light nuclei can be combined, their mutual Coulomb repulsion must be overcome. Fission induced by neutrons has no Coulomb barrier and thus very low-energy incident particles can be used; indeed, the cross section for ^{235}U increases as we reduce the neutron energy. On the other hand, cross sections for reactions induced by charged particles tend to decrease with decreasing energy.

Consider the fission of two ^{20}Ne nuclei to form ^{40}Ca. The Q value is about 20.7 MeV, or about 0.5 MeV/nucleon, comparable to the energy released in fission. However, before the nuclear forces of the two ^{20}Ne nuclei can interact, we must move them close enough together so that their nuclear distributions begin to overlap. At the point where their surfaces are just touching, the Coulomb repulsion is 21.2 MeV. If we were to perform a nuclear reaction in which two ^{20}Ne were brought together with a total of 21.2 MeV of kinetic energy, the final energy of the system would be 41.9 MeV, representing the initial 21.2 MeV of kinetic energy *plus* the 20.7 MeV released in the reaction (the Q value). The energy gain is therefore a factor of two—21 MeV goes in and 42 MeV comes out.

Accelerating ^{20}Ne to 21.2 MeV against a ^{20}Ne target is certainly no problem, but heavy-ion accelerators (^{20}Ne is called a "heavy ion" by accelerator physicists, for whom "light ion" means only H or He) produce beams in the nanoampere to microampere range. At a current of 10^{-6} A, even if every particle in the beam were to react (an unlikely prospect—scattering is several orders of magnitude more likely than fusion) the power output would be about 2 W, hardly enough even to light the accelerator laboratory!

An alternative approach would be to heat a container of neon gas until the thermal energy is large enough to have a high probability of two nuclei approaching one another and colliding with 21.2 MeV of energy. Because the thermal energy is used to overcome the Coulomb barrier that inhibits fusion, this process is called *thermonuclear* fusion. For the mean kinetic energy per molecule of a gas ($\frac{3}{2}kT$) to be $\frac{1}{2}$ of 21.2 MeV, we must have $kT = 7$ MeV. At room temperature, $kT = 0.025$ eV, and so this process requires a temperature about 3×10^8 times room temperature, or about 10^{11} K!

Despite these various drawbacks, fusion energy is at present a subject of vigorous and intensive research to perfect techniques for heating fusible nuclei and for increasing their density so the number of reactions becomes large enough that the energy output is comparable to that of a fission reactor (10^9 W). Of course, fusion also powers the sun and other stars and is therefore ultimately responsible for the evolution of life on Earth. Understanding fusion is critical for understanding the end products of stellar reactions, when the thermonuclear fuel is mostly exhausted and a star may pass through a nova or supernova stage, ending as a chunk of cosmic ash or as a neutron star or black hole. Most horribly, thermonuclear weapons are the curse of our civilization and a constant threat to our very existence.

In this chapter, we cover the basic physics of fusion processes and direct applications to solar fusion, controlled fusion reactors, and thermonuclear weapons. In Chapter 19, we consider further applications in nuclear astrophysics.

14.1 BASIC FUSION PROCESSES

As we discussed in the introduction, fusion is not at all a "natural" process on Earth (as fission is) because of the substantial limitations imposed by the Coulomb barrier. Once we overcome the barrier, fusion becomes very likely, as the two overlapping nuclei quickly reach a state of minimum energy. The basic fusion processes are thus considerably simpler to understand and explain than fission processes. The most elementary fusion reaction, $p + p \rightarrow {}^2He$, is not possible, owing to the instability of ${}^2He$ (but an alternative process analogous to β decay and leading to ${}^2H$ is a primary first step in solar fusion; see Section 14.3). Another elementary reaction is

$$^2H + {}^2H \rightarrow {}^4He + \gamma$$

where the γ is essential for energy balance, since ${}^4He$ has no excited states. The energy release (Q value) is 23.8 MeV, which happens to be greater than both the neutron and proton separation energies of ${}^4He$. More likely reactions are thus

$$^2H + {}^2H \rightarrow {}^3He + n \qquad (Q = 3.3 \text{ MeV})$$

$$^2H + {}^2H \rightarrow {}^3H + p \qquad (Q = 4.0 \text{ MeV})$$

These are called *deuterium-deuterium or D-D* reactions.

Of course, the more stable the end product formed, the greater is the energy release in the reaction. A reaction that forms ${}^4He$ would be likely to show a

particularly large energy release:

$$^2\text{H} + ^3\text{H} \rightarrow ^4\text{He} + \text{n} \qquad (Q = 17.6 \text{ MeV})$$

This reaction is called the *deuterium-tritium or D-T* reaction. If the incident particles have negligibly small kinetic energies, the ^{4}He and n share 17.6 MeV consistent with linear momentum conservation, and a monoenergetic neutron with energy 14.1 MeV emerges. This reaction often serves as a source of fast neutrons. Because of the large energy release (and because the Coulomb barrier is no higher than in the D-D reactions), the D-T reaction has been selected for use in controlled fusion reactors. A disadvantage is that most of the energy is given to the neutron, in which form it is not particularly easy to extract. In fission, very little of the energy release is given to the neutrons, and the kinetic energy of the fission fragments is easy to extract.

The fusion of four protons ultimately to form ^{4}He (in several steps) is responsible for the thermonuclear energy released in stars similar to the sun. The next step, once the hydrogen fuel has been used up, is helium fusion. The simplest reaction, $^4\text{He} + ^4\text{He} \rightarrow ^8\text{Be}$, is not observed because ^{8}Be breaks up into two ^{4}He again almost as fast as it is formed (10^{-16} s). Instead, a more complicated process takes place:

$$3\,^4\text{He} \rightarrow ^{12}\text{C}$$

The probability of bringing together three particles at one point is negligibly small. Instead, the process (in stars) first produces a small equilibrium concentration of ^{8}Be, and capture of a third α particle by the ^{8}Be happens to occur through a resonance in ^{12}C where the cross section becomes large enough to give a reasonable probability for capture before the ^{8}Be splits apart. The larger Coulomb barrier of the helium reactions relative to hydrogen reactions means that helium burning occurs only in hotter (and older) stars. At still higher temperatures, other reactions occur that can produce energy from ^{12}C and heavier products (up to ^{56}Fe). In Section 14.3 we consider the hydrogen-burning processes in the sun, and in Chapter 19 we consider other aspects of nuclear reactions in stars.

14.2 CHARACTERISTICS OF FUSION

Energy Release The calculation of the energy release in fusion is much more direct than that for fission. It is necessary simply to calculate the Q value of the appropriate reaction. For most applications of fusion, from controlled fusion reactors to solar processes, the reacting particles have energies in the range of 1–10 keV. The initial kinetic energies are thus small compared with the Q values of several MeV. The energy released, and the final total energy of the product particles, will then be equal to the Q value:

$$\tfrac{1}{2}m_\text{b}v_\text{b}^2 + \tfrac{1}{2}m_\text{Y}v_\text{Y}^2 \simeq Q \tag{14.1}$$

for product particles b and Y. Again neglecting the initial motions, the final momenta are equal and opposite:

$$m_\text{b}v_\text{b} \simeq m_\text{Y}v_\text{Y} \tag{14.2}$$

and thus

$$\tfrac{1}{2}m_b v_b^2 \simeq \frac{Q}{1 + m_b/m_Y} \tag{14.3}$$

$$\tfrac{1}{2}m_Y v_Y^2 \simeq \frac{Q}{1 + m_Y/m_b} \tag{14.4}$$

from which we can calculate the distribution in energy for the elementary fusion reactions given in the previous sections.

One consequence of this energy sharing is immediately apparent—the lighter product particle takes the larger share of the energy. The ratio of the kinetic energies is, from Equation 14.2, just

$$\frac{\tfrac{1}{2}m_b v_b^2}{\tfrac{1}{2}m_Y v_Y^2} = \frac{m_Y}{m_b} \tag{14.5}$$

Thus in the case of the D-T reaction, the product neutron has 80% of the energy. In the D-D reactions, the product proton or neutron has 75% of the available energy.

Coulomb Barrier If R_a and R_X are the radii of the reacting particles, the Coulomb barrier is

$$V_c = \frac{e^2}{4\pi\epsilon_0}\frac{Z_a Z_X}{R_a + R_X} \tag{14.6}$$

when the particles just touch at their surfaces. The effect of the Coulomb barrier on the fusion reaction is very similar to the effect of the Coulomb barrier on α decay. The product $Z_a Z_X$ will ultimately appear in an exponential barrier penetration probability, and so the fusion cross section is extremely sensitive to the Coulomb barrier. The fusion probability therefore decreases rapidly with $Z_a Z_X$, and the barrier is lowest for the hydrogen isotopes. For the D-T reaction, $V_c = 0.4$ MeV, but even though the barrier is lowest, it is still far above the typical incident particle energy of 1–10 keV. Of course, it is not necessary for the particles to be above the barrier; just as in α decay, it is the barrier penetration probability that determines the outcome.

Cross Section The fusion cross section can be adapted from the basic expression for nuclear reaction cross sections, Equation 11.70. For particles reacting at thermal energies, it is likely that the reaction will occur far from any resonance, and thus the energy dependence of the cross section comes mainly from two terms: the k^{-2} factor (which gives a v^{-2} dependence), and the partial reaction probability, which for two charged particles includes a barrier penetration factor of the form e^{-2G} as in the case of α decay, Equation 8.15. Thus

$$\sigma \propto \frac{1}{v^2} e^{-2G} \tag{14.7}$$

where G is essentially given by Equation 8.17, substituting for Q the center-of-mass energy E of the reacting particles. Since $E \ll B$, we can approximate

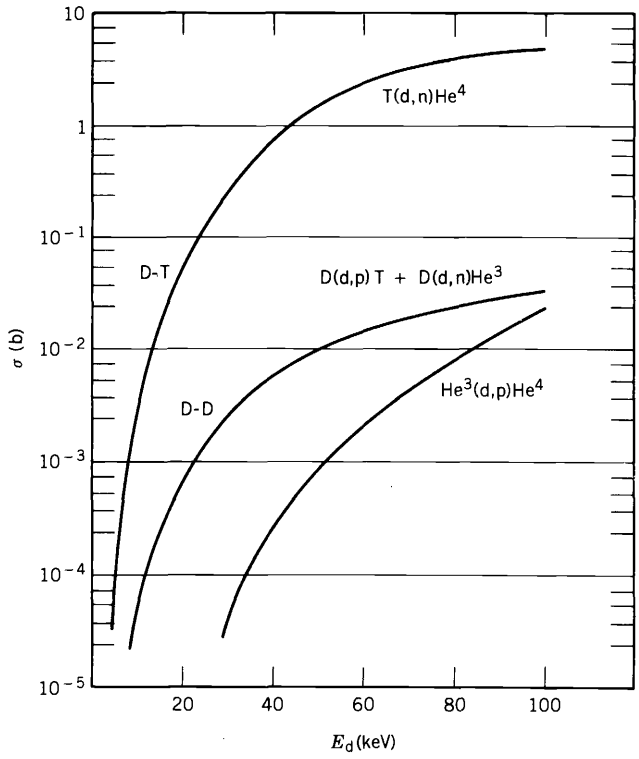


Figure 14.1 Cross sections for fusion reactions.

Equation 8.17 as

$$G \simeq \frac{e^2}{4\pi\epsilon_0}\frac{\pi Z_a Z_X}{\hbar v} \tag{14.8}$$

In these expressions v represents the relative velocity of the reacting particles. The proportionality factor needed in Equation 14.7 will involve nuclear matrix elements and statistical factors depending on the spins of the particles, but the entire energy dependence is accounted for by the factors included in Equation 14.7. Figure 14.1 shows a plot of the resulting expression.

Reaction Rate As discussed in Sections 6.3 and 12.3, the rate for a nuclear reaction depends on the product σv. For neutron-induced reactions outside the resonance region, $\sigma \propto 1/v$ and so σv = constant. For fusion reactions, this is not the case. Moreover, in thermonuclear fusion there will be a distribution of particle speeds described by the usual Maxwell-Boltzmann velocity distribution:

$$n(v) \propto e^{-mv^2/2kT} \tag{14.9}$$

where $n(v)v^2\,dv$ gives the relative probability to find a particle with speed between v and $v + dv$ in a collection of particles in thermal equilibrium at

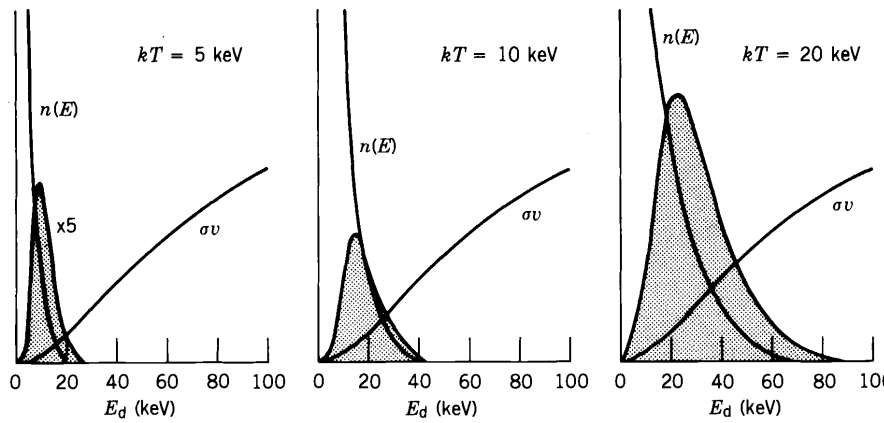


Figure 14.2 Folding of the product σv with a Maxwell-Boltzmann energy distribution at temperatures corresponding to $kT = 5$, 10, and 20 keV. The curve $n(E)$ shows the Maxwell-Boltzmann distribution, proportional to $E^{1/2}\exp(-E/kT)$; the curve $n(E)$ falls to zero at low energies, which is not shown in the graphs. The shaded area shows the product. Note the great increase in shaded area with kT, corresponding to an increase of $\langle \sigma v \rangle$ as is shown in Figure 14.3. The deuteron energy E_d is one-half of the total center-of-mass reaction energy E.

temperature T. In such a collection of nuclei undergoing thermonuclear fusion, it is appropriate to calculate σv averaged over all speeds or energies:

$$\langle \sigma v \rangle \propto \int_0^\infty \frac{1}{v} e^{-2G} e^{-mv^2/2kT} v^2 \, dv \tag{14.10}$$

or

$$\langle \sigma v \rangle \propto \int_0^\infty e^{-2G} e^{-E/kT} \, dE \tag{14.11}$$

Figure 14.2 shows an example of the folding of the product σv with the Maxwell-Boltzmann distribution function for various temperatures. At low temperature, there is little overlap between $n(E)$ and σv, and the average is small. At very high T, the area of the Maxwell-Boltzmann distribution becomes small and again the average value of σv is small. At intermediate temperatures, $\langle \sigma v \rangle$ rises to a maximum. Figure 14.3 shows $\langle \sigma v \rangle$ for several fusion reactions as a function of the temperature. At extremely high temperatures ($T \sim 10^{10}$ K, corresponding to MeV energies), the D-T reaction may become less favorable than others, but in the temperature region that is likely to be achievable in a thermonuclear fusion reactor (1–10 keV or $T \sim 10^7$–10^8 K) the D-T reaction is clearly favored.

The simple theory used in this section to evaluate $\langle \sigma v \rangle$ would be appropriate only for the D-D reaction. For reactions involving two different nuclei (D-T, for example), we should take better account of the velocities of the different species. The cross section and reaction rate should involve a relative velocity, $\sigma(v_{rel})$ and $\langle \sigma(v_{rel}) v_{rel} \rangle$, and the average should be done over the Maxwell-Boltzmann distribution of both species. Even though the specific details may be more complicated, the general conclusions regarding fusion reaction rates remain valid.

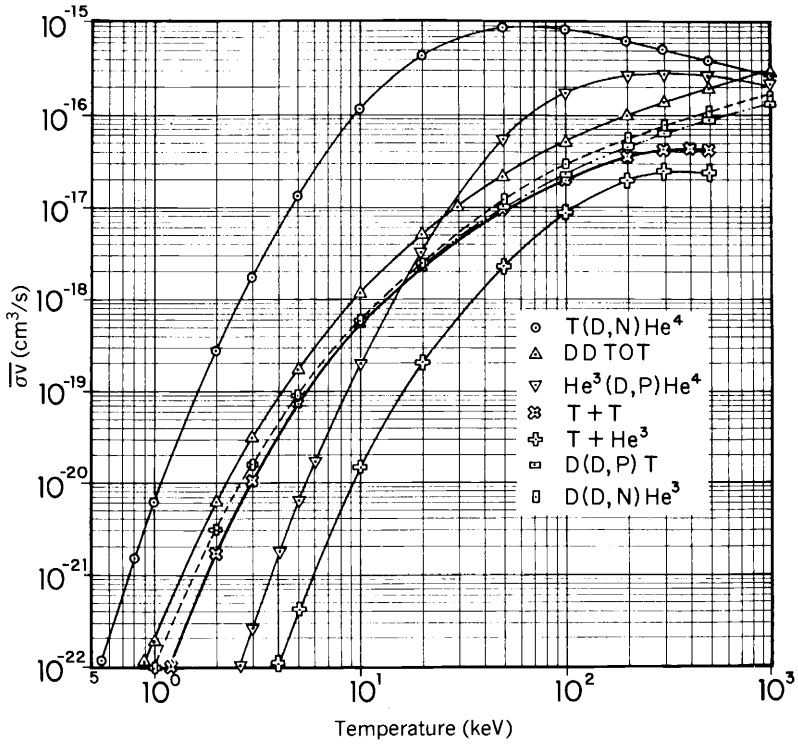


Figure 14.3 Values of σv averaged over a Maxwell-Boltzmann energy distribution for various fusion reactions. From D. Keefe, *Ann. Rev. Nucl. Particle Sci.* **32**, 391 (1982).

14.3 SOLAR FUSION

Before discussing how we achieve thermonuclear fusion on Earth, let's consider the sun, which we can regard as an extremely successful prototype of a self-sustaining thermonuclear reactor. As far as we can tell from the fossil records on Earth, the sun's output has been nearly constant over a time scale of more than 10^9 years.

The basic process in the sun (and most other stars) is the fusion of hydrogen into helium. Hydrogen is by far the most abundant material in the universe—more than 90% of the atoms in the universe are hydrogen, and all but less than 1% of the remainder are helium. (This helium was formed during the early stages of the evolution of the universe and not as a result of later stellar processes.) All reactions in any fusion cycle must be two-body reactions (two particles in the initial state) because the simultaneous collision of three particles is too improbable an event to be significant. The first step in the fusion process must be the combination of two protons to form the only stable two-nucleon system:

$$^1\mathrm{H} + {}^1\mathrm{H} \rightarrow {}^2\mathrm{H} + \mathrm{e}^+ + \nu \qquad (Q = 1.44\ \mathrm{MeV})$$

The ν in the final state signals a weak interaction process, which must occur to turn a proton into a neutron (not enough energy is available to create a π meson and to have $\mathrm{p} \rightarrow \mathrm{n} + \pi^+$). The cross sections for weak interaction processes are very small; for the formation of deuterium, the cross section is calculated to be of

the order of 10^{-33} b at keV energies and 10^{-23} b at MeV energies. The central temperature of the sun is about 15×10^6 K, corresponding to a mean proton energy of about 1 keV, but to calculate the reaction rate it is necessary to find $\langle \sigma v \rangle$ averaged over all energies, and the easy penetration of the Coulomb barrier for MeV particles in the high-energy tail of the Maxwell-Boltzmann distribution compensates somewhat for the low intensity in the tail. The reaction rate is nevertheless very small, and even at the high densities at the core of the sun (about 125 g/cm^3, or 7.5×10^{25} protons/cm^3) the reaction rate is only about 5×10^{-18}/s per proton. What keeps the sun radiating is the enormous number of reacting protons, of the order of 10^{56}, so that the total reaction rate is of the order of 10^{38}/s. This step in the solar fusion cycle is often called the "bottleneck" because it is the slowest and least probable step.

Following deuteron formation, it becomes very likely for the following reaction to occur:

$$^2\mathrm{H} + {}^1\mathrm{H} \rightarrow {}^3\mathrm{He} + \gamma \qquad (Q = 5.49\ \mathrm{MeV})$$

It is very unlikely at this point to observe D-D reactions because of the small number of deuterons present—only one deuteron is formed for every $\sim 10^{18}$ protons, and thus it is about 10^{18} times more likely that a deuteron will react with a proton than with another deuteron. Deuterons are thus "cooked" to ^{3}He nearly as rapidly as they are formed.

Reactions of ^{3}He with protons are not possible:

$$^3\mathrm{He} + {}^1\mathrm{H} \rightarrow {}^4\mathrm{Li} \rightarrow {}^3\mathrm{He} + {}^1\mathrm{H}$$

The isotope ^{4}Li does not exist as a bound system, and it breaks up as soon as it is formed. It is also unlikely for ^{3}He to react with ^{2}H because the density of ^{2}H is very low and because the ^{2}H is converted to ^{3}He very rapidly. The fate of a ^{3}He is thus to wander until it finds another ^{3}He:

$$^3\mathrm{He} + {}^3\mathrm{He} \rightarrow {}^4\mathrm{He} + 2\,{}^1\mathrm{H} + \gamma \qquad (Q = 12.86\ \mathrm{MeV})$$

The complete process is indicated schematically in Figure 14.4, and is known as the *proton-proton cycle*. The net reaction is the conversion of four protons to helium:

$$4\,{}^1\mathrm{H} \rightarrow {}^4\mathrm{He} + 2e^+ + 2\nu$$

To find the total Q value, we must keep in mind that we have been discussing reactions with bare nuclear particles. Let's add four electrons to each side of this process, giving four neutral H atoms on the left, and a neutral He atom on the right with two additional electrons to annihilate the positrons. The net process is thus $4\ {}^1\mathrm{H} \rightarrow {}^4\mathrm{He}$, with a Q value of 26.7 MeV. The energy converted to solar radiation per cycle is slightly less, for the neutrinos emerge directly from the core without contributing to the heating of the *photosphere*, the outer region of the sun where the energy released in nuclear reactions is converted to light.

An alternative fate for the ^{3}He is to encounter an α particle:

$$^3\mathrm{He} + {}^4\mathrm{He} \rightarrow {}^7\mathrm{Be} + \gamma$$

followed either by

$$^7\mathrm{Be} + e^- \rightarrow {}^7\mathrm{Li} + \nu$$

and

$$^7\mathrm{Li} + \mathrm{p} \rightarrow 2\,{}^4\mathrm{He}$$

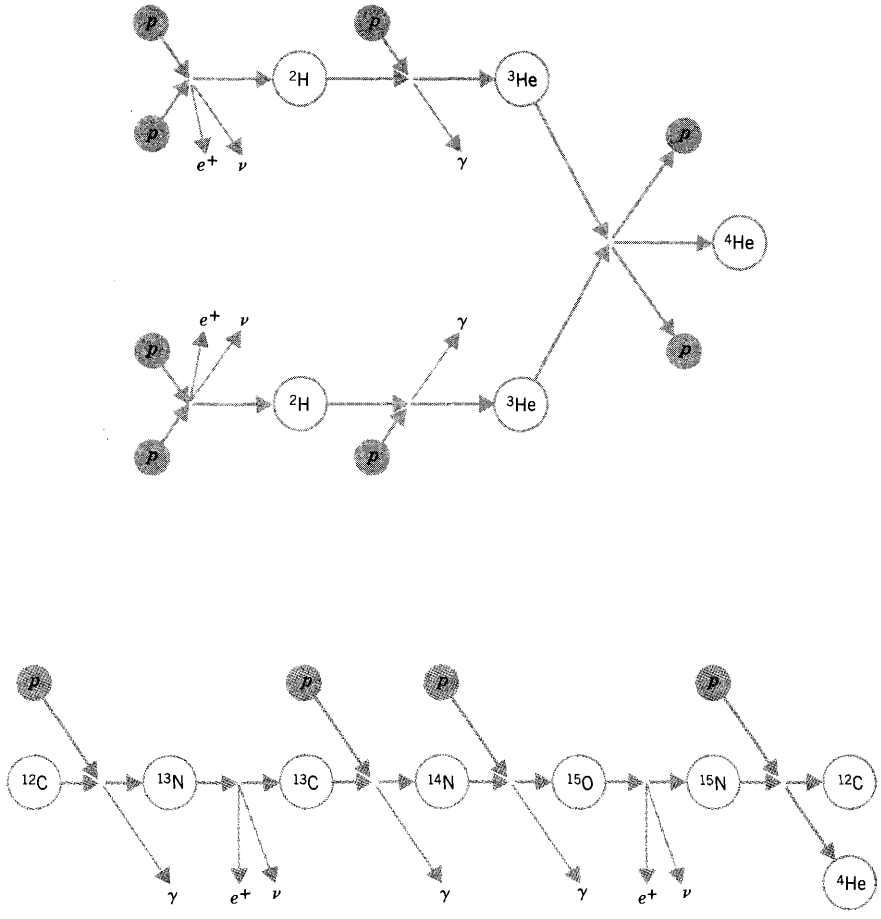


Figure 14.4 (Top) Sequence of processes in proton-proton chain of fusion reactions. (Bottom) Carbon (CNO) cycle of fusion reactions.

or perhaps by the sequence

$$^{7}\text{Be} + \text{p} \rightarrow {}^{8}\text{B} + \gamma$$
$$^{8}\text{B} \rightarrow {}^{8}\text{Be} + \text{e}^{+} + \nu$$
$$^{8}\text{Be} \rightarrow 2\,{}^{4}\text{He}$$

The net reaction and the net Q value are the same for these three possible paths. Which one is actually chosen depends on the composition of the star and on its temperature. In the case of the sun, we can test for these three alternatives by observing the neutrinos. In the first case, we get a continuous distribution of neutrinos with a maximum energy of 0.42 MeV. In the second case, the two-body ^{7}Be electron capture gives a monoenergetic neutrino of energy 0.862 MeV, while the ^{8}B decay gives a continuous neutrino distribution with an endpoint of 14 MeV. To observe these neutrinos, Davis has devised a sensitive experiment which was previously described in Section 9.6. After many years of experiments, Davis

has observed only a small fraction (one-third or less) of the expected number of neutrinos from the sun.

Neutrino observation gives us in effect a window to the deep solar interior, for the visible light that reaches us from the sun is characteristic of its surface and represents γ rays from reactions in the core that are scattered many thousands of times on their journey to the surface. It also takes perhaps millions of years for the radiation to reach the surface, so the light we see today results from solar processes that occurred millions of years ago. The neutrinos, on the other hand, come to us directly from the core at the speed of light. It is therefore very important to try to understand why the results of the Davis experiment disagree with theory and to devise other experiments that are sensitive to other components of the neutrino spectrum.

If in addition to hydrogen and helium there are heavier elements present in the interior of a star, a different series of fusion reactions can occur. One such series is the *carbon or CNO cycle*:

$$
\begin{aligned}
{}^{12}\mathrm{C} + {}^{1}\mathrm{H} &\rightarrow {}^{13}\mathrm{N} + \gamma \\
{}^{13}\mathrm{N} &\rightarrow {}^{13}\mathrm{C} + \mathrm{e}^{+} + \nu \\
{}^{13}\mathrm{C} + {}^{1}\mathrm{H} &\rightarrow {}^{14}\mathrm{N} + \gamma \\
{}^{14}\mathrm{N} + {}^{1}\mathrm{H} &\rightarrow {}^{15}\mathrm{O} + \gamma \\
{}^{15}\mathrm{O} &\rightarrow {}^{15}\mathrm{N} + \mathrm{e}^{+} + \nu \\
{}^{15}\mathrm{N} + {}^{1}\mathrm{H} &\rightarrow {}^{12}\mathrm{C} + {}^{4}\mathrm{He}
\end{aligned}
$$

In this case the ^{12}C is neither created nor destroyed, but acts as a catalyst to aid in the fusion process. The net process is $4\ {}^{1}H \rightarrow {}^{4}He + 2e^{+} + 2\nu$, exactly as in the proton-proton cycle, and the Q value is the same. The carbon cycle can proceed more rapidly than the proton-proton cycle because it does not have a process analogous to the deuterium bottleneck. However, the Coulomb barrier is 6 or 7 times higher for proton reactions with carbon and nitrogen than for proton-proton reactions. The carbon cycle will thus be dominant at higher temperatures, where the additional thermal energy is needed to increase the probability to penetrate the Coulomb barrier (Figure 14.5).

The mean solar radiation reaching the Earth is about 1.4×10^{3} W/m^2, which (if distributed uniformly in space) means the sun's total output is about 4×10^{26} W. Each fusion reaction produces about 25 MeV, and thus there must be about 10^{38} fusion reactions per second, consuming 4×10^{38} protons per second. At this rate, the sun can be expected to continue to burn its hydrogen fuel for another 10^{10} y.

Once a star has exhausted its hydrogen fuel, helium fusion reactions can take place, with $3\ {}^{4}He \rightarrow {}^{12}C$ at the higher temperature needed to penetrate the Coulomb barrier. Other reactions involving fusion of light nuclei and α-particle capture can continue to release energy, until the process ends near ^{56}Fe, beyond which there is no energy gain in combining nuclei. This relatively simple recipe not only helps to explain some of the many categories of stars we observe, but it also gives us a means to understand the relative abundances of various atomic species (light even-Z atoms, made through successive α captures on ^{12}C, are far

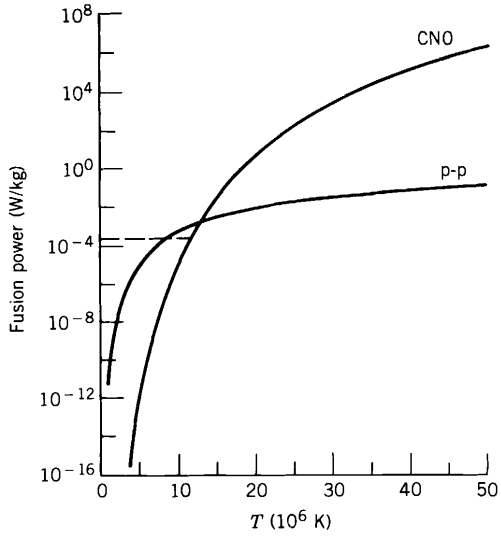


Figure 14.5 Power generation per unit mass of fuel for proton-proton and CNO processes. The dashed line indicates the sun's power of about 2×10^{-4} W / kg.

more abundant then neighboring odd-Z atoms; nearly everything above Fe is less abundant than almost everything below Fe). We consider further details of nuclear astrophysics, including the evolution of stars and the production of the elements, in Chapter 19.

14.4 CONTROLLED FUSION REACTORS

The essence of controlling fusion reactions and extracting usable energy is to heat a thermonuclear fuel to temperatures of the order of 10^8 K (mean particle kinetic energies of 10 keV) while simultaneously maintaining a high enough density for a long enough time that the rate of fusion reactions will be large enough to generate the desired power. At these temperatures, the atoms must become ionized (for hydrogen, only 13.6 eV is needed to strip the electron), and so the fuel is a hot mixture of clouds of positive ions and negative electrons but is overall electrically neutral. Such a situation is called a *plasma*, and the dynamical equations that govern plasma behavior are beyond the scope of this text. The electrostatic properties of a plasma determine a length scale called the *Debye length*,

$$L_D = \left(\frac{4\pi\epsilon_0}{e^2} \frac{kT}{4\pi n} \right)^{1/2} \tag{14.12}$$

where n is the mean ion or electron density (which will of course be subject to considerable local fluctuations on a microscopic scale). Using solid densities (10^{28} m^{-3}) as a rough scale factor, the Debye length for a 10-keV plasma is of the order of 10^{-8} m and the number of particles in a volume of the plasma of dimension of one Debye length is about 10^4. For a more rarified plasma, say of density only 10^{22}/m^3, the Debye length is 10^{-5} m and the number of particles in a volume of dimension one Debye length is 10^7. In either of these two extreme

cases, there are two basic properties: the physical size of the reacting plasma is far larger than the Debye length in dimension, and there are many particles in any characteristic volume. It is these two properties that permit the use of plasma equations to describe the hot thermonuclear fuel.

A major problem is obviously to confine the plasma—for the hot fuel to exchange energy with the walls of its container would simultaneously cool the fuel and melt the container. There are at present two schemes under investigation for confining the thermonuclear fuel: *magnetic confinement* and *inertial confinement*. In magnetic confinement, the plasma is confined by a carefully designed magnetic field. In inertial confinement, a solid pellet is suddenly heated and compressed by being struck simultaneously from many directions with intense beams of photons or particles.

Confinement of a plasma is of course not absolute—there will be many ways for a plasma to lose energy. The primary mechanism is *bremsstrahlung*, in which the Coulomb scattering of two particles produces an acceleration which in turn gives rise to the emission of radiation. The largest accelerations are suffered by the lightest particles (electrons), but because the electrons and ions are approximately in thermal equilibrium, any loss by the electrons is felt also by the ions, which are then less energetic and less successful in penetrating the Coulomb barrier. The power radiated by an electron experiencing an acceleration a is

$$P = \frac{e^2 a^2}{6\pi\epsilon_0 c^3} \tag{14.13}$$

If the electron is at a distance r from an ion of charge Z, the acceleration is

$$a = \frac{F}{m_e} = \frac{Ze^2}{4\pi\epsilon_0 m_e r^2} \tag{14.14}$$

If τ is the characteristic time during which the ion and electron interact, then the number of ions encountered at a distance r will be (see Figure 14.6) $(n)(v_e\tau)(2\pi r\,dr)$, where n is the density of positive ions. Thus

$$dP = \frac{e^2 n}{6\pi\epsilon_0 c^3} \frac{Z^2 e^4 v_e \tau (2\pi r\,dr)}{(4\pi\epsilon_0)^2 m_e^2 r^4} \tag{14.15}$$

where we let dP be the contribution to the total power from electrons scattered at impact parameters between r and $r + dr$. The characteristic interaction time τ can be estimated as r/v_e and thus

$$dP = \frac{4\pi e^6 Z^2 n}{3(4\pi\epsilon_0)^3 m_e^2 c^3} \frac{dr}{r^2} \tag{14.16}$$

Integrating from r_{min} to r_{max} gives the total power radiated by a single electron, and multiplying the result by the density of electrons n_e gives the power per unit volume radiated by the plasma. We can take $r_{max} \sim \infty$ and for r_{min} it is tempting to try the distance of closest approach, which for 10 keV electrons turns out to be $144Z$ fm. If we calculate the quantum mechanical uncertainty in the electron's position, taking $\Delta p \sim p \simeq 100$ keV/c, then Δx is of the order of 2000 fm. We therefore cannot specify r_{min} as precisely as $144Z$ fm, and we should take as a

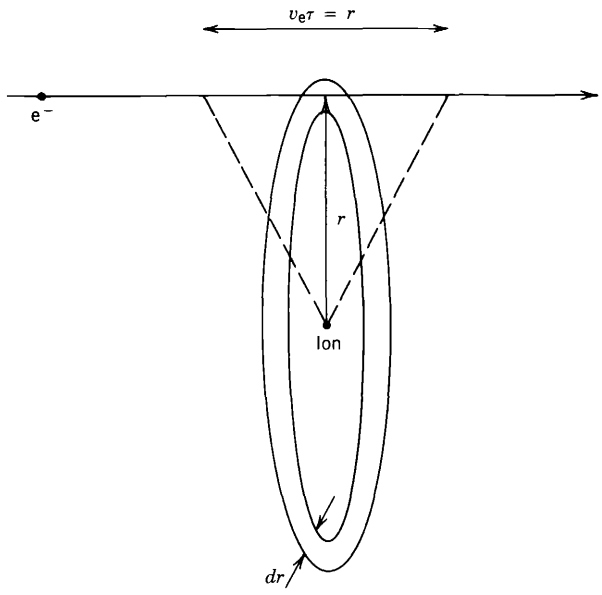


Figure 14.6 Geometry for estimating bremsstrahlung losses. The interaction time τ is approximately r/v_e from the portion of the path where the Coulomb force has the greatest effect. All electrons that pass through the ring of radius r and thickness dr suffer similar losses.

better estimate $r_{min} = \hbar/m_e v_e$. Carrying out the integration, the power per unit volume radiated in bremsstrahlung becomes

$$P_{br} = \frac{4\pi n n_e Z^2 e^6 v_e}{3(4\pi\epsilon_0)^3 m_e c^3 \hbar} \tag{14.17}$$

Continuing the estimate, we put for v_e the velocity corresponding to the mean kinetic energy of the Maxwell-Boltzmann distribution, $v_e \simeq \sqrt{3kT/m_e}$. Evaluating all the numerical coefficients, the final estimate is

$$P_{br} = 0.5 \times 10^{-36} Z^2 n n_e (kT)^{1/2} \text{ W/m}^3 \tag{14.18}$$

where kT is in keV. The reaction rate for fusion reactions is $n_1 n_2 \langle \sigma v \rangle$, where n_1 and n_2 are the densities of the two kinds of fusing ions; if there is only one kind of ion, as in D-D fusion, the product $n_1 n_2$ should be replaced with $\frac{1}{2}n^2$, where the factor of $\frac{1}{2}$ corrects for double counting of reactions. Comparing Equation 14.18 with the fusion rates in Figure 14.7, we see that there is a temperature at which the fusion output will exceed the bremsstrahlung loss, which is of the order of 4 keV for D-T and 40 keV for D-D reactions. This suggests the superiority of the choice of D-T for fuel. Note also that the bremsstrahlung losses increase as Z^2; therefore fusion reactions using nuclei other than hydrogen have substantially greater bremsstrahlung losses as well as generally smaller reaction rates in the keV region (because of the Coulomb barrier).

We therefore choose to operate our fusion reactor at a temperature where the power gain from fusion exceeds the bremsstrahlung losses. Other radiation losses, including synchrotron radiation from charged particles orbiting about magnetic

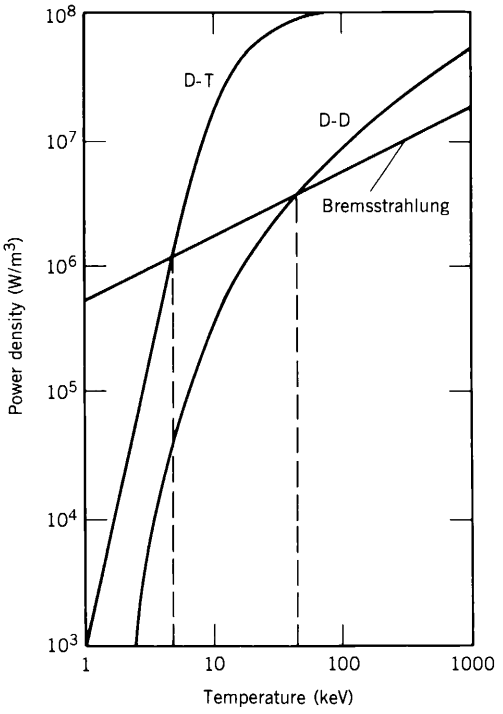


Figure 14.7 Comparison of bremsstrahlung losses with power outputs of D-D and D-T reactions, assuming an ion density of $10^{21}/m^3$. The vertical lines show the temperatures above which fusion power exceeds bremsstrahlung losses.

field lines, can also be neglected. The fusion reactor will have a net energy gain if the energy released in fusion reactions exceeds the radiation losses *and* the original energy investment in heating the plasma to the operating temperature. If we operate at a temperature above 4 keV, even at 10 keV, the D-T fusion gain is greater than the radiation loss, and we can neglect the loss in energy to radiation. The energy released per unit volume from fusion reactions in the plasma is

$$E_f = \tfrac{1}{4}n^2\langle\sigma v\rangle Q\tau \tag{14.19}$$

where we assume that the densities of D and T are each equal to $\frac{1}{2}n$ (so that the total n is equal to n_e), Q is the energy released per reaction (17.6 MeV for D-T), and τ is the length of time the plasma is confined so that reactions can occur. Note that Equation 14.19 is of the form: reactions per unit time (reaction rate) per unit volume times energy release per reaction times the time during which reactions take place.

The thermal energy per unit volume needed to raise the ions and electrons to temperature T is $\frac{3}{2}nkT$ (for the ions) and $\frac{3}{2}n_ekT$ (for the electrons). With $n = n_e$, the thermal energy is

$$E_{th} = 3nkT \tag{14.20}$$

Let us review the sequence. We supply an energy of E_{th} to heat the plasma, then if we are able to confine it for a time τ we can extract fusion energy E_f. The

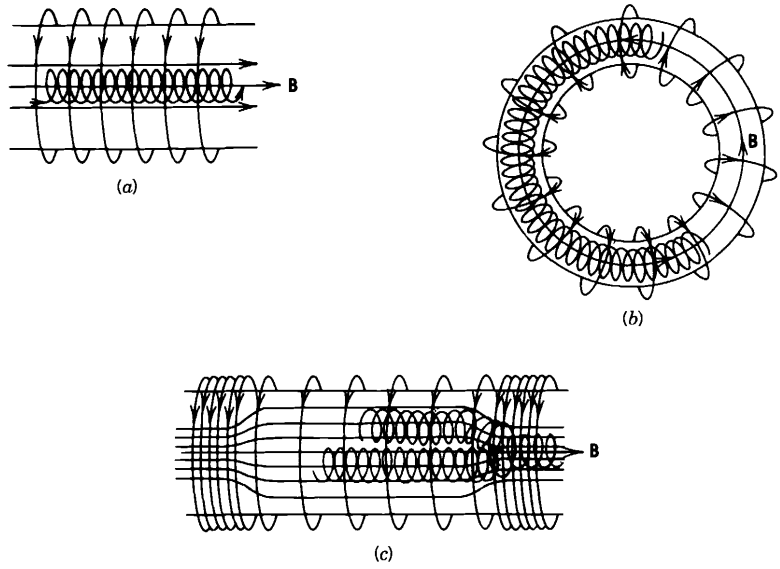


Figure 14.8 (*a*) Confinement by uniform axial magnetic field. The field ***B*** is established by the large current-carrying coils. The particles spiral about ***B***. (*b*) In a toroidal geometry, the particles follow the magnetic field lines as they spiral, but there is a gradual drift toward the outer wall. (*c*) In a magnetic mirror, the particles again follow the field lines, but are reflected from the high-field region.

reactor shows a net energy gain if

$$E_f > E_{th}$$

$$\tfrac{1}{4}n^2\langle\sigma v\rangle Q\tau > 3nkT \tag{14.21}$$

or

$$n\tau > \frac{12kT}{\langle\sigma v\rangle Q} \tag{14.22}$$

For an operating temperature of 10 keV for the D-T reaction, $\langle\sigma v\rangle \sim 10^{-22}$ m^3/s and thus $n\tau > 10^{20}$ s/m^3. This estimate of the minimum necessary product of ion density and confinement time is called the *Lawson criterion* and represents the goal of reactor designers. It will, of course, be different for different operating temperatures and for different fuels. For D-D reactions, Figure 14.7 shows that 10 keV is too low an operating temperature (bremsstrahlung losses are too great). Operating at $kT = 100$ keV gives $\langle\sigma v\rangle \simeq 0.5 \times 10^{-22}$ and thus $n\tau > 10^{22}$ s/m^3. We therefore need a hundredfold increase in the density of ions or the confinement time or some combination of both to gain energy in a D-D reactor.

Let's turn now to an examination of the basic reactor types and see how close they come to meeting the Lawson criterion. The simplest magnetic confinement is a uniform magnetic field—charged particles spiral about the field direction, as indicated in Figure 14.8. This is sufficient to confine the particle in only two directions. To prevent the loss of particles along the axis, there are two solutions shown: we can form a torus, thus keeping the spiral in a ring, or we can form a high density of magnetic field lines which reflects the particles back into the

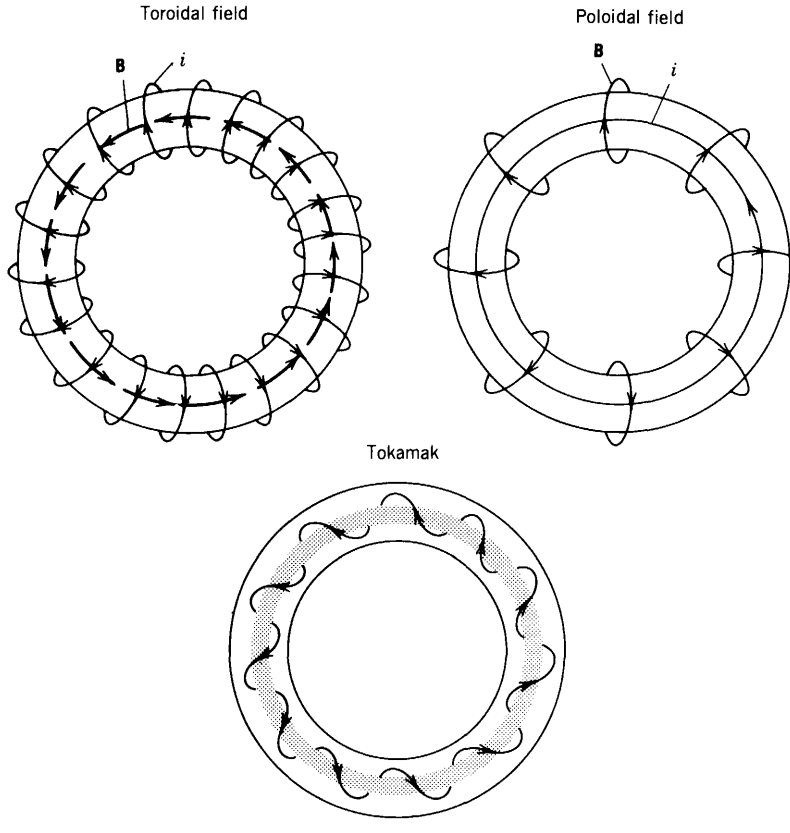


Figure 14.9 Principle of tokamak method of magnetic confinement. A toroidal field is produced by a winding of coils, and a poloidal field is produced by an axial current; these two fields are combined in the tokamak design. (The current-carrying coils are not shown.) The resulting field lines form a helix, through which the ions can travel in closed orbits.

low-field region and is hence known as a *magnetic mirror*. In any real toroidal winding, the field is weaker at larger radii, and thus as a particle spirals it sees a region of lower field which lets the spiral radius become larger and lets the particle approach the outer wall. To reduce this effect, a magnetic field component along the surface of the toroid is introduced; this is called a *poloidal* field. It can be achieved using a set of external coils, as illustrated in Figure 14.9, or by passing a current along the axis of the toroid through the plasma itself. The current serves the dual purpose of heating the plasma and confining the particles. The basic design is called a *tokamak* after the Russian acronym for the device.

The tokamak is at present one of the two most promising candidates for the basic design of a fusion power reactor. In actual tokamak developmental facilities, such as the one illustrated in Figure 14.10, the poloidal field is provided not by a set of external coils (which are used in a different device, known as a stellerator), but by a current induced in the plasma itself by a set of external windings that function in essence as the primary of a transformer. The ohmic heating resulting from the current (which is of the order of a few MA) also helps

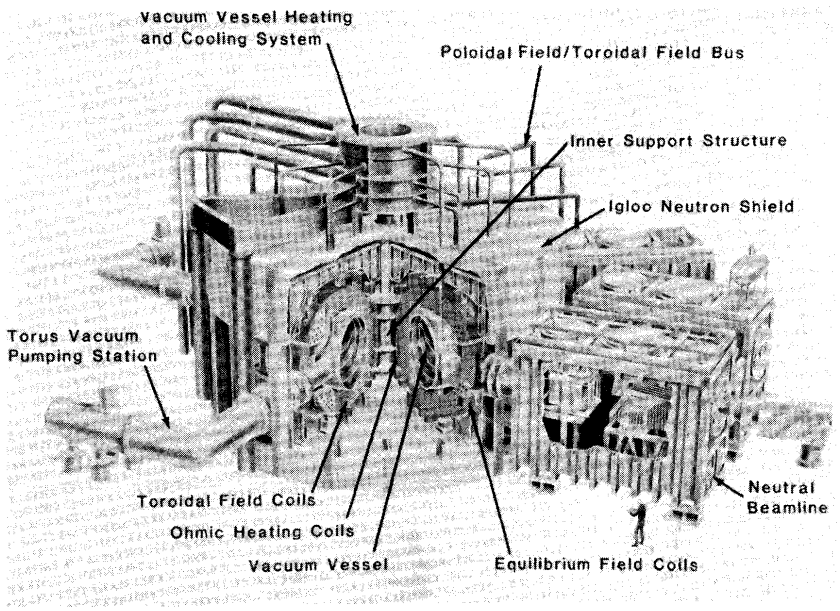


Figure 14.10 The Tokamak Fusion Test Reactor (TFTR). The radius of the vacuum chamber is about 2 m. The ohmic heating coils produce a plasma current of 2.5×10^6 A. Neutral-beam heating of about 10 MW contributes to the plasma. Drawing courtesy Princeton Plasma Physics Laboratory.

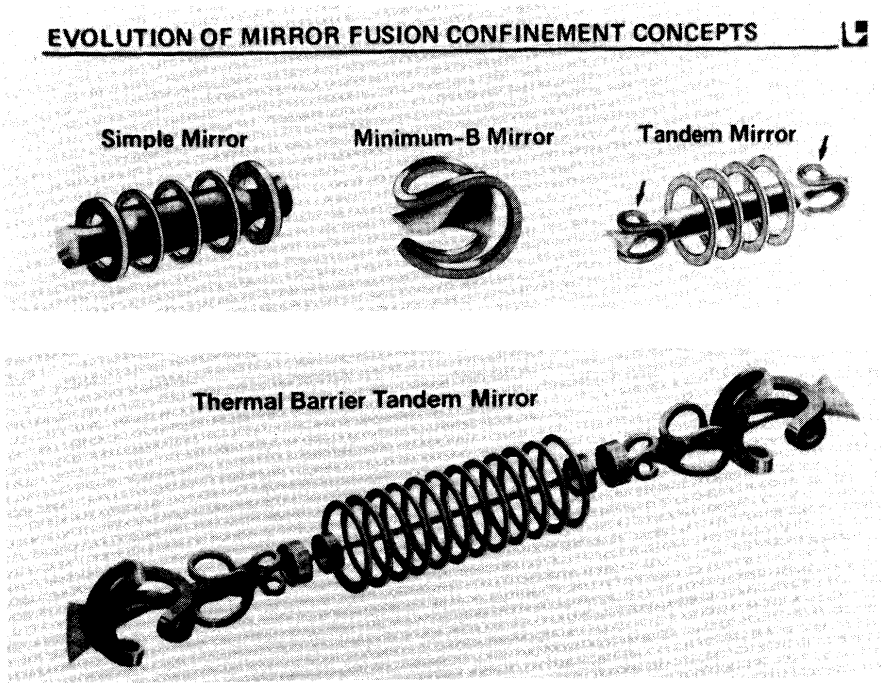


Figure 14.11 Basic concepts of linear mirror devices. The bottom drawing shows the combination of devices that would be used in a design such as that shown in Figure 14.12. Courtesy Lawrence Livermore National Laboratory, University of California, and U.S. Department of Energy.

to heat the plasma. The use of transformers requires the tokamak to operate in a pulsed mode, which is a fundamental limitation on the operation of the device; current pulses in the present generation of tokamaks have a duration of the order of 1 s.

Additional heating must be provided to raise the plasma to temperatures of the order of 10–100 keV. Two methods under investigation are radiofrequency (rf) heating and neutral beam injection (NBI). The rf waves radiated into the plasma drive the electrons and induce toroidal currents that heat the plasma. In the NBI technique, a beam of H or D ions is accelerated to energies of 10–100 keV and then neutralized (for example, by charge-exchange reactions in passing through a cell of neutral H or D atoms). The neutral atoms can pass undeviated through the magnetic fields of the tokamak and into the plasma, where they rapidly lose energy to the plasma through Coulomb scattering from ions and electrons.

Auxiliary heating systems of tens of MW will be required to achieve ignition of the plasma, after which the 3.5-MeV α's resulting from D-T fusion will provide the necessary heat to sustain the reactions. The charged α particles are confined to the plasma by the magnetic fields and eventually lose energy to the plasma through collisions.

Magnetic mirror machines generally try to make a three-dimensional "magnetic well" to confine the plasma because the simple linear mirror device is not effective in confining the plasma if it tries to bulge toward the walls in the low-field region. A so-called "minimum-B" configuration consists of a single coil shaped like the seams on a baseball or tennis ball as indicated in Figure 14.11. A combination of the simple mirror principle and the minimum-B coils to trap particles in tandem (called a *tandem mirror* device) is illustrated in Figure 14.11.

A design for a tandem mirror facility is shown in Figure 14.12. The actual operating parameters are similar to those of the tokamak. Auxiliary heating by rf waves and NBI are essential to raise the temperature of the plasma, as in the tokamak design.

Inertial confinement fusion takes a very different approach. A tiny pellet containing deuterium and tritium is suddenly struck with an intense laser pulse that both heats the pellet and compresses it to high density. The goal of this technique is to achieve densities and temperatures that are high enough that fusion can occur before the pellet simply expands and blows apart. In the design for a power plant based on this process, it is anticipated that many (10–100) pellets per second would be used, and the cycle of fuel injection, compression, ignition, and power stroke is somewhat similar in principle to the cycle of the internal combustion engine.

To make a crude estimate of the requirements for such a device, let's note that the time necessary for the compressed pellet to blow apart will be determined by the speed of propagation of mechanical waves in the medium, which will be of the same order as the mean thermal speed of the particles in the medium. (For an ordinary solid at room temperature, the mean thermal velocities are of the order of 10^3 m/s; the speed of mechanical waves, sound for instance, is of the same order.) At $kT \sim 10$ keV, the mean thermal speed is about 10^6 m/s. If we consider a pellet compressed to a diameter of 0.1–1 mm, it could be expected to blow apart in about 10^{-9}–10^{-10} s. Applying Lawson's criterion for a D-T mixture, if the confinement time were as short as 10^{-9}–10^{-10} s, we would need a

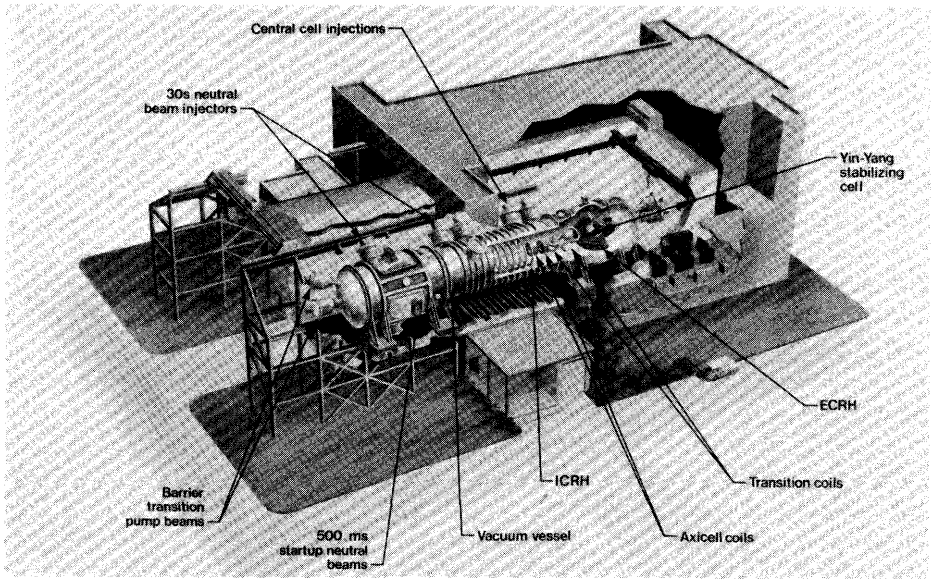


Figure 14.12 Design of Magnetic Fusion Test Facility (MFTF-B). The cutaway portion shows the mirror devices drawn in Figure 14.11. Courtesy Lawrence Livermore National Laboratory, University of California, and U.S. Department of Energy.

density of at least 10^{29}–$10^{30}/\text{m}^3$, which is two orders of magnitude greater than ordinary liquid or solid densities for hydrogen.

To heat a spherical pellet of diameter 1 mm to a mean thermal energy of 10 keV per particle, the total thermal energy that must be supplied is about

$$E_{\text{th}} \sim \tfrac{4}{3}\pi(0.5\text{ mm})^3 \times 10^{29}\text{ m}^{-3} \times 10^4\text{ eV} \approx 10^5\text{ J}$$

That is, we must supply an energy of the order of 10^5 J in about 10^{-9} s for a net power of 10^{14} W! Our estimate for the power that must be supplied is surely too low, for a large portion of the energy supplied to the pellet is sure to be absorbed in "boiling off" of surface particles, so we probably should increase by another order of magnitude the estimate of the total energy we must supply actually to heat and compress the core of the pellet. Furthermore, lasers are notoriously inefficient devices for converting electrical energy into radiation; 10% is probably the best that can be hoped for, but 1% is more typical. Therefore, the electrical power needed for the lasers may approach 10^{17} W. Fortunately, that power need be provided only for short intervals of time, but nevertheless the magnitude of 10^{17} W is a staggering number—compare it for instance with the entire electrical generating capacity of the United States, which is of the order of 10^{12} W!

To run an inertial confinement reactor at a net energy gain, it is apparent that we must exceed considerably the Lawson criterion. We should hope to achieve compressions perhaps approaching 1000 times ordinary density, and to operate well above 10 keV thermal energy per particle.

The sequence of processes in laser-driven fusion might be as follows: A pellet is injected into the machine and is simultaneously struck from many directions

by an intense laser pulse. The outer layer of the solid pellet is immediately vaporized and forms a plasma, which continues to absorb the laser radiation. The plasma itself is unconfined and it rapidly "blows off" or *ablates*, which (by Newton's third law) drives a compressional shock wave back into the remaining core of the pellet; this shock wave compresses and heats the core to the point at which thermonuclear ignition can occur at the highest density region near the center. The α particles resulting from the fusion rapidly lose their energy in collisions with ions in the dense fuel. This contributes additional heating, and the thermonuclear burn propagates outward, finally blowing the pellet apart and ending the reaction.

The requirements on lasers imposed by the break-even energy condition are severe, and certainly beyond the capability of present lasers. Particularly serious is the low efficiency (1–10%) for converting electrical energy into radiation. Therefore, alternative approaches to inertial confinement fusion are being explored using beams of charged particles instead of lasers. The particles must deposit their energy in a distance which is of the order of the radius of the pellet, thus contributing the maximum amount of the heating and shock wave. Taking a pellet of about 100 times solid density with a diameter of 0.1–1 mm, the range for the particles should be about 0.1 g/cm^2. From Figure 7.2 for protons in dense matter (take Pb, for example), a particle energy of 5 MeV is required. Adopting the previous estimate of 10^5 J as the thermal energy needed to heat the fuel, we

Table 14.1 Magnetic Confinement Fusion Devices

Size[a] (m)	B_{max} (T)	Device	Location	Type	Year	$n\tau$ (10^{20} s/m^3)	kT (keV)
1.3	3.5	PLT (Princeton Large Torus)	Princeton (USA)	Tokamak	1978	0.4	10
2.5	5.2	TFTR (Tokamak Fusion Test Reactor)	Princeton (USA)	Tokamak	1984	0.15	6
2.8	2.8	JET (Joint European Torus)	England	Tokamak	1983	0.5	5
0.64	12	Alcator-C	MIT (USA)	Tokamak	1983	0.8	1.7
3.0	5.0	JT-60	Japan	Tokamak	1986	0.2–0.6	5–10
2.4	3.5	T-20	USSR	Tokamak	1986	1.0	7–10
5	0.1	TMX (Tandem Mirror Experiment)	Livermore (USA)	Tandem mirror	1980	0.01	10
16	1.0	MFTF-B (Mirror Fusion Test Facility)	Livermore (USA)	Tandem mirror	1988	0.1	15

[a] For tokamaks, the size entry gives the major radius of the toroid; for the linear mirrors, the size indicates the length of the central chamber.

would require

$$10^5 \text{ J} \times \frac{1}{1.6 \times 10^{-19} \text{ J/eV}} \times \frac{1 \text{ proton}}{5 \times 10^6 \text{ eV}} \simeq 10^{17} \text{ proton}$$

in a pulse of 10^{-9} s duration; that is, we would need a current of the order of 20×10^6 A! Using electrons instead of protons, Figures 7.3 and 7.4 indicate an energy of about 0.5 MeV, and to obtain 10^{14} W we would need a current of 200×10^6 A. If we use beams of heavy ions (U, for instance), we can use Equation 7.6 to estimate that a range of 0.1 g/cm^2 for U would be equivalent to a range of protons of about 3 g/cm^2. Figure 7.2 does not show ranges as high as 3 g/cm^2, but we can extrapolate the line for heavy matter to obtain an energy of about 35 MeV for protons to have such a range, and since Equation 7.6 is based on a comparison of ranges of different particles with the same velocity, the energy of the U would be about $240 \times 35 = 8$ GeV. The necessary current would be about 10^4 A. Although the energies we have estimated for the beams of electrons, light ions (protons) and heavy ions (U) are all quite reasonable and well within present accelerator technology, the currents are far beyond present accelerators, which are limited to mA. Research therefore is now in progress to solve the beam transport and focusing problems that will arise at these high currents, and it is hoped that charged-particle beams will offer a reasonable alternative to lasers.

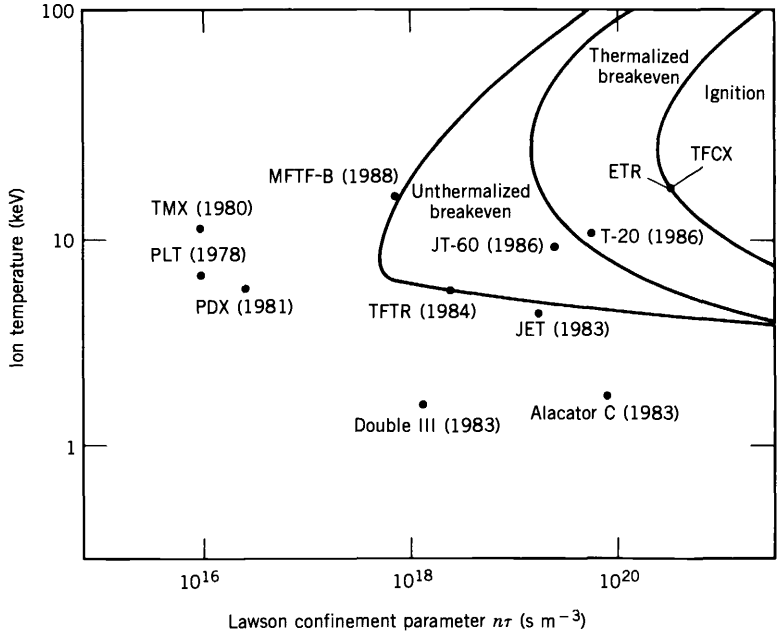


Figure 14.13 Approach to the Lawson criterion of various past and future magnetic confinement fusion devices. Some of these are listed in Table 14.1. The region of thermalized breakeven corresponds to exceeding the Lawson criterion; ignition indicates the region in which heat from fusion products will sustain the reaction. ETR (Engineering Test Reactor) and TFCX (Toroidal Fusion Core Experiment) are planned or proposed facilities.

As of this writing, there is a great deal of research and development activity throughout the world on the various aspects of controlled fusion we have briefly outlined. The entire area is extremely fast-moving, and new discoveries and achievements are rapidly announced. Rather than try to project into a very uncertain future, let's instead look at the steady progress that has been made up to now at approaching the Lawson criterion or providing the necessary ignition power. Table 14.1 lists some of the magnetic confinement devices that have been built and tested and some that are expected to become operational during the

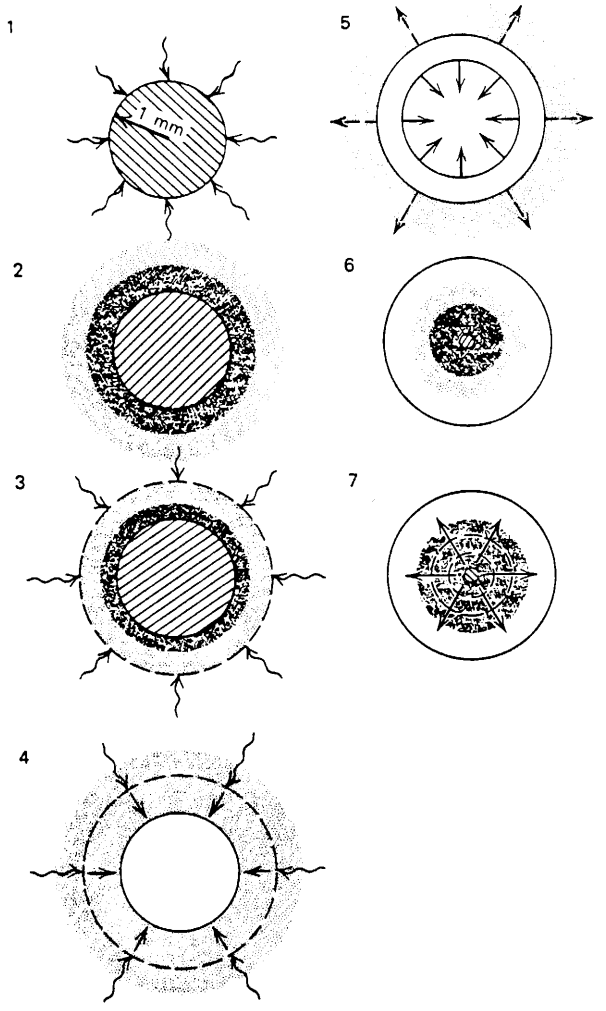


Figure 14.14 Sequence of stages in inertial confinement fusion: (1) irradiation of fuel pellet by lasers; (2) formation of plasma atmosphere; (3) additional laser beam absorption in atmosphere; (4) ablation and resulting imploding shock wave; (5) shock wave compressing core; (6) ignition of core; (7) burn propagating outward. From J. J. Duderstadt and G. A. Moses, *Inertial Confinement Fusion* (New York: Wiley, 1982).

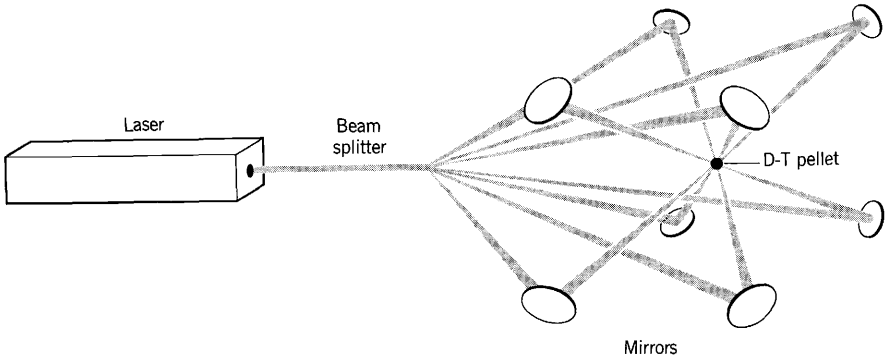


Figure 14.15 Irradiation of D-T pellet by multiple laser beams.

next several years. Figure 14.13 shows the steady march toward satisfying the Lawson criterion that has been made in the past decade.

By comparison, research in inertial confinement techniques has not made nearly as much progress, although the physics is perhaps better understood than in the case of magnetic confinement. The major technological difficulty has been in achieving the necessary laser power. Figure 14.14 shows the sequence of events that occur in the pellet, and Figure 14.15 shows a schematic diagram of how the pellet might be exposed to the laser radiation.

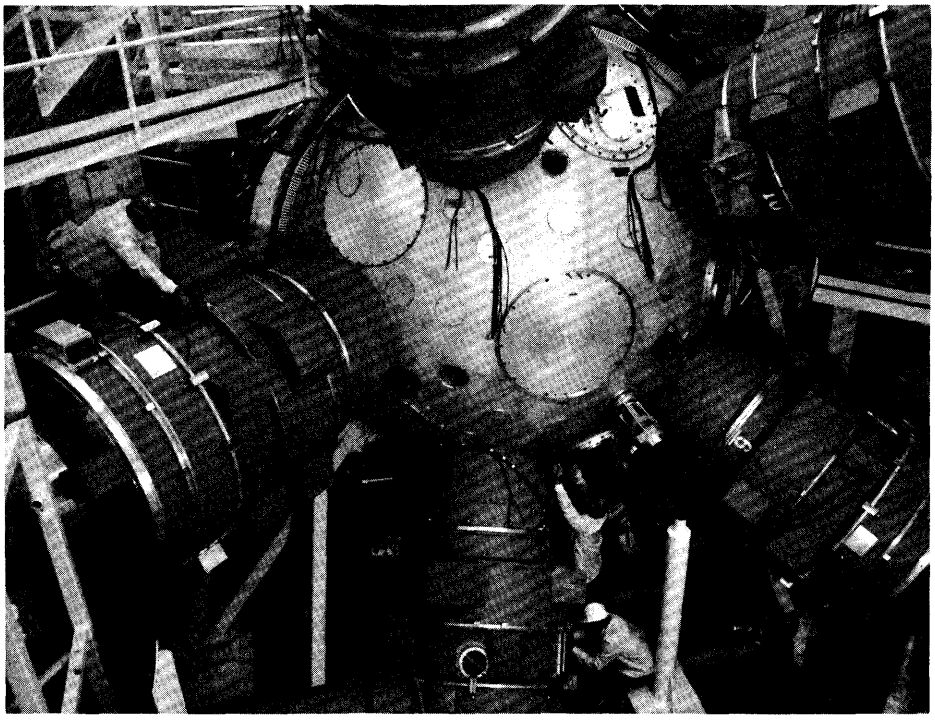


Figure 14.16 The Nova inertial confinement fusion facility of the Lawrence Livermore Laboratory. The photo shows the target chamber and 5 of the 10 laser beam tubes. Courtesy Lawrence Livermore National Laboratory, University of California, and U.S. Department of Energy.

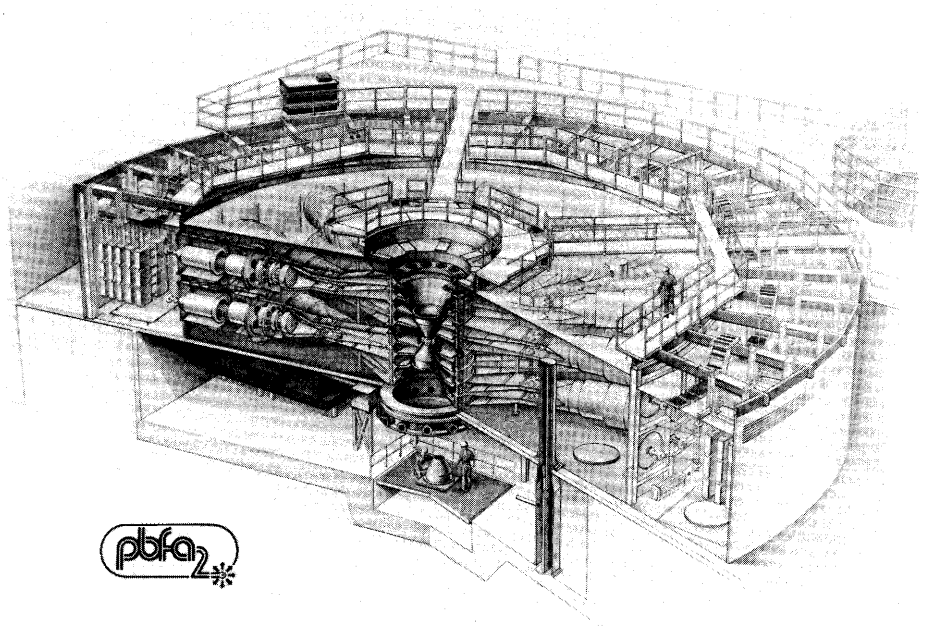


Figure 14.17 Particle beam fusion accelerator. Thirty-six beams of lithium ions are focused on a D-T target, in a pulse of 10^{14} W of duration 20 ns. Because the efficiency of absorption of the beam's energy is nearly 100%, this device may be able to achieve ignition of the D-T fuel. Drawing courtesy Sandia National Laboratory.

At the Lawrence Livermore Laboratory in California, the Nova laser (Figure 14.16) provides 10 beams to strike the target. The laser itself is based on Nd, in which the primary lasing transition is 1060 nm, in the infrared region. Absorption of the laser light is enhanced by going to shorter wavelengths, so the lasing medium incorporates a crystal of potassium dihydrogen phosphate (KDP), which acts as a nonlinear optical medium and produces higher harmonics ($\lambda/2$, $\lambda/3$, $\lambda/4, \ldots$) of the incident light. There is a particularly high efficiency for converting to the first harmonic at 530 nm. The Nova system is expected to produce 100-kJ nanosecond pulses, for a power of order 100 TW.

Valuable basic research has been and will be done with the Nd laser systems, but they are not suitable for practical fusion devices because the Nd glass must cool for about one hour after a laser pulse (thus repetition rates of 10–100/s are impossible) and the lasers themselves are quite inefficient, about 0.1%. Research is presently underway to study the use of CO_2 gas lasers, which permit high repetition rates and high laser efficiency ($\sim$ 10%). A disadvantage is the long wavelength (10.6 μm), where absorption by the pellet's plasma surface layer to create ablation is less efficient.

A particle-beam test device is illustrated in Figure 14.17. Thirty-six individual light-ion (or electron) accelerators are arranged around the pellet injection region. The latest development of this device will focus beams of 100 TW on the pellet, with about 4 MJ of ion energy in a 35-ns pulse. The time necessary for charging

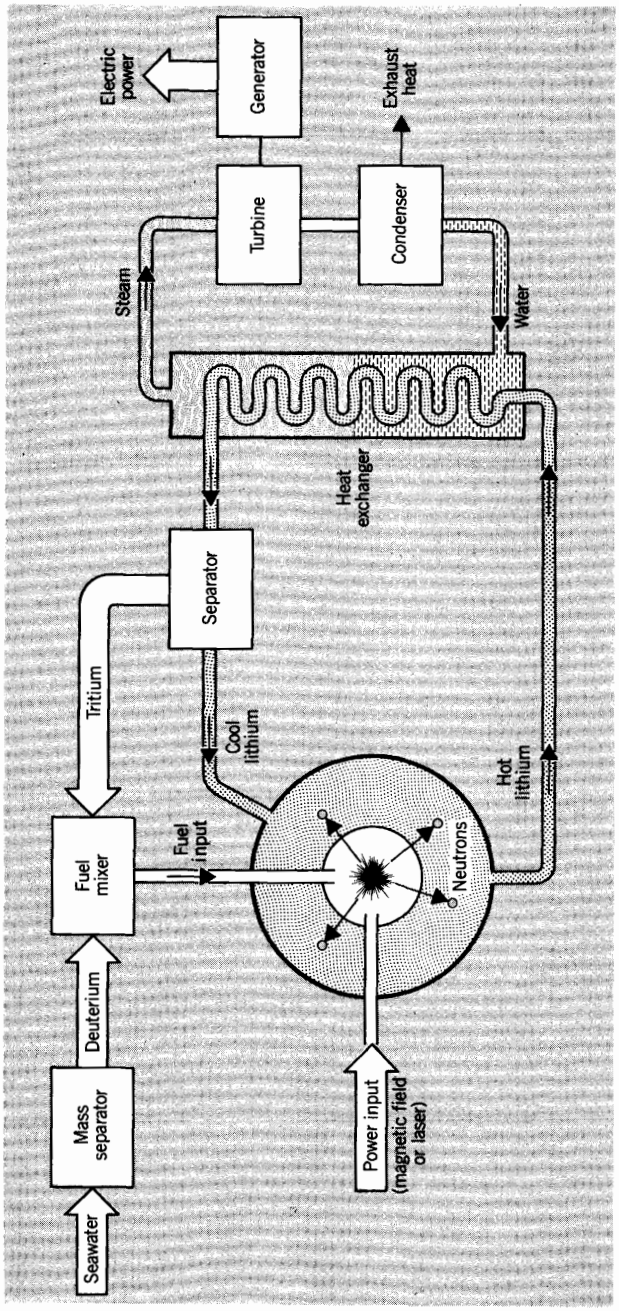


Figure 14.18 Design for a fusion power plant.

the enormous capacitative energy storage devices may limit the repetition rate of this system.

This introduction to controlled fusion devices is by no means complete but it represents a realistic summary of the state of the art as of late 1986. Research is taking place simultaneously on many fronts, and while many magnetic confinement and inertial confinement devices are well within the last order of magnitude (or even factor of 2) of exceeding the Lawson criterion, there is as yet no single leading candidate for the basic design of a controlled fusion reactor. Despite the many technological problems, progress in the last decade has been considerable, and it is not overly optimistic to extrapolate to the break-even point within the next decade or two.

A proposed design for a fusion power reactor is shown in Figure 14.18. The D-T reaction gives a neutron and an α particle, which deposits its energy within the fuel and contributes to the heating of the D-T mixture. The neutron carries 80% of the energy (14.1 MeV) and can be captured by a blanket of lithium through the reactions $^6\text{Li} + \text{n} \rightarrow {}^4\text{He} + {}^3\text{H}$ or $^7\text{Li} + \text{n} \rightarrow {}^4\text{He} + {}^3\text{H} + \text{n}$. The energetic ^{4}He and ^{3}H then deposit their energy in the lithium as heat. The hot liquid lithium then drives a steam generator which is used to run a turbine. The ^{3}H is extracted to produce fuel for the reactor.

14.5 THERMONUCLEAR WEAPONS

Once the first thermonuclear explosives were detonated by the United States and the USSR in the early 1950s, the fission explosives in the strategic arsenals of both nations were soon replaced with thermonuclear weapons of explosive energy 2–3 orders of magnitude greater than the early fission weapons. The kiloton-range explosives that devastated Hiroshima and Nagasaki have given way to megaton explosives. It gives but small comfort to note that the effective destructive capability of a weapon increases only as the square or cube root of its explosive energy.

Most of the details of the construction of thermonuclear weapons are classified, but enough is publicly known that we may make some general observations about their operation. As a starting point, all of the previous discussions regarding the ignition temperature of fusable fuel remain valid, and the only rapid and mobile source capable of achieving such temperatures is a nuclear explosion. Thus a fusion weapon includes a fission explosive as an initiator. The radiation from the fission explosion is responsible for heating and compressing the thermonuclear fuel.

The first thermonuclear explosive used a liquified fuel mixture, which required a cumbersome refrigeration apparatus to achieve and maintain the low temperatures necessary to liquify hydrogen. Present-day weapons use solid lithium deuteride as fuel, made with separated isotope ^{6}Li. The neutrons released from the primary fission explosion (and the subsequent fusions) convert the ^{6}Li into tritium:

$$^6\text{Li} + \text{n} \rightarrow {}^3\text{H} + {}^4\text{He} \qquad (Q = 4.78 \text{ MeV})$$

Even for low-energy neutrons, the tritium carries enough energy (2.7 MeV) to penetrate easily the D-T Coulomb barrier and initiate the fusion reactions.

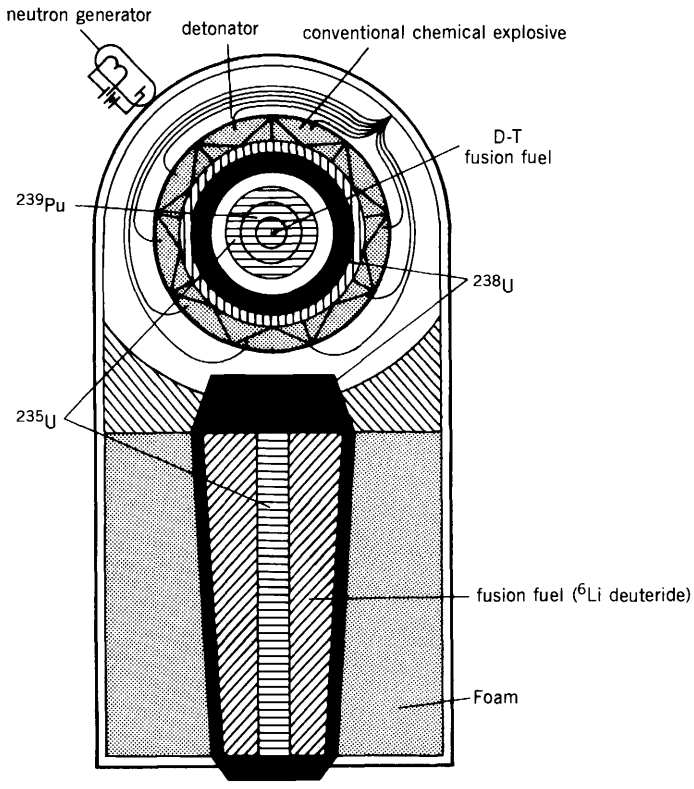


Figure 14.19 Schematic diagram of thermonuclear explosive. The detonation of the chemical explosive compresses a ^{238}U shell about ^{235}U and ^{239}Pu, driving them into criticality and initiating a fission explosion. The fission reaction is "boosted" by a small amount of D-T fuel at the center of the sphere; D-T fusion provides additional neutrons for the fission explosion. The X rays and γ rays from the fission explosion vaporize the polystyrene foam which compresses the ^{238}U tamper about the main fusion fuel and also heats the fusion fuel to its ignition temperature, beginning the thermonuclear reaction. The fast neutrons released in the fusion reactions cause fissions in ^{235}U and ^{238}U, increasing the total yield of the weapon. The diagram and description are from an article by Howard Morland published in the November 1979 issue of *The Progressive*; a more complete version can be found in H. Morland, *The Secret That Exploded* (New York: Random House, 1981).

Somewhat similar to the inertial confinement technique of controlled fusion, the heat, neutrons, and α particles contribute to sustaining the reaction until the expansion of the fuel terminates the reaction.

The fast neutrons released in the fusion can be used to add additional energy to the explosive by surrounding the fusion fuel with a casing of ^{238}U, which fissions with fast neutrons. The operation and energy release in a thermonuclear weapon are thus dependent on a fission-fusion-fission cycle. About half the yield of a typical strategic weapon may come from the final fission processes.

A highly schematic diagram of a thermonuclear weapon is shown in Figure 14.19 and from the photograph of an actual weapon housing shown in Figure 14.20 it is not difficult to infer the relative size and placement of the components.

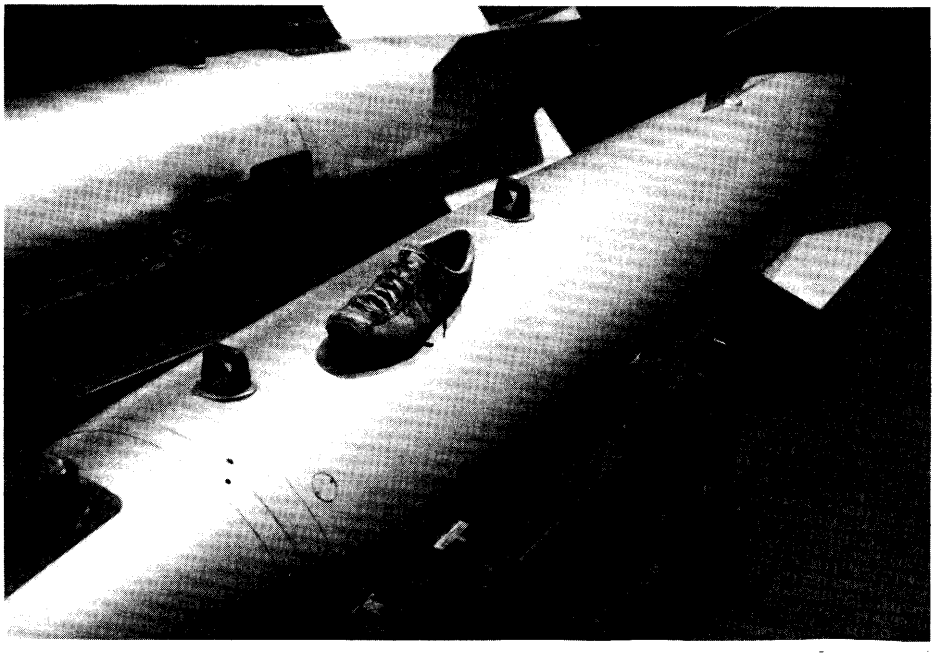


Figure 14.20 The casing of a thermonuclear weapon. From H. Morland, *The Secret That Exploded* (New York: Random House, 1981).

The destructive effects of a 1–10-megaton thermonuclear weapon can be anticipated from the discussion of fission weapons in Chapter 13. The radius within which there would be virtually complete destruction by blast effects and firestorm varies roughly as the cube root of the weapon yield, and is thus an order of magnitude beyond the 1 km distance characteristic of a typical fission weapon. Over a radius of perhaps 10 km, a single weapon produces essentially complete destruction.

Reducing the fission yields (by eliminating the ^{238}U casing) eliminates most of the radioactive fission products from the debris of the explosion and creates a relatively "clean" explosion, that is, free of the long-term effects of fallout and surface radioactivity associated with fission products. Because the yield of an explosion is the primary goal of a strategic weapon, it is believed that most of the strategic weapons in the U.S. arsenal are "dirty" weapons of the fission-fusion-fission variety.

There are also relatively low-yield battlefield nuclear explosives, of the tactical category. Among these is the enhanced-radiation or neutron weapon. By eliminating the ^{238}U casing, these small weapons (in the kiloton range) produce an intense burst of neutrons, the object of which is to deliver a lethal dose of radiation to an army advancing in armored vehicles, such as tanks. It is estimated that a 1-kiloton neutron bomb will subject personnel shielded by armor plate to a radiation dose of about 10^3 rads over a radius of 1 km. Such a dose will cause death within days. The enhanced radiation weapons were designed to penetrate armor and thus halt an advancing army, particularly one that is invading in the defender's home territory (in which case minimizing blast damage is highly

desirable; the use of megaton explosives would destroy the country in order to save it).

The effects of fusion weapons on population and structures are similar to those of fission weapons, discussed in Section 13.9, with appropriate scale factors introduced to account for differences in explosive yields. One additional effect not considered in Chapter 13 is the electromagnetic pulse (EMP). The prompt γ rays and X rays released in the explosion interact with air molecules (through Compton scattering and ionization) to create a large current of negative electrons flowing outward from the point of the explosion. These electrons are accelerated by the Earth's magnetic field and give rise to a traveling electromagnetic wave in the form of a pulse. An explosion several hundred kilometers above the center of the United States would be within the line of sight of the entire United States and would expose the country to electric fields of the order of 10^4 V/m for a 1-megaton blast. Such a pulse could be destructive of electrical power networks and communications grids necessary for decisive action in time of war.

The scenario of an all-out nuclear war is thus particularly horrible—perhaps 1000 or more strategic warheads in the megaton range explode within a few minutes over the entire United States. Perhaps 50% of the U.S. population would die in such an attack, from the combination of blast, heat, fire, and radiation. Blast damage and firestorms would lay waste to most cities, and EMP effects would destroy electrical power and communication facilities. The remaining population would have to contend with the long-term effects of fallout and with the disease and starvation that are likely to follow from the general destruction. Recent calculations indicate that the dust and smoke created from a general exchange of nuclear weapons will circulate throughout the atmosphere, blocking enough sunlight that agriculture would become impossible and major climate changes would bring about a perpetual "nuclear winter." Surely all petty disagreements among nations must become insignificant when measured against such outcomes of a general nuclear war.

The present strategic arsenal of the United States includes 1000 Minuteman land-based intercontinental ballistic missiles (ICBMs), approximately half of which carry a single warhead (1.5 megatons) and half of which carry three multiple independently targeted re-entry vehicles (MIRVs) with a total yield of 0.5–1 megaton; 33 Poseidon and Trident submarines, each with 16 or 24 missiles having 8 or 10 MIRV warheads of about 50–100 kilotons each; and 332 B-52 bombers, each carrying at least four warheads of 1 megaton each. The total number of strategic warheads in the U.S. arsenal is 2152 in ICBMs (1572 megatons), 4960 in submarine-launched ballistic missiles (344 megatons), and 2698 in bombers, some equipped with air-launched missiles (1621 megatons); the totals are 9810 warheads (3537 megatons). Equivalent totals for the Soviet Union are 7741 warheads (6618 megatons). An additional 10,000–20,000 small (kiloton range) tactical weapons are also held by each side. The total megatonnage is thus of order 10,000!

Let's attempt to put this staggering figure in perspective. The total explosive energy is of the order of 10^{10} tons of TNT; the population of the Earth is of order 5×10^9, and thus we are each allotted a share of about 2 tons of TNT, roughly a cubic meter. Every person on Earth is thus living precariously with his or her personal cubic meter of high explosive. It is apparent to any reasonable

thinker that this silly overkill capability compromises everyone's security, and the only sensible course is a reduction in the number of weapons and control of their proliferation. Achieving this reduction is a major challenge facing both physicists and politicians in the next decade.

REFERENCES FOR ADDITIONAL READING

Among the references for the basic physics of fusion processes are those that deal also with the technology of controlled fusion and the design of fusion reactors: S. Glasstone and R. H. Lovberg, *Controlled Thermonuclear Reactions* (Princeton, NJ: Van Nostrand, 1960); W. M. Stacey, Jr., *Fusion: An Introduction to the Physics and Technology of Magnetic Confinement Fusion* (New York: Wiley, 1984); H. Motz, *The Physics of Laser Fusion* (London: Academic, 1979); J. J. Duderstadt and G. A. Moses, *Inertial Confinement Fusion* (New York: Wiley, 1982); M. O. Hagler and M. Kristiansen, *An Introduction to Controlled Thermonuclear Fusion* (Lexington, MA: Heath, 1977); *Fusion*, edited by Edward Teller (New York: Academic, 1981).

For reviews of fusion reactor research, see: F. L. Ribe, *Rev. Mod. Phys.* **47**, 7 (1975); R. F. Post, *Ann. Rev. Nucl. Sci.* **20**, 509 (1970); D. Keefe, *Ann. Rev. Nucl. Part. Sci.* **32**, 391 (1982); K. I. Thomassen, *Ann. Rev. Energy* **9**, 281 (1984).

An interesting nontechnical description of the social and political background of the controlled fusion research program is Joan Lisa Bromberg, *Fusion: Science, Politics, and the Invention of a New Energy Source* (Cambridge, MA: MIT Press, 1982).

Several general popular-level articles on controlled fusion have appeared in *Scientific American*: B. Coppi and J. Rem, "The Tokamak Approach in Fusion Research" (July 1972); J. L. Emmett, J. Nuckolls, and L. Wood, "Fusion Power by Laser Implosion" (June 1974); W. C. Gough and B. J. Eastland, "The Prospects of Fusion Power" (February 1971); M. J. Lubin and A. P. Fraas, "Fusion by Laser" (June 1971); Harold P. Furth, "Progress Toward a Tokamak Fusion Reactor" (August 1979); R. W. Conn, "The Engineering of Magnetic Fusion Reactors" (October 1983); R. S. Craxton, R. L. McCrory, and John M. Soures, "Progress in Laser Fusion" (August 1986).

References to work on fusion in stars will be presented in Chapter 19.

In contrast to the considerable body of literature on the technology of fission weapons, there is little published on fusion weapons. Perhaps the best-known work, at least in terms of the publicity it generated, is: Howard Morland, *The Secret That Exploded* (New York: Random House, 1981). There is much more written about the effects of nuclear weapons and about the political issues that relate to the reduction of weapon inventories. A summary of the entire literature in this area can be found in the resource letter "Physics and the Nuclear Arms Race," by D. Schroeer and J. Dowling, *Am. J. Phys.* **50**, 786 (1982). The American Association of Physics Teachers has published a collection of reprints, including the above resource letter and Morland's original article, in *Physics and the Nuclear Arms Race: Selected Reprints* (1984). Particularly worthwhile for its technical detail (and included in the above collection) is H. L. Brode, *Ann. Rev.*

Nucl. Sci. **18**, 153 (1968). More recent work includes: the entire March 1983 issue of *Physics Today*, which features articles on the effects of nuclear weapons and descriptions of present arsenals; A. A. Broyles, *Am. J. Phys.* **50**, 586 (1982); D. Schroeer, *Science, Technology, and the Nuclear Arms Race* (New York: Wiley, 1984), a well-written and comprehensive (but introductory) work treating weapon technologies, delivery systems, strategies, and arms control; and *Physics, Technology and the Nuclear Arms Race*, edited by D. W. Hafemeister and D. Schroeer (New York: American Institute of Physics, 1983), a collection of articles by experts in the areas of the technology, strategy, and politics of nuclear weapons.

PROBLEMS

1. Calculate (1) the temperature necessary to overcome the Coulomb barrier and (2) the fusion energy release in a gas of: (a) ^{16}O; (b) ^{12}C; (c) ^{24}Mg; (d) ^{14}N; (e) ^{10}B.
2. (a) Compute the Q values for the basic D-D reactions: $^2H + {}^2H \rightarrow {}^3He + n$ and $^2H + {}^2H \rightarrow {}^3H + p$. (b) Assuming the incident particle kinetic energies to be negligible, find the energies of the outgoing particles in both reactions.
3. (a) Calculate the ratio of the D-D fusion cross sections at 100 and 20 keV from Equation 14.7 and show that it agrees with Figure 14.1. (b) Do the same for the D-T cross section.
4. (a) Estimate the shaded areas in Figure 14.2 and show that they are consistent with the D-D curve of Figure 14.3. (b) Extend the calculation upward to 100 keV and downward to 1 keV; again compare with Figure 14.3. (Duplicate the 5 and 20 keV calculations as well, so that your calculation can be normalized against that of Figure 14.2.) Remember that for D-D reactions, $E = 2E_D$; also remember that $n(E)$ includes a $T^{-3/2}$ dependence that must be included before comparisons can be made of results at different temperatures.
5. By calculating the energy released in each of the six reactions of the carbon cycle, show that the total energy release is 26.7 MeV.
6. In analogy with the carbon cycle, fusion of hydrogen to helium can occur with ^{20}Ne as a catalyst. Suggest a sequence of reactions, similar to the carbon cycle, in which this could occur. Calculate the energy release from each reaction and evaluate the total energy release. (*Hint*: Two successive proton captures must occur in the carbon cycle, because ^{14}N is stable and does not β decay. This will not necessarily happen in the neon-based cycle.)
7. Calculate the threshold for neutrino capture by ^{37}Cl. Which of the reactions of the proton-proton cycle can produce neutrinos above this threshold? Does the carbon cycle produce detectable neutrinos?
8. Making (and justifying) any necessary assumptions about conversion efficiencies, estimate the number of D-T pellets that must be irradiated each second to operate a 1000-MW generating plant.

15

ACCELERATORS

The purpose of an accelerator of charged particles is to direct against a target a beam of a specific kind of particles of a chosen energy. There are many varieties of methods for accomplishing this task, all using various arrangements of electric and magnetic fields, and in this chapter we review the general features of some of the more common types of accelerators.

As an electronic device, the accelerator shares many features in common with an ordinary television picture tube. Both require a source of charged particles (electrons from a hot filament or ionized atoms from an ion source), an electric field to accelerate the particles (10^4 V in a TV tube and perhaps 10^7 V in some accelerators), focusing elements to counteract the natural tendency of the beam to diverge, deflectors to aim the beam in the desired direction, a target of selected material for the beam to strike, and a chamber to house all the components in high vacuum to prevent the beam from scattering in collisions with molecules in the air.

The design of accelerators varies greatly with the purpose for which they will be used. In some cases high energy is desired, and in other cases high intensity. Accelerators for electrons (which become relativistic at reasonably low voltages and which have long ranges in matter) differ greatly from those for heavy ions (which are generally nonrelativistic and have extremely short ranges in matter). As a practical problem, the short range of heavy ions means that the entire accelerator must be one continuous vacuum for heavy ions cannot cleanly penetrate even the thinnest "window" that would separate one vacuum chamber from another.

We can somewhat loosely classify accelerators as low, medium, or high energy. Low-energy accelerators are used to produce beams in the 10–100-MeV range, often for reaction or scattering studies to elucidate the structure of specific final states, perhaps even individual excited states. Such accelerators should have accurate energy selection and should have reasonably high currents because the ultimate precision of many experiments is limited by counting statistics. The heating of targets by intense beams can be considerable, and often targets must be cooled to prevent the heat from destroying the target.

Medium-energy accelerators operate in the range of roughly 100–1000 MeV. At these energies, collisions of nucleons with nuclei can release π mesons, and so these accelerators are often used to study the role of meson exchange in the

6. Analyze the following decays or reactions for possible violations of the basic conservation laws. In each case state which conservation laws, if any, are violated and through which interaction the process will most likely proceed (if at all):

 (a) $\pi^+ + p \rightarrow p + p + \bar{n}$
 (b) $\Sigma^+ \rightarrow n + e^+ + \nu_e$
 (c) $K^+ \rightarrow \pi^+ + e^+ + e^-$
 (d) $\pi^- + p \rightarrow \Lambda^0 + \Sigma^0$
 (e) $K^+ \rightarrow \pi^+ + \pi^+ + \pi^0 + \pi^-$
 (f) $K^+ \rightarrow \pi^+ + e^+ + \mu^-$
 (g) $\Lambda^0 + p \rightarrow \Sigma^+ + n$
 (h) $\Lambda^0 \rightarrow p + K^-$

7. Analyze the following decays according to their quark content:

 (a) $\Omega^- \rightarrow \Lambda^0 + K^-$
 (b) $K^+ \rightarrow \pi^+ + \pi^0$
 (c) $\Xi^- \rightarrow \Lambda^0 + \pi^-$
 (d) $\Lambda_c^+ \rightarrow p + \overline{K}^0$

8. Analyze the following reactions according to their quark content:

 (a) $K^- + p \rightarrow \Omega^- + K^+ + K^0$
 (b) $p + p \rightarrow p + \pi^+ + \Lambda^0 + K^0$
 (c) $K^- + p \rightarrow \Xi^- + K^+$
 (d) $\pi^- + n \rightarrow \Delta^- + \pi^0$

19

NUCLEAR ASTROPHYSICS

To nuclear and particle physicists, the early universe represents the ultimate particle accelerator, in which energies and densities of particles were beyond what we can ever hope to achieve with artificially constructed accelerators. Reactions occurred with rates and varieties almost incomprehensible, but (perhaps surprisingly) by studying the end products of those reactions, we can infer many details of the reaction processes that cannot be measured on Earth. Essential to the understanding of these evolutionary reactions are known details (cross sections, etc.) of reactions that *can* be measured in our laboratories. What is now called the *standard model* of the hot Big Bang cosmology includes an overall framework based on the General Theory of Relativity, nuclear and particle properties directly measured, inferences from the standard model of elementary particles discussed in Chapter 18, and some extrapolations based on reasonable hypotheses. The input data must yield results in agreement with observations, the primary ones being the relative amounts of various light isotopes produced during the earliest epoch of element formation. The observed abundances can then put severe constraints on the fundamental processes that occurred during the formation epoch.

A much more difficult task is to understand the formation of the heavier elements following fusion reactions and neutron captures in stellar interiors. Not only is the nuclear physics more complicated (and the reactions more difficult to duplicate in the laboratory), but the mechanics and thermodynamics are less well understood. Here the observational evidence consists primarily of astronomical observations, not only with conventional optical telescopes, but more recently with particle and γ-ray spectrometers carried in orbiting spacecraft. In this case also, nuclear decays and reactions observed in Earth-bound laboratories can determine fundamental limits on the nature and especially the duration of nuclear reactions in stars.

The evolution of the universe can, from our Earthly perspective, be divided into four stages: primordial nucleosynthesis and atomic formation, galactic condensation, stellar nucleosynthesis, and evolution of the Solar System. What we call the age of the universe is merely the sum of the durations of these four sequential periods. The first stage lasts from the Big Bang ($t = 0$) to the formation of stable atomic hydrogen and helium (plus a very small concentration of other products). Although there are many uncertainties about this era (result-

ing from uncertainties in our knowledge of fundamental nuclear and particle properties), they have very little effect on estimates of the duration of this era, and moreover its duration is so small (about 10^6 years) that uncertainties are relatively unimportant. Galactic condensation occurs under the influence of gravitational forces alone, and nuclear and particle physics have no influence on this epoch, which has been estimated to last from 1 to 2 Gy (gigayear = 10^9 y). The era of stellar nucleosynthesis contributes the greatest uncertainty, perhaps ± 2 Gy, but we will see how recent nuclear reaction studies have given results for this era in excellent agreement with independent astronometric deductions. Finally, the duration of the evolution of the Solar System is well known, with little uncertainty.

19.1 THE HOT BIG BANG COSMOLOGY

One of the most significant discoveries of twentieth-century physics is the expansion of the universe. This deduction was made by Edwin Hubble following many observations of the absorption line spectra of distant galaxies. Hubble discovered that the spectra are red-shifted; that is, the absorption lines appear closer to the long-wavelength (red) end of the visible spectrum than they do when emitted by terrestrial sources. This red shift is similar to the Doppler shift of electromagnetic radiation, and from the degree of the red shift Hubble was able to deduce the velocities of recession of the galaxies relative to Earth. From independent observations, he knew the distance to the galaxy, and he observed that there was a linear relationship between the distance d and the speed of recession v:

$$v = Hd \tag{19.1}$$

where H is called the Hubble parameter. Figure 19.1 illustrates the linear Hubble relationship. The present best value of the Hubble parameter is about

$$H = 67 \frac{\text{km/s}}{\text{Mpc}}$$

where one megaparsec (Mpc) is 3.26×10^6 light years. The uncertainty in this value is large; the permitted range is about 50–100 km/s/Mpc.

According to the present model, this expansion is a general property of the universe, but one that is likely to vary with time, owing to the effect of gravity. The recession of the galaxies is a result of the general expansion of the universe, but if the universe is infinite we cannot define a radius. Instead, we define a *scale factor* $R(t)$, which gives the time dependence of any typical length. The distance between galaxies, for instance, increases in proportion to the increase of the scale factor. In terms of the scale factor, the Hubble parameter can be written as

$$H = \frac{1}{R}\frac{dR}{dt} \tag{19.2}$$

If the universe is expanding at a constant rate, then H is a constant, but the mutual gravitational attraction of the galaxies means that the recessional speed will decrease, in which case H is a function of the time.

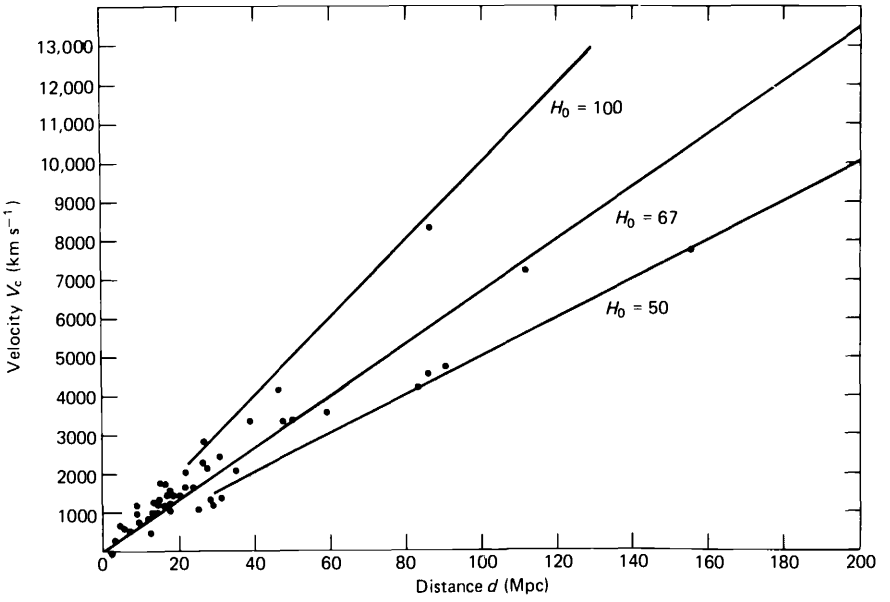


Figure 19.1 Velocity-distance relationship for groups and clusters of galaxies. The straight line demonstrates the Hubble relationship. From M. Rowan-Robinson, *The Cosmological Distance Ladder* (New York: Freeman, 1985).

As in the case of any mechanical system, the time evolution of the behavior can be obtained by solving the dynamical equations, in this case the tensor equations of the General Theory of Relativity. The mechanics of the theory are beyond the level of this text, but the result can be expressed in simple form:

$$H^2 = \frac{(dR/dt)^2}{R^2} = \frac{8\pi G}{3}\rho(t) - \frac{kc^2}{R^2} + \frac{\Lambda}{3} \tag{19.3}$$

where G is the gravitational constant of Newton (6.67×10^{-11} N · m^2/kg^2) and $\rho(t)$ is the mean mass + energy density of the universe. The geometrical factor k is determined by the fundamental geometry of space-time: $k = 0$ for a "flat" universe, in which the laws of geometry are Euclidian; $k = +1$ for a closed, spherical universe (corresponding to positive curvature); $k = -1$ for a curved universe with a shape analogous to a saddle. The cosmological constant Λ is assumed to vanish for the present discussion.

If the expansion had been at a constant rate dR/dt since $t = 0$, then the distance and recession velocity of Equation 19.1 would be connected by $d = vt$, where t is the age of the universe. Thus $t = H^{-1} = 15$ Gy, with an uncertainty of about ± 5 Gy. This is of course an upper limit on the true age of the universe, for we are deducing the Hubble parameter by observing galaxies that have already slowed from their original recession speed. In the past, H would have had a larger value, leading to a shorter deduced age. Figure 19.2 shows how the dependence of various scale factors on time leads to ages of the universe that are less than H^{-1}.

In these calculations, the age of the universe is operationally defined as the time since $R = 0$; that is, the expansion of the universe suggests that if we look

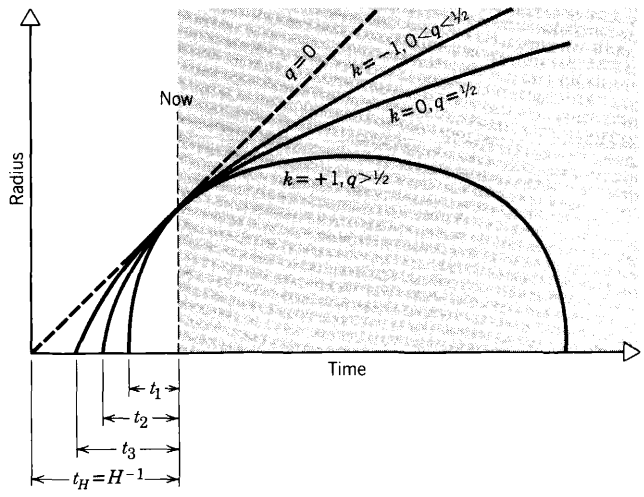


Figure 19.2 The dependence of the radius or scale factor of the universe on the time for various types of universes: $q = 0$, a universe with a constant rate of expansion; $k = -1$, an open, curved universe; $k = 0$, an open, flat universe; $k = +1$, a closed universe which expands and then contracts. The dimensionless deceleration parameter q is defined as $-R(d^2R/dt^2)/(dR/dt)^2$ and is a measure of the effect of gravitational interactions in slowing (or even reversing) the expansion.

far enough back into time, we find the galaxies so close together that they occupy a state of enormous energy and matter density. Extrapolating further back to $t = 0$, we come to a mathematical singularity, the Big Bang.

Before we examine the state of the universe just after the Big Bang, we should look at the form of solutions to Equation 19.3. We assume $k = 0$, allowing us to neglect what is basically an uninteresting term in the equation. Following the Big Bang, the universe was dominated by radiation (or by matter moving at such high speed that the radiation-like relationship $E = pc = hc/\lambda$ was obeyed), and the radiant energy density ρ_R is

$$\rho_R = \frac{\text{energy}}{\text{volume}} = \text{energy per quantum} \times \text{quanta per volume}$$
$$\propto \frac{1}{R} \times \frac{1}{R^3}$$

where the R^{-1} factor comes from the λ^{-1} factor in the energy quantum and the R^{-3} factor comes from the volume. We can thus take $\rho_R = C/R^4$ (the constant C will disappear) and Equation 19.3 becomes

$$\frac{1}{R}\frac{dR}{dt} = \sqrt{\frac{8\pi GC}{3}}\frac{1}{R^2} \tag{19.4}$$

which integrates to give

$$t = \sqrt{\frac{3}{32\pi G\rho_R}} \tag{19.5}$$

If we base ρ_R on the energy density $u(T)$ of blackbody radiation for a radiating system at temperature T:

$$u(T) = \sigma T^4 \tag{19.6}$$

where σ is the Stefan-Boltzmann constant, then we have an important fundamental relationship between age t (in seconds) and temperature T (in kelvins) during the radiation-dominated era:

$$T = \frac{1.5 \times 10^{10}}{t^{1/2}} \tag{19.7}$$

The temperature is an important parameter to describe the early universe. If the temperature is high enough, matter and radiation are in equilibrium, and particle-antiparticle creation occurs as often as annihilation; in the case of electrons, for example

$$e^+ + e^- \leftrightarrow 2\gamma$$

For $2\gamma \rightarrow e^+ + e^-$ to occur, the radiant photons must have an energy of at least 0.511 MeV; if on the average the photons have an energy of kT (here k is the Boltzmann constant of thermodynamics), the energy corresponds to a temperature of $T = 6 \times 10^9$ K. That is, when $T \lesssim 6 \times 10^9$ K (corresponding to $t > 6$ s), the radiation field is no longer energetic enough to balance $e^+ + e^- \rightarrow 2\gamma$ reactions with $2\gamma \rightarrow e^+ + e^-$, and the former reaction begins to dominate.

This is then the overall scheme of the Big Bang cosmology: The present universe is created from a space-time singularity at essentially infinite temperature and density. It consists of a mixture of the most fundamental particles and their antiparticles plus radiation. As the universe expands and cools, each species of particles in turn goes out of equilibrium with the radiation. We observe today the relics of the particle interactions plus the residual radiation which has had negligible interactions with matter since the final decoupling within the first 10^6 y.

The experimental discovery which, along with Hubble's expansion, provided dramatic confirmation of the Big Bang theory was the universal microwave background radiation, immediately associated with the residual radiation from the Big Bang. The original discovery was made by Arno Penzias and Robert Wilson in 1964. They were attempting to use a radio receiver, tuned to 7.35 cm wavelength, which had been built for contact with an early communications satellite. In the process, they observed a background "noise" that, despite their best efforts, could not be eliminated from the system. They finally identified the noise as a real signal, and discovered that it came uniformly from all directions and at all times of day and night. By measuring the energy density of the radiation at $\lambda = 7.35$ cm, they were able to deduce the blackbody temperature of 3.1 ± 1.0 K. Other measurements subsequently made at different wavelengths demonstrate that the radiation does indeed have the expected blackbody spectrum (Figure 19.3); the present best temperature is 2.7 ± 0.1 K.

The essential features of the Big Bang cosmology are thus confirmed, but many details remain to be filled in. The exact mechanism that triggers galaxy condensation from what must have originated as a homogeneous mixture of particles is not yet clear, nor is the mechanism that guarantees that opposite sides of our

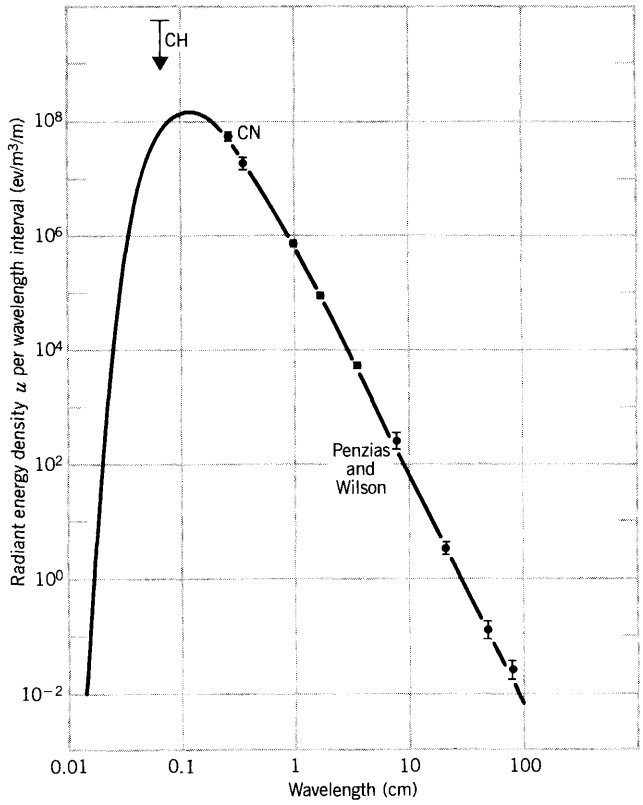


Figure 19.3 The wavelength spectrum of the cosmic microwave background radiation. The dots are data points and the solid curve is a blackbody spectrum for $T = 2.7$ K.

observable universe, though not causally connected (i.e., a light beam could not have traveled from one end to the other within their present age), appear to have similar properties. Exotic particles may have been available at the large energies and densities of the early universe and may have played an important role; on the other hand, the list of particles generated in Chapter 18 may be nearly complete, as some high-energy physicists suspect, leaving no place for exotics.

19.2 PARTICLE AND NUCLEAR INTERACTIONS IN THE EARLY UNIVERSE

Although we do not yet understand how to extrapolate back to the earliest instants after the Big Bang, many of the fine details of the structure of the universe in that era are irrelevant for the particular part of the story in which we are interested.

For example, we consider the times around $t = 10^{-12}$ s. At that point the temperature is, from Equation 19.7, about 10^{16} K, corresponding to a mean energy quantum kT of 1000 GeV. With the possible exception of free quarks, whose masses we do not know (and which may not be permitted to exist in a free state), all known particles can be readily created at this energy. All species of

particles must exist in equilibrium concentrations; for example, the lepton-production reactions

$$\gamma + \gamma \rightarrow e^+ + e^-$$
$$\gamma + \gamma \rightarrow \mu^+ + \mu^-$$
$$\gamma + \gamma \rightarrow \tau^+ + \tau^-$$

will occur with a probability determined by the density of states available for the final particles, but since the rest energies of all particles are far below 1000 GeV, the available momentum is about the same for each and the birth rates are identical. If there are additional generations of leptons, these also would be produced in equilibrium with the photons.

The number density of photons can be found from the basic expressions for blackbody radiation. The energy density is

$$u(E)\,dE = \frac{8\pi E^3}{(hc)^3}\frac{1}{e^{E/kT}-1}dE \tag{19.8}$$

and the number per energy interval is

$$n(E)\,dE = \frac{u(E)}{E}\,dE = \frac{8\pi E^2}{(hc)^3}\frac{1}{e^{E/kT}-1}dE \tag{19.9}$$

Integrating Equations 19.8 and 19.9 over all energies and evaluating the constants gives the total energy density and number density of photons at temperature T:

$$\rho_\gamma = 4.7 \times 10^3\, T^4\ \text{eV/m}^3 \tag{19.10}$$

$$N_\gamma = 2.0 \times 10^7\, T^3\ \text{photons/m}^3 \tag{19.11}$$

where T is in kelvins. At the present temperature of 2.7 K, the number density is $4 \times 10^8/\text{m}^3 = 400/\text{cm}^3$. These photons have a present mean energy of less than 0.001 eV, which is the reason we do not detect them under ordinary circumstances; each cubic centimeter has a mass energy of about 0.25 eV in primordial photons.

The present matter density of the universe is difficult to estimate. The best estimates for visible (luminous) matter suggest $\rho_0 \sim 3 \times 10^{-31}\ \text{g/cm}^3$; clusters of galaxies, however, seem to be bound by additional nonluminous matter, and the matter density may be uncertain by as much as one order of magnitude. We will arbitrarily increase the value by a factor of 2 to account for nonluminous matter and take

$$\rho_0 \sim 6 \times 10^{-31}\ \text{g/cm}^3$$
$$\sim 0.4\ \text{nucleon/m}^3$$

The present density of nucleons is only about 10^{-9} the present density of photons. Because there is no mechanism by which nucleons can be destroyed on a time scale of the age of the universe, our cosmological model must account for the great imbalance of photons over nucleons.

We also believe that the universe is made almost exclusively of matter, rather than antimatter. This is a difficult assumption to test, for galaxies made of antimatter would differ in no observable way from galaxies made of matter. If

there were a rough balance of matter and antimatter, we might expect occasional encounters between one and the other in interstellar dust and gas, resulting in annihilation reactions with the emission of high-energy photons. Observational limits on such photons are very low, suggesting little antimatter-matter annihilation. We will therefore assume our universe to be composed of ordinary matter.

If we look back to the time when $T > 10^{13}$ K ($t < 10^{-6}$ s), photons had enough energy to create nucleon-antinucleon pairs, as

$$\text{photons} \leftrightarrow \text{p} + \bar{\text{p}}, \text{n} + \bar{\text{n}}$$

We would therefore expect *exactly* equal numbers of nucleons and antinucleons. Even if free quarks could have been created in a much earlier epoch, we would still expect a balance:

$$\text{photons} \leftrightarrow \text{q} + \bar{\text{q}}$$

The balance between matter and antimatter is upset by CP-violating decays (see Section 17.6), which *do* favor one type over the other. The era of the massive X particles, associated with the Grand Unified Theories (GUTs, Section 18.8) distinguishes between matter and antimatter, and the relative rates of

$$\text{X} \rightarrow \text{q} + \text{q}$$

and

$$\bar{\text{X}} \rightarrow \bar{\text{q}} + \bar{\text{q}}$$

may not be equal. If this is the case, there will be a slight imbalance of matter over antimatter; after 10^{-6} s, when nucleons and antinucleons can no longer be created by the radiation field, the antimatter will annihilate with an equal quantity of matter, and the remaining matter is what we observe today. The imbalance must have been very small, about 1 part in 10^9, for us to observe the present 10^{-9} nucleon-to-photon ratio. With the unification mass estimated to be 10^{15} GeV, the temperature at which this imbalance becomes established must be about 10^{28} K, corresponding to an age of about 10^{-36} s.

Let's now jump to the era of $t > 10^{-6}$ s, where $T \lesssim 10^{13}$ K ($E \lesssim 1$ GeV). Nucleon-antinucleon annihilation occurs, but no longer in equilibrium with the reverse creation process. An abundance of leptons and neutrinos is present, so weak interactions can occur to convert protons to neutrons:

$$\text{p} + \bar{\nu}_\text{e} \leftrightarrow \text{n} + \text{e}^+$$

$$\text{n} + \nu_\text{e} \leftrightarrow \text{p} + \text{e}^-$$

If $\text{e}^\pm$ and ν_e, $\bar{\nu}_\text{e}$ are plentiful, these reactions will go in either direction, and at this early time the number of neutrons and protons should be equal.

At $t = 10^{-2}$ s, $T = 10^{11}$ K ($E = 10$ MeV). Now electrons are the only remaining charged leptons; μ ($mc^2 = 105$ MeV) and τ ($mc^2 = 1784$ MeV) are no longer produced (and have long since decayed to electrons or annihilated to photons), but through neutral weak interactions, all species of neutrinos can be made:

$$\text{e}^+ + \text{e}^- \leftrightarrow \text{Z}^0 \leftrightarrow \nu_\text{e} + \bar{\nu}_\text{e}$$

$$\text{e}^+ + \text{e}^- \leftrightarrow \text{Z}^0 \leftrightarrow \nu_\mu + \bar{\nu}_\mu$$

$$\text{e}^+ + \text{e}^- \leftrightarrow \text{Z}^0 \leftrightarrow \nu_\tau + \bar{\nu}_\tau$$

If the neutrinos are massless (or if their masses are small compared with 10 MeV), then these reactions will be at equilibrium, and the relative numbers of neutrino species will remain constant.

Associated with each kind of particle is a statistical weight g_i ($i = e^+, e^-, \nu_e, \bar{\nu}_e, \nu_\mu, \bar{\nu}_\mu, \nu_\tau, \bar{\nu}_\tau, \ldots$), which essentially gives the permitted number of spin or polarization states. For convenience we group together e^+ and e^- (as e) and each $\nu_i, \bar{\nu}_i$ pair (as ν_i), so that

$$\begin{aligned} g_e &= 4 \qquad (2 \text{ spin states for each of } e^+ \text{ and } e^-) \\ g_{\nu_i} &= 2 \qquad (\nu_i \text{ and } \bar{\nu}_i \text{ states for } i = e, \mu, \tau, \ldots) \end{aligned} \tag{19.12}$$

The number and energy densities associated with each species are governed by the Fermi-Dirac distribution:

$$u(E)\,dE = g_i \frac{4\pi E^3}{(hc)^3} \frac{1}{e^{E/kT} + 1}\,dE \tag{19.13}$$

with an analogous result for the number density $n(E)$ as in Equation 19.9.

Carrying out the required integrals gives the total volume density of particles and energy for electrons

$$N_e = \tfrac{3}{2} N_\gamma \tag{19.14}$$

$$\rho_e = \tfrac{7}{4} \rho_\gamma \tag{19.15}$$

where N_γ and ρ_γ are the photon total number and energy densities given by Equations 19.10 and 19.11. The corresponding contribution from neutrinos will be

$$N_\nu = \tfrac{3}{4} n_\nu N_\gamma \tag{19.16}$$

$$\rho_\nu = \tfrac{7}{8} n_\nu \rho_\gamma \tag{19.17}$$

where n_ν is the number of different neutrino species ($n_\nu = 3$ for e, μ, τ only).

Neutrons are slightly more massive than protons, so there are slightly fewer of them in an equilibrium mixture at temperature T, owing to the Boltzmann factor:

$$\frac{N_n}{N_p} = e^{-(m_n - m_p)c^2/kT} \tag{19.18}$$

The mass difference is about 1.3 MeV, and at $kT = 10$ MeV (at $t \sim 0.01$ s), $N_n/N_p \simeq 0.88$. Maintaining an equilibrium condition requires the presence of sufficient $e^\pm$ and $\nu_e, \bar{\nu}_e$ to allow the $n \leftrightarrow p$ conversion.

At $t = 1$ s ($T = 10^{10}$ K; $E = 1$ MeV), neutrino interactions are no longer important; neither the charged nor the neutral interactions of neutrinos contribute to the reactions. This is the era of *neutrino decoupling*, from which time the neutrinos expand freely with the universe, virtually unaffected by nuclear reactions.

Immediately following the decoupling, $e^+ + e^- \rightarrow 2\gamma$ is possible, but not the reverse. The photon energy density therefore increases somewhat, and in effect the temperature of the photons decreases less rapidly than that of the freely

expanding neutrinos. The effect can be shown to be

$$\frac{T_\gamma}{T_\nu} = \left(\frac{11}{4}\right)^{1/3} \cong 1.4 \tag{19.19}$$

for three families of leptons. The present neutrino temperature is thus about 2 K.

Following the annihilation of the positrons and electrons, we are left with a large collection of photons, about 10^{-9} as many electrons and protons (equal numbers, to keep the net electric charge zero), and a slightly smaller number of neutrons (from the Boltzmann factor). This ends the era of particle interactions and begins the time of nuclear reactions. After the stable, light nuclei have formed (^{2}H, ^{3}He, ^{7}Li), the universe continues to expand and cool until the photons decouple; that is, neutral atoms can form when the photons lack the energy necessary to ionize them. This occurs at a temperature of perhaps 3000 K and an age of about 700,000 y. With the continuing expansion of the universe, the photons continue to cool, independent of the interactions of matter (which are restricted to gravity since the other interactions can no longer operate on the large scale) until they reach the presently observed temperature of 2.7 K.

19.3 PRIMORDIAL NUCLEOSYNTHESIS

To begin production of heavy nuclei, the first reaction that must occur is

$$\mathrm{n} + \mathrm{p} \rightarrow \mathrm{d} + \gamma$$

At high temperatures, the reverse reaction occurs as quickly as deuterium production, and there is no accumulation of deuterium nuclei. The photon energy necessary for photodissociation is 2.225 MeV (the binding energy of deuterium), but it must be remembered that there are about 10^9 times as many photons as protons or neutrons. The photons have a blackbody spectrum, given by Equation 19.9, which of course extends to very large E (Figure 19.4). When the number of photons in the high-energy tail above the energy 2.225 MeV is less than the

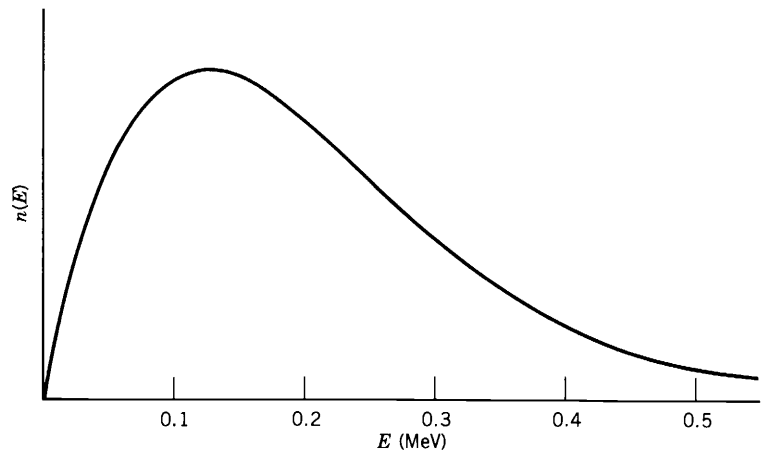


Figure 19.4 The number of blackbody photons at energy E for a temperature of $T = 9 \times 10^8$ K.

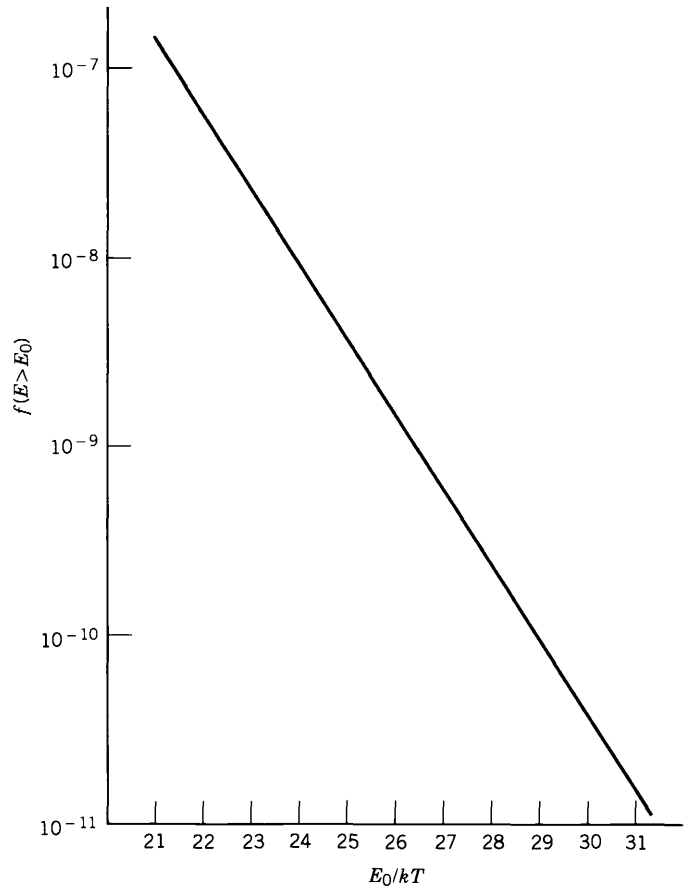


Figure 19.5 The fraction f of photons of energies above E_0.

number of nucleons participating in deuterium formation, there will be too few photons to inhibit deuterium production. We can establish the temperature at which this will occur by approximating the tail as an exponential

$$n(E)\,dE \cong \frac{8\pi E^2}{(hc)^3}\,e^{-E/kT}\,dE \tag{19.20}$$

and integrating for energies above E_0 gives

$$N_\gamma(E > E_0) = \frac{8\pi}{(hc)^3}(kT)^3\,e^{-E_0/kT}\left[\left(\frac{E_0}{kT}\right)^2 + 2\left(\frac{E_0}{kT}\right) + 2\right] \tag{19.21}$$

Dividing by the total number density gives the fraction f above E_0

$$f(E > E_0) = 0.42\,e^{-E_0/kT}\left[\left(\frac{E_0}{kT}\right)^2 + 2\left(\frac{E_0}{kT}\right) + 2\right] \tag{19.22}$$

Figure 19.5 illustrates this function in the range $10^{-11} < f < 10^{-7}$, corresponding to $21 < E_0/kT < 31$.

The number of nucleons available for deuterium formation is determined by the number of neutrons because there are fewer neutrons than protons. The ratio

N_n/N_p decreases with decreasing temperature, according to Equation 19.18, only as long as $e^{\pm}$ are sufficiently plentiful and react quickly enough for $n \leftrightarrow p$ conversion to take place. At a certain temperature T_*, the ratio N_n/N_p becomes "frozen" when the rate of weak interactions becomes too small. Based on the known cross sections for weak interactions, we can estimate this temperature as $T_* = 9 \times 10^9$ K, corresponding to $N_n/N_p \simeq 0.2$; this occurs at a time of about 3 s.

Neutrons therefore originally constitute a fraction of the total number of nucleons equal to 0.2. If the nucleon-to-photon ratio is 10^{-9}, then the critical fraction of high-energy photons necessary to prevent deuterium formation will be 0.2×10^{-9}, corresponding to $T = 9 \times 10^8$ K from Equation 19.22 and thus to $t \simeq 250$ s. As can be seen from Figure 19.5, this estimate is very insensitive to the value of f and thus to the N_n/N_p ratio.

Once we have formed deuterium in sufficient quantity, other nuclear reactions become possible. We can form the mass-3 nuclei:

$$d + n \rightarrow {}^3H + \gamma$$

$$d + p \rightarrow {}^3He + \gamma$$

or by

$$d + d \rightarrow {}^3H + p$$

$$d + d \rightarrow {}^3He + n$$

Finally, ^{4}He can be formed:

$${}^3H + p \rightarrow {}^4He + \gamma$$

$${}^3He + n \rightarrow {}^4He + \gamma$$

The binding energies of all these reaction products are greater than that of deuterium; thus if the photons are cool enough to permit deuterium to form, they will certainly permit the remaining reactions.

Because there is no stable mass-5 nucleus, ^{4}He is the primary end product of this process. Also ^{8}Be is unstable, so two ^{4}He cannot combine directly. There will be a small production of mass-7 nuclei:

$${}^4He + {}^3H \rightarrow {}^7Li + \gamma$$

$${}^4He + {}^3He \rightarrow {}^7Be + \gamma$$

but the Coulomb barriers for these reactions are about 1 MeV, and the nuclei are well below that value in energy (in equilibrium at $T = 9 \times 10^8$ K, the mean kinetic energy is less than 0.1 MeV). Therefore essentially all of the neutrons end as part of ^{4}He nuclei, which has a relative abundance $N_{He}/N_p = 0.081$ (calculated from the "frozen" N_n/N_p ratio after correcting for the radioactive β decays of the neutrons between $t = 3$ s and $t = 250$ s). The relative primordial abundance of ^{4}He by weight, Y_p, is thus about 0.24, and except for additional burning of H and He in stars, this relative abundance should have remained constant in the universe from $t = 250$ s until today.

The observed abundance (by weight) of ^{4}He is about $Y_p = 0.24 \pm 0.01$, based on observations from a variety of astronomical systems, including gaseous nebulae, planetary nebulae, and stars (including the Sun). This excellent agree-

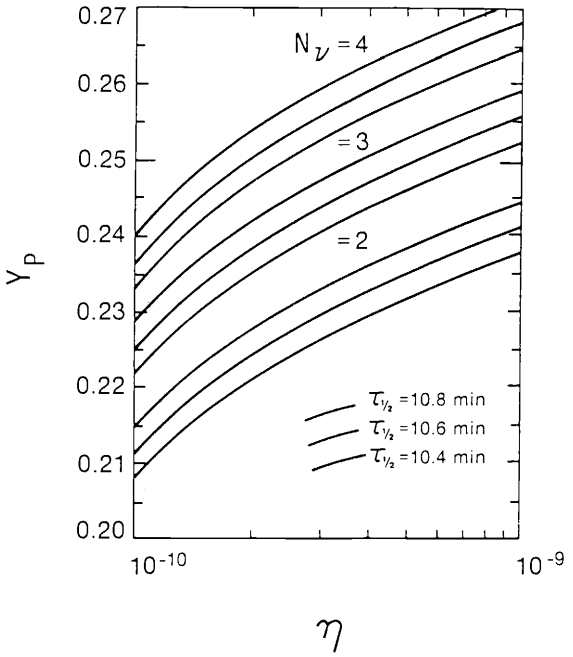


Figure 19.6 Dependence of primordial helium abundance Y_p on the nucleon-to-photon ratio. The expected dependence is shown for 2, 3, or 4 types of massless neutrino; for each case the three curves show the range corresponding to the uncertainty in the experimental value of the neutron half-life of 10.6 $\pm$ 0.2 min. From D. N. Schramm and G. Steigman, *Phys. Lett. B* **141**, 337 (1984).

ment between the calculated abundance and that observed should not be taken as a confirmation of the theory, for the final ^{4}He abundance is very sensitive to the assumed frozen N_n/N_p ratio, which in turn is sensitive to the calculated temperature at which the freeze-out occurs. This calculation depends critically on the half-life of neutron decay (which is not extremely well known, $t_{1/2} = 10.6 \pm 0.2$ min) and on the assumed number of species of leptons. Figure 19.6 shows the dependence of Y_p on the number of massless species of neutrinos (at least three, according to the standard model) and on the nucleon-to-photon ratio. You can see that the observed ^{4}He abundance allows an additional species of neutrinos (another generation of leptons and presumably also quarks) only for a nucleon-to-photon ratio below 2×10^{-10}. It permits only two massless neutrinos (allowing, for instance, the τ neutrino to be massive, which is contrary to the standard model but not disallowed by the presently rather poor experimental limits on its mass) for correspondingly large nucleon-to-photon ratios ($> 6 \times 10^{-10}$).

In addition to ^{4}He, there will be a small concentration of primordial ^{2}H, ^{3}He, and ^{7}Li in the present universe. Deuterium in particular is critical for a determination of the nucleon-to-photon ratio—at large nucleon abundances, ^{2}H is more rapidly "cooked" into heavy nuclei and its concentration is accordingly reduced. The ratio N_d/N_p can be deduced from the shift in the absorption spectrum of atomic hydrogen caused by the heavier nuclear mass of ^{2}H. The observed value is subject to uncertainties arising from the destruction of primor-

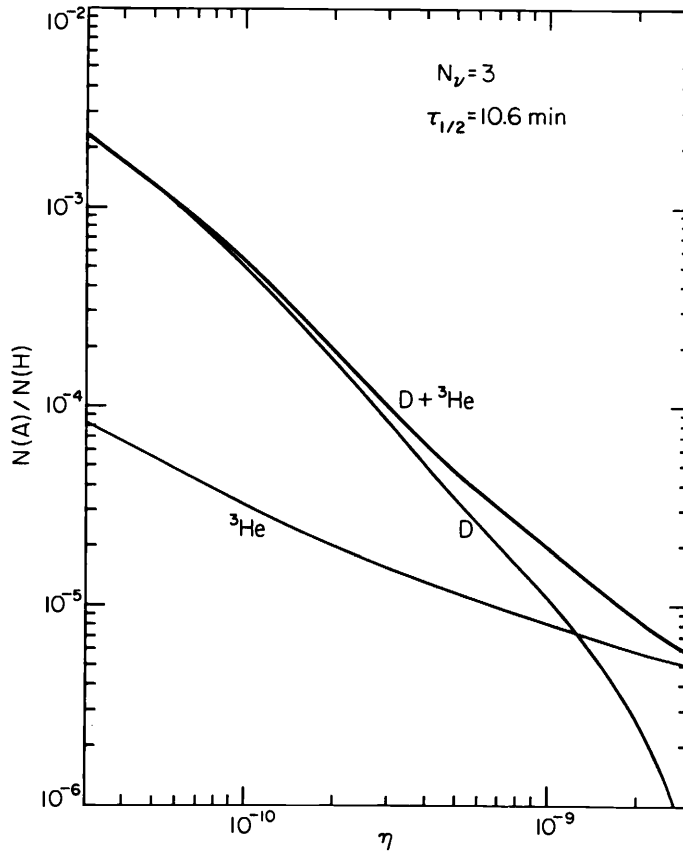


Figure 19.7 Dependence of the abundance of ^{2}H and ^{3}He on the nucleon-to-photon ratio. From J. Yang et al., *Astrophys. J.* **281**, 493 (1984).

dial ^{2}H in the evolution of galaxies, but the best current value is $N_d/N_p \sim 1\text{–}3 \times 10^{-5}$.

The isotope ^{3}He is, like ^{2}H, a result of incomplete primordial processes, and the abundance of ^{3}He decreases as the primordial nucleon density increases. Here again, observed present-day abundances may not reflect primordial values, for "new" ^{3}He can be produced, in particular from deuterium. The ^{3}He abundance observed presently is therefore possibly a measure of the primordial combined ^{3}He + ^{2}H abundance. Based on observed solar abundances, it is suggested that $(N_{^2H} + N_{^3He})/N_p < 6 \times 10^{-5}$.

Figure 19.7 shows the abundances calculated with the standard model (three varieties of massless neutrinos). It is quite clear that the deuterium and ^{3}He abundances constrain the nucleon-to-photon ratio to be greater than about 4×10^{-10}, and returning to Figure 19.6, we see that this value is inconsistent with a fourth neutrino. Although much work, both theoretical and experimental, remains to be done to solidify these conclusions, it appears that these cosmological arguments may indicate that there are no new fundamental particles beyond the present three generations of leptons and quarks.

19.4 STELLAR NUCLEOSYNTHESIS ($A \lesssim 60$)

The dominant process in the formation of the elements with $A \lesssim 60$ is charged-particle reactions, primarily those induced by protons and α particles. The probability for these reactions to occur will depend on the overlap between the thermal distribution of particle energies and the Coulomb barrier penetration probability, exactly as in the case of fusion reactions discussed in Section 14.2.

Stars begin life as a mixture of hydrogen and 24% (by weight) helium. As the original gas cloud collapses, the individual atoms exchange their gravitational potential energy for kinetic energy, thereby increasing the temperature of the cloud. Eventually, the temperature is high enough that the protons can overcome the repulsive Coulomb energy, and fusion reactions can begin. The outward pressure from the radiation released in fusion effectively halts the gravitational collapse, and the star enters an equilibrium phase (like our Sun) that may last 10^{10} y.

The basic reactions of the proton-proton fusion cycle have already been discussed in Section 14.3 and need not be repeated here. When a star's hydrogen fuel is depleted, gravitational collapse can begin again, and eventually a higher temperature is reached (perhaps $1\text{–}2 \times 10^8$ K, compared with 10^7 K for the present Sun) where the Coulomb barrier for ^{4}He-^{4}He fusion can be overcome. The increased ignition temperature results in a larger radiation pressure, which expands the outer envelope of the star's surface by a large factor, perhaps by a factor of 100 or 1000. The apparent energy density of the surface decreases, and the star appears at a lower effective surface temperature. This is the *red giant* stage.

As there is no stable mass-8 nucleus, there are no observable end products of the reaction

$$^4\text{He} + {}^4\text{He} \rightarrow {}^8\text{Be}$$

for ^{8}Be breaks apart (into two ^{4}He again) in a time of the order of 10^{-16} s. The Q value is 91.9 keV, and so even at 2×10^8 K (mean thermal energy of 17 keV) there will be a fair number of energetic α's in the high-energy tail of the thermal distribution to form ^{8}Be. There will be a small equilibrium concentration of ^{8}Be, of the order of the Boltzmann factor $e^{-91.9\ \text{keV}/17\ \text{keV}} = 4 \times 10^{-3}$, and the reaction rate can be calculated, exactly as we did in Section 14.2 for the D-D or D-T reactions.

We know that ^{12}C is plentiful in the universe, but the calculated rates of $2\alpha \rightarrow {}^8\text{Be}$ and $^8\text{Be} + \alpha \rightarrow {}^{12}\text{C}$ are not sufficient to produce the observed large abundances of ^{12}C, as was first realized by Fred Hoyle in the early 1950s. The Q value for $^8\text{Be} + \alpha \rightarrow {}^{12}\text{C}$ is 7.45 MeV, and Hoyle argued that the large production of ^{12}C requires this reaction to occur readily, which in turn requires a resonance to account for what must be an increase in the cross section at this energy. He made this suggestion to W. A. Fowler, whose research group at Cal Tech began in the 1950s an extended program concerning the study of nuclear reactions of astrophysical importance. The Cal Tech group discovered the ^{12}C resonance corresponding to an excited state at 7.65 MeV, just above the energy predicted by Hoyle, but well within the capability of being reached at temperatures of $1\text{–}2 \times 10^8$ K. The net Q value for $3\ ^4\text{He} \rightarrow {}^{12}\text{C}^*$ is 285 keV. Subse-

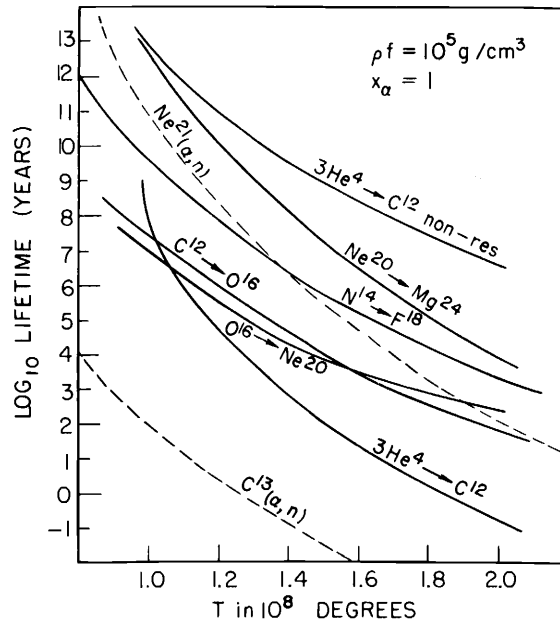


Figure 19.8 Mean lifetime in years for various α-particle reactions as a function of temperature. The reaction rate is the inverse of the lifetime, so reactions near the bottom of the graph are the ones with the highest rates. From Burbidge, Burbidge, Fowler, and Hoyle, *Rev. Mod. Phys.* **29**, 547 (1957).

quently, Fowler and his colleagues were able to populate the 7.65-MeV excited state in ^{12}C following β decay of ^{12}B. They identified it as a 0^+ state and observed its decay into three α particles, thereby suggesting that it could indeed be formed by three α particles. The 0^+ assignment is consistent with the probable s-state couplings in these low-energy reactions.

Once ^{12}C is formed, other α-particle reactions become possible:

$$^{12}C + {}^4He \rightarrow {}^{16}O + \gamma \qquad (Q = 7.16 \text{ MeV}, E_B = 3.57 \text{ MeV})$$

$$^{16}O + {}^4He \rightarrow {}^{20}Ne + \gamma \qquad (Q = 4.73 \text{ MeV}, E_B = 4.47 \text{ MeV})$$

$$^{20}Ne + {}^4He \rightarrow {}^{24}Mg + \gamma \qquad (Q = 9.31 \text{ MeV}, E_B = 5.36 \text{ MeV})$$

As the Coulomb barrier E_B increases for heavier nuclei, it becomes decreasingly likely to continue this sequence of reactions. Figure 19.8 shows the calculated mean lifetime for nuclei participating in these reactions, taken from the classic work on nucleosynthesis by Burbidge, Burbidge, Fowler, and Hoyle. Notice in particular the importance of the ^{12}C resonance, which effectively increases the reaction rate by about 8 orders of magnitude.

When the helium fuel begins to be exhausted, gravitational collapse sets in again (only if the star is sufficiently massive—otherwise the gravitational force is not strong enough to oppose the "degeneracy pressure" of the electrons that are reluctant to have overlapping wave functions). The star then heats up enough to ignite ^{12}C and ^{16}O burning, which permits such reactions as

$$^{12}C + {}^{12}C \rightarrow {}^{20}Ne + {}^4He \quad \text{or} \quad {}^{23}Na + p$$

$$^{16}O + {}^{16}O \rightarrow {}^{28}Si + {}^4He \quad \text{or} \quad {}^{31}P + p$$

at temperatures of the order of 10^9 K, where the Coulomb barrier can be more easily penetrated.

In addition to these reactions, other α-particle and nucleon capture reactions can occur as well. For example, ^{14}N may be present in second-generation stars, formed originally from ^{12}C as part of the carbon cycle of proton-proton fusion discussed in Section 14.3. Alpha-capture reactions can produce the chain $^{14}N \rightarrow {}^{18}O \rightarrow {}^{22}Ne \rightarrow {}^{26}Mg \ldots$. Reactions other than (α,γ), including (α,n) or (p,γ) will occur, with somewhat less probability.

The final stage in the production of nuclei near mass 60 is silicon burning, which is in actuality a complex sequence of reactions that take place rapidly but under nearly equilibrium conditions deep in the hot stellar interiors. The Coulomb barrier is too high to permit direct formation by such reactions as $^{28}Si + {}^{28}Si \rightarrow {}^{56}Ni$; instead, what occurs are combinations of photodissociation reactions (γ, α), (γ, p), or (γ, n) followed by capture of the dissociated nucleons:

$$^{28}Si + \gamma \rightarrow {}^{24}Mg + {}^{4}He$$

$$^{28}Si + {}^{4}He \rightarrow {}^{32}S + \gamma$$

and many other similar reactions. In the equilibrium process, the Si that resulted from oxygen burning is partly "melted" into lighter nuclei and partly "cooked" into heavier nuclei. The end products of chains of such reactions are the mass-56 nuclei (^{56}Ni, ^{56}Co, ^{56}Fe). At this point there is no longer energy released in the capture reactions, and the process is halted.

Confirmation of this scenario can be seen with reference to Figure 19.9; the abundances of the elements formed by α capture (Z = even) are far greater (an order of magnitude or more) than the neighboring odd-Z elements. Notice also

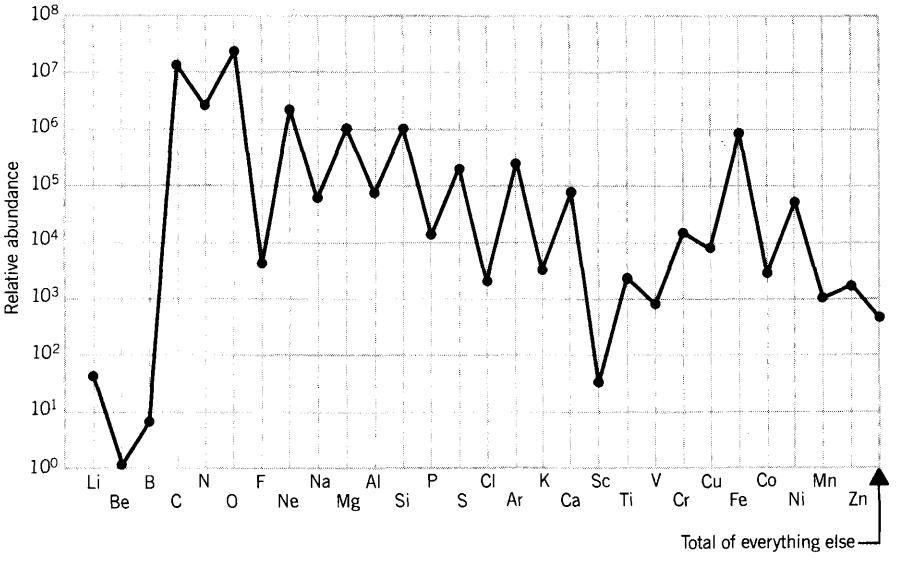


Figure 19.9 Relative abundances (by weight) of the elements beyond helium.

the dramatic (6 orders of magnitude) drop for elements below C; these elements are not formed in the stellar processes discussed so far.

To understand the rate of charged-particle reactions in stellar interiors, we must try to duplicate the reaction conditions using accelerators on Earth. The required energies are not large (~ MeV), but we require beams of the highest possible intensity (because these charged-particle reactions are strongly inhibited at low energy by the Coulomb barrier penetration factors) and best possible energy resolution (to study the behavior near discrete resonances or specific excited states).

The reaction probability in a stellar environment can be calculated in a way similar to the fusion reaction rate, as in Section 14.2. The reacting particles (a + X) are described by a thermal distribution

$$n(E)\,dE \propto e^{-E/kT}\sqrt{E}\,dE \tag{19.23}$$

while the cross section has the basic form of

$$\sigma(E) \propto \frac{1}{E}\,e^{-2G} \tag{19.24}$$

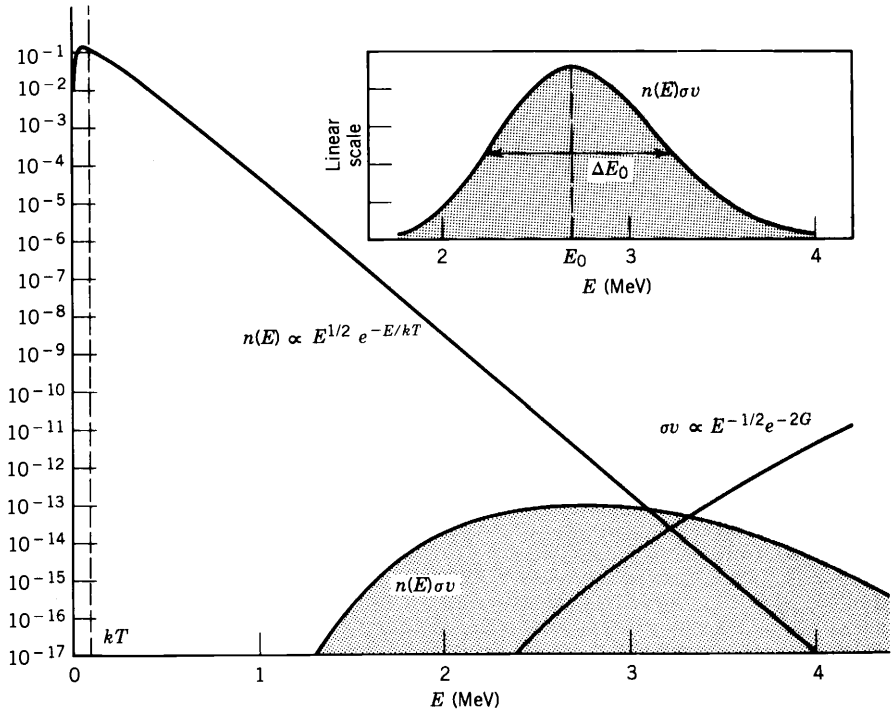


Figure 19.10 The dependence of $n(E)$ and σv on energy. Their product, which is proportional to the reaction rate, is the shaded region. The inset at the top shows the reaction rate plotted on a linear scale, illustrating the peak energy E_0 and the width ΔE_0. Notice that the reaction rate peaks at energies far above kT. The curves are drawn for the reaction $^{12}C + {}^{12}C$ at a temperature corresponding to $kT = 0.1$ MeV.

where G is the Gamow factor, as in Equation 8.17:

$$G \cong \frac{e^2}{4\pi\epsilon_0}\frac{\pi Z_a Z_X}{\hbar v} \tag{19.25}$$

$$2G \cong Z_a Z_X A_{\text{eff}}^{1/2} E^{-1/2} \tag{19.26}$$

All energies and velocities are given in the center of mass. The "effective mass number" A_{eff} is $A_a A_X/(A_a + A_X)$. In Equation 19.26, E is given in MeV.

The barrier penetration factor increases with increasing energy, while the number of particles decreases. Figure 19.10 shows the overlap region between the two functions of energy. The reaction probability is large only in the shaded region where the two distributions overlap, and thus the usual measure of the "effective energy" of a thermal distribution, kT, is totally inappropriate to characterize these reactions, which occur exclusively at energies much larger than kT.

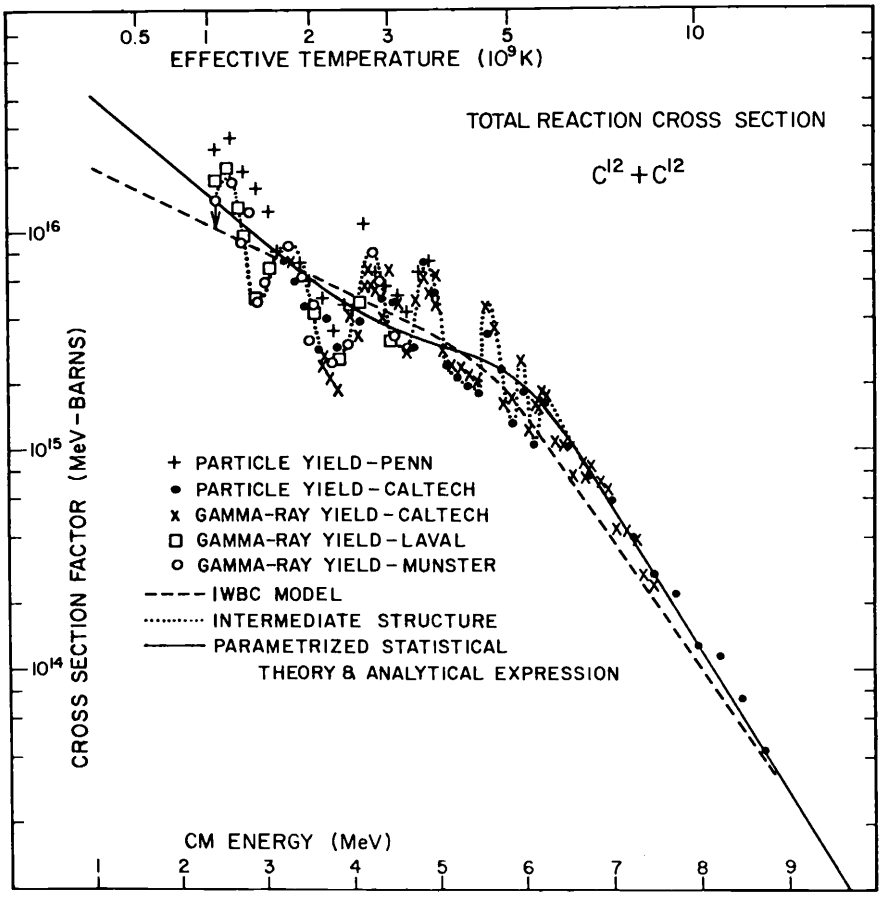


Figure 19.11 The cross-section factor $S(E)$ for $^{12}C + ^{12}C$. From W. A. Fowler, *Rev. Mod. Phys.* **56**, 149 (1984).

The reaction rate depends on the product σv and on the number of particles available at a specific energy

$$\begin{aligned} \text{rate} &\propto n(E)\sigma(E)v \\ &\propto (\sqrt{E}\, e^{-E/kT})\left(\frac{1}{E}\, e^{-2G}\right)\sqrt{E} = e^{-E/kT-2G} \end{aligned} \tag{19.27}$$

which describes the overlap region in Figure 19.10. The characteristic energy of the process can be evaluated in terms of the peak energy E_0 and width ΔE_0 of the distribution:

$$E_0 = \left(\tfrac{1}{2}kTZ_aZ_XA_{\text{eff}}^{1/2}\right)^{2/3} \tag{19.28}$$

$$\Delta E_0 = 2^{7/6}3^{-1/2}\left(Z_aZ_XA_{\text{eff}}^{1/2}\right)^{1/3}(kT)^{5/6} \tag{19.29}$$

To obtain information on the reaction rate in the interior of a star, we should study reactions with accelerators, not at energies of kT, but at energies of E_0. In the case of $^{12}C + {}^{12}C$, for example, to duplicate stellar conditions at $kT = 0.1$ MeV (that is, $T = 10^9$ K), we should do the reaction at center-of-mass energy $E_0 = 2.3$ MeV.

Let's rewrite Equation 19.24 as

$$\sigma(E) = \frac{1}{E}\, e^{-2G} S(E) \tag{19.30}$$

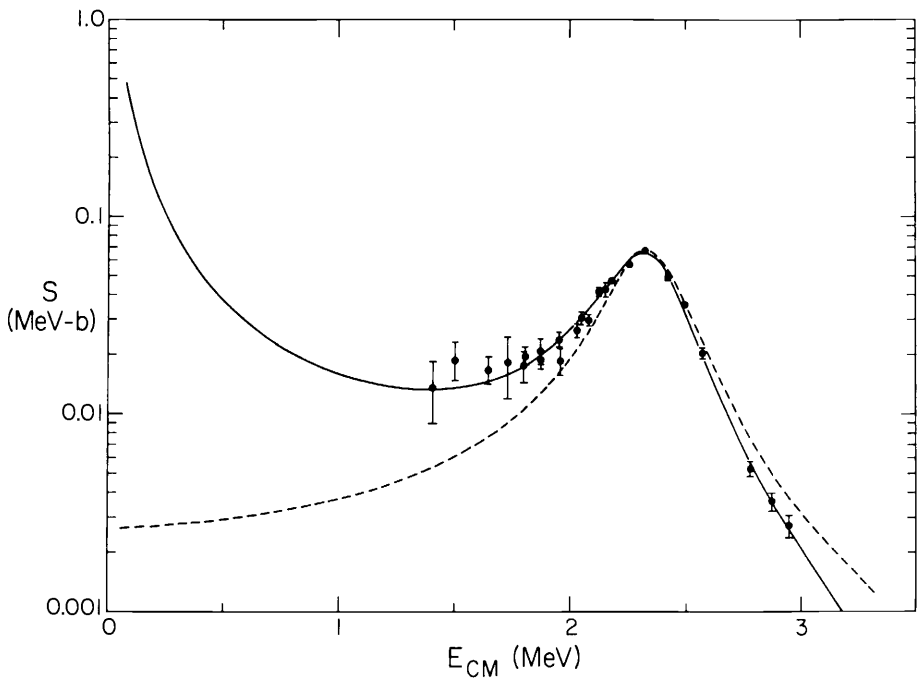


Figure 19.12 Cross-section factor $S(E)$ for $^{12}C + \alpha \rightarrow {}^{16}O + \gamma$. The dashed curve is a theoretical fit that ignores the contributions of the ^{16}O bound states, while the solid curve is a fit that includes the effect of the bound states and gives much better agreement with the experimental data. From S. E. Koonin, T. A. Tombrello, and G. Fox, *Nucl. Phys. A* **220**, 221 (1974).

where $S(E)$ includes all nuclear-structure information other than the barrier penetration factor. For example, if the cross section is to be measured near a resonance, then

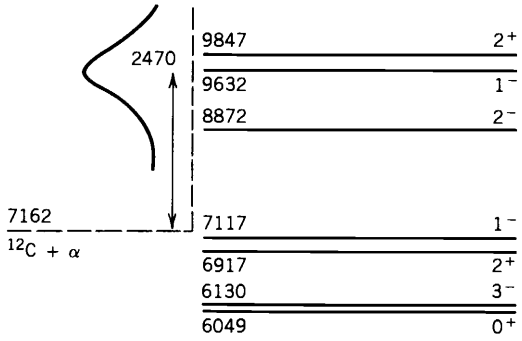
$$S(E) = g\Gamma_{aX}\Gamma_{bY}\frac{1}{(E - E_R)^2 + \Gamma^2/4} \tag{19.31}$$

where Γ_{aX} is the noncoulomb contribution to the entrance width (involving only nuclear wave functions). To compute the reaction rate, we must determine the factor $S(E)$, which can be directly obtained from the cross sections:

$$S(E) = E\sigma(E)\, e^{2G} \tag{19.32}$$

Figure 19.11 shows the $^{12}C + ^{12}C$ cross section factor $S(E)$, which has a smooth nonresonant background along with several peaks illustrating some resonant structure. The Q value for the $^{12}C + ^{12}C \rightarrow ^{24}Mg$ reaction is large (13.9 MeV), so the structure corresponds to very highly excited states of the compound system.

Figure 19.12 shows the cross section factor $S(E)$ for $^{12}C + ^{4}He \rightarrow ^{16}O$. The structure is dominated by a single broad resonance, corresponding to an α-unsta-



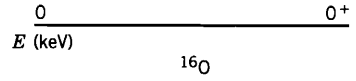


Figure 19.13 Excited states of ^{16}O. The broad resonance (which is also shown in Figure 19.12) at 2470 keV above the $^{12}C + \alpha$ threshold includes the 1^- and 2^+ states at 9632 and 9847 keV. The interference of the 1^- and 2^+ states just below the $^{12}C + \alpha$ threshold (7117 and 6917 keV) has a substantial effect on the calculated cross section.

ble state at about 2.5 MeV above the $^{12}C + {}^4He$ threshold (Figure 19.13). The calculated cross section agrees very well with the measured values, but the two ^{16}O excited states just below the $^{12}C + {}^4He$ energy have a substantial influence on the calculated cross section and cannot be neglected.

Careful determinations of charged-particle reaction cross sections for energies in the MeV range, in addition to the most complete knowledge about the structure and properties of excited states, are essential in calculating the reaction rates and interior temperatures for models of stellar interiors. For his work in measuring such reactions, W. A. Fowler was honored with the 1983 Nobel Prize.

19.5 STELLAR NUCLEOSYNTHESIS ($A > 60$)

As Figure 3.16 shows, fusion reactions are not energetically favored above about $A = 60$. For these nuclei, neutron capture is the primary production mechanism. Let's consider, for example, ^{56}Fe, which is the most abundant stable isotope of the most abundant element formed near the end of the chain of fusion reactions. In a flux of neutrons, a sequence of neutron-capture reactions will take place:

$$^{56}Fe + n \rightarrow {}^{57}Fe + \gamma$$

$$^{57}Fe + n \rightarrow {}^{58}Fe + \gamma$$

$$^{58}Fe + n \rightarrow {}^{59}Fe + \gamma$$

The next step in the process depends on the intensity of the neutron flux. The isotope ^{59}Fe is radioactive, with a half-life of 45 days. If the neutron flux is so low that the probability of neutron capture is far smaller than once per 45 days, then ^{59}Fe will β decay to stable ^{59}Co, which can then undergo neutron capture leading to radioactive ^{60}Co. If, on the other hand, the probability of neutron capture is so great that the average time necessary to capture a neutron is small (seconds or less), then the sequence of neutron-capture reactions can continue to ^{60}Fe ($t_{1/2} = 3 \times 10^5$ y), ^{61}Fe ($t_{1/2} = 6$ min), ^{62}Fe ($t_{1/2} = 68$ s), and beyond. When we finally reach an isotope that is so neutron rich that its half-life becomes shorter than the mean life before neutron capture, it will β^- decay to an isotope with one higher atomic number. The sequence of neutron captures will begin again, until an extremely unstable isotope of this new sequence is reached, at which time β^- decay increases the atomic number by one step again.

These two processes are responsible for the formation of the vast majority of the stable isotopes of the nuclei beyond $A = 60$. The first process, in which neutron capture occurs only on a long time scale, leaving time for all intervening β decays to occur, is called the s (for slow) process. The second process, which does not leave time for any but the most short-lived decays, is called the r (for rapid) process. Figure 19.14 shows the s- and r-process paths near ^{56}Fe.

Before we discuss the neutron-capture processes in detail, let's consider the origin of neutrons. Neutron emission following α-particle reactions will be likely only if the original target nucleus is already neutron rich (and thus has a relatively weakly bound neutron). The neutron separation energies of α-particle nuclei tend to be quite large (^{12}C, 18.7 MeV; ^{16}O, 15.7 MeV; ^{20}Ne, 16.9 MeV; ^{24}Mg, 16.5 MeV; ^{28}Si, 17.2 MeV . . .) and beyond the range of the incident alphas

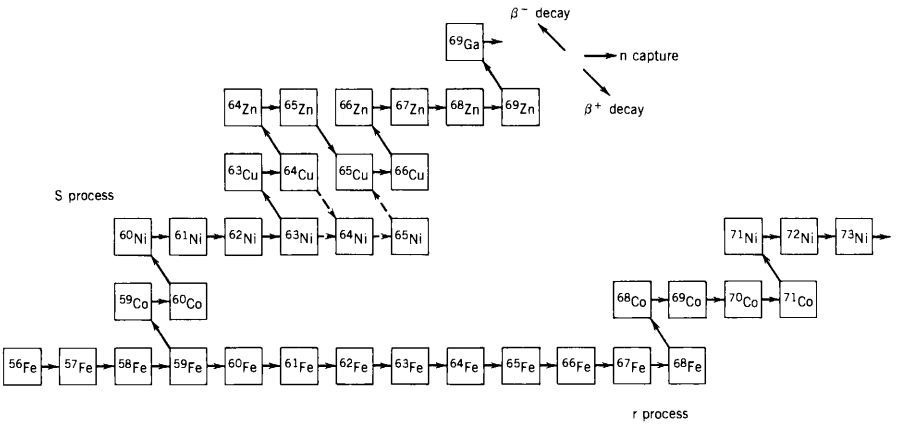


Figure 19.14 The r- and s-process paths from ^{56}Fe. The dashed lines in the s process represent possible alternative paths to ^{65}Cu. Many different r-process paths are possible, as the short-lived nuclei β decay; only one such path is shown.

in the stellar environment. More likely candidates are those with less tightly bound neutrons: $^{13}\mathrm{C}(\alpha, \mathrm{n})^{16}\mathrm{O}$ ($Q = 2.2$ MeV) and $^{22}\mathrm{Ne}(\alpha, \mathrm{n})^{25}\mathrm{Mg}$ ($Q = -0.48$ MeV). These reactions will occur during the helium burning or red-giant phase of stellar evolution, and the reaction rates can be calculated using the methods described in the last section. The results indicate that, in the red-giant temperature range of $1\text{–}2 \times 10^8$ K, the neutron density n_n is of order $10^{14}/\mathrm{m}^3$. We can estimate the reaction rate per target atom to be

$$r \simeq n_n \langle \sigma v \rangle \tag{19.33}$$

and at a temperature of 2×10^8 K, the velocity of a thermalized neutron is about 2×10^6 m/s. A typical neutron-capture cross section at these energies (~ 20 keV) is about 0.1 b, and so

$$r \sim (10^{14}\ \mathrm{m}^{-3})(2 \times 10^6\ \mathrm{m/s})(10^{-29}\ \mathrm{m}^2) = 2 \times 10^{-9}/\mathrm{s}$$

or about one per 20 years. This is obviously an s-process situation.

To increase the reaction rate by some 10 orders of magnitude, as is needed for the r process, we obviously require a vast increase in the neutron flux. This is thought to occur in the violent stellar explosions known as supernovae, but there is as yet no general agreement on this hypothesis, nor is there an acceptable theory of the properties of supernovae. Yet the experimental evidence for the production of r-process nuclei is firm, and we will therefore accept that somewhere in the universe is a source (supernova, neutron star, etc.) that is capable of producing the necessary fluxes.

In the production of s-process nuclei, which occurs over a very long time, we expect the establishment of an approximate equilibrium situation. That is, each species has sufficient time to reach its equilibrium abundance, in which the production rates and destruction rates are equal. In a species A, with abundance N_A, the rate of change of N_A is

$$\frac{dN_A}{dt} \propto \sigma_{A-1} N_{A-1} - \sigma_A N_A \tag{19.34}$$

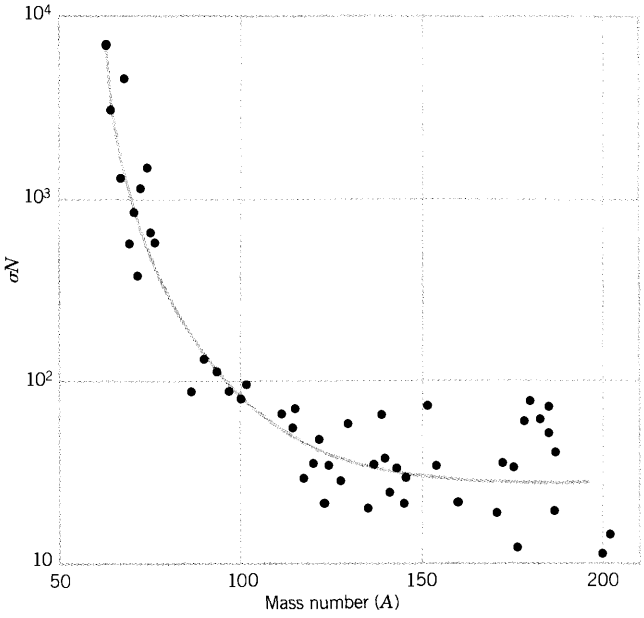


Figure 19.15 The product σN approaches a constant value well above the Fe peak.

because A is produced through neutron capture by nuclei of mass number $A - 1$, and N_A is depleted by neutron captures of A leading to $A + 1$. In equilibrium, $dN_A/dt = 0$, and we expect

$$\sigma_{A-1}N_{A-1} = \sigma_A N_A = \text{constant} \tag{19.35}$$

Figure 19.15 shows the product σN plotted for the nuclei beyond $A = 60$. Just above the peak in the abundance at iron, Equation 19.35 is not satisfied, for the Fe abundance is not obtained through the s process. The product σN begins near Fe with very large values, but then decreases to an equilibrium value above $A = 100$. This smooth and gradual behavior indicates that the basic assumptions regarding s-process behavior are valid.

Figure 19.16 shows a small section of the chart of the nuclides, illustrating s- and r-process paths. Certain nuclei are accessible to both r- and s-process paths; trying to account for the abundances of these isotopes means we must be able to separate the two contributions. Where there is a gap in an isotopic sequence of stable nuclei (as between ^{120}Sn and ^{122}Sn, or between ^{121}Sb and ^{123}Sb), the s process cannot continue along the sequence and must proceed after β decay to the next higher atomic number. Thus ^{122}Sn and ^{124}Sn can be produced only in the r process. Their abundances are roughly equal, 4.5 and 5.6%, but much smaller than that of ^{120}Sn, 32.4%. As a first guess, we might estimate that about 5% of the ^{120}Sn abundance of 32% is from the r process, while the remaining 27% is from the s process. On the other hand, the β decays at mass 122, 123, and 124 from r-process nuclei terminate at stable ^{122}Sn, ^{123}Sb, and ^{124}Sn, and are thus unable to reach the Te isotopes ^{122,123,124}Te, which are *shielded* from the r process. They can be produced only through the s process.

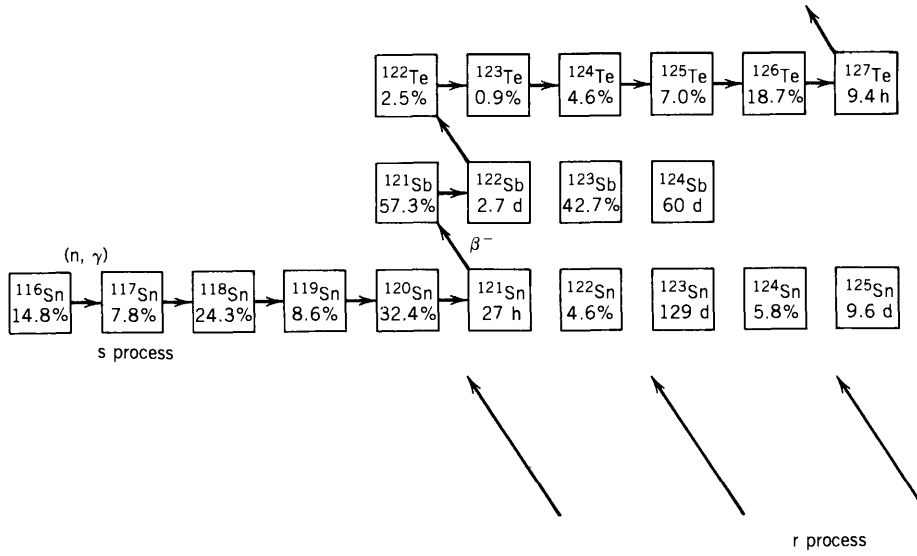


Figure 19.16 r- and s-process paths leading to Sn, Sb, and Te isotopes.

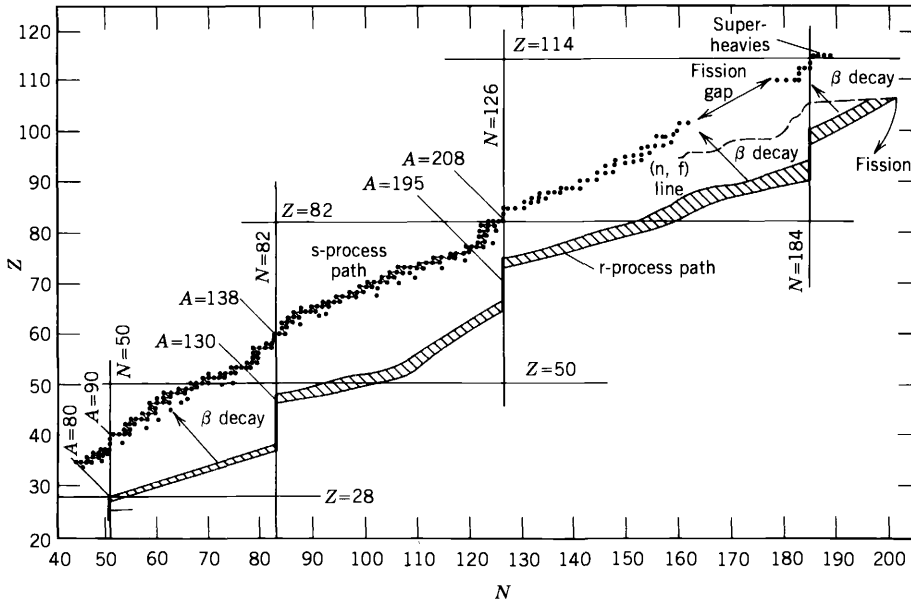


Figure 19.17 Neutron capture paths for r and s processes.

Figure 19.17 shows the complete r- and s-process paths leading to the stable isotopes in the chart of the nuclides. The s process proceeds in zigzag fashion through most of the stable isotopes, terminating at ^{209}Bi, because there are no stable (or metastable) isotopes just above $A = 209$ through which the s process could continue. The r process has no such restriction and can continue until the fission half-lives are as short as the r-process capture times. Near the termination of the r process, it may be possible to produce superheavy nuclei; such a

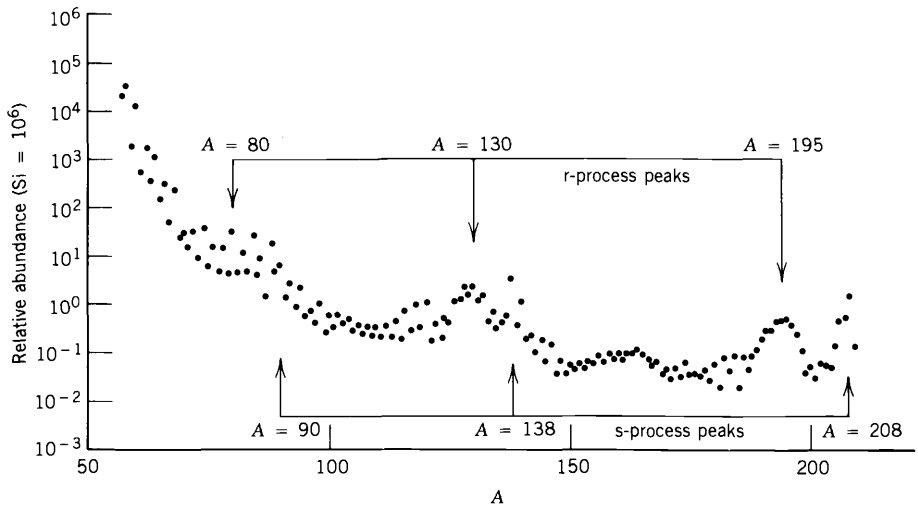


Figure 19.18 Abundances of isobars. The peaks near $A = 80$, 130, and 195 originate from the β decays of r-process progenitors with $N = 50$, 82, or 126. The peaks near $A = 90$, 138, and 208 result from s-process stable nuclei with $N = 50$, 82, or 126. Note the difference in abundance between odd-A and even-A nuclei.

possibility has inspired the search for evidence for superheavy nuclei in natural materials, thus far without success.

Near the magic numbers, the β decay times become so short that an added neutron decays to a proton in a time small compared with the r-process capture time. This accounts for the vertical rises in the r-process path at $N = 50$, 82, and 126. As these nuclei subsequently β decay toward the stable isobars, a slight overabundance of stable nuclei will result. This will occur near $A = 80$, 130, and 195, as indicated in Figure 19.18.

19.6 NUCLEAR COSMOCHRONOLOGY

In Section 6.7, we reviewed the use of radioactive dating methods to determine the age of the Earth (and of other solid objects in the Solar System). By examining the relative numbers of parent and daughter nuclei in decays with half-lives in the proper range ($\sim$ 1–10 Gy), it is possible to deduce the time since the condensation of the object. The fundamental assumption of the method is that the "ingredients" of the Earth were thoroughly mixed before condensation, so that the previous decay products of a given species would be unlikely to be found close to a collection of atoms of that species. Since condensation, there was little opportunity for migration or loss of decay products and we can, with suitable care to account for the possibility of such losses, measure the ratio of parent and daughter nuclei and deduce the length of time that the daughters have been accumulating in that particular site. Using a variety of decay processes ($^{40}K \rightarrow {}^{40}Ar$, $^{87}Rb \rightarrow {}^{87}Sr$, $^{232}Th \rightarrow {}^{208}Pb$, $^{238}U \rightarrow {}^{206}Pb$) the oldest materials from the Earth, Moon, and meteorites are dated at 4.55 Gy. The good agreement obtained with decays of differing half-lives, and using materials from differing

locations that have differing exposures to conditions that may cause loss of daughter activities, serves to confirm the validity of the method. The age of the Solar System is just a bit older than this, perhaps 4.6–4.8 Gy, representing the additional time necessary for the condensation of the solid material from the "protostar" or nebula.

The sequence of events leading to the present day is then as follows:

1. Big Bang, leading to formation of neutral atoms ($\sim 10^6$ y);
2. Condensation of galaxies and first-generation stars (time interval $\equiv \delta \sim$ 1–2 Gy);
3. Nucleosynthesis in stars and supernovae, leading to the formation of the present chemical elements (time interval $\equiv \Delta$);
4. Condensation of Solar System from debris of earlier stars (time interval $\equiv A_e$ = 4.6 Gy).

The total age of the universe (A_u) is then

$$A_u = \delta + \Delta + A_e \tag{19.36}$$

neglecting the first contribution, which is certainly very small compared with the others. The time δ for the gravitational interaction to bring together original galaxies and stars has been calculated to be in the range of 1–2 Gy. Since A_e is well known, we can determine the age of the universe if it is possible to determine the duration Δ of nucleosynthesis in first-generation stars.

The basic procedure in this process is to compare observed abundances with those calculated according to a certain model and based on fundamental processes whose rate we can determine independently, primarily through measurements in our laboratories on Earth. Because of the many uncertainties in determining the magnitude of r- and s-process contributions in nuclei that can be produced through both processes, we choose for this procedure nuclei whose production is exclusively through only one process. For the r process, we use heavy nuclei ($A > 209$), which cannot be produced through the s process. We have already alluded to one technique of this sort in Chapter 13. The $^{235}U/^{238}U$ ratio changes with time, owing to their differing half-lives (0.7 Gy for ^{235}U, 4.5 Gy for ^{238}U). The present ratio (0.00720) is then considerably different from the value at the time of condensation of the Solar System (0.29). To extrapolate back beyond that time, to formation of ^{235}U and ^{238}U in the r process, we must know something of the production processes that ultimately result in ^{235}U and ^{238}U. The r-process advance to heavier nuclei is halted when the fission half-lives become sufficiently short, and the heavy nuclei produced (which range up to $A \simeq 300$) then α and β decay to produce ^{235}U and ^{238}U. The isotope ^{238}U can be formed through β decays from the r-process nucleus at mass 238, and from α decays of nuclei at mass 242, 246, and 250 that result (ultimately) from β decays of r-process nuclei at those masses. Figure 19.19 illustrates the process. Nuclei above $A = 250$ decay primarily through spontaneous fission and thus do not contribute to the uranium abundances. We can therefore make a calculation of the "original" ratio $^{235}U/^{238}U$, based on these estimates of r-process production. Figure 19.20 is an example of the calculated results, illustrating two extreme cases—a steady-state

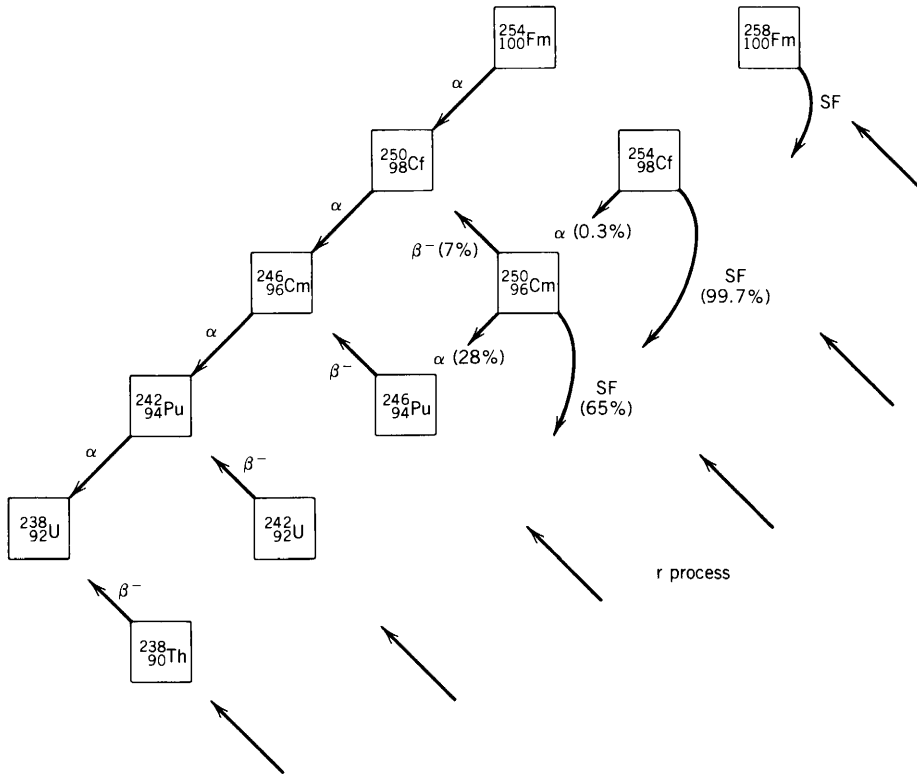


Figure 19.19 Progenitors of ^{238}U. When spontaneous fission (SF) becomes the most likely decay process (for ^{254}Cf, ^{258}Fm, and beyond), the r process cannot feed the α-decay chain leading to ^{238}U. Production of ^{238}U from the r process therefore occurs only at A = 238, 242, 246, and 250.

production, in which the ratio is constant in time until production ends, following which the ratio decays to its present value over 4.5 Gy, and a sudden production, which produces all of the ^{235}U and ^{238}U in their original abundance ratio (1.64), which then decays freely to the present value. In the former case, we can make no prediction of the length of time during which this production occurred; in the latter case, the time Δ between nucleosynthesis and condensation of the Solar System is 2 Gy.

A more acceptable scenario is that during the interval Δ, r-process events went on gradually and continuously, as also did the relative decays of ^{235}U and ^{238}U. Constructing an appropriate model for the production of r-process nuclei, we can then check it against abundances directly measured for stable nuclei produced exclusively through the r process. Finally, we can use the model to compute the unmeasurable abundances of the r-process progenitors of ^{235}U and ^{238}U, and we can extrapolate the production-plus-decay rates backward in time until they match the calculated abundance ratio at the beginning of galactic nucleosynthesis. Figure 19.21 shows the result of this calculation, along with a similar result for the ^{232}Th/^{238}U ratio. The deduced most probable value for Δ is 6 Gy, with a

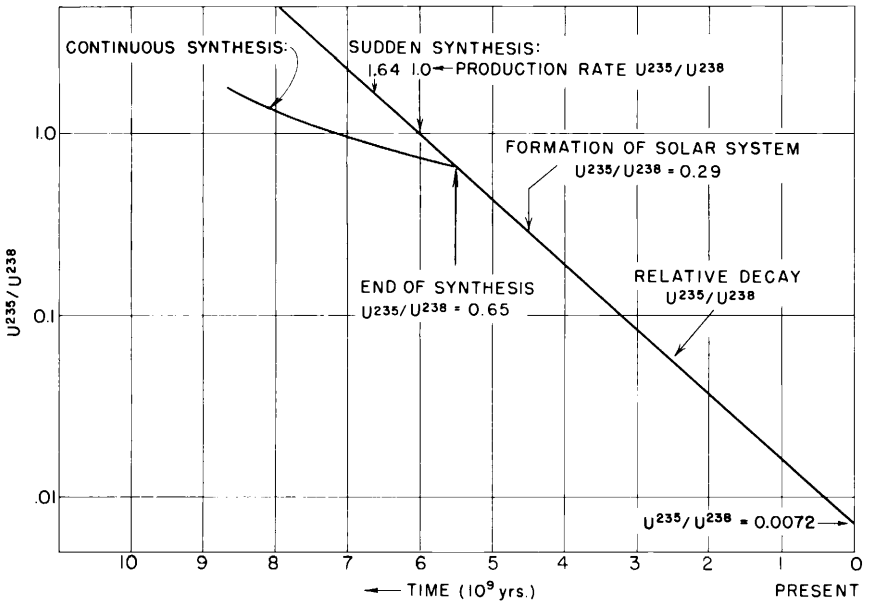


Figure 19.20 Ratio of abundances of ^{235}U and ^{238}U over time, leading to the present value of 0.0072. Various scenarios are shown which may have produced the original nuclides. From Burbidge, Burbidge, Fowler, and Hoyle, *Rev. Mod. Phys.* **29**, 547 (1957).

permitted range (based on the uncertainties inherent in the calculations) from about 4 to 9 Gy.

Such models may also include a "pre-solar spike," a sudden deposit of r-process products just at the time condensation began. (Indeed, there are some theories that suggest a cataclysmic event such as a supernova was responsible for the condensation of the Solar System.) Evidence in support of the spike comes from the abundances of the products of short-lived (on the Gy time scale) decays of r-process nuclei, including ^{129}I (16 My), ^{244}Pu (81 My), and ^{26}Al (0.72 My).

An alternative approach to determining Δ comes from an s-process argument. Figure 19.22 shows the s- and r-process paths through the Os and Re nuclei. The isotope ^{187}Re is an r-process nucleus and decays to ^{187}Os with a half-life of 40 Gy, in just the proper range to be used as a decay chronometer. If we could compare the abundance of ^{187}Re with that of its ^{187}Os daughter, we could deduce the interval during which the ^{187}Re has been decaying. Unfortunately, ^{187}Os is also produced directly in the s process, so this determination requires a careful computation of the s-process abundance of the Os isotopes. We can use the standard s-process formula, $\sigma_A N_A = \sigma_{A-1} N_{A-1}$, for this purpose if we know the cross sections for neutron capture, given that the abundance of ^{186}Os is from the s process alone, since it is shielded from the r-process by ^{186}W. A difficulty with this procedure is that the first excited state of ^{187}Os is at an energy of only 10 keV; at stellar temperatures, $kT \approx 20$ keV, and the excited state is expected to be strongly populated. Moreover, the excited state has spin $I = \frac{3}{2}$, while the ground state has $I = \frac{1}{2}$; thus the statistical weight $(2I + 1)$ of the excited state is

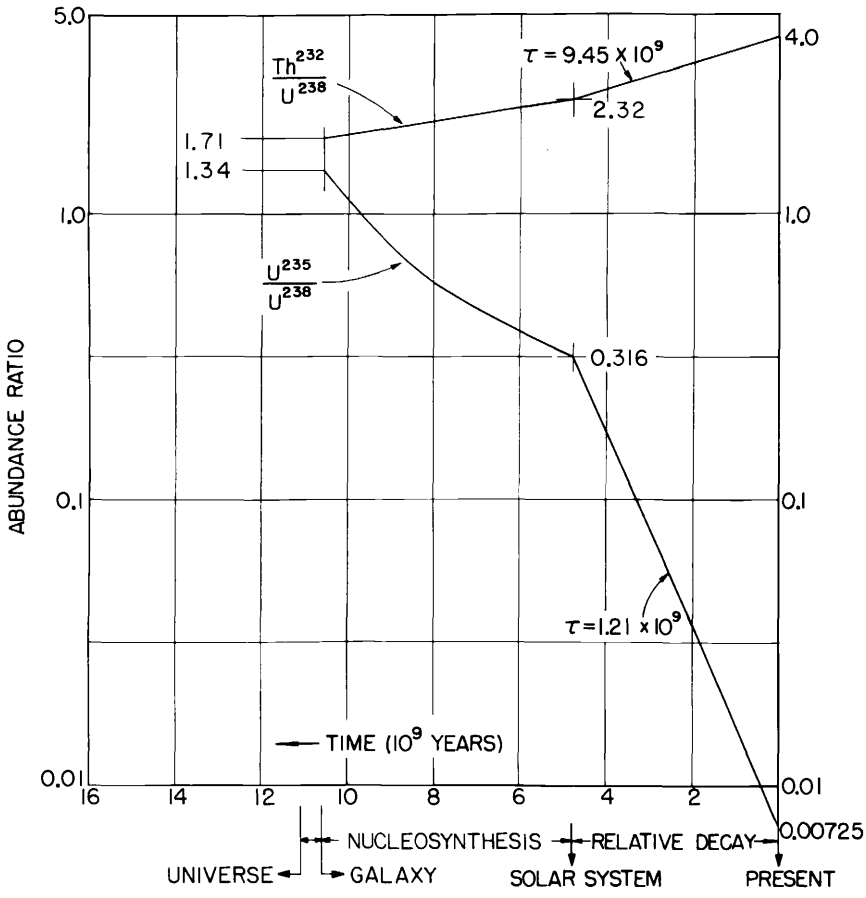


Figure 19.21 Possible scenario leading to present abundance ratio of ^{235}U and ^{238}U. The r process and decay contribute during the nucleosynthesis era (Δ), perhaps resulting from many supernovas ejecting r-process nuclei into the interstellar medium. After the solar system began to condense, no new r-process nuclei were added; the abundance ratio then decayed freely to its present value. From W. A. Fowler, *Quarterly Journal of the Royal Astronomical Society* (1987); courtesy W. A. Fowler.

twice that of the ground state. The analysis therefore requires measurement of the neutron-capture cross section of the excited state as well as the ground state. The measurement of the ground-state capture cross section is relatively easy, but the excited state is not populated in 300 K Earthly laboratories, and it cannot serve as a target for neutron reactions. Two differing approaches have been used to attack this problem. In one, the capture cross section of the ^{189}Os ground state is measured. This state happens to have the same nuclear structure as the ^{187}Os excited state, and its measurement can be applied to the determination of the cross section of the ^{187}Os excited state. In the second method, the inelastic

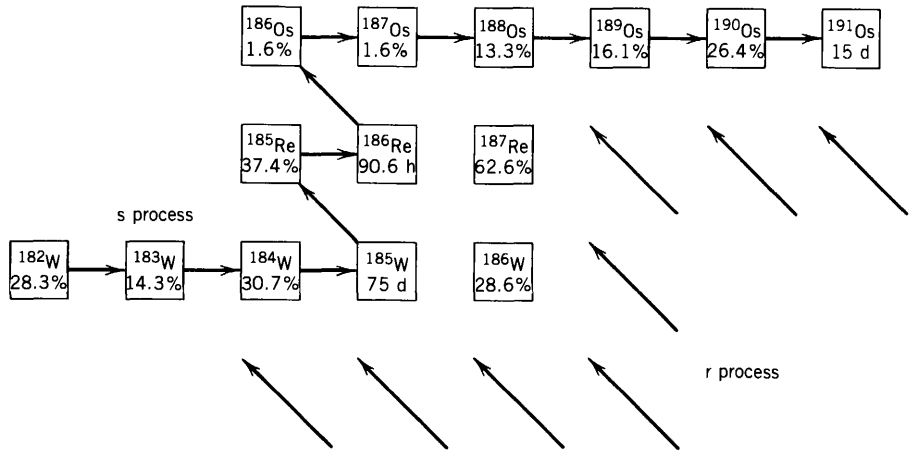


Figure 19.22 r- and s-process formation of Re and Os isotopes.

scattering cross section has been measured for ^{187}Os(n, n′)^{187}Os*, permitting a determination of the scattering amplitudes and phase shifts, from which the capture cross section can be calculated. Both measurements are done with neutron energies in the astrophysical range (30–60 keV). These methods give values for Δ in the range of 9–12 Gy, with uncertainties of about $\pm 20\%$. The lower end of this range is consistent with the value of Δ determined from the $^{235}U/^{238}U$ ratio, but both methods depend on assumptions that need further theoretical and experimental tests before either calculation is accepted as reliable. If we accept the value $\Delta = 8 \pm 2$ Gy as a fair compromise, then

$$A_u = 14 \pm 2 \text{ Gy}$$

Other model-dependent determinations of the age of the universe may be consistent with this value. The Hubble age H^{-1} is 15 Gy for $H = 67$ km/s/Mpc, but H^{-1} is equal to A_u only in a universe that has been expanding at a constant rate since $t = 0$. Any realistic cosmology includes a gravitational deceleration, and so $A_u < H^{-1}$. If there is just enough matter to "close" the universe (that is, eventually to halt the expansion only as $R \to \infty$), then $A_u = \frac{2}{3}H^{-1} = 10$ Gy, in rough agreement with the above value deduced from nucleosynthesis. However, the Hubble parameter itself is uncertain by a factor of 2 (the present literature includes values as high as 100 km/s/Mpc), so perhaps the agreement is accidental; there are also claims for values of Δ from nucleosynthesis that would lead to an age of about 18 Gy. In any case, the determination of the value of Δ is likely to remain an active pursuit in experimental and theoretical nuclear physics, demonstrating once again the fundamental importance of nuclear physics for understanding astrophysical processes.

REFERENCES FOR ADDITIONAL READING

There are many excellent and inspiring popular-level books on cosmology that provide interesting background reading for this chapter. Among them are T. Ferris, *The Red Limit* (New York: Morrow, 1977); S. Weinberg, *The First Three Minutes* (New York: Basic Books, 1977); J. Silk, *The Big Bang* (San Francisco: Freeman, 1980).

Other elementary and intermediate (in mathematical level) texts are E. R. Harrison, *Cosmology* (Cambridge: Cambridge University Press, 1981); M. Rowan-Robinson, *Cosmology* (Oxford: Clarendon Press, 1981); P. J. E. Peebles, *Physical Cosmology* (Princeton: Princeton University Press, 1971); M. Berry, *Principles of Cosmology and Gravitation* (Cambridge: Cambridge University Press, 1976); P. T. Landsberg and D. A. Evans, *Mathematical Cosmology* (Oxford: Clarendon Press, 1977); J. V. Narlikar, *Introduction to Cosmology* (Portola Valley, CA: Jones and Bartlett, 1983); H. S. Goldberg and M. D. Scadron, *Physics of Stellar Evolution and Cosmology* (New York: Gordon & Breach, 1981).

The advanced mathematical theory can be found in S. Weinberg, *Gravitation and Cosmology* (New York: Wiley, 1972) and C. W. Misner, K. S. Thorne, and J. A. Wheeler, *Gravitation* (San Francisco: Freeman, 1973).

No detailed study of nucleosynthesis would be complete without a reading of the classic review article known in the literature as B^2FH: G. R. Burbidge, E. M. Burbidge, W. A. Fowler, and F. Hoyle, *Rev. Mod. Phys.* **29**, 547 (1957). Additional details on nucleosynthesis can be found in H. Reeves, *Stellar Evolution and Nucleosynthesis* (New York: Gordon & Breach, 1968) and in D. D. Clayton, *Principles of Stellar Evolution and Nucleosynthesis* (New York: McGraw-Hill, 1968). More recent review papers on nucleosynthesis include J. W. Truran, *Ann. Rev. Nucl. Part. Sci.* **34**, 53 (1984), G. J. Mathews and R. A. Ward, *Reports on Progress in Physics* **48**, 1371 (1985), and A. M. Boesgaard and G. Steigman, *Ann. Rev. Astron. Astrophys.* **23**, 319 (1985).

The contributions of George Gamow and William A. Fowler to the fields of cosmology and nucleosynthesis have been celebrated in two volumes of short contributions by their colleagues: *Cosmology, Fusion, and Other Matters*, edited by F. Reines (Boulder: Colorado Associated University Press, 1972) and *Essays in Nuclear Astrophysics*, edited by C. A. Barnes, D. D. Clayton, and D. N. Schramm (Cambridge: Cambridge University Press, 1982). Fowler's contributions to nuclear astrophysics are also summarized in his Nobel Prize address, reprinted in *Rev. Mod. Phys.* **56**, 149 (1984).

The strong relationship between nuclear physics and astrophysics is emphasized in the review by C. Rolfs and H. P. Trautvetter, *Ann. Rev. Nucl. Part. Sci.* **28**, 115 (1978). The similarly strong connection between cosmology and particle physics is discussed by G. Steigman, *Ann. Rev. Nucl. Part. Sci.* **29**, 313 (1979).

For recent work on the determination of the age of the universe from the Os abundances and neutron cross sections, see: J. C. Browne and B. L. Berman, *Phys. Rev. C* **23**, 1434 (1981); R. R. Winters and R. L. Macklin, *Phys. Rev. C* **25**, 208 (1982); R. L. Hershberger et al., *Phys. Rev. C* **28**, 2249 (1983).

PROBLEMS

1. (a) In an expanding universe dominated by matter, the mass density should decrease like R^{-3}. Use Equation 19.3 with $k = 0$ and $\Lambda = 0$ to find $R(t)$. This case is called the Einstein-deSitter model. (b) Calculate the corresponding relationship between H^{-1} and the age of the universe in this model.
2. Derive Equation 19.5 from Equation 19.4.
3. Show that the constants in Equations 19.5 and 19.6 evaluate to give Equation 19.7.
4. Integrate Equations 19.8 and 19.9, and evaluate the constants to obtain Equations 19.10 and 19.11.
5. (a) During what era would the universe have been rich in K^0 and $\overline{K}^0$ mesons? (b) Could the interactions of these mesons with the existing nucleons and antinucleons have been responsible for the imbalance of matter and antimatter?
6. On a logarithmic time scale from 10^{-6} s to 10^3 s, make a qualitative sketch showing the time dependence of the relative numbers of free p, n, ^{2}H, ^{3}H, ^{3}He, and ^{4}He.
7. (a) Assuming a nucleon-to-photon ratio of 10^{-10}, repeat the calculation of Section 19.3 for the age of the universe when deuterium formation is permitted. (b) Assume all of the neutrons combine with an equal number of protons to make α particles. After taking into account the decrease in the number of neutrons during the time calculated in part (a) from their radioactive decay, find the resulting ratio N_{He}/N_p.
8. (a) Calculate the energy E_0 at which the stellar reaction rate, Equation 19.27, reaches its peak. (b) Calculate the width ΔE_0 by expanding Equation 19.27 in a Taylor series about E_0 and finding the energy $E_{1/2}$ at which the rate drops by half. For this calculation the width ΔE_0 is the full width at half maximum, $2(E_{1/2} - E_0)$.
9. (a) At what center-of-mass energy should we study the silicon-burning reaction $^4\text{He} + {}^{28}\text{Si}$ to duplicate stellar conditions? (b) If ^{4}He are incident in the laboratory on ^{28}Si at rest, what energy should be chosen?
10. The CNO cycle that may contribute to energy production in stars similar to the Sun begins with the reaction $\text{p} + {}^{12}\text{C} \rightarrow {}^{13}\text{N} + \gamma$. Assuming the temperature near the center of the Sun to be 15×10^6 K, find the peak energy and width of the reaction rate.
11. Trace the s-process path, in analogy with Figure 19.14, from ^{69}Zn to ^{90}Zr. Identify any stable nuclei in this region that cannot be reached in the s process, and note which nuclei are shielded from the r process.
12. Continue the previous problem from ^{90}Zr to ^{116}Sn.

Appendix B

CENTER-OF-MASS REFERENCE FRAME

Reactions are most conveniently analyzed in the center-of-mass (CM) reference frame, in which the total linear momentum of the reacting particles is zero. (As we see in the following discussion, the effects of special relativity cause the center-of-mass frame to differ from the center-of-momentum frame. For the low-energy decays and reactions that are discussed in this text, the nonrelativistic equations can be safely applied and the distinction is relatively unimportant. To be strictly correct, the CM frame should be defined as the center-of-momentum frame, as in Equation B.2 below, but with the relativistic expression for momentum, Equation A.4, replacing the classical mv.) In the laboratory (L) system, reactions are usually performed by bringing a beam of incident particles against a target of particles at rest. The observed properties of the reaction (energy and momentum of product particles, cross sections) must therefore be transformed from the L to the CM reference frame before the theory and the experiment can be compared.

B.1 REACTION KINEMATICS

The reaction to be considered will be of the form

$$\mathrm{a} + \mathrm{X} \rightarrow \mathrm{Y} + \mathrm{b}$$

in which the beam of particles of type a has a laboratory kinetic energy T_a; the target particles X are at rest in the laboratory. To avoid the confusion of multiple subscripts, all L coordinates will be represented by unprimed variables (T_a, v_a, T_Y, T_b, θ_Y, θ_b, ...), while all corresponding CM coordinates will be represented by primed variables (T_a', v_a', T_Y', ...).

For convenience we choose the incident momentum of a to be along the x direction. Then, for low energy reactions in which nonrelativistic kinematics may be used, the initial linear momenta are

$$p_x = m_\mathrm{a} v_\mathrm{a} \tag{B.1}$$

$$p_x' = m_\mathrm{a} v_\mathrm{a}' + m_\mathrm{X} v_\mathrm{X}' = 0 \tag{B.2}$$

in the L and CM frames, respectively. If v_CM represents the velocity of the CM as

measured in the L frame, then

$$v'_a = v_a - v_{CM} \tag{B.3}$$

$$v'_X = -v_{CM} \tag{B.4}$$

and it can be immediately shown that Equation B.2 is satisfied if

$$v_{CM} = v_a \frac{m_a}{m_a + m_X} \tag{B.5}$$

After the collision, the particles b and Y must move in opposite directions in the CM frame (so that the total linear momentum remains zero). The final momentum in the L frame has x and y components

$$p_x = m_b v_b \cos\theta_b + m_Y v_Y \cos\theta_Y \tag{B.6}$$

$$p_y = m_b v_b \sin\theta_b - m_Y v_Y \sin\theta_Y \tag{B.7}$$

where for convenience the relative signs of the y-components are indicated explicitly in Equation B.7 by defining θ_b and θ_Y on opposite sides of the x axis.

In the CM frame, the final particles move in the directions θ'_b and $\theta'_Y = -\theta'_b$. Along the line of motion, the total momentum must vanish, and so

$$m_b v'_b + m_Y v'_Y = 0 \tag{B.8}$$

The manipulation of Equations B.6 to B.8 leads to an interesting result: the velocity of the center of mass after the reaction is not the same as its velocity before the reaction. (This may seem to violate the classical restriction on the uniformity of CM motion under internal forces in an isolated system, but classical physics does not permit the total mass of the system to change. Because the initial mass is not equal to the final mass, their difference being the Q value, the classical equations do not strictly apply.) The relationship between the final and initial CM velocities is

$$v_{CM,f} = \left(\frac{m_a + m_X}{m_b + m_Y}\right) v_{CM,i} \tag{B.9}$$

Note that in elastic collisions, $v_{CM,f} = v_{CM,i}$. The ratio between the masses in Equation B.9 is normally very close to unity; the initial and final masses differ by the Q value, which is typically only 10^{-3} to 10^{-5} of the total mass energy for reactions at low energy.

The application of conservation of energy in the L and CM frames gives the following result for the energy of particle b:

$$T'_b = \frac{m_b}{m_Y + m_b}\left[Q + \left(1 - \frac{m_a}{m_Y + m_b}\right) T_a\right] \tag{B.10}$$

The corresponding equation for T_b in the L frame was given as Equation 11.5.

A corresponding analysis of the velocity and momentum equations gives the transformation between the angles:

$$\tan\theta_b = \frac{\sin\theta'_b}{\cos\theta'_b + \gamma} \tag{B.11}$$

where

$$\gamma = \frac{v_{\mathrm{CM}}}{v'_{\mathrm{b}}} \tag{B.12}$$

$$= \left[\frac{m_{\mathrm{a}} m_{\mathrm{b}}}{m_{\mathrm{X}} m_{\mathrm{Y}}} \frac{T_{\mathrm{a}}}{T_{\mathrm{a}} + Q(1 + m_{\mathrm{a}}/m_{\mathrm{X}})} \right]^{1/2} \tag{B.13}$$

B.2 CROSS SECTIONS

Total cross sections involve only absolute probabilities for reactions to occur, and are therefore unaffected by the transformation between the L and CM frames. Differential cross sections, however, involve angular variables and are therefore dependent on the frame of reference.

The number of particles hitting a small detector is $d\sigma$ in both frames, and writing $d\sigma = (d\sigma/d\Omega)\, d\Omega \equiv \sigma(\theta)\, d\Omega$, the relationship between the differential cross sections follows:

$$d\sigma = \sigma(\theta)\, d\Omega = \sigma(\theta')\, d\Omega' \tag{B.14}$$

Given a measured laboratory differential cross section $\sigma(\theta)$, the CM differential cross section can be obtained as

$$\sigma(\theta') = \sigma(\theta) \frac{d\Omega}{d\Omega'} \tag{B.15}$$

Integrating over the uninteresting azimuthal variable in both frames, we have $d\Omega = 2\pi \sin\theta\, d\theta$ and $d\Omega' = 2\pi \sin\theta'\, d\theta'$, and from Equation B.11, it follows that

$$\frac{d\Omega}{d\Omega'} = \frac{|1 + \gamma \cos\theta'|}{(1 + 2\gamma \cos\theta' + \gamma^2)^{3/2}} \tag{B.16}$$

B.3 THE CM SCHRÖDINGER EQUATION

The Schrödinger equation that governs the mutual interaction of the reacting particles can also be reduced to a CM form. For two particles, the combined equation in Cartesian coordinates can be written

$$-\frac{\hbar^2}{2m_{\mathrm{a}}}\left(\frac{\partial^2\Psi}{\partial x_{\mathrm{a}}^2} + \frac{\partial^2\Psi}{\partial y_{\mathrm{a}}^2} + \frac{\partial^2\Psi}{\partial z_{\mathrm{a}}^2}\right) - \frac{\hbar^2}{2m_{\mathrm{X}}}\left(\frac{\partial^2\Psi}{\partial x_{\mathrm{X}}^2} + \frac{\partial^2\Psi}{\partial y_{\mathrm{X}}^2} + \frac{\partial^2\Psi}{\partial z_{\mathrm{X}}^2}\right)$$
$$+ V(\boldsymbol{r}_{\mathrm{a}}, \boldsymbol{r}_{\mathrm{X}})\Psi = E\Psi \tag{B.17}$$

where $\boldsymbol{r}_{\mathrm{a}} = (x_{\mathrm{a}}, y_{\mathrm{a}}, z_{\mathrm{a}})$ and $\boldsymbol{r}_{\mathrm{X}} = (x_{\mathrm{X}}, y_{\mathrm{X}}, z_{\mathrm{X}})$ represent the coordinates of the particles and Ψ represents the combined wave function. Defining the CM coordinate $\boldsymbol{R} = (X, Y, Z) = (m_{\mathrm{a}}\boldsymbol{r}_{\mathrm{a}} + m_{\mathrm{X}}\boldsymbol{r}_{\mathrm{X}})/(m_{\mathrm{a}} + m_{\mathrm{X}})$ and the relative coordinate $\boldsymbol{r} = (x, y, z) = \boldsymbol{r}_{\mathrm{a}} - \boldsymbol{r}_{\mathrm{X}}$, then the partial derivatives can be written in terms

of the new coordinates. For example,

$$\frac{\partial \Psi}{\partial x_a} = \frac{\partial \Psi}{\partial X}\frac{\partial X}{\partial x_a} + \frac{\partial \Psi}{\partial x}\frac{\partial x}{\partial x_a}$$
$$= \frac{m_a}{m_a + m_X}\frac{\partial \Psi}{\partial X} + \frac{\partial \Psi}{\partial x}$$

and so on for all first and second partials. The result is

$$-\frac{\hbar^2}{2M}\left(\frac{\partial^2 \Psi}{\partial X^2} + \frac{\partial^2 \Psi}{\partial Y^2} + \frac{\partial^2 \Psi}{\partial Z^2}\right) - \frac{\hbar^2}{2m}\left(\frac{\partial^2 \Psi}{\partial x^2} + \frac{\partial^2 \Psi}{\partial y^2} + \frac{\partial^2 \Psi}{\partial z^2}\right) + V\Psi = E\Psi \tag{B.18}$$

where the terms involve respectively the total mass $M = m_a + m_X$ and the *reduced mass* $m = m_a m_X/(m_a + m_X)$. If the potential depends only on the relative coordinate $\boldsymbol{r}$, then the equation is *separable* into one part that depends only on the CM motion and another relative part that involves the interaction. The wave function separates as $\Psi = \psi_{CM}(X, Y, Z)\psi(x, y, z)$. The CM part has the form of a single particle of mass M moving freely (that is, a plane wave). The relative part ψ is the solution of

$$-\frac{\hbar^2}{2m}\left(\frac{\partial^2 \psi}{\partial x^2} + \frac{\partial^2 \psi}{\partial y^2} + \frac{\partial^2 \psi}{\partial z^2}\right) + V(\boldsymbol{r})\psi = E\psi \tag{B.19}$$

where $\psi(x, y, z)$ is the wave function representing the interaction of the particles. This simplified form of the two-body equation now only requires that we solve the Schrödinger equation for a single particle of the reduced mass m moving in a fixed potential $V(\boldsymbol{r})$ that is identical with the two-body laboratory potential. The resulting solution can be used to evaluate cross sections that can then be compared with laboratory cross sections using the transformation Equations B.15 and B.16. Equation B.19 can also be written in spherical polar coordinates; see Equation 2.16.

Appendix C

TABLE OF NUCLEAR PROPERTIES

The following table shows some properties of a selection of isotopes. For each element only the stable and relatively long-lived radioactive isotopes are included. Ground-state atomic masses and spin-parity assignments are shown for all isotopes; uncertain spin-parity assignments are in parentheses. Abundances are given for stable isotopes, and for radioactive isotopes the half-life and principal decay mode are shown (ε—electron capture, possibly including positron emission; β^-—negative beta decay; α—alpha decay; f—spontaneous fission). The masses are those of the corresponding neutral atoms and were taken from the 1983 atomic mass evaluation: A. H. Wapstra and G. Audi, *Nucl. Phys.* **A432**, 1 (1985). In the half-life entries, My = 10^6 y. Uncertainties in the masses are typically 10^{-5} u (10^{-4} u for some cases far from stability); uncertainties in the abundances and half-lives are typically at or below the level of the last digit tabulated.

	Z	A	Atomic mass (u)	I^π	*Abundance* or Half-life
H	1	1	1.007825	$\frac{1}{2}^+$	*99.985%*
		2	2.014102	1^+	*0.015%*
		3	3.016049	$\frac{1}{2}^+$	12.3 y (β^-)
He	2	3	3.016029	$\frac{1}{2}^+$	*1.38 × 10⁻⁴%*
		4	4.002603	0^+	*99.99986%*
Li	3	6	6.015121	1^+	*7.5%*
		7	7.016003	$\frac{3}{2}^-$	*92.5%*
		8	8.022486	2^+	0.84 s (β^-)
Be	4	7	7.016928	$\frac{3}{2}^-$	53.3 d (ε)
		8	8.005305	0^+	0.07 fs (α)
		9	9.012182	$\frac{3}{2}^-$	*100 %*
		10	10.013534	0^+	1.6 My (β^-)
		11	11.021658	$\frac{1}{2}^+$	13.8 s (β^-)
B	5	8	8.024606	2^+	0.77 s (ε)
		9	9.013329	$\frac{3}{2}^-$	0.85 as (α)
		10	10.012937	3^+	*19.8%*
		11	11.009305	$\frac{3}{2}^-$	*80.2%*
		12	12.014353	1^+	20.4 ms (β^-)
		13	13.017780	$\frac{3}{2}^-$	17.4 ms (β^-)
C	6	9	9.031039	$\frac{3}{2}^-$	0.13 s (ε)
		10	10.016856	0^+	19.2 s (ε)
		11	11.011433	$\frac{3}{2}^-$	20.4 m (ε)
		12	12.000000	0^+	*98.89%*
		13	13.003355	$\frac{1}{2}^-$	*1.11%*
		14	14.003242	0^+	5730 y (β^-)
		15	15.010599	$\frac{1}{2}^+$	2.45 s (β^-)
N	7	12	12.018613	1^+	11 ms (ε)
		13	13.005739	$\frac{1}{2}^-$	9.96 m (ε)
		14	14.003074	1^+	*99.63%*
		15	15.000109	$\frac{1}{2}^-$	*0.366%*
		16	16.006100	2^-	7.13 s (β^-)

	Z	A	Atomic mass (u)	I^π	*Abundance* or Half-life
		17	17.008450	$\frac{1}{2}^-$	4.17 s (β^-)
		18	18.014081	1^-	0.63 s (β^-)
O	8	14	14.008595	0^+	71 s (ε)
		15	15.003065	$\frac{1}{2}^-$	122 s (ε)
		16	15.994915	0^+	*99.76%*
		17	16.999131	$\frac{5}{2}^+$	*0.038%*
		18	17.999160	0^+	*0.204%*
		19	19.003577	$\frac{5}{2}^+$	26.9 s (β^-)
		20	20.004076	0^+	13.5 s (β^-)
F	9	17	17.002095	$\frac{5}{2}^+$	64.5 s (ε)
		18	18.000937	1^+	110 m (ε)
		19	18.998403	$\frac{1}{2}^+$	*100 %*
		20	19.999981	2^+	11 s (β^-)
		21	20.999948	$\frac{5}{2}^+$	4.3 s (β^-)
		22	22.003030	$(3,4)^+$	4.2 s (β^-)
		23	23.003600	$(\frac{3}{2},\frac{5}{2})^+$	2.2 s (β^-)
Ne	10	17	17.017690	$\frac{1}{2}^-$	0.11 s (ε)
		18	18.005710	0^+	1.7 s (ε)
		19	19.001880	$\frac{1}{2}^+$	17.3 s (ε)
		20	19.992436	0^+	*90.51%*
		21	20.993843	$\frac{3}{2}^+$	*0.27%*
		22	21.991383	0^+	*9.22%*
		23	22.994465	$\frac{5}{2}^+$	37.6 s (β^-)
		24	23.993613	0^+	3.4 m (β^-)
		25	24.997690	$(\frac{1}{2},\frac{3}{2})^+$	0.60 s (β^-)
Na	11	20	20.007344	2^+	0.45 s (ε)
		21	20.997651	$\frac{3}{2}^+$	22.5 s (ε)
		22	21.994434	3^+	2.60 y (ε)
		23	22.989768	$\frac{3}{2}^+$	*100 %*
		24	23.990961	4^+	15.0 h (β^-)
		25	24.989953	$\frac{5}{2}^+$	60 s (β^-)
		26	25.992586	3^+	1.1 s (β^-)
		27	26.993940	$\frac{5}{2}^+$	0.30 s (β^-)
Mg	12	21	21.011716	$(\frac{3}{2},\frac{5}{2})^+$	0.123 s (ε)
		22	21.999574	0^+	3.86 s (ε)
		23	22.994124	$\frac{3}{2}^+$	11.3 s (ε)
		24	23.985042	0^+	*78.99%*
		25	24.985837	$\frac{5}{2}^+$	*10.00%*
		26	25.982594	0^+	*11.01%*
		27	26.984341	$\frac{1}{2}^+$	9.46 m (β^-)
		28	27.983877	0^+	21.0 h (β^-)
		29	28.988480	$\frac{3}{2}^+$	1.4 s (β^-)
Al	13	24	23.999941	4^+	2.07 s (ε)
		25	24.990429	$\frac{5}{2}^+$	7.18 s (ε)
		26	25.986892	5^+	0.72 My (ε)
		27	26.981539	$\frac{5}{2}^+$	*100 %*
		28	27.981910	3^+	2.24 m (β^-)
		29	28.980446	$\frac{5}{2}^+$	6.6 m (β^-)
		30	29.982940	3^+	3.7 s (β^-)
Si	14	26	25.992330	0^+	2.21 s (ε)
		27	26.986704	$\frac{5}{2}^+$	4.13 s (ε)
		28	27.976927	0^+	*92.23%*
		29	28.976495	$\frac{1}{2}^+$	*4.67%*
		30	29.973770	0^+	*3.10%*
		31	30.975362	$\frac{3}{2}^+$	2.62 h (β^-)
		32	31.974148	0^+	105 y (β^-)
		33	32.997920	$(\frac{3}{2}^+)$	6.2 s (β^-)
P	15	29	28.981803	$\frac{1}{2}^+$	4.1 s (ε)
		30	29.978307	1^+	2.50 m (ε)
		31	30.973762	$\frac{1}{2}^+$	*100 %*
		32	31.973907	1^+	14.3 d (β^-)
		33	32.971725	$\frac{1}{2}^+$	25.3 d (β^-)
		34	33.973636	1^+	12.4 s (β^-)
S	16	30	29.984903	0^+	1.2 s (ε)
		31	30.979554	$\frac{1}{2}^+$	2.6 s (ε)
		32	31.972071	0^+	*95.02%*
		33	32.971458	$\frac{3}{2}^+$	*0.75%*
		34	33.967867	0^+	*4.21%*
		35	34.969032	$\frac{3}{2}^+$	87.4 d (β^-)
		36	35.967081	0^+	*0.017%*
		37	36.971126	$\frac{7}{2}^-$	5.0 m (β^-)
		38	37.971162	0^+	170 m (β^-)
Cl	17	33	32.977452	$\frac{3}{2}^+$	2.51 s (ε)
		34	33.973763	0^+	1.53 s (ε)
		35	34.968853	$\frac{3}{2}^+$	*75.77%*
		36	35.968307	2^+	0.30 My (β^-)
		37	36.965903	$\frac{3}{2}^+$	*24.23%*
		38	37.968011	2^-	37.3 m (β^-)
		39	38.968005	$\frac{3}{2}^+$	56 m (β^-)
		40	39.970440	2^-	1.35 m (β^-)
		41	40.970590	$(\frac{1}{2},\frac{3}{2})^+$	31 s (β^-)
Ar	18	34	33.980269	0^+	0.844 s (ε)
		35	34.975256	$\frac{3}{2}^+$	1.78 s (ε)
		36	35.967546	0^+	*0.337%*
		37	36.966776	$\frac{3}{2}^+$	35.0 d (ε)
		38	37.962732	0^+	*0.063%*
		39	38.964314	$\frac{7}{2}^-$	269 y (β^-)
		40	39.962384	0^+	*99.60%*
		41	40.964501	$\frac{7}{2}^-$	1.83 h (β^-)

	Z	A	Atomic mass (u)	I^π	*Abundance* or Half-life
		42	41.963050	0^+	33 y (β^-)
		43	42.965670		5.4 m (β^-)
		44	43.965365	0^+	11.9 m (β^-)
K	19	37	36.973377	$\frac{3}{2}^+$	1.23 s (ε)
		38	37.969080	3^+	7.61 m (ε)
		39	38.963707	$\frac{3}{2}^+$	*93.26%*
		40	39.963999	4^-	1.28 Gy (β^-)
		41	40.961825	$\frac{3}{2}^+$	*6.73%*
		42	41.962402	2^-	12.4 h (β^-)
		43	42.960717	$\frac{3}{2}^-$	22.3 h (β^-)
		44	43.961560	2^-	22.1 m (β^-)
		45	44.960696	$\frac{3}{2}^+$	17 m (β^-)
		46	45.961976	(2^-)	115 s (β^-)
		47	46.961677	$\frac{1}{2}^+$	17.5 s (β^-)
Ca	20	38	37.976318	0^+	0.44 s (ε)
		39	38.970718	$\frac{3}{2}^+$	0.86 s (ε)
		40	39.962591	0^+	*96.94%*
		41	40.962278	$\frac{7}{2}^-$	0.10 My (ε)
		42	41.958618	0^+	*0.647%*
		43	42.958766	$\frac{7}{2}^-$	*0.135%*
		44	43.955481	0^+	*2.09%*
		45	44.956185	$\frac{7}{2}^-$	165 d (β^-)
		46	45.953689	0^+	*0.0035%*
		47	46.954543	$\frac{7}{2}^-$	4.54 d (β^-)
		48	47.952533	0^+	*0.187%*
		49	48.955672	$\frac{3}{2}^-$	8.72 m (β^-)
		50	49.957519	0^+	14 s (β^-)
Sc	21	42	41.965514	0^+	0.68 s (ε)
		43	42.961150	$\frac{7}{2}^-$	3.89 h (ε)
		44	43.959404	2^+	3.93 h (ε)
		45	44.955910	$\frac{7}{2}^-$	*100 %*
		46	45.955170	4^+	83.8 d (β^-)
		47	46.952409	$\frac{7}{2}^-$	3.35 d (β^-)
		48	47.952235	6^+	43.7 h (β^-)
		49	48.950022	$\frac{7}{2}^-$	57.0 m (β^-)
		50	49.952186	5^+	1.71 m (β^-)
Ti	22	43	42.968523	$\frac{7}{2}^-$	0.51 s (ε)
		44	43.959690	0^+	54 y (ε)
		45	44.958124	$\frac{7}{2}^-$	3.09 h (ε)
		46	45.952629	0^+	*8.2%*
		47	46.951764	$\frac{5}{2}^-$	*7.4%*
		48	47.947947	0^+	*73.7%*
		49	48.947871	$\frac{7}{2}^-$	*5.4%*
		50	49.944792	0^+	*5.2%*
		51	50.946616	$\frac{3}{2}^-$	5.80 m (β^-)
		52	51.946898	0^+	1.7 m (β^-)
		53	52.949730	$(\frac{3}{2})^-$	33 s (β^-)
V	23	46	45.960198	0^+	0.42 s (ε)
		47	46.954906	$\frac{3}{2}^-$	32.6 m (ε)
		48	47.952257	4^+	16.0 d (ε)
		49	48.948517	$\frac{7}{2}^-$	330 d (ε)
		50	49.947161	6^+	*0.250%*
		51	50.943962	$\frac{7}{2}^-$	*99.750%*
		52	51.944778	3^+	3.76 m (β^-)
		53	52.944340	$\frac{7}{2}^-$	1.6 m (β^-)
		54	53.946442	$(3,4,5)^+$	50 s (β^-)
Cr	24	46	45.968360	0^+	0.26 s (ε)
		47	46.962905	$\frac{3}{2}^-$	0.51 s (ε)
		48	47.954033	0^+	21.6 h (ε)
		49	48.951338	$\frac{5}{2}^-$	41.9 m (ε)
		50	49.946046	0^+	*4.35%*
		51	50.944768	$\frac{7}{2}^-$	27.7 d (ε)
		52	51.940510	0^+	*83.79%*
		53	52.940651	$\frac{3}{2}^-$	*9.50%*
		54	53.938882	0^+	*2.36%*
		55	54.940842	$\frac{3}{2}^-$	3.50 m (β^-)
		56	55.940643		5.9 m (β^-)
Mn	25	50	49.954240	0^+	0.28 s (ε)
		51	50.948213	$\frac{5}{2}^-$	46.2 m (ε)
		52	51.945568	6^+	5.59 d (ε)
		53	52.941291	$\frac{7}{2}^-$	3.7 My (ε)
		54	53.940361	3^+	312 d (ε)
		55	54.938047	$\frac{5}{2}^-$	*100 %*
		56	55.938907	3^+	2.58 h (β^-)
		57	56.938285	$\frac{5}{2}^-$	1.6 m (β^-)
		58	57.940060	3^+	65 s (β^-)
Fe	26	51	50.956825	$(\frac{5}{2})^-$	0.25 s (ε)
		52	51.948114	0^+	8.27 h (ε)
		53	52.945310	$\frac{7}{2}^-$	8.51 m (ε)
		54	53.939613	0^+	*5.8%*
		55	54.938296	$\frac{3}{2}^-$	2.7 y (ε)
		56	55.934939	0^+	*91.8%*
		57	56.935396	$\frac{1}{2}^-$	*2.15%*
		58	57.933277	0^+	*0.29%*
		59	58.934877	$\frac{3}{2}^-$	44.6 d (β^-)
		60	59.934078	0^+	1.5 My (β^-)
		61	60.936748	$(\frac{3}{2},\frac{5}{2})^-$	6.0 m (β^-)
		62	61.936773	0^+	68 s (β^-)
Co	27	54	53.948460	0^+	0.19 s (ε)

	Z	A	Atomic mass (u)	I^π	*Abundance* or Half-life
		55	54.942001	$\frac{7}{2}^-$	17.5 h (ε)
		56	55.939841	4^+	78.8 d (ε)
		57	56.936294	$\frac{7}{2}^-$	271 d (ε)
		58	57.935755	2^+	70.8 d (ε)
		59	58.933198	$\frac{7}{2}^-$	*100 %*
		60	59.933820	5^+	5.27 y (β^-)
		61	60.932478	$\frac{7}{2}^-$	1.65 h (β^-)
		62	61.934060	2^+	1.5 m (β^-)
		63	62.933614	$(\frac{7}{2})^-$	27.5 s (β^-)
Ni	28	55	54.951336	$\frac{7}{2}^-$	0.19 s (ε)
		56	55.942134	0^+	6.10 d (ε)
		57	56.939799	$\frac{3}{2}^-$	36.0 h (ε)
		58	57.935346	0^+	*68.3%*
		59	58.934349	$\frac{3}{2}^-$	0.075 My (ε)
		60	59.930788	0^+	*26.1%*
		61	60.931058	$\frac{3}{2}^-$	*1.13%*
		62	61.928346	0^+	*3.59%*
		63	62.929670	$\frac{1}{2}^-$	100 y (β^-)
		64	63.927968	0^+	*0.91%*
		65	64.930086	$\frac{5}{2}^-$	2.52 h (β^-)
		66	65.929116	0^+	54.8 h (β^-)
		67	66.931570	?	21 s (β^-)
Cu	29	59	58.939503	$\frac{3}{2}^-$	82 s (ε)
		60	59.937366	2^+	23.4 m (ε)
		61	60.933461	$\frac{3}{2}^-$	3.41 h (ε)
		62	61.932586	1^+	9.73 m (ε)
		63	62.929599	$\frac{3}{2}^-$	*69.2%*
		64	63.292766	1^+	12.7 h (ε)
		65	64.927793	$\frac{3}{2}^-$	*30.8%*
		66	65.928872	1^+	5.10 m (β^-)
		67	66.927747	$\frac{3}{2}^-$	61.9 h (β^-)
		68	67.929620	1^+	31 s (β^-)
Zn	30	61	60.939514	$\frac{3}{2}^-$	89 s (ε)
		62	61.934332	0^+	9.2 h (ε)
		63	62.933214	$\frac{3}{2}^-$	38.1 m (ε)
		64	63.929145	0^+	*48.6%*
		65	64.929243	$\frac{5}{2}^-$	244 d (ε)
		66	65.926035	0^+	*27.9%*
		67	66.927129	$\frac{5}{2}^-$	*4.10%*
		68	67.924846	0^+	*18.8%*
		69	68.926552	$\frac{1}{2}^-$	56 m (β^-)
		70	69.925325	0^+	*0.62%*
		71	70.927727	$\frac{1}{2}^-$	2.4 m (β^-)
		72	71.926856	0^+	46.5 h (β^-)
		73	72.929780	$(\frac{3}{2})^-$	24 s (β^-)
Ga	31	64	63.936836	0^+	2.6 m (ε)
		65	64.932738	$\frac{3}{2}^-$	15.2 m (ε)
		66	65.931590	0^+	9.4 h (ε)
		67	66.928204	$\frac{3}{2}^-$	78.3 h (ε)
		68	67.927982	1^+	68.1 m (ε)
		69	68.925580	$\frac{3}{2}^-$	*60.1%*
		70	69.926028	1^+	21.1 m (β^-)
		71	70.924701	$\frac{3}{2}^-$	*39.9%*
		72	71.926365	3^-	14.1 h (β^-)
		73	72.925169	$\frac{3}{2}^-$	4.87 h (β^-)
		74	73.926940	$(4)^-$	8.1 m (β^-)
		75	74.926499	$\frac{3}{2}^-$	2.1 m (β^-)
Ge	32	66	65.933847	0^+	2.3 h (ε)
		67	66.932737	$(\frac{1}{2})^-$	19.0 m (ε)
		68	67.928096	0^+	271 d (ε)
		69	68.927969	$\frac{5}{2}^-$	39.0 h (ε)
		70	69.924250	0^+	*20.5%*
		71	70.924954	$\frac{1}{2}^-$	11.2 d (ε)
		72	71.922079	0^+	*27.4%*
		73	72.923463	$\frac{9}{2}^+$	*7.8%*
		74	73.921177	0^+	*36.5%*
		75	74.922858	$\frac{1}{2}^-$	82.8 m (β^-)
		76	75.921402	0^+	*7.8%*
		77	76.923548	$\frac{7}{2}^+$	11.3 h (β^-)
		78	77.922853	0^+	1.45 h (β^-)
		79	78.925360	$(\frac{1}{2})^-$	19 s (β^-)
As	33	70	69.930929	4^+	53 m (ε)
		71	70.927114	$\frac{5}{2}^-$	61 h (ε)
		72	71.926755	2^-	26.0 h (ε)
		73	72.923827	$\frac{3}{2}^-$	80.3 d (ε)
		74	73.923928	2^-	17.8 d (ε)
		75	74.921594	$\frac{3}{2}^-$	*100 %*
		76	75.922393	2^-	26.3 h (β^-)
		77	76.920646	$\frac{3}{2}^-$	38.8 h (β^-)
		78	77.921830	(2^-)	91 m (β^-)
		79	78.920946	$\frac{3}{2}^-$	9.0 m (β^-)
Se	34	71	70.932270	$\frac{5}{2}^-$	4.7 m (ε)
		72	71.927110	0^+	8.4 d (ε)
		73	72.926768	$\frac{9}{2}^+$	7.1 h (ε)
		74	73.922475	0^+	*0.87%*
		75	74.922522	$\frac{5}{2}^+$	119.8 d (ε)
		76	75.919212	0^+	*9.0%*
		77	76.919913	$\frac{1}{2}^-$	*7.6%*
		78	77.917308	0^+	*23.5%*
		79	78.918498	$\frac{7}{2}^+$	< 0.065 My (β^-)

	Z	A	Atomic mass (u)	I^π	*Abundance* or Half-life
		80	79.916520	0^+	*49.8%*
		81	80.917991	$(\frac{1}{2})^-$	18.5 m (β^-)
		82	81.916698	0^+	*9.2%*
		83	82.919117	$(\frac{9}{2})^+$	22.5 m (β^-)
		84	83.918463	0^+	3.3 m (β^-)
Br	35	76	75.924528	1^-	16.1 h (ε)
		77	76.921378	$\frac{3}{2}^-$	57.0 h (ε)
		78	77.921144	1^+	6.46 m (ε)
		79	78.918336	$\frac{3}{2}^-$	*50.69%*
		80	79.918528	1^+	17.6 m (β^-)
		81	80.916289	$\frac{3}{2}^-$	*49.31%*
		82	81.916802	5^-	35.3 h (β^-)
		83	82.915179	$(\frac{3}{2})^-$	2.39 h (β^-)
		84	83.916503	2^-	31.8 m (β^-)
		85	84.915612	$(\frac{3}{2})^-$	2.9 m (β^-)
Kr	36	75	74.931029	?	4.3 m (ε)
		76	75.925959	0^+	14.8 h (ε)
		77	76.924610	$\frac{5}{2}^+$	75 m (ε)
		78	77.920396	0^+	*0.356%*
		79	78.920084	$\frac{1}{2}^-$	35.0 h (ε)
		80	79.916380	0^+	*2.27%*
		81	80.916590	$\frac{7}{2}^+$	0.21 My (ε)
		82	81.913482	0^+	*11.6%*
		83	82.914135	$\frac{9}{2}^+$	*11.5%*
		84	83.911507	0^+	*57.0%*
		85	84.912531	$\frac{9}{2}^+$	10.7 y (β^-)
		86	85.910616	0^+	*17.3%*
		87	86.913360	$\frac{5}{2}^+$	76 m (β^-)
		88	87.914453	0^+	2.84 h (β^-)
		89	88.917640	$(\frac{5}{2})^+$	3.18 m (β^-)
Rb	37	82	81.918195	1^+	1.25 m (ε)
		83	82.915144	$\frac{5}{2}^-$	86.2 d (ε)
		84	83.914390	2^-	32.9 d (ε)
		85	84.911794	$\frac{5}{2}^-$	*72.17%*
		86	85.911172	2^-	18.8 d (β^-)
		87	86.909187	$\frac{3}{2}^-$	*27.83%*
		88	87.911326	2^-	17.8 m (β^-)
		89	88.912278	$(\frac{3}{2})^-$	15.2 m (β^-)
		90	89.914811	(1^-)	153 s (β^-)
Sr	38	81	80.923270	$(\frac{1}{2}^-)$	22 m (ε)
		82	81.918414	0^+	25.0 d (ε)
		83	82.917566	$\frac{7}{2}^+$	32.4 d (ε)
		84	83.913430	0^+	*0.56%*
		85	84.912937	$\frac{9}{2}^+$	64.8 d (ε)
		86	85.909267	0^+	*9.8%*
		87	86.908884	$\frac{9}{2}^+$	*7.0%*
		88	87.905619	0^+	*82.6%*
		89	88.907450	$\frac{5}{2}^+$	50.5 d (β^-)
		90	89.907738	0^+	28.8 y (β^-)
		91	90.910187	$(\frac{5}{2})^+$	9.5 h (β^-)
		92	91.910944	0^+	2.7 h (β^-)
		93	92.913987	$(\frac{7}{2}^+)$	7.4 m (β^-)
Y	39	84	83.920310	(5^-)	39 m (ε)
		85	84.916437	$(\frac{1}{2})^-$	2.7 h (ε)
		86	85.914893	4^-	14.7 h (ε)
		87	86.910882	$\frac{1}{2}^-$	80.3 h (ε)
		88	87.909508	4^-	106.6 d (ε)
		89	88.905849	$\frac{1}{2}^-$	*100%*
		90	89.907152	2^-	64.1 h (β^-)
		91	90.907303	$\frac{1}{2}^-$	58.5 d (β^-)
		92	91.908917	2^-	3.54 h (β^-)
		93	92.909571	$\frac{1}{2}^-$	10.2 h (β^-)
		94	93.911597	2^-	18.7 m (β^-)
Zr	40	87	86.914817	$(\frac{9}{2}^+)$	1.6 h (ε)
		88	87.910225	0^+	83.4 d (ε)
		89	88.908890	$\frac{9}{2}^+$	78.4 h (ε)
		90	89.904703	0^+	*51.5%*
		91	90.905644	$\frac{5}{2}^+$	*11.2%*
		92	91.905039	0^+	*17.1%*
		93	92.906474	$\frac{5}{2}^+$	1.5 My (β^-)
		94	93.906315	0^+	*17.4%*
		95	94.908042	$\frac{5}{2}^+$	64.0 d (β^-)
		96	95.908275	0^+	*2.80%*
		97	96.910950	$\frac{1}{2}^+$	16.9 h (β^-)
		98	97.912735	0^+	31 s (β^-)
Nb	41	89	88.913449	$(\frac{1}{2})^-$	2.0 h (ε)
		90	89.911263	8^+	14.6 h (ε)
		91	90.906991	$(\frac{9}{2})^+$	700 y (ε)
		92	91.907192	$(7)^+$	35 My (ε)
		93	92.906377	$\frac{9}{2}^+$	*100%*
		94	93.907281	6^+	0.020 My (β^-)
		95	94.906835	$\frac{9}{2}^+$	35.0 d (β^-)
		96	95.908100	6^+	23.4 h (β^-)
		97	96.908097	$\frac{9}{2}^+$	72 m (β^-)
Mo	42	90	89.913933	0^+	5.67 h (ε)
		91	90.911755	$\frac{9}{2}^+$	15.5 m (ε)
		92	91.906808	0^+	*14.8%*
		93	92.906813	$\frac{5}{2}^+$	3500 y (ε)
		94	93.905085	0^+	*9.3%*
		95	94.905841	$\frac{5}{2}^+$	*15.9%*

	Z	A	Atomic mass (u)	I^π	*Abundance* or Half-life
		96	95.904679	0^+	*16.7%*
		97	96.906021	$\frac{5}{2}^+$	*9.6%*
		98	97.905407	0^+	*24.1%*
		99	98.907711	$\frac{1}{2}^+$	66.0 h (β^-)
		100	99.907477	0^+	*9.6%*
		101	100.910345	$\frac{1}{2}^+$	14.6 m (β^-)
Tc	43	94	93.909654	7^+	293 m (ε)
		95	94.907657	$\frac{9}{2}^+$	20.0 h (ε)
		96	95.907870	7^+	4.3 d (ε)
		97	96.906364	$\frac{9}{2}^+$	2.6 My (ε)
		98	97.907215	$(6)^+$	4.2 My (β^-)
		99	98.906254	$\frac{9}{2}^+$	0.214 My (β^-)
		100	99.907657	1^+	15.8 s (β^-)
Ru	44	94	93.911361	0^+	52 m (ε)
		95	94.910414	$\frac{5}{2}^+$	1.65 h (ε)
		96	95.907599	0^+	*5.5%*
		97	96.907556	$\frac{5}{2}^+$	2.88 d (ε)
		98	97.905287	0^+	*1.86%*
		99	98.905939	$\frac{5}{2}^+$	*12.7%*
		100	99.904219	0^+	*12.6%*
		101	100.905582	$\frac{5}{2}^+$	*17.0%*
		102	101.904348	0^+	*31.6%*
		103	102.906323	$\frac{3}{2}^+$	39.4 d (β^-)
		104	103.905424	0^+	*18.7%*
		105	104.907744	$\frac{3}{2}^+$	4.44 h (β^-)
		106	105.907321	0^+	372 d (β^-)
		107	106.910130	$(\frac{5}{2}^+)$	3.8 m (β^-)
Rh	45	98	97.910716	$(2)^+$	8.7 m (ε)
		99	98.908192	$(\frac{1}{2}^-)$	16.1 d (ε)
		100	99.908116	1^-	20.8 h (ε)
		101	100.906159	$\frac{1}{2}^-$	3.3 y (ε)
		102	101.906814	6^+	2.9 y (ε)
		103	102.905500	$\frac{1}{2}^-$	*100 %*
		104	103.906651	1^+	42.3 s (β^-)
		105	104.905686	$\frac{7}{2}^+$	35.4 h (β^-)
		106	105.907279	1^+	29.8 s (β^-)
Pd	46	99	98.911763	$(\frac{5}{2}^+)$	21.4 m (ε)
		100	99.908527	0^+	3.6 d (ε)
		101	100.908287	$\frac{5}{2}^+$	8.5 h (ε)
		102	101.905634	0^+	*1.0%*
		103	102.906114	$\frac{5}{2}^+$	17.0 d (ε)
		104	103.904029	0^+	*11.0%*
		105	104.905079	$\frac{5}{2}^+$	*22.2%*
		106	105.903478	0^+	*27.3%*
		107	106.905127	$\frac{5}{2}^+$	6.5 My (β^-)
		108	107.903895	0^+	*26.7%*
		109	108.905954	$\frac{5}{2}^+$	13.4 h (β^-)
		110	109.905167	0^+	*11.8%*
		111	110.907660	$\frac{5}{2}^+$	23 m (β^-)
		112	111.907323	0^+	21.0 h (β^-)
Ag	47	103	102.908980	$\frac{7}{2}^+$	65.7 m (ε)
		104	103.908623	5^+	69.2 m (ε)
		105	104.906520	$\frac{1}{2}^-$	41.3 d (ε)
		106	105.906662	1^+	24.0 m (ε)
		107	106.905092	$\frac{1}{2}^-$	*51.83%*
		108	107.905952	1^+	2.4 m (β^-)
		109	108.904756	$\frac{1}{2}^-$	*48.17%*
		110	109.906111	1^+	24.4 s (β^-)
		111	110.905295	$\frac{1}{2}^-$	7.45 d (β^-)
		112	111.907010	2^-	3.14 h (β^-)
Cd	48	104	103.909851	0^+	58 m (ε)
		105	104.909459	$\frac{5}{2}^+$	56.0 m (ε)
		106	105.906461	0^+	*1.25%*
		107	106.906613	$\frac{5}{2}^+$	6.50 h (ε)
		108	107.904176	0^+	*0.89%*
		109	108.904953	$\frac{5}{2}^+$	463 d (ε)
		110	109.903005	0^+	*12.5%*
		111	110.904182	$\frac{1}{2}^+$	*12.8%*
		112	111.902757	0^+	*24.1%*
		113	112.904400	$\frac{1}{2}^+$	*12.2%*
		114	113.903357	0^+	*28.7%*
		115	114.905430	$\frac{1}{2}^+$	53.4 h (β^-)
		116	115.904755	0^+	*7.5%*
		117	116.907228	$\frac{1}{2}^+$	2.4 h (β^-)
		118	117.911700	0^+	50.3 m (β^-)
In	49	110	109.907230	2^+	69.1 m (ε)
		111	110.905109	$\frac{9}{2}^+$	2.83 d (ε)
		112	111.905536	1^+	14.4 m (ε)
		113	112.904061	$\frac{9}{2}^+$	*4.3%*
		114	113.904916	1^+	71.9 s (β^-)
		115	114.903882	$\frac{9}{2}^+$	*95.7%*
		116	115.905264	1^+	14.1 s (β^-)
		117	116.904517	$\frac{9}{2}^+$	43.8 m (β^-)
Sn	50	109	108.911294	$\frac{7}{2}^+$	18.0 m (ε)
		110	109.907858	0^+	4.1 h (ε)
		111	110.907741	$\frac{7}{2}^+$	35 m (ε)
		112	111.904826	0^+	*1.01%*
		113	112.905176	$\frac{1}{2}^+$	115.1 d (ε)
		114	113.902784	0^+	*0.67%*
		115	114.903348	$\frac{1}{2}^+$	*0.38%*

	Z	A	Atomic mass (u)	I^π	*Abundance* or Half-life
		116	115.901747	0^+	*14.6%*
		117	116.902956	$\frac{1}{2}^+$	*7.75%*
		118	117.901609	0^+	*24.3%*
		119	118.903311	$\frac{1}{2}^+$	*8.6%*
		120	119.902199	0^+	*32.4%*
		121	120.904239	$\frac{3}{2}^+$	27.1 h (β^-)
		122	121.903440	0^+	*4.56%*
		123	122.905722	$\frac{11}{2}^-$	129 d (β^-)
		124	123.905274	0^+	*5.64%*
		125	124.907785	$\frac{11}{2}^-$	9.62 d (β^-)
		126	125.907654	0^+	0.1 My (β^-)
		127	126.910355	$(\frac{11}{2}^-)$	2.1 h (β^-)
Sb	51	118	117.905534	1^+	3.6 m (ε)
		119	118.903948	$\frac{5}{2}^+$	38.0 h (ε)
		120	119.905077	1^+	15.8 m (ε)
		121	120.903821	$\frac{5}{2}^+$	*57.3%*
		122	121.905179	2^-	2.70 d (β^-)
		123	122.904216	$\frac{7}{2}^+$	*42.7%*
		124	123.905938	3^-	60.2 d (β^-)
		125	124.905252	$\frac{7}{2}^+$	2.7 y (β^-)
		126	125.907250	8^-	12.4 d (β^-)
		127	126.906919	$\frac{7}{2}^+$	3.85 d (β^-)
Te	52	117	116.908630	$\frac{1}{2}^+$	62 m (ε)
		118	117.905908	0^+	6.00 d (ε)
		119	118.906411	$\frac{1}{2}^+$	16.0 h (ε)
		120	119.904048	0^+	*0.091%*
		121	120.904947	$\frac{1}{2}^+$	16.8 d (ε)
		122	121.903050	0^+	*2.5%*
		123	122.904271	$\frac{1}{2}^+$	*0.89%*
		124	123.902818	0^+	*4.6%*
		125	124.904429	$\frac{1}{2}^+$	*7.0%*
		126	125.903310	0^+	*18.7%*
		127	126.905221	$\frac{3}{2}^+$	9.4 h (β^-)
		128	127.904463	0^+	*31.7%*
		129	128.906594	$\frac{3}{2}^+$	69 m (β^-)
		130	129.906229	0^+	*34.5%*
		131	130.908528	$\frac{3}{2}^+$	25.0 m (β^-)
		132	131.908517	0^+	78.2 h (β^-)
		133	132.910910	$(\frac{3}{2}^+)$	12.5 m (β^-)
I	53	123	122.905594	$\frac{5}{2}^+$	13.2 h (ε)
		124	123.906207	2^-	4.18 d (ε)
		125	124.904620	$\frac{5}{2}^+$	60.2 d (ε)
		126	125.905624	2^-	13.0 d (ε)
		127	126.904473	$\frac{5}{2}^+$	*100 %*
		128	127.905810	1^+	25.0 m (β^-)
		129	128.904986	$\frac{7}{2}^+$	16 My (β^-)
		130	129.906713	5^+	12.4 h (β^-)
		131	130.906114	$\frac{7}{2}^+$	8.04 d (β^-)
		132	131.907987	4^+	2.30 h (β^-)
Xe	54	121	120.911450	$(\frac{5}{2}^+)$	40.1 m (ε)
		122	121.908170	0^+	20.1 h (ε)
		123	122.908469	$(\frac{1}{2}^+)$	2.08 h (ε)
		124	123.905894	0^+	*0.096%*
		125	124.906397	$(\frac{1}{2})^+$	17 h (ε)
		126	125.904281	0^+	*0.090%*
		127	126.905182	$(\frac{1}{2}^+)$	36.4 d (ε)
		128	127.903531	0^+	*1.92%*
		129	128.904780	$\frac{1}{2}^+$	*26.4%*
		130	129.903509	0^+	*4.1%*
		131	130.905072	$\frac{3}{2}^+$	*21.2%*
		132	131.904144	0^+	*26.9%*
		133	132.905888	$\frac{3}{2}^+$	5.25 d (β^-)
		134	133.905395	0^+	*10.4%*
		135	134.907130	$\frac{3}{2}^+$	9.1 h (β^-)
		136	135.907214	0^+	*8.9%*
		137	136.911557	$\frac{7}{2}^-$	3.82 m (β^-)
Cs	55	130	129.906753	1^+	29.2 m (ε)
		131	130.905444	$\frac{5}{2}^+$	9.69 d (ε)
		132	131.906431	2^-	6.47 d (ε)
		133	132.905429	$\frac{7}{2}^+$	*100 %*
		134	133.906696	4^+	2.06 y (β^-)
		135	134.905885	$\frac{7}{2}^+$	3 My (β^-)
		136	135.907289	5^+	13.1 d (β^-)
		137	136.907073	$\frac{7}{2}^+$	30.2 y (β^-)
		138	137.911004	3^-	32.2 m (β^-)
Ba	56	127	126.911130	$(\frac{1}{2}^+)$	12.7 m (ε)
		128	127.908237	0^+	2.43 d (ε)
		129	128.908642	$\frac{1}{2}^+$	2.2 h (ε)
		130	129.906282	0^+	*0.106%*
		131	130.906902	$\frac{1}{2}^+$	12.0 d (ε)
		132	131.905042	0^+	*0.101%*
		133	132.905988	$\frac{1}{2}^+$	10.7 y (ε)
		134	133.904486	0^+	*2.42%*
		135	134.905665	$\frac{3}{2}^+$	*6.59%*
		136	135.904553	0^+	*7.85%*
		137	136.905812	$\frac{3}{2}^+$	*11.2%*
		138	137.905232	0^+	*71.7%*
		139	138.908826	$\frac{7}{2}^-$	82.9 m (β^-)
		140	139.910581	0^+	12.7 d (β^-)
		141	140.914363	$\frac{3}{2}^-$	18.3 m (β^-)

	Z	A	Atomic mass (u)	I^π	*Abundance* or Half-life
La	57	135	134.906953	$\frac{5}{2}^+$	19.5 h (ε)
		136	135.907630	1^+	9.87 m (ε)
		137	136.906460	$\frac{7}{2}^+$	0.06 My (ε)
		138	137.907105	5^+	*0.089%*
		139	138.906347	$\frac{7}{2}^+$	*99.911%*
		140	139.909471	3^-	40.3 h (β^-)
		141	140.910896	$\frac{7}{2}^+$	3.90 h (β^-)
		142	141.914090	2^-	91.1 m (β^-)
Ce	58	133	132.911360	$\frac{1}{2}^+$	5.4 h (ε)
		134	133.908890	0^+	76 h (ε)
		135	134.909117	$\frac{1}{2}^+$	17.6 h (ε)
		136	135.907140	0^+	*0.190%*
		137	136.907780	$\frac{3}{2}^+$	9.0 h (ε)
		138	137.905985	0^+	*0.254%*
		139	138.906631	$\frac{3}{2}^+$	137.2 d (ε)
		140	139.905433	0^+	*88.5%*
		141	140.908271	$\frac{7}{2}^-$	32.5 d (β^-)
		142	141.909241	0^+	*11.1%*
		143	142.912383	$\frac{3}{2}^-$	33.0 h (β^-)
		144	143.913643	0^+	284 d (β^-)
		145	144.917230	$\frac{5}{2}^+$	2.98 m (β^-)
Pr	59	138	137.910748	1^+	1.45 m (ε)
		139	138.908917	$\frac{5}{2}^+$	4.4 h (ε)
		140	139.909071	1^+	3.39 m (ε)
		141	140.907647	$\frac{5}{2}^+$	*100 %*
		142	141.910039	2^-	19.2 h (β^-)
		143	142.910814	$\frac{7}{2}^+$	13.6 d (β^-)
		144	143.913301	0^-	17.3 m (β^-)
Nd	60	139	138.911920	$\frac{3}{2}^+$	29.7 m (ε)
		140	139.909306	0^+	3.37 d (ε)
		141	140.909594	$\frac{3}{2}^+$	2.5 h (ε)
		142	141.907719	0^+	*27.2%*
		143	142.909810	$\frac{7}{2}^-$	*12.2%*
		144	143.910083	0^+	*23.8%*
		145	144.912570	$\frac{7}{2}^-$	*8.3%*
		146	145.913113	0^+	*17.2%*
		147	146.916097	$\frac{5}{2}^-$	11.0 d (β^-)
		148	147.916889	0^+	*5.7%*
		149	148.920145	$\frac{5}{2}^-$	1.73 h (β^-)
		150	149.920887	0^+	*5.6%*
		151	150.923825	$(\frac{3}{2}^+)$	12.4 m (β^-)
		152	151.924680	0^+	11.4 m (β^-)
Pm	61	142	141.912970	1^+	40.5 s (ε)
		143	142.910930	$\frac{5}{2}^+$	265 d (ε)
		144	143.912588	5^-	349 d (ε)
		145	144.912743	$\frac{5}{2}^+$	17.7 y (ε)
		146	145.914708	3^-	5.5 y (ε)
		147	146.915135	$\frac{7}{2}^+$	2.62 y (β^-)
		148	147.917473	1^-	5.37 d (β^-)
		149	148.918332	$\frac{7}{2}^+$	53.1 h (β^-)
		150	149.920981	(1^-)	2.68 h (β^-)
Sm	62	142	141.915206	0^+	72.5 m (ε)
		143	142.914626	$\frac{3}{2}^+$	8.83 m (ε)
		144	143.911998	0^+	*3.1%*
		145	144.913409	$\frac{7}{2}^-$	340 d (ε)
		146	145.913053	0^+	103 My (α)
		147	146.914894	$\frac{7}{2}^-$	*15.1%*
		148	147.914819	0^+	*11.3%*
		149	148.917180	$\frac{7}{2}^-$	*13.9%*
		150	149.917273	0^+	*7.4%*
		151	150.919929	$\frac{5}{2}^-$	90 y (β^-)
		152	151.919728	0^+	*26.6%*
		153	152.922094	$\frac{3}{2}^+$	46.8 h (β^-)
		154	153.922205	0^+	*22.6%*
		155	154.924636	$\frac{3}{2}^-$	22.4 m (β^-)
Eu	63	148	147.918125	5^-	54.5 d (ε)
		149	148.917926	$\frac{5}{2}^+$	93.1 d (ε)
		150	149.919702	0^-	36 y (ε)
		151	150.919847	$\frac{5}{2}^+$	*47.9%*
		152	151.921742	3^-	13 y (ε)
		153	152.921225	$\frac{5}{2}^+$	*52.1%*
		154	153.922975	3^-	8.5 y (β^-)
		155	154.922889	$\frac{5}{2}^+$	4.9 y (β^-)
		156	155.924752	0^+	15 d (β^-)
		157	156.925418	$\frac{5}{2}^+$	15 h (β^-)
Gd	64	149	148.919344	$\frac{7}{2}^-$	9.4 d (ε)
		150	149.918662	0^+	1.8 My (α)
		151	150.920346	$\frac{7}{2}^-$	120 d (ε)
		152	151.919786	0^+	*0.20%*
		153	152.921745	$\frac{3}{2}^-$	242 d (ε)
		154	153.920861	0^+	*2.1%*
		155	154.922618	$\frac{3}{2}^-$	*14.8%*
		156	155.922118	0^+	*20.6%*
		157	156.923956	$\frac{3}{2}^-$	*15.7%*
		158	157.924099	0^+	*24.8%*
		159	158.926384	$\frac{3}{2}^-$	18.6 h (β^-)
		160	159.927049	0^+	*21.8%*
		161	160.929664	$\frac{5}{2}^-$	3.7 m (β^-)
Tb	65	156	155.924742	3^-	5.34 d (ε)
		157	156.924023	$\frac{3}{2}^+$	150 y (ε)

	Z	A	Atomic mass (u)	I^π	*Abundance* or Half-life
		158	157.925411	3^-	150 y (ε)
		159	158.925342	$\frac{3}{2}^+$	*100 %*
		160	159.927163	3^-	72.1 d (β^-)
		161	160.927566	$\frac{3}{2}^+$	6.90 d (β^-)
		162	161.929510	1^-	7.76 m (β^-)
Dy	66	153	152.925769	$\frac{7}{2}^-$	6.4 h (ε)
		154	153.924429	0^+	3 My (α)
		155	154.925747	$\frac{3}{2}^-$	10.0 h (ε)
		156	155.924277	0^+	*0.057%*
		157	156.925460	$\frac{3}{2}^-$	8.1 h (ε)
		158	157.924403	0^+	*0.100 %*
		159	158.925735	$\frac{3}{2}^-$	144.4 d (ε)
		160	159.925193	0^+	*2.3%*
		161	160.926930	$\frac{5}{2}^+$	*19.90%*
		162	161.926795	0^+	*25.5%*
		163	162.928728	$\frac{5}{2}^-$	*24.9%*
		164	163.929171	0^+	*28.1%*
		165	164.931700	$\frac{7}{2}^+$	2.33 h (β^-)
		166	165.932803	0^+	81.6 h (β^-)
Ho	67	162	161.929092	1^+	15 m (ε)
		163	162.928731	$(\frac{7}{2})^-$	33 y (ε)
		164	163.930285	1^+	29.0 m (ε)
		165	164.930319	$\frac{7}{2}^-$	*100 %*
		166	165.932281	0^-	26.8 h (β^-)
		167	166.933127	$(\frac{7}{2}^-)$	3.1 h (β^-)
Er	68	160	159.929080	0^+	28.6 h (ε)
		161	160.929996	$\frac{3}{2}^-$	3.24 h (ε)
		162	161.928775	0^+	*0.14%*
		163	162.930030	$\frac{5}{2}^-$	75.1 m (ε)
		164	163.929198	0^+	*1.56%*
		165	164.930723	$\frac{5}{2}^-$	10.4 h (ε)
		166	165.930290	0^+	*33.4%*
		167	166.932046	$\frac{7}{2}^+$	*22.9%*
		168	167.932368	0^+	*27.1%*
		169	168.934588	$\frac{1}{2}^-$	9.40 d (β^-)
		170	169.935461	0^+	*14.9%*
		171	170.938027	$\frac{5}{2}^-$	7.52 h (β^-)
		172	171.939353	0^+	49.3 h (β^-)
Tm	69	166	165.933561	2^+	7.70 h (ε)
		167	166.932848	$\frac{1}{2}^+$	9.25 d (ε)
		168	167.934170	3^+	93.1 d (ε)
		169	168.934212	$\frac{1}{2}^+$	*100 %*
		170	169.935798	1^-	128.6 d (β^-)
		171	170.936427	$\frac{1}{2}^+$	1.92 y (β^-)
		172	171.938397	2^-	63.6 h (β^-)

	Z	A	Atomic mass (u)	I^π	*Abundance* or Half-life
Yb	70	166	165.933875	0^+	56.7 h (ε)
		167	166.934946	$\frac{5}{2}^-$	17.5 m (ε)
		168	167.933894	0^+	*0.135%*
		169	168.935186	$\frac{7}{2}^+$	32.0 d (ε)
		170	169.934759	0^+	*3.1%*
		171	170.936323	$\frac{1}{2}^-$	*14.4%*
		172	171.936378	0^+	*21.9%*
		173	172.938208	$\frac{5}{2}^-$	*16.2%*
		174	173.938859	0^+	*31.6%*
		175	174.941273	$\frac{7}{2}^-$	4.19 d (β^-)
		176	175.942564	0^+	*12.6%*
		177	176.945253	$\frac{9}{2}^+$	1.9 h (β^-)
		178	177.946639	0^+	74 m (β^-)
Lu	71	172	171.939085	(4^-)	6.70 d (ε)
		173	172.938929	$\frac{7}{2}^+$	1.37 y (ε)
		174	173.940336	1^-	3.3 y (ε)
		175	174.940770	$\frac{7}{2}^+$	*97.39%*
		176	175.942679	7^-	*2.61%*
		177	176.943752	$\frac{7}{2}^+$	6.71 d (β^-)
		178	177.945963	1^+	28.4 m (β^-)
Hf	72	171	170.940490	$(\frac{7}{2}^+)$	12.1 h (ε)
		172	171.939460	0^+	1.87 y (ε)
		173	172.940650	$\frac{1}{2}^-$	24.0 h (ε)
		174	173.940044	0^+	*0.16%*
		175	174.941507	$\frac{5}{2}^-$	70 d (ε)
		176	175.941406	0^+	*5.2%*
		177	176.943217	$\frac{7}{2}^-$	*18.6%*
		178	177.943696	0^+	*27.1%*
		179	178.945812	$\frac{9}{2}^+$	*13.7%*
		180	179.946546	0^+	*35.2%*
		181	180.949096	$\frac{1}{2}^-$	42.4 d (β^-)
		182	181.950550	0^+	9 My (β^-)
		183	182.953530	$(\frac{3}{2}^-)$	64 m (β^-)
Ta	73	178	177.945750	1^+	9.31 m (ε)
		179	178.945930	$(\frac{7}{2}^+)$	665 d (ε)
		180	179.947462	1^+	*0.0123%*
		181	180.947992	$\frac{7}{2}^+$	*99.9877%*
		182	181.950149	3^-	115 d (β^-)
		183	182.951369	$\frac{7}{2}^+$	5.1 d (β^-)
W	74	178	177.945840	0^+	21.5 d (ε)
		179	178.947067	$(\frac{7}{2}^-)$	38 m (ε)
		180	179.946701	0^+	*0.13%*
		181	180.948192	$\frac{9}{2}^+$	121 d (ε)
		182	181.948202	0^+	*26.3%*
		183	182.950220	$\frac{1}{2}^-$	*14.3%*

	Z	A	Atomic mass (u)	I^π	*Abundance* or Half-life
		184	183.950928	0^+	*30.7%*
		185	184.953416	$\frac{3}{2}^-$	75.1 d (β^-)
		186	185.954357	0^+	*28.6%*
		187	186.957153	$\frac{3}{2}^-$	23.9 h (β^-)
		188	187.958480	0^+	69.4 d (β^-)
Re	75	182	181.951210	2^+	12.7 h (ε)
		183	182.950817	$(\frac{5}{2})^+$	71 d (ε)
		184	183.952530	3^-	38 d (ε)
		185	184.952951	$\frac{5}{2}^+$	*37.40%*
		186	185.954984	1^-	90.6 h (β^-)
		187	186.955744	$\frac{5}{2}^+$	*62.60%*
		188	187.958106	1^-	16.9 h (β^-)
		189	188.959219	$(\frac{5}{2})^+$	24.3 h (β^-)
Os	76	182	181.952120	0^+	21.5 h (ε)
		183	182.953290	$(\frac{9}{2})^+$	13.0 h (ε)
		184	183.952488	0^+	*0.018%*
		185	184.954041	$\frac{1}{2}^-$	93.6 d (ε)
		186	185.953830	0^+	*1.6%*
		187	186.955741	$\frac{1}{2}^-$	*1.6%*
		188	187.955830	0^+	*13.3%*
		189	188.958137	$\frac{3}{2}^-$	*16.1%*
		190	189.958436	0^+	*26.4%*
		191	190.960920	$\frac{9}{2}^-$	15.4 d (β^-)
		192	191.961467	0^+	*41.0%*
		193	192.964138	$\frac{3}{2}^-$	30.6 h (β^-)
		194	193.965173	0^+	6.0 y (β^-)
Ir	77	188	187.958830	(2^-)	41.5 h (ε)
		189	188.958712	$\frac{3}{2}^+$	13.1 d (ε)
		190	189.960580	(4^+)	11.8 d (ε)
		191	190.960584	$\frac{3}{2}^+$	*37.3%*
		192	191.962580	4^-	74.2 d (β^-)
		193	192.962917	$\frac{3}{2}^+$	*62.7%*
		194	193.965069	1^-	19.2 h (β^-)
		195	194.965966	$(\frac{3}{2}^+)$	2.8 h (β^-)
Pt	78	187	186.960470	$\frac{3}{2}^-$	2.35 h (ε)
		188	187.959386	0^+	10.2 d (ε)
		189	188.960817	$\frac{3}{2}^-$	10.9 h (ε)
		190	189.959917	0^+	*0.013%*
		191	190.961665	$\frac{3}{2}^-$	2.9 d (ε)
		192	191.961019	0^+	*0.78%*
		193	192.962977	$(\frac{1}{2}^-)$	50 y (ε)
		194	193.962655	0^+	*32.9%*
		195	194.964766	$\frac{1}{2}^-$	*33.8%*
		196	195.964926	0^+	*25.3%*
		197	196.967315	$\frac{1}{2}^-$	18.3 h (β^-)
		198	197.967869	0^+	*7.2%*
		199	198.970552	$(\frac{5}{2}^-)$	30.8 m (β^-)
		200	199.971417	0^+	12.5 h (β^-)
Au	79	194	193.965348	1^-	39.5 h (ε)
		195	194.965013	$\frac{3}{2}^+$	186 d (ε)
		196	195.966544	2^-	6.18 d (ε)
		197	196.966543	$\frac{3}{2}^+$	*100 %*
		198	197.968217	2^-	2.696 d (β^-)
		199	198.968740	$\frac{3}{2}^+$	3.14 d (β^-)
		200	199.970670	1^-	48.4 m (β^-)
Hg	80	193	192.966560	$\frac{3}{2}^-$	3.8 h (ε)
		194	193.965391	0^+	520 y (ε)
		195	194.966640	$\frac{1}{2}^-$	9.5 h (ε)
		196	195.965807	0^+	*0.15%*
		197	196.967187	$\frac{1}{2}^-$	64.1 h (ε)
		198	197.966743	0^+	*10.0%*
		199	198.968254	$\frac{1}{2}^-$	*16.8%*
		200	199.968300	0^+	*23.1%*
		201	200.970277	$\frac{3}{2}^-$	*13.2%*
		202	201.970617	0^+	*29.8%*
		203	202.972848	$\frac{5}{2}^-$	46.6 d (β^-)
		204	203.973467	0^+	*6.9%*
		205	204.976047	$\frac{1}{2}^-$	5.2 m (β^-)
Tl	81	200	199.970934	2^-	26.1 h (ε)
		201	200.970794	$\frac{1}{2}^+$	73 h (ε)
		202	201.972085	2^-	12.2 d (ε)
		203	202.972320	$\frac{1}{2}^+$	*29.5%*
		204	203.973839	2^-	3.77 y (β^-)
		205	204.974401	$\frac{1}{2}^+$	*70.5%*
		206	205.976084	0^-	4.20 m (β^-)
Pb	82	201	200.972830	$\frac{5}{2}^-$	9.3 h (ε)
		202	201.972134	0^+	0.05 My (ε)
		203	202.973365	$\frac{5}{2}^-$	51.9 h (ε)
		204	203.973020	0^+	*1.42%*
		205	204.974458	$\frac{5}{2}^-$	15 My (ε)
		206	205.974440	0^+	*24.1%*
		207	206.975872	$\frac{1}{2}^-$	*22.1%*
		208	207.976627	0^+	*52.3%*
		209	208.981065	$\frac{9}{2}^+$	3.25 h (β^-)
		210	209.984163	0^+	22.3 y (β^-)
		211	210.988735	$(\frac{9}{2}^+)$	36.1 m (β^-)
		212	211.991871	0^+	10.6 h (β^-)
Bi	83	206	205.978478	6^+	6.24 d (ε)
		207	206.978446	$\frac{9}{2}^-$	32 y (ε)

Z	A	Atomic mass (u)	I^π	*Abundance* or Half-life
	208	207.979717	(5^+)	0.368 My (ε)
	209	208.980374	$\frac{9}{2}^-$	*100 %*
	210	209.984095	1^-	5.01 d (β^-)
	211	210.987255	$\frac{9}{2}^-$	2.15 m (α)
	212	211.991255	1^-	60.6 m (β^-)
Po 84	206	205.980456	0^+	8.8 d (ε)
	207	206.981570	$\frac{5}{2}^-$	5.8 h (ε)
	208	207.981222	0^+	2.90 y (α)
	209	208.982404	$\frac{1}{2}^-$	102 y (α)
	210	209.982848	0^+	138.4 d (α)
	211	210.986627	$\frac{9}{2}^+$	0.52 s (α)
At 85	208	207.986510	6^+	1.63 h (ε)
	209	208.986149	$\frac{9}{2}^-$	5.4 h (ε)
	210	209.987126	5^+	8.3 h (ε)
	211	210.987469	$\frac{9}{2}^-$	7.21 h (ε)
	212	211.990725	(1^-)	0.31 s (α)
	213	212.992911	$\frac{9}{2}^-$	0.11 μs (α)
Rn 86	207	206.990690	$\frac{5}{2}^-$	9.3 m (ε)
	210	209.989669	0^+	2.4 h (α)
	211	210.990576	$\frac{1}{2}^-$	14.6 h (ε)
	212	211.990697	0^+	24 m (α)
	218	218.005580	0^+	35 ms (α)
	222	222.017571	0^+	3.82 d (α)
	224		0^+	107 m (β^-)
Fr 87	209	208.995870	$\frac{9}{2}^-$	50 s (α)
	212	211.996130	5^+	20 m (ε)
	215	215.000310	$\frac{9}{2}^-$	0.12 μs (α)
	220	220.012293	1	27.4 s (α)
	223	223.019733	$(\frac{3}{2})$	21.8 m (β^-)
Ra 88	222	222.015353	0^+	38 s (α)
	223	223.018501	$\frac{1}{2}^+$	11.4 d (α)
	224	224.020186	0^+	3.66 d (α)
	225	225.023604	$(\frac{3}{2})^+$	14.8 d (β^-)
	226	226.025403	0^+	1602 y (α)
	227	227.029171	$(\frac{3}{2}^+)$	42 m (β^-)
Ac 89	224	224.021685	(0^-)	2.9 h (ε)
	225	225.023205	$(\frac{3}{2}^-)$	10.0 d (α)
	226	226.026084	(1^-)	29 h (β^-)
	227	227.027750	$\frac{3}{2}^-$	21.77 y (β^-)
	228	228.031015	(3^+)	6.1 h (β^-)
Th 90	228	228.028715	0^+	1.91 y (α)
	229	229.031755	$\frac{5}{2}^+$	7300 y (α)
	230	230.033128	0^+	75,400 y (α)
	231	231.036299	$\frac{5}{2}^+$	25.52 h (β^-)
	232	232.038051	0^+	*100 %*
	233	233.041577	$(\frac{1}{2}^+)$	22.3 m (β^-)
Pa 91	229	229.032073	$(\frac{5}{2}^+)$	1.4 d (ε)
	230	230.034527	(2^-)	17.7 d (ε)
	231	231.035880	$\frac{3}{2}^-$	32,800 y (α)
	232	232.038565	(2^-)	1.31 d (β^-)
	233	233.040243	$\frac{3}{2}^-$	27.0 d (β^-)
U 92	233	233.039628	$\frac{5}{2}^+$	0.1592 My (α)
	234	234.040947	0^+	0.245 My (α)
	235	235.043924	$\frac{7}{2}^-$	*0.720%*
	236	236.045563	0^+	23.42 My (α)
	237	237.048725	$\frac{1}{2}^+$	6.75 d (β^-)
	238	238.050785	0^+	*99.275%*
	239	239.054290	$\frac{5}{2}^+$	23.5 m (β^-)
Np 93	236	236.046550	(6^-)	0.11 My (ε)
	237	237.048168	$\frac{5}{2}^+$	2.14 My (α)
	238	238.050941	2^+	2.117 d (β^-)
	239	239.052933	$\frac{5}{2}^+$	2.36 d (β^-)
Pu 94	237	237.048401	$\frac{7}{2}^-$	45.3 d (ε)
	238	238.049555	0^+	87.74 y (α)
	239	239.052158	$\frac{1}{2}^+$	24,100 y (α)
	240	240.053808	0^+	6570 y (α)
	241	241.056846	$\frac{5}{2}^+$	14.4 y (β^-)
	242	242.058737	0^+	0.376 My (α)
	243	243.061998	$\frac{7}{2}^+$	4.96 h (β^-)
Am 95	240	240.055278	(3^-)	50.9 h (ε)
	241	241.056824	$\frac{5}{2}^-$	433 y (α)
	242	242.059542	1^-	16.0 h (β^-)
	243	243.061375	$\frac{5}{2}^-$	7370 y (α)
	244	244.064279	(6^-)	10.1 h (β^-)
Cm 96	246	246.067218	0^+	4700 y (α)
	247	247.070347	$\frac{9}{2}^-$	16 My (α)
	248	248.072343	0^+	0.34 My (α)
	249	249.075948	$\frac{1}{2}^+$	64 m (β^-)
Bk 97	246	246.068720	2^-	1.8 d (ε)
	247	247.070300	$(\frac{3}{2}^-)$	1380 y (α)
Cf 98	251	251.079580	$\frac{1}{2}^+$	898 y (α)
	252	252.081621	0^+	2.64 y (α)
Es 99	252	252.082944	$(4^+, 5^-)$	472 d (α)
	253	253.084818	$\frac{7}{2}^+$	20.5 d (α)

	Z	A	Atomic mass (u)	I^π	*Abundance* or Half-life
Fm	100	256	256.091767	0^+	2.63 h (f)
		257	257.095099	$(\frac{9}{2}^+)$	100 d (α)
Md	101	257	257.095580	$(\frac{7}{2}^-)$	5.2 h (ε)
		258	258.098570	(8^-)	55 d (α)
No	102	258	258.098150	0^+	1.2 ms (f)
		259	259.100931	$(\frac{9}{2}^+)$	60 m (α)
Lr	103	260	260.105320		180 s (α)
Rf	104	261	261.108690		65 s (α)
Ha	105	261	261.111820		1.8 s (α)
		262	262.113760		34 s (f)
	106	263	263.118220		0.8 s (f)
	107	262	262.122930		115 ms (α)

CREDITS

The following illustrations were taken from the works listed below and are used with the permissions of the author and publisher: from David Halliday, *Introductory Nuclear Physics*, 2nd edition (New York: Wiley, 1955)—figures 3.14, 4.2, 4.7, 4.10, 6.2, 6.5, 7.1, 12.12, 12.24, 12.25, 15.13, 15.26, 15.28, 16.12, 16.14, 16.15; from Kenneth S. Krane, *Modern Physics* (New York: Wiley 1983)—figures 1.1, 3.1, 3.11, 3.12, 3.16, 5.1, 6.1, 7.19, 10.27, 11.7, 11.8, 11.10, 12.20, 13.5, 14.4, 14.15, 14.18, 15.11, 15.31, 18.10, 19.2, 19.3, 19.9, 19.15. All other figures that are not original to the present work are used with the permissions of the authors and publishers listed in the accompanying legends.

INDEX

Absorbed dose, 186
Absorption coefficient:
 Compton, 202
 energy dependence, 203
Abundance:
 elements in solar system, 771
 isotopic, 63
Accelerator, Fermilab:
 Berkeley 184-inch synchrocyclotron, 575
 Bevatron, 583
 Brookhaven AGS, 586
 Cambridge Electron Accelerator, 582–583
 CERN ISR, 595–596
 CERN Proton Synchrotron, 586
 CERN Super Proton Synchrotron, 586–588, 597
 Cockcroft-Walton, 593
 colliding-beam, 593–598
 Cosmotron, 583–584
 cyclotron, 571–574
 AVF, 576–578
 fringing field, 573–574
 relativistic limit, 574
 sector-focused, 576
 superconducting, 580
 DESY, 597–598
 Fermilab, 586, 597
 heavy-ion, 579–581
 Holifield Heavy Ion Research Facility, 568–570
 LAMPF, 591–592
 linear, 588–593
 drift tube, 589
 electron, 591, 593
 phase stability, 590
 proton, 591–592
 traveling wave, 590
 Oak Ridge Isochronous Cyclotron, 576, 579
 SLAC, 591, 593, 597–598
 storage ring, 596
 Superconducting Supercollider, 597
 SuperHILAC, 593
 synchrocyclotron, 574
 phase stability, 574
 synchrotron, 581–588
 AG focusing, 582
 electron, 582
 proton, 583
 TRIUMF, 577–579
 Van de Graaff, 565–569
 tandem, 567–569
Accelerators, 559–598
 mass spectrometry using, 794
Activity, 162
 decay of, 162–163
 mixture of, 165
 units of, 162
Alpha decay, 174, 246–269
 ^{229}Pa, 266–269
 ^{242}Cm, 258
 ^{251}Fm, 262–266
 ^{253}Es, 259
 angular distribution, 260
 angular momentum transfer in, 257
 applications of, 796–800
 barrier penetration, 251–252
 basic process, 247
 coincidences with gammas, 263, 265–267
 Coulomb barrier, 251–252
 deformed nuclei, 260
 energy release, 248
 favored, 268
 fine structure, 258
 Gamow factor, 253
 Geiger-Nuttall rule, 249
 half-life calculated, 253
 half-life *vs.* energy, 249
 long-range, 302
 nuclear recoil energy, 248
 parity change in, 257

Alpha decay (*Continued*)
parity-violating, 315
Q value, 248
Q value *vs.* A, 250
Q value from semiempirical mass formula, 250
quantum theory of, 252–253
shell structure, 250
smoke detectors using, 798
systematics, 249
thermal power from, 798
Alpha decay spectroscopy, 261–269
Alpha particle, first identification of, 246
Alpha-particle reactions, in stellar fusion, 769
Amplifier, 220
Analog state, *see* Isobaric analog state
Angular correlation, 338–339
perturbed, 642
electric quadrupole, 648
magnetic dipole, 642–644, 646–647
time differential, 642–643, 648
time integral, 644–647
Angular distribution, perturbed, 640
Angular momentum:
quantum theory of, 34
total, 36
Angular momentum projection quantum number, 36
Angular momentum quantum number, 34
Associated production, 687
Atomic beam magnetic resonance, 627
Atomic number, 4
Attenuation coefficient, total linear, 201

Backbending, 437
Barn, 75
Barrier penetration, 19
Barrier potential, 18
Baryon number, conservation of, 715
Baryons, 653, 710
Bateman equations, 173
Bessel functions, spherical (table), 28
Beta decay, 174, 272–322
^{3}H, 287–288
^{10}Be, 315
^{12}B, 320–321
^{12}N, 320–321
^{40}K, 316
^{64}Cu, 281
^{66}Ga, 283
^{72}Zn, 318
^{91}Y, 284
^{126}I, 319–321
^{176}Lu, 317
^{177}Lu, 317–319
^{210}Bi, 273, 275
allowed, selection rules, 289
allowed approximation, 279
angular momentum selection rules, 289
charge conjugation noninvariance in, 312
coincidence spectroscopy, 318
conserved vector current (CVC) hypothesis, 290
continuous electron spectrum, 273
Coulomb effects on, 280–281
CP symmetry, 312
density of states, 278
double, 70, 298–302
decay rate, 299
direct observation, 300
geochemical observation, 300
and lepton conservation, 300
neutrinoless, 301
electron capture, Q value, 276
energy release, 273
energy spectrum, 280–281
Fermi decay, 289–290
Fermi function, 280
Fermi integral, 282, 293
Fermi-Kurie plot, 282, 315–316, 318–320
allowed, 283
first forbidden, 284
Fermi theory, 277
forbidden, 281
selection rules, 291–292
shape factor, 282, 284
ft value, 283, 294, 295
Gamow-Teller decay, 289–290
helicity of electrons and neutrinos, 298
to isobaric analog state, 304, 308, 321
isospin selection rules, 391
matrix element, 278
mirror nuclei, 290
momentum spectrum, 279–281
negative, Q value, 275
neutrino mass limits from, 274, 286–288
neutron, 274, 289
nuclear matrix element, 279
parity change in, 289
parity nonconservation in, 312–314
positive, Q value, 276
shell-model effects on, 322
strength constant, 284–285
superallowed, 283–285
total decay rate, 282
Beta-delayed nucleon emission, 302
to continuum of final states, 308
to discrete final states, 303
energy conservation in, 304
Big Bang, 178
Big Bang cosmology, 756–760
Binding energy:
electronic, 65
fission release of, 479
nuclear, 65
Binding energy per nucleon, 67
Binomial distribution, 218

Blackbody radiation, energy spectrum, 761
B meson, 739
Bohr magneton, 73, 606
Born approximation, 421
Bragg-Kleeman rule, 194
Branching ratio, 176
Breit-Wigner formula, 428
Breit-Wigner resonance, 681
Bremsstrahlung, 196

Calibration, energy, standards for, 226
Carbon-14 dating, *see* Radiocarbon dating
CAT scanner, 805, 806
^{14}C emission by heavy nuclei, 254, 255
Central potential, 27
Centrifugal potential, 28
Centrifugal repulsion, 30, 32, 35
Centrifugal stretching, 436
Charge conjugation, 309
Charge independence, 102
Charge radius and matter radius, equivalence of, 58
Charge symmetry, 102
Charm, 717
Charmonium, 735
Coincidence, 228
 chance, 228
 dependence on source activity, 229
 lifetime measurement from delayed, 233
 true, 228
Collective model, 134–149
 magnetic dipole moments, 147
 rotational, 142
 excited states, 145, 147
 vibrational, 139
 excited states, 141
Compound nucleus, 416
Compton continuum, 222
Compton edge, 222, 223
Compton linear absorption coefficient, 202
Compton scattering, 199, 220–221
 differential cross section, 200–201
 energy distribution, 200
 polarization dependence, 241
 total cross section, 200
Computerized axial tomography (CAT), 804
Cosmochronology, 780–785
Coulomb energy difference, 54
Coulomb excitation, 402–405
Coulomb scattering, *see* Rutherford scattering
Coulomb scattering by electrons, energy loss, 196–197
Coulomb scattering by heavy particles, energy loss, 193
Counter telescope, 238
CP symmetry, 312
CPT theorem, 661, 667
CP violation:
 cosmological implications, 698
 K^0 decay, 692–698
 theories of origin, 698
Cross section:
 differential, 90, 393
 reaction, 392
 and induced radioactivity, 169
 total, 90
Curie (unit), 162
Current density, 14
Cyclotron resonance frequency, 571

De Broglie postulate, 10
De Broglie wavelength, 10
Decay constant, 161
 partial, 164, 176
 total, 164
Deep inelastic scattering, 721
Deformation parameter, 142
Degeneracy, 26
Delta resonance, 675–679
D meson, 717, 735, 737
Density of final states, 41, 166, 277, 296
Deuterium, 80
 abundance in universe, 767
 formation in early universe, 764
Deuteron, 80
 binding energy, 81
 d-state admixture, 84–85
 electric quadrupole moment, 85, 627
 magnetic dipole moment, 84, 627
 mass, 81
 parity, 84
 spin, 83
Diffraction, electron, 45
Dipole moment, 72. *See also* Electric dipole moment; Magnetic dipole moment
Dipole radiation, *see* Electromagnetic radiation
Doppler shift, use in lifetime measurements, 234–235
Dose equivalent, 187
Double-escape peak, 222

Effective range, neutron–proton scattering, 95
Effective range approximation, 95
Efficiency, photons, Ge *vs.* NaI, 227
Eigenvalue, 12
Electric dipole moment, 329
Electric quadrupole hyperfine parameter, 616
Electric quadrupole interaction, 609–610
Electric quadrupole moment, 72, 74–75, 607–608
 deformed nuclei, 143
 deuteron, 85
 measurement of, 627
 prolate and oblate, 609
 shell model, 127, 129, 130

Electric quadrupole moment (*Continued*)
systematics of 2^+ states, 138
Electromagnetic radiation:
angular distribution, 330
decay probability, 331
dipole, 328–330
angular distribution, 330
radiated power, 330
matrix element, 331
monopole, nonexistence of, 334
multipole moments, 331
parity of, 330–331
radiated power, 331
Weisskopf estimate, 332–335
Electron capture, 174. *See also* Beta decay
Electron-positron annihilation, 681, 682
Electron radius, classical, 200
Electron scattering, 196
energy loss, 197
radiative *vs.* collisional losses, 197
range-energy relationship, 198
Electrons (nuclear), evidence against, 4
Electroweak theory, 704
Energy calibration standards, 226
Energy resolution, 223
Ge detector, 225
scintillator, 224
Escape peaks, 222
Eta meson, 682, 683, 684
Exchange force, 108
Expectation value, 13
Exposure, 185

Fermi function, 280
Fermi's Golden Rule, 41, 166, 168, 277, 296
Fermi (unit), 7
Feynman diagram, 702
Field particles, 709
Fission, 66, 478–524
activation energy, 481
barrier against, 481
chain reaction, 479, 501
critical assembly, 501
cross section, 488
thermal, 490
decay heat of fragments, 513
delayed neutrons, 485
discovery of, 478
effects of nuclear deformation, 483
energy of fragments, 492
energy of neutrons, 492–493
energy release in, 479, 488, 492
four-factor formula, 503
mass distribution of fragments, 484–485, 494
multiplication time of neutrons, 505
neutron emission, 484, 486
neutron reproduction factor, 501–504
pairing effects on, 489
prompt neutrons, 485
radioactive fragments, 487, 512–516
resonance capture of neutrons, 503
resonances in, 497–500
secondary well, 495–496
shell effects on, 494
spontaneous, 175, 481
lifetimes for, 483
neutrons from, 446
Fission explosives, 520–524
^{235}U, 521
^{239}Pu, 521
effects, 522–524
fallout, 523
yield, 521
Fission isomers, 495
Fission reactors, boiling water, 509, 511
breeders, 507
control rods, 506
converters, 507
coolant, 509
deuterium, moderated, 510, 512
fast breeder, 511
fuel, 508
gas-cooled, 510, 512
moderator, 508
natural (Oklo), 516–520
poisoning, 515, 526
power, 506
pressurized water, 509, 511
F meson, 717, 737
Free particle, 15
Fusion, 66, 528–557
CNO cycle, 537
Coulomb barrier, 531
cross section, 531–532
deuterium–deuterium, 529
deuterium–tritium, 530
energy release, 530
proton–proton cycle, 535
reaction rate, 532
solar, 534
neutrino emission, 536
stellar, 769
reaction rate, 774
thermonuclear, 529
Fusion explosives, *see* Thermonuclear weapons
Fusion reactors, 538–553
bremsstrahlung losses, 539
energy release, 541
inertial confinement, 545, 550
laser-driven, 546
Lawson criterion, 542
magnetic confinement, 542, 547
magnetic mirror, 543–544
power plant design, 552
tokamak, 543–544

Gamma decay, 175, 327–373. *See also* Electromagnetic radiation
^{72}Ge, 348
^{72}Se, 348
^{108}Cd(from ^{108m}Ag), 351–355
^{108}Pd(from ^{108m}Ag), 351–355
^{177}Hf (from ^{177}Lu), 358–360
^{180m}Hf, 355–359
angular correlation, 338–340
angular distribution, 337
angular momentum selection rules, 333–334
coincidence spectroscopy, 354, 360
*E*1, systematics, 350
*E*2, systematics, 350
isospin selection rules, 391
*M*4, systematics, 350
multipole mixtures, 335, 340, 361
neutron capture state, 463
nuclear recoil, 328
oriented nuclei, 337
parity selection rules, 333–334
partial decay constant, 348–351
polarization of, 340–341
Gamma decay spectroscopy, 351–361
Gamma-ray camera, 803
Gamma rays:
medical imaging with, 800
radiotherapy with, 811
Gamma-ray scanner, 801
Gamow factor, 253, 773
Gaussian distribution, 219
Geiger counter, 206
quenching gas, 206
Geiger-Nuttall rule, 249
Gell-Mann–Nishijima formula, 717
g factor:
neutron, 73
orbital, 73, 607
proton, 73
spin, 73, 607
Gluons, 724
colored, 728
exchange of, 742
multiplicity, 726
observation in jets, 727
Grand Unified Theories, 746–752
proton decay, 750
Gray (unit), 186

Half-life, 161
partial, 176
Harmonic oscillator:
one-dimensional, 23
wave functions (table), 24
radial probability density (graphs), 32
three-dimensional, energy levels, 31–32
wave functions (table), 31
Heisenberg uncertainty relationship, 11
Helicity, 297
Helium, abundance in universe, 766
Hubble parameter, 756–757
Hubble relationship, 756
Hydrogenic atom, energy levels, 32, 34
radial wave functions, 33, 35
Hyperfine anomaly, 616
Hyperfine interaction:
electric quadrupole, 371–373
magnetic dipole, 370–371
Hyperfine structure, 610–619
muonic, 632
optical, 631, 635
Hypernuclei, 690–692
Hyperon, 688, 689

Impact parameter, 396
Intermediate vector bosons, *see* Weak bosons
Internal conversion, 175, 341–348
electron energy, 343
matrix element, 345
monopole transitions, 334, 346
partial decay constant, 349
X rays following, 342
Internal conversion coefficient, 343
determination from electron intensity, 353
estimate, 345
L subshells, 345, 361
Internal conversion spectrum, ^{203}Hg, 344
Intrinsic angular momentum (spin), 36
Invariant mass, 680
Ionization chamber, 204
avalanche, 205
speed of ions, 204
Ion source, 560
Isobar, 5
Isobaric analog state, 304, 321, 391
Isobaric spin, *see* Isospin
Isobar model, 679
Isomer, 175
Isomer shift, 369, 371
Isospin, 388–392
conservation in particle interactions, 684, 717
conservation in reactions, 391
nucleon, 389
nucleus, 389
in particle multiplets, 716
selection rule, beta decay, 391
gamma decay, 390
symmetry, 390
two-nucleon system, 389
Isotone, 5
Isotope, 5
Isotope separation, laser, 64
Isotope shift, 636
muonic, 52–54
optical, 51, 64
nuclear radius from, 53

Isotope shift (*Continued*)
X-ray, 51
nuclear radius from, 52
Isotopic spin, *see* Isospin

J resonance, *see* Psi resonance

Klein-Gordon equation, 654
Klein-Nishina formula, 200
K meson, 687, 688, 692–698
CP-violating decay, 696–698
decay lifetimes of neutral, 695
regeneration, 695

Landé *g* factor, 613
Larmor frequency, 642
Lepton number, conservation of, 716
Leptons, 653, 709
conservation of, 296, 300
symmetry with quarks, 747
Lifetime, mean, 161
Lifetime measurement:
from decay of activity, 230–231
from delayed time coincidence, 232–233
from Doppler shift, 234–235
Linear energy transfer, 811
Liquid-drop model, 68

Magnetic dipole hyperfine parameter, 613
Magnetic dipole moment, 72, 74, 329, 605–606
collective model, 147
deuteron, 84
measurement of, 625–627
electron, 619
many-particle shell model, 151
neutron, 624
measurement of, 623–624
proton, 623
measurement of, 620–623
in shell model, 125
systematics of 2^+ states, 138
Magneton, 73, 606
Bohr, 73, 606
nuclear, 73, 606
Mass defect, 65
Mass doublet method, 62
Mass number, 4
Mass spectrometry, accelerator-based, 794
Mass spectroscope, 60, 61
Matrix element, 41, 166, 277
Mean lifetime, 161
Mesons, 653
Metastable state, 175
Microwave background radiation, 759
Mirror nuclei, Coulomb energy difference, 55–56
Molecular beam magnetic resonance, 625
Moment of inertia, 144, 436–438
Monopole moment, 72
Mössbauer effect, 364–373
hyperfine splitting, 370–373
isomer shift, 369, 371
linewidth, 366
magnetic dipole hyperfine splitting, 645, 649–650
recoil-free fraction, 367
test of General Relativity, 367–369
Multichannel analyzer, 220
Multipole moment, 72
Multiwire proportional counter, 240, 242
Muonic atom, 52
Muonic X rays, 53–54
hyperfine splitting, 634
nuclear radius from, 55

Negatron decay, 174
Neutral current weak interaction, 707
Neutrino, 174
cosmological constraints on number of, 767
detection of, 297
helicity of, 297
mass limits, 274, 286–288
solar, 298, 536
Neutrino capture, 295
cross section, 296
Neutrino decoupling, 763
Neutrino physics, 295–298
Neutrinos, in early universe, 762–763
Neutron, 5
beta decay of, 274, 289
discovery, 444
electric dipole moment, 445
magnetic dipole moment, 444, 624
Neutron activation analysis, 465, 788
sensitivity, 789
Neutron capture, activity from, 465
Neutron capture cross section, shell structure, 120
Neutron-capture gamma rays, 463
Neutron–proton mass difference, 444
Neutron–proton ratio, early universe, 763, 766
Neutrons:
Bragg diffraction of, 455
Bragg reflection of, 471, 472
capture (radiative) of, 462
cross section, resonance, 457
total, 456, 460
velocity dependence of, 451–452, 459
crystal structure determinations using, 473–475
detection of, 451–452
diffraction of, 465–475
elastic scattering of, 448
gravitational effects on, 468
interferometer for, 467
moderation of, 448–451

monochromator for, 473
proton recoil detectors of, 455
radiotherapy with, 811
resonance scattering, 427
spin precession in magnetic field, 468
thermalization of, 450
time-of-flight method, 453–454
velocity selection, 453
Neutron sources, 445–447
Normal distribution, *see* Gaussian distribution
Normalization, 12
Nuclear deformation, 142
effect on shell structure, 151
electric quadrupole moment and, 143
Nuclear magnetic resonance, 629, 639
imaging by, 807, 808
Nuclear magneton, 73, 606
Nuclear medicine, 800–812
Nuclear molecule, 433
Nuclear orientation, 637
Nucleon, 5
internal structure, 721, 727
Nucleon emission, 176
Nucleon–nucleon interaction:
central force, 100
charge independence, 102
charge symmetry, 102
diagrams for, 704
exchange forces, 108
potentials, 107
properties, 80, 100
repulsive core, 103–104
spin dependence, 92, 100
spin-orbit term, 104
square-well potential, 82
tensor force, 101
Nucleon–nucleon scattering, *see* Scattering, nucleon–nucleon
Nucleosynthesis:
$^{235}U/^{239}U$ chronometer, 783–784
duration of, 781–782
primordial, 764–768
Re-Os chronometer, 783
stellar, charged-particle processes, 769–776
neutron capture processes, 776
Nuclide, 5

Oklo reactor, *see* Fission reactors, natural
Omega meson, 682, 683, 684
Optical model, 413–416, 461
Oriented nuclei:
alpha decay, 260
beta decay, 312
gamma decay, 337
Oxygen effect, 810
Oxygen enhancement ratio, 811

Pairing, breakdown at high angular momentum, 438
Pairing force, 68, 74
effect on fission, 489
Pair production, 201, 221
Parity, 37, 714
nonconservation of, 309–315
in alpha decay, 315
in nuclear states, 313, 315
nuclear, 71
Parity violation, 38
Partial wave expansion, 409
Particle current density, 14
Particle decays:
angular momentum conservation, 714
energy of products, 711
parity conservation, 715
Particle identifier, 239–241
Particle reactions:
angular momentum conservation, 714
energy of products, 713
threshold energy, 594, 714
Particle-induced X-ray emission, 791
cross sections, 792–793
Paschen-Back effect, 618–619
Pauli exclusion principle, 40
Peak fitting, 225
PET scan, 806, 807
Phase shift, 88, 89, 411, 425
Phase stability, 574, 590
Photoelectric absorption, 221
Photoelectric cross section, 199
Photoelectric effect, 198
Photomultiplier tube, 208, 212, 213
Photopeak, 222
Pi-mesic X rays, 656
Pi meson, 111
decay, 658, 665, 667
electron *vs.* muon modes, 668
discovery, 655
exchange of, 111
exchange potential, 112
isospin, 656
lifetime, 665–666
mass, 656–661
parity, 663
production reactions, 669–671
reactions with nucleons, 671–679
resonances with nucleons, 675–679
spin, 661, 663
strong coupling constant, 112
Pi mesons, radiotherapy with, 811
Pion, *see* Pi meson
Poisson distribution, 219
Polarimeters, 241–243
Polarization, linear, of gamma rays, 341
Polarized beams, 104
Positron decay, 174

Positron emission tomography (PET), 806
Potential, central, 27
Potential barrier, *see* Barrier potential
Potential step, *see* Step potential
Potential well:
 one-dimensional:
 finite, 22
 infinite, 20
 three-dimensional Cartesian, infinite, 25
 three-dimensional spherical, infinite, 27
Preamplifier, 220
Probability density, 12
 radial, 29
Proportional counter, 205
 avalanche, 206
 drift time, 206
 electric field, 205
 Geiger-Müller region, 206
 multiwire, 240, 242
Proton, 4
 decay of, 750
 magnetic dipole moment, 623
Proton emission, 255, 256, 257
Psi resonance, 733–736
 excited states, 740, 744–745
 Zweig-suppressed decays, 735–736

Quadrupole lens, 561, 562
Quadrupole moment, *see* Electric quadrupole moment
Quality factor, 186
Quark:
 bottom, 739–740
 charm, 733, 735–737
 top, 740, 742
Quark model, 718–721
 asymptotic freedom, 742
 charm included, 733
 colorless, 722
 decay analysis using, 729–732
 disconnected diagrams in, 729
 evidence for color, 724
 flavor-changing weak decays, 727, 732
 gluon exchange, 724
 infrared slavery, 742
 quantum chromodynamics, 742
 reaction analysis using, 727
Quarks:
 color field, 743
 colors of, 722
 existence of free, 746
 existence within nucleon, 721
 flavors of, 720
 fractional charges, 720
 experimental indication, 740
 free, in early universe, 762
 experimental searches, 746
 magentic dipole moments, 745–746
 masses, 744–746
 Pauli principle, 721
 symmetry with leptons, 747
Q value, reaction, 380
 mass determined from, 62, 384

Radial equation, 27
Radiation:
 effects on living tissue, 809
 units for measuring, 184, 187
Radiation damage, 328
Radiation standards, 187
Radioactive dating, 181
Radioactive decay:
 chain of, 170
 exponential law, 161
 growth of daughter, 171
 statistical theory, 161
Radioactivity:
 artificial, 160
 induced, 160, 169
 natural, 178
Radiocarbon dating, 184
 accelerator use in, 795
Radium-beryllium neutron source, 445
Radius, nuclear, 44, 48
 from alpha decay, 57, 254
 charge *vs.* matter, 58
 from Coulomb energy difference, 56
 from electron scattering, 50
 from muonic isotope shifts, 55
 from neutron cross sections, 462
 from optical isotope shifts, 53
 from pi-mesic X rays, 57
 from Rutherford scattering, 57, 402
 shell structure, 120
 from X-ray isotope shifts, 52
Rad (unit), 186
Range:
 alpha particle, 193, 195, 203
 deuteron, 195
 different particles in same material, 196
 electron, 198, 203
 energy dependence, 194
 extrapolated, 203
 mean, 193, 203
 photon, 203
 proton, 195
Range-energy relationship:
 electrons, 198
 heavy particles, 195
Reaction:
 $^{3}H(d,n)^{4}He$, 447
 $^{3}H(p,n)^{3}He$, 382
 $^{3}He(n,p)^{3}H$, 384
 $^{9}Be(\alpha,n)^{12}C$, 445

$^{12}C(^{12}C, ^{12}C)^{12}C$, 432
$^{14}C(p,n)^{14}N$, 383
$^{14}N(d,n)^{15}O$, 454
$^{14}N(n,p)^{14}C$, 384
$^{16}O(^{16}O, ^{20}Ne)^{12}C$, 439
$^{16}O(^{2}H, ^{4}He)^{14}N$, 391
$^{23}Na(p,\gamma)^{24}Mg$, 430
$^{25}Mg(p,p)^{25}Mg$, 418
$^{26}Mg(^{7}Li, ^{8}B)^{25}Ne$, 387
$^{27}Al(p,p)^{27}Al$, 429
$^{58}Ni(^{4}He,p)^{61}Cu$, 385
$^{59}Cu(n,\gamma)^{60}Cu$, 427, 464
$^{59}Cu(n,n)^{59}Cu$, 427
$^{90}Zr(d,p)^{91}Zr$, 421–422
$^{162}Dy(\alpha,8n)^{159}Er$, 437
$^{176}Yb(\alpha,6n)^{174}Hf$, 437
$^{208}Pb(n,n)^{208}Pb$, 406
$^{208}Pb(p,p)^{208}Pb$, 406

Reactions:
- angular distribution of products, 382
- channels, 410
- compound nucleus model, 416–419
 - angular dependence, 418
 - experimental verification, 417
- conservation laws, 380
- Coulomb elastic scattering, *see* Rutherford scattering
- Coulomb inelastic scattering, *see* Coulomb excitation
- cross section, 392–394, 408–413
 - differential, 393
 - elastic scattering, 411
 - partial wave analysis, 411
 - total, 412
- direct, 419–424
 - angular dependence, 421
 - angular momentum transfer, 421
 - spectroscopic factor, 424
- energy of products, 382
- evaporation, 419
- experimental techniques, 395–396
- heavy-ion, 431–440
- inelastic, 408
- interference between resonance and potential scattering, 428
- isospin conservation, 391
- observables, 379
- optical model analysis, 413–416
- phase shifts, 411
- pickup, 420
- *Q* value, 381
 - excited states, 387
 - mass determination from, 62, 384
- resonance, 414–431
 - Breit-Wigner formula, 428
 - cross section, 426
 - energy width, 425–426
 - phase shift, 425
 - scattering (nuclear), 405–408
 - stripping, 420
 - threshold energy, 382
 - transfer, 420
 - types, 379

Relative biological effectiveness (RBE), 186
Rem (unit), 187
Resolution, *see* Energy resolution; Time resolution
Resonance fluorescence, nuclear, 361
Resonances:
- meson, 679–686
- nucleon, 671, 678

Resonant photon absorption:
- cross section, 361–362
- Doppler broadening, 363–365
- recoil correction, 362, 364–365
- width, 362

Rho meson, 680, 681, 684
Roentgen (unit), 185
Rotational band, 144
Rotational model, 142
- deviation at large angular momentum, 436

r process nucleosynthesis, 776
Rubidium-strontium dating method, 183
Rutherford backscattering, 797, 798, 799
Rutherford scattering, 396–405
- closest approach of projectile, 397
- differential cross section, 399
- electron-quark, 723
- experimental verification, 400–401
- nuclear radius determination, 57, 402
- quantum effects, 404–405
- scattered fraction, 397

Scattering:
- electron, 45
 - by ^{12}C and ^{16}O, 46
 - by ^{208}Pb, 47
 - charge distribution from, 49
 - nuclear radius from, 50
- neutron, from molecular H_2, 93
- neutron–neutron, 96, 99
 - effective range, 99
 - scattering length, 99
- neutron–proton, differential cross section, 109
 - effective range, 95
 - scattering length, 95
 - singlet *vs.* triplet, 92
 - total cross section, 92
- nucleon–nucleon, 86
 - charge symmetry, 102
 - differential cross section, 90
 - phase shift, 88
 - phase shifts (intermediate energy), 103
 - polarized, 104

Scattering (*Continued*)
square-well wave functions, 88
s-wave phase shift, 88
total cross section, 90–91
proton–proton, 96
differential cross section, 97
effective range, 99, 102
phase shifts (low energy), 99
scattering length, 99, 102
Scattering length, 93
neutron–proton scattering, 95
singlet and triplet, 94–95
Schmidt lines, 126
Schrödinger equation, 12
one-dimensional, time independent, 12
radial, 27
spherical coordinates, 14
three-dimensional, time independent, 14
Scintillation detectors, 207, 211
activated, 211
energy resolution, 224
inorganic, 209
organic, 209
time resolution, 230
Secular equilibrium, 170, 171, 172
Semiconductor detectors, 213
band structure, 214–215
depletion region, 216
Ge, 217
energy resolution, 225
time resolution, 230
Si, 217
surface barrier, 217
timing, 217
Semiempirical mass formula, 68, 250
Separation energy:
neutron, 65
proton, 65
two-nucleon, systematics and shell structure, 119
Shell model, 68, 117–134
deformed nuclei, 151
effect on alpha decay, 250
effect on beta decay, 322
effect on fission, 494
effect on nucleosynthesis, 780
electric quadrupole moments, 127, 129, 130
energy levels, 123
evidence for, 117, 119, 120
excited states, 131
independent particle assumption, 131
magnetic dipole moments, 125, 127, 128
many-particle, 149
potential, 122
spin-orbit interaction, 124
Sievert (unit), 187
Silicon burning, stellar, 771
Single-escape peak, 222
Skin thickness, 48
Specific activity, 184, 230
Specific γ-ray constant, 185, 186
Spectrometer, magnetic, 236
Spectroscopic notation, 35, 37, 610
Spectrum, γ-ray, comparison of Ge and NaI, 223
pulse-height, 220
Spherical Bessel functions (table), 28
Spherical harmonics (graphs), 30
Spherical harmonics, parity, 38
Spherical harmonics (table), 27
Spin, 36
nuclear, 70
quantum number, 603
odd–odd nuclei, 604
Spin-lattice relaxation, 630
Spin-orbit coupling, atomic, 611
Spin-orbit interaction:
in nucleon–nucleon scattering, 104
in shell model, 124
s process abundances, 778, 780
s process nucleosynthesis, 776
Standard deviation, 218
of repeated measurement, 219
Stationary state, 13, 40, 165
Statistics, counting, 217
Step potential, 16, 17
Stopping power, 194
Strangeness, 686, 717
conservation of, 687
Superheavy elements, 433
production in r process, 779
Symmetry:
exchange, 39
reflection (parity), 37

Tau lepton, 709
Telescope, counter, 238
Thermonuclear weapons, 553–557
design, 554
effects, 556
strategic arsenals, 556
Theta-tau puzzle, 312
Threshold energy, 382, 594, 714
Time-of-flight method, 239–240
Time resolution, 229
Ge, 230
scintillators, 230
Time reversal, 309
Time-to-amplitude converter (TAC), 228
Tomography, 803
Transient equilibrium, 173
Transition probability, 40
Transuranic elements, 478
Tunneling, 19

Upsilon resonance, 738–740, 744–745

Variance, 218
Vibrational model, 139

Wave function, 12
 free particle, 15
Weak bosons, 286, 703
 decay of, 707
 discovery of, 706–707
 exchange of, 747
 mass, 705
Weak interaction, 285
 diagrams for, 704
 neutral current, 707
Weak interaction coupling constant, 705
Weinberg angle, 705
 in GUTs, 750
Weinberg-Salam theory, 704–705, 707. *See also* Electroweak theory
Width of decaying state, 40, 167

X particle, 762
 exchange in GUTs, 749
X ray, K, 51
X rays, medical imaging with, 803–806

Zeeman effect, 616–617
 nuclear, 336, 370–371. *See also* Hyperfine interaction
Zweig's rule, 729, 735, 739

PERIODIC TABLE OF THE ELEMENTS

1 H 1.0079																	2 He 4.0026
3 Li 6.941	4 Be 9.012											5 B 10.81	6 C 12.011	7 N 14.007	8 O 15.999	9 F 18.998	10 Ne 20.179
11 Na 22.990	12 Mg 24.305											13 Al 26.982	14 Si 28.086	15 P 30.974	16 S 32.06	17 Cl 35.453	18 Ar 39.948
19 K 39.098	20 Ca 40.08	21 Sc 44.956	22 Ti 47.90	23 V 50.942	24 Cr 51.996	25 Mn 54.938	26 Fe 55.847	27 Co 58.933	28 Ni 58.70	29 Cu 63.546	30 Zn 65.38	31 Ga 69.72	32 Ge 72.59	33 As 74.922	34 Se 78.96	35 Br 79.904	36 Kr 83.80
37 Rb 85.468	38 Sr 87.62	39 Y 88.906	40 Zr 91.22	41 Nb 92.906	42 Mo 95.94	43 Tc (97)	44 Ru 101.07	45 Rh 102.91	46 Pd 106.4	47 Ag 107.87	48 Cd 112.41	49 In 114.82	50 Sn 118.69	51 Sb 121.75	52 Te 127.60	53 I 126.90	54 Xe 131.30
55 Cs 132.91	56 Ba 137.33	57–71 Rare Earths	72 Hf 178.49	73 Ta 180.95	74 W 183.85	75 Re 186.21	76 Os 190.2	77 Ir 192.22	78 Pt 195.09	79 Au 196.97	80 Hg 200.59	81 Tl 204.37	82 Pb 207.2	83 Bi 208.98	84 Po (209)	85 At (210)	86 Rn (222)
87 Fr (223)	88 Ra (226)	89–103 Acti-nides	104 Rf (257)	105 Ha	106 (263)	107	108	109									

Rare Earths (Lanthanides)	57 La 138.91	58 Ce 140.12	59 Pr 140.91	60 Nd 144.24	61 Pm (145)	62 Sm 150.4	63 Eu 151.96	64 Gd 157.25	65 Tb 158.93	66 Dy 162.50	67 Ho 164.93	68 Er 167.26	69 Tm 168.93	70 Yb 173.04	71 Lu 174.97
Actinides	89 Ac (227)	90 Th 232.04	91 Pa (231)	92 U 238.03	93 Np (237)	94 Pu (244)	95 Am (243)	96 Cm (247)	97 Bk (247)	98 Cf (251)	99 Es (254)	100 Fm (257)	101 Md (258)	102 No (259)	103 Lr (260)

For each element, the bottom line gives either the atomic mass or (in parentheses, for radioactive elements) the mass number of the most stable isotope.